Issue 53

International Journal of Energy and Environmental Engineering

International Journal of Energy and Environmental Engineering (2023) 14:973–989
https://doi.org/10.1007/s40095-023-00560-6

ORIGINAL RESEARCH

Development of a day-ahead solar power forecasting model chain for a 250 MW PV park in India

Arindam Roy[1] · Aravindakshan Ramanan[2] · Barun Kumar[3] · Chris Alice Abraham[3] · Annette Hammer[1] · Elena Barykina[4] · Detlev Heinemann[5] · Naveen Kumar[3] · Hans-Peter Waldl[4] · Indradip Mitra[2] · Prasun Kumar Das[3] · R. Karthik[3] · K. Boopathi[3] · K. Balaraman[3]

Received: 13 May 2022 / Accepted: 10 March 2023 / Published online: 1 April 2023

Abstract

Due to the steep rise in grid-connected solar Photovoltaic (PV) capacity and the intermittent nature of solar generation, accurate forecasts are becoming ever more essential for the secure and economic day-ahead scheduling of PV systems. The inherent uncertainty in Numerical Weather Prediction (NWP) forecasts and the limited availability of measured datasets for PV system modeling impacts the achievable day-ahead solar PV power forecast accuracy in regions like India. In this study, an operational day-ahead PV power forecast model chain is developed for a 250 MWp solar PV park located in Southern India using NWP-predicted Global Horizontal Irradiance (GHI) from the European Centre of Medium Range Weather Forecasts (ECMWF) and National Centre for Medium Range Weather Forecasting (NCMRWF) models. The performance of the Lorenz polynomial and a Neural Network (NN)-based bias correction method are benchmarked on a sliding window basis against ground-measured GHI for ten months. The usefulness of GHI transposition, even with uncertain monthly tilt values, is analyzed by comparing the Global Tilted Irradiance (GTI) and GHI forecasts with measured GTI for four months. A simple technique for back-calculating the virtual DC power is developed using the available aggregated AC power measurements and the inverter efficiency curve from a nearby plant with a similar rated inverter capacity. The AC power forecasts are validated against aggregated AC power measurements for six months. The ECMWF derived forecast outperforms the reference convex combination of climatology and persistence. The linear combination of ECMWF and NCMRWF derived AC forecasts showed the best result.

Keywords Numerical Weather Prediction · PV power forecast · Model chain · Combination of AC power forecasts · Availability of limited design parameters · Indian meteorological conditions

Introduction

The intermittent nature of solar resource poses a challenge in producing reliable generation forecasts for grid-connected solar Photovoltaic (PV) systems. As the initial bid or generation schedule needs to be provided on a day-ahead basis, accurate day-ahead predictions are essential for the financial security of PV plant owners. Grid operators of power systems with a high penetration of solar PV require these forecasts to ensure the maintenance of load-generation balance. Due to the ever-increasing emphasis on climate targets, as seen recently at the COP26, renewable electricity capacity is expected to surpass 4800 GW by 2026 [1]. According to the International Energy Agency (IEA), Solar PV is alone expected to account for half of all renewable power expansion worldwide from 2021 to 2026. India has the highest

✉ Arindam Roy
arindam.roy@uni-oldenburg.de

1 German Aerospace Center (DLR) Institute of Networked Energy Systems, Carl-Von-Ossietzky-Straße 15, 26129 Oldenburg, Germany

2 Deutsche Gesellschaft Für Internationale Zusammenarbeit (GIZ) GmbH, B-5/2, Safdarjung Enclave, New Delhi 110029, India

3 Solar Radiation Resource Assessment, National Institute of Wind Energy, Velachery-Tambaram Main Road, Pallikaranai, Chennai 600100, India

4 Overspeed GmbH & Co. KG, Technologiepark 4, 26129 Oldenburg, Germany

5 Institute of Physics, Carl von Ossietzky University of Oldenburg, 26111 Oldenburg, Germany

growth rate in renewable power capacity relative to the existing capacity [1]. As of August 2022, the nationwide installed capacity of grid-connected solar PV is 63 GW [2]. In a recent update to its Nationally Determined Contribution (NDC), the Indian Government has decided to reduce the emissions intensity of its GDP by 45% till 2030 [3]. Solar PV is expected to play a leading role in achieving its ambitious target. However, the data availability from these PV systems is often restricted to measurements of irradiance, module temperature, and inverter AC power output. To cope with the increasing demand for accurate solar PV forecasts, our forecast model chain is developed and benchmarked for Indian meteorological conditions with a limited availability of measured datasets from the site.

Solar irradiance forecasts from Numerical Weather Prediction (NWP) model produce accurate and reliable results for day-ahead and multiday-ahead forecast horizons [4–6]. In the subsequent steps, forecasted irradiance is converted into the PV power output using statistical, physical, or a combination of both models. Statistical and machine learning models are trained with past irradiance measurements, module and meteorological parameters, and the final PV power output to derive a direct relationship between them. The accuracy of such models depends on the available length of historical training data [7–10]. Alternatively, physical models are used for the transposition of Global Horizontal Irradiance (GHI) to Global Tilted Irradiance (GTI), modeling the DC power output as a function of GTI and PV module temperature, or modeling the inverter DC to AC power conversion efficiency in a stepwise manner [11, 12], as shown in Fig. 1. A hybrid combination of the physical and machine learning-based methods can also serve specific purposes, such as the removal of data points with curtailment before model training [13].

The NWP model output GHI needs to be temporally interpolated to match the time resolution of the generation

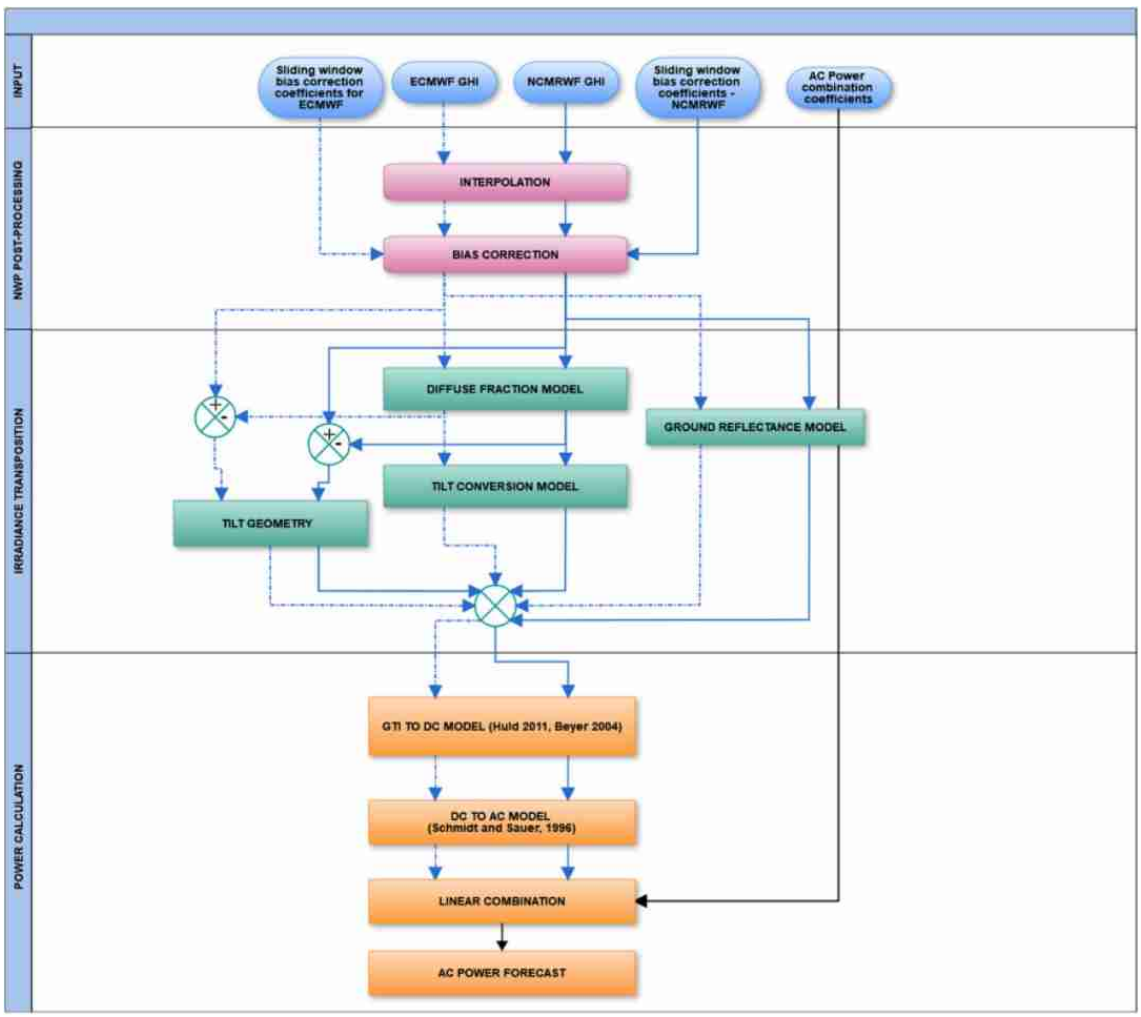

Fig. 1 Schematic of the forecasting model chain from NWP input (top) to final combined power forecast (bottom)

schedule mandated by regulations [14, 15]. An initial bias correction of the NWP modeled GHI is useful for the removal of systematic deviations and improves the accuracy of the predicted GHI. Various bias correction techniques using ground measurements are found in the literature, including polynomial functions [14, 16, 17], Kalman Filtering [18, 19], and Neural Networks (NN) [20–22]. Methods for bias correction of NWP solar irradiance output using geostationary satellite data images are also reported [23]. Diffuse fraction and diffuse sky models transform forecasted GHI into GTI [24]. The diffuse fraction model splits the GHI into its beam and diffuse components [25–27]. This is usually achieved in the simplest case by modeling the diffuse fraction (ratio of the diffused irradiance to the global irradiance) as a function of the clearness index (ratio of the global irradiance to the top of the atmosphere irradiance). Advanced methods can use multiple astronomical and meteorological parameters as predictors [29–31]. GTI incident on the module and the cell temperature influence efficiency and, consequently, the DC power output. PV module efficiency can be modeled using detailed diode equivalent circuits [32, 33] or as empirical functions of incident irradiance and cell temperature [12, 34–37]. An increase in operating cell temperature beyond 25 °C has a negative impact on the electrical efficiency of PV modules, and the losses can be significant for regions like India [38–40]. Detailed inverter efficiency curves at different voltage levels can be obtained from the manufacturer's data sheet [41]. The conversion efficiency of the module DC power output into AC power by the inverter can also be modeled in multiple ways: constant efficiency, polynomial efficiency curve, and voltage-dependent polynomial efficiency curves [42–46].

In this study, an operational day-ahead PV power forecast model is developed using a combination of the NWP datasets from the European Centre of Medium Range Weather Forecasts (ECMWF) and the National Centre for Medium Range Weather Forecasting (NCMRWF) models. Its components are benchmarked for a 250 MWp solar PV plant located in Southern India. In [47], the authors proposed using the Lorenz polynomial bias correction function as a reference for benchmarking newer methods. In [48], the authors validated the improvement in accuracy due to NN-based bias correction against ground-measured data from four stations located on the La Réunion Island. In [22], the authors developed an optimally configured NN-based corrective algorithm for NWP output GHI and validated it against ground measurements from two sites in southern Portugal. However, a benchmark of the NN-based technique against the Lorenz polynomial method is not shown. In this work, the accuracy of the two bias correction techniques is intercompared for ten months. [7] suggested that assuming a tilt value could be better than using the GHI directly in the case of irradiance transposition with an unknown module tilt. However, the validation of forecasted GTI obtained from an assumed tilt against ground measurements is lacking. Especially for situations where the module tilt is changed manually on a seasonal basis, with every readjustment cycle lasting multiple days, as in the case of the PV plant analyzed in this work. The utility of using even approximate module tilt values for irradiance transposition is shown in this study. In [7], the author studied the power output simulation of 16 PV plants for five data availability scenarios but did not consider the case in which the AC power output dataset is available while DC power is not. In the current analysis, DC power is back-calculated from the AC power due to the lack of the inverter DC side measurements. However, this situation is encountered quite frequently in India; therefore, the current work provides a practical solution for such cases. In [48], the authors implemented and tested a site-specific bias correction technique for NWP-based AC power forecasts across 23 PV sites in Finland. However, the method uses NWP forecast data from a single model and does not combine multiple NWP model outputs. In [49], the authors generated solar power forecasts from two different parameterizations of the same Weather Research and Forecasting (WRF) model and subsequently performed a linear combination of the two power forecasts. However, they did not use a reliable standard of reference, such as, the convex combination of persistence and climatology [50, 51], for analyzing the utility of the forecasts.

This study has the following specific objectives: -

- Benchmarking the performances of the Lorenz polynomial and Neural Network (NN)-based bias correction methods on a sliding window basis.
- Validation of the benefit of using a GHI transposition model even with uncertain or approximate PV module tilt information.
- Estimating DC power from aggregated AC power meter readings.
- Development of an operational physical model chain for solar PV power forecast.
- Analyzing the utility of AC power forecasts derived from ECMWF and NCMRWF against the reference convex combination of persistence and climatology.
- Linear combination of the two AC power forecasts and validation of the improvement against the convex combination of persistence and climatology.

Data and methods

The forecast model chain is a collection of individual models that convert the GHI output from the NWP dataset into GTI at the PV module tilt and then finally into the plant AC power output by modeling each stage of energy conversion

in the PV plant. A conceptual schematic of the model chain is shown in Fig. 1.

Numerical weather prediction data

NWP datasets from ECMWF and the NCMRWF are used in this work. The ECMWF High Resolution Forecast (HRES) model runs twice daily at 00 and 12 UTC, and produces three hourly predictions up to three days ahead at a spatial resolution of $0.25^{\circ} \times 0.25^{\circ}$. NCMRWF provides global, regional, deterministic and ensemble predictions. The deterministic global model is run twice daily at 00 and 12 UTC, and provides hourly forecast up to nine days ahead with a spatial resolution of $0.25° \times 0.25°$. Each global model's 00 UTC run output is used for generating solar power forecasts in this analysis.

Solar radiation resource assessment network data

Quality controlled ground-measured irradiance data from the nearest Solar Radiation Resource Assessment (SRRA) station at Kadiri is also used in training the bias correction model. SRRA is a network of long-term solar radiation monitoring stations spread across 115 locations over India. These stations are equipped for sampling GHI, Diffuse Horizontal Irradiance (DHI), Direct Normal Irradiance (DNI), ambient temperature, humidity, wind speed, wind direction, rain accumulation and barometric pressure every

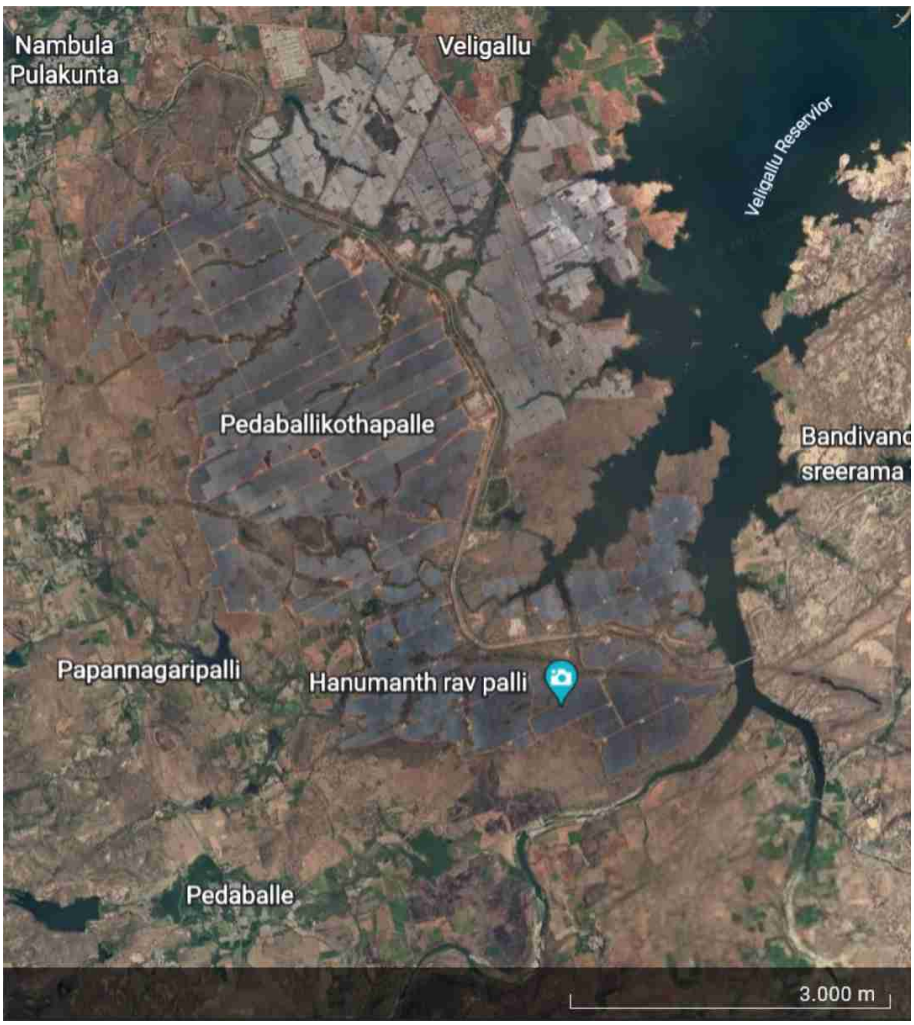

Fig. 2 Location of the power plant (Google earth image)

Table 1 Averaged tilt of the 5 individual blocks on a seasonal basis

Month Number	1	2	3	4	5	6	7	8	9	10	11	12
Module Tilt	27°	27°	9°	4°	4°	4°	4°	4°	6°	14°	23°	26°

second before averaging them over every one minute and recording them [52].

Power plant data

The test site shown in Fig. 2 consists of five 50 MWp blocks of solar PV plants co-located within the same Solar Park, with each block having a different module type, size and manufacturer. The module tilt angle of each block varies independently on a seasonal basis. An average monthly module tilt schedule for all blocks combined has been prepared (see Table 1) from the approximate tilt change schedule obtained from site survey. Dynamic datasets from the power plant include time series measurements of GHI, GTI, PV module temperature and the aggregated AC power output of the park at an interval of 15 min. DC measurements from the inverter are not available. The irradiance measurements are quality controlled using the same checks as used for the SRRA stations [53]. These include the missing value test, tracking error test, minimum diffuse radiation test, coherence test, clear-sky test, maximum physical limit test and minimum physical limit test. The power measurements are quality-controlled using stuck value check, non-zero nighttime value check, maximum possible ramp check and physical limit check.

Interpolation of numerical weather prediction data

The raw GHI predictions from NWP data are available only for a pre-defined number of grid points. The average of the predicted GHI at the four grid points closest to the center coordinate of the plant is computed. The average GHI can be subsequently interpolated to 15 min from its original hourly or three hourly resolution by using the clear sky index interpolation method [14, 15]. Furthermore, in [54] it is shown that using a more intricate clear sky model does not necessarily imply better forecasts. The computationally simple model proposed in [55] is used in this analysis to compute clear sky indices $k_t^{\text{orig res}}$ from the NWP output GHI dataset at the original temporal resolution, as shown in Eq. 1. Clear sky indices $k_t^{15\text{ min}}$ in 15 min temporal resolution is derived by assuming that the original clear sky indices remain constant within each hourly or three hourly period depending on the actual time resolution of the NWP output. The 15-min resolution GHI dataset can be estimated, as shown in Eq. 2.

$$k_t^{\text{orig res}} = \frac{\text{GHI}_{\text{NWP}}^{\text{orig res}}}{\text{GHI}_{\text{clear sky}}^{\text{orig res}}} \tag{1}$$

$$\text{GHI}_{\text{NWP}}^{15\text{ min}} = k_t^{15\text{ min}} \cdot \text{GHI}_{\text{clear sky}}^{15\text{ min}} \tag{2}$$

Bias correction of irradiance data from numerical weather prediction model

NWP models have a coarse resolution spanning a large area (grid cell), and a systematic bias in the prediction may be observed when compared with site-specific ground measurements of GHI. The mathematical expression for bias is shown in Eq. 3. This is influenced by the local conditions at the site.

$$bias = \text{GHI}_{\text{NWP}} - \text{GHI}_{\text{meas}} \tag{3}$$

Lorenz polynomial method

In this method, the bias in NWP output GHI for a given location is modeled as a bi-variate fourth order polynomial function of the cosine of the solar zenith angle $cos(\theta_z)$ and the clear sky index k_t^*[15, 56], as shown in Eq. 4. k_t^* is defined as the ratio of the actual GHI to the GHI expected under clear sky conditions (Eq. 5).

$$\begin{aligned}\text{bias} =& a_0 \cdot (\cos\theta_z)^4 + a_1 \cdot k_t^{*4} + a_2 \cdot (\cos\theta_z)^3 + a_3 \cdot k_t^{*3} \\ &+ a_4 \cdot (\cos\theta_z)^2 + a_5 \cdot k_t^{*2} + a_6 \cdot (\cos\theta_z) + a_7 \cdot k_t^* + a_8\end{aligned} \tag{4}$$

$$k_t^* = \frac{\text{GHI}}{\text{GHI}_{\text{clear sky}}} \tag{5}$$

The coefficients a_1 to a_8 are obtained by curve fitting Eq. 4 with a historical dataset for which the bias in the NWP output GHI is already known. Equation 4 with known coefficients is then used for estimating and removing the bias from actual operational forecasts.

Feedforward neural network

Feedforward NNs are the simplest networks in which the information can move in only one direction-from the input layer to hidden layers and finally to the output layer. There is no loop or cycle transporting information in the backward direction. The NN architecture implemented in [20] is used here. It comprises of one input layer with two input nodes, one hidden layer with four hidden nodes and the final output layer with one node. A tangent hyperbolic activation function is used in the hidden nodes. The two inputs to the model are-(a) $\cos(\theta_z)$ and (b) k_t^*. The inputs are kept identical to that in the Lorenz polynomial method (Sect. 3.2.1.) to benchmark the methods based on equal information. The model's output is the bias in NWP output GHI, as shown in Eq. 1. The weights and offsets of the NN model are tuned by training on a historical dataset. In the final step, $\cos(\theta_z)$ and forecasted k_t^* are fed into the

model to estimate and remove the bias from the operational forecasts.

Irradiance transposition

Diffuse fraction model is used to split the GHI into its direct and diffuse irradiance components. The GHI and its two components are fed into a transposition model to produce the three components of irradiance on a tilted plane, namely, beam irradiance at tilt, diffused irradiance at tilt and ground reflected irradiance at tilt.

Diffuse fraction model

Betcke, 2018 validated seven diffuse fraction models with two years of GHI and DHI measurements from 33 SRRA stations across India. The result of this analysis is presented in Appendix A (Table 3). It can be seen that the model described in [25] estimates the diffused irradiance at the horizontal plane from GHI with the highest accuracy in terms of the normalized Root Mean Square Error (nRMSE). The nRMSE metric is used as the reference since the deviation of power production from forecast at each timestamp leads to additional costs or penalties in grid management. Therefore, the focus on average nRMSE rather than the average R^2 is more appropriate here, and the Chandrasekaran model is used in this analysis. For clearness index (k_t) less than 0.24, the diffuse fraction (k_d) decreases linearly with k_t (Eq. 6). In the k_t range of 0.24 to 0.8, k_d decreases as a fourth order polynomial function of k_t (Eq. 7). For k_t values beyond 0.8, k_d is assumed to be constant at 0.197 (Eq. 8). The coefficients of Eqs. 6, 7, and 8 are valid for all seasons.

$$k_{\mathrm{d}} = 1.0086 - 0.178k_{\mathrm{t}},\ \forall k_{\mathrm{t}} \le 0.24 \tag{6}$$

$$k_{\mathrm{d}} = 0.9686 + 0.1325k_{\mathrm{t}} + 1.4183k_{\mathrm{t}}^2 - 10.1860k_{\mathrm{t}}^3 + 8.3733k_t^4,\ \forall k_{\mathrm{t}} \in (0.24, 0.8] \tag{7}$$

$$k_{\mathrm{d}} = 0.197,\ \forall k_{\mathrm{t}} > 0.8 \tag{8}$$

Diffuse Sky model

Betcke, 2018 validated three commonly used diffuse sky models with two years ground-measured datasets of GHI and GTI from two AMS stations of the SRRA network (Table 4). The Klucher model outperformed the other models in terms of nRMSE. The first term of Eq. 9 $\frac{(I_{\mathrm{H}}-I_{\mathrm{D}})\cdot\cos\psi}{\sin\alpha}$ describes the transposition of the beam irradiance. The second term $I_{\mathrm{D}}\cdot\left(\frac{1+\cos\varepsilon}{2}\right)$ represents the transposition of diffused irradiance while considering horizon $\left(1+F\cdot\sin^3\frac{\varepsilon}{2}\right)$ and circumsolar $\left(1+F\cdot\cos^2\psi\sin^3(90-\alpha)\right)$ brightening. The third term models the ground-reflected irradiance on a tilted plane. Under overcast conditions, the adjustment factor F (Eq. 10) tends to 0, and the model reduces to the isotropic model proposed by [57]. Under a clear sky, the model reduces to the anisotropic model developed by [58].

$$I_{\mathrm{T}} = \frac{(I_{\mathrm{H}}-I_{\mathrm{D}}).\cos\psi}{\sin\alpha} + I_{\mathrm{D}}.\left(\frac{1+\cos\varepsilon}{2}\right).\left(1+F.\sin^3\frac{\varepsilon}{2}\right).\left(1+F.\cos^2\psi\sin^3(90-\alpha)\right) + I_{\mathrm{H}}.\rho.\left(\frac{1-\cos\varepsilon}{2}\right) \tag{9}$$

$$F = 1 - \left(I_{\mathrm{D}}/I_{\mathrm{H}}\right)^2 \tag{10}$$

where I_{T} total irradiance incident on a surface tilted toward the equator at an angle ε, I_{H} total irradiance received on a horizontal surface, I_{D} diffused irradiance received on a horizontal surface, α solar elevation angle, ψ angle between the sun direction and the normal direction of the tilted surface, ρ ground reflectance or albedo.

Photovoltaic module output model

In this analysis, the models proposed in [34, 36] are tested as they do not require module voltage and current measurements. In either case, the efficiency and the relative efficiency (Eq. 11) are modeled as functions of incident irradiance and module temperature.

$$\eta_{\mathrm{rel}} = \frac{\eta_{\mathrm{MPP}}}{\eta_{\mathrm{STC}}} = \frac{P_{\mathrm{MPP}}/G}{P_{\mathrm{STC}}/1000} \tag{11}$$

where η_{MPP} maximum power point efficiency of the PV module, η_{rel} relative efficiency of the PV module, η_{STC} efficiency of the PV module under standard test conditions (STC) of 1000 W/m^2 irradiance and 25 °C module temperature, P_{MPP} module power output at the MPP, P_{STC} module DC power output at STC, G irradiance incident on the module surface.

Existing methods for estimating PV module or cell temperature incorporate weather and PV system parameters into their models [39]. In [40], the authors used ambient temperature, incident irradiance, overall thermal loss coefficient of the module, transmittance of the module cover, absorptance of PV layer, nominal operating cell temperature (NOCT) and nominal terrestrial environment (NTE) condition parameters to estimate the operating cell temperature. [59] estimated the module temperature as a function of incident irradiance, ambient temperature and wind speed. [60] proposed a simple linear expression for estimating cell temperature as a function of the ambient temperature and the incident irradiance. The Ross model, described in Sect. "PV module temperature

model", is used for module temperature estimation as the input parameter requirement matches the data availability.

Huld model

The relative efficiency of the PV module is modeled as a second order polynomial function of the normalized module temperature T' and the natural logarithm of the normalized incident irradiance $\ln G'$, as shown in Eq. 12. By combining Eqs. 11 and 12, the DC power output at the MPP can be modeled directly as a function of T' and $\ln G'$ (Eq. 13).

$$\eta_{\mathrm{rel}}\left(G',T'\right) = 1 + k_1 \cdot \ln G' + k_2 \cdot \left[\ln G'\right]^2 + T' \cdot \left(k_3 + k_4 \cdot \left[\ln G'\right] + k_5 \cdot \left[\ln G'\right]^2\right) + k_6 \cdot T'^2 \tag{12}$$

$$P\left(G',T'\right) = G' \cdot P_{\mathrm{STC}}\left(1 + k_1 \cdot \ln G' + k_2 \cdot \left[\ln G'\right]^2 + T' \cdot \left(k_3 + k_4 \cdot \left[\ln G'\right] + k_5 \cdot \left[\ln G'\right]^2\right) + k_6 \cdot T'^2\right) \tag{13}$$

where G' incident irradiance normalized by 1000 W/m^2, T' normalized module temperature $\left(T_{\mathrm{mod}} - 25\ ^\circ\mathrm{C}\right)$, P DC power output at the MPP under actual operating conditions, k_1 to k_6 coefficients.

The coefficients k_1 to k_6 can be computed by curve fitting Eq. 13 with a historic dataset of DC power, incident irradiance (GTI) and module temperature measurements. Thereafter, Eq. 13 with known coefficient values can be used to estimate the module DC power output at any given value of irradiance G and module temperature T.

Beyer model

The MPP efficiency of a PV module with an operating temperature of 25 °C is represented as a function of incident irradiance G, as shown in Eq. 14 [34]. The MPP efficiency at any operating temperature T is estimated using Eq. 15. Based on Eqs. 11 and 15, the MPP DC power output can be expressed as shown in Eq. 16. Thus, the four coefficients of the model can be estimated by curve fitting Eq. 16 with historical measurements of DC power, incident irradiance (GTI) and module temperature measurements.

$$\eta_{\mathrm{MPP}}(G, 25\ ^\circ\mathrm{C}) = a_1 + a_2 \cdot G + a_3 \cdot \ln G \tag{14}$$

$$\eta_{\mathrm{MPP}}(G,T) = \eta_{\mathrm{MPP}}(G, 25\ ^\circ\mathrm{C}) \cdot \left[1 + \alpha(T - 25\ ^\circ\mathrm{C})\right] \tag{15}$$

$$\Rightarrow \eta_{\mathrm{MPP}}(G,T) = \left(a_1 + a_2 \cdot G + a_3 \cdot \ln G\right) \cdot \left[1 + \alpha(T - 25\ ^\circ\mathrm{C})\right]$$

$$P(G,T) = \frac{G' \cdot P_{\mathrm{STC}}}{\eta_{\mathrm{STC}}} \cdot \left(a_1 + a_2 \cdot G + a_3 \cdot \ln G\right) \cdot \left[1 + \alpha(T - 25\ ^\circ\mathrm{C})\right] \tag{16}$$

where $\eta_{\mathrm{MPP}}(G,T)$ MPP efficiency at irradiance G and module temperature T, a_1, a_2, a_3 = Irradiance coefficients, a = Temperature Coefficient.

PV module temperature model

The Ross model expresses the operating cell temperature T_{c} as the sum of the ambient temperature T_{a} and the product of the incident irradiance G with the proportionality factor k (Eq. 17). The proportionality factor k is known as the Ross parameter, and its values found in the literature lie in the range of 0.02–0.06 °C m^2 W^{-1} [39]. The k value of a PV plant depends on the module and installation type. The lowest values correspond to cases where the modules are well-ventilated, while the highest values correspond to situations with limited ventilation possibilities. The cooling effect of wind is not considered here.

$$T_{\mathrm{c}} = T_{\mathrm{a}} + k \cdot G \tag{17}$$

where T_{c} Operating cell temperature of the module, T_{a} Ambient temperature, k Ross parameters.

Module temperature forecasts T_c are obtained by inserting the ambient temperature and GTI predictions based on NWP forecasts into Eq. 17.

DC power to AC power conversion

During the conversion of DC power to AC power at the inverter, a portion of the power is lost. The inverter efficiency (or loss) can vary as a function of the inverter output AC power, DC side voltage and the output power factor, if applicable [45]. The models presented in [42] and [44] express the inverter efficiency as a function of the inverter 's AC power output and the DC side voltage. [46] expresses the inverter efficiency as a function of the input DC power. As the model does not require DC voltage measurements, it is selected in this study.

Schmidt and Sauer model

In [46], the authors modeled the inverter loss as a quadratic polynomial function of the inverter AC power output, as shown in Eq. 19. The inverter loss p_{loss} is defined as the difference between DC power and AC power measurements (Eq. 18). The three coefficients p_{self}, v_{loss} and r_{loss} represent distinct physical losses in the inverter and can be computed by curve fitting Eq. 19 with measured datasets of DC

power p_{in} and AC power p_{out}. The inverter's efficiency at a given DC power input p_{in} can then be estimated, as shown in Eq. 20. The final AC power output p_{out} is derived from Eq. 21.

$$p_{\text{loss}} = p_{\text{in}} - p_{\text{out}} \tag{18}$$

$$p_{\text{loss}} = p_{\text{self}} + v_{\text{loss}} \cdot p_{\text{out}} + r_{\text{loss}} \cdot \left(p_{\text{out}}\right)^2 \tag{19}$$

$$\eta = -\frac{1 + v_{\text{loss}}}{2 \cdot r_{\text{loss}} \cdot p_{\text{in}}} + \sqrt{\left(\frac{1 + v_{\text{loss}}}{2 \cdot r_{\text{loss}} \cdot p_{\text{in}}}\right)^2 + \frac{p_{\text{in}} - p_{\text{self}}}{r_{\text{loss}} \cdot \left(p_{\text{in}}\right)^2}} \tag{20}$$

$$\eta = \frac{p_{\text{out}}}{p_{\text{in}}} \tag{21}$$

where p_{loss} DC to AC power conversion loss in inverter per unit rated capacity, p_{in} DC power input to the inverter per unit rated capacity, p_{out} AC power output from the inverter per unit rated capacity, p_{self} self-consumption of the inverter per unit rated capacity, v_{loss} Loss due to voltage drop across the semi-conductor per unit rated capacity, r_{loss} Ohmic loss per unit rated capacity, η Inverter efficiency.

Combination of AC power forecasts

The two different AC power forecasts obtained using the ECMWF and NCMRWF output GHI are further combined in this study to improve the accuracy of the final forecast. The combined AC power forecast $P_{\text{AC}}^{\text{comb}}$ is modeled as a linear function of the NCMRWF-based AC power forecast and ECMWF-based AC power forecast, as shown in Eq. 22. The coefficients a_1 and a_2 are computed by curve fitting Eq. 22 with datasets of $P_{\text{AC}}^{\text{NCMRWF}}$, $P_{\text{AC}}^{\text{ECMWF}}$ and measured AC power in place of $P_{\text{AC}}^{\text{comb}}$.

$$P_{\text{AC}}^{\text{comb}} = a_1 \cdot P_{\text{AC}}^{\text{NCMRWF}} + a_2 \cdot P_{\text{AC}}^{\text{ECMWF}} \tag{22}$$

Evaluation of forecast accuracy

System deviation or bias in irradiance forecast is represented in Eq. 23 with the normalized mean bias error (nMBE). The power forecasts are validated using the normalized root mean square error (nRMSE) metric shown in Eq. 24.

$$n\text{MBE} = \frac{\frac{1}{N}\sum_{n=1}^{N}\left(\text{GHI}_{\text{pred}} - \text{GHI}_{\text{meas}}\right)}{\left(\frac{\sum_{n=1}^{N}\text{GHI}_{\text{meas}}}{N}\right)} \times 100 \tag{23}$$

$$n\text{RMSE} = \frac{\sqrt{\frac{1}{N}\sum_{n=1}^{N}\left(\text{GHI}_{\text{pred}} - \text{GHI}_{\text{meas}}\right)^2}}{\left(\frac{\sum_{n=1}^{N}\text{GHI}_{\text{meas}}}{N}\right)} \times 100 \tag{24}$$

Results and discussions

Interpolation

The two GHI forecasts for the plant are obtained by pre-processing the two NWP outputs to site-level spatial resolution and 15 min temporal resolution, as described in Sect. "Interpolation of numerical weather prediction data". Figure 3 shows the ECMWF forecast in its original three hourly resolution and after it is interpolated to the 15 min resolution. Similarly, the NWP output GHI from NCMRWF is also interpolated to 15 min from its original hourly resolution. The interpolated ECMWF-based GHI prediction exhibits an average bias of + 0.46% (over-estimation) against GHI measured at the PV plant over the validation period from 17.12.2018 to 23.10.2019. The interpolated GHI from NCMRWF shows a bias of + 1.71% (over-estimation). In [4], the nMBE in the forecast for single sites across North America and Europe over individual days ranged from − 1% to + 10%. In [61], the authors validated the GHI forecasts from multiple NWP models against ground measurements from stations in Southern Germany, Switzerland, Austria and Southern Spain for one year. They calculated the average bias to be between − 2.9% and + 5.9% across the sites.

Bias correction

Two bias correction techniques—(i) polynomial function and (ii) NN-based bias correction methods, are validated on

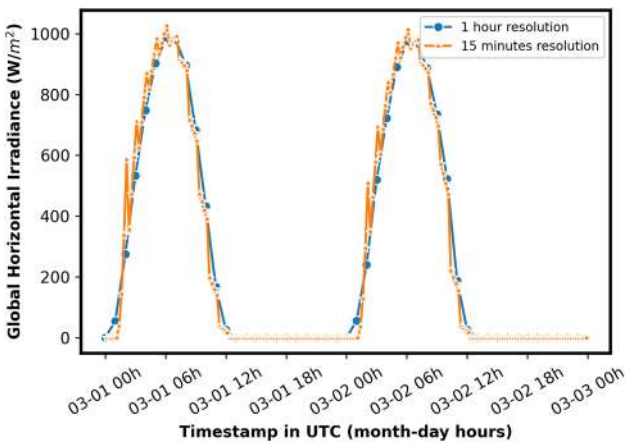

Fig. 3 Interpolation of hourly GHI to 15-min resolution

a sliding window basis against the ground-measured GHI from the PV plant for the period 17th December 2018 to 23rd October 2019. Ground measured GHI datasets from both the PV plant and the nearest SRRA station is used for training the two bias correction algorithms. The sliding window is varied from 15 to 40 days in 5-day steps to determine the optimum number of training days for the bias correction algorithms. The variation in bias with the change in the number of days of training in the sliding window is shown in Figs. 4 and 5 for ECMWF and NCMRWF, respectively. To select a bias correction technique for the model chain, the maximum reduction in bias with the minimum number of training days is used as a criterion. The Lorenz polynomial method reduces the bias in ECMWF predicted GHI to − 0.001% with 25 days of training. The bias in NCMRWF predicted GHI is reduced to − 0.08% with 20 days of training. After the NN-based correction, the bias lies between 0 and − 0.2% and − 1 and − 2% for ECMWF and NCMRWF respectively. Consequently, the Lorenz polynomial method is used for bias correction in the model chain. With the NN method, a negative bias is observed for all sets of training days. In [61], the authors performed bias correction of ECMWF predicted GHI for a period of one year. The corrected GHI predictions showed an average bias of − 0.2% against ground measurements from 87 stations distributed across north-eastern Germany.

Tilt conversion

The diffuse fraction model by Chandrasekaran and Kumar" and the diffuse sky model by "Klucher" are combined in the forecasting chain for the conversion from GHI to GTI due to their suitability for Indian solar climatology (see Sect. "Irradiance transposition"). The PV module tilt varies seasonally at each of the five blocks. Furthermore, each block follows its own independent tilt variation schedule, and the entire manual tilt change procedure requires multiple days in each case. During the tilt changing, the PV modules in each block can have two different types of tilt values. Approximate information on tilt variation schedule was obtained from a site survey.

Two forecasted GTI datasets are obtained by transposing the bias-corrected GHI forecasts from the ECMWF and NCMRWF using the tilt angles from Table 1. The forecasted GTI and forecasted GHI for the period 6th February 2019 to 6th June 2019 are plotted against the measured GTI t from a block, as shown in Figs. 6 and 7. It can be seen that the

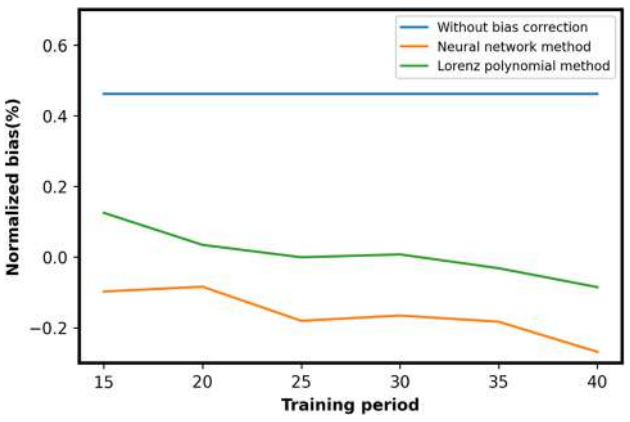

Fig. 4 The variation of normalized bias in ECMWF output GHI with the increasing number of training days for the two bias correction methods

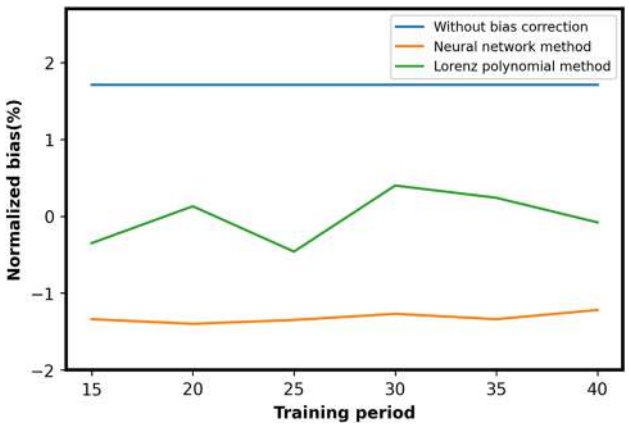

Fig. 5 The variation of normalized bias in NCMRWF output GHI with the increasing number of training days for the two bias correction methods

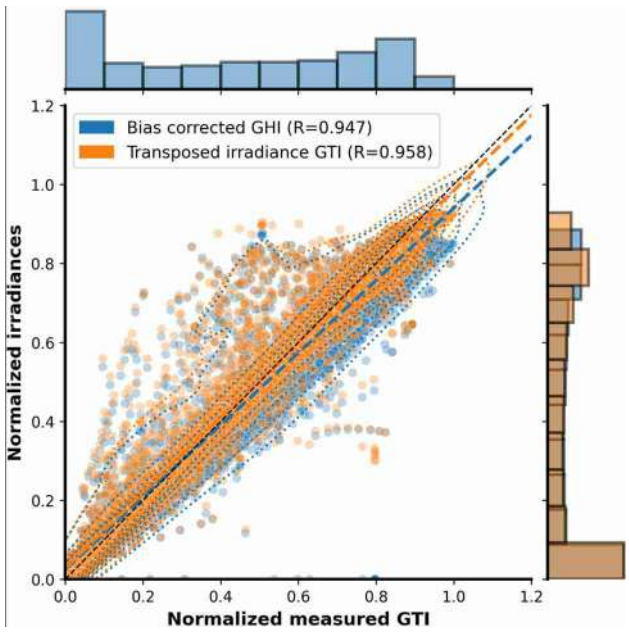

Fig. 6 Comparison of bias corrected ECMWF output GHI and its transposition against measured GTI

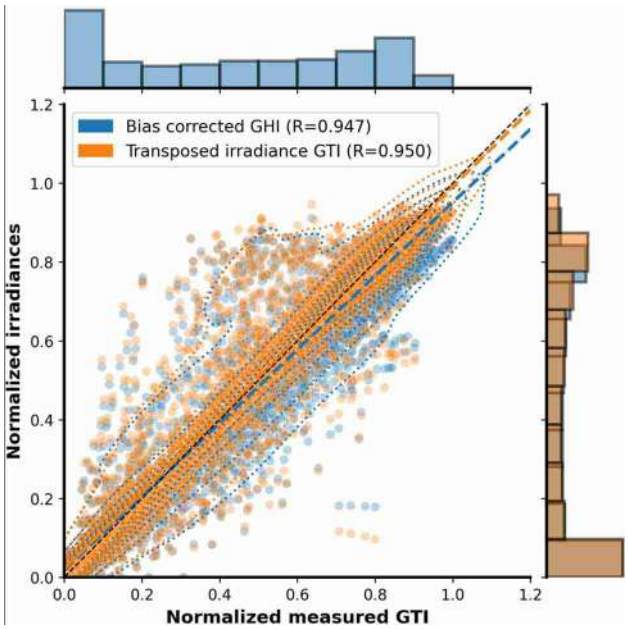

Fig. 7 Comparison of bias corrected NCMRWF output GHI and its transposition against measured GTI

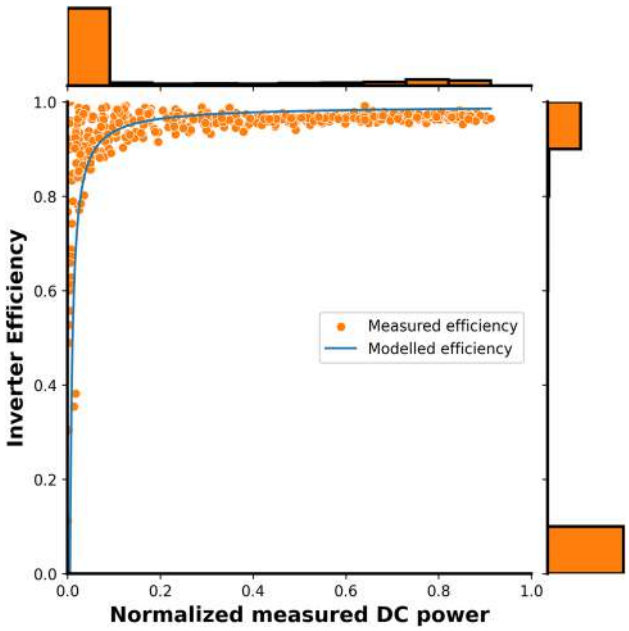

Fig. 8 Inverter efficiency curve estimated from a nearby PV site using Schmidt and Sauer model

forecasted GTI obtained by transposing GHI shows a better correlation to the measured GTI at uncertain tilt angles than the forecasted GHI. The benefit of the irradiance transposition model can be particularly observed in high-irradiance situations. [7] tested the performance of PV power output modeling under different scenarios—where the module tilt information is available and where it is not. By analyzing the accuracy of simulated power against measurements, it was observed that assuming a value of tilt could be better than using the GHI directly in the case of irradiance transposition with an unknown module tilt. It was also found beneficial to reduce the module tilt by 5° to 10° from its actual value. However, analyzing the final AC power accuracy has caveats as this also incorporates errors due to inaccuracies in PV module and inverter performance modeling. It can be observed from Figs. 6 and 7 that the highest utility of GHI transposition over using raw GHI is observed during periods of high irradiance, i.e., clear sky period. The benefit of using even approximate module tilt values for irradiance transposition is shown here. Especially for situations where the module tilt is changed manually on a seasonal basis, with every readjustment cycle lasting multiple days.

DC power model

Virtual DC power data

Due to the complete lack of DC measurements and blockwise AC power output data from the PV park, a synthetic or virtual DC power dataset is back-calculated from the aggregated AC power output of the entire PV park. The inverter efficiency curve from a nearby PV plant with a similar rated capacity is derived and used for this purpose, as shown in Fig. 8. The inverter efficiency curve is obtained by training the voltage-independent Schmidt and Sauer model with actual DC and AC power output measurements from the nearby site. This efficiency curve is used to produce an aggregated virtual DC power dataset from the available aggregated AC power dataset of the PV park under analysis. [62] showed that the efficiency curves of grid-connected inverters vary depending on the optimization approach used. A low self-consumption strategy leads to high efficiency at small partial loads while compromising the performance at the higher end of the curve. A small input power level strategy leads to a good performance at the higher end of the curve but reduces the efficiency at small partial loads.

PV model coefficients

The coefficients of the Huld and Beyer models are obtained by curve fitting Eqs. 13 and 16 with Virtual DC power data,

Table 2 nRMSE of AC power forecasts

NWP data	Huld model (%)	Beyer model (%)
ECMWF	11.01	11.03
NCMRWF	12.72	12.76

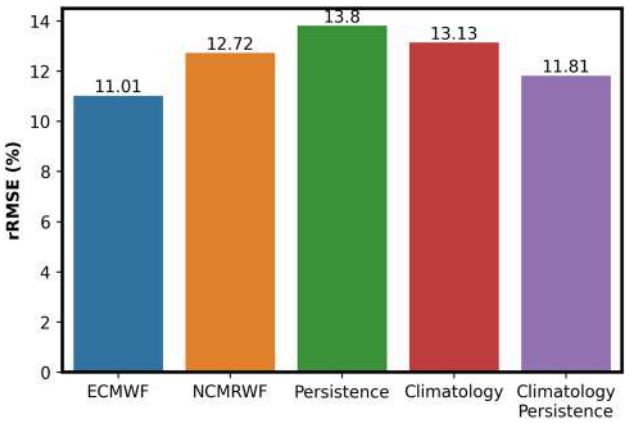

Fig. 9 Comparison of the AC power forecasts obtained from ECMWF and NCMRWF with persistence, climatology and the convex combination of persistence and climatology

GTI measurement and module temperature measurement for the period 7th November 2018 to 15th April 2019. The Beyer model additionally requires the PV module efficiency at η_{STC} (Eq. 16). An efficiency of 15% is assumed here as the PV modules are predominantly polycrystalline with a minor share of monocrystalline and thin film modules.

AC power predictions

The AC power predictions are calculated from the ECMWF and NCMRWF predicted GHI with the entire forecast model chain (see Fig. 1) for the validation period of 16th April 2019 to 23rd October 2019. The Ross parameter k in Eq. 17 is set to 0.03 °C m^2 W^{-1} based on a pre-study. With two NWP models and two GTI to DC conversion models, four forecasted AC power datasets are obtained. The error observed for these four datasets of AC power forecasts is shown in Table 2. No significant difference could be observed between the performances of Huld and Beyer models. However, as the Huld model performs marginally better, it is used in the final forecast model chain. Forecasts derived from the ECMWF and NCMRWF datasets outperform climatology and persistence, as shown in Fig. 9. However,

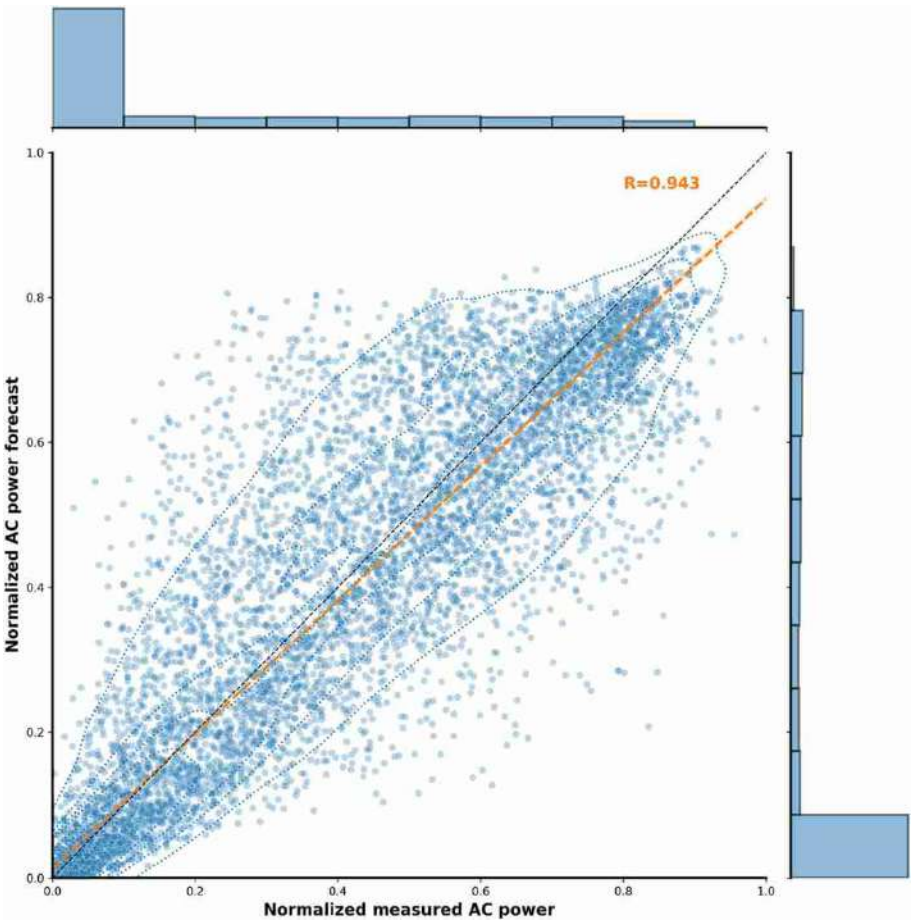

Fig. 10 AC power forecast derived from the ECMWF data

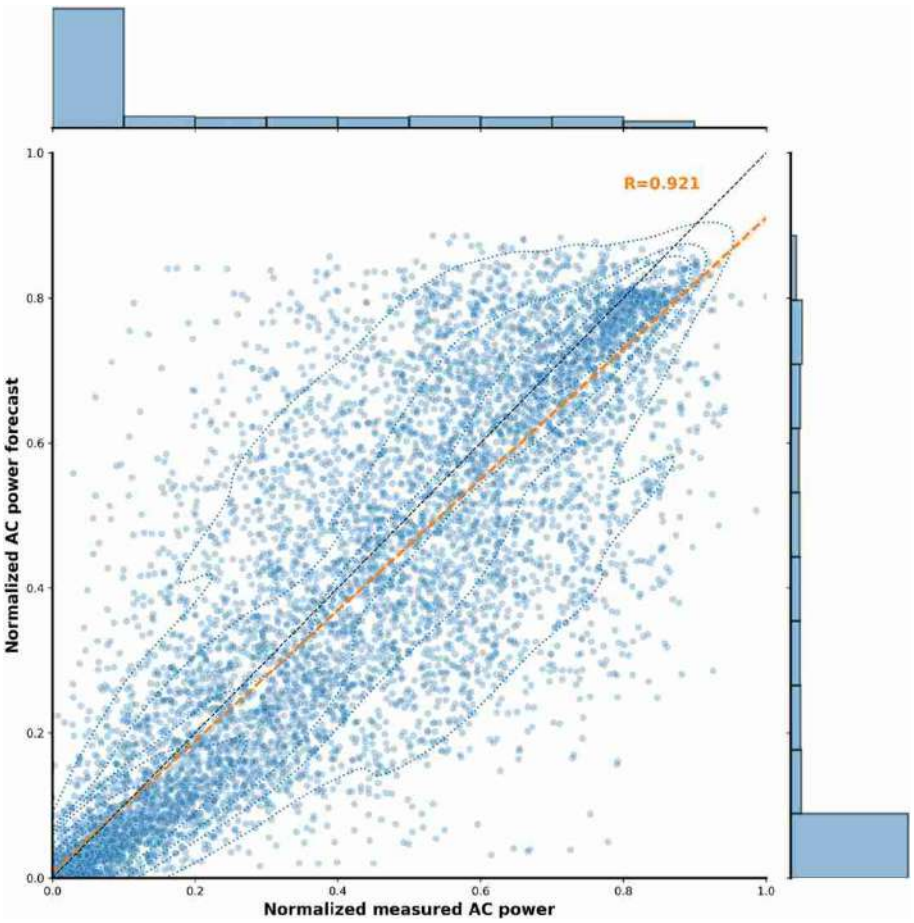

Fig. 11 AC power forecast derived from the NCMRWF data

the NCMRWF derived forecast shows higher rRMSE than the convex combination of climatology and persistence (as defined in [50] and [51]). Figures 10 and 11 also show that NCMRWF derived forecasts show lower correlation than ECMWF. [11] evaluated the accuracy of their forecasting model chain against PV power measurements from China for eight exemplary days and found the nRMSE to vary between 8 and 19%. [49] found that the nRMSE of their model chain varied from 8.21% at 1 h ahead to 13.84% at 48 h ahead on an average for one year of PV power measurements from a site in Hungary.

Combination of power forecasts based on the two NWP sources

For the final combined AC power prediction, the coefficients of the combination equation are trained on 15 days sliding window basis. The accuracy of the combined AC power forecast is validated for the period 1st May 2019 to 23rd October 2019. Although the NCMRWF derived forecast shows higher rRMSE than the convex combination of climatology and persistence, the final combination of ECMWF and NCMRWF derived forecasts shows the best performance, as shown in Fig. 12. From Figs. 10, 11, 12 and 13, it can be observed that there is always an underestimation of AC power for periods of higher generation that correspond

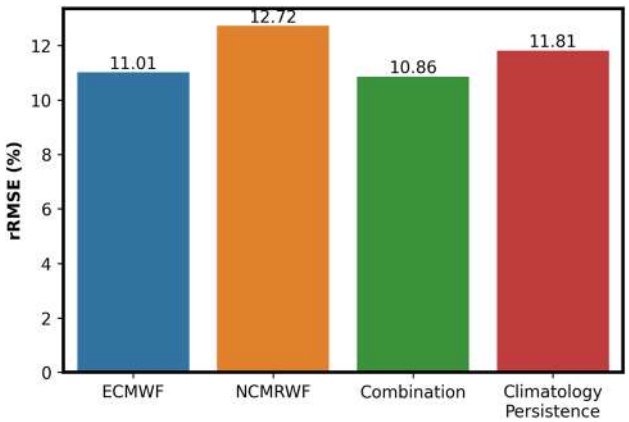

Fig. 12 Comparison of the AC power forecasts obtained from ECMWF and NCMRWF with persistence, climatology and the convex combination of persistence and climatology

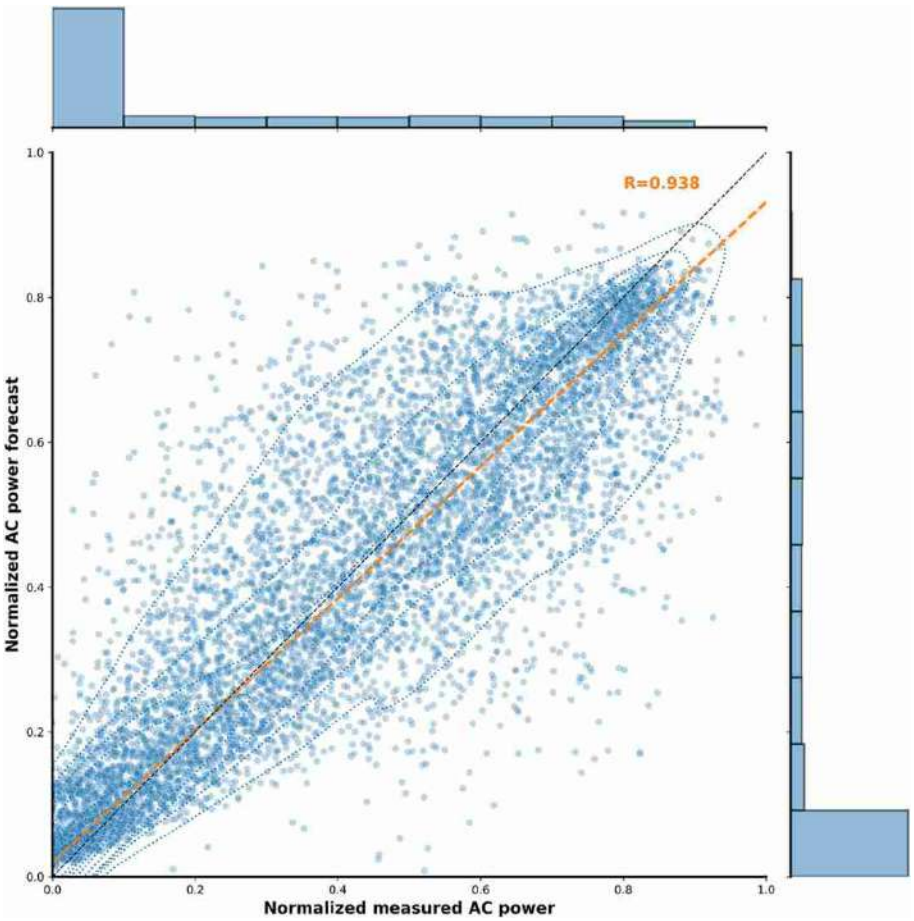

Fig. 13 Combination of the AC power forecasts derived from ECMWF and NCMRWF

to high solar elevation angles. For the periods of lower generation, an overestimation in the forecast can be observed. [49] showed that combination of AC power forecasts leads to a considerable improvement in accuracy at all times of the day except the early morning.

Conclusion

In this study, an NWP-based day ahead solar PV power forecast model chain has been developed, and each of its model component benchmarked against measurements from a 250 MWp PV park located in Southern India. Without any post-processing, the GHI output from both the ECMWF and NCMRWF models overestimated the GHI compared to the ground measurements. The Lorenz polynomial method outperformed the one hidden layer with four nodes NN architecture based bias correction method with both the NWP datasets for the PV Park site. The NN-based method also showed a consistent under-estimation of GHI with both the NWP data-sets. [7] opined that an assumed tilt angle may be better than using the GHI directly in situations with an unknown tilt angle. The usefulness of irradiance transposition even in situations with uncertain seasonal tilt information was established by the fact that the forecasted GTI dataset showed a better correlation with the measured GTI at uncertain tilt than the forecasted GHI with measured GTI. [7] did not analyze the scenario in which the AC power output dataset is available while the DC power is not. In this study, it was possible to back-calculate an aggregated virtual DC power dataset from the available aggregated AC power measurements by using a voltage-independent inverter efficiency curve derived from another nearby PV site with a similar PV capacity rating. This virtual DC power dataset was used in training the Beyer and Huld PV efficiency models. The Huld model performed only marginally better than the Beyer model and was therefore used in the final forecast model chain.. The ECMWF and NCMRWF derived forecasts outperformed both climatology and persistence. However, the NCMRWF derived forecast showed higher error than the convex combination of climatology and persistence. Nevertheless, the linear combination of the AC power forecasts

derived from the ECMWF and NCMRWF datasets showed the best accuracy and outperformed the convex combination of climatology and persistence. This possibly points to the fact that the underlying atmospheric effects are modeled differently in the two NWP models, and a combination of both therefore leads to more information about the atmospheric condition. However, the global NWP models are inherently limited by their low resolution (25 km) and assume the same cloud situation or irradiance over a large area. To summarize, we demonstrated that it is possible to produce reliable day-ahead PV power forecasts, derived from numerical weather data, for the Indian subcontinent even in situations where the PV tilt information and the inverter DC measurements are lacking. Furthermore, we compared our result against a standard reference—the convex combination of persistence and climatology. Each individual step of the forecast model chain has been optimized to provide a benchmark of the expected day-ahead solar PV power forecast accuracy. As the deviation of the actual power feed-in from the forecast is penalized beyond a deviation threshold, the accuracy metrics provide solar PV plant operators information about the financial risks involved. Furthermore, as the global NWP model grid size is large (25 kms) and as there are other large solar PV parks located in the surrounding, this also gives the grid operators an idea about the expected deviation of GW scale solar PV feed-in from its day-ahead schedule. This will allow them to procure the necessary reserves in advance. The limitations in this study include:

(i) Interpolation from 3 h or 1 h to 15 min assuming a constant clear sky index. This is not a realistic assumption, but could be improved by using a machine learning based classification.
(ii) The model chain assumes a constant tilt for the entire PV park, which is not true. Although assuming a single tilt provides better results than using GHI directly, this could be further improved upon
(iii) Although there are different kinds of PV modules connected to multiple inverters, in this study all the PV modules together and the inverters were lumped together. All properties were calculated at the aggregate level, which is not realistic. A more detailed representation of the PV park could be developed.

Table 3 rRMSE, rMBE, |rMBE| and correlation coefficient of the diffuse fraction models averaged over all stations (Betcke, 2018)

Model	$<rRMSE>$ (%)	$<rMBE>$ (%)	$<\|rMBE\|>$ (%)	$<r^2>$
Orgill and Hollands	25.0	7.5	8.0	0.833
Erbs	25.0	2.6	6.1	0.781
Chandrasekaran and Kumar	23.9	3.6	5.9	0.842
Reindl 1	25.9	2.9	5.8	0.869
Reindl 2	28.4	4.6	6.1	0.769
Suehrcke and McCormick, built-in clear sky model	50.3	35.1	35.1	0.746
Suehrcke and McCormick, Ineichen clear sky model, Remund turbidity	38.5	23.4	23.4	0.781
Skartveit et al., without variability, built in clear sky model	25.3	3.1	8.6	0.884
Skartveit et al., with variability, built in clear sky model	25.9	9.7	9.8	0.885
Skartveit et al., without variability, Ineichen sky model, Remund turbidity	27.4	− 6.1	7.6	0.857
Skartveit et al., with variability, Ineichen sky model, Remund turbidity	24.8	0.4	5.1	0.874

Table 4 Results of the analysis of the tilt conversion models (Betcke, 2018)

Station	Gandhinagar	Gurgaon
latitude/tilt (°)	23.2	28.4
Data completeness (%)	86	83
Tilt factor from measurement (%)	105.4	102.7
Diffuse fraction from measurement (%)	51	50
rRMSE/rMBE isotropic (%)	15.7/− 1.4	24.9/2.9
rRMSE/rMBE Klucher (%)	11.9/1.4	19.1/6.4
rRMSE/rMBE Perez I (%)	13.0/1.3	20.4/7.6
rRMSE/rMBE Perez II (%)	12.8/0.9	20.1/7.3

(iv) Global NWP models with a low spatial resolution (25 kms × 25 kms) were used in this study, whereas the solar PV park has a dimension of 3 kms × 3 kms. Regional models with higher spatial resolution will be tested in the future.

(v) The combined AC forecast over-estimated the power production during periods with lower generation. This may be due to the inappropriate modeling of the atmospheric turbidity and scattering at low solar elevation angles. Clear sky models that incorporate near real time aerosol information could be explored for this purpose. At higher generation levels, the forecasts under-estimate the AC power. Further analysis is necessary to determine whether this under-estimation is due to the inability of NWP models to resolve clouds at the coarse resolution and the consequent averaging effect.

Appendix

Tables 3, 4.

Acknowledgements The authors thank the operator of the solar farm, who supported our work with historic and real-time data, the Indian Meteorological Department, who supported us with NCMRWF datasets, and GIZ GmbH, who financed a major part of the work presented. This work was carried out during 2017–2019 under the Green Energy Corridors project of the Indo-German Energy Programme. The authors declare that they have no conflict of interest.

Funding Open Access funding enabled and organized by Projekt DEAL.

References

1. International Energy Agency: Renewables 2021. https://www.iea.org/reports/renewables-2021. Accessed 31 Dec 2022
2. Ministry of New and Renewable Energy: Physical Progress. https://mnre.gov.in/the-ministry/physical-progress. Accessed 31 Dec 2022
3. Government of India: India's Updated Nationally Determined Contribution. https://pib.gov.in/PressReleaseIframePage.aspx?PRID=1847812. Accessed 31 Dec 2022
4. Perez, R., Lorenz, E., Pelland, S., Beauharnois, M., Van Knowe, G., Hemker, K., Heinemann, D., Remund, J., Müller, S.C., Traunmüller, W., Steinmauer, G., Pozo, D., Ruiz-Arias, J.A., Lara-Fanego, V., Ramirez-Santigosa, L., Gaston-Romero, M., Pomares, L.M.: Comparison of numerical weather prediction solar irradiance forecasts in the US, Canada and Europe. Sol. Energy **94**, 305–326 (2013). https://doi.org/10.1016/j.solener.2013.05.005
5. Inman, R.H., Pedro, H.T.C., Coimbra, C.F.M.: Solar forecasting methods for renewable energy integration. Prog. Energy Combustion Sci. **39**, 535–576 (2013)
6. Wan, C., Zhao, J., Song, Y., Xu, Z., Lin, J., Hu, Z.: Photovoltaic and solar power forecasting for smart grid management. CSEE J. Power Energy Syst. **1**(4), 38–46 (2015). https://doi.org/10.17775/CSEEJPES.2015.00046
7. Mayer, M.J.: Influence of design data availability on the accuracy of physical photovoltaic power forecasts. Sol. Energy **227**, 532–540 (2021). https://doi.org/10.1016/j.solener.2021.09.044
8. Leva, S., Dolara, A., Grimaccia, F., Mussetta, M., Ogliari, E.: Analysis and validation of 24 hours ahead neural network forecasting of photovoltaic output power. Math. Comput. Simul. **131**, 88–100 (2017). https://doi.org/10.1016/j.matcom.2015.05.010
9. Theocharides, S., Makrides, G., Georghiou, G.E., Kyprianou, A.: Machine learning algorithms for photovoltaic system power output prediction. In: IEEE International Energy Conference (ENERGYCON), pp. 1–6 (2018). https://doi.org/10.1109/ENERGYCON.2018.8398737
10. Wolff, B., Kühnert, J., Lorenz, E., Kramer, O., Heinemann, D.: Comparing support vector regression for PV power forecasting to a physical modeling approach using measurement, numerical weather prediction, and cloud motion data. Sol. Energy **135**, 197–208 (2016). https://doi.org/10.1016/j.solener.2016.05.051
11. Cui, C., Zou, Y., Wei, L., Wang, Y.: Evaluating combination models of solar irradiance on inclined surfaces and forecasting photovoltaic power generation. IET Smart Grid **2**, 123–130 (2019). https://doi.org/10.1049/iet-stg.2018.0110
12. Mayer, J.M., Gyula, G.: Extensive comparison of physical models for photovoltaic power forecasting. Appl. Energy **283**, 116239 (2021). https://doi.org/10.1016/j.apenergy.2020.116239
13. Holland, N., Pang, X., Herzberg, W., Bor, J., Lorenz, E.: Combination of physics based simulation and machine learning for PV power forecasting of large power plants. In: EU PVSEC Programme Online, 6–10 September (2021)
14. Huang, J., Thatcher, M.: Assessing the value of simulated regional weather variability in solar forecasting using numerical weather prediction. Sol. Energy **144**, 529–539 (2017). https://doi.org/10.1016/j.solener.2017.01.058
15. Lorenz, E., Hurka, J., Heinemann, D., Beyer, H.G.: Irradiance forecasting for the power prediction of grid-connected photovoltaic systems. IEEE J. Sel. Top. Appl. Earth Obs. Remote Sens. **2**, 2–10 (2009)
16. Joshi, B., Kay, M., Jessie, C.K., Sproul, A.B.: Evaluation of solar irradiance forecasting skills of the Australian Bureau of Meteorology's ACCESS models. Sol. Energy **188**, 386–402 (2019). https://doi.org/10.1016/j.solener.2019.06.007
17. Yagli, G.M., Monika, Yang, D., Srinivasan, D.: Using combinational methods for forecast improvement in PV power plants. In: IEEE Innovative Smart Grid Technologies-Asia (ISGT Asia), pp. 540–545 (2018). https://doi.org/10.1109/ISGT-Asia.2018.8467878
18. Suksamosorn, S., Hoonchareon, N., Songsiri, J.: Post-processing of NWP forecasts using kalman filtering with operational constraints for day-ahead solar power forecasting in Thailand. IEEE Access **9**, 105409–105423 (2021). https://doi.org/10.1109/ACCESS.2021.3099481

19. Yang, D.: On post-processing day-ahead NWP forecasts using Kalman filtering. Sol. Energy **182**, 179–181 (2019). https://doi.org/10.1016/j.solener.2019.02.044
20. Lauret, P., Diagne, H.M., David, M.: A neural network post-processing approach to improving NWP solar radiation forecasts. Energy Procedia **57**, 1044–1052 (2014). https://doi.org/10.1016/j.egypro.2014.10.089
21. Lauret, P., Lorenz, E., Mathieu, D.: Solar forecasting in a challenging insular context. Atmosphere **7**, 214 (2016)
22. Pereira, S., Canhoto, P., Salgado, R., Costa, M.J.: Development of an ANN based corrective algorithm for the operational ECMWF global horizontal irradiation forecasts. Sol. Energy **185**, 387–405 (2019). https://doi.org/10.1016/j.solener.2019.04.070
23. Watanabe, T., Takenaka, H., Nohara, D.: Post-processing correction method for surface solar irradiance forecast data from the numerical weather model using geostationary satellite observation data. Sol. Energy **223**, 202–216 (2021). https://doi.org/10.1016/j.solener.2021.05.055
24. Tschopp, D., Jensen, A.R., Dragsted, J., Ohnewein, P., Furbo, S.: Measurement and modeling of diffuse irradiance masking on tilted planes for solar engineering applications. Sol. Energy **231**, 365–378 (2022). https://doi.org/10.1016/j.solener.2021.10.083
25. Chandrasekaran, J., Kumar, S.: Hourly diffuse fraction correlation at a tropical location. Sol. Energy **53**, 505–510 (1994). https://doi.org/10.1016/0038-092X(94)90130-T
26. Reindl, D.T., Beckman, W.A., Duffie, J.A.: Diffuse fraction correlations. Sol. Energy **45**(1), 1–7 (1990). https://doi.org/10.1016/0038-092X(90)90060-P
27. Skartveit, A., Olseth, J.A., Tuft, M.E.: An hourly diffuse fraction model with correction for variability and surface albedo. Sol. Energy **63**(3), 173–183 (1998). https://doi.org/10.1016/S0038-092X(98)00067-X
28. Paulescu, E., Blaga, R.: A simple and reliable empirical model with two predictors for estimating 1-minute diffuse fraction. Sol. Energy **180**, 75–84 (2019). https://doi.org/10.1016/j.solener.2019.01.029
29. Boland, J., Scott, L., Luther, M.: Modelling the diffuse fraction of global solar radiation on a horizontal surface. Environmetrics **12**, 103–116 (2001)
30. Furlan, C., Oliveira, A.P., Soares, J., Codato, G., Escobedo, J.F.: The role of clouds in improving the regression model for hourly values of diffuse solar radiation. Appl. Energy **92**, 240–254 (2012). https://doi.org/10.1016/j.apenergy.2011.10.032
31. Ridley, B., Boland, J., Lauret, P.: Modelling of diffuse solar fraction with multiple predictors. Renew. Energy **35**(2), 478–483 (2010). https://doi.org/10.1016/j.renene.2009.07.018
32. Batzelis, E.I.: Simple PV performance equations theoretically well founded on the single-diode model. IEEE J. Photovoltaics **7**, 1400–1409 (2017). https://doi.org/10.1109/JPHOTOV.2017.2711431
33. Yaqoob, S.J., Saleh, A.L., Motahhir, S., Agyekum, E.B., Nayyar, A., Qureshi, B.: Comparative study with practical validation of photovoltaic monocrystalline module for single and double diode models. Sci. Rep. **11**, 19153 (2021). https://doi.org/10.1038/s41598-021-98593-6
34. Beyer, H.G., Betcke, J., Drews, A., Heinemann, D., Lorenz, E., Heilscher, G., Bofinger, S.: Identification of a general model for the MPP performance of PV-modules for the application in a procedure for the performance check of grid connected systems. In: 19th European Photovoltaic Solar Energy Conference and Exhibition, p. 7, (2014)
35. Deotti, L., Júnior, I.S., Honório, L., Marcato, A.: Empirical models applied to distributed energy resources-an analysis in the light of regulatory aspects. Energies **14**(2), 326 (2021). https://doi.org/10.3390/en14020326
36. Huld, T., Friesen, G., Skoczek, A., Kenny, R.P., Sample, T., Field, M., Dunlop, E.D.: A power-rating model for crystalline silicon PV modules. Sol. Energy Mater. Sol. Cells **95**, 3359–3369 (2011). https://doi.org/10.1016/j.solmat.2011.07.026
37. Soler-Castillo, Y., Rimada, J.C., Hernández, L., Martínez-Criado, G.: Modelling of the efficiency of the photovoltaic modules: grid-connected plants to the Cuban national electrical system. Sol. Energy **223**, 150–157 (2021). https://doi.org/10.1016/j.solener.2021.05.052
38. Padmavathi, K., Arul, D.S.: Performance analysis of a 3 MWp grid connected solar photovoltaic power plant in India. Energy Sustain. Dev. **17**, 615–625 (2013). https://doi.org/10.1016/j.esd.2013.09.002
39. Santiago, I., Trillo-Montero, D., Morena-Garcia, I.M., Pallarés-López, V., Luna-Rodríguez, J.J.: Modeling of photovoltaic cell temperature losses: a review and a practice case in South Spain. Renew. Sustain. Energy Rev. **90**, 70–89 (2018). https://doi.org/10.1016/j.rser.2018.03.054
40. Skoplaki, E., Boudouvis, A.G., Palyvos, J.A.: A simple correlation for the operating temperature of photovoltaic modules of arbitrary mounting. Sol. Energy Mater. Sol. Cells **92**, 1393–1402 (2008). https://doi.org/10.1016/j.solmat.2008.05.016
41. Roumpakias, E., Stamatelos, A.: Performance analysis of a grid-connected photovoltaic park after 6 years of operation. Ren. Energy **141**, 368–378 (2019). https://doi.org/10.1016/j.renene.2019.04.014
42. Driesse, A., Jain, P., Harrison, S.: Beyond the curves: modeling the electrical efficiency of photovoltaic inverters. In: 33rd IEEE Photovoltaic Specialists Conference, pp. 1–6 (2008). https://doi.org/10.1109/PVSC.2008.4922827
43. King, D.L., Boyson, W.E., Kratochvil, J.A.: Photovoltaic array performance model. Sandia Rep. No. 2004–3535 (2004). https://doi.org/10.2172/919131
44. King, D.L., Gonzalez, S., Galbraith, G.M., Boyson, W.E.: Performance model for grid-connected photovoltaic inverters. Sandia National Laboratories SAND2007-5036 (2007)
45. Lave, M., Ellis, A., Stein, J.S.: Simulating solar power plant variability: a review of current methods. Sandia National Laboratories: Alburquerque, NM, USA (2013)
46. Schmidt, H., Sauer, D.: Wechselrichter-Wirkungsgrade. Sonnenenergie **4**, 43–47 (1996)
47. Yang, D., Meer, D.: Post-processing in solar forecasting: ten overarching thinking tools. Renew. Sustain. Energy Rev. **5**, 140 (2021). https://doi.org/10.1016/j.rser.2021.110735
48. Böök, H., Lindfors, A.V.: Site-specific adjustment of a NWP-based photovoltaic production forecast. Sol. Energy **211**(15), 779–788 (2020). https://doi.org/10.1016/j.solener.2020.10.024
49. Filipe, J.M., Bessa, R.J., Sumaili, J., Tomé R., Sousa, J.N.: A hybrid short-term solar power forecasting tool. In: 18th International Conference on Intelligent System Application to Power Systems (ISAP), pp. 1–6 (2015). doi: https://doi.org/10.1109/ISAP.2015.7325543
50. Yang, D.: Standard of reference in operational day-ahead deterministic solar forecasting. J. Renew. Sustain. Energy **11**, 053702 (2019)
51. Yang, D.: Making reference solar forecasts with climatology, persistence, and their optimal convex combination. Sol. Energy **193**, 981–985 (2019). https://doi.org/10.1016/j.solener.2019.10.006
52. Kumar, A., Gomathinayagam, S., Giridhar, G., Mitra, I., Vashishtha, R., Meyer, R., Schwandt, M., Chhatbar, K.: Field experiences with the operation of solar radiation resource assessment stations in India. Energy Procedia (2014). https://doi.org/10.1016/j.egypro.2014.03.249
53. Schwandt, M., Chhatbar, K., Meyer, R., Mitra, I., Vashistha, R., Giridhar, G., Gomathinayagam, S., Kumar, A.: Quality check

procedures and statistics for the Indian SRRA solar radiation measurement network. Energy Procedia **57**, 1227–1236 (2014)
54. Yang, D., Alessandrini, S., Antonanzas, J., Antonanzas-Torres, F., Badescu, V., Beyer, H.G., Blaga, R., Boland, J., Bright, J.M., Coimbra, C.F.M., David, M., Frimane, Â., Gueymard, C.A., Hong, T., Kay, M.J., Killinger, S., Kleissl, J., Lauret, P., Lorenz, E., Meer, D., Paulescu, M., Perez, R., Lamigueiro, O.P., Peters, I.M., Reikard, G., Renné, D., Saint-Drenan, Y., Shuai, Y., Urraca, R., Verbois, H., Vignola, F., Voyant, C., Zhang, J.: Verification of deterministic solar forecasts. Sol. Energy **210**, 20–37 (2020)
55. Ineichen, P., Perez, R.: A new airmass independent formulation for the linke turbidity coefficient. Sol. Energy **73**, 151–157 (2002). https://doi.org/10.1016/S0038-092X(02)00045-2
56. Rincón, A., Jorba, O., Frutos, M., Alvarez, L., Barrios, F.P., González, J.A.: Bias correction of global irradiance modelled with weather and research forecasting model over Paraguay. Sol. Energy **170**, 201–211 (2018). https://doi.org/10.1016/j.solener.2018.05.061
57. Liu, B., Jordan, R.: The long-term average performance of flat-plate solar-energy collectors: with design data for the U.S., it's outlying possessions and Canada. Sol. Energy **7**(2), 53–74 (1963)
58. Temps, R.C., Coulson, K.L.: Solar radiation incident upon slopes of different orientations. Sol. Energy **19**(2), 179–184 (1977). https://doi.org/10.1016/0038-092X(77)90056-1
59. Faiman, D.: Assessing the outdoor operating temperature of photovoltaic modules. Prog. Photovolt. Res. Appl. **16**, 307–315 (2008). https://doi.org/10.1002/pip.813
60. Ross, R.G.: Interface design considerations for terrestrial solar cell modules. In: 12th Photovoltaic Specialists Conference, pp. 801–806 (1976). https://doi.org/10.1109/ENERGYCON.2018.8398737. https://ui.adsabs.harvard.edu/abs/1976pvsp.conf..801R
61. Lorenz, E., Remund, J., Müller, S. C., Traunmüller, W., Steinmaurer, G., Pozo, D., Ruiz-Arias J.A., Fanego, V.L., Ramirez, L., Romeo, M.G., Kurz, C., Pomares, L.M., Guerrero, C. G.: Benchmarking of different approaches to forecast solar irradiance. In: 24th European Photovoltaic Solar Energy Conference, pp. 21–25 (2009). Hamburg, Germany
62. Notton, G., Lazarov, V., Stoyanov, L.: Optimal sizing of a grid-connected PV system for various PV module technologies and inclinations, inverter efficiency characteristics and locations. Renew. Energy **35**(2), 541–554 (2010)

International Journal of Energy and Environmental Engineering (2023) 14:841–869
https://doi.org/10.1007/s40095-022-00552-y

ORIGINAL RESEARCH

Green and renewable resources: an assessment of sustainable energy solution for Far North Queensland, Australia

M. K. Islam[1] · N. M. S. Hassan[1] · M. G. Rasul[2] · Kianoush Emami[1] · Ashfaque Ahmed Chowdhury[3]

Received: 10 May 2022 / Accepted: 13 November 2022 / Published online: 30 November 2022

Abstract

Remote communities, which do not have a connection to the national grid in Far North Queensland (FNQ), depend on dirty and costly diesel generators to meet their energy demands. The cost of power generation is considerable in those areas, because the diesel fuel must be carried by truck or ship and a fuel reserve must be held on-site in case of expected demand or weather closure. Moreover, Australia has an energy security issue in relation to liquid fuels. Australia is reliant on imported fuel such as diesel to fill the shortage, as domestic production and supply are unable to fulfil domestic demand. As a result, by deploying hybrid integrated renewable energy systems in remote areas, isolated communities may lower their power prices, enjoy a more secure and dependable source of electricity and minimise their carbon footprint by eliminating or reducing the usage of diesel. In this study, an extensive literature review has been conducted focussing on renewable resources for Australia and Far North Queensland, different hybrid energy systems including energy storage, and finally highlights the alternative clean and renewable energy options for Far North Queensland (FNQ) remote communities. In addition, this study has performed an assessment of renewable energy available from solar and wind resources considering climatic, geographical and economic aspects for FNQ. The literature review and the assessment show that solar and wind resources including hydrogen storage have significant potential for energy solution of FNQ. The assessment results indicate that selected regions of FNQ have suitable land area of 142,294.86 km^2 (55.94% of total selected areas) for solar and 144,563.80 km^2 (56.83% of total selected areas) for wind. The total calculated potential power can be 14,448 GW from solar PV and 1040.97 GW from wind energy. This study provides a significant pathway for parties interested in investing in renewable energy in FNQ. Moreover, knowing a land's suitability will increase confidence and hence speed up the renewable energy investment.

Keywords Renewable energy · Hydrogen · Solar farm · Wind farm · Electrical power potential · GIS

Introduction

The rapid socio-economic uplift, including population growth, technology upgradation, trade, increased production and consumption, has made the relations between Earth and human beings deeper than ever. Consequently, fossil fuel reserves are depleting so quickly to meet the energy demands, which are the globe's current issue. The gathering of greenhouse gases in the atmosphere, causing global warming and the urgent requirement of renewable and eco-friendly energy resources has been a great concern. Apart from that, energy demands are growing every day with the globe's population which may grow up to roughly 9.9 billion by 2050 [1]. At the same time, developing countries will have to enhance energy expenditure intensely because of their spreading economy [2].

To be sustainable, a society needs high and constant amounts of energy with limited environmental impact. There are many remote areas in the FNQ, and they have to rely on diesel power generation for fulfilling their basic energy requirements [3]. However, diesel is one kind of fossil fuel which has limited stock. In addition, the diesel power generation is costly [4] and harmful to the ecosystem because of its greenhouse gas emissions [5]. To

✉ M. K. Islam
m.islam2@cqu.edu.au

[1] School of Engineering and Technology, Central Queensland University, Abbott Street, Cairns, QLD 4870, Australia

[2] School of Engineering and Technology, Central Queensland University, Yaamba Rd, Rockhampton, QLD 4701, Australia

[3] School of Engineering and Technology, Central Queensland University, Bryan Jordan Dr, Gladstone, QLD 4680, Australia

keep the globe environmentally sustainable, so that the civilisation can continue for a longer time, the resources of the earth should not be changed from the equilibrium levels which help to sustain the ecosystem for thousands of years. Simultaneously, the world has to limit carbon emissions. The incoming energy resources, the solar and wind, should be trapped, not the energy system innate in the globe. Solar energy can be exploited in several ways: utilising solar cells to convert solar to electricity [6], and wind energy to generate electricity [7]. Wind energy is, in reality, a secondary effect consequencing from solar energy [7, 8].

FNQ has an abundance of solar and wind resources that have bright potential towards the fruitful sustainable pathways. However, the intermittency or unsteady nature makes solar and wind less secure, incapable of providing energy at all times [9]. There is one that sounds to be consistent with promoting energy security and cleanliness, that is hydrogen. Hydrogen is an energy carrier, convenient to transform from different energy sources, and possesses the highest amount of energy by weight compared to any common fuels [10, 11]. Hydrogen leverages the utilisation of solar and wind, as they can be used to generate hydrogen, which can then be utilised at any time for fulfilling energy needs [12]. Furthermore, if hydrogen is generated through water splitting and used in fuel cell for power production, it will produce only water as a by-product, with no hazardous emissions [11]. This is called green hydrogen. Therefore, solar and wind including green hydrogen, with their promising clean features, could be the best option for the future energy system of FNQ and Australia in general.

The motive of this study is to find out the solution for reducing the impact of diesel generation so that the remote communities can sustainably lead their life in a sustainable way. In this study, an extensive literature review has been conducted. The review focuses on renewable resources in an Australian context, emerging hybrid renewable energy systems, hydrogen storing options, renewable generation in Australia and the renewable energy potential in FNQ. In addition, a potential assessment of solar and wind resources has been conducted in terms of climatic, geographical and economic to see the suitability for the growth of solar and wind projects. The main objectives of this study to find a sustainable solution for FNQ's energy system can be summarized as follows:

1. Survey on renewable resources and its' potentiality, renewable generation in Australia;
2. Explore suitable resources for FNQ's energy system;
3. Investigate suitable lands to install solar and wind power stations, using the multi-criteria Geographical Information System (GIS) modelling technique.

To date, this is the first elaborate study where FNQ has been explored to identify potential resources as well as to investigate the suitability of places for solar and wind analysis using GIS. Finally, as this study covers the potential of renewable resources, especially the two most mature technologies, namely solar and wind including hydrogen storage, and location suitability for the installation of solar and wind farm, hence it can be expected that it will give valuable insights for hybrid versions of solar and wind including hydrogen energy applications. The present article is structured into six sections, including introduction (Sect. 1), global weather pattern (Sect. 2), global energy demand and consumption (Sect. 3), literature review that presents overview on renewable resources of global and Australian perspective, electricity energy value chain and different hybrid energy systems, potential of hydrogen energy storage, renewable generation in Australia and renewable resource potential in FNQ (Sect. 4), assessment of solar and wind resources presenting climatological, geographical and economic potential including discussion about the importance of solar and wind energy development for FNQ's energy system (Sect. 5). The last section presents the main conclusions and future perspectives.

Weather pattern

The weather pattern has been changing; for example, the global surface temperature increment, narrowing the cryosphere extensively including weight loss from ice sheets and glaciers, depletion in snow cover and Arctic Sea ice extent and thickness [13]. Global warming is responsible for extreme events, such as more extended periods of heat, heavy rainstorms and oceans acidification because of absorbing carbon dioxide [14]. All weather-related problems are happening because of the greenhouse gas (GHG) emissions in the atmosphere. Global surface temperature increment may cause more drought and damage of agricultural land. In addition, extremely hot weather may push people from their motherlands and compel them to move to other areas, eventually driving them to compete for depleting resources in their areas of arrival. Coastal regions can be invaded by multiple natural hazards such as tornado, extreme sea levels and flooding. The ocean temperature increment will also pose marine lives at possible food insecurity risk. Ultimately, a change in the weather pattern will result in changing ecosystem structure and functioning, which may cause losing the globe's unique biodiversity [13, 15]. Figure 1 highlights some indicators of global warming that were examined over the past decades [16, 17]. The globe's climate system comprises the land surface, atmosphere, oceans and ice. As seen in Fig. 1, white arrows indicate rising trends and black arrows indicate declining trends.

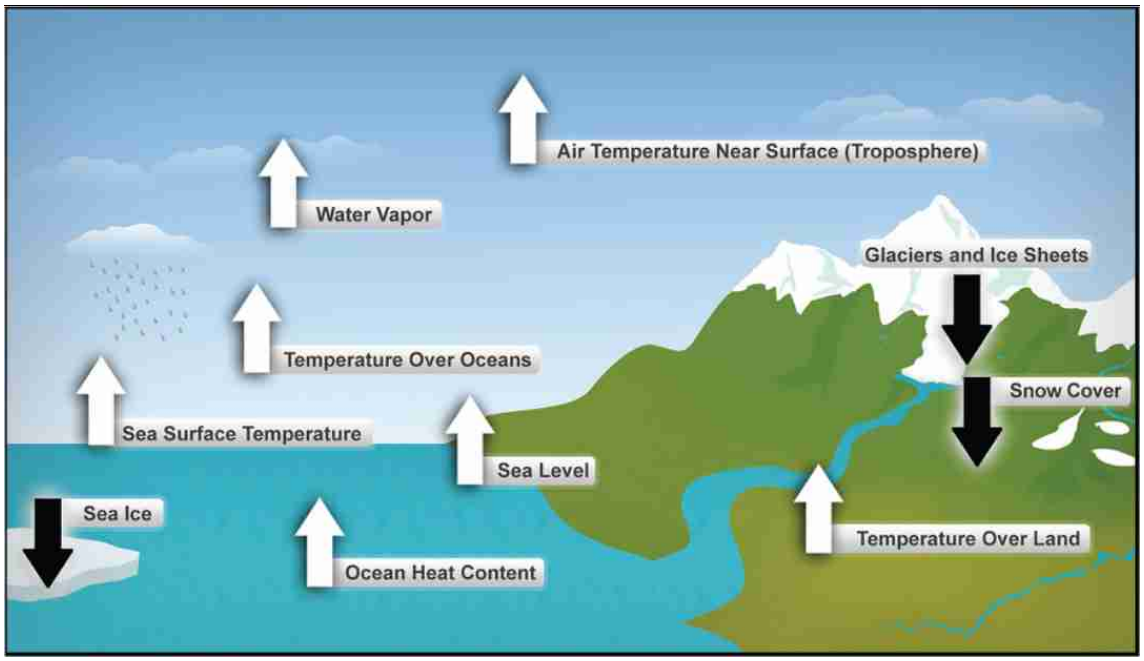

Fig. 1 Ten indicators of the global warming [16, 17]

Global warming is augmented at an average rate of 0.08 °C per decade since 1980 and over twice that rate since 1981. In 2020, the global surface temperature augmented at an average of 0.98 °C, which is the second highest record in the last 141 years [18]. If the present trend continues, the global temperature may reach to 1.5 °C between 2030 and 2052 [18, 19]. The Intergovernmental Panel on Climate Change (IPCC) [20] reported that the global mean sea level was augmented from 1.4 mm per annum (1901–1990) to 3.6 mm per annum (2006–2015); the 0–700 m and 700–2000 m layers of the ocean were warmed at rates of 6.28 ± 0.48 ZJ and 3.86 ± 2.09 ZJ, respectively, from 1993 to 2017. In addition, the continual ocean acidification because of carbon uptake (the ocean surface water pH level has been falling at a range of 0.017–0.027 pH units per decade since the 1980s) including oxygen vanished with a loss of 0.5–3.3% between 1970 and 2010 from the ocean surface to 1000 m [20]. Numerous peer-reviewed literature has already been reported about the weather extremes around the world, such as droughts in South Africa [21], extreme heatwaves in Sweden [22], excessive 6-day rainfall in Bangladesh [23] and hurricanes in the Caribbean [24]. These extreme weather events are due to the global surface temperature increment which are likely to be the results of the accumulation of GHG (carbon di-oxide, nitrous oxide, methane, halocarbons) in the atmosphere [25].

The global atmospheric concentration of carbon di-oxide has raised from a preindustrial (1750) level of 280 ppm to 417.64 ppm (March 2021), nitrous oxide from 270 to 333.6 ppb (Nov 2020), methane from 715 to 1892.3 ppb (Dec 2020) [26, 27]. As seen in Fig. 2, maximum greenhouse gas (GHG) emissions come from fossil fuel sources that are used in different economic sectors [28]. Among the GHG, carbon di-oxide is the most abundant in the atmosphere, hence the main contributor to global warming. Figure 3 depicts the trend of the increment of the global annual mean temperature anomaly with the concentration of carbon dioxide in the atmosphere [29, 30].

Australia's climate is changing in response to global warming, with an average temperature increment of 1.44 ± 0.24 °C since the Australian observations commenced in 1910 [31]. The most warming has been happening since 1950, and since then, Australia is getting warmer and warmer every decade. For instance, Australia suffered 43 exceedingly hot days in 2019, more than three times as many as in any year before 2000. High monthly maximum temperatures, around 2% during 1960–1989 and over 4% during 1990–2004, have recently been over 12% during 2005–2019. [31]. This number is more significant than a sixfold increment over the 60 years. Climate change is observed across the whole Australia. All areas of Queensland are warming since 1910, with an average annual temperature increment of 1.5 °C. Rainfall has increased in most parts of Queensland during the summer or humid season [32]. The number of days including threatening weather conditions for bushfires has augmented in all regions across the state. Sea levels are predicted to rise by nearly 26 cm along the coast of

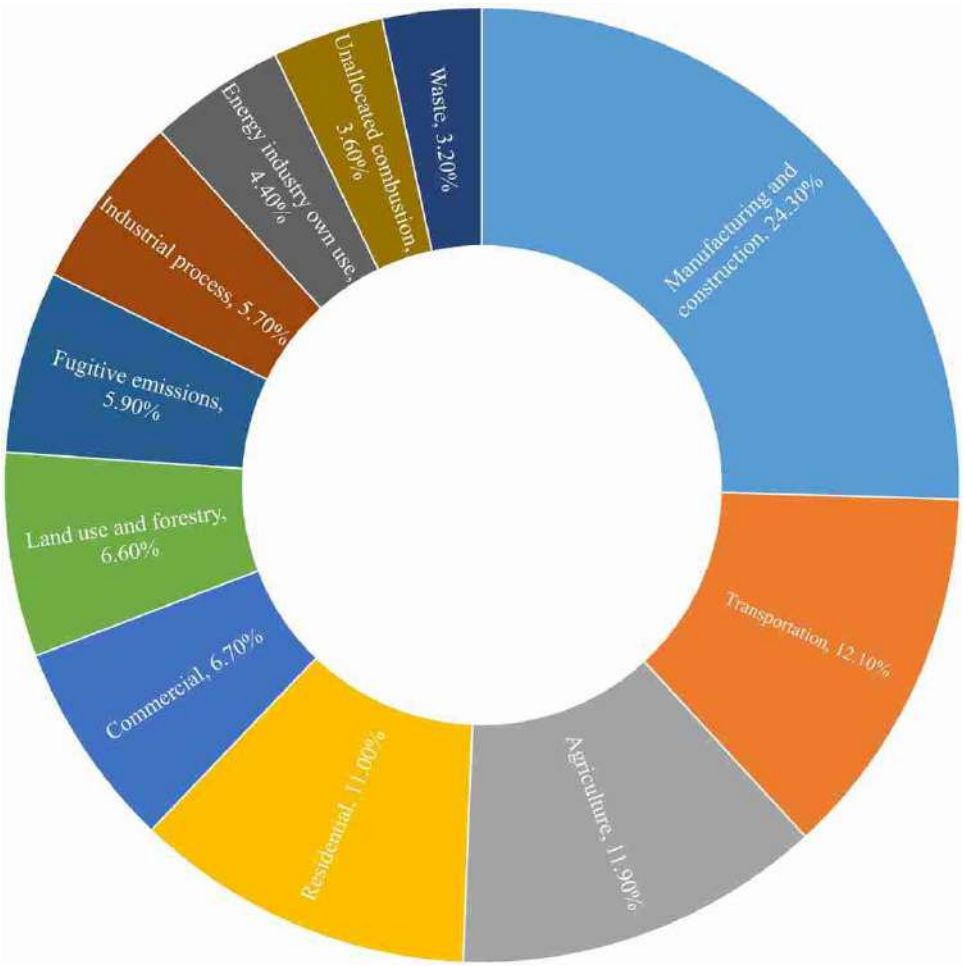

Fig. 2 Global GHG emissions by economic sectors in 2016 [28]

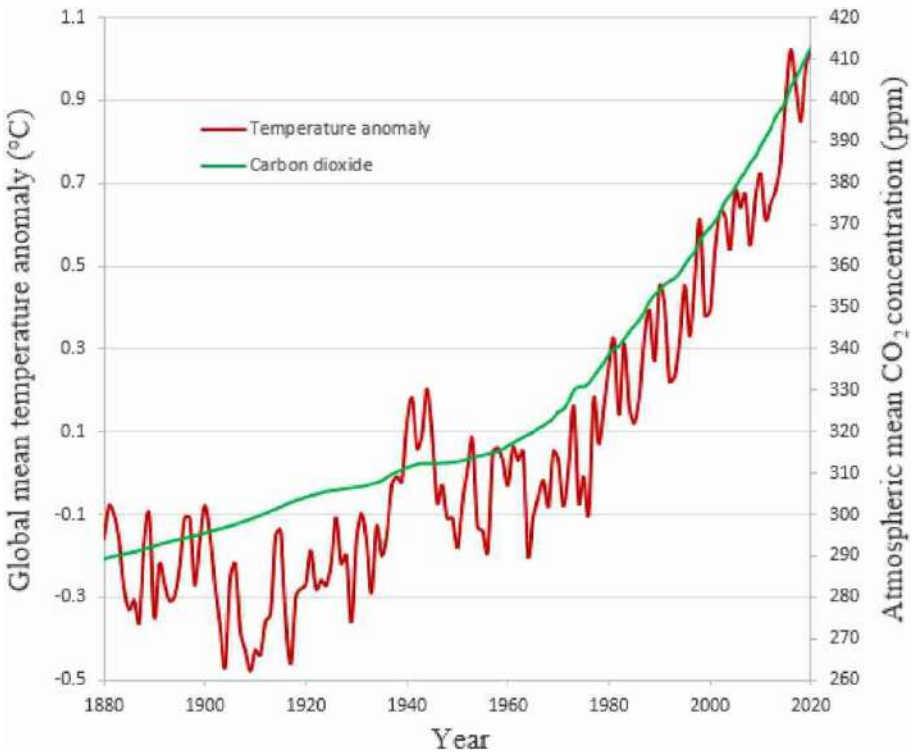

Fig. 3 Global annual mean temperature anomaly and carbon dioxide concentration [29, 30]

Queensland. Queensland may face more extreme rain events in the near future [32].

The FNQ region is specifically in danger because of the impact of climate change. Alteration in temperature or rainfall may impact significantly on the tourism, agriculture, dairy, cane and fisheries sectors [33]. Local community will also be affected, as climate change may augment heat-related health problems and potentially increase catastrophic occurrences, such as cyclones and floods, with endangering lives and infrastructure. Healthy reef and rainforest environs are the core for the tourism industry. These ecosystems are particularly at risk because of the adverse effect of climate change. Raising temperatures may constantly cause coral bleaching in the Great Barrier Reef, and this impact will become more severe if the temperature continues to increase [33]. The deterioration of the reef will be a destroy of the distinguished innate value for FNQ, which will ultimately adversely affect the tourism industry. Furthermore, sea water acidification has been occurring due to the continuous absorption of carbon dioxide. Continual acidification can affect coral formation [33, 34], which would further exacerbate the vulnerability of the Great Barrier Reef.

The globe is warming continuously, and if the GHG emissions are not controlled immediately and strong development of fossil fuel plants continues, then the globe's surface temperature may rise by 4 °C, or more, within 2100 [35], including terrible impacts on the globe's ecology and substantial demolition of the world's major coastal parts [36]. A maximum of 2 °C of global mean surface temperature deviation from pre-industrial level is the widely accepted climate policy target, but the temperatures above 2 °C will cause the ecosystems to be highly vulnerable [37]. In addition, without taking any action against GHG emissions, climate change might cost as high as 5–20% of the global gross domestic product (GDP) per year [36]. Specially, developing countries like Africa may face more difficult situations with the GDP losses as high as 26.6% per year [38]. Instead, taking action might cost 1% of the global GDP per year [36]. So, it is from an economic point of view that worldwide investment is inevitable now for the drawdown of GHG emissions and fossil fuel utilisation by alternative approaches to energy production that could potentially arrest the current climate trend.

Energy demand and consumption

Energy is the crucial and fundamental element for the global civilisation. There is a close and firm relation among the energy supply, national and international security, human basic needs and economic growth and the ecological pollution. Hence, energy is a complicated issue now, while the global energy demand continues to rise. Energy, as a production input or as a direct component of human well-being, is the key component of economic development. Its uninterrupted supply with increased global demand continuously poses a significant challenge to society. The global energy demand may rise by 30% within 2035, driven by emerging economies such as China, Brazil, Russia and India [39]. But the demands are fulfilled mainly by fossil fuels. The ongoing fossil fuel utilisation is posing a threat to the planet by emitting GHG [39]. Figure 4 depicts the energy consumption of different fuels in 2020, where it is seen that fossil fuels are dominating the energy regime. However, the pandemic Covid-19 causes global energy demand to decline by 4.5% in 2020, which is the biggest fall since World War II [39].

The downfall in demand in 2020 did not influence all fuels evenly. Oil was the hardest hit, with restrictions on transport resulting in demand dropping by a remarkable 9.3%—the biggest drop in history [39]. However, the oil demand bounced back by 5.7 mb/d in 2021 [40], which is faster than any other fuel. Coal demand declines globally by 4% in 2020, but the coal utilisation for power generation in advanced economies dropped down by 15%, more than a half of coal's global decline.

Low power demand increased renewable power generation and low gas prices squeezed coal utilisation in power generation. However, coal demand rebounded strongly in 2021, although with vast, diverse geography [39]. In contrast, natural gas showed far greater resiliency in 2020, with demand dropping only by 2.3%. Due to low prices and rapid growth in economies across Asia and the Middle East, in 2021, global gas consumption rebounded by 4.6%, the most substantial rebound among all fossil fuels and double the decline that occurred in 2020 [41]. In 2020, the low gas prices caused a gas generation to obtain a share in the US power market as well as sustain in the European Union (EU) [39].

Global power consumption experienced a smallest drop, 0.9% in 2020. Despite the drop in overall power

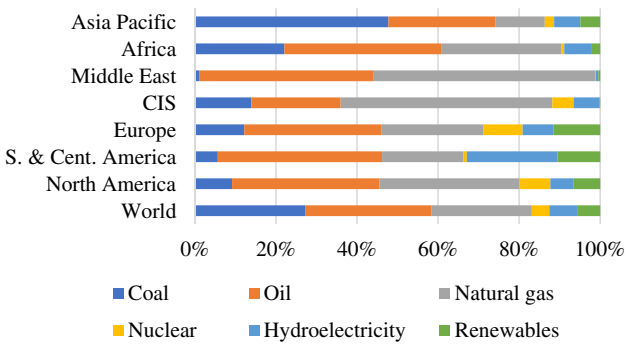

Fig. 4 Global energy consumption by fuel in 2020 [39], note: CIS-Commonwealth of Independent States

consumption, renewable generation (wind, solar, geothermal energy, bioenergy, and excluding hydroelectricity) boomed to 358 TWh, the highest ever increase. This achievement was gained by the strong growth in both wind (173 TWh) and solar (148 TWh) generation. The continued deployment of renewables including power demand falls hurt coal utilisation in 2020, losing competitiveness especially in the USA and EU. However, 'more than doubling' in the wind and solar power generation over the last 5 years has not made even a tiny dent in total coal production. Essentially coal production level in 2020 was unchanged from that's level in 2015, since last year's decline just counterbalanced the previous few years' increments [39]. Although the continued deployment of renewable, it cannot keep up with the rising demand. The world will need more than a just strong growth in renewable energy to banish coal from the power sector. It is still long to put coal out of the power sector.

Global power demand rebounded strongly in 2021, boosted by more than 6%. 2021 have experienced the biggest ever annual rise, over 1500 TWh [42]. Coal served more than half of the additional demand in 2021, raising in absolute terms faster than renewable energy for the first time since 2013. Global power demand is expected to grow by around 3 to 4% in 2022, 2.6% in 2023 and above 2% in 2024 [42], as energy efficiency measures start showing effects. However, fossil fuel-based power generation may grow by 0.2% annually from 2022 to 2024, but still is expected to serve 58% of total power generation in 2024, with coal-based power generation to serve 34% in 2024 [42]. Hence, the world will be still affected by fossil fuels including GHG increment in the upcoming years.

The increment of GHG should be minimised as soon as possible to avoid severe ecological damage [43]. Therefore, time is crucial now and an urgent energy transition is pivotal. The German Advisory Council on Global Climate Change [44] has drawn attention to the energy transition that it could benefit a double dividend: 'Not only will it prevent a fatal degradation of the global environment, but it could also create the basis for a new economic dynamism, with positive effects on employment, prosperity and equity'. To narrate it more pointedly, there are many indications that the renewable energy transition is an opportunity to reshape the prevalent energy regime to sustain the natural life support system, which will rescue the global economy. Decarbonisation is at the centre of the path of transition towards sustainability to battle against climate change, which can be succeeded by massively expanding renewable energies while giving access to modern energy for the billions of people living in energy poverty.

The remote communities of FNQ are leading their lives in a very unsustainable way. Currently, for their basic energy needs, they are heavily reliant on the diesel generator [3] which is associated with limited resource diesel including higher, unstable fuel prices [4] and greenhouse gas emissions, damaging the biota including trees, vegetation and marine lives. In addition, the diesel fuel must be shipped by truck or ship to the remote areas. Fuel reservation on-site is necessary in case of higher power demand than expected or the area being cut-off by any weather event. Therefore, this worse situation underscores the requirement for developing a new energy system with the minimal environmental impacts. By utilising hybrid renewable energy systems at isolated locales, remote communities can minimise their power costs and can have a more secure and consistent power supply with diminished carbon emissions because of no or less diesel.

FNQ region, with an area of 380,748.3 square kilometres [45], is one of the most attractive tourist destinations in Australia. The region has a number of World Heritage Sites, including the Great Barrier Reef, the Wet Tropics of Queensland and Riversleigh, Australia's largest fossil mammal site [33, 46]. But climate change, mainly due to the use of fossil fuels, is exacerbating extreme weather events that threaten FNQ's unique features and tourism industry [33].

Literature review

Renewable resources

Energy resources are categorised into three types: (1) fossil fuels, (2) renewable and (3) nuclear. Renewable resources are non-depletable sources that emit very low or no greenhouse gases. A superabundance of renewable resources exists, namely: wind, solar, hydro, biomass, geothermal, tidal and ocean—all these resources are vastly available and easily exploitable in Australia's geographical and political context. Solar and wind power generation have been proved to be the most logical and easily harvested option of all renewable resources available. Solar is vast, and the globe receives solar irradiation on an average 1.6 MWh/m^2, which is potent to fulfil the annual world energy requirements [47].

The red sea regions including Saudi Arabia and Egypt are receiving the highest amount of solar irradiation, while Australia and the USA receive above average solar irradiation [49]. Figure 5 reports that the largest solar radiation greatly blesses the north-west and central regions of Australia. Australia is receiving on an average 35 megajoules per square metre per day or 58 million petajoules per annual of solar irradiation (around 10,000 times Australia's annual energy consumption), the world's highest solar radiation [50]. There is also notable solar potential in areas with access to the electricity grid. The annual solar irradiation fallen onto the areas within 25 km of existing transmission lines is around 500 times larger than the yearly Australian energy consumption [50].

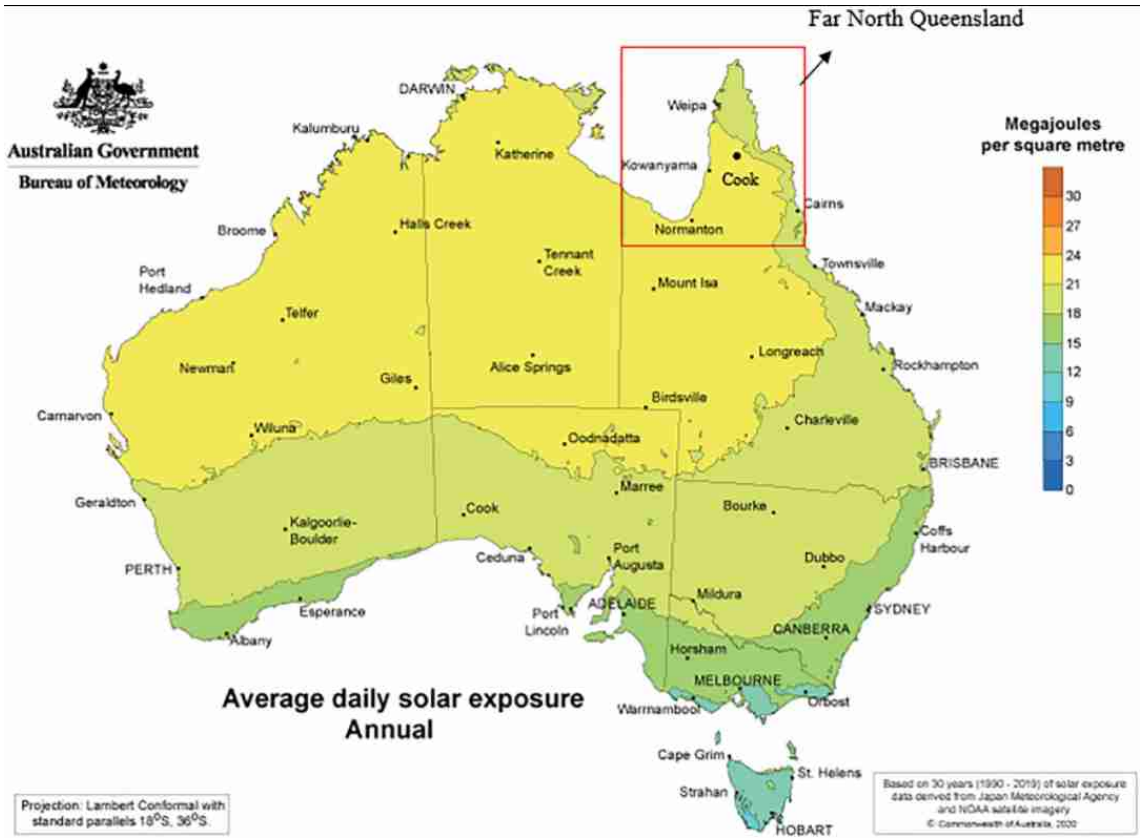

Fig. 5 Australian average daily solar exposure [48]

With the prospective and rapid growth in solar energy exploitation, wind energy is the fastest-growing source in Australia. Australia is one of the best continents in the world for having high wind resources that primarily are located in south-western, southern and south-eastern regions and extending hundreds of kilometres inland and including highland areas in south-eastern regions [51, 52]. Wind has already been proven as one of the least-cost power options. Small-scale wind turbines are sufficient to serve the remote community power needs, as well as large-scale wind farms could be a feasible option instead of fossil fuels [53].

Hydropower has been utilised for 135 years to convert the energy of water to electrical energy. Hydropower was developed in Australia in the nineteenth century within the areas of high rainfall and elevation such as Tasmania and New South Wales. Hydropower, including installed capacity of 8790 MW, is the 2nd largest renewable resource in Australia, and Australia is the world's fourth-largest producer of hydropower [54]. However, Australia's hydropower development trend is relatively slow due to a notable lack of viable on-river locations, variable annual rainfall, high temperature, very high evaporation rates [55].

Ocean renewable energy from ocean waves, tidal and ocean currents, has significant potency in Australia. The first ocean power patent was reported in Australia in 1909; after that the twenty-first century has seen significant government investment and private venture capital-funded developments [56]. Australia's wave energy resource is the most significant source on earth [57]. Australia's best wave energy resources are located along the southern and western coastlines. The total wave energy on entire Australia is on average, approximately 3.125 petajoules (PJ) [57], and it could meet a maximum of 11% of Australia's total energy demand by 2050 [58]. Australia also has good opportunity to exploit mechanical energy from tides, current and waves, and ocean thermal energy from the sun's heat. The Australian government has funded projects aiming to make this inborn energy as a major contributor to the country's energy mix by 2050. The Australian Wave Energy Atlas (as shown in Fig. 6) is one of the first outputs of this agenda which forms the Australian Renewable Energy Mapping Infrastructure [59]. However, ocean energy technologies are relatively new and still need to be proven in pilot and demonstration plants. Also, these technologies are significantly more expensive than other, more mature forms of variable renewable energy.

Australia has notable hot rock geothermal resources, capable of producing superheated water or steam suitable for base load electricity generation. There are also

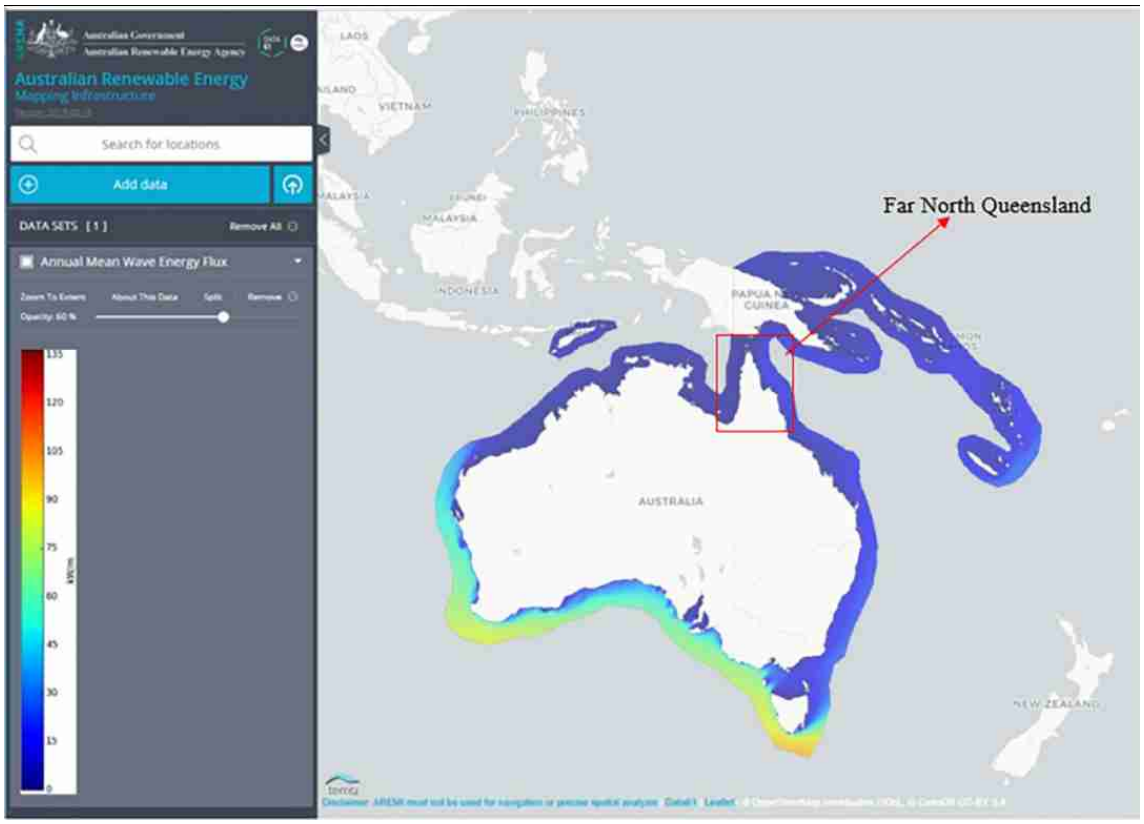

Fig. 6 The Australian wave energy atlas, displaying the annual mean wave energy flux (in kW/m) and the Australian Renewable Energy Mapping Infrastructure (AREMI) [59]

potential lower temperature geothermal resources in a number of sedimentary basins for power generation or direct-use applications.

The global electricity energy value chain and emerging hybrid renewable energy systems

The electricity energy value chain comprises all functions required to generate, distribute and consume power. Figure 7 presents the electricity energy value chain, which can be segmented into five major parts: fuel procurement, electricity generation, transmission, distribution and end user [60]. Due to the irresistible challenges of increasing power demand, depletion of fossil fuels, the emergency for decarbonisation and power accessibility, the energy communities [4] are reshaping the energy value chain:

(1) A paradigm shift-decentralised or distributed generation network has appeared as an alternative to highly centralised architecture; decentralisation is observed and reflected through the envelopment of micro-grids which comprise distributed renewable resources, battery storage, load and controlling systems;
(2) The deployment of hybrid integrated renewable energy system is continuously increasing for maximising the usage of locally distributed and dispersed renewable resources;
(3) The scope of hybrid energy system for grid connection or Power-to-X applications.

A hybrid energy system constitutes more than one energy source: either renewable or non-renewable sources so that one source being unavailable can be substituted by another available sources to ensure sustainable power supply. This is a worthy option to meet the power demand from locally available energy sources for regions where grid extension is expensive or power transmission from centralised utility is difficult. Utilising only locally available renewable resources to provide power is a sustainable option for human beings. A hybrid system constituting only renewable resources has benefits where fuel cost inclines, fuel transport is expensive, and globe's ecological system is worsening. But due to the unpredictable, seasonal and time-dependent natures, renewable resources are not entirely reliable options. In this regard, including an energy storage system is one kind of approach for hybrid systems [61].

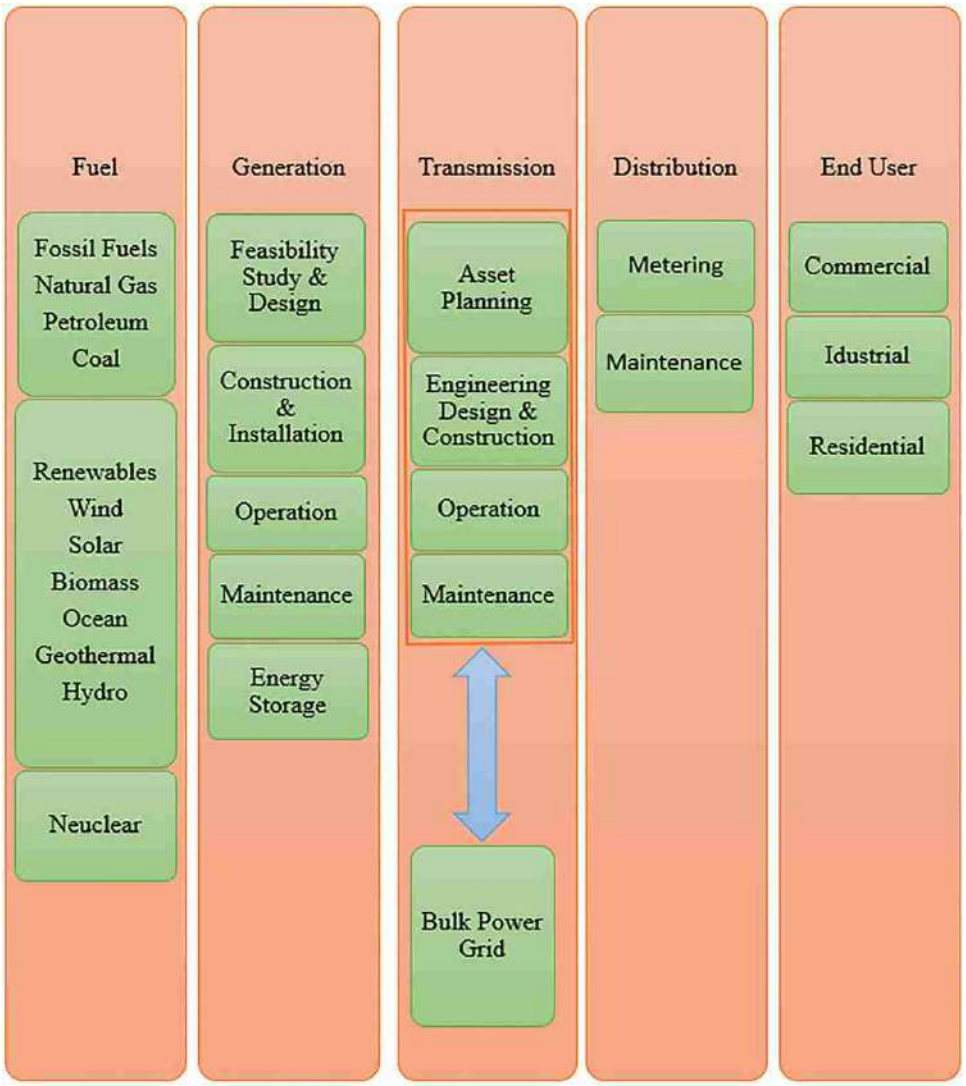

Fig. 7 The electricity energy value chain [60]

Solar PV is dominating in off-grid installation among all renewable systems [62, 63]. Lower maintenance and more straightforward implementation make PV a common and more suitable option in many off-grid applications [64]. Along with the PV, wind power has already shown itself as a very low-cost and promising option. Albeit solar PV and wind can supplement each other to handle intermittent nature and can enhance overall reliability [65], an energy-storing stuff, such as batteries, ultra-capacitors and fuel cells, is normally an essential option to manage renewable intermittency, enhance energy efficiency and assure secure and good-quality power supply [66, 67]. Diesel generators are sometimes used as back-ups to reduce power loss probability in off-grid hybrid systems [68, 69].

Widespread implementation of solar and wind energy generation system accredits to the global reachability of these resources and naturally complements characteristic of solar and wind resources. Research regarding complementing effects of different renewable resources has been conducted in recent studies [70, 71]. In addition, integrating hydro [72, 73], geothermal [74], biomass [68, 75, 76] and tidal [77] energy resources alongside solar and wind resources, instead of diesel generator, which is related to higher fuel and maintenance cost, have been suggested in recent research work. Recent research indicates that HRES can be implemented not only in remote areas or in off-grid conditions such as sites away from the national grid or at satellite earth stations [78], but also in a grid-connected conditions or Power-to-X applications such as direct charging of electric vehicles (EV) [79], renewable hydrogen generation [80], chemical production [81], desalination [82, 83] and multi-generation [84].

Hydrogen: a new opportunity towards the decarbonisation

The ecological damage due to global warming and excessive energy needs has put unprecedented pressure on the world to seek clean alternative energy options. The most important and immediate factors to be considered in seeking alternatives are their prospective curtailment of high levels of GHG and other emissions hazardous to the ecosystem. Clean renewable energy sources have become a global concern in this context. Recently, along with the available renewable resources, hydrogen is regarded as the major option in this sustainable journey of seeking. Hydrogen has far reached significance for energy security, emission mitigation and green economic development.

Theoretically, hydrogen could be imagined as an infinite supplement, if renewable energy is implemented to generate hydrogen through water electrolysis and then discharge the chemical energy through the reaction of hydrogen gas and oxygen gas to water. It is the greatest attraction of hydrogen to be present in water, which covers about 71% of globe's surface [85]. If hydrogen can be generated from water economically, it can be a future energy provider as well as can concurrently diminish emissions in various sectors such as the power sector, transportation and industry [86]. Moreover, compared to solar, wind and geothermal resources, which have limitation of their own volatile and intermittent nature, hydrogen with no toxic emissions and greater energy content (higher energy density: between 120 and 142 $MJkg^{-1}$, around 3 times greater than fossil fuels) can be an excellent option for future energy systems [10, 11, 87].

The world was experienced energy transition a long time ago. Wood was the main source of energy since several 1000 years ago. The usage of coal did energy transition to fossil fuel, while the industrial revolution happened in the eighteenth century [88]. Then the transition from coal to petroleum occurred by 1930. The invention of the internal combustion engine accelerated oil utilisation, which peaked in 2000 to meet the world's energy needs. Since 1970 natural gas utilisation enhanced gradually and is hoped to reach a climax by 2050 [88], when the hydrogen energy carrier may take the global lead in fulfilling energy needs. However, shifting from one fuel to another has not wiped out the previous ones; rather, their exploitation has been superimposed with much higher amounts. Wood, coal, oil and natural gas are providing energy concomitantly and recently in complement to that modern windmills and solar PV are supplying energy also.

A noticeable fuel transition has happened. Wood contains more complex chemical structure and lower specific energy (20.6 $MJkg^{-1}$) than coal (23.9 $MJkg^{-1}$) [89]. Similarly, coal has more complex chemical structure and lower specific energy than oil (45.5 $MJkg^{-1}$), which continues this trend with natural gas (52.2 $MJkg^{-1}$) [89]. Additionally, this shifting seems to be the continual decarbonisation of fuels. Because, the carbon quantity declined from wood to coal, to oil, to natural gas. It is also surprising that the hydrogen quantity enhances continuously from wood, to coal, to oil, to natural gas, ultimately to arrive at the perennial, carbon-free hydrogen.

Figure 8 depicts the trend towards the decarbonisation of the global energy supply, from one based on mainly carbon to one that is based on hydrogen. This trend reflects the hydrogenation of the global energy supply, which means the global movement towards the hydrogen energy carrier. It is noteworthy that clean hydrogen or ammonia has no relation with any carbon emission.

The transition to the hydrogen energy era has already been started worldwide with marked participation of renewable resources. Australia is not out of this hydrogen race. Clean hydrogen production at low cost is one of the priority stretch goals under the Australian government's 2020 Low Emissions Technology Statement [94]. FNQ needs clean, versatile, flexible, storable and safe fuels to support the energy needs with mitigating carbon emissions. Hydrogen possesses all of these features. When hydrogen is generated using renewable energy through water electrolysis, and fuelled into fuel cells to generate power, it produces only water, with no carbon emissions [11]. In addition, renewable energy's inherent intermittency can be complemented well by the production and storage of hydrogen. Thus, hydrogen can be a mode of reserving renewable energies for utilising at a later time when it is required, resulting in a yearly, renewable and sustainable circular cycle. Storing hydrogen can act as a buffer for enhancing the resiliency of the energy system of the remote parts of FNQ, thereby stabilising the regional electrical network. Eventually, utilising renewable resources to produce hydrogen is of immense potential for

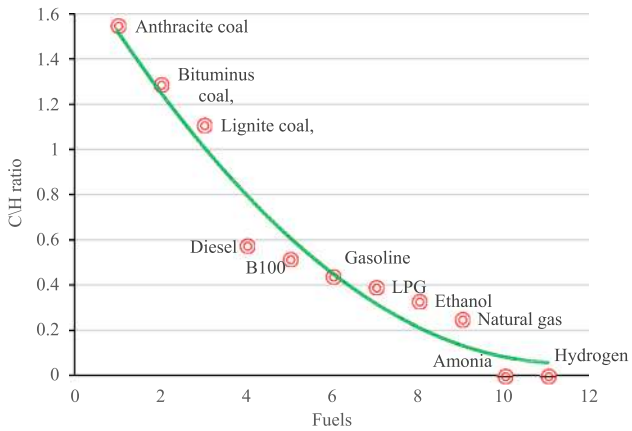

Fig. 8 Carbon/hydrogen ratio of common fuels [89–93]

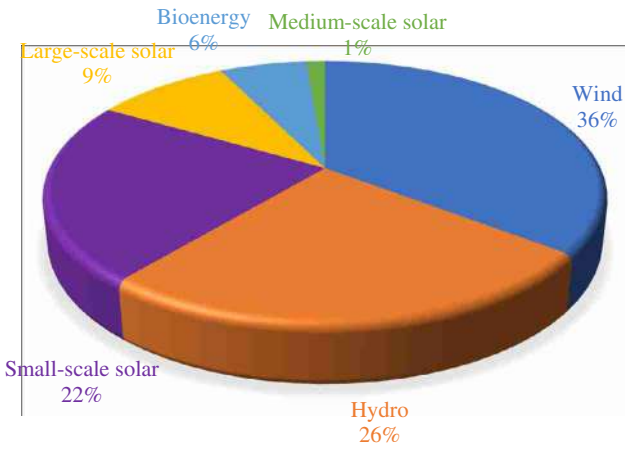

Fig. 9 Renewable energy generation in Australia by different technology [52]

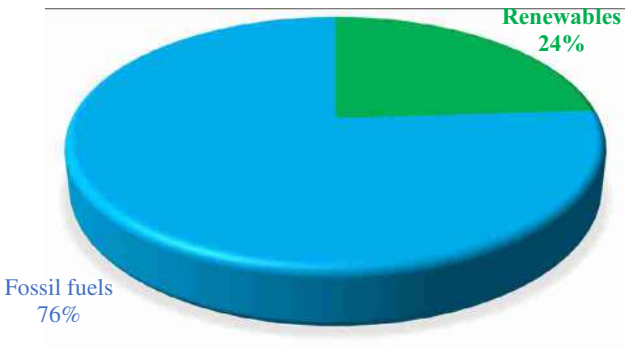

Fig. 10 Total electricity generation in Australia in 2019 [52]

the remote parts of FNQ, with their own local specificities in terms of raw materials and energy sources.

Renewable energy generation in Australia

Australia has a rich, diverse renewable resource ranging from solar, wind, bioenergy, geothermal to ocean energy. The exploitation of solar and wind energy has been increasing since 2010 and continues rapidly. Before 2019, hydro energy was the most significant generator of renewable electricity among all renewable resources. In 2018, hydro energy provided 35.2% of generation (17,002 GWh) of total renewables. 2019 is the best year for wind, which has taken over the mantle as Australian's clean energy leader, accounting for 35.4% renewable power generation (as shown in Fig. 9). Australia has demonstrated record in 2019, that renewable power generation accounts 24% of total electricity generation (as shown in Fig. 10), an increase of 2.7% on 2018 [52].

The completion of the Large-scale Renewable Energy Target (LRET) was the largest achievement for 2019, which is more than a year ahead of the 2020 deadline. Australia has attained the LRET in September 2019 following the 148 MW Cattle.

Hill Wind Farm [52]. This remarkable milestone has transformed renewable energy from one of the most expensive energy generations to the cheapest. The contribution of different renewable sources to national power generation is presented in Table 1.

Australia has six states: New South Wales, South Australia, Tasmania, Victoria, Queensland and Western Australia with two mainland the Australian Capital Territory and the Northern Territory. Figure 11 illustrates the contribution of renewable generation to supply consumers in each state in 2019.

Tasmania is in the leading position for using renewable energy with a penetration level of 95.6%. Due to the shutting down of Northern coal-fired power stations [95], renewables provide 52.1% of South Australia's electricity, special thanks to hydro and wind energy. Still, Queensland has the largest fossil fuel power generation and is very low in renewable generation, while Tasmania has the biggest total renewable generation [95].

Renewable energy potential in FNQ

Queensland is the fastest-growing and most energy-intensive state in Australia. The GHG emissions in Queensland are

Table 1 Power generation by renewable resources in Australia [52]

Resources	Generation (GWh)	Percentage of renewable generation (%)	Percentage of total generation (%)	Equivalent number of households powered over course of the year
Wind	19,487	35.4	8.5	4,240,013
Hydro	14,166	25.7	6.2	3,082,150
Small-scale solar	12,269	22.3	5.3	2,669,440
Large-scale solar	5141	9.3	2.2	1,118,596
Bioenergy	3314	6.0	1.4	7,21,005
Medium-scale solar	716	1.3	0.3	155,867
Total	55,093	100.0	24.0	11,987,070

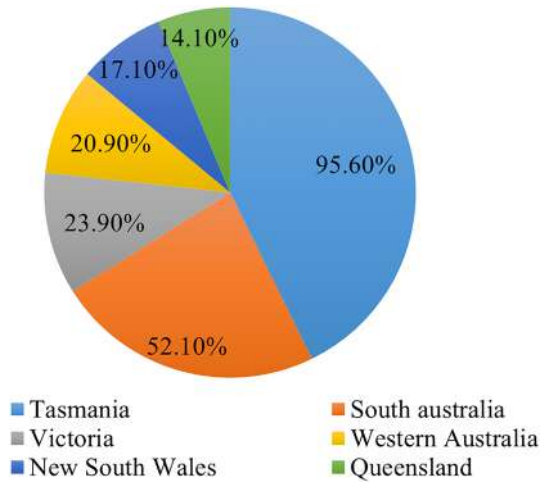

Fig. 11 Renewable power penetration in Australia by state in 2019 [52]

approximately 43 tonnes per capita, greater than that in any other state [96]. With the strong growth in power demand, Queensland is facing the challenge of mitigating the rise in GHG emissions. Because of the vast geographical area and highly decentralised population, Queensland faces challenges in ensuring cost-effective and reliable power supply to remote and sparsely populated regions [96]. The remote parts of Queensland still meet their power demand by mainly the diesel power generation, which needs fuel with fluctuating prices and maintenance. Renewable energy could be an option in addressing all these challenges, and FNQ has a vital role to play in this regard.

The FNQ has a powerful combination of solar, wind, hydro and bioenergy resources. The region has dozens of sites suitable for off-river pumped hydro to store and release clean power on demand. Solar and wind farms in FNQ can generate 20–50% more electricity per unit than most other countries. Even wind generators in the region often can be operated at times when southern wind farms are idle [97]. However, hydropower plants have geographical constraints including harmful dams for marine species. Biomass resources are not entirely green as they emit some GHG. They are also associated with transportation and processing costs. On the other hand, solar and wind have less impact than hydro and biomass.

In this study, the main concern is about the remote areas of FNQ such as Cook shire, Doomadgee, Burke, Pormpuraaw, Northern Peninsula, Umagico, Mapoon, Torres shire, etc. There are some renewable solutions including community-scale solar PV in few remote parts such as Doomadgee, Mapoon, Pormpuraaw, the Northern Peninsula Area, but diesel power generation is still dominating in the remote areas of FNQ [3]. These areas are full of abundant solar and wind resources. Solar irradiation and wind speed are considered high in these regions which is the proof of potency for the development of renewable energy systems, that can replace the present diesel power generation system [3].

Assessment of solar and wind resources

Climatological potential

Solar irradiation in Central and North Queensland including FNQ can be considered as one of the highest amounts in the globe, only the Northern and the Southern African desert and the Southwestern United States receive a comparable amount [98]. The combined sunny climate and latitude of FNQ exhibit potentiality for solar electricity generation. Any area receiving solar irradiation of greater than 4 kWh/m^2/day can be geographically potential for harnessing solar energy [99].

FNQ receives average daily solar irradiation, that is greater than 5.5 KWh per square metre per day [98], more than enough with annual average daily sunshine hours of 7 to 8 (as shown in Fig. 12). Figure 13 presents monthly mean daily global horizontal irradiation for some selected remote areas of FNQ, which varies between 4 and 7.5 kWh/m^2/day [101], which is the proof of FNQ's promising potential to harness solar energy. It is also seen that Mornington Island has peaked in November recording 7.3 kWh/m^2/day, followed by Cook at 7 kWh/m^2/day, Lockhart at 6.8 kWh/m^2/day and Burke at 5.9 kWh/m^2/day. On the other hand, Aurukun, Carpentaria and Kowanyama have recorded a maximum of 7.2 kWh/m^2/day in October, followed by Doomadgee and Pormpuraaw at 7.1 kWh/m^2/day, Napranum and Torres shire at 7.0 kWh/m^2/day, Mapoon and Northern Peninsula area at 6.7 kWh/m^2/day.

Similarly, wind resource in FNQ is another potential option for power generation, with annual average wind velocity at 80 m above ground level ranging from 5.6 to 10 m/s (as shown in Fig. 14). Previous studies considered the minimum mean daily wind velocity 4 m/s [103] and 5 m/s [104] for installing wind farm. In addition, the mean operational cut in velocity for the Vestas V117-3.45, horizontal axis wind turbine, which is used in Mount Emerald wind farm in Arriga (FNQ), is 3 m/s [105, 106] and this indicates that FNQ is the best suited to wind energy.

Geographical potential

Suitable place identification to install solar and wind farm is a complicated task. Moreover, issues such as meteorological needs, ecological concerns and financial gains, also need to be considered for plant installation and operation [107, 108]. Area with the abundant resources such as solar irradiation

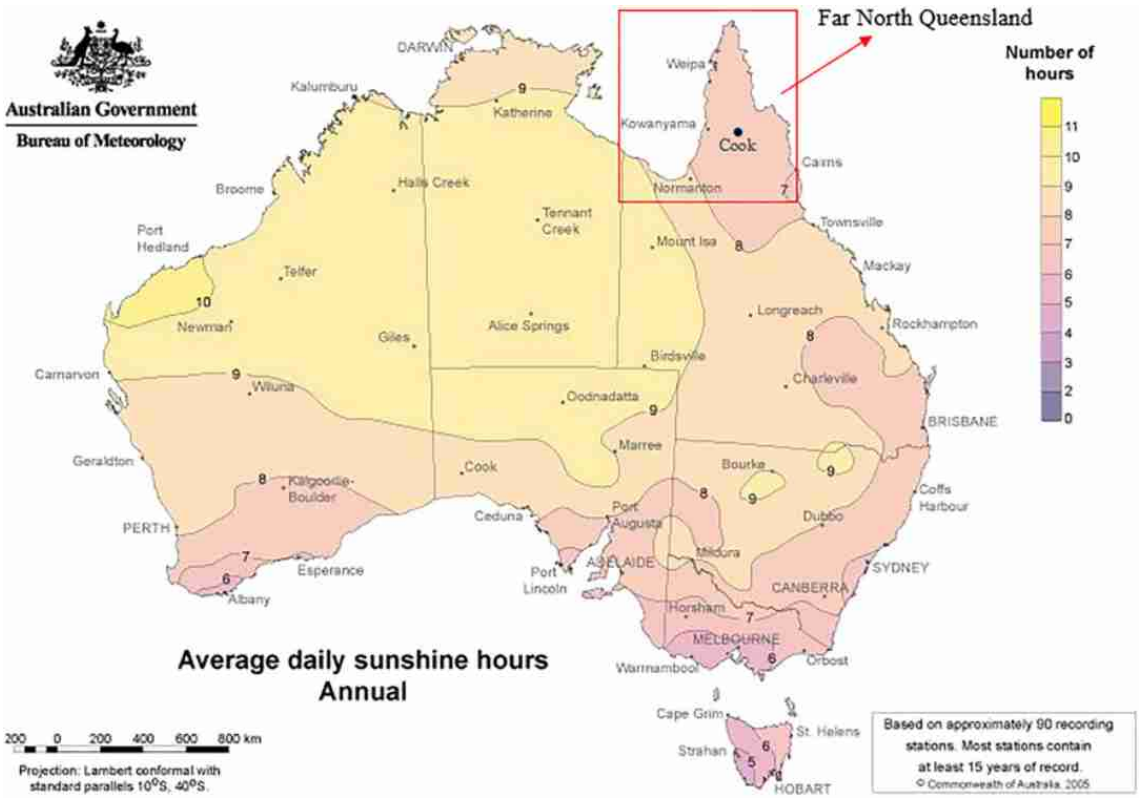

Fig. 12 Annual average daily sunshine hours in Australia including FNQ [100]

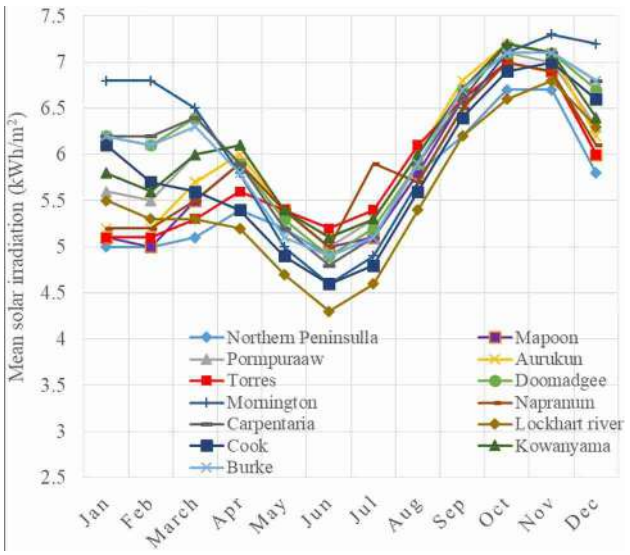

Fig. 13 Monthly mean daily solar irradiation in selected regions of FNQ [101]

and wind velocity may not be the only feasible thing. Some other factors that can also be crucial for the evaluation of suitable places, such as social, economic and environmental constraints [109, 110]. Recently, Geographical Information System (GIS) has appeared as the most convenient and proficient tool, and is being employed by many countries for assessing renewable energy potentiality [111, 112]. GIS tool can digitise, convert, analyse and visualise spatial data [113]. GIS can handle a range of environmental, financial, social and regional aspects for planning renewable energy development. It has inbuilt abilities to investigate the territories, generate and sort data, capture the geographical information, manage commands and visualise the output [113]. GIS data give an appropriate path to ascertain a suitable place considering location-specific circumstances (social and environmental limitations and resource availability) [114–116]. GIS includes various built-in tools; the present study principally utilises data management, conversion and spatial analysis tools. In this study, to perform GIS-based analysis, several remote areas from FNQ have been selected, namely Cook, Carpentaria, Burke, Doomadgee, Mornington Island, Kowanyama, Pormpuraaw, Aurukun, Injinoo, Torres, New Mapoon, Umagico, Mapoon and Lokhart river.

All topographical data are extracted from different digital databases that are given in Table 2. Unsuited locations have been omitted utilising different tools of ArcGIS. Firstly, data management toolbox is used to make projection of all GIS data layers (vector and raster) on a similar coordinate system, project tool for vector data and project raster tool for

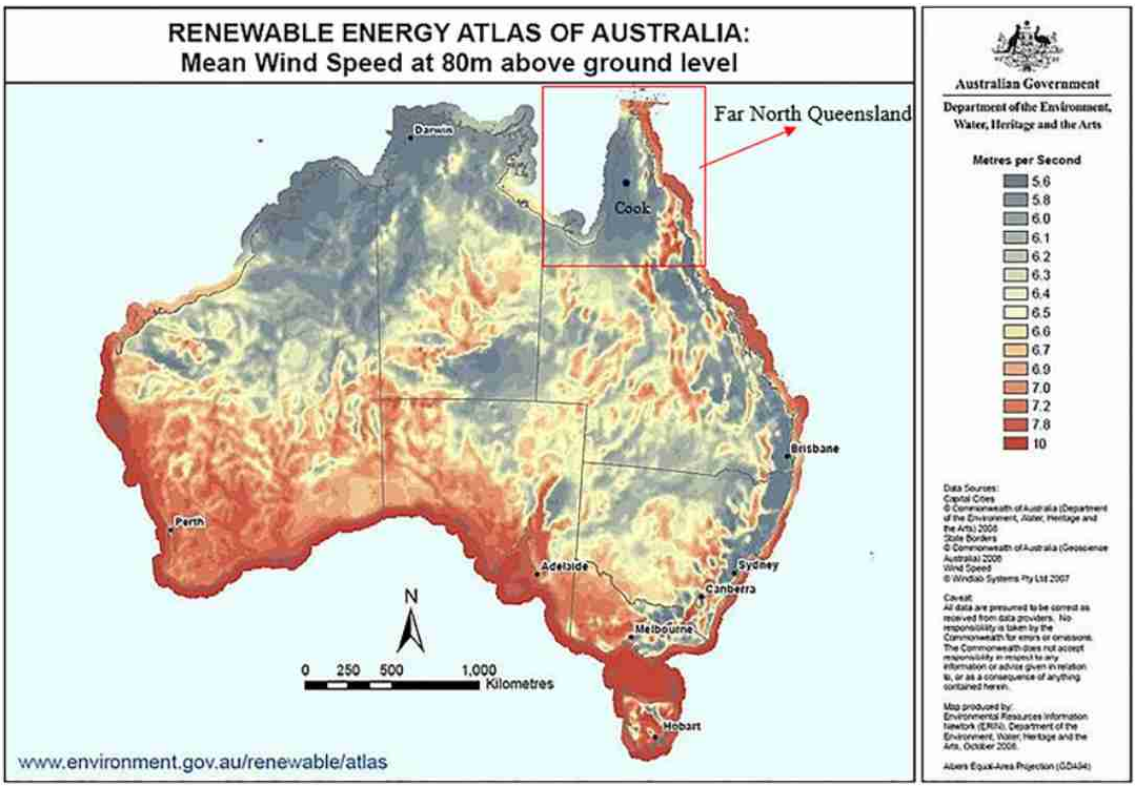

Fig. 14 Mean wind speed at 80 m above ground level in Australia including FNQ [102]

Table 2 GIS data set for identifying suitable locations

Thematic theme	Type of data	Source	Spatial resolution
Administrative boundary	Vector	GADM, version 1.0 [117]	–
Water bodies	Vector	DIVA-GIS [117]	–
Protected areas	Vector	WDPA [118]	–
Airports	Vector	Data Share [119]	-
Urban built-up area	Vector	SEDAC [120]	–
Rail network	Vector	DIVA-GIS [117]	–
Road network	Vector	DIVA-GIS [117]	–
Land-use land cover	Raster	GlobCover [121]	10 arcsec
Digital elevation model	Raster	CGIAR SRTM [117]	30 s

raster data. Then different GIS activities have been executed for each layer to fulfil the renewable energy development criterion, as described below:

(1) Extraction of land cover and digital elevation models of selected areas of FNQ from the land-use land cover and global digital elevation models, respectively, by utilising Extract by Mask tool.
(2) Extraction of slope model from the elevation model by Slope tool.
(3) Reclassification of raster model of a slope by Reclassify tool.
(4) Identification of suitable and unsuitable land cover from land cover data by Weighted Overlay tool.
(5) Conversion of all raster models into vector data set by Raster to Polygon tool.
(6) Implementation of a suitable buffer by Buffer tool on each layer that further expands the omitting criterion according to the assumptions considered in this study and merging unsuited layers by Merge tool.
(7) Removal of merged unsuitable areas from the suitable land cover (vector data) by Erase tool.
(8) Finally, the Clip tool is utilised to extract the administrative boundary of selected regions with the aid of the

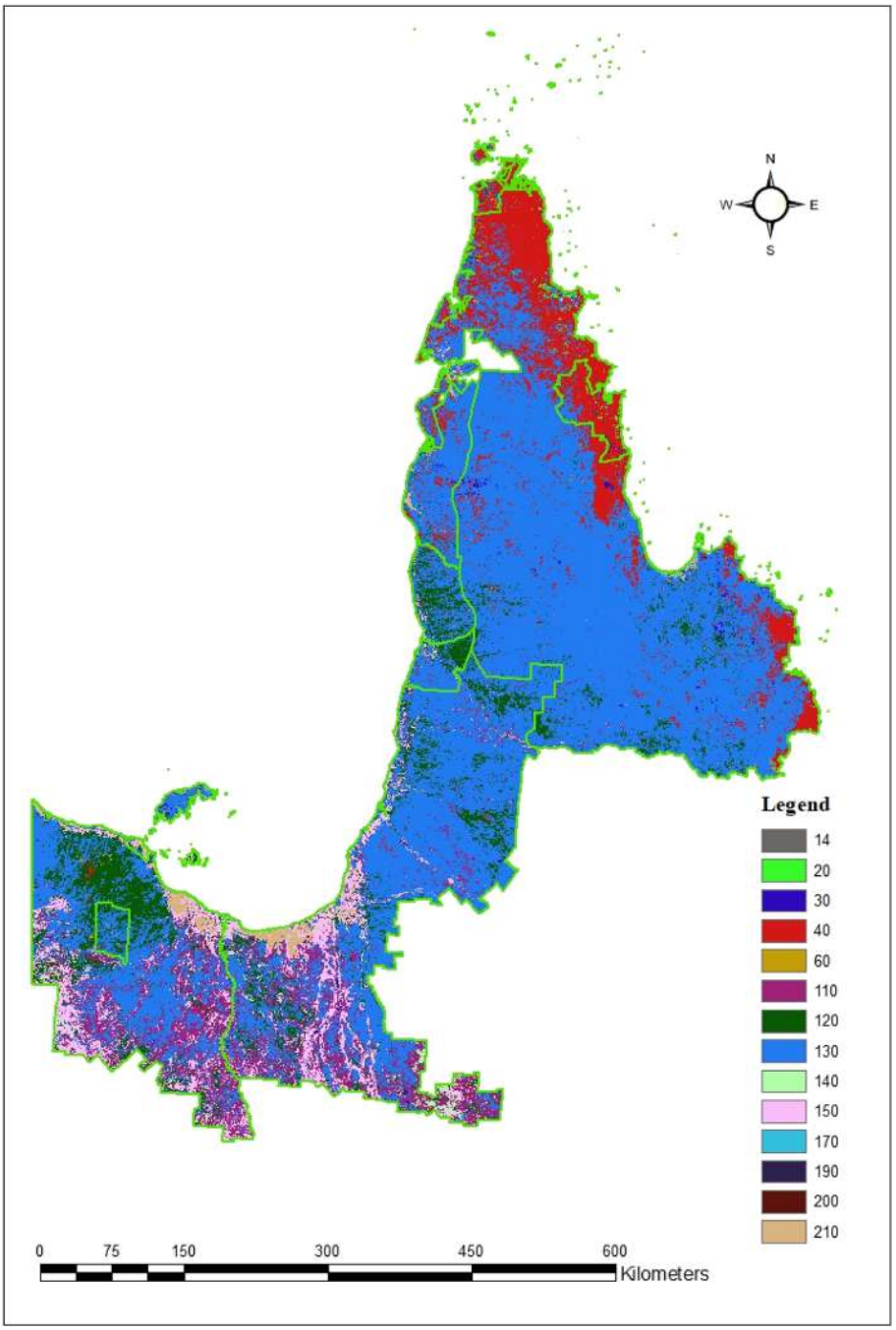

Fig. 15 GlobCover land-use land cover for selected regions of FNQ

administrative boundaries of Australia from the final suitable layer.

At last, the total suitable places for each administrative boundary of the selected regions are acquired by computing their geometry in the attribute table. Based on the appropriate land-use factors, the maximal limits of solar and wind power generation capacity are evaluated for each selected region that illustrates the geographical potential of renewable energy. Several exclusion criterion included for the assessment is outlined below:

(1) Land-use land cover (LULC): In this assessment, UN global land cover data are utilised. As per the criterion of a previous study [122], irrigated (class 11), rain-fed croplands (class 14), mosaic cropland (class 20), shrubland (class 130), grassland (class 140), sparse vegetation (class 150) and bare areas (class 200) are considered suitable for wind plants. For solar, similar

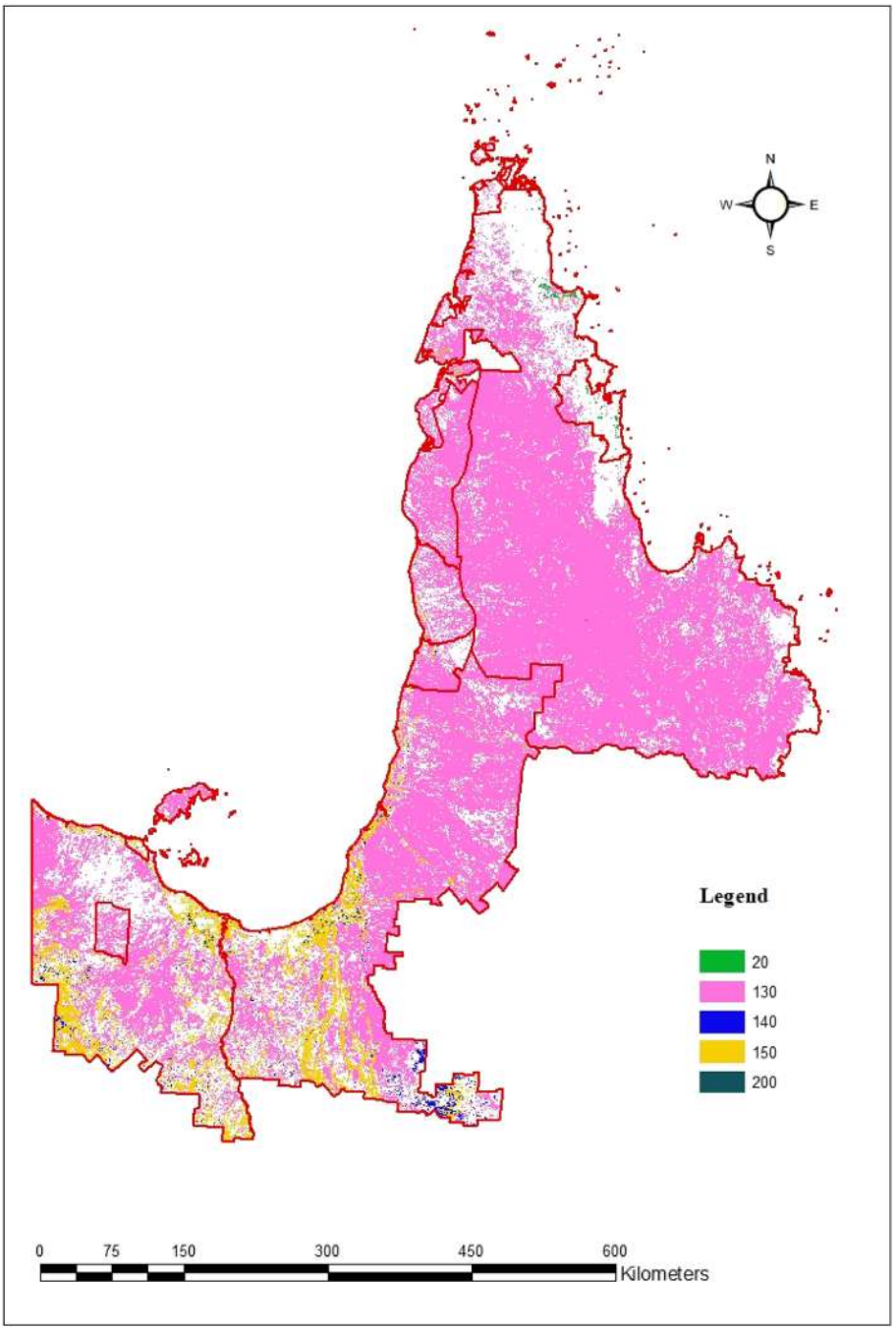

Fig. 16 Suitable land cover for solar in selected regions of FNQ

suitability criterion which is implemented for wind, is used, except irrigated (11), rain-fed croplands (14). Other land categories such as mosaic vegetation (class 30), broad-leaved deciduous (classes 50, 60) or semi-deciduous forest (class 40), needle-leaved ever green forest (classes 70, 90), mixed forest (class 100), mosaic forest (class 110) and grassland (class 120), woody wetlands (classes 160, 170), artificial areas (class 190), water bodies (class 210), snow or ice (class 220) are considered unsuitable for any power plant installation.

(2) Water bodies: In some studies, to conserve natural resources, reservoirs such as seas, rivers and lakes were omitted with a buffer of 100 m [123] and 400 m [109] for wind application; 400 m for both solar and wind application [103]. In this study, 400 m is considered for both solar and wind analysis.

(3) Protected area: Previous studies [124, 125] applied 1 km buffer for protected areas in wind application to preserve the protected areas such as world heritage sites, national parks and sanctuaries, which are not

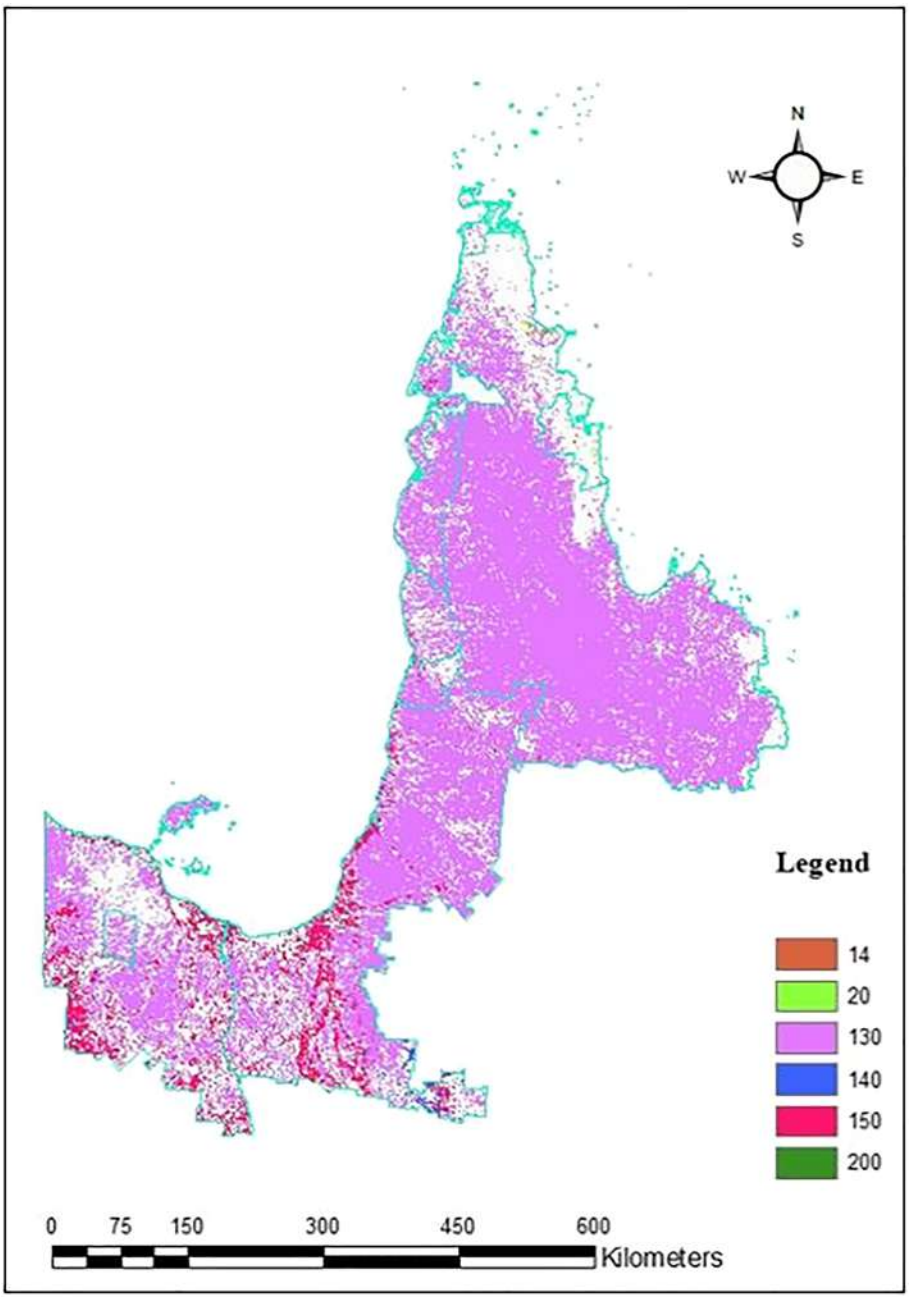

Fig. 17 Suitable land cover for wind in selected regions of FNQ

suitable for power plant installation. This study has adopted 1 km buffer for wind analysis.

(4) Urban and rural built-up area: In deploying renewable energies at a large-scale, densely populated and urbanised areas are not practicable for avoiding inconvenience to human life. Previous studies applied a buffer of 5 km [124] for wind applications, 500 m [126, 127] for solar and wind applications. This study has adopted 5 km buffer for wind analysis. And no buffer zone is applied for solar analysis.

(5) Rail and road network: Rail and road networks are not also practicable for renewable energy installation. Previous studies applied a 300 m [124] buffer to road and rail networks considering their future expansion and a 500 m [128] buffer for reducing visual disturbance and ensuring electrical safety. In this study, 500 m buffer is maintained with existing rail and road networks for solar and wind analysis.

(6) Airports: In some studies [114, 129, 130], distance to airport is used for wind analysis, as wind turbines may disturb air traffic control by muddling the airport surveillance radar signals. Previous studies have implemented a buffer of 2500 m [104, 123] and 3000 m

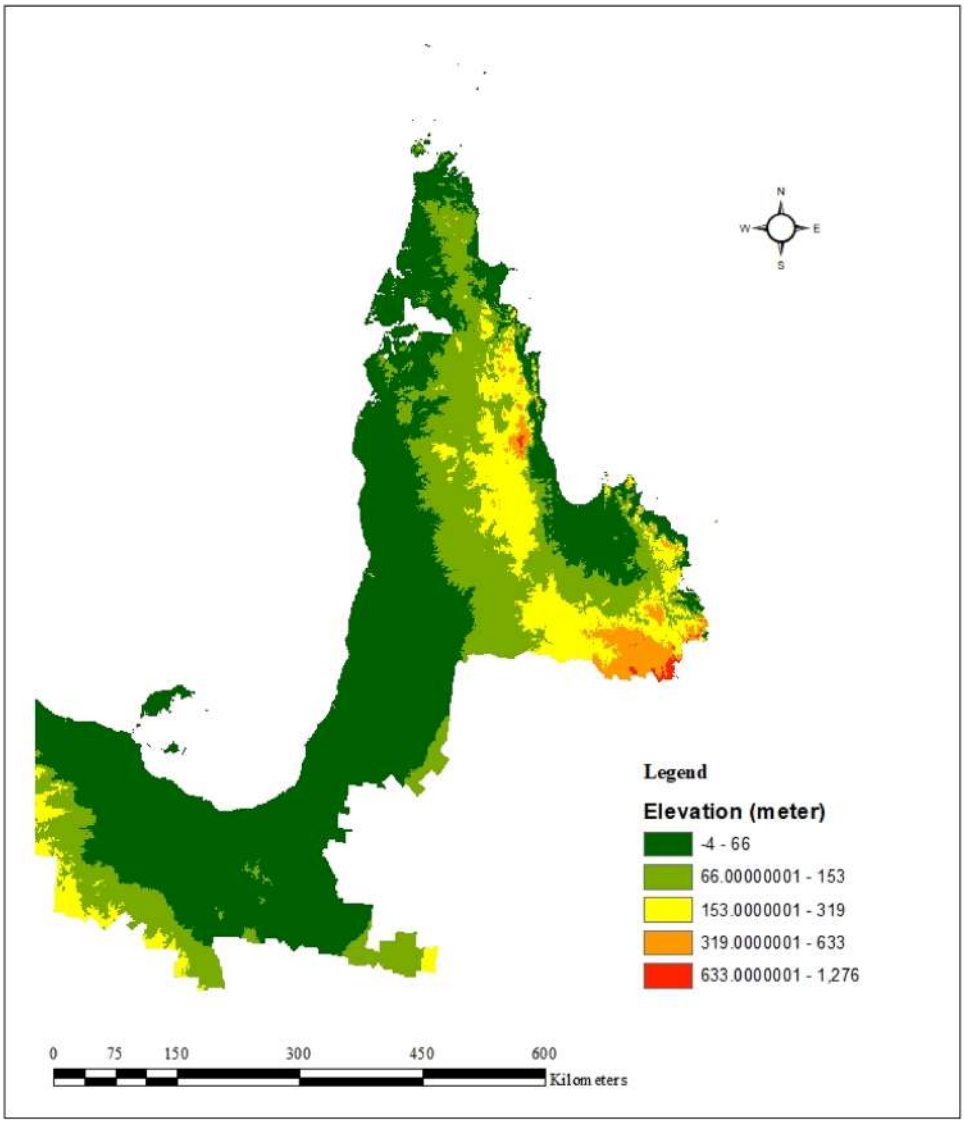

Fig. 18 Elevation of selected regions of FNQ

[129], and in this study, 3000 m is considered as a safer option.

(7) However, consultation is inevitable for installing any wind farm within a range of 30 km [131] of an airport. In the case of solar, glimpse and glint [132, 133] from panels may mystify pilots' vision and may also affect the radar systems. Hence, a 1000 m buffer is applied between airports and solar plant for the present study.

(8) Slope and elevation: Slope and elevation are the elementals of topography. Almost all studies recommend land with low slopes and low elevations for developing solar and wind projects [114, 126, 134, 135]. For wind projects, the allowable range of slope may vary within 10 to 30 degrees [134] and for solar can vary between 3 and 5 degrees [126, 134]. The elevation above sea level varies from place to place, and previous studies proposed elevation of 2000 m for solar and wind farms [126, 136], 4500 m for solar farms [104], 2000 m for wind farms [128]. This study considers slope up to 5°for solar analysis and maximum 15° for wind analysis. From the slope map (as shown in Fig. 19), it is found that the selected regions of FNQ have maximum slope 14.82°. So, the slopes of the areas are fully suitable for wind power installation. Figure 18 represents the elevation of the regions. The maximum elevation is 1276 m, which is considered suitable for both solar and wind projects development.

Results

The current study is the first ever work to explore suitable locations in FNQ for the development of solar and wind projects using GIS multi-criterion decision making. ArcMap 10.8.1 is used for GIS-based analysis. The assessment

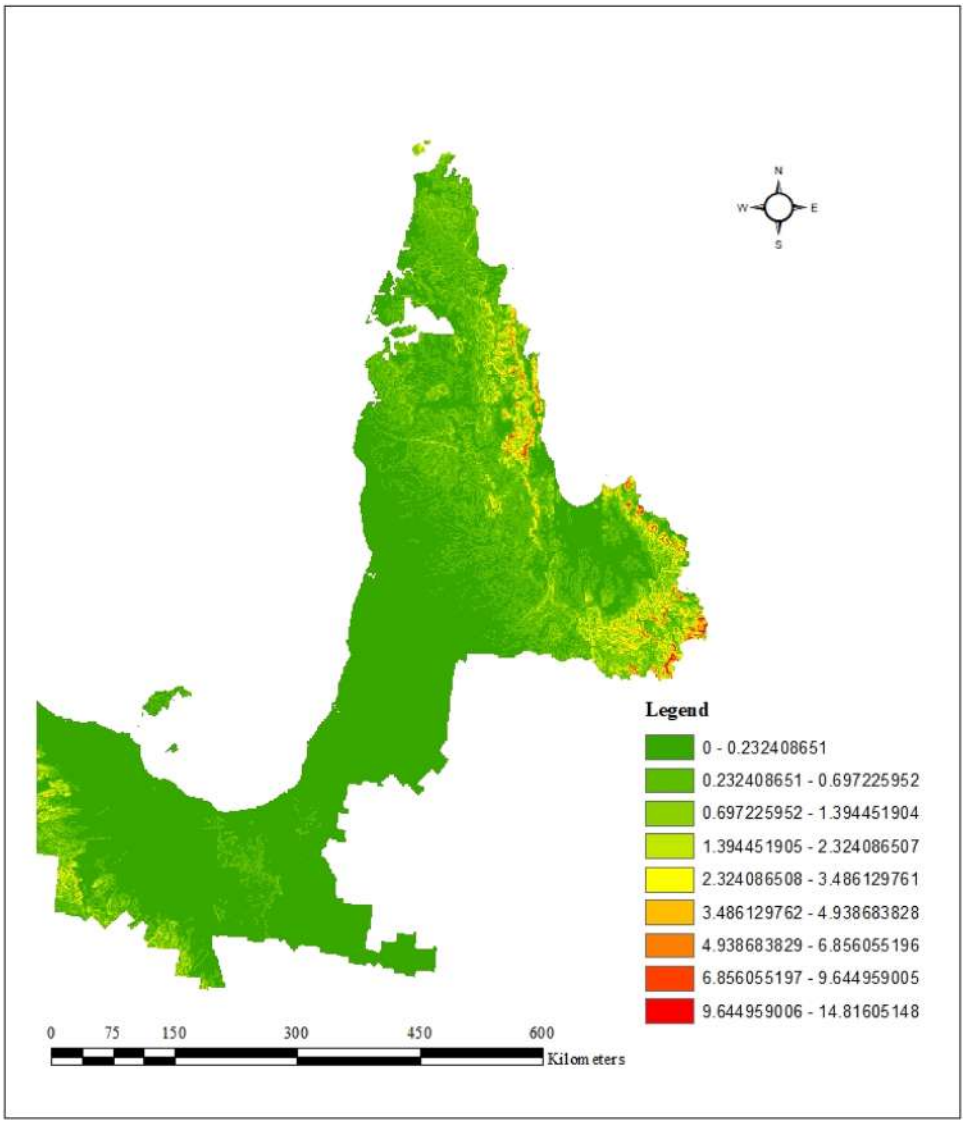

Fig. 19 Slope map for selected regions of FNQ

is conducted using GIS-based multi-layer approach. The outcome of different GIS activities executed for location suitability analysis, is displayed in Figs. 15, 16, 17, 18, 19, 20, 21. Figure 15 represents land cover information for the selected regions of FNQ such as classes 14 (rainfed croplands), 20 (mosaic croplands), 30 (mosaic vegetation), 40 (semi-deciduous forest), 60 (broadleaved deciduous forest), 110 (mosaic forest), 120 (mosaic grassland), 130 (shrubland), 140 (grassland), 150 (sparse vegetation), 170 (woody wetlands), 190 (artificial areas), bare areas (200) and water bodies (210). Figures 16 and 17 represent the suitable land cover for solar and wind, respectively, which are found after excluding unsuitable land cover. Figure 18 shows the elevation map. The elevation map shows that maximum areas of the selected regions are within −4 m to 66 m. Other areas have different ranges of elevation such as 66–153 m, 153–319 m, 319–633 m and 633–1276 m. It is noticeable that the selected regions have a maximum elevation of 1276 m, which is well below previous studies' adopted elevation of 2000 m [126, 136]. So, the selected whole regions are considered suitable for both solar and wind. Figure 19 represents the slope map. From the slope map, it is seen that maximum areas of the selected regions have slope below 1.4° that means that maximum areas are almost flat and very much suitable for installing power plant. Few areas are within the range of 1.4° to 4.94°. Very few areas are within the range of 4.94–14.82°. The slope map is reclassified within the range of 0–5° and 5–14.82°, which is presented in Fig. 20. This figure has given more better understanding that almost all areas have a slope within 5°, which is suitable for solar. In addition, the maximum slope is 14.82°, so all the selected regions are fully suitable for wind, as this study adopts maximum 15° slope for wind analysis. Figure 21 represents the unsuitable GIS layers that include

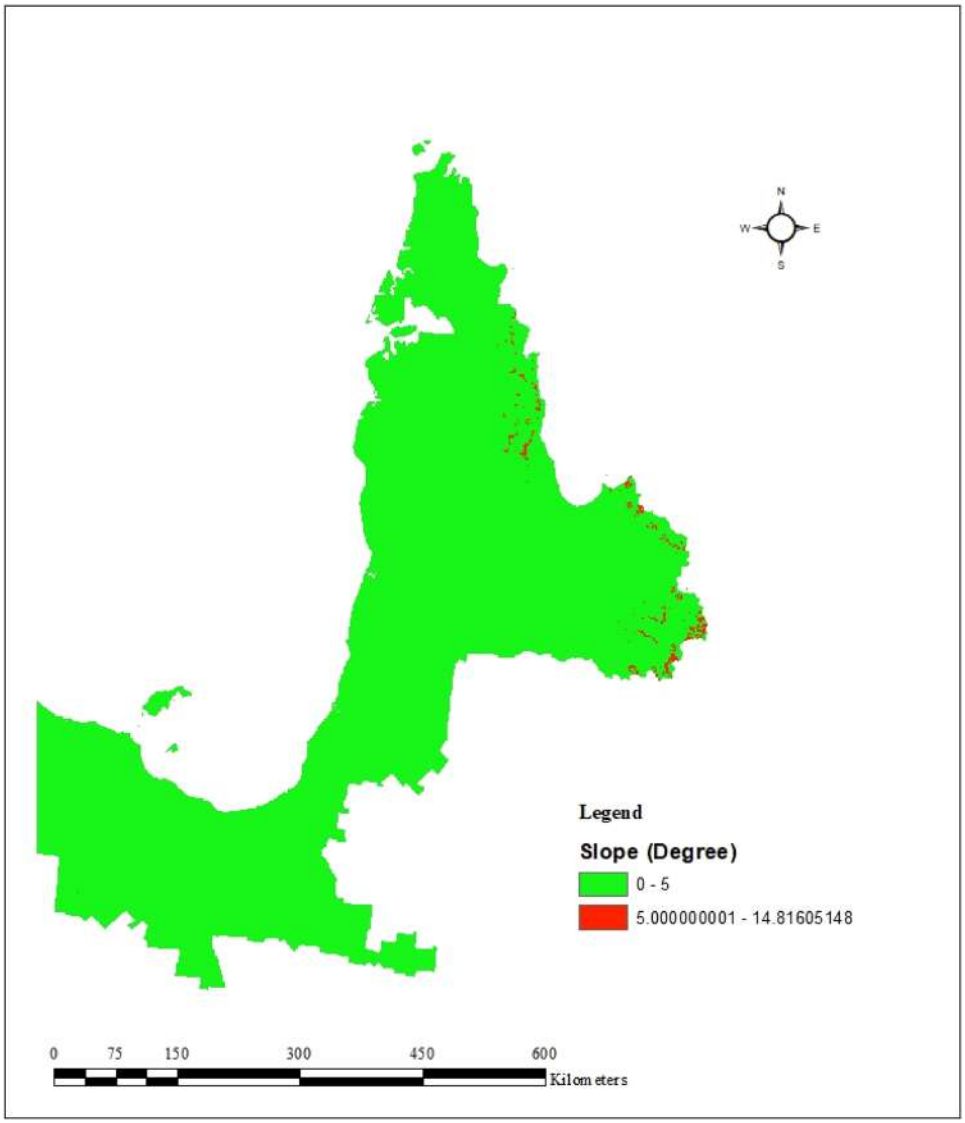

Fig. 20 Reclassified slope map for solar of selected regions of FNQ

urban areas, protected areas, rail and road networks, water bodies and airports. Excluding these unsuitable layers with suitable buffer and considering suitable land cover, elevation and slope, final suitable places for solar and wind farms installation in selected administrative areas have been generated that are presented in Figs. 22 and 23, respectively. Suitable locations for solar and wind in every administrative region are calculated in the attribute table that are presented in Tables 3 and 4, respectively.

The suitable land evaluation process has been conducted for solar and wind separately. Initially, the selected regions are assumed only for being solar project and later only for wind project. Finally, the total land area suitable for solar power has been found to be 142,294.85 km^2 and for wind 144,563.83 km^2. The solar energy potential can be evaluated considering mean horizontal solar irradiation, suitable land area and solar panel efficacy. Solar power potential can be calculated by the following equation [137]:

$$P_{\text{solar}} = G \times \text{SA} \times \text{AF} \times \eta \tag{1}$$

where P_{solar} is the solar power potential, G is annual mean horizontal solar irradiation in $kWh/m^2/day$, SA is the suitable land area (m^2), AF is the area factor (%), and η is the solar panel efficacy (%). Here, the area factor reveals the maximal places covered by the solar panels with minimal shadow effect. Area factor is considered 70% as used in the previous studies [113, 137]. Daily average solar irradiation data for selected regions are collected from Bureau of Meteorology. The study has used the First solar series 4™ PV module (advanced thin-film solar module), used in Kidston solar farm on the site of Kidston gold mine of FNQ. The maximum efficiency, 17%, of the module is used in this

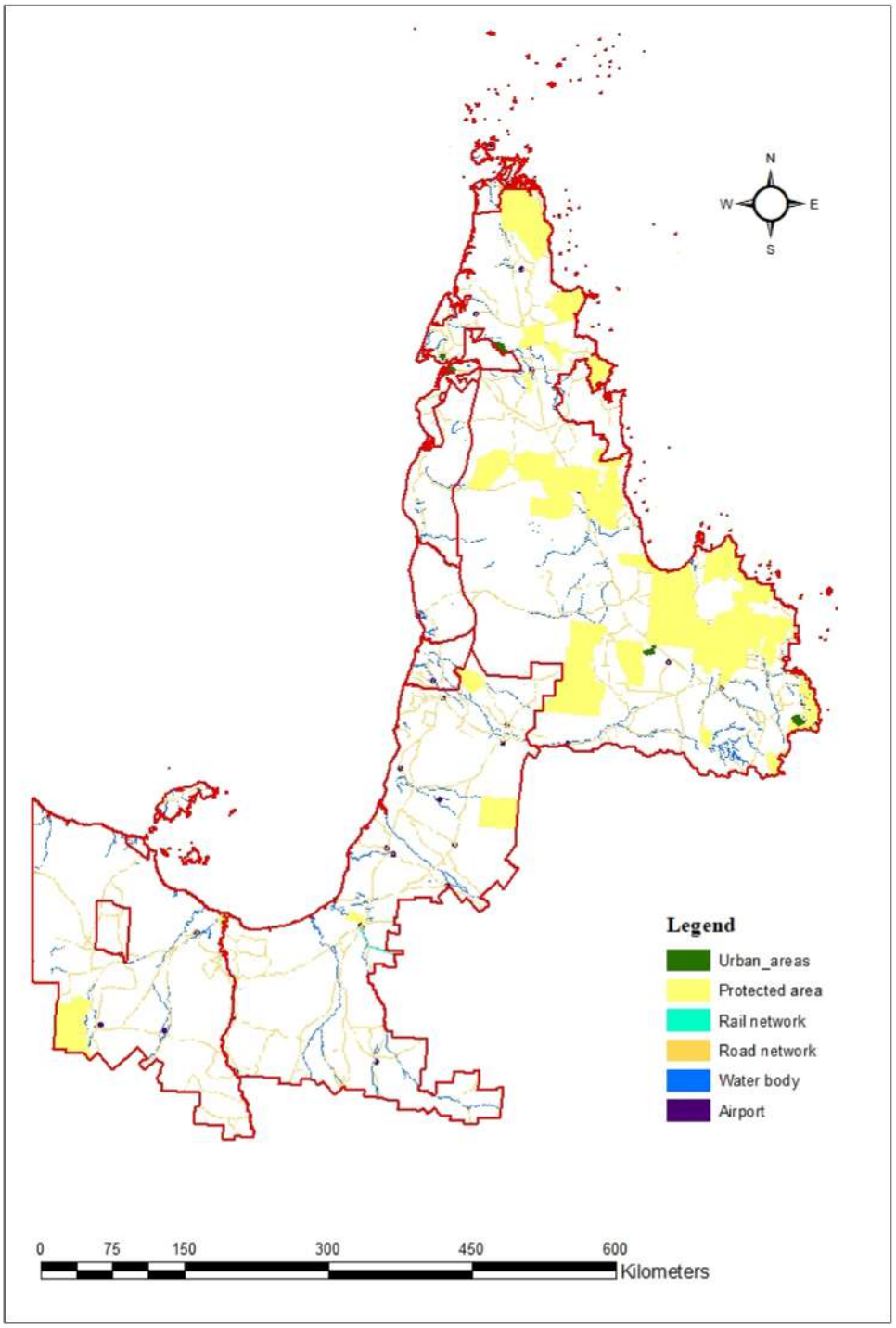

Fig. 21 Unsuitable GIS layers for selected regions of FNQ

study to get the maximum possible solar power. Table 3 represents calculated solar power potential for the selected sites. The biggest area Cook is suitable for 6,107.30 GW solar power production, whereas the smallest area Umagico is suitable for 23.30 MW solar power production.

Wind power potential can be evaluated by the following equation [134]:

$$P_{\text{wind}} = \text{SA} \times \text{AF} \tag{2}$$

where P_{wind} is the wind power potential (MW), SA is the suitable land area (m^2), and AF is the area factor (kW/m^2). In this study, wind turbines have been arranged at a distance of 7D × 5D [113], where D is the rotor diameter. Area factor (AF) can be calculated as follows [134],

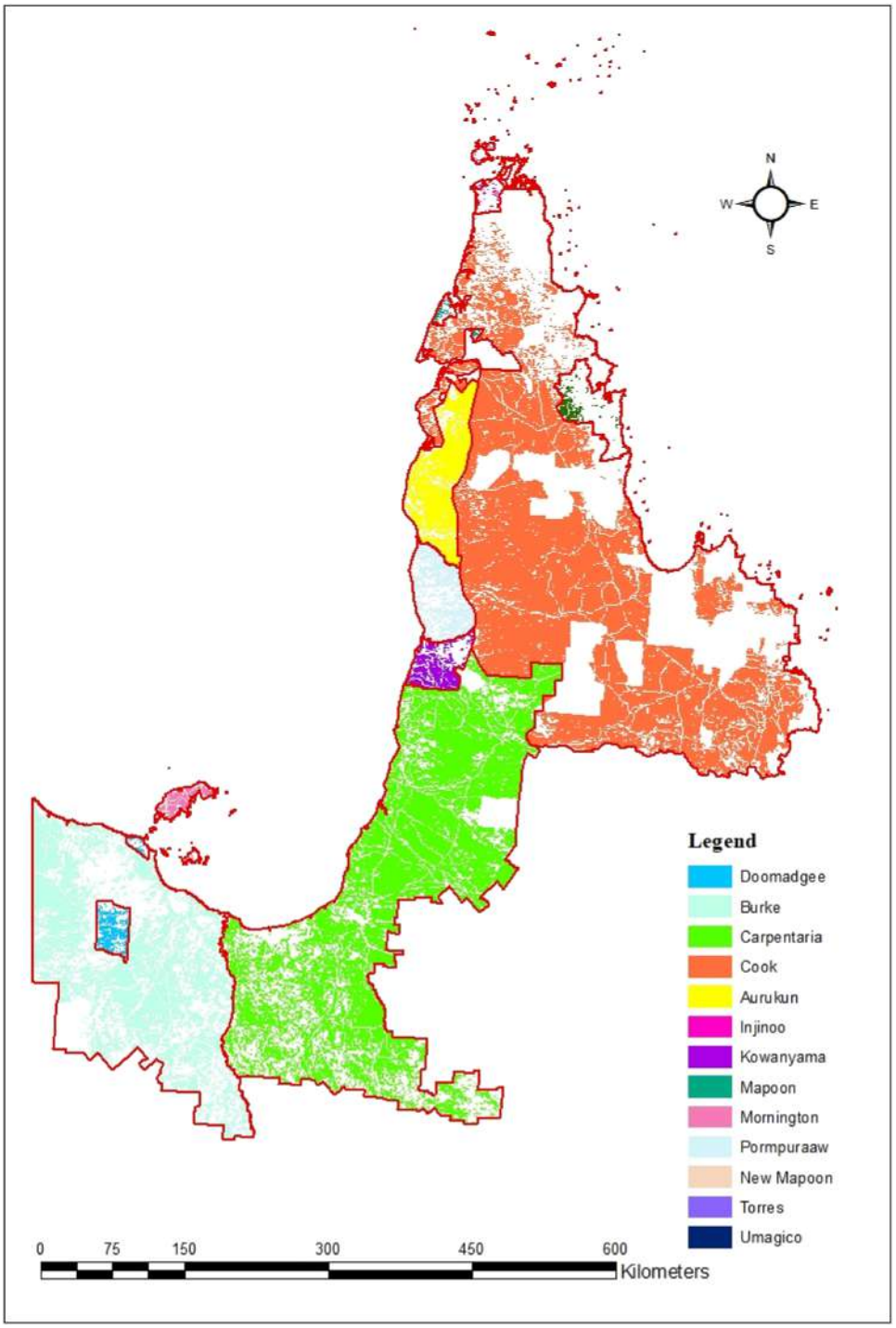

Fig. 22 Final suitability map for solar power installation in selected regions of FNQ

$$\mathrm{AF} = \mathrm{Capacity}/(7D \times 5D) \tag{3}$$

The study has used Vestas V117-3.45 wind turbine specification to calculate wind power potential. The turbine capacity and rotor diameter are 3.45 MW and 117 m, respectively [138]. Table 4 represents calculated theoretical wind power potential for the selected regions. The biggest area Cook can be suitable for 450 GW wind power production, whereas the smallest area Umagico is suitable for 1.38 MW wind power production.

Economic potential

Another important thing is that renewable power generation cost needs to be cheap or cost competitive. According to Roam consulting Pty Ltd, compared to fossil fuel power

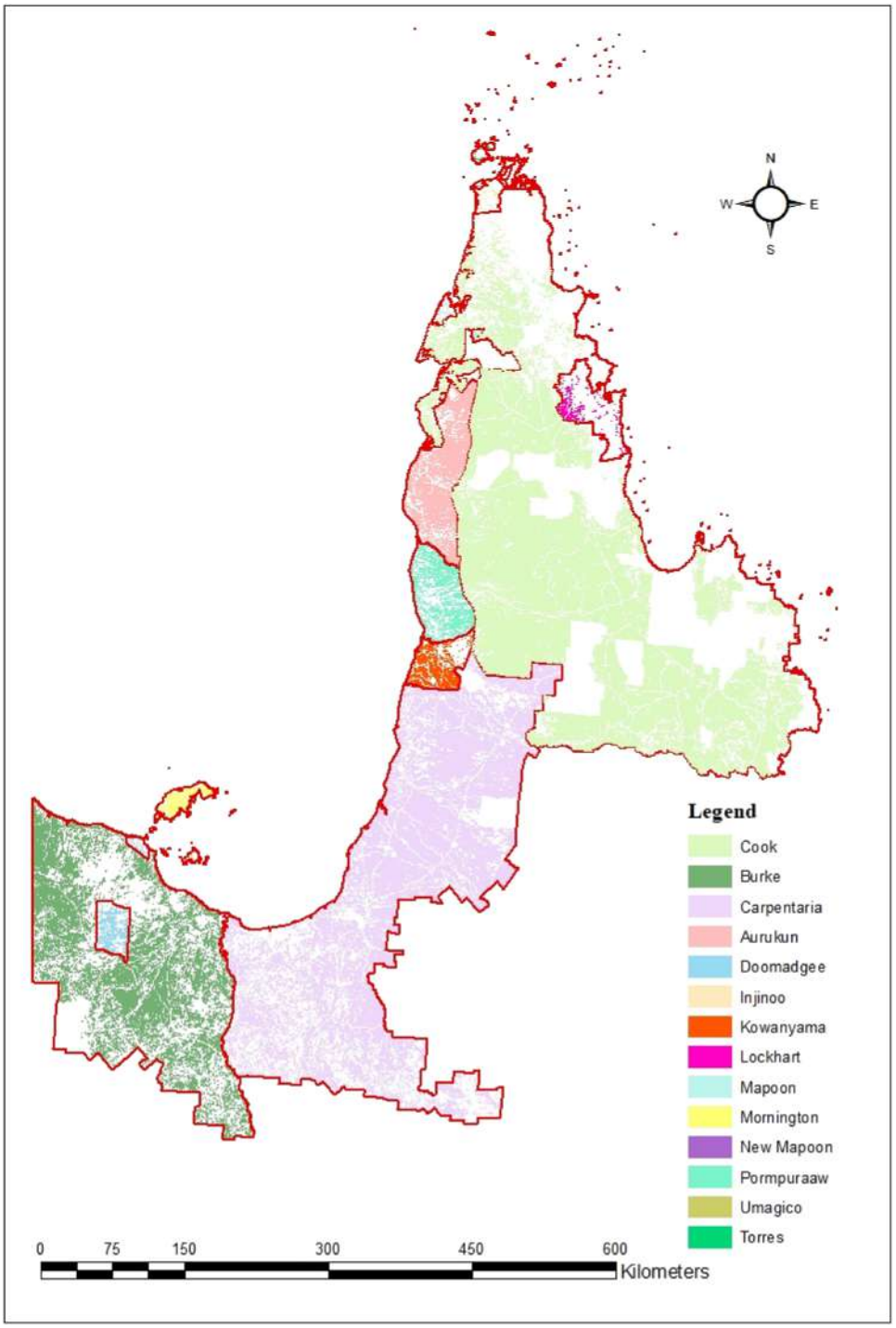

Fig. 23 Final suitability map for wind power installation in selected regions of FNQ

generation, renewable generation could be cheaper in the remote communities that would be advantageous and crucial for local economic growth. The Australian Climate Council [139] has reported that renewable power generation is the cheapest option now compared to new built coal and gas power generation, even with all of the existing subsidies associated with coal and gas. Table 5 depicts the power generation cost by sources [139].

Table 3 Theoretical solar power potential

Selected site	Annual solar mean radiation (G) (kWh/m^2/day)	Suitable area (m^2)	Theoretical power potential (MW)
Cook	5.8	61,940,133,432.00	6,107,297.16
Carpentaria	6.1	45,689,555,002.00	4,738,006.85
Burke town	6.2	22,407,859,618.00	2,361,788.40
Doomadgee	6.1	1,049,736,835.00	108,857.71
Mornington Island	5.9	632,097,742.50	63,399.40
Kowanyama	6.1	1,546,394,148.00	160,361.07
Pormpuraaw	6.0	2,733,477,907.00	278,814.75
Aurukun	5.9	5,948,460,436.00	596,630.58
Injinoo	5.6	105,737,663.10	10,066.23
Torres	5.8	48,331,606.32	4,765.49
New Mapoon	5.7	1,264,375.11	122.52
Umagico	5.6	244,564.76	23.28
Mapoon	5.5	191,562,294.40	17,911.07
Lockhart River	5.6	521,935,891.28	347,818.08

Table 4 Theoretical wind power potential

Selected site	Suitable area (m^2)	Theoretical power potential (MW)
Cook	62,514,737,696.00	450,154.65
Carpentaria	46,115,274,994.00	332,065.78
Burke town	22,636,366,913.00	162,999.42
Doomadgee	1,035,985,866.00	7,459.90
Mornington Island	811,595,814.20	5,844.12
Kowanyama	1,581,502,920.00	11,388.05
Pormpuraaw	2,806,975,362.00	20,212.40
Aurukun	5,993,704,069.00	43,159.32
Injinoo	137,748,431.80	991.89
Torres	80,323,315.77	578.39
New Mapoon	1,288,902.50	9.28
Umagico	191,127.54	1.38
Mapoon	251,693,470.70	1,812.39
Lockhart River	596,438,879.30	4,294.82

Table 5 Cost of new built power plants [139]

Power technology	Levellised cost of energy (LCOE) $(aus)/MWh
Wind	$50–65
Solar PV	$78–140
Solar thermal plant	$78
Gas combined cycle	$78–90
Coal	$134–203
Coal with carbon capture system (CCS)	$352

Recently, Queensland solar and wind projects show possibility to be the cheapest power generation option in Australia. For instance, the Coopers Gap wind farm of 453 MW in Queensland can deliver power with cost bellow $60/MWh [139]. Large-scale solar PV in Queensland has already reached bellow $80/MWh [140]. However, remote communities of FNQ have access to electricity, but emissions, cost and reliability are the major concern. They have to rely on expensive imported diesel. In 2018–19, the Queensland government [141] paid $465 million to Ergon Energy Retail for ensuring remote customers paid similar electricity prices to other users. Hence, many remote places are not paying the real cost of power supply. In addition, the utilisation of diesel-based power generation is contributing to environmental pollution such as noise, carbon emissions and oil spillage, high supply cost and increased road maintenance costs [141]. On the other hand, continued fall in the cost of solar and wind generation, including storage, can lessen the power supply cost and the need for diesel power generation [141]. The cost competitiveness of solar and wind open up the prospect of utilising local renewable energy resources in place of the existing diesel power generation system of FNQ. In addition, a vast deployment of renewable energy can fuel economic growth in FNQ, with creating new job opportunities, enhancing human well-being and eventually can contribute to a climate-safe future.

Queensland has a high ambitious target for installing renewable energy in FNQ, by expanding especially solar and wind energy resources. However, the installation of renewable power plant is very slow compared to their targets. The possible barriers may include lack of evidence of energy resources, poor infrastructure, high investment costs,

limited planning and lack of political motive. However, the results of the study can help various government agencies, policy and decision makers, researchers and parties in bringing renewables into the FNQ's energy system. The present study has performed a GIS-based analysis to assess favourable locations to develop two eminent resources, namely solar and wind. From the analysis, it is found that the FNQ has significant potential for exploiting solar and wind. Then the study has highlighted the LCOE or investment for solar and wind energy including conventional power systems, which proves that solar and wind resources have significant economic potential. The present study can give worthy guidance to the research community as well as potential parties regarding the location suitability to install solar and wind power stations. The current study assesses suitable places for solar and wind projects, including power potential, and presents an overview on economic potential. Hopefully, the results of the study will assist in attaining future renewable energy targets.

Conclusion

Since the world progressively incorporates renewable power generation and switching away from expensive or emissions-intensive technologies, the demand is rising for hybrid renewable energy assets that combine multiple forms of generation and storage. Renewable energy sources are promising for eliminating ecological damage. From the technical and economic context, different methodologies have been developed to size and analyse techno-economic characteristics regarding renewable energy adoption. This study has presented a global survey on the renewable energy availability, development and an essential to implement renewable energy system within remote regions of Far North Queensland in Australia. This study has performed potential assessment for solar and wind resources in terms of climatic, geographical and economical. The assessment shows significant potential for solar and wind development in every aspect.

This study concludes that the selected areas from Far North Queensland are highly potential for solar and wind. The total maximum potential areas are found at 142,294.86 km^2 (55.94% of total selected areas) with power potential of 14,448 GW for solar and 144,563.80 km^2 (56.83% of total selected areas) with power potential 1040.97 GW for wind. Along with the solar and wind, hydrogen presents a clear perspective for a clean and affordable energy supply in the remote areas as well as deep decarbonisation which is the global target, needed to be reached by 2050 for limiting global surface temperature increment to 2 °C. In addition, the possibility to store hydrogen opens the opportunity for the integration of high renewable resources (solar and wind) shares with positive effects on Australia's sustainable development goals through reduced GHG emissions. Hence, utilisation of renewable resources: solar and wind with water splitting hydrogen is the ultimate solution for energy system and sustainable ecology.

This study has presented a potential overview to the complexity of decision making in the renewable energy sector and a scientific basis for selecting efficient, cost-effective clean solutions for the energy system of remote communities of Far North Queensland, Australia. This knowledge will increase stakeholder confidence in investing in renewable energy, which will be integral to Australia's efforts to reduce reliance on dirty and costly diesel-based energy systems.

Data availability Data will be made available on request.

Declarations

Conflict of interest The authors declare that they have no known competing financial interest or personal relationships that could have appeared to influence the work reported in this paper.

References

1. IISD: World population to reach 9.9 billion by 2050. (2020) Accessed 12 Sep 2021
2. Mandal, T.K., Gregory, D.H.: Hydrogen: A future energy vector for sustainable development. Proc. Instit. Mech. Eng. Part C J. Mech. Eng. Sci. **224**(3), 539–558 (2010)
3. Ergon Energy: Renewables in Far North Queensland. (2020) Accessed 20 April 2021
4. Li, L., Wang, X.: Design and operation of hybrid renewable energy systems: current status and future perspectives. Curr. Opin. Chem. Eng. **31**, 100669 (2021)
5. Mwangi, J.K., Lee, W.J., Chang, Y.C., Chen, C.Y., Wang, L.C.: An overview: energy saving and pollution reduction by using green fuel blends in diesel engines. Appl. Energy **159**, 214–236 (2015)
6. Kannan, N., Vakeesan, D.: Solar energy for future world:-a review. Renew. Sustain. Energy Rev. **62**, 1092–1105 (2016)
7. Energy Matters: Wind energy: how a wind turbine works. (2005). Accessed 22 Sep 2022
8. Tong, W.: Fundamentals of wind energy, vol. 44. WIT Press Southampton, UK (2010)
9. Solomon, A.A., Child, M., Caldera, U., Breyer, C.: Exploiting wind-solar resource complementarity to reduce energy storage need. AIMS Energy **8**(5), 749–770 (2020)
10. Maggio, G., Nicita, A., Squadrito, G.: How the hydrogen production from res could change energy and fuel markets: a review of recent literature. Int. J. Hydrogen Energy **44**(23), 11371–11384 (2019)
11. Sazali, N.: Emerging technologies by hydrogen: a review. Int. J. Hydrogen Energy **45**(38), 18753–18771 (2020)
12. Zhang, W., Maleki, A., Rosen, M.A., Liu, J.: Sizing a stand-alone solar-wind-hydrogen energy system using weather forecasting and a hybrid search optimization algorithm. Energy Convers. Manag. **180**, 609–621 (2019)

13. IPCC: The ocean and cryosphere in a changing cli-mate. Special report. *Geneva: IPCC, final draft*, (2019a)
14. Melillo, J.M., Richmond, T.T., Yohe, G.: Climate change impacts in the United States: The third national climate assessment. *Global Change Research Program*, p 841, (2014)
15. Gleditsch, N.P.: This time is different! Or is it? Neomalthusians and environmental optimists in the age of climate change. J. Peace Res. **58**(1), 177–185 (2021)
16. NOAA: Climate change and variability. 2021. Accessed 09 April 2021
17. Kennedy, J.J., Thorne, P.W., Peterson, T.C., Reudy, R.A., Stott, P.A., Parker, D.E., Good, S.A., Titchner, H.A., Willett, K.M.: How do we know the world has warmed? state of the climate in 2009. Bull. Am. Meteorol. Soc. **91**, 26–27 (2010)
18. NOAA: Global climate report - annual 2020. 2020. Accessed 07 April 2021
19. IPCC: Global warming of .5°c, special report
20. Bindoff, N.L., Cheung, W.W.L., Kairo, J.G., Ar´ıstegui, J., Guinder, V.A., Hallberg, R., Hilmi, N., Jiao, N., Karim, M.S., Levin, L., O'Donoghue, S., Purca Cuicapusa, S.R., Rinkevich, B., Suga, T., Tagliabue, A., Williamson, P.: Changing ocean, marine ecosystems, and dependent communities. *In: IPCC Special Report on the Ocean and Cryosphere in a Changing Climate*, 2019
21. Pascale, S., Kapnick, S.B., Delworth, T.L., Cooke, W.F.: Increasing risk of another cape town "day zero" drought in the 21st century. Proc. Natl. Acad. Sci. **117**(47), 29495–29503 (2020)
22. Wilcke, R.A.I., Kjellstrom, E., Lin, C., Matei, D., Moberg, A., Tyrlis, E.: The extremely warm summer of 2018 in sweden – set in a historical context. Earth Syst. Dyn. **11**(4), 1107–1121 (2020)
23. Rimi, R.H., Haustein, K., Allen, M.R., Barbour, E.J.: Risks of pre-monsoon extreme rainfall events of Bangladesh: is anthropogenic climate change playing a role? Bull. Am. Meteorol. Soc. **100**(1), S61–S65 (2019)
24. Keellings, D., Hernández Ayala, J.J.: Extreme rainfall associated with hurricane Maria over Puerto Rico and its connections to climate variability and change. Geophys. Res. Lett. **46**(5), 2964–2973 (2019)
25. Meinshausen, M., Nicholls, Z.R.J., Lewis, J., Gidden, M.J., Vogel, E., Freund, M., Beyerle, U., Gessner, C., Nauels, A., Bauer, N., Canadell, J.G., Daniel, J.S., John, A., Krummel, P.B., Luderer, G., Meinshausen, N., Montzka, S.A., Rayner, P.J., Reimann, S., Smith, S.J., van den Berg, M., Velders, G.J.M., Vollmer, M.K., Wang, R.H.J.: The shared socio-economic pathway (ssp) greenhouse gas concentrations and their extensions to 2500. Geosci. Model Dev. **13**(8), 3571–3605 (2020)
26. Pachauri, R.K., Reisinger, A.: Climate change 2007: synthesis report. *IPCC, Geneva, Switzerland*, (2007)
27. Ed Dlugokencky. Carbon cycle greenhouse gases, noaa/gml. *Global Monitoring Laboratory*. (2021). Accessed 20 April 2021
28. EarthCharts: Global greenhouse gas emissions by sector. (2016). Accessed 21 April 2021
29. Meinshausen, M., Vogel, E., Nauels, A., Lorbacher, K., Meinshausen, N., Etheridge, D.M., Fraser, P.J., Montzka, S.A., Rayner, P.J., Weiss, R.: Historical greenhouse gas concentrations for climate modelling (cmip6). Geosci. Model Dev. **10**(5), 2057–2116 (2017)
30. NASA: Global climate change: vital signs of the planet. *NASA's Jet Propulsion Laboratory, California Institute of Technology*. (2021). Accessed 22 April 2021
31. Bureau of Meteorology: State of the climate 2020. (2020). Accessed 28 Jan 2022
32. CCA: Queensland's changing climate. (2021). Accessed 28 Jan 2022
33. Syktus, J.: Climate change in the Far North Queensland region. (2009). Accessed 17 Jan 2022
34. De'ath, G., Lough, J.M., Fabricius, K.E.: Declining coral calcification on the great barrier reef. Science **323**(5910), 116–119 (2009)
35. Riahi, K., Van Vuuren, D.P., Kriegler, E., Edmonds, J., Oneill, B.C., Fujimori, S., Bauer, N., Calvin, K., Dellink, R., Fricko, O., et al.: The shared socioeconomic pathways and their energy, land use, and greenhouse gas emissions implications: an overview. Global Environ. Change **42**, 153–168 (2017)
36. Stern, N.: The economics of climate change. *HM Treasury; UK*, (2006)
37. Glikson, D.A.: Beyond 2 degrees celsius. *Earth and paleoclimate science Australian National University*, (2011)
38. Kompas, T., Pham, V.H., Che, T.N.: The effects of climate change on GDP by country and the global economic gains from complying with the Paris climate accord. Earth's Future **6**(8), 1153–1173 (2018)
39. BP: Statistical review of world energy 2021. (2021). Accessed 08 August 2021
40. OPEC: Opec monthly oil market report. (2022). Accessed 5 Feb 2022
41. IEA: Gas market report, q1–2022. (2022). Accessed 5 Feb 2022
42. IEA: Electricity market report. (2022). Accessed 8 Feb 2022
43. Clarke, L., Jiang, K., Akimoto, K., Babiker, M., Blanford, G., Fisher-Vanden, K., Hourcade, J.C., Krey, V., Kriegler, E., Loschel, A. et al.: Climate change 2014: Mitigation of climate change. contribution of working group iii to the fifth assessment report of the intergovernmental panel on climate change. (2014)
44. Kraas, F., Leggewie, C., Lemke, P., Matthies, E., Messner, D., Nakicenovic, N., Joachim Schellnhuber H., Schlacke, S., Schneidewind, U., Brandi, C. et al. Entwicklung und Gerechtigkeit durch Transformation: die vier großen I; Sondergutachten. WBGU, (2016)
45. Wiki: Far North Queensland. (2021). Accessed 17 Jan 2022
46. PIFU-QG: The economic and social impacts of tourism in the Far North Queensland planning region. (2015). Accessed 17 Dec 2021
47. Geoscience Australia: Solar. (2020). Accessed 22 Feb 2021
48. Bureau of meteorology: Average daily solar exposure. (2016). Accessed 8 Jun 2021
49. Li, H.X., Edwards, D.J., Reza Hosseini, M., Costin, G.P.: A review on renewable energy transition in Australia: an updated depiction. J. Clean. Prod. **242**, 118475 (2020)
50. ARENA: Australian energy resource assessment. (2018). Accessed 01 March 2021
51. Prasad, A.A., Taylor, R.A., Kay, M.: Assessment of solar and wind resource synergy in Australia. Appl. Energy **190**, 354–367 (2017)
52. Clean Energy Council: Clean energy Australia report 2020. (2020). Accessed 20 Jan 2021
53. Yusaf, T., Goh, S., Borserio, J.A.: Potential of renewable energy alternatives in Australia. Renew. Sustain. Energy Rev. **15**(5), 2214–2221 (2011)
54. IHA: Hydropower status report 2017, (2017)
55. Bahadori, A., Zahedi, G., Zendehboudi, S.: An overview of Australia's hydropower energy: status and future prospects. Renew. Sustain. Energy Rev. **20**, 565–569 (2013)
56. Manasseh, R., McInnes, K.L., Hemer, M.A.: Pioneering developments of marine renewable energy in Australia. Int. J. Ocean Clim. Syst. **8**(1), 50–67 (2017)
57. Hemer, M.A., Zieger, S., Durrant, T., O'Grady, J., Hoeke, R.K., McInnes, K.L., Rosebrock, U.: A revised assessment of Australia's national wave energy resource. Renew. Energy **114**, 85–107 (2017)
58. Behrens, S., Griffin, D., Hayward, J., Hemer, M., Knight, C., McGarry, S., Osman, P., Wright, J.: Ocean renewable energy:

2015–2050. An analysis of ocean energy in Australia. In *Commonwealth Scientific and Industrial Research Organisation Report*, p 212. (2012)
59. Hemer, M.A., Pitman , T., McInnes, K. Rosebrock, U.: The Australian wave energy atlas. Project overview and final report, (2018)
60. Bamber, P., Guinn, A., Gereffi, G.: Burundi in the energy global value chain: Skills for private sector development, 02 (2014)
61. Courtecuisse, V., Sprooten, J., Robyns, B., Petit, M., Francois, B., Deuse, J.: A methodology to design a fuzzy logic based supervision of hybrid renewable energy systems. Math. Comput. Simul. **81**(2), 208–224 (2010)
62. Dresselhaus, M., Thomas, I.: Alternative energy technologies. Nature **414**, 332–337 (2001)
63. Vaishya, M.T.P., Khambra, B.: A review of solar energy based heat and power generation systems. (2021)
64. Parida, B., Iniyan, S., Goic, R.: A review of solar photovoltaic technologies. Renew. Sustain. Energy Rev. **15**(3), 1625–1636 (2011)
65. Nema, P., Nema, R.K., Rangnekar, S.: A current and future state of art development of hybrid energy system using wind and PV-solar: a review. Renew. Sustain. Energy Rev. **13**(8), 2096–2103 (2009)
66. Kim, M., Bae, S.: Decentralized control of a scalable photovoltaic (PV)-battery hybrid power system. Appl. energy **188**, 444–455 (2017)
67. Li, L., Liu, P., Li, Z., Wang, X.: A multi-objective optimization approach for selection of energy storage systems. Comput. Chem. Eng. **115**, 213–225 (2018). (**cited By 22**)
68. Singh, S., Singh, M., Kaushik, S.C.: Feasibility study of an islanded microgrid in rural area consisting of pv, wind, biomass and battery energy storage system. Energy Convers. Manag. **128**, 178–190 (2016)
69. Qoaider, L., Steinbrecht, D.: Photovoltaic systems: a cost competitive option to supply energy to off-grid agricultural communities in arid regions. Appl. Energy **87**, 427–435 (2010)
70. Canales, F.A., Jurasz, J., Beluco, A., Kies, A.: Assessing temporal complementarity between three variable energy sources through correlation and compromise programming. Energy **192**, 116637 (2020)
71. Jurasz, J., Canales, F.A., Kies, A., Guezgouz, M., Beluco, A.: A review on the complementarity of renewable energy sources: concept, metrics, application and future research directions. Solar Energy **195**, 703–724 (2020)
72. Ramesh, M., Saini, R.P.: Dispatch strategies based performance analysis of a hybrid renewable energy system for a remote rural area in India. J. Clean. Prod. **259**, 120697 (2020)
73. Zhang, Y., Lian, J., Ma, C., Yang, Y., Pang, X., Wang, L.: Optimal sizing of the grid-connected hybrid system integrating hydropower, photovoltaic, and wind considering cascade reservoir connection and photovoltaic-wind complementarity. J. Clean. Prod. **274**, 123100 (2020)
74. Alirahmi, S.M., Dabbagh, S.R., Ahmadi, P., Wongwises, S.: Multi-objective design optimization of a multi-generation energy system based on geothermal and solar energy. Energy Convers. Manag. **205**, 112426 (2020)
75. Murugaperumal, K., Raj, P.A.D.V.: Feasibility design and techno-economic analysis of hybrid renewable energy system for rural electrification. Solar Energy **188**, 1068–1083 (2019)
76. Li, J., Liu, P., Li, Z.: Optimal design and techno-economic analysis of a solar-wind-biomass off-grid hybrid power system for remote rural electrification: a case study of west china. Energy **208**, 118387 (2020)
77. Khooban, M.H., Gheisarnejad, M.: A novel deep reinforcement learning controller based type-ii fuzzy system: frequency regulation in microgrids. IEEE Trans. Emerg. Top. Comput. Intell. **5**(4), 689–699 (2020)
78. Zhou, W., Lou, C., Li, Z., Lin, Lu., Yang, H.: Current status of research on optimum sizing of stand-alone hybrid solar–wind power generation systems. Appl. energy **87**(2), 380–389 (2010)
79. Fathabadi, H.: Novel stand-alone, completely autonomous and renewable energy based charging station for charging plug-in hybrid electric vehicles (phevs). Appl. Energy **260**, 114194 (2020)
80. Glenk, G., Reichelstein, S.: Economics of converting renewable power to hydrogen. Nat. Energy **4**(3), 216–222 (2019)
81. Wang, G., Mitsos, A., Marquardt, W.: Renewable production of ammonia and nitric acid. AIChE J. **66**(6), e16947 (2020)
82. Gökçek, M.: Integration of hybrid power (wind-photovoltaic-diesel-battery) and seawater reverse osmosis systems for small-scale desalination applications. Desalination **435**, 210–220 (2018)
83. Maleki, A.: Design and optimization of autonomous solar-wind-reverse osmosis desalination systems coupling battery and hydrogen energy storage by an improved bee algorithm. Desalination **435**, 221–234 (2018)
84. Zhang, Q., Martín, M., Grossmann, I.E.: Integrated design and operation of renewables-based fuels and power production networks. Comput. Chem. Eng. **122**, 80–92 (2019)
85. McCay, M.H., Shafiee, S.: Hydrogen: an energy carrier. In *Future Energy*, pp 475–493. Elsevier, (2020)
86. Nagpal, M., Kakkar, R.: An evolving energy solution: intermediate hydrogen storage. Int. J. Hydrogen Energy **43**(27), 12168–12188 (2018)
87. Okolie, J.A., Patra, B.R., Mukherjee, A., Nanda, S., Dalai, A.K., Kozinski, J.A.: Futuristic applications of hydrogen in energy, biorefining, aerospace, pharmaceuticals and metallurgy. Int. J. Hydrogen Energy **46**(13), 8885–8905 (2021)
88. de Miranda, P.E.V.: Hydrogen energy: sustainable and perennial. In Science and Engineering of Hydrogen-Based Energy Technologies, pp 1–38. Elsevier, (2019)
89. Dinçer, İ, Zamfirescu, C.: Sustainable Hydrogen Production. Elsevier, Amsterdam (2016)
90. Ren, Yi., Huang, Z., Miao, H., Di, Y., Jiang, D., Zeng, Ke., Liu, B., Wang, X.: Combustion and emissions of a di diesel engine fuelled with diesel-oxygenate blends. Fuel **87**(12), 2691–2697 (2008)
91. Mohammed, H.A., Abdulhaleem, S.M.: Experimental study of spark ignition engine operated with naphtha or gasoline blended LPG fuel. MEJ. Mansoura Eng. J. **41**(2), 9–17 (2020)
92. Coronado, C.R., de Carvalho Jr, J.A., Yoshioka, J.T., Silveira, J.L.: Determination of ecological efficiency in internal combustion engines: the use of biodiesel. Appl. Thermal Eng. **29**(10), 1887–1892 (2009)
93. Bhoi, S., Banerjee, T., Mohanty, K.: Insights on the combustion and pyrolysis behavior of three different ranks of coals using reactive molecular dynamics simulation. RSC Adv. **6**(4), 2559–2570 (2016)
94. AG: Global leadership in low emissions technologies first low emissions technology statement – 2020. (2020). Accessed 12 Nov 2021
95. Heidari, A., Esmaeel Nezhad, A., Tavakoli, A., Rezaei, N., Gandoman, F.H., Miveh, M.R., Ahmadi, A., Malekpour, M.: A comprehensive review of renewable energy resources for electricity generation in Australia. Front. Energy **14**(3), 510–529 (2020)
96. Solar Citizens: Welcome to Queensland's renewable energy boom. (2020). Accessed 2 April 2021
97. RE: Renewable energy industry profile. (2018). Accessed 10 July 2021

98. Baniyounes, A., Liu, G., Rasul, M. G., Khan, M. M. K. Review on renewable energy potential in Australian subtropical region (central and north Queensland). In Advanced Materials Research, vol 347, pp 3846–3855. Trans Tech Publ, (2012)
99. Mishra, T., Rabha, A., Kumar, U., Arunachalam, K., Sridhar, V.: Assessment of solar power potential in a hill state of India using remote sensing and geographic information system. Remote Sens. Appl. Soc. Environ. **19**, 100370 (2020)
100. Bureau of Meteorology: Average daily sunshine hours. (2005). Accessed 8 Jun 2021
101. Bureau of Meteorology: Monthly mean daily global solar irradiation. (2021). Accessed 20 Dec 2021
102. Bureau of Meteorology: Renewable energy atlas of Australia, mean wind speed at 80 m above ground level. (2008). Accessed 15 Feb 2021
103. Ali, S., Taweekun, J., Techato, K., Waewsak, J., Gyawali, S.: Gis based site suitability assessment for wind and solar farms in Songkhla, Thailand. Renew. Energy **132**, 1360–1372 (2019)
104. Noorollahi, E., Fadai, D., Akbarpour Shirazi, M., Ghodsipour, S.H.: Land suitability analysis for solar farms exploitation using GIS and fuzzy analytic hierarchy process (FAHP)—a case study of Iran. Energies **9**(8), 643 (2016)
105. WIKI: Mount emerald wind farm. (2017). Accessed 14 Dec 2021
106. RATCH-Australia: Wind turbine model: V117–3.45 mw®. (2017). Accessed 14 Dec 2021
107. Aragones-Beltran, P., Chaparro-Gonzalez, F., Pastor-Ferrando, J.P., Rodrıguez-Pozo, F.: An ANP-based approach for the selection of photovoltaic solar power plant investment projects. Renew. Sustain. Energy Rev. **14**(1), 249–264 (2010)
108. Yun-na, Wu., Yi-sheng, Y., Tian-tian, F., Li-na, K., Wei, L., Luojie, Fu.: Macro-site selection of wind/solar hybrid power station based on ideal matter-element model. Int. J. Electr. Power Energy Syst. **50**, 76–84 (2013)
109. Van Haaren, R., Fthenakis, V.: GIS-based wind farm site selection using spatial multi-criteria analysis (SMCA): evaluating the case for New York State. Renew. Sustain. Energy Rev. **15**(7), 3332–3340 (2011)
110. Tavana, M., Santos, F.J., Arteaga, S.M., Alimohammadi, M.: A fuzzy multi-criteria spatial decision support system for solar farm location planning. Energy Strategy Rev. **18**, 93–105 (2017)
111. Chu, C.T., Hawkes, A.D.: A geographic information system-based global variable renewable potential assessment using spatially resolved simulation. Energy **193**, 116630 (2020)
112. Watson, J.J., Hudson, M.D.: Regional scale wind farm and solar farm suitability assessment using GIS-assisted multi-criteria evaluation. Landsc. Urban Plan. **138**, 20–31 (2015)
113. Saraswat, S.K., Digalwar, A.K., Yadav, S.S., Kumar, G.: MCDM and GIS based modelling technique for assessment of solar and wind farm locations in India. Renew. Energy **169**, 865–884 (2021)
114. Latinopoulos, D., Kechagia, K.: A GIS-based multi-criteria evaluation for wind farm site selection. A regional scale application in Greece. Renew. Energy **78**, 550–560 (2015)
115. de Assis Tavares, L.F., Shadman, M., de Freitas Assad, L.P., Silva, C., Landau, L., Estefen, S.F.: Assessment of the offshore wind technical potential for the Brazilian southeast and south regions. Energy **196**, 117097 (2020)
116. Sun, Y., Wang, R., Li, J., Liu, J.: Gis-based multiregional potential evaluation and strategies selection framework for various renewable energy sources: a case study of eastern coastal regions of china. Energy Sci. Eng. **5**(3), 123–140 (2017)
117. DIVA-GIS: Diva-GIS spatial data download. Accessed 14 Dec 2021
118. PP: Protected planet. Accessed 14 Dec 2021
119. Pope, A., Sietinsone, L.: Airports, University of Edinburgh. (2017). Accessed 14 Dec 2021
120. SEDAC: Global rural-urban mapping project, cent. int. earth sci. inf. netw. (ciesin), columbia univ. cuny inst. demogr. res. (cidr), int. food policy res. inst. (ifpri), World Bank. Accessed 14 Dec 2021
121. DUE: Esa data user element. Accessed 14 Dec 2021
122. Phadke, A., Bharvirkar, R., Khangura, J.: Reassessing Wind Potential Estimates for India: Economic and Policy Implications. Technical report, Lawrence Berkeley National Lab.(LBNL), Berkeley, CA (United States), (2011)
123. Siyal, S.H., Mörtberg, U., Mentis, D., Welsch, M., Babelon, I., Howells, M.: Wind energy assessment considering geographic and environmental restrictions in Sweden: a GIS-based approach. Energy **83**, 447–461 (2015)
124. Jain, A., Das, P., Yamujala, S., Bhakar, R., Mathur, J.: Resource potential and variability assessment of solar and wind energy in India. Energy **211**, 118993 (2020)
125. Aydin, N.Y., Kentel, E., Duzgun, H.S.: GIS-based site selection methodology for hybrid renewable energy systems: a case study from western turkey. Energy Convers. Manag. **70**, 90–106 (2013)
126. Uyan, M.: GIS-based solar farms site selection using analytic hierarchy process (AHP) in Karapinar region, Konya/Turkey. Renew. Sustain. Energy Rev. **28**, 11–17 (2013)
127. Jangid, J., Bera, A.K., Joseph, M., Vishal Singh, T.P., Singh, B.K. P., Das, S.: Potential zones identification for harvesting wind energy resources in desert region of India–a multi criteria evaluation approach using remote sensing and GIS. Renew. Sustain. Energy Rev. **65**, 1–10 (2016)
128. Ayodele, T.R., Ogunjuyigbe, A.S.O., Odigie, O., Munda, J.L.: A multi-criteria GIS based model for wind farm site selection using interval type-2 fuzzy analytic hierarchy process: the case study of Nigeria. Appl. Energy **228**, 1853–1869 (2018)
129. Bennui, A., Rattanamanee, P., Puetpaiboon, U., Phukpattaranont, P., Chetpattananondh, K.: Site selection for large wind turbine using GIS. In PSU-UNS International Conference on Engineering and Environment, pp 561–566 (2007)
130. Aydin, N.Y., Kentel, E., Duzgun, S.: GIS-based environmental assessment of wind energy systems for spatial planning: a case study from western turkey. Renew. Sustain. Energy Rev. **14**(1), 364–373 (2010)
131. Infrastructure Australia: National airport safeguarding framework. Accessed 14 Dec 2021
132. Ho, C.K., Ghanbari, C.M.: Hazard Analyses of Glint and Glare from Concentrating Solar Power Plants. Technical report, Sandia National Lab.(SNL-NM), Albuquerque, NM (United States), (2009)
133. Ho, C.K., Sims, C.A., Christian, J.M.: Evaluation of glare at the Ivanpah solar electric generating system. Energy Proced. **69**, 1296–1305 (2015)
134. Anwarzai, M.A., Nagasaka, K.: Utility-scale implementable potential of wind and solar energies for Afghanistan using GIS multi-criteria decision analysis. Renew. Sustain. Energy Rev. **71**, 150–160 (2017)
135. Krewitt, W., Nitsch, J.: The potential for electricity generation from on-shore wind energy under the constraints of nature conservation: a case study for two regions in Germany. Renew. Energy **28**(10), 1645–1655 (2003)
136. Noorollahi, Y., Yousefi, H., Mohammadi, M.: Multicriteria decision support system for wind farm site selection using GIS. Sustain. Energy Technol. Assess. **13**, 38–50 (2016)

137. Dhunny, A.Z., Doorga, J.R.S., Allam, Z., Lollchund, M.R., Boojhawon, R.: Identification of optimal wind, solar and hybrid wind-solar farming sites using fuzzy logic modelling. Energy **188**, 116056 (2019)
138. Vestas: Wind turbine model: V117–3.45 mw®. Accessed 17 Dec 2021
139. Climate Council: Rnewables: powering Queensland's future. (2017). Accessed 3 Nov 2021
140. Renew Economy: Australian wind delivers more record low prices, as private sector piles in. (2017). Accessed 3 Nov 2021
141. Infrastructure Australia: Australian infrastructure audit 2019: energy. (2019). Accessed 10 Nov 2021

International Journal of Energy and Environmental Engineering (2023) 14:699–718
https://doi.org/10.1007/s40095-022-00544-y

ORIGINAL RESEARCH

Prediction of biomass corrosiveness over different coatings in fluidized bed combustion

M. L. Contreras[1] · M. Benito[1] · A. Bahillo[1]

Received: 23 May 2022 / Accepted: 1 October 2022 / Published online: 18 October 2022

Abstract
Energy production in biomass fired boilers is increasing rapidly due to the advantages of CO_2 neutrality and renewability, however damaging agents present in biomass composition accelerates power plant components corrosion. This study evaluates the influence of the biomass burned in fluidized bed combustion processes on high-temperature corrosion, by means of thermodynamic equilibrium modelling, considering those reactions occurring between the combustion atmosphere and different protective coatings (isFeAl, isNiAl and isSiCrAl). Fuels composition and operating conditions from a 10 kW BFB boiler were introduced as input data to improve the performance of the model. Representative samples from agricultural waste, industrial wood and forestry wood waste were selected for evaluation. Results showed industrial wood waste as highly damaging for most coatings studied, with high risk of salt stickiness, deposits formation and release of acidic gases. The elevated volatiles percentage together with significant ash content determined might lead to a major ash components release to the gas phase, available to later condense in the metals surfaces. Silication of alkali and deposited alkali chlorides were the dominant corrosion mechanisms observed for most cases. An increase in alloys corrosion resistance was detected through the model when nickel or chromium was present, showing isSiCrAl as the most resistant. However, alloys protection exhibited significant variations depending upon the biomass burned, thus materials selection should consider the compatibility with conditions for its final use. Thermodynamic modelling, based on real conditions and fuels composition, provides a useful tool to identify key factors for protective coatings design when employing new waste fuels.

Keywords Biomass combustion · High-temperature corrosion · Thermodynamic equilibrium model · Corrosion-resistant coatings

Introduction

Energy from biomass, a renewable and CO_2-neutral source, has become the most globally used renewable energy source, corresponding to more than 60% of all renewable energy sources (RES) in Europe. Biomass includes a large variety of different fuels with different chemical composition and combustion characteristics [1].

In spite of the benefits, biomass composition could be a potential problem in the thermal conversion of low-grade fuels, as it contains an important concentrations of ash-forming elements (K, Na, S, Cl, Ca, Mg, Si, P, Al, and Fe) which can be released during the thermal conversion to form bottom and fly ashes, which at a later stage affect the thermal process, giving rise to operational problems such as deposit formation, corrosion, slagging and bed agglomeration in fluidized-bed boilers [1–3]. Deposit formation on the surface of the superheater tubes reduces the boiler efficiency. High concentrations of alkali and chlorine in the deposit also cause severe corrosion of the steel surfaces [2]. During biomass combustion, chlorine is released as HCl and Cl_2, reacting with the metal heating surface, causing severe active oxidation corrosion [3]. Also, it can promote the gasification of the alkali metal elements in the fuel and react with alkali metals to form volatile alkali chloride in the gas phase. The vast majority of gaseous alkali metals are deposited and condensed on the low-temperature metal heating surface. Furthermore, they trap solid particles in flue gas, which leads to serious slagging, fouling and corrosion [4].

✉ M. L. Contreras
mluisa.contreras@ciemat.es

[1] Sustainable Thermochemical Valorization, Department of Energy, CIEMAT, Av. Complutense 40, 28040 Madrid, Spain

High-temperature corrosion has always been a major obstacle to improve the boiler steam parameters [5]. With the increase in the boiler combustion temperature and the presence of corrosion elements, intense corrosion in the furnace has made the traditional alloys no longer satisfactory.

A corrosion attack can be mitigated in two ways: improving the materials or changing the surrounding environment of the materials. Several field and laboratory studies [6–10] have investigated both corrosion mechanisms and ways of minimizing this problem, such as the use of chemical additives [11–13]. A great deal of research has also been devoted to the development of new materials and technologies to meet the high-temperature environment in the furnace [14–22]. Modifying the surface of boiler components by depositing protective *coatings* based on the formation of corrosion-resistant oxide scales is also a possible mitigation route [23]. Coatings provide a way of extending the limits of use of materials at the upper end of their performance capabilities. The phases that constitute the coating layer should be thermodynamically stable in the operating environment. A large number of coating processes are available to provide surface protection [24]. Several authors have pursued efficient coatings to prevent the high-temperature corrosion of metallic materials in biomass fuelled boilers and waste incinerators [25–27].

Despite the growing interest in metallic coatings, a comprehensive treatment of the coatings from the experimental methodologies to the fundamentals and of their corrosion behaviour in real conditions is lacking. There are studies on different aspects of coatings, including wear [28] or erosion-corrosion performance [29], hot corrosion [30] low-temperature corrosion [31] and corrosion in supercritical boilers [32]. However, to date, studies developed exhibit difficulties in relating specific parameters to corrosion observed, as there are too many parameters such as temperature, ash deposit composition and gas composition which are continually fluctuating. For this reason, most studies carried out to check coatings efficiency are developed at laboratory reactors employing synthetic gas mixtures with addition of salts to simulate real boiler conditions, while there is a lack of research on the effect of coating composition in real corrosive environments typical of biomass energy power plants.

On the other hand, to understand corrosion mechanisms, it is necessary to know more about chemical reactions happening in the boiler. In this sense, it is fundamental to predict the ash transformation behaviour and also to find methods in order to estimate the degree of ash-related problems for specific fuels and fuel mixtures [2].

The first step to determine the adequacy of a given fuel, from the ash behaviour point of view corrosion, is the elemental analysis of the fuel ash content. Apart from the analytical methods, thermodynamic equilibrium modelling has also become a commonly used tool to better understand the ash transformation behaviour. Most of reported thermodynamic studies have been focused in various ash-related processes such as deposition related issues, slag formation in furnaces, bed agglomeration of fluidized-beds and smelt bed behaviour [33–36]. Other authors have also evaluated corrosion of heat transfer surfaces through the prediction of the potential reactions that may take place among the metals of the superheaters with the combustion atmosphere [1, 2, 23]. However, these studies are usually based on the evaluation of one specific fuel and, with respect to the composition of the combustion atmosphere (gases and ashes), representative compositions of biomass combustion atmospheres are often employed as input data for the model. Until the moment, there are not reported studies which evaluate and compare the affection of different biomass fuels over a specific material, employing real combustion conditions.

In this sense, this study aims to assess the risk of corrosion of representative biomass fuels over different protective coatings, considering the reactions that take place among the alloying elements with the combustion atmosphere and the deposits. Thermodynamic equilibrium modelling was used as a predictive tool, simulating different atmospheres arising from the combustion of representative biomasses from diverse categories (agricultural, forestry and industrial) over three different alloys (isFeAl, isNiAl and isSiCrAl).

The first part of this research includes a previous physicochemical characterization of the biomass fuels, in order to both anticipate the potential ash corrosiveness of the diverse biomass types and also, to better interpret the results obtained in the model. The second part evaluates the influence of the biomass composition on corrosion during FBC, by modelling the exposition of each selected alloy to the diverse combustion atmospheres. In this sense, modelling results have been divided into three main sections corresponding to three target coatings.

The final objective of this work consists of determining which of these alloys may involve a major protection in boilers when employing a specific type of biomass, thus last part of this article compares the potential resistance provided by the diverse coatings against a given biomass combustion atmosphere.

Material and methods

Biomass fuels analysis

The selection of the biomass fuels was conducted on the basis of covering the main biomass categories employed as power plant boiler fuels. In this sense, representative samples from agricultural waste (wheat straw, WS), industrial wood (industrial waste wood, IWW) and wood residues

(forestry residues, FR, and eucalyptus wood, EW) were chosen for the study.

The first step in developing a thermodynamic equilibrium modelling is to carry out a complete characterization of the fuels. For effective utilization of biomass fuel, the knowledge of their characterization is essential. The constituents of biomass fuel vary from region to region and depend upon sources from which biomass is collected and method of preparation of biomass.

Characterization of the solid biofuels was carried out, based on the latest European standards for biomass materials. The proximate and ultimate analyses of the fuels were undertaken by utilizing LECO Truspec equipment. Minor elements content in fuels (ash analyses) was quantified by ICP-AES and ICP-MS techniques. Trace elements (TEs) concentrations were also determined through more specific techniques. For mercury case, a direct analyser (DMA 80) based on EPA Method 7473 was employed. As and Se were determined through HGAAS, while for Cd, GFAAS technique was used. The rest of TEs analyses were carried out through ICP-AES.

Coatings selection

The chemical composition of three promising coatings was used for the study. The selection includes the composition of two slurry aluminides coatings with and without silicon addition (isSiCrAl, isFeAl,) and one hybrid coating, consisting in a slurry aluminide coating combined with nickel electrodeposition (isNiAl). These slurry aluminide coatings have been produced on different substrates and have demonstrated excellent high-temperature corrosion resistance under steam, fire-side corrosion and metal dusting conditions among others.

In addition to the coating microstructure, its chemical composition is also of great relevance to the corrosion protection ability during biomass combustion. The chemical composition of selected alloys (Sect. 2.3) was used to introduce metallic elements contents.

Ni- and Fe-based coatings are the most commonly used alloy systems in boiler applications. The main motivation for using *Fe-based* alloys is that they are rather cheaper and more environmentally friendly compared to many other alloying elements. *Ni-based* thermal spray coatings often display good resistance to high-temperature corrosion. The Ni matrix is preferred over other metal matrices like Fe in Cl-containing environments as the formation of $NiCl_2$ is thermodynamically less favoured than other detrimental metallic chlorides such as $FeCl_2$.

Cr is a commonly used alloying element in materials for high-temperature applications (850 °C) that can form a stable oxide (Cr_2O_3).

Similar to Cr, *Al* is also widely used in thermal spray powder composition, particularly for high-temperature corrosion applications.

Low concentrations of *Si* are often used in high-temperature alloys. A small level of Si can also be found in thermal spray powder compositions to provide the high-temperature corrosion resistance by the formation of a protective SiO_2 layer on the coating surface. A small level of Si can also facilitate formation of other protective oxide scales such as Al-rich or Cr-rich oxides. If Cr is also available in the composition, the high O affinity of Si leads to the formation of a SiO2 layer beneath the chromia scale.

As was stated before, under oxidizing–chloridizing conditions, the situation is much more complex as an internal selective attack can occur, depending on the alloying elements present in the material. In this sense, detailed knowledge of the behaviour of different alloying elements in commercial materials, in particular, coatings, is important.

Modelling approach

The modelling was performed using HSC Chemistry 6.1 software. Thermodynamic equilibrium modelling is based on the Gibbs energy minimization, which calculates the chemical the most stable composition of the system (equilibrium composition) at specified conditions, considering thermodynamic data from all the phases and compounds. As a simplification, activity coefficients were taken as 1.0.

In the fluidized-bed environment, ash reactions could approach equilibrium due to a good gas–solid contact and mixing and a relatively long residence time for the solids. However, in spite of the advantages found for thermodynamic equilibrium modelling in combustion systems, it is important to consider the limitations of this program. Firstly, not all the possible species that may occur under different conditions are included in the thermodynamic databases. Secondly, physical processes are not taken into account, while in experimental conditions, reactions are highly dependent on the reactants mixing, residence time and on the kinetics of the reactions.

The first step in the equilibrium calculation is the definition of the system. In this study, calculations have been carried out considering combustion parameters obtained at a 10 kWth BFB pilot plant, located at Ciemat (Fig. 1), considering the combustion pattern in the fluidized-bed system and the temperature profile in the combustion zone, although results obtained are considered to be valid for bigger scales.

As input data for the model, chemical composition of atmosphere (air) and biomass fuels (Table 1) as well as recorded operating data, such as temperature, pressure and air/fuel ratio, were introduced in the theoretical reactor, simulating the conditions in the real BFB boiler.

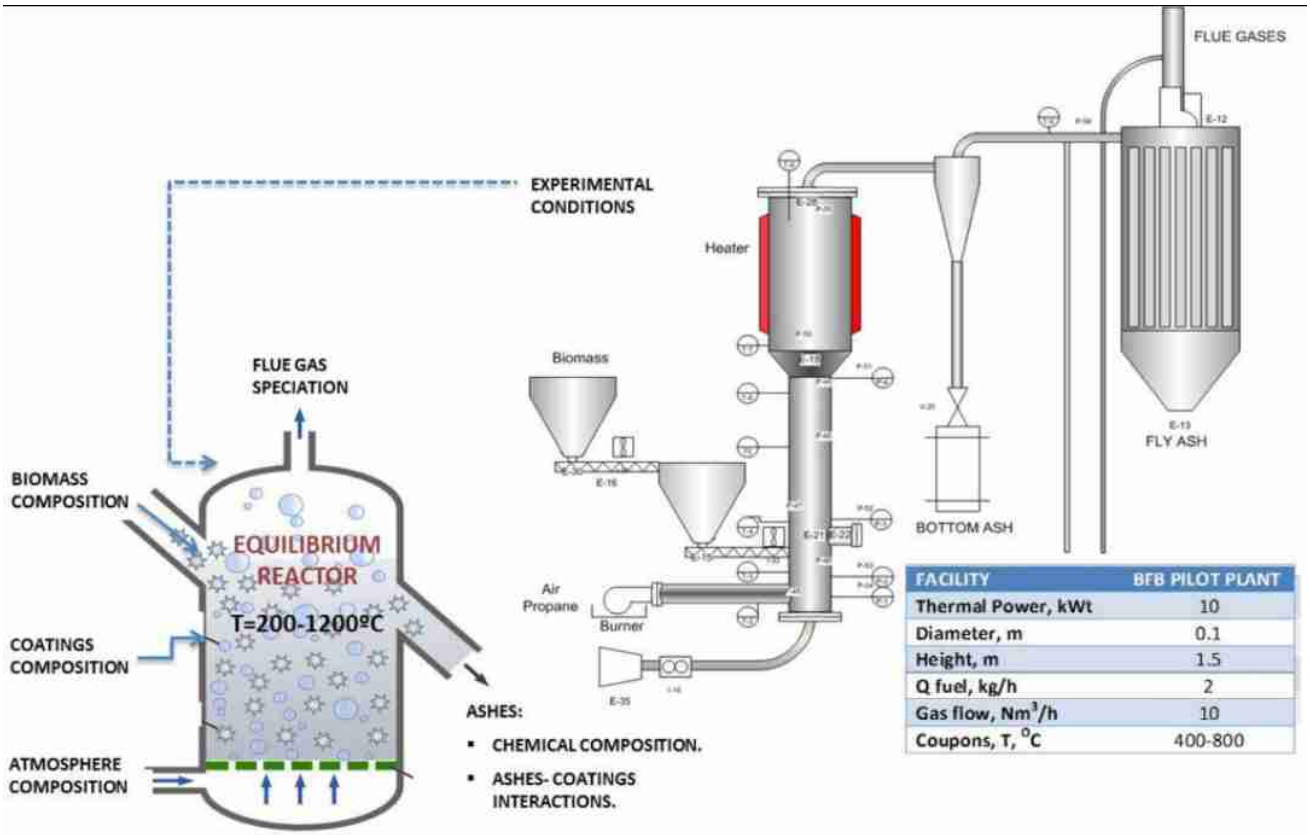

Fig. 1 Scheme of the equilibrium reactor. Inputs, outputs and operation conditions

Secondly, the chemical compositions of selected alloys (Table 2) were used to introduce the values of the metallic elements.

By crossing these coatings with the different biomass fuels, the theoretical matrix carried out for the study can be drawn as shown in Fig. 2. The study will thus compare both the effectiveness of the different coatings for a specific biomass and also the resistance of each coating versus the different types of biomasses.

The maximum temperature that the flue gas reaches in the FBC system (850 °C) was considered; however, the main emphasis was to predict the condensation behaviour of the flue gas in the superheater section. Therefore, calculations were performed at atmospheric pressure into a global temperature range of 300–800 °C, giving a special attention to the temperature interval of 500–650 °C) where the flue gas meets the superheater steel tubes making it possible to evaluate the fouling tendency.

For discussion of the results, only species contributing more than 1% of total compounds were considered.

Results and discussion

Biomass fuels characterization

Table 1 shows physical and chemical characterization results achieved for selected biomass samples, through the methodology described in Sect. 2.1. Figures 3a and b shows, respectively, major and trace elements contents determined in the biomasses analyses, in order to compare and predict the potential corrosiveness of the samples.

Physicochemical characterization results have shown great variability among the different biomass fuels selected. From proximate analysis, it can be checked how the major ash content corresponds to forestry residues (FR) samples. The highest sulphur content is also detected for FR sample. However, the elevated calcium concentration present in this biomass may counteract sulphur released to the gas phase during combustion.

In addition, TEs content determined for this biomass together with that obtained for industrial waste wood (IWW)

Table 1 Biomass fuels characterization

	Unit	WS	FR	IWW	EW
Proximate analysis					
Moisture content	wt.% w.b	8.30	4.30	4.40	17.9
Ash content	wt.% d.b	4.90	8.80	2.60	0.90
Volatiles	wt.% d.b	69.5	74.7	78.7	80.1
Ultimate analysis					
C	wt.% d.b	41.80	46.10	48.50	49.20
H	wt.% d.b	6.40	6.10	6.10	5.90
N	wt.% d.b	0.56	0.70	1.76	< 0.10
S	wt.% d.b	0.11	0.30	0.05	0.01
O	wt.% d.b	37.75	33.62	36.51	43.84
Cl	wt.% d.b	0.18	0.08	0.08	0.05
Ash analysis					
Major elements					
Al	mg/kg d.b	240	3400	770	8300
Ca	mg/kg d.b	4500	11,000	3300	270,000
Fe	mg/kg d.b	230	4500	570	8100
K	mg/kg d.b	8200	1800	730	61,000
Mg	mg/kg d.b	1100	1200	490	28,000
Na	mg/kg d.b	190	1400	670	18,000
Si	mg/kg d.b	17,000	14,000	2100	69,000
P	mg/kg d.b	700	300	150	11,000
Mn	mg/kg d.b	29	170	70	12,000
Trace elements					
Hg	µg/kg d.b	4.18	32.20	33.56	8.21
Cr	mg/kg d.b	28	62	34	< 1.0
Ni	mg/kg d.b	17	61	19	< 1.0
Cu	mg/kg d.b	10	2600	60	2.4
Ti	mg/kg d.b	8	900	860	350
Pb	mg/kg d.b	< 6	550	84	< 1.0
Zn	mg/kg d.b	14	1700	230	410

w.b.: wet basis; d.b.: dry basis; wt.%: weight percent

shows the highest values, with significant concentrations detected for elements such as Cu, Ti, Pb and Zn. In contrast, the lowest TEs contents were found for wheat straw (WS). These results indicate a more elevated TEs content (including mercury) in woody biomasses than in agro-residues. This statement is in agreement with previous studies of biomass materials characterization. Previous researchers [37] observed that fly ashes from wood samples have generally higher As, Cd, Pb and Hg contents than those of agricultural residues. Stromberg B [38] denoted a typical elevated content of impurities in waste wood materials.

It is also noteworthy ash analyses results obtained for eucalyptus wood samples, with significantly higher amount of ash-forming light metals (Al, Ca, Mg, Na and K) in contrast to the rest of the biomasses studied. These elements have great influence on ash-related problems in combustion plants.

With respect to agro-residues, wheat straw samples exhibit the most elevated chlorine concentration. This fact, joined to the important potassium content of this fuel, may lead to potential corrosive atmosphere during combustion.

Corrosiveness of biomass ashes

In order to anticipate and compare the potential risk of selected biomass materials in the combustion process, different *fuel indexes* (key numbers) were calculated for the diverse samples, based on the chemical composition results of biomass fuel ashes. These indexes relate the various substances in the ash to one another, being useful to find out the critical quantity relationships between different substances that can be directly related to risk components or risky mixtures of components [39]. A comprehensive overview on different fuel indexes has been provided in the literature [40, 41].

$$\text{Vaporization Ratio}: \mathrm{Cl}/(\mathrm{K}+\mathrm{Na}) \quad (1)$$

$$\text{Salt Ratio}: (\mathrm{Cl}+2\mathrm{S})/(\mathrm{K}+\mathrm{Na}) \quad (2)$$

$$\text{Sulphating number}: 2\mathrm{S}/\mathrm{Cl} \quad (3)$$

Table 3 shows key numbers values determined for biomass fuels ashes. The major *vaporization ratio*, which indicates *high risk of corrosive chlorine-rich deposits* formation, was obtained for industrial waste wood. Higher values for *salt ratio* index were also detected for this biomass together with forestry residues, predicting hazardous for salt stickiness, formation of deposits and free corrosive acidic gases. Hazardous for alkaline sintering is expected for wheat straw, with salt ratio values below 0.7.

Sulphating number exhibit elevated values for all biomasses except for eucalyptus wood, with significantly major numbers calculated for forestry residues case. This key number shows whether there is *sufficient surplus sulphur*

Table 2 K moles of metallic elements introduced in the thermodynamic calculations

Coating acronym	Fe	Ni	Al	Si	Cr
isFeAl	5.2×10^{4}	–	5.2×10^{-4}	–	–
isNiAl	–	7.5×10^{-5}	7.5×10^{-5}	–	–
isSiCrAl	–	–	2.34×10^{-3}	1.3×10^{-4}	1.3×10^{-4}

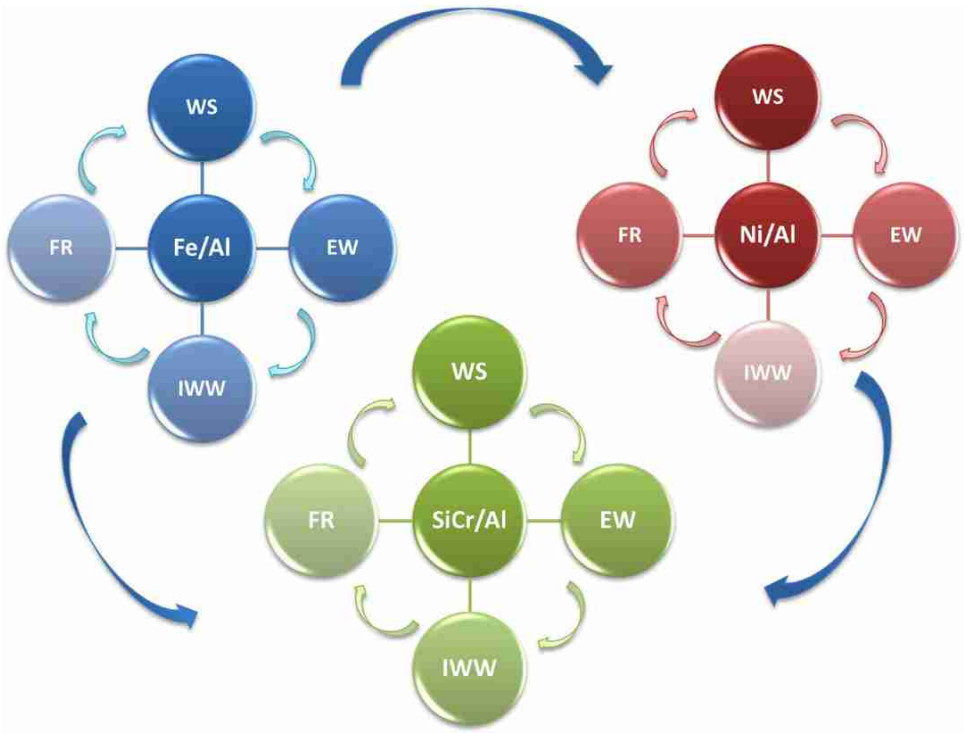

Fig. 2 Matrix of the modelling tests

to reduce the risk of corrosion in conjunction with alkali chlorides. It has been found from experience that if the molar ratio S/Cl is between 2 and 4, the risk of chloride-induced corrosion will be reduced [38]. In this sense, chloride-induced corrosion may be offset by sulphur in forestry residues case. On contrast, low valued found for eucalyptus wood ashes denotes potential chloride-induced corrosion when employing this biomass.

Figure 4 summarizes the potential risks determined for the diverse biomass ashes studied, revealing that significant hazard might be caused if industrial waste wood or forestry residues were fed in a combustion process, leading to salt stickiness and free corrosive acidic gases.

Thermodynamic equilibrium modelling for isFeAl coating

Impact of wheat straw combustion on isFeAl coatings

Main solid species formed from Fe/Al interactions with ash-forming elements during conventional combustion of wheat straw were determined. Figure 5a shows equilibrium composition of main species determined at a wide temperature range from 300 to 800 °C. Only those species resulting from interactions towards isFeAl coating are shown in this figure, although other corrosive forms have also been detected to be originated in this atmosphere.

In these conditions, results exhibit $CaAl_2Si_3O_{10}(OH)_2$ as the main compound formed, assuming more than 35% of total species, coming from the reaction of calcic components in fuel and being enhanced by both silica concentration and water content. Dodson JR research on wheat straw ashes use [42] also reported the occurrence of insoluble calcium silicate precipitates in wheat straw ashes combusted at 600 °C or above. Secondly, $KFe_3(FeSi_3O_{10})(OH)_2$ accounts for approximately 20% of total species predicted to be formed in this scenery. Previous researchers have stated about the formation of insoluble potassium silicates and aluminosilicates during wheat straw combustion [43]. Nielsen et al. [44] gave a useful analysis of the deposition of potassium salts on superheater tubes during straw firing, showing how potassium was present as K_2OSiO_2(s), KCl(s) and K_2SO_4(s) and at low temperatures.

Results obtained (Fig. 5a) exhibits how both compounds are stable in a wide thermal range (300–780 °C). Dodson JR [42] also showed how u*p to 500 °C, potassium solubility remains constant irrespective of the extent of combustion or the cooling condition.*

The presence of these compounds indicates *corrosion processes associated with silication of alkali chlorides*, which can be described through Eqs. 4–6:

$$2MCl\,(s,\ l,\ g) + \left(2SiO_2 + Al_2O_3\right)(s,\ l) + H_2O\,(g) \rightarrow 2MAlSiO_4(s,\ l) + 2HCl\,(g) \quad (4)$$

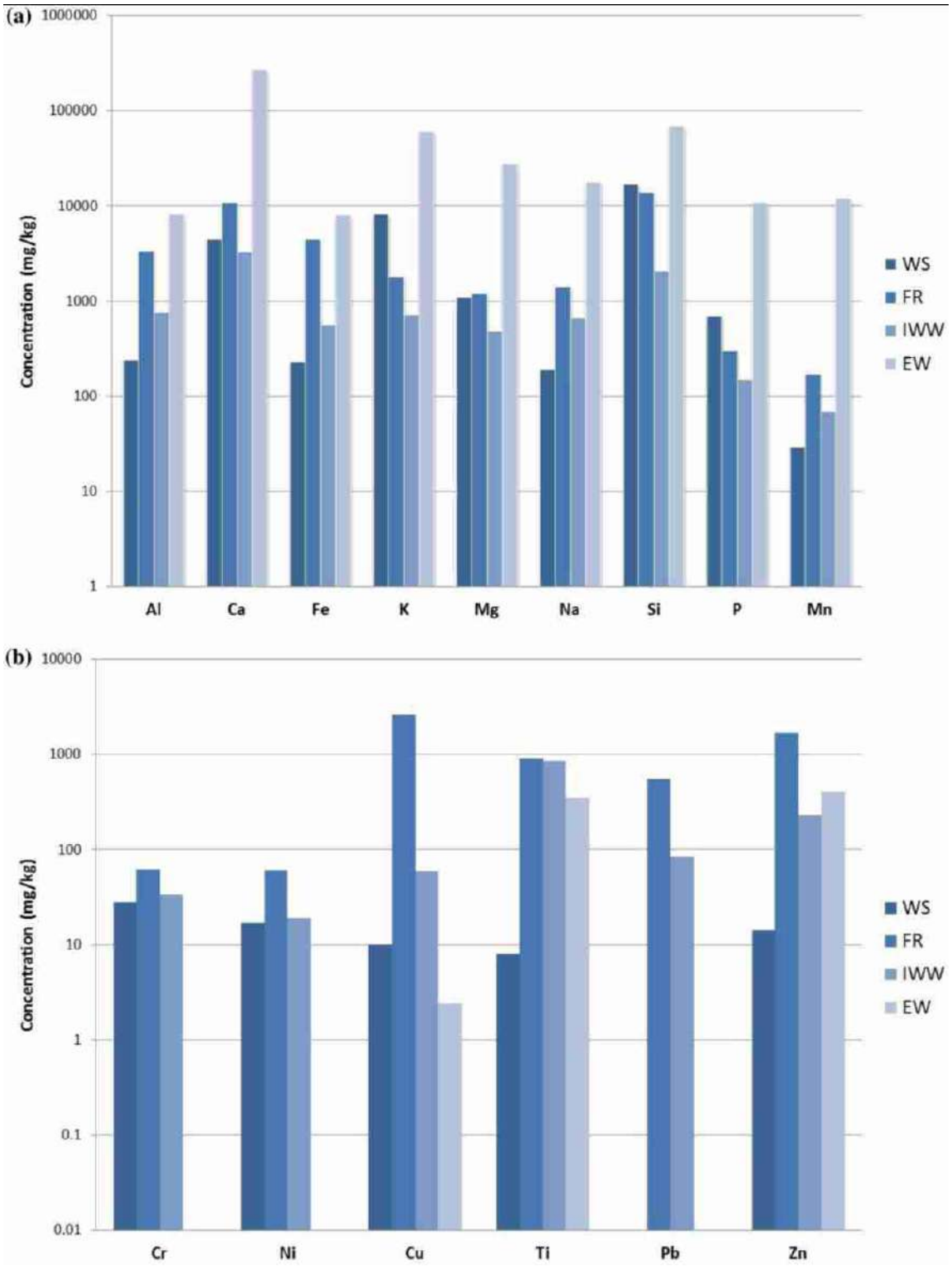

Fig. 3 Biomass fuels characterization **a** Major elements concentrations; **b** Trace elements concentrations

$$2\mathrm{MCl\ (s,\ l,\ g)} + \left(4\mathrm{SiO_2} + \mathrm{Al_2O_3}\right)\mathrm{(s,\ l)} + \mathrm{H_2O\ (g)} \rightarrow 2\mathrm{MAlSi_2O_6(s,\ l)} + 2\mathrm{HCl\ (g)} \quad (5)$$

$$2\mathrm{MCl\ (s,\ l,\ g)} + \left(6\mathrm{SiO_2} + \mathrm{Al_2O_3}\right)\mathrm{(s,\ l)} + \mathrm{H_2O\ (g)} \rightarrow 2\mathrm{MAlSi_3O_8(s,\ l)} + 2\mathrm{HCl\ (g)} \quad (6)$$

Table 3 Key numbers for biomass materials studied

	WS	FR	IWW	EW		
Vaporization ratio						
Cl/(K + Na)	0.23	0.21	0.47	0.01	*> 0.3:*	*High risk of the formation of corrosive chlorine-rich deposits*
					> 1:	*High risk of formation of other volatile chloride than with Na and K*
						Also high risk of homogeneous chloride-induced corrosion
						or low-temperature corrosion with Cl admixture by excess HCl
Salt ratio						
(Cl + 2S)/(K + Na)	0.55	1.96	1.12	0.01	*> 1:*	*All free alkali metal can be bound as chloride or sulphate*
					< 1:	*All chlorine and sulphur can be bound to alkali (if all alkalis are free)*
					< 0.7:	*Hazardous for alkaline sintering*
					> 0.7:	*Hazardous for salt stickiness, formation of deposits and free corrosive acidic gases*
Sulphating number						
2S/Cl	1.35	8.29	1.38	0.44	*< 1:*	*All chloride cannot be transformed to sulphate*
					> 1:	*All chloride can be transformed to sulphate*

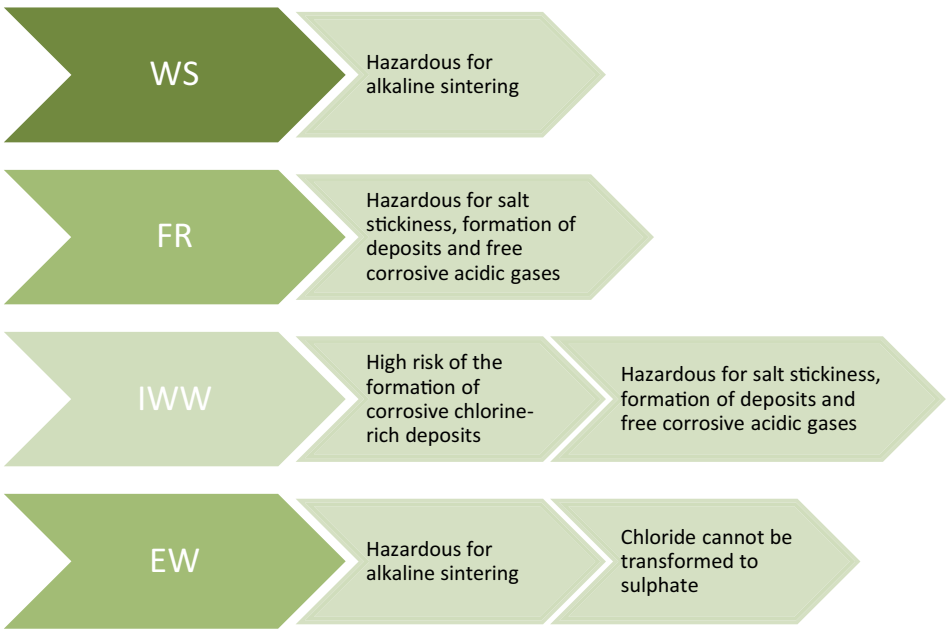

Fig. 4 Potential risk determined for biomass ashes studied, based on fuel index calculations

M in equations denotes the metal from alkali chlorides. HCl generated through Eqs. 4–6 is responsible for corrosion, as it diffuses towards the metal surface to form volatile metal chlorides, such as $FeCl_2$ leading to the continuous transport of the metal scale interface to the bulk gas [45, 46].

The bar graph in Fig. 5a compares the percentages of Fe/Al-ash compounds predicted to be originated at the selected temperature range of 500–700 °C. From the graphic, it can be checked how, apart from calcium, *potassium* also exerts a high influence in the formation of most deposits predicted for this biomass. On the other hand, silicon has been detected as an important precursor for most of determined chemical forms. Straw samples analyses (Fig. 3) exhibited great contents of *silicon* and *potassium*, in contrast to other biomasses, and *calcium*, which may have given rise to these chemical forms.

Berlanga et al. [1], in their thermodynamic calculations for wheat straw corrosion, detected metal oxidation initiated by the presence of potassium. During combustion, soluble K is released as K(g), KOH(g), KCl(g), and other species which may further react with other compounds of the flue gas. The most important secondary reaction is the conversion of alkali vapours (e.g. KOH(g), KCl(g), K2SO4(g)) into corresponding alkali silicates [28, 37]. Aluminium silicates may capture volatile potassium during combustion, thereby reducing the risk of deposit and corrosion. [39]. However,

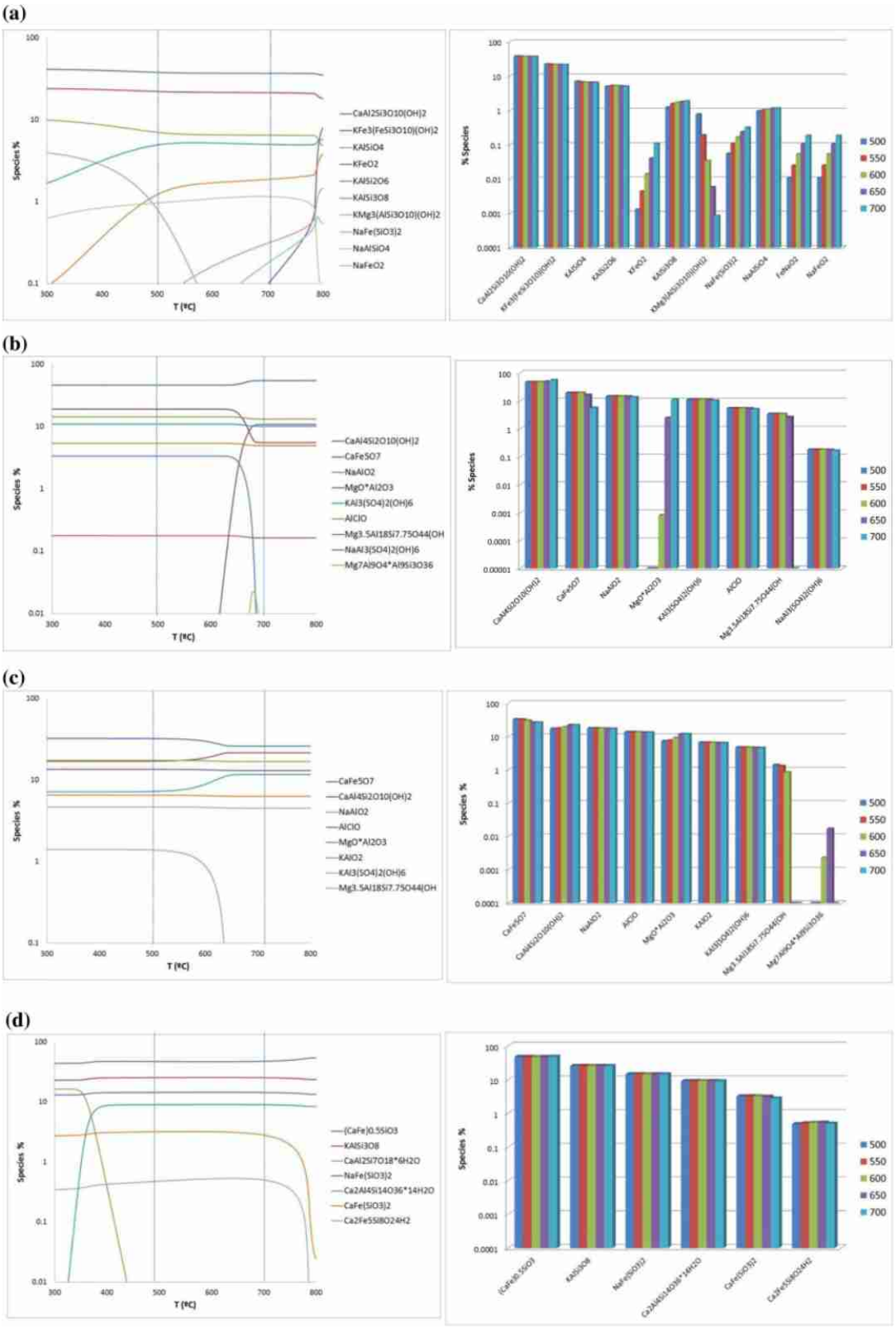

Fig. 5 Equilibrium composition and temperature influence of main species resulting from isFeAl–ash interactions during combustion of: **a** WS; **b** FR; **c** IWW; and **d** EW

high contents of silica together with potassium are directly linked to the formation of tenacious surface deposits on firesides and heating surfaces [40].

In this sense, silica can modify the chemistry of other ash-forming elements, such as K, Na, and Ca, through secondary reactions and thus indirectly affect the deposition and corrosion properties of fly ash. Otherwise, the presence of hydroxyl groups in main chemical forms originated reveals that water content in fuel may increase the formation of main deposits.

With respect to minor components predicted, Fe oxides formation is observed to be strongly affected by temperature.

Impact of forestry residues combustion on is FeAl coatings

Figure 5b shows the equilibrium diagram of main compounds arising from reactions of forestry residues ash components with Fe/Al materials. The percentages of those species formed at 500–700ºC temperature range are exhibited in the bar graph from Fig. 5b.

Forestry residues was seen to contain significant concentrations of calcium (Fig. 3a), in comparison with the rest of the fuels studied (with the exception of eucalyptus). In this sense, main forms originated in the process (≥ 10%) are result of Al and Fe interactions with *calcium* components in the fuel, giving rise to $CaAl_4Si_2O_{10}(OH)_2$ and $CaFe_5O_7$. Silicon is also present in significant contents in this fuel, promoting Ca/Mg–aluminium silicates formation. As it was described for WS, the occurrence of alumina-silicates such as $CaAl_4Si_2O_{10}(OH)_2$ involves corrosion mechanisms associated with silication of alkali chlorides, (Eqs. 4–6) [45, 46]. $CaFe_5O_7$ indicates *active oxidation of iron* in these conditions, but the formation of this specie is seen to decrease at temperatures above 650 °C (Fig. 5b). Grabke et al. [47] gave the basis for understanding this mechanism.

A second group of aluminium compounds (5–10%) are result of aluminium interactions with Na, Mg, K and Cl ($NaAlO_2$, $Mg^*Al_2O_3$, $KAl_3(SO_4)_2(OH)_6$ and AlClO). $NaAlO_2$ formation is related to *corrosion associated with deposited alkali chlorides*. Potential reactions for this corrosion mechanism are listed below (7, 8). M denotes the metal involved (i.e. Al, Fe, etc.):

$$M_2O_3(s) + 2NaCl\,(s) + 1/2\,O_2(g) \rightarrow 2NaMO_2(s,\ l) + Cl_2(g) \quad (7)$$

$$M_2O_3(s) + 2KCl\,(s) + 1/2\,O_2(g) \rightarrow 2KMO_2(s,\ l) + Cl_2(g) \quad (8)$$

These reaction products have been observed in previous corrosion testing reports [45, 48]. For this fuel, K and Na capture are seen to be more influenced by sulphur than by silica, as it occurs in wheat straw case. Sulphur reduces KCl concentration in the flue gas by sulphation. In addition, Kassman et al. [11] confirmed that the presence of gaseous SO_3 is of greater importance than that of SO_2 for the sulphation of gaseous KCl.

$K/NaAl_3(SO_4)_2(OH)_6$ observed in Fig. 5b, indicates *corrosion processes associated with sulphation of alkali chlorides*, which can be described by reactions 9, 10 [23]:

$$2MCl(s,\ l,\ g) + SO_2(g) + 1/2O_2(g) + H_2O(g) \leftrightarrow M_2SO_4(s,\ l) + 2HCl(g) \quad (9)$$

$$2MCl(s,\ l,\ g) + SO_2(g) + O_2(g) \leftrightarrow M_2SO_4(s,\ l) + 2Cl_2(g) \quad (10)$$

Different authors have shown how, during combustion, sulphur reduces the formation of KCl in the flue gas by sulphation [49–51]. The presence of gaseous SO_3 is of greater importance than that of SO_2 for the sulphation of gaseous KCl. This was confirmed by Kassman et al. [49, 50].

Impact of Industrial Waste Wood combustion on is FeAl coatings

Figure 5c presents equilibrium composition of main species determined for industrial waste wood combustion into Fe-Al system, at a wide temperature range from 300 to 800 ºC. Dominant compounds within the temperature range of 500–700 ºC are extracted in the bar chart from Fig. 5c.

Calcium and silicon are seen as the dominant major ash-forming elements content in industrial waste wood (Fig. 3a), thus $CaFe_5O_7$ and $CaAl_4Si_2O_{10}(OH)_2$) represent the main deposits (≥ 10 species %) formed during the combustion of this fuel. Na/Cl-aluminium oxides are also encountered in important amounts ($NaAlO_2$, AlClO).

In lower percentages (5–10%), aluminium is observed to react with magnesium and potassium components in fuel ($MgO^*Al_2O_3$, $KAlO_2$, $KAl_3(SO_4)_2(OH)_6$). In this case, sulphur also participates in, primary, potassium and, secondly, sodium capture ($K/Na–Al_3(SO_4)_2(OH)_6$).

In a minor extent (˂5%), diverse Mg–Al silicates have also been determined ($Mg_35Al_{18}Si_7O_{44}(OH)$, $Mg_7Al_9O_{4*}Al_9Si_3O_{36}$). In this case, silicates and sulphates also react with alkali vapours, thus affecting the alkali chemistry in flue gas.

Predicted species calculated in these conditions may indicate that main corrosion mechanisms in this case are primary related to deposited alkali chlorides, 7, 8 ($CaFe_5O_7$, $NaAlO_2$), followed by silication of alkali chlorides, 4–6 ($CaAl_4Si_2O_{10}(OH)_2$) and direct corrosion by $Cl_2(g)$ (AlClO). Sulphation of alkali chlorides (Eqs. 9–10) is also detected in minor concentrations ($KAl_3(SO_4)_2(OH)_6$).

Impact of Eucalyptus combustion on isFeAl coatings

Equilibrium composition of main compounds resulting from eucalyptus combustion into Fe-Al system is shown in Fig. 5d. Eucalyptus biomass was seen to contain major concentration for all major ash-forming elements than the rest of the biomasses studied, with significantly high silicon content (Fig. 3a), being silication of alkali chlorides the main corrosion mechanism involved with this fuel.

Main compounds within the temperature range of 500–700 ºC are exposed in the bar graph from Fig. 5d. $(CaFe)_{0.5}SiO_3$ is observed as the major compound originated, followed by $KAlSi_3O_8$ and $NaFe(SiO_3)_2$, which are also determined in important percentages (10–50%), as result of the high potassium and sodium concentration present in this biomass.

Other calcium silicates are detected in lower concentrations (1–5%), resulting from interactions with both Al and Fe ($Ca_2Al_4Si_{14}O_{36}$*$14H_2O$, $CaFe(SiO_3)_2$).

Thereby, in eucalyptus case, silica reactions are the governing factor affecting the chemistry of other ash-forming elements (K, Na, and Ca), which indirectly affects the deposition and corrosion properties of fly ash.

Conclusions of biomass influence on FeAl-based coating corrosion

When a FeAl-based coating is introduced in the hypothetical combustion reactor, different conclusions are drawn according to the biomass fed. Table 4 shows main compounds formed through Fe-Al/ biomass ashes interactions.

In the case of *wheat straw,* both calcium and silicon present in the biomass tend to interact with aluminium to form *Ca–Al–Si hydroxides*, as dominant compounds. Potassium also exerts a high influence in the formation of most deposits predicted, with $KFe_3(FeSi_3O_{10})(OH)_2$ as the second main compound (20% of total species) and diverse K/Na-Al-silicates in lower concentrations, which may reduce alkali vapours in the gas phase.

In *forestry residues case*, main forms originated in the process (≥ 10%) are also result of calcium interactions, but in this case, with both Al and Fe ($CaAl_4Si_2O_{10}(OH)_2$, $CaFe_5O_7$). Silicon is also present in significant contents in this fuel, promoting Ca/Mg–aluminium silicates formation.

On contrast, when *eucalyptus* is employed, iron is involved in main reactions, giving rise to diverse *Ca/Na–Fe silicates*. In addition, $KAlSi_3O_8$ is detected as the secondary dominant compound.

In industrial waste wood case, equal order of concentrations are determined for the different ash-forming elements present in this fuel, giving rise to similar interactions towards both iron and aluminium through diverse oxides, silicates, aluminates and sulphates compounds.

With respect to corrosion mechanisms towards this coating, silication of alkali and deposited alkali chlorides are dominant, followed by minor reactions of sulphation and oxidation by $Cl_2(g)$.

Thermodynamic equilibrium modelling for isNiAl coating

Impact of wheat straw combustion on isNiAl coatings

Main chemical forms originated from isNiAl interactions with wheat straw ash-forming elements were determined.

Table 4 Main species formed through Fe-Al/ biomass ashes interactions, at T = 500–700ºC, and corrosion mechanisms involved

% SPECIES	WS	FR	IWW	EW
≥ 10%	*(2)* $CaAl_2Si_3O_{10}(OH)_2$ *(2)*$KFe_3(FeSi_3O_{10})(OH)_2$	*(2)*$CaAl_4Si_2O_{10}(OH)_2$ *(1)* $CaFe_5O_7$ *(1)* $NaAlO_2$	*(1)* $CaFe_5O_7$ *(2)*$CaAl_4Si_2O_{10}(OH)_2$ *(1)* $NaAlO_2$ *(4)* AlClO	*(2)* $(CaFe)_{0.5}SiO_3$ *(2)* $KAlSi_3O_8$ *(2)* $NaFe(SiO_3)_2$
5–10%	*(2)* $KAlSiO_4$ *(2)* $KAlSi2O_6$	$Mg*Al_2O_3$ *(3)* $KAl_3(SO_4)_2(OH)_6$ *(4)* AlClO	$MgO*Al_2O_3$ (1) $KAlO_2$ *(3)* $KAl_3(SO_4)_2(OH)_6$	*(2)*$Ca_2Al_4Si_{14}O_{36}$*$14H_2O$
1–5%	$KAlSiO_3O_8$ $NaAlSiO_4$	$Mg_35Al_{18}Si_7O_{44}(OH)$	$Mg_35Al_{18}Si_7O_{44}(OH)$	$CaFe(SiO_3)_2$
≤ 1%	$KMg_3(AlSi_3O_{10})(OH)_2$ $NaFe(SiO_3)_2$ $KFeO_2$ $NaFeO_2$	$NaAl_3(SO_4)_2(OH_)_6$	$Mg_7Al_9O_{4*}Al_9Si_3O_{36}$	$Ca2Fe_5Si_8\ O_{24}H_2$

Corrosion associated with solid/deposited alkali chlorides

Corrosion associated with silication of alkali chlorides

Corrosion associated with sulphation of alkali chlorides

Corrosion associated with Cl2(g)

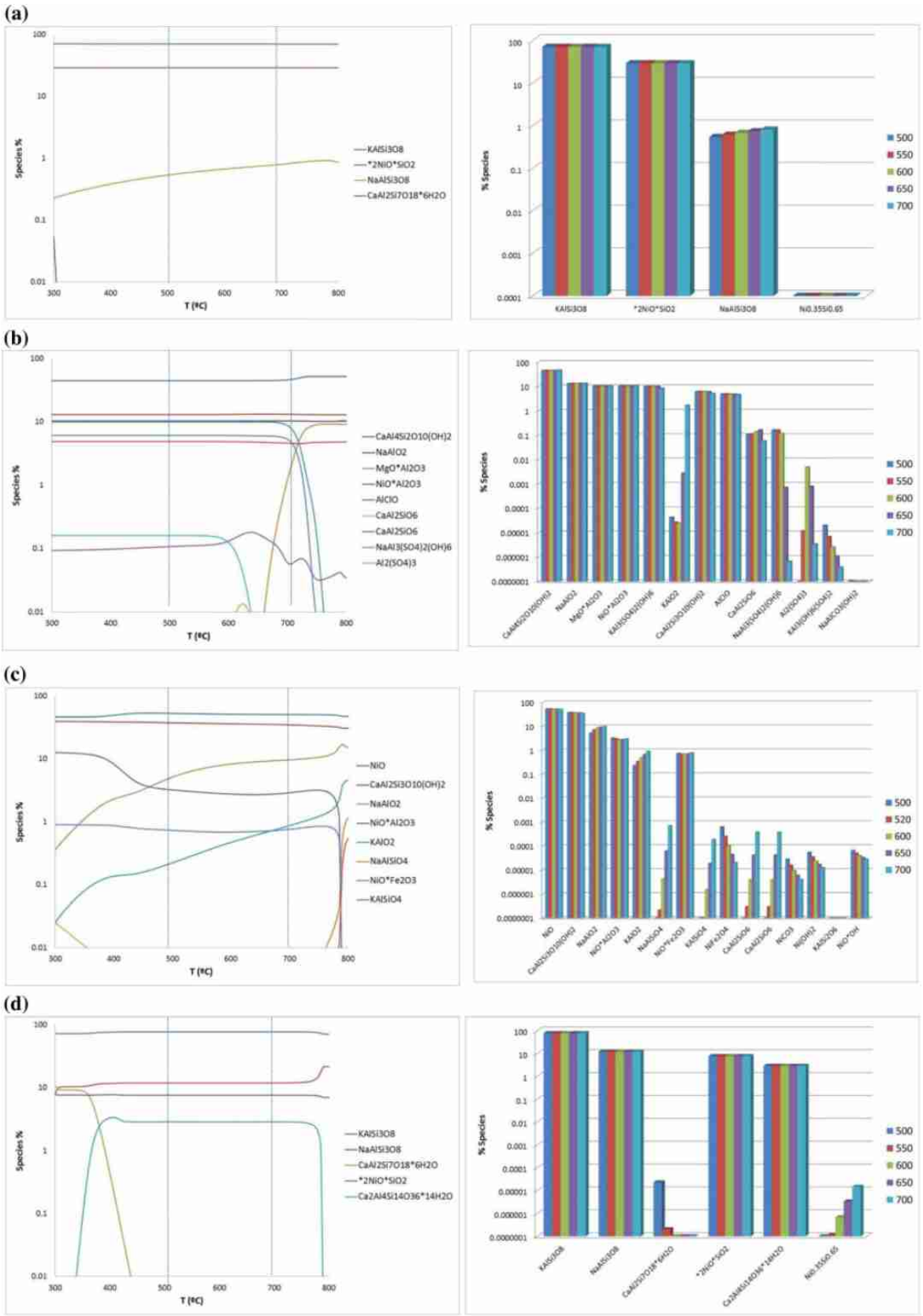

Fig. 6 Equilibrium composition and temperature influence of main species resulting from isNiAl–ash interactions during combustion of: **a** WS; **b** FR; **c** IWW; and **d** EW

Figure 6a shows equilibrium composition of main species determined at a temperature range of 300–800 ºC. The bar chart in Fig. 6a shows Ni/Al-ash compounds predicted to be originated at 500–700ºC.

When wheat straw composition is introduced in the combustion process, both aluminium and nickel are involved in main interactions, with silication of alkali chlorides (Eqs. 4–6) as the primary corrosion mechanism involved with this biomass. $KAl_2Si_3O_8$ is observed as the main specie predicted from metal interactions with wheat straw combustion ashes, which may be related by the important potassium and silicon concentration present in this fuel. The concentration of this compound ($KAl_2Si_3O_8$) is seen to be enhanced with potassium content in fuel.

$2NiO*SiO_2$ is the secondary compound formed in significant amounts. For this fuel, silicon is also observed as an important agent involved in the formation of main chemical species ($KAl_2Si_3O_8$, $2NiO*SiO_2$ and $NaAlSi_3O_8$).

With regard to temperature effect, only minor compounds formed (under 1% of total species) are seen to be affected by this factor.

Impact of forestry residues combustion on isNiAl coatings

Chemical equilibrium compounds derived from forestry residues combustion is shown in Fig. 6b.

Percentages of main Ni/Al-ash species formed at different temperatures are plotted in the bar graph from Fig. 6b. In this scenery, there are few interactions with Ni materials, with only one compound predicted to be formed ($NiO*Al_2O_3$) in percentages around 10% of total compounds formed.

Dominant corrosion mechanisms in this case are related with silication processes ($CaAl_4Si_2O_{10}(OH)_2$) followed by deposited alkali chlorides ($NaAlO_2$). In this case, potassium seems to be removed from the combustion atmosphere by sulphation ($KAl_3(SO_4)_2(OH)_6$).

As in the previous case, minor compounds are more influenced by temperature than main forms.

Impact of industrial waste wood combustion on isNiAl coatings

Main chemical species produced from isNiAl reactions with waste wood ash-forming elements were determined. Figure 6c shows equilibrium composition of main species originated from 300 to 800 ºC.

In contrast to previous fuels, when waste wood is employed as fuel, high oxidation occurs towards nickel, as NiO (more than 45% of total compounds formed), although a significant number of interactions with aluminium are also observed, with $CaAl_2Si_3O_{10}(OH)_2$ as the dominant form, which is linked to silication reactions.

Nickel oxidation is seen to be slightly increased (around 4%) with temperature, but this factor exerts a major influence in the formation of other species which appear in lower concentrations (below 10%).

The bar chart in Fig. 6c shows main predicted compounds at selected temperatures. Major aluminium interactions are observed to be related with the presence of Ca, Si, K and Na. On the other hand, water content is seen to influence the formation of calcic species.

Impact of Eucalyptus combustion on isNiAl coatings

Equilibrium composition obtained, when eucalyptus composition is introduced in the isNiAl system, is charted in Fig. 6d. In this case, ash-forming elements primarily interact with aluminium, and main species formed are influenced by silicon presence. When this fuel is employed, corrosion is mainly associated with silication of alkali chlorides (4–6).

The bar graph in Fig. 6d presents Ni/Al-ash compounds predicted to be originated at selected temperatures. Dominant forms originated in the system are primary $KAlSi_3O_8$, (> 70%) and secondly, $NaAlSi_3O_8$ (12%) and $Ca_2Al_4Si_{14}O_{36}*14H_2O$ (9%). The latest compound is highly influenced by temperature, being sharply reduced above 360ºC. Main nickel compound ($2NiO*SiO_2$) is produced in percentages around 7–8%, and is stable in the whole thermal range studied. The rest of predicted compounds are formed in concentrations under 1%.

Conclusions of biomass influence on NiAl-based coating corrosion

In summary, Sect. 3.2 indicates that the biomass type introduced in the system also influences in a high extent the results obtained for NiAl-based coatings.

In this case, biomass ashes are seen to react, in a major extent, with aluminium, giving rise to diverse compounds which are detailed in Table 5.

Main differences are detected when industrial waste wood is employed. The composition of this fuel showed lower contents for most major ash-forming elements than the rest biomasses studied. The absence of these elements in the combustion atmosphere makes decrease the potential aluminium interactions, determined for other fuels. Lower silication and sulphation reactions are produced when this biomass is burned, which reduces alkali capture, increasing potential corrosion. For this reason, in this case, Ni oxides are the dominant predicted.

With regard to corrosion, silication of alkali chlorides is observed as the dominant mechanism involved, followed by deposited alkali chlorides and minor reactions of sulphation and oxidation by $Cl_2(g)$.

Table 5 Main species formed through Ni–Al/ biomass ashes interactions

% SPECIES	WS	FR	IWW	EW
≥ 10%	*(2)* $KAl_2Si_3O_8$ *(2)* $2NiO*SiO_2$	*(2)* $CaAl_4Si_2O_{10}(OH)_2$ *(1)* $NaAlO_2$	*(1)* NiO *(2)*$CaAl_2Si_3O_{10}(OH)_2$	*(2)* $KAlSi_3O_8$ *(2)* $NaAlSi_3O_8$
5–10%	–	$MgO*Al_2O_3$ $NiO*Al_2O_3$ *(3)* $KAl_3(SO_4)_2(OH)_6$ *(2)* $CaAl_2Si_3O_{10}(OH)_2$	$NaAlO_2$	$*2NiO*SiO_2$ $Ca2Al_4Si_{14}O_{36}*14H_2O$
1–5%	–	AlClO $KAlO_2$	$NiO*Al_2O_3$	-
≤ 1%	$NaAlSi_3O_8$	$CaAl_2Si_3O_6$ $NaAl_3(SO_{4)2}(OH)_6$ $Al_2(SO_4)_3$ $KAl_3(OH)_6(SO_4)_2$	$NiO*Fe_2O_3$ $KAlO_2$	$CaAl_2Si_7O_{18}*6H_2O$ $Ni_{0.35}Si_{0.65}$

Corrosion associated with solid/deposited alkali chlorides

Corrosion associated with silication of alkali chlorides

Corrosion associated with sulphation of alkali chlorides

Corrosion associated with $Cl_2(g)$

Thermodynamic equilibrium modelling for isSiCrAl coating

Impact of wheat straw combustion on isSiCrAl coatings

Main chemical species formed from isSiCrAl interactions with wheat straw ashes were determined. Figure 7a exhibits the equilibrium chemical composition determined at the selected temperature range. The bar graph in Fig. 7a shows SiCr/Al-ash compounds predicted to be originated at selected temperatures. Major aluminium species detected (≥ 10%) are K-Al oxides and hydroxides ($KAlO_2$, $KAl_2(AlSi_3O_{10})(OH)_2$, $KAl_3(AlSi_3O_{10})(OH)_2$, which may be related by the high potassium content in this fuel. These chemical forms come from mechanisms of both silication of alkali chlorides and reactions with deposited alkali chlorides. In these conditions, equilibrium calculations exhibit how oxides and hydroxides formation is strongly affected by temperature, above 600 °C. On the other hand, hydroxides formation seems to be related with the water content in the biomass.

Corrosion is also associated with Cl_2 present in the gas phase, giving rise to AlClO, as important percentages (˃ 10%).

In percentages of 5–10%, Cr_2O_3 and $KAl_3(SO_4)_2(OH)_6$ are observed as secondary forms produced with this fuel. With respect to the former, alloyed chromium is known to improve steel by forming a protective oxide layer consisting of Cr_2O_3 if the chromium content of the steel is sufficiently high. However, previous studies have shown how the protective chromium oxide may be destroyed by reaction with alkali chlorides (11, 12) and carbonates (13) with alkali chromate as the intermediate [48, 52]:

$$2Cr_2O_3(s) + 8MCl(s, l, g) + 5O_2(g) \rightarrow 4K_2CrO_4(s) + 4Cl_2(g) \quad (11)$$

$$2Cr_2O_3(s) + 8MCl(s, l, g) + 4H_2O(g) + 3O_2(g) \rightarrow 4K_2CrO_4(s) + 8HCl(g) \quad (12)$$

$$2Cr_2O_3(s) + 4M_2CO_3(s) + 3O_2(g) \rightarrow 4K_2CrO_4(s) + 4CO_2(g) \quad (13)$$

Other species such as CrO_2 and $NaAlO_2$ are also predicted to be originated in minor percentages (2–3%).

Impact of forestry residues combustion on isSiCrAl coatings

Main chemical compounds resulting from isSiCrAl interactions with forestry residues ashes were determined. Figure 7b shows equilibrium composition of main predicted species. Percentages obtained for each predicted compound at selected temperatures are shown in the bar chart from Fig. 7b. Silication reactions are seen as the dominant mechanisms leading to the major compounds formed in this case.

In this scenery, mainly deposits of, primary, SiO_2 and, secondly, $CaAl_4Si_2O_{10}(OH)_2$ are seen to be formed. Fast reactions are observed to occur at temperatures below 350 °C, with a sharp decrease in the concentration of diverse compounds (SiO_2(l), Al, CrO_2, $CaAl_4Si_2O_{10}(OH)_2$ and $NaAl_2(AlSi_3O_{10})(OH)_2$), with temperature increase.

In minor percentages, an important number of alkali-Al silicates are detected, together with CrO_2, CrO_3, AlClO and different Al-sulphates ($Al_2(SO_4)_3$, $Al_2(SO_4)_3*6H_2O$). Chromium oxidation is detected at lower percentages as Cr_2O_3 and at temperatures above 420 °C. Al-sulphates reactions are observed at low temperatures (≤ 420 °C). Sulphur content

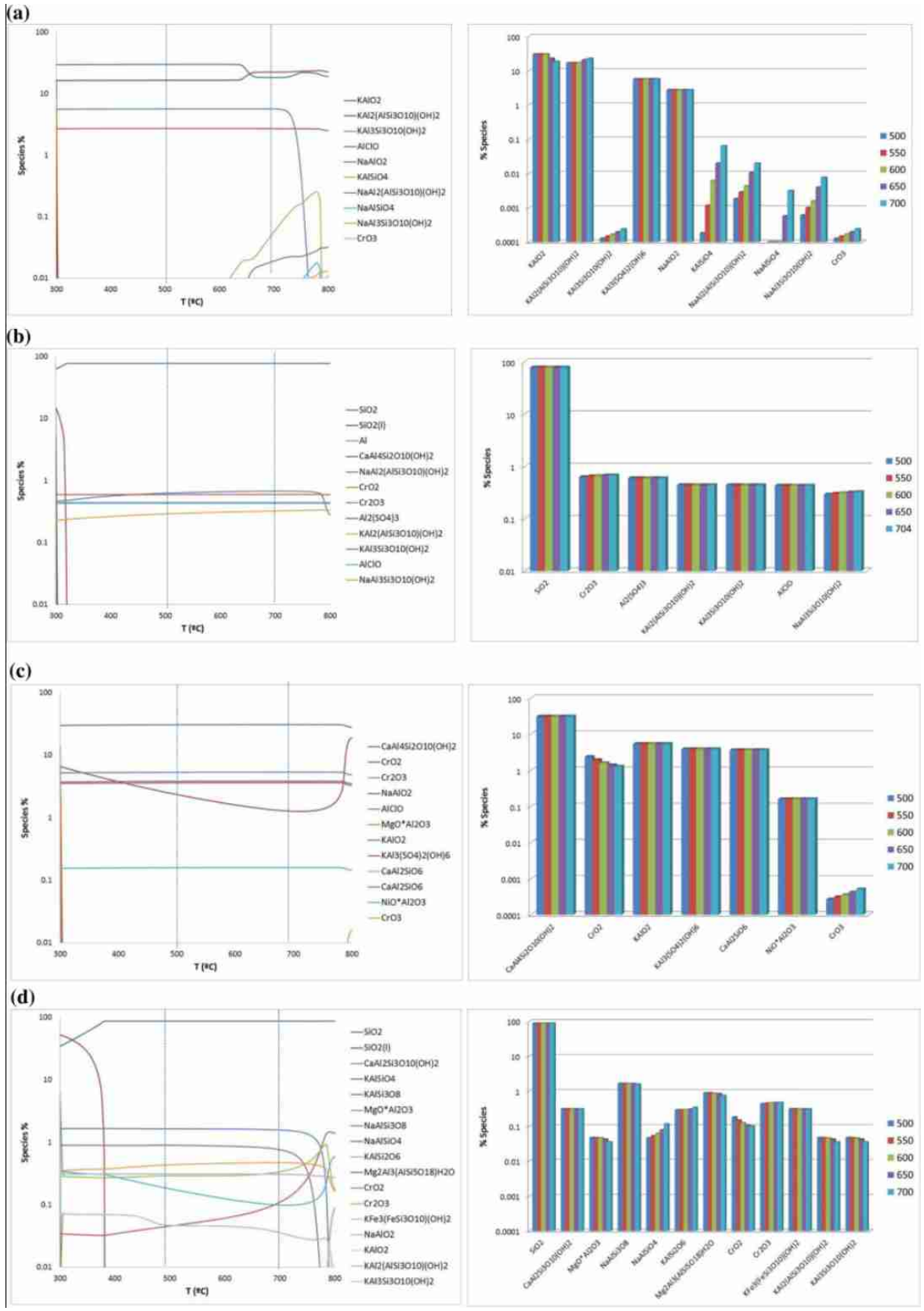

Fig. 7 Equilibrium composition and temperature influence of main species resulting from isSiCrAlAl–ash interactions during combustion of: **a** WS; **b** FR; **c** IWW; and **d** EW

in this fuel (Table 1) was determined to be quite low in comparison with the rest of the biomasses studied, which may have reduced the concentration of condensed sulphates formed. Ca, Na and water content are seen to favour silicates hydroxides formation at low T ≤ 300 °C.

Impact of industrial waste wood combustion on isSiCrAl coatings

Main condensed species formed from isSiCrAl interactions with industrial waste wood ashes were determined. Evolution of these compounds with temperature is shown in Fig. 7c.

In this case, $CaAl_4Si_2O_{10}(OH)_2$ is predicted as the dominant compound formed, which is stable with temperature increase. The second main effect observed in these conditions is chromium oxidation as Cr_2O_3, which would give rise to a protective oxide layer.

Other oxidized forms (CrO_2, $NaAlO_2$, AlClO, $MgO*Al_2O_3$) are predicted to appear in percentages over 5% at temperatures below 300 °C.

In minor percentages (< 5%), alkali sulphates ($KAl_3(SO_4)_2(OH)_6$), alkali carbonates ($NaAlCO_3(OH)_2$) and Ca-Al silicates ($CaAl_2SiO_6$) are also detected to be formed, which would reduce the concentration of available alkali, reducing corrosion risk.

Percentages obtained for each predicted compound at selected temperatures are shown in the bar graph from Fig. 7c, with $CaAl_4Si_2O_{10}(OH)_2$ as the main specie, followed by diverse aluminium interactions with potassium and calcium in form of oxides, sulphates and silicates ($KAlO_2$, $KAl_3(SO_4)_2(OH)_6$, $CaAl_2SiO_6$).

Diverse types of corrosion mechanisms are detected for this fuel, as it was also observed for wheat straw, which are primary related to by silication of alkali chlorides, Eqs. 4–6 ($CaAl_4Si_2O_{10}(OH)_2$), deposited alkali chlorides, Eqs. 7–8 ($NaAlO_2$) and direct corrosion by Cl_2(g) (AlClO). Sulphation, Eqs. 9–10 ($KAl_3(SO_4)_2(OH)_6$) of alkali chlorides, is also detected, but in minor concentrations (1–5% species).

Impact of Eucalyptus combustion on isSiCrAl coatings

Finally, eucalyptus composition was introduced in the isSiCrAl system. Figure 7d plots equilibrium diagrams calculated for main predicted species. The bar chart from Fig. 7d shows the percentages obtained for each compound at selected temperature range (500–700ºC).

Results obtained for dominant compounds in the equilibrium system show silicon oxidation, as oxides (87% species), as the main reaction involved.

In a lesser extent (≤ 2%), different compounds such as $NaAlSi_3O_8$, $Mg_2Al_3(AlSi_5O_{18})H_2O$ and $KFe_3(FeSi_3O_{10})(OH)_2$ are also observed. Thereby silication of alkali chlorides is produced in much lower percentages than it was

Table 6 Main species formed through SiCrAl/ biomass ashes interactions

% SPECIES	WS	FR	IWW	EW
≥ 10%	*(2)* $KAlO_2$ *(2)* $KAl_2(AlSi_3O_{10})(OH)_2$ *(2)* $KAl_3Si_3O_{10}(OH)_2$ *(4)* AlClO	SiO_2, SiO_2 (l)	*(2)* $CaAl_4Si_2O_{10}(OH)_2$ Cr_2O_3 *(1)* $NaAlO_2$ *(4)* AlClO	SiO_2, SiO_2 (l)
5–10%	Cr_2O_3 *(3)* $KAl_3(SO_4)_2(OH)_6$	*(2)* $CaAl_4Si_2O_{10}(OH)_2$	CrO_2 $MgO*Al_2O_3$ *(1)* $KAlO_2$	*(2)* $CaAl_2Si_3O_{10}(OH)_2$
1–5%	CrO_2 $NaAlO_2$	–	$KAl_3(SO_4)_2(OH)_6$ $CaAl_2SiO_6$	$KAlSi_3O_8$ $NaAlSi_3O_8$
≤ 1%	$NaAl_2(AlSi_3O_{10})(OH)_2$ $NaAlSiO_4$ $NaAl_3Si_3O_{10}(OH)_2$ CrO_3 SiO_2 $KAl_3(OH)_6(SO_4)_2$ $NaAlCO_3(OH)_2$	$NaAl_2(AlSi_3O_{10})(OH)_2$ CrO_2 $Al_2(SO_4)_3$ $KAl_2(AlSi_3O_{10})(OH)_2$ $KAl_3Si_3O_{10}(OH)_2$ AlClO $NaAl_3Si_3O_{10}(OH)_2$ CrO_3 $Al_2(SO_4)_3*6H_2O$	$NiO*Al_2O_3$ CrO_3 $NaAlCO_3(OH)_2$ $KAl_3(OH)_6(SO_4)_2$	$NaAlSiO_4$ $KAlSi_2O_6$ $Mg_2Al_3(AlSi_5O_{18})H_2O$ CrO_2 Cr_2O_3 $KFe_3(FeSi_3O_{10})(OH)_2$ $NaAlO_2$ $KAlO_2$ $KAl_2(AlSi_3O_{10})(OH)_2$ $KAl_3Si_3O_{10}(OH)_2$

Corrosion associated with solid/deposited alkali chlorides

Corrosion associated with silication of alkali chlorides

Corrosion associated with sulphation of alkali chlorides

Corrosion associated with Cl_2(g)

observed for other biomasses, so corrosion associated with this mechanism is not relevant in this case.

On the other hand, the formation of the protective chromium oxide (Cr_2O_3) is also detected, in minor percentages (0.5%).

Conclusions of biomass influence on SiCrAl-based coating corrosion

When isSiCrAl is introduced in the system, results obtained differ depending on the biomass used. Table 6 shows main interactions resulting from biomasses ash components with Si-Cr-Al-based coatings.

When either *forestry residues* or *eucalyptus* are employed, silica and Ca-Al silicates are observed as the dominant forms, while alkali capture by silicates/sulphates formation occurs at much lower percentages than in the other biomasses. In addition, chromium oxidation as Cr_2O_3, which would involve the formation of a protective layer, is also produced in a minor extent.

On contrast, when *wheat straw or industrial waste wood* is introduced in the system, an important amount of aluminium interactions with K, Na and Ca are observed, as oxides, silicates and, in a minor extent, of sulphates, which would involve a lower concentration of alkali in the gas phase, thus reducing corrosion risk. On the other hand, for these fuels, chromium oxides (Cr_2O_3, CrO_2) are detected in significant percentages (˃5% species), mainly in the case of industrial waste wood.

With respect to corrosion mechanisms, silication reactions are dominant for all biomasses studied, while in wheat straw and industrial waste wood cases, mechanisms associated with solid alkali chlorides and direct oxidation by $Cl_2(g)$ are also relevant. Chromium oxidation as Cr_2O_3 is mainly detected for industrial waste wood case and, secondly, for wheat straw, while for the rest of the biomasses this effect is negligible.

Comparison of results obtained through the global matrix of the modelling tests

By comparing the results obtained in the diverse modelling tests (Fig. 2), where different alloys were exposed to varied combustion atmospheres burning diverse biomass types, a definition of the most corrosive biomass fuels over a specific coating has been reached and schematized in Fig. 8. The corrosion mechanisms associated with each biomass, as well as the number of metals–ash compounds interactions determined through the model, were also included in this figure.

In the case of isFeAl, major potential corrosion was observed when, primary, IWW or, secondly, FR were used as fuels in the combustion process, which is reflected by the significantly higher amount of interactions between the coating metal composition and the atmosphere chemical compounds when these biomasses are burned. The elevated volatiles content determined in these fuels might have led to a major release of ash components to the gas phase, available to later condense in the metals surfaces. The low sulphur concentration found in IWW samples also reduces ash-forming elements capture in the bottom ash thus increasing volatilization. On contrast, FR contains high sulphur content but this is counteracted by the important content of ash-forming elements. *Ca-Al-Si hydroxides* were seen as the main compounds formed in most sceneries tested for this coating.

With respect to isNiAl, main number of interactions was seen to be primary produced in the corrosive FR atmosphere, and secondly detected during EW combustion. EW also contains an elevated volatiles percentage and very important major elements content. However, the ash percentage in this fuel was determined in low values. In addition, results summarized in Table 5 for this coating, reflected how in IWW tests, isNiAl is affected by nickel oxidation reactions, while silication and sulphation reactions prevailed for the rest of the biomasses.

In the case of isSiCrAl, when either *wheat straw or industrial waste wood* compositions were introduced, significant number of reactions were observed related to diverse corrosion mechanisms (associated with $Cl_2(g)$, with solid alkali chlorides and with silication processes).

In this sense, results reveal that the protective character of a specific alloy is highly depending upon the biomass burned. Figure 8 shows *IWW and FR as highly damaging in most cases, which is in agreement with conclusions from fuels indexes calculations*.

Predicting metal interactions, based on real combustion conditions and fuel composition, was seen to be useful to identify key factors for protective coatings design when employing new waste fuels. However, results obtained through this modelling require of field verification. In this sense, further research will be focused on coatings testing in real conditions through the insertion of coated coupons in the BFBC plant and the development of different combustion experiments operating with biomass fuels evaluated in this study.

Conclusions

A modelling of chemical interactions produced between the metals composing different coatings and the chemicals compounds released during the combustion of diverse biomass types was developed as a corrosion risk prediction strategy in biomass boilers.

Previous characterization of the biomass fuels showed great variability, with higher values obtained for both ash content and trace metals concentrations in FR case.

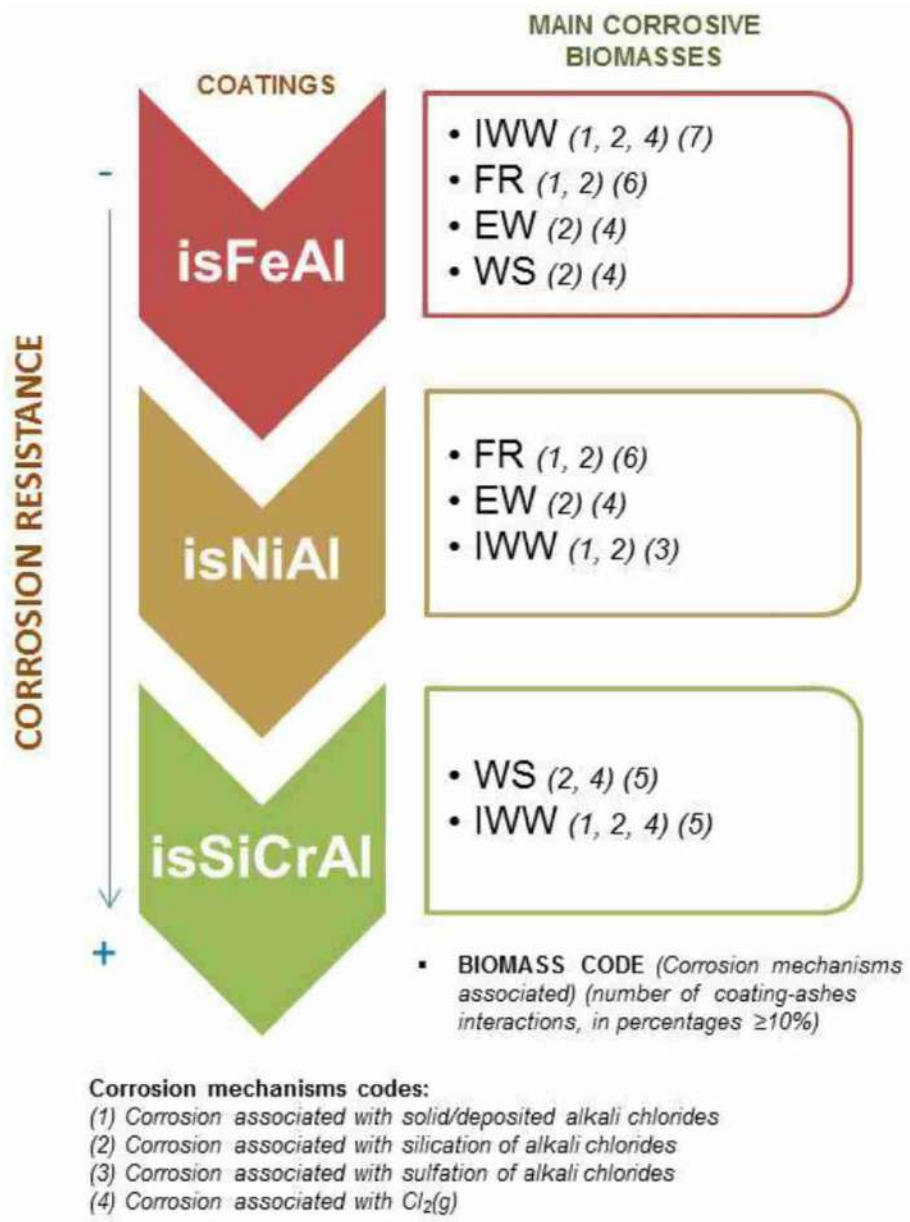

Fig. 8 Most damaging biomass fuels determined for each coating

Fuels indexes calculations, based on ash chemical composition, have revealed that major hazard may be caused if IWW, in a major extent, or FR were fed in a combustion process, showing high risk of salt stickiness, deposits formation and release of free corrosive acidic gases.

Results obtained through the thermodynamic equilibrium model were in in agreement with conclusions from fuels indexes calculations, showing, primarily, IWW and secondarily, FR as highly damaging for most coatings studied. The significant ash content determined in FR samples together with the elevated volatiles content determined in both IWW and FR biomasses, might have led to a major release of ash components to the gas phase, available to later condense in the metals surfaces.

An increase in alloys corrosion resistance was detected through the model when nickel and/ or chromium was present, showing isSiCrAl as the most resistant followed by isNiAl. However, results showed how even highly alloyed materials could be severely corroded depending on the biomass composition, thus materials selection should be carried out regarding the compatibility with the environment conditions for its final use.

The model also provided information on the *corrosion mechanisms* occurring in each scenario, revealing both silication of alkali and deposited alkali chlorides as dominant processes, followed by minor reactions of sulphation and direct oxidation by $Cl_2(g)$.

Predicting metal interactions, based on real combustion conditions and fuel composition, was seen as a useful tool to identify key factors for protective coatings design when employing new waste fuels.

Acknowledgements The presented results were obtained through the activities performed within BELENUS Project, under the support received from the European Union's Horizon 2020 Research and Innovation Programme under Grant agreement No 815147.

Author contributions All authors contributed to the study development. All authors read and approved the final manuscript.

Funding Open Access funding provided thanks to the CRUE-CSIC agreement with Springer Nature. Funding was provided by European Union's Horizon 2020 Research and Innovation Programme under Grant agreement No. 815147.

Data availability The datasets generated in this study are not publicly available to ensure the confidentiality of the project but are available from the corresponding author on reasonable request.

Declarations

Conflict of interest The authors have not disclosed any competing interests.

References

1. Berlanga, C., Ruiz, J.: A: study of corrosion in a biomass boiler. J. Chem. **2013**, 1–8 (2013)
2. Moradian, F.: Ash behavior in fluidized-bed combustion and gasification of biomass and waste fuels experimental and modeling approach. Thesis. University of Borås, Sweden (2016)
3. Gruber, T., Schulze, K., Scharler, R., Obernberger, I.: Investigation of the corrosion behavior of 13CrMo4-5 for biomass fired boilers with coupled online corrosion and deposit probe measurements. Fuel. **144**, 15–24 (2015)
4. Wang, Y., Sun, Y., Yue, M., Li, Y.: Reaction kinetics of chlorine corrosion to heating surfaces during coal and biomass cofiring. J. Chem. **2020**, 1–10 (2020)
5. Wang, Y., Sun, Y., Jiang, L., Liu, L., Li, Y.: Characteristics of corrosion related to ash deposition on boiler heating surface during cofiring of coal and biomass. J. Chem. **2020**, 1–9 (2020)
6. Luo, W., Liu, Z., Wang, Y., Yang, R.: High temperature corrosion behaviors of the superheater materials. Proc. Eng. **36**, 212–610 (2012)
7. Khodier, A.H.M., Hussain, T., Simms, N.J., Oakey, J.E., Kilgallon, P.J.: Deposit formation and emissions from co-firing miscanthus with Daw Mill coal: pilot plant experiments. Fuel **101**, 53–61 (2012)
8. Nordgren, D., Hedman, H., Padban, N., Boström, D., Öhman, M.: Ash transformations in pulverised fuel co-combustion of straw and woody biomass. Fuel Process. Technol. **105**, 52–58 (2013)
9. Enestam, S., Bankiewicz, D.P., Tuiremo, J., Makela, K., Hupa, M.: Are NaCl and KCl equally corrosive on superheater materials of steam boilers? Fuel **104**, 294–306 (2013)
10. Berlanga-Labari, C., Fernández-Carrasquilla, J.: Study of the oxidation to high temperature of eight alloys in atmospheres of combustion of biomass. Rev. Metal. **44**(4), 343–354 (2008)
11. Kassman, H., Pettersson, J., Steenari, B.-M., Åmand, L.-E.: Two strategies to reduce gaseous KCl and chlorine in deposits during biomass combustion. Injection of ammonium sulphate and co-combustion with peat. Fuel Process. Technol. **105**, 170–180 (2013)
12. Wang, L., Hustad, J.E., Skreiberg, Ø., Skjevrak, G., Grønli, M.: A critical review on additives to reduce ash related operation problems in biomass combustion applications. Energy Proc. **20**, 20–29 (2012)
13. Aho, M., Vainikka, P., Taipale, R., Yrjas, P.: Effective new chemicals to prevent corrosion due to chlorine in power plant superheaters. Fuel **87**(6), 647–654 (2008)
14. Duoli, W., Yuan, Z., Liu, S., Zheng, J., Wei, X., Zhang, C.: Recent development of corrosion factors and coating applications in biomass firing plants. Coatings **10**, 1001 (2020)
15. Dębowska, A., Magdziarz, A., Kopia, A., Kalemba-Rec, I., Petrzak, P.: Influence of fuel ashes on corrosion of surface coatings cladded by CMT method. Energy Sources **41**, 427–437 (2019)
16. Sadeghi, E., Markocsan, N., Joshi, S.: Advances in corrosion-resistant thermal spray coatings for renewable energy power plants: Part II—effect of environment and outlook. J. Therm. Spray Technol. **28**, 1789–1850 (2019)
17. Vijaya Lakshmi, D., Suresh Babu, P., Rama Krishna, L., Vijay, R., Srinivasa Rao, D.: Corrosion and erosion behaviour of iron aluminide (FeAl(Cr)) coating deposited by detonation spray technique. Adv. Powder Technol. **32**(7), 2192–2201 (2021)
18. Aliyu, A., Srivastava, C.: Corrosion behaviour and protective film constitution of AlNiCoFeCu and AlCrNiCoFeCu high entropy alloy coatings. Surfaces Interfaces. **27**, 101481 (2021)
19. Chi, H., Pans, M.A., Bai, M., Sun, C., Hussain, T., Sun, W., et al.: Experimental investigations on the chlorine-induced corrosion of HVOF thermal sprayed Stellite-6 and NiAl coatings with fluidised bed biomass/ anthracite combustion systems. Fuel **288**, 119607 (2021)
20. Wu, D.L., Dahl, K.V., Grumsen, F.B., Christiansen, T.L., Montgomery, M., Hald, J.: Breakdown mechanism of γ-Al_2O_3 on Ni_2Al_3 coatings exposed in a biomass fired power plant. Corros. Sci. **170**, 108583 (2020)
21. Li, Z., Liu, C., Chen, Q., Yang, J., Liu, J., Yang, H., et al.: Microstructure, high-temperature corrosion and steam oxidation properties of Cr/CrN multilayer coatings prepared by magnetron sputtering. Corros. Sci. **191**, 109755 (2021)
22. Sun, M., Song, J., Du, C., Yang, Y., Yan, D.: Fundamental understanding on the microstructure and corrosion resistance of Cr-$(Cr, Al)_2O_3$ composite coatings in-situ synthetized by reactive plasma spraying. Surf. Coat. Technol. **423**, 127608 (2021)
23. Antunes, R.A., De Oliveira, M.C.L.: Corrosion in biomass combustion: a materials selection analysis and its interaction with corrosion mechanisms and mitigation strategies. Corros. Sci. **76**, 6–26 (2013)

24. Sadeghimeresht, E. (2018) Ni-Based Coatings for High Temperature Corrosion Protection. PhD Thesis. Production Technology. No. 23. University West.
25. Bendix, D., Tegeder, G., Crimmann, P., Metschke, J., Faulstich, M.: Development of thermal sprayed layers for high temperature areas in waste incineration plants. Mater. Corros. **59**, 389–392 (2008)
26. Mahesh, R.A., Jayaganthan, R., Prakash, S.: Evaluation of hot corrosion behaviour of HVOF sprayed Ni–5Al and NiCrAl coatings in coal fired boiler environment. Surf. Eng. **26**, 413–421 (2010)
27. Naganuma, H., Ikeda, N., Ito, T., Satake, H., Matsuura, M., Ueki, Y., Yoshiie, R., Naruse, I.: Control of ash deposition in solid fuel fired boiler. Fuel Process. Technol. **105**, 77–81 (2013)
28. Fauchais, P., Vardelle, A.: Thermal sprayed coatings used against corrosion and corrosive wear. In: Advanced Plasma Spray Applications. InTech, London (2012)
29. Szymański, K., Hernas, A., Moskal, G., Myalska, H.: Thermally sprayed coatings resistant to erosion and corrosion for power plant boilers—a review. Surface Coat. Technol. **268**, 153–164 (2015)
30. Mudgal, D., Singh, S., Prakash, S.: Corrosion problems in incinerators and biomass-fuel-fired boilers. Int. J. Corros. **2014**, 1–14 (2014)
31. Abualigaledari, S., Mahdavi, A., Azarmi, F., Huang, Y., McDonald, A.: A comprehensive review of corrosion resistance of thermally-sprayed and thermally-diffused protective coatings on steel structures. J. Therm. Spray Technol. **28**(4), 645–677 (2019)
32. Viswanathan, R., Coleman, K., Rao, U.: Materials for ultra- supercritical coal-fired power plant boilers. Int. J. Press. Vessels Pip. **83**(11–12), 778–783 (2006)
33. Lindberg, D., Backman, R., Chartrand, P., Hupa, M.: Towards a comprehensive thermodynamic database for ash-forming elements in biomass and waste combustion. Current situation and future developments. Fuel Process. Technol. **105**, 129–141 (2013)
34. Poole, D., Argent, B.B., Sharifi, V.N., Swithenbank, J.: Prediction of the distribution of alkali and trace elements between the condensed and gaseous phases in a municipal solid waste incinerator. Fuel **87**, 1318–1333 (2008)
35. Nutalapati, D., Gupta, R., Moghtaderi, B., Wall, T.F.: Assessing slagging and fouling during biomass combustion: a thermodynamic approach allowing for alkali/ash reactions. Fuel Process. Technol. **88**, 1044–1052 (2007)
36. Zevenhoven-Onderwater, M., Blomquist, J.P., Skrifvars, B.J., Backman, R., Hupa, M.: The prediction of behaviour of ashes from five different solid fuels in fluidised bed combustion. Fuel **79**, 1353–1361 (2000)
37. Pastircakova, K.: Determination of trace metal concentrations in ashes from various biomass materials. Energ. Educ. Sci. Technol. **13**(2), 97–104 (2004)
38. Stromberg, B.: Fuel Handbook. Varmeforsk, Stockholm (2006)
39. Dizaji, H.B., Zeng, T., Enke, D.: New fuel indexes to predict ash behavior for biogenic silica production. Fuel **310**, 122345 (2022)
40. Bryers, R.W.: Fireside slagging, fouling, and high-temperature corrosion of heat transfer surface due to impurities in steam-raising fuels. Prog. Energy Combust. Sci. **22**(1), 29–120 (1996)
41. Garcia-Maraver, A., Mata-Sanchez, J., Carpio, M., Perez-Jimenez, J.A.: Critical review of predictive coefficients for biomass ash deposition tendency. J. Energy Inst. **90**(2), 214–228 (2017)
42. Dodson, J.R.: Wheat straw ash and its use as a silica source. PhD. University of York Chemistry (2011)
43. Liu, Q., Zhong, W., Yu, Z. et al. Potassium precipitation and transformation during the combustion of torrefied wheat straw—effect of additives. Biomass Conv. Bioref. (2022).
44. Nielsen, H.P., Baxter, L.L., Sclippab, G., Morey, C., Frandsen, F.J., Dam-Johansen, K.: Deposition of potassium salts on heat transfer surfaces in straw-fired boilers: a pilot-scale study. Fuel **79**, 131–139 (2000)
45. Niu, Y., Tan, H., Hui, S.: Ash-related issues during biomass combustion: alkali-induced slagging, silicate melt-induced slagging (ash fusion), agglomeration, corrosion, ash utilization, and related countermeasures. Prog. Energy Combust. Sci. **52**, 1–61 (2016)
46. Metsajoki, J., Huttunen-Saarivirta, E., Lepisto, T.: Elevated-temperature corrosion of uncoated and aluminized 9–12% Cr boiler steels beneath KCl deposit. Fuel **133**, 173–181 (2014)
47. Grabke, H.J., Reese, E., Spiegel, M.: The effects of chlorides, hydrogen chloride and sulfur dioxide in the oxidation of steels below deposits. Corros. Sci. **37**, 1023–1043 (1995)
48. Li, Y.S., Niu, Y., Spiegel, M.: High temperature interaction of Al/Si-modified Fe-Cr alloys with KCl. Corros. Sci. **49**, 1799–1815 (2007)
49. Kassman, H., Bafver, L., Amand, L.-E.: The importance of SO2 and SO3 for sulphation of gaseous KCl—an experimental investigation in a biomass fired CFB boiler. Combust Flame. **157**, 1649–1657 (2010)
50. Kassman, H., Pettersson, J., Steenari, B.-M., Amand, L.-E.: Two strategies to reduce gaseous KCl and chlorine in deposits during biomass combustion—injection of ammonium sulphate and co-combustion with peat. Fuel Process. Technol. **105**, 170–180 (2013)
51. Kassman, H., Brostrom, M., Berg, M., Amand, L.E.: Measures to reduce chlorine in deposits: application in a large-scale circulating fluidised bed boiler firing biomass. Fuel **90**, 1325–1334 (2011)
52. Li, Y.S., Spiegel, M., Shimada, S.: Corrosion behaviour of various model alloys with NaCl-KCl coating. Mater. Chem. Phys. **93**, 217–223 (2005)

International Journal of Energy and Environmental Engineering (2023) 14:671–686
https://doi.org/10.1007/s40095-022-00542-0

ORIGINAL RESEARCH

Negative impact of constant RPM control strategy on ship NOx emission in waves

Mohammad Hossein Ghaemi[1] · **Hamid Zeraatgar**[2]

Received: 7 June 2022 / Accepted: 18 September 2022 / Published online: 3 October 2022

Abstract

In severe wave conditions, the ship propulsion system is loaded with high fluctuations due to external disturbances. The highly fluctuating loads enforce radical changes in the main engine torque, which in turn demands variation of the fuel rate injected into the cylinders if a constant rotational speed strategy is applied. Therefore, the temperature of gases varies to a large extent during the combustion process in the cylinders. The emitted NOx is a function of this highly fluctuating temperature. The main goal of this study is to investigate NOx emission under the aforementioned conditions when a usual constant RPM control strategy is applied in waves similar to the calm water condition. The paper presents a mathematical model of the whole system, which is applied to a selected ship both in regular waves and in calm water conditions. The results show that the sea waves, in comparison with the calm water condition, can radically increase the emitted NOx under the constant rotational speed strategy. This change can reach even 10^{14} times more, averagely. The results also show that the higher the wave height the higher the emitted NOx. It is concluded that the control strategy of keeping the engine rotational speed in waves at a constant level is the most important reason for the significantly increased NOx emission in waves in comparison with the calm water condition.

Keywords NOx emission · Ship control strategy · Marine diesel engine · Ship operation · Sea waves · Governor

Abbreviations

CII	Carbon intensity indicator
ECA	Emission control areas
EEDI	Energy Efficiency Design Index
EEXI	Energy Efficiency of Existing Ship Index
EGR	Exhaust gas recirculation
EIAPP	Engine International Air Pollution Prevention
GHG	Greenhouse gases
HC	Unburned hydrocarbons
IVMD	Instantaneous-value multidimensional model
IVZD	Instantaneous-value zero-dimensional model
HCCI	Homogeneous charge compression ignition
NMVOC	Non-methane volatile organic compounds
MVZD	Mean-value zero-dimension model
PAH	Polycyclic aromatic hydrocarbons
PM	Particular matter
SCR	Selective catalytic reduction
TWCEL	Total weighted cycle emission limit

Letters

a	Added (due to wave)
A	Area, equivalent area, advance
c	Specific heat coefficient
C	Coefficient
D	Diameter
E	Engine
h	Propeller immersion height
J	Moment of inertia, number
k	Coefficient, wave number
K	Coefficient
m	Mass, model
M	Torque (moment)
n	Rate of revolution
p	Pressure
pw	Orbital inflow
P	Power
q	Heat calorific value
Q	Torque

✉ Mohammad Hossein Ghaemi
ghaemi@pg.edu.pl

[1] Faculty of Mechanical Engineering and Ship Technology, Institute of Ocean Engineering and Ship Technology, Gdańsk University of Technology, G. Narutowicza 11/12, 80-233 Gdańsk, Poland

[2] Department of Maritime Engineering, Amirkabir University of Technology, Tehran, Iran

R	Gas constant, resistance, radius
t	Thrust deduction factor, time, total (due to wave)
T	Temperature, total, thrust
u	Velocity in the x-direction ($\overline{u}$: amplitude)
V	Volume
w	Wake fraction coefficient
x	Longitudinal axis, surge (added mass)
y	Transverse axis
z	Vertical axis
Z	Number of cylinders

Greek letters

β	Diminution factor
Δ	Overall ship mass
ζ	Wave profile function
η	Efficiency, coordinate
κ	Adiabatic exponent
λ	Coefficient, the ratio of ship length to model length
μ	Heading angle
π	Pressure ratio
ρ	Density
φ	Phase angle
ψ	Flow function
ω	Angular velocity

Lower indexes

0	Ambient condition
1	Point before compressor, x-direction
2	Point after compressor, y-direction
3	Point after charge air cooler (before cylinders), z-direction
4	Point after cylinders, roll (angle)
5	Point after the turbine, pitch (angle)
6	Yaw (angle)
am	Air intake manifold (receiver)
at	Atmosphere
b	Burnt (fuel)
C	Compressor
clr	Charge air cooler
comb	Combustion
cr.	Critical
cyl	Engine cylinders
e	Encounter
E	Engine
f	Fuel
gr	Exhaust gas receiver
loss	Energy/power/torque losses
n	Net
p	(At constant) pressure, prismatic
P	Propeller
T	Turbine
TC	Turbocharger
v	(At constant) volume
w	Cooling water

Upper index

*	Equivalent

Introduction

Higher efficiency, large availability, reliability, high power capacity, and easier maintenance are some of the advantages of diesel engines. That is why they are still considered as the main prime movers of ships [1]. They are being also utilized as auxiliary engines for electricity generation on shipboards. Simultaneously, they emit a relatively high amount of greenhouse gases (GHGs) due to the type of fuel they consume, and their characteristics. The main GHGs that diesel engines emit are NOx, SOx, COx, PM, and HC, among which CO and NO are the most toxic and harmful gases [2]. The emission of NOx from fossil fuels dominantly increases tropospheric ozone and hydroxyl-radical concentrations over their natural 'background' levels, thereby increasing the oxidizing power of the atmosphere [3]. Recent advances in studying air quality and the health effects of shipping emissions are discussed by Contini and Merico [4].

Reduction of emission of GHG in shipping has been one of the main goals of the International Maritime Organisation (IMO) with adopting an amendment to the MARPOL Chapter VI, providing mandatory Energy Efficiency Design Index (EEDI). Additionally, IMO currently proposed applying the Energy Efficiency of Existing Ships Index (EEXI) and Carbon Intensity Indicator (CII). These measures impose radical change on the maritime industry. Based on Annex VI, Regulations 13.8 and 5.32, starting from 2000, the Engine International Air Pollution Prevention (EIAPP) certificate is required for all ships that are equipped with marine diesel engines over 130-kW output power independent of the ship's tonnage [5]. This mainly addresses the level of NOx emission and is put in order by defining three levels (Tiers) depending on the year of building and the rate of shaft revolution. All new buildings after January 1, 2016, must satisfy the criterion of Tier III. This limitation is related to those ships that are operating in the emission control areas (ECAs). Bouman has presented a comprehensive review of the technologies, measures, and potential for reducing GHG emissions from shipping taking into account 150 up-to-date research studies [6].

Regarding the above requirements, many technological solutions during the last two decades have been provided, which can be divided into two parts: primary and secondary. The main primary methods are decrease in injection duration, delay of the start of injection and pre-injection, modification of fuel injectors, controlling the combustion

pressure, increasing the ability and efficiency of scavenging air cooler, Miller cycle, water injection, and exhaust gas recirculation (EGR) [7, 8]. There are several secondary methods, while selective catalytic reduction (SCR) method is the most well-accepted solution, today [9]. There are many studies in which different solutions, methods, and strategies are compared to each other, e.g. [9–11].

Additionally, the possibility of using different fuels and their impact has been included in other studies. As an example, Jeevahan et al. have shown that although biodiesel produces higher NOx emissions with slightly lower brake thermal efficiency and advantages of reduced emissions of CO2, CO, HC, and smoke, there are some strategies such as fuel treatments, low-temperature combustion, mixing fuel additives and reformulating fuel composition that leads to the reduction of NOx emission [12].

Research on the reduction of NOx increased starting in 1970, and the fundamental keys were mathematical models (both analytical and numerical), intensive experimental tests and measurements, and related simulations. Cakir presented a combustion model to account for the nitric oxide formation in diesel engines and compared the analytical model results with experimental data [13]. Way introduced methods for calculating the exhaust gas compositions and determining the NOx amount [14]. Miller described the mechanism and modelling of nitrogen chemistry in the combustion process [15].

Correa measured NOx emissions for a 250-MW-class combined-cycle unit for power generation with gaseous fuel and concluded that NO is formed in a distributed zone manner when the equilibrium and super-equilibrium effects can broaden the NOx-forming zones beyond the fine scales of turbulence, even in non-premixed flames [16]. Additionally, the experimental results showed that the pressure and the structure of the turbulent flow field have a diminishing effect on NOx emissions in progressively leaner premixed combustion [16]. Chikahisa et al. investigated the process of NO formation and its characteristics in diesel engines using different emission control ideas and showed that the NO formation rate is independent of the mixing of combustion gas [17]. The most important result of this study was identifying that NO emission is roughly proportional to the inverse of engine speed. Kikuta et al. analysed combustion and NO formation in large diesel engines using scale model experiments and compared them with the theoretical predictions [18]. Particularly, the study describes flow patterns and flame distribution leading to determining the heat release rates and thermal efficiency. Then, based on these identifications, an algorithm to predict NO emissions was suggested.

Rausen et al. introduced several empirical formulae for identifying the combustion duration and heat release for a homogeneous charge compression ignition (HCCI) using a mean-value model [19]. Merker provided integrated information on the simulation of combustion and pollutant formation for engine development [20]. Aspiron presented combined physics-based equations and empirical formula, which takes engine speed, injected fuel mass, the cylinder charge, its composition, and the start of combustion with the corresponding pressure and temperature as inputs and calculates the NOx emission [21]. Arregle et al. showed that the accuracy of the in-cylinder air mass and the in-cylinder total mass is much more critical than that of the instantaneous in-cylinder pressure and the injected fuel mass for NOx prediction [22]. Therefore, accurate modelling of the intake air and EGR mixture temperature and fresh air mass is crucial to be able to rationally predict the NOx emission.

Egnell presented a multi-zone combustion diagnostic method, where measured pressure data were used to calculate the heat release, local temperatures and concentrations of NO and other species [23]. Lamaris et al. also employed a multi-zone combustion model to estimate the performance characteristics and the NOx emissions of a 12.5-MW large-scale two-stroke diesel engine [24]. Mocerino et al. developed a model using Ricardo WAVE software to simulate the dynamics and emissions of an internal combustion engine [25]. The model was employed as a tool for the evaluation of emissions, particularly NO. Papagiannakis [26], Benvenuto [27] and Stoumpos [28] analysed the emission characteristics of dual-fuel engines. Scappin et al. introduced and utilized a zero-dimensional two-zone combustion model to simulate the performance and NOx emissions of a low-speed marine diesel engine using the extended Zeldovich mechanism [29]. They achieved an accuracy of 95% in comparison with a full-scale experiment. In the context of multi-zone models, Hountalas, Savva and Raptotasios studies are also important [30–32].

Hybrid propulsion solutions and their impact on emissions have also reached the great attention of scholars [33]. Last but not least, it should be mentioned that the accurate measurement of the gas composition has also assisted to improve the models and better setting up their parameters [34, 35].

The goal of this study is the evaluation of the consumed fuel and emitted NOx as one of the most harmful components of GHG in sea waves in comparison with calm water. To define the problem, it should be noted that ships are mostly navigating in sea waves rather than in the calm water. A ship and its propulsion system in the calm water are in the steady condition, whereas, in sea waves, their performances are dominated by wave oscillations. In these circumstances, engine torque and speed fluctuate in response to the ship's motion, which in turn enforce the engine's subsystems' performances to behave oscillatory. The above literature review reveals that the problem of GHG emission in sea waves has not been addressed by them. Therefore, the investigation of NOx as one of the main elements of GHG in sea waves

under the control strategy of constant engine speed (as usual practice) seems to be necessary, and it is the main objective of this study. This problem is related to several areas of research such as ship motion, propeller hydrodynamic performances in waves, engine, and subsystem performances in waves. On that basis, the simplification for the modelling of whole systems is inevitable. Here, to study the impact of sea waves on the ship emissions, when the engine is equipped with a conventional speed governor, first a mathematical model is developed in which the dynamic of the hull, propeller and engine in wave conditions is combined with the control strategy of the constant rotational speed of the engine. The mathematical model allows us to evaluate the consumed fuel as well as NOx as an important part of GHG. In the second stage of the study, a computer code is developed in MATLAB-SIMULINK for simulation purposes. Thirdly, this model is simulated for a selected ship in two regular waves and compared to the calm water conditions. In the fourth stage, a comparative analysis is conducted, where the system performances for calm and wave conditions are compared. The results show a radical increase of NOx in waves in comparison with the calm water when the same control strategy is applied in all conditions. The new elements and contribution of the results of the study in the related research field include describing the impact of the traditional control strategy of constant rotational speed for ships on the fuel consumption and NOx emission profile in wave conditions, as well as explaining the changing of ship NOx emission of a ship in response to the sea wave.

Methodology and modelling

Generally, to evaluate the consumed fuel and the emitted GHG of ships in waves, several dynamic systems have to be coupled. They include hull motion in waves, propeller performance in waves, diesel engine behaviour under the selected control strategy to control the fuel rate, as well as engine subsystems. Having the mathematical model, then its parameters should be selected and set up. This can be done based on the model and experimental test or manufacturers' data. Here, the results of model tests have been used both for ship hull resistance and for propeller open water characteristics. The engine parameters have been set using the manufacturer's data. Next, the model is coded for simulation. The simulations are conducted for two regular sea head waves and in the related calm water under three different ship speeds. The results of simulation in the time domain that include the variables of the coupled system are then used to evaluate the impact of waves and constant rotational speed control strategy on the NOx emission. The developed mathematical model enables determining the average NO emission.

In this section, a justification for the selected type of mathematical model of the engine has been presented, firstly. Then, a description of the subsystems is provided, and finally, the mathematical models of each subsystem are delivered.

Selecting the type of engine model

The diesel engine performances in unsteady states are usually analysed using four model types.

Engine model type A set of simple first- or second-order transfer functions, which determine output variables, mainly engine torque, average indicated pressure, or temperature, in response to the input variables (fuel rack or fuel rate) as a black box.

Engine model type 2 Mean-Value Zero-Dimension (MVZD) model in which the mean value of variables such as mass flow rate, temperature, and the fuel-to-air ratio is determined for each block of diesel engine (for example including compressor, turbine, manifolds, charge air cooler, etc.), while all cylinders are considered as a single block.

Engine model type 3 Instantaneous-Value Zero-Dimensional (IVZD) model, in comparison with MVZD, all variables are calculated instantaneously and individually for each cylinder.

Engine model type 4 Instantaneous-Value Multidimensional (IVMD) model that is similar to IVZD, while the output variables are additionally determined depending on the geometric coordinates.

IVZD and IVMD models can be one-zone or multi-zone, and single-phase or multi-phase flow models, particularly with respect to the combustion process. Generally, IVZD or IVMD models with two-phase flow consideration including pure air and air mixed with exhaust gases are able to simulate the instantaneous unsteady values of NOx formation. However, the MVZD model evaluates the NOx emission as a function of averaged temperature along a cycle, which is less than the real combustion temperature, for which the NOx emission should be calculated for a period of combustion. This approach has one significant weakness, which is assuming a linear distribution of NOx emission over time. The assumption, to some extent, disregards the strong nonlinearity of NOx formation as a function of combustion temperature. Since the present study aims to compare the NOx emission under different operation conditions in sea waves with respect to calm water, applying an MVZD model seems to be justified when simultaneously reducing the time and cost of simulation.

The subsystems

To achieve the goal of the study, it is necessary to develop the mathematical model of the following subsystems: (1)

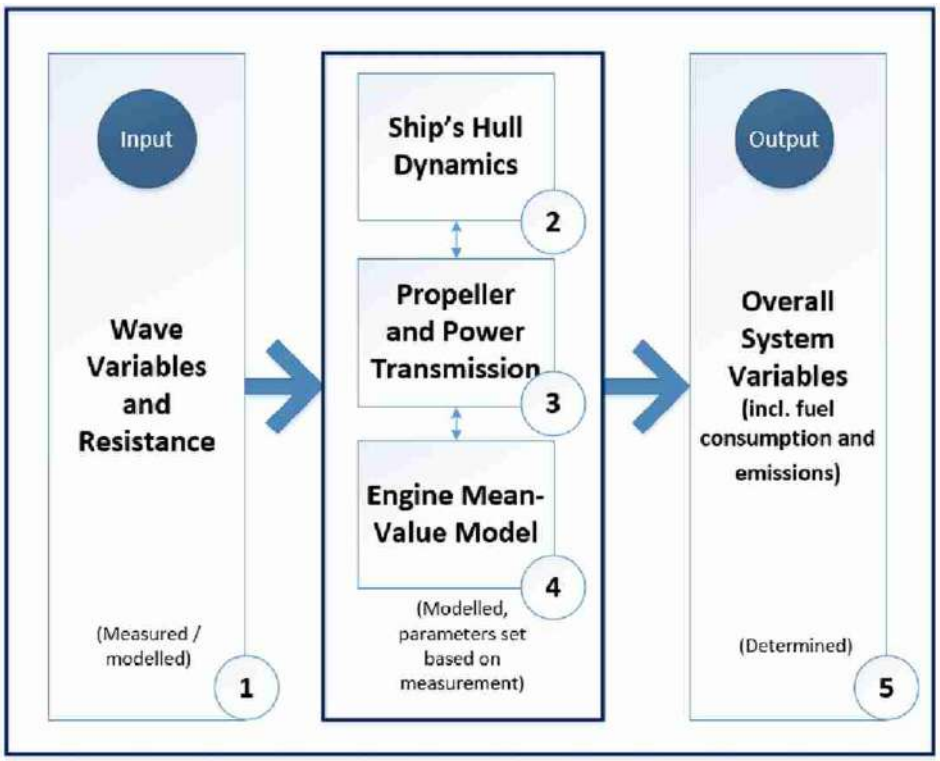

Fig. 1 The layout of the mathematical model

coupled equations of dynamics of ship motion, propeller, and engine, (2) total resistance that involves instantaneous wave forces in the x-direction (their mean value is known as added resistance), and (3) engine dynamics with the capability of determining the variables of the combustion process, and particularly combustion temperature. These subsystems are interacting with each other, and therefore, they had to be integrated under one overall system. To set up the model parameters, the steady-state data delivered by the manufacturers as well as some empirical relationships are used. Such a built model is then coded in MATLAB-SIMULINK. The simulation is conducted for a selected ship, in the calm water and head sea waves of two regular waves. Each subsystem of the model has been individually verified. Ship resistance, propeller characteristics, and wave variables are based on the model tests. The engine performances are verified for a wide range of steady-state conditions by simulating the engine variables when a selected operating point is changed from 100 to 10% of SMCR and vice versa. The increment of these changes was set from 10 to 50%.

Mathematical model

The layout of the mathematical model is presented in Fig. 1. It comprises five main modules, where the first (wave variables and resistance) and the fifth (overall system variables) modules stand as the input and output, respectively. Three other modules present the coupling equations of ship hull dynamics, propeller performances, and engine unsteady-state variables.

Referring to Fig. 1, the first module has been already presented in [36]. The wave parameters were set in advance, and the variables of the generated wave are measured. It contains the calm water resistance and time series of wave force in the *x*-direction, which have been concluded from model tests. The second and third modules are described in [37]. The fourth module has been adapted so that the steady-state model applied in [36] is replaced by the mean-value zero-dimensional (MVZD) model described in [38]. The fifth module is elaborated to determine the overall system outputs, which integrates the outputs of modules 2, 3, and 4 by including their interrelations. A submodule for the NOx evaluation is developed and integrated under module 5, where the NOx formation model is evaluated based on the mathematical model presented in detail by Heywood [39]. The developed mathematical model enables determining the average NO emission directly, where NO_2 emission can be estimated roughly as 10% of the calculated NO emission [38]. The coupled system of equations representing the described mathematical model is shown in Table 1. The assumptions applied for these equations are: (1) all gases are semi-ideal, (2) the pressure and mass losses are negligible for all gases, (3) the mechanical losses are negligible, (4) the waves are regular, (5) the ship moves only along its longitudinal axes, when roll and pitch are omitted, and (6) ship is a rigid body.

Table 1 The mathematical model

Module 1	$R_{am}(t) = R_{tm}(t) - R_{Tm}(u(t))$	(1)
	$R_a(t) = \lambda^3 \cdot R_{am}(t)$	(2)
	$\omega_e = \omega\left(1 - u\frac{\omega}{g}\cos\mu\right)$	(3)
	$h(x, y, \mu, t) = \eta_3(t) + y \cdot \eta_4(t) - x \cdot \eta_5(t) - \zeta(x, y, \mu, t)$, where:	(4)
	$\eta_3(t) = \overline{\eta}_3 \cos\left(\omega_e t + \varphi_3\right)$	(5)
	$\eta_4(t) = \overline{\eta}_4 \cos\left(\omega_e t + \varphi_4\right)$	(6)
	$\eta_5(t) = \overline{\eta}_5 \cos\left(\omega_e t + \varphi_5\right)$	(7)
	$\zeta(x, y, \mu, t) = \overline{\zeta} \cos\left(kx\cos\mu + ky\sin\mu - \omega_e t\right)$	(8)
Module 2	$T_n(t) - R_T(u(t)) - R_a(t) = \left(\Delta + x_u\right)\dot{u}(t)$	(9)
Module 3	$J_A(t) = \frac{u_A(t)}{D_p\lvert n_P(t)\rvert}$	(10)
	$u_A(t) = u(t)(1 - w(t)) + \overline{u}_{PW}\cos\left(\omega_e t - kx_p\cos\mu\right)$, where: $w = 0.45\,C_p - 0.05$(Robertson)	(11)
	$T(t) = \beta \cdot K_{T0}\left(J_A(t)\right)\rho n_P(t)\lvert n_P(t)\rvert D_P^4$, where $\beta = \text{ real}\left(1 - \frac{\text{acos}\varepsilon}{\pi} + \frac{\varepsilon}{\pi}\sqrt{1 - \varepsilon^2}\right)$ and $\varepsilon = \frac{h}{R_P}$	(12)
	$Q_P(t) = K_Q\left(J_A(t)\right)\rho n_P(t)\lvert n_P(t)\rvert D_P^5$	(13)
	$T_n(t) = T(t)\left(1 - t_T(t)\right)$, where $t_T = 0.5C_p - 0.12$(Hecker)	(14)
	$Q_E(t) - Q_P(t) = J\,\dot{\omega}(t)$	(15)
Module 4	Turbine:	
	$\dot{m}_5 = A_T^* \cdot \psi_T \cdot \sqrt{P_{gr} \cdot \rho_{gr}}$, where:	(16)
	$\psi_T\left(\pi_T\right) = \begin{cases} \left[\frac{2\kappa_T}{\kappa_T - 1}\left(\pi_T^{\frac{2}{\kappa_T}} - \pi_T^{\frac{\kappa_T+1}{\kappa_T}}\right)\right]^{\frac{1}{2}}; & \pi_T \geq \pi_{T_{cr.}} \\ \left[\kappa_T.\left(\frac{2}{\kappa_T+1}\right)^{\frac{\kappa_T+1}{\kappa_T-1}}\right]^{\frac{1}{2}}; & \pi_T < \pi_{T_{cr.}} \end{cases}$	(17)
	and	
	$\pi_{T_{cr.}} = \left(\frac{2}{\kappa_T+1}\right)^{\frac{\kappa_T}{\kappa_T-1}}$	(18)
	$P_T = \dot{m}_5 \cdot \eta_T \cdot \frac{\kappa_T}{\kappa_T - 1} \cdot R_5 \cdot T_5 \cdot \left[1 - \pi_T^{\left(\frac{\kappa_T-1}{\kappa_T}\right)}\right]$	(19)
	Compressor:	
	$\dot{m}_1 = \dot{m}_1\left(\omega_{TC}, \pi_C, T_0\right)$; (compressor map)	(20)
	$P_C = \frac{1}{\eta_C} \cdot \dot{m}_1 \cdot \frac{\kappa_C}{\kappa_C - 1} \cdot R_{at} \cdot T_{at} \cdot \left[1 - \pi_C^{\left(\frac{\kappa_C-1}{\kappa_C}\right)}\right]$	(21)
	$T_1 = \frac{1}{\eta_C} T_{at} \cdot \pi_C^{\frac{\kappa_T-1}{\kappa_T}}$	(22)
	Turbocharger shaft:	
	$\left(J_{TC}\dot{\omega}_{tc} = M_T - M_C - M_{TC_{loss}}\right)$	(23)
	Charge air cooler:	
	$T_2 = T_1 - \eta_{clr} \cdot \left(T_1 - T_w\right)$	(24)
	Intake air receiver:	
	$V_{am} \cdot \overset{\circ}{\rho}_{ia} = \dot{m}_1 - \dot{m}_3$	(25)

Table 1 (continued)

$$\frac{dT_{am}}{dt} = \frac{1}{m_{am}}\left[\left(\frac{c_{p2}}{c_{v_{am}}}\right)\cdot \dot{m}_2 \cdot T_2 - \left(\frac{c_{p_{am}}}{c_{v_{am}}}\right)\cdot \dot{m}_3 \cdot T_3 - T_{am}\cdot \dot{m}_{am}\right] \quad (26)$$

Exhaust gas receiver:

$$V_{gr}\cdot \overset{\circ}{\rho}_{gr} = \dot{m}_4 - \dot{m}_5 \quad (27)$$

$$\frac{dT_{gr}}{dt} = \frac{1}{m_{gr}}\left[\left(\frac{c_{p4}}{c_{v_{gr}}}\right)\cdot \dot{m}_4 \cdot T_4 - \left(\frac{c_{p_{gr}}}{c_{v_{gr}}}\right)\cdot \dot{m}_5 \cdot T_5 - T_{gr}\cdot \dot{m}_{gr}\right] \quad (28)$$

Engine cylinders and combustion process:

$$\dot{m}_3 = A^*_{cyl}\cdot \psi_{cyl}(\pi_{cyl})\cdot \sqrt{p_3\cdot \rho_3} \quad (29)$$

$$\dot{m}_{combt} = \frac{\omega}{2\pi}\cdot V_{cyl}\cdot \rho_3 \cdot Z \quad (30)$$

$$\eta_{fill} = 1 - \exp\left(-k_b\cdot \lambda_b\right), \text{ where:} \lambda_b \approx \frac{\dot{m}_3}{\dot{m}_{combt}} \quad (31)$$

$$\dot{m}_{comb} = \frac{\omega}{2\pi}\cdot Z\cdot V_{cyl}\cdot \frac{R_{am}T_{am}}{p_{am}}\cdot\left[1-\exp\left(-k_b\cdot\lambda_b\right)\right], \text{ where:} \quad (32)$$

$$\lambda_b = \frac{2\pi\cdot \dot{m}_3\cdot R_{am}\cdot T_{am}}{\omega\cdot Z\cdot V_{cyl}} \quad (33)$$

$$P_E = \eta_E\cdot \dot{m}_f\cdot q_f \quad (34)$$

$$T_4 = T_{am}\cdot \frac{c_{p_3}}{c_{p_4}}\cdot \frac{\dot{m}_3-\dot{m}_{comb}}{\dot{m}_4} + T_{comb}\cdot \frac{\dot{m}_{comb}}{\dot{m}_4}\cdot \frac{c_{p_{comb}}}{c_{p_4}} \quad (35)$$

$$T_{comb} = \frac{q_f\cdot \dot{m}_f\cdot(1-k_{loss})-P_E}{(\dot{m}_{comb}+\dot{m}_f)\cdot c_{p_4}} + T_{am}\cdot \frac{\dot{m}_{comb}}{\dot{m}_{comb}+\dot{m}_f}\cdot \frac{c_{p_{am}}}{c_{p_4}} \quad (36)$$

NOx emission

$$\frac{d[NO]}{dt} = \frac{6.10^{16}}{\sqrt{T_{comb}}}\exp\left(\frac{-69090}{T_{comb}}\right)[O_2]_e^{1/2}[N_2]_e \quad (37)$$

Results and discussion

In this section, the case study is presented, and the simulation process is described. Next, the results of the simulation are illustrated and interpreted. Finally, a detailed discussion is provided.

The selected ship is a container vessel, presented in [36], where the data regarding ship resistance and propeller parameters, as well as propulsive coefficients, are described based on the model tests, Zeraatgar and Ghaemi [37]. For clarification purposes, the ship and propeller specifications are given in Table 2. The engine is MAN-B&W 8S65ME-C8.5, equipped with a MAN B&W High Eff. TCA88 turbocharger [40, 41]. The fuel oil's low calorific value is assumed to equal 42,707 kJ/kg. The ambient conditions are 20 °C and 101,325 Pa. The kinematics of ship motion and the related coordination are set based on [42].

Ship motion and instantaneous wave force in the *x*-direction in two regular waves are recorded in towing tank in model scale of 40.75 as shown in Table 3.

Simulation is conducted for two considered waves as abbreviated W1 and W2 in Table 3. The simulation is continued in three more conditions, i.e., ship speed of 11.761, 10. 541 and 10.156 in the calm water. The results include the variables of the hull, propeller, and engine, including the internal variables of the engines. Additionally, fuel consumption and formation rate of NOx emission both in molar and mass terms are concluded and reported. The simulation time was set to 1800 s. The first 500 s are devoted to operation in the calm water, for the next approximately 800 s ship is in the wave, and finally, the last 500 s it is in the calm water.

When the ship is simulated for wave condition, based on the ship speed behaviour, it is concluded that the steady state has been approached approximately after 500 s. Therefore, the steady-state values of different variables could be selected for the time between 1200 and 1250, as the sample period. It should be noticed that the time during which the model in the experiment was in wave condition was not enough long to cover the whole simulation time. Therefore, the wave total force in the x-direction is repeated several times to cover 800 s for simulation purposes.

The variables that have been determined within the simulation process are about 43 (see Appendix). Some of the more important variables are depicted and discussed below.

The recorded resistance, as input, and the time traces of a set of selected variables are illustrated in Figs. 2, 3, 4, 5, 6, 7, 8, 9 and 10. Only those variables that play a fundamental role to demonstrate the NOx emission with respect to the ship operation conditions are selected, presented, and analysed.

Figure 2 depicts resistance fluctuation in two regular waves, W1 and W2, scaled up for ship from the model test [37]. The ship speed is 11. 7 m/s (22.8 Kn) and the calm water resistance is 1160.9 kN which its range of fluctuation is several times higher than the calm water resistance.

Figure 3 illustrates the time trends of ship speed. Starting from the calm water condition, the ship enters to head regular waves under the control strategy of constant engine speed. As a result, the ship speed reduces and fluctuates. Its mean value reaches 10.7 m/s and 10.2 m/s in W1 and W2, respectively. The fluctuation is not regular, and it repeats in each encounter period. Its amplitude is about 0.1 m/s and 0.15 m/s in W1 and W2, respectively. The ship speed reduction, however, could be more by excluding the governor, which tries to maintain the engine rotational speed at a constant level.

Figure 4 shows almost the same behaviour of engine rotational speed that was observed for ship speed due to the application of the same governor and its command signal. The mean value of the engine rotational speed changes from 9.72 to 9.82 and 9.80 RPM in W1 and W2, respectively. The amplitude of fluctuations is 1.0 RPM in W1 and 1.1 RPM in W2, which is not relatively too much. It is interesting to underline that the RPM fluctuation is a response to the resistance fluctuation in waves when the command rotational speed is kept at a constant level. Forcing the rotational speed to be maintained almost at a constant level means increasing the fuel consumption, and consequently higher emissions.

Figure 5 illustrates the fluctuation of propeller power demand. Its mean value is changed to 11,889 kW and 13,066 kW in W1 and W2, respectively. The propeller power demand amplitude is extremely high as much as ten times of the mean value where the higher wave height causes higher fluctuation amplitude.

Table 3 Parameters of the generated regular waves for the model tests [37]

No	H		T	
	Model (cm)	Ship (m)	Model (s)	Ship (s)
W1	4	1.63	1.13	7.23
W2	8	3.26	1.60	10.21

Figure 6 demonstrates the engine delivered power. It is achieved under circumstances of constant engine speed strategy as well as engine limiters. Its mean value in the calm water is 19319 kW and reduces to 10,908 kW and 11,240 kW in W1 and W2, respectively. It is extremely high and is in impact form fluctuating as time marches. It should be noted that this is mostly related to the control strategy, as well as the diesel engine characteristics.

Figure 7 shows the spatial average of the temperature of combustion as a function of time. It follows the same trend as engine-delivered power following the constant rotational speed control strategy. Considering that the NOx emission is strongly dependent on this temperature, it changes in a vast range and very large fluctuations of the emissions should be expected in waves.

Fuel rate and consumed fuel are shown in Fig. 8. The mean fuel rate changes from 0.879 kg/s to 0.536 kg/s and 0.561 kg/s in W1 and W2, respectively. To avoid any confusion, the fuel rate at a ship speed of 10.561 m/s and 10.156 m/s in the calm water condition (equivalent to the mean ship speed at W1 and W2) is calculated and shown in Table 4. They are 0.570 kg/s and 0.536 kg/s, respectively. It is well known that the ship power is a function of power 3 to 4 of ship speed, while fuel rate is in the proportion of ship power. That is why a marginal change in the mean value of ship speed results in a significant change in the fuel rate.

The values of the consumed fuel in W1 and W2 are marginally different. Again, it is mainly related to the selected control strategy, which keeps the rotational speed at a constant level independent of the external and environmental conditions.

To show the impact of wave parameters, hull, propeller, and engine dynamics in sea waves on the NOx formation, the mean values of the variables presented in Figs. 2, 4, 5,

Table 2 Ship and propeller specifications [36, 37]

Ship	Δ (ton)	L_{BP} (m)	B (m)	T (m)	u (m/s)	C_B (–)	C_P (–)
	26,980.22	182.880	24.414	9.782	23.82	0.600	0.615
Propeller		D_P (m)	Z_P (–)		A_E/A_0 (–)		H/D_P (–)
		7.590	5		0.5808		1.00

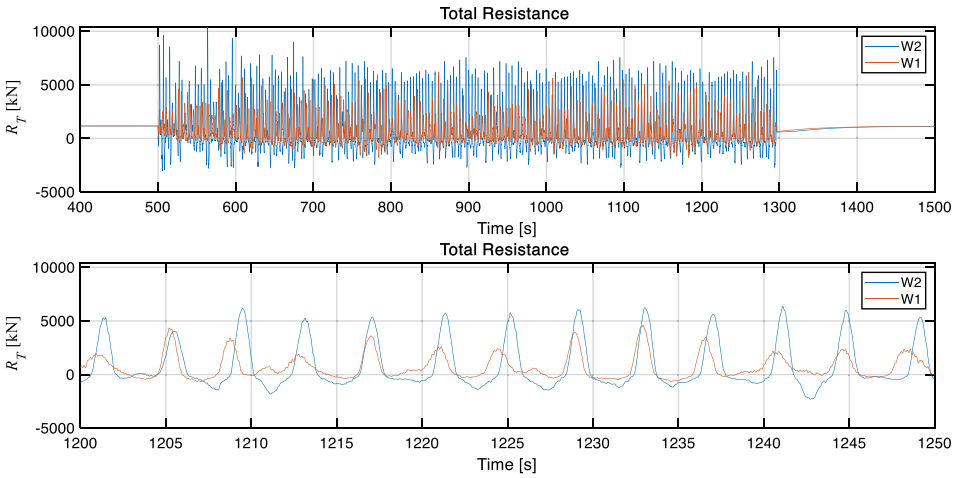

Fig. 2 Total resistance fluctuations for two wave conditions (upper part: overall, lower part: during the selected period in steady state)

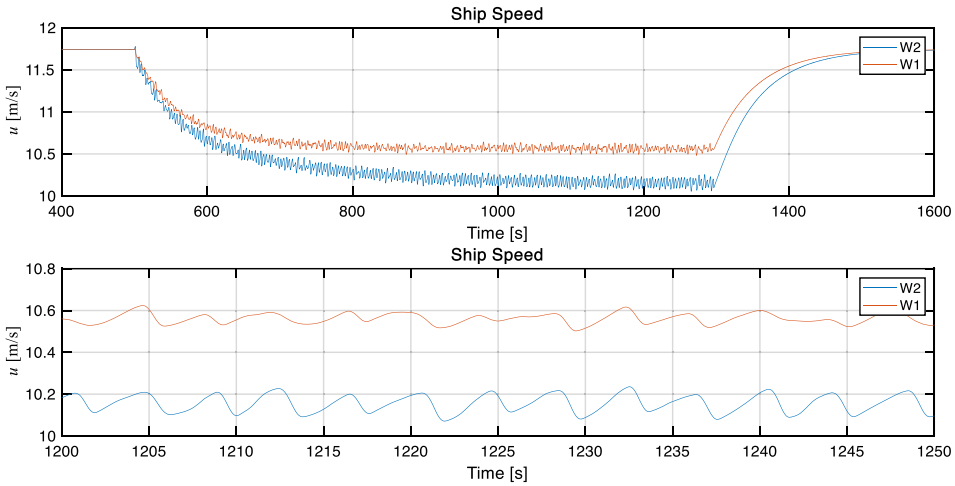

Fig. 3 Ship speed versus time for two wave conditions (upper part: overall, lower part: during the selected period in steady state)

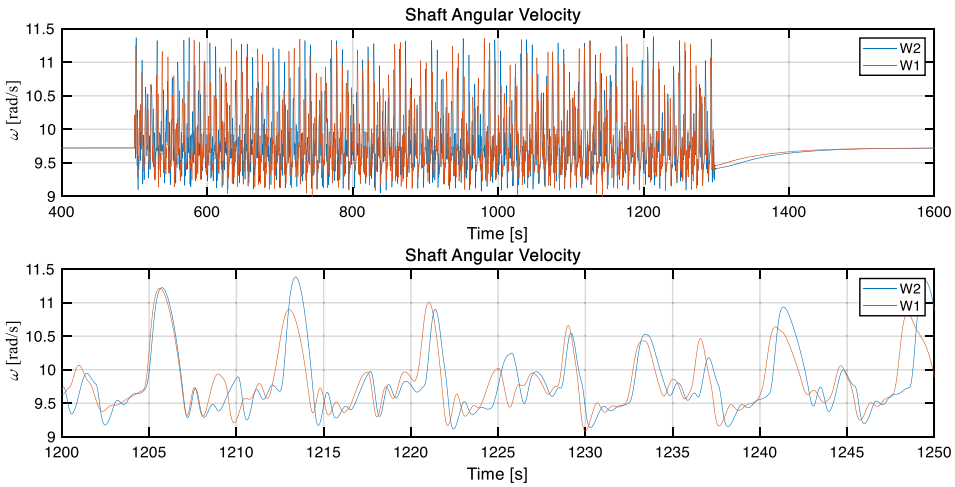

Fig. 4 Engine speed versus time for two wave conditions (upper part: overall, lower part: during the selected period in steady state)

6, 7, 8, 9 and 10 are evaluated and given in Table 4. Since the comparison to the calm water condition is necessary, the selected variables are calculated for three ship speeds: (1) $u = 11.741$ m/s, and no wave, (2) $u = 10.561$ m/s, equivalent to the ship mean speed in W1 navigating in the calm water, and (3) $u = 10.156$ m/s, equivalent to ship mean speed in

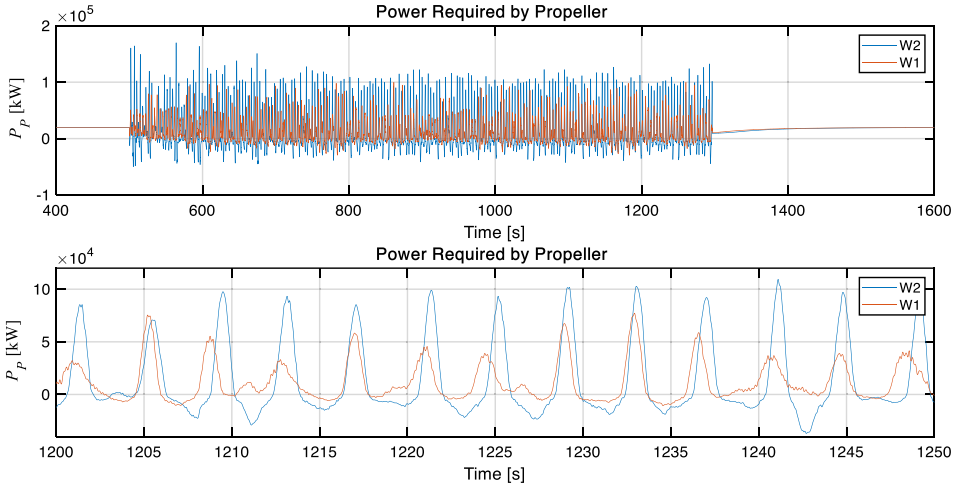

Fig. 5 Propeller power demand versus time for two wave conditions (upper part: overall, lower part: during the selected period in steady state)

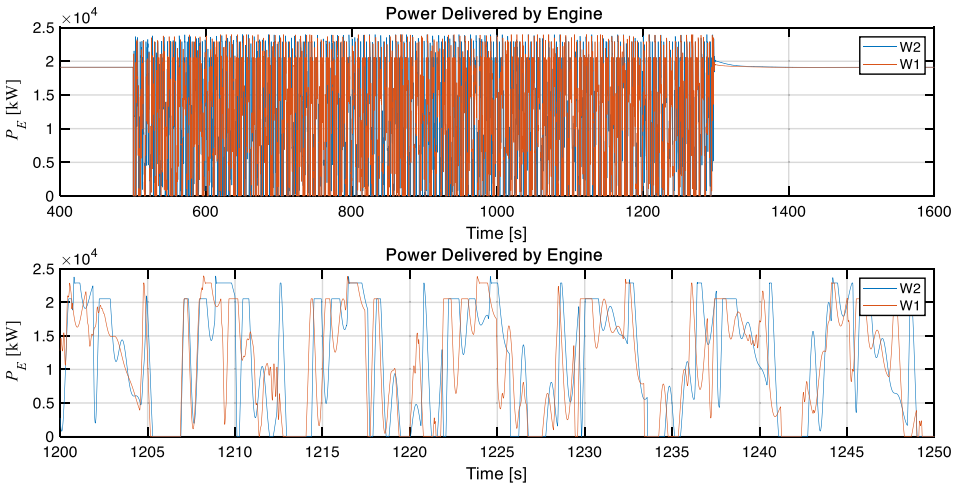

Fig. 6 Engine delivered power versus time for two wave conditions (upper part: overall, lower part: during the selected period in steady state)

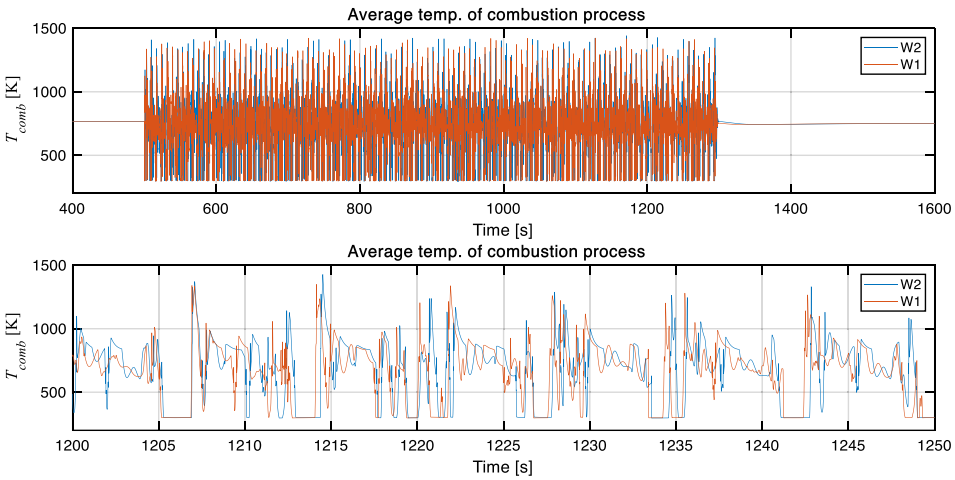

Fig. 7 Average combustion temperature versus time for two wave conditions (upper part: overall, lower part: during the selected period in steady state)

W2 navigating in the calm water. The mean value of the variables under the wave condition is calculated for the selected period of 50 s (from 1200 to 1250 s), where the ship is assumed to be in steady repeating oscillation.

Hereafter, the discussion is provided. Referring to the system of Eqs. (1) to (37) total resistance and fuel rate controlled by the speed governor are dominating inputs that decide the time trend of other variables. As it is shown in

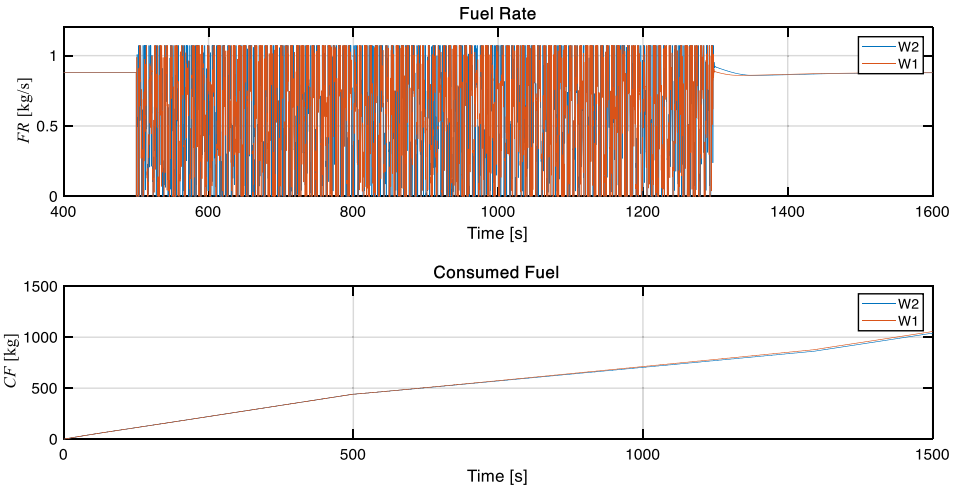

Fig. 8 Fuel rate (upper part) and consumed fuel (lower part) versus time for two wave conditions

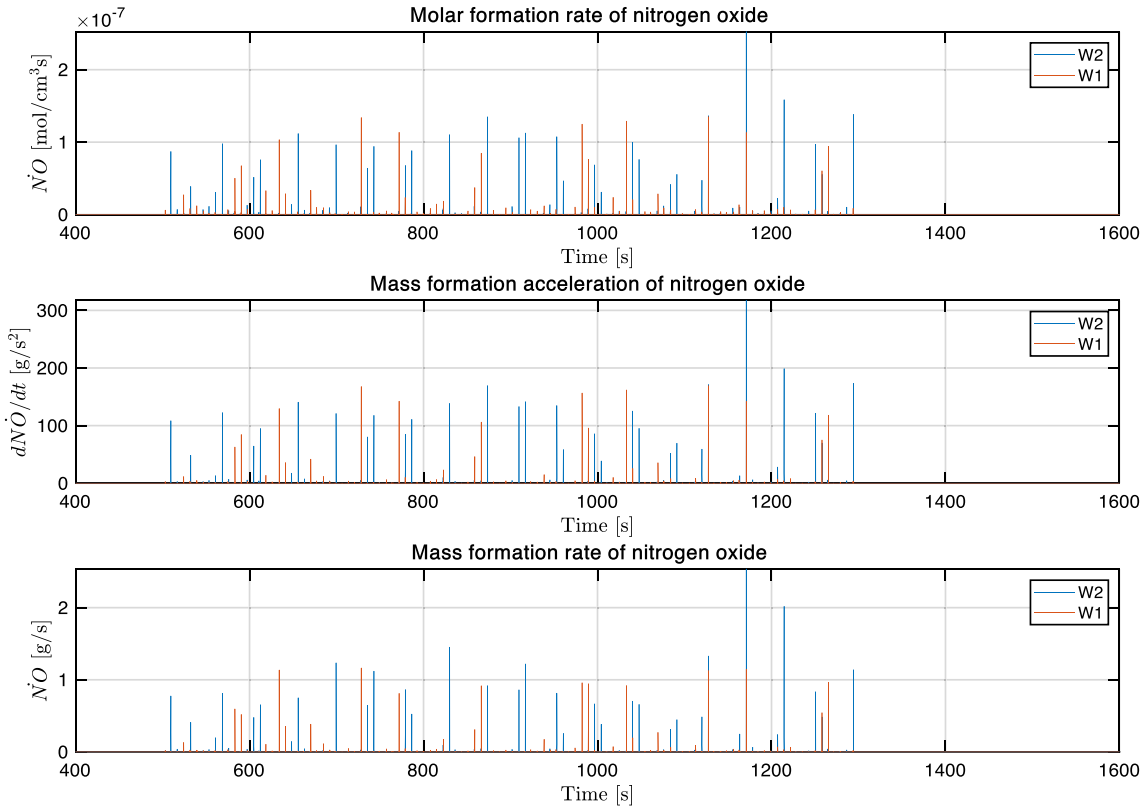

Fig. 9 Formation of NO: molar formation rate (upper part), mass formation acceleration (middle part), and mass formation rate (lower part) versus time for two wave conditions

Fig. 2, the fluctuations of the total resistance due to the encountered wave are quite large. It becomes negative in some instances along a period, which means the ship is pushed forward by the sea wave despite the head sea condition. The negative values of total resistance are observed when the ship encounters the wave trough, depending on the wavelength to ship length ratio. However, the magnitude of the total resistance in such a condition is much less than the magnitude of the total resistance at the maximum level. Referring to the results given in Table 4, the added resistance in W1 and W2 is approximately 52 kN and 176 kN, respectively. However, the min and max values of total resistance are −670 kN and +4609 kN in W1, and −2315 kN and +6380 kN in W2. The impact of resistance fluctuations

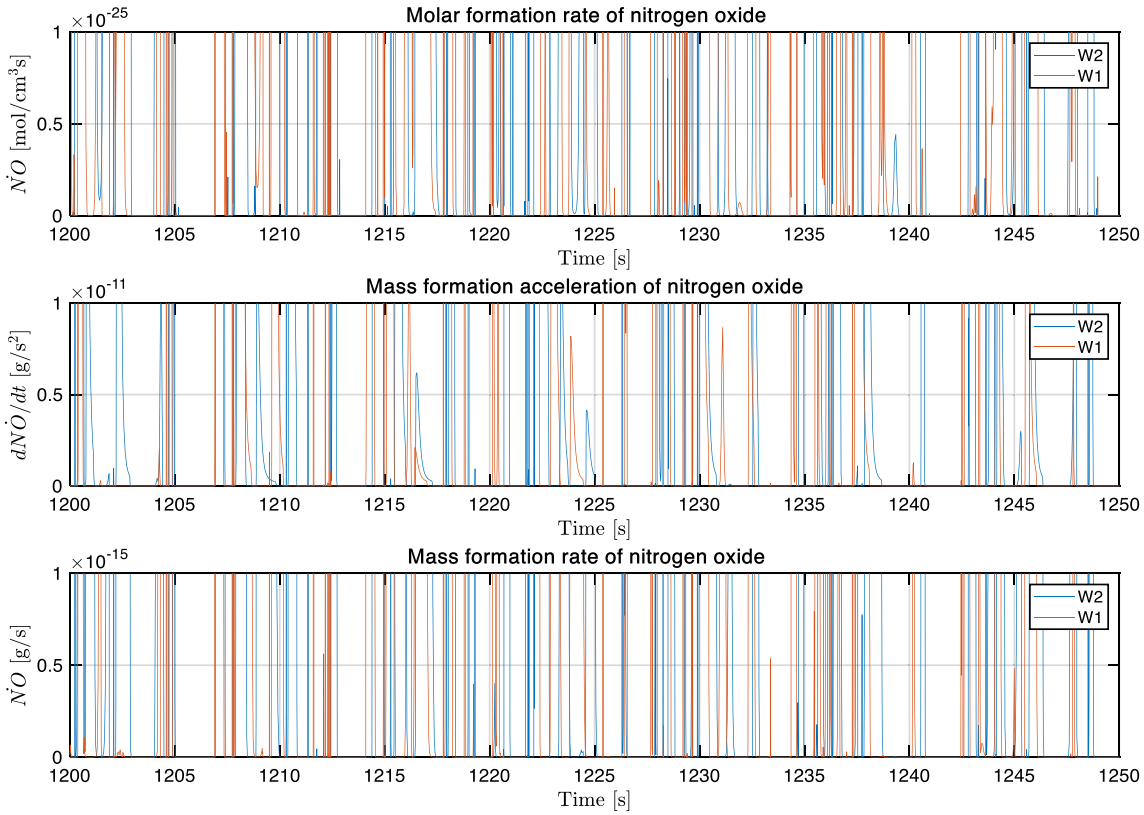

Fig. 10 A selected period in a steady state of formation of NO or NOx: molar formation rate (upper part), mass formation acceleration (middle part), and mass formation rate (lower part) for two wave conditions

Table 4 Mean values of the selected variables of the system

Variable	Unit	Calm ($u = 11.741$ m/s)	Calm ($u = 10.561$ m/s)	Calm ($u = 10.156$ m/s)	W1	W2
Total resistance	kN	1160,889	660,272	599,131	712,436	775,719
Ship speed	m/s	11,741	10,561	10,156	10,561	10,156
Engine rotational speed	rad/s	9721	9723	9828	9824	9804
Required power by propeller	kW	19,301	6706	6085	11,889	13,066
Delivered power by engine	kW	19,319	6710	6089	10,908	11,240
Average combustion temperature	K	767	695	691	689	702
Voyaged distance	m	587.049	528.050	507.800	528.055	507.798
Fuel rate	kg/s	0.879	0.570	0.536	0.536	0.561
Consumed fuel	kg	43.928	28.489	26.826	26.823	28.074
Consumed fuel per metre	kg/m	0.075	0.054	0.053	0.051	0.055
Molar formation of nitrogen oxide	mol/m3.s	1.731E−25	1.71E−29	9.060E−30	2.334E−11	1.689E−10
Mass formation acceleration of nitrogen oxide	g/s^2	1.895E−16	1.38E−20	6.926E−21	2.212E−02	2.065E−01
The mass formation rate of nitrogen oxide	g/s	6.377E−17	6.915E−19	3.463E−19	1.914E−04	2.131E−03
Emitted nitrogen oxide	kg	9.630E−18	3.96E−16	1.98E−16	4.967E−04	5.566E−04
Specific emitted nitrogen oxide	g/kWh	1.188E−17	3.710E−19	2.048E−19	6.317E−05	6.825E−04

in a large range of variation on the rate of formation of NOx can be observed in Figs. 9 and 10. The NOx itself is the result of the frequent and large variation of average combustion temperature shown in Fig. 7., which represents approximately 1200 °C oscillations, periodically. The latter has a direct influence on NOx emission, which is described by Eq. (37). The relationship between combustion temperature and molar formation rate of NO is shown in Fig. 11. It illustrates how temperatures higher than 1211 °C lead to molar formation rates of NO beyond 1E−6 mol/cm^{3}s. It can be regarded as a limit that causes higher NOx emission than 1 to 2 g/kWh (the lower bound of IMO Tier III is 1.96 g/kWh) for the considered case depending on the mass flow rate to the engine cylinders.

It should be also noted that the combustion temperature considered in this study is an average value that is calculated based on the MVZD model of the engine. It means that the combustion continuously happens in time but at a lower temperature. The instantaneous value in comparison with the mean value of this temperature during the combustion process is several times higher, and consequently, the instantaneous emission rate is significantly higher, too. Therefore, the results are generally underestimated and must be regarded as conservative just for comparative analysis. However, the simulation results in the calm water, W1, and W2 conditions, relatively well describe the sea waves' impact on the NOx emissions. In other words, the MVZD model can help to compare the impact of ship environment on the NOx emission but is not able to provide a real and exact figure for NOx formation rate. The present study can be further developed to adopt IVZD or IVMD as an engine model to improve the NOx emission determination.

As an example, the mass formation rate of NO, given in Table 4, of 6915E−19 and 3463E−19 in calm water jumps up to 1914E−04 and 2131E−03 in W1 and W2 conditions, respectively. Even though the mean value of averaged combustion temperature changes in a small range. That is due to large fluctuations of the NO formation rate shown in Fig. 9. These radical, large, and frequent fluctuations are the results of the applied control strategy, which is based on using a conventional governor to keep the engine rotational speed at a constant level. Such a strategy leads to a quick response to the environmental disturbances and significant change in the fuel rate in wave conditions, see Fig. 8. It is also the reason for the rapid fluctuations of the engine power as shown in Fig. 6. To summarize, based on the given values in the last row of Table 4, it is determined that emitted nitrogen oxide in terms of kg/kWh has been increased approximately 1.7E14 times more in the W1 condition and 3.3E15 times in the W2 condition, compared to their related calm water conditions, i.e. for ship speeds 10.561 m/s and 10.156 m/s, respectively. This addresses the need of changing the control strategy to decrease the emissions in wave conditions, which of course should be adjusted with no safety sacrificing.

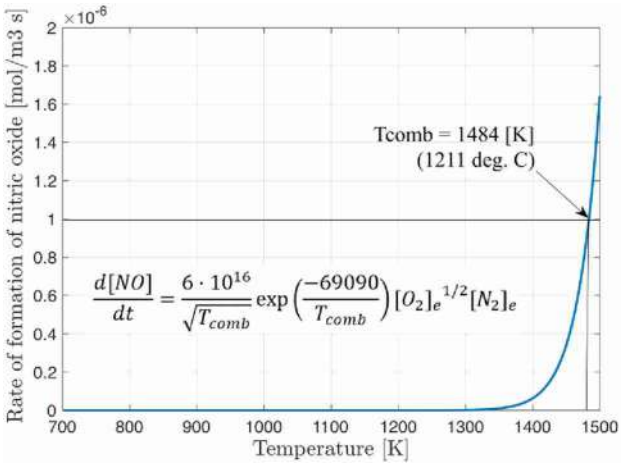

Fig. 11 The rate of formation of nitrogen dioxide as a function of combustion temperature

Conclusions

The present study aims to investigate the influence of sea waves on the NOx emission of a selected ship equipped with a conventional marine diesel engine that is controlled by a governor to keep the engine and propeller rotational speed at a constant level. For this purpose, a proper mathematical model is developed in which the hull, propeller, and engine interactions are taken into consideration. The model is then adapted for numerical simulation. The parameters of the model have been set based on the experimental tests or manufacturers' data. To do the comparative analysis, the simulation is conducted in two regular waves and three ship speeds in the calm water condition. There are five main findings of this study. Firstly, it is concluded that sea waves have a significant impact on the emitted NOx in comparison with the calm water condition at the same ship speed. Secondly, the simulation results show that the higher wave height causes higher total resistance in waves and in turn the emitted NOx becomes higher. The third one describes the reason for the radical increase of NOx in waves. It indicates that such a significant increase is associated with the conventional control strategy that is based on constant engine rotational speed using a conventional speed governor, which is a usual practice in ship navigation. Following this finding, the fourth one can be formulated. The traditional control strategy of the constant engine rotational speed rapidly changes the instantaneous fuel rate to compensate the influence of instantaneous wave added resistance. This leads to the high variation

Table 5 The list of output variables of the computer code

1. Ship speed
2. Engine speed
3. Advance number
4. Propeller thrust and torque diminution factor
5. Net thrust
6. Propeller torque
7. Engine torque
8. Required brake power
9. Delivered brake power
10. Mass of air in the air manifold
11. Temp. of air in the air manifold
12. Mass of ex. gases in the ex. gases receiver
13. Temp. of ex. gases in the ex. gases receiver
14. The mass flow rate of exhaust gases after the turbine
15. Temp. of ex. gases after turbine
16. Average temp. of combustion process
17. Average temp. of outflow gases from engine cylinders
18. Fuel rate
19. The flow rate of air after the compressor
20. The flow rate of air into cylinders
21. The flow rate of air that takes part in combustion
22. The flow rate of exhaust gases after cylinders
23. The flow rate of exhaust gases into the turbine
24. The temperature of the air after the compressor
25. The temperature of air into cylinders
26. The temperature of air that takes part in combustion
27. The temperature of exhaust gases into turbine
28. The temperature of exhaust gases after the turbine
29. The pressure ratio of the compressor
30. The pressure ratio of the turbine
31. The tip speed of the compressor wheel
32. Power of compressor
33. Power of turbine
34. Angular velocity of the turbocharger shaft
35. Mass of air in the intake air manifold
36. The temperature of the air in the intake air manifold
37. The pressure of air in the intake air manifold
38. Mass of gases in exhaust gas receiver
39. The temperature of gases in the exhaust gas receiver
40. The pressure of gases in the exhaust gas receiver
41. Angular velocity of the engine shaft
42. Fuel-to-air ratio
43. The formation rate of nitrogen oxide

in temperature of gases in the combustion process which is blamed for the radical increase of emitted NOx. Summing up these four findings and the extent of the impact of sea wave conditions on the emissions in waves puts under question employing the traditional control strategy of constant engine rotational speed, and this is the final finding and overall conclusion of the study. It underlines that an alternate control strategy is necessary which avoids high and radical changes in fuel rate, prevents sharp and frequent change in combustion temperature and tremendously improves the emission performance of the engine. In addition to this future research need, adequate control of the air mass flow into the engine that leads to reduction of NOx emission should be carefully studied. Further investigations should be accompanied by employing an IVZD or IVMD model of the engine for stimulation purposes since the MVZD model is suitable for comparative analysis of NOx emission rather than determining its absolute values.

Appendix 1

The variables that are determined as the outputs of the simulation code are given in Table 5.

Author contributions MHG did conceptualization, methodology, software, visualization, formal analysis, writing—original draft preparation; HZ.: done data curation, investigation, validation, writing—reviewing and editing.

Funding This research did not receive any specific grant from funding agencies in the public, commercial, or not-for-profit sectors.

Declarations

Conflict of interest The authors declare that they have no known competing financial interests or personal relationships that could have appeared to influence the work reported in this paper.

Consent for publication The work described in this manuscript has not been published previously and is not under consideration for publication elsewhere, its publication is approved by both authors, and if accepted for publishing, it will not be published elsewhere in the same form, in English or any other language, including electronically without the written consent of the copyright holder.

References

1. Vasilescu, M.V.: Advantages and disadvantages of different types of modern marine propulsions. J. Mar. Technol. Environ. **2**, 57–63 (2018)
2. Reşitoğlu, İA., Altinişik, K., Keskin, A.: The pollutant emissions from diesel-engine vehicles and exhaust aftertreatment systems. Clean Tech. Environ. Policy **17**, 15–27 (2015). https://doi.org/10.1007/s10098-014-0793-9
3. Lawrence, M.G., Crutzen, P.J.: Influence of NO(x) emissions from ships on tropospheric photochemistry and climate. Nature **402**(6758), 167–170 (1999). https://doi.org/10.1038/46013
4. Contini, D., Merico, E.: Recent advances in studying air quality and health effects of shipping emissions. Atmosphere **12**(1), 92 (2021). https://doi.org/10.3390/ATMOS12010092
5. Joung, T.H., Kang, S.G., Lee, J.K., Ahn, J.: The IMO initial strategy for reducing Greenhouse Gas(GHG) emissions, and its follow-up actions towards 2050. J. Int. Mar. Saf. Environ. Aff. Shipp. **4**(1), 1–7 (2020). https://doi.org/10.1080/25725084.2019.1707938
6. Bouman, E.A., Lindstad, E., Rialland, A.I., Stromman, A.H.: State-of-the-art technologies, measures, and potential for reducing GHG emissions from shipping – a review. Transp. Res. Part D Transp. Environ. **52**, 408–421 (2017). https://doi.org/10.1016/j.trd.2017.03.022
7. Lamas, M.I., Rodriguez, C.G.: Emissions from marine engines and NOx reduction methods. J. Marit. Res. **9**, 77–81 (2012)
8. Park, W., Lee, J., Min, K., Yu, J., Park, S., Cho, S.: Prediction of real-time NO based on the in-cylinder pressure in Diesel engines. Proc. Combust. Inst. **34**(2), 3075–3082 (2013). https://doi.org/10.1016/j.proci.2012.06.170
9. Lu, X., Geng, P., Chen, Y.: NOx emission reduction technology for marine engine based on tier-III: a review. J. Therm. Sci. **29**(5), 1242–1268 (2020). https://doi.org/10.1007/S11630-020-1342-Y
10. Liang, X.Y., Zhou, P.L., Yu, H.Z.N., Cao, X.Y., Sun, X.X.P.L.: Computational study of NOx reduction on a marine diesel engine by application of different technologies. Energy Procedia **158**, 4447–4452 (2019)
11. Deng, J., Wang, X., Wei, Z., Wang, L., Wang, C., Chen, Z.: A review of NOx and SOx emission reduction technologies for marine diesel engines and the potential evaluation of liquefied natural gas fuelled vessels. Sci. Total Environ **766**, 144319 (2021)
12. Jeevahan, J., Mageshwaran, G., Britto, J.G., Durai Raj, R.B., Thamarai, K.R.: Various strategies for reducing NOx emissions of biodiesel fuel used in conventional diesel engines: a review. Chem. Eng. Commun. **204**(10), 1202–1223 (2017). https://doi.org/10.1080/00986445.2017.1353500
13. Cakir, H.: Nitric oxide formation in diesel engines. Inst. Mech. Eng. (Lond) Proc. **188**(46), 477–483 (1974). https://doi.org/10.1243/PIME_PROC_1974_188_057_02]
14. Way, R.J.B.: Methods for determination of composition and thermodynamic properties of combustion products for internal combustion engine calculations. Inst. Mech. Eng. Lond. Proc. **190**(60), 686–697 (1976). https://doi.org/10.1243/PIME_PROC_1976_190_073_02
15. Miller, J.A., Bowman, C.T.: Mechanism and modelling of nitrogen chemistry in combustion. Prog. Energy Combust. Sci. **15**(4), 287–338 (1989). https://doi.org/10.1016/0360-1285(89)90017-8
16. Correa, S.M.: A review of NOx formation under gas-turbine combustion conditions. Combust. Sci. Technol. **87**(1–6), 329–362 (1993). https://doi.org/10.1080/00102209208947221
17. Chikahisa, T., Konno, M., Murayama, T., Kumagai, T.: Analysis of NO formation characteristics and its control concepts in diesel engines from NO reaction kinetics. JSAE Rev. **15**(4), 297–303 (1994). https://doi.org/10.1016/0389-4304(94)90210-0
18. Kikuta, K., Chikahisa, T., Hishinuma, Y.: Study on predicting combustion and NOx formation in diesel engines from scale model experiments. JSME Int. J. Ser. B **43**(1), 89–96 (2000). https://doi.org/10.1299/JSMEB.43.89
19. Rausen, D.J., Stefanopoulou, A.G., Kang, J.M., Eng, J.A., Kuo, T.W.: A mean-value model for control of homogeneous charge compression ignition (HCCI) engines. J. Dyn. Syst. Meas. Control Trans. ASME **127**(3), 355–362 (2005). https://doi.org/10.1115/1.1985439
20. Merker, G.P.: Simulating Combustion: Simulation of Combustion and Pollutant Formation for Engine-Development. Springer, New York (2006)
21. Asprion, J., Chinellato, O., Guzzella, L.: A fast and accurate physics-based model for the NOx emissions of diesel engines. Appl. Energy **103**, 221–233 (2013). https://doi.org/10.1016/J.APENERGY.2012.09.038
22. Arregle, J., Lopez, J.J., Guardiola, C., Monin, C.: Sensitivity Study of a NOx Estimation Model for On-board Applications. SAE Technical Papers, SAE International (2008). https://doi.org/10.4271/2008-01-0640
23. Egnell, R.: Combustion Diagnostics by Means of Multizone Heat Release Analysis and NO Calculation. SAE Technical Papers, SAE International (1998). https://doi.org/10.4271/981424
24. Lamaris, V.T., Hountalas, D.T., Zannis, T.C., Glaros, S.E.: Development and validation of a multi-zone combustion model for predicting performance characteristics and NOx emissions in large scale two-stroke diesel engines. ASME Int. Mech. Eng. Congr. Expo. Proc. **3**, 317–327 (2010). https://doi.org/10.1115/IMECE2009-11382
25. Mocerino, L., Soares, C.G., Rizzuto, E., Balsamo, F., Quaranta, F.: Validation of an emission model for a marine diesel engine with data from sea operations. J. Mar. Sci. Appl. (2021). https://doi.org/10.1007/S11804-021-00227-W/FIGURES/13
26. Papagiannakis, R.G., Rakopoulos, C.D., Hountalas, D.T., Rakopoulos, D.C.: Emission characteristics of high speed, dual fuel, compression ignition engine operating in a wide range of natural gas/diesel fuel proportions. Fuel **89**(7), 1397–1406 (2010). https://doi.org/10.1016/J.FUEL.2009.11.001
27. Benvenuto, G., Laviola, M., Campora, U.: Simulation Model of a Methane-Fuelled Four Stroke Marine Engine for Studies on Low Emission Propulsion Systems. Developments in Maritime Transportation and Exploitation of Sea Resources, pp. 591–598. CRC Press, Florida (2013)
28. Stoumpos, S., Theotokatos, G., Boulougouris, E., Vassalos, D., Lazakis, I., Livanos, G.: Marine dual fuel engine modelling and parametric investigation of engine settings effect on performance-emissions trade-offs. Ocean Eng. **157**, 376–386 (2017). https://doi.org/10.1016/J.OCEANENG.2018.03.059
29. Scappin, F., Stefansson, S.H., Haglind, F., Andreasen, A., Larsen, U.: Validation of a zero-dimensional model for prediction of NOx and engine performance for electronically controlled marine two-stroke diesel engines. Appl. Therm. Eng. **37**, 344–352 (2012). https://doi.org/10.1016/J.APPLTHERMALENG.2011.11.047
30. Hountalas, D.T., Zovanos, G.N., Sakellarakis, D., Antonopoulos A.K.: Validation of multi-zone combustion model ability to predict two stroke diesel engine performance and NOx emissions using on board measurements. In: Proceedings of the Spring Technical Conference of the ASME Internal Combustion Engine Division, pp. 47—60 (2012). https://doi.org/10.1115/ICES2012-81100
31. Savva, N.S., Hountalas, D.T.: Evolution and application of a pseudo-multi-zone model for the prediction of NOx emissions from large-scale diesel engines at various operating conditions. Energy Convers. Manag. **85**, 373–388 (2014). https://doi.org/10.1016/j.enconman.2014.05.103
32. Raptotasios, S.I., Sakellaridis, N.F., Papagiannakis, R.G., Hountalas, D.T.: Application of a multi-zone combustion model to

investigate the NOx reduction potential of two-stroke marine diesel engines using EGR. Appl. Energy **157**, 814–823 (2015). https://doi.org/10.1016/J.APENERGY.2014.12.041
33. Larsen, U., Pierobon, L., Baldi, F., Haglind, F., Ivarsson, A.: Development of a model for the prediction of the fuel consumption and nitrogen oxides emission trade-off for large ships. Energy **80**, 545–555 (2015). https://doi.org/10.1016/J.ENERGY.2014.12.009
34. Cooper, D.A.: Exhaust emissions from high-speed passenger ferries. Atmos Environ. (2001). https://doi.org/10.1016/s1352-2310(01)00192-3
35. Kowalski, J., Tarelko, W.: NOx emission from a two-stroke ship engine Part 1: modeling aspect. Appl. Therm. Eng. **29**(11–12), 2153–2159 (2009). https://doi.org/10.1016/j.applthermaleng.2008.06.032
36. Zeraatgar, H., Ghaemi, M.H.: The analysis of overall ship fuel consumption in acceleration manoeuvre using hull-propeller-engine interaction principles and governor features. Pol. Marit. Res. **26**, 162–173 (2019). https://doi.org/10.2478/pomr-2019-0018
37. Ghaemi, M., Zeraatgar, H.: Analysis of hull, propeller and engine interactions in regular waves by a combination of experiment and simulation. J. Mar. Sci. Technol. (2020). https://doi.org/10.1007/s00773-020-00734-5
38. Ghaemi, M.H.: Performance and emission modelling and simulation of marine diesel engines using publicly available engine data. Pol. Marit. Res. **28**(4), 63–87 (2021). https://doi.org/10.2478/POMR-2021-0050
39. Heywood, J.: Internal Combustion Engine Fundamentals. McGraw-Hill Education Ltd, New York (2018)
40. MAN-B&W: Computerized Engine Application System (CEAS). https://www.man-es.com/marine/products/planning-tools-and-downloads/ceas-engine-calculations. Accessed 05 Apr 2022
41. MAN B&W S65ME-C8.5-TII Project Guide Electronically Controlled Two-stroke Engines, https://www.academia.edu/35674638/MAN_B_and_W_S90ME_C8_TII_Project_Guide_Electronically_Controlled_Two_stroke_Engine. Accessed 03 Apr 2022
42. Fossen, T.I.: Handbook of marine craft hydrodynamics and motion control [bookshelf]. IEEE Control Syst. **36**, 78–79 (2016). https://doi.org/10.1109/mcs.2015.2495095

International Journal of Energy and Environmental Engineering (2023) 14:613–626
https://doi.org/10.1007/s40095-022-00538-w

ORIGINAL RESEARCH

Scope for feed-in tariff in a hydro-rich energy market—a case of Bhutan

Andu Dukpa[1]

Received: 8 June 2022 / Accepted: 9 September 2022 / Published online: 30 September 2022

Abstract
To promote the use of renewable energy (RE), several types of RE policies have been implemented globally. Among these, feed-in tariff (FiT) is one of the most accepted mechanisms of pricing policy. However, choosing the best policy for a market with a high RE penetration is a challenge. A case of Bhutan is considered in this paper as the source of electrical energy is predominantly hydropower. Additionally, a generous subsidy is provided by the government to keep the electricity tariff to a minimum. Recently, there has been an increase in the advocacy and motivation for other forms of RE sources (RES) to supplement hydropower and increase energy security in Bhutan. Bhutan aims to achieve a total of 20 MW of non-hydro RES by 2025 as per the RE policy of Bhutan. However, Bhutan still does not have an RE pricing policy, and therefore, there is a need to institute a suitable pricing mechanism to accommodate the penetration of the planned non-hydro RES. This paper discusses the challenges in introducing FiT for non-hydro RES in an electricity market dominated by hydropower in Bhutan. Subsequently, recommendations are made in the wake of subsidised electricity tariff, which is the lowest in the region at 0.0171 USD/kWh for low voltage customers. FiTs for solar photovoltaic based on different categories of customers have been computed and proposed.

Keywords Deregulation · Renewable energy · Feed-in tariff · Electricity pricing · Electricity market

Introduction

Globally, there has been an increase in the use of renewable energy sources (RES) primarily to discourage the use of fossil-fuelled energy generation, reduce greenhouse gas emissions and increase energy security. Policy schemes such as feed-in tariff (FiT), net-metering and other mechanisms have been instituted to promote the use of RES. However, in regions where the share of RE is dominant, designing and implementing RE policy becomes a challenge. One such region is Bhutan, where the source of electricity is predominantly hydropower and a policy to provide incentives for the installation of RE is yet to be instituted.

Bhutan is blessed with a huge hydropower potential of 36,900 MW with annual production capacity of 154,000 GWh [1]. Chukha Hydropower Plant, the country's first hydropower plant (HP) was established in 1986–88. Since then, there has been a considerable progress in the development of HPs in Bhutan. The total installed capacity of hydropower in Bhutan today stands at 2335 MW [1], which is 6.32% of the total potential. About 70% of the total generation is exported and sold to India [2], Bhutan's closest neighbour and ally because of which there has been a surge in the country's economy. The electricity exported to India topped 4,465 MU fetching Indian Rupees (Rs.) 10,080 million (~USD 136 million) in 2020, and the revenue from hydropower is approximately 7.5% of the country's gross domestic product (GDP) [2].

In addition, Bhutan had set up an ambitious target of providing 100% electricity coverage to all households by 2020, but this target was brought forward, to be achieved by the year 2013 [3]. In May 2008, Bhutan and India signed the *Protocol to the 2006* Agreement concerning Cooperation in the Field of Hydroelectric Power and agreed to achieve a total generation of 10,000 MW by the year 2020 in Bhutan [4]. However, considering the current pace of development and complexities involved in the construction of HPs and the fact that excessive dependence on a single resource for electricity would imperil the country's energy security, the country has recently started identifying RES that would be most appropriate for Bhutan. Wind power and solar

✉ Andu Dukpa
a.dukpa@pb.edu.pl; andudukpa@gmail.com

[1] Faculty of Electrical Engineering, Bialystok University of Technology, Bialystok, Poland

power are the front runners among others in Bhutan. The theoretical solar potential in Bhutan is estimated at 6 TW, while the restricted technical potential is estimated at 12 GW [5]. As per [5], the wind energy potential is estimated at around 760 MW, mostly in the northern region of Bhutan, with Wangduephodrang district in the north accounting for around 19% of the total potential. The two districts in southern Bhutan; Chukha has 12% and Dagana, 10% of the total wind power potential [5]. Other renewable technologies such as biomass and biogas are mainly limited to cooking purposes in rural areas. RE policy has not been implemented yet in Bhutan and there are no private generation companies (GenCos). As the country look towards diversifying the sources of energy in Bhutan, there is a need to institute an appropriate RE pricing scheme. Among the existing RE policies, FiT is considered the most effective and widely implemented RE policy in the world [6],[6]. This paper discusses the challenges in introducing FiT in Bhutan and subsequently proposes recommendations in the wake of subsidised electricity tariff and a non-liberalised market dominated by hydropower.

Methodology

Energy sector in Bhutan

The energy sector in Bhutan has been restructured to address the need of the changing market scenario and to keep pace with the global change. The restructuring of the energy sector in Bhutan has not been long. It was only in 2002, when the energy sector, which was fully state-owned was restructured to derive maximum benefits for the country and the consumers.

Bhutan Power Corporation Limited (BPC), established on July 1, 2002, serves as the system operator for Bhutan and is responsible for both transmission and distribution of electricity in the country. In addition, BPC also looks after the Bhutan Power System Operator (BPSO), small/micro HPs and wind power plant comprised of two wind power generators of 2×300 kW in Rubessa, Wangduephodrang. Therefore, the role of BPC is comparatively unique from that of a conventional system operator elsewhere. Besides providing electricity services to the nation, BPC as one of the companies of Druk Holding and Investments (DHI) is also mandated to generate revenue for the company. Figure 1 shows the overall structure of energy sector in Bhutan. In general, the power and energy sector in Bhutan is comprised of only government entities and currently, there are no private GenCos, except as end-user consumers.

Renewable energy in Bhutan

Driven by the increasing domestic demand, risks due to reliance on a single source of electricity and the need to harness other forms of clean energy, the Ministry of Economic Affairs of Bhutan (MoEA) had come up with a draft RE policy in 2011, which was finalised and released as the 'Alternative Renewable Energy Policy 2013 (AREP)', the first edition of the renewable energy policy in Bhutan. Bhutan shall strive to generate 20 MW by 2025 through a mix

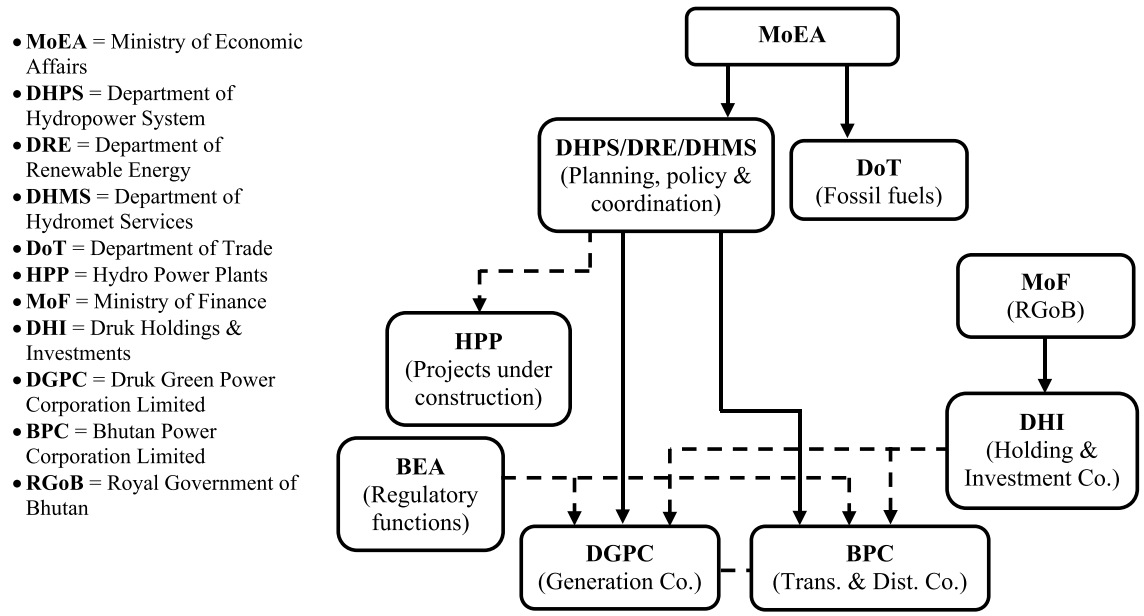

Fig. 1 Structure of energy sector in Bhutan

of renewable technologies such as solar power, wind power, biomass, and others [8]. However, the targets set in AREP [8] as shown in Table 1 are comparatively lower than what is available [5].

Although focus on small hydropower has been made in [8], no specific target has been set for small hydropower less than 25 MW.

In Bhutan, the development and implementation of wind power and solar photovoltaic (PV) and their integration into the national grid is prioritised over other non-hydro RES [9]. The current priorities are small hydropower, wind power and solar PV as they seem most appropriate and viable considering the rugged mountain terrains of Bhutan [8]. In a country where hydropower is the main source of electricity and that major portion of the country's economy depends on hydropower, penetration of other sources of renewable energy is seen as a challenge, primarily due to the overall costs and associated turnover. Keeping in view the challenges associated with hydropower generation, the threat to energy security due to reliance on a single source of electricity, and the increasing imports of fossil fuels, Bhutan has started diversification of its energy resources [8]. As per [9], major activities have been planned to promote RE and include the following types of RES:

(i) Wind power
(ii) Solar PV
(iii) Biomass, and
(iv) Small hydropower.

In 2014, two wind electric generators were installed in Rubessa, Wangduephodrang. The 2×300 kW wind power plant was established mainly to reduce the import of electricity during the lean period, increase sale during summer and diversify energy resources in the country. Although non-hydro RES for the generation of electricity (RES-E) has penetrated the market, BPC does not levy a separate tariff to its customers.

BPC is responsible for the transmission and distribution of electricity to residential, commercial, and industrial customers irrespective of the type of source of electricity. However, with the increase in the percentage of RE penetration, there will be a need to appropriately design and implement a pricing mechanism to suitably benefit investors as well as meet the objectives of the government. Additionally, the RE policy of Bhutan also indicates a FiT scheme to be introduced [8]. At the moment, non-hydro RES penetration has remained insignificant and therefore, the electricity pricing modality and the tariff thereof continue to remain unchanged. The electricity generation from various sources in 2020 is shown in Fig. 2. [10].

Electricity generation from non-hydro RES-E will grow and the share of these RES-E is expected to reach 20 MW by 2025. The DRE had planned to install three major renewable power plants: A 30 MW solar power plant at Shingkhar, Bumthang, a 17 MW solar power plant at Sephu, Wangduephodrang and a 23 MW wind power plant at Gaselo, Wangduephodrang [11]. The planned solar power plants will be the first of their kind and the largest solar power plants in the country. While the plan to install the 17 MW Solar PV plant in Sephu is in progress, the 30 MW solar PV plant in Shingkhar has been suspended due to community issues.

Table 1 Renewable energy scenarios proposed in Bhutan by 2025 [5, 8]

Source	Capacity by 2025 (MW)			
	AREP target	Low case	Base case	High case
Small Hydro	–	37.2	67.5	110
Wind	5	2.4	5.1	7.8
Solar PV	5	2	6.1	11.9
Biomass	5	0.6	1	8.1
Others	5	–	–	–
Total	20	42.2	79.7	137.8

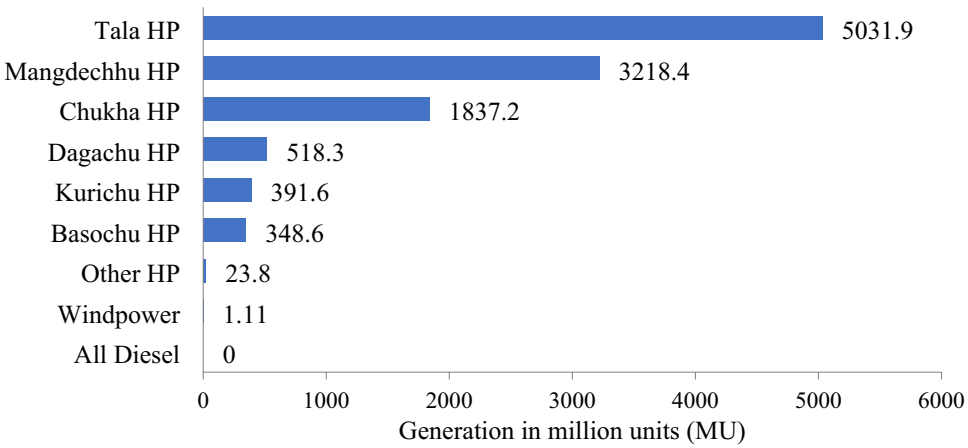

Fig. 2 Electricity generation from various sources in 2020

Additionally, a utility scale 180 kW grid-tied ground mounted solar power plant was inaugurated on October 4, 2021, in Rubessa, Wangduephodrang as a pilot project. The solar power plant is expected to provide electricity to around 90 households in the locality through the grid. Therefore, FiT, or other pricing mechanisms will have to be carefully planned to suit the needs of the country in view of the increase in non-hydro RES-E.

Feed-in tariff

Feed-in tariff in general is a government driven policy to promote and support investments in renewable power generation. FiT scheme enables the RE GenCos, such as solar, wind or small hydropower to receive an incentive for electricity generation.

As per [7], there are two types of FiT models: (i) Market-dependent or Feed-in Premium (FiP) model and (ii) Market-independent or Fixed Price model, where the main distinction is the dependency on the actual electricity market price. While the market-dependent model is associated with an additional premium on top of the market price, the market-independent model offers a guaranteed minimum payment for every unit of electricity injected into the grid. FiTs facilitate long-term financial incentive to those who participate as GenCos and contribute electricity to the grid. Unlike the current system of unit-based pricing, the pricing is based on the conditions of the FiT contract with the utility company. A well-planned FiT can create a robust market for RE and encourage increased participation of RES-E. In addition to FiT, the following types of regulatory instruments in the promotion of RE are implemented:

(i) Feed-in Premium
(ii) Auction
(iii) Quota
(iv) Certificate system
(v) Net-metering
(vi) Mandate, and
(vii) Registry

Fiscal incentives and other benefits such as grid access, access to finance and socio-economic benefits are also being implemented in the promotion of RE technologies. FiT schemes have been conducive to RE development since the early 2010's, however the focus has now shifted from FiTs to competitive tendering schemes such as auctions [12]. In [13], they have carried out an analysis to determine the effectiveness of the FiT policy and conclude that there are multiple avenues that can be leveraged to achieve a larger representation of RE. There is a preference for auctioning, net-metering and mini-grids as alternative mechanisms to FiT policies. It is reported that the implementation of these options should be done effectively to avoid challenges faced with the FiT policy [13]. In Malaysia, successful utilisation of RES for electricity generation and the global implementation of FiT has encouraged the implementation of FiT. Although FiT can be conveniently implemented for biomass, biogas and solid waste energy, FiT has not attracted expected investment in solar and wind RES due to their requirement of higher FiTs [14]. In Taiwan, the government has adopted FiTs coupled with a bidding process to determine subsidised tariffs due to difficulties in setting tariff each year and because FiTs often cannot catch up with the market and technology-varying conditions [15]. Several nations have introduced technology-specific FiTs combined with net-metering scheme.

Although FiT is an effective RE policy, it is interesting to note that several countries have either revised or discontinued their FiT policy. In few cases, due to reduction in the solar PV costs, FiTs were replaced by combined policies and to prevent over-subsidisation in the markets [16]. More number of countries have opted auctions modality over FiTs as their renewable energy pricing policy [17]. The number of countries following FiT and Auction modality from the year 2014 to 2016 is shown in Fig. 3 [17]. As seen from the trend, by the end of 2016, more than 70 countries had adopted auctions as opposed to FiT. A substantial increase in the number of countries adopting auctions is noted as opposed to FiT, mostly due to their flexibility of design and because they can be made country specific.

Results and discussions

Feed-in tariff in Bhutan

At the moment, there is a lack of FiT and other incentive schemes for RES in Bhutan. It would require a robust enabling policy environment for Bhutan to achieve a total of 20 MW of alternative RE generation by 2025 as planned. To enable a promising policy environment for alternate RE resources in Bhutan, the following are considered the highest priorities [18]:

(i) formulation of renewable energy master plan to identify, assess, and forecast the resources,
(ii) formulation of feed-in tariff framework, and
(iii) preparation of implementation rules and guidelines of the alternative renewable energy policy.

With a feed-in policy in place, regulatory agencies such as the Bhutan Electricity Authority (BEA) and the DRE could initiate the development, implementation, and monitoring of the FiT programme. Further, the lack of private

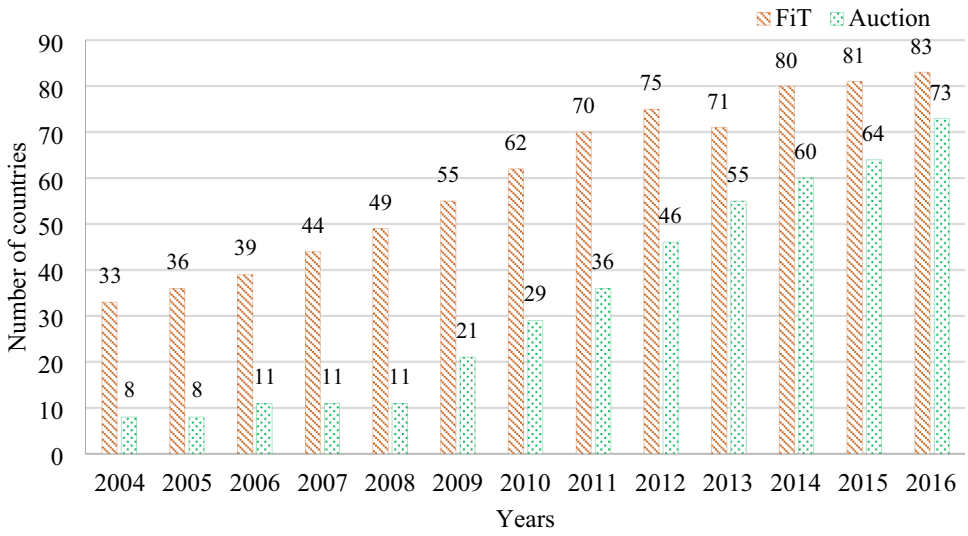

Fig. 3 Number of countries adopting FiT and Auction [17]

GenCos in Bhutan has not conditioned the government to pursue such feed-in policies. Further, in a study conducted by [19], it has been opinioned that there is a barrier to promoting non-hydro RES due to the absence of a FiT policy in Bhutan. Based on the nature of the feed-in policy (feed-in tariff or feed-in premium), several types of incentives can be developed. As per [8], BEA shall design and develop the following:

(i) fed-in tariff as per the principles contained in the policy, and
(ii) norms related to grid connectivity/interfacing and load dispatch, etc.

Considering all circumstances, the current choice of RE pricing policy in Bhutan is FiT [8].

Electricity pricing in Bhutan

Bhutan's current electricity market structure is unique as all components of the power sector (generation, transmission, and distribution) operate under one entity, the DHI, which is the largest and only government-owned holding company in Bhutan. To encourage additional participants in the electricity market, the government will have to devise various strategies, and this will necessitate a major reform in the electricity market structure. Further, Bhutan currently exports electricity to only a single customer, which is India. To benefit more customers, enhance cross-border energy trade, and increase energy security, Bhutan will have to continue exploring opportunities to export energy to other neighbouring countries such as Bangladesh, Nepal, and Myanmar. Additionally, Bhutan's dependency on energy export from hydropower, a single source of energy comes with a challenge to its energy security.

The electricity pricing in general is determined by the generation cost, transmission cost, distribution cost, interests and depreciation of assets, salaries of employees, and profit. These costs further depend on numerous factors, such as connected load, load conditions, demand factor, load factor, diversity factor, plant capacity factor, etc., which makes the fixation of tariff in an electricity market rigorous. BPC as the state-owned system operator, levies electricity costs on customers and these prices are regulated by BEA. The past and current end-user tariff is shown in Table 2 [20, 21].

Over the years, there has been a steady rise in the domestic electricity tariff based on numerous factors. Although small, the rise has been steady, and an extrapolation of the tariff gives an average annual increase of 1.8%. The variation in the tariff for low voltage (LV) customers from 2017 to 2022 (projected) is shown in Fig. 4. It can be concluded that the rise over the years is held minimum due to subsidies provided by the government.

The electricity prices in Bhutan are determined by the BEA and fixed in accordance with the *Tariff Determination Regulation 2016* of Bhutan. The regulation provides for the electricity prices in accordance with the *Electricity Act of Bhutan 2001* and the *Domestic Electricity Tariff Policy 2016*. These prices apply to all licensees including the following [22]:

(i) Generation licensee.
(ii) Transmission licensee.
(iii) Distribution and supply licensee.
(iv) System operation licensee.

Table 2 Electricity tariff in Bhutan

Tariff Structure	Unit**	1/1/2017 – 30/6/2017	1/7/2017 – 30/6/2018	1/7/2018 – 30/6/2019	1/10/2019 – 30/6/2020	1/7/2020 – 30/6/2021	1/7/2021 – 30/6/2022
Low Voltage (LV)							
LV Block I (Rural) *0–100 kWh*	Nu./kWh	0	0	0	0	0	0
LV Block I (Highlanders) *0–200 kWh*	Nu./kWh	–	–	–	0	0	0
LV Block I (Others) *0–100 kWh*	Nu./kWh	1.28	1.28	1.28	1.28	1.28	1.28
LV Block II (All) *101–500 kWh**	Nu./kWh	2.52	2.60	2.68	2.68	2.68	2.68
LV Block III (All) *> 500 kWh**	Nu./kWh	3.33	3.43	3.53	3.57	3.60	3.64
LV Bulk	Nu./kWh	3.79	3.90	4.02	4.06	4.10	4.14
Medium Voltage (MV)							
Energy Charge	Nu./kWh	2.00	2.07	2.16	2.24	2.45	2.65
Demand Charge	Nu./kWh	250	275	300	325	325	325
High Voltage (HV)							
Energy Charge	Nu./kWh	1.59	1.59	1.59	1.50	1.50	1.50
Demand Charge	Nu./kVA/Month	262	262	262	292	292	292
Wheeling	Nu./kWh	0.195	0.195	0.195	0.27	0.27	0.27

*For 2017–2018, it is only up to 300 kWh instead of 500 kWh

**Conversion rate as of Feb 2022 is approximately, USD 1 = Nu. 74.8

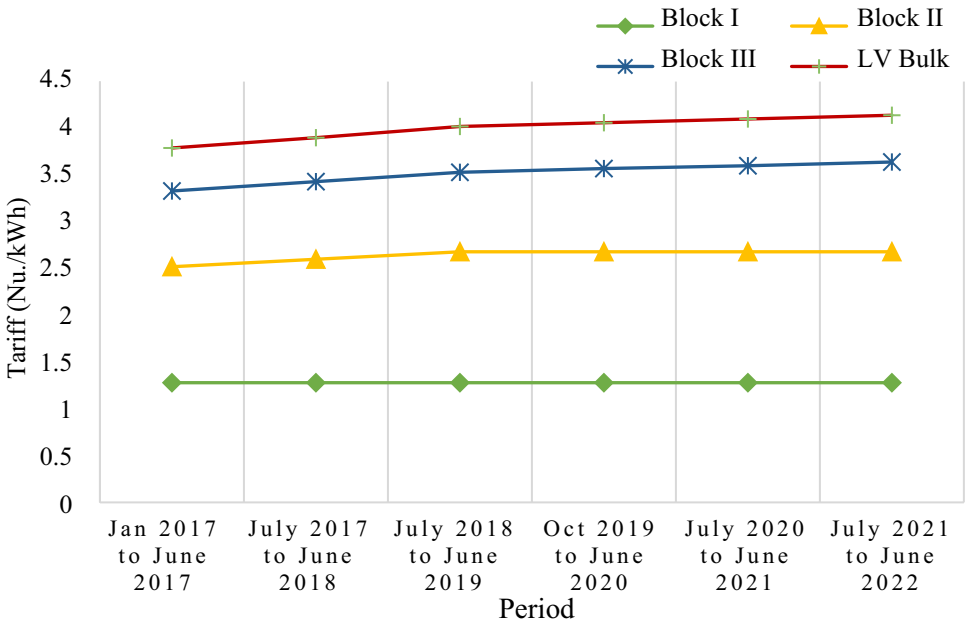

Fig. 4 Increase in the LV tariff from 2017 to 2022

Further, all electricity tariffs for the sale of electricity must comply with the terms of the regulation, except for the following [22]:

(i) import of electricity from other countries,
(ii) export of electricity to other countries, and
(iii) sale of electricity from generators under *Power Purchase Agreements* (PPA).

The existing low tariff has enabled significant success in the overall socio-economic growth in Bhutan. There has also been an increase in the small, medium, and large energy intensive industries due to the access to reliable and affordable electricity. This is evident from the government's initiative of establishing various special economic zones in the country [7], where citizens are encouraged to establish various industries through government-led schemes. However, hydropower projects have their own share of shortfalls. Environmentalists continue to question whether hydropower projects in Bhutan can really be considered as 'clean' sources of electricity.

In addition, there have been bottlenecks in the construction of hydropower projects, such as the construction of the 1200 MW Punatshangchhu-I which began in 2008 and was scheduled to be completed in 2016, but the completion date has been further delayed. The project has been facing serious challenges due to geological conditions in the construction of the dam. The delay in the completion of the project has caused serious financial and resource implications to the government.

Considering all circumstances, the government has now started embracing other forms of RE. Several projects are in the pipeline and constructions will begin soon. A pricing modality needs to be developed to encourage the establishment of non-hydro RES-E projects in the country. As per [8], all RE projects for electricity generation except for mini, micro, and small hydropower are to be developed under Build, Own, Operate (BOO) model.

Electricity tariff computation

The electricity tariff payable to BPC is derived as follows [23]:

$$E_T = \mathrm{CoS} - S_R(\mathrm{USD/kWh}) \tag{1}$$

where $CoS = \mathrm{G_C} + \mathrm{N_C}$.

The cost of supply *CoS* is the sum of generation cost G_C from DGPC and network cost N_C (transmission and distribution) from BPC. *CoS* includes the allowances for operation and maintenance costs, depreciation, return on fixed assets, i.e., including an allowance for company taxation, cost of working capital and any regulatory fees, duties, or levies that the licensee is liable to pay.

The network cost N_C, includes the operation and maintenance costs, depreciation, return on fixed assets i.e., including an allowance for company taxation, cost of working capital and any regulatory fees, duties, or levies that the licensee is liable to pay, cost of losses to transmit, distribute and supply electricity to the customers. S_R is the subsidy granted by the royal government of Bhutan (RGoB) to BPC to keep the MV and LV customer tariffs lower than the *CoS*.

The end-user tariff for LV, MV and HV works out as shown in Table 3 for the tariff sample of 2017 [23]. From the table, we see that the unit price of LV for all levels of block is Nu. 5.81 (USD 0.0776). The subsidy provided by the government ranges from 0 to 5.81 Nu./kWh (0 to 0.0776 USD/kWh), based on the customer type and consumption. For the LV customers, it ranges from 1.91 to 5.81 Nu./kWh (0.0255

Table 3 Computation of end-user tariff [23]

Customer group	Generation cost, DGPC (Nu/kWh)	Network cost, BPC (Nu/kWh)	Total COS (Nu/kWh)	Subsidy (Nu/kWh)	Tariff (Nu.)
	G_C	N_C	*CoS*	S_R	E_T
LV Consumers (230/415 V)					
Block I (Rural Domestic) ≤ 100 kWh				5.81	0.00/kWh
Block I (Others) ≤ 100 kWh				4.53	1.28/kWh
Block II ≥ 101 kWh to ≤ 300 kWh	1.59	4.22	5.81	3.21	2.60/kWh
Block III ≥ 301 kWh				2.38	3.43/kWh
LV Bulk				1.91	3.90/kWh
MV Consumers (6.6/11/33 kV)					
Demand charge	1.59	3.79	5.38	1.53	275/kVA/month
Energy charge					2.07/kWh
HV Consumers (66 kV and above)					
Demand charge	1.59	0.64	2.23	0	262/kVA/month
Energy charge				0	1.59/kWh

to 0.0776 USD/kWh), which works out to a minimum of 32.87% to a maximum of 100% for LV customers. Likewise, subsidy is also provided to MV customers. Therefore, it is evident from Table 3 that the government provides electricity subsidy based on different category of customers, mainly supporting those in rural areas.

In Bhutan, all generation plants fully owned by the RGoB must provide 15% of the annual generation as royalty energy to the government free of charge [24]. This enables the government to grant significant subsidies so that the domestic tariff is kept at minimum. To ascertain the impact of the subsidy provided by the government which eventually benefits the end-user customers in Bhutan, electricity pricing in the South Asian region is compared.

Table 4 gives a comparison of the average electricity pricing across South Asian countries and Fig. 5 compares the average electricity price for household customers as of October 2015 [24]. From the comparisons, it is evident that Bhutan has the lowest unit price for household customers among the South Asian countries, while Sri Lanka has the highest unit price with a monthly consumption of 600 kWh. The comparison also indicates that the average unit prices of household customers as well as that for commercial and industrial customers are the lowest in Bhutan. Unfortunately, these lead to bigger challenges for those wishing to venture into non-hydro RES-E in Bhutan. Consequently, designing a renewable pricing policy becomes a bigger challenge.

Pricing mechanism

In the context of the current discussion, the following two objectives among others given in [25] are relevant and important:

Table 4 Average electricity price in South Asian countries in US cents/kWh at unity power factor [24]

Customer category	Class	Electricity use (kWh/month)	Max. demand (kW)	Bangladesh	Bhutan	India (Assam)	Maldives	Nepal	Sri Lanka
Household	Small	30	–	4.82	0.00	5.09	20.47	4.76	2.50
	Medium	90	–	5.42	1.92	6.32	20.47	7.35	6.84
	Large	180	–	6.21	2.70	10.68	21.18	8.16	15.89
	Very Large	600	–	8.24	3.97	10.68	23.93	9.99	27.35
Commercial	Small	1000	–	12.76	5.53	12.15	30.99	9.82	15.52
	Medium	58,000	180	9.97	4.74	12.18	34.05	9.46	17.99
	Large	600,000	1500	9.83	3.62	12.18	34.11	9.46	16.90
Industrial	Small	5000	–	10.07	5.53	8.05	33.49	7.83	8.71
	Medium	65,000	180	9.97	4.63	10.51	34.06	7.39	11.30
	Large	270,000	600	9.84	3.54	11.48	34.10	6.65	10.86
	Very Large	1,050,000	2250	9.83	3.52	11.48	34.11	6.31	10.85

USD conversion rate as of Oct 31, 2015: USD 1.00 = Nu. 65.40

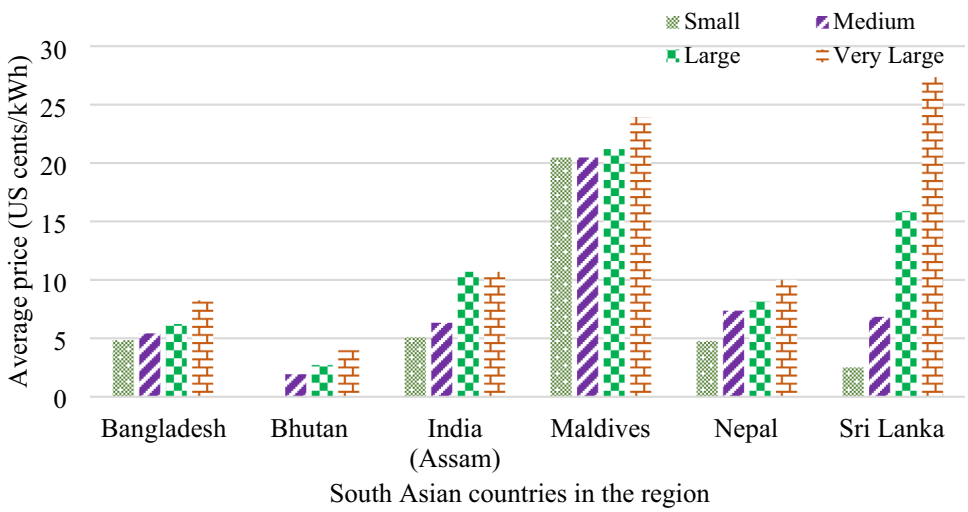

Fig. 5 Comparison of average electricity price for household customers in South Asian countries

(i) to promote a safe and reliable supply of electricity throughout the country (leading to increased energy security), and
(ii) to promote development of renewable energy resources.

It has been established that a well-designed FiT scheme offer multiple benefits to all stakeholders as the tariff can be both cost-effective and cost-efficient. However, in a RE-rich market with subsidised electricity prices, designing an effective FiT scheme will demand careful analysis and planning. Additionally, once these subsidies are withdrawn, private players may see promising prospects while the general population may end up paying an increased tariff. Further, the introduction of a FiT without careful analysis may drive the existing electricity tariff to rise considerably. This may put economic pressure on the general mass, while only a handful of private participants operating as GenCos may benefit financially. Currently, there is a lack of standard for private sectors to participate in RE generation and the rate of subsidy provided by the government makes it difficult for private individuals and business entities to participate in RE business in Bhutan. This also poses one of the biggest challenges in implementing a FiT policy, aggravated by the lack of adequate grid infrastructure to support such schemes. As the overall design of FiT scheme is also influenced by the market design and the availability of resources, the FiT scheme may not allow an effective market integration of RE. FiT in a non-liberalised, monopolised electricity market is not encouraging, perhaps only when there are adequate number of private participations. Further, as recommended by [26], FiT policies must be kept transparent, less complex and consider local conditions such as RES-E potential.

This work proposes FiT scheme taking into consideration the following factors:

(i) Energy is almost entirely hydropower based.
(ii) Subsidy is provided by the government that results in a lower tariff for end-users.
(iii) Lack of private participation and knowledge of the benefits of investing in RES.

Globally, favourable policies such as FiTs, renewable portfolio standards, tenders, and tax incentives have contributed to the growth in RES-E although these were aimed at overcoming initial barrier to the development of RES-E when compared to the costs related to conventional sources of generation [27]. Further, increase in the RES-E penetration could impact electricity prices and consequently, the revenue opportunities for RES-E plants. It will be a challenge to maintain rapid RES-E supply growth against decreasing costs and technical and market operation challenges associated with high penetration levels of RES-E [27]. In the case of Bhutan, where such initiatives are yet to take place, modifications in the FiTs will have to be made to address the required needs of the investors and the government in future.

The levelised cost of energy (LCOE), which serves as a cost indicator for various RE technologies has an influence on the design of pricing strategies for RES-E. LCOE will continue to decrease for solar PV and wind power, while for hydropower, it will increase, primarily due to inflation and labour cost [28–30]. Therefore, it is more viable to opt for non-hydro RES-E, especially solar PV.

In terms of evolution in the incentive schemes, [31] gives a historical perspective of the introduction of the Grid Feed-in Law in 1990 in Germany, which was replaced by the Renewable Energy Sources Act (EEG 2000) based FiT scheme in 2000. They further give the underlying reasons for moving from fixed FiT scheme to auctions since 2016, although exceptions have been made for smaller-sized installations of less than 750 kW where these installations continue to receive FiTs. In Germany, solar PV investors between 300 to 750 kW are provided with the following two options [32]:

(i) Tender scheme for utility scale PV without self-consumption, and
(ii) FiT, halved compared to smaller systems, allowing self-consumption is allowed.

For the existing market in Bhutan, subsidy provided by the government is based on 'blocks' of consumers. Currently, there are no grid regulations and no incentives for private participants. Therefore, to determine FiT for effective implementation, the following components of the FiT pricing as per the traditional definition of FiT will need to be considered:

(i) Generation tariff – where the generator is paid for every kWh of electricity generated.
(ii) Export tariff – where the generator is paid for every kWh injected into the grid.
(iii) Rate of own usage – rate at which deficit energy is bought from the grid.

The existing pricing modality in Bhutan is shown in Fig. 6. Customers pay subsidised electricity tariff E_T and the rate at which power is exported to the third country PE_E is based on the power purchase agreement (PPA) signed with the third country. In absence of fossil-fuelled energy sources in the country, and the existence of a well-established energy sector with hydropower as the primary source, support for other forms of RE is not well pronounced. Further, as per the energy policy, there is a cap of 25 MW of total generation

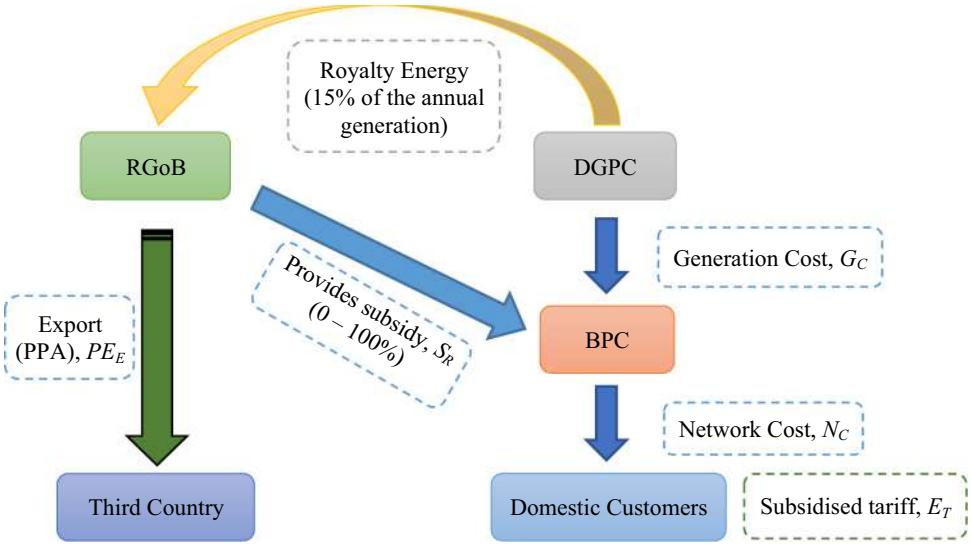

Fig. 6 Existing pricing mechanism

from non-hydro RES-E by 2025. Therefore, based on the prioritised non-hydro RES-E in [8], a suitable FiT scheme needs to be designed for solar power and wind power.

While designing the scheme, it must be noted that the non-hydro RES-E investors do not suffer any losses. FiT is based on several economic and cost aspects, including LCOE for various RE technologies. The LCOE of residential PV systems in 2019 was between 0.063 USD/kWh and 0.265 USD/kWh [33]. India and China had the lowest country/market average LCOE for commercial PV up to 500 kW. Further, for onshore wind, the global weighted-average LCOE in 2019 was 0.053 USD/kWh. The most competitive weighted average LCOE below 0.050 USD/kWh was observed in India and China and the LCOE is expected to further reduce [33].

While information on LCOE for different RE technologies in Bhutan would be ideal for this study, reliable information and data is not available. Therefore, data from India, 0.063 USD/kWh is used instead, owing to the proximity, and having a similar market scenario. The average residential load is assumed to be 5 kW.

To assess LCOE since it has an influence on the pricing strategy, LCOE in select countries have been reviewed. Table 5 shows the LCOE for residential solar PV and onshore wind power in various countries. Further, the lifetime of solar PV is between 20 and 35 years [33]. Therefore, it is safe to assume the project lifetime n of solar PV to be 25 years in the current work. For wind power plants, [34] has concluded that the useful life of wind power plant has changed over time and today it stands at an average of 30 years.

An investor or a homeowner will only opt for non-hydro RES-E if it offers an undue advantage over that from the grid. If TC_{RES-E} is the total cost in its lifetime n with electricity from non-hydro RES-E and TC_{grid} is the total earnings in its lifetime n with energy into the grid, the following preliminary condition for an investor to invest in RES-E must be satisfied:

$$TC_{\text{RES - E}} < \text{TC}_{\text{grid}} \tag{2}$$

The total costs $TC_{\text{RES - E}}$ and TC_{grid} are given by,

$$TC_{\text{RES - E}} = nE_g\text{LCOE} \tag{3}$$

$$TC_{\text{grid}} = nmE_iE_T(1+r)^{n-1} \tag{4}$$

where E_g is the total energy generation in n number of years and m is the number of months in a year, E_i is the kWh injected into the grid, and E_T is the retail LV tariff with an annual increase r at 1.8% per year as indicated in Fig. 4. The simplest forms of determining the total costs are considered in Eq. (3) and it does not account for taxes, discount rates and other associated costs pertaining to Bhutan.

Results

Considering the current market scenario, it is proposed that the FiT is pegged with the block-wise subsidy to enable each category of customer to make net savings for injecting equivalent kWh into the grid. FiT is computed based on the maximum

Table 5 LCOE (USD/kWh) for residential solar PV & onshore wind power in various countries in 2019 [33]

RES-E		India	Japan	China	USA	Germany
Wind	USD/ kWh	0.049	0.113	0.047	0.046	0.068
PV		0.063	0.163	0.067	0.171	0.138

subsidy $S_{R\_\max}$ and electricity tariff E_T for each category of LV customer. As a sample, FiT for LV Block-I (others) FiT_{LVB1_o} is fixed as given below:

$$FiT_{LVB1\_o} = S_{R\_\max} - E_{T\_LVB1\_0} \quad (5)$$

$FiT_{LVB1\_o} = 5.81 - 1.28 = 4.53$ Nu./kWh $= 0.0606$ USD/kWh, and LCOE is 0.063 USD/kWh. The proposed FiTs with net savings that each category of customer/investor can make, considering a plant life of 25 years with 1.8% annual increase in the retail tariff have been computed and shown in Table 6.

The preliminary condition for an investor to opt for non-hydro RES-E based on Eq. (2) is shown in Fig. 7.

The following conclusions can be drawn from Table 6 and Fig. 7:

(i) The proposed FiT will not be effective for LV customers in rural, highland areas, Block I (others) and Block II (all) as they receive subsidies of 0.0777, 0.0777, 0.0606 and 0.0418 USD/kWh respectively.

(ii) Only LV Block III and LV Bulk customers with net injection of 500 and 1000 kWh per month respectively will be able to make savings if they opt for RES-E (solar PV). The proposed FiTs are 0.0290 and 0.0223 USD/kWh respectively, when export tariff component is pegged with the subsidy.

(iii) To encourage maximum number of participants in the RE market, a generation tariff pegged with the lowest tariff (0.0171 USD/kWh) can also be provided in addition to the export tariff. This will result in a higher net savings for all categories of LV customers, including rural and highlanders.

Further, FiTs for different countries in the region and other areas where it has gained significant success are shown in Table 7 for the purpose of drawing comparison with the proposed FiT.

For the purpose of drawing comparison between the proposed FiT and the FiTs given in Table 7, the lowest values of FiTs in these respective countries are considered. The comparative analysis is drawn and shown in Fig. 8. From the comparative analysis, it can be concluded that the proposed FiT in Bhutan remains the lowest for all categories of customers, as it is pegged with the rate of subsidy provided by the government. This will not be encouraging for the private investors who wish to participate in FiT scheme in Bhutan, and therefore, a more rigorous scheme will have to be instituted to encourage private investors.

To encourage private participants to invest in non-hydro RES-E in a country with high ratio of RE (hydropower) and to achieve reasonable return on investment, the following recommendations are made:

Table 6 Comparison of costs and the proposed FiT

Category of Customer	kWh injected into grid/ month, E_i	Retail electricity tariff, E_T	Proposed FiT (USD/kWh)	Total earnings from grid, TC_{grid} (USD)	Total cost for RES-E, TC_{RES-E} (USD)	Net savings (USD/kWh)
LV Block I (Rural)	100	0.0000	0.0777	0	1890	−1890
LV Block I (Highlanders)	200	0.0000	0.0777	0	3780	−3780
LV Block I (Others)	100	0.0171	0.0606	788	1890	−1102
LV Block II (All)	500	0.0358	0.0418	8247	9450	−1203
LV Block III* (All)	1000	0.0487	0.0290	22,401	18,900	3501
LV Bulk*	5000	0.0553	0.0223	127,390	94,500	32,890

*The upper limits have been suitably assumed for the purpose of the study

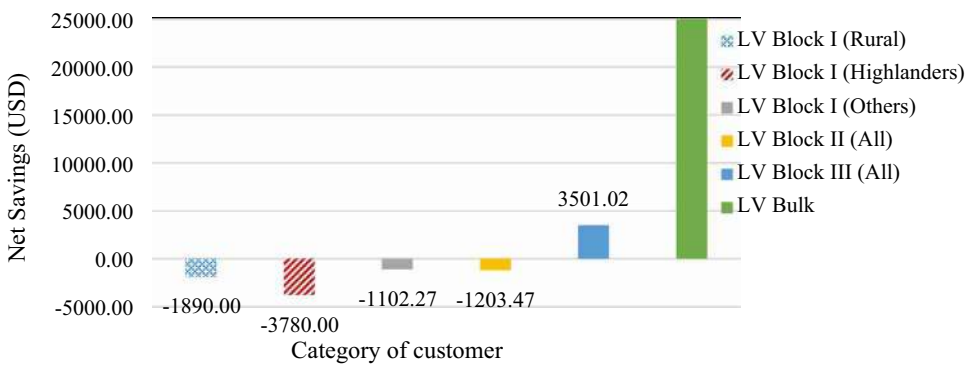

Fig. 7 Condition for investors to opt for RES-E

Table 7 FiTs (USD/kWh) in select countries for solar PV

India[a]	Japan[b]	China[c]	USA[d]	Germany[e]
~0.0405/kWh (1 – 5 MW)	~0.19/kWh (< 10 kW)	~0.0757 (region I)	~0.1450 (30–500 kW)	~0.1220 (0–10 kW)
	~0.12/kWh (10–50 kW) ~0.11/kWh (50 to 250 kW) Tender > 250 kW	~0.0908 (region II) ~0.1059 (region III)	~0.1300 (> 500 kW–3 MW) ~0.1350 (> 3 MW)	~0.1187 (10–40 kW) ~0.1061 (40–100 kW)

[a]Based on [35] since it is the closest Indian state to Bhutan. Although competitive bidding is largely followed, the proposed FiT for 1 MW to 5 MW solar PV in 2021 was 3 Rs./kWh (0.0405 USD/kWh)[35]

[b]Provisional solar PV FiTs for the fiscal year April 2020–March 2021 in Japan based on the Ministry of Economy, Trade and Industry (METI) [36]

[c]FiT is based on large PV projects in three different regions in China [37]

[d]Fit for Los Angeles Department of Water & Power [38]

[e]FiT in Germany [39]

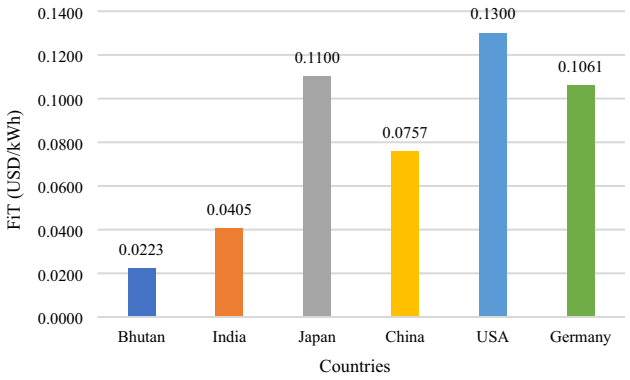

Fig. 8 Proposed FiT and FiTs in countries where it has been successfully implemented

(i) For a system with block rate tariff, FiTs can be fixed based on the 'blocks' of kWh injected into the grid.
(ii) Export tariff component of FiT can be pegged with the block rate tariff. LV customers will continue to draw benefits for their investment in non-hydro RES-E. Any sale of electricity after *n* years can be considered as 'profit.'
(iii) The generation tariff (FiT) can be pegged to the lowest subsidy rate. However, for the government to make marginal profit, the FiT remains lower or equal to the power export tariff (PE_E) based on the power purchase agreement, which may also include framework for future bilateral cooperation in the field of energy between two nations.
(iv) In place of 'generation tariff,' a tax credit can also be provided. As the percentage of non-hydro RES-E installation is going to be minimal due to the 25 MW cap on the installation of RES-E, this will not have any major financial constraints on the government. This strategy will encourage a greater number of participants.

The above analysis pertains to a rooftop solar PV, however, LCOE is technology-based and to make the proposal generic, pricing modality is proposed as shown in Table 8 for both wind and solar PV for a period of 25 years.

It must be noted that the retail tariff as well as the power export tariff keeps varying based on the market scenario and PPA, respectively. These variations must be taken into consideration while designing FiT so that the government nor the investor incurs loss. Although many RE-matured countries like United Kingdom and Germany are moving towards tendering scheme, for Bhutan, where there is lack of i) deregulated market ii) RE pricing modality, and iii) private participants, the pricing modality can be initiated with FiT scheme as proposed. With experience and increase in the number of participants, the following alternatives as shown in Table 9 can be proposed in place of FiT.

Table 8 Proposal for FiT scheme

Option	FiT	Benefit to the investor/generator	Benefit to the government
A	Generation tariff+Export tariff	Yes	Yes
B	Export tariff	Yes, but only to higher category of customers	Yes, more than Option A

Table 9 Alternatives to FiT scheme

1. Net-metering	There is no time-bound obligation or project time-period
	Additional design complications, such as those related to block rate tariff, project cost, LCOE will be minimised
	Allows investors to sell or use the units generated at any time without a specific contract
2. Auction	As the bid is evaluated by the government, it offers flexibility to make appropriate decisions
	Creates a competitive electricity market

Limitations and future work

The proposed schemes are based on a simplified method where assumptions are made on the LCOE of the two variable renewable energy (VRE) sources due to lack of data specific to Bhutan. Recommendations made in this paper would serve as a guideline for decision making, planning, and instituting a more robust system to introduce RE policy for non-hydro RES-E. As it would be a challenge to introduce an RE policy in Bhutan primarily due to the source of electricity being hydropower and generous subsidies provided by the government, it would necessitate the cooperation of all players: MoEA, BEA and DHI (BPC & DGPC) to work on a suitable RE policy. One of the immediate research works would be to determine LCOE for various RE technologies in Bhutan, in particular wind power and solar PV. Thereafter, we draw comparisons on different RE policies suitable for Bhutan's unique energy market on the basis of LCOE and subsidies provided by the government.

Conclusion

In a market with high share of RE, promotion and investment in additional RES-E is seen as a challenge. With the increase in the share of RE installations globally, several countries have started moving away from the traditional FiT scheme into tendering and other revised schemes. In the case of Bhutan, it is a challenge to promote and invest in non-hydro RES-E since the electricity tariff is the lowest in the South Asian region. However, apart from the financial aspects, there is a need to consider energy security and related challenges, such as dependency on a single source of energy in the country. Therefore, as Bhutan gradually begins diversifying its energy resources, suitable RE policy will need to be instituted.

Two RE technologies, solar power and wind power are considered in this paper. FiT for solar power has been computed and proposed for different blocks of customers. The analysis indicates that LV Block I customers would not benefit from the FiT scheme as they receive subsidies ranging from 0.0418 to 0.0777 USD/kWh/month. Only two categories of customers, LV Block III and LV Bulk, are able to make savings if they opt for the FiT scheme of 0.0290 and 0.0223 USD/kWh respectively. Further, two favourable alternatives, (i) net-metering and (ii) auction have been proposed. However, these recommendations are subject to change based on the market scenario and the government policies. A more robust RE policy will need to be instituted to benefit all players.

Data availability All data generated or analysed during this study are included in this published article.

Declarations

Conflict of interest The author has no conflict of interest to declare.

References

1. Ministry of Economic Affairs, Royal Government of Bhutan. Sustainable Hydropower Development Policy 2021. https://www.moea.gov.bt/wp-content/uploads/2017/07/Sustainable-Hydropower-Development-Policy-2021.pdf (2021).
2. Druk Green Power Corporation Ltd. Annual Report 2019.pdf. https://www.drukgreen.bt/wp-content/uploads/2020/09/CAD_Publication_AnnualReport19_2019.pdf (2019).
3. Gross National Happiness Commission, Royal Government of Bhutan. Tenth Five Year Plan 2: Programme Profile 2008–2013 (2009).
4. Royal Bhutanese Embassy, New Delhi. Bhutan-India Hydropower Relations. https://www.mfa.gov.bt/rbedelhi/?page_id=28.
5. IRENA. Renewables Readiness Assessment: Kingdom of Bhutan. 52 https://www.irena.org/-/media/Files/IRENA/Agency/Publication/2019/Dec/IRENA_RRA_Bhutan_2019.pdf (2019).
6. Couture, T.D., Cory, K., Kreycik, C., Williams, E.: Policymaker's Guide to Feed-in Tariff Policy Design. (2010) https://www.osti.gov/biblio/984987 doi: https://doi.org/10.2172/984987

7. Couture, T., Gagnon, Y.: An analysis of feed-in tariff remuneration models: implications for renewable energy investment. Energy Policy **38**, 955–965 (2010). https://doi.org/10.1016/j.enpol.2009.10.047
8. Department of Renewable Energy, Ministry of Economic Affairs. Alternative Renewable Energy Policy—2013. https://www.moea.gov.bt/wp-content/uploads/2017/07/Final-Alternative-RE-Policy-April-2013.pdf (2013).
9. Royal Government of Bhutan. Economic Development Policy 2016. https://www.moea.gov.bt/wp-content/uploads/2017/07/Economic-Development-Policy-2016.pdf (2016).
10. National Statistics Bureau, Royal Government of Bhutan. Statistical Year Book of Bhutan 2021. (2021).
11. Lhaden, Y.: Hydropower besides, Bhutan looks at renewable energy. Kuensel (2020).
12. REN21. Renewables 2020 Global Status Report. (Paris: REN21 Secretariat, 2020).
13. Ndiritu, S.W., Engola, M.K.: The effectiveness of feed-in-tariff policy in promoting power generation from renewable energy in Kenya. Renewable Energy **161**, 593–605 (2020). https://doi.org/10.1016/j.renene.2020.07.082
14. Chua, S.C., Oh, T.H., Goh, W.W.: Feed-in tariff outlook in Malaysia. Renew. Sustain. Energy Rev. **15**, 705–712 (2011). https://doi.org/10.1016/j.rser.2010.09.009
15. Wang, K.M., Cheng, Y.J.: The evolution of feed-in tariff policy in Taiwan. Energ. Strat. Rev. **1**, 130–133 (2012). https://doi.org/10.1016/j.esr.2012.05.002
16. REN21. Asia and the Pacific Renewable Energy Status Report. (Paris: REN21 Secretariat, 2019).
17. IRENA, IEA & REN21. Renewable Energy Policies in a Time of Transition. (2018).
18. ADB. Promoting Clean Energy Development in Bhutan. 17 https://www.adb.org/projects/documents/promoting-clean-energy-development-bhutan-tar (2014).
19. Yangka, D., Rauland, V., Newman, P.: Carbon neutral policy in action: the case of Bhutan. Climate Policy **19**, 672–687 (2019). https://doi.org/10.1080/14693062.2018.1551187
20. BEA, Royal Government of Bhutan. Approved Tariff | Bhutan Electricity Authority. http://bea.gov.bt/approved-tariff/.
21. BPC. Bhutan Power Corporation Limited. https://www.bpc.bt/electricity-tariff/.
22. Bhutan Electricity Authority. Tariff Determination Regulation 2016. (2016).
23. Bhutan Electricity Authority. Electricity Tariff in Bhutan. (2017).
24. Siyambalapitiya, T. Tariff Appraisal Study: Balancing Sustainability and Efficiency with Inclusive. Access. https://doi.org/10.22617/WPS179075-2 (2018).
25. Electricity Act of Bhutan 2001. (2001).
26. Klein, A. et al. Evaluation of Different Feed-In Tariff Design Options: Best Practice Paper for the International Feed-In Cooperation. https://cleanenergysolutions.org/es/resources/evaluation-different-feed-tariff-design-options-best-practice-paper-international-feed (2008).
27. Miller, M. et al. RES-E-NEXT: Next Generation of RES-E Policy Instruments. https://www.osti.gov/biblio/1260509-res-next-next-generation-res-policy-instruments (2013). doi: https://doi.org/10.2172/1260509
28. Yao, Y., Xu, J.-H., Sun, D.-Q.: Untangling global levelised cost of electricity based on multi-factor learning curve for renewable energy: wind, solar, geothermal, hydropower and bioenergy. J. Clean. Prod. **285**, 124827 (2021). https://doi.org/10.1016/j.jclepro.2020.124827
29. Ram, M., et al.: A comparative analysis of electricity generation costs from renewable, fossil fuel and nuclear sources in G20 countries for the period 2015–2030. J. Clean. Prod. **199**, 687–704 (2018). https://doi.org/10.1016/j.jclepro.2018.07.159
30. Jung, T., Kim, D., Moon, J., Lim, S.: A scenario analysis of solar photovoltaic grid parity in the Maldives: the Case of Malahini Resort. Sustainability **10**, 4045 (2018). https://doi.org/10.3390/su10114045
31. Leiren, M.D., Reimer, I.: Historical institutionalist perspective on the shift from feed-in tariffs towards auctioning in German renewable energy policy. Energy Res. Soc. Sci. **43**, 33–40 (2018). https://doi.org/10.1016/j.erss.2018.05.022
32. Germany's Renewable Energy Act 2021: how to implement the fine policy detail of emissions reduction targets. *Energy Post* https://energypost.eu/germanys-renewable-energy-act-2021-how-to-implement-the-fine-policy-detail-of-emissions-reduction-targets/ (2021).
33. IRENA. *Renewable Power Generation Costs in 2019*. https://www.irena.org/publications/2020/Jun/Renewable-Power-Costs-in-2019 (2020).
34. Wiser, R.H., Bolinger, M.: Benchmarking Anticipated Wind Project Lifetimes: Results from a Survey of U.S. Wind Industry Professionals. Lawrence Berkeley National Laboratory (2019).
35. Discussion Paper with Notice. West Bengal Electricity Regulatory Commission https://wberc.gov.in/sites/default/files/Discussion%20Paper%20with%20Notice.pdf (2021).
36. Japan sets solar PV feed-in tariffs for the 2020–2021 year. https://www.enerdata.net/publications/daily-energy-news/japan-sets-solar-pv-feed-tariffs-2020-2021-year.html (2020).
37. Dong, C., Zhou, R., Li, J.: Rushing for subsidies: the impact of feed-in tariffs on solar photovoltaic capacity development in China. Appl. Energy **281**, 116007 (2021). https://doi.org/10.1016/j.apenergy.2020.116007
38. Feed-in Tariff (FiT) Program. https://www.ladwp.com/ladwp/faces/ladwp/commercial/c-gogreen/c-gg-commsolarprograms/c-gg-csp-fit?_afrLoop=229395052857132&_afrWindowMode=0&_afrWindowId=null#%40%3F_afrWindowId%3Dnull%26_afrLoop%3D229395052857132%26_afrWindowMode%3D0%26_adf.ctrl-state%3D1ccjrf1ijd_42.
39. Winter, S., Schlesewsky, L.: The German feed-in tariff revisited: an empirical investigation on its distributional effects. Energy Policy **132**, 344–356 (2019). https://doi.org/10.1016/j.enpol.2019.05.043

International Journal of Energy and Environmental Engineering (2023) 14:949–960
https://doi.org/10.1007/s40095-023-00558-0

ORIGINAL RESEARCH

Performance evaluation of monocrystalline and polycrystalline-based solar cell

Mithun Ray[1] · Md. Firoz Kabir[1] · Md. Raihan[1] · A. B. M. Noushad Bhuiyan[1,2] · Tawhida Akand[1,2] · Nur Mohammad[2]

Received: 8 October 2022 / Accepted: 14 January 2023 / Published online: 24 January 2023

Abstract

This paper exhibits the performance of crystalline-based solar cells (polycrystalline and monocrystalline) as well as the comparative analysis of these solar cells following various types of orientation in the solar plant. Since the global energy demand is increasing rapidly, different sorts of renewable energy have been used in the last decades to meet this massive demand all over the world. From recent studies, solar has been considered the most promising among these renewable sources. To analyze the performance, the geographical site (Savar, Dhaka) was selected which has a latitude of 23.8538° and a longitude of 90.2534°. In this study, the most effective polycrystalline and monocrystalline solar cell has been founded which is 440 and 370 wp, respectively. Regarding this, a grid-connected PV system (12.3 Kwp) has been simulated which showed the performance ratio of the monocrystalline cell was 83.55%, which was better than the polycrystalline-based solar cell which was 79.6%. In terms of different kinds of orientations, monocrystalline at dual-axis tracking planes showed the highest value of energy injection to the grid was 25.8 MWh/year, while the least value has been founded in the fixed orientation plane which was 20.6 MWh/year. In this perspective, polycrystalline showed 23.9 and 19.5 MWh/year for dual-axis tracking and fixed orientation planes, respectively. Monocrystalline showed more energy injected into the grid compared to polycrystalline technologies for every orientation in the plant as well as the highest value of performance ratio.

Keywords Grid-connected · Solar radiation · PVSYST · Orientation · E_Array · E_Grid

Abbreviations

Poly	Polycrystalline
Mono	Monocrystalline
PV	Photovoltaic
STC	Standard test condition
G_{STC}	Total solar radiation under STC (KW/m^2)
G_{opt}	Total in-plane solar insolation (KWh/m^2)
E_{AC}	AC energy output (KWh)
E_{daily}	Total daily total AC energy output (KWh)
Y_f	Final yield (KWh/KWp)
Y_{rf}	Reference yield (KWh/KWp)
PR	Performance ratio
E_Grid	Energy injected into grid
E_Array	Effective energy at the output of the array
T_Amb	Ambient average temperature °C

✉ A. B. M. Noushad Bhuiyan
noushad.cuet@gmail.com

Mithun Ray
mithunray.eee@gmail.com

Md. Firoz Kabir
firozkabir354@gmail.com

Md. Raihan
mdrahid484@gmail.com

Tawhida Akand
tawhidacuet@gmail.com

Nur Mohammad
nur.mohammad@cuet.ac.bd

[1] Department of Electrical and Electronic Engineering, City University, Dhaka, Bangladesh

[2] Department of Electrical and Electronic Engineering, Chittagong University of Engineering & Technology(CUET), Chittagong, Bangladesh

Introduction

We have come to know the worth of renewable energy to accomplish our assertion of daily life. Solar energy is the most promising among all renewable energy. To mitigate our pollution from fossil fuels while generating energy, solar energy will be able to play a vital role to meet our demands for daily life. Solar power can be used to heat water, electrify homes and buildings, and even power cars. It causes no

pollution even at the time of installation. The use of solar energy is swiftly increasing day by day all over the world. Many developing and developed countries [1–3] are working on how to reduce the use of fossil fuel and for reducing environmental pollution through it. Grid-connected solar systems are playing a vital role to improve the whole area of this solar system. Many countries have been working on the grid-connected solar system. In ten years, for developing renewable energy Morocco has implemented a favorable national energy strategy to mitigate greenhouse gas emission and for decreasing the cost of energy service which is produced by fossil fuel, oil and so on. Morocco has an enormous source for renewable energy, including solar energy with 5.5 KWh /m^2/ day; with the sunshine of 3000 h per year [4, 5].

The different types of PV technologies performance strongly depend on the meteorological condition, geographical site, solar radiation, and plane orientation [6, 7]. This system also includes the maximum capacity of solar, ambient temperature, final yield, and system loss.

In Dubai-based 200 Kwp power plant, they found total production of energy 352.6 MWh/year and specific production of energy was 1757 KWh/KWp/year. The annual performance ratio of the system was found as 81.67% [8]. Between monocrystalline and polycrystalline solar cell, there is an established statement that the efficiency and the performance rate of monocrystalline were better than the polycrystalline [9]. At 1000 w/m^2 solar radiation [9], the efficiency of monocrystalline and polycrystalline was 15.27 and 13.53%, respectively. In Germany, they arranged 1000 rooftop photovoltaic system to analyze the performance of the solar cell. Using the annual in-plane irradiation, the annual performance ratio was ascertained in the range 47.5–81% (mean 66.5%) [10]. In Ref. [11], a higher monthly total average final yield than polycrystalline modules. In paper [12], a remarkable annual performance ratio of the solar module has been found that is about 74% including capacity factor 9.27% and system efficiency 8.3% with the application of PVSYST software. Saeed Edalati and Mehran Ameri [13] composed two types of PV modules with almost similar characteristics. This investigation concludes with PR ratio of 82.92% including the final yield 5.38 KWh/KWp day. For the grid-connected PV system, in the park of Island, they found that the park can supply 229MWh in 2007, the annual pair 67.37% as well [14]. For a summer region, the PR ratio always decrease for the dust accumulation which lies between − 0.04% to − 0.13% for positive ambient temperature [15]. In 2005, Italian management grant to produce electricity by PV plants [16]. In India, the demonstration for PV system was organized in 2008 and the analyzation was about 3 MWp plant to generate electrical energy [17, 18]. The economic liability in KUET, Khulna, Bangladesh, they found traditional electricity and CO_2 emission rate also saved [19, 20].

Because of energy shortage in Bangladesh, for meeting citizens demand as a renewable energy, solar energy should be used [21]. Recent study shows that almost 55% people in Bangladesh is facing problem with electricity production [22, 23]. Furthermore, among them 30% of people [24] are those who are in below poverty line. The unsatisfactory factor of receiving energy is raising around 10% yearly in the citizens of Bangladesh [25, 26]. Since, the electricity production is not enough [27, 28] comparatively to others south Asian countries we have to keep our eyes on this perspective.

In this study, polycrystalline and monocrystalline-based solar cell has been used to show the most effectivity between these cells regarding field orientation. According to affordability, polycrystalline is promising over monocrystalline or other cells due to its manufacturing procedure [3, 26]. According to recent researches, monocrystalline has been chosen for its significant efficiency [29, 30] so we can compare with a convenient way and the availability of crystalline-based solar cell are higher as well which is more than 85% [31] over others cell.

The objectives of this paper are to figure out the most efficient crystalline-based solar cell regarding effective energy, energy injected into the grid in terms of different orientations. In the previous studies, these types of orientations have not been considered for obtaining simulated values.

Description of solar PV power plant

Geographical site

The selected site for the PV plant at Savar, which is situated in Dhaka, Bangladesh. The latitude and longitude of that place are 23.8538° and 90.2534° and, respectively. This place was selected to analyze due to its enough potential to set a PV plant.

For the orientation of solar modules, azimuth is -5° concerning its tilt angle. The reason for choosing this azimuth angle showed by Fig. 1.

The global horizontal irradiation and total diffuse irradiation all year round is given in Fig. 2.

PV installation for the plant

For the installation of the plant two types of solar panels are selected. One is monocrystalline and the other is a polycrystalline solar panel. It includes a 12 KW AC inverter to generate and reserve. For the monocrystalline panel, the plant includes a 370wp modules, the total module numbers are 34

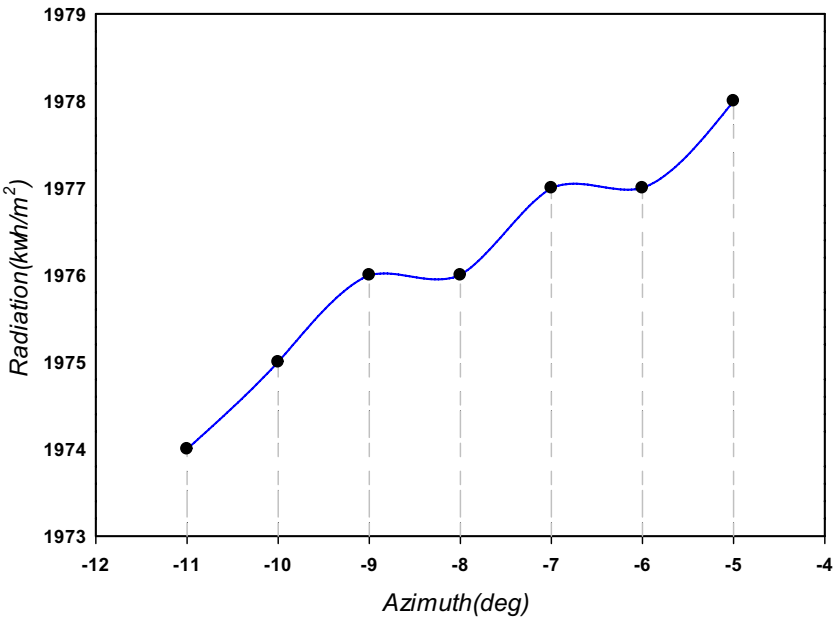

Fig. 1 Solar radiation according to azimuth angle for the tilt angle 23° to capture maximum radiation

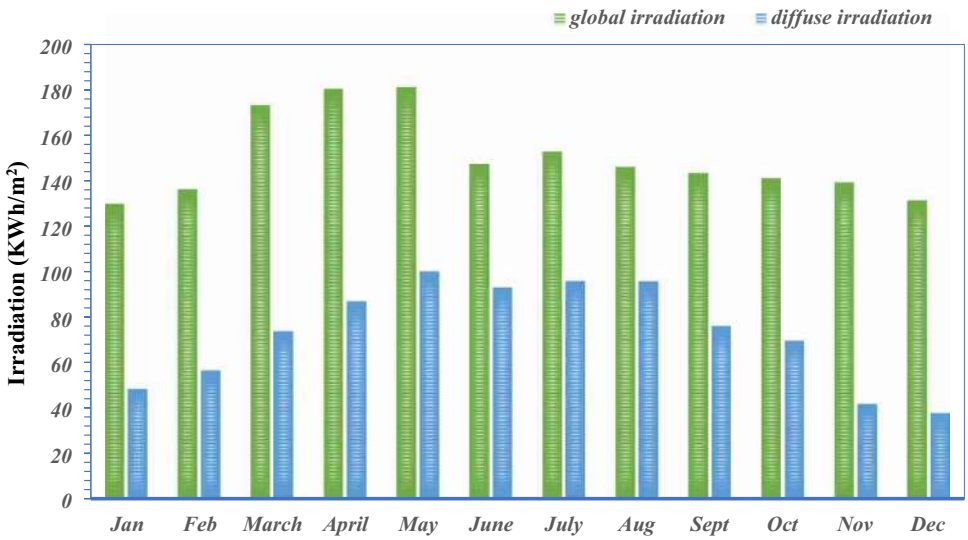

Fig. 2 Horizontal global irradiation (KWh/m^2) and horizontal diffuse irradiation (KWh/m^2) for every month

Table 1 Characteristics of various types of solar modules

Trademark	GENERIC		SOLARWORLD	
Solar panel	Monocrystalline	Polycrystalline	Monocrystalline	Polycrystalline
Optimum operating voltage (V_{mp})	34.10 V	17.10 V	30.9 V	31.4 V
Optimum operating current (I_{mp})	10.86 A	3.5 A	8.32 A	8.15A
Open circuit voltage (V_{oc})	41.30 V	21.80 V	38 V	37.8 V
Short circuit current (I_{sc})	11.37 A	3.8 A	8.88 A	8.66A
Module efficiency (%)	19.84	10.79	15.2	15.2
Length (mm)	1776	1109	1675	1675
Width (mm)	1052	502	1001	1001
Weight (kg)	20	7.20	21.2	21.2

which are connected with series, and two parallel strings are added to those modules.

On the contrary, for polycrystalline 60wp module is formed which includes a total of 204 modules in series with 6 parallel strings.

The characteristics of these modules and the properties which are investigated in Ref. [5] are showed in Table 1.

Methodology

The required system of solar system was calculated according to the grid-connected solar plant. This plant illustrates the performance ratio and total E_Grid of the plant all over the year. To get the simulation report and the accuracy analysis PVSYST is used. The geographical location of the site that found in the Meteonorm 7.2 database.

To meet the validity of PV plants different sort of parameters for instance-final yield, reference yield, performance ratio, and daily and monthly energy generation that is related to system loss of the PV plants. The rest of the parameters that were related to the required PV plant appreciation were

- Horizontal global irradiation.
- Horizontal diffuse irradiation.
- Ambient temperature.
- Effective energy at the output of the array.
- Energy injected into the grid.
- Energy output for the system.

These parameters were considered for every solar panel according to the whole month of the year.

- Energy output for the system

Let, the total daily energy generated E_{daily} and monthly energy generated E_{monthly} by the PV system [12, 13] are given as follows:

$$E_{(\text{daily})} = \sum_{d=1}^{24} E_{(\text{hourly})} \tag{1}$$

$$E_{(\text{monthly})} = \sum_{d=1}^{n} E_{(\text{daily})} \tag{2}$$

where $E_{(daily)}$, $E_{(hourly)}$, and $E_{(monthly)}$ are the daily AC energy output, hourly AC energy output, monthly AC energy output, respectively, and n is the number of days in a month.

- Final yield

This final yield [16] is defined as the total AC energy generated by the PV system for day, month, and year which is divided by the rated output:

$$Y_{(f,\text{daily})} = \frac{E_{\text{AC}}}{P_{(\text{photovoltaic,rated})}} \tag{3}$$

$$Y_{(f,\text{monthly})} = \sum_{d=1}^{n} E_{(\text{AC,daily})} Y_{(f,\text{daily})} \tag{4}$$

- Reference yield:

Reference yield (Y_{rf}) presents the ratio of total insolation which is divided by the array reference irradiance:

$$Y_{\text{rf}} = \frac{G_{\text{total in plane solar insolation}}}{G_{\text{stc}}} \tag{5}$$

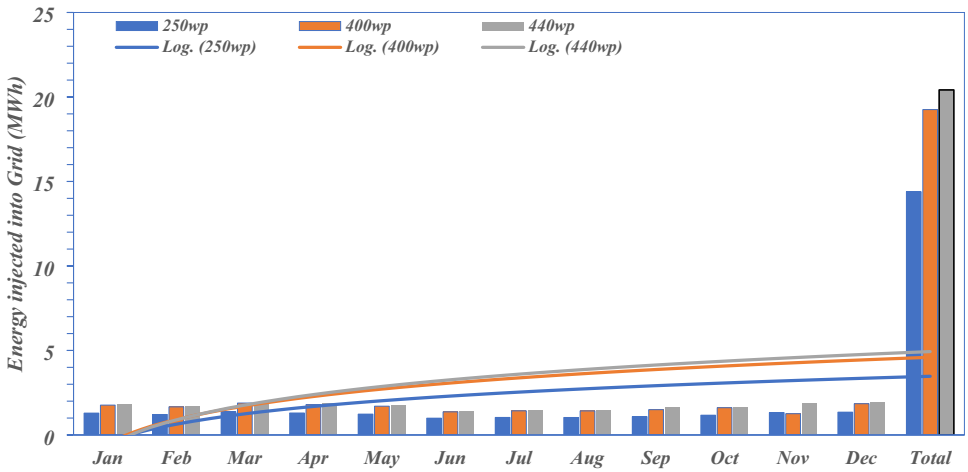

Fig. 3 Analogy of three bifacial (250, 400 and 440 wp) monocrystalline-based solar modules

where G_{opt} is total in-plane solar insolation and G_{stc} (1 KWh/$m^{2)}$ is array reference irradiance.

Results and discussions

Between the monocrystalline and polycrystalline solar modules, there have two types of modules, the bifacial type, and the Vmax 1500 V solar module. Figure 3 manifests the E_Grid of the bifacial modules according to the whole month of solar radiation of that particular place.

The energy injected into the grid showed a superior value when the 440wp module has been used which was about 20 MWh/year, which was from bifacial modules. And the minimal value shown for the 250wp module was just about over 14 MWh/year.

Figure 4 shows the E_Grid of five Vmax 1500 V modules for every month of the year. The simulation results of these modules show that the E_Grid value of 300, 340, 370, 400, and 440 are 17.389, 18.461, 20.793, 19.822, and 20.305 MWh, respectively, which shows in Fig. 4. The peak value experienced in 370wp module that belongs to the monocrystalline-based solar cell Fig. 5**.**

The remaining modules are 60, 110, and 190 wp showing 27.972, 25.934, and 12.527 MWh, respectively, per year. The highest value was in the 60wp module that belongs to polycrystalline.

Residual polycrystalline modules (60, 110, 190 wp) E_Grid value for every month of a year illustrates in Fig. 5.

For the orientation of a fixed tilted plane from a monocrystalline module, 370 wp gives the higher value 20.793 MWh which is from V_{max} 1500 V that belongs to a monocrystalline-based solar module, for bifacial module 440 wp gives the superior value 20.318 MWh which is monocrystalline-based cell as well. Between these two modules, 370 wp showed the highest effectivity.

For this reason, the chosen module for the PV power plant was 370wp monocrystalline module. The PR ratio of these modules shows in Fig. 6**.** From this figure we have come to know the performance of the 370wp module is better than the other polycrystalline residual module.

The value of E_Array and E_Grid for the bifacial module, V_{max} 1500 V, and the remaining polycrystalline

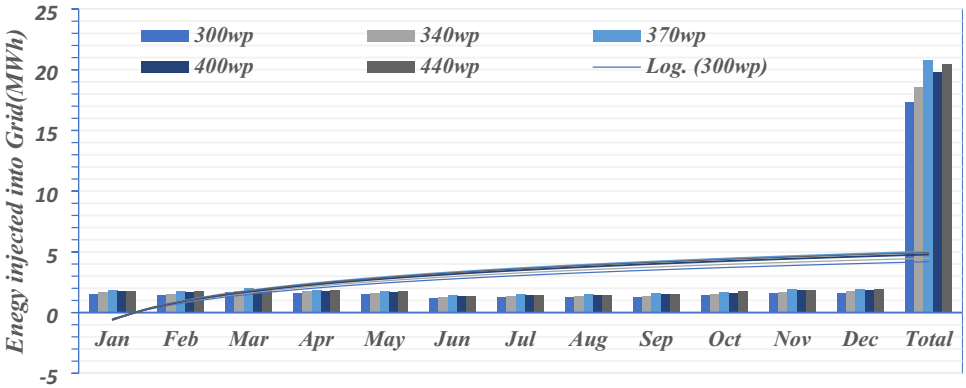

Fig. 4 Analogy of five Vmax 1500 V (300, 340, 370, 400, 440 wp) monocrystalline modules

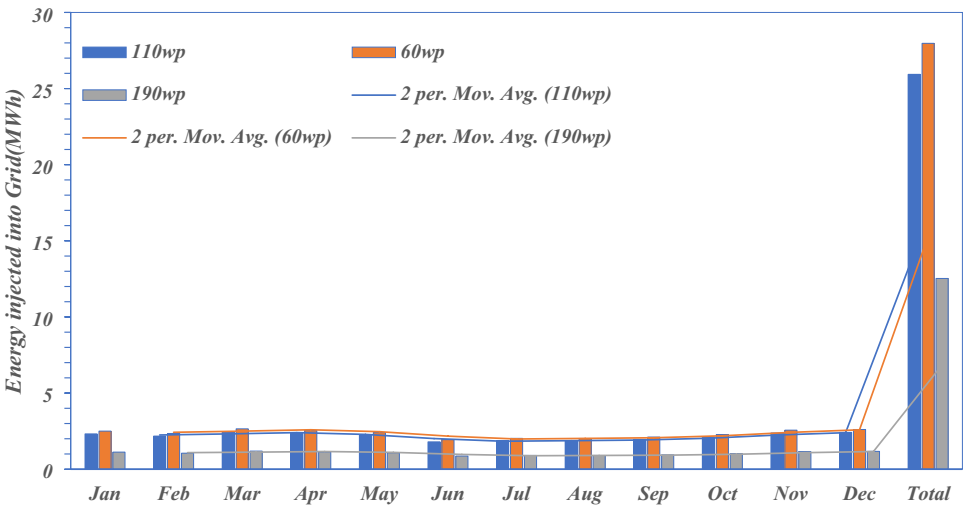

Fig. 5 Analogy of 60wp, 110wp, and 190wp modules

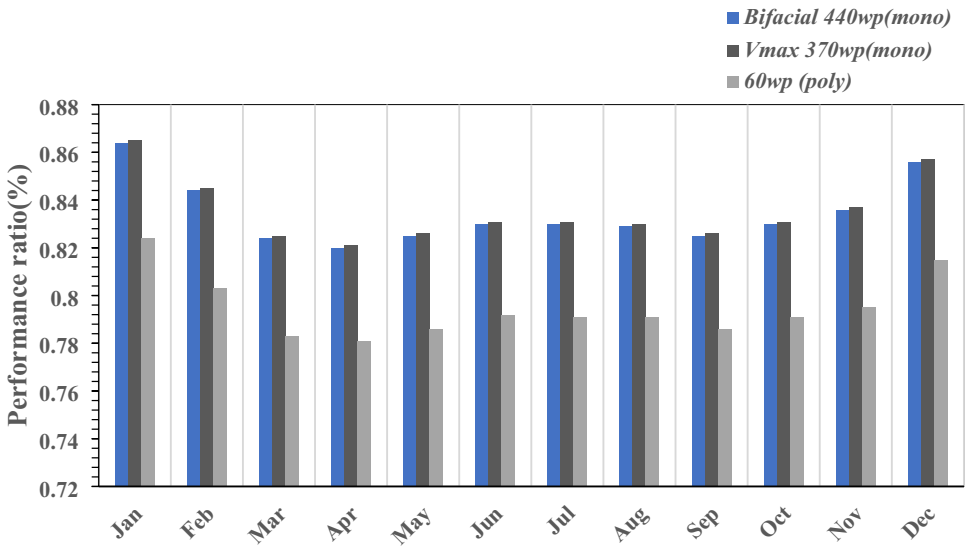

Fig. 6 Yearly PR ratio for fixed tilted plane, analogy of bifacial 440 wp (monocrystalline), V_{max} 1500 V 370 wp (monocrystalline) and 60 wp (polycrystalline) modules

modules demonstrates in Tables 5, 6, and 7 have been put in the appendix part.

For fixed tilted plane, the yearly PR ratio of 370 wp (mono), 440 wp (mono), and 60 wp (poly) are 0.840, 0.838, and 0.790, respectively, from the PR we have also known that the monocrystalline solar module superior to the polycrystalline solar module.

Energy Injected into Grid (MWh) for several orientations:

The simulated value for the fixed orientation plane, single axis tracking plane, and dual-axis tracking plane is portrayed in Table 2. Since the highest value is depicted in 370 wp (monocrystalline), this module has been used to figure out the most effective orientation of solar plants.

From previous simulations, we have come to know about the most effective solar cell to use in a grid-connected system was 370 wp monocrystalline and 60 wp polycrystalline module. Moreover, the simulation showed the most promising orientations were the horizontal N–S axis, two-axis tracking, and fixed tilted plane; these belong to single axis tracking plane, dual-axis tracking plane, and fixed orientation plane, respectively.

For further experiments, those modules which showed the peak value in the projected plant (370 wp monocrystalline, 60 wp polycrystalline) have been selected regarding field orientations of horizontal N–S axis, two-axis tracking planes, and fixed tilted planes.

Figure 7 shows the energy that entering into the grid in terms of different field types according to the mentioned polycrystalline and monocrystalline-based solar cells. Here, the monocrystalline cell experienced the highest level of energy producing capacity at dual-axis tracking planes which was 25.8 MWh/year. On the contrary, the minimum value was 20.6 MWh/year at fixed orientation planes.

Additionally, the polycrystalline cell also witnessed the pick value in dual-axis tracking planes which was 23.9 MWh/year, while the lowest energy providing capacity showed in fixed orientation planes which were only 19.5 MWh/year. Energy injected according to field types illustrated in Fig. 7.

Table 2 E_Grid and E_Array value of for several orientations

Field type	Orientations	E_Grid (MWh)	E_Array (MWh)
Single axis tracking planes	Horizontal N–S axis	25.378	25.948
	Horizontal axis E–W	21.888	22.399
	Vertical axis tracking	24.577	25.135
Dual-axis tracking planes	Tracking two	25.774	26.358
	Tracking two axis, frame N–S	25.227	25.796
	Tracking two axis, frame E–W	26.130	26.720
Fixed orientation planes	Fixed tilted plane	20.793	21.281
	Several orientations	18.041	18.463
	Seasonal tilt adjustment	20.569	21.054

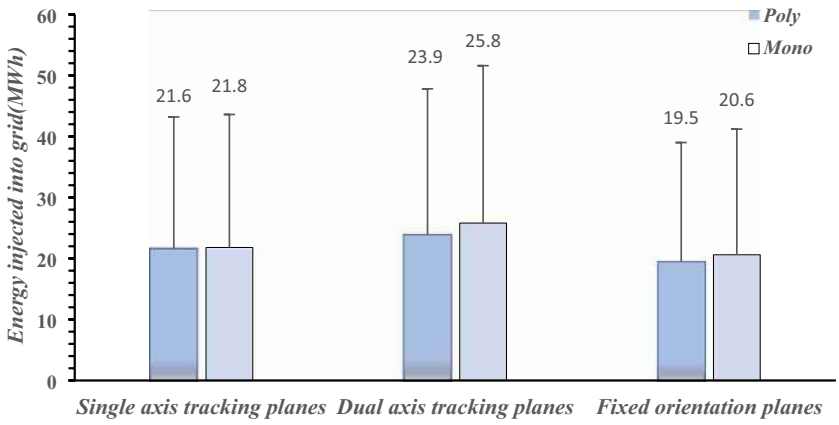

Fig. 7 Illustration of energy injection of poly and monocrystalline solar cell into grid regarding orientation types of field

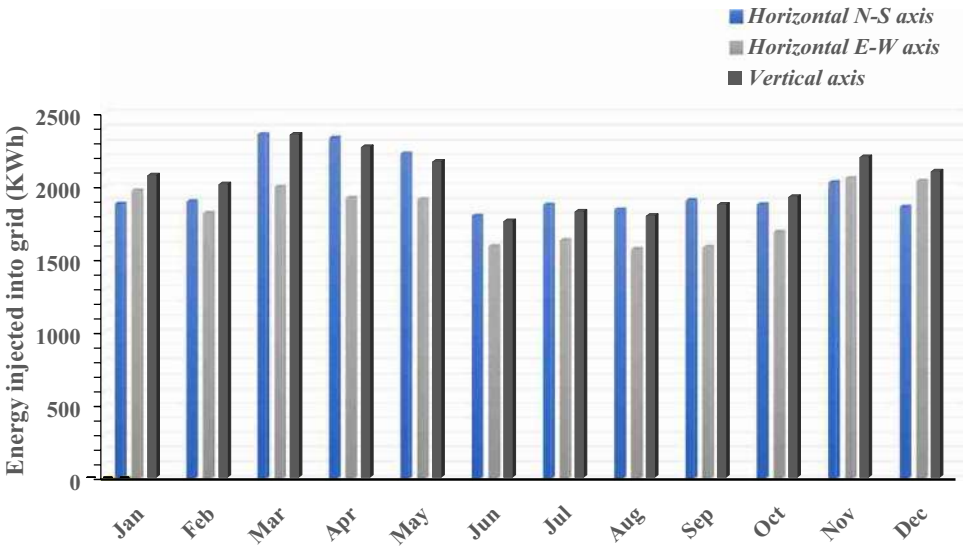

Fig. 8 Comparison of single axis (horizontal N–S, horizontal E–W, and vertical axis) tracking plane

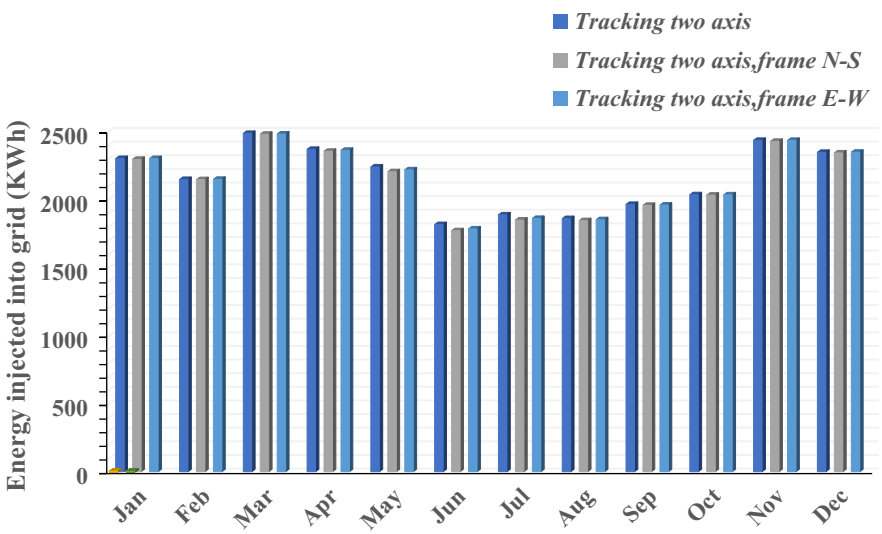

Fig. 9 Comparison of dual-axis tracking (tracking two axis, tracking two axis; frame N–S, tracking two axis; frame E–W) plane

Figures 8, 9 and 10 show the comparison of E_Grid for single axis tracking planes, dual-axis tracking planes, and fixed orientation planes.

According to our projected plant and the earlier study, a comparison of those values has been shown below in the following Table 3. Since tracking two axis frames showed comparatively superior value than other orientations; therefore, it was the selected orientation type for experiments. In addition, 370 wp mono and 60wp poly have been used for simulation (Figs. 11, 12).

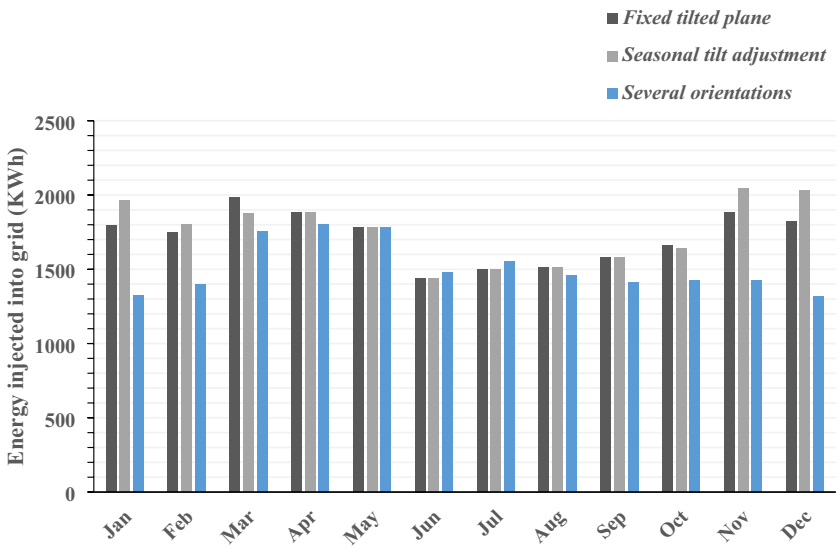

Fig. 10 Comparison for fixed orientation (fixed tilted plane, seasonal tilt adjustment, and several orientation) planes

Table 3 Comparison of results regarding solar cell (a) and irradiation consumption (b) between projected plant and reference plant

(a)		
	Polycrystalline	Monocrystalline
Projected yield (MWh/year)	23.955	25.774
Reference yield (MWh/year)	3.8338	3.8347
(b)		
	Projected yield (KWh/m^2)	Reference yield (KWh/m^2)
Received radiation(poly)	1802	1841
Effective radiation(mono)	2441	1955

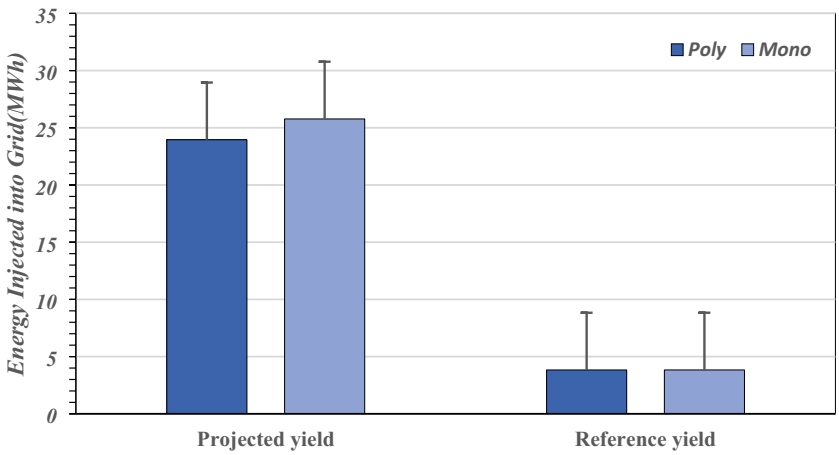

Fig. 11 Comparison of energy produced to the grid in terms of projected and reference field

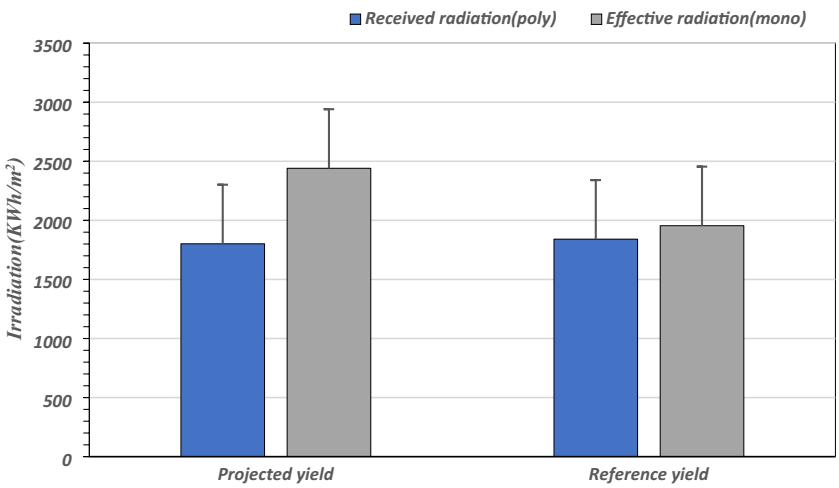

Fig. 12 Comparison of receiving irradiation according to the projected and reference plant considering poly and monocrystalline-based solar cell

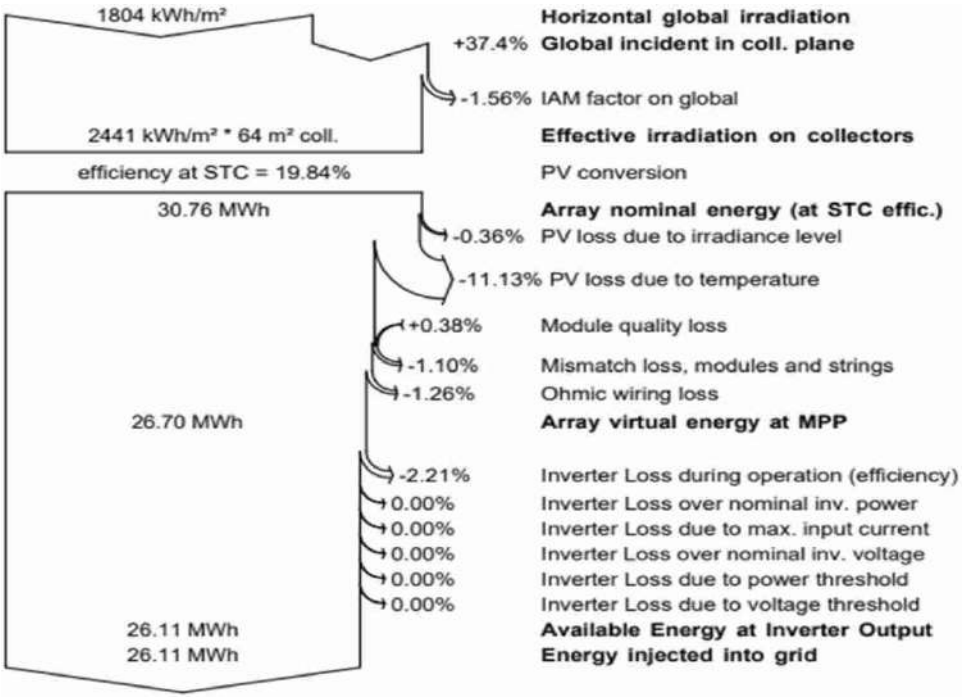

Fig. 13 System loss diagram over the whole year

The overall system loss diagram illustrated in Fig. 13.

Economic evaluation and cost calculation for the plant:

The investment through this power plant is considered for 20 years without considering any financial help from bank. For the plant, different types of orientations which are the most promising for installation and most relevant as well demonstrates in Table 4:

According to the orientations in a fixed tilted plane, tracking two axis and horizontal N–S axis showed the pick values among all field types. To obtain financial results, those types of the field have been chosen that illustrated in Fig. 14.

Table 4 Economic evaluation and CO_2 emission rate of chosen module for promising orientation plane

	Fixed tilted plane	Tracking two axis frame E–W	Horizontal N–S axis
E Grid (MWh)	20.793	26.130	25.378
Net profit	38,050.8 $	51,021.6 $	49,009.1 $
Payback period	2.7 years	2.1 years	2.1 years
Return on investment (ROI)	640.2%	858.4%	824.6%
CO_2 Emissions	293.220 tons	374.078 tons	361.533 tons

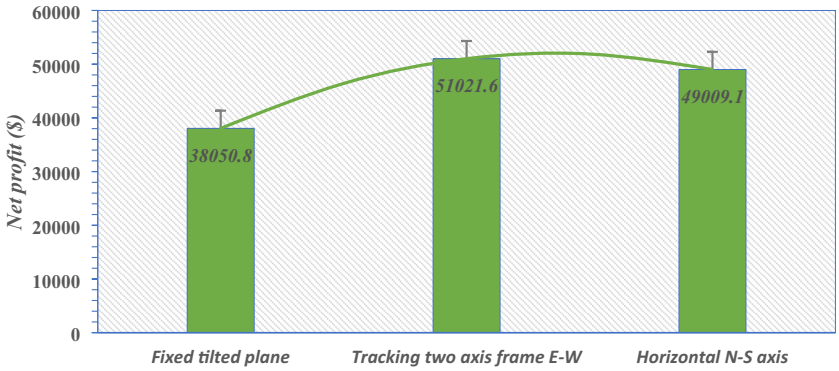

Fig. 14 Financial results of 20 years for the fixed tilted plane, tracking 2 axis frame E–W and horizontal N–S

Figure 14 represents the financial result of 20 years for that orientation.

Conclusion

In this research, we have explored the performance of polycrystalline and monocrystalline modules without considering any shading effects. The monocrystalline solar cell has been founded as the most effective cell over the polycrystalline-based solar cell whose performance ratio is 83.55%. Additionally, tracking two axis; frame E-W has been figured out as the most feasible orientation that belongs to the dual-axis tracking plane, which can inject energy to the projected grid 26.130 MWh/year, while the minimal injected value experienced in the fixed orientation plane that was 18.041 MWh/year. These obtained values can vary minimally due to the deficiency of applied information in the reference as well as for not using shading effects on the plant. In the coming years, this study can facilitate the way of making crystalline-based solar power plants considering different regions.

Data availability statement

The data that support the findings of this study are available from PVsyst photovoltaic software but restrictions apply to the availability of these data, which were used under license for the current study, and so are not publicly available. Data are however available from the authors upon reasonable request and with permission of PVsyst (https://www.pvsyst.com/meteo-data-source/).

Appendix

See Appendix Tables 5, 6, and 7.

Table 5 Simulation results for several types of bifacial modules (250wp 26Vmono, 400wp 32 V mono, 440wp 35 V mono, 440wp 35 V mono)

Months	Jan	Feb	March	April	May	June	July	Aug	Sept	Oct	Nov	Dec
250 wp												
E Array (MWh)	1.323	1.239	1.400	1.331	1.265	1.021	1.066	1.062	1.113	1.198	1.356	1.375
E Grid (MWh)	1.293	1.211	1.367	1.299	1.233	0.993	1.037	1.034	1.084	1.169	1.325	1.349
400 wp												
E Array (MWh)	1.807	1.702	1.934	1.838	1.743	1.402	1.464	1.458	1.543	1.651	1.866	1.890
E Grid (MWh)	1.767	1.663	1.889	1.797	1.703	1.367	1.428	1.423	1.497	1.613	1.258	1.849
440 wp												
E Array (MWh)	1.853	1.746	1.948	1.884	1.786	1.435	1.498	1.492	1.577	1.692	1.915	1.940
E Grid (MWh)	1.813	1.706	1.938	1.842	1.744	1.399	1.461	1.456	1.635	1.653	1.872	1.897

Table 6 Simulation results for several types of Vmax 1500 V modules (300wp 27 V mono, 340wp 28 V mono, 370wp 29 V mono, 400wp 32 V mono, 440wp 35 V)

Months	Jan	Feb	March	April	May	June	July	Aug	Sept	Oct	Nov	Dec
300 wp												
E Array (MWh)	1.596	1.496	1.691	1.607	1.506	1.232	1.285	1.279	1.343	1.446	1.637	1.665
E Grid (MWh)	1.561	1.406	1.652	1.570	1.490	1.200	1.253	1.248	1.311	1.412	1.601	1.629
340 wp												
E Array (MWh)	1.694	1.588	1.795	1.705	1.619	1.306	1.363	1.357	1.405	1.534	1.738	1.768
E Grid (MWh)	1.658	1.553	1.754	1.776	1.581	1.273	1.329	1.324	1.391	1.499	1.700	1.730
370 wp												
E Array (MWh)	1.896	1.786	1.029	1.928	1.828	1.470	1.534	1.528	1.609	1.731	1.957	1.984
E Grid (MWh)	1.854	1.746	1.983	1.885	1.786	1.433	1.497	1.492	1.571	1.692	1.915	1.941
400 wp												
E Array (MWh)	1.807	1.702	1.934	1.834	1.743	1.402	1.464	1.458	1.534	1.651	1.866	1.890
E Grid (MWh)	1.767	1.663	1.889	1.797	1.703	1.367	1.428	1.423	1.497	1.613	1.825	1.849
440 wp												
E Array (MWh)	1.852	1.745	1.983	1.883	1.784	1.434	1.496	1.490	1.571	1.691	1.914	1.938
E Grid (MWh)	1.811	1.766	1.937	1.841	1.742	1.398	1.460	1.455	1.534	1.758	1.872	1.897

Table 7 Simulation results for several types of polycrystalline modules (110wp 29 V, 60wp 14 V poly, 190wp 22 V poly)

Months	Jan	Feb	March	April	May	June	July	Aug	Sept	Oct	Nov	Dec
110 wp												
E Array (MWh)	2.373	2.226	2.520	2.398	2.279	1.841	1.922	1.914	2.005	2.158	2.435	2.474
E Grid (MWh)	2.320	2.175	2.462	2.343	2.227	1.797	1.877	1.870	1.958	2.108	2.379	2.418
60 wp												
E Array (MWh)	2.561	2.401	2.717	2.586	2.459	1.987	2.074	2.066	2.163	2.327	2.627	2.669
E Grid (MWh)	2.502	2.346	2.653	2.526	2.402	1.940	2.026	2.018	2.112	2.274	2.565	2.608
190 wp												
E Array (MWh)	1.149	1.078	1.221	1.161	1.104	0.891	0.930	0.927	0.971	1.045	1.179	1.198
E Grid (MWh)	1.123	1.052	1.190	1.133	1.075	0.865	0.904	0.901	0.944	1.018	1.152	1.171

Declarations

Conflict of interest The authors declare that they have no conflict of interest.

References

1. Islam, R., Bhuiyan, A.B.M.N., Ullah, M.W.: An overview of concentrated solar power (CSP) technologies and its opportunities in Bangladesh (2017). https://doi.org/10.1109/ECACE.2017.7913020
2. Hui, S.C.M., Chan S.C.: Integration of green roof and solar photovoltaic systems. In: Jt. Symp. 2011 Integr. Build. Des. New Era Sustain., vol. 2011, no. November, pp. 1–12 (2011)
3. IEA-PVPS Task 2, Analysis of Photovoltaic Systems. Report IEA-PVPS T2-01, December 2000. [Online]. http://www.iea-pvps-task2.org/
4. Bhuiyan, N., Ullah, W., Islam, R., Ahmed, T., Mohammad, N.: Performance optimisation of parabolic trough solar thermal power plants–a case study in Bangladesh. Int. J. Sustain. Energy **39**(2), 113–131 (2020). https://doi.org/10.1080/14786451.2019.1649263
5. Baghdadi, I., El Yaakoubi, A., Attari, K., Leemrani, Z., Asselman, A.: Performance investigation of a PV system connected to the grid. Procedia Manuf. **22**, 667–674 (2018). https://doi.org/10.1016/j.promfg.2018.03.096
6. Hui, S., Hei-Man, C.: Development of modular green roofs for high-density urban cities. In: World Green Roof Congr., pp. 1–18 (2008) [Online]. https://www.elteasygreen.com
7. Hui, S.C.M.: Low energy building design in high density urban cities. Renew. Energy **24**(3–4), 627–640 (2001). https://doi.org/10.1016/S0960-1481(01)00049-0
8. Satish, M., Santhosh, S., Yadav, A.: Simulation of a Dubai based 200 KW power plant using PVsyst software. In: 2020 7th Int. Conf. Signal Process. Integr. Networks, SPIN 2020, pp. 824–827 (2020). https://doi.org/10.1109/SPIN48934.2020.9071135
9. Nayan, M.F., Ullah, S.M.S., Saif, S.N.: Comparative analysis of PV module efficiency for different types of silicon materials considering the effects of environmental parameters. In: 2016 3rd Int. Conf. Electr. Eng. Inf. Commun. Technol. iCEEiCT 2016, no. Dc (2017). https://doi.org/10.1109/CEEICT.2016.7873089
10. Decker, B., Jahn, U.: Performance of 170 grid connected PV plants in northern Germany—analysis of yields and optimization potentials. Sol. Energy **59**(4–6–6 pt 4), 127–133 (1997). https://doi.org/10.1016/S0038-092X(96)00132-6
11. Allouhi, A., Saadani, R., Kousksou, T., Saidur, R., Jamil, A., Rahmoune, M.: Grid-connected PV systems installed on institutional buildings: technology comparison, energy analysis and economic performance. Energy Build. **130**, 188–201 (2016). https://doi.org/10.1016/j.enbuild.2016.08.054

12. Sharma, V., Chandel, S.S.: Performance analysis of a 190 kWp grid interactive solar photovoltaic power plant in India. Energy **55**, 476–485 (2013). https://doi.org/10.1016/j.energy.2013.03.075
13. Edalati, S., Ameri, M., Iranmanesh, M.: Comparative performance investigation of mono- and poly-crystalline silicon photovoltaic modules for use in grid-connected photovoltaic systems in dry climates. Appl. Energy **160**, 255–265 (2015). https://doi.org/10.1016/j.apenergy.2015.09.064
14. Kymakis, E., Kalykakis, S., Papazoglou, T.M.: Performance analysis of a grid connected photovoltaic park on the island of Crete. Energy Convers. Manag. **50**(3), 433–438 (2009). https://doi.org/10.1016/j.enconman.2008.12.009
15. Ferrada, P., Araya, F., Marzo, A., Fuentealba, E.: Performance analysis of photovoltaic systems of two different technologies in a coastal desert climate zone of Chile. Sol. Energy **114**, 356–363 (2015). https://doi.org/10.1016/j.solener.2015.02.009
16. Ghiani, E., Pilo, F., Cossu, S.: Evaluation of photovoltaic installations performances in Sardinia. Energy Convers. Manag. **76**, 1134–1142 (2013). https://doi.org/10.1016/j.enconman.2013.09.012
17. Padmavathi, K., Daniel, S.A.: Performance analysis of a 3MWp grid connected solar photovoltaic power plant in India. Energy Sustain. Dev. **17**(6), 615–625 (2013). https://doi.org/10.1016/j.esd.2013.09.002
18. Kumar, N.M., Dasari, S., Reddy, J.B.: Availability factor of a PV power plant: evaluation based on generation and inverter running periods. Energy Procedia **147**, 71–77 (2018). https://doi.org/10.1016/j.egypro.2018.07.035
19. Kandasamy, C.P., Prabu, P., Niruba, K.: Solar potential assessment using PVSYST software. In: Proc. 2013 Int. Conf. Green Comput. Commun. Conserv. Energy, ICGCE 2013, pp. 667–672 (2013). https://doi.org/10.1109/ICGCE.2013.6823519
20. Shiva Kumar, B., Sudhakar, K.: Performance evaluation of 10 MW grid connected solar photovoltaic power plant in India. Energy Rep. **1**, 184–192 (2015). https://doi.org/10.1016/j.egyr.2015.10.001
21. Radka, M.: Swera: solar and wind energy resource assessment. In: 38th ASES Natl. Sol. Conf. 2009, Sol. 2009, vol. 8, no. February, pp. 4318–4323 (2009)
22. BBS: Statistical year book. Bangladesh Bureau of Statistics, Statistics Division, Ministry of Planning, no. September, pp. 1–14 (2012)
23. Rahman, M.M., Ahmed, A.U., Dey, P., Habib, A., Reza, C.M.F.S., Aziz, F.: Solar energy potential in Bangladesh. In: International conference on mechanical engineering and renewable energy 2013 (ICMERE2013), vol **2013**, pp 24–27
24. Rahim, M.M.M., Hosam-E-Haider, M.: Renewable energy scenario in Bangladesh: opportunities and challenges. In: 2nd Int. Conf. Electr. Eng. Inf. Commun. Technol. iCEEiCT 2015, no. May, pp. 21–23 (2015). https://doi.org/10.1109/ICEEICT.2015.7307466
25. Islam, A.K.M.S., Islam, M., Rahman, T.: Effective renewable energy activities in Bangladesh. Renew. Energy **31**(5), 677–688 (2006). https://doi.org/10.1016/j.renene.2005.08.004
26. Cabraal, A., Ward, W.A., Bogach, V.S., Jain, A.: Living in the light : the Bangladesh solar home systems story. © World Bank, License: CC BY 3.0 IGO, World Bank, Washington, DC (2021). https://openknowledge.worldbank.org/handle/10986/35311
27. Halder, P.K., Paul, N., Joardder, M.U.H., Sarker, M.: Energy scarcity and potential of renewable energy in Bangladesh. Renew. Sustain. Energy Rev. **51**, 1636–1649 (2015). https://doi.org/10.1016/j.rser.2015.07.069
28. Campbell, J., Zemen, Y., Richardson, B., Striner, B.: Photovoltaic module performance and degradation as compared in distinct climatic regions. In: Conf. Rec. IEEE Photovolt. Spec. Conf., pp. 1250–1255 (2012). https://doi.org/10.1109/PVSC.2012.6317829
29. Zhao, J., Wang, A., Green, M.A., Ferrazza, F.: 19.8% Efficient 'Honeycomb' textured multicrystalline and 24.4% monocrystalline silicon solar cells. Appl. Phys. Lett. **73**(14), 1991–1993 (1998). https://doi.org/10.1063/1.122345
30. Nandi, S.K., Hoque, M.N., Ghosh, H.R., Chowdhury, R.: Assessment of wind and solar energy resources in Bangladesh. Arab. J. Sci. Eng. **38**(11), 3113–3123 (2013). https://doi.org/10.1007/s13369-012-0429-5
31. Um H.D., Hwang, I., Choi, D., Seo, K.: Flexible crystalline-silicon Photovoltaics: light management with surface structures. Acc. Mater. Res. **2**(9):701–713 (2021). https://doi.org/10.1021/accountsmr.1c00038

International Journal of Energy and Environmental Engineering (2023) 14:757–776
https://doi.org/10.1007/s40095-022-00547-9

ORIGINAL RESEARCH

Influence of solar and solid oxide fuel cell in AGC learning by utilizing spotted hyena optimized cascade controller

Arindita Saha[1] · **Puja Dash**[2] · **Naladi Ram Babu**[3]

Received: 4 April 2022 / Accepted: 21 October 2022 / Published online: 3 November 2022

Abstract

The present work explores automatic generation control learning for manifold area and sources under traditional situations. Sources in area-1 are thermal, biodiesel; thermal and gas plant in area-2; and thermal, split-shaft gas turbine (Ss(GT)) in area-3. An original strive has been set out to execute cascade controller with the amalgamation of proportional with tilt–integral–derivative with filter (TIDN) and fractional-order integral–derivative (FOID). TIDN and FOID are in series connection, hence named TIDN-FOID. Various scrutiny expresses excellency of TIDN-FOID controller over proportional–integral–derivative filter (PIDN) and TIDN from outlook regarding the lessened level of peak overshoot, extent of oscillations, peak undershoot as well as settling time. In an endeavour to procure the controller's gains and parameters, bioinspired meta-heuristic spotted hyena optimizer (SHO) is applied. It is also observed that the presence of a renewable solar source makes the system significantly better compared to the base thermal–biodiesel–gas–Ss(GT) system. TIDN-FOID performance is also observed to be excellent in the presence of solar for both 1% step load disturbance and random load pattern individually. Fixed as well as variable insolation for solar is analysed separately. The performance of solid oxide fuel cell (SoFC) is also examined using the TIDN-FOID controller, which provides with noteworthy outcome in dynamic performance for both types of disturbances. Also, sensitivity analysis is performed, and it is observed that the values of the TIDN-FOID parameters at nominal conditions are appropriate for a higher value of disturbance.

Keywords Automatic generation control · Biodiesel plant · Solar thermal power plant · Solid oxide fuel cell · Spotted hyena optimizer · TIDN-FOID controller

List of symbols

f	Frequencies set point value. Hertz (Hz) is unit
*	Exponent implies best number
i	Subscripted value implies to area number
B_i	Coefficient of frequency bias of the concerned area
T_{ij}	Coefficient of synchronization
T	Time of simulation in seconds
Δf_i	Alteration of frequency of concerned area
ΔP_{Di}	Amount of load alteration of concerned area
H_i	Amount of inertia constant of concerned area
D_i	$\Delta P_{Di}/\Delta f_{\mathrm{i}}$ (p.u MW/Hz)
R_i	Parameter of speed regulation of governor of concerned area
β_i	Characteristics of frequency response of concerned area
K_{pi}	Gain of power system block
T_{pi}	Time constant of power system block
P_{ri}	Considered rated power of an area
a_{ij}	(P_{ri}/P_{rj})
pf_{iv}	Area participation factor for area-i, $i=1$, 2, 3 and $v=1$, 2, 3
T_{gi}, T_{ti}, T_{ri}	Time constants of governor, turbine and reheater of thermal generating units in seconds (s) of concerned area

✉ Arindita Saha
sahaarindita.91@gmail.com

[1] Department of Electrical Engineering, Regent Education & Research Foundation Group of Institutions, Kolkata, West Bengal, India

[2] Department of Electrical and Electronics Engineering, Gayatri Vidya Parishad College of Engineering (Autonomous), Visakhapatnam, Andhra Pradesh, India

[3] Department of Electrical and Electronics Engineering, Aditya Engineering College, Surampalem, East-Godavari, Andhra Pradesh, India

K_{ri}	Gain of reheater of thermal generating units of concerned area
T_{sgi}, T_{GSi}, T_{TSi}	Time constants of solar field, governor and turbine of solar thermal units in seconds (s) of concerned area
B_g	Valve positioner time constant in seconds (s) of gas turbine
C_g	Gas turbine valve positioner
X_g	Governor's lead time constant of gas turbine
Y_g	Governor's lag time constant of gas turbine
T_{cr}	Time delay of combustion reaction of gas turbine
T_f	Time constant of fuel of gas turbine
T_{cd}	Time constant of compressor's discharge volume
K_{Pi}, K_{Ii}, K_{Di}	Proportional, integral, derivative gains of integer-order controller
K_{FIi}, K_{FDi}, K_{Ti}	Integral, derivative and tilt gains of fractional-order controller
n_j, λ_j and μ_j	Tilt, integral and derivative parameters of fractional-order controller
N_j	Filter coefficient
αD_t^{α}	Fractional operator
$\Gamma(.)$	Euler's gamma function
ω	Undammed frequency

Introduction

A power system is healthy if proper balance coordination is maintained between the amounts of power generation and demand along with losses. This is very intricate during periods of high demands and leads to disparity in power. Further, if this disparity in the form of aberration in frequency and tie line power connecting areas are not noticed it will lead to huge damage [1–3]. This disparity leads to instability and blackouts of the power system which is overcome by the concept of automatic generation control (AGC). Elgerd et al.[4] have provided with the basic mathematical formulation of AGC. Back in earlier days, most of the works in AGC were confined to a single area system [5–7]. Later, works have carried forward to multi-systems [8–12] with the inclusion of nonlinearity like generation rate constraint and also sometimes governor dead band. Most of the works were using thermal as generating units. Nanda et al.[13] have assessed the hydro–thermal system. Saikia et al.[14] performed assessment for the gas–thermal system. Pradhan et al. [15] have performed an analysis for a system having sources like thermal, gas and hydro. Saha et al. [16] have reported the use of split-shaft gas turbine (Ss(GT)) in a three-area system. Thus, the combination of sources like thermal, gas and Ss(GT) is yet to be examined; hence, it calls for assessment.

Fossil fuels are generously used to generate electricity. But, constant usage of these fuels are depleting them, as their depletion rate is much faster compared to its formation time. Moreover, the by-products formed are hampering the environment. So, it is high time to involve the usage of renewable sources of energy like solar and wind. And most of the issues are to some extent alleviated by their involvement. Few pieces of the literature are available that point to the usage of renewable source solar in AGC. Das et al.[6] have reported about the usage of solar thermal power plants (STPP) in an isolated system. Their studies were limited to only a single area. Later, Sharma et al. [17] briefed about the usage of STPP for the integrated systems along with thermal for a conventional system. The authors in [18, 19] have mentioned the usage of STPP for AGC systems under a restructured scenarios with thermal plants. Now, the conventional diesel plants are getting replaced by biodiesel plants [20] which leads to less toxic production. Therefore, these combinations of system with solar (with constant and variable solar insolation at different types of disturbances one at a time) and biodiesel plants are not yet reported in studies in AGC learning. Hence, it demands extensive investigations.

In an interconnected system, the system can be stabilized in terms of reduced change in errors with the help of various energy storage devices (ESD). Some of the ESDs reported in the literature related to the AGC study are battery energy storage systems [19, 21], redox flow batteries [22], superconducting magnetic energy storage [23], capacitive energy storage [22] and ultra-capacitor [18]. Similarly, there is another storage system named solid oxide fuel cell (SoFC) [24]. SoFC belongs to the category of fuel cell which uses solid oxide material in the form of electrolyte. SoFC are efficient and cause fewer emissions. They operate at very high temperatures, where they do not need a costly catalyst. The involvement of SoFC in AGC learning is yet to be explored.

Primary and secondary controls are the two types of control in AGC. The main focus in AGC learning regarding control is the proper selection of secondary controllers. Many studies reflect about the usage of various integer-order (IO) controllers like integral (I) [25], proportional–integral (PI) [26], proportional–integral–derivative with filter (PIDN) [27]. Two [28] or three [29] higher-degree-of-freedom controllers have also been analysed in this field of study and are also of IO type. Few fractional-order (FO) controllers which found application are FOPI [30], FOPID [31, 32], proportional with tilt–integral–derivative with filter (TIDN) [33], FO-TIDN [34] and model predictive controller [35]. The AGC learning literature also points out the usage of IO cascade controllers (proportional–integral–proportional derivative (PI-PD)) [36], FO cascade controllers (FO proportional–integral–FO proportional–derivative (FOPI-FOPD))

[23] and the combination of IO and FO controllers (PIDN-FOPD) [18]. But, a series cascade combination of TIDN with FO integral–derivative named TIDN-FOID has not been yet stated in the AGC literature. Moreover, application of the TIDN-FOID controller in this three-area thermal–biodiesel–gas–Ss(GT) system has not been reported previously, so it demands the need for investigation.

The performance of any secondary controller is excellent only if the best values of its gain and parameters are properly chosen. These can be done with the help of either conventional or optimization techniques. But, the use of the conventional techniques is quite laborious and provides sub-optimum outcomes. Some of the optimization techniques which found their demand in AGC learning are particle swarm optimization (PSO) [37], firefly algorithm (FA) [38], cuckoo search (CS) [28], grey wolf optimization (GWO) [17], biogeography-based optimization (BBO) [29], flower pollination algorithm (FPA) [36], differential evolution (DE) [39], whale optimization algorithm (WOA) [40], grass hoper [41], lightening search [42] and quasi-learning [43], genetic algorithm [44], crow search algorithm [45]. A newly developed bioinspired meta-heuristic algorithm titled spotted hyena optimized (SHO) [46] is obtainable from the literature. SHO was established from the behavioural nature of spotted hyenas which portrays the social bond between spotted hyena and their collaborative deeds. To a great wonder, SHO has not identified its implementation in AGC learning for obtaining the best values of controller gains and parameters, thus demanding advanced investigation.

With regard to overhead discussions, the prime purpose of the present article is as follows:

a) Formulation of three-area system with thermal–biodiesel in area$_{-1}$, thermal–gas in area$_{-2}$ and thermal–Ss(GT) in area$_{-3}$.
b) The gains of PIDN/FOPID/TIDN/TIDN-FOID are simultaneously optimized individually using the SHO algorithm to obtain an excellent controller.
c) The system mentioned in a) is integrated with solar in all areas. After that, the excellent controller is looked forward to comparing their performances with constant and variable solar insolation separately for each case for 1% step load disturbance.
d) The system mentioned in c) is considered for fixed solar insolation at random load as a disturbance. Again the performances of PIDN/FOPID/TIDN/TIDN-FOID controllers are studied separately to obtain the best controller in this case.
e) The impact of solar on system dynamics is studied for both 1% step load and random load disturbance for fixed insolation with the best-obtained controller from b), c) and d).
f) The impact of SoFC on system dynamics is studied for both 1% step load and random load disturbance for fixed insolation with the best-obtained controller from b), c) and d).
g) Sensitivity analysis is carried out to examine the robustness of the best controller's gains with a higher value of step load disturbance.

For easy understanding, the present article is schematically presented in Fig. 1.

The main contributions of the present work are:

a) A maiden effort was made to study the effect of SoFC on AGC system dynamics.
b) A new cascade TIDN-FOID controller is suggested for AGC studies for the first time.
c) A comparative analysis of fixed and variable solar insolation one at a time considering step and random load perturbations is carried out.
d) AGC study with combined solar and SoFC improves system dynamics over solar system alone.
e) Sensitivity analysis discovers that SHO optimized TIDN-FOID controller values are robust and need not be reset again.

Investigated system and SoFC

Investigated system

A three-area system of unequal type is taken into account for the survey having the area capacity ratio in the form of 1:3:4. The system involves thermal and biodiesel plants as generating units in area-1 and in the same manner, thermal and gas plants in area-2 and thermal and split-shaft gas turbines (Ss(GT)) in area-3. Even the system is associated with generation rate constraint and governor dead band as non-linearities. The participation factors (pf) of each generating units of respective areas are: $pf_{11}=0.7$, $pf_{12}=0.3$ in area$_{-1}$, $pf_{21}=0.6$, $pf_{22}=0.4$ in area$_{-2}$ and $pf_{31}=0.65$, $pf_{32}=0.35$ in area$_{-3}$. This is supposed to be system-1. The conventional diesel plant is nowadays getting replaced by biodiesel plants as they are non-toxic, as well as biodegradable, slightly more density and lower viscosity; moreover, it releases less CO. Thus, they can be utilized as a standby for power generation. It consists of a valve regulator and combustion engine. The first-order transfer function (Tf) of valve regulator and combustion engine of biodiesel plant is given by Eqs. (1) and (2), respectively [20].

$$Tf_{\text{valve regulatorBio - diesel}} = \frac{K_{VR}}{1 + sT_{VR}} \tag{1}$$

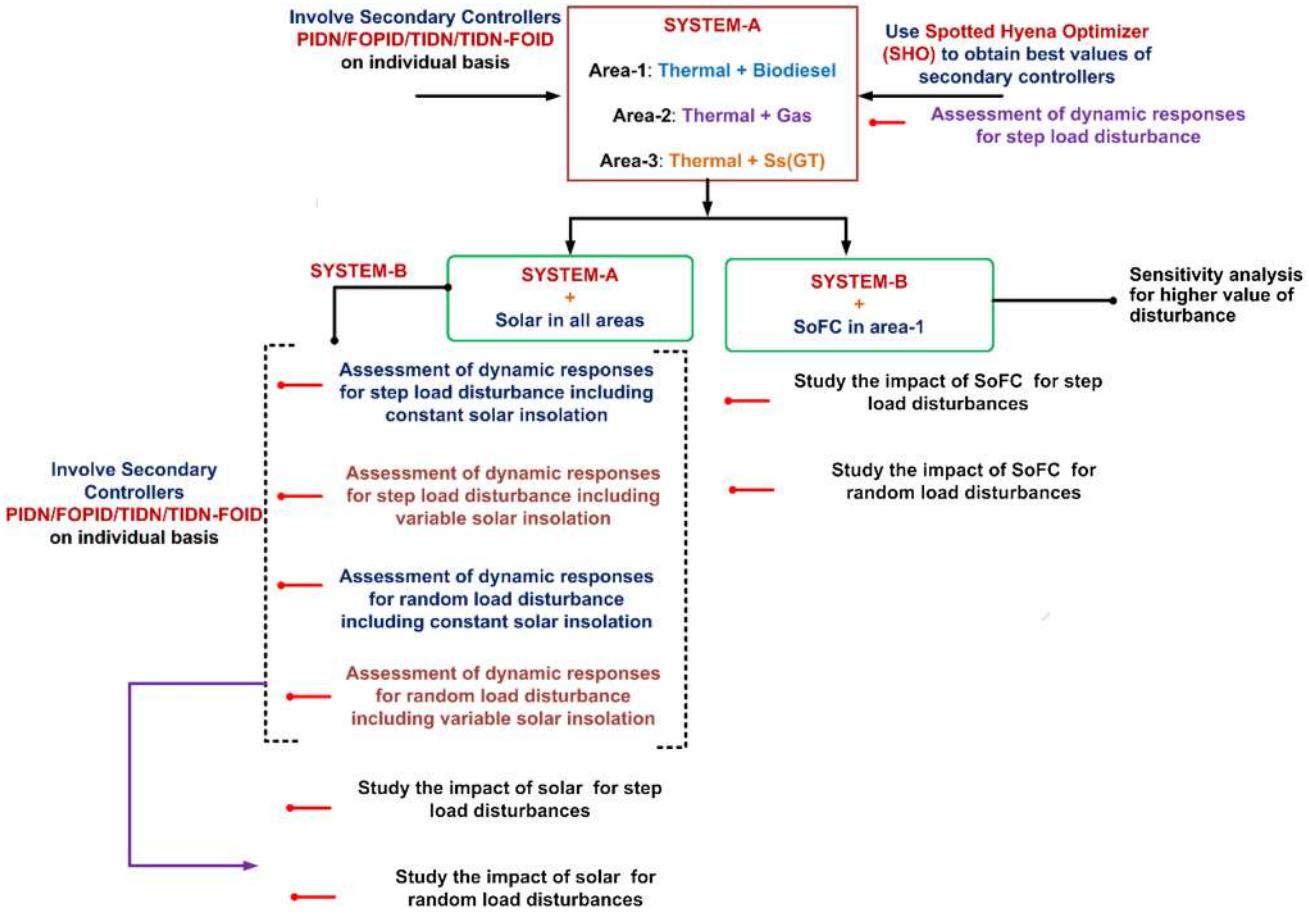

Fig. 1 Schematic representation of present article work

K_{VR} and T_{VR} are the gain and time constants of valve regulators of biodiesel plants, respectively [20].

$$Tf_{\text{Combustion engineBio-diesel}} = \frac{K_{CE}}{1 + sT_{CE}} \tag{2}$$

K_{CE} and T_{CE} are the gain and time constants of the combustion engine of biodiesel plants, respectively. Consequently, system-1 is integrated with the solar thermal power plants in all areas. This is treated as system-2. The pf's are as $pf_{11} = 0.6$, $pf_{12} = 0.25$, $pf_{13} = 0.15$ in area-1, $pf_{21} = 0.5$, $pf_{22} = 0.35$, $pf_{23} = 0.15$ in area-2 and $pf_{31} = 0.5$, $pf_{32} = 0.4$, $pf_{33} = 0.2$ in area-3. After that, an energy storing component namely solid oxide fuel cell (SoFC) is included in area-1. The schematic and transfer function (Tf) model of systems is shown in Fig. 2. The nominal values of system parameters are provided in Appendix. The Tf model of Ss(GT) is obtained from Reference [17]. The best values of controller gains and parameters are obtained with the help of the spotted hyena optimizer algorithm considering integral squared error as a performance index (Pi_{ISE}) given by Eq. (3) [8].

$$Pi_{ISE} = \int_0^T \left\{ \left(\Delta f_i\right)^2 + \left(\Delta P_{tie_{i-j}}\right)^2 \right\} dt \tag{3}$$

Solid oxide fuel cell (SoFC)

The energy storing component solid oxide fuel cell (SoFC) [24] is a static electrochemical device that is utilized to transform hydrogen as well as oxygen's chemical form of energy into electrical energy. This is done by employing ceramic-type electrolytes and porous electrodes. The three main components associated with power generation from

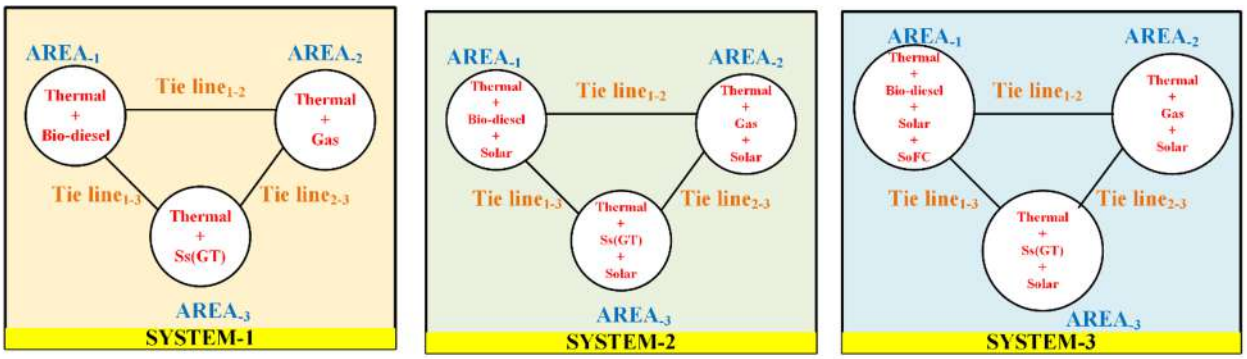

(a)

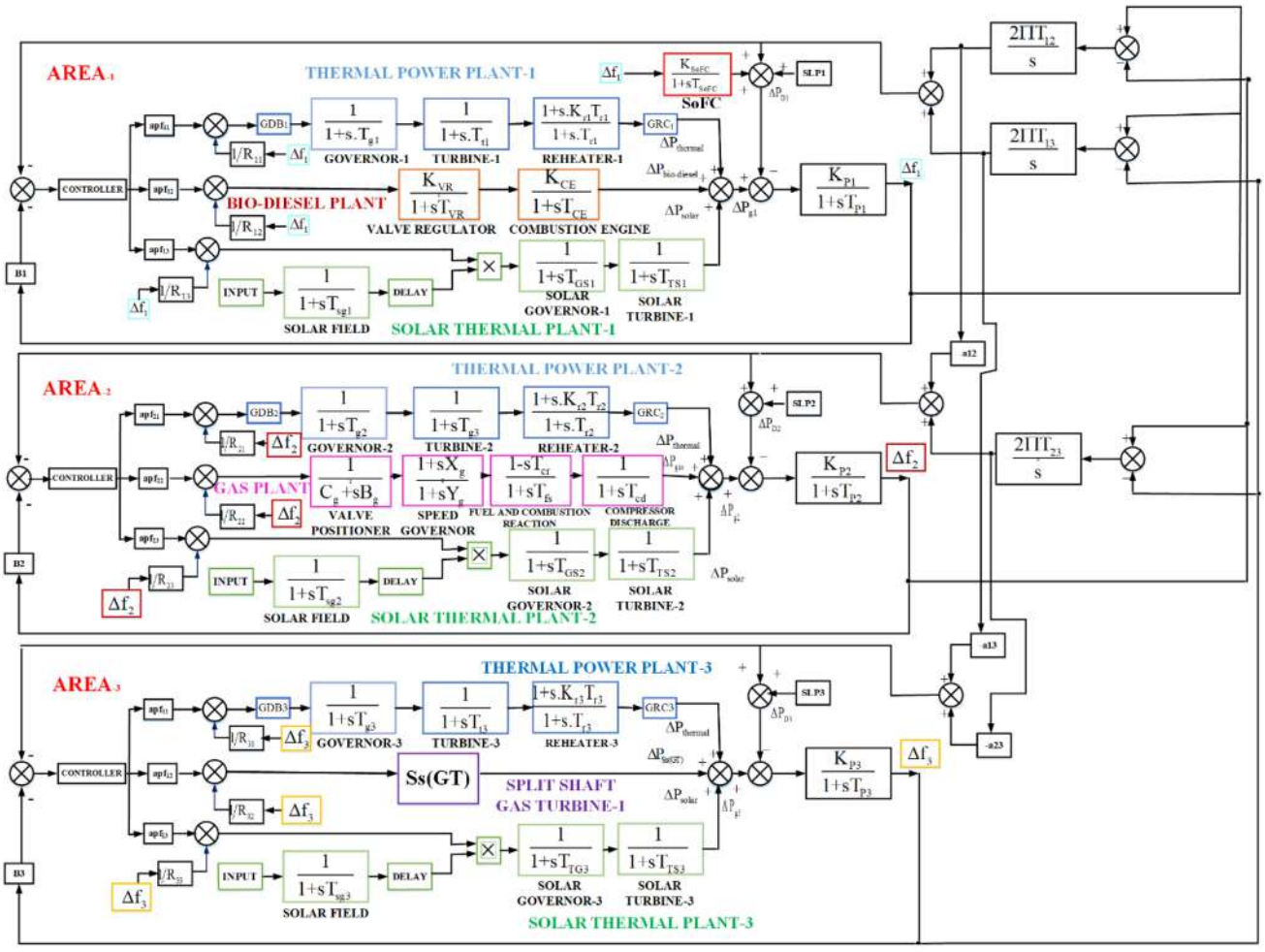

(b)

Fig. 2 Schematic diagram and Tf model of unequal three-area system with thermal–biodiesel–solar in area-1, thermal–gas–solar in area-2 and thermal–Ss(GT)–solar in area-3 along with SoFC in area-1: **a** Schematic diagram of three different systems in step by step method, **b** Tf model of ultimate system with both solar and SoFC

SoFC are the fuel processing unit, power unit and power conditioning section. SoFC has a few features like higher temperature, high efficiency, high catalytic reaction, less prone to corrosion, profitable, the lesser release of exhaust gases and many more. The Tf of SoFC is given by Eq. (4) [24].

$$\mathrm{Tf}_{\mathrm{SoFC}}(\mathrm{s}) = \frac{\mathrm{K}_{\mathrm{SoFC}}}{1 + \mathrm{sT}_{\mathrm{SoFC}}} \tag{4}$$

$\mathrm{K}_{\mathrm{SoFC}}$ and $\mathrm{T}_{\mathrm{SoFC}}$ are the gain and time constants of SoFC, respectively.

Proposed controller

The proposed controller in this article is the combination of tilt–integral–derivative with filter (TIDN) and integral–derivative in fractional form (FOID). A fractional-order controller (FO) provides more flexibility and enhances the overall performance of the system by providing some additional degrees of freedom [40]. The two parts of the controller, i.e. TIDN and FOID, are in a series combination. The block outline of TIDN-FOID is demonstrated in Fig. 3. Block-1 (B1) and Block-2 (B2) are the arrangements of TIDN and FOID, respectively. $\mathrm{R}_{\mathrm{si}}(\mathrm{s})$ and $\mathrm{O}_{\mathrm{si}}(\mathrm{s})$ are the reference and output signals for the TIDN-FOID controller, respectively.

The Riemann–Liouville (R–L) description for FO integrator and derivative can be acquired from Eqs. (5), (6) [18], [47].

$$\alpha D_t^{-\alpha} f(t) = \frac{1}{\Gamma(n)} \int_{\alpha}^{t} (t-\tau)^{\alpha-1} f(\tau) d\tau \tag{5}$$

$$\alpha D_t^{\alpha} f(t) = \frac{1}{\Gamma(n-\alpha)} \frac{d^n}{dt^n} \int_{\alpha}^{t} (t-\tau)^{n-\alpha-1} f(\tau) d\tau \tag{6}$$

In Eqs. (5), (6), $\mathrm{n}-1 \leq \alpha < \mathrm{n}$, n is an integer, $\alpha \mathrm{D}_{\mathrm{t}}^{\alpha}$ is the fractional operator and $\Gamma(.)$ is the Euler's gamma function. The Laplace transformation of Eqs. (5), (6) is given by Eqs. (7), (8), respectively [18].

$$L\left\{\alpha D_t^{\alpha} f(t)\right\} = s^{\alpha} F(s) - \sum_{k=0}^{n-1} s^k \alpha D_t^{\alpha-k-1} f(t)|_{t=0} \tag{7}$$

$$L\left\{\alpha D_t^{\alpha} f(t)\right\} = s^{\alpha} F(s) - \sum_{k=0}^{n-1} s^k \alpha D_t^{\alpha-k-1} f(t)|_{t=0} \tag{8}$$

The disadvantage of the infinite count of poles and zeros due to perfect approximation is overwhelmed by Oustaloup et al. [48]. In [48], a proper Tf is suggested which can be estimated FO derivatives as well as integrators via recursive distribution about poles and zeros demonstrated by Eq. (9) [48].

$$s^{\alpha} = K \prod_{n=1}^{M} \frac{1 + \left(s/\omega_{Z,n}\right)}{1 + \left(s/\omega_{p,n}\right)} \tag{9}$$

If K = 1 (attuned gain) then and their gain = zero db with 1 rad/s frequency, M = number of poles as well as zeros (already set) and frequencies range for poles and zeros are provided by Eqs. (10)–(14) [18].

$$\omega_{Z,l} = \omega_l \sqrt{n} \tag{10}$$

$$\omega_{p,n} = \omega_{Z,n} \varepsilon \; n \; 1, \ldots, M, \tag{11}$$

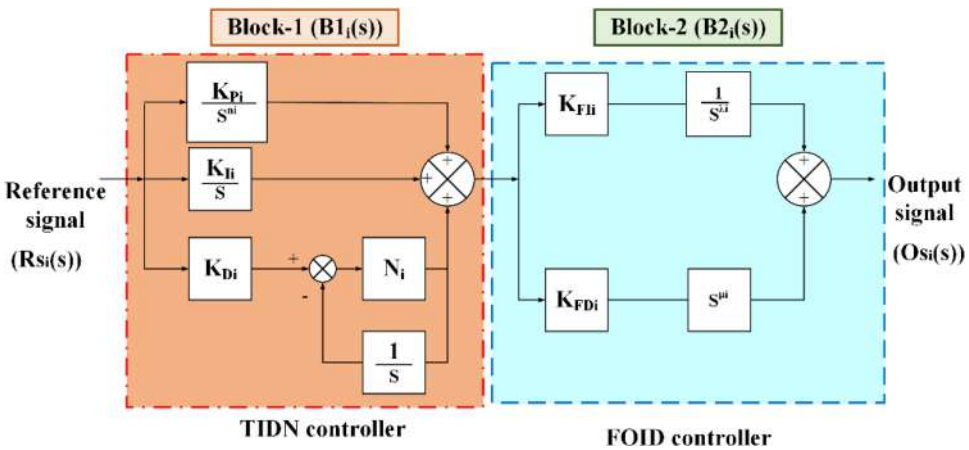

Fig. 3 Arrangement of proposed controller (TIDN-FOID)

Table 1 Best values of gains and parameters of PIDN, FOPID, TIDN and TIDN-FOID controllers for system-1 (excluding solar) for step load disturbance

Name of controllers	Corresponding gains and parameters	Area-1	Area-2	Area-3
PIDN	K_{Pi}*	0.0017	0.0028	0.0039
	K_{Ii}*	0.8276	0.8365	0.8265
	K_{Di}*	0.3592	0.4059	0.4185
	N_i*	10.77	12.41	15.25
FOPID	K_{Pi}*	0.1347	0.2739	0.3633
	K_{Ii}*	0.8995	0.9997	0.9743
	λ_i*	0.9956	0.9694	0.8564
	K_{Di}*	0.9239	0.4798	0.3740
	μ_i*	0.7172	0.9586	0.6429
TIDN	K_{Pi}*	0.5015	0.6470	0.6013
	K_{Ii}*	0.3048	0.3442	0.4582
	K_{Di}*	0.3607	0.4761	0.5708
	N_i*	46.00	42.00	40.00
	n_i*	0.9409	1.9508	2.9107
TIDN-FOID	K_{Pi}*	0.9293	0.8412	0.8041
	K_{Ii}*	0.8642	0.8754	0.8643
	K_{Di}*	0.6548	0.7160	0.7683
	N_i*	63.53	52.23	65.35
	n_i*	4.9202	6.8256	7.9288
	K_{FIi}*	0.7408	0.8507	0.8573
	λ_i*	0.0214	0.0855	0.0475
	K_{FDi}*	0.8484	0.5148	0.4178
	μ_i*	0.0625	0.0250	0.0588

$$\omega_{Z,n+1} = \omega_{p,n}\sqrt{\eta} \tag{12}$$

$$\varepsilon = \left(\omega_h/\omega_l\right)^{v/M} \tag{13}$$

$$\eta = \left(\omega_n/\omega_l\right)^{(1-v)/M} \tag{14}$$

The TIDN controller is the modified form of PIDN controller where the proportional gain is associated with a tilted constituent in the form of $s^{-(1/n)}$ or $1/s^{(1/n)}$. TIDN is chosen as it facilitates hassle-free tuning, an excellent ratio of disturbance rejection; also, it is least affected by the alteration of system parameters.

The Tf of $B1_i(s)$ is given by Eq. (15).

$$B1_i(s) = \left\{\frac{K_{Pi}}{\left(s^{1/n_i}\right)}\right\} + \left\{\frac{K_{Ii}}{(s)}\right\} + K_{Di}\frac{N_i}{1+N_i/s} \tag{15}$$

The Tf of $B2_i(s)$ is given by Eq. (16).

$$B2_i(s) = \frac{K_{FIi}}{s^{\lambda_i}} + s^{\mu_i}K_{FDi} \tag{16}$$

where λ and μ are the non-integer order of FO integrator and derivative parts, respectively. K_{FIi} and K_{FDi} are the integral and derivative gain of FO part of the related area.

Thus,

$$O_{si}(s) = \left(B1_i(s)B2_i(s)\right)* R_{si}(s) \tag{17}$$

The adjusting parameters of TIDN and FOID are obtained using SHO by Pi_{ISE}. Stated boundaries of frequency [ωl, ωh] reflected for assessment is [0.01, 50], for controller gains like K_{Pi}, K_{Ii}, K_{Di}, K_{FIi}, K_{FDi}, is within 0–1, filter coefficient (N_i) is between 0 and 100, controller parameters (λ_i, μ_i) are within 0–1 and n_i between 1 and 12 [33]. The Tf model of TIDN-FOID is shown in Fig. 3

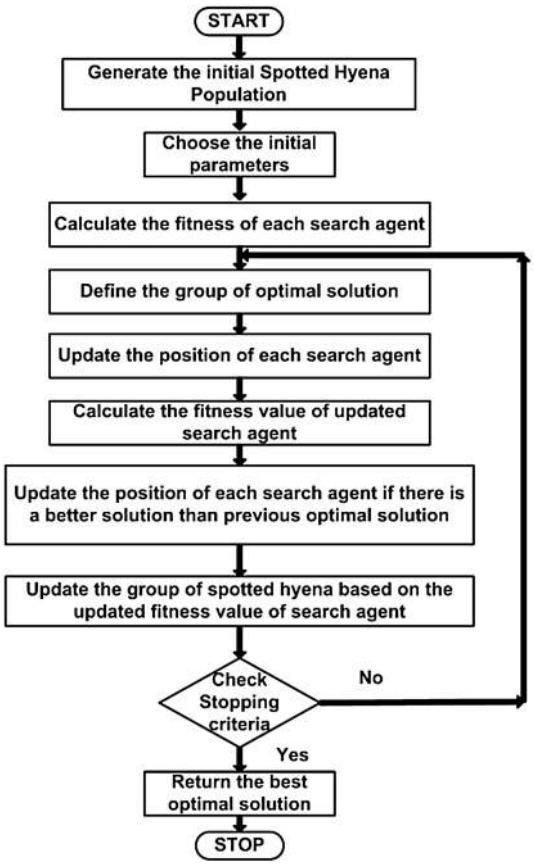

Fig. 4 Flowchart of SHO algorithm

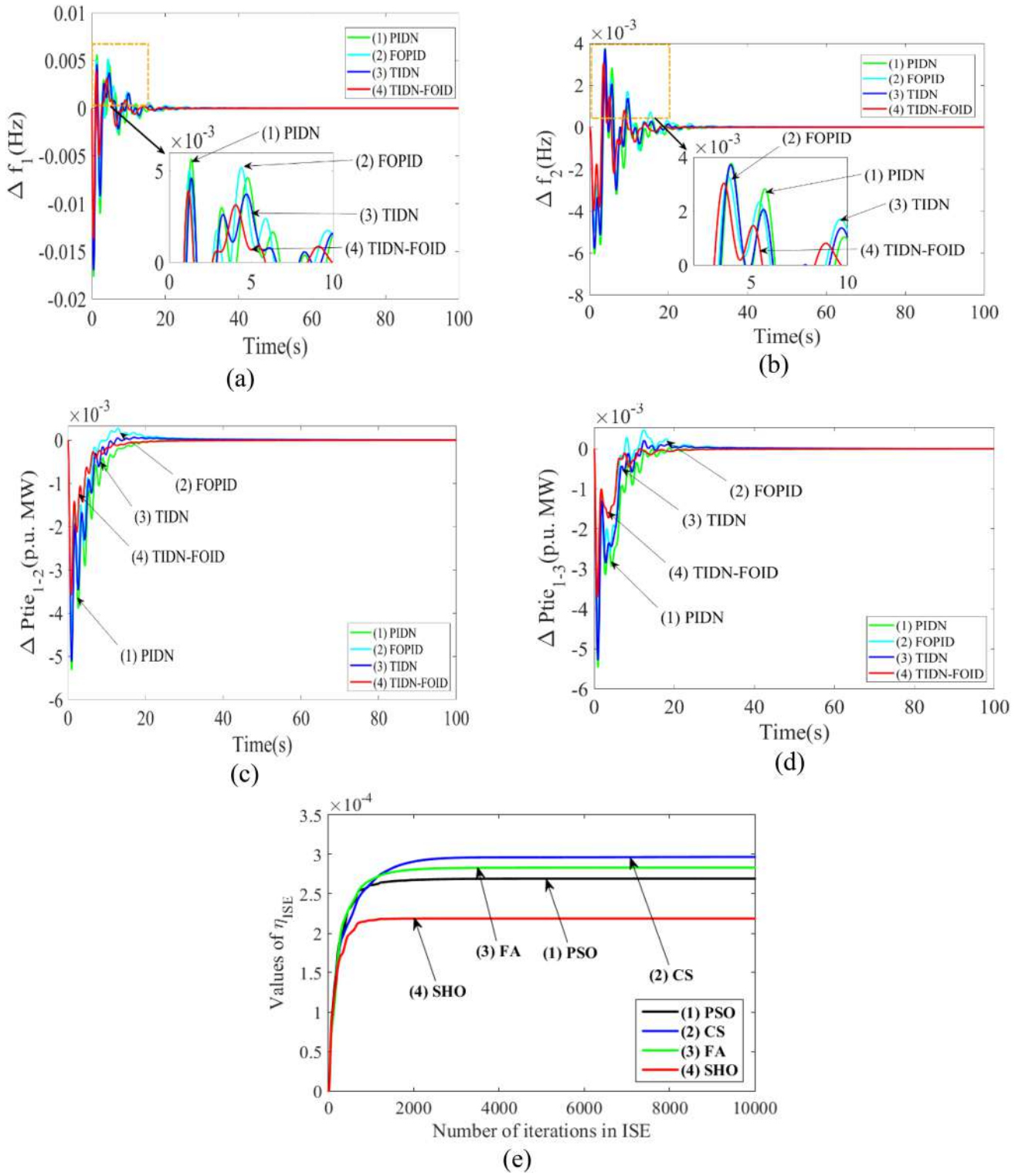

Fig. 5 Assessment of responses of controllers PIDN, FOPID, TIDN and TIDN-FOID for system-1 (excluding solar and SoFC) for 1% step load disturbance. **a** Area-1 frequency aberration Vs. time, **b** area-2 frequency aberration Vs. time, **c** tie line power aberration for line interconnecting area-1 and area-2 Vs. time, **d** tie line power aberration for line interconnecting area-1 and area-3 Vs. time, **e** characteristics of convergence

Table 2 Best values of gains and parameters of PIDN, FOPID, TIDN and TIDN-FOID controllers for system-2 (including constant solar insolation) for step load disturbance

Name of controllers	Corresponding gains and parameters	Area-1	Area-2	Area-3
PIDN	K_{Pi}*	0.0016	0.0017	0.0010
	K_{Ii}*	0.7632	0.7552	0.7395
	K_{Di}*	0.3655	0.3674	0.8049
	N_i*	39.77	30.41	35.25
FOPID	K_{Pi}*	0.2245	0.2546	0.4123
	K_{Ii}*	0.3476	0.9897	0.8907
	λ_i*	0.8692	0.9868	0.8977
	K_{Di}*	0.9897	0.5123	0.4123
	μ_i*	0.6896	0.9123	0.7199
TIDN	K_{Pi}*	0.2644	0.5375	0.5274
	K_{Ii}*	0.5765	0.4568	0.5764
	K_{Di}*	0.5613	0.4624	0.5748
	N_i*	44.23	25.00	32.76
	n_i*	2.9202	4.9697	3.9782
TIDN-FOID	K_{Pi}*	0.9764	0.8874	0.9975
	K_{Ii}*	0.5344	0.6444	0.6853
	K_{Di}*	0.7855	0.7415	0.9814
	N_i*	65.23	73.23	85.76
	n_i*	7.9202	8.2674	9.5555
	K_{FIi}*	0.9987	0.9988	0.9998
	λ_i*	0.0091	0.0092	0.0084
	K_{FDi}*	0.9658	0.8972	0.9635
	μ_i*	0.1070	0.1075	0.1108

Table 3 Best values of gains and parameters of PIDN, FOPID, TIDN and TIDN-FOID controllers for system-2 (including variable solar insolation) for step load disturbance

Name of controllers	Corresponding gains and parameters	Area-1	Area-2	Area-3
PIDN	K_{Pi}*	0.5432	0.5390	0.4726
	K_{Ii}*	0.6494	0.5323	0.4215
	K_{Di}*	0.2478	0.3005	0.3488
	N_i*	15.35	16.82	18.45
FOPID	K_{Pi}*	0.2145	0.2867	0.4787
	K_{Ii}*	0.5744	0.8979	0.8787
	λ_i*	0.9876	0.9136	0.8097
	K_{Di}*	0.9086	0.6121	0.5221
	μ_i*	0.6544	0.9087	0.8979
TIDN	K_{Pi}*	0.8430	0.9509	0.8520
	K_{Ii}*	0.6453	0.6516	0.7607
	K_{Di}*	0.4876	0.5753	0.6887
	N_i*	30.25	37.82	42.45
	n_i*	2.9165	3.1882	3.9425
TIDN-FOID	K_{Pi}*	0.5415	0.6123	0.7332
	K_{Ii}*	0.5431	0.5325	0.5473
	K_{Di}*	0.4766	0.4855	0.4884
	N_i*	56.01	54.11	62.12
	n_i*	8.5420	7.2340	8.9800
	K_{FIi}*	0.6530	0.6425	0.7523
	λ_i*	0.0567	0.0174	0.0161
	K_{FDi}*	0.8531	0.8638	0.8842
	μ_i*	0.1405	0.0112	0.1518

Spotted hyena optimizer (SHO)

The bioinspired meta-heuristic algorithm designated as spotted hyena optimizer (SHO) was developed by Dhiman et. al [46]. SHO was developed after being motivated by behaviour of spotted hyenas. This depicts the social connection amid spotted hyena and their cooperative action. The three measures associated with SHO are tracking down the hunt, enclosing and striking the hunt. In SHO, an appropriate balance is maintained in between exploitation and exploration. This increases the opportunity to achieve overall optima. SHO is markedly different from other algorithms as it performs exploitation and exploration by separate relations. With a vector, $\vec{h}$ the appropriate balance is maintained in between exploitation and exploration by decreasing its value from 5 to 0 over a number of iterations. The coefficient vector $\vec{E}$ half of iterations are specific for exploitation and others for exploration. If $\overrightarrow{|E|} \geq 1$, it indicates exploration, i.e. searching, whereas $\overrightarrow{|E|} \leq 1$ indicates exploitation, i.e. hunting. Thus, this arrangement avoids difficulties related to local optima. The detailed mathematical and theoretical explanation is given in Reference [48]. In SHO, each spotted hyena is allotted with a collection of parameters to be optimized to the extent of higher and lesser limits. Within the extent of values, the perfect measure of parameters should settle. Secondary controllers PIDN/FOPID/TIDN/TIDN-FOID are utilized individually, and individual gains are optimized.

After subsequent initialization concerning input variables related to SHO like a total of search agents and iteration, assessment by simulation is conducted by keeping any of these parameters changing and others unchanging, and the value of Pi_{ISE} is attained using parameters relevant to each hyena. So, later with numerous runs, the value of the varying parameter is carefully chosen associated with least value of Pi_{ISE}. Likewise, the similar procedure is conducted for further parameter maintaining the by now optimized one unchanging. In this manner, best values of SHO parameters are acquired. Tuned values of parameters are number of search agents $n = 50$ and number of iterations = 100. SHO's flowchart is provided in Fig. 4.

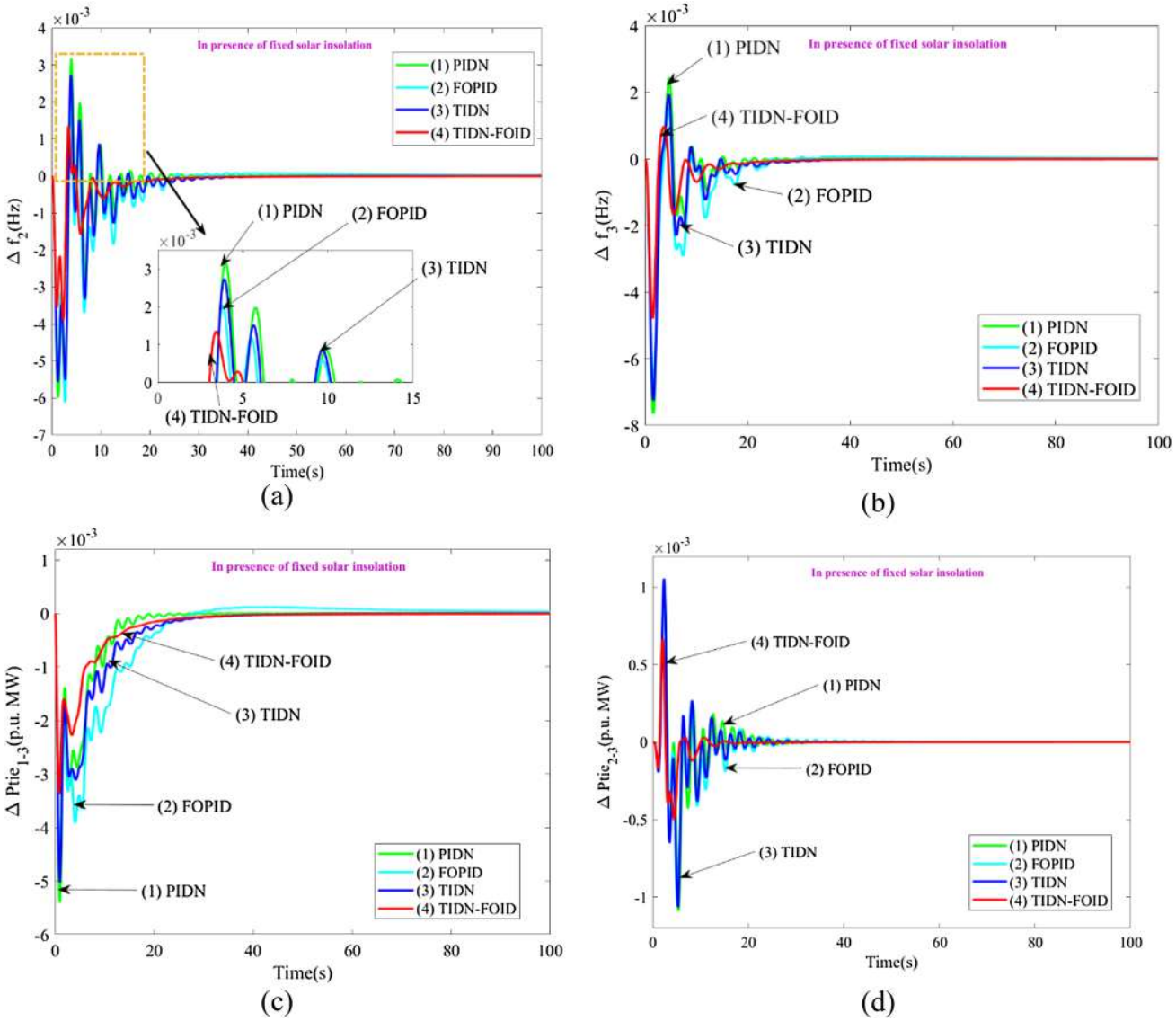

Fig. 6 Assessment of responses of controllers PIDN, FOPID, TIDN and TIDN-FOID for system-2 (only constant solar insolation) for 1% step load disturbance. **a** Area-2 frequency aberration Vs. time, **b** area-3 frequency aberration Vs. time, **c** tie line power aberration for line interconnecting area-1 and area-3 Vs. time, **d** tie line power aberration for line interconnecting area-2 and area-3 Vs. time

The proposed methodology

A three-area system with capacity ratio of 1:3:4 is considered. The investigated system comprises of thermal, solar, SoFC and biodiesel in area-1, thermal, gas and solar in area-2 and thermal, split-shaft gas turbine and solar in area-3. Investigations are carried out by considering proposed TIDN-FOID controller and its gains are optimized by SHO technique considering ISE as a performance index. The optimization technique is coded in MATLAB R2020a software, and the investigated system is modelled in Simulink with the FOMCON toolbox.

Studies are performed for: (a) controller comparison in systems-1 and 2 considering with and without solar having fixed and variable solar insolation; (b) comparison of system dynamics with step and random perturbations in system (a); (c) impact of SoFC on step and random perturbations in system (b); and (d) sensitivity analysis in system (c).

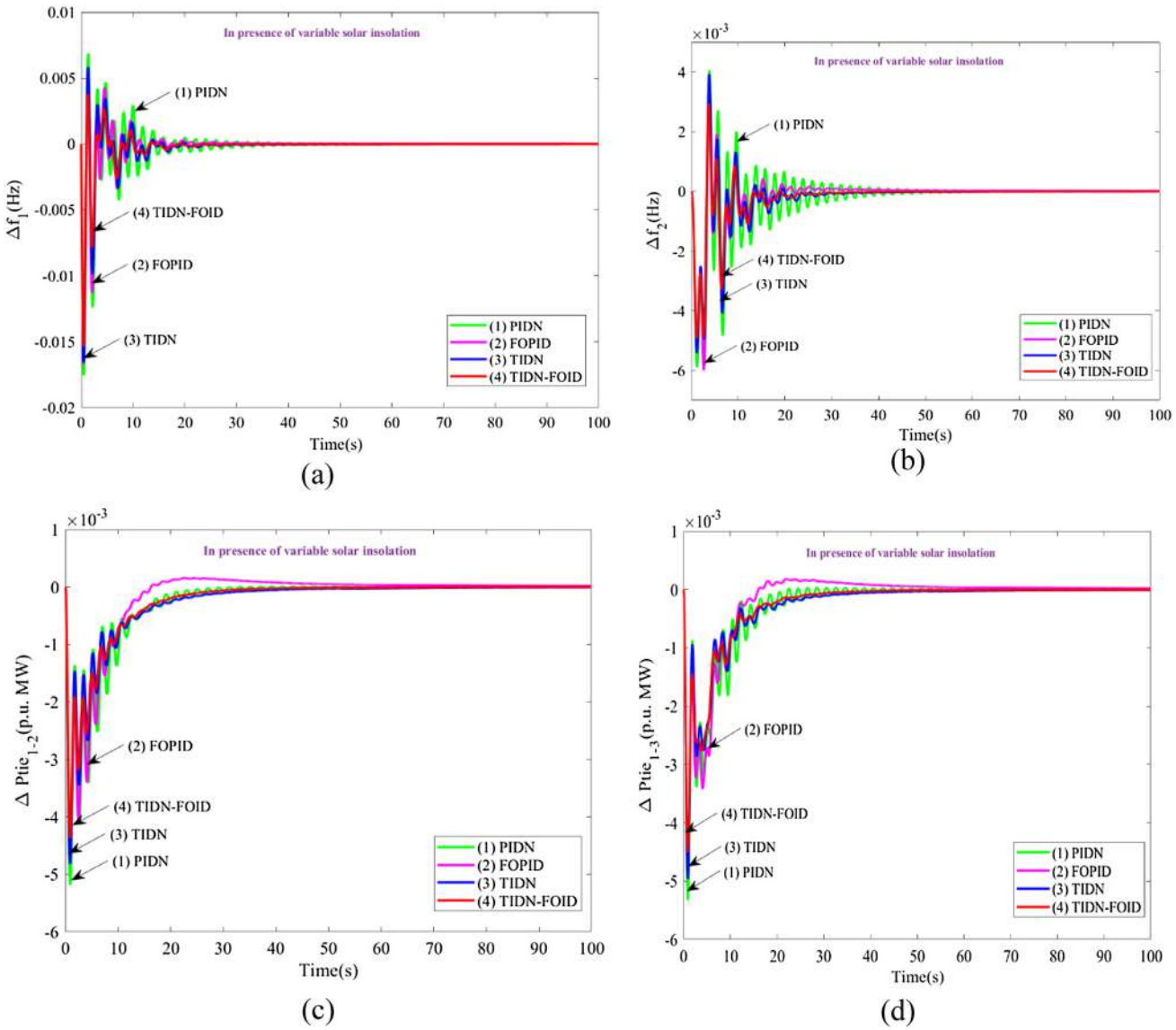

Fig. 7 Assessment of responses of controllers PIDN, FOPID, TIDN and TIDN-FOID for system-2 (only variable solar insolation) for 1% step load disturbance. **a** Area-1 frequency aberration Vs. time, **b** area-2 frequency aberration Vs. time, **c** tie line power aberration for line interconnecting area-1 and area-2 Vs. time, **d** tie line power aberration for line interconnecting area-1 and area-3 Vs. time

Results and assessment

Assessment of dynamic responses for step load disturbance (excluding solar)

The system examined here for assessment includes thermal–biodiesel in area-1, thermal–gas in area-2 and thermal–Ss(GT) in area-3 (system-1). This system is introduced with PIDN/FOPID/TIDN/TIDN-FOID controllers on individual basis. Assessment is performed along with 1% step load disturbance in area-1. The best available values of each of the controller gains and parameters are acquired using SHO, by using Pi_{ISE}. The best possible values are given in Table 1, and with these values, dynamic responses are acquired as shown in Fig. 5a–d. Critical view of each response says about the excellence of TIDN-FOID over other controllers regarding lessened level of peak overshoot, extent of oscillations, peak undershoot as well as settling time. The productivity of SHO is also examined with few other algorithms like PSO, CS and FA for optimization of TIDN-FOID controller parameter values, and in each case, convergence characteristics are acquired and compared in Fig. 5e. It is seen that the convergence characteristics of SHO for the particular system are faster and have lesser value of Pi_{ISE}. The best values

Table 4 Best values of gains and parameters of PIDN, FOPID, TIDN and TIDN-FOID controllers for system-2 (including fixed solar insolation) for random pattern of load

Name of controllers	Corresponding gains and parameters	Area-1	Area-2	Area-3
PIDN	K_{Pi}*	0.6258	0.4721	0.7477
	K_{Ii}*	0.5784	0.5684	0.5648
	K_{Di}*	0.1347	0.2401	0.2271
	N_i*	16.15	11.25	18.50
FOPID	K_{Pi}*	0.3212	0.3656	0.4121
	K_{Ii}*	0.6767	0.8907	0.7907
	λ_i*	0.9778	0.9232	0.9123
	K_{Di}*	0.9898	0.7190	0.6132
	μ_i*	0.6869	0.9876	0.8665
TIDN	K_{Pi}*	0.4514	0.7545	0.7505
	K_{Ii}*	0.6475	0.6462	0.6406
	K_{Di}*	0.5831	0.6401	0.5311
	N_i*	15.25	21.01	21.31
	n_i*	1.2550	1.2551	1.2555
TIDN-FOID	K_{Pi}*	0.9075	0.9381	0.9922
	K_{Ii}*	0.7514	0.7414	0.7315
	K_{Di}*	0.7552	0.7063	0.6824
	N_i*	67.51	63.25	70.51
	n_i*	6.2520	7.1810	5.2851
	K_{FIi}*	0.5110	0.6125	0.7102
	λ_i*	0.7112	0.6288	0.3310
	K_{FDi}*	0.6966	0.9245	0.7558
	μ_i*	0.5555	0.5515	0.5558

of gains and parameters employing varied algorithms are not provided here.

Assessment of dynamic responses for step load disturbance including constant solar insolation

In Sect. 5.1, it is noted that SHO optimized TIDN-FOID controller's response is enhanced compared to other classical controllers. Now, the system with thermal–biodiesel in area-1, thermal–gas in area-2 and thermal–Ss(GT) in area-3 at 1% step load as disturbance is incorporated with solar thermal power plant in each area to perform analysis**.** This system with solar at fixed insolation is introduced with PIDN/FOPID/TIDN/TIDN-FOID controllers on individual basis. The best available values of each of the controller gains and parameters are acquired using SHO, by using Pi_{ISE}. The best possible values are given in Table 2, and with these values, dynamic responses are acquired as shown in Fig. 6. Critical view of each response says about the excellence of TIDN-FOID over other controllers regarding lessened level of peak overshoot, extent of oscillations, peak undershoot as well as settling time even in the presence of fixed solar insolation.

Assessment of dynamic responses for step load disturbance including variable solar insolation

In Sects. 5.1 and 5.2, it is noted that SHO optimized TIDN-FOID controller's response is enhanced compared to other classical controllers in both the absence and the presence of solar, respectively. Now, the system with thermal–biodiesel in area-1, thermal–gas in $area_{-2}$ and thermal–Ss(GT) in area-3 at 1% step load as disturbance is incorporated with solar thermal power plant (variable solar insolation) in each area to perform analysis**.** This system with solar at variable insolation is introduced with PIDN/FOPID/TIDN/TIDN-FOID controllers on individual basis. The best available values of each of the controller gains and parameters are acquired using SHO, by using Pi_{ISE}. The best possible values are given in Table 3, and with these values, dynamic responses are acquired as shown in Fig. 7. Critical view of each response says about the excellence of TIDN-FOID over other controllers regarding lessened level of peak overshoot, extent of oscillations, peak undershoot as well as settling time even in the presence of variable solar insolation.

Assessment of dynamic responses for random pattern of load including solar for fixed insolation

The system examined here for assessment includes thermal–biodiesel in $area_{-1}$, thermal–gas in $area_{-2}$ and thermal–Ss(GT) in $area_{-3}$ along with solar thermal power plant in all areas. This system is introduced with PIDN/FOPID/TIDN/TIDN-FOID controllers on individual basis. Assessment is performed along with random pattern of load as disturbance in area-1. The best available values of each of the controller gains and parameters are acquired using SHO, by using Pi_{ISE}. The best possible values are given in Table 4, and with these values, dynamic responses are acquired as shown in Fig. 8. The random pattern of load considered here is shown in Fig. 8a marked in black bold line. Critical view of each response says about the excellence of TIDN-FOID over other controllers regarding lessened level of peak overshoot, extent of oscillations and peak undershoot.

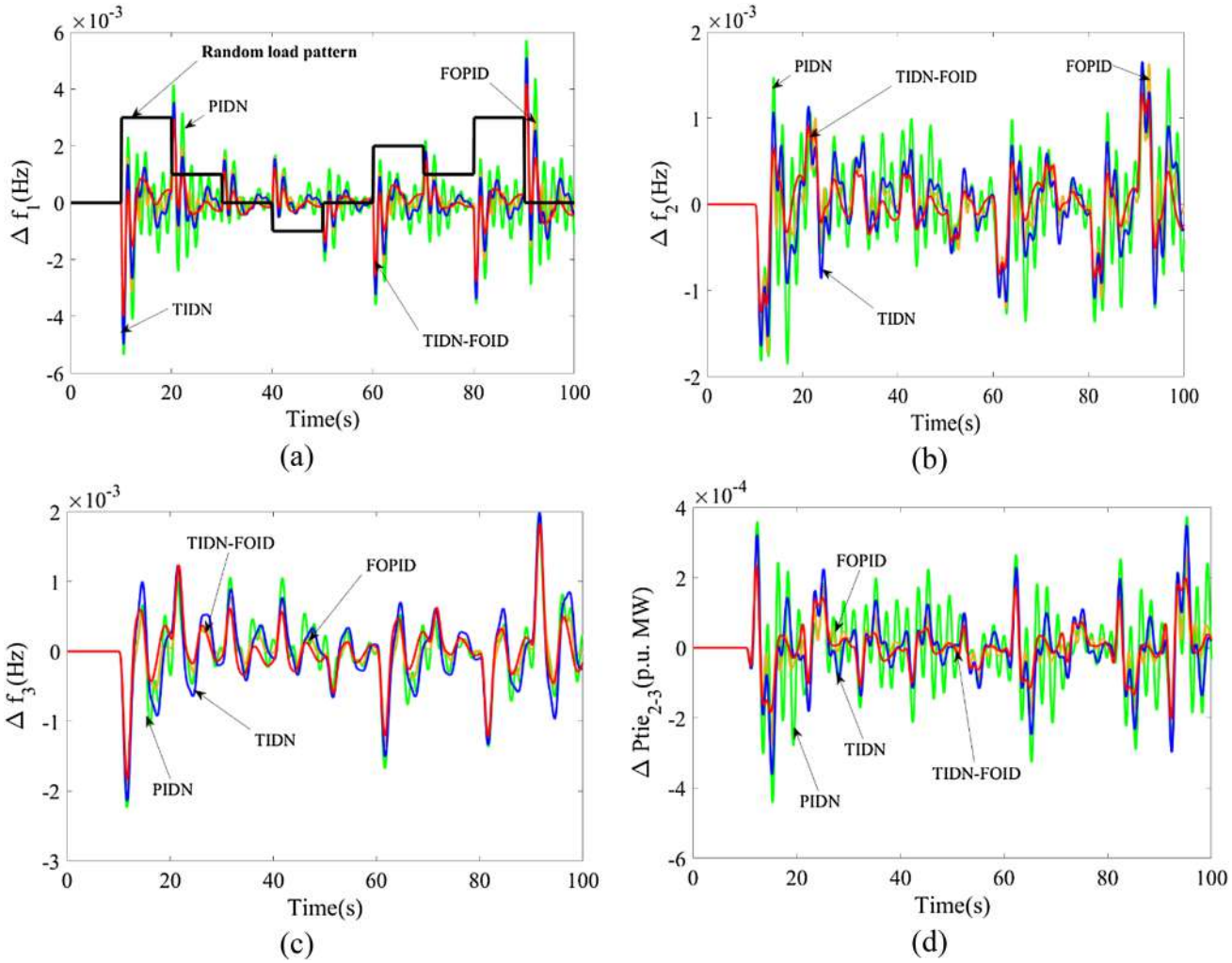

Fig. 8 Assessment of responses of controllers PIDN, FOPID, TIDN and TIDN-FOID for system-2 (only fixed solar insolation) for random load disturbance. **a** Area-1 frequency aberration Vs. time, **b** area-2 frequency aberration Vs. time, **c** area-3 frequency aberration Vs. time, **d** tie line power aberration for line interconnecting area-2 and area-3 Vs. time

Impact of solar on system dynamics considering step load and random load separately

In the above section, it is noted that SHO optimized TIDN-FOID controller's response is enhanced compared to other classical controllers. Now, the impact of solar is examined by comparing its responses with the responses of three-area system excluding solar thermal power plant. TIDN-FOID is considered as secondary controller. The best values of gains are given in Table 1. With these values, the responses are shown in Fig. 9 for systems with and without solar for both 1% step load disturbance and random pattern of load in area-1 as disturbance separately. Critical view of each response says about the excellence of system dynamics in the presence of solar regarding lessened level of peak overshoot, extent of oscillations, peak undershoot as well as settling time using TIDN-FOID controller for 1% step load disturbance. Similarly, in case of random pattern of load TIDN-FOID controller's supremacy is reflected in terms of lessened peak overshoot, extent of oscillations and peak undershoot. Only three responses are provided here for each case.

Impact of SoFC on system dynamics considering step load and random load separately

In the above subsections, it is noted that SHO optimized TIDN-FOID controller's response is enhanced in the presence of solar. Now, the impact of solid oxide fuel cell (SoFC) is examined by comparing its responses with the responses of three-area system including solar thermal power plant. TIDN-FOID is considered as secondary controller. The best values of gains are given in Table 5 for system with 1% step load and random pattern of load

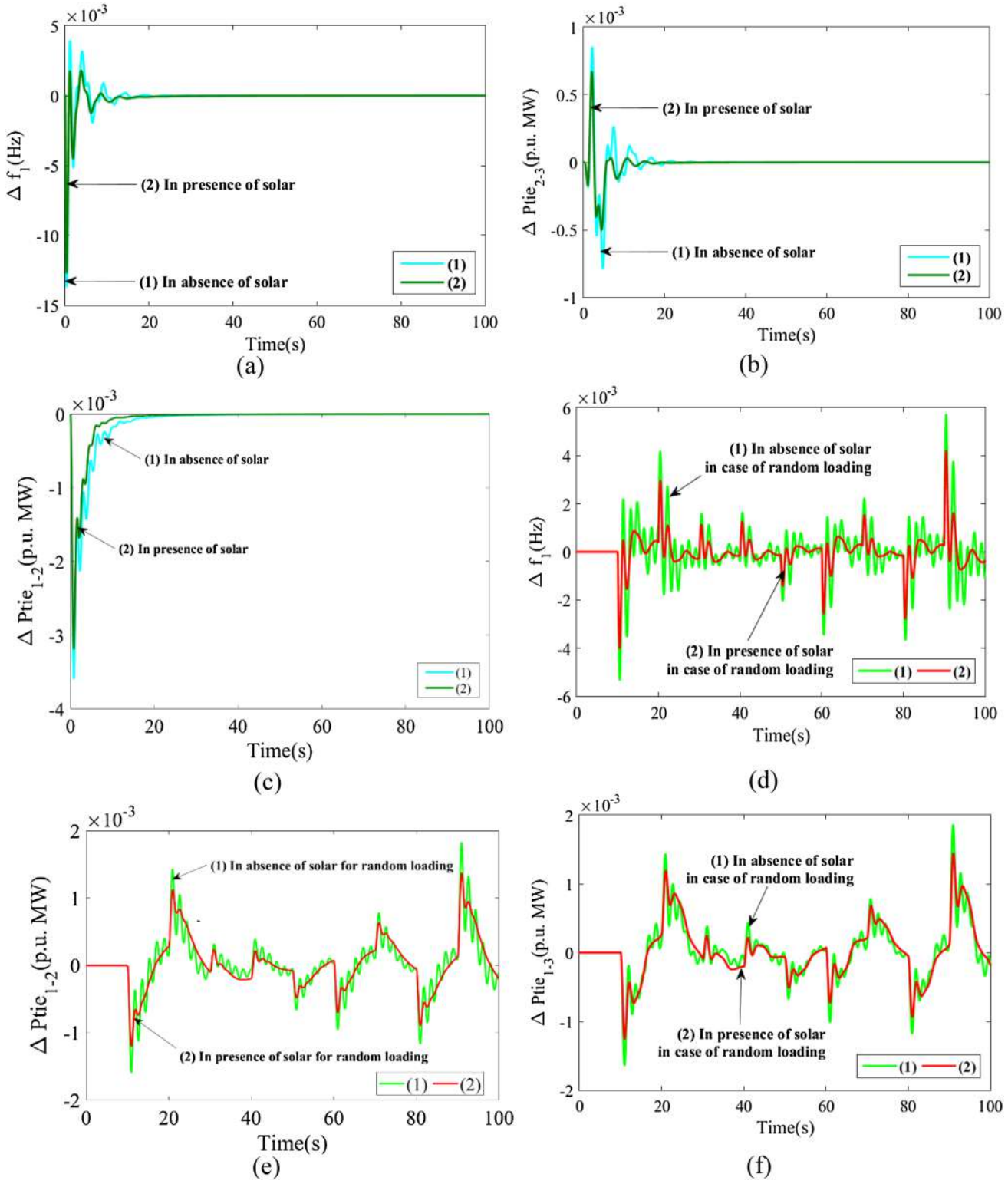

Fig. 9 Assessment of impact of fixed solar insolation on system dynamics using SHO optimized TIDN-FOID controller considering 1% step load and random load pattern of disturbances on individual basis for system-2: **a** area-1 frequency aberration Vs. time (for 1% step load disturbance), **b** tie line power aberration for line interconnecting area-2 and area-3 Vs. time (for 1% step load disturbance), **c** tie line power aberration for line interconnecting area-1 and area-2 Vs. time (for 1% step load disturbance), **d** area-1 frequency aberration Vs. time (random load pattern of disturbance), **e** tie line power aberration for line interconnecting area-1 and area-3 Vs. time (for random load pattern of disturbance), (f) tie line power aberration for line interconnecting area-1 and area-2 Vs. time (for random load pattern of disturbance)

Table 5 Best values of gains and parameters of TIDN-FOID controller for system including solar and SoFC (system-3) for 1% step load and random pattern of load disturbances separately

For 1% step load disturbance				
Name of controllers	Corresponding gains and parameters	Area-1	Area-2	Area-3
TIDN-FOID	K_{Pi}*	0.5998	0.6955	0.6986
	K_{Ii}*	0.4230	0.2341	0.2345
	K_{Di}*	0.9488	0.9519	0.9969
	N_i*	90.53	91.23	94.89
	n_i*	6.2140	8.2250	10.014
	K_{FIi}*	0.9746	0.4079	0.4170
	λ_i*	0.1025	0.2464	0.4607
	K_{FDi}*	0.9864	0.9876	0.9975
	μ_i*	0.2810	0.3206	0.4333
For random pattern of load as disturbance				
TIDN-FOID	K_{Pi}*	0.7435	0.6477	0.7057
	K_{Ii}*	0.4006	0.3007	0.3812
	K_{Di}*	0.8874	0.7649	0.8641
	N_i*	51.23	48.55	62.35
	n_i*	8.2140	9.2250	10.014
	K_{FIi}*	0.4125	0.3314	0.3258
	λ_i*	0.0014	0.0041	0.0041
	K_{FDi}*	0.6452	0.6852	0.5324
	μ_i*	0.0002	0.0001	0.0001

separately. With these values, the responses are shown in Fig. 10 for systems with and without SoFC for both 1% step load disturbance and random pattern of load in area-1 as disturbance separately. Critical view of each response says about the excellence of system dynamics in the presence of SoFC regarding lessened level of peak overshoot, extent of oscillations, peak undershoot as well as settling time using TIDN-FOID controller for 1% step load disturbance. Similarly, in case of random pattern of load TIDN-FOID controller's supremacy is reflected in terms of lessened peak overshoot, extent of oscillations and peak undershoot. Only two responses are provided here for each case.

Sensitivity analysis for higher value of disturbance

Analysis of sensitivity is done to observe the robustness of SHO optimized TIDN-FOID controller gains tracked down at base circumstance to broad alteration in system situation in thermal–biodiesel in $area_{-1}$, thermal–gas in $area_{-2}$ and thermal–Ss(GT) in $area_{-3}$ system along with solar and SoFC. Over here, the examined system is exposed with 3% step load disturbance in $area_{-1}$. The optimized gains of TIDN-FOID controller are given in Table 6 is acquired employing SHO. The dynamic responses for best values comparable to base and varied responses are shown in Fig. 11. Comparison turns out that responses are pretty much alike which insist no additional resetting of best values for alteration in conditions.

Discussion of results

According to the results acquired in the preceding subsections, the remarks are as follows:

a. The proposed TIDN-FOID controller is providing the best results compared to PIDN, FOPID and TIDN for the base system without solar. Critical understanding of each result of Fig. 5 says about the excellence of TIDN-FOID over PIDN/FOPID/TIDN concerning diminished level of peak overshoot ($\Delta f_1 = 0.0041$ Hz, $\Delta f_2 = 0.0034$ Hz, $\Delta Ptie_{1\text{-}2} = 0$ p.u. MW, $\Delta Ptie_{1\text{-}3} = 0$ p.u. MW), extent of oscillations, peak undershoot ($\Delta f_1 = 0.0132$ Hz, $\Delta f_2 = 0.0041$ Hz, $\Delta Ptie_{1\text{-}2} = 0.0036$ p.u. MW, $\Delta Ptie_{1\text{-}3} = 0.0035$ p.u. MW) as well as settling time ($\Delta f_1 = 32.73$ s, $\Delta f_2 = 36.89$ s, $\Delta Ptie_{1\text{-}2} = 33.70$ s, $\Delta Ptie_{1\text{-}3} = 35.45$ s).
b. Also, Fig. 5 shows that SHO optimized TIDN-FOID controller is providing with least value of $PI_{ISE} = 0.00021$, whereas PI_{ISE} values for PSO, CS, FA are 0.00026, 0.00029, 0.00027, respectively.
c. When the base system is inculcated with solar for fixed insolation, it is observed the excellent performance of TIDN-FOID over PIDN/FOPID/TIDN. Critical understanding of each result of Fig. 6 says about

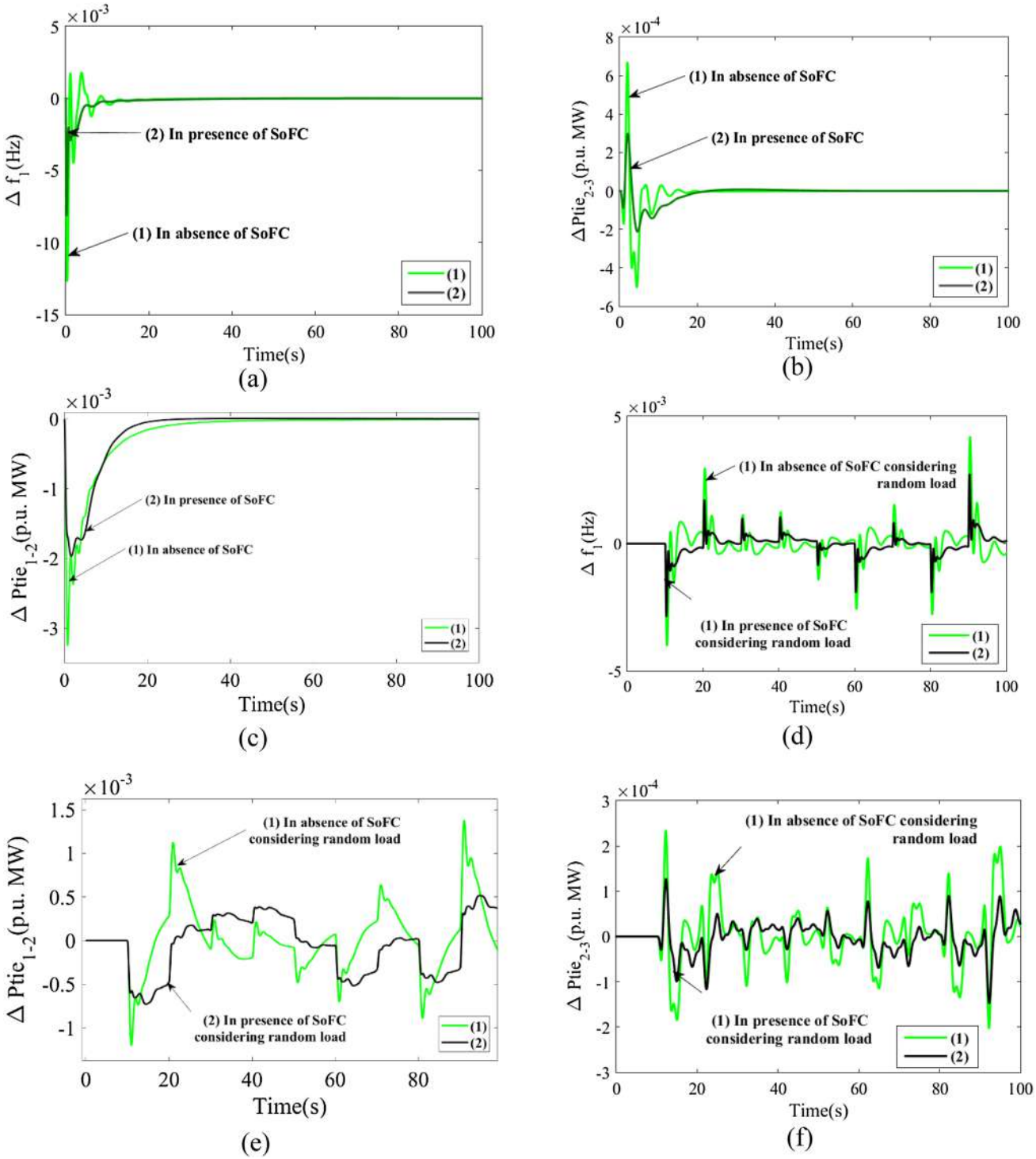

Fig. 10 Assessment of impact of SoFC on system dynamics using SHO optimized TIDN-FOID controller considering 1% step load and random load pattern of disturbances on individual basis for system-3 (in the presence of solar): **a** area-1 frequency aberration Vs. time (for 1% step load disturbance), **b** tie line power aberration for line interconnecting area-2 and area-3 Vs. time (for 1% step load disturbance), **c** tie line power aberration for line interconnecting area-1 and area-2 Vs. time (for 1% step load disturbance), **d** area-1 frequency aberration Vs. time (random load pattern of disturbance), **e** tie line power aberration for line interconnecting area-1 and area-2 Vs. time (for random load pattern of disturbance), **f** tie line power aberration for line interconnecting area-2 and area-3 Vs. time (for random load pattern of disturbance)

Table 6 Best values of gains and parameters of TIDN-FOID controller for system including solar and SoFC for 3% step load disturbance

Name of controllers	Corresponding gains and parameters	Area-1	Area-2	$Area_{-3}$
TIDN-FOID	K_{Pi}*	0.6059	0.7095	0.7012
	K_{Ii}*	0.4562	0.3254	0.3147
	K_{Di}*	0.9120	0.9124	0.9705
	N_i*	89.56	90.36	92.36
	n_i*	6.3021	7.9991	9.9851
	K_{FIi}*	0.9807	0.5141	0.3985
	λ_i*	0.1033	0.3122	0.4512
	K_{FDi}*	0.9877	0.8950	0.9784
	μ_i*	0.2800	0.3155	0.4514

the excellence of TIDN-FOID over PIDN/FOPID/TIDN concerning diminished level of peak overshoot ($\Delta f_2 = 0.0026$ Hz, $\Delta f_3 = 0.0015$ Hz, $\Delta Ptie_{1\text{-}3} = 0$ p.u. MW, $\Delta Ptie_{2\text{-}3} = 0.0061$ p.u. MW), extent of oscillations, peak undershoot ($\Delta f_2 = 0.0038$ Hz, $\Delta f_3 = 0.0044$ Hz, $\Delta Ptie_{1\text{-}3} = 0.0032$ p.u. MW, $\Delta Ptie_{2\text{-}3} = 0.0051$ p.u. MW) as well as settling time ($\Delta f_2 = 28.65$ s, $\Delta f_3 = 33.45$ s, $\Delta Ptie_{1\text{-}3} = 32.34$ s, $\Delta Ptie_{2\text{-}3} = 27.88$ s).

d. Figures 7 and 8 show that the TIDN-FOID controller has better performance over PIDN/FOPID/TIDN when variable solar insolation for step load and fixed solar insolation for random load disturbances, respectively.
e. Figure 9 shows that solar has a noticeable impact on system dynamics while considering fixed solar insolation for step load disturbance in terms of lessened peak undershoot, peak overshoot and settling time. Even

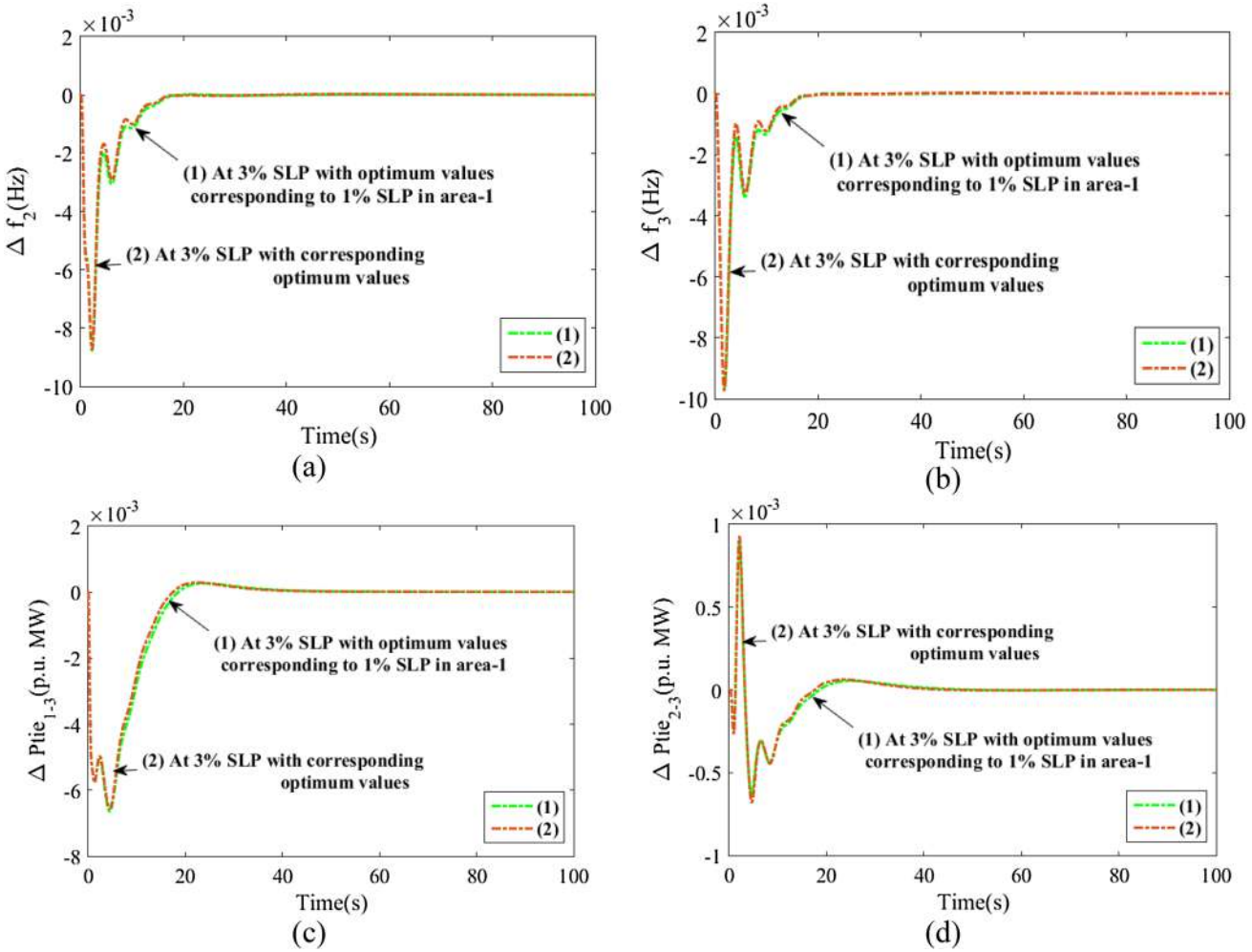

Fig. 11 Assessment of system responses using SHO optimized TIDN-FOID controller when step load disturbance is increased to 3% from 1%: **a** area-2 frequency aberration Vs. time, **b** area-3 frequency aberration Vs. time, **c** tie line power aberration for line interconnecting area-1 and area-3 Vs. time, **d** tie line power aberration for line interconnecting area-2 and area-3 Vs. time

when solar is used with random load, the system dynamics improved with reduced intensity of oscillations.

f. Figure 10 shows that system with SoFC in the presence of fixed insolation has great impact in terms of diminished level of peak overshoot ($\Delta f_1 = 0$ Hz, $\Delta Ptie_{2\text{-}3} = 0.0032$ p.u. MW, $\Delta Ptie_{1\text{-}2} = 0$ p.u. MW), extent of oscillations, peak undershoot overshoot ($\Delta f_1 = 0.0076$ Hz, $\Delta Ptie_{2\text{-}3} = 0.0023$ p.u. MW, $\Delta Ptie_{1\text{-}2} = 0.0019$ p.u. MW) as well as settling time overshoot ($\Delta f_1 = 18.23$ s, $\Delta Ptie_{2\text{-}3} = 22.78$ s, $\Delta Ptie_{1\text{-}2} = 19.56$ s). Also, when SoFC is integrated into the system with random load, the extent of oscillations is improved a lot.

Conclusion

In the present material of work, solar-SoFC has been incorporated first ever in the field of automatic generation control (AGC) under traditional situation. An original effort has been laid down to implement cascade controller with the combination of tilt–integral–derivative with filter (TIDN) and fractional-order integral–derivative (FOID) in AGC. A recently developed bioinspired meta-heuristic algorithm expressed as spotted hyena optimizer (SHO) is efficiently utilized for achieving gains and parameters of different controllers. The excellence of the proposed cascade TIDN-FOID is considered with and without solar and is better than other classical controllers like PIDN, FOPID and TIDN in terms of peak undershoot, peak overshoot and settling time. Also, the performance of the proposed SHO optimization technique provides quick responses and converges faster than cuckoo search (CS), firefly algorithm (FA) and particle swarm optimization (PSO). Also, SHO technique exhibits less error values by 1.941% for CS, 2.415% for FA and 2.884% for PSO techniques. Moreover, the proposed cascade TIDN-FOID controller with the SHO technique enhances system dynamics with variable and random solar insolation over classical controllers. Further, it is evident that with solar integration, considering both fixed and random insolation, the system dynamics are better than the base system alone. Furthermore, investigations are carried out with SoFC integration, considering both fixed and random solar insolation. Studies reveal that with SoFC incorporation, the proposed system has significantly improved responses over solar thermal system. Likewise, system with solar and SoFC, system dynamics such as shown significant improvement in terms of peak overshoot by 86.67%, 98%; peak undershoot by 41.67%, 9.803% and settling time by 33.33%, 18.18% for the system with solar-SoFC and solar alone. A survey of sensitivity analysis for the higher value of disturbance is carried out and it is found that controller values obtained at nominal conditions are robust and need not be reset again.

Similarly, in future the above proposed method of frequency control can also be applied in the combined control of voltage and frequency by connecting automatic voltage regulator with the proposed AGC system. Besides, it can be applied with the combinations of other artificial intelligence techniques.

Appendix

Thermal unit: Tri = 10 s, Kri = 5, Tti = 0.3 s, Tgi = 0.08 s;
Biodiesel: Kvr = 1, Tvr = 0.05 s, Kce = 1, Tce = 0.5 s;
Gas unit: Cg = 1, Xg = 0.6 s, Bg = 0.049 s, Tcd = 0.2 s, Yg = 1.1 s, Tf = 0.239 s, Tcr = -0.01 s;
Ss(GT): $L_{max} = 1$, $T_3 = 3$ s, $T_1 = T_2 = 1.5$ s, $K_T = 1$, $FOV_{max} = 1$, $FOV_{min} = -0.02$, $D_{tur} = 0$ p.u;
Solar: $T_s = 1.8$ s, $K_s = 1.8$, $T_{ts} = 3.0$ s, $T_{gs} = 1.0$ s;
SoFC: $K_{SoFC} = 1$, $T_{SoFC} = 0.2$ s.

Acknowledgements The authors express their thankfulness to the administrative section and EE department of Regent Education & Research Foundation Group of Institutions for providing essential amenities to achieve the current effort.

Declarations

Conflict of interest The authors affirm that they have not any recognized challenging fiscal interests or private associations that could have seemed to affect the effort stated in this work.

References

1. Elgerd, O.I.: Electric energy systems theory: an introduction. Tata McGraw-Hill, New Delhi (2007)
2. Kundur, P.: Power system stability and control. Mc Graw Hill, New York (1993)
3. Ibraheem Kumar, P., Kothari, D.P.: Recent philosophies of automatic generation control strategies in power systems. IEEE Trans. Power Syst. **20**(1), 346–357 (2005)
4. Elgerd, O.I., Fosha, C.E.: Optimum megawatt-frequency control of multiarea electric energy systems. IEEE Trans. Power Appar. Syst. **89**(4), 556–563 (1970)
5. Das, D., Adityaa, S.K., Kothari, D.P.: Dynamics of diesel and wind turbine generators on an isolated power system. Electr. Power Energy Syst. **21**, 183–189 (1999)
6. Ch, D.D., Roy, A.K., Sinha, N.: GA based frequency controller for solar thermal–diesel–wind hybrid energy generation/energy storage system. Int J Elect Pow Ener Sys. **43**(1), 262–279 (2012)
7. Ismayil, C., Sreerama, K.R., Sindhu, T.K.: Automatic generation control of single area thermal power system with fractional

order PID ($PI^{\lambda}D^{\mu}$) controllers. In Third Int. Conf. on Advances in Control and Optimization of Dynamical Systems, March 13–15, (2014). Kanpur, India: pp.552–557.
8. Babu, N.R., Saikia, L.C.: AGC of a multiarea system incorporating accurate HVDC and precise wind turbine systems. Int. Trans. Elect. Energy Sys. **30**(4), e12277 (2020)
9. Ramoji, S.K., Saikia, L.C.: Optimal coordinated frequency and voltage control of CCGT-thermal plants with TIDF CONTROLLER. IETE J. Res. (2021). https://doi.org/10.1080/03772063.2021.1959420
10. Sharma, M., Dhundhara, S., Arya, Y., Prakash, S.: Frequency excursion mitigation strategy using a novel COA optimised fuzzy controller in wind integrated power systems. IET Renew Power Generat **14**, 4071–4085 (2020)
11. Kumar, B., Adhikari, S., Datta, S., Sinha, N.: Real time simulation for load frequency control of multisource microgrid system using grey wolf optimization based modified bias coefficient diagram method (GWOMBCDM) controller. J. Electr. Eng. Technol. **16**(1), 205–221 (2021)
12. Mandeep, S., Bansal, R.K., Prakash, S., Sajjad, A.M.V.O.: Algorithm based LFC design of a six-area hybrid diverse power system integrating IPFC and RFB. IETE J. Res. **67**(3), 394–407 (2021)
13. Nanda, J., Mangla, A., Suri, S.: Some new findings on automatic generation control of an interconnected hydrothermal system with conventional controllers. IEEE Trans Energy Convers **21**(1), 187–194 (2006)
14. Saikia, L.C., Chowdhury, A., Shakya, N., et al.: AGC of a multi area thermal system using firefly optimized IDF controller. India Conf. (INDICON), IEEE, Mumbai, India (2013)
15. Pradhan, P.C., Sahu, R.K., Panda, S.: Firefly algorithm optimized fuzzy PID controller for AGC of multi-area multi-source power systems with UPFC and SMES. Eng Sci Technol, Int J. **19**(1), 338–354 (2016)
16. Saha, A., Saikia, L.C.: Renewable energy source-based multiarea AGC system with integration of EV utilizing cascade controller considering time delay. Int Trans Electr Energy Sys. **29**(1), e2646 (2019)
17. Sharma, Y., Saikia, L.C.: Automatic generation control of a multi-area ST—thermal power system using grey wolf optimizer algorithm based classical controllers. Electr. Power Energy Syst. **73**, 853–862 (2015)
18. Saha, A., Saikia, L.C.: Utilisation of ultra-capacitor in load frequency control under restructured STPP-thermal power systems using WOA optimised PIDN-FOPD controller. IET Gener. Transm. Distrib. **11**(13), 3318–3331 (2017)
19. Dutta, A., Prakash, S.: Load frequency control of multi-area hybrid power system integrated with renewable energy sources utilizing FACTS & energy storage system. Environ Prog Sustain Energy. **39**, e13329 (2020). https://doi.org/10.1002/ep.13329
20. Barik, A.K., Das, D.C.: Expeditious frequency control of solar photobiotic/biogas/biodiesel generator based isolated renewable microgrid using grasshopper optimisation algorithm. IET Renew. Power Gener. **12**(14), 1659–1667 (2018)
21. Gupta, N., Kumar, N.: Particle swarm optimization based automatic generation control of interconnected power system incorporating battery energy. Procedia Computer Science. **132**, 1562–1569 (2018)
22. Arya, Y.: Effect of energy storage systems on automatic generation control of interconnected traditional and restructured energy systems. Int. J. Energy Res. **43**, 6475–6493 (2019)
23. Tasnin, W., Saikia, L.C.: Performance comparison of several energy storage devices in deregulated AGC of a multi-area system incorporating geothermal power plant. IET Renew. Power Gener. **12**(7), 761–772 (2018)
24. Deng, Z., Cao, H., Li, X., et al.: Generalized predictive control for fractional order dynamic model of solid oxide fuel cell output power. J. Power Sources. **195**, 8097–8103 (2010)
25. Pathak, N., Verma, A., Bhatti, T.S., Nasiruddin, I.: Modeling of HVDC tie-links and their utilization in AGC/LFC operations of multi-area power systems. IEEE Trans Ind Electr (2019). https://doi.org/10.1109/TIE.2018.2835387
26. Kumari, N., Malik, N., Jha, A.N., Mallesham, G.: Design of PI controller for automatic generation control of multi area interconnected power system using bacterial foraging optimization. Int. J. Eng Tech. **8**(6), 2779–2786 (2016)
27. Jagatheesan, K., Anand, B., Samanta, S., Dey, N., Ashour, A.S., Balas, V.E.: Design of a proportional-integral-derivative controller for an automatic generation control of multi-area power thermal systems using firefly algorithm. IEEE/CAA J Autom Sinica (2019). https://doi.org/10.1109/JAS.2017.7510436
28. Dash, P., Saikia, L.C., Sinha, N.: Comparison of performances of several FACTS devices using Cuckoo search algorithm optimized 2DOF controllers in multi-area AGC. Electr. Power Energy Syst. **65**, 316–324 (2015)
29. Rahman, A., Saikia, L.C., Sinha, N.: AGC of dish-stirling solar thermal integrated thermal system with biogeography based optimised three degree of freedom PID controller. IET Renew. Power Gener. **10**(8), 1161–1170 (2016)
30. Reddy P. J., Kumar T. A.: AGC of three-area hydro-thermal system in deregulated environment using FOPI and IPFC. 2017 International Conference on Energy, Communication, Data Analytics and Soft Computing (ICECDS), Chennai; 2017: pp.2815–2821, doi: https://doi.org/10.1109/ICECDS.2017.8389969
31. Pan, I., Das, S.: Fractional order AGC for distributed energy resources using robust optimization. IEEE Trans on Smart Grid. **7**(5), 2175–2186 (2016)
32. Ismayil, C., Sreerama, K.R., Sindhu, T.K.: Fractional order PID controller for automatic generation control of multiarea power systems. Int Trans Electr Energy Sys. **25**, 3329–3348 (2015)
33. Rambabu N., Narrisetty V., Saikia L.C.: Maiden Application of Coyote Optimizer Algorithm with TIDN Controller in AGC of a Multi-Area Multi-Source System. 2019 IEEE 16th India Council International Conference (INDICON); pp. 1–4.
34. Sharma, M., Prakash, S., Saxena, S., Dhundhara, S.: Optimal fractional-order tilted-integral-derivative controller for frequency stabilization in hybrid power system using Salp swarm algorithm. Electr Power Comp Sys **48**(18), 1912–1931 (2020). https://doi.org/10.1080/15325008.2021.1906792
35. Elsisi, M.: Optimal design of nonlinear model predictive controller based on new modified multitracker optimization algorithm. Int J Intell Syst. **35**, 1857–1878 (2020). https://doi.org/10.1002/int.22275
36. Dash, P., Saikia, L.C., Sinha, N.: Flower pollination algorithm optimized PI-PD cascade controller in automatic generation control of a multi-area power system. Int. J. Electr. Power Energy Syst. **82**, 19–28 (2016)
37. Haroun, A.H.G., Li, Y.-Y.: A novel optimized hybrid fuzzy logic intelligent PID controller for an interconnected multi-area power system with physical constraints and boiler dynamics. ISA Trans. **71**(2), 364–379 (2017)
38. Padhan, S., Sahu, R.K., Panda, S.: Application of firefly algorithm for load frequency control of multi-area interconnected power system. Electr. Power Compon. Syst. **42**(13), 1419–1430 (2014)
39. Sahu, R.K., Panda, S., Rout, U.K.: DE optimized parallel 2-DOF PID controller for load frequency control of power system with governor dead-band nonlinearity. Electr Power Energy Sys **49**, 19–33 (2013)

40. Saha, A., Saikia, L.C.: Combined application of redox flow battery and DC link in restructured AGC system in the presence of WTS and DSTS in distributed generation unit. IET Gener. Transm. Distrib. **12**(9), 2072–2085 (2018)
41. Choudhary, A.K., Prakash, S., Sharma, M., Dhundhara, S.: Grasshopper optimisation based robust power/frequency regulator for shipboard micro-grid. IET Renew. Power Gener. **14**(17), 3568–3577 (2020)
42. Elsisi, M., Abdelfattah, H.: New design of variable structure control based on lightning search algorithm for nuclear reactor power system considering load-following operation. Nucl. Eng. Technol. **52**(3), 544–551 (2020)
43. Elsisi, M.: Improved grey wolf optimizer based on opposition and quasi learning approaches for optimization: case study autonomous vehicle including vision system. Artif Intell Rev (2022). https://doi.org/10.1007/s10462-022-10137-0
44. Bhatt, P., Roy, R., Ghoshal, S.P.: GA/particle swarm intelligence-based optimization of two specific varieties of controller devices applied to two-area multi-units automatic generation control. Int. J. Electr. Power Energy Syst. **32**(4), 299–310 (2010)
45. Babu, N.R., Saikia, L.C.: Automatic generation control of a solar thermal and dish-stirling solar thermal system integrated multi-area system incorporating accurate HVDC link model using crow search algorithm optimised FOPI Minus FODF controller. IET Renew. Power Gener. **13**(12), 2221–2231 (2019)
46. Dhiman, G., Kumar, V.: Spotted hyena optimizer: a novel bio-inspired based metaheuristic technique for engineering applications. Adv. Eng. Softw. **114**, 48–70 (2017)
47. Ranganayakulua, R., Bhaskar, R.U., Babu, G., Seshagiri, A.R., Dipesh, S.P.: A comparative study of fractional order PIλ/PIλDμ tuning rules for stable first order plus time delay processes. Resour-Effic Technol **12**(1), S136–S152 (2016)
48. Oustaloup, A., Mathieu, B., Lanusse, P.: The CRONE control of resonant plants: application to a flexible transmission. Eur J Contr **1**(2), 113–121 (1995)

International Journal of Energy and Environmental Engineering (2023) 14:889–903
https://doi.org/10.1007/s40095-022-00554-w

ORIGINAL RESEARCH

Spatial modelling and policy evaluation of the offshore wind potential for a small oceanic island: the case of Mauritius

Jay Rovisham Singh Doorga[1] · Zyaad Boodoo[1] · Tyagaraja S. M. Cunden[1] · Yogeshwarsing Calleecharan[1] · Rajeev Khoodeeram[1]

Received: 14 June 2022 / Accepted: 29 November 2022 / Published online: 15 December 2022

Abstract

The identification of offshore wind farms necessitates the consideration of multiple factors, including technical, social, economic, and ecological ones, amongst others. In the current study, a multi-criterial model is applied by incorporating wind speed, water depth, grid proximity, tourism activities, and marine spatial constraint factors to determine optimum sites for offshore wind farm placements in the Republic of Mauritius. The North-Eastern region, off the coast of Grand Gaube, has been found to be promising, with an annual electricity potential of 1650 GWh, owing to favourable wind regime of about 7.95 m/s at 100 m height. Moreover, the site location, at an average water depth of 38 m, favours the adoption of conventional jacket foundation. A levelized cost analysis reveals that the electricity generated from the offshore farm would be priced at $163/MWh, which makes it cost-competitive as compared to heavy fuel oil at $218/MWh. A scenario looking at the installation of a 608 MW offshore wind plant, which represents the theoretical maximum that may be attained in the optimum region identified, revealed that exploitation of this site has the potential to decrease up to 1.5 times the share of imported fuel oil and diesel for electricity needs. Besides providing guidelines for the implementation of offshore wind technology in Mauritius, the paper reflects on important gaps for adoption, including factors that seek to ease policy uptake.

✉ Jay Rovisham Singh Doorga
jdoorga@udm.ac.mu

Zyaad Boodoo
zboodoo@udm.ac.mu

Tyagaraja S. M. Cunden
tcunden@udm.ac.mu

Yogeshwarsing Calleecharan
ycalleecharan@udm.ac.mu

Rajeev Khoodeeram
rkhoodeeram@udm.ac.mu

[1] Faculty of Sustainable Development and Engineering, Université Des Mascareignes, Beau Bassin-Rose Hill, Mauritius

Graphical abstract

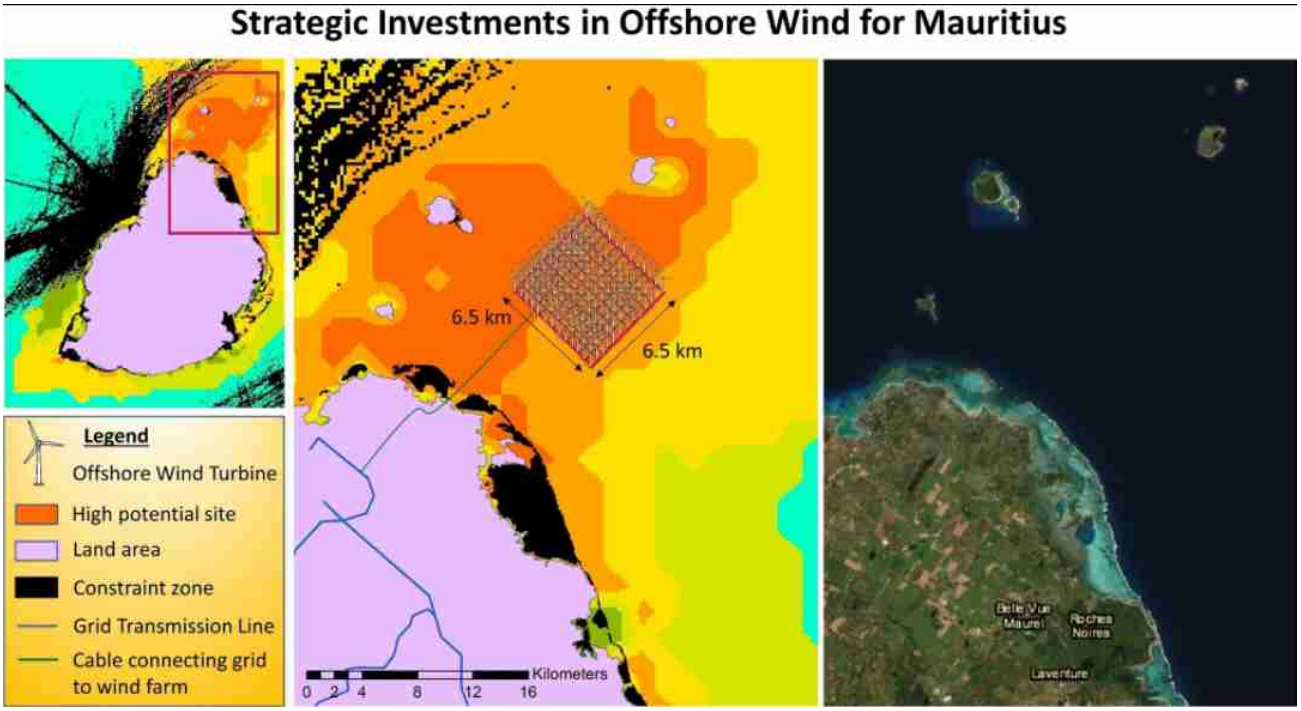

Keywords Offshore wind · GIS · MCDA · Decarbonization · Renewable energy · Mauritius

Introduction

Founded on a mixed developing economic system based on the agricultural, tourism, exportation, and financial services sectors, the island of Mauritius is heavily reliant on the importation of fossil fuels to power its economy. An estimated 84% of the primary energy requirement of the country is met by imported fossil fuels, notably oil and coal, with the energy sector alone accounting for nearly 62% of the national greenhouse gas emissions [47]. This heavy dependence on imported fossil fuels is further compounded by the high vulnerability of the country to fossil fuel market dynamics, including price volatility, quality and availability, resulting in unwavering energy security issues. Supply interruptions and shocks in the global energy system, prevalent during the COVID pandemic period, have had significant repercussions in the power and transport sectors of vulnerable fossil fuel-dependent island nations like Mauritius [20]. It is essential for the country to improve its resilience whilst stimulating economic recovery and sustainable development in the post-pandemic period. This requirement has been even more stressed recently, whereby energy prices have soared to unprecedented levels following the ripple effects of the conflict between Russia and Ukraine. An accelerated energy transition through investments in renewable energy would, therefore, help the country in its key endeavour to attain energy security and at the same time contribute to the overarching goal of decarbonizing its carbon-intensive grid in line with its latest Nationally Determined Contribution under the Paris Agreement [9, 49].

Over the past two decades, a panoply of policy instruments and programs has been implemented in Mauritius to boost the renewable energy sector. A Small-Scale Distributed Generation (SSDG) scheme, funded by the Government of Mauritius with UNDP support in 2010, supported the integration of small-scale (< 50 kW) photovoltaic (PV) panels and wind turbines through a targeted Feed-in Tariff (FiT) scheme [15]. Another more recent policy instrument employed includes a net-meting scheme which is benefiting around 2000 small power producers around the island who are generating electricity using PV and wind energy technologies for a total capacity of 5 MW [19]. The recent budget 2021/2022 of Mauritius provides incentives towards sustainable energy generation and proposes the renewable energy sector as a new pillar of economic growth [10]. As part of the measures put forward to ramp up renewable energy generation from 13 to 60% by 2030, a detailed feasibility study is planned to be conducted in order to investigate the offshore wind energy potential for electricity generation [10]. In this vein, the findings of the present paper can support for

science-based policy decision-making by guiding the cost-effective implementation of an offshore wind farm, thereby enabling to increase the share of renewables in the energy mix of Mauritius. The electricity generated from renewables was estimated at 688 GWh in 2020, representing a share of 23.9% of the electricity generation mix [39]. Onshore wind, with an electricity generation potential of 18 GWh in 2020, contributed only 0.6% of the electricity requirement of the country [39]. Generating electricity from offshore wind can significantly increase the share of renewables in the mix.

Offshore wind potential assessments of Mauritius have revealed the higher energy resource potentials of the offshore regions of the island as compared to onshore sites. It is estimated that at 80 m height, about 2.3–3.4 times higher wind power densities are yielded near the south-eastern offshore coast, with values attaining 420 W/m^2, as compared to inland regions at 66 m height [38]. The Southern and North-Eastern offshore regions of the island yield 1.8–2.5 times higher wind power densities attaining about 450 W/m^2 at 100 m height as compared to the onshore region at 110 m height [38]. As of 2020, the global offshore wind energy capacity was 34.4 GW, representing an increase of 21.2% as compared to 2019 [21]. The experience gained through the growth of installed offshore wind capacity in addition to material and technological developments has contributed in lowering the upfront investment costs associated with offshore wind turbines. The construction of offshore wind facilities has registered the fastest cost reduction of any renewable energy source in 2019 attaining $78/MWh, which represents a drop in price of 32% as compared to 2018 [1]. In Europe, offshore wind power has become cost-competitive with conventional fossil fuels since 2017 [4]. Projections made by the European Union for offshore wind turbines suggest that a reduction in the capital investment cost of more than 50% and a prolongation of the technical lifetime from 20 to 30 years could be attained by 2050 [23]. In addition to the promising future economic prospects offered by offshore wind facilities, the fact that they are placed at sea is a huge benefit, especially for an island like Mauritius with land scarcity issues.

The suitable planning of offshore wind farms necessitates the consideration of multiple factors, ranging from the climatic suitability of the site pertaining to appropriate offshore wind regimes, geotechnical land properties of the bottom seafloor section, and geospatial constraints associated with shipping routes, amongst others. Multi-Criteria Decision Analysis (MCDA) is a useful tool that allows the structuring of a complex multi-dimensional problem [32]. Schillings et al. [37] resorted to the MCDA technique to investigate the offshore wind potential of the North Sea and to limit conflicts that may arise due to existing sea uses that may interfere with the placement of an offshore wind farm. The offshore wind energy potential of the UK was investigated using a multi-criterial model set up by Cavazzi and Dutton [3] which enables the simulation of technical and economic aspects for proper offshore wind farm planning. An assessment of the offshore wind potential using the MCDA approach in the Gulf of Thailand revealed a technical power potential amounting to 7000 MW, with a generation potential of 15 TWh/year [53]. Mahdy and Bahaj [25] conducted an MCDA to investigate the offshore wind potential of Egypt and was able to identify three highly suitable areas with minimum restrictions, with the capacity to generate 33 GW of wind power.

The innovation of the current study is that it seeks to fill the important gap in literature pertaining to unveiling the techno-economic offshore wind potential of small islands. Such locations have specificities inherent to their physical characteristic and socio-economic contexts—characterized by space and resource limitations, economies that are highly vulnerable to external shocks, reliance on foreign direct investment coming from tourism, which, in turn, is dependent upon fragile ecosystems, amongst others. There are relatively few papers in literature regarding assessments of offshore wind potentials for small islands, and the research presented in this paper aims to address this gap. Moreover, the current paper is amongst the few ones to incorporate tourism activities as an important factor which dictates the placement of offshore wind farms. Being an island, which is heavily dependent on the tourism economy, implies that the inclusion of the tourism activity factor is key for optimum siting of offshore wind power plants in Mauritius.

In the current study, the MCDA technique is adopted to identify highly suitable sites for the constructions of offshore wind farms in the territorial waters of Mauritius. The technical power potential of the farm is revealed, and an economic feasibility assessment is performed to evaluate its economic potential as compared to conventional fossil fuel use for electricity generation. We also reflect on important gaps for adoption, including factors that seek to ease policy uptake.

We begin by contextualizing the research and by describing the area of study. The materials and methodology adopted in the current study are thereafter elaborated. The theoretical foundations underlying the methods used to investigate the offshore wind potential of Mauritius are described in the methodological section. The results of the study are then presented, followed by an in-depth discussion that aims to provide for a scientifically informed guide for the development of offshore wind farms at the identified sites.

Study area

The Republic of Mauritius, situated in the South-West Indian Ocean to the east of Madagascar, has a large Exclusive Economic Zone (EEZ) of 2.3 million km^2 (Fig. 1a).

Since 2012, it shares a joint management area with the Seychelles which extends over 396,000 km^2 of the Continental Shelf. Mauritius Island sits on the Mascarene Plateau (Fig. 1b) which arches about 2000 km across the western Indian Ocean up to the Seychelles, and hosts a rich and diverse ecosystem on the mid-oceanic plateau at water depths of about 100 m [7]. The shallower regions are found on the plateau extending in the Northern offshore waters of the island, in contrast with the deeper sections on the southern latitudes where the bathymetric gradient is steeper. Marine spatial constraints are mainly concentrated within the vicinity of the lagoon (Fig. 1c), enclosed by a near-continuous coral reef, and which comprises of fishing reserves and Marine Parks which are secured under the Fisheries and Marine Resources Act 2007. Inscribed as a UNESCO World Heritage Site, Le Morne Cultural Landscape is protected by a strict legal framework under the National Heritage Trust Fund Act 2004, as delineated in Fig. 1c.

Materials and methods

Framework overview

The framework adopted to investigate the offshore wind energy potential of Mauritius is shown in Fig. 2. Initially, the geospatial constraints prohibiting the construction of an offshore wind facility are identified. The MCDA process begins with the identification of criteria that influence the placement of the offshore wind farm. Analytical Hierarchy Process (AHP) technique is thereafter used to determine the importance of each criterion through a pairwise comparison process which results in the allocation of factor weights. Suitably weighted factors are then combined using the Weighted Linear Combination (WLC) process to identify feasible and unfeasible regions for exploitation. Prohibited regions identified at an earlier stage are then excluded from the analysis to reveal only feasible sites that are graded based on their potential for exploitation. The highest potential regions identified are further probed to determine the technical and economic appropriateness for offshore wind farm implementation.

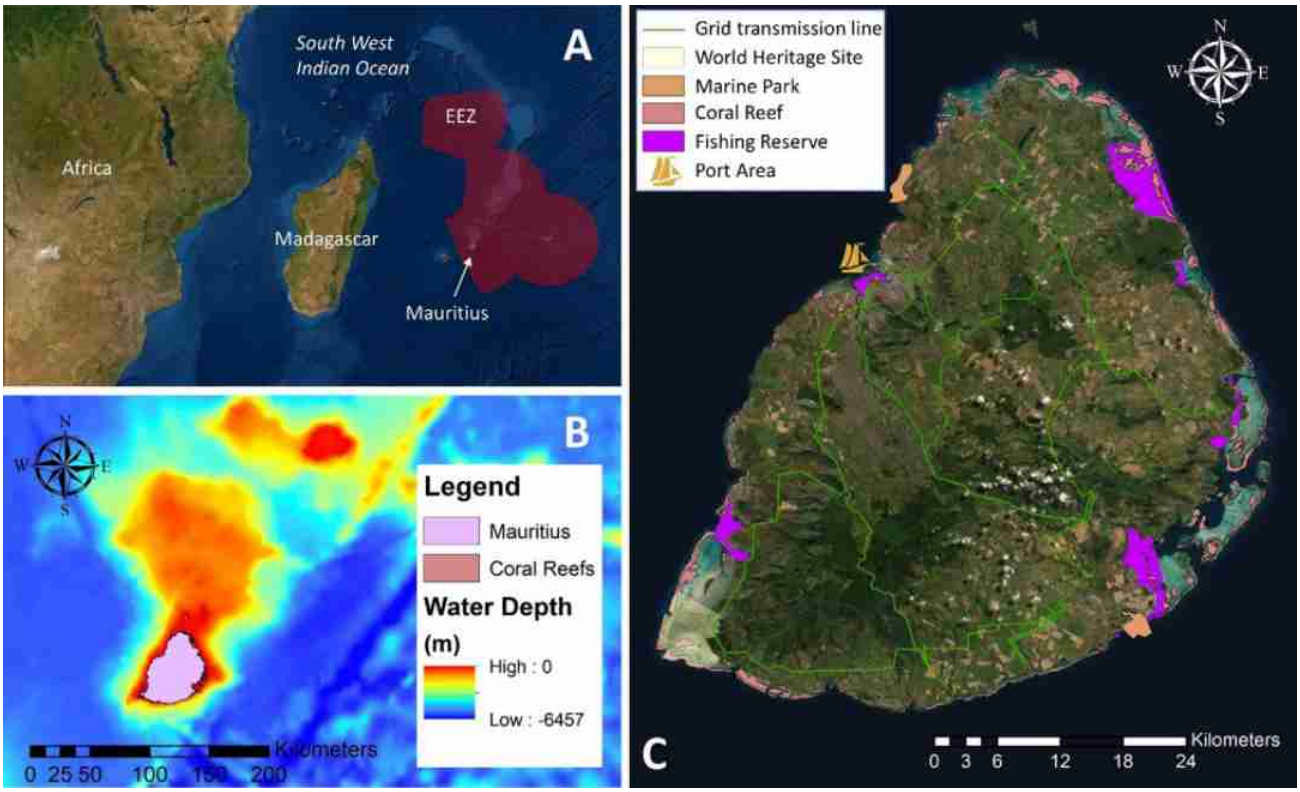

Fig. 1 **a** Location of Mauritius in the South-West Indian Ocean and extent of its Exclusive Economic Zone (EEZ). **b** Bathymetric chart of the South-Western Indian Ocean in the vicinity of Mauritius Island. **c** Location of some nearshore marine spatial constraints for Mauritius

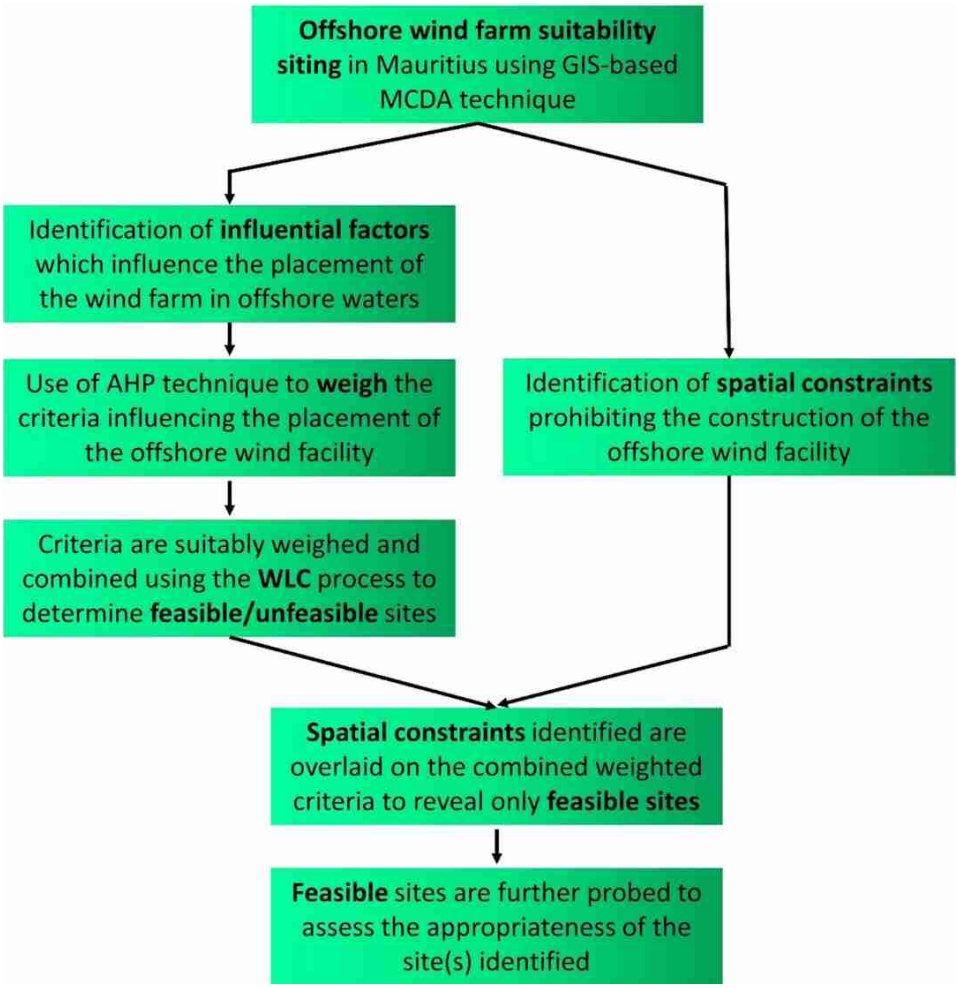

Fig. 2 Methodology adopted to determine the optimum siting and arrangement of an offshore wind facility in waters of Mauritius

Geospatial optimization

GIS-based MCDM

The main processes underlying the GIS-based MCDA approach involve deriving criteria weights through the Analytical Hierarchy Process (AHP) and combining the factors using the WLC process. Both processes are illustrated in the following subsections.

Analytical hierarchy process (AHP) Offshore wind farm siting necessitates the consideration of multiple quantitative and qualitative factors that may influence its placement in the offshore waters. The unstructured nature of the site-suitability analysis confers some degree of complexity to this multi-dimensional problem. Consequently, the AHP approach introduced by Saaty [35] is generally used to reduce the level of complexity through the proper structuring of a decision-making problem into a hierarchical representation. The process involves pairwise comparisons of criteria based on a common scale of measurement, referred to as the Saaty Scale, as presented in Table 1. The result of this pairwise comparison leads to a decision matrix which influences the weights of the elements that make up the analysis, hence giving a structure to the decision problem.

Evaluation matrix A, shown next in Eq. 1, is acquired through the pairwise comparisons of n criteria. The element a_{ij} $(i, j = 1, 2, 3, \ldots, n)$ indicates the quotient of weight.

$$A = \begin{bmatrix} a_{11} & a_{12} & \ldots & a_{1n} \\ a_{21} & a_{22} & \ldots & a_{2n} \\ \vdots & \vdots & \ddots & \vdots \\ a_{n1} & a_{n2} & \ldots & a_{nn} \end{bmatrix}, a_{ii} = 1, a_{ij} = \frac{1}{a_{ji}}, a_{ji} \neq 0 \quad (1)$$

The relative weights, A_w, of the decision matrix above is calculated using the right eigenvector, w, corresponding to the maximum eigenvalue, $\lambda_{\max}$, as shown in Eq. 2:

$$A_w = \lambda_{\max} w \quad (2)$$

In order to ensure that consistency is maintained in the pairwise comparisons performed, a consistency check is performed, as presented in Eq. 3. The check is performed

Table 1 Saaty's fundamental scale for pairwise comparisons

Intensity of importance	Definition	Explanation
1	Equally significant	Two elements contributing equally to the objective
3	Moderate significance	Experience and judgement slightly favour one element over another
5	Strong significance	Experience and judgement strongly favour one element over another
7	Very strong significance	Activity is strongly favored and its dominance is demonstrated in practice
9	Extreme significance	The evidence favouring one parameter over another is of the highest possible order
2, 4, 6, 8	Intermediate values	Used to represent compromise between priorities listed above

prior to applying the weights to the criteria making up the decision problem. The consistency ratio (CR) measuring the degree of departure from pure inconsistency is derived as follows:

$$\mathrm{CR} = \frac{\mathrm{CI}}{\mathrm{RI}} \tag{3}$$

where RI represents the consistency of a randomly generated pairwise comparison matrix and CI indicates the consistency index, as expressed in Eq. 4:

$$\mathrm{CI} = \frac{\lambda_{\max} - n}{n - 1} \tag{4}$$

The pairwise comparison test is iterated until CR $\leq$ 10%, which indicates an acceptable level.

Weighted linear combination (WLC) After deriving the weights through the AHP technique, the different factors are combined through the WLC technique to generate the offshore wind farm suitability map of Mauritius. This aggregation involves assigning derived weights acquired from AHP to individual criterion and then summing them up. The Offshore Wind Suitability Index (OWSI) is given by:

$$\mathrm{OWSI} = \sum_{j=1}^{n} w_j a_{ij} \tag{5}$$

where w_j is the weight of factor j, a_{ij} is the normalized value of area i under factor j, and n is the number of criteria.

Review of offshore wind models

Site suitability analysis for an offshore wind farm requires the consideration of multiple factors We present in Table 2 a synthesis of the influential and constraint factors employed by multiple offshore wind farm studies around the world.

Selected offshore constraint factors

Marine protected areas (MPAs) In view of protecting marine habitats and maintaining biodiversity, MPAs have been set up which consists of six fishing reserves and two marine parks, as illustrated in Fig. 1c. MPAs are secured under strict legal frameworks which would pose a legal constraint to the laying of submarine cables from the offshore wind farm to the shore. The data were made available by UNEP-WCMC and IUCN [48].

World heritage site With the objective to preserve the cultural heritage of Le Morne Brabant, which is regarded as a symbol of marronage during the nineteenth century in Mauritius, strict policy frameworks have been set up and a buffer zone (Fig. 1c) has been traced by the Ministry of Housing and Lands [28]. Georeferencing and digitization of the buffer area was performed using QGIS.

Coral reef Coral reefs are regarded as important ecological habitats for marine organisms and may pose a constraint with regards to the laying of underwater electric cables for the offshore wind farm that may entail significant reef damage [8]. Coral reef distribution around Mauritius was vectorized (Fig. 1c) in QGIS through visual inspection of satellite imageries.

Exclusive economic zone (EEZ) With one of the largest EEZ globally, a key endeavour of the Republic of Mauritius is the promotion of its ocean economy. According to the United Nations Convention on the Law of the Sea (UNCLOS), the country has exclusive rights to implement offshore projects within the limits of its national jurisdiction, as delineated by the EEZ (Fig. 1a). The demarcation of EEZ region for Mauritius was made available by Flanders Marine Institute [13].

Shipping route The location of the offshore wind farm may pose a navigational constraint for marine traffic. The shipping routes around Mauritius were determined from the ship density maps of Marine Traffic from 2019 and 2020 [27]. The map was georeferenced and the ship routes around Mauritius were extracted using QGIS, as illustrated in Fig. 3.

Unfeasible water depths The offshore wind industry has experienced significant growth over the past decade. Monopile foundation has been reported to be the most popular

Table 2 Specifications of offshore wind farm suitability models implemented worldwide

Country	Technique	Constraint	Influential factor and weight	Reference
Egypt	AHP WLC	Military area Natural parks Oil and gas well Shipping routes Cables	Wind power density (54%) Depth (24%) Soil properties (7%) Distance to grid (4%) Distance to shore (11%)	Mahdy and Bahaj [25]
Hong Kong	AHP WLC	Fishing port Restricted areas Fairways Mud disposal Anchorage site Fish culture Recreation zone Artificial reef	Distance to shore (6%) Distance to flora/fauna (3.5%) Distance to recreation zones (3.5%) Distance to port (24%) Distance to fishing areas (5%) Distance to grid (10%) Wind speed (14%) Depth (33%)	Gavériaux et al. [14]
Morocco	AHP WLC	Submarine cables Shipping routes Protected areas Migratory bird route Blue flag beach EEZ	Wind speed (38.5%) Water depth (20.7%) Distance to grid (12.9%) Distance to port (6%) Distance to shoreline (6%) Tourism density (2%) Distance to airport (3.4%) Sediment thickness (10.4%)	Taoufik, M. and Fekri [44]
Brazil	AHP WLC	Low wind speed Unfeasible depth Fishing site Pipeline Conservation site Priority area	Wind speed (53%) Water depth (30%) Distance to shore (11%) Distance to ports (6%)	Vinhoza and Schaeffer [52]
Mauritius (present paper)	AHP WLC	Shipping route Unfeasible depth EEZ Marine protected areas Coral reef World heritage	Wind speed Water depth Distance to grid Tourism density	Doorga et al. [9]

typology with a global market share of 60% [36]. Monopiles are generally used in shallow (0–15 m) and intermediate (15–30 m) depths. Tripod and jacket structures are better suited for transitional water depths between 30 and 50 m [31]. Floating foundations are generally used for deep waters above 50 m and can be implemented in water depths of up to 1000 m based on currently proposed technologies [54]. In the current analysis, we identify and exclude water depths greater than 2000 m using bathymetric data from [16], as shown in Fig. 3.

Selected influential factors

Wind speed Considered as being the most influential factor in offshore wind farm siting studies worldwide, as presented in the offshore wind farm models implemented in Table 2, the wind speed parameter is integrated in the formulated model for Mauritius. The wind speed parameter is directly related to the cost-effectiveness of wind farms [43]. The wind data (Fig. 4) in the vicinity of Mauritius were made available by the Technical University of Denmark (DTU) in collaboration with the World Bank Group. Wind speed values vary from 3.1 to 13.6 m/s at 100 m height, with the strongest wind speeds registered in the Southern and Northern offshore regions, as observed in Fig. 4, and reported by Cunden and Lollchund [5]. Higher scores are given to regions witnessing higher wind speeds and the lower scores are attributed to the regions with the lower wind speeds.

Water depth Due to its influence on the type and cost of foundation necessary to accommodate and offshore wind farm, the bathymetry factor is an important one. Water depth data (Fig. 5) were made available by GEBCO [16]. Higher scores are given to regions lying closer to the shore (0–30 m depth) owing to the popular and cost-effective use of monopiles as compared to the other foundation types.

Proximity to grid The nearness of the offshore wind farm site to the grid transmission line has the benefit of saving on electric cable costs and facilitating the injection of electricity to the grid network. The grid transmission lines of Mauritius were made available by OpenStreetMap [30]. The

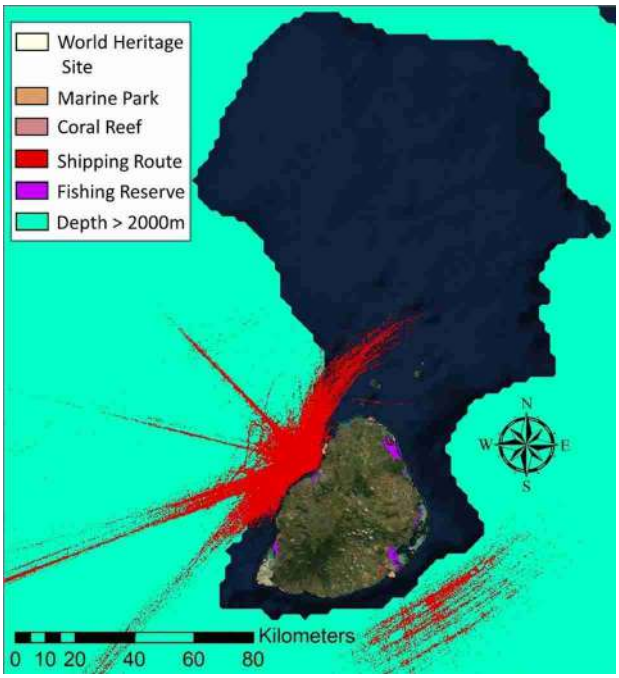

Fig. 3 Geospatial constraints prohibiting the implementation of offshore wind farms in the territorial waters of Mauritius

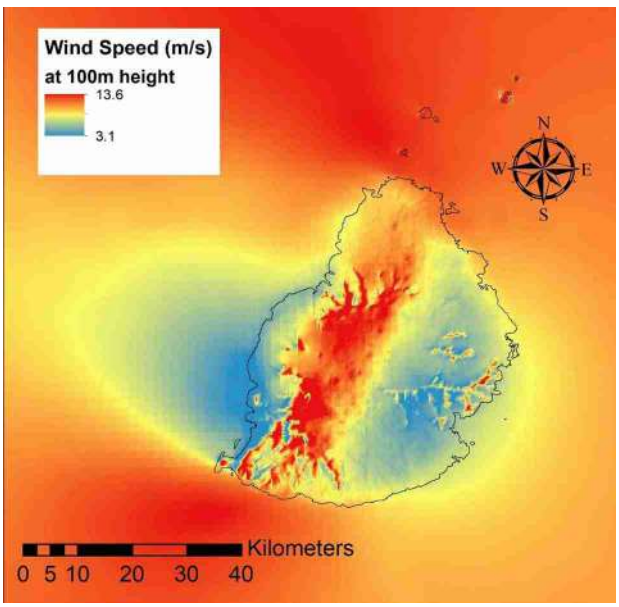

Fig. 4 Map of Mauritius delineating the geospatial variations in wind speeds across the inland and offshore regions of the country

electricity transmission line data were used to derive the chart illustrated in Fig. 6 which delineate offshore regions around Mauritius which lie nearer and further from the grid network. Higher scores are given to nearshore waters in close proximity to the grid network of Mauritius in order to

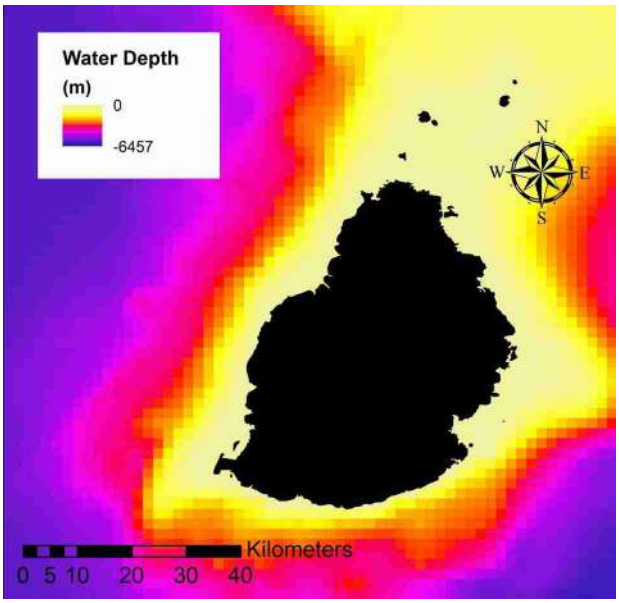

Fig.5 Map of Mauritius delineating the variations in water depths off the coastal areas of the country

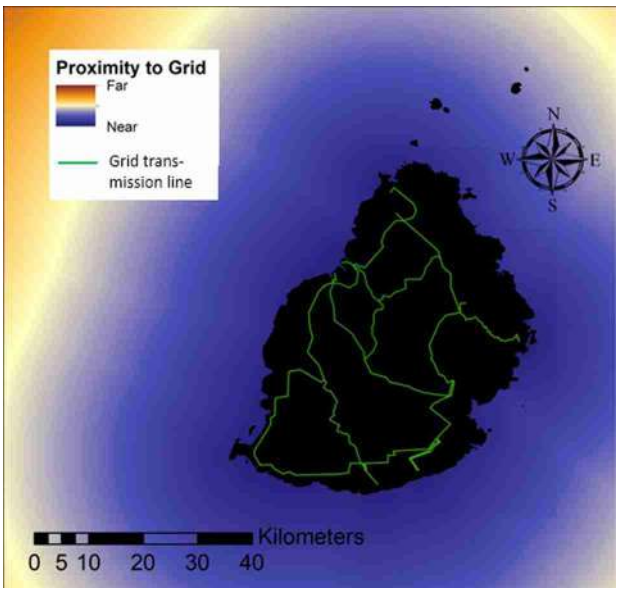

Fig.6 Map of Mauritius delineating the grid transmission network and the proximity of offshore sites to the latter

facilitate injection of electricity from the plant to the electricity grid.

Proximity to popular tourist areas A major inconvenience posed by the implementation of offshore wind turbines is its visibility from the shoreline which decreases the attractiveness of the region where they are installed. Mauritius, being popular touristic destination, whose economy relies on rev-

enues generated from the tourist industry, would necessitate that the offshore wind facility be placed in a region away from tourist activities. The dataset with the main tourist sites on the island (comprising of hotels and popular tourist attractions) was acquired from OpenStreetMap [30] and is presented in Fig. 7. Higher scores are attributed to regions lying far from highly touristic areas in view of dampening the impact of the farm's placement on tourist activities in the region.

Wind energy modelling

A Weibull distribution may be used to represent the probabilistic distributions of wind speeds at a certain region of interest and is given by the probability density function, $f(U)$, as:

$$f(U) = \frac{k}{A}\left(\frac{U}{A}\right)^{k-1} \exp\left[-\left(\frac{U}{A}\right)^{k}\right] \tag{6}$$

where U denotes the wind velocities. The shape factor, k, and the scale factor, A, can be computed using the following equations:

$$k = \left(\frac{\sigma_U}{U_{\text{avg}}}\right)^{-1.086} \tag{7}$$

$$A = \frac{U_{\text{avg}}}{\tau\left(1+\frac{1}{k}\right)} \tag{8}$$

where σ_U represents the standard deviation whilst the average wind speed is given by U_{avg}.

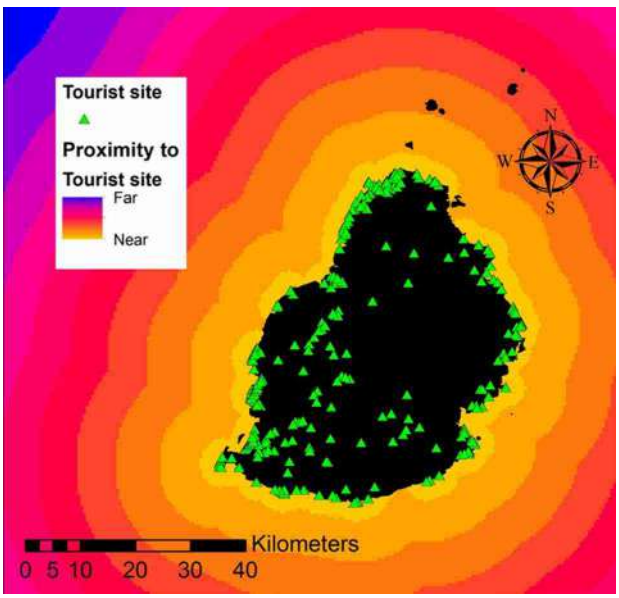

Fig.7 Map of Mauritius delineating offshore regions around the island lying near and far from tourist sites

The wind energy yield from the turbine may be obtained using the probability density function given next. In Eq. 9, given next, v_c, v_r and v_f are the cut-in, rated and cut-out speeds of the turbine.

$$P(v) = P_r \begin{cases} 0 \text{ for } v < v_c \\ \frac{v^3 - v_c^3}{v_r^3 - v_c^3} \text{ for } v_c \le v \le v_r \\ 1 \text{ for } v_r \le v \le v_f \\ 0 \text{ for } v \ge v_f \end{cases} \tag{9}$$

We assume the use of the wind turbine model: Siemens SWT-3.6-120, rated at 3600 kW, having a 120 m rotational blade diameter and 90 m hub height in the derivation of wind energy yield [55]. We also assume a linear wind flow incident on the wind turbines.

Capacity factor

The capacity factor, CF, defined as the ratio of the actual energy yield (derived from the wind energy model) to the maximum possible electrical energy output from the turbine, is estimated as follows:

$$\text{CF} = \frac{\text{Actual energy yield [MWh]}}{\text{Capacity of turbine \{MW\}} \times 8760 \text{ [h]}} \tag{10}$$

The estimated capacity factor will be used to calculate the levelized cost of electricity associated with the implementation of the offshore wind facility.

Economic modelling

The Levelized Cost of Electricity (LCOE) is defined as the full life-cycle costs of electricity derived from an installed technology per MWh of electricity generated [46]. The advantage of LCOE is that it helps compare multiple technology options to determine the most cost-competitive one. The LCOE [$/MWh] may be estimated as follows, assuming constant annual maintenance costs and energy generation throughout the technology's life-cycle.

$$\text{LCOE} = \frac{K_c K_{\text{RF}} + O_f}{E} \tag{11}$$

where K_c is the capital cost [$], K_{RF} represents the capital recovery factor, O_f indicates the fixed annual operating costs [$], whilst E denotes the annual electricity yield [MWh].

The capital recovery factor, K_{RF}, may be estimated as follows:

$$K_{\text{RF}} = \frac{i(1+i)^t}{(1+i)^t - 1} \tag{12}$$

where i represents the discount rate [%] and t denotes the economic life [years] of the offshore wind technology energy under consideration.

In deriving the LCOE, the main assumptions are that we employ a capital cost value of $3,400,000/MW, a fixed annual and maintenance cost of $95,000/MW, assuming a project lifetime of 20 years and a discount rate of 8%, as suggested by Lazard [24] for offshore wind energy systems.

Results and discussions

Unveiling the techno-economic offshore wind potential

Using the AHP technique, pairwise comparison is performed between a pair of influential factors, yielding the decision matrix shown in Table 3a. Four pairwise comparisons were performed which resulted in an acceptable consistency ratio of 2.6%. The derived weights presented in Table 3b were based on the principal eigenvalue of 4.07. The general order of importance is such that wind speed is attributed the highest weightage owing to its highest degree of importance in determining optimum offshore wind farm sites. Water depth is then attributed the next highest weightage followed by proximity to grid transmission lines and distance to high touristic areas. This order of importance adopted reflects the ones generally employed in various offshore wind farm models implemented worldwide, as shown in Table 2. The factors are then standardized to bring them on a comparable scale prior to applying the derived weights in Table 3b. Combination of weighted and standardized factors then proceeds using the WLC technique which results in the offshore wind farm potential map of Mauritius, shown in Fig. 8. Geospatial constraints identified in Fig. 3 are then overlaid on the map to delineate only regions feasible for exploitation.

Feasible regions around Mauritius are graded from high to low potentials for the implementation of offshore wind energy facilities. From Fig. 8, it can be observed that the regions of highest potentials are found in the Northern, North-Eastern, and South-Western offshore areas which are indicative of locations having high wind velocities, suitable water depths, are located near grid transmission lines, and are adequately situated in zones of fairly low touristic activities. The offshore wind potential map is further probed to

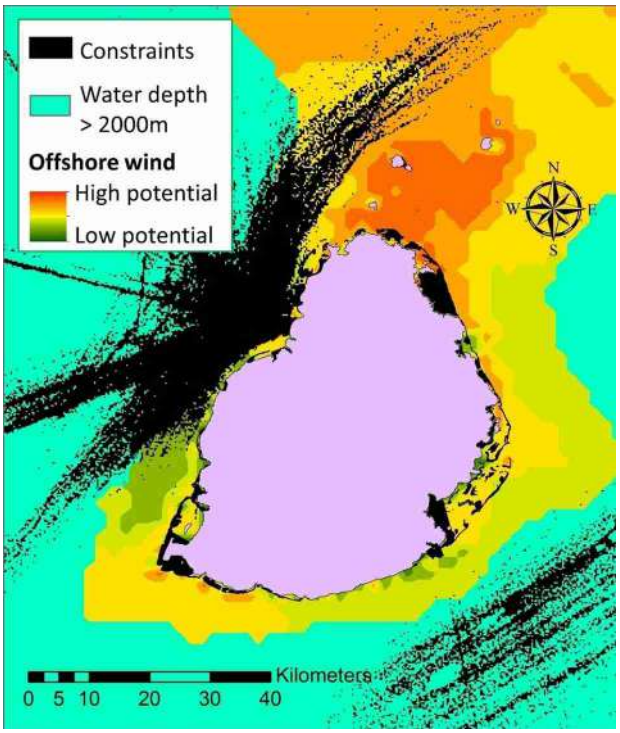

Fig. 8 Map of the maritime zone of Mauritius delineating the offshore wind farm resource potential around the island

Table 3 Results of the AHP method for the **a** decision matrix and **b** factor weights pertaining to the offshore wind farm model

Decision matrix

	Z_1	Z_2	Z_3	Z_4
Z_1	1	2.00	3.00	3.00
Z_2	0.50	1	2.00	3.00
Z_3	0.33	0.50	1	2.00
Z_4	0.33	0.33	0.50	1

Factor weights

Cat	Criteria	Weight	Rank
Z_1	Wind speed	44.8%	1
Z_2	Water depth	28.3%	2
Z_3	Proximity to grid	16.4%	3
Z_4	Proximity to touristic sites	10.6%	4

reveal a proposed ideal site in the North East off the coast of Grand Gaube, as illustrated in Fig. 9. Specifications of the proposed site are presented in Table 4. This identified North-Eastern site witnesses high wind speed (7.95 m/s) at 100 m height, whilst being located in an average water depth of 38 m which would favour conventional jacket foundation. Additionally, the site has the added benefit of being located at some distance from the shore (7.2 km), such that the offshore turbines would be practically out of sight from the North-Eastern coast. The relatively lower coral distributions opposite to the farm layout in that region, as illustrated in Fig. 9b, would imply less ecological impacts as the laying of underwater electric cables would not entail significant reef damage. Moreover, the identified site has been strategically located at some distance from Round, Flat, Gunners Quoin, and Ambre Islets which are ecologically sensitive regions and host a rich biodiversity.

Assuming that an offshore wind turbine model: Siemens SWT-3.6-120 with rated power 3,600 kW, 120 m diameter and 90 m hub height [55] is used in the implementation of an offshore wind farm for Mauritius, the annual energy yield may be estimated as presented in Table 4. For an arrangement of 169 turbines proposed at the Northern Eastern site, the estimated annual energy generation potential is around 1650 GWh. The marginal cost for implementing the wind farm in the identified propitious site is estimated at \$163/MWh and is even lower than the average LCOE of heavy fuel oil (\$218/MWh) in Mauritius [38], making it cost-competitive even without considering energy subsidies. The implementation of an offshore wind farm in the Northern Eastern site can decrease by about 1.5 times, the importation of fuel oil and diesel (1056 GWh in 2020 [39]) to meet electricity demand. Consequently, the investment in an offshore wind farm in a high potential region has the benefit of dampening the reliance on imported fossil fuels for electricity generation and decarbonize the carbon-intensive

Table 4 Specifications of the proposed sites for the implementation of offshore wind farms

	North-east site
GPS locations	– 19.96°; 57.77°
Area	42.3 km^2
Number of wind turbines	169
Offshore wind farm capacity	608 MW
Average water depth at site	38 m
Type of foundation needed	Jacket
Annual mean wind speed at 100 m height	7.95 m/s
Distance to grid transmission line	13.2 km
Visibility of farm/distance to shore	Low/7.2 km
Tourist density near the site	Relatively low
Estimated annual energy yield	1,650 GWh
Capacity factor	0.31
LCOE	\$163/MWh
Wave regime	Moderate

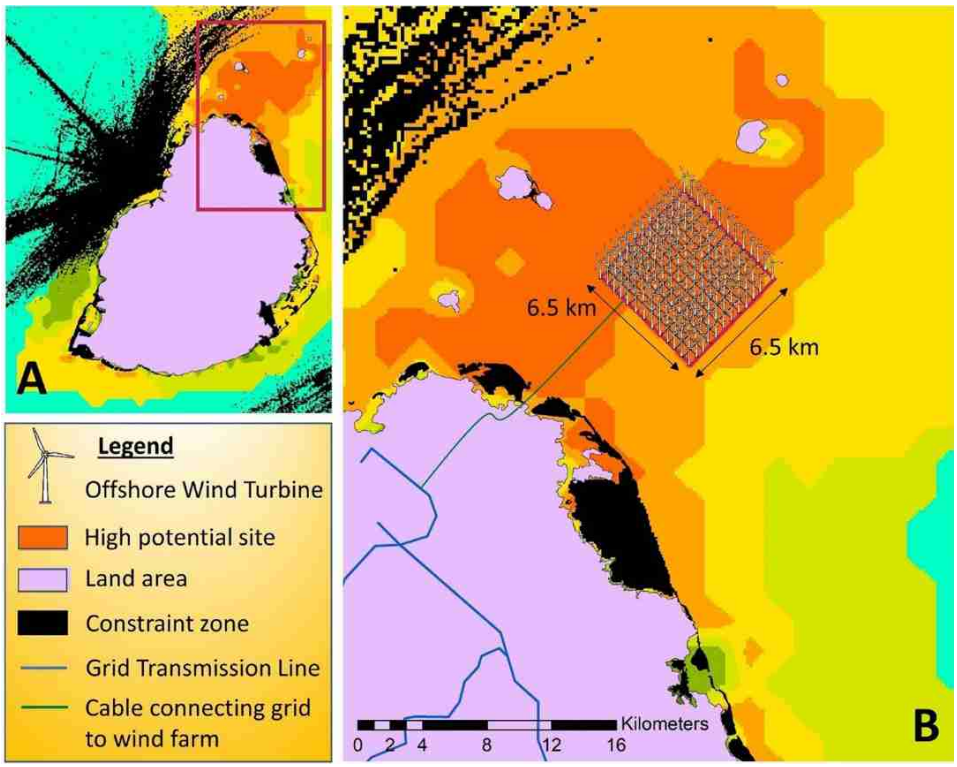

Fig. 9 **a** Location of proposed site identified in the North-East region of Mauritius for the implementation of an offshore wind facility. **b** Offshore wind farm layout comprising of 169 turbines with a 500 m spacing between adjacent turbines and installed in a high potential region identified off the coast of Grand Gaube

power sector whilst yielding long-term economic benefits. Sizing of the farm will be based on energy demand and grid integration capacity.

In comparison with previous studies by Gavériaux et al. [14] for Hong Kong, Mahdy and Bahaj [25] for Egypt, and Vinhoza and Schaeffer [52] for Brazil, which identify sites with higher probabilities for wind speeds occurring in the range of 4–8 m/s, the siting of the proposed offshore wind farm benefits from wind speeds averaging 7.95 m/s. The high wind speed values will be translated into higher energy yields and, therefore, more economic energy generation. However, as also contemplated by other literature studies, the paper considers a range of factors from tourist activities to ecological impacts in order to properly site the wind farm.

The results from the current paper reveal the technical and economic viability of implementing a network of offshore wind turbines in the nearshore north-eastern waters of Mauritius. A network of 169 turbines has been contemplated in the current study to reveal the maximum offshore wind power extraction permissible in a high wind resource area off the coast of Grand Gaube. From this analysis, it was revealed that the installation of typical jacket foundation in water depths averaging 38 m has the technical annual potential of generating around 1,650 GWh, resulting in an LCOE value of about $163/MWh and found to be more economic than fossil fuel oil and diesel. However, based on the energy demand and grid integration capacity of Mauritius, the sizing of a suitable network for offshore wind power turbines in the segment of the optimum site identified that is closer to the shore and that could even favour conventionally used monopiles (intermediate depths of 15–30 m) should be envisaged. The identified site benefits from the ecological advantage of less damage from cable laying due to the lower coral distributions, in addition of the low tourist activities in the vicinity.

Policy uptake and roadblocks

In the Republic of Mauritius, the Department of Continental Shelf, Maritime Zone Administration and Exploration (DCSMZAE) has the legal mandate for Marine Spatial Planning [6]. Such responsibilities include the identification of zones for development of offshore wind farms. However, the DCSMZAE has not yet identified suitable zones for such development (confirmed via email exchanges). Given the national [29] and international commitments [50] taken by Mauritius to develop clean energy, and the fact that the Mauritius Renewable Energy Agency has recently launched an expression of interest from suitable consortiums to develop offshore wind energy in Mauritius [26], not only do the findings of this paper have a high policy relevance, but they are also timely aligned with the country's current ambitions and efforts to unlock the development of offshore wind farms.

However, the transition from scientific assessments to policy uptake is not a straightforward task. For instance, it should be recalled that none of the projects referred to in Table 2 [25], Gavérieux et al. 2019; [44, 52] has been implemented as at-date, although Brazil has registered six environmental impact assessment licences applications for offshore wind as at 2020 [12]. Moreover, at a global level, Zhang et al. [57] infer that global rollout of offshore wind is still in its initial stages, with 6924 wind turbines having been constructed in only 14 coastal nations by 2019 (1 wind farm located in the US, 21 in the UK, 8 in Germany, 8 in Denmark, 7 in China, 2 in Sweden and 3 in the Netherlands).

Whilst this situation may be symptomatic of the recent (and still growing) maturity of research and development on offshore wind technologies that make them cost-competitive with respect to fossil fuel-based energy sources, it also prompts some reflection on the underlying causes accounting for limited diffusion of offshore wind farms as a clean energy source globally, and within the ambit of this paper, utilising those lessons to derive policy implications for the case of the Republic of Mauritius.

In the first instance, this situation could be attributed to a number of gaps in the literature that may have hampered policy uptake across nations involved in offshore wind farm development. For instance, there are currently scarce assessments digging deep into (i) cumulative environmental impacts on marine habitats and species and ecosystem functioning of the benthic community, as well as regulatory risk assessments and other governance and financing challenges [18], [22], (ii) hydrodynamics and hydrographic conditions in the immediate vicinity of sites [51], (iii) impact of offshore wind farms on birds [56] (iv) conducive policy instruments and stakeholder engagement mechanisms [2], (v) potential tourism value-added in terms of 'curiosity trips' [45], (vi) studies on levels of support from island residents [34], (vii) the use of ethnographic studies to inform on the impacts on tourism and recreation around selected sites [40], and the use of integrated strategic planning and a long-term multidisciplinary approach to site selection [42], amongst others.

Given the inherent characteristics of the Republic of Mauritius as a Small Island Developing state, the need for local empirical case studies covering those gaps is heightened. However, with a view to, pragmatically, address national imperatives to decarbonize the energy sector by increasing renewable energy sources to 60% by 2030 [29], it may not be judicious to wait for detailed scientific studies that explore the full-scope of gaps in the literature as previously mentioned. Within this context, this paper provides for an insight of possible sites (Fig. 5) whereby offshore wind farm development is technically feasible, along with a preferred location (Fig. 6) based on an analytically sound methodology ("Materials and methods" section).

Furthermore, scarce diffusion of offshore wind technologies may also reflect a broader limitation of standardized engineering-based assessments of the technical and economic feasibility of technologies. Indeed, another branch of scholarly work posits that technology uptake is essentially path dependent, whereby technology development and diffusion are influenced by a complex interplay between technological and social factors such as user preferences, adequacy of regulatory frameworks, cultural aspects and infrastructure requirements amongst others [17, 33]. These literatures suggest the use of other theoretical frameworks that better integrate socio-technical considerations within analyses that study offshore wind farm development, the lessons of which may better inform policy uptake [11].

Along those reflections, Sovacool [41] calls for energy studies to "become more socially oriented, interdisciplinary and heterogeneous" and "centre on both physical and social processes, include diverse actors and mix qualitative and quantitative methods" so as to better positioned to have a social impact. Comparing the underlying approach adopted in this paper, one may reflect on the reliance on the sole judgement of the authors to choose influential and constraint factors, as well as assign weights that, ultimately, shape the results obtained. To address this gap, the method used and analyses undertaken within this study may be tested with local actors (such as the environment, land use planning, energy ministries, as well as fishermen, NGOs and the public) so as to discuss and agree on most appropriate sites for offshore wind development. To this end, Fig. 5 provides for a basis for such discussions.

Conclusions

In the current study, the feasibility of offshore wind potential is explored for the small island developing state of Mauritius in view of responding to the need to decarbonize the power system and reduce dependence on expensive imported fossil fuel sources for electricity generation. The paper is one of the few for small islands with emphasis on accounting for tourism activities. The marine spatial constraints, such as shipping routes and marine protected areas, are identified and combined with influential factors including wind conditions, water depths, and techno-economic criteria such as proximity to grid transmission lines and tourism density, for proper wind farm planning. The results revealed that the Northern, North-Eastern, and South-Western offshore regions are propitious for offshore wind farm development owing to favourable climatic, economic, and technical conditions.

An in-depth assessment revealed that the North-Eastern site is more suitable for immediate implementation owing to the fact that it is located in an average water depth of 38 m, which would favour the conventionally used jacket foundation. The adequate wind regime of the site, which averages 7.95 m/s at 100 m height over an annual time span, would make it possible to generate up to 1650 GWh of electricity annually. Based on this energy yield, a levelized cost of electricity value of $163/MWh has been estimated for the farm which is found to be cost-competitive as compared to heavy fuel oil ($218/MWh). The highly suitable offshore wind farm site identified in the North-East has a theoretical maximum wind resource potential that can contribute in decreasing up to about 1.5 times the importation of fuel oil and diesel to meet electricity demand whilst catering for the sustainable energy supply of a growing population.

However, this paper also highlights a number of gaps in the literature, covering environmental, policy, regulatory, and methodological factors. The main limitation of the current study is that it has been conducted in a highly academic and siloed approach and without the involvement of other stakeholders. Reflecting on those gaps and with a view to ease policy uptake of the results of this paper, it is proposed to replicate this study with actors having a stake in the development of offshore wind farms.

Suggested avenues for future research should look at sizing of a nearshore wind farm in a segment of the area identified based on (a) the energy demand of the population and grid capacity, as well as on (b) further in-depth ecological considerations pertinent to the site. Moreover, another line of research could focus on the optimum arrangement for wind turbines to increase energy yield in the face of the generated wake effects.

Acknowledgements The authors are grateful to the Université des Mascareignes for the support provided for conducting the research presented in this paper. The authors are thankful for the contributions of the Technical University of Denmark (DTU) in collaboration with the World Bank Group, GEBCO, OpenStreetMap, UNEP-WCMC, Ministry of Housing and Lands, Flanders Marine Institute, and Marine Traffic for the provision of data to conduct the offshore wind potential analysis. The authors acknowledge the use of QGIS v3.16.8 for the purpose of research. Thanks are extended to the two anonymous reviewers.

Authors' contribution JRSD (Corresponding Author) involved in the conception and design of the study, acquisition of data, analysis and interpretation of data, and drafting of the manuscript. ZB contributed in drafting the policy relevance section. TSMC revised the paper for important intellectual content. YC revised the paper for important intellectual content. RK revised the paper for important intellectual content.

Funding The authors declare that no funds, grants, or other support were received during the preparation of this manuscript.

Data availability The datasets generated during and/or analysed during the current study are not publicly available due to costly data involved and that needs to be regularly maintained but are available from the corresponding author on reasonable request].

Declarations

Conflict of interest The authors have no relevant financial or non-financial interests to disclose.

Ethical approval On behalf of all authors, I, Dr Jay Doorga, the corresponding author of this paper wish to assure you that for the manuscript (Feasibility study for the implementation of an offshore wind farm in the nearshore waters of Mauritius: A techno-economic analysis) the following is fulfilled: (1) This material is the authors' own original work, which has not been previously published elsewhere. (2) The paper is not currently being considered for publication elsewhere. (3) The paper reflects the authors' own research and analysis in a truthful and complete manner. (4) The paper properly credits the meaningful contributions of co-authors and co-researchers. (5) The results are appropriately placed in the context of prior and existing research. (6) All sources used are properly disclosed (correct citation). Literally copying of text must be indicated as such by using quotation marks and giving proper reference. (7) All authors have been personally and actively involved in substantial work leading to the paper, and will take public responsibility for its content. The violation of the Ethical Statement rules may result in severe consequences. We agree with the above statements and declare that this submission follows the policies of the Journal of Clean Technologies and Environmental Policy.

References

1. Andrew, L.: Offshore wind power price plunges by a third in a year. https://www.rechargenews.com/transition/offshore-wind-power-price-plunges-by-a-third-in-a-year-bnef/2-1-692944 (2019). Accessed 6 Sept 2021
2. Carey, D.A., Wilber, D.H., Read, L.B., Guarinello, M.L., Griffin, M., Sabo, S.: Effects of the block island wind farm on coastal resources. Oceanography **33**(4), 70–81 (2020)
3. Cavazzi, S., Dutton, A.G.: An offshore wind energy geographic information system (OWE-GIS) for assessment of the UK's offshore wind energy potential. Renew. Energy **87**, 212–228 (2016)
4. Coren, M.: After a decade of dithering, the US east coast went all in on offshore wind power this week. https://qz.com/1290429/three-us-states-signed-up-for-1200-mw-of-offshore-wind-power-this-week/ (2018). Accessed 6 Sept 2021
5. Cunden, T.S. and Lollchund, M.R.: High-resolution wind speed mapping for the island of Mauritius using mesoscale modelling. In: Progress in Advanced Computing and Intelligent Engineering, pp. 719–734. Springer, Singapore (2021)
6. DCSMZAE. Strategic actions. https://csmzae.govmu.org/Pages/Strategic%20Actions/Strategic-Actions.aspx (2020). Accessed 3 Nov 2021
7. Doorga, J.R.S., Gooroochurn, O., Motah, B.A., Ramchandur, V., Sunassee, S.: A novel modelling approach to the identification of optimum sites for the placement of ocean thermal energy conversion (OTEC) power plant: application to the tropical island climate of Mauritius. Int. J. Energy Environ. Eng. **9**(4), 363–382 (2018)
8. Doorga, J.R., Sadien, M., Bheeroo, N.A., Pasnin, O., Gooroochurn, O., Modoosoodun-Nicolas, K., Ramchandur, V., Ramharai, D.: Assessment and management of coastal erosion: insights from two tropical sandy shores in Mauritius Island. Ocean Coast. Manag. **212**, 105823 (2021)
9. Doorga, J.R.S.: Climate change and the fate of small islands: the case of Mauritius. Environ. Sci. Policy **136**, 282–290 (2022)
10. EDB. Budget 2021/22: Better together. https://news.edbmauritius.org/budget-newsletter/pdf/EDB_Budget_Newsletter_2021-22.pdf (2021). Accessed 23 Aug 2021
11. Enevoldsen, P., Permien, F.H., Bakhtaoui, I., von Krauland, A.K., Jacobson, M.Z., Xydis, G., Sovacoola, B., Valentine, S.V., Luecht, D., Oxley, G.: How much wind power potential does europe have? Examining European wind power potential with an enhanced socio-technical atlas. Energy Policy **132**, 1092–1100 (2019). https://doi.org/10.1016/j.enpol.2019.06.064
12. ERO. Brazilian Offshore Wind Roadmap. Energy Research Office. https://storymaps.arcgis.com/stories/1565a407d4a443029e035b1844c8437b (2020). Accessed 5 Nov 2021
13. Flanders Marine Institute. Maritime Boundaries geodatabase: maritime boundaries and exclusive economic zones (200NM), version 11. http://www.marineregions.org/. https://doi.org/10.14284/386 of the European Union. (2019)
14. Gavériaux, L., Laverrière, G., Wang, T., Maslov, N., Claramunt, C.: GIS-based multi-criteria analysis for offshore wind turbine deployment in Hong Kong. Ann. GIS **25**(3), 207–218 (2019)
15. GCF.: Accelerating the Transformational shift to a low-carbon economy in the Republic of Mauritius. https://www.greenclimate.fund/sites/default/files/document/funding-proposal-fp033-undp-mauritius.pdf (2016). Accessed 23 Aug 2021
16. GEBCO Compilation Group. GEBCO 2021 Grid. https://www.gebco.net/data_and_products/gridded_bathymetry_data/ (2021). Accessed 10 Sept 2021
17. Geels, F.: Technological transitions as evolutionary reconfiguration processes: a multi-level perspective and a case-study. Res. Policy **31**(8–9), 1257–1274 (2002)
18. Gordon, J.A.: Impacts and implications of offshore wind power research: a review of techno-economic, socio-technical. https://tethys.pnnl.gov/sites/default/files/publications/Gordon-2020.pdf (2020). Accessed 3 Nov 2021
19. Hadush, S.Y., and Ravi Kumar Bhagwat, S.: A comparative study of renewable energy and electricity access policies and regulatory frameworks in the Indian Ocean islands: the case of Mauritius, Seychelles, Madagascar and Comoros. (2019)
20. IRENA. SIDS High-level dialogue: accelerating energy transition in small island developing states to stimulate post-pandemic recovery. https://www.irena.org/events/2020/Jun/SIDS-High-Level-Dialogue-with-AOSIS (2020). Accessed 23 Aug 2021
21. IRENA. Renewable capacity statistics 2021. https://www.irena.org/publications/2021/March/Renewable-Capacity-Statistics-2021 (2021). Accessed 6 Sept 2021
22. Pezy, J.-P., Raoux, A., Dauvin, J.-C.: An ecosystem approach for studying the impact of offshore wind farms: a French case study. ICES J. Mar. Sci. **77**(3), 1238–1246 (2020). https://doi.org/10.1093/icesjms/fsy125
23. Lacal, Arantegui, R., Jaeger-Waldau, A., Vellei, M., Sigfusson, B., Magagna, D., Jakubcionis, M., Perez, Fortes, M., Lazarou, S., Giuntoli, J., Weidner, Ronnefeld, E., De, Marco, G., Spisto, A., Gutierrez, Moles, C., authors Carlsson, J., editor. ETRI 2014-Energy technology reference indicator projections for 2010–2050. EUR 26950. Luxembourg (Luxembourg): Publications Office of the European Union; 2014. JRC92496
24. Lazard. 'Lazard's levelized cost of energy analysis-Version 11.0'. https://www.lazard.com/media/450337/lazard-levelized-cost-of-energy-version-110.pdf (2017). Accessed 15 Sept 2020
25. Mahdy, M., Bahaj, A.S.: Multi criteria decision analysis for offshore wind energy potential in Egypt. Renew. Energy **118**, 278–289 (2018)
26. MARENA. Expression of interest SC/EOI/M2021/010 for provision of consultancy services required for conducting a "feasibility study of ocean renewable Energy technologies in the Republic Of Mauritius". https://www.marena.org/work-with-us/procurement/eoi-2021 (2021). Accessed 3 Nov 2021

27. MarineTraffic. Global ship tracking intelligence. www.marinetraffic.com (2021). Accessed 9 Sept 2021
28. MHL. Planning policy guidance 2 Le Morne cultural Landscape. http://www.lemorneheritage.org/assets/policy.pdf (2007). Accessed 9 Sept 2021
29. MOF. Budget Speech 2021–2022, Ministry of finance, economic planning and development. https://budgetmof.govmu.org/Documents/2021_22budgetspeech_english.pdf (2021). Accessed 3 Nov 2021
30. OpenStreetMap. https://www.openstreetmap.org/ (2021). Accessed 10 Sept 2021
31. Plodpradit, P., Dinh, V.N., Kim, K.D.: Tripod-supported offshore wind turbines: modal and coupled analysis and a parametric study using X-SEA and FAST. J. Mar. Sci. Eng. **7**(6), 181 (2019)
32. Polatidis, H., Haralambopoulos, D.A., Munda, G., Vreeker, R.: Selecting an appropriate multi-criteria decision analysis technique for renewable energy planning. Energy Sources, Part B **1**(2), 181–193 (2006)
33. Rip, A. & Kemp, R.: Technological change. In: Rayner, S. & Malone, E. L., (eds.) Human choice and climate change. Vol. II, Resources and Technology. Columbus: Battle, pp. 327–399. (1998)
34. Russell, A., Firestone, J., Bidwell, D., Gardner, M.: Place meaning and consistency with offshore wind: an island and coastal tale. Renew. Sustain. Energy Rev. **132**, 110044 (2020)
35. Saaty, T.L.: A scaling method for priorities in hierarchical structures. J. Math. Psychol. **15**(3), 234–281 (1977)
36. Sánchez, S., López-Gutiérrez, J.S., Negro, V., Esteban, M.D.: Foundations in offshore wind farms: evolution, characteristics and range of use. Analysis of main dimensional parameters in monopile foundations. J. Mar. Sci. Eng. **7**(12), 441 (2019)
37. Schillings, C., Wanderer, T., Cameron, L., van der Wal, J.T., Jacquemin, J., Veum, K.: A decision support system for assessing offshore wind energy potential in the North Sea. Energy Policy **49**, 541–551 (2012)
38. Shea, R.P., Ramgolam, Y.K.: Applied levelized cost of electricity for energy technologies in a small island developing state: a case study in Mauritius. Renew. Energy **132**, 1415–1424 (2019)
39. SM. Energy and water statistics 2020. https://statsmauritius.govmu.org/Documents/Statistics/ESI/2021/EI1587/Energy_Yr20_070621.pdf (2020). Accessed 28 Aug 2021
40. Smith, H., Smythe, T., Moore, A., Bidwell, D., McCann, J.: The social dynamics of turbine tourism and recreation: Introducing a mixed-method approach to the study of the first US offshore wind farm. Energy Res. Soc. Sci. **45**, 307–317 (2018)
41. Sovacool, B.: Diversity: energy studies need social science. Nature **511**, 529–530 (2014). https://doi.org/10.1038/511529a
42. Spyridonidou, S., Vagiona, D.G., Loukogeorgaki, E.: Strategic planning of offshore wind farms in Greece. Sustainability **12**(3), 905 (2020)
43. Sunak, Y., Höfer, T., Siddique, H., Madlener, R. and De Doncker, R.W.: A GIS-based decision support system for the optimal siting of wind farm projects. Universitätsbibliothek der RWTH Aachen. (2015)
44. Taoufik, M. and Fekri, A.: GIS-based multi-criteria analysis of offshore wind farm development in Morocco. Energy Convers. Manag. X:100103 (2021)
45. Trandafir, S., Gaur, V., Behanan, P., Uchida, E., Lang, C., Miao, H.: How are tourists affected by offshore wind turbines? A case study of the first US offshore wind farm. J. Ocean Coast. Econ. **7**(1), 1 (2020)
46. Ueckerdt, F., Hirth, L., Luderer, G., Edenhofer, O.: System LCOE: what are the costs of variable renewables? Energy **63**, 61–75 (2013)
47. UNDP. Three reasons why energy transition is important for Mauritius COVID-19 economic recovery. https://www.mu.undp.org/content/mauritius_and_seychelles/en/home/blog/2020/how-mauritius_-energy-transition-will-support-its-covid-19-recov.html (2020). Accessed 19 Aug 2021
48. UNEP-WCMC and IUCN. Protected planet: the world database on protected areas (WDPA) [Online], September 2021, Cambridge, UK: UNEP-WCMC and IUCN. www.protectedplanet.net (2021). Accessed 9 Sept 2021
49. UNFCCC. Adoption of the Paris agreement. https://unfccc.int/documents/184656 (2015). Accessed 21 Sept 2022
50. UNFCCC. Update of the nationally determined contribution of the Republic Of Mauritius. https://www4.unfccc.int/sites/ndcstaging/Pages/Party.aspx?party=MUS&prototype=1 (2021). Accessed 3 Nov 2021
51. van Berkel, J., Burchard, H., Christensen, A., Mortensen, L.O., Petersen, O.S., Thomsen, F.: The effects of offshore wind farms on hydrodynamics and implications for fishes. Oceanography **33**(4), 108–117 (2020)
52. Vinhoza, A., Schaeffer, R.: Brazil's offshore wind energy potential assessment based on a spatial multi-criteria decision analysis. Renew. Sustain. Energy Rev. **146**, 111185 (2021)
53. Waewsak, J., Landry, M., Gagnon, Y.: Offshore wind power potential of the Gulf of Thailand. Renew. Energy **81**, 609–626 (2015)
54. World Bank. Expanding offshore wind to emerging markets. Available online at https://documents1.worldbank.org/curated/en/716891572457609829/pdf/Going-Global-Expanding-Offshore-Wind-To-Emerging-Markets.pdf (2019). Accessed 9 Sept 2021
55. WTM. Siemens SWT-3.6–120 Offshore. Available online at https://en.wind-turbine-models.com/turbines/669-siemens-swt-3.6-120-offshore (2021). Accessed 14 Sept 2021
56. WWF. Environmental impacts of offshore wind power production in the North Sea–A Literature Overview. WWF-World Wide Fund For Nature, Oslo. 48 pp. Available online at: https://www.wwf.no/assets/attachments/84-wwf_a4_report___havvindrapport.pdf (2014). Accessed 5 Nov 2021
57. Zhang, T., Tian, B., Sengupta, D., et al.: Global offshore wind turbine dataset. Sci. Data **8**, 191 (2021). https://doi.org/10.1038/s41597-021-00982-z

International Journal of Energy and Environmental Engineering (2023) 14:803–827
https://doi.org/10.1007/s40095-022-00550-0

ORIGINAL RESEARCH

Economic energy scheduling through chaotic gorilla troops optimizer

Ashutosh Bhadoria[1] · **Sanjay Marwaha**[1]

Received: 24 June 2022 / Accepted: 11 November 2022 / Published online: 12 December 2022

Abstract
This research proposes a novel solution to the power generation scheduling problem based on the chaotic gorilla troop's optimizer algorithm (CGTO). Power system operational planning is a large-scale, highly constrained combinatorial optimization problem known as the Energy Generation Scheduling Problem. The Gorilla Troops optimizer is a bio-inspired heuristic optimizer that uses gorilla hierarchy and hunting notions to resolve challenging scheduling issues. The gorilla update method is initially obtain binary string of generators in order to determine the global best solution (s), which is followed by a chaotic operation. Chaotic search avoids local minima while GTO seeks out global optima, resulting in a better balance of exploitation and exploration. A simple and effective strategy for wind power integration placement and sizing is presented in this research. The messy behavior of the wind is predicted to follow the Weibull PDF. Examining the viability and effectiveness of units between 10 and 100, the results are compared to those attained using various techniques mentioned in the literature. The results unequivocally demonstrate that the recommended technique provides superior solutions than competing alternatives. The solution was improved further in the wind power sharing scenario. Convergence curve amply demonstrates the optimizer's robustness.

Keywords Artificial gorilla troops optimizer · Metaheuristic algorithm · Generation Scheduling Problem · Chaotic search · Hybrid optimizer

Introduction

A big electric power system today typically comprises of thousands of transmission lines and hundreds of generators. Such a large-scale system's functioning should take into consideration the ongoing fluctuation in customer needs. Power system scheduling is based on two crucial decision-making processes in order to guarantee there is liability and the efficient running of this type of systems. First, each time interval of the scheduling time horizon should be used to establish the commitment states (on or off) of the systems generating units. The "Unit Commitment" problem is the name for this issue. The power demand will be distributed among the committed units according to another choice, known as the "Economic Dispatch." Such a distribution is chosen based on the traits of the component units. For a least-cost solution, the results of these two choices must be taken into account concurrently. The scheduled power generation should be able to meet the anticipated demand in the scheduling problem, where the time horizon typically runs from one day to one week. However, there is always a chance that some of the committed units would fail owing to the unique outages or unexpected challenges in the operation of a power system; therefore, a hot reserve which is not in operation must be considered. In this case, the extra capacity (spinning reserve) might be able to supply the mismatch power and deliver electricity to the portion of the load that was originally attributed to the failing units. Another system need that must be met in the scheduling problem is the supply of the spinning reserve. A deterministic spinning reserve constraint is typically used to simulate such dependability requirements, and this constraint necessitates a specific amount of spinning reserve capacity. This, however, is an incorrect formulation of system limitations [I] since it does not accurately reflect the risk that the system actually faces. The ideal timetable for a power system's operation should also take into account the system's component

✉ Ashutosh Bhadoria
drashutosh.bhadoria@gmail.com

[1] Sant Longowal Institute of Technology and Engineering SLITE, Sangrur, Punjab, India

producing units' characteristics. According to how they use energy resources, generating units in a power system can also be categorized. The term "thermal units" refers to the generators that convert heat energy into electricity and have an endless supply of fuel. The majority of the units in the current power systems belong to this type of generating units. A different kind of generating units consists of fuel-constrained units that operate similarly to thermal units. However, there is a maximum amount of gasoline that can be made accessible to any fuel-constrained unit at any given time. A unit is subject to this constraint for a number of reasons, including the scarcity of natural resources, utility and fuel supplier contracts, and transportation issues. Assigning a preset total fuel consumption to each unit within the scheduled time horizon is a typical set of fuel restrictions used in modern power systems. These constraints are known as "Take or Pay" contracts. The third category of generators includes wind generators, which produce electricity by harnessing the kinetic energy of moving wind. Utilizing wind resources may result in a number of operational restrictions depending on the rate of the wind intake and environmental restrictions. In power system operation, unit commitment (UC) is a mixed-integer, frequently nonlinear, NP-hard issue. It necessitates determining the binary on/off state of power generation units as well as the real-valued power output of on-line units at the same time, all while adhering to different limitations such as power balance, capacity limit, and minimum up/down time limits. Since global warming has been a major challenge for mankind in the last decade, owing to widespread use of fossil fuels. Fuel releases pollutants including CO2, SO2, and NOx that are harmful to the environment. By enacting emission taxes, many nations are promoting the creation of clean energy in an effort to reduce the impact of global warming. The burning of fossil fuels is the main source of greenhouse gases. Three main forms of conventional fuels—oil, gas, and coal—produce emissions that are represented by greenhouse gases like NOx, CO2, and SO2. The Paris Climate Conference 2015 created a global commitment to keep maximum temperature rises under 2 degrees Celsius by the end of the century [1]. Significant reductions in GHG emissions from both major drivers of emissions, notably power production and transportation, are ultimately a fundamental way to achieving this objective [2]. As a result, both industrialized and developing countries work to utilize abundantly available alternative energy sources that are also environmentally beneficial. As a result, current studies and research have given renewable energy sources a lot of attention. The UC has already been widely investigated for traditional power systems with limited or no participation of variable renewable production. However, in recent years, there has been a significant increase in the use of variable renewable energy sources around the world, posing new issues for power system operators. Modern power systems with a considerable renewable share must be able to respond to fast and large variations in renewable energy output due to the uncertainty and variability of renewable generation, making flexibility a hot topic of research in recent years. A number of studies have been conducted in this area, with the goal of maximizing the use of flexible resources in the operation of highly renewable systems. In renewable energy share wind and generation gain utmost importance and have increased dramatically, allowing them to play a substantial role in wholesale energy markets while lowering fossil fuel consumption. Wind and solar power generation, which are generally classified as negative loads, have substantial swings in their load curves and are likely to induce repeated ramping and start-ups/shut-downs for thermal units [17]. Over the last few decades, extensive research has been performed to answer the problem, leading to the proposal of a variety of traditional approaches, intelligent methods, and hybrid or analytical methods. Generation scheduling problem has long been matter of concern various approaches have been applied to solve this complex problem conventional methods such as exhaustive enumeration [1] in which all possible combinations are tried, this is very complex and tiresome. Priority list [2] is simple sub-optimal approach which sorts units according to their priority, and whose priority is first participate first, followed by next best units. Dynamic programing [3] approach suffers with dimensionality problem. Lagrangian relaxation [4, 5 suffers with its sub-optimal nature as duality gap may not always reduce to zero. Branch and bound [6] Tabu search [7, 8] Unit decommitment method [9].

Performance of conventional approach fails when objective functions are either discontinuous or having multiple optima points. Since almost all classical techniques require objective function and gradient information of objective function since generation scheduling is complex non-convex curve classical method usually stuck in local minima. Soft computation-based solutions primarily make use of theoretical and applied understanding of the inference generated to address UCP. With the use of these techniques, it is possible to qualitatively describe a system's behavior, characteristics, and response without using precise mathematical formulas. Fuzzy logic, artificial neural networks, and evolutionary and GA-based approaches are three main categories in which growth in the field of soft computation techniques can

be hypothesized. Hence soft computing-based method is widely adopted to solve generation scheduling problem, such as simulated annealing fuzzy logic [10, 11], genetic algorithm [12], ant colony optimization [13], evolutionary programming [14], harmony search [15], binary gravitational algorithm [16], fire fly algorithm [17], differential evolution [18], teaching–learning-based optimization [19], sine cosine optimizer [20], moth flame optimizer [21]. Various other hybrid optimization approaches owing to their batter balance between exploitation and exploration are quite common nowadays such as BMFO-SIG [22], GWA-SA [23], Hybrid SMA-SCA [24], BGWO [25], Hybrid optimizer [26, 27, 28]

Numerous scientific disciplines have used meta-heuristic optimization techniques. Meta-heuristics are straightforward to comprehend. They draw inspiration from natural phenomena, animal behaviors, and evolutionary theories. Meta-heuristics are easily adaptable to different issues since they typically treat them as "black boxes." Third, the majority of meta-heuristics use processes without derivation. Meta-heuristics stochastically optimize issues as opposed to gradient-based methods. Finally, compared to traditional optimization strategies, meta-heuristics are better able to avoid local optima. Since the search space for real issues is frequently unknown, extremely complicated, and home to a large number of local optima, meta-heuristics are effective tools for optimizing these difficult real-world problems. Applying meta-heuristics to a variety of issues is simple. Finally, meta-heuristics outperform conventional optimization techniques when it comes to avoiding local optima. Meta-heuristics are workable solutions for optimizing these challenging real-world problems since the search space of realistic difficulties is frequently unknown and complex, with a high number of local optima. There isn't a single meta-heuristic that can handle all optimization issues. This outcome was reached according to the "No Free Lunch Theorem" [37]. In other words, a meta-heuristic can produce incredibly promising outcomes for a set of issues. On a different set of tasks, however, the same algorithm might not perform well. We can also suggest new meta-heuristics, integrate multiple meta-heuristics, or enhance existing meta-heuristics thanks to their simplicity. A new hybrid meta-heuristic search algorithm is being created as a result. In order to achieve hybridization, newly developed, well-known metaheuristic algorithms, GTO Hybridizes with chaotic search should integrate both exploration and exploitation search methodologies to address unit commitment and dispatch issues in real-world power systems.

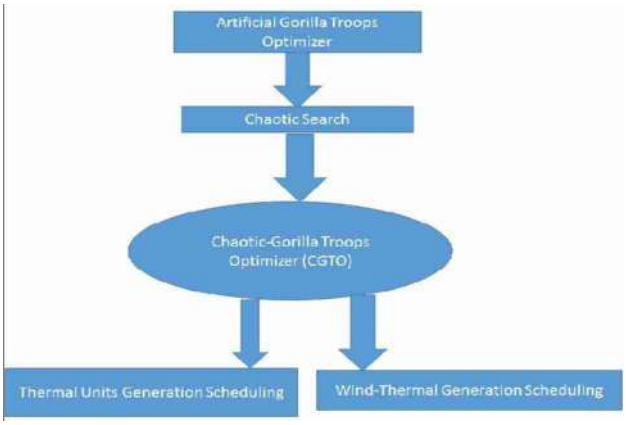

Fig. 1 Graphical Abstract of the objective of the Study

Novel contribution/innovation

Study's original contribution is the creation of a special hybrid optimizer. By moving the optimizer from the exploration side, GTO enables the optimizer to look for fresh, fruitful search locations. Its exploitation capability which is in charge of hunting for global solutions inside the search space has been boosted by the addition of a chaotic search operator. Its exploration and exploitation capabilities are more stable than its original version. This paper advances the current understanding of hybrid metaheuristic search algorithms. Fig. 1 expresses intent of proposed work.

Reason of choosing CGTO optimizer

It is important to note that one element related to the broader notion of exploration and exploitation is diversity. AGTO has high diversity. Low diversity does not necessarily imply exploitation, while high diversity stimulates exploration because exploitation calls for the utilization of both population and landscape data gathered during the search process. Literature survey further divulges that optimizer has quick convergence rate. However, when they are hybridizes, they tend to show further quick convergence; hence chaotic strategy further improves their shortcoming.

Objective of study

Clear objective of study is to find cost-effective generation schedule which should satisfy the load demand and spinning reserve requirement with lowest fuel cost. This objective has been achieved with the help of proposed hybrid optimizer. The suggested approach achieves the objective of

research in three parts. In the first, the CGTO resolves the unit commitment issue without taking into account the various limitations. Second, using a heuristic constraints repair mechanism, prior solutions are made to agree with unavoidable restrictions. Lastly, the suggested method is utilized to determine the best cost-effective solution within a given timeframe. This study looks into wind energy in more detail. The Chaos of Wind pattern is believed to follow the Weibull probability distribution function and be stochastic in nature.

Comprehensive benchmarking against some of the top techniques in the literature and in-depth simulation studies demonstrate that system operators can experience significant cost savings by deploying the CGTO optimizer. Saving in cost further increases if wind power share is taken into consideration along with thermal system.

Organization of the paper

The rest of the paper is organized as follows: The basic survival strategy adopted by the Gorilla Troops and the new improved chaotic Gorilla troop's optimizer is framed in Sect. 2. Section 3 proposes a mathematical problem formulation of generation scheduling. The characteristic equation in this section shows objective functions with all hard bound constrained. Section 4 for generation of uncertain renewable energy generation scenarios; scenarios of wind power generation in four specific seasons, probabilistic wind power model and estimated wind power for each hour calculation is done in this segments. Section 5 deals with modus operandi of optimizer to solve generation scheduling problem. Result and discussion for large-scale thermal and wind thermal test system constitute Sect. 6. Conclusive result and scope for improvements as well as limit of optimizer is discussed in Sect. 7.

Artificial gorilla troops optimizer

Gorilla troops optimizer is recent metaheuristic optimizer proposed by Benyamin el al [29]. All optimization processes were carried out by five distinct operators. Three distinct operators were utilized throughout the exploration phase, including migration to an uncharted area to advance GTO research. The gorilla movement, the second operator, enhances the harmony between exploration and exploitation. The third machinist in the exploration phase, migration towards a known location, significantly improves the GTO's capacity to explore for various optimization spaces. On the other hand, the use of two operators during the exploitation phase greatly improves search performance.

Artificial gorilla troops: exploration phase

All gorillas in the GTO approach are potential solutions, and the silverback gorilla at each optimization stage is the top candidate solution. The optimizer uses three distinct strategies for the exploration phase: migration to new sites, migration to existing areas, and migration to other gorillas. Each of these three approaches is chosen using a conventional technique. The random parameter determines how migration to an unknown site is decided (p). However, the strategy of approaching other gorillas is chosen if rand is less than 0.5. However, the migration to a known site technique is selected if rand is less than 0.5. Each of the employed techniques offers the GTO algorithm a significant amount of power. While the second mechanism restores algorithm exploration performance and the third technique aids the GTO dropping from local minima, the first mechanism enables the algorithm to keep a close eye on the entire solution universe.

$$GX^{\text{iter}+1} = \begin{cases} \text{Lowerbound} + r_1 \times (\text{Upperbound} - \text{Lowerbound}) ; & \mu < p \\ L \times H + (r_2 - C) \times X_r(iter) ; & \mu \geq 0.5 \\ X_i - L \times [L \times \{X(\text{iter}) - \text{GX}_r(\text{iter})\} + r_3 \times \{X(\text{iter}) - \text{GX}_r(\text{iter})\}] ; & \mu < 0.5 \end{cases} \quad (1)$$

As described in Eq. (1) in iteration t, $GX^{\text{iter}+1}$ is the gorilla candidate position vector. The current vector of the gorilla location is X (t). Furthermore, each iteration updates the values of and random number, which are random numbers ranging from 0 to 1 and play an important part in the optimization process. P is a 0–1 parameter that must be specified prior to the optimization procedure; it affects the possibility of choosing a migration method to an unknown site. The upper and lower limits of the variables are denoted by

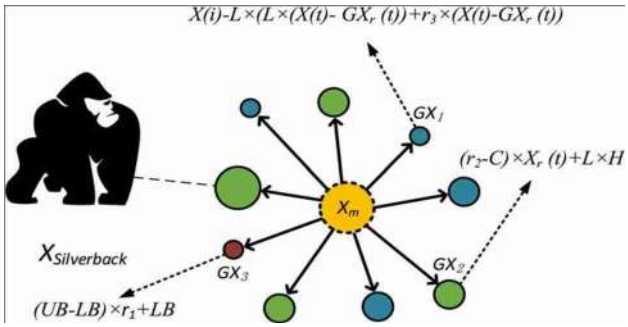

Fig. 2 Vector follows the silverback in 2D Search space [29]

its original name as "Lower bound", and "upper bound", respectively, the places adjusted in each phase were incorporated into one of the gorilla candidate locations vectors, which was chosen at random. Finally, C, L, and H, respectively, are obtained as describe in [29]

Artificial gorilla troops: exploitation phase

The silverback has a long-lasting effect on the other gorillas since he is the strongest and fittest one in the group, drawing them all to him. Additionally, they comply with Silverback's commands to travel to various locations in search of food supplies and to remain with him. Members could also have an effect on how the group moves as a whole. This method is picked when the C & W value is selected. When C ≥ W, Follow the silverback mechanism is selected and when C<W adult females competition is taken. W is variable to be set before optimization operation. Equation is used to model this phenomenon (2).This is dipicted in Fig. 2

$$\mathrm{GX}^{\mathrm{iter}+1} = X^{iter} + L \times M \times [X^{\mathrm{iter}} - X_{\mathrm{silverback}}] \tag{2}$$

$\mathrm{GX}^{\mathrm{iter}+1}$ In the following t iteration of Equation is the gorilla candidate position vector (1). The gorilla's current location vector is X. (t). Furthermore, the values of r1, r2, r3, and rand, which are random numbers ranging from 0 to 1, are updated with each iteration. p is a 0–1 range parameter that must be specified before to the optimization stage.

$$M\left(\left|\frac{1}{N}\sum_{i-1}^{N}\mathrm{GX}_i(\mathrm{iter})\right|^{g}\right)^{\frac{1}{g}} \tag{3}$$

$$g = 2^{L} \tag{4}$$

Competition for adult female

In the event where C is less than W, the second mechanism is used. When teenage gorillas reach puberty, they engage in violent competition with other males to choose adult females to add to their group. These fights can go for days and involve numerous participants. Equation is used to model this phenomenon (5)

$$\mathrm{GX}_i^{\mathrm{iter}} = X(\mathrm{Silverback}) - A \times [X(\mathrm{silverback}) \times Q - X(\mathrm{iter}) \times Q] \tag{5}$$

$$Q = 2 \times r_5 - 1 \tag{6}$$

$$A = \beta \times E \tag{7}$$

$$E = \begin{cases} N_1 \ ; \ \mathrm{rand} \geq 0.5 \\ N_2 \ ; \ \mathrm{rand} < 0.5 \end{cases} \tag{8}$$

In the exploitation phase of the algorithm, two behaviors are used: first is imitation of the silverback and second phase is fatal Competition for fully grown females. The group's leader is a silverback gorilla, who makes all of the decisions, directs the gorillas to food sources, and controls their movements. The silverback is in charge of the gorillas' safety and well-being, and they all obey his commands. The silverback gorilla, on the other hand, may become feeble and elderly, eventually dying, and the group's silverback gorilla may take over as leader, or other male gorillas may challenge the silverback gorilla and seize control of the group. The addition of a chaotic search tool boosts its local search power.

Different chaotic functions

Present manuscripts use a special kind of chaotic function, and hybridize with gorilla troop's optimizer. The intention behind the same is it improves its exploitation capability since GTO optimizer already proved to be one of best optimizer as far as exploration phase is concerned [29]; hence chaotic gorilla optimizer has batter balance between exploitation and exploration search capability. Many meta-heuristic algorithms employ the notion of probability distribution, which incorporates a degree of randomness in the optimizer, to boost local search capabilities. If unpredictability due to periodicity and idleness is correctly utilized, chaotic maps may be helpful. Equation 21 satisfies all of these chaotic requirements

$$Z(q+1) = f(z_q) \tag{9}$$

In Eq. (9) z_{k+1} &$f(z_k)$ are the $(k+1)^{th}$ & k^{th} chaotic number, respectively. Following popular chaotic functions are usually adopt to improve optimization process. In the propose research singer map function is used to enhance optimizer local search capability. List of chaotic curve has been given in Appendix-A.

Pseudo code of CGTO

Algorithm: Pseudo code of CGTO

% Parametric Settings for CGTO setting

Input: Parameters: T, β, p, Number of population (N), Maximum number of iterations ($iter_{\max}$)
Output: The location of Gorilla and its fitness value

% Initialization of parameters

Initialize the random population $X_i\,(i=1,2,3,...,N)$
Calculate the fitness value of Gorilla

% Main loop

While (stopping criterion is not met) do

Update the C using $C=F\times\left(1-\frac{Iter}{Iter_{\max}}\right)$

Update the L using $L=C\times l$

% Exploration Phase

For (Each Gorilla Position X_i) do

Update the location of Gorilla using

$$GX(iter+1)=\begin{cases} lb+r_1\times(UB-LB); & \mu<p \\ L\times H+(r_2-C)\times X_r(iter); & \mu\geq 0.5 \\ X_i-L\times[L\times\{X(iter)-GX_r(iter)\}+r_3\times\{X(iter)-GX_r(iter)\}]; & \mu<0.5 \end{cases}$$

end for

% Create Group

Calculate the fitness value of the Gorilla
If GX is better than X, replace them
Set $X_{silverback}$ as the location of silverback (best location)

% Exploitation Phase

For (each Gorilla (X_i **))** do

If $|c|\geq 1$, then

Update the Gorilla Location using $GX(iter+1)=X(iter)+L\times M\times[X(iter)-X_{silverback}]$

else

Initialize $r_0=rand$

Update r_5 using $r_5(iter+1)=1.7\left(7.86r_0-23.3r_0^2+28.75r_0^3-13.301875r_0^4\right)$

Update the Gorilla Location using $GX(i)=X_{silverback}-A\times[X_{silverback}\times(2r_5-1)-X(iter)\times(2r_5-1)]$

End if
End for
% Create Group
Calculate the fitness values of Gorilla
If New Solutions are better than previous solutions, replace them
Set $X_{silverback}$ as the location of silverback (best location)

End while loop

Return Best fitness and best position of Gorilla

Unit commitment problem formulation

The unit commitment problem's goal is to reduce the total operational cost of generating power by as much as possible over a given planning horizon:

$$\mathrm{NOC} = \sum_{t=1}^{t=T}\sum_{i=1}^{i=N}[\mathrm{FC}_i(P_i^t) * \psi_i^t + \psi_i^t(1-\psi_i^{t-1})\mathrm{SUC}_i^t + \psi_i^{t-1}(1-\psi_i^t)\mathrm{SD}_i^t \tag{10}$$

$$\mathrm{FC}_i(P_i^t) = a_i * (P_i^t)^2 + b_i * (P_i^t) + c_i \tag{11}$$

$$\mathrm{SUC}_i^t = \left\{ \begin{array}{l} \mathrm{HOTS}_i^t, \quad \text{if } \mathrm{MDT}_i \le T_{i,\mathrm{off}}^t + T_i^{\mathrm{cold}} \\ \mathrm{COLDS}_i^t, \text{if } T_{i,\mathrm{off}}^t > \mathrm{MDT}_i + T_i^{\mathrm{cold}} \end{array} \right\} \tag{12}$$

This objective function is subject to following constraints.

System constraints

Power balance, spinning reserve, and tie line capacity restrictions are all examples of system constraints. These restrictions affect all of the system's generating units, hence they're referred to as coupling constraints. The following is a detailed description of each constrain

Power balance constraint

Power demand plus losses must be met by generation. The load ratio share, or load conferred, in any system is random variable; hence power generation has to be adjusted at every instant of time in accordance with load.

$$\sum_{i=1}^{\mathrm{NG}} P_i^t * \psi_i^t = P_D \quad (t = 1, 2, ..., T) \tag{13}$$

For wind thermal system this constraints amended as follows

$$\sum_{i=1}^{\mathrm{NG}} P_i^t * \psi_i^t + P_{\mathrm{wind}}^t = P_D \quad (t = 1, 2, ..., T) \tag{14}$$

Spinning reserve constraint

On-line units' total maximum capacity must be larger than demand + losses and the spinning reserve required. This spinning reserve is required to meet unexpected increases in demand or forced generating unit outages. The required spinning reserve is normally defined by the maximum capacity of one of the system's two largest generating units or a percentage of predicted peak demand for the time frame in question. In the present manuscript spinning reserve is considered as 10% of peak load demand. The formula for the spinning reserve restriction is provided in

$$\sum_{i=1}^{\mathrm{NG}} P_{i(\max)} * \psi_i^t \ge P_D + \mathrm{SR}_t \quad (t = 1, 2, ..., T) \tag{15}$$

Thermal unit constraints

The beginning condition, minimum and maximum generation output limits, minimum up-time and down-time, and unit status restriction constraints are all unique to each thermal unit. Non-coupling limitations are what they're called. The following is a description of each limitation.

Each constraint is described as follows.

Initial condition

Initial condition of a generating unit includes number of hours that it has consecutively been on-line or off-line and its generation output at an hour before the scheduled time horizon starts. Both initial number of on- line/off-line hours and initial generation output, when associated with the other unit constraints, may limit the on-line/off-line status and the generation output of the unit in the scheduled time horizon.

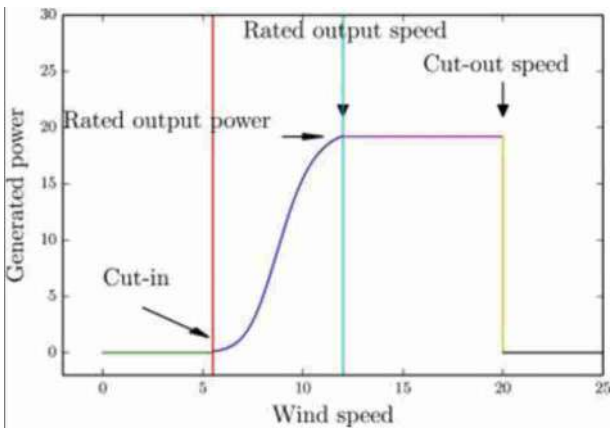

Fig. 3 The variation of generated power with wind speed

Minimum and maximum generation output limits

Machine output limits or economic output limits specify a range of unit power outputs. Due to unit ramp rate constraints, the minimum and maximum limits that bound the generation output of each generating unit in a given hour, as stated in Eq. 28, can be adjusted within the range of unit power outputs. The next sections go over these restrictions.

$$P_i^{\min} \le P_i \le P_i^{\max} \tag{16}$$

Minimum up-time

A unit's minimum up-time is the amount of time it must be on-line once it has been turned on. The number of hours that a unit must be off-line after it has been turned off is known as the minimum down-time

$$T_{t,i}^{\mathrm{ON}} \ge \mathrm{MUT}(i)\ (i = 1, 2, ..., \mathrm{NG}; t = 1, 2, ..., T) \tag{17}$$

Minimum down-time constraints

Unit once gets off it should not turned on until it reaches certain minimum time to get completely cooled off. This minimum time is known as minimum down time.

$$T_{t,i}^{\mathrm{OFF}} \ge \mathrm{MDT}(i)\ (i = 1, 2, ..., \mathrm{NG}; t = 1, 2, ..., T) \tag{18}$$

Wind speed modelling

For the sake of describing stochastic behavior of wind speed in predefined time period, Weibull document has been considered. Weibull division at t th time segment for the wind speed u^t (m/s) can be shown as

$$f_u^t(u) = \frac{k^t}{c^t}.\left(\frac{v^t}{c^t}\right)^{k^t-1}.\exp\left(-\left(\frac{u^t}{c^t}\right)^{k^t-1}\right) \ for\ c^t > 1;\ k^t > 0 \tag{19}$$

At the tth time segment, the shape parameter (k^t) and scale factor (c^t) are expressed as shown.

$$k^t = \left(\frac{\sigma^t}{\mu_u^t}\right)^{-1.086} \tag{20}$$

$$c^t = \left(\frac{\mu_u^t}{\Gamma(1 + 1/k^t)}\right) \tag{21}$$

Power generation model

Any device that can slow down a mass of moving air, such as a sail or propeller, may extract some of the energy that the wind possesses due to its speed and utilize it to do meaningful work. The wind energy converter's output power is determined by three parameters. Due to chaotic wind dynamics, it is nearly hard to predict wind power reliably and precisely for the following three factors: wind speed, cross-sectional area of wind swept by the rotor, and total rotor conversion efficiency. The hourly output power of wind turbine corresponds to a specific t^{th} time segment

$$P_{\mathrm{WT}}^t = \sum_{g=1}^{N_v} PG_{\mathrm{WTg}} * P_u(u_g^t) \tag{22}$$

The probability of wind speed for each state during any specific time frame is calculated as below.

$$P_u(u_g^t) = \left\{ \begin{array}{l} \int_0^{(u_g^t+u_{g+1}^t)/2} f_v^t(u)dv \ for\ g = 1 \\ \int_{(s_{g-1}^t+s_g^t)/2}^{(u_g^t+u_{g+1}^t)/2} f_u^t(u)du \ for\ g = 2...(N_s - 1) \\ \int_{(u_{g-1}^t+u_g^t)/2}^{\infty} f_u^t(u)du \ \ for\ g = N \end{array} \right\} \tag{23}$$

Wind speed variability must be taken into account when designing large WEC machines; for each turbine, there is a minimum wind speed called the cut-in wind speed at which rotation can begin, and a rated wind speed at which the generator produces its rated power; the rotation rate is kept constant by varying the generator output. When wind speeds surpass the rated value, the pitch of the blades is automatically adjusted to maintain rotor speed. The blades are feathered, similar to air craft, at very high wind speeds, and spinning stops. Cut off speed is the wind speed at which this occurs, and the electric power production is practically constant.

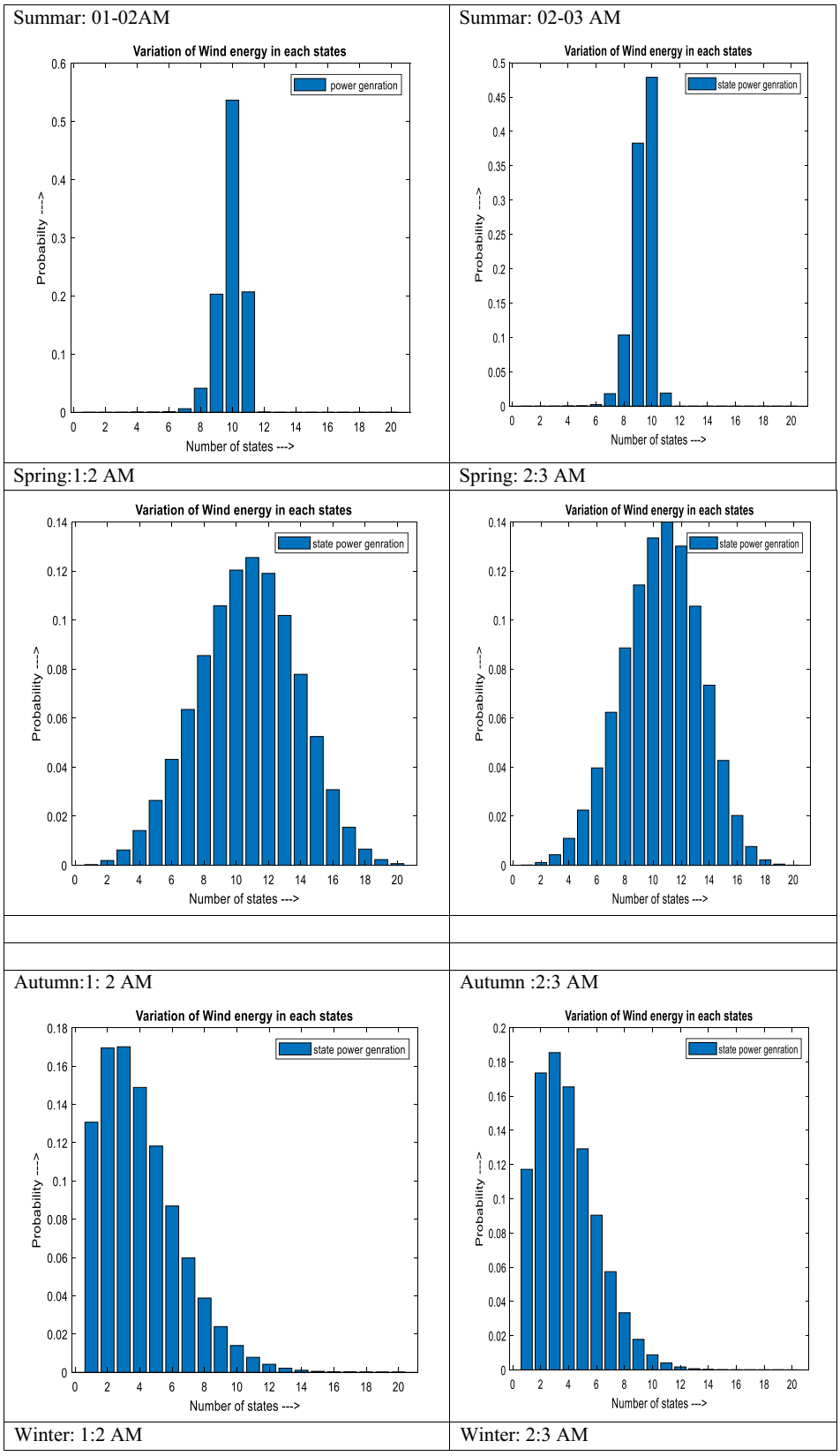

Fig. 4 Wind power probability profile with respect to number of state

Fig. 4 (continued)

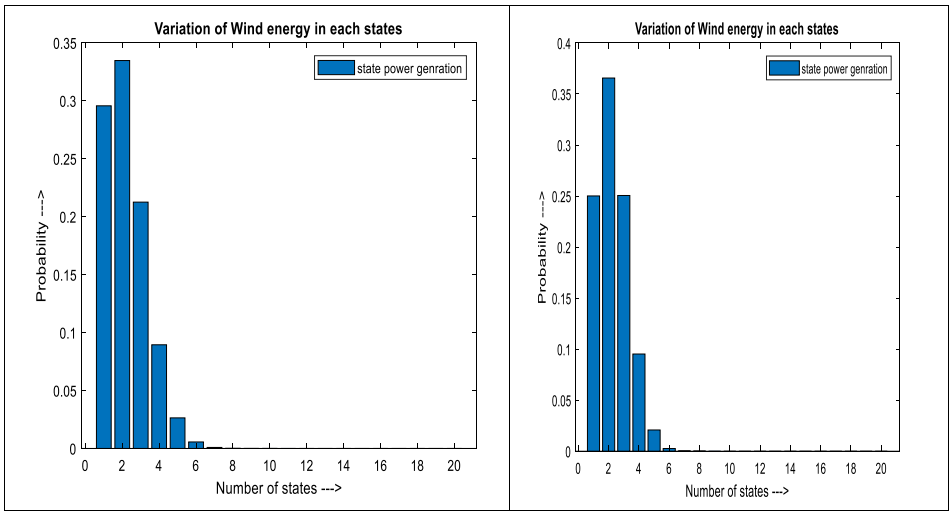

The variation of generated power with wind speed is approximately shown in Fig. 3

The power generation of the wind turbine depends on its performance curve. For nonlinear performance characteristics power generation of wind turbine at average speed for state g is calculated as

$$PG_{\mathrm{WT}}^{g}=\begin{cases}0 & u_{\mathrm{ag}}<c_{\mathrm{in}},\, or\, u_{\mathrm{ag}}>u_{\mathrm{count}}\\ \left(a*u_{\mathrm{ag}}^{3}+b*P_{\mathrm{rated}}\right) & u_{\mathrm{cin}}\le u_{\mathrm{ag}}\le u_{N}\\ P_{\mathrm{rated}} & u_{N}\le u_{\mathrm{ag}}\le u_{\mathrm{count}}\end{cases} \tag{24}$$

where P_{rated} is the maximum power that can be generated by Wind turbine, v_{cout} is cutout wind speed; constant a and b are function of cut in wind speed v_{cin}. And Nominal wind speed v_N, obtained as

$$a=\frac{P_{\mathrm{rated}}}{\left(u_{N}^{3}-u_{\mathrm{cin}}^{3}\right)} \tag{25}$$

$$b=\frac{u_{\mathrm{cin}}^{3}}{\left(u_{N}^{3}-u_{\mathrm{cin}}^{3}\right)} \tag{26}$$

Wind data

Practical wind data was collected from the Kakdwip area, which is located close to the Bay of Bengal at 21.8830 N and 88.183E. A particular characteristic of dramatic weather change is provided by its closeness to the tropic of cancer [26]. In addition, the study time is separated into four seasons: spring, summer (May to July), autumn (August to October), and winter (November to January) (February to April). Each season is represented by 24 segments, which correspond to the season's hourly intervals. 96 time periods make up the year, then (24 for each season). Wind speed in meters per second, mean and standard deviation. Appendix-B provides full data (Mean and Standard deviations) for all the seasons. Each hour is separated into 20 states (scenarios). Practical wind turbine data is given in Appendix-C. In Appendix-D, a wind power given from wind turbine's for all the season's summer, autumn winter and spring is listed and described. Wind erratic pattern follows Weibull probability function. Probabilistic power in each states has been shown in Fig. 4. Over all power for that hour is sum of all states power generation, and shown in Fig. 5.

Number of states for Weibull probability function has been chosen 20. This helps to realize the distribution in discrete form. The discrete probability distribution for all seasons, i.e. summer, spring, and autumn and winter, for four hour has been illustrated in Fig. 4.

Wind power for 24-h

In this work, the wind speed distribution and statistical analysis are determined using the Weibull distribution approach. To derive the Weibull probability density function, you must know the figure and scale parameters. The equation may be used to demonstrate the generic form of the two-parameter Weibull probability density function for wind speed (25).

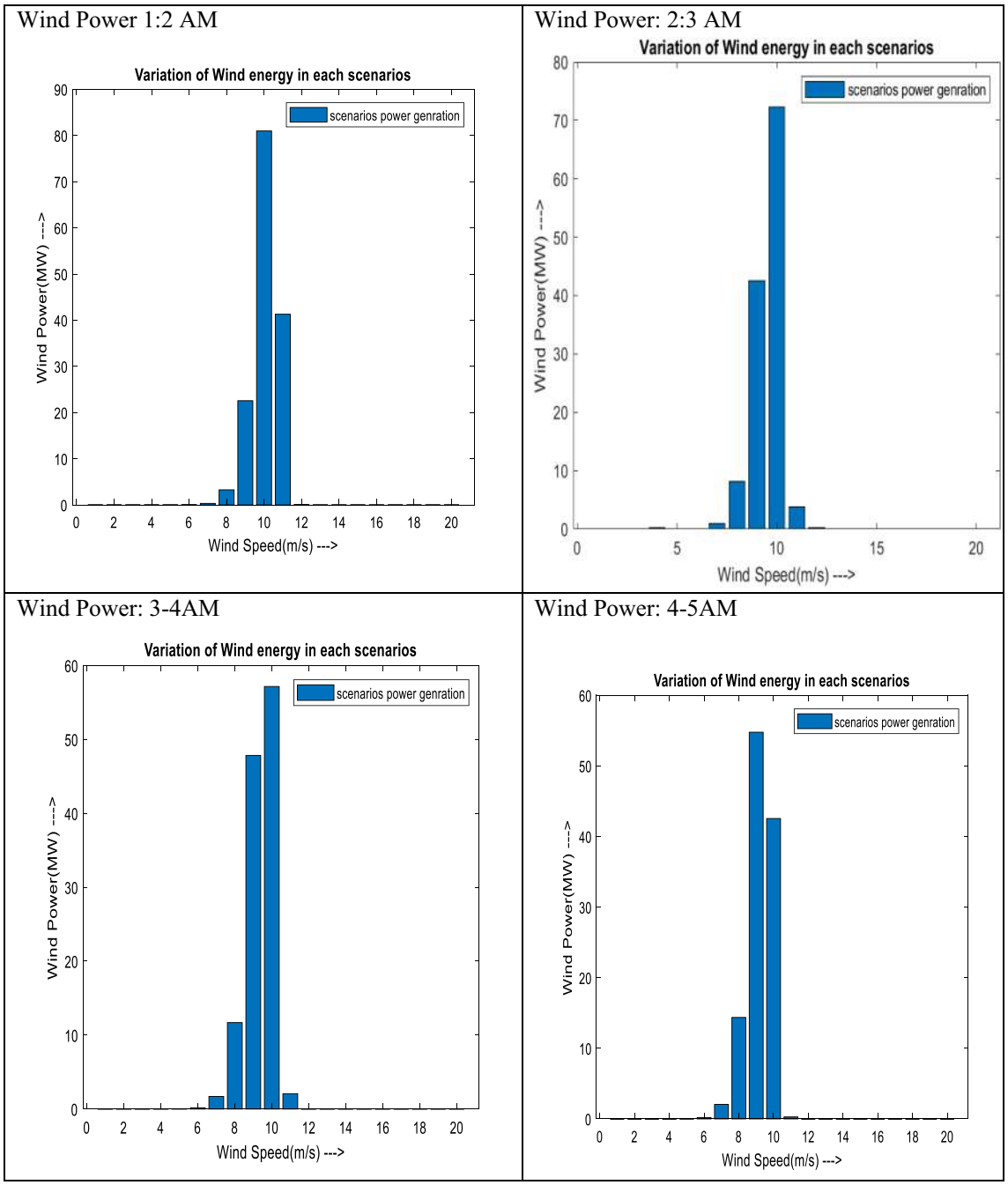

Fig. 5 Wind power generation in each stat

Equation may be used to compute the shape function and scale factor values for each observed time (22–23).

The parameters of the Weibull distribution can be determined using a variety of approaches. The most commonly used strategy is the graphical method, which is a maximum possibility method. The graphical technique was employed in this investigation. The veracity of this technique is based on the minimization of vertical discrepancies between observed and segmented wind speed data. The following equation may be used to represent the average wind speed of the Weibull distribution. In this, the wind power over a 24-h period has been computed and tallied (4). In addition,

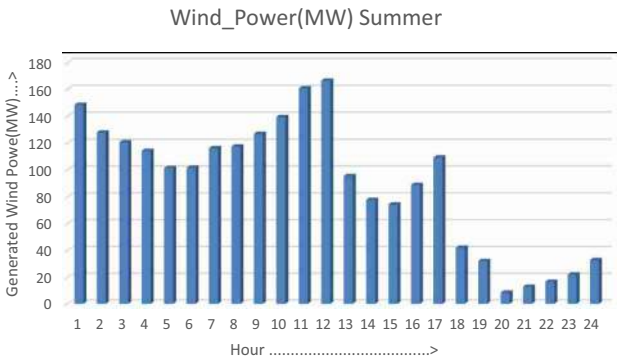

Fig. 6 Wind Power Generation Profile in Summer Seasons for 24-Hours

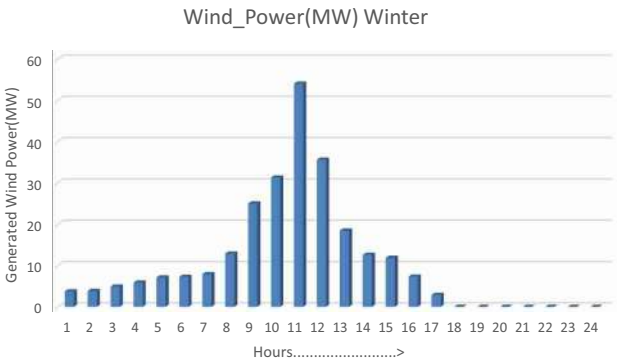

Fig. 7 Wind Power Profile For 24-Hour In the winter seasons for 24-h

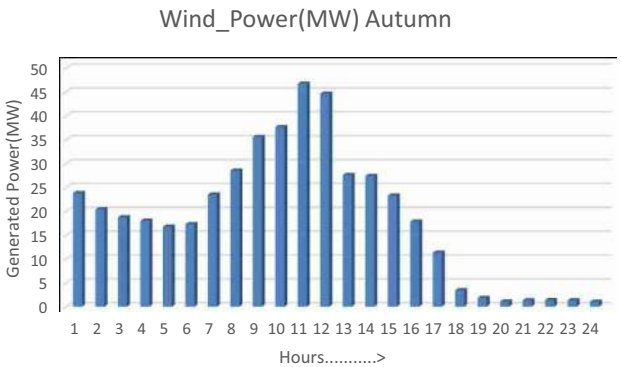

Fig. 8 Wind Power Profile For 24-Hour In the autumn seasons for 24-h

in Fig. (5), wind power is plotted against wind speed (in m/s2) in each state. Wind power for all the seasons is obtained and tabulated in Appendix-D.

In this manuscripts an only wind data in the seasons of spring has been considered. A composite wind-thermal system has

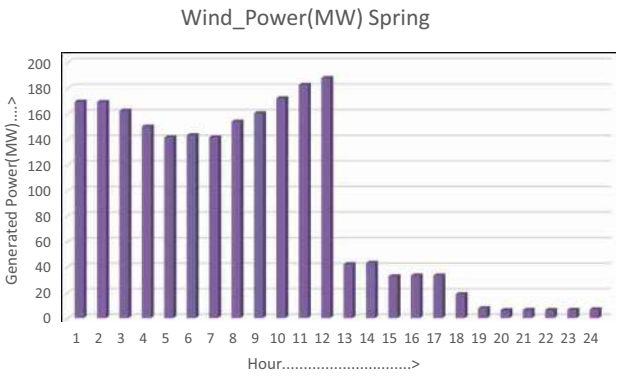

Fig. 9 Wind Power Profile For 24-Hour In the spring for 24- hour

been proposed in witch wind power for 24 h has already calculated. Wind owing to cost free has got precedence over the thermal units hence utilized first in this way effective load on thermal units get reduced. $(P_D(t) = P_{\text{Load}}(t) - P_{\text{wind}}(t)$These under stressed load is now subject to tack by the thermal units with their all constraints in to considerations.

Wind Power Profile for 24 h for spring seasons has been calculated based on the mean and average speed as depicted in Appendix-B. Using Weibull probability distribution wind power for all the four seasons is calculated and given in Appendix-D. Its profile for 24 h is shown in Figs. 6, 7, 8, 9

Solution approach for generation scheduling problem

This strategy exploits and explores their placement in a suitable search space while taking into account all constraints using a hybrid CGTO method. Finding out the status of committed units is necessary before fixing a scheduling issue. The entire generation schedule issue can be solved using the following steps.

Step 1: The demonstration of particle is defined in order to tackle the unit commitment problem using CGTO. A particle is a discrete entity that has a binary state of either 1 or 0. These states are similar to the on and off states of a unit. These discrete individuals would exhibit the unit commitment schedule across a time horizon T, and the full set of individuals would be recorded in a binary metrics of order GT*T, the population matrix illustrated below.

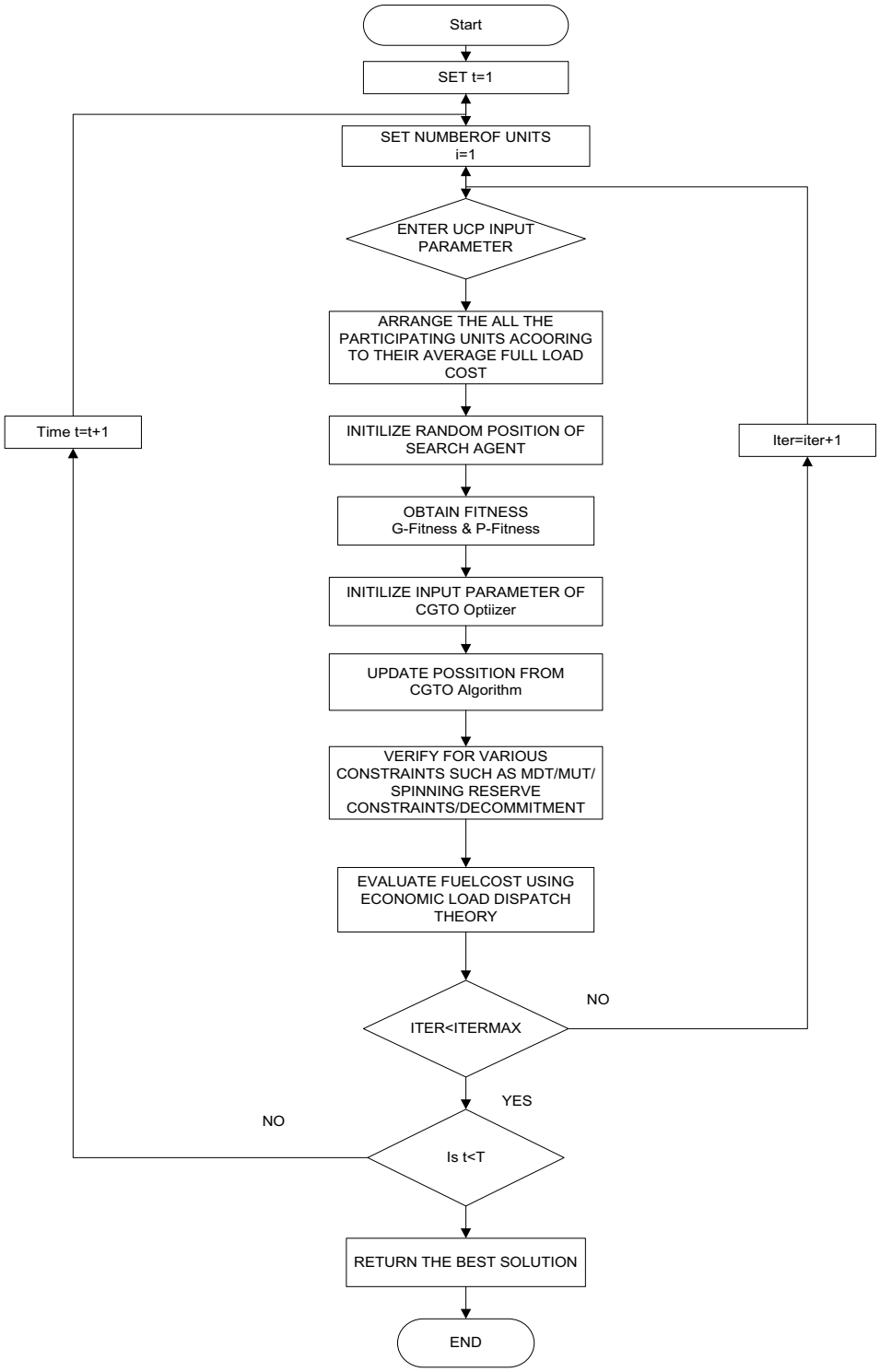

Fig. 10 Flow chart of Generation Scheduling Process by CGTO Optimizer

$$u_{NP} = \begin{bmatrix} u_1^1 & u_1^2 & .. & .. & u_1^T \\ u_2^1 & u_2^2 & .. & .. & u_2^T \\ . & & & & \\ . & & & & \\ u_N^1 & u_N^2 & .. & .. & u_N^T \end{bmatrix}_{N\times T}$$

Power generation schedule, P(i:t) for i^{th} generating unit at t^{th} hour within maximum and minimum power generation limits can be found as below

$$P(i:t) = P(i)_{\min} + rand() * \left\{P(i)_{\max} - P(i)_{\min}\right\} \quad (28)$$

Step 2: all the generating units are prioritize according to the average full load cost.
Step 3: available wind power for each hour has been calculated beforehand with the help of Weibull probability density function. Effective hourly load has now been reduced to $P_{d,t}^{\text{new}} = P_{d,t}^{\text{old}} - P_{\text{wind}}^{t}$. As available wind power for each hour must be utilized and has priority over thermal units, as wind power does not impose any fuel cost on the system. In this study wind power for the spring seasons has been considered for generation scheduling problem.
Step 4: Because computed priority units may fail to meet spinning reserve restrictions, heuristic methods are used to fix spinning reserve limitations.
Step 5: For time violation limitations, all individual units of the population matrix are repaired. Because all individual units must have the shortest possible up and down times, if the suggested method violates these restrictions, it should be fixed using an aggressive heuristics method. As a result of this reasoning, the algorithm is compelled to meet these limits at the expense of fitness value.
Step 6: Repairing the MDT/MUT might result in a larger mismatch in the spinning reserve, resulting in increased operational costs. The program determines the most redundant unit using a heuristic methodology used to repair de-commitment of units. The most redundant units are those with the lowest priority rank, and these units may frequently be turned off without causing further MDT/MUT violations.
Step 7: When complete patterns of committing and decommitting units within a stipulated time horizon are known, then most economic load problem is solved.
Step 8: Calculate the fitness value of each particle in entire population using objective function.
Step 9: Define Artificial Gorilla troops optimizer parameter as described in Sect. (2), obtain position with AGTO and allow chaotic search for local search and obtain new position according to its governing equations, obtained by CGTO Optimizer.
Step 10: Modify the new updated position given by CGTO by passing through function that handles all vital constraints such as MDT/MUT, Spinning reserve, and decommitment. This process is known as grey zone modification. Detail of constraints handling strategies and their heuristic code have been presented in Appendix-E.
Step11: obtain final gbest position through CGTO optimizer.
Step12: Since after grey zone modification their exist modification in unit schedule, so obtained optimal economic generation schedule.
Step13: Obtain Startup cost units, startup may be different in all cases when unit is started from cold start, warm start or hot start.
Step14: If maximum iteration is achieved stop it otherwise increase the iteration number.
Step 15: Stop the optimal solution for generation scheduling through the particle whose index is g-best.

Entire process has been shown in Fig. 10.

Result and discussion

For solving UCP, the proposed CGTO is tested on different system sizes based on a basic system of 10 units from literature [30]. The scheduling time horizon T is chosen as one day with 24 intervals of one hour each. The spinning hour requirement is set to 10% of total demand. For the system 20, 40, 60, and 100 unit the basic 10 unit system is duplicated and load demands are adjusted proportionally to the system size. General experimental setup has been carried out with number of trial run = 30, maximum iteration = 100. And matlab-2019a (8.1.0.604) software on windo10, home basic CPU @2.10Ghz, RAM 6 GB, Processor i5, 64 bit operating system is used. Tables 1, 2, 3 show generation scheduling of thermal unit system. Rest of the Table and figures are present in Appendix –F.

Test system-I (10 -Unit Thermal System With 5% SR)

Table 1 Generation scheduling of committed units for 10 unit thermal system (with 5%SR)

Hours	Generation scheduling										Cost		
	U1	U2	U3	U4	U5	U6	U7	U8	U9	U10	Startup	Fuel	Total
1	455	245	0	0	0	0	0	0	0	0	0	13,683.13	13,683.13
2	455	295	0	0	0	0	0	0	0	0	0	14,554.5	14,554.5
3	455	395	0	0	0	0	0	0	0	0	0	16,301.89	16,301.89
4	455	455	0	0	40	0	0	0	0	0	560	18,597.67	19,157.67
5	455	390	130	0	25	0	0	0	0	0	1910	20,051.16	21,961.16
6	455	455	130	0	60	0	0	0	0	0	0	21,891.43	21,891.43
7	455	410	130	130	25	0	0	0	0	0	0	23,261.98	23,261.98
8	455	455	130	130	30	0	0	0	0	0	0	24,150.34	24,150.34
9	455	455	130	130	110	20	0	0	0	0	0	26,588.96	26,588.96
10	455	455	130	130	162	43	25	0	0	0	520	29,365.95	29,885.95
11	455	455	130	130	162	80	25	13	0	0	60	31,219.63	31,279.63
12	455	455	130	130	162	80	25	53	10	0	60	33,205.25	33,265.25
13	455	455	130	130	162	43	25	0	0	0	0	29,365.95	29,365.95
14	455	455	130	130	110	20	0	0	0	0	0	26,588.96	26,588.96
15	455	455	0	130	140	20	0	0	0	0	0	24,318.01	24,318.01
16	455	440	0	130	25	0	0	0	0	0	0	20,895.88	20,895.88
17	455	390	0	130	25	0	0	0	0	0	260	20,020.02	20,280.02
18	455	455	0	130	60	0	0	0	0	0	0	21,860.29	21,860.29
19	455	455	0	130	135	0	25	0	0	0	0	24,569.99	24,569.99
20	455	455	130	130	162	0	25	0	43	0	170	29,867.32	30,037.32
21	455	455	130	130	105	0	25	0	0	0	0	26,842.13	26,842.13
22	455	385	130	130	0	0	0	0	0	0	60	21,879.33	21,939.33
23	455	315	130	0	0	0	0	0	0	0	0	17,795.28	17,795.28
24	455	215	130	0	0	0	0	0	0	0	0	16,052.85	16,052.85
	Overall cost	3600	552,927.9	556,527.9									

Test system-II (10 -Unit Thermal System With 10%SR.)

Table 2 Generation scheduling of committed units for 10 unit thermal system (With 10% SR)

Hours	Generation scheduling										Cost		
	U1	U2	U3	U4	U5	U6	U7	U8	U9	U10	Startup	Fuel	Total
1	455	245	0	0	0	0	0	0	0	0	1620	13,683.13	15,303.13
2	455	295	0	0	0	0	0	0	0	0	560	14,554.5	15,114.5
3	455	370	0	0	25	0	0	0	0	0	0	16,809.45	16,809.45
4	455	455	0	0	40	0	0	0	0	0	0	18,597.67	18,597.67
5	455	390	0	130	25	0	0	0	0	0	0	20,020.02	20,020.02
6	455	360	130	130	25	0	0	0	0	0	0	22,387.04	22,387.04
7	455	410	130	130	25	0	0	0	0	0	690	23,261.98	23,951.98
8	455	455	130	130	30	0	0	0	0	0	0	24,150.34	24,150.34
9	455	455	130	130	85	20	25	0	0	0	0	27,251.06	27,251.06
10	455	455	130	130	162	33	25	10	0	0	60	30,057.55	30,117.55
11	455	455	130	130	162	73	25	10	0	10	120	31,926.21	32,046.21
12	455	455	130	130	162	80	25	43	10	10	30	33,890.16	33,920.16
13	455	455	130	130	162	33	25	10	0	0	0	30,057.55	30,057.55
14	455	455	130	130	85	20	25	0	0	0	0	27,251.06	27,251.06
15	455	455	130	130	30	0	0	0	0	0	0	24,150.34	24,150.34
16	455	310	130	130	25	0	0	0	0	0	0	21,513.66	21,513.66
17	455	260	130	130	25	0	0	0	0	0	0	20,641.82	20,641.82
18	455	360	130	130	25	0	0	0	0	0	170	22,387.04	22,557.04
19	455	455	130	130	30	0	0	0	0	0	0	24,150.34	24,150.34
20	455	455	130	130	162	33	25	10	0	0	320	30,057.55	30,377.55
21	455	455	130	130	85	20	25	0	0	0	0	27,251.06	27,251.06
22	455	455	0	0	145	20	25	0	0	0	0	22,735.52	22,735.52
23	455	425	0	0	0	20	0	0	0	0	0	17,645.36	17,645.36
24	455	345	0	0	0	0	0	0	0	0	0	15,427.42	15,427.42
	Overall cost										3570	559,857.8	563,427.8

Test system-II (20 -Unit Thermal System)

Table 4 Generation scheduling of committed units for 10 and 20 unit thermal system (Comparison With other optimizer)

Method	Best cost ($)	Mean cost($)	Worst cost ($)	Mean time (second)	Best cost($)	Mean cost($)	Worst cost ($)	Mean time(second)
10 UNIT					20 UNIT			
EPL [31]	563,977	–	–	0.72	1,124,369	–	–	2.97
ILA [32]	565,828	–	–	0.32	1,125,997	–	–	4.99
QM [32]	565,828	–	–	1.29	1,125,997	–	–	115.8
LR[33]	565,825	–	–	–	1,130,660	–	–	–
GA [33]	565,825	–	570,032	221	1,126,243	–	1,132,059	733
EP [34]	564,551	565,352	566,231	100	1,125,494	1,127,257	1,129,793	340
SA [35]	565,828	565,988	566,260	3.35	1,126,251	1,127,955	1,129,112	16.8
IBPSO [36]	563,977	564,155	565,312	27	1,125,216	1,125,448	1,125,730	55
DE [18]	563,938	–	–	27.4	1,124,291	–	–	52.8
BFA [37]	564,842	–	–	110	1,124,892	–	–	350
ICA [38]	563,938	564,408	–	48	1,124,274	–	–	63
HSA [39]	564,368	–	–	6.9	1,127,177	–	–	61
BGSA [40]	563,937	564,031	564,241	–	1,123,996	1,124,738	1,125,156	–
Fuzzy SADP [10]	563,978	–	–	–	1,123,390	–	–	–
GMTLBO-BH[41]	563,938	–	–	6.75	1,123,297	–	–	17
BRABC [42]	563,938	564,040	565,640	40.75	–	–	–	–
MBABC [43]	563,977	563,999	564,036	16.12	1,124,556	1,124,877	1,125,342	47.61
CGTO	563,427.8	564,297	565,017	0.01462	1,123,449	1,125,435	1,126,660	0.015625

Comparison of results with other similar state of the art algorithm

The proposed algorithm is tested on medium and large dimensional system 10, 20, 40, 60, 80 and 100 unit system (small test system for 7 unit also tested). The system data and load pattern for basic 10 unit, 24-h test system is adopted from [30]. For 20 unit system the 10 unit system data is taken as a reference, but it is multiplied by two, similarly load demand is duplicated. In all the test system cases cost function is quadratic as shown in equation 11; the spinning reserve is taken 10% of load demand for all the cases. However for 10 unit system 5% SR is also used to evaluate cost solution Wind integrated dynamic generation scheduling and. Convergence curve has been shown in Appendix-F. The amount of dollar saving is depicted in Table 6. Tables 4 and 5 show cost comparison of CGTO algorithm with other state of art optimizer. These tables clearly show the total operational costs achieved by the new improved CGTO algorithm is best for all the test system.

Detail discussion in accordance to the main objective

The CGTO technique is used to resolve generation scheduling for various test systems with 10 to 100 units. To successfully use the CGTO for addressing the highly constrained, non-convex generation scheduling problem, the best values for various parameters must be determined. This test system has been used to execute a number of tests. The experiments show that the factors listed below are ideal for the CGTO algorithm's greatest performance: population size is four times larger than the system size (i.e. for 10 unit population size is 40). The Appendix- F description is used to set the CGTO parameters. The highest iterative generations is 100. Under the chosen parameters, we run CGTO 30 times from different initial populations in succession and select the best result as the final optimization solution. In the meantime, for each test system we also performed CGTO 30 trials from different initial populations in succession to examine the variation in their total production costs. Test results are

Table 3 Generation scheduling of committed units for 20 unit thermal system

Hours	Generation scheduling																				Cost		
	U1	U2	U3	U4	U5	U6	U7	U8	U9	U10	U11	U12	U13	U14	U15	U16	U17	U18	U19	U20	Startup	Fuel	Total
1	455	245	0	0	0	0	0	0	0	0	455	245	0	0	0	0	0	0	0	0	0	27,366.26	27,366.26
2	455	295	0	0	0	0	0	0	0	0	455	295	0	0	0	0	0	0	0	0	1240	29,109	30,349
3	455	382.5	0	0	0	0	0	0	0	0	455	382.5	0	0	25	0	0	0	0	0	0	33,111.24	33,111.24
4	455	417.5	0	130	0	0	0	0	0	0	455	417.5	0	0	25	0	0	0	0	0	2010	37,197.46	39,207.46
5	455	402.5	0	130	0	0	0	0	0	0	455	402.5	0	130	25	0	0	0	0	0	550	39,532.69	40,082.69
6	455	425	0	130	25	0	0	0	0	0	455	425	130	130	25	0	0	0	0	0	0	44,157.72	44,157.72
7	455	455	0	130	45	0	0	0	0	0	455	455	130	130	45	0	0	0	0	0	0	46,008.84	46,008.84
8	455	455	130	130	30	0	0	0	0	0	455	455	130	130	30	0	0	0	0	0	1120	48,300.68	49,420.68
9	455	455	130	130	97.5	20	25	0	0	0	455	455	130	130	97.5	20	0	0	0	0	860	53,838.78	54,698.78
10	455	455	130	130	162	33	25	10	0	0	455	455	130	130	162	33	25	10	0	0	640	60,115.1	60,755.1
11	455	455	130	130	162	73	25	10	10	0	455	455	130	130	162	73	25	10	10	0	180	63,832.12	64,012.12
12	455	455	130	130	162	80	25	43	10	10	455	455	130	130	162	80	25	43	10	10	90	67,780.33	67,870.33
13	455	455	130	130	162	33	25	10	0	10	455	455	130	130	162	33	25	0	0	0	0	60,143.56	60,143.56
14	455	455	130	130	97.5	20	0	0	0	0	455	455	130	130	97.5	20	25	0	0	0	0	53,838.78	53,838.78
15	455	455	130	130	30	0	0	0	0	0	455	455	130	130	30	0	0	0	0	0	0	48,300.68	48,300.68
16	455	310	130	130	25	0	0	0	0	0	455	310	130	130	25	0	0	0	0	0	0	43,027.32	43,027.32
17	455	260	130	130	25	0	0	0	0	0	455	260	130	130	25	0	0	0	0	0	0	41,283.65	41,283.65
18	455	360	130	130	25	0	0	0	0	0	455	360	130	130	25	0	0	0	0	0	0	44,774.09	44,774.09
19	455	455	130	130	30	0	0	0	0	0	455	455	130	130	30	0	0	0	0	0	0	48,300.68	48,300.68
20	455	455	130	130	162	33	25	10	0	0	455	455	130	130	162	33	25	10	0	0	1150	60,115.1	61,265.1
21	455	455	130	130	85	20	25	0	0	0	455	455	130	130	85	20	25	0	0	0	0	54,502.11	54,502.11
22	455	455	0	130	160	20	25	0	0	0	455	455	0	0	0	20	25	0	0	0	0	45,255.23	45,255.23
23	455	432.5	0	0	25	0	0	0	0	0	455	432.5	0	0	0	0	0	0	0	0	0	34,862.51	34,862.51
24	455	345	0	0	0	0	0	0	0	0	455	345	0	0	0	0	0	0	0	0	0	30,854.84	30,854.84
	Overall cost																				7840	1,115,609	1,123,449

Table 5 Generation scheduling of committed units for 40, 60, 80 and 100. Unit thermal system (Comparison with other Optimizer)

Method	Best cost ($)	Mean cost($)	Worst cost ($)	Mean time (second)	Best cost ($)	Mean cost($)	Worst cost ($)	Mean time (second)
40 UNIT					60 UNIT			
EPL [31]	2,246,508	–	–	11.9	3,366,210	–	–	23
ILA [32]	2,248,285	–	–	63.3	3,368,950	–	–	534
QM [32]	2,248,285	–	–	6080	–	–	–	–
LR [33]	2,258,503	–	–	–	3,394,066	–	–	–
GA [33]	2,251,911	–	2,259,706	2697	3,376,625	–	3,384,252	5840
EP [34]	2,249,093	2,252,612	2,256,085	1176	3,371,611	3,376,255	3,381,012	2267
SA [35]	2,250,063	2,252,125	2,254,539	88.28	–	–	–	–
IBPSO [36]	2,248,581	2,248,875	2,249,302	110	3,367,865	3,368,278	3,368,779	172
DE [18]	2,246,274	–	–	161.9	3,365,784	–	–	370.7
BFA [37]	2,246,223	–	–	620	3,369,237	–	–	1400
ICA [38]	2,247,078	–	–	151	3,371,722	–	–	366
HSA [39]	2,250,968	–	–	234	3,375,138	–	–	562
BGSA [40]	2,246,445	2,247,400	2,247,962	–	3,364,665	3,366,257	3,368,394	–
SADP [10]	2,244,334	–	–	–	3,366,975	–	–	–
GMTLBO-BH [41]	2,245,602	–	–	36.5	–	–	–	–
IMBABC [43]	2,245,720	2,246,373	2,247,275	113.88	3,366,202	3,367,088	3,368,277	20,115
CGTO	2,245,648	2,249,802	2,252,392	0.047396	3,366,104	3,370,803	3,374,159	0.078125
80 UNIT					100 UNIT			
EPL [31]	4,489,322	–	–	44.4	5,608,440	–	–	64.5
ILA [32]	4,492,173	–	–	54 330	5,612,686	–	–	15 625
CSMA-SCA [44]	–4521585	–	–	–	5635734	–	–	
LR [33]	4,526,022	–	–	–	5,657,277	–	–	–
GA [33]	4,504,933	–	4,510,129	10 036	5,627,437	–	5,637,914	15 733
EP [34]	4,498,479	4,505,536	4,512,739	3584	5,623,885	5,633,800	5,639,138	6120
SA [35]	4,498,076	4,501,156	4,503,987	405.01	5,617,876	5,624,301	5,628,506	696.43
IBPSO [36]	4,491,083	4,491,681	4,492,686	235	5,610,293	5,611,181	5,612,265	295
DE [18]	4,488,450	–	–	568.6	5,607,900	–	–	663.9
BFA [37]	4,491,287	–	–	3200	5,611,514	–	–	5800
ICA [38]	4,497,919	–	–	994	5,617,913	–	–	1376
HSA [39]	4,500,745	–	–	1103	5,622,350	–	–	1911
BGSA [40]	4,488,039	4,490,053	4,491,993	–	5,607,838	5,609,585	5,611,188	–
SADP [10]	4,490,844	–	–	–	5,610,217	–	–	–
GMTLBO-BH [41]	–	–	–	–	5,611,105	–	–	236
MBABC [43]	4,488,401	4,489,514	4,491,172	360.90	5,607,965	5,609,621	5,611,118	486.45
CGTO	4,488,147	4,493,483	4,494,937	0.127604	5,605,708	5,606,095	5,705,756	10.65

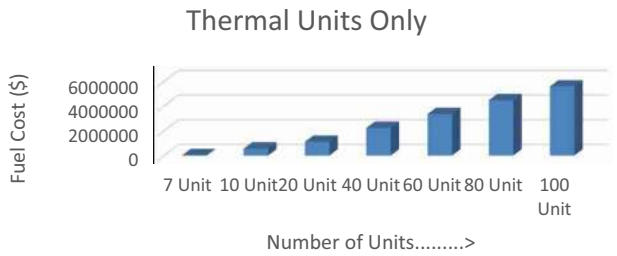

Fig. 11 Variation of the fuel cost as a function of number of generating units for Thermal units

shown in Tables 4 and 5. The best, worst, and average total production costs findings of the CGTO are obtained. From Tables 4 and 5, the average production costs of 30 trials generated variation in a small range and the standard deviation are small and tolerable. Simultaneously, average production costs are near to the middle position between their maximum

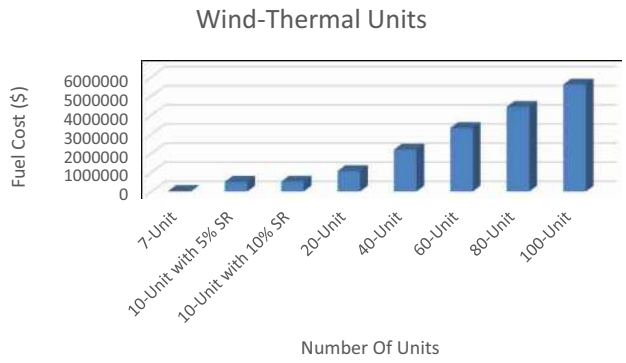

Fig. 12 Variation of the fuel cost as a function of number of generating units for wind-thermal units

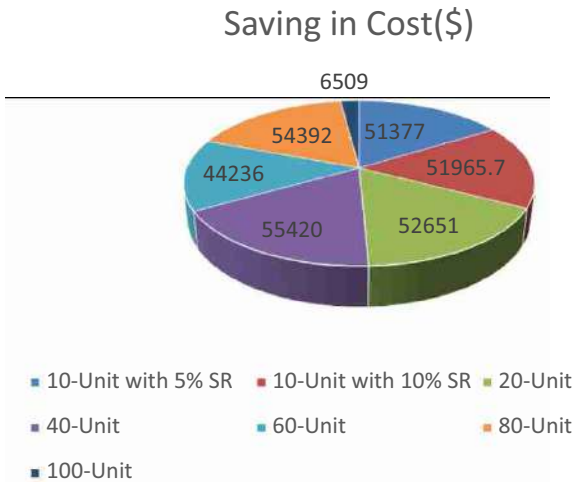

Fig. 13 Saving in Fuel cost by considering wind-power share (unit wise)

and minimum values. Therefore, it is evident that solutions are impartial and equally dispersed among the best and worst options. The 10-unit system's optimal solution as determined by the suggested algorithm is displayed in Table 4. While waiting, we look at how the test system's overall fuel cost varies with the number of evolutionary generations. The convergence processes of the top solution after 30 trials are listed in APPENDIX-F for various test systems. It is simple to see from Figs. 15 and 16 that the CGTO has satisfactory convergence and that, at later iterations, the algorithm escaped from the local optima. It demonstrated the effectiveness of the CGTO stochastic searching mechanism, which relies on chaotic interactions between agents. Additionally, the CGTO's performance was enhanced by the suggested mutation procedures.

Interpretation of the results

Tables 4 and 5 demonstrate how the test system's overall fuel cost has changed as a function of the evolutionary generation numbers, same is depicted by Figs. 11 and 12. Wind integrated thermal unit's solution for generation scheduling further more superior as depicted in Fig. 13 which clearly shows that introducing wind power at available instant reduces the effective load requirement of that hour hence it imposes less unit commitment stress on thermal unit which results in economic saving C solution after 30 trials are shown for several test systems in Figs. 14 and 15

The distribution of the best solutions is shown in Fig. 11 through 7 to allow for a visual representation of the outcome. The 10 unit system's optimal solution as determined by the suggested algorithm is taken from [28]. In the for the time being, we investigate how the test system's overall fuel cost varies with the number of evolutionary generations. 30 trial runs for various test systems are reported in Fig. 14. It is clear from convergence curve of Figs. 15 and 16 that the recommended CGTO algorithm converges satisfactorily and escapes the local optima thus perform stochastic searching mechanism of CGTO. The proposed chaotic search technique increased the performances of CGTO.

It proved that the stochastic searching mechanism of CGTO, which is conducted by chaotic forces among agents, is efficient and the proposed mutation strategies improved the performance of CGTO. To validate the results obtained with the CGTO, we compare the performance of the CGTO to those of other approaches with respect to the best total production cost. The results were reported in literature when the same problem were solved using EPL [31], ILA [32], QM [32], LR [33], GA [33], EP [34], SA [35], IBPSO[36], DE[18], BFA[37], ICA [38] HSA [39], BGSA [40], Fuzzy SADP [10], GMTLBO-BH [41], BRABC [42] MBABC [43]. Tables 4 and 5 show comparison of cost with other state of the art algorithm. From Table 5, it is clearly shown that the total operation costs achieved by the proposed improved CGTO is the best in terms of the test systems of 10, 40, 60, 80 units. For the test systems with 20 units and 100 units, the result of BGSA is second best. It is obvious that the proposed improved CGTO is superior to the mentioned methods. As the results shown above, the total production costs of the CGTO are demonstrated to be less expensive than those of other methods on generating unit systems. Obviously, the CGTO vastly improves performance than other methods in terms of both solution quality and CPU times especially on the large-scale UCP. The proposed

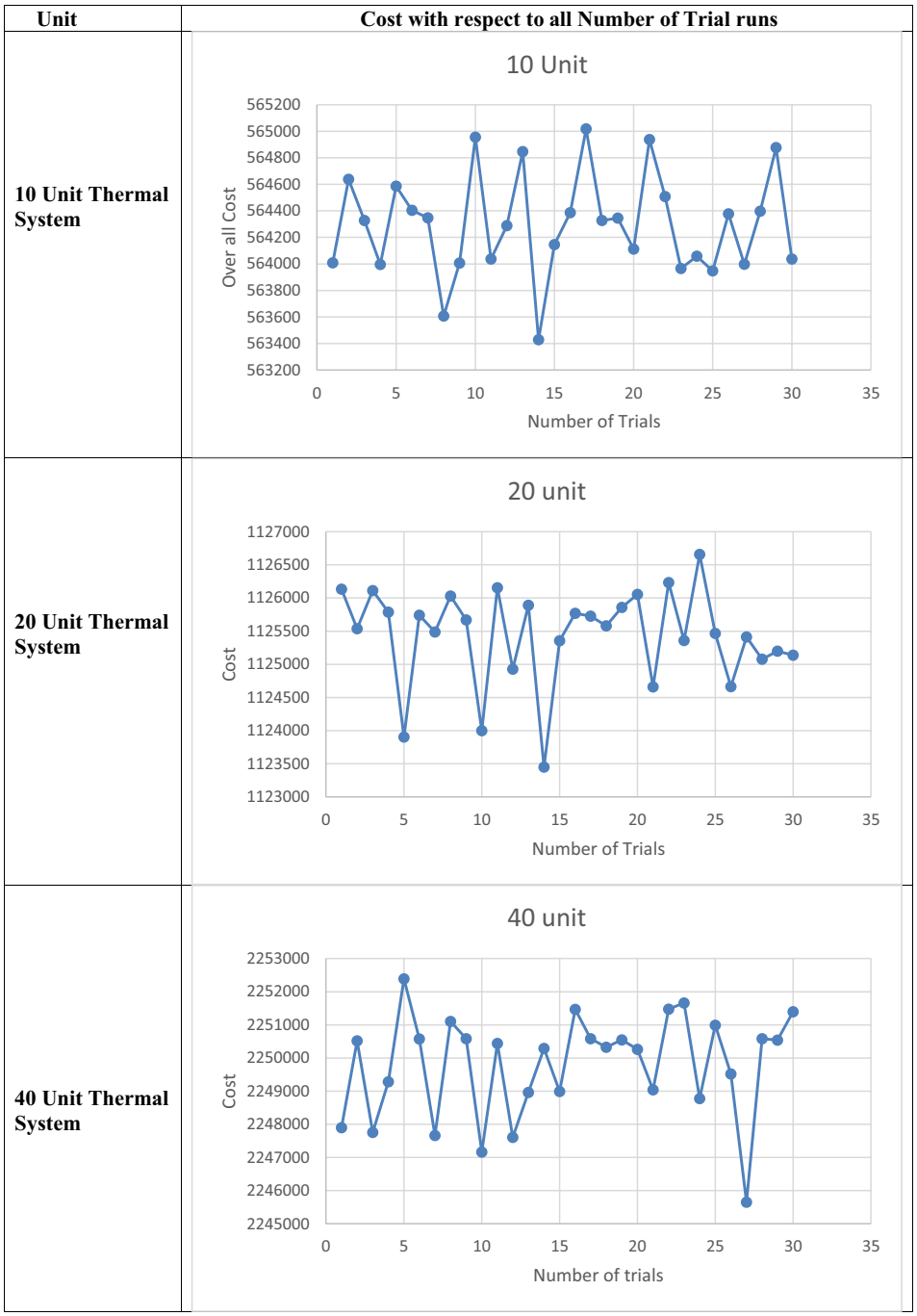

Fig. 14 Cost as a function of Number of trial runs

CGTO converges to the solution at a faster rate than the other methods reported in the literature.

From Table 6 it is obvious that for 7 unit wind-integrated thermal unit saving in fuel cost is maximum and is 14.5%, and as the number of units go on increasing percentage cost saving gets reduces and for 100 unit wind-thermal units it is less than 1%.

Fig. 14 (continued)

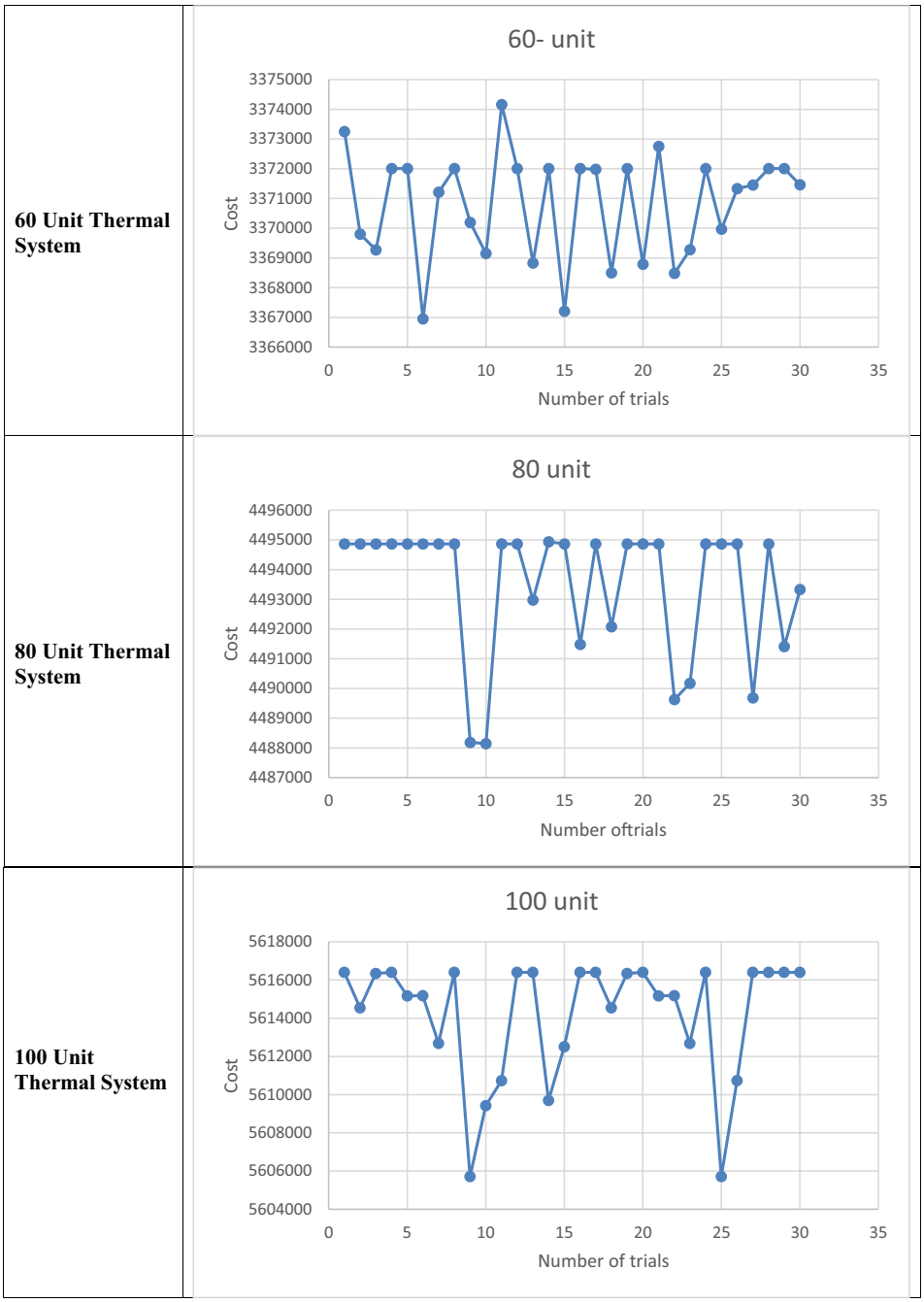

Conclusions

The chaotic Gorilla troop's optimizer (CGTO), a groundbreaking global optimization method that was developed to address the Generation Scheduling Problem, was inspired by and derived from the multi-phased Social process of gorilla groups. This optimizer presents a new chaotic updating strategy known as singer map based position updating, which logically divides the population into selection of silverback and adopts the strategy used by silverback (CMBCS). A better balance between exploration and exploitation is achieved by using the GTO approach, which looks for global optima, as opposed to chaotic search, which prevents the algorithm from slipping into local minima. The

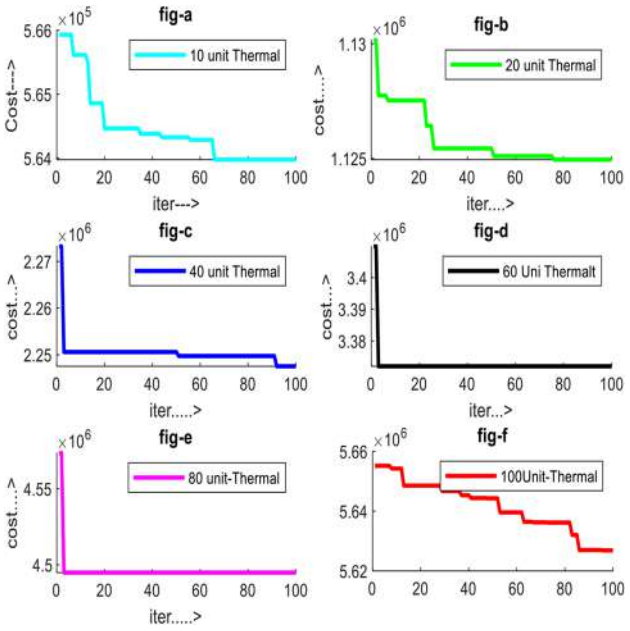

Fig. 15 Convergence curve for unit 10–100 for thermal unit system

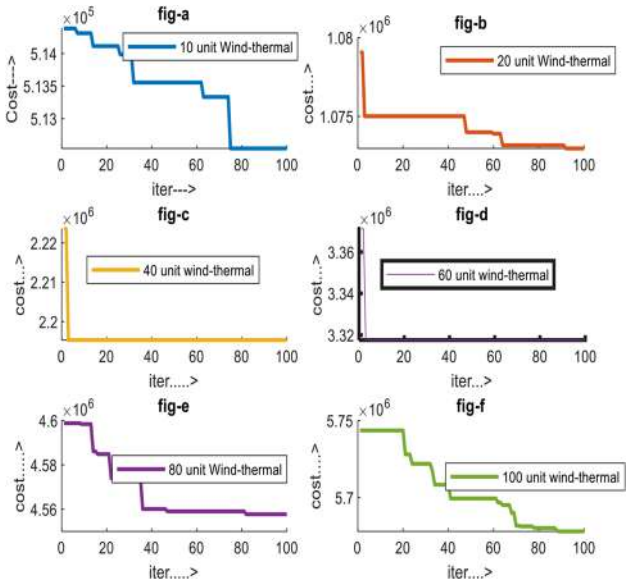

Fig. 16 Convergence curve for unit 10-100 for wind-thermal units

Table 6 Economic analysis of results while considering effect of wind power share

SN	Number of units	Cost ($)		Economic benefit	
		Thermal unit	Wind-thermal unit	Saving in cost($)	% Saving
1	7-Unit	34,321.74	29,319.14	5002.6	14.5%
2	10-Unit with 5% SR	556,527.9	505,150.6	51,377	9.23%
3	10-Unit with 10% SR	563,427.8	511,462.1	51,965.7	9.22%
4	20-Unit	1,123,449	1,070,758	52,651	4.68%
5	40-Unit	2,245,648	2,190,228	55,420	2.46%
6	60-Unit	3,366,104	3,321,868	44,236	1.32%
7	80-Unit	4,488,147	4,433,755	54,392	1.21%
8	100-Unit	5,605,708	5,599,199	6509	0.11%

impact of renewable energy on the issue of generation scheduling is further explored in this manuscript. The experiment has used thermal and wind thermal systems with 10 units, 20 units, 40 units, 60 units, and 80 units and 100 unit the extensive computational studies demonstrate that the CGTO strategy suggested in this paper performs better than the majority of the current methods to create high-quality solutions close to global minima. The influence of wind energy on the scheduling of power generation was also emphasized in this research. The precise calculation of wind power using wind data has successfully shown that a significant amount of money may be saved by using a wind integrated thermal system.

The following are potential areas for further research:

- The hydro generating units can be combined along with conventional thermal generating units, renewable and EV based energy sources.

- The maintenance cost and shut down cost of the thermal units can be included in addition to production cost as futuristic overall objective function.
- The generation scheduling problem can be consider with heat as combined cycle consider plants which is the most important concern for the Antarctic countries.
- Hybrid energy sources such as super capacitor based hybrid battery packs and ancillary services based energy sources can be included to fulfill the futuristic power demand in smart grid system.
- The proposed CGTO approach has been tested for single objective function; however same can be used to develop with multi objective function.

Supplementary Information The online version contains supplementary material available at https://doi.org/10.1007/s40095-022-00550-0.

Data availability The authors certify that all the data generated or analyzed during this study are available (and its additional file) may be found in link given below. https://drive.google.com/file/d/1pMAJBW--BBxRHaZ0C0iq6W06cjjCWHOc/view?usp=sharing Request for code should be made to corresponding author.

Declarations

Conflict of interest The authors certify that they have NO affiliations with or involvement in any organization or entity with any financial interest (such as honoraria; educational grants; participation in speakers' bureaus; membership, employment, consultancies, stock ownership, or other equity interest; and expert testimony or patent-licensing arrangements), or non-financial interest (such as personal or professional relationships, affiliations, knowledge or beliefs) in the subject matter or materials discussed in this manuscript.

References

1. Sheble, G.B., Fahd, G.N.: Unit commitment literature synopsis. IEEE Trans. Power Syst. **9**(1), 128–135 (1994). https://doi.org/10.1109/59.317549
2. Quan, R., Jian, J., Yang, L.: An improved priority list and neighborhood search method for unit commitment. Int. J. Electr. Power Energy Syst. **67**, 278–285 (2015). https://doi.org/10.1016/J.IJEPES.2014.11.025
3. Snyder, W.L., Powell, H.D., Rayburn, J.C.: Dynamic programming approach to unit commitment. IEEE Trans. Power Syst. **2**, 339–347 (1987)
4. Fisher, M.L.: The Lagrangian relaxation method for solving integer programming problems. Manage. Sci. **50**(12), 1861–1871 (2004). https://doi.org/10.1287/mnsc.1040.0263
5. Borghetti, A. et al.: Lagrangian relaxation and tabu search approaches for the unit commitment problem. IEEE Porto. Power Tech. Conf., (2001)
6. Cohen, A.I., Yoshimura, M.: A branch-and-bound algorithm for unit commitment. IEEE Trans. Power Appar. Syst. **2**, 444–451 (1983)
7. Glover, F.: Tabu Search Part I. Orsa J. Comput. **1**(3), 190–206 (1989)
8. Mantawy, A.H., Abdel-Magid, Y.L., Selim, S.Z.: Unit commitment by tabu search. IEE Proc. Gener. Transm. Distrib. **145**(1), 56 (1998). https://doi.org/10.1049/ip-gtd:19981681
9. Tseng, C.L., Li, C.A., Oren, S.S.: Solving the unit commitment problem by a unit decommitment method. J. Optimization Theory Appl. **105**(3), 707–730 (2000)
10. Patra, S., Goswami, S.K., Goswami, B.: Fuzzy and simulated annealing based dynamic programming for the unit commitment problem. Expert Syst. Appl. **36**(3), 5081–5086 (2009). https://doi.org/10.1016/j.eswa.2008.06.039
11. Arif, S., Mohammedi, R.D., Hellal, A., Choucha, A.: A memory simulated annealing method to the unit commitment problem with ramp constraints. Arab. J. Sci. Eng. **37**(4), 1021–1031 (2012). https://doi.org/10.1007/s13369-012-0217-2
12. Senjyu, T., Yamashiro, H., Shimabukuro, K., and Uezato, K., Unit commitment problem using genetic algorithm, pp. 1611–1616, (2002)
13. Sum-im, T., Ongsakul, W.: Ant colony search algorithm for unit commitment. IEEE Int. Conf. Ind. Technol. **1**, 72–77 (2003). https://doi.org/10.1109/ICIT.2003.1290244
14. Rajan, C.C.A. and Mohan, M.R., An evolutionary programming-based tabu search method for solving the unit commitment problem, vol. 19, no. 1, pp. 577–585, (2004)
15. Geem, Z.W., Kim, J.H., Loganathan, G.V.: A new heuristic optimization algorithm: harmony search. Simulation **76**(2), 60–68 (2001). https://doi.org/10.1177/003754970107600201
16. Ji, B., Yuan, X., Li, X., Huang, Y., Li, W.: Application of quantum-inspired binary gravitational search algorithm for thermal unit commitment with wind power integration. Energy Convers. Manag. **87**, 589–598 (2014). https://doi.org/10.1016/j.enconman.2014.07.060
17. Yang, X.S.: Firefly algorithm, stochastic test functions and design optimization. Int. J. Bio-Inspired Comput. **2**(2), 78–84 (2010). https://doi.org/10.1504/IJBIC.2010.032124
18. Datta, D., Dutta, S.: A binary-real-coded differential evolution for unit commitment problem. Int. J. Electr. Power Energy Syst. **42**(1), 517–524 (2012). https://doi.org/10.1016/j.ijepes.2012.04.048
19. Roy, P.K., Paul, C., Sultana, S.: Oppositional teaching learning based optimization approach for combined heat and power dispatch. Int. J. Electr. Power Energy Syst. **57**, 392–403 (2014). https://doi.org/10.1016/j.ijepes.2013.12.006
20. Bhadoria, A., Marwaha, S., Kamboj, V.K.: An optimum forceful generation scheduling and unit commitment of thermal power system using sine cosine algorithm. Neural Comput. Appl. (2020). https://doi.org/10.1007/s00521-019-04598-8
21. Bhadoria, A., Marwaha, S.: Moth flame optimizer-based solution approach for unit commitment and generation scheduling problem of electric power system. J. Comput. Des. Eng. **7**(5), 668–683 (2020). https://doi.org/10.1093/jcde/qwaa050
22. Bhadoria, A., Marwaha, S., and Kamboj, V. K., BMFO-SIG: A novel binary moth flame optimizer algorithm with sigmoidal transformation for combinatorial unit commitment and numerical optimization problems, vol. 5, no. 4. Springer Singapore, (2020)
23. Bhadoria, A., Marwaha, S., Kamboj, V.K.: A solution to statistical and multidisciplinary design optimization problems using hGWO-SA algorithm. Neural Comput. Appl. **33**(8), 3799–3824 (2021). https://doi.org/10.1007/s00521-020-05229-3
24. Bhadoria, A., Marwaha, S.: Optimal generation scheduling of electrical power system by using hybrid metaheuristic search technique. IEEE 2nd Int Conf. Electr. Power Energy Syst. ICEPES

2021(2), 1–5 (2021). https://doi.org/10.1109/ICEPES52894.2021.9699749
25. Panwar, L.K., Reddy, S., Verma, A., Panigrahi, B.K., Kumar, R.: Binary grey wolf optimizer for large scale unit commitment problem. Swarm Evol. Comput. **38**, 251–266 (2018). https://doi.org/10.1016/j.swevo.2017.08.002
26. Vatanpour, M., et al.: Profit based unit commitment using hybrid optimization technique. Energy **49**, 65–86 (2017). https://doi.org/10.1016/j.energy.2018.01.138
27. Li, X., et al.: Analysis of operation cost and wind curtailment using multi-objective unit commitment with battery energy storage. Energy **178**, 101–114 (2019). https://doi.org/10.1016/j.energy.2019.04.108
28. Bhadoria, A. and Marwaha, S. Optimal generation scheduling of electrical power system by using hybrid metaheuristic search technique. In: 2021 IEEE 2nd International conference on electrical power and energy systems (ICEPES), no. 2, pp. 1–5. (2022) https://doi.org/10.1109/icepes52894.2021.9699749.
29. Abdollahzadeh, B., Soleimanian Gharehchopogh, F., Mirjalili, S.: Artificial gorilla troops optimizer: a new nature-inspired metaheuristic algorithm for global optimization problems. Int. J. Intell. Syst. **36**(10), 5887–5958 (2021). https://doi.org/10.1002/int.22535
30 Bhadoria, A., Marwaha, S.: Moth flame optimizer-based solution approach for unit commitment and generation scheduling problem of electric power system. J. Comput. Des. Eng. (2020). https://doi.org/10.1093/jcde/qwaa050
31. Senjyu, T., Shimabukuro, K., Uezato, K., Funabashi, T.: A fast technique for unit commitment problem by extended priority list. IEEE Trans. Power Syst. **18**(2), 882–888 (2003). https://doi.org/10.1109/TPWRS.2003.811000
32. Viana, A., Pedroso, J.P.: A new MILP-based approach for unit commitment in power production planning. Int. J. Electr. Power Energy Syst. **44**(1), 997–1005 (2013). https://doi.org/10.1016/j.ijepes.2012.08.046
33. Kazarlis, S.A., Bakirtzis, A.G., Petridis, V.: A genetic algorithm solution to the unit commitment problem. IEEE Trans. Power Syst. **11**(1), 83–92 (1996). https://doi.org/10.1109/59.485989
34. Juste, K.A.: An evolutionary programming solution to the unit commitment problem. IEEE Trans. Power Syst. **14**(4), 1452–1459 (1999). https://doi.org/10.1109/59.801925
35. Simopoulos, D.N., Kavatza, S.D., Vournas, C.D.: Unit commitment by an enhanced simulated annealing algorithm. IEEE Trans. Power Syst. **21**(1), 68–76 (2006)
36. Yuan, X., Nie, H., Su, A., Wang, L., Yuan, Y.: An improved binary particle swarm optimization for unit commitment problem. Expert Syst. Appl. **36**(4), 8049–8055 (2009). https://doi.org/10.1016/j.eswa.2008.10.047
37. Eslamian, M., Hosseinian, S.H., Vahidi, B.: Bacterial foraging-based solution to the unit-commitment problem. IEEE Trans. Power Syst. **24**(3), 1478–1488 (2009). https://doi.org/10.1109/TPWRS.2009.2021216
38. Moghimi Hadji, M., Vahidi, B.: A solution to the unit commitment problem using imperialistic competition algorithm. IEEE Trans. Power Syst. **27**(1), 117–124 (2012). https://doi.org/10.1109/TPWRS.2011.2158010
39. Pourjamal, Y., Najafi Ravadanegh, S.: HSA based solution to the UC problem. Int. J. Electr. Power Energy Syst. **46**(1), 211–220 (2013). https://doi.org/10.1016/j.ijepes.2012.10.042
40. Yuan, X., Ji, B., Zhang, S., Tian, H., Hou, Y.: A new approach for unit commitment problem via binary gravitational search algorithm. Appl. Soft Comput. J. **22**, 249–260 (2014). https://doi.org/10.1016/j.asoc.2014.05.029
41. Azizipanah-Abarghooee, R., Niknam, T., Bavafa, F., Zare, M.: Short-term scheduling of thermal power systems using hybrid gradient based modified teaching-learning optimizer with black hole algorithm. Electr. Power Syst. Res. **108**, 16–34 (2014). https://doi.org/10.1016/j.epsr.2013.10.012
42. Chandrasekaran, K., Hemamalini, S., Simon, S.P., Padhy, N.P.: Thermal unit commitment using binary/real coded artificial bee colony algorithm. Electr. Power Syst. Res. **84**(1), 109–119 (2012). https://doi.org/10.1016/j.epsr.2011.09.022
43. Singhal, P.K., Naresh, R., Sharma, V.: A modified binary artificial bee colony algorithm for ramp rate constrained unit commitment problem. Int. Trans. Electr. Energy Syst. **25**(12), 3472–3491 (2015). https://doi.org/10.1002/etep.2046
44. Bhadoria A, Sanjay M (2022) A chaotic hybrid optimization technique for solution of dynamic generation scheduling problem considering effect of renewable energy sources. MRS Energy Sustain. https://doi.org/10.1557/s43581-022-00050-y

International Journal of Energy and Environmental Engineering (2023) 14:573–599
https://doi.org/10.1007/s40095-022-00536-y

ORIGINAL RESEARCH

A state-of-the-art of experimentally studied adsorption water desalination systems

A. E. Zohir[1] · Ehab S. Ali[1] · A. M. Farid[1] · Ramadan N. Elshaer[1] · Ramy H. Mohammed[2] · Ahmed S. Alsaman[3] · Hamdy H. El-Ghetany[4] · Ahmed A. Askalany[3]

Received: 11 April 2022 / Accepted: 9 September 2022 / Published online: 23 September 2022

Abstract
Energy, freshwater, and the environment are interrelated features that infuse all human activities. Addressing this nexus in an integrated energy conversion system is a big challenge for the research community. Adsorption desalination system, which is a good alternative to traditional desalination systems, could solve this problem because it uses eco-friendly working fluids and can be powered by renewable energy. Many experimental prototypes for the adsorption desalination cycle were built and tested in the last decades. Also, different adsorbent materials were developed and characterized. Therefore, this paper reviews adsorbent materials with water vapor utilized in experimental adsorption desalination studies, which is considered the first step in constructing an efficient system. After that, the paper comprehensively reviews all previous experimental adsorption desalination studies. It focuses on the design of the experimental test rig, the mass of adsorbent material, and system performance, such as the specific daily water production, coefficient of performance, and specific cooling power. This work also discusses the properties of heat exchangers (i.e., adsorbent beds) employed in adsorption desalination systems.

Keywords Adsorption cycles · Adsorbents · Desalination · Energy-efficient

Introduction

Energy, freshwater, and the environment are interrelated features that infuse all our activities on the earth. Furthermore, they are becoming the most significant and common areas in recent research fields [1]. World energy consumption is projected to increase by 2.6% annually to 2030 [2]. The electrical energy utilization growth rate in Egypt is about 7% annually. It would need to increase its current generation capacity by a higher rate (more than 7%). The energy rate utilized by refrigeration air conditioning systems represents 30% of the total worldwide consumed energy and 32% in Egypt [3].

Due to population growth, desalination is a practical solution to the water shortage problem [4]. Distillation, membrane, and crystallization are examples of traditional desalination methods. Membrane-based reverse osmosis (RO), multi-stage flashing (MSF), and multi-effect distillation (MED) are examples of commercial desalination technologies [5]. Table 1 expresses comparing analysis for almost all common desalination technologies [6]. On the other hand, traditional desalination technologies have a significant initial investment and running cost [7, 8]. The energy costs of producing unit water by MSF or RO are higher than producing potable water from surface and subterranean water resources. Desalination costs vary depending on the location. The cheapest seawater reverse osmosis cost was 0.5 US$/m^3 in 2016 [9]. Traditional energy-based desalination plants consume a lot of natural resources. As a result, solar, geothermal, wind, and other pollutant-free renewable energy sources are becoming increasingly popular for desalination. However, more research is needed to identify the most suitable technology for desalination applications [10].

✉ Ehab S. Ali
eng_ehab1987@yahoo.com

1 Mechanical Engineering Department, Tabbin Institute for Metallurgical Studies, Cairo 11912, Egypt

2 Department of Mechanical Power Engineering, Zagazig University, Zagazig 44519, Egypt

3 Mechanical Department, Faculty of Technology and Education, Sohag University, Sohag 82524, Egypt

4 Solar Energy Department, National Research Centre, Cairo 12622, Egypt

Table 1 Comparing analysis for almost common desalination technologies [6]

Items	MSF	MED	MED-TVC	SWRO	MD	(MED + AD)
Driving temperature (°C)	90–110	65–70	65–70	Ambient	60–90	65–70
Capital cost ($/m^3/day)	1598	2000	1860	1313	1131	2200
Thermal energy (kWh$_{thermal}$/m^3)	53–70	40–65	50–80	–	100	30–40
Electrical energy (kWh$_{elec}$/m^3)	2.5–5.0	2.0–2.5	2.0–2.5	4.0–6.0	1.5–3.65	2.8
Water cost ($/m^3)	0.56–1.75	0.52–1.01	1.12–1.50	0.26–0.54	1.17–2.0	0.48

Adsorption desalination system (ADS) is becoming a promising future technology for saving the required freshwater [11, 12]. It is based on using porous material that could be regenerated via low-grade thermal energy [13, 14]. The ADS has the advantage of efficiently utilizing low heat sources such as waste heat and/or solar energy [15–17]. It has some advantages over the commercial desalination methods, such as (i) the employment of the low-temperature excess or waste heat, (ii) lesser corrosion and fouling, (iii) and low maintenance cost. In addition, the ADS has two significant outcomes over the current desalination technologies, namely, (i) removing any "bio-contamination" and (ii) decreasing global warming due to the employment of excess waste heat [2, 18, 19]. The adsorption system can also be driven by renewable energy, reducing global warming resulting from carbon dioxide emissions of electricity generation [20]. The adsorption systems can be utilized for cooling purposes [21, 22]. The idea for utilizing these systems in desalination was firstly presented by Zejli et al. [23] in 2004, in which the earliest ADS simulation was performed. Till now, mathematical results [4–6, 24–28] achieved high values of specific daily water production (SDWP) and coefficient of performance (COP) of 98 m^3/ton.day and 2.1, respectively [4]. However, this performance was not proven experimentally on either lab-scale, prototype, or pilot scale. Experimental measurements are still low as SDWP did not increase more than 18 m^3/ton.day [29], and COP did not increase than 0.77 [30]. This trend shows a research gap between the theoretical and experimental studies in this field because of the lack of understanding of the effect of heat and mass transfer mechanisms on cycle performance. Also, many adsorbent materials have been developed in the last years, and however, their performance was tested theoretically without considerable investigation about their thermal effect on the system performance [14, 31].

Therefore, the present review presents an innovative review focusing on experimental studies of ADS. It also discusses the effect of the employed adsorbents' heat and mass transfer characteristics on the system efficiency for the first time in reviewing ADS. Thus, the paper identifies the huge difference in performance between the experimental and numerical studies in adsorption desalination. It also discusses this technology's future perspective, challenges, and outlook to fill the world water demand and supply gap. The present review is divided into two main sections besides the introduction. The first section explores research that expresses experimental adsorbent materials with water vapor, which is the first step in constructing an ADS. The second section explores experimental investigations for ADS with and without evaporator condenser heat recovery. This work emphasizes the experimental test rig design, the mass of adsorbent material adsorption, and desalination system performance as SDWP, COP, and specific cooling power (SCP) for each experimental device. This review states the properties of utilized heat exchangers of adsorbent beds in ADS.

Adsorbent materials used in ADS

Many researchers focused on developing new adsorbent material or improving its adsorption uptake to enhance ADS effectiveness. Therefore, this section presents adsorption materials tested with water vapor as adsorbate.

Silica gel

Silica gel is the common material utilized in the ADS. Silica gel is a category of amorphous synthetic silica that consists of a rigid and continuous net of colloidal silica associated with SiO_4 particles. The main advantages of silica gel are that it can regenerate with temperatures as low as 100 °C and thermal stability. Still, they have low adsorption capacity compared to new adsorbents such as MOF [15]. White [32] theoretically illustrated the effect of silica gel granular diameter (1, 2, 3 mm) on the water adsorption rate. The study showed that reducing granule size raises the adsorption rate. Table 2 summarizes different types of silica gel and their adsorption uptakes.

Zeolite

Zeolite is a crystalline alumina silicate composed of alkali/alkali soil, namely molecular sieve, and alumina silicate skeletal has 0.2–0.5 cm^3/g of porosity. The adsorption capability of zeolite is related to the proportion between aluminum and silicon. The main advantages of zeolite are non-toxic, non-flammable, and environmentally friendly. It

Table 2 Different types of silica gel and their adsorption uptakes

Silica gel	Max. equilibrium uptake (gwater g^{-1}_{ads})	BET surface area (m^2 g^{-1})	References
Silica gel, type 3A/H_2O	0.33	n.d	[33]
Silica gel, type A/H_2O	0.40	n.d	[33]
Silica gel, type A + +/H_2O	0.52	863.6	[33]
Silica gel, type 2560/H_2O	0.32	636.4	[33]
Silica gel, type RD/H_2O	0.45	838	[34]
Fuji silica gel, type RD/H_2O	0.48	780	[35]
Fuji silica gel, type 2060/H_2O	0.37	707	[35]

n.d. means no data

Table 3 Different types of zeolite and their adsorption uptakes

Zeolite	Max. equilibrium uptake (gwater g^{-1}_{ads})	BET surface area (m^2 g^{-1})	References
Natural zeolite/H_2O	0.12	643	[38]
Zeolite 4A/H_2O	0.20	n.d	[38]
AQSOA-Z01/H_2O	0.21	189.6	[39]
AQSOA-Z02/H_2O	0.31	717.8	[39]
AQSOA-Z05/H_2O	0.23	187.1	[39]
Zeolite-13X/H_2O	0.30	n.d	[40]

n.d. means no data

needs high regeneration temperatures and low adsorption capacity compared to new adsorbents such as MOF [36]. About 40 types of natural zeolite and around 150 types of artificial zeolite regarding a synthesis method [37]. Table 3 summarizes different types of zeolite and their adsorption uptakes.

Metal–organic frameworks (MOFs)

Heat transformation technologies require the creation of adsorbent materials. In this regard, new materials appropriate to adsorption–desorption working fluid must yet be discovered for this technology to be remarkable [41, 42]. Metal–organic frameworks (MOFs), also known as porous coordination polymers (PCPs), have shown outstanding adsorbent properties and were investigated for heat transformation uses. MOFs also comprise hydrophilic and hydrophobic moieties, each with adsorption characteristics. Because of their high adsorption capacity for guest molecules such as water, MOF materials offer significant potential for heat transformation compared to a large range of natural and manufactured adsorbents. However, their stability and long-time synthesis process are the main challenges facing this family of nanoporous materials [42, 43]. Compared to silica gel, MOFs with hydrophilic characteristics have the preference since they have an unlimited water uptake capacity at high pressures. At first, MOFs were demonstrated as adsorbent materials by looking at their ability to use solid–gas adsorption for energy transformations. MOF materials offer a wide range of energy storage and heat transformation (cooling/heating) uses. Because water is commonly utilized as a working fluid, the examined adsorbent materials were evaluated using water adsorption–desorption properties. MOFs have also been examined for water adsorption studies to investigate structural characteristics and adsorption performance. The metal clusters must first coordinate water molecules before the poetical condensation procedure in the solid adsorbent's pores (MOFs) occurs in water adsorption [42, 44]. Therefore, metal groups categorize MOF materials for water adsorption and heat/energy transformation applications. In addition, several frameworks showed geometric plasticity and reversible structural change in guest adsorption. Thus, water adsorption on MOF materials was previously used to estimate their heat transformation performance.

MOFs have significantly more promise for this use than current adsorbents for heat transformation applications, like alumina phosphates or zeolites, owing to their composition, pore structure, also topology. Furthermore, additional improvement of the porosity structure of the MOFs, allowing for tailoring of their adsorption capabilities, modification or functionalization of metal clusters/ions, and biological linkers are still achievable [42, 45]. This opens up exciting possibilities for MOF production with specified properties optimized for specific working situations, such as heat transformations [42, 43]. Interestingly, development in MOF chemistry has progressed. Numerous techniques to synthesize and develop water-stable MOFs have paved the path for water-sorbent candidates with improved water adsorption and associated applications, see Table 4 [46–50]. From where water uptake capacity and corresponding relative pressure at which the pore filling occurs, the adsorption capabilities of MOFs are highly variable from a qualitative standpoint. Hydrolytically stable porous materials with large pore volumes, on the other hand, are likely to have large water adsorption capabilities. Hunt for hydrolytically stable

Table 4 List of possible MOFs and their water adsorption properties

MOFs	Metals	Uptake[a] (gwater g^{-1}ads)	Surface area (m^2 g^{-1})	References
CAU-6	Al	0.485	620	[54]
CAU-10	Al	0.31	635	[55]
CAU-10-H	Al	0.382	635	[55]
CAU-10-NH_2	Al	0.19	n.d	[55]
CAU-10-NO_2	Al	0.15	440	[55]
CAU-10-OCH_3	Al	0.07	n.d	[55]
CAU-10-OH	Al	0.27	n.d	[55]
DUT-4	Al	0.28	1360	[44]
DUT-67	Zr	0.625	1560	[56]
MIL-100	Cr	0.41	1517	[57]
MIL-100	Fe	0.81	1549	[44]
		0.77	1917	[58]
MIL-100	Al	0.50	1814	[58]
MIL-100	Cr	0.40	1330	[59]
		1.01	2059	[60]
		1.28	3017	[44]
		1.40	3124	[61]
MIL-100-DEG	Cr	0.33	580	[59]
MIL-100-EG	Cr	0.43	710	[59]
MIL-101-NH_2	Cr	0.90	2509	[61]
		1.06	2690	[62]
MIL-101-NO_2	Cr	1.08	2146	[61]
		0.44	1245	[62]
MIL-101-pNH_2	Cr	1.05	2495	[62]
MIL-101-pNO_2	Cr	0.60	2195	[62]
MIL-101-soc	Cr	1.95	4549	[53]
MIL-125	Ti	0.36	1160	[45]
MIL-125-NH_2	Ti	0.36	830	[45]
		0.37	1220	[63]
MIL-53	Al	0.09	1040	[45]
		0.09	n.d	[64]
MIL-53-NH_2	Al	0.05	940	[45]
		0.09	n.d	[64]
MIL-53-OH	Al	0.40	n.d	[64]
MIL-53	Ga	0.05	1230	[45]
MIL-53-NH_2	Ga	0.02	210	[45]
MIL-53-$(COOH)_2$	Fe	0.16	n.d	[64]
MIL-68	In	0.32	1100	[45]
MIL-68-NH_2	In	0.32	850	[45]
MOF(NDI-SEt)	Zn	0.25	888	[65]
MOF(NDI-SO2Et)	Zn	0.25	764	[65]
MOF(NDI-SOEt)	Zn	0.30	927	[65]
MOF-199	Cu	0.55	1340	[44]
		0.64	921	[66]
		0.49	1270	[67]
MOF-74	Co	0.63	1130	[56]
MOF-74	Mg	0.75	1250	[56]
		0.62	1400	[67]
MOF-74	Ni	0.615	1040	[56]
		0.48	639	[56]
MOF-801-P	Zr	0.45	990	[56]
MOF-801-SC	Zr	0.35	690	[56]
MOF-802	Zr	0.11	1290	[56]
MOF-804	Zr	0.29	1145	[56]
MOF-805	Zr	0.415	1230	[56]
MOF-806	Zr	0.425	2220	[56]
MOF-808	Zr	0.735	2060	[56]
MOF-841	Zr	0.64	1390	[56]
PIZOF-2	Zr	0.85	2080	[56]
SIM-1	Zn	0.14	570	[45]
UiO-60	Zr	0.535	1290	[56]
		0.40	1032	[63]
		0.39	1105	[68]
		0.37	1160	[67]
UiO-66–1,4-Naphy1	Zr	0.26	757	[68]
UiO-66–2.5-$(OMe)_2$	Zr	0.42	868	[68]
UiO-66-NH_2	Zr	0.38	1328	[63]
		0.34	1123	[68]
		0.37	1040	[67]
UiO-66-NO_2	Zr	0.37	792	[68]
UiO-67	Zr	0.18	2064	[63]
ZIF-8	Zn	0.02	1255	[44]
		0.01	1530	[45]

[a]Adsorption properties of water measured at 25 °C and almost saturated vapor pressure

and recyclable MOFs with higher total water uptake is a major focus of MOF chemistry research [45, 47, 51–53].

Comparison among MOF materials and conventional materials

The authors showed and compared various MOF materials that outperform existing porous materials like silica gel and zeolites in water adsorption [69, 70], see Fig. 1. The water adsorption isotherms of MOF materials are shown in Fig. 2. When comparing Figs. 1 and 2, it is clear that the MIL-101(Cr) outperformed the typical greatest adsorption capacity. For the adsorption (desalination and cooling) process, desalinated water and cooling effects are influenced by the value of the adsorption capacity of the adsorbent material. The available adsorbed amount in water vapor adsorption uptake (Δw) at adsorption and adsorption pressures are mainly affected by the available adsorbed amount. The Δw represents the difference between expected material concentrations in the adsorption and desorption model

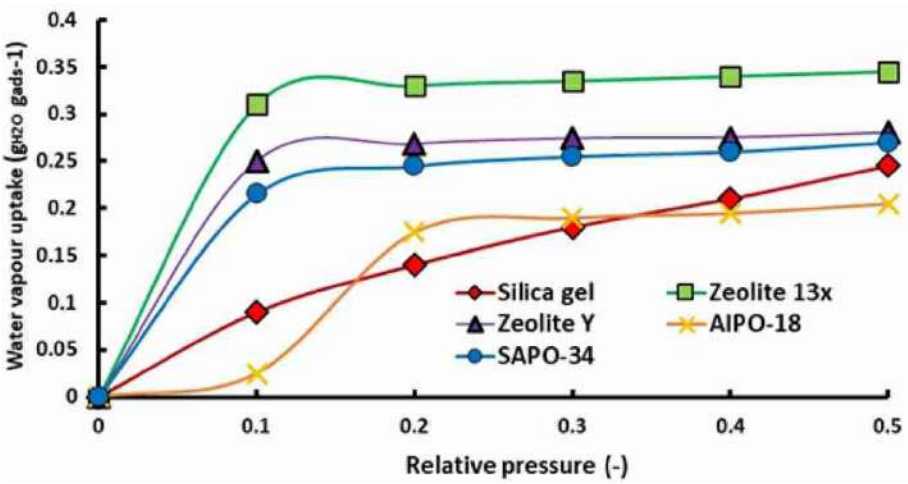

Fig. 1 Isotherms for water adsorption of traditional adsorbents like silica gel RD [75], SAPO-34 [72], Zeolite Y [76], Zeolite 13X [77]and AlPO-18 [77] at 25 °C

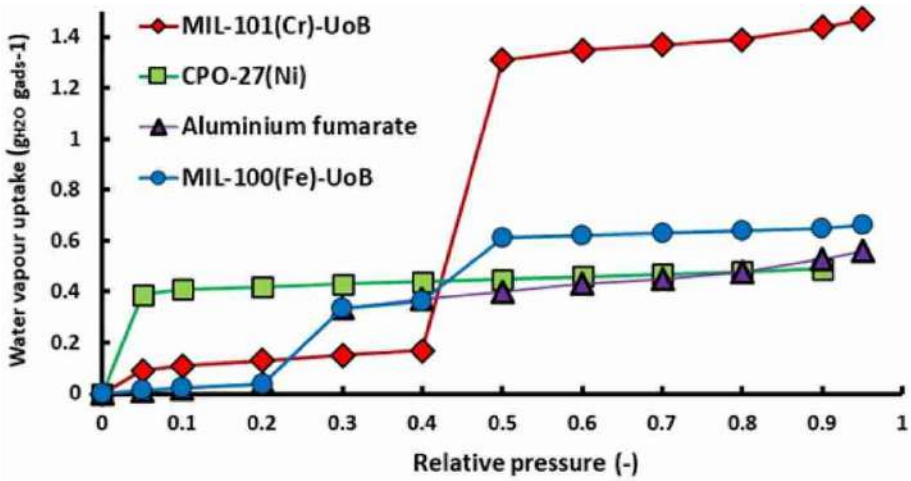

Fig. 2 Isotherm of water adsorption for some MOF materials like MIL-101(Cr)-UoB, CPO-27(Ni), Aluminum fumarate, and MiL-100(Fe)-UoB [69] at 25 °C

(cycle sorption quantity). The adsorbent material with a step increase in water vapor uptake before ($P/P_s = 0.25$) is suitable for cooling applications. Some adsorbent materials take their most adsorption capacity after $P/P_s = 50\%$, which indicates that it is more suitable for desalination than cooling applications. In cooling applications, the evaporator pressure could be considered 1 kPa to get a cooling effect at around 7 °C, while in the desalination application, the evaporator pressure could be higher, around 2.25 kPa to take benefit most adsorption capacity of material as Δw [36]. Based on this Figure, MIL-101(Cr), MIL-100(Fe), and aluminum fumarate are suitable for applications requiring high P/P_s, like desalination [68] or energy storage, whereas CPO-27(Ni) is better suited for applications requiring low P/P_s like energy storage [71], cooling [72] or dual effect desalination [73, 74]. For more illustration of whether an adsorbent is suitable more in desalination or cooling applications, or both. This is calculated based on Δw at evaporation and condensation pressures and temperatures using the Gibbs energy change ($-\mathrm{RT}\ \ln(P/P_s)$) relationship as illustrated in Fig. 3. The figure expresses that the MIL-101(Cr)-UoB has the best performance in desalination mode. It is achieved Δw (1.22 kg/kg) in desalination application. But it has not a good performance in cooling mode as it achieves Δw (0.06 kg/kg) due to its isotherm performance, which has a jump in adsorbed vapor uptake after $P/P_s = 0.4$. The figure also expresses that Aluminum fumarate and MIL-100(Fe)-UoB have the best performance in cooling mode as they achieve around Δw (0.32 kg/kg) in cooling mode.

Enhancing the properties of MOF materials

Because of its huge pore size and high free volume, MIL-101(Cr) has exceptional features, including exceptionally low thermal conductivity. During both adsorption and desorption stages, low thermal conductivity makes it difficult for heat transfer processes to reach the required operating temperatures fast. To enhance the thermal conductivity of parent MIL-101, a composite of MIL-101(Cr)/GrO was utilized (Cr) [78]. Two approaches were used to create a composite of MIL-101(Cr)

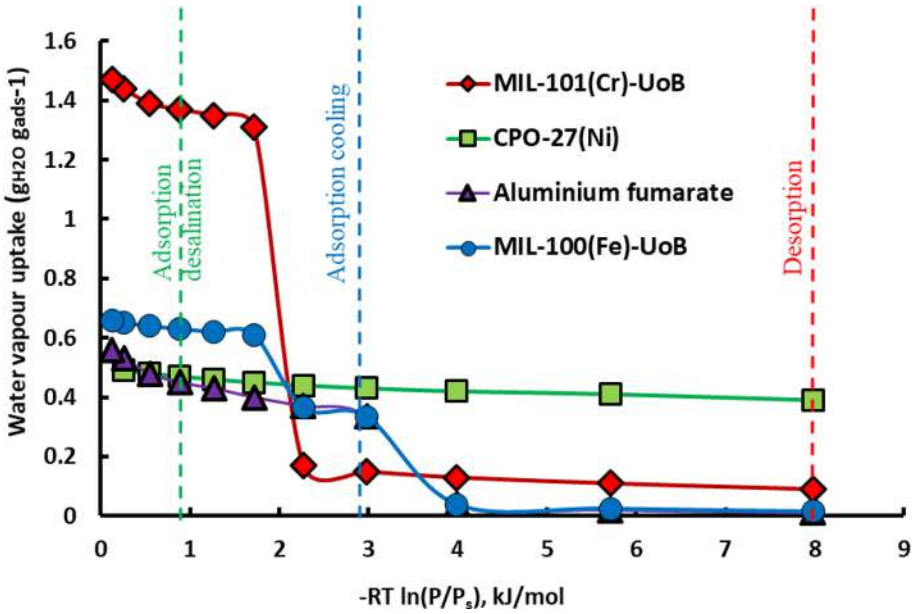

Fig. 3 Adsorption characteristic of MOF [69] at 25 °C

and GrO: physically mixing the two components and integrating them into the synthesis process. Owing to the limited porosity of GrO, it was discovered that the composites made via the physical mixing method had a decreased water uptake. In the synthesis process, the 2% GrO synthesis composite demonstrated comparable water uptake at low relative pressures and outperformed the pristine material at high relative pressures. Because of the crystal structural distortion, 5% GrO synthesis composite reduced water uptake [78].

Composite adsorption materials

Many researchers have improved the current adsorbent materials by the composition method, whether by compositing two or more host matrix materials together or by compositing a host matrix with a salt hydrate to improve the performance of systems that use those materials [36]. Table 5 summarizes the adsorption characteristics of composite materials. The table illustrates that composite adsorbent materials achieved higher adsorption water capacity than the base materials, which expresses that composite materials can achieve higher performance as cooling power or desalination effect. But these composite adsorbents need to be examined experimentally in adsorption desalination/cooling devices to realize what can enhance performance.

Experimental adsorption desalination systems

This section explores all presented experimental investigations for ADS separated into two categories. Experimental investigation types are ADS with and without evaporator condenser heat recovery. This section explores all experimental adsorption desalination (AD) studies; the work emphasizes the experimental test rig design, the mass of adsorbent material adsorption, and desalination system performance as SDWP, COP, and specific cooling power (SCP) of each experimental device. This work also reviews the properties of the used heat exchangers of adsorbent beds in ADS.

Experimental adsorption desalination studies

In this sub-section, experimental investigations of ADS are presented. These experimental investigations are for producing both desalination and cooling effects. The first excremental test rig for ADS was presented by Wang et al. [8], as illustrated in Fig. 4. The highest SDWP obtained was 4.7 m^3/ton of silica gel at T_{des} = 85 °C and T_{cw} = 30 °C. This study also reported that SDWP yielded from the plant could be further boosted by adopting a higher chilled water temperature supply (T_{chi}) and lowering adsorption cooling water (T_{cwi}). It demonstrated that ADS was also more efficient when the heat source temperature was lowered to 65 °C. Thu et al. [118] reported ADS performances with two-bed and four-bed operational modes. Figure 5 shows the used test rig for ADS. The tested results are estimated in terms of (i) SDWP, cycle time, and (ii) performance ratio (PR) for several driving temperatures (T_{drv}). It was found that the maximum SDWP is about 10 m^3 /tone.day with PR 0.61. The study also provided a valuable guideline for the operational approach of ADS. The study employed four adsorption units with 36 kg of silica gel per adsorption unit. Wu et al. [119] presented ADS as an alternative to traditional desalination systems that could be utilized by waste heat

Table 5 Summary of the adsorption characteristics of composite materials

Composite	Uptake (g g^{-1})	BET surface area (m^2 g^{-1})	V_{por} (cm^3 g^{-1})	P/P_s (–)	T_{ads} (°C)	Refs.
SG/$CaCl_2$	1			> 0.6	20	[79]
SG	0.4	785	1.31	0.95	23	[80]
SG/$CaCl_2$	0.57	224	1.039			
SG/16.7wt.% $CaCl_2$	0.57	886	3.9	0.75	25	[81]
SG/28.9wt.% $CaCl_2$	0.9	640	1.9	0.75		
SG/16.6wt.% $CaCl_2$	0.48	276	0.45	0.75		
SG/28.9wt.% $CaCl_2$	1.1	200	0.54	0.75		
SG/31.6wt.% $CaCl_2$	0.68	152	0.54	0.7		
SG	0.16	529	0.806	0.8	30	[82]
SG/10wt.% $CaCl_2$	0.44		0.698			
SG/20wt.% $CaCl_2$	0.53		0.567			
SG/30wt.% $CaCl_2$	0.6		0.53			
SG/40wt.% $CaCl_2$	0.74		0.395			
SG	0.1	550	0.43	0.75		[83]
SG/28.6wt.% LiBr (Aerogel)	0.5	520	1.05	0.7	25	
SG/28.6wt.% LiBr (Densified)	0.68	351	1.13	0.75		
SG/28.0wt.% LiBr (Xerogel)	0.63	324	0.38	0.75		
SG/35.5wt.% LiBr (Impregnation)	0.8	262	0.39	0.65		
SG/13.5wt.% $MgSO_4$	0.27				25	[84]
SG/24wt.% $MgSO_4$	0.37					
SG/38wt.% $MgSO_4$	0.47					
KSM SG		600	0.3			[85]
KSM SG/21.7 wt.% $CaCl_2$	0.25			0.7	20	
KSK SG		260	1			[86]
KSK SG/45wt.% $Ca(NO_3)_2$	0.2–0.3	60	0.24	< 0.7	30	
KSK SG		350	1		35	[87]
KSK SG/34.5wt.% $LiNO_3$	0.22					
KSK SG			1		20	[88]
KSK SG/42wt.% $CaCl_2$	0.45		0.6–0.64			
KSK SG/48wt.% LiBr-	0.39		0.6–0.64			
KSK SG/33wt.% $MgCl_2$	0.51		0.6–0.64			
KSKG SG		350	1			[89]
KSKG SG/33.7 wt.% $CaCl_2$	0.7–0.75			0.7	20	
KSKG SG/32 wt.% LiBr	0.6–1			0.7–0.8	40	[90]
KSKG SG/57 wt.% LiBr						
PHTS	0.16–0.65	810	0.705	0.4–0.95	40	[91]
PHTS/4wt.% $CaCl_2$	0.25–0.78	461	0.492			
PHTS/10wt.% $CaCl_2$	0.38–1.20	322	0.377			
PHTS/20wt.% $CaCl_2$	0.58–2.24	163	0.189			
SBA-15		519	0.73		50	[92]
SBA-15/43wt.% $CaCl_2$	0.615	52	0.17	0.4		
SBA-15	0.02	554	0.8	0.3	20	[93]
SBA-15/2.80wt.% $Al_2(SO_4)_3$	0.05	550	0.75			
SBA-15/5.32wt.% $Al_2(SO_4)_3$	0.065	549	0.73			
SBA-15/6.77wt.% $Al_2(SO_4)_3$	0.09	541	0.7			
Syloid72FP/Emim-Oms	1.64			0.9	25	[94]
Syloid AL-1FP	0.28	605–740	0.23–0.4	0.9	25	[95]
Syloid AL-1FP/60wt.% Emim-Oms	1.86					
Syloid AL-1FP/20wt.% Emim-Ac	0.92					

Table 5 (continued)

Composite	Uptake (g g^{-1})	BET surface area (m^2 g^{-1})	V_{por} (cm^3 g^{-1})	P/P_s (–)	T_{ads} (°C)	Refs.
Syloid72FP	0.44	340–405	1.2			
Syloid72FP/60wt.% Emim-Oms	1					
Syloid72FP/60wt.% Emim-Ac	1.32					
Syloid AL-1FP/60.0% [Emim][CH_3SO_3]	0.85			0.9	25	[96]
Syloid AL-1FP/41.7% [Emim][CH_3SO_3]	0.75					
Syloid AL-1FP/17% [Emim][CH_3SO_3]	0.5					
Syloid AL-1FP/1.8% [Emim][CH_3SO_3]	0.25					
AC	0.35	678	2.365	0.94	23	[97]
AC/$CaCl_2$	0.42	224	1.039			
AC/38.6wt.% $MgCl_2$	0.941	716	0.3924	0.7	25	[98]
AC/31.2wt.% MgCl2 + 3.2wt.% Ce	1.05	494.8	0.3846			
AC	0.19	1117	0.5329	atm	25	[99]
AC + 16wt.%SG	0.244	610	0.2934			
AC + 26wt.%SG	0.246	664	0.3121			
AC + 19wt.%SG	0.25	682	0.3242			
AC + 2wt.%SG/68wt.%$CaCl_2$	0.41	118	0.074			
AC + 4wt.%SG/57wt.%$CaCl_2$	0.699	82	0.0449			
AC + 3wt.%SG/64wt.%$CaCl_2$	0.805	83	0.0589			
AC + 20wt.%SG/11wt.%$CaCl_2$	0.243	602	0.2895			
AC + 24wt.%SG/13wt.%$CaCl_2$	0.236	626	0.2975			
AC + 22wt.%SG/4wt.%$CaCl_2$	0.264	680	0.327			
AC + 22wt.%SG/5wt.%$CaCl_2$	0.412	156	0.0812			
AC + 13wt.%SG/21wt.%$CaCl_2$	0.433	160	0.0882			
AC + 10wt.%SG/15wt.%$CaCl_2$	0.332	188	0.0958			
AC1		1370	0.109	0.4–0.9		[100]
AC1/10wt.% Na_2O_3Si	0.12–0.52	690	0.095		25	
AC2		1300	0.158			
AC2/10wt.% Na_2O_3Si	0.12–0.42	1080	0.048			
Carbon Sibunit		450 ± 25	0.9 ± 0.05			[97]
Carbon Sibunit/29wt.% LiBr	0.4–1.1			0.7	30	
Expanded graphite		12.3 ± 1.2	3.3 ± 0.1			
Expanded graphite/33wt.% LiBr	0.4–1.1			0.7	30	
MWCNT		270	3	> 0.4	37	[101]
MWCNT/44wt.% LiCl	1.1	140	1.4			
MWCNT/53wt.% $CaCl_2$	0.94	75	0.9			
MWCNT		270	5.3		35	[102]
GP(MWCNT/41wt.% LiCl)	1	145	2.7			
PB(MWCNT/42wt.% LiCl)	1	124	4.7			
PP(MWCNT/41wt.% LiCl)	1	144	2.7			
MWCNT/PVA/55wt.% LiCL	0.6	80	0.9	0.2	35	[103]
Zeolite		921	0.374			[104]
Zeolite/15wt.% $MgSO_4$	0.15	400	0.18	0.7	30	
Zeolite13X	0.28	468	1.527	0.94	23	[80]
Zeolite13X/$CaCl_2$	0.6	233	1.489			
Zeolite13X	0.0761	667	0.32	< 0.3	25	[105]
Zeolite13X/10wt.% $CaCl_2$	0.0914	608	0.34			
Zeolite13X/20wt.% $CaCl_2$	0.1592	608	0.36			
Zeolite13X/30wt.% $CaCl_2$	0.1953	605	0.36			
Zeolite13X/40wt.% $CaCl_2$	0.3953	601	0.34			

Table 5 (continued)

Composite	Uptake (g g^{-1})	BET surface area (m^2 g^{-1})	V_{por} (cm^3 g^{-1})	P/P_s (–)	T_{ads} (°C)	Refs.
Zeolite13X/46wt.% $CaCl_2$	0.8	622	0.54			
Alumina/Zeolite13X	1.16	455	0.283	0.94	20	[106]
Alumina			0.75		20	[92]
IK-02-200 alumina/31wt.% $CaCl_2$	0.3		0.6–0.64			
MIL-101	0.18	3402.69	1.59	0.4	25	[107]
MIL-101/LiCl	0.5	2054.03	0.94			
MIL-101/NaCl	0.46	2000.66	0.91			
MIL-101	1.22	2789	1.32	0.9	25	[108]
MIL-101/2wt.% GO	1.53	3472	1.69			
MIL-101/4wt.% GO	1.56	3501	1.77			
MIL-101/6wt.% GO	1.58	3522	1.78			
MIL-101/8wt.% GO	1.42	3126	1.57			
MIL-101(Cr)	0.1–1.35	3354.84	1.73	0.3–0.9	25	[109]
MIL-101(Cr)/3wt.% $CaCl_2$	0.16–1.2	2976.77	1.49			
MIL-101(Cr)/4wt.% $CaCl_2$	0.16–1.3	3117.14	1.58			
MIL-101(Cr)/5wt.% $CaCl_2$	0.26–1.2	2675.9	1.35			
MIL-101(Cr)/6wt.% $CaCl_2$	0.22–1.25	2641.5	1.32			
MIL-101(Cr)/8wt.% $CaCl_2$	0.65–1.75	1876.01	0.99			
MIL-101(Cr)	0.18–1.05	2824	1.362	0.4–0.9	25	[110]
MIL-101(Cr)/10% $CaCl_2$	0.5–0.88	1977	0.745			
MIL-101(Cr)/20% $CaCl_2$	0.53–1.13	1307	0.509			
MIL-101(Cr)/30% $CaCl_2$	0.6–1.35	193	0.071			
MIL-101(Cr)	0.4	3460	1.753	0.95	25	[78]
MIL-101(Cr)/0.5wt.%GrO (Synthesis)	1.4	3137.8	1.641			
MIL-101(Cr)/0.5wt.%GrO (Physical)	1.22	2608.5	1.346			
MIL-101(Cr)/1wt.%GrO (Synthesis)	1.45	3028.1	1.619			
MIL-101(Cr)/1wt.%GrO (Physical)	1.17	2425.7	1.265			
MIL-101(Cr)/2wt.%GrO (Synthesis)	1.55	3674	2.14			
MIL-101(Cr)/2wt.%GrO (Physical)	1.32	2077	1.035			
MIL-101(Cr)/5wt.%GrO (Synthesis)	1.47	2810	1.879			
MIL-101(Cr)/5wt.%GrO (Physical)	1.27	2626	1.33			
Vermiculite	0.06	15.1	4.11	0.94	23	[80]
Vermiculite/$CaCl_2$	1.45	10.9	1.491			
Vermiculite/$MgSO_4$	0.41	3.6	2.054			
Vermiculite/$Ca(NO_3)_2$	1.52	2.4	1.274			
Vermiculite/$Li(NO_3)_2$	1.73	2.4	1.109			
Vermiculite/LiBr	1.94	1.9	1.172			
Vermiculite/63wt.% $LiNO_3$	0.4–0.5			< 0.5	33	[111]
Vermiculite	0.04	9	1.8		25	[112]
Vermiculite/57.3wt.% $CaCl_2$	1.13		1.55			
MCM-41	0.04	1137	1.3	0.3	20	[93]
MCM-41/3wt.% $Al2(SO_4)_3$	0.1	1021	1.12			
MCM-41/5wt.% $Al2(SO_4)_3$	0.15	993	1.12			
MCM-41/7wt.% $Al2(SO_4)_3$	0.17	941	1.01			
MCM-41		1050	1.1			[113]
MCM-41/37.7wt.% $CaCl_2$	0.7–0.75	325		0.7	20	
WSS	0.15	111.7	0.309	0.95	25	[114]
WSS/9.6wt.% LiCl	1.1	64.5	262			
WSS	0.15	111.7	0.309	0.95	25	[115]

Table 5 (continued)

Composite	Uptake (g g^{-1})	BET surface area (m^2 g^{-1})	V_{por} (cm^3 g^{-1})	P/P_s (–)	T_{ads} (°C)	Refs.
WSS/2.2wt.% $CaCl_2$	0.26	100.9	0.29			
WSS/13wt.% $CaCl_2$	0.66	49.9	0.209			
WSS/22.4wt.% $CaCl_2$	1.12	38.4	0.152			
WSS	0.26	149	0.37	0.95	25	[116]
WSS/5wt.% $CaCl_2$	0.31	119	0.33	0.95		
WSS/10wt.% $CaCl_2$	0.32	101	0.32	0.75		
WSS/5wt.% NaCl	0.35	129	0.33	0.95		
WSS/10wt.% NaCl	0.48	128	0.34	0.95		
WSS/5wt.% LiCl	0.38	124	0.33	0.95		
WSS/10wt.% LiCl	0.57	134	0.35	0.95		
SP	1.5	105.3	0.168	0.9	25	[117]
SP/$CaCl_2$	1.33	103.953	0.1657			

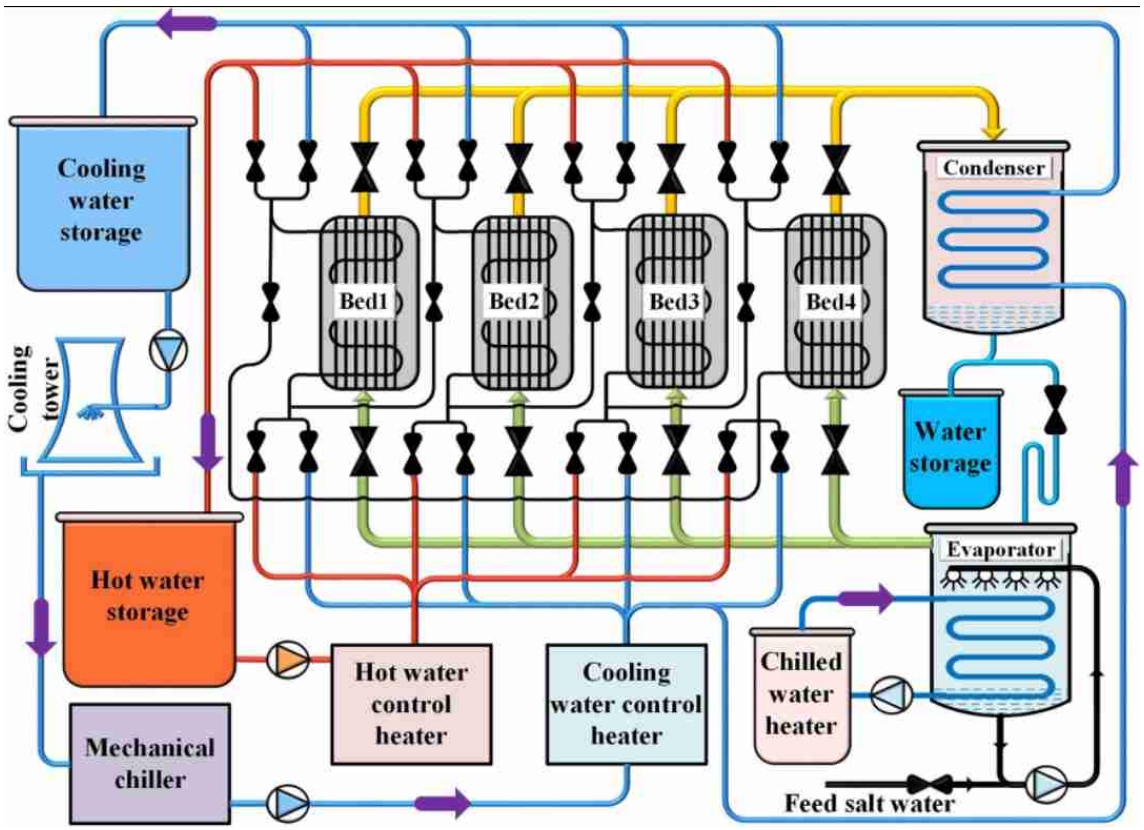

Fig. 4 Schematic diagram of the ADS used test facility [8]

or solar energy to generate potable. The study investigated a practical implementation of theoretical ADS cycles and their validity experimentally. As shown in Fig. 6, the study employed one adsorption unit with 2.124 kg of silica gel.

Ng et al. [120] analyzed the performance of ADS utilized by waste heat for producing desalinated water and cooling effect. A theoretical simulation for ADS was preceded. The cycle was explored using key performance parameters like

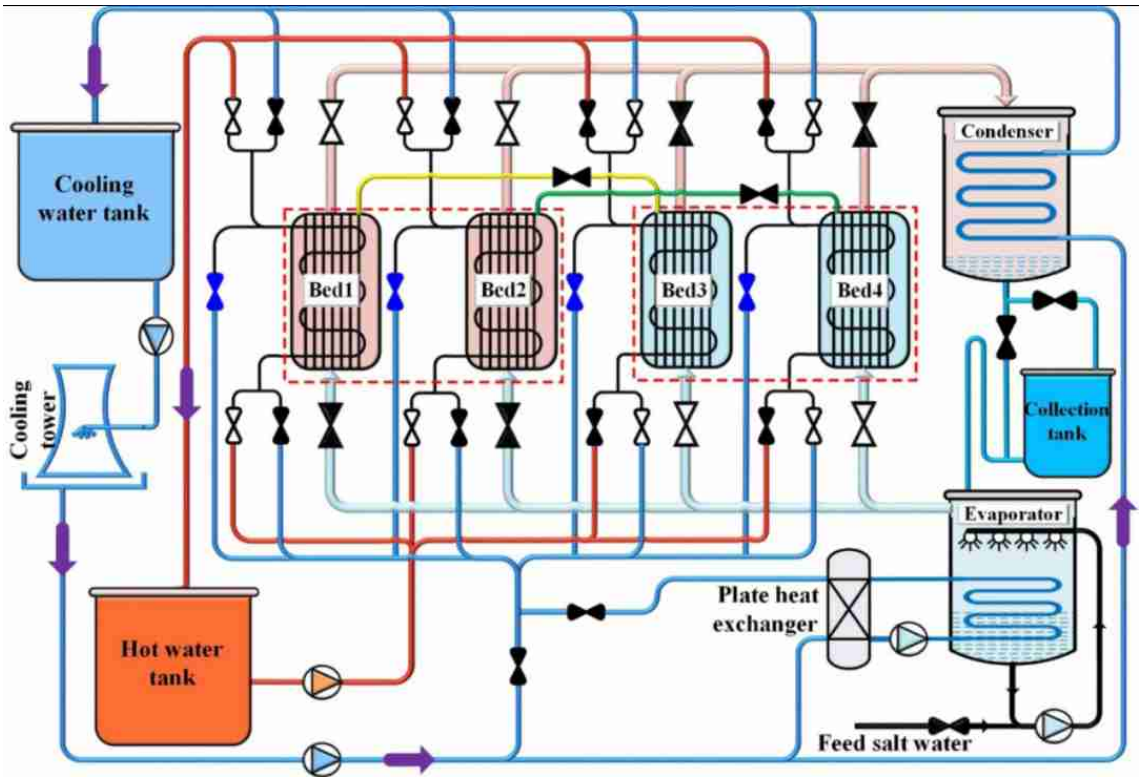

Fig. 5 Schematic diagram of used ADS experimental test rig stated in [118]

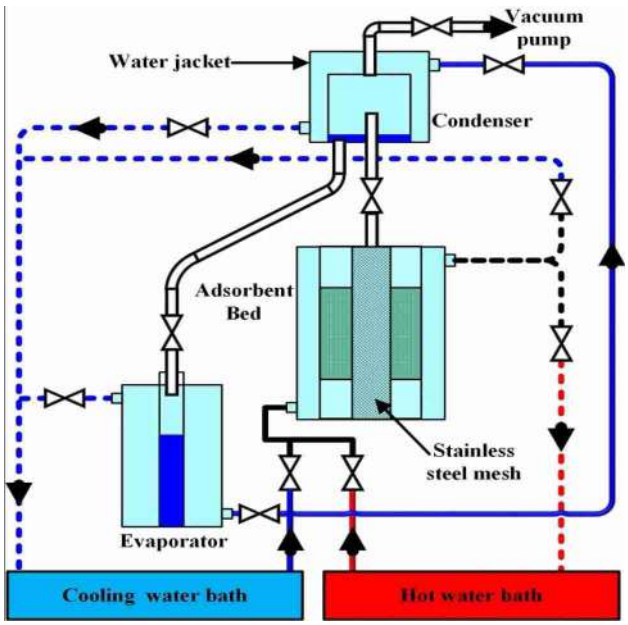

Fig. 6 One adsorption unit with 2.124 kg of silica gel [119]

(i) SCP, (ii) SDWP, (iii) COP, and (iv) overall conversion ratio (OCR). The mathematical results were certified by experimental data. Figure 7 expresses the advanced ADS cycle with 4 adsorption units with 36 kg silica gel per unit. At $T_{whi} = 85$ °C, the cycle produced 3.6 m^3 of desalinated water and 23 Raton at $T_{cho} = 10$ °C.

Mitra et al. [121] evaluated two-stage ADS for both cooling-cum-desalination. Figure 8 shows a schematic of the experimental facility. The study showed that a single-stage ADS system could not be used with an air-cooled condenser under tropical conditions, and this was realized by operating the system in a 2-stage model. Also, the study expressed a developed simulation model that was closer to experimental results than the previous one.

Gao et al. [122] investigated an innovative single-stage vacuum evaporator to extract saltwater. The system was settled to utilize an ultra-low-grade heat source of 50 °C. Figure 9 illustrates the investigated system. The adsorbent bed comprised 5 arrays of U-shaped aluminum finned tube heat-exchanger with 0.8 kg of silica gel (Type A). It was conducted that utilizing lower T_{cwi} enhanced the desorption process, which boosted the performance of the developed system.

Alsaman et al. [15] proposed and designed a new solar ADS for cooling and desalination. The proposed ADS was built and tested under Egypt's climate conditions. Figure 10

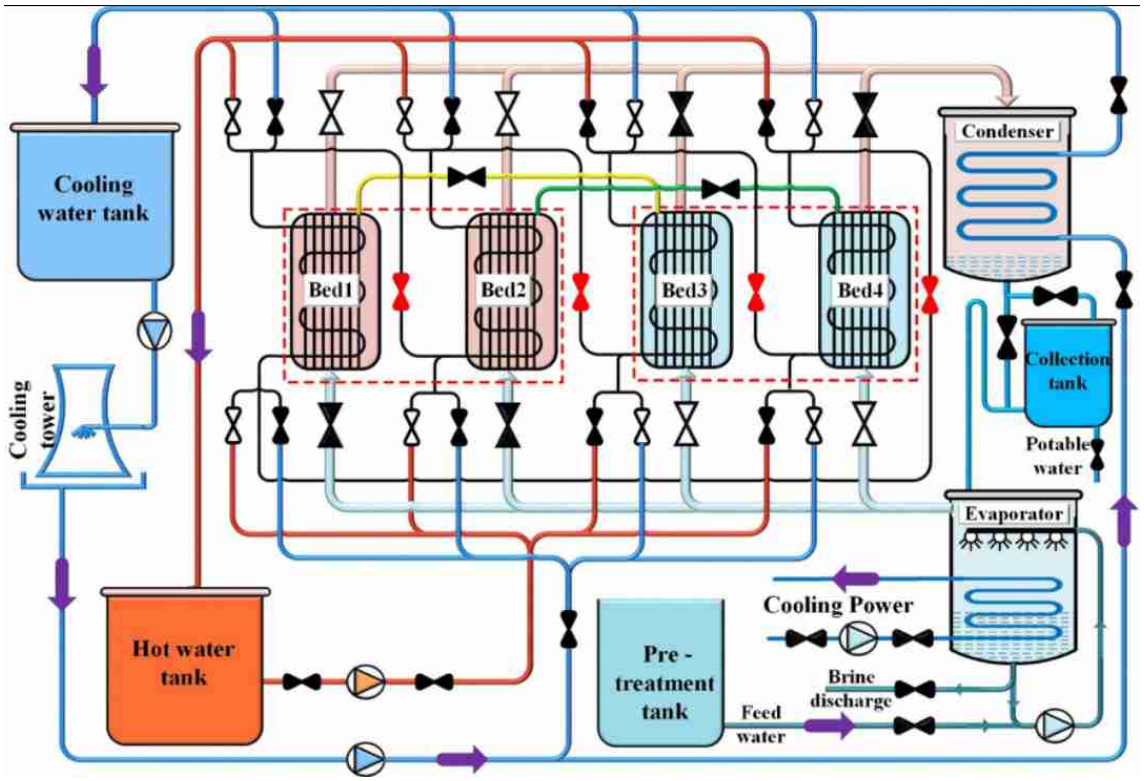

Fig. 7 Advanced ADS cycle with 4 adsorption units [120]

expresses the designed ADS 13.5 kg with silica gel. The Adsorption characteristics were also presented for the selected material. The theoretical model was close to experimental results. The results showed that SCP was 112 W/kg and SDWP was 4 m^3/day.ton with COP of 0.45. Dakkama et al. [74] investigated MOF development for producing ice and freshwater. Figure 11 expresses a schematic diagram of the investigated system. The adsorber bed contained 670 g of CPO-27 (Ni). Results indicated that the optimal operating salinity concentration was 35,000 ppm to produce ice (8.3 m^3/day/ton) with COP 0.9. The SDWP was 1.8 m^3/day/ton.

Youssef et al. [73] explored experimentally using CPO-27 (Ni) as adsorbent material for ADS applications. Experimental and numerical investigation for utilizing 0.67 kg of CPO-27(Ni) with a one-bed ADS system was obtained, as expressed in Fig. 12. Results demonstrated that by increasing T_{eva} and reducing T_{cond}, SCP was improved. The ADS created 65 Rton/ton at (T_{evap} = 20 °C). SDWP was improved to 22.8 m^3/ton.day at (T_{evap} = 40 °C, T_{con} = 5 °C and T_{des} = 95 °C). Olkis et al. [123–126] presented three papers illustrating the design of an experimental small-scale ADS desalinator for producing freshwater. The study introduced the world's smallest ADS with 0.2 kg silica gel, as shown in Fig. 12. The system achieved an SDWP of 7.7 kg/kg_{sg}.day. The ADS demonstrated the profits of heat combination between the adsorbent beds to reduce the consumed energy by 25% and raise the PR to 0.6.

Elsayed et al. [127] reported that MOF materials were recommended to substitute the traditional adsorbents. The study presented an experimental test of 0.375 kg aluminum fumarate in ADS. The performance of aluminum fumarate was higher than that of ADS utilizing silica gel and CPO-27(Ni) for desalination effect only at high P/P_s. Zhang et al. [128] presented a pilot-scale ADS with freshwater production of 100 kg/h, as illustrated in Fig. 13. The system was constructed based on small-scale system optimization and enhancement. The results exhibited that the desalinated water was less than 100 kg/h at T_{hwi} = 55 °C. At higher T_{hwi}, the desalinated water rate was improved to 191.3 kg/h at T_{hwi} = 80 °C.

Advanced experimental desalination investigations

In this section, the advanced adsorption desalination experimental investigations will be expressed. These experimental investigations are for only the desalination effect. In these systems, a heat recovery between evaporator and condenser

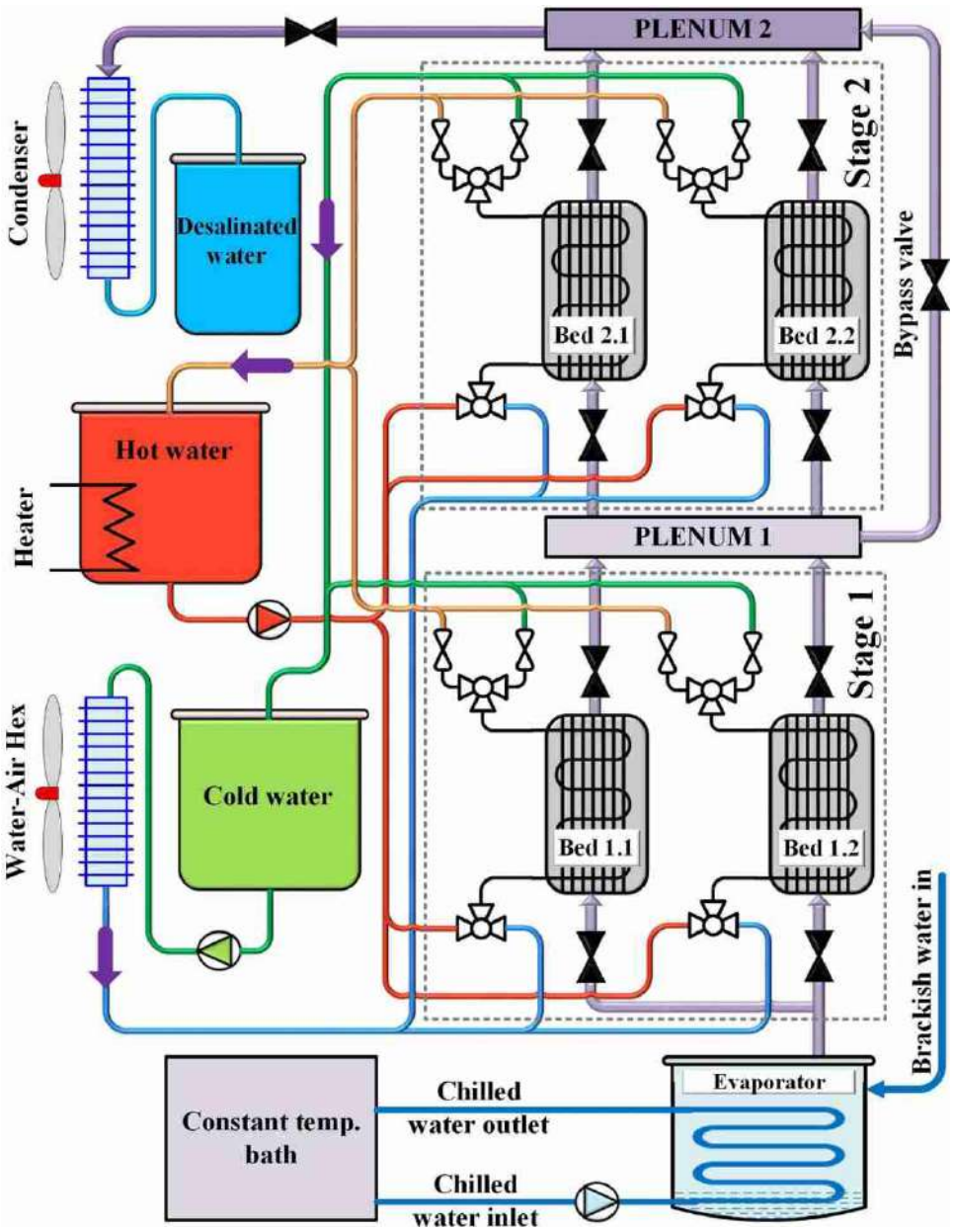

Fig. 8 Schematic of 2-bed two-stage ADS [121]

was utilized. Thu et al. [25]expressed the results of an investigation advanced AD cycle with internal heat recovery between condenser and evaporator. Figure 14 expresses the advanced AD cycle with 4 adsorption units with 36 kg silica gel per unit. A mathematically advanced AD cycle was developed and validated with experimental results. The advanced ADS could yield an SDWP of 9.24 m^3/ton daily at 70 °C with PR = 0.77. The proposed system could be operated at 50 °C T_{hwi} with SDWP 4.3. The advanced cycle SDWP was two times that of the traditional AD cycle.

Ma et al. [30] investigated an experimental heat recovery between adsorber and desorber beds for ADS with 29.17 kg silica gel per adsorption bed, as illustrated in Fig. 15. The results showed that the SDWP and PR were 4.69 and 0.766, respectively.

This heat recovery employment could not rise SDWP, but it could save consuming energy. Kim et al. [129] investigated the water quality measurements of AD plants. Feedwater was taken from the Red Sea. Figure 16 expresses the schematic AD cycle with 4 adsorption units. Water quality was assessed by complying with the Environmental Protection Agency (EPA) principles with major primary and minor inorganic drinking water contaminants and other usually tested water quality considerations. Desalinated water

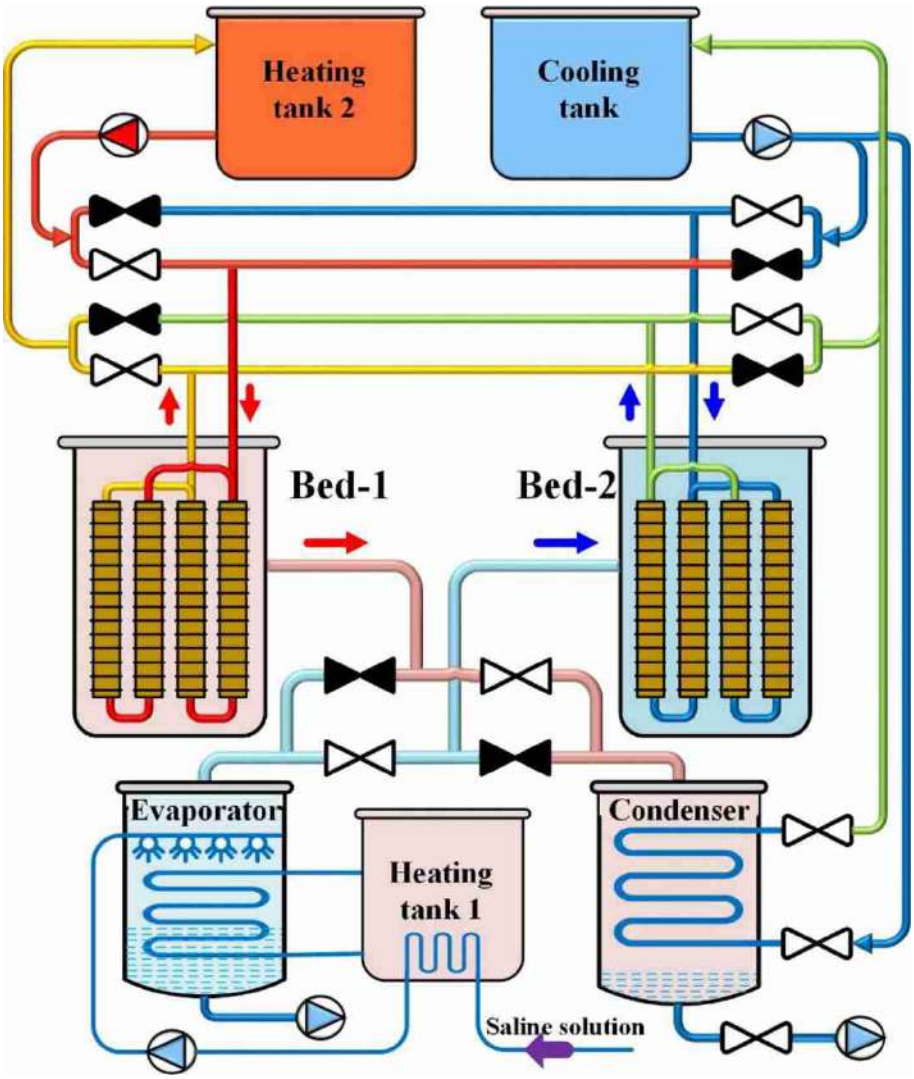

Fig. 9 Schematic of the used experimental facility [122]

testing ensured the good quality of generated freshwater. Test results showed that ADS effectively removes all forms of salts to less than 10 ppm. Bai et al. [29] investigated the mass recovery between adsorber and desorber beds for ADS and the feedwater quality effect on ADS performance. The results showed that the SDWP and SCP were 18.08 and 490, respectively.

Hybrid adsorption desalination with MED system

There are many studies on hybrid ADS with other systems such as RO-AD, AD-MVC, and AD-HDH. Still, many of these studies are theoretically investigated. The only experimental hybrid investigation systems were expressed between AD and MED. Shahzad et al. [130] presented an experimentally new hybrid "MEDAD" system, a coupling of the conventional MED and ADS, as expressed in Fig. 17. The main advantage of the MEDAD cycle is that it allowed some MED stages to work below ambient temperature, indifferent to the conventional MED. The hybrid system significantly increases desalinated water to 2.5–3 folds of conventional MED.

Son et al. [131] explored experimentally hybrid "MEDAD" desalination, applying synergetic impact for utilizing energy to improve the MEDAD performance, as expressed in Fig. 18. The MEDAD system significantly increased desalinated water up to 2–5 folds of conventional MED of the same rating.

Table 6 summarizes the results of previous experimental ADS studies. The SDWP for ADS that utilized silica gel varied from 3.6 to 14.2 m^3/day.ton. This wide range illustrates the significant effect of ADS system design and operating conditions. Therefore, the next section summarizes

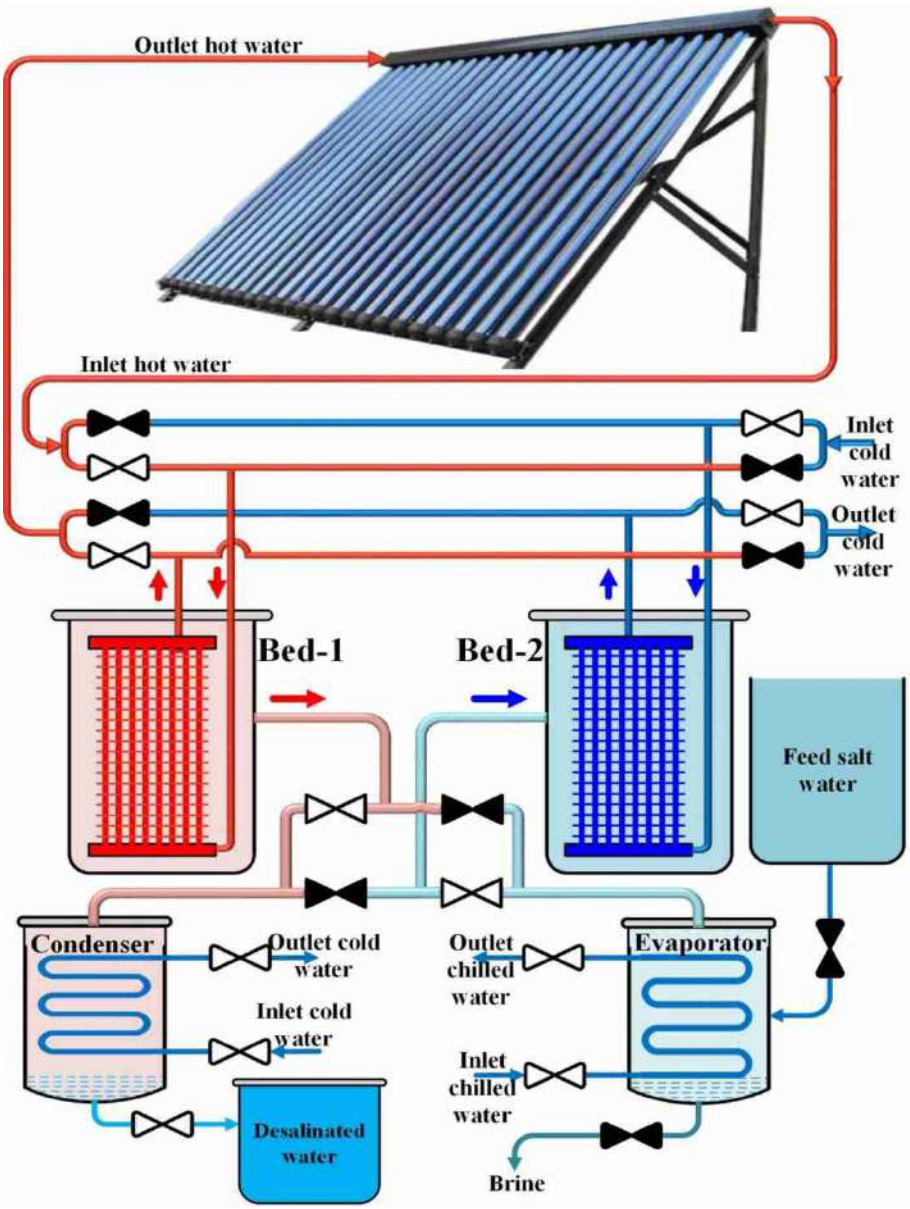

Fig. 10 Schematic diagram of the solar ADC test rig [15]

the heat exchanger configurations and their effect on ADS performance.

Effect of heat transfer of adsorption bed on ADS performance

In this section, the effect of heat transfers of adsorption bed on ADS performance. The current study expresses all adsorption desalination experimental investigations. The heat transfer parameters of adsorption beds are expressed in Table 7. The following equation illustrates heat transfer parameters.

To simplify the computation, the $TM_{inherent}$ of sorbed refrigerant was ignored. It is simplified in two ways: (1) the computed thermal mass no longer includes the sorbent's equilibrium composition, and (2) the thermal mass may be viewed as constant in sorption and desorption operations. Neglecting the TM of sorbed refrigerant will have a minor influence on TM_{total} for many adsorption heat exchangers (HXs).

The thermal mass of the adsorption bed is given by

$$TM_{total} = TM_{inherent} + TM_{design} \quad (1)$$

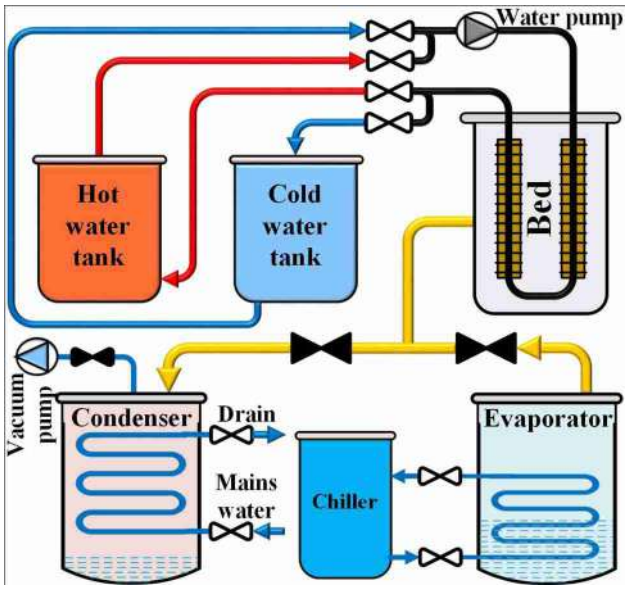

Fig. 11 Schematic diagram of ADS for ice making and freshwater [74]

$$TM_{inherent} = M_{adsorbent} Cp_{adsorbent} \quad (2)$$

$$TM_{design} = \rho_{HTF} V_{HTF} CP_{HTF} + \sum M_{metal} Cp_{metal} \quad (3)$$

where HTF represents heating thermal fluid.

The specific thermal mass is given by.

$$STM = \frac{TM_{design}}{M_{adsorbent}} \quad (4)$$

Figures 19 and 20 express the effect of bed design representing thermal masses of heat exchangers on ADS performance through the previous experimental studies. In the previous experimental studies, the STM varied from 1.74 to 6.58 kJ/kg. Figure 19 illustrates the COP variation by changing the adsorption bed's specific thermal mass (STM). The COP decreases from 0.766 to 0.36 with STM increasing 1.74–6.05 kJ/kg for silica gel adsorbent duo to increase the adsorption bed's thermal mass, which means more heat losses in the heating adsorption bed. This heat loss is represented in the heating of the heat exchanger. Figure 20 expresses the SDWP variation by changing the adsorption bed's specific thermal mass (STM). STM has a significant effect on SDWP. The SDWP increases from 3.6 to 18 m^3/day.ton (about 500% increasing) with STM increasing from 1.74 to 6.58 kJ/kg as a result of increasing the overall heat transfer coefficient due to increasing the thermal mass of the adsorption bed. This means more adsorbent vapor is released

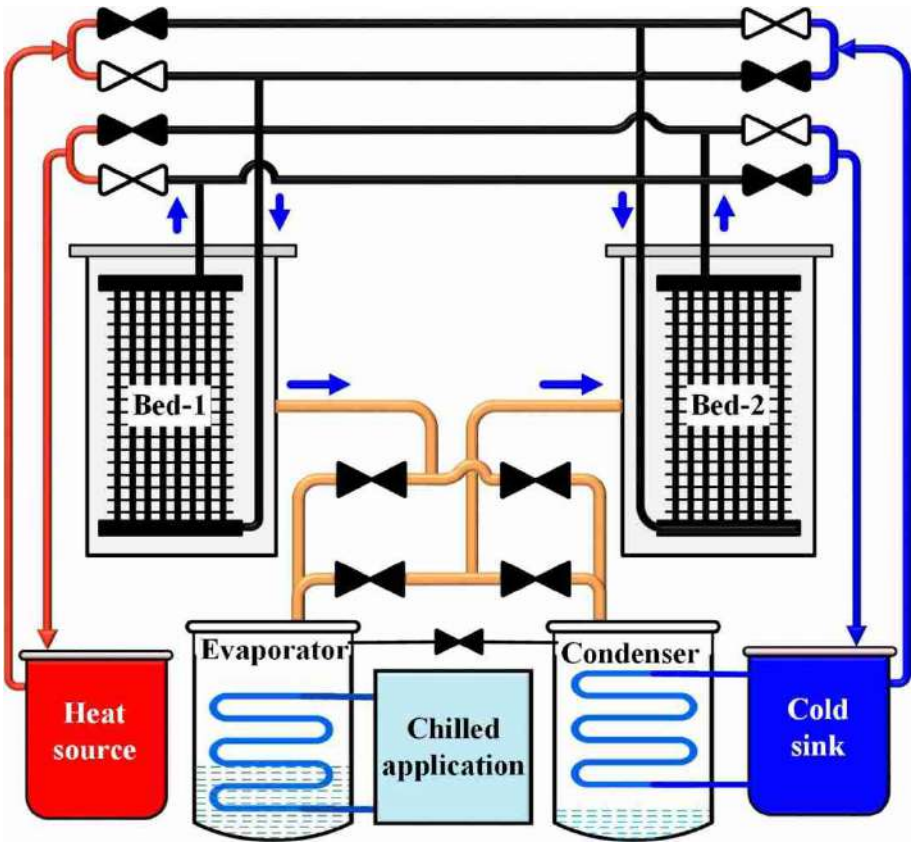

Fig. 12 Schematic diagram of small-scale ADS desalinator [123–125]

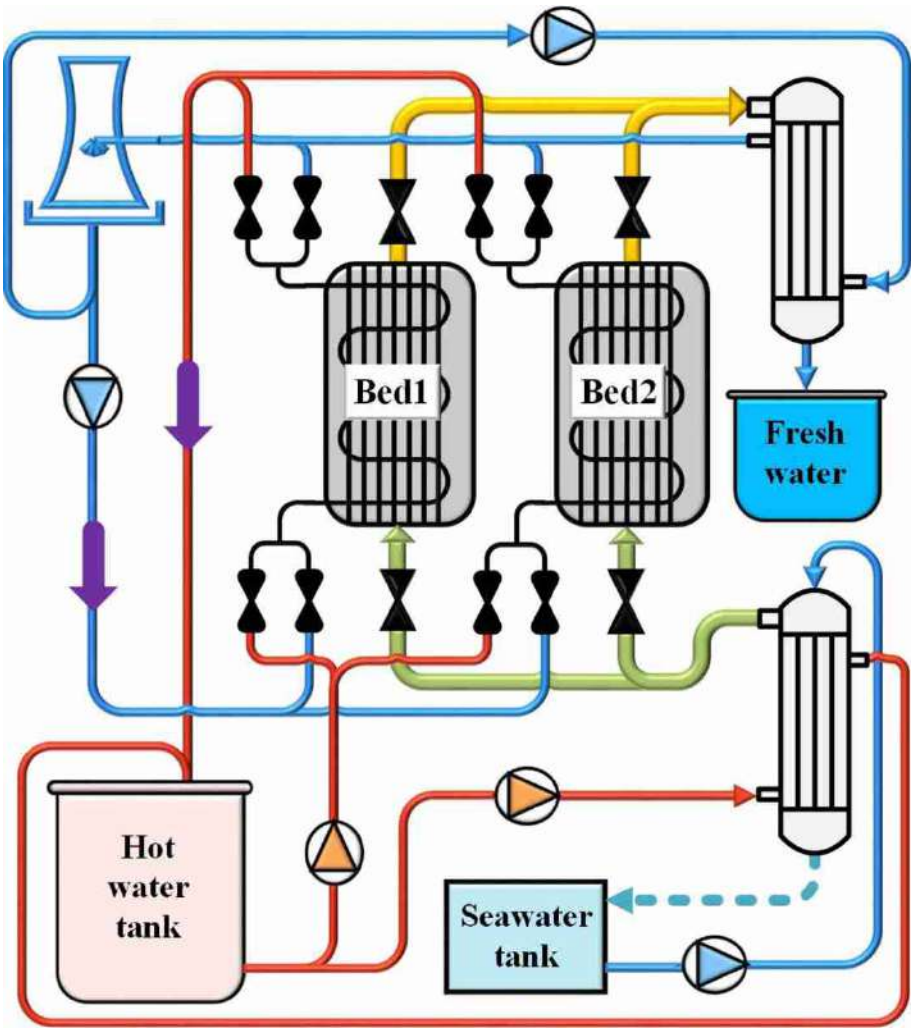

Fig. 13 Schematic diagram of pilot-scale ADS [76]

in desorption mode, leading to more desalinated water production in the condenser.

Challenges and perspectives

This section expresses the research gap, the required research topics in ADS, and future marketing challenges of marketing these ADS. Despite the many advantages of ADS, as they can be driven by renewable and/or waste energy, they still face difficulties in marketing and dissemination. This is because it suffers from high volume and relatively low efficiency compared to traditional devices, which decreases the productivity of these systems and makes them unattractive. Moreover, the number of experimental researches in this field is still limited compared to its importance. From this standpoint, it was necessary to show the gap and clarify the deficiency in this area. This is what this work is trying to show, as after reviewing the published research, it was found that the number of devices built to study desalination systems does not exceed a dozen. This clearly shows that the field still needs more effort, research, and the development of new methods and materials to raise the efficiency of this system. Therefore, it is recommended to do more experimental research to encourage the industrial sector and investors to build AD plants. The authors recommend these future researches focus on the following:-

1 Finding new adsorbent materials with a high adsorption capacity to reduce AD plant volume and increase performance in terms of SDWP and COP.
2 Finding new composite adsorbent materials for higher adsorption capacity

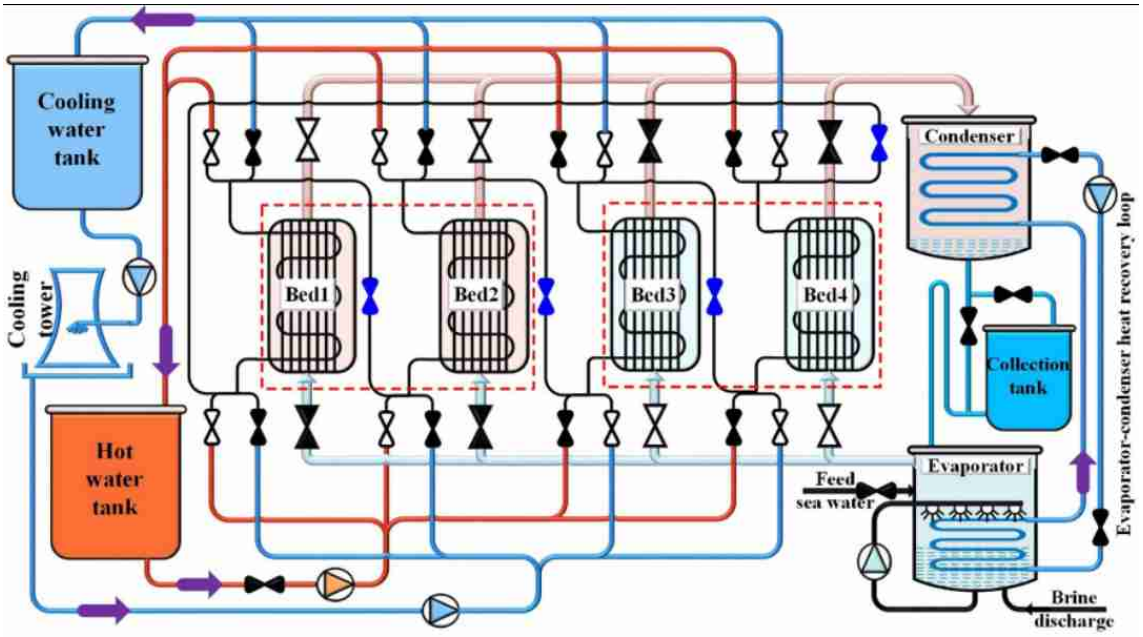

Fig. 14 Advanced ADS cycle with 4 adsorption units [25]

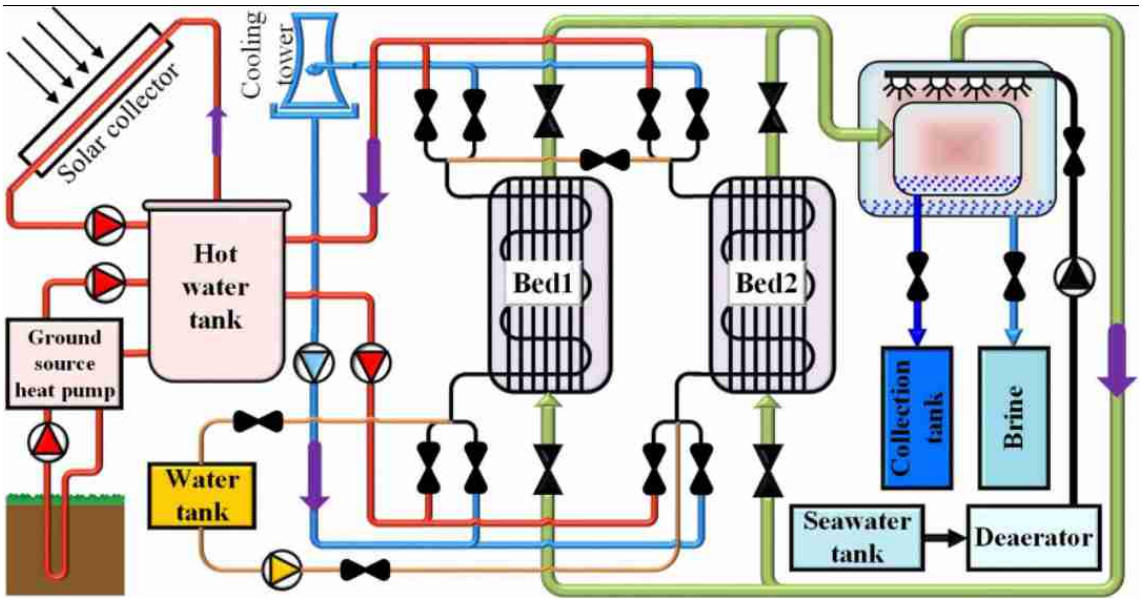

Fig. 15 Schematic diagram for heat recovery between adsorber and desorber beds [30]

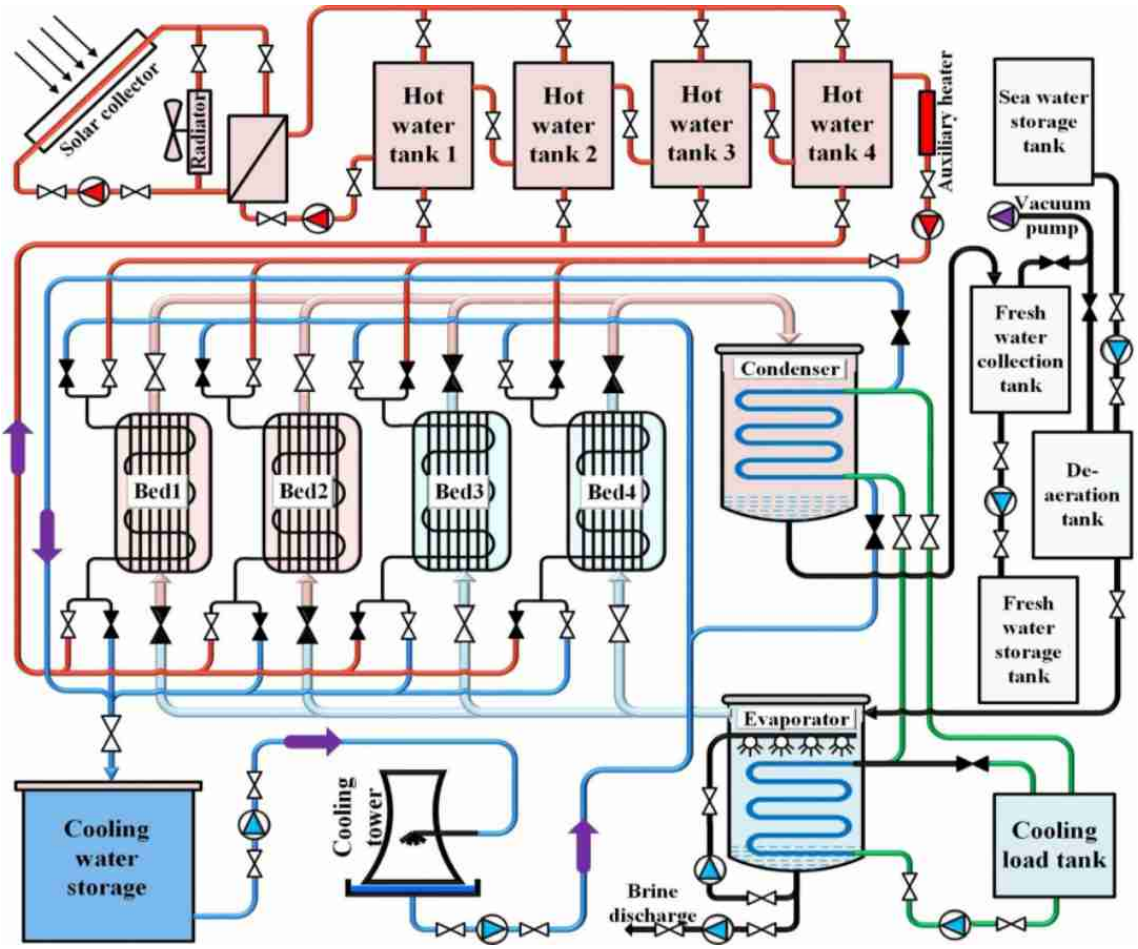

Fig. 16 schematic ADS cycle with 4 adsorption units [129]

3 How to increase the COP of the AD cycle by increasing the overall heat transfer coefficient of adsorption beds and evaporator and condenser.
4 Applying the recent theoretical research of ADS experimentally to close the gap between theoretical and experimental studies. Mathematical results [4–6, 24–28] achieved high values of SDWP and COP of 98 m^3/ton.day and 2.1, respectively [4]. However, this performance was not proven experimentally on either lab-scale, prototype, or pilot scale. Experimental measurements are still low as SDWP did not increase more than 18 m^3/ton.day, and COP did not increase than 0.78.
5 Applying the theoretical hybridization between ADS and RO, HDH, salt hydrate, and absorption system experimentally to realize the benefits of these combinations. Also, study new combinations of ADS and other desalination systems.
6 Establish more pilot plants and scale up adsorption desalination plants to encourage the industrial sector to invest in these ADS. Finding new adsorbent materials with a high adsorption capacity to reduce AD plant volume and increase performance in terms of SDWP and COP.

Conclusions

This review presents a survey about the constructed and tested experimental water distillation systems that consider adsorption technology. Not so many systems have been found, as less than ten systems were built worldwide to take off freshwater from the salty water by adsorption evaporation technology. One of these few systems had been built in Egypt. The majority of these systems

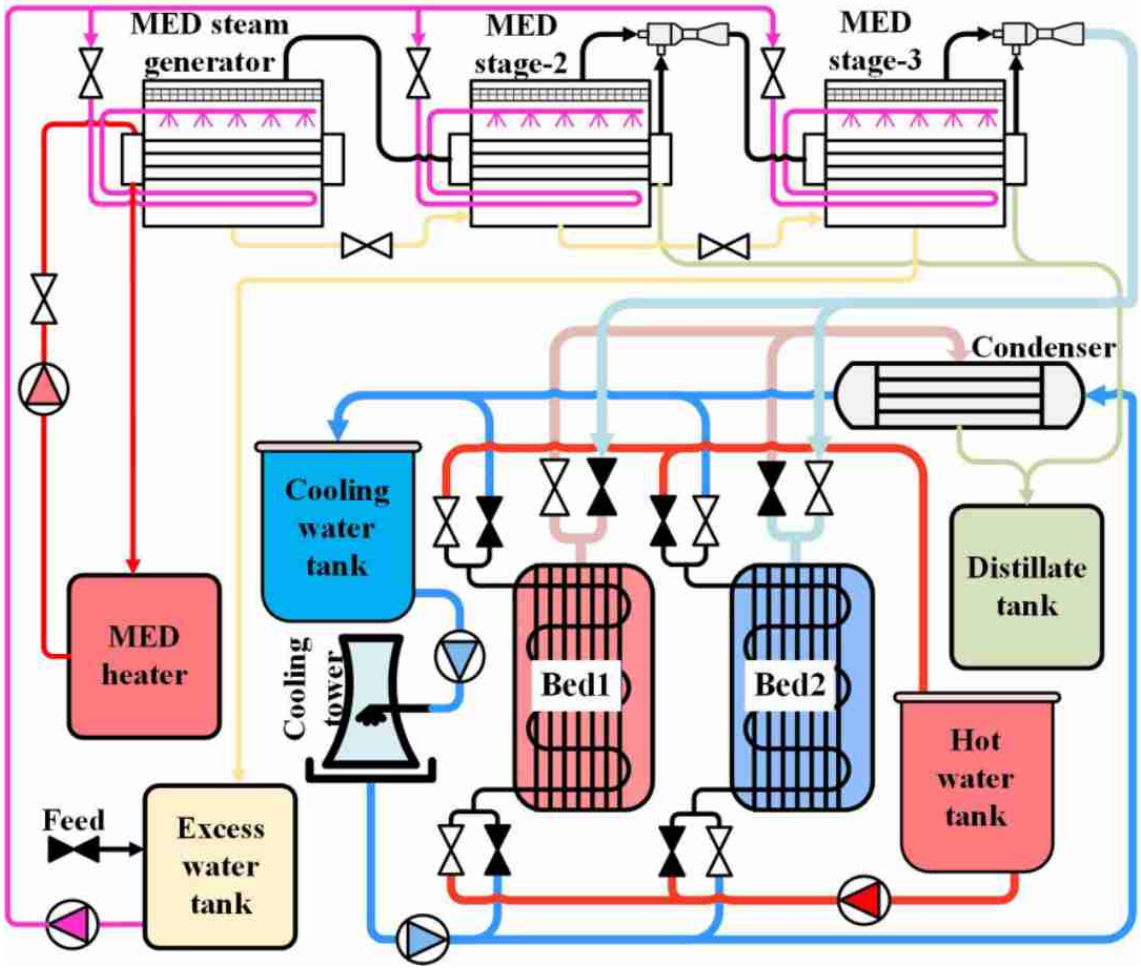

Fig. 17 MEDAD schematic diagram for experimental rig installed in NUS [130]

employed silica gel as an adsorbent material; its composites and metal–organic framework were also used. The amounts of the used adsorbents varied from less than 1 kg, reaching 1440 kg. Produced amount of pure water per day per ton of adsorbent has been varied as well, from 1.8 m^3/ton/day up to 25 m^3/ton/day. The whole presented system used a fin tube-type heat exchanger. It is clear that the technology is still in the cradle, and more experimental test rigs are required to be built and tested at different operating conditions. Also, more adsorbent materials are needed to be employed in such systems.

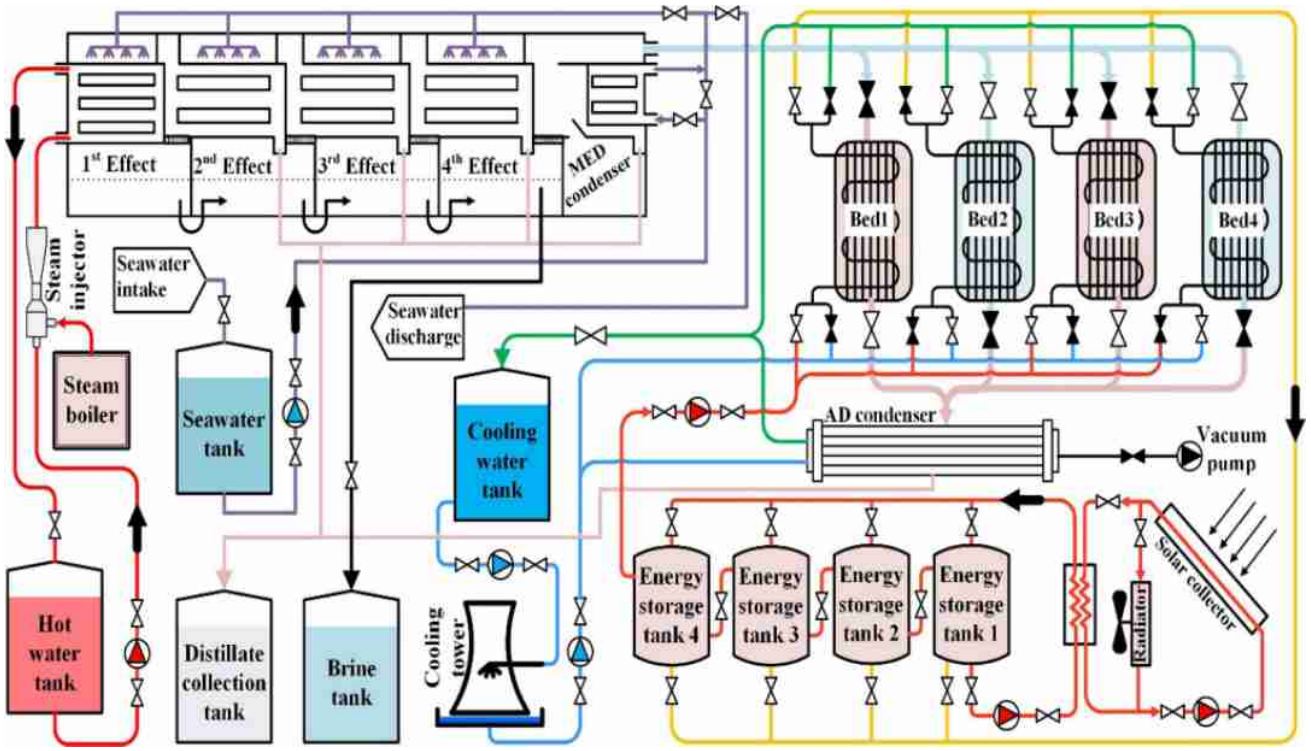

Fig. 18 Pictorial view of MED-AD system [131]

Table 6 Comparison between previous experimental ADS studies

Adsorbent material	Half cycle time (s)	No. of bed	Adsorbent weight (kg)	T_{cw} (°C)	T_{hw} (°C)	SDWP (m^3/ton)	SCP (W/kg)	COP (–)	Refs.
Silica gel	180	4	36	30	85	4.7	–	0.28	[8]
Silica gel	650	2	6.75	30	85	4	112	0.45	[15]
Silica gel	600	4	36	30	85	14.2	–	0.74	[25]
Silica gel	900	2	29.17	27	83	4.69	–	0.766	[30]
Silica gel	600	4/2	36	30	85	10	–	0.61	[118]
Silica gel	480	4	36	29.5	85	8	181	–	[120]
Silica gel	1200	2	0.2	25	80	7.7	80	0.6	[123–126]
Silica gel	900	2	1440	27	80	3.6	–	0.72	[128]
CPO-27Ni MOF	720	1	0.670	20	110	6.9	200	–	[73, 132, 133]
CPO-27Ni MOF	900	1	0.670	24	95	1.8	–	0.48	[74]
Aluminum fumarate	900	2	0.375	30	90	8.5	250	0.13	[127]
Aluminum fumarate	250	2	23.2	25	85	8.66	226	0.5	[134]
Aluminum fumarate	500	1	0.3	30	90	14.4	549.7	0.26	[135]
Montmorillonite/HCl	450	2	2.65	25	85	4.4	110	0.41	[12]
MWCNT embedded zeolite13X/$CaCl_2$	542	2	1.1	24	85	18.08	490	0.3	[29]

Table 7 The heat transfer parameters of adsorption beds for different excremental test rigs

Component (section) shape of HX	Working pair	Heat transfer fluid	Sorbent mass (kg)	HX Mass (kg)	TM_{total} (kJ/K)	$m_{sorb}/m_{H.X}$	STM (TM/$m_{sorb.}$)	Refs.
Tube fin HX packed	Silica gel/water	Water	6.75	25.44	16.2	0.26533	2.4	[15]
Tube fin HX packed	Silica gel/water	Water	0.21	0.81	0.737	0.259259	3.5	[123–126]
Tube fin HX packed	Silica gel/water	Water	29.17	60.34	50.83	0.483427	1.74	[30]
Tube fin HX packed	Silica gel/water	Water	36	–	184.1	–	5.11	[120]
Tube fin HX packed	Silica gel/water	Water	1440	1293.6	2458.8	1.082251	1.756	[128]
Shell and tube HX stage 1	Silica gel/water	Water	5.6	25	17.152	0.224	3.06	[121]
Shell and tube HX stage 2	Silica gel/water	Water	3.2	22	13.5	0.145455	4.22	[121]
Tube fin HX packed	Silica gel/water	Water	36	–	217.22	–	6.03	[25]
Tube fin HX packed	CPO-27Ni MOF/water	Water	0.67	29.97	–	0.022356	–	[73, 132, 133]
Tube fin HX packed	MWCNT embedded zeolite13X/$CaCl_2$	Water	1.1	8	7.24	0.137	6.58	[29]
Tube fin HX packed	Montmorillonite/HCl	Water	2.65	12.97	8.19	0.204	3.09	[12]

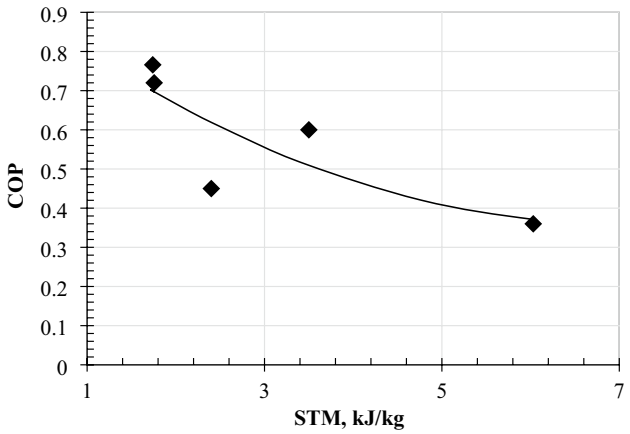

Fig. 19 Effect of STM on COP of ADS

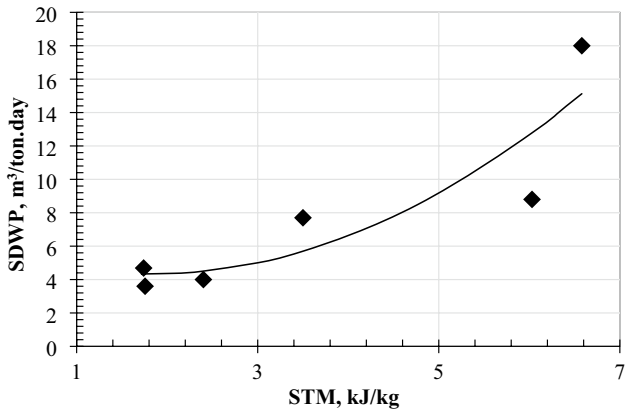

Fig. 20 Effect of STM on SDWP of ADS

Acknowledgements This research is a part of a research project supported by the Academy of Scientific Research and Technology (ASRT) through call Egypt scientists -2. Call no. 2/2019/ASRT-Nexus.

Declarations

Conflict of interest The authors declare that they have no conflict of interest.

References

1. Harby, K., Ali, E.S., Almohammadi, K.M.: A novel combined reverse osmosis and hybrid absorption desalination-cooling system to increase overall water recovery and energy efficiency. J. Clean. Prod. **287**, 125014 (2021). https://doi.org/10.1016/j.jclepro.2020.125014
2. Thu, K., Chakraborty, A., Kim, Y.D., Myat, A., Saha, B.B., Ng, K.C.: Numerical simulation and performance investigation of an advanced adsorption desalination cycle. Desalination **308**, 209–218 (2013). https://doi.org/10.1016/j.desal.2012.04.021
3. Sadri, S., Khoshkhoo, R.H., Ameri, M.: Optimum exergo-economic modeling of novel hybrid desalination system (MEDAD+RO). Energy **149**, 74–83 (2018). https://doi.org/10.1016/j.energy.2018.02.006
4. Ali, E.S., Mohammed, R.H., Qasem, N.A.A., Zubair, S.M., Askalany, A.: Solar-powered ejector-based adsorption desalination system integrated with a humidification-dehumidification system. Energy Convers. Manag. **238**, 114113 (2021). https://doi.org/10.1016/j.enconman.2021.114113
5. Ali, E.S., Mohammed, R.H., Askalany, A.: A daily freshwater production of 50 m3/ton of silica gel using an adsorption-ejector combination powered by low-grade heat. J. Clean. Prod. **282**, 124494 (2021). https://doi.org/10.1016/j.jclepro.2020.124494
6. Askalany, A.A., Ali, E.S.: A new approach integration of ejector within adsorption desalination cycle reaching COP higher than one. Sustain. Energy Technol. Assess. **41**, 100766 (2020). https://doi.org/10.1016/j.seta.2020.100766
7. Ng, K.C., Shahzad, M.W., Son, H.S., Hamed, O.A.: An exergy approach to efficiency evaluation of desalination. Appl. Phys. Lett. **110**, 184101 (2017). https://doi.org/10.1063/1.4982628
8. Wang, X., Ng, K.C.: Experimental investigation of an adsorption desalination plant using low-temperature waste heat. Appl. Therm. Eng. **25**, 2780–2789 (2005). https://doi.org/10.1016/j.applthermaleng.2005.02.011
9. Shemer, H., Semiat, R.: Sustainable RO desalination – Energy demand and environmental impact. Desalination **424**, 10–16 (2017). https://doi.org/10.1016/j.desal.2017.09.021
10. Ding, D., Huang, J., Deng, X., Fu, K.: Recent advances and perspectives of nanostructured amorphous alloys in electrochemical water electrolysis. Energy Fuels **35**, 15472–15488 (2021). https://doi.org/10.1021/acs.energyfuels.1c02706
11. Kim, Y.D., Woo, S.Y., Lee, H.S., Ji, H.: Adsorption isotherm model for analyzing the adsorption characteristics of water vapor to commercially available silica gel adsorbents for adsorption desalination applications. J. Chem. Eng. Data. **66**, 1144–1156 (2021). https://doi.org/10.1021/acs.jced.0c00927
12. Ali, E.S., Askalany, A.A., Harby, K., Diab, M.R., Hussein, B.R.M., Alsaman, A.S.: Experimental adsorption water desalination system utilizing activated clay for low grade heat source applications. J. Energy Storage **43**, 103219 (2021). https://doi.org/10.1016/j.est.2021.103219
13. Yang, M., Wang, X., Li, J., Zheng, J.N., Jiang, L.: Effects of particle sizes on growth characteristics of propane hydrate in uniform/nonuniform sands for desalination application. Energy Fuels **36**, 1003–1014 (2022). https://doi.org/10.1021/acs.energyfuels.1c03709
14. Ali, E.S., Askalany, A.A., Harby, K., Diab, M.R., Alsaman, A.S.: Adsorption desalination-cooling system employing copper sulfate driven by low grade heat sources. Appl. Therm. Eng. **136**, 169–176 (2018). https://doi.org/10.1016/j.applthermaleng.2018.03.014
15. Alsaman, A.S., Askalany, A.A., Harby, K., Ahmed, M.S.: Performance evaluation of a solar-driven adsorption desalination-cooling system. Energy **128**, 196–207 (2017). https://doi.org/10.1016/j.energy.2017.04.010
16. Amin, Z.M., Hawlader, M.N.A.: Analysis of solar desalination system using heat pump. Renew. Energy **74**, 116–123 (2015). https://doi.org/10.1016/j.renene.2014.07.028
17. Ali, E.S., Mohammed, R.H., Zohir, A.E., Farid, A.M., Elshaer, R.N., El-Ghetany, H.H., Askalany, A.A.: Novel ultrasonic dynamic vapor sorption apparatus for adsorption drying, cooling and desalination applications. Energy Rep. **8**, 8798–8804 (2022). https://doi.org/10.1016/j.egyr.2022.06.026
18. Askalany, A., Habib, K., Ghazy, M., Assadi, M.K.: Adsorption cooling system employing activated carbon/ hfc410a adsorption pair. ARPN J. Eng. Appl. Sci. **11**, 12253–12257 (2016)
19. Ghazy, M., Askalany, A.A., Ibrahim, E.M.M., Mohamed, A.S.A., Ali, E.S., AL-Dadah, R.: Solar powered adsorption desalination system employing CPO-27(Ni). J. Energy Storage **53**, 105174 (2022). https://doi.org/10.1016/j.est.2022.105174
20. Ghazy, M., Ibrahim, E.M.M., Mohamed, A.S.A., Askalany, A.A.: Cooling technologies for enhancing photovoltaic–thermal (PVT) performance: a state of the art. Int. J. Energy Environ. Eng. (2022). https://doi.org/10.1007/s40095-022-00491-8
21. Ghazy, M., Askalany, A., Kamel, A., Khalil, K.M.S., Mohammed, R.H., Saha, B.B.: Performance enhancement of adsorption cooling cycle by pyrolysis of Maxsorb III activated carbon with ammonium carbonate. Int. J. Refrig. **126**, 210–221 (2021). https://doi.org/10.1016/j.ijrefrig.2020.12.036
22. Askalany, A.A., Saha, B.B.: Towards an accurate estimation of the isosteric heat of adsorption—a correlation with the potential theory. J. Colloid Interface Sci. **490**, 59–63 (2017). https://doi.org/10.1016/j.jcis.2016.11.040
23. Zejli, D., Benchrifa, R., Bennouna, A., Bouhelal, O.K.: A solar adsorption desalination device: first simulation results. Desalination **168**, 127–135 (2004). https://doi.org/10.1016/j.desal.2004.06.178
24. Thu, K., Yanagi, H., Saha, B.B., Ng, K.C.: Performance investigation on a 4-bed adsorption desalination cycle with internal heat recovery scheme. Desalination **402**, 88–96 (2017). https://doi.org/10.1016/j.desal.2016.09.027
25. Thu, K., Saha, B.B., Chakraborty, A., Chun, W.G., Ng, K.C.: Study on an advanced adsorption desalination cycle with evaporator-condenser heat recovery circuit. Int. J. Heat Mass Transf. **54**, 43–51 (2011). https://doi.org/10.1016/j.ijheatmasstransfer.2010.09.065
26. Ali, E.S., Askalany, A.A., Zohir, A.E.: Innovative employing of salt hydration with adsorption to enhance performance of desalination and heat transformation systems. Appl. Therm. Eng. **179**, 115614 (2020). https://doi.org/10.1016/j.applthermaleng.2020.115614
27. Askalany, A., Ali, E.S., Mohammed, R.H.: A novel cycle for adsorption desalination system with two stages-ejector for higher water production and efficiency. Desalination **496**, 114753 (2020). https://doi.org/10.1016/j.desal.2020.114753
28. Ali, E.S., Muhammad Asfahan, H., Sultan, M., Askalany, A.A.: A novel ejectors integration with two-stages adsorption

desalination: away to scavenge the ambient energy. Sustain. Energy Technol. Assess. **48**, 101658 (2021). https://doi.org/10.1016/j.seta.2021.101658
29. Bai, S., Ho, T.C., Ha, J., An, A.K., Tso, C.Y.: Study of the salinity effects on the cooling and desalination performance of an adsorption cooling cum desalination system with a novel composite adsorbent. Appl. Therm. Eng. **181**, 115879 (2020). https://doi.org/10.1016/j.applthermaleng.2020.115879
30. Ma, H., Zhang, J., Liu, C., Lin, X., Sun, Y.: Experimental investigation on an adsorption desalination system with heat and mass recovery between adsorber and desorber beds. Desalination **446**, 42–50 (2018). https://doi.org/10.1016/j.desal.2018.08.022
31. Askalany, A.A., Ernst, S.J., Hügenell, P.P.C., Bart, H.J., Henninger, S.K., Alsaman, A.S.: High potential of employing bentonite in adsorption cooling systems driven by low grade heat source temperatures. Energy **141**, 782–791 (2017). https://doi.org/10.1016/j.energy.2017.07.171
32. White, J.: A CFD simulation on how the different sizes of silica gel will affect the adsorption performance of silica gel. Model. Simul. Eng. **2012**, 1–12 (2012). https://doi.org/10.1155/2012/651434
33. Thu, K., Chakraborty, A., Saha, B.B., Ng, K.C.: Thermo-physical properties of silica gel for adsorption desalination cycle. Appl. Therm. Eng. **50**, 1596–1602 (2013). https://doi.org/10.1016/j.applthermaleng.2011.09.038
34. Robens, E., Wang, X.: Investigation on the isotherm of silica gel+water systems. J. Therm. Anal. Calorim. **76**, 659–669 (2004). https://doi.org/10.1023/b:jtan.0000028045.96239.7e
35. Mohammed, R.H., Mesalhy, O., Elsayed, M.L., Su, M., Chow, C.L.: Revisiting the adsorption equilibrium equations of silica-gel/water for adsorption cooling applications. Int. J. Refrig. **86**, 40–47 (2018). https://doi.org/10.1016/j.ijrefrig.2017.10.038
36. Alsaman, A.S., Ibrahim, E.M.M., Ahmed, M.S., Askalany, A.A.: Composite adsorbent materials for desalination and cooling applications: a state of the art. Int. J. Energy Res. **46**, 10345–10371 (2022). https://doi.org/10.1002/er.7894
37. Bahgaat, A.K., Hassan, H.E., Melegy, A.A., Abd-El Kareem, A.M., Mohamed, M.H.: Synthesis and characterization of zeolite-Y from natural clay of Wadi Hagul Egypt. Egypt J Chem **63**, 3791–3800 (2020). https://doi.org/10.21608/EJCHEM.2020.23195.2378
38. Sayilgan, ŞÇ., Mobedi, M., Ülkü, S.: Effect of regeneration temperature on adsorption equilibria and mass diffusivity of zeolite 13x-water pair. Microporous Mesoporous Mater. **224**, 9–16 (2016). https://doi.org/10.1016/j.micromeso.2015.10.041
39. Kayal, S., Baichuan, S., Saha, B.B.: Adsorption characteristics of AQSOA zeolites and water for adsorption chillers. Int. J. Heat Mass Transf. **92**, 1120–1127 (2016). https://doi.org/10.1016/j.ijheatmasstransfer.2015.09.060
40. Teo, H.W.B., Chakraborty, A., Han, B.: Water adsorption on CHA and AFI types zeolites: modelling and investigation of adsorption chiller under static and dynamic conditions. Appl. Therm. Eng. **127**, 35–45 (2017). https://doi.org/10.1016/j.applthermaleng.2017.08.014
41. Henninger, S.K., Schmidt, F.P., Henning, H.M.: Water adsorption characteristics of novel materials for heat transformation applications. Appl. Therm. Eng. **30**, 1692–1702 (2010). https://doi.org/10.1016/j.applthermaleng.2010.03.028
42. Chaemchuen, S., Xiao, X., Klomkliang, N., Yusubov, M., Verpoort, F.: Tunable metal-organic frameworks for heat transformation applications. Nanomaterials **8**, 661 (2018). https://doi.org/10.3390/nano8090661
43. Tatlier, M., Munz, G., Henninger, S.K.: Relation of water adsorption capacities of zeolites with their structural properties. Microporous Mesoporous Mater. **264**, 70–75 (2018). https://doi.org/10.1016/j.micromeso.2017.12.031
44. Furukawa, H., Gándara, F., Zhang, Y.B., Jiang, J., Queen, W.L., Hudson, M.R., Yaghi, O.M.: Water adsorption in porous metal-organic frameworks and related materials. J. Am. Chem. Soc. **136**, 4369–4381 (2014). https://doi.org/10.1021/ja500330a
45. Canivet, J., Bonnefoy, J., Daniel, C., Legrand, A., Coasne, B., Farrusseng, D.: Structure-property relationships of water adsorption in metal-organic frameworks. New J. Chem. **38**, 3102–3111 (2014). https://doi.org/10.1039/c4nj00076e
46. Burtch, N.C., Jasuja, H., Walton, K.S.: Water stability and adsorption in metal-organic frameworks. Chem. Rev. **114**, 10575–10612 (2014). https://doi.org/10.1021/cr5002589
47. Administrator, O.J.S.T.: Metal-organic frameworks applied for water purification. Resour Technol (2018). https://doi.org/10.18799/24056537/2018/1/177
48. Taylor, J.M., Vaidhyanathan, R., Iremonger, S.S., Shimizu, G.K.H.: Enhancing water stability of metal-organic frameworks via phosphonate monoester linkers. J. Am. Chem. Soc. **134**, 14338–14340 (2012). https://doi.org/10.1021/ja306812r
49. Canivet, J., Fateeva, A., Guo, Y., Coasne, B., Farrusseng, D.: Water adsorption in MOFs: fundamentals and applications. Chem. Soc. Rev. **43**, 5594–5617 (2014). https://doi.org/10.1039/c4cs00078a
50. Jasuja, H., Burtch, N.C., Huang, Y.G., Cai, Y., Walton, K.S.: Kinetic water stability of an isostructural family of zinc-based pillared metal-organic frameworks. Langmuir **29**, 633–642 (2013). https://doi.org/10.1021/la304204k
51. Li, S., Chen, Y., Pei, X., Zhang, S., Feng, X., Zhou, J., Wang, B.: Water purification: adsorption over metal-organic frameworks. Chin J. Chem. **34**, 175–185 (2016). https://doi.org/10.1002/cjoc.201500761
52. Li, N., Xu, J., Feng, R., Hu, T.L., Bu, X.H.: Governing metal-organic frameworks towards high stability. Chem. Commun. **52**, 8501–8513 (2016). https://doi.org/10.1039/c6cc02931k
53. Towsif Abtab, S.M., Alezi, D., Bhatt, P.M., Shkurenko, A., Belmabkhout, Y., Aggarwal, H., Weseliński, ŁJ., Alsadun, N., Samin, U., Hedhili, M.N., Eddaoudi, M.: Reticular chemistry in action: a hydrolytically stable mof capturing twice its weight in adsorbed water. Chem. **4**, 94–105 (2018). https://doi.org/10.1016/j.chempr.2017.11.005
54. Reinsch, H., Marszalek, B., Wack, J., Senker, J., Gil, B., Stock, N.: A new Al-MOF based on a unique column-shaped inorganic building unit exhibiting strongly hydrophilic sorption behaviour. Chem. Commun. **48**, 9486–9488 (2012). https://doi.org/10.1039/c2cc34909d
55. Reinsch, H., van der Veen, M.A., Gil, B., Marszalek, B., Verbiest, T., de Vos, D., Stock, N.: Structures, sorption characteristics, and nonlinear optical properties of a new series of highly stable aluminum mOFs. Chem. Mater. **25**, 17–26 (2013). https://doi.org/10.1021/cm3025445
56. Akiyama, G., Matsuda, R., Kitagawa, S.: Highly porous and stable coordination polymers as water sorption materials. Chem. Lett. **39**, 360–361 (2010). https://doi.org/10.1246/cl.2010.360
57. Jeremias, F., Khutia, A., Henninger, S.K., Janiak, C.: MIL-100(Al, Fe) as water adsorbents for heat transformation purposes—a promising application. J. Mater. Chem. **22**, 10148–10151 (2012). https://doi.org/10.1039/c2jm15615f
58. Wickenheisser, M., Jeremias, F., Henninger, S.K., Janiak, C.: Grafting of hydrophilic ethylene glycols or ethylenediamine on coordinatively unsaturated metal sites in MIL-100(Cr) for improved water adsorption characteristics. Inorg. Chim. Acta. **407**, 145–152 (2013). https://doi.org/10.1016/j.ica.2013.07.024
59. Ehrenmann, J., Henninger, S.K., Janiak, C.: Water adsorption characteristics of MIL-101 for heat-transformation applications of MOFs. Eur. J. Inorg. Chem. **2011**, 471–474 (2011). https://doi.org/10.1002/ejic.201001156

60. Akiyama, G., Matsuda, R., Sato, H., Hori, A., Takata, M., Kitagawa, S.: Effect of functional groups in MIL-101 on water sorption behavior. Microporous Mesoporous Mater. **157**, 89–93 (2012). https://doi.org/10.1016/j.micromeso.2012.01.015
61. Khutia, A., Rammelberg, H.U., Schmidt, T., Henninger, S., Janiak, C.: Water sorption cycle measurements on functionalized MIL-101Cr for heat transformation application. Chem. Mater. **25**, 790–798 (2013). https://doi.org/10.1021/cm304055k
62. Jeremias, F., Lozan, V., Henninger, S.K., Janiak, C.: Programming MOFs for water sorption: amino-functionalized MIL-125 and UiO-66 for heat transformation and heat storage applications. Dalt. Trans. **42**, 15967–15973 (2013). https://doi.org/10.1039/c3dt51471d
63. Shigematsu, A., Yamada, T., Kitagawa, H.: Wide control of proton conductivity in porous coordination polymers. J. Am. Chem. Soc. **133**, 2034–2036 (2011). https://doi.org/10.1021/ja109810w
64. Wade, C.R., Corrales-Sanchez, T., Narayan, T.C., Dincă, M.: Postsynthetic tuning of hydrophilicity in pyrazolate MOFs to modulate water adsorption properties. Energy Environ. Sci. **6**, 2172–2177 (2013). https://doi.org/10.1039/c3ee40876k
65. Liu, J., Wang, Y., Benin, A.I., Jakubczak, P., Willis, R.R., LeVan, M.D.: CO2/H2O adsorption equilibrium and rates on metal-organic frameworks: HKUST-1 and Ni/DOBDC. Langmuir **26**, 14301–14307 (2010). https://doi.org/10.1021/la102359q
66. Schoenecker, P.M., Carson, C.G., Jasuja, H., Flemming, C.J.J., Walton, K.S.: Effect of water adsorption on retention of structure and surface area of metal-organic frameworks. Ind. Eng. Chem. Res. **51**, 6513–6519 (2012). https://doi.org/10.1021/ie202325p
67. Cmarik, G.E., Kim, M., Cohen, S.M., Walton, K.S.: Tuning the adsorption properties of uio-66 via ligand functionalization. Langmuir **28**, 15606–15613 (2012). https://doi.org/10.1021/la3035352
68. Elsayed, E., Al-Dadah, R., Mahmoud, S., Elsayed, A., Anderson, P.A.: Aluminium fumarate and CPO-27(Ni) MOFs: characterization and thermodynamic analysis for adsorption heat pump applications. Appl. Therm. Eng. **99**, 802–812 (2016). https://doi.org/10.1016/j.applthermaleng.2016.01.129
69. Al Dadah, R., Mahmoud, S., Elsayed, E., Youssef, P., Al-Mousawi, F.: Metal-organic framework materials for adsorption heat pumps. Energy **190**, 116356 (2020). https://doi.org/10.1016/j.energy.2019.116356
70. Mohammed, R.H., Rezk, A., Askalany, A., Ali, E.S., Zohir, A.E., Sultan, M., Ghazy, M., Abdelkareem, M.A., Olabi, A.G.: Metal-organic frameworks in cooling and water desalination: synthesis and application. Renew. Sustain. Energy Rev. **149**, 111362 (2021). https://doi.org/10.1016/j.rser.2021.111362
71. Elsayed, A., Elsayed, E., Al-Dadah, R., Mahmoud, S., Elshaer, A., Kaialy, W.: Thermal energy storage using metal–organic framework materials. Appl. Energy. **186**, 509–519 (2017). https://doi.org/10.1016/j.apenergy.2016.03.113
72. Shi, B.: Development of an Mof based adsorption air conditioning system for automotive. http://etheses.bham.ac.uk/id/eprint/6017 (2015)
73. Youssef, P.G., Dakkama, H., Mahmoud, S.M., Al-Dadah, R.K.: Experimental investigation of adsorption water desalination/cooling system using CPO-27Ni MOF. Desalination **404**, 192–199 (2017). https://doi.org/10.1016/j.desal.2016.11.008
74. Dakkama, H.J., Youssef, P.G., Al-Dadah, R.K., Mahmoud, S.: Adsorption ice making and water desalination system using metal organic frameworks/water pair. Energy Convers. Manag. **142**, 53–61 (2017). https://doi.org/10.1016/j.enconman.2017.03.036
75. Rezk, A., Al-Dadah, R., Mahmoud, S., Elsayed, A.: Experimental investigation of metal organic frameworks characteristics for water adsorption chillers. Proc. Inst. Mech. Eng. Part C J. Mech. Eng. Sci. **227**, 992–1005 (2013). https://doi.org/10.1177/0954406212456469
76. Kummer, H., Füldner, G., Henninger, S.K.: Versatile siloxane based adsorbent coatings for fast water adsorption processes in thermally driven chillers and heat pumps. Appl. Therm. Eng. **85**, 1–8 (2015). https://doi.org/10.1016/j.applthermaleng.2015.03.042
77. Cheung, O., Hedin, N.: Zeolites and related sorbents with narrow pores for CO_2 separation from flue gas. RSC Adv. **4**, 14480–14494 (2014). https://doi.org/10.1039/c3ra48052f
78. Elsayed, E., Wang, H., Anderson, P.A., Al-Dadah, R., Mahmoud, S., Navarro, H., Ding, Y., Bowen, J.: Development of MIL-101(Cr)/GrO composites for adsorption heat pump applications. Microporous Mesoporous Mater. **244**, 180–191 (2017). https://doi.org/10.1016/j.micromeso.2017.02.020
79. Jänchen, J., Ackermann, D., Stach, H., Brösicke, W.: Studies of the water adsorption on zeolites and modified mesoporous materials for seasonal storage of solar heat. Sol. Energy. **76**, 339–344 (2004). https://doi.org/10.1016/j.solener.2003.07.036
80. Casey, S.P., Elvins, J., Riffat, S., Robinson, A.: Salt impregnated desiccant matrices for "open" thermochemical energy storage-selection, synthesis and characterisation of candidate materials. Energy Build. **84**, 412–425 (2014). https://doi.org/10.1016/j.enbuild.2014.08.028
81. Mrowiec-Białoń, J., Jarzębski, A.B., Lachowski, A.I., Malinowski, J.J., Aristov, Y.I.: Effective inorganic hybrid adsorbents of water vapor by the sol-gel method. Chem. Mater. **9**, 2486–2490 (1997). https://doi.org/10.1021/cm9703280
82. Wu, H., Wang, S., Zhu, D.: Effects of impregnating variables on dynamic sorption characteristics and storage properties of composite sorbent for solar heat storage. Sol. Energy. **81**, 864–871 (2007). https://doi.org/10.1016/j.solener.2006.11.013
83. Mrowiec-Bialoń, J., Lachowski, A.I., Jarzębski, A.B., Gordeeva, L.G., Aristov, Y.I.: SiO2-LiBr nanocomposite sol-gel adsorbents of water vapor: preparation and properties. J. Colloid Interface Sci. **218**, 500–503 (1999). https://doi.org/10.1006/jcis.1999.6406
84. Gordeeva, L.G., Glaznev, I.S., Malakhov, V.V., Aristov, Y.I.: Influence of calcium chloride interaction with silica surface on phase composition and sorption properties of dispersed salt. Russ. J. Phys. Chem. **77**, 1843–1847 (2003)
85. Aristov, Y.I., Tokarev, M.M., Restuccia, G., Cacciola, G.: Selective water sorbents for multiple applications, 2 $CaCl_2$ confined in micropores of silica gel: sorption properties. React. Kinet. Catal. Lett. **59**, 335–342 (1996). https://doi.org/10.1007/BF02068131
86. Simonova, I.A., Freni, A., Restuccia, G., Aristov, Y.I.: Water sorption on composite "silica modified by calcium nitrate." Microporous Mesoporous Mater. **122**, 223–228 (2009). https://doi.org/10.1016/j.micromeso.2009.02.034
87. Aristov, Y.I., Sapienza, A., Ovoshchnikov, D.S., Freni, A., Restuccia, G.: Reallocation of adsorption and desorption times for optimisation of cooling cycles. Int. J. Refrig. **35**, 525–531 (2012). https://doi.org/10.1016/j.ijrefrig.2010.07.019
88. Tanashev, Y.Y., Krainov, A.V., Aristov, Y.I.: Thermal conductivity of composite sorbents "salt in porous matrix" for heat storage and transformation. Appl. Therm. Eng. **61**, 401–407 (2013). https://doi.org/10.1016/j.applthermaleng.2013.08.022
89. Tokarev, M.M., Aristov, Y.I.: Selective water sorbents for multiple applications, 4 $CaCl_2$ confined in silica gel pores: sorption/desorption kinetics. React. Kinet. Catal. Lett. **62**, 143–150 (1997). https://doi.org/10.1007/BF02475725
90. Gordeeva, L.G., Restuccia, G., Cacciola, G., Aristov, Y.I.: Selective water sorbents for multiple applications, 5 LiBr confined in mesopores of silica gel: sorption properties. React. Kinet. Catal. Lett. **63**, 81–88 (1998). https://doi.org/10.1007/BF02475434
91. Ristić, A., Logar, N.Z.: New composite water sorbents $CaCl_2$-PHTS for low-temperature sorption heat storage:

determination of structural properties. Nanomaterials **9**, 27 (2019). https://doi.org/10.3390/nano9010027
92. Ponomarenko, I.V., Glaznev, I.S., Gubar, A.V., Aristov, Y.I., Kirik, S.D.: Synthesis and water sorption properties of a new composite "$CaCl_2$ confined into SBA-15 pores." Microporous Mesoporous Mater. **129**, 243–250 (2010). https://doi.org/10.1016/j.micromeso.2009.09.023
93. Jabbari-Hichri, A., Bennici, S., Auroux, A.: Effect of aluminum sulfate addition on the thermal storage performance of mesoporous SBA-15 and MCM-41 materials. Sol. Energy Mater. Sol. Cells. **149**, 232–241 (2016). https://doi.org/10.1016/j.solmat.2016.01.033
94. Dong, H., Askalany, A.A., Olkis, C., Zhao, J., Santori, G.: Hydrothermal stability of water sorption ionogels. Energy **189**, 116186 (2019). https://doi.org/10.1016/j.energy.2019.116186
95. Askalany, A., Olkis, C., Bramanti, E., Lapshin, D., Calabrese, L., Proverbio, E., Freni, A., Santori, G.: Silica-supported ionic liquids for heat-powered sorption desalination. ACS Appl. Mater. Interfaces. **11**, 36497–36505 (2019). https://doi.org/10.1021/acsami.9b07602
96. Askalany, A.A., Freni, A., Santori, G.: Supported ionic liquid water sorbent for high throughput desalination and drying. Desalination **452**, 258–264 (2019). https://doi.org/10.1016/j.desal.2018.11.002
97. Gordeeva, L.G., Restuccia, G., Freni, A., Aristov, Y.I.: Water sorption on composites "LiBr in a porous carbon." Fuel Process. Technol. **79**(3), 225–231 (2002)
98. Yu, Q., Zhao, H., Sun, S., Zhao, H., Li, G., Li, M., Wang, Y.: Characterization of $MgCl_2$/AC composite adsorbent and its water vapor adsorption for solar drying system application. Renew. Energy. **138**, 1087–1095 (2019). https://doi.org/10.1016/j.renene.2019.02.024
99. Tso, C.Y., Chao, C.Y.H.: Activated carbon, silica-gel and calcium chloride composite adsorbents for energy efficient solar adsorption cooling and dehumidification systems. Int. J. Refrig. **35**, 1626–1638 (2012). https://doi.org/10.1016/j.ijrefrig.2012.05.007
100. Huang, H., Oike, T., Watanabe, F., Osaka, Y., Kobayashi, N., Hasatani, M.: Development research on composite adsorbents applied in adsorption heat pump. Appl. Therm. Eng. **30**, 1193–1198 (2010). https://doi.org/10.1016/j.applthermaleng.2010.01.036
101. Grekova, A., Gordeeva, L., Aristov, Y.: Composite sorbents "li/Ca halogenides inside multi-wall carbon nano-tubes" for thermal energy storage. Sol. Energy Mater. Sol. Cells. **155**, 176–183 (2016). https://doi.org/10.1016/j.solmat.2016.06.006
102. Grekova, A.D., Gordeeva, L.G., Lu, Z., Wang, R., Aristov, Y.I.: Composite "LiCl/MWCNT" as advanced water sorbent for thermal energy storage: sorption dynamics. Sol. Energy Mater. Sol. Cells. **176**, 273–279 (2018). https://doi.org/10.1016/j.solmat.2017.12.011
103. Brancato, V., Gordeeva, L.G., Grekova, A.D., Sapienza, A., Vasta, S., Frazzica, A., Aristov, Y.I.: Water adsorption equilibrium and dynamics of LICL/MWCNT/PVA composite for adsorptive heat storage. Sol. Energy Mater. Sol. Cells. **193**, 133–140 (2019). https://doi.org/10.1016/j.solmat.2019.01.001
104. Hongois, S., Kuznik, F., Stevens, P., Roux, J.J.: Development and characterisation of a new $MgSO_4$-zeolite composite for long-term thermal energy storage. Sol. Energy Mater. Sol. Cells. **95**, 1831–1837 (2011). https://doi.org/10.1016/j.solmat.2011.01.050
105. Chan, K.C., Chao, C.Y.H., Sze-To, G.N., Hui, K.S.: Performance predictions for a new zeolite 13X/$CaCl_2$ composite adsorbent for adsorption cooling systems. Int. J. Heat Mass Transf. **55**, 3214–3224 (2012). https://doi.org/10.1016/j.ijheatmasstransfer.2012.02.054
106. Oh, H.T., Lim, S.J., Kim, J.H., Lee, C.H.: Adsorption equilibria of water vapor on an alumina/zeolite 13X composite and silica gel. J. Chem. Eng. Data. **62**, 804–811 (2017). https://doi.org/10.1021/acs.jced.6b00850
107. Teo, H.W.B., Chakraborty, A.: Water adsorption on various metal organic framework. IOP Conf. Ser. Mater. Sci. Eng. **272**, 012019 (2017). https://doi.org/10.1088/1757-899X/272/1/012019
108. Yan, J., Yu, Y., Ma, C., Xiao, J., Xia, Q., Li, Y., Li, Z.: Adsorption isotherms and kinetics of water vapor on novel adsorbents MIL-101(Cr)@GO with super-high capacity. Appl. Therm. Eng. **84**, 118–125 (2015). https://doi.org/10.1016/j.applthermaleng.2015.03.040
109. Elsayed, E., Anderson, P., Al-Dadah, R., Mahmoud, S., Elsayed, A.: MIL-101(Cr)/calcium chloride composites for enhanced adsorption cooling and water desalination. J. Solid State Chem. **277**, 123–132 (2019). https://doi.org/10.1016/j.jssc.2019.05.026
110. Liu, Z., Gao, W., Qi, X., Lou, F., Lang, H.: Experimental study on salt–metal organic framework composites for water absorption. Inorg. Chim. Acta. **500**, 119214 (2020). https://doi.org/10.1016/j.ica.2019.119214
111. Sapienza, A., Glaznev, I.S., Santamaria, S., Freni, A., Aristov, Y.I.: Adsorption chilling driven by low temperature heat: new adsorbent and cycle optimization. Appl. Therm. Eng. **32**, 141–146 (2012). https://doi.org/10.1016/j.applthermaleng.2011.09.014
112. Aristov, Y.I., Restuccia, G., Tokarev, M.M., Buerger, H.D.D., Freni, A.: Selective water sorbents for multiple applications. 11 $CaCl_2$ confined to expanded vermiculite. React. Kinet. Catal. Lett. **71**, 377–384 (2000). https://doi.org/10.1023/A:1010351815698
113. Tokarev, M., Gordeeva, L., Romannikov, V., Glaznev, I., Aristov, Y.: New composite sorbent $CaCl_2$ in mesopores for sorption cooling/heating. Int. J. Therm. Sci. **41**, 470–474 (2002). https://doi.org/10.1016/S1290-0729(02)01339-X
114. Liu, H., Nagano, K., Togawa, J.: A composite material made of mesoporous siliceous shale impregnated with lithium chloride for an open sorption thermal energy storage system. Sol. Energy. **111**, 186–200 (2015). https://doi.org/10.1016/j.solener.2014.10.044
115. Liu, H., Nagano, K., Sugiyama, D., Togawa, J., Nakamura, M.: Honeycomb filters made from mesoporous composite material for an open sorption thermal energy storage system to store low-temperature industrial waste heat. Int. J. Heat Mass Transf. **65**, 471–480 (2013). https://doi.org/10.1016/j.ijheatmasstransfer.2013.06.021
116. Nakabayashi, S., Nagano, K., Nakamura, M., Togawa, J., Kurokawa, A.: Improvement of water vapor adsorption ability of natural mesoporous material by impregnating with chloride salts for development of a new desiccant filter. Adsorption **17**, 675–686 (2011). https://doi.org/10.1007/s10450-011-9363-1
117. Alsaman, A.S., Ibrahim, E.M.M., Salem Ahmed, M., Ali, E.S., Farid, A.M., Askalany, A.A.: Experimental investigation of sodium polyacrylate-based innovative adsorbent material for higher desalination and cooling effects. Energy Convers. Manag. **266**, 115818 (2022). https://doi.org/10.1016/j.enconman.2022.115818
118. Thu, K., Ng, K.C., Saha, B.B., Chakraborty, A., Koyama, S.: Operational strategy of adsorption desalination systems. Int. J. Heat Mass Transf. **52**, 1811–1816 (2009). https://doi.org/10.1016/j.ijheatmasstransfer.2008.10.012
119. Wu, J.W., Biggs, M.J., Pendleton, P., Badalyan, A., Hu, E.J.: Experimental implementation and validation of thermodynamic cycles of adsorption-based desalination. Appl. Energy. **98**, 190–197 (2012). https://doi.org/10.1016/j.apenergy.2012.03.022
120. Ng, K.C., Thu, K., Saha, B.B., Chakraborty, A.: Study on a waste heat-driven adsorption cooling cum desalination cycle. Int. J. Refrig. **35**, 685–693 (2012). https://doi.org/10.1016/j.ijrefrig.2011.01.008

121. Mitra, S., Kumar, P., Srinivasan, K., Dutta, P.: Performance evaluation of a two-stage silica gel + water adsorption based cooling-cum-desalination system. Int. J. Refrig. **58**, 186–198 (2015). https://doi.org/10.1016/j.ijrefrig.2015.06.018
122. Gao, W., Li, C., Xu, C., Wang, D., Wu, D.: An experimental investigation of salt-water separation in the vacuum flashing assisted with heat pipes and solid adsorption. Desalination **399**, 116–123 (2016). https://doi.org/10.1016/j.desal.2016.08.016
123. Olkis, C., Brandani, S., Santori, G.: Cycle and performance analysis of a small-scale adsorption heat transformer for desalination and cooling applications. Chem. Eng. J. **378**, 122104 (2019). https://doi.org/10.1016/j.cej.2019.122104
124. Olkis, C., Brandani, S., Santori, G.: Design and experimental study of a small scale adsorption desalinator. Appl. Energy. **253**, 113584 (2019). https://doi.org/10.1016/j.apenergy.2019.113584
125. Olkis, C., Brandani, S., Santori, G.: A small-scale adsorption desalinator. Energy Procedia **158**, 1425–1430 (2019). https://doi.org/10.1016/j.egypro.2019.01.345
126. Olkis, C., Al-Hasni, S., Brandani, S., Vasta, S., Santori, G.: Solar powered adsorption desalination for Northern and Southern Europe. Energy **232**, 120942 (2021). https://doi.org/10.1016/j.energy.2021.120942
127. Elsayed, E., Al-Dadah, R., Mahmoud, S., Anderson, P., Elsayed, A.: Experimental testing of aluminium fumarate MOF for adsorption desalination. Desalination **475**, 114170 (2020). https://doi.org/10.1016/j.desal.2019.114170
128. Zhang, H., Ma, H., Liu, S., Wang, H., Sun, Y., Qi, D.: Investigation on the operating characteristics of a pilot-scale adsorption desalination system. Desalination **473**, 114196 (2020). https://doi.org/10.1016/j.desal.2019.114196
129. Kim, Y.D., Thu, K., Masry, M.E., Ng, K.C.: Water quality assessment of solar-assisted adsorption desalination cycle. Desalination **344**, 144–151 (2014). https://doi.org/10.1016/j.desal.2014.03.021
130. Shahzad, M.W., Thu, K., Kim, Y.D., Ng, K.C.: An experimental investigation on MEDAD hybrid desalination cycle. Appl. Energy. **148**, 273–281 (2015). https://doi.org/10.1016/j.apenergy.2015.03.062
131. Son, H.S., Shahzad, M.W., Ghaffour, N., Ng, K.C.: Pilot studies on synergetic impacts of energy utilization in hybrid desalination system: multi-effect distillation and adsorption cycle (MED-AD). Desalination **477**, 114266 (2020). https://doi.org/10.1016/j.desal.2019.114266
132. Askalany, A., Alsaman, A.S., Ghazy, M., Mohammed, R.H., Al-Dadah, R., Mahmoud, S.: Experimental optimization of the cycle time and switching time of a metal organic framework adsorption desalination cycle. Energy Convers. Manag. **245**, 114558 (2021). https://doi.org/10.1016/j.enconman.2021.114558
133. Ghazy, M., Ibrahim, E.M.M., Mohamed, A.S.A., Askalany, A.A.: Experimental investigation of hybrid photovoltaic solar thermal collector (PV/T)-adsorption desalination system in hot weather conditions. Energy **254**, 124370 (2022). https://doi.org/10.1016/j.energy.2022.124370
134. Albaik, I., Badawy Elsheniti, M., Al-Dadah, R., Mahmoud, S., Solmaz, İ: Numerical and experimental investigation of multiple heat exchanger modules in cooling and desalination adsorption system using metal organic framework. Energy Convers. Manag. **251**, 114934 (2022). https://doi.org/10.1016/j.enconman.2021.114934
135. Saleh, M.M., Elsayed, E., Al-Dadah, R., Mahmoud, S.: Experimental testing of wire finned heat exchanger coated with aluminium fumarate MOF material for adsorption desalination application. Therm. Sci. Eng. Prog. **28**, 101050 (2022). https://doi.org/10.1016/j.tsep.2021.101050

International Journal of Energy and Environmental Engineering (2023) 14:643–660
https://doi.org/10.1007/s40095-022-00540-2

ORIGINAL RESEARCH

Solar photovoltaic array fed single-stage sensorless vector control of induction motor drive for water pumping applications

Bhanu Prakash Rachaputi[1] · **Josephine Rathinadurai Louis**[1] · **Moorthi Sridharan**[1]

Received: 16 April 2022 / Accepted: 18 September 2022 / Published online: 15 November 2022

Abstract

This paper proposes a novel photovoltaic (PV) array-fed induction motor (IM) drive in irrigation applications. The energy conversion includes a single-stage conversion procedure. The output voltage obtained from the PV array is given to the conventional voltage source inverter (VSI), which uses a sensorless vector control approach to drive the IM. A novel approach in vector control with the reduced number of sensors is attempted to improve the performance and handle proper energy conversion. The novel vector control approach incorporates modified maximum power extraction (MPE) algorithms. The system assimilates the single-stage VSI to operate effectively, making the IM-pump drive work superior to other methods. The paper compares the proposed single-stage conversion process exposed to different MPE algorithms, such as P&O and PSO, with the proposed MPSO algorithm. The validation of the proposed system is accomplished through both simulations in MATLAB/SIMULINK and experimental results. The simulation results compare all three MPE algorithms and conclude that MPSO employed for novel vector control extracts maximum power with an accuracy not less than 99.5% subjected to different partial shading conditions. The experimental results validate the proposed MPE algorithm for the induction motor pump drive and obtain maximum power attainment with an accuracy of 98.2% without partial shading effect and 90.84% and 88.89% for partial shading conditions. The overall efficiency of the proposed system varies from 81.2 to 73.4% for different insolation conditions.

Keywords Motor control · Stator control · Peak power extraction · Solar photovoltaic array · Water pumping applications · Sensorless control · Induction motor

Abbreviations

IM	Induction motor
DC	Direct current
VSI	Voltage source inverter
IMPD	Induction motor-pump drive
IMDC	Induction motor drive control
SPV	Solar photovoltaic
SPVA	Solar photovoltaic array
VSI	Voltage source inverter
MPE	Maximum power extraction
OT	Optimization technique
MPPT	Maximum power point tracking
MPT	Maximum power tracking
PPT	Peak power tracking
SFOC	Stator field-oriented control
MPD	Motor pump drive
PSO	Particle swarm optimization
MPSO	Modified particle swarm optimization
P&O	Perturb and observe
MPA	Maximum power attainment
DSP	Digital signal processor
RMS	Root-mean-square

Introduction

Water supply to the farming lands is a primary requirement and is generally fed from a motor-pump setup. Farming lands in rural areas at remote locations lack the utility power supply to drive these motor-pump drives (MPD). Bringing the utility grid to such remote locations may not be viable or may not be economical. The solution to resolve this power deficit shall be to eliminate using renewable systems as sources of electricity. The countries such as India are rich sources of solar energy, and about 5 billion GWh per year

✉ Josephine Rathinadurai Louis
josephinerl@nitt.edu

[1] Electrical and Electronics Engineering Department, National Institute of Technology, Tiruchirappalli, India

is falling over India's surface [1]. Employing photovoltaic systems to harness solar energy imitates an autonomous power source of electricity [2]. Solar PV systems are evolving with several applications from small scale to large scale and have a huge inflow of investments [3]. The adoption of solar photovoltaic (SPV) generation globally is shown in Fig. 1 [4]. The solar PV systems are meant to increase their demand to 370 GW by 2030 and 1050 GW by 2050 [5]. Utility, commercial, residential and off-grid are the major areas of PV applications as they employ PV systems in large scale as shown in Fig. 2 [6]. Off-grid systems are not explored much so far and still has far potential because nearly 33% of the rural areas do not have access to electricity [7]. Therefore, SPV systems can evolve as an autonomous source of electricity to electrify the remote villages. Off-grid and grid-connected solar photovoltaic array (SPVA) systems on a nanoscale are evolving [8] to meet domestic appliance requirements. The Indian government initiates new policies and programs for off-grid SPVA systems [9]. An important application of off-grid solar photovoltaic (PV) systems concerning the policies and programs of the Indian government is solar water pumps [10]. The advancements in the power semiconductor devices allow solar PV systems to extend their applications to water pumping applications [11].

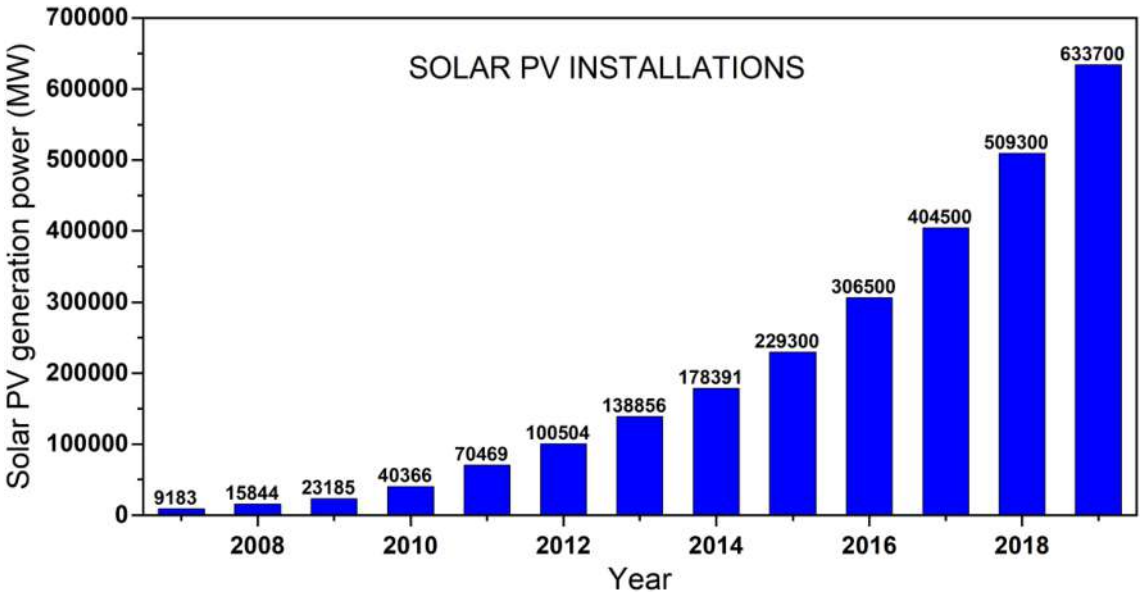

Fig. 1 Installation of solar photovoltaic systems globally from 2007 to 2019 [4]

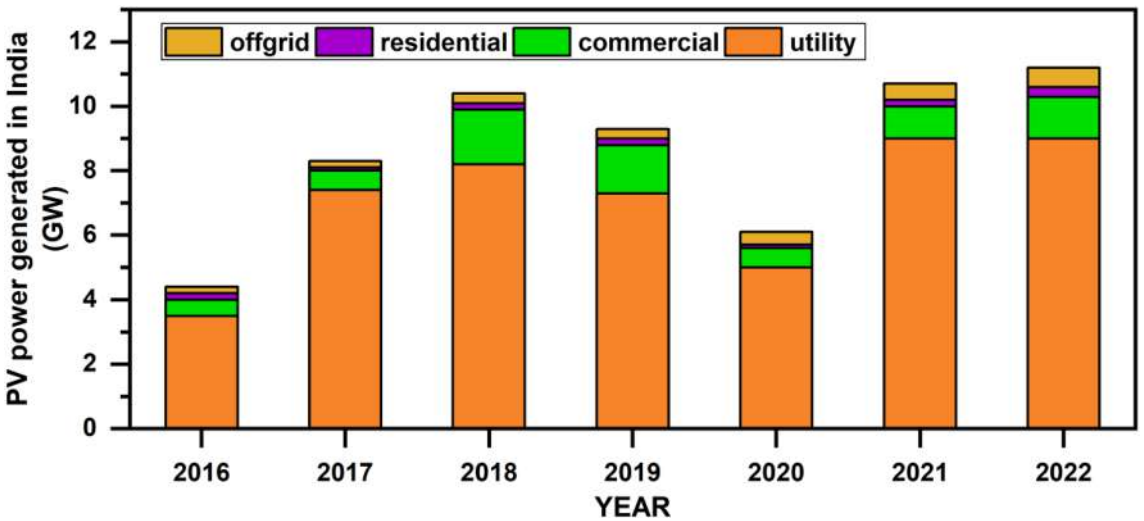

Fig. 2 Generation of solar photovoltaic power generation in India for various segments [6]

Motor pump drives for SPVA system applications through the power electronic converters have complexities such as the significant drop in the SPVA voltage [12] due to variable insolation and the high incurred cost of SPVA systems at the time of installation [13] due to multiple DC-DC and DC-AC conversion stages.

The MPD in the farming lands will be fed through a solar PV array (SPVA) through the different converter stages [13]. These photovoltaic arrays will act as a primary power source to MPD in remote locations or as an auxiliary power source with the utility grid [14]. The SPVA systems initially employ two-stage power conversion, such as a DC-DC converter followed by a DC-AC converter [15]. DC-DC converter employs an MPE algorithm, and the DC-AC inverter adopts motor control algorithms to deploy in the circuit. The cost is increased with a multi-stage converter and requires two different controller mechanisms to drive the motor pump setup. Other forms of motor-pump drives adopt battery systems to increase the utilization further [15]. Due to their remote locations and battery-driven control requiring additional converter circuits [16][17] with extra control algorithms, the cost of the circuit increases and safety for batteries became the primary concern. Hence, single-stage converters are becoming conformed for MPD applications. Single-stage converters reduce the cost of the system by eliminating multiple converters employment and further increases the efficiency of the system. The primary concern of the SPVA water pumping systems is the selection of the motor and it plays a vital role in the effective operation of MPD. An induction motor is chosen for water pumping applications because of its rugged performance with long life [18, 19]. A conventional three-phase VSI is employed in the power conversion process of MPD, and a novel extended vector control is deployed to control the three-phase VSI.

As the vector control is superior in controlling the induction motor, it is employed to control the voltage source inverter (VSI) [20–22]. But the same vector control algorithm fails to maintain the induction motor when driven from SPVA. The starting current demanded by the induction motor makes the PV array operate in a short circuit mode of operation and thus fails to develop a voltage across the PV array. As a result of low voltage across the induction motor, it fails to rotate [23–28]. Hence, the vector control requires modification that makes DC voltage regulation also. DC voltage regulation is used as speed reference generation for vector control to govern the input side of the three-phase VSI [13–31]. The service of DC bus voltage regulation itself is not sufficient for the maximum utilization of SPVA. The voltage reference to the DC bus voltage regulation is obtained from the maximum power extraction (MPE) algorithm to extract maximum power. This voltage reference is converted to the speed reference required for the vector control of induction motor pump drive (IMPD). The actual speed is necessary for the vector control and can be determined using an encoderless mechanism such as model reference adaptive control [32, 33].

The selection and the development of MPE algorithms are significant in speed reference generation. To extract maximum power from SPVA, algorithms such as hill-climbing [34, 35], incremental conductance [36], and optimization methods [37] are used. Optimization techniques, such as particle swarm optimization [38], cuckoo search [39], and grey-wolf algorithms [40] are popular methods to extract the peak power from SPVA irrespective of partial shading conditions. These MPE algorithms are popular based on PPT speed, complexity, and robustness subjected to different environmental conditions. Particle swarm optimization effectively extracts the peak power under partial shading conditions and has reduced complexity in its deployment to hardware compared to Cuckoo search and grey wolf algorithms. The PPT speed of the particle swarm optimization can be improved by modifying its local tracking segment of the particle equation and is explained in detail in MPE algorithm selection and design section.

The motive is to propose a low-cost PV array fed MPD through an energy-efficient single-stage power electronic converter network pertaining to sophisticated control by validating it with the hardware setup. The main objectives of the proposed system are as follows.

1. To eliminate the speed sensor by estimating it with the voltage and current values at the motor terminals.
2. To develop the speed reference required for the SFOC of IMPD, which is equivalent to the peak power point of SPVA. This peak power point is extracted from MPE algorithms and should work for partial shading conditions also without fail.
3. To attain better accuracy of PPT of the MPE algorithm by modifying the existing PSO algorithm and should be superior to the existing methods.
4. To validate the proposed system with the experimental hardware setup.

The novelty of the proposed system is described as follows.

1. Single-stage VSI feeding an IMPD employing MPE-based modified vector control that effectively works for partial shading conditions also.
2. A modified particle swarm optimization algorithm was adopted for MPE to increase the accuracy of PPT.
3. A comparison of existing MPE algorithms with the proposed MPSO algorithm for PPT was presented meticulously.

Methodology

The block diagram representation of the proposed system is shown in Fig. 3. The main circuitry consists of a SPVA driving an induction motor pump setup through a conventional voltage source inverter. The control section starts with an optimization technique (OT MPPT)-based maximum power extraction algorithm for the SPVA. The optimization methods give the dc link voltage reference as maximum power equivalent value. This dc-link voltage reference is compared with the actual dc-link voltage value to attain proper dc voltage regulation. This voltage regulation is generated as speed reference for the vector control of induction motor drive. The system eliminates the voltage sensors at the motor terminals by estimating them with the dc-link voltage measurement.

The second section consists of the design and methodology of the proposed approach. The design of the proposed systems includes the design of SPVA, MPE algorithm selection and its design, input capacitor, and pump design. The methodology describes the determination of motor terminal voltages from the photovoltaic DC-link voltage, modified encoderless vector control of IMD and estimation of speed reference. The third section depicts results and discussion. The results of the proposed system are realized using simulations and are validating the same with the help of an experimental setup. The fourth section conveys the conclusions realized from the practical and simulated results. The design of the single-stage SPVA-fed IMPD comprises SPVA design, MPE algorithm selection with its design, DC-link capacitor design, and design of the pump.

Design of SPVA

It is necessary to choose the rating of SPVA to drive the induction motor pump setup. The power rating of the SPVA is determined to control the induction motor as an alternative to the utility grid. The motor selected for the irrigation applications is a 2.2 kW (3 hp), 440 V, 1440 rpm induction motor. The PV array should be able to develop 3KW of power to drive the induction motor. Table 1 shows the values of SPVA to feed the motor-pump setup. The solar photovoltaic array at maximum power attainment is selected to meet the motor-rated power of 2.2 kW (P_{ppa}). The SPVA voltage is considered as the peak value of the line voltage of motor terminals. For a line voltage of 440 V at the motor terminals, the peak value of the line voltage is $440 * \sqrt{2} = 622V$. This SPVA voltage at MPA is considered with a safety margin of 1.045 (a^*) and leads to 650 V (V_{ppa}) of SPVA voltage to be attained at maximum power value. The rated SPVA current for a 2.2 kW load is the ratio of SPVA-rated power (P_{ppa}) to SPVA-rated voltage. The rated value of SPVA current is 2200/650 = 3.38 A (I_{ppa}). The electrical specifications of each PV module of a Coleman manufacturer are mentioned in Table 1. With the help of formulas mentioned in Table 1, its relevant specifications of SPVA are determined and are updated in the same Table 1.

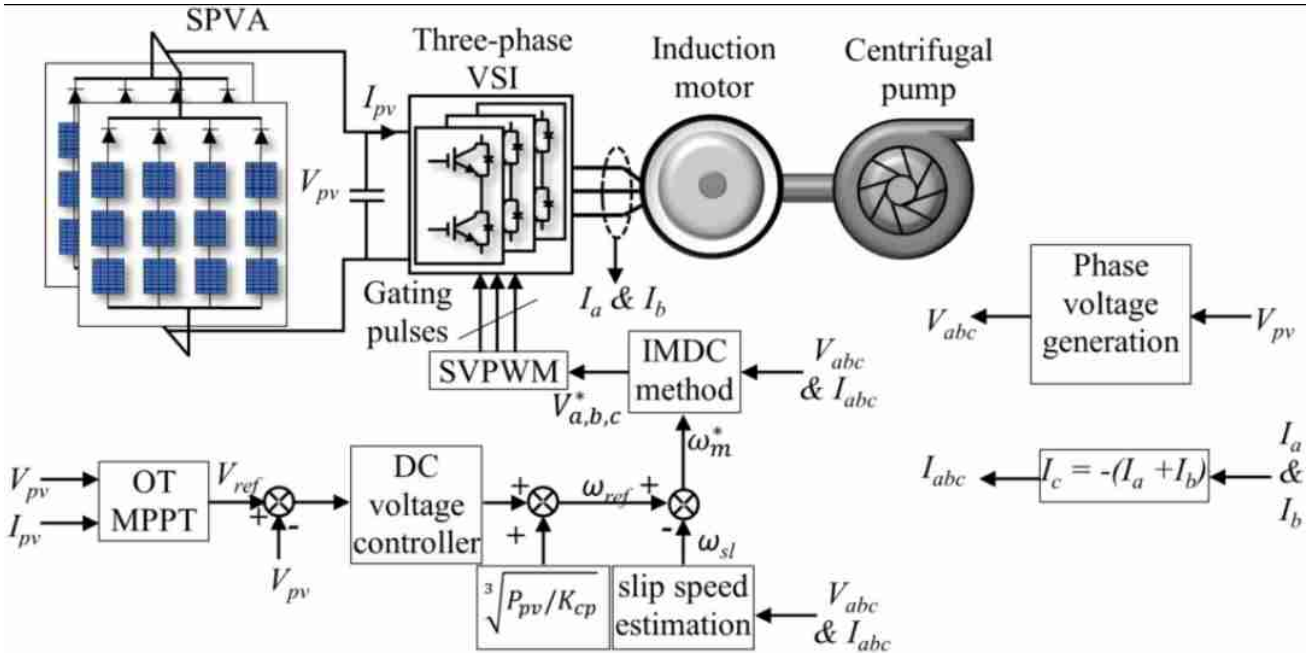

Fig. 3 A single-stage converter for PV array fed IMPD

Table 1 Specifications of SPVA for simulations

S.No	Specifications	Value
1	Array power capacity at peak power attainment (P_{ppa})	**2200 W**
2	Initial array voltage at maximum power (V_{ppa})=$V_{L(motor)} * \sqrt{2} * a^*$	650 V
3	Array current at peak power attainment (I_{ppa}=P_{ppa} / V_{ppa})	3.38 A
4	Open circuit voltage of each PV module (V_{ocm})	32 V
5	PPA voltage of each module (V_{ppam})	28 V
6	Short circuit current of each PV module (I_{scm})	1.38 A
7	PPA current of each module (I_{ppam})	1.21 A
8	Number of SPVA modules in series connection, N_{se}=(V_{ppa})/ (V_{ppam})	24
9	Number of SPVA modules in parallel connection, N_{pa}=(I_{ppa})/ (I_{ppam})	3
10	Open circuit voltage of SPVA (V_{oc})=V_{ocm}*N_{se}	**768 V**
11	Short circuit current of SPVA (I_{sc})=I_{scm}*N_{pa}	**A**
12	SPVA voltage at peak power attainment (V_{SPVA})$_{PPA}$=V_{ppam}*N_{se}	**672 V**
13	SPVA current at peak power attainment (I_{SPVA})$_{PPA}$=I_{ppam}*N_{pa}	**3.63 A**

The values in the bold are the final values used for the solar photovoltaicarray design

MPE algorithm selection and design

The choice of the algorithm plays a vital role in attaining peak power values from SPVA. One algorithm that ensures peak power attainment irrespective of partial shading conditions is particle swarm optimization (PSO). The PSO algorithm was derived from the movement and direction of flock birds searching for their food. Mathematically, it employs two equations to calculate the velocity and position of each bird/particle. The birds/particles will choose local and global best locations for food. After a continuous search, the best global location of the particle among all the particles will be obtained from this PSO algorithm. This best position of the particle/bird is the best peak power attainment position, referred to as the best DC link voltage reference. The equations of velocity and position of the DC link voltage reference are given in Eqs. (1) and (2).

$$v_{dc}^{j}(i+1) = k * v_{dc}^{j}(i) + k_1 \text{rand}\left(\left(V_{dcl}^{j}\right)^2 - \left(V_{dc}^{j}(i)\right)^2\right) + k_2 \text{rand}\left(V_{dcg} - V_{dc}^{j}(i)\right) \quad (1)$$

$$V_{dc}^{j}(i+1) = V_{dc}^{j}(i) + \min\{\max\left\{v_{dc(min)}^{j}, v_{dc}^{j}(i+1)\right\}, v_{dc(max)}^{j}\} \quad (2)$$

V_{dc}^{j} and v_{dc}^{j} are the position and velocity of the particle 'j'. The best dc-link voltage reference of particle 'j' is given by V_{dcl}^{j} and best dc-link voltage reference so far is given by V_{dcg}. The constants k, k_1, and k_2 are the weights to make the convergence quickly and are determined with PSO equations [41, 42]. The second term in the velocity equation identifies the best local dc-link voltage reference and is modified to achieve fast local convergence. The power values are determined for each dc-link voltage reference value ($V_{dc}^{j}(i)$) and are updated in the local dc-link voltage reference (V_{dc}^{j}) of which the highest power is developed. This process continues to update the global dc-link voltage reference. As the counter value 'i' is completed, the best global dc-link voltage reference will be achieved. This PSO is best suitable for peak power extraction from SPVA irrespective of partial shading conditions.

Selection of DC link capacitor and design of the pump

As the circuit employs single-stage VSI, the change in SPVA voltage will hugely impact the three-phase voltage generated by the VSI. This imbalanced voltage increases the harmonic content on the motor side. Voltage regulation on the DC side is required to reduce the ripple on the DC side. A capacitor is placed at the terminals of the SPVA to mitigate the voltage ripple content on the DC side of the inverter. The value of the capacitor is chosen for a permissible ripple in the voltage. The DC-link capacitor [43] is given by $C_{pv} = \{6sV_{ph}I_p t\} / \left\{V_{dc}^2 - V_{dc(min)}^2\right\}$

$$C_{pv} = \frac{6sV_{ph}I_p t}{V_{dc}^2 - V_{dc(min)}^2} \quad (3)$$

The centrifugal pump will be employed, and its mathematical equation is derived as follows. The relation between torque and speed of the centrifugal pump [44] is given by Eq. (4).

$$\tau_l = p_k \omega_p^2 \tag{4}$$

The constant P_k is the proportionality constant and is given by $P_{\text{motor}}/\omega_{\text{motor}}^3$.

Once the system is designed, the deployment of the modified SFOC of IMPD should be done and the modeling of the same is explained as follows.

Modified sensorless vector control of Induction motor drive

The voltage at the motor terminals can be estimated from the dc-link voltage. $v_{\text{ad}}(t)$, $v_{\text{bd}}(t)$, and $v_{\text{cd}}(t)$ are the derived three-phase terminal voltages from the SPVA voltage as shown in Eq. (5). S_a, S_b, and S_c are either zero or one and are called switching functions of the voltage source inverter. These derived three-phase terminal voltages are in the form of pulses and are not useful to determine the other parameters such as flux and speed. Hence it is necessary to use a filter for smoothing the waveform.

$$\begin{bmatrix} v_{ad}(t) \\ v_{bd}(t) \\ v_{cd}(t) \end{bmatrix} = \begin{bmatrix} 2S_a & -S_b & -S_c \\ -S_a & 2S_b & -S_c \\ -S_a & -S_b & 2S_c \end{bmatrix} \frac{V_{pv}}{3} \tag{5}$$

The derived voltages are then passed through a low-pass filter of 100 Hz cut-off frequency to generate the actual three-phase voltage measurements V_{abc} for the vector control mechanism. As the motor stator currents are balanced, only two of the three phases are sensed using current sensors, as shown in Fig. 3. The measurement of speed is quite important for the execution of SFOC of IMPD and is predicted as follows.

Estimation of speed in induction motor drive

Speed estimation of induction motor can be done without the help of a speed sensor or encoder but by measuring the instantaneous voltage and currents drawn by the induction motor.

Transformation of three-phase voltage generation from PV terminal voltage and measured three-phase currents are transformed to the α-β frame of reference to determine the flux quantities from which the motor speed can be estimated (Figs. 4 and 5).

$$\begin{bmatrix} v_\alpha(t) \\ v_\beta(t) \end{bmatrix} = \begin{bmatrix} \frac{2}{3} & -\frac{1}{3} & -\frac{1}{3} \\ 0 & \sqrt{3} & -\sqrt{3} \end{bmatrix} \begin{bmatrix} v_a(t) \\ v_b(t) \\ v_c(t) \end{bmatrix} \tag{6}$$

$$\begin{bmatrix} i_\alpha(t) \\ i_\beta(t) \end{bmatrix} = \begin{bmatrix} \frac{2}{3} & -\frac{1}{3} & -\frac{1}{3} \\ 0 & \sqrt{3} & -\sqrt{3} \end{bmatrix} \begin{bmatrix} i_a(t) \\ i_b(t) \\ i_c(t) \end{bmatrix} \tag{7}$$

The stator reference value of the flux component is derived [45] as follows.

$$p(\Psi_\beta) = \left(v_\beta - R_s i_\beta\right), p(\Psi_\alpha) = \left(v_\alpha - R_s i_\alpha\right) \quad \text{(Where p is the derivative representation)} \tag{8}$$

$$\Psi_s = \sqrt{\Psi_\alpha^2 + \Psi_\beta^2} \tag{9}$$

$$i_{\text{qs}} = i_\beta\left(\Psi_\alpha/\Psi_s\right) - i_\alpha\left(\Psi_\beta/\Psi_s\right) \tag{10}$$

$$i_{ds} = i_\beta\left(\Psi_\beta/\Psi_s\right) + i_\alpha\left(\Psi_\alpha/\Psi_s\right) \tag{11}$$

$$\omega_e = \left[\left(v_\beta - R_s i_\beta\right)\Psi_\alpha - \left(v_\alpha - R_s i_\alpha\right)\Psi_\beta\right]/\Psi_s^2 \tag{12}$$

$$\psi_{ds} = \psi_\beta\left(\frac{\psi_\beta}{\psi_s}\right) + \psi_\alpha\left(\frac{\psi_\alpha}{\psi_s}\right) \tag{13}$$

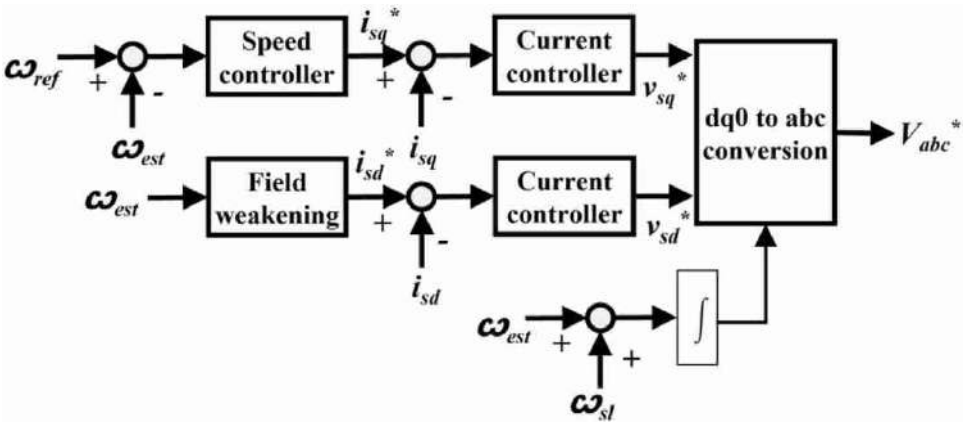

Fig. 4 SFOC mechanism for PV array fed IMPD

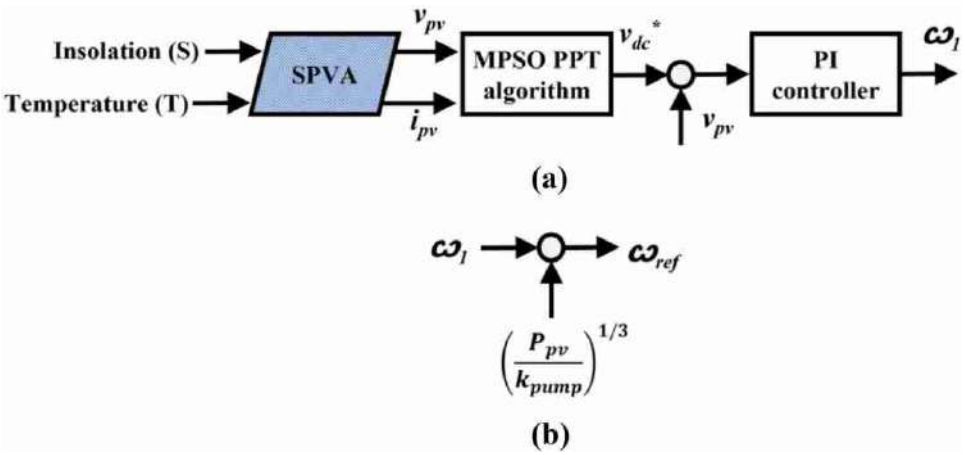

Fig. 5 Generation of speed reference. **a** Estimation of ω_1. **b** Feedforward component of speed

where i_{qs} and i_{ds} are the components of stator currents in the synchronized dq0 reference frame with $\sigma = 1 - L_m^2/(L_s L_r)$, $\tau_r = L_r/R_r$. L_r, L_m, and L_{lr} are the rotor inductance, magnetizing inductance, and rotor leakage inductance. The parasitic resistances R_r and R_s are referred to as stator and rotor, respectively. ω_e is the synchronous speed, and ω_{sl} is the slip speed. The mechanical speed of the induction motor is estimated from Eq. (15).

$$\omega_{sl} = \frac{\left(1 + \sigma S \tau_r\right) L_s i_{qs}}{\tau_r \left(\psi_{ds} - \sigma L_s i_{ds}\right)} \tag{14}$$

$$\omega_m = \omega_e - \omega_{sl} \tag{15}$$

ω_m is the estimated speed used for the SFOC of the IMPD and is represented as ω_{est} in Fig. 6.

Stator field-oriented control (SFOC) of IMPD

Figure 4 depicts the control scheme of the vector control method used for controlling the flux and stator currents. The speed and current controllers are the basic proportional-integral controllers that minimize their respected errors. The field weakening block consists of two main segments. The

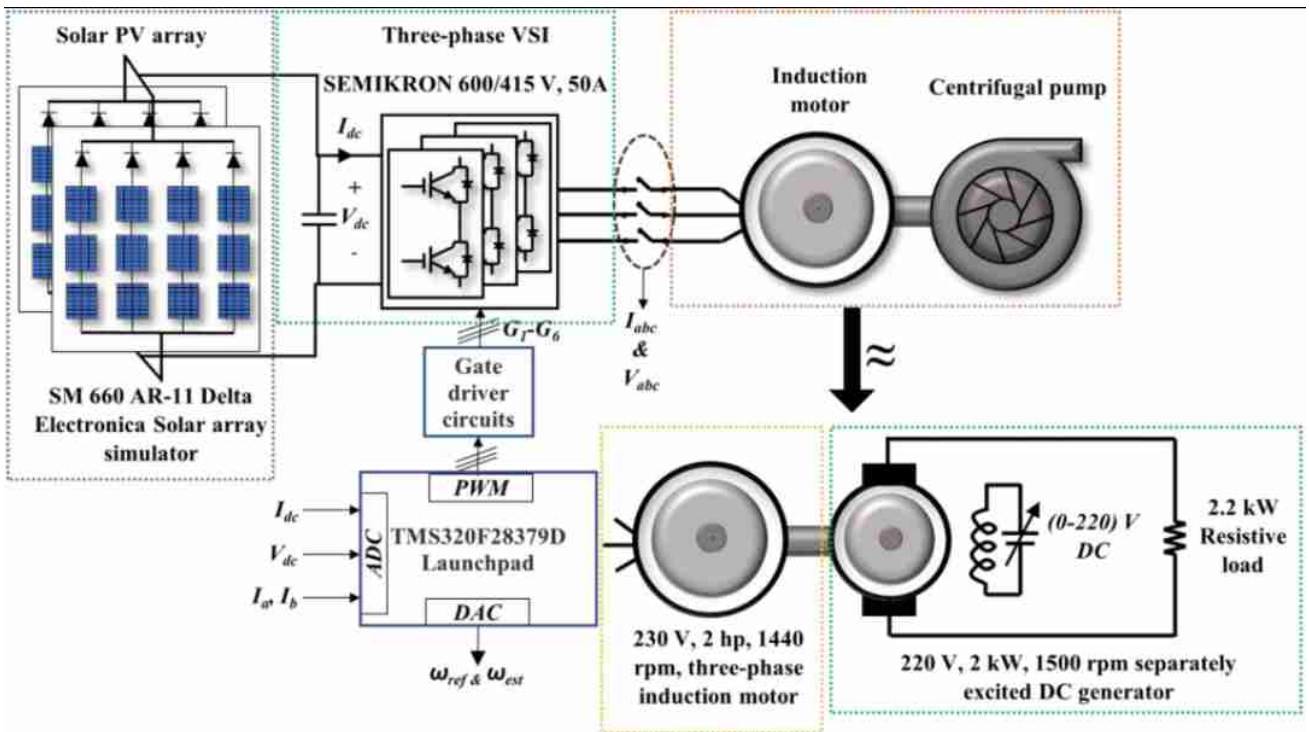

Fig. 6 Block diagram representation of the proposed experimental set-up

first segment is the d-component of current from magnetizing current (I_{mg}), and the second segment is the reference of the d-component of current.

$$I_{dx}^{*} = I_{mg} \text{ for } \omega_m\left(or\omega_{est}\right) \le \omega_{rated} \tag{16}$$

$$I_{dx}^{*} = \frac{\omega_{rated}}{\omega_{est}} I_{mg} \text{ for } \omega_m\left(or\omega_{est}\right) > \omega_{rated} \tag{17}$$

$$I_{dx}^{*} = I_{dx}^{e*} + \tau_r p I_{dx}^{e*} \tag{18}$$

$pI_{dx}^{e*} \to 0$ in the normal operation. The reference flux (Ψ_{ds}^{*}) is determined as $\Psi_{ds}^{*} = L_m I_{dm}^{e*}$

An exciting current I_{ds}^{*} is considered as the output of the flux generated error is directed to the input of the PI controller.

$$I_{ds(j)}^{e*} = I_{ds(j-1)}^{e*} + K_{p\Psi}\left\{\Psi_{e(j)} - \Psi_{e(j-1)}\right\} + K_{i\Psi}\Psi_{e(j)} \tag{19}$$

$$\text{where } \Psi_e = \Psi_{sd}^{*} - \Psi_{sd} \tag{20}$$

The decoupling component is introduced in the FOC to control the flux and torque individually by introducing a feedforwarded path. The decoupling part *(I_{dcp})* of the current [43] is mentioned as follows:

$$I_{dec} = \frac{\tau_r \sigma \omega_{sl}}{1 + \sigma \tau_r S} i_{qs} \tag{21}$$

$$i_{sd}^{*} = i_{sd}^{e*} + I_{dec} \tag{22}$$

Reference speed generation

The PSO algorithm generates an output of V_{dc}^{*} to generate an error signal. This error signal is given to the input of a PI controller to generate a speed estimation ω_1, as shown in Fig. 5a. To meet the power requirement of the pump, this estimated speed ω_1 is added to the pump speed, which results in ω_{ref}. The reference generation is developed using a feedforward speed component to meet the maximum power requirement, as shown in Fig. 5b.

The solar PV specifications and motor parameters for the hardware are mentioned in "A: Solar PV array hardware" and "B: Induction motor parameters" Appendix section, respectively. As mentioned in the block diagram shown in Fig. 6, a solar array simulator SM-660 V AR-11 is used as an alternative to a solar PV array that drives an induction motor coupled with a DC generator through SEMIKRON three-phase VSI rated for 600 V (DC) and 415 V (AC) at 50 A V (DC) capability. Due to laboratory constraints, the induction motor coupled with the DC generator is considered identical to the induction motor with a centrifugal pump, approximating the torque-speed relation from quadratic to linear conversion. Voltage sensors and current sensors on either side of the VSI are used in the hardware circuit to debug the system. The DSP controller TMS320F28379D launchpad was fed by the DC voltage (LV-25P) and DC current (LA-55P) sensors along with motor current (LA-55P) measurement sensors and is shown in Fig. 6. The speed encoder is eliminated, and the motor speed is estimated in the real-time controller TMS320F28379D. This estimated speed is generated through the DAC terminals of the controller to understand the response of the proposed system. The reference speed generation from the MPE algorithm also generated from the DAC terminals of the same DSP controller board. The program is deployed in the DSP-based controller to generate the required PWM pulses to control three-phase VSI. The rated voltage and current limitations in the solar array simulator restricted the operating of the induction motor drive below the rated value. The primary consideration is that the output power transfer to the load should be operated at the peak power point. The modified PSO method is implemented to transfer the peak power. The simulations are performed for the proposed PV array configuration under the change in insolation. The insolation changes apply to the 24 series-connected modules with three such parallel-connected arrays. The proposed system is exposed to different PV graphs of SPVA, as shown in Fig. 7, considering the effect of partial shading conditions to validate the maximum power extraction (MPE) algorithms. Figure 7 offers the series-connected and parallel-connected modules exposed to different insulations. These three different insolation P–V graphs are considered three different operation modes.

Among them, mode-I is an entirely normal mode without the effect of partial shading conditions. Mode-II and mode-III are exposed to different insolation among the SPVA and replicate other characteristics, as shown in Fig. 7. Three different modes of operation, as in Fig. 7, are implemented such that the first 0.5 s is operated in mode-I, and mode-II is operated for 0.2 s and is between 0.5 and 0.7 s. In contrast, mode-III is performed for 0.3 s and is from 0.7 to 1 s.

Results and discussion

Figure 8 shows the comparative representation of MPE algorithms implemented in the deployment of induction motor drive vector control. The overall comparison of all the MPE algorithms adopted to vector control of induction motor drive gives the variation of currents, reference speed, and electromagnetic torque variations. As shown in Fig. 7, the modes of operation I, II and III are implemented in the MATLAB simulation and the results are explained as follows. The proportional-integral controller parameters are estimated using the symmetrical optimum method [46].

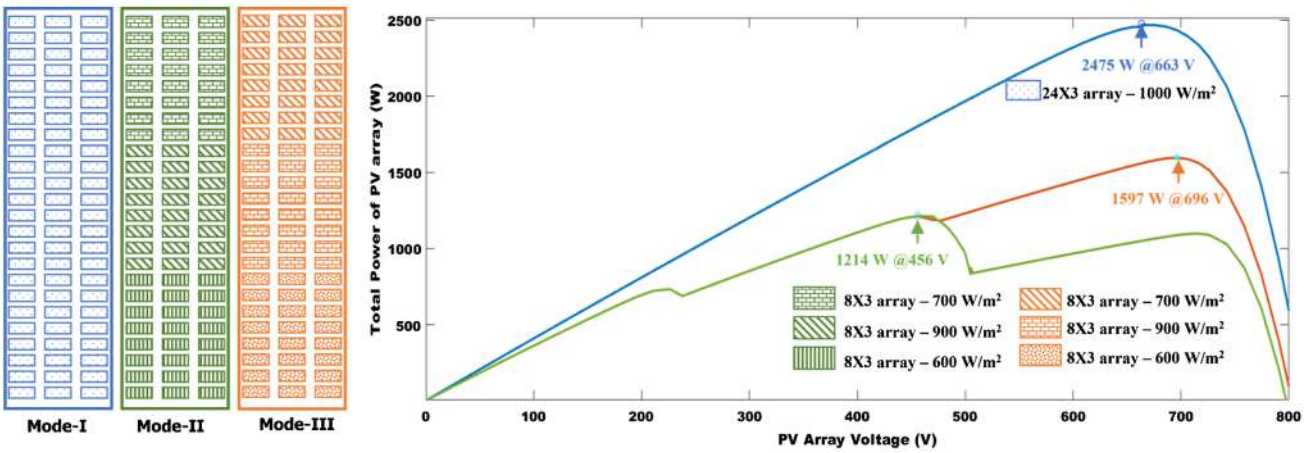

Fig. 7 SPVA characteristics of the proposed system exposed to different insolation conditions

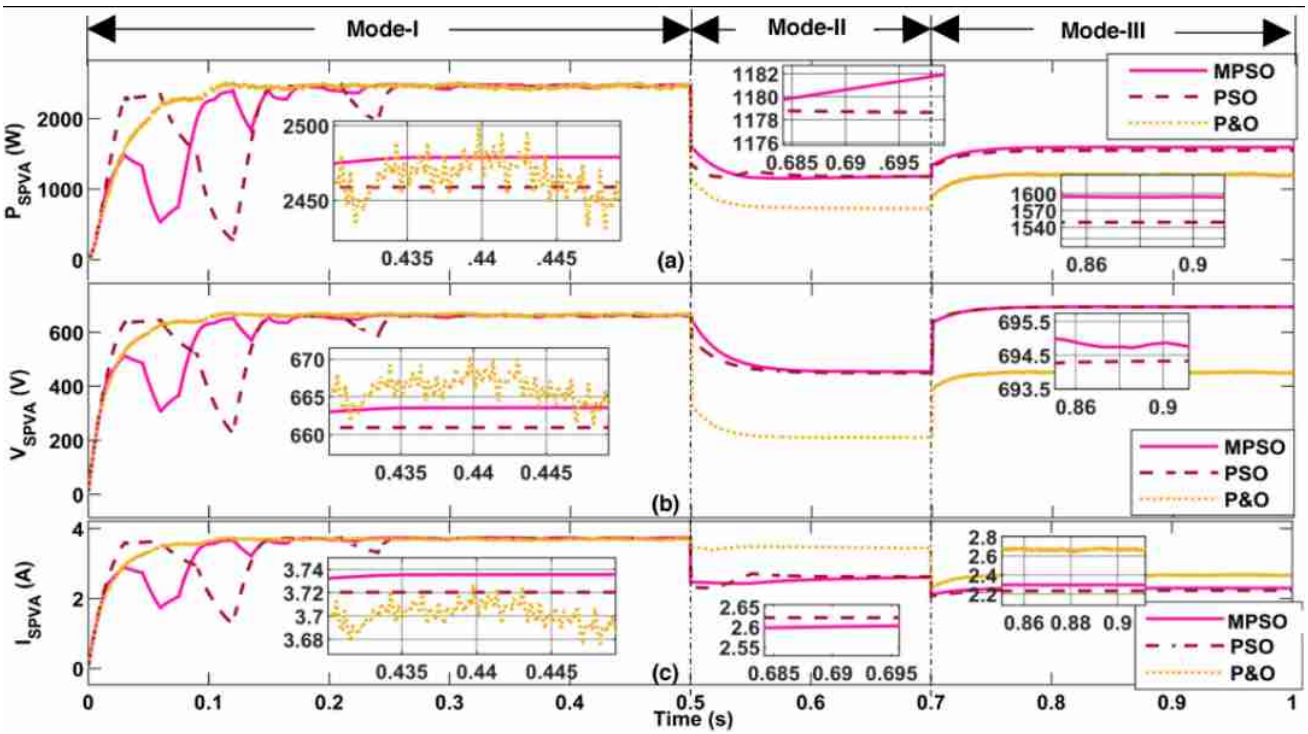

Fig. 8 Simulation results at the terminals of SPVA. **a** SPVA power comparison of modified PSO, PSO [38] and P&O [13] algorithms, **b** SPVA voltage comparison of modified PSO, PSO [38] and P&O [13] algorithms, **c** SPVA current comparison of modified PSO, PSO [38] and P&O [13] algorithms

The power delivery of SPVA at MPE value to the motor drive is presented in Fig. 8a. The steady state reaching time and their corresponding values are mentioned in Table 2.

As the first mode of operation (mode-I) is performing without partial shading conditions, all the MPE algorithms are tracking the peak power point (PPT) to the

$$\text{accuracy} = 100 - \frac{\text{true maximum power} - \text{measured maximum power}}{\text{true maximum power}} * 100 \tag{23}$$

Table 2 Comparison of MPE algorithms in terms of maximum power attainment (MPA) and steady state reaching time

S. No	MPE algorithm	Parameter	Mode-1	Mode-II	Mode-III
1	MPSO	Power (W) (accuracy in % with respect to ideal maximum power value)	2470.2 (99.81%)	**1208.7 (99.56%)**	**1590 (99.56%)**
2	PSO		2458.9 (99.35%)	1186.1 (97.7%)	1547.6 (96.91%)
3	P&O [13]		**2471.5 (99.86%)**	722.4 (59.5%)	1201.5 (75.23%)
4	MPSO	Steady state time (s)	0.23	0.045	0.035
5	PSO		0.26	0.055	0.035
6	P&O [13]		**0.1**	**0.035**	**0.015**

There are two sets of bold values for different modes. In power, it represents the maximum power value and in settling time, it represents the minimum settling time

nearby ideal value. The zoomed version of steady state power, steady state voltage, and steady state current of the all the MPE algorithms are presented in Fig. 8. It can be observed that the P&O algorithm is operating with ripple in the power. There exists a smoother operation of PSO and MPSO power values during the steady state operation. The power obtained in P&O is more than PSO and MPSO algorithms. The PSO and MPSO algorithms are tracking at a lesser speed than P&O algorithms. It can be observed that the P&O algorithm is very good at attaining the highest accuracy in Mode-I without accounting for the effect of partial shading conditions and fails to attain the accurate value in Mode-II and Mode-III considering the effect of partial shading conditions. While observing the MPSO algorithm, irrespective of partial shading conditions it is superior to the PSO algorithm and can meet the accuracy of not less than 99%. The steady state reaching time is higher in MPSO and PSO algorithms than in the P&O algorithm. From, Fig. 8b and c, the voltage and current values of all the MPE algorithms are following solar PV characteristics. The power developed by the P&O algorithm has failed to attain the maximum power under partial insolation conditions. The MPSO algorithm with changes in insolation tracks faster in comparison with

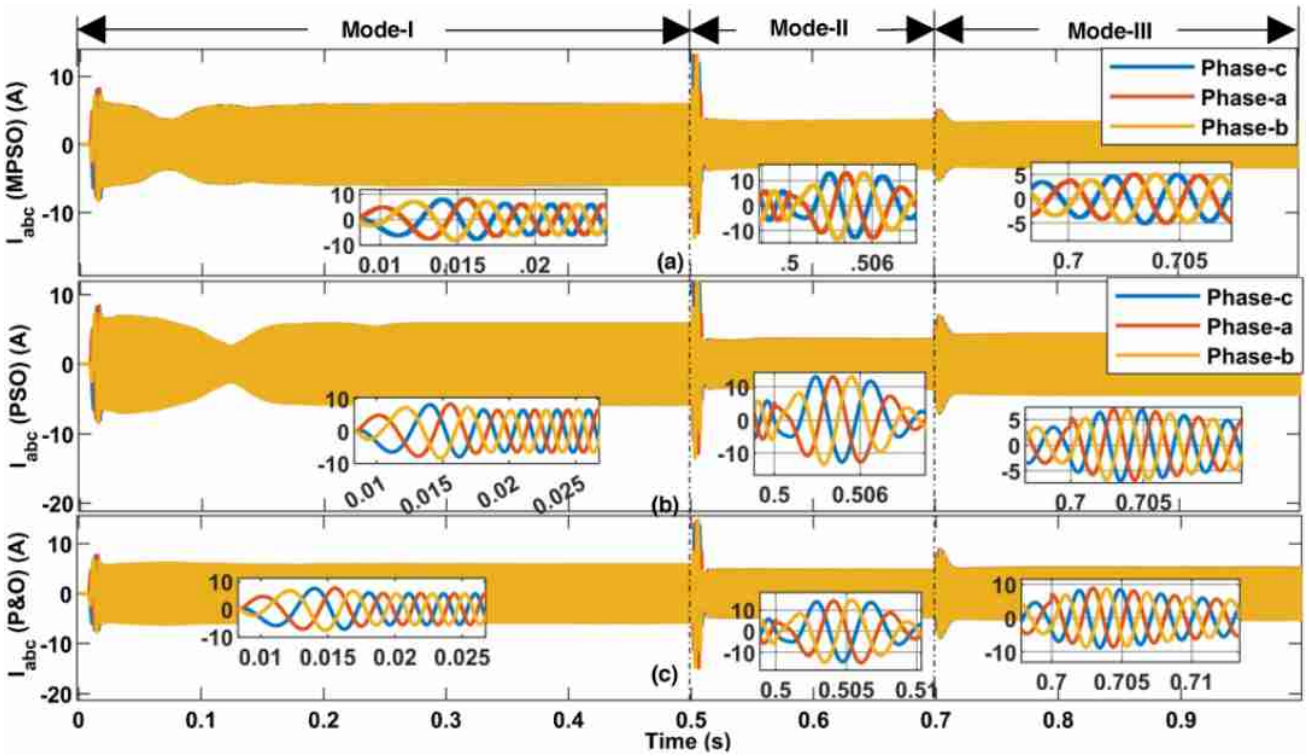

Fig. 9 Simulation results of stator currents for the different MPE algorithms. **a** Three-phase stator currents of induction motor drive for MPSO MPE algorithm, **b** Three-phase stator currents of induction motor drive for PSO MPE algorithm [38], **c** Three-phase stator currents of induction motor drive for P&O MPE algorithm [13]

the PSO method because of its fast convergence in local maxima point and is presented in Fig. 8. Figure 8 shows the proposed MPSO algorithm implementation in the vector control of induction motor-pump drive.

During Mode-I, the motor currents are compared in Fig. 9a, b and c, and can be realized that the starting of the motor is reduced irrespective of the MPE algorithm used. The actual responses of the currents during the transition of modes are shown in zoomed version for the clear understanding of the currents.

The current during the transients indicates the large demand of flux to attain the required speed. The starting current of the induction motor is adequately controlled and in turn, reduced from the actual starting current. This starting current reduction is due to decoupling the current term from the vector control. The ripple in the stator currents is reduced during mode-II to Mode-III transition compared to PSO and P&O methods as shown in Fig. 9. The SPVA current, motor currents and torque are compared in Fig. 10a, b, and c. To ensure that the motor is driving the load without losing the stability, the developed electromagnetic torque (T_e) should meet the load torque (pump torque, T_{pump}). This tracking of load torque (T_{pump}) and electromagnetic torque (T_e) is depicted in Fig. 10c. The validation of the simulation results is accomplished as the torque follows the SPVA current as shown in Fig. 10b and c.

The proposed system validates the reference speed tracking with the estimated speed is shown in Fig. 11c. Similarly, the estimated speed of the motor follows the SPVA voltage as shown in Fig. 11b with Fig. 11c. The steady state values of the proposed system are presented in the zoomed version for all the three modes of operation also presented in Fig. 11.

The comparison of stator current of each algorithm is presented in Fig. 12a and replicates the values corresponding to power attained at SPVA. The deviation of motor reference speed and torque during the transition from Mode-I to Mode-II is presented in Fig. 12c and d. This reference speed is faster in the P&O algorithm in comparison with PSO and MPSO algorithm due to its iteration time but still takes a similar time to reach the steady-state. The electromagnetic torque and estimated speed correspond to the maximum power tracked by the MPE algorithms, as shown in Fig. 12b and d and can be concluded that the MPSO algorithm is delivering the maximum power to the motor load in comparison with PSO and P&O algorithms. The PSO algorithm is almost the same as the MPSO algorithm, but MPSO is superior to PSO and P&O as it attains near-ideal values. The response of all the MPE algorithms remains the same for IMD vector control as they exhibit similar movements for the changes in the insolation.

To test the simulated system in the experimental hardware setup, the induction motor pump drive needs to be replaced with an induction motor coupled with a DC generator due to laboratory constraints. The hardware setup is exposed to three variants of PV graphs, as shown in Fig. 13. The parameters of the SPVA used in the solar array simulator are mentioned in "A: Solar PV array hardware" Appendix section. All these three variants are considered three different modes of operation. The three modes of operation are performed for similar time-sharing

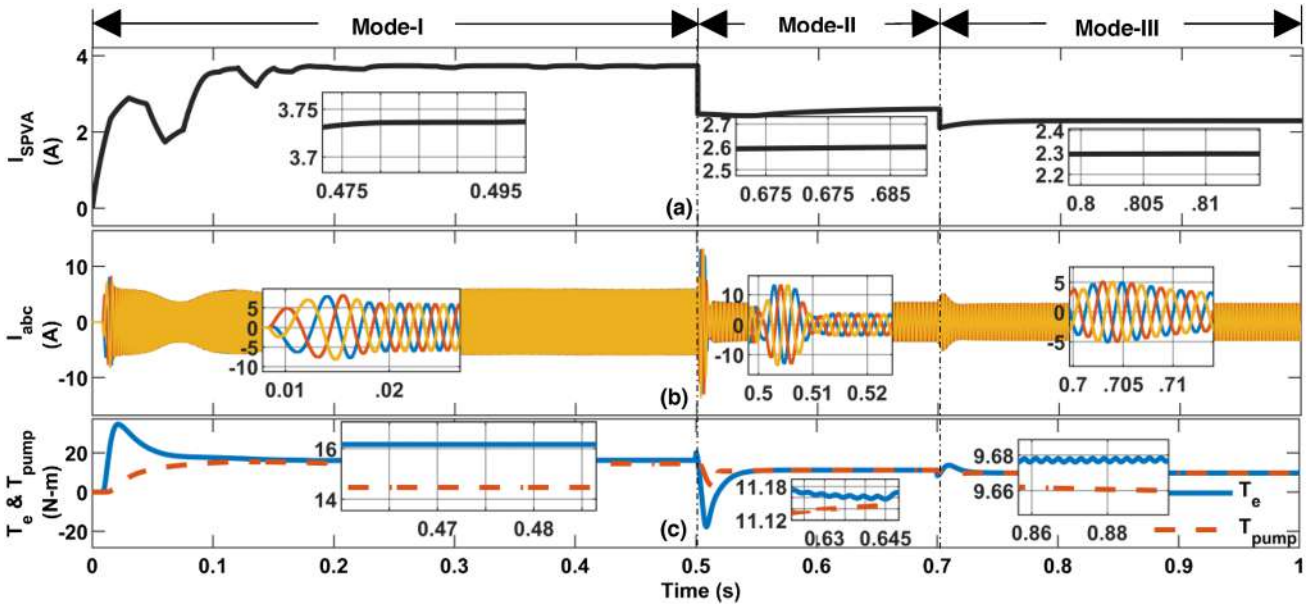

Fig. 10 Simulation of vector control of IMD for insolation graphs with MPSO MPE algorithm part-1. **a** SPVA current, (**b**) three-phase stator currents of induction motor, (**c**) electromagnetic torque (T_e) and pump torque (Tpump)

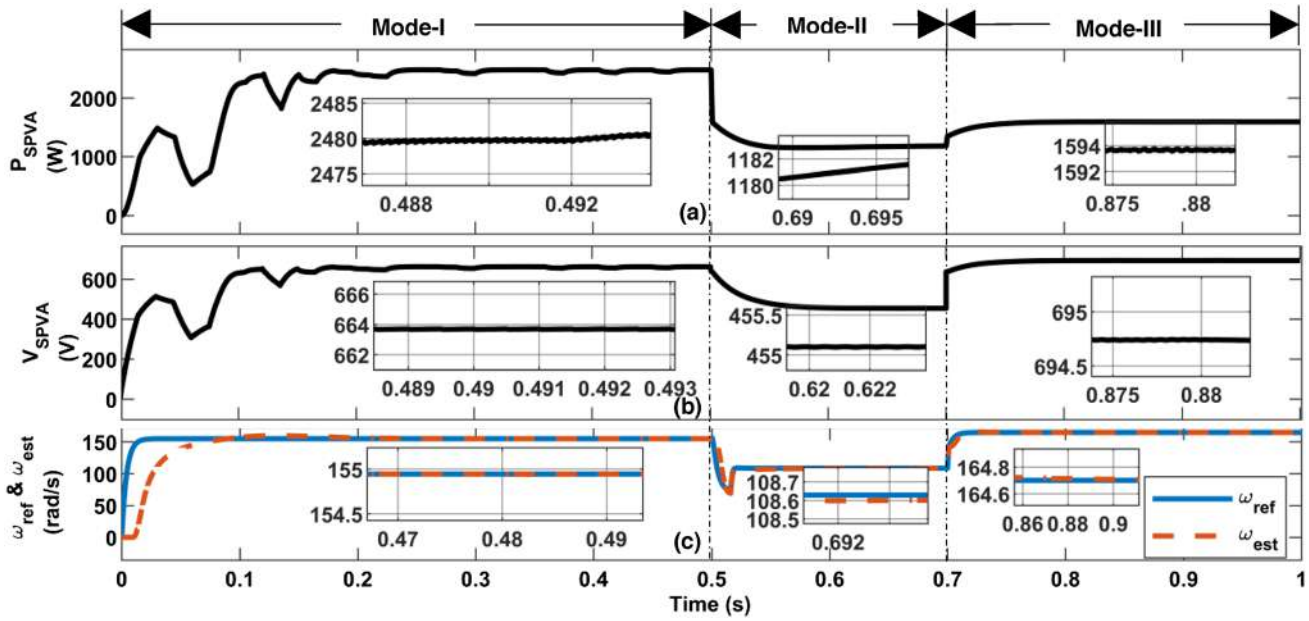

Fig. 11 Simulation of vector control of IMD for insolation graphs with MPSO MPE algorithm part-2. **a** SPVA power, **b** SPVA voltage, **c** Tracking of reference speed (ω_{ref}.) and estimated speed (ω_{est})

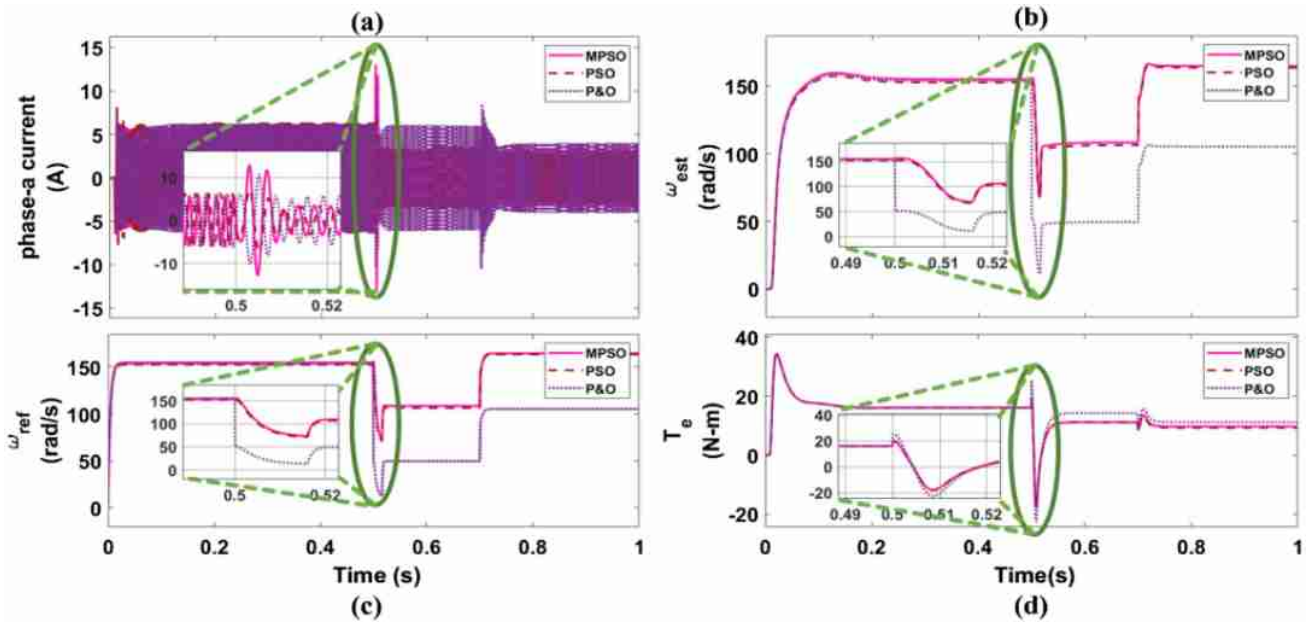

Fig. 12 Comparison of motor drive parameters for different MPE algorithms. **a** comparison of phase current (I_a), (**b**) comparison of estimated speed (ω_{est}), (**c**) comparison of reference speed (ω_{ref}.), (**d**) comparison of electro-magnetic torque (T_e)

as presented in simulations and are tested for the MPSO algorithm alone as it performs better than other mentioned MPE methods. In mode 1, the SPVA power should be 2469 W at 336 V. Similarly, in mode-II and mode-III, the power attainments are1380 W at 220 V and 1598 W at 348 V, respectively.

The motor parameters required for implementing SFOC of IMPD are mentioned in "B: Induction motor parameters" Appendix section. The MPE algorithm incorporated in SFOC of IMD is deployed in the DSP-based microcontroller board TMS320F28379D launchpad using the Code Composer Studio platform. The primary objective of the hardware deployment is to validate the simulation results

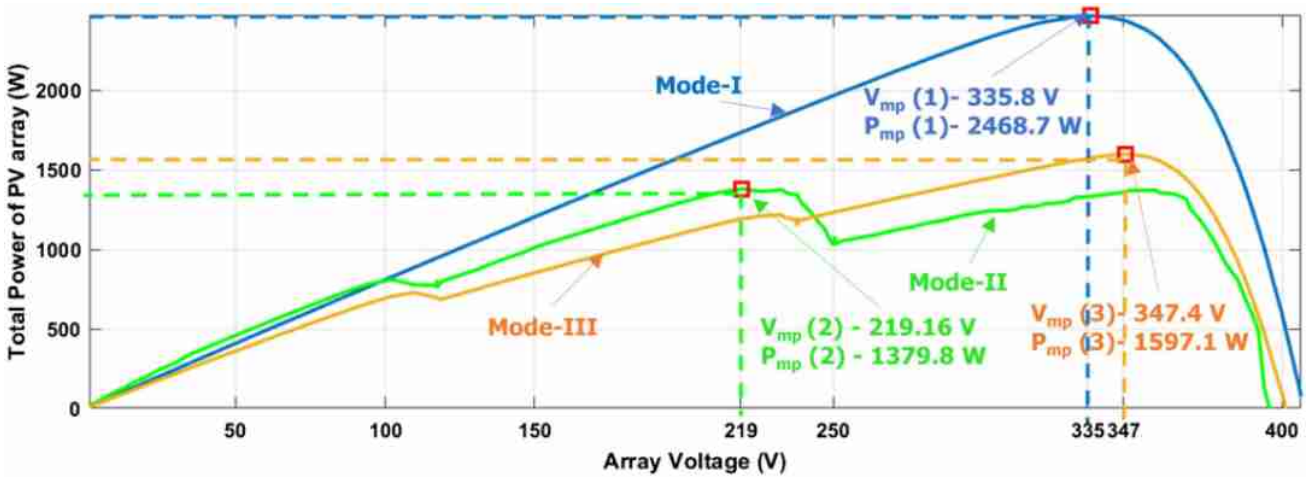

Fig. 13 Variant PV graphs for PV simulator deployment

of the proposed system, such as MPE algorithm validation, verification of reduced starting current, and similarities in voltage and current parameters of SPVA. As shown in Fig. 6, the induction motor employed in the hardware is rated for 230 V, 2-hp motor and demands an RMS current of 6.73 A at 0.82 power factor. But the maximum current generated from the solar array simulator is limited to 6 A, thus operating the induction motor below the rated value. This trade-off in laboratory constraints changes the SPVA graphs, as indicated in Fig. 13. So, the hardware deployment should ensure the attainment of peak power values during three modes of operation (Figs. 14 and 15).

The peak power delivered by SPVA during mode-I is 2468.7 W, mode-II is 1379.8 W, and mode-III is 1597.1 W. These maximum power values are indicated in Fig. 13 and are fed to the solar array simulator as 128 data point PV graphs. The peak power attainment of the given SPVA graphs was validated with the results mentioned in Fig. 16.

The hardware results of the proposed system are presented in Figs. 16, 17, and 18. As indicated in Fig. 14, the

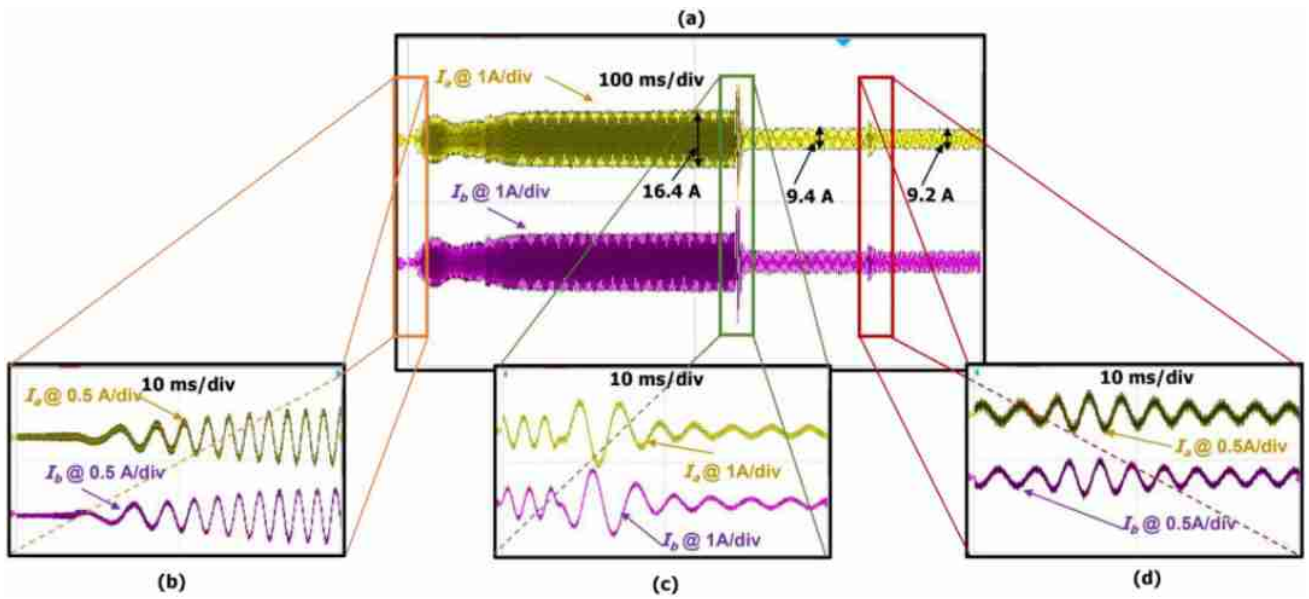

Fig. 14 **a** Induction motor stator currents of phase-a and phase-b for all the three mode of PV characteristics, (**b**) smooth starting of stator currents of three-phase induction motor operating under Mode-I PV characteristics, (**c**) phase-a and phase-b stator currents of induction motor operating under Mode-II PV characteristics, and (**d**) Phase-a and Phase-b stator currents of induction motor operating under Mode-III PV characteristics

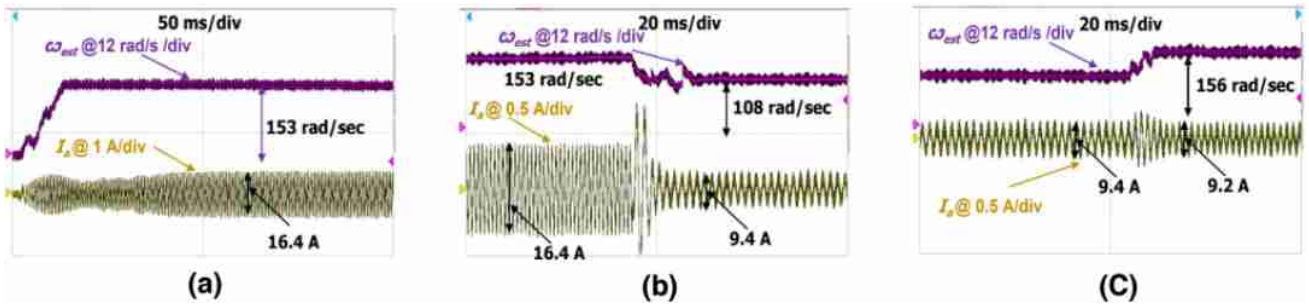

Fig. 15 **a** Estimated speed (ω_{est}) and stator current (I_a) of three-phase induction motor operating under Mode-I, (**b**) estimated speed (ω_{est}) and stator current (I_a) of three-phase induction motor operating under Mode-II transition, (**c**) estimated speed (ω_{est}) and statocurrent (I_a) of three-phase induction motor operating under Mode-III transition

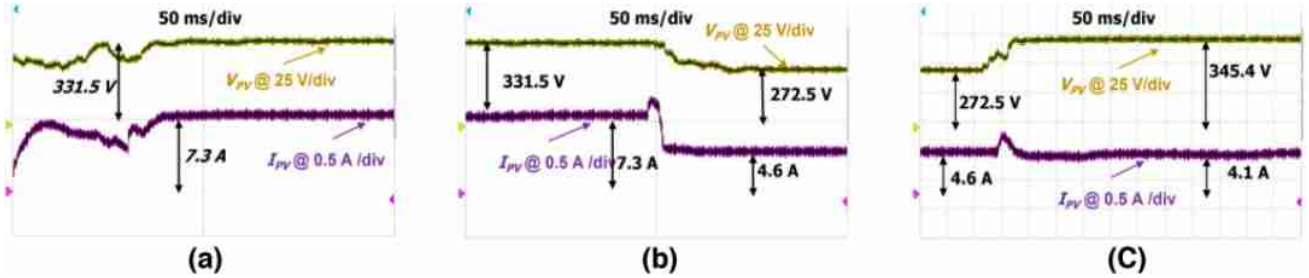

Fig. 16 **a** SPVA voltage (V_{PV}) and SPVA current (I_{PV}) under Mode-I, (**b**) SPVA voltage (V_{PV}) and SPVA current (I_{PV}) under Mode-II, (**c**) SPVA voltage (V_{PV}) and SPVA current (I_{PV}) under Mode-III

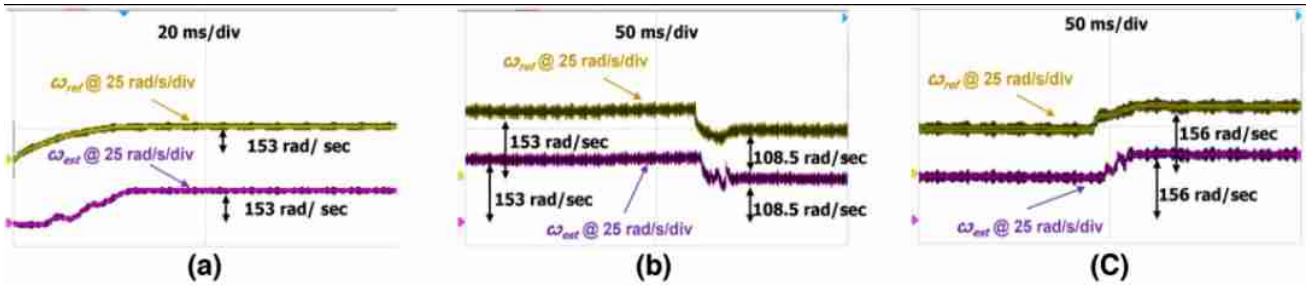

Fig. 17 **a** Comparison of reference speed (ω_{ref}), and estimated speed (ω_{est}) under Mode-I, (**b**) comparison of reference speed (ω_{ref}), and estimated speed (ω_{est}) from Mode-I to Mode-II transition, and (**c**) comparison of reference speed (ω_{ref}), and estimated speed (ω_{est}) from Mode-I to Mode-II transition

stator currents have a smooth starting and are similar in structure to the current waveform obtained in Fig. 9a.

The variation of estimated speed concerning motor stator current for mode-I, mode-II, and mode-III are presented in Fig. 15a, b, and c, respectively. The estimated speed follows the transient behavior of the stator currents as depicted in Fig. 15a, b, and c. The stator current changed from 16.4 A (peak to peak) during steady-state in mode-1 to 9.4 A (peak to peak) during steady-state in mode-II and 9.2 A (peak-to-peak) during steady-state in mode-III. The rest of the details are tabulated in Table 3, and the relevant waveform details are presented in Fig. 15a, b, and c.

The PPA of SPVA is quite important to deliver to the load and can be determined from the SPVA voltage and SPVA current, which are obtained as depicted in Fig. 16a, b, and c. The steady values of SPVA voltage and SPVA current are mentioned in Fig. 16a, b, and c. The power attainment in Table 3 is compared with Fig. 13, and there exists a deviation in the power output during partial shading conditions. Mode-I almost attained the peak power of 2419.95 W with an accuracy of 98.02%, mode-II achieved a power of

1253.5 W with an accuracy of 90.84% from the ideal peak power, and mode-III attained power of 1419.6 W with an accuracy of 88.89% from ideal peak power.

Another major concern of hardware deployment is the verification of reference speed tracking with the estimated speed. The tracking of estimated speed with the reference speed for mode-I, mode-II and mode-III are lucidly depicted in Fig. 17a, b and c. The reference speed is the equivalent value obtained from MPE algorithm and the estimated speed obtained from motor voltages and currents are in perfect harmony for all the three modes of operation as depicted in Fig. 17a, b and c.

Figure 18a presents the relevance between stator current and SPVA current for all three modes of operation. The SPVA current controls the motor current as the transition is synchronized. Figure 18b illustrates MPE reference voltage tracking by SPVA voltage and ensures the dc voltage regulation is successful. Thus, the proposed MPSO algorithm is validated by inheriting it in the SFOC of the IMD mechanism.

Table 4 gives the efficiency of the system under variable partial shading conditions. The SPVA peak power obtained and SPVA ideal peak power are considered as two important parameters to consider the efficiency. The main efficiency of the entire system with the effect of peak power tracking is a major concern. The efficiency of the system is highly dependent on insolation conditions and falls drastically for lower insolation conditions (low power conditions).

From these simulated and experimental results, it can be concluded that the MPSO algorithm is superior in accurate

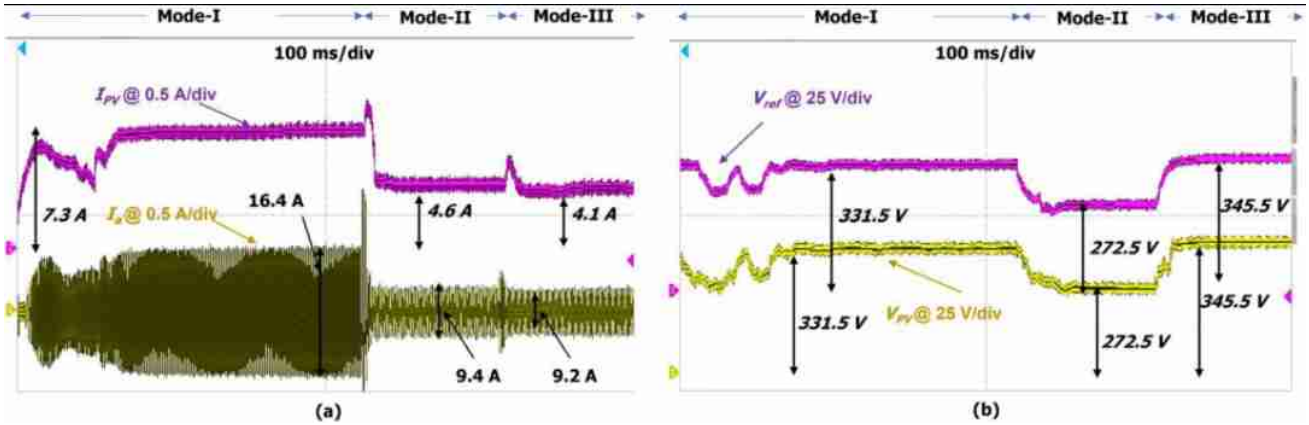

Fig. 18 **a** Comparison of SPVA current (I_{PV}) and motor stator current (I_a) operating under all the three modes of PV characteristics and, (**b**) comparison of PPT reference voltage (V_{ref}) and SPVA voltage (V_{PV}) operating under all the three modes of PV characteristics

Table 3 Comparison of parameters of the proposed system under steady state in each mode of operation obtained from experimental setup

S. No	Parameter	Mode-1	Mode-2	Mode-3
1	SPVA voltage (V_{PV})	331.5 V	272.5 V	345.4 V
2	SPVA current (I_{PV})	7.3 A	4.6 A	4.1 A
3	SPVA power (P_{PV}) (accuracy in % with respect to ideal maximum power value)	2419.95 W **(98.02%)**	1253.5 W (90.84%)	1419.6 W (88.89%)
4	Estimated speed (ω_{est})	153 rad/sec	108.5 rad/sec	153 rad/sec

The bold one is the maximum accuracy of all them and should be identified

Table 4 Efficiency of the induction motor drive system from the experimental setup

Mode	Ideal SPVA power (W) (Fig. 16)	Obtained SPVA power (W) (Fig. 18)	DC armature terminal voltage (V)	DC generator load current (A)	Efficiency $\eta_{obtained}$. (%) $=\frac{\text{DC generator power}}{\text{obtained SPVA power}}$ *100	Efficiency η_{final}(%) $=\frac{\text{DC generator power}}{\text{Ideal SPVA power}}$ *100
I	2468.7	2419.5	215.5	9.3	82.83	**81.18%**
II	1379.8	1253.5	210.8	4.81	80.89	**73.48%**
III	1597.1	1419.6	212.8	5.74	86.04	**76.48%**

The final obtained efficiency for different modes of operation is important and is mentioned in bold values

tracking of maximum power but lacks in speed tracking in comparison with the conventional P&O algorithm. Further research is required to improve the speed tracking of the MPSO algorithm for maximum power extraction. The deployment of the experimental hardware setup due to multiple tuning of PI controllers is a tedious and time-consuming process. The tuned PI controller parameters obtained from the simulation are initially considered for deployment in the controller. This deployment may or may not work because of hardware constraints. Some parameters such as rotor resistance and rotor time constant of the motor are variable subject to the environment. Due to its deviation from the realized motor parameters, the tuning process of the PI controllers should be manually adjusted to nearby values. There are four PI controllers in the vector control, one PI controller for the DC bus voltage regulation and one PI controller for estimating speed. The top priority of manual tuning is given to the PI controller that estimates the speed. Once the speed estimation PI controller is cross-checked with the tachometer, vector control PI controllers need to be tuned. The four PI controllers of vector control usually work directly for the simulated PI-tuned parameters. The PI controller for the DC bus regulation will finally be adjusted to make the control algorithm work properly. The manual tuning and testing the hardware to run the experiment takes multiple trials and is a tedious process. The safety of the equipment should be considered at all times and operated accordingly. Hence developing a simple control algorithm without compromising maximum power attainment, reduction in starting current, and regulation of SPVA voltage with the reduced number of sensors is the future research area for single-stage SPVA-driven water pumping applications.

Conclusions

An SPVA driving an IMPD through a single-stage voltage source inverter was proposed with the design of all the sections in the system. A sensorless approach was adopted to control IMPD by eliminating the voltage sensors at the motor terminals, which are predicted from SPVA voltage through matrix manipulations. One of the three current sensors at the motor terminals for current measurement is eliminated with the help of three-phase current balance equations. The SFOC of IMD is adopted with the encoderless mechanism for the motor speed estimation and is determined by estimating the synchronous speed and slip speed of the motor. The reference speed required for the vector control algorithm is the maximum power equivalent value of SPVA and is predicted using the MPSO algorithm. The proposed system is tested for three operating modes, out of which mode-I represents the SPVA characteristic without partial shading conditions, and mode-II and mode-III represent the characteristic of SPVA with the effect of partial shading conditions. The speed reference from the MPE point was incorporated in field-oriented control and was used to control the conventional three-phase voltage source inverter to minimize the error between the reference speed and estimated speed. The speed reference is generated from the voltage reference obtained from the MPSO MPE algorithm. This generated reference is used as a control reference for modified field-oriented control. The simulation of all the three modes of operation employing the proposed MPSO algorithm was compared with the relevant MPE algorithms such as PSO and P&O algorithms. The MPSO algorithm is superior to PSO and P&O algorithms in terms of accurate tracking of maximum power, and it can be concluded that it attains 99%, irrespective of the effect of partial shading conditions. P&O algorithm is faster in achieving the steady state value than the MPSO algorithm and PSO algorithm. The main limitation of the MPSO algorithm is its tracking speed compared to the conventional P&O algorithm. Further research is required to advance the MPSO algorithm to track faster with the reduced number of iterations. The estimated motor speed tracks the reference speed and thus validates the algorithm. The motor torque can meet the load torque without compromising the maximum power extraction and is depicted through simulations. The simulated system is implemented through the hardware to validate the MPA of the MPSO algorithm deployed in the SFOC of IMPD, tracking the estimated speed with the reference speed and reducing starting current. The MPA of the MPSO algorithm in the hardware deployment attains the least accuracy of 88% in mode-III during partial shading conditions of PV characteristics. The hardware circuitry comprising induction motor coupled with DC generator is a linear approximated model of induction motor-pump set up, but the validation of the proposed controller is adequately deployed. The variation of speed, voltage, and current concerning the change in PV graphs indicates the attainment of maximum power and its delivery to the load, thus ensuring its suitability for water pumping applications. The overall efficiency of the proposed system varied from 81.18% to 73.48% for the chosen modes of operation. The efficiency of the system decreases with the insolation applied on the PV array.

Appendix

A: Solar PV array hardware

$V_{oc} = 384$ V, $V_{mp} = 330$ V, $I_{sc} = 6.9$ A, $I_{mp} = 6.05$ A, $N_{ser} = 34$, Npar = 25, number of cells in one module (Ns) = 36, DC-link capacitor (C_{dc}) = 4700μF, switching frequency (fs) = 10 kHz.

B: Induction motor parameters

1.5 kW, 3-phase, 400 V (L-L), 2 poles, $R_s = 0.7384\Omega$, $L_{ls} = 0.003045H$, $R_r = 0.7043\Omega$, $L_{lr} = 0.003045H$, $L_m = 0.1241H$, $J = 0.0343\ kg - m^2$, DC voltage controller gains $K_{pd} = 0.04$, $K_{id} = 1.35$.

Supplementary Information The online version contains supplementary material available at https://doi.org/10.1007/s40095-022-00540-2.

Funding The authors have no competing interests to declare that are relevant to the content of this article and the authors receive partial funding from the Institute of Engineers (India) under research Grant-in-aid scheme (with the project ID: DR2022005) for the submitted work.

Declarations

Conflict of interest On behalf of all authors, the corresponding author states that there is no conflict of interest.

References

1. Ministry of New and Renewable Energy.: Government of India, https://mnre.gov.in/solar/current-status/. Accessed 14 May 2022 (2022).
2. Azad, R., Chakraborty, S.: Green growth and the right to energy in India. Energy Policy **141**, 111456 (2020). https://doi.org/10.1016/j.enpol.2020.111456
3. Majid, M.A.: Renewable energy for sustainable development in India: current status, future prospects, challenges, employment, and investment opportunities. Energy Sustain. Soc. **10**(1), 1–36 (2020). https://doi.org/10.1186/s13705-019-0232-1
4. Market Report Series: IEA (2021), Solar PV, IEA, Paris https://www.iea.org/reports/solar-pv.
5. Vinod Kumar, S., et al.: Imperative role of photovoltaic and concentrating solar power technologies towards renewable energy generation. Int. J. Photoenergy (2022). https://doi.org/10.1155/2022/3852484
6. IEA: Renewables 2020, IEA, Paris (2020) https://www.iea.org/reports/renewables-2020/solar-pv.
7. Zahira, R., et al.: Stand-alone microgrid concept for rural electrification: a review. Resid. Microgrids Rural Electrifications (2022). https://doi.org/10.1016/B978-0-323-90177-2.00013-X
8. Kumar, A., Patel, N., Gupta, N., Gupta, V.: Photovoltaic power generation in Indian prospective considering off-grid and grid-connected systems. Int. J. Renew. Energy Res. IJRER **8**(4), 1936–1950 (2018)
9. Rajagopalan, S., Breetz, H.L.: Niches, narratives, and national policy: How India developed off-grid solar for rural electrification. Environ. Innov. Soc. Trans. **43**, 41–54 (2022). https://doi.org/10.1016/j.eist.2022.02.004
10. Ministry of New and Renewable Energy: Government of India, https://mnre.gov.in/solar/solar-offgrid. Accessed 14 May 2022, (2022).
11. Li, W.T., Thirugnanam, K., Tushar, W., Yuen, C., Chew, K.T., Tai, S.: Improving the operation of solar water heating systems in green buildings via optimized control strategies. IEEE Trans. Ind. Inf. **14**(4), 1646–1655 (2018). https://doi.org/10.1109/TII.2018.2797018
12. Hafez, B., Abdel-Khalik, A.S., Massoud, A.M., Ahmed, S., Lorenz, R.D.: Single-sensor-based three-phase permanent-magnet synchronous motor drive system with Luenberger observers for motor line current reconstruction. IEEE Trans. Ind. Appl. **50**(4), 2602–2613 (2014). https://doi.org/10.1109/TIA.2013.2296625
13. Shukla, S., Singh, B.: Single-stage pv-grid interactive induction motor drive with improved flux estimation technique for water pumping with reduced sensors. IEEE Trans. Power Electron. **35**(12), 12988–12999 (2020). https://doi.org/10.1109/TPEL.2020.2990833
14. Sharma, U., Singh, B.: Utility-tied solar water pumping system for domestic and agricultural applications. J. Inst. India Eng. Ser. B **101**(1), 79–91 (2020). https://doi.org/10.1007/s40031-020-00426-z
15. Hadole, M.V., Tiwari, K.N., Bajpai, P.: Energy generation and flow rate prediction of photovoltaic water pumping system for irrigation. Environ. Dev. Sustain. **23**(5), 6722–6733 (2021). https://doi.org/10.1007/s10668-020-00886-9
16. Adle, R., Renge, M., Muley, S.: Improvement in performance of series Z-source inverter with an application as solar PV fed water pump. Iran. J. Sci. Tech. Trans. Electr. Eng. **44**(3), 1263–1279 (2020). https://doi.org/10.1007/s40998-020-00310-y
17. Shukla, S., Singh, B., Shaw, P., Al-Durra, A., El-Fouly, T.H., El-Saadany, E.F.: A new analytical mppt based induction motor drive for solar pv water pumping system with battery backup. IEEE Trans. Ind. Electron. (2021). https://doi.org/10.1109/TIE.2021.3091929
18. Priyadarshi, N., Sanjeevikumar, P., Bhaskar, M.S., Azam, F., Taha, I.B., Hussien, M.G.: An adaptive TS-fuzzy model-based RBF neural network learning for grid integrated photovoltaic applications. IET Renew. Power Gener. (2022). https://doi.org/10.1049/rpg2.12505
19. Raghuwanshi, S.S., Khare, V.: Sizing and modelling of stand-alone photovoltaic water pumping system for irrigation. Energy Environ. **29**(4), 473–491 (2018). https://doi.org/10.1177/0958305X17752739
20. Jones, W.V.: Motor selection made easy: choosing the right motor for centrifugal pump applications. IEEE Ind.Appl. Mag. **19**(6), 36–45 (2013). https://doi.org/10.1109/MIAS.2012.2215649
21. Neha, B., Hussain, I., Singh, B.: Vector-based synchronization method for grid integration of solar PV-battery system. IEEE Trans. Ind. Inf. **15**(9), 4923–4933 (2019). https://doi.org/10.1109/TII.2019.2921034
22. Kumar, N., Singh, B., Panigrahi, B.K., Chakraborty, C., Suryawanshi, H.M., Verma, V.: Integration of solar PV with low-voltage weak grid system: using normalized Laplacian kernel adaptive Kalman filter and learning based InC algorithm. IEEE Trans. Power Electron. **34**(11), 10746–10758 (2019). https://doi.org/10.1109/TPEL.2019.2898319
23. Singh, B., Kumar, S.: Grid integration of 3P4W solar PV system using M-LWDF-based control technique. IET Renew. Power Gen. **11**(08), 1174–1181 (2016). https://doi.org/10.1049/iet-rpg.2016.0495
24. Pradhan, S., Hussain, I., Singh, B., Panigrahi, B.K.: Performance improvement of grid-integrated solar PV system using DNLMS control algorithm. IEEE Trans. Ind. Appl. **55**(1), 78–91 (2018). https://doi.org/10.1109/TIA.2018.2863652
25. Shukl, P., Singh, B.: Grid integration of three-phase single-stage PV system using adaptive laguerre filter based control algorithm under nonideal distribution system. IEEE Trans. Ind. Appl. **55**(6), 6193–6202 (2019). https://doi.org/10.1109/TIA.2019.2931504
26. Patra, S., Kishor, N., Mohanty, S.R., Ray, P.K.: Power quality assessment in 3-Φ grid connected PV system with single and dual stage circuits. Int. J. Electr. Power Energy Syst. **75**, 275–288 (2016). https://doi.org/10.1016/j.ijepes.2015.09.014
27. Tomar, A., Mishra, S., Bhende, C.N.: AOMH–MISO based PV–VCI irrigation system using ASCIM pump. IEEE Trans. Ind.

Appl. **54**(5), 4813–4824 (2018). https://doi.org/10.1109/TIA.2018.2839728
28. Vitorino, M.A., de Rossiter Corrêa, M.B., Jacobina, C.B., Lima, A.M.N.: An effective induction motor control for photovoltaic pumping. IEEE Trans. Ind. Electron. **58**(4), 1162–1170 (2010). https://doi.org/10.1109/TIE.2010.2054053
29. Mudlapur, A., Ramana, V.V., Damodaran, R.V., Balasubramanian, V., Mishra, S.: Effect of partial shading on PV fed induction motor water pumping systems. IEEE Trans. Energy Convers. **34**(1), 530–539 (2018). https://doi.org/10.1109/TEC.2018.2876132
30. Muljadi, E.: PV water pumping with a peak-power tracker using a simple six-step square-wave inverter. IEEE Trans. Ind. Appl. **33**(3), 714–721 (1997). https://doi.org/10.1109/28.585862
31. Correa, O.P., Seleme, S.I., Silva, S.R.: Efficiency optimization in stand-alone photovoltaic pumping system. Renew. Energy **41**, 220–226 (2012)
32. Yang, C., Finch, J.W.: "A Comparison of Induction Motor Speed Estimation Using Conventional MRAS and an AI-Based MRAS Parallel System". In: Ao, SI., Gelman, L. (eds) Advances in Electrical Engineering and Computational Science. Lecture Notes in Electrical Engineering, vol 39. Springer, (2021). https://doi.org/10.1007/978-90-481-2311-7_7.
33. Özdemir, S.: A new stator voltage error-based MRAS model for field-oriented controlled induction motor speed estimation without using voltage transducers. Electr. Eng. **102**, 2465–2479 (2020). https://doi.org/10.1007/s00202-020-01043-1
34. Shabaan, S., El-Sebah, M.I.A., Bekhit, P.: Maximum power point tracking for photovoltaic solar pump based on ANFIS tuning system. J. Electr. Syst. Inf. Technol. **5**(1), 11–12 (2018). https://doi.org/10.1016/j.jesit.2017.12.001
35. Lasheen, M., Abdel-Salam, M.: Maximum power point tracking using Hill Climbing and ANFIS techniques for PV applications: a review and a novel hybrid approach. Energy Convers. Manag. **171**, 1002–1019 (2018). https://doi.org/10.1016/j.enconman.2018.06.003
36. Rebei, N., Hmidet, A., Gammoudi, R., Hasnaoui, O.: Implementation of photovoltaic water pumping system with MPPT controls. Front. Energy **9**(2), 187–198 (2015). https://doi.org/10.1007/s11708-015-0359-5
37. Ghoneim, A.A.: Design optimization of photovoltaic powered water pumping systems. Energy Convers. Manag. **47**(11–12), 1449–1463 (2006). https://doi.org/10.1016/j.enconman.2005.08.015
38. Murali, S., Panda, K.P. and Panda, G.: PV-HESS fed BLDC driven water pumping system with PSO-based MPP tracking employing zeta converter, In: 2018 IEEE Innovative Smart Grid Technologies-Asia (ISGT Asia) (pp. 196–201), (2018). https://doi.org/10.1109/ISGT-Asia.2018.8467896.
39. Mosaad, M.I., Abed El-Raouf, M.O., Al-Ahmar, M.A., Banakher, F.A.: Maximum power point tracking of PV system based cuckoo search algorithm, review and comparison. Energy Procedia **162**, 117–126 (2019). https://doi.org/10.1016/j.egypro.2019.04.013
40. Guo, K., Cui, L., Mao, M., Zhou, L., Zhang, Q.: An improved gray wolf optimizer MPPT algorithm for PV system with BFBIC converter under partial shading. IEEE Access **8**, 103476–103490 (2020). https://doi.org/10.1109/ACCESS.2020.2999311
41. Ufnalski, B., Grzesiak, L.M.: A plug-in direct particle swarm repetitive controller for a single-phase inverter. Electr. Rev. **90**(6), 6–11 (2014). https://doi.org/10.12915/PE.2014.06.02
42. Ufnalski, B., Grzesiak, L.M.: Plug-in direct particle swarm repetitive controller with a reduced dimensionality of a fitness landscape–a multi-swarm approach. Bull. Polish Acad. Sci. Tech. Sci. (2015). https://doi.org/10.1515/bpasts-2015-0098
43. Caracas, J.V.M., de Carvalho Farias, G., Teixeira, L.F.M., de Souza Ribeiro, L.A.: Implementation of a high-efficiency, high-lifetime, and low-cost converter for an autonomous photovoltaic water pumping system. IEEE Trans. Ind. Appl. **50**(1), 631–641 (2013). https://doi.org/10.1109/tia.2013.2271214
44. Shukla, S., Singh, B.: Reduced current sensor based solar PV fed motion sensorless induction motor drive for water pumping. IEEE Trans. Ind. Inf. **15**(7), 3973–3986 (2018). https://doi.org/10.1109/TII.2018.2885795
45. Bose, B.K.: Power electronics and AC drives, Englewood Cliffs (1986).
46. Hailemariam, Z.M., Leidhold, R., Tesfamariam, G.T.: Real-Time speed control of a PMSM for wind turbine application. IEEE PES/IAS PowerAfrica Conf. (2019). https://doi.org/10.1109/PowerAfrica.2019.8928919

International Journal of Energy and Environmental Engineering (2023) 14:791–802
https://doi.org/10.1007/s40095-022-00549-7

ORIGINAL RESEARCH

Investigation of waste cooking oil–diesel blend with copper oxide additives as fuel for diesel engine under variations in compression ratio

Madhuri G. Chatur[1] · Anil Maheshwari[1] · Srinidhi Campli[2]

Received: 13 September 2022 / Accepted: 5 November 2022 / Published online: 19 November 2022

Abstract
The current day energy expenses contribute cripplingly to inflation rates and hamper the day-to-day needs of the common man. Biodiesel which is a hopeful fuel to muscle diesel needs to be researched extensively such that when brought to day-to-day use must not hamper the traditional engines working. So in the current work, a conventional diesel engine that can be modified to various compression ratios is used to testify to the performance and emissions results. Copper oxide nano additives are used as fuel additives. The copper oxide nano-sized particle characteristics and various parameters were determined using appropriate characterization methods. The additives are mixed in waste cooking oil methyl ester blend and later subjected to property check and engine testing. The addition of nano-sized additives does enhance the thermal performance of the engine by incrementing the thermal efficiency and retarding the fuel consumption rates by 6.3 and 4.9%. The emissions discharged from the engine were also retarded by 4.3%, 26.1 for CO and HC emissions.

Keywords Engine compression ratio · Performance · Emission · Nano fuel additives · Waste cooking oil biodiesel

Abbreviations

WCO20	Waste cooking oil methyl ester 20% vol and conventional diesel 80% vol
ppm	Part per million
DI	Direct injection
CI	Compression ignition
BDD	Biodiesel–diesel blend
BTHE	Brake thermal efficiency
BSFC	Brake specific fuel consumption
PD	Pure diesel
SB	Straight biodiesel
NiO	Nickel oxide
CNT	Carbon nanotubes
HRR	Heat release rate
CuO	Copper oxide nanoparticles
EGT	Exhaust gas temperatures

Introduction

Diesel Engines which are known as heavy-duty engines dominate the logistics and the mass transportation sector and with rising fuel cost does impact largely on the common man's savings. The Current day's Inflation rate depends on the cost of fuel crises. Today Fossil fuel cost varies according to the OPEC nation's declared prices, which factors a lot in developing nations. Biodiesel which is a promising source to run diesel engines does provide good results and which are in line with diesel in certain aspects. Biodiesel or Transesterified Oil esters alone can be fuelled in diesel engines, but their cloud point and viscosity cost heavily when used in cold environments and cold starting of CI engine. Also, the density of transesterified ester is quite high which leads to larger fuel injection droplets into the combustion chamber leading to higher soot formation. A Solution to this problem is the blending of Biodiesel with diesel. The properties of the 10 and 20% of Biodiesel–diesel blend are quite comparable when equated to the properties of diesel. Also, many researchers have reported that the 20% blend gives good performance and reduces emissions such as CO and HC [1, 2]. Despite these favorable responses, the fuel consumption

✉ Madhuri G. Chatur
madhurisdeokar@gmail.com

[1] Department of Mechanical Engineering, Sandip University, Nashik, India

[2] Department of Mechanical Engineering, JSPM's Rajarshi Shahu College of Engineering, Pune-33, India

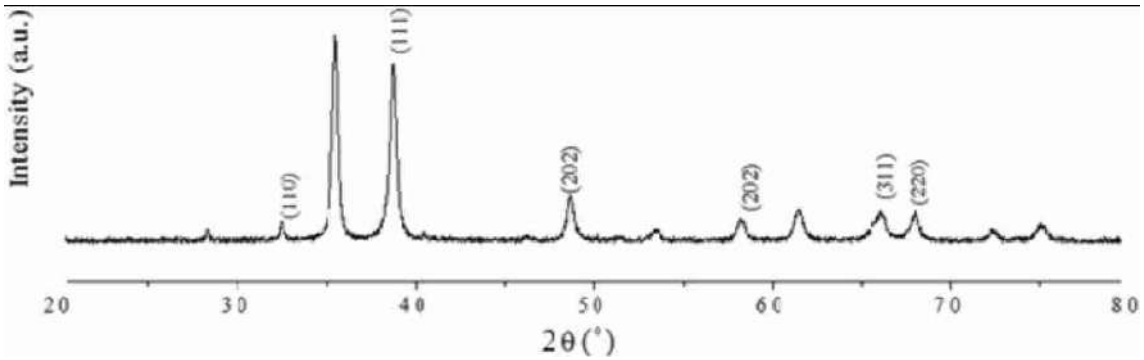

Fig. 1 X-ray diffraction of CuO nanoparticles

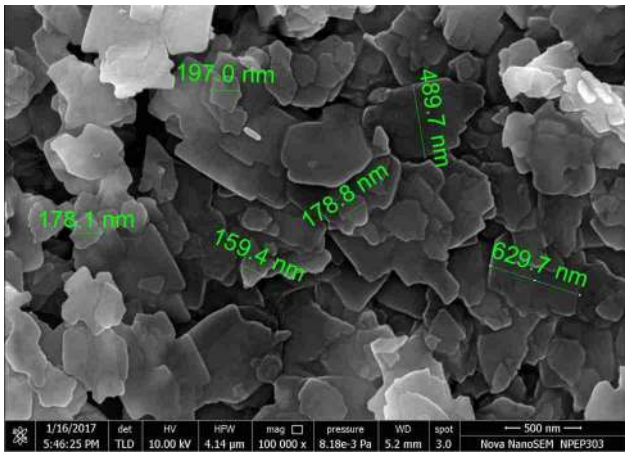

Fig. 2 FESEM of CuO nanopartilces

Table 1 Characterization of copper oxide nano additives

Parameters	Size
Lattice constant (c)	4.259
% Phase	5.41
Crystalline size	89.35
Theoratical density	37.36 nm
Axial ratio (C/A)	5.95e5 g/cm^3
Average particle size	305.59 nm

rates and Peak cylinder pressure values do limit the use of these blended fuels. Also, the soot formation when these blended fuels are combusted does tend retard the combustion performance of diesel engines in long run [3]. A Lot of research has been focused on addressing these issues, which include the use of varying engine variables such as advancing fuel injection and fuel injection at higher pressure but both lead to tribological problems and increase the thermal oxides of nitrogen emission. Most authors have also highlighted the studies of variable compression ratios. Muralidharan and Vasudevan [4] used the same feedstock, but the blending of esters in BDD was 20, 40, 60, and 80% and with engine CR values of 18, 19, 20, 21, and 22. However, they found that the BTHE at 50% load was the maximum. Prabhu et al. [5] used lower biodiesel blends of algal feedstocks such as B10 and B20 biodiesel blends in the CI engine. With lower Biodiesel in BDD, the results such as thermal performance and emissions were in line with conventional fuel. Another study conducted by Sayin et al. [6] investigated the variation of compression ratio and fuel injection parameters on the engine performance

Fig. 3 EDS of CuO particles

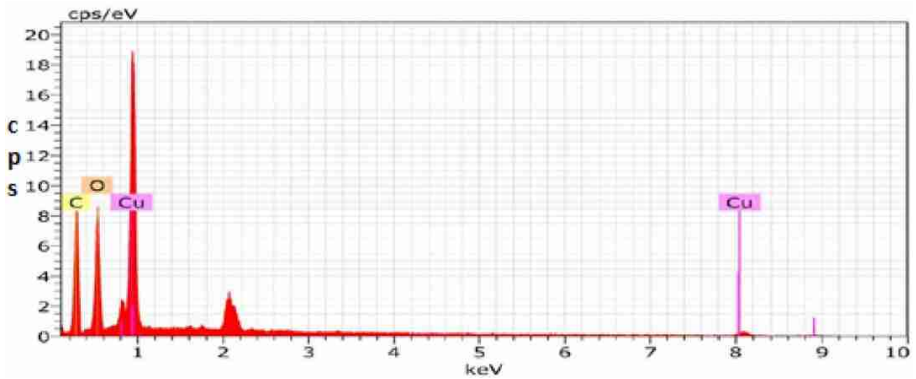

Table 2 Thermo physical properties of test fuels

Property	Standard	WCO20	WCO20 + 10 ppm	WCO20 + 20 ppm	WCO20 + 30 ppm	WCO20 + 40 ppm	Diesel
Chemical composition		FAME(C12-C22)	–	–	–	–	HC(C10-C21)
Density, kg/m^3	IS 1448 P:16	844	847	851	855	859	825
Calorific value, MJ/kg	IS 1448 P:6	40.52	40.66	40.69	40.72	40.67	42.62
Kinematic viscosity @ 40 °C	IS 1448 P:25	4.25	4.23	4.21	4.15	4.14	2.83
Flash point, °C	IS 1448 P:20	91	96	95	96	96	69
Cloud point, °C	IS 1448 P:10	8.9	9.1	9.2	9.2	9.2	6.2
Pour point, °C	IS 1448 P:10	4.5	4.6	4.6	4.7	4.7	3.4
Cetane index	Calculative method	–	–	–	–	–	48

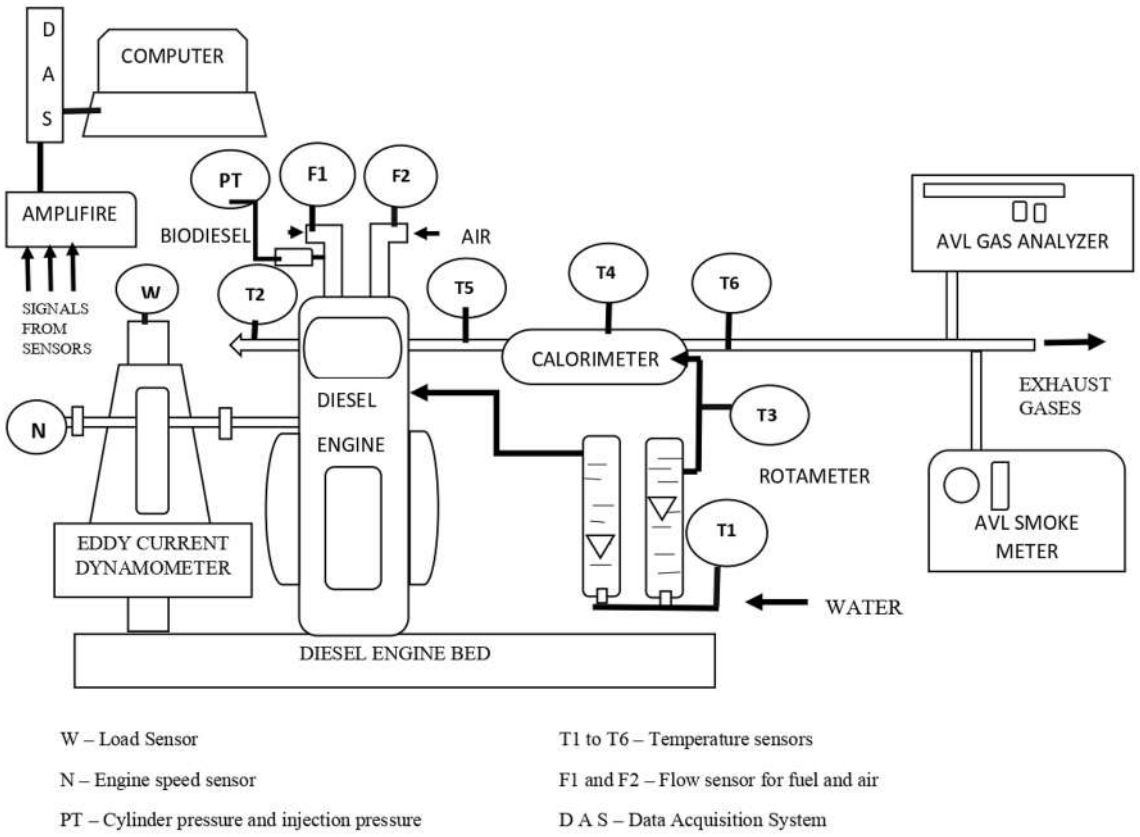

Fig. 4 Schematic diagram of experimental engine test setup

and emission features. With the rising in the engine compression ratio, the fuel consumption values and a similar trend were shown by the engine NOx discharge. Other emissions such as CO and HC plummeted with higher CR values. Most researchers have emphasized that the rise of engine CR does provide an advantage in fuel atomization

Table 3 Engine specifications

Manufacture	Kirloskar oil
SFC	251 g/kWh
Rated power	5.4 kW @ 1500 rpm
Standard CR	18:1
Bore	87.5 mm
Stroke	110 mm
Injection timing	23° before TDC

Table 4 Device specifications and terminology

Device specification	Range	Accuracy	Uncertainties
Carbon monoxides (CO)	0–10.00%	±0.01%	±0.1
Carbon dioxides (CO_2)	0–20.00%	±0.01%	±0.2
Oxides of nitrogen (NOx)	0–5000 ppm	±1 ppm	±0.2
Oxygen (O2)	0–25.00%	±0.01%	±0.2
Hydrocarbons (HC)	1–1500 ppm	±1 ppm	±0.1
Exhaust gas temp. (EGT)	0–500 °C	±1 °C	±0.1
Tachometer	0–10,000 rpm	±10 rpm	±0.1
Fuel flow meter	1–30 cc	±0.1 cc	±0.1

and reduction of BDD ignition delay but the cost of this was paid by the rising levels of NOx in emission. El-Adawy et al. [7] studied engines fuelled with waste oil ester blends under CRs 14, 16, and 18. They found that the specific fuel consumption reduces with rising in engine compression ratio and a rise in output thermal efficiency. Also, emissions such as CO_2 rose by 14.28% and unburnt hydrocarbon emissions plummeted heavily. However, a good reduction of the above emission was taken a hit in NOx. Till date, there are many bioesters-diesel fuel blends used in the engine but the right compression ratio is yet to be explored. Compression ratio studies related to biodiesel marks of paramount importance as biodiesel diesel blend properties vary with feedstock, and blending levels, and the right compression ratio for a variety of feedstock and blending ratios is yet to be explored. To address this issue of BDD combusted in the engine leading to higher NOx, researchers have focused on various fuel additives. One possibility for addressing this is the use of alcohols and other aryl fuel additives [8, 9], but the problem with such additives is they tend to nourish the combustion of fuel by micro-explosion but increase the amount of CO and HC emissions. Another possible approach that is explored in the current day is the use of nano fuel additives [10, 11]. These nano-sized additives are usually metallic/non-metallic oxide additives that are known to enhance the combustion aspects of BDD blends [12–15].

Novelty in current research

Based on the above-related literature, there is minimal work conducted using feedstocks of waste cooking oil, and variation studies of esterified diesel blends with Nano additives under variation in engine compression ratio. The current research explains the use of Waste cooking oil is taken as feedstock and transesterified to Waste cooking esters and blended with diesel to form a WCO20 blend. Later, copper oxide nano additives are dosed in 10 ppm, 20 ppm, 30 ppm, and 40 ppm levels. Later, these CuO nano-dosed WCO20 blend is fueled in a diesel engine for performance and emissions assessment with diesel and base blend under variations in engine compression ratio.

Materials and methods

Waste cooking oil was collected from local restaurants and filtered to remove impurities. The filtered oil was poured into a transesterification set up with a known volume of LR garde methanol and KOH (LR grade) was added as a reaction catalyst. The reaction time was kept for 2 h and a temperature of 60 °C scale. Later the transesterified ester was separated from the total mixture by the gravity separation process. The methyl ester was later washed several times to remove excel KOH and methanol. The pure waste cooking oil methyl ester was blended with diesel with a volumetric proportion of 20%:80% to form a WCO20 Biodiesel–diesel blend. Collaterally, Copper oxide nano additives were synthesized using a homogenous method using cuprous chloride as precursor salt and potassium hydroxide. The salts were mixed in solvent and filtered and later sintered at 600 °C. The collected CuO particles were noticed for significance and studies using techniques such as XRD, FESEM, and EDS. The XRD studies display the various diffraction peaks which bear a resemblance to JCPDS No 48-1548. Table 1 exhibits the obtained data from XRD (Fig. 1). The FESEM images are shown in Fig. 2 and the average particle size was around 289 nm. Also Fig. 3 provides the Energy-dispersive X-ray spectroscopy of CuO particles. Later, these characterized particles were dissolved in Isopropyl alcohol (100 ml) in levels of 10 mg, 20 mg, 30 mg, and 40 mg and later added to the WCO20 blend to form WCO10 CuO, WCO20 CuO, WCO30 CuO, and WCO40 CuO. So a total of six test fuels four from the above, Diesel and Base WCO20 Blend were taken as diesel engine test fuels (Table 2).

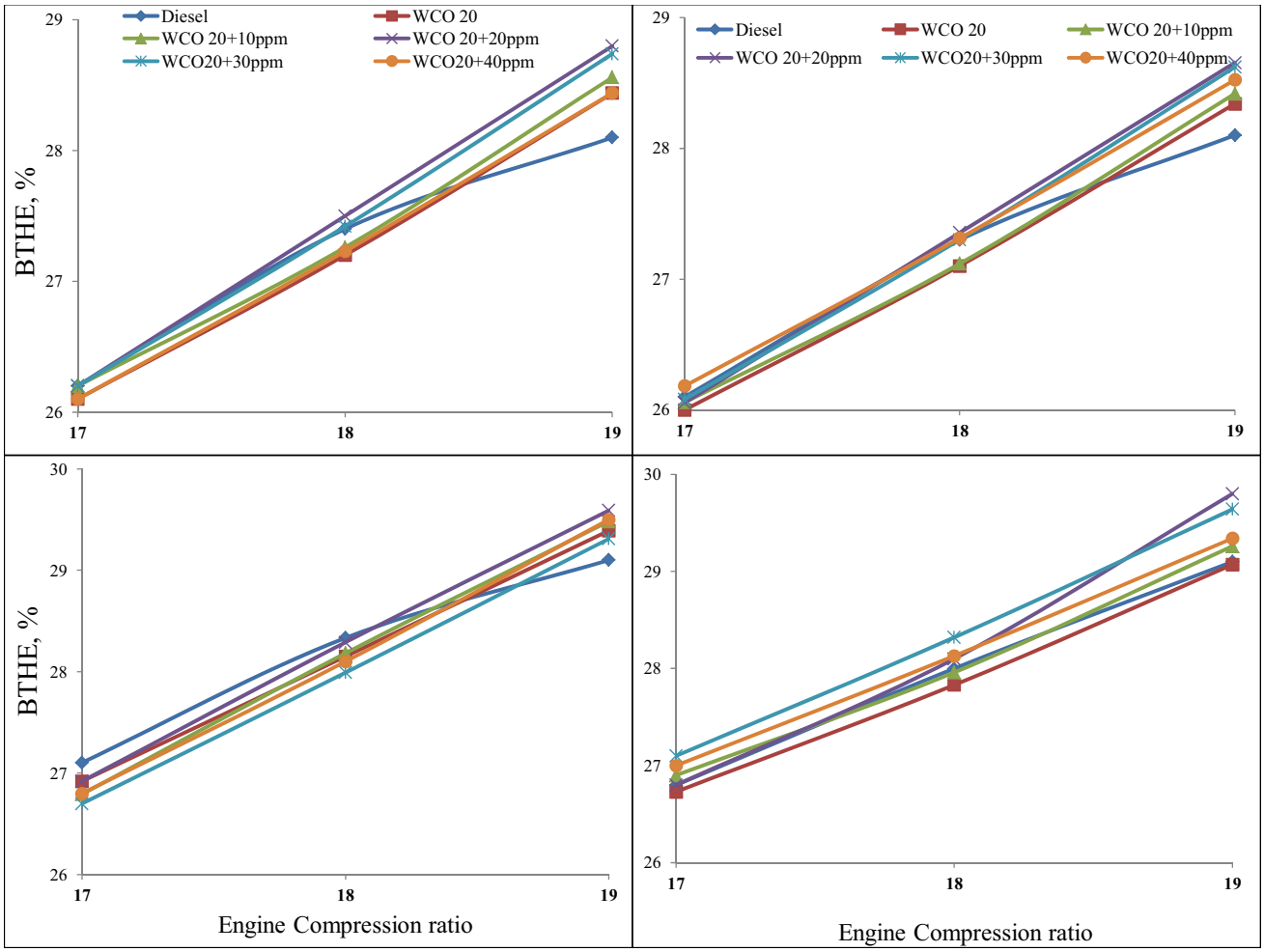

Fig. 5 Variation of brake thermal efficiency at varying engine compression ratios, engine loads and amounts of copper oxides

Experimental test setup

The experimental results were obtained from a modified diesel engine test rig which had a tilting cylinder block assembly to adjust the compression ratio. The schematic diagram of the test setup is shown in Fig. 4 and the test rig specifications are tabulated in Table 3. The Compression ratios were varied at a constant engine crank speed of 1500 rpm and fuel injection timing of 23° bTDC. The engine was coupled to an eddy current dynamometer and was water-cooled. The test fuel properties are tabulated in Table 3. The features of various measuring instruments can be obtained from Table 4 and the overall uncertainty was around ± 2.28%.

Results and discussion

The results observed for all six-test fuels were noted at varying engine loads and Compression ratios. The compression ratios used were 17, 18, and 19. The primary cause for these CRs was that biodiesel–diesel blends bear higher density and viscosity and the Loads were increased by 25%. Each reading was taken 3 times and averaged for observations. All standard procedures were followed during the experimentation process. The results are discussed in two phases. In the first phase, the thermal performance of the engine fuelled with the above fuels is discussed and in the secondary phase, the discussion of the amount of various gases was observed.

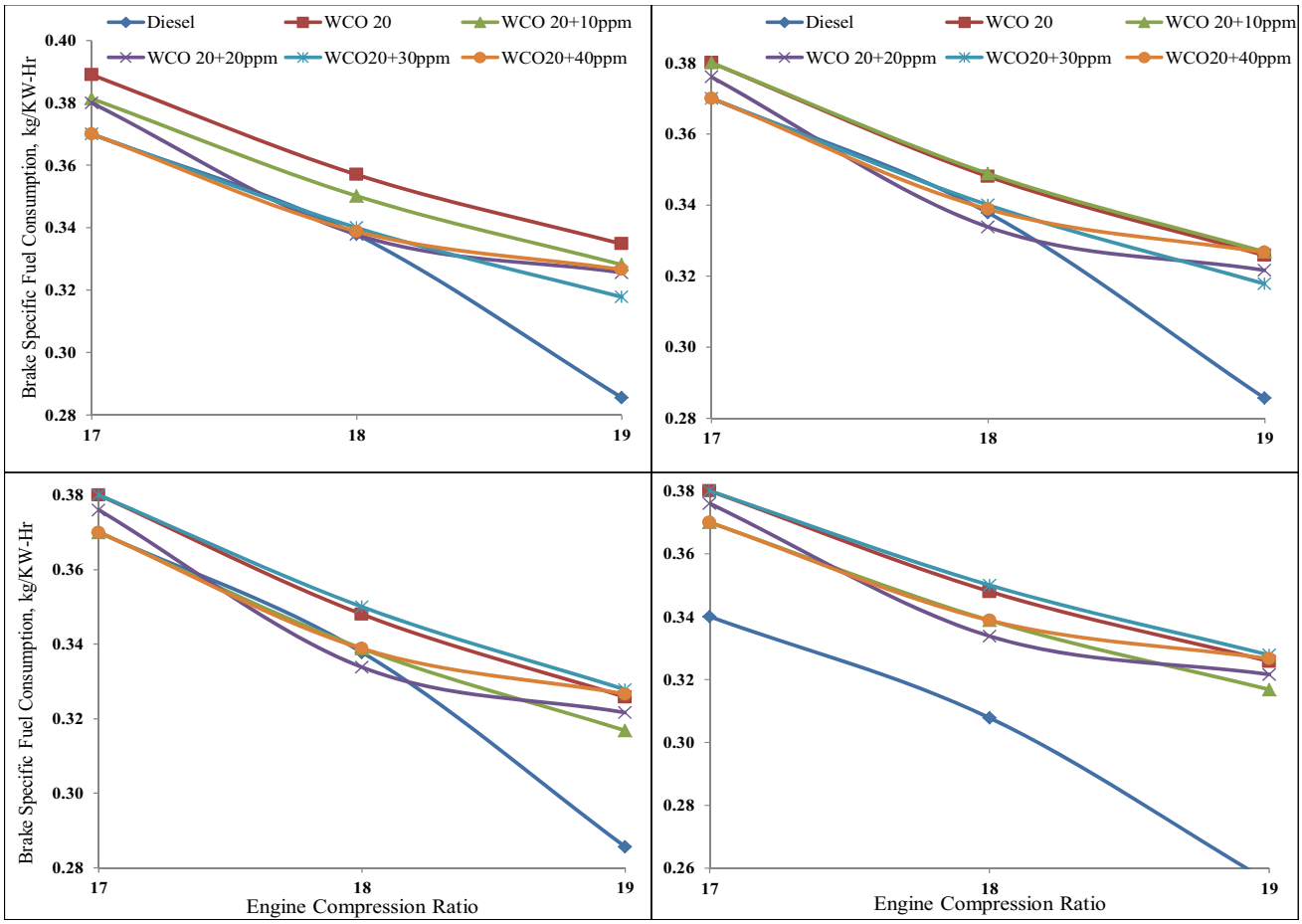

Fig. 6 Variation of brake specific fuel consumption at varying engine compression ratios, engine loads and amounts of copper oxides

Performance characteristics

The Performance parameters observed were thermal efficiency, fuel consumption, and exhaust gas temperature.

Brake thermal efficiency

The thermal performance of the engine fuelled with the above test fuels can be observed in Fig. 5. At all loads, the thermal performance of the engine increased with load incrementation. Also, the Thermal performance observed was higher for the Higher engine volumetric ratio. The main reason for this rise was higher CR leads to greater cylinder air compression, thereby increasing the pressure and compressed air temperature, which leads to quick fuel atomization. Moreover, the addition of CuO in WCO does boost heavily the thermal efficiency of the engine. The percentile hike in the thermal efficiency with the addition of CuO in WCO20 was 2.7, 4.9, 5.6 and 4.7% respectively for 10 ppm, 20 ppm, 30 ppm, and 40 ppm adulteration when compared to WCO20 blend. The amount of rising in thermal efficiency when the engine's volumetric ratio was changed from 18 to 19 for WCO 20, WCO + 10 ppm of CuO, WCO + 20 ppm of CuO, WCO20 + 30 ppm of CuO, and WCO20 + 40 ppm of CuO was 3.19, 4.72, 4.23 and 4.62% respectively. The cause for rising in thermal efficiency was due to the micro explosion of encapsulated isopropyl alcohol having CuO particles and later they pass on the heat to the WCO20 blend and thereby leading to secondary atomization of WCO20. The results were in line with the findings of Srinidhi et al. [16] when they used Nickel oxide nano additives were used as fuel additives in a neem biodiesel blend. They found a similar rise in the BTHE values.

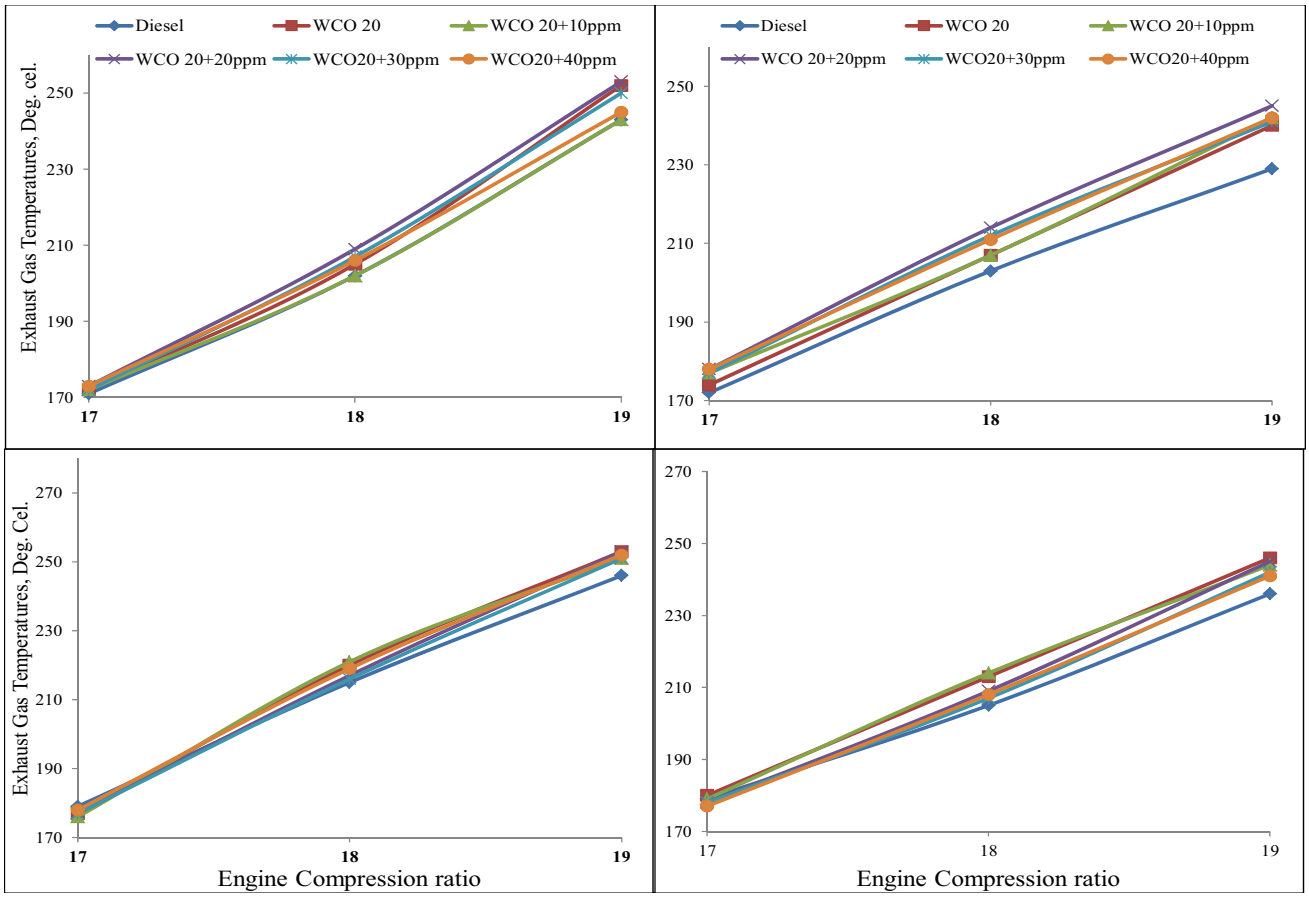

Fig. 7 Variation of exhaust gas tempratures at varying varying engine compression ratios, engine loads and amounts of copper oxides

Brake specific fuel consumption

The specific fuel consumption (SFC) rates for all test fuels could be found in Fig. 6. It's quite prejudiced that biodiesel has a lower calorific value and does have to combust in a greater amount for the same power derived from conventional fuel [17–19]. Figure 6 provides a trend of the SFC of the engine that with rising CR and engine loads, the SFC is lower. Also, the adulteration of Copper oxide does tend to lower the engine SFC values by a small margin. The decline observed in SFC when WCO was dosed with 10 ppm, 20 ppm, 30 ppm, and 40 ppm of CuO was 2.1, 4.1, 3.6 and 3.5% respectively. The least SFC values were observed by Diesel fuel as they bear higher heat content compared to the rest of the 05 test fuels. Furthermore, The decline of SFC values when CR was shifted from 18 to 19 for WCO 20, WCO + 10 ppm of CuO, WCO + 20 ppm of CuO, WCO20 + 30 ppm of CuO, and WCO20 + 40 ppm of CuO was 2.4, 3.6, 3.2 and 3.2%, respectively. The trend of reducing SFC was also observed by Muralidharan and Vasudevan [4] when they used waste frying oil as fuel and at varying compression ratios.

Exhaust gas temperatures

The exhaust temperatures of gases are a critical factor for biodiesel as alternate fuel as EGT plays a vital role in the formation of NOx [1, 20]. Biodiesel which has more oxygen for combustion, than diesel, factors for better combustion features. Due to this, BDD blends are found to factor more EGT than Diesel [21, 22]. Figure 7 explains the EGT for various fuels at varying CR and Engine loads. With the rise in CR values and the engine loads, the EGT values also rose. Also, the addition of CuO in WCO20 does factor in plummeting the EGT of discharge gases. The escalation in EGT was found, when the Engine CR was changed from 17 to 19 for WCO 20, WCO + 10 ppm of CuO, WCO + 20 ppm of CuO, WCO20 + 30 ppm of CuO, and WCO20 + 40 ppm

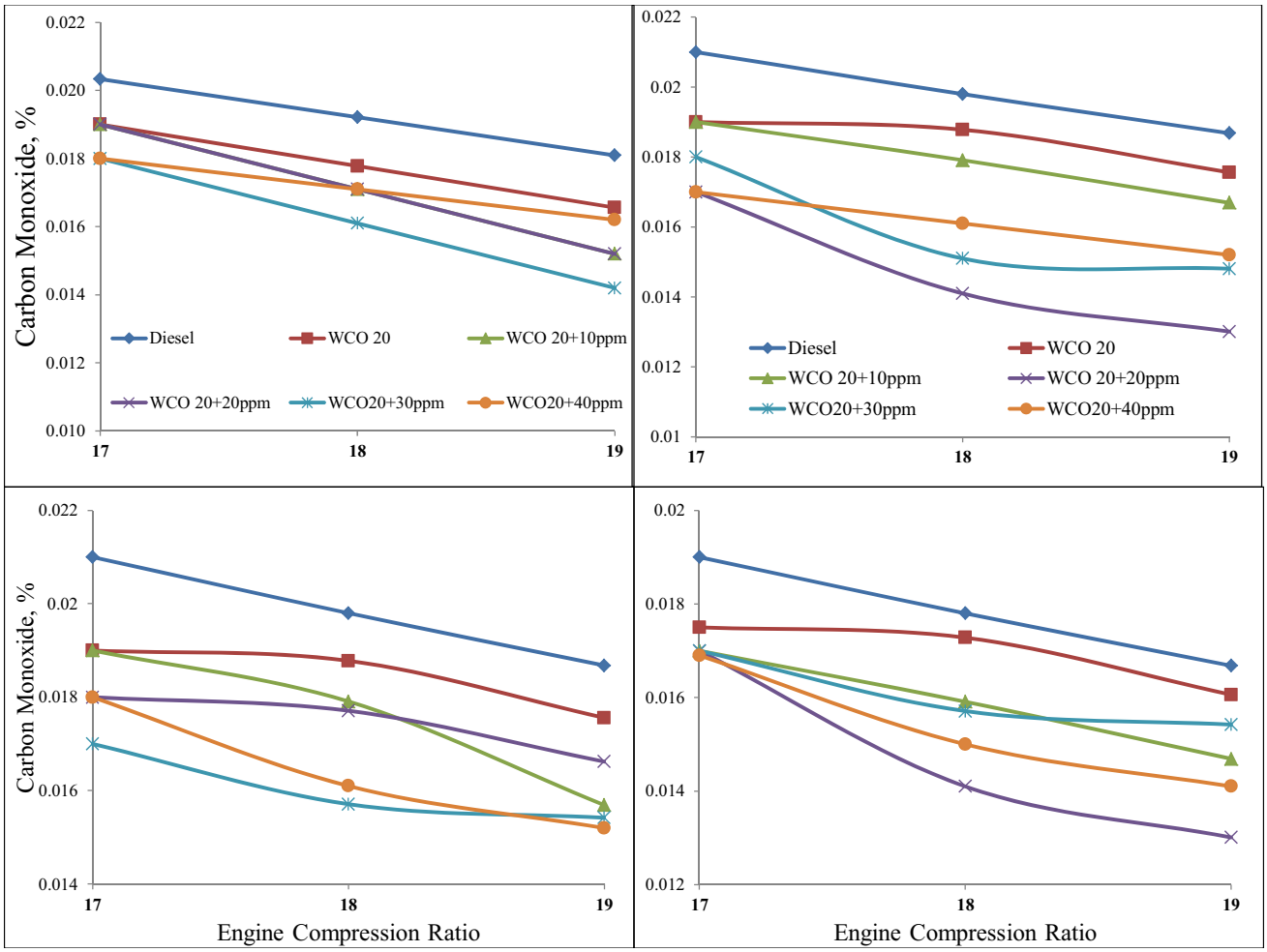

Fig. 8 Variation of CO emissions at varying engine compression ratios, engine loads and amounts of copper oxides

of CuO was 7.6, 8.2, 9.8, 8.8 and 8.9%, respectively when compared to diesel These findings are in line Bora et al. [23] used rice brain type biodiesel with the addition of biogas under varying engine compression ratio.

Emission features

The oxides of carbon emissions

These determine the quality of fuel combustion in the engine. The amount of CO_2 determines the cleanliness of combustion, whereas, CO in the exhaust gases results in the imperfect combustion of fuel blends [24, 25]. Figures 8 and 9 explain the CO and CO_2 gases in the combusted gases. With rising CR and engine loads the CO_2 emission tends to rise whereas the CO emission acts in a reverse trend. The value of Diesel for all engine loads and CR was lowest for CO_2 emission and highest for CO emissions. The primary reason might be due to the combustion phenomenon of the fuel inside the engine. The addition of CuO does add to the quality of fuel combustion of the WCO20 fuel blend. The rise in CO_2 emission due to the doping of CuO in WCO20 with levels of 10 ppm, 20 ppm, 30 ppm, and 40 ppm was 4.8,6.3, 5.9 and 5.8% when compared with WCO20. Also, with the incrementation of engine CR from 18 to 19, the ascent in CO_2 was found to be 5.3, 7.2, 7.9, 7, 6.8 and 7 for Diesel, WCO 20, WCO + 10 ppm of CuO, WCO + 20 ppm of CuO, WCO + 30 ppm of CuO, and WCO + 40 ppm of CuO respectively. On the other hand, the CO emission decent recorded for CuO in WCO20 with levels of 10 ppm, 20 ppm, 30 ppm, and 40 ppm was 3.7, 5.2, 5.1 and 4.9% when compared with WCO20 and with step increase in CR from 18 to 19 was 5.6, 7.1, 7.2, 7.8, 7 and 7.2% for conventional diesel, WCO20 blend, WCO + 10 ppm of CuO, WCO + 20 ppm of

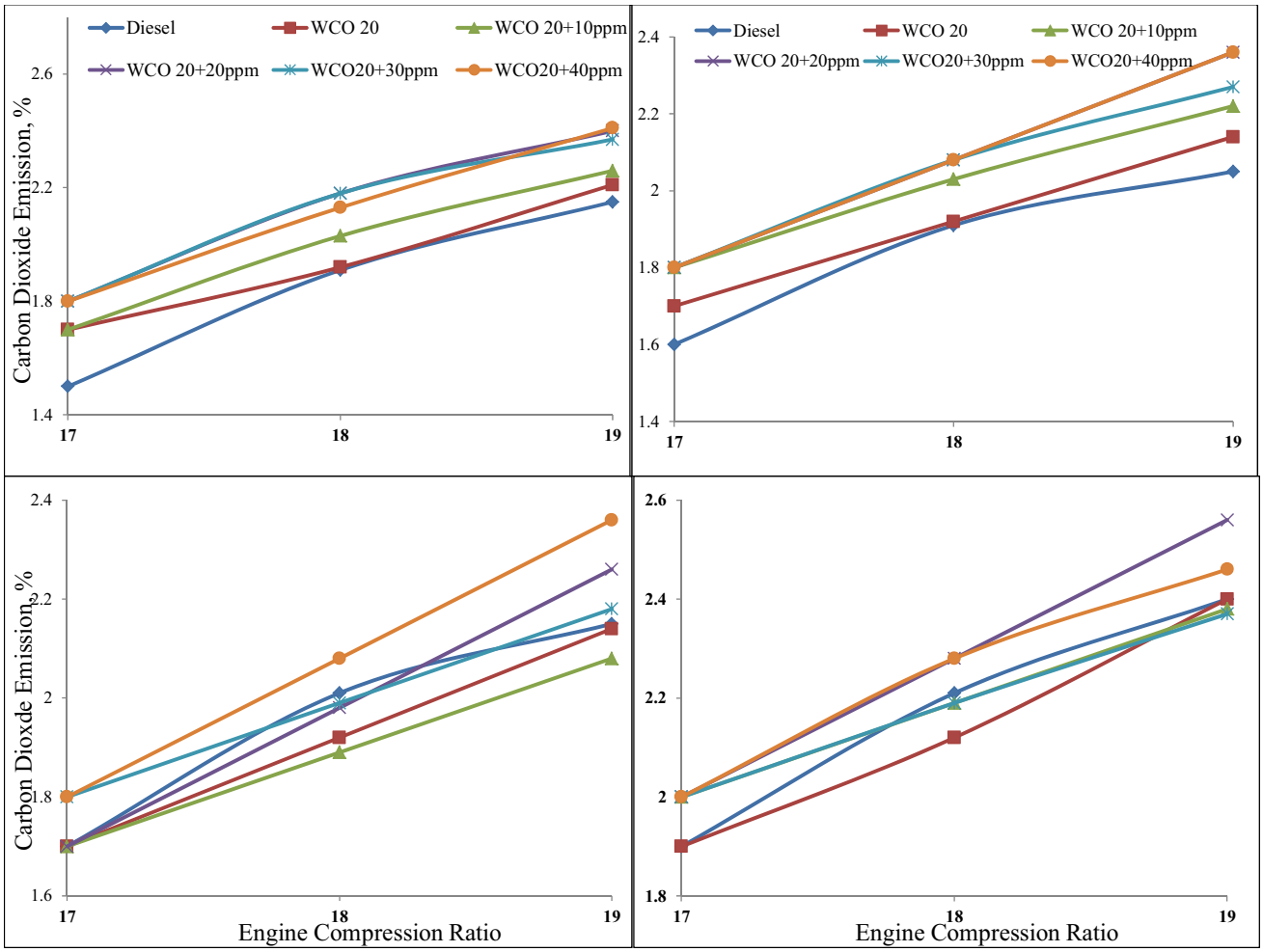

Fig. 9 Variation of CO_2 emissions at Varying Engine Compression Ratios, Engine Loads and amounts of copper oxides

CuO, WCO + 30 ppm of CuO, and WCO + 40 ppm of CuO respectively.

Hydrocarbon emissions

Follow the same trend as that CO emissions. BDD blend shows very low HC emissions, as diesel engines run under lean Air–fuel mixtures [26–28]. Figure 10 depicts the amount of HC emission for all six fuels at varying CR and engine loads. The change in CR from 18 to 19, does promote the combustion activity of fuel and the percentile descent in HC emission for Diesel, WCO 20, WCO + 10 ppm of CuO, WCO + 20 ppm of CuO, WCO + 30 ppm of CuO, and WCO + 40 ppm of CuO is 6.5, 10.76, 11.5, 13.5, 12.75 and 13.1% correspondingly. The addition of Copper oxide particles in WCO20 blends does retard the HC emission largely. The addition of Copper oxide additives in WCO20, plummeted the HC emission by 5.9, 14, 15.7 and 14.6% for 10 ppm, 20 ppm, 30 ppm, and 40 ppm respectively. The findings are in line with Venu et al. [29] when they fuelled diesel engines with diesel–ethanol blends with alumina as a fuel additive. They too postulated that HC emissions tend to retard to a greater extent with the use of nano additives.

NOx emissions

Thermal NOx emissions are one of the limiting points for Biodiesel–diesel blend usage. With the current global emission scenario, alternate fuel researchers are put in a pickle to reduce [30, 31]. Figure 11 draws the representation of NOx for all test fuels, at varying loads and CR. It could be distinguished that NOx emissions were Biodiesel–diesel test fuels. The contamination of CuO in the WCO20 blend scales up the NOx levels to a trivial magnitude. It was witnessed

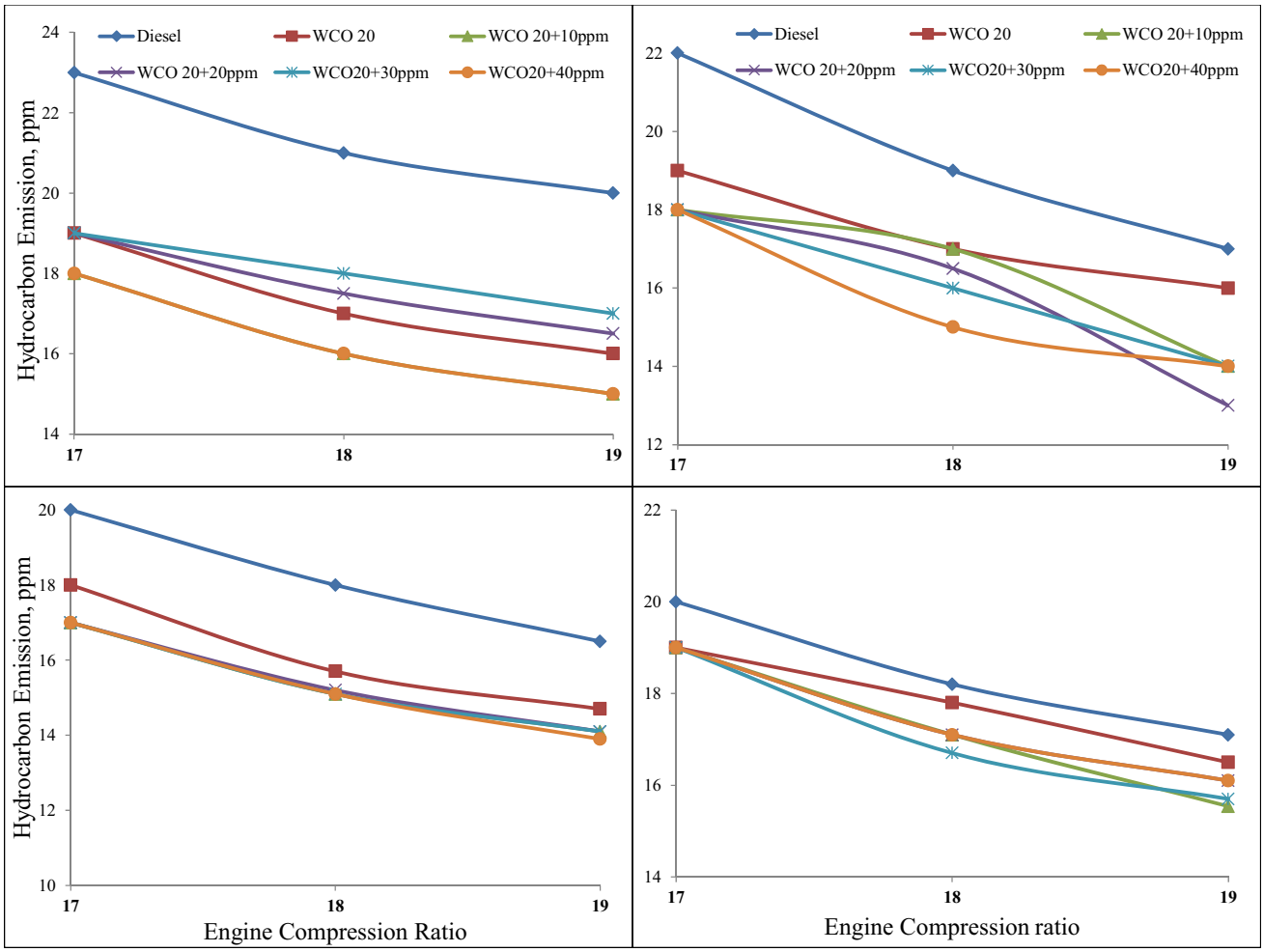

Fig. 10 Variation of HC emissions at varying engine compression ratios, engine loads and amounts of copper oxides

that with CR of 19, the ascent found for NOx with 10 ppm, 20 ppm, 30 ppm, and 40 ppm addition of CuO in WCO20 was found to be 4.3, 5.9, 5.2 and 5.3%, respectively. Srinidhi et al. [16] found a similar rise in NOx levels when the engines were fired with Neem Biodiesel blends under varying compression ratios of 16, 17, and 18 with Nickel oxide levels varying from 25 to 100 ppm.

Conclusion

The current work elaborates on the variance of engine compression ratio studies on the performance and emission features displayed when fuelled with waste cooking oil fuel blends with and without the addition of copper oxide fuel addition. The compression ratio of the engine varied from 17 to 19 and the load of the engine (25, 50, 75 and 100%) for all the above-said test fuels, keeping the fuel injection pressure and timing of fuel entry constant. Based on the above levels of Variation below are some major inferences witnessed.

- The addition of copper oxide nano additives in WCO20 does tend to favor the WCO blend by impeding the viscosity of fuel and but the tradeoff's the density of the fuel.
- The inculcation of Copper oxide Nano-additives in the WCO20 blend subsidizes reducing the ignition delay of fuel thereby reducing the CO and HC emission.
- The inculcation of oxide of Copper and higher CR does accelerate thermal efficiency and Specific Fuel Consumption values. The rise in thermal efficiency when the engine's CR was changed from 18 to 19 for WCO 20, WCO + 10 ppm of CuO, WCO + 20 ppm of CuO, WCO20 + 30 ppm of CuO, and WCO20 + 40 ppm of CuO

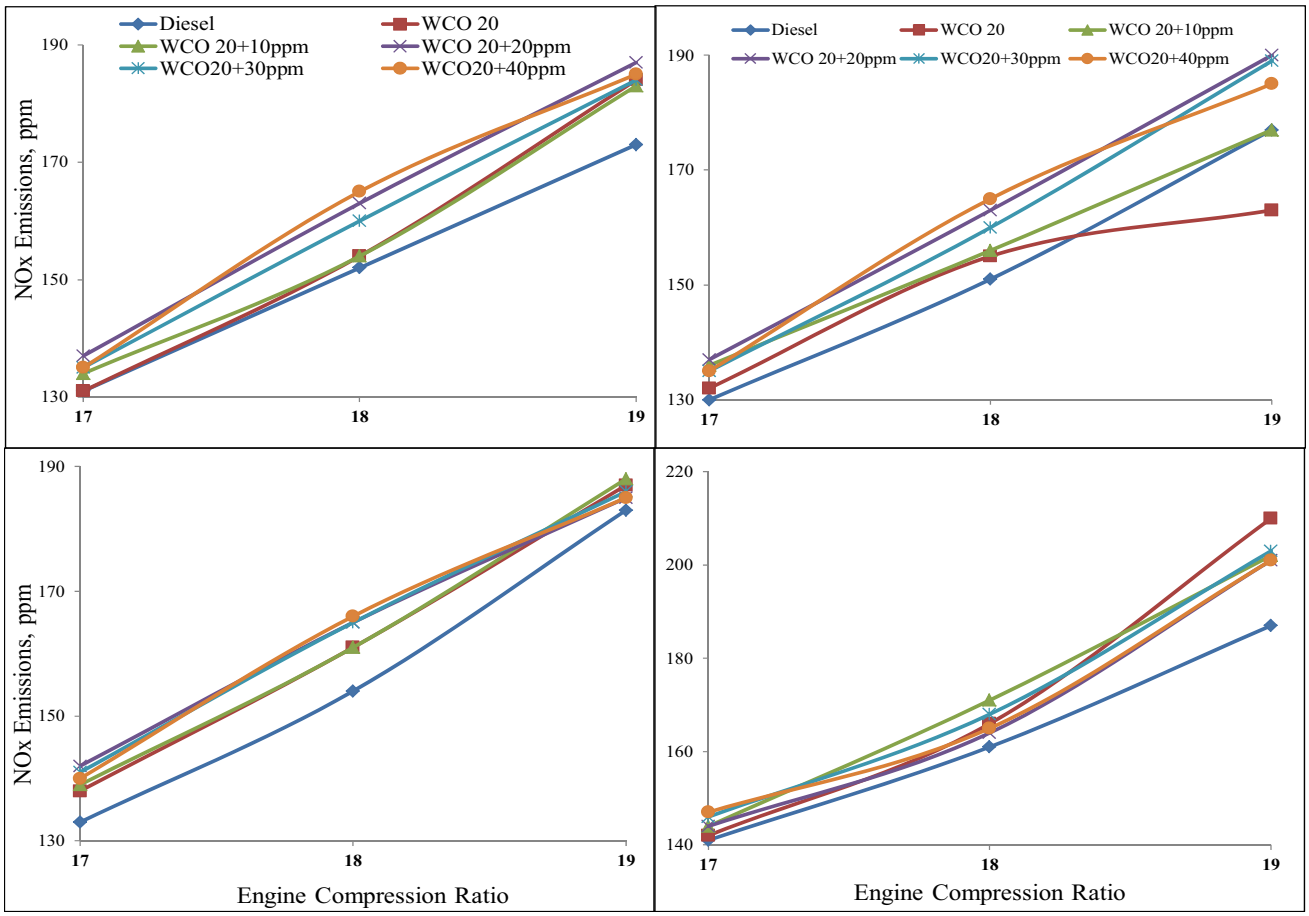

Fig. 11 Variation Of NOx emissions at varying engine compression ratios, engine loads and amounts of copper oxides

was 3.19, 4.72, 4.23 and 4.62% respectively. The decline of SFC values when CR was shifted from 18 to 19 for WCO 20, WCO + 10 ppm of CuO, WCO + 20 ppm of CuO, WCO20 + 30 ppm of CuO, and WCO20 + 40 ppm of CuO was 2.4, 3.6, 3.2 and 3.2% respectively

- Rising CR values do provide a higher NOx amount of rising observed with copper oxides addition was averaged to around 5.9%. The release of unburnt hydrocarbon emissions greatly. Also, the use of Nano additives diminishes the HC release by an average of 26.1%.

Scope for future work

Studies related to the toxicity of combusted fuel and particulate matter could be explored to such to forecast the impact on living beings and environmental aspects.

Data availability Data available on request from the authors.

Declarations

Conflict of interest The authors declare that they have no conflict of interest.

References

1. Srinidhi, C., Kshirsagar, P., Joshi, M., et al.: Effect of fuel injection timing on CI engine fuelled with neem biodiesel blends—a comparative study of experimental and numerical simulation. Int. J. Energy Environ. Eng. **13**, 395–406 (2022). https://doi.org/10.1007/s40095-021-00429-6
2. Srinidhi, C., Jawale, M., Utikar, V., Shraddha, J., Acharya, M., Arakerimath, R., Hole, J.A., Channapattana, S.V.: A comparative performance and emission investigation CI engine fuelled with neem oil esters with varying engine compression ratios. Heat Transf. **51**(8), 7990–8004 (2022)
3. Srinidhi, C., Madhusudhan, A., Channapattana, S.V.: Effect of NiO nanoparticles on performance and emission characteristics

at various injection timings using biodiesel–diesel blends. Fuel **235**, 185–193 (2019). https://doi.org/10.1016/j.fuel.2018.07.067
4. Muralidharan, K., Vasudevan, D.: Performance, emission and combustion characteristics of a variable compression ratio engine using methyl esters of waste cooking oil and diesel blends. Appl. Energy **88**(11), 3959–3968 (2011)
5. Prabhu, A., VenkataRamanan, M., Jayaprabakar, J.: Effect of compression ratio on the performance of CI engine fuelled with freshwater algae biodiesel. Int. J. Ambient Energy **41**(1), 80–83 (2020)
6. Sayin, C., Gumus, M.: Impact of compression ratio and injection parameters on the performance and emissions of a DI diesel engine fueled with biodiesel-blended diesel fuel. Appl. Therm. Eng. **31**(16), 3182–3188 (2011)
7. El-Adawy, M., El-Kasaby, M., Eldrainy, Y.A.: Performance characteristics of a supercharged variable compression ratio diesel engine fueled by biodiesel blends. Alex. Eng. J. **57**(4), 3473–3482 (2018)
8. Srinidhi, C., Madhusudhan, A., Channapattana, S.V., Gawali, S.V.: Comparative investigation of performance and emission features of methanol, ethanol, DEE, and nanoparticles as fuel additives in diesel–biodiesel blends. Heat Transf. **50**, 2624–2642 (2021). https://doi.org/10.1002/htj.21997
9. Selvan, V.A.M., Anand, R.B., Udayakumar, M.: Effects of cerium oxide nanoparticle addition in diesel and diesel, biodiesel, ethanol blends on the performance and emission characteristics of a CI engine. ARPN J. Eng. Appl. Sci. **4**, 1–6 (2009)
10. Soudagar, M.E.M., Nik-Ghazali, N.N., Kalam, M.A., Badruddin, I.A., Banapurmath, N.R., Akram, N.: The effect of nano-additives in diesel–biodiesel fuel blends: a comprehensive review on stability, engine performance and emission characteristics. Energy Convers. Manag. **178**, 146–177 (2018). https://doi.org/10.1016/j.enconman.2018.10.019
11. Srinidhi, C., Madhusudhan, A.: A diesel engine performance investigation fuelled with nickel oxide nano fuel-methyl ester. Int. J. Renew. Energy Res. **7**(2), 676–681 (2017)
12. Saxena, V., Kumar, N., Saxena, V.K.: A comprehensive review on combustion and stability aspects of metal nanoparticles and its additive effect on diesel and biodiesel fuelled C.I. engine. Renew. Sustain. Energy Rev. **70**, 563–588 (2017). https://doi.org/10.1016/j.rser.2016.11.067
13. Kannan, G.R., Karvembu, R., Anand, R.: Effect of metal based additive on performance emission characteristics of diesel engine fuelled with biodiesel. Appl. Energy **88**, 3694–3703 (2011)
14. Nanthagopal, K., Ashok, B., Tamilarasu, A., Johny, A., Mohan, A.: Influence on the effect of zinc oxide and titanium dioxide nanoparticles as an additive with *Calophyllum inophyllum* methyl ester in a CI engine. Energy Convers. Manage. **146**, 8–19 (2017)
15. Ranjan, A., Dawn, S., Jayaprabakar, J., Nirmala, N., Saikiran, K., Sriram, S.S.: Experimental investigation on effect of MgO nanoparticles on cold flow properties, performance, emission and combustion characteristics of waste cooking oil biodiesel. Fuel **220**, 780–791 (2018)
16. Campli, S., Acharya, M., Channapattana, S.V., Pawar, A.A., Gawali, S.V., Hole, J.: The effect of nickel oxide nano-additives in *Azadirachta indica* biodiesel–diesel blend on engine performance and emission characteristics by varying compression ratio. Environ. Prog. Sustain. Energy **40**, e13514 (2021)
17. Agarwal, A.K., Srivastava, D.K., Dhar, A., Maurya, R.K., Shukla, P.C., Singh, A.P.: Effect of fuel injection timing and pressure on combustion, emissions and performance characteristics of a single-cylinder diesel engine. Fuel **111**, 374–383 (2013). https://doi.org/10.1016/j.fuel.2013.03.016
18. Shaafi, M.B., Daneshvar, F., Jahani, N., Mobini, K.: Effect of ferrofluid on the performance and emission patterns of a four stroke diesel engine. Adv. Mech. Eng. **3**, 1–5 (2011)
19. Sarvestany, S.N., Farzad, A., Bajestan, E.E., Mir, M.: Effects of magnetic nanofluid fuel combustion on the performance and emission characteristics. J. Dispers. Sci. Technol. **08**, 1745–1750 (2014)
20. Rajak, U., Verma, T.N.: Influence of combustion and emission characteristics on a compression ignition engine from a different generation of biodiesel. Int. J. Eng. Sci. Technol. **23**(1), 10–20 (2020)
21. Raheman, H., Ghadge, S.V.: Performance of diesel engine with biodiesel at varying compression ratio and ignition timing. Fuel **87**(12), 2659–2666 (2008). https://doi.org/10.1016/j.fuel.2008.03.006
22. Sharma, A., Murugan, S.: Potential for using a tyre pyrolysis oil–biodiesel blend in a diesel engine at different compression ratios. Energy Convers. Manag. **93**, 289–297 (2015)
23. Bora, B.J., Saha, U.K.: Experimental evaluation of a rice bran biodiesel–biogas run dual fuel diesel engine at varying compression ratios. Renew. Energy **87**, 782–790 (2016)
24. Ong, H.C., Masjuki, H.H., Mahlia, T.M., Silitonga, A.S., Chong, W.T., Leong, K.Y.: Optimization of biodiesel production and engine performance from high free fatty acid *Calophyllum inophyllum* oil in CI diesel engine. Energy Convers. Manag. **81**, 30–40 (2014)
25. Ong, H.C., Silitonga, A.S., Masjuki, H.H., Mahlia, T.M., Chong, W.T., Boosroh, M.H.: Production and comparative fuel properties of biodiesel from non-edible oils: *Jatropha curcas*, *Sterculia foetida* and *Ceiba pentandra*. Energy Convers. Manag. **73**, 245–255 (2013)
26. Debnath, B.K., Saha, U.K., Sahoo, N.: A comprehensive review on the application of emulsions as an alternative fuel for diesel engines. Renew. Sustain. Energy Rev. **42**, 196–211 (2015)
27. Ithnin, A.M., Ahmad, M.A., Bakar, M.A., Rajoo, S., Yahya, W.J.: Combustion performance and emission analysis of diesel engine fuelled with water-in-diesel emulsion fuel made from low-grade diesel fuel. Energy Convers. Manag. **90**, 375–382 (2015)
28. Serrano, J., Jiménez-Espadafor, F.J., López, A.: Analysis of the effect of different hydrogen/diesel ratios on the performance and emissions of a modified compression ignition engine under dual-fuel mode with water injection. Hydrogen-diesel dual-fuel mode. Energy **172**, 702–711 (2019). https://doi.org/10.1016/j.energy.2019.02.027
29. Venu, H., Madhavan, V.: Effect of Al_2O_3 nanoparticles in biodiesel–diesel–ethanol blends at various injection strategies: performance, combustion and emission characteristics. Fuel **186**, 176–189 (2016). https://doi.org/10.1016/j.fuel.2016.08.046
30. Srinidhi, C., Madhusudhan, A., Channapattana, S.V.: Comparative analysis of exhaust gas recirculation and nanoparticles on the performance and emission of diesel engine fuelled with neem biodiesel blend. Int. J. Ambient Energy (2019). https://doi.org/10.1080/01430750.2019.1636876
31. Channapattana, S.V., Pawar, A.A., Kamble, P.G.: Investigation of DI-CIfour stroke VCR engine at different fuel injection timing using bio-fuel derived from non-edible oil source as a fuel. Biofuels (2016). https://doi.org/10.1080/17597269.2016.1187540

International Journal of Energy and Environmental Engineering (2023) 14:829–839
https://doi.org/10.1007/s40095-022-00551-z

ORIGINAL RESEARCH

Evaluation of adsorption properties of organic wastes in aqueous media for arsenic removal

Augustine Nana Sekyi Appiah[1,3] · Lucas Nana Wiredu Damoah[1] · Yaw Delali Bensah[1] · Peace Korshiwor Amoatey[1] · Daniel Nukpezah[2] · Aubin Aholouvi[1] · Ebenezer Annan[1]

Received: 7 June 2022 / Accepted: 12 November 2022 / Published online: 21 November 2022

Abstract

Arsenic is toxic and one of the most prominent environmental challenges especially in water quality. The World Health Organization recommends 10 µg/L as the acceptable level limit in drinking water. The use of materials that are easily reproducible, economical and are envisaged as 'waste' is paramount in water treatment technologies sustainability. In this study, organic wastes: rice husks (RH) and orange peels powder (OPP) were used as adsorbents in arsenate contaminated drinking water treatment to ascertain purification properties. The adsorbents were processed into two different particle sizes: 841 µm and 42.5 µm powders via sieve analysis. These adsorbents were characterized using scanning electron microscopy and Fourier transform infrared spectroscopy for morphological and functional group studies, respectively. The batch adsorption studies show that arsenic removal efficiency of the adsorbents with smaller particle size (425 µm) was greater than with larger particle size (841 µm) being 96.38% and 82.2%, respectively, for the same mass of rice husk (RH). The adsorption mechanisms for the rice husk (RH) can be described as chemisorption process since it best fits the pseudo-second-order model. The isotherm modeling of the adsorption data was found to be described using the Freundlich isotherm model. The adsorption data for orange peels powder (OPP) were, however, best described by Langmuir isotherm and pseudo-second-order kinetics models. The organic wastes, RH and OPP were found to be efficient in the removal of Arsenic(V) from contaminated waters.

Keywords Arsenic · Contaminated water · Rice husk · Orange peels · Adsorption

Introduction

Arsenic is toxic and one of the most prominent environmental challenges. The World Health Organization (WHO) recommends 10 µg/L as the acceptable level of arsenic in drinking water. When the concentration exceeds the 10 µg/L limit, the exposed population experiences serious health problems [1, 2]. The health issues include stomach, intestinal, liver, kidney, and heart disorders, neurological, dermal hematopoietic, reproductive, and carcinogenic diseases [3]. Many countries have reported arsenic contamination, and some are under the threat of arsenic pollution. Turkey has been identified as one of the countries under the threat with

✉ Ebenezer Annan
ebannan@ug.edu.gh

Augustine Nana Sekyi Appiah
ansappiah@st.ug.edu.gh; augustine.appiah@polsl.pl

Lucas Nana Wiredu Damoah
lnwdamoah@ug.edu.gh

Yaw Delali Bensah
ydbensah@ug.edu.gh

Peace Korshiwor Amoatey
pkamoatey@ug.edu.gh

Daniel Nukpezah
dnukpezah@staff.ug.edu.gh

Aubin Aholouvi
aubinaholouvi@gmail.com

[1] Department of Materials Science and Engineering, School of Engineering Sciences, University of Ghana, Legon, Ghana

[2] Institute for Environment and Sanitation Studies, University of Ghana, Legon, Ghana

[3] Materials Research Laboratory, Faculty of Mechanical Engineering, Silesian University of Technology, 18A, Konarski Street, 44-100 Gliwice, Poland

high values ranging from 10 to 7754 mg/L being reported in the western regions of the country [4].

In Africa, low concentrations of arsenic contamination have been reported in countries such as Tanzania, Botswana, and Bukina Faso [5, 6] and high levels have been observed in water bodies in Ghana, Ethiopia, Morocco, and Zimbabwe [7, 8]. Most mining communities are found to have high arsenic levels [9, 10]. Prestea, a city in Ghana, is reported to have range of arsenic levels from 150 to 8250 µg/L. Ahmed and Carboo [11] published on speciation of As (+3) and As (+5) in some Ghanaian gold tailings and observed that the absence of As (+3) in riverbed sediment, attributable to the fact that As (+3) is oxidized to As (+5) by dissolved oxygen. However, Smedley et al. [12] found some streams which have high As (+3) content ([As (+3)]/[As total] > 0.5), probably as a result of methylation and reduction reactions mediated by bacteria and algae. Arsenic (+5) is the most common type in ground water in Ghana.

Arsenic can exhibit various oxidation states (−3, 0, +3, +5 oxidation states) depending on the redox conditions with arsenite (+3) and arsenate (+5) existing as main oxyanions. While the monovalent anionic species of arsenate ($H_2AsO_4^-$) is predominant at a pH of 2–6, arsenite $H_2AsO_3^-$ is significant at the pH of 9–12. In surface waters, the oxidized forms: arsenite and arsenate are the most widespread species [13, 14]. In soils, arsenate is the predominant form under oxidizing conditions whereas arsenite is the major form of arsenic that occurs under reducing conditions [15]. Arsenic(III) (As (+3)) is more toxic and difficult to remove with conventional physiochemical treatment methods as compared with Arsenic(V), As (+5).

Many methods, including co-precipitation with iron or alum, adsorption unto coagulated floc, ion-exchange resin, reverse osmosis and membrane techniques, have been used in removing arsenic from drinking water [16, 17]. The most economical, reliable, and convenient technique is adsorption [18]. Arsenic removal via adsorption can be accomplished using natural iron containing minerals, titanium dioxide, zerovalent iron, red mud, magnetic nanoparticles, however high costs are associated with these adsorbents [19]. Current literature has explored and reported the arsenic removal tendencies of inexpensive adsorbents such as shrimp shells [20], modified zeolite [21], modified fungal biomass [22], and modified coconut coir pith [23]. Most of these reported materials in their natural form, need further chemical or physical treatments before being used. The low concentration effectiveness of these materials has also not been of priority in the reported literature. Therefore, alternative low-cost options especially agricultural waste such as corn cobs, corn husks, coconut coir, rice husk and banana peels usage as adsorbent without any chemical or extensive physical treatment might hold potential for water treatment application and requires to be explored. It is important to choose an adsorbent which have key compositions to reduce or remove completely targeted contaminant.

Rice husk is available in many countries as an agricultural waste. It has been identified as a potential adsorbent due to its granular structure, low cost, insolubility in water, high chemical stability, and mechanical strength. Every ton of rice produces about 23% of rice husk which is normally burnt, releasing carbon dioxide and other pollutants into the atmosphere. Thus, using rice husk as a potential bio-adsorbent will ultimately result in better waste management and a reduction in pollution. The main composition of rice husk are carbon and silica with geographically varying percentages of cellulose, hemicellulose, lignin, water, mineral ash (of about 96.34% silica content) [24].

This study therefore explores the arsenic adsorption tendencies of locally available inexpensive rice husks and orange peels in their powdered form, without modification, in reducing arsenic content in aqueous media to acceptable levels in drinking water. The success of this approach will make it easy for such an arsenic remediation procedure to be replicated without extensive technical know-how. The objectives include the selection and preparation of organic wastes as adsorbents for arsenic removal, characterization of the adsorbents using Fourier transform infrared spectroscopy (FTIR) and scanning electron microscopy (SEM). The removal efficiency of the adsorbents will be investigated as well as the isotherm models. The two most basic and widely used isotherm models, Langmuir and Freundlich models, will be employed in the isotherm modeling of the adsorption data.

Materials and methods

Preparation and characterization of adsorbents

Preparation of rice husks (RH)

Raw rice husks were obtained from the University of Ghana (UG) farms. It was thoroughly washed to remove all dirt and other physically adhered foreign materials until the decanted deionized water was observed to be colorless, and then air-dried for 1 week at room temperature (35 °C). The air-dried RH was further dried in an oven at 80 °C for 24 h. The dried RH was then milled and sieved into 425 µm and 841 µm particle sizes using the RETSCH sieve shaker AS 200 (RETSCH Mill, Germany).

Preparation of orange peel powders (OPP)

Orange peels obtained from local market, Madina Market in the Greater Accra region in Ghana were washed thoroughly with de-ionized water to remove all physically attached

particles and surface impurities. The peels were then air-dried for 1 week at room temperature 24 °C and later kept in an oven at 60 °C for 6 h to ensure effective removal of moisture. The dry peels were then milled into powder with a CB15 blender (Waring Commercial, USA) and sieved to particle sizes of 425 µm and 841 µm using the RETSCH sieve shaker AS 200.

Characterization

The adsorbents (RH and OPP) were characterized using FTIR and SEM. The Fourier transform infrared spectroscopy (FTIR, Bruker Tensor 2027 FTIR spectrometer) was used to identify the functional groups present on the surface of the adsorbent samples whereas Supra 35 (Zeiss, Oberkochen, Germany) was used for the morphology studies.

Chemicals

All chemicals used in this study were analytical grade purchased from Sigma-Aldrich. The experiments were carried out using distilled water and the pH adjusted with either sodium hydroxide (NaOH) or hydrochloric acid (HCl) where necessary. A 1000 µg/L stock solution (Sodium Arsenate) was prepared and diluted when required for experiments.

Batch adsorption experiments

The prepared RH was used without any further physical or chemical treatment. A gram of each size of RH was used separately in the batch adsorption process of 100 ml stock solution of sodium arsenate for respective times: 20, 40, 60, 80, 100 and 120 min. The adsorbent in the sodium arsenate solution (which has a concentration of 100 µg/L) was thoroughly mixed using Orbital shaker (4500 rpm) for the allowed duration. The solution was then sieved using Whartman 1 filter paper with 11 µm as the pore size. The effluent from filtration was then analyzed for the concentration of Arsenic(V) ions using Atomic Absorption Spectroscopy (GTA 120 Graphite Tube Atomizer, Agilent Technologies, USA). This procedure was repeated in increment steps of 2 from 2 to 10 g for each of the RH particle sizes.

The removal efficiency was calculated using the equation

$$R\% = \left(\frac{C_o - C_e}{C_o}\right) \times 100 \tag{1}$$

where $R\%$ is the percentage of Arsenic(V) ions adsorbed. Again, the adsorptive capacity, q, is given by the expression,

$$q = \left(C_o - C_e\right)V/m \tag{2}$$

where q is the As(V) adsorbed (mg/g), C_o is the initial concentration of Arsenic(V) in solution (mg/L), C_e is the concentration of Arsenic(V) in solution at equilibrium time (mg/L), V is the solution volume (L), and m is the adsorbent dosage (g).

Adsorption isotherm models

Freundlich model

The Freundlich isotherm model is based on the assumption that an increase in the concentration of the adsorbate increases quantity of adsorbate on the adsorbent surface, and this exponentially decreases the sorption energy upon completion of the sorption centers of the adsorbent [25, 26]. A linear form of the Freundlich isotherm model is given as

$$\log q_e = \log k_f + \frac{1}{n}\log C_e \tag{3}$$

where q_e is the amount of adsorbate adsorbed at equilibrium; k_f is the Freundlich constant; $1/n$ is the heterogeneity factor relating to the capacity and intensity of the adsorption; C_e is the concentration of the solution at equilibrium. The adsorption characteristics can be deduced from the value of n; when $n=1$, adsorption is linear; when $n<1$, adsorption is unfavorable and when $n>1$, adsorption is favorable.

Langmuir model

The Langmuir model assumes that the point of valance exists on the surface of the adsorbent and that each of these sites is capable of adsorbing one molecule. Again, it is assumed that the adsorption sites have equal affinities for molecules of adsorbate and that the presence of adsorbed molecules at one site will not affect the adsorption of molecules at an adjacent site [27]. The Langmuir model expression can be linearized as in Eq. (4).

$$\frac{C_e}{q_e} = \frac{C_e}{q_m} + \frac{1}{q_m b_L} \tag{4}$$

where q_e is the amount of adsorbate adsorbed in mg/g; C_e is the concentration of the adsorbate at equilibrium in mg/L; q_m and b_L are Langmuir constants related to maximum adsorption capacity (mg/g) and energy of adsorption (L/mg). A graph of C_e/q_e versus C_e, which is a straight line, will have a slope of $1/q_m$ and an intercept of $1/q_m b_L$. For an adsorption to obey the Langmuir isotherm model, it must satisfy the conditions of a dimensionless factor, R_L based on the slope and intercept of the graph. The dimensionless factor is related to the Langmuir constant b_L, and the initial adsorbate concentration C_0 as

$$R_{L=} = \frac{1}{1 + b_L + C_0} \tag{5}$$

The type of adsorption is indicated by the value of R_L such that when R_L is less than 1, adsorption is favorable; when R_L is equal to 1, adsorption is linear; when R_L is between 0 and 1, adsorption is favorable; when R_L is 0, adsorption is irreversible [28].

Adsorption kinetics models

The experimental data for the arsenic adsorption can be simulated by the pseudo-first-order (PFO) and pseudo-second-order (PSO) kinetic models [29]. The linear forms of the two equations were adopted to aid understanding of the uptake of arsenic from aqueous medium.

Pseudo-first order

The equation for the pseudo-first order is given in Eq. (6) and it assumes that the rate of change in solute adsorption over time is directly proportional to the difference in saturation concentration and the amount of adsorptive solid uptake over time [30]. The adsorption data obtained experimentally were fitted to the equation. When the *R*-square of the fit is superior compared with others, the adsorption data can be described by physio-sorption mechanism.

$$\mathrm{Log}\left(q_e - q_t\right) = \mathrm{Log}q_e - \frac{k_1}{2.303}t \tag{6}$$

where q_e and q_t are the amount of Arsenic(V) adsorbed (mg/g) at equilibrium and any time t, respectively, and k_1 (min^{-1}) is the rate of constant of adsorption for pseudo-first order.

Pseudo-second order

The equation for the pseudo-second order is given in Eq. (7). Adsorption data that fits this model can be described by chemisorption.

$$\frac{t}{q_t} = \frac{1}{\left(k_2 q_t^2\right)} + \frac{t}{q_t} \tag{7}$$

k_2 (min^{-1}) is the rate of constant for pseudo-second order constant.

Results

The performance of RH and OPP was evaluated for the removal of arsenate from aqueous solution. Two different sizes of the RH at different contact times (up to 120 min maximum) were used for the adsorption studies. The potential of OPP to adsorb arsenic was also explored.

Morphology of adsorbent powders

The SEM images of the adsorbents are shown in Fig. 1. Figure 1a shows numerous curved surfaces on the rick husks. Each plate appears to have uniform mini indentations. Figure 1b can be observed to have several smaller cavities on the surfaces of the OPP. The sample has channels that supports removal of contaminants.

FTIR characterization

Figure 2 shows the FTIR spectra for adsorbents rice husk and orange peels before and after adsorption. Table 1 indicates the assignments for the various regimes of the spectra. In the case of RH, the peak at 3400 cm^{-1} represents OH stretching. The band within 1000–1200 cm^{-1} from this region indicate the presence of C–O–C bonds from organic compounds. The high intensity of the peak at 1040 cm^{-1} was attributed to the superimposition of the vibrations from these two bonds [31]. Vibrations within the range of wave numbers 469–800 cm^{-1} were attributed to Si–H bonds within the husk.

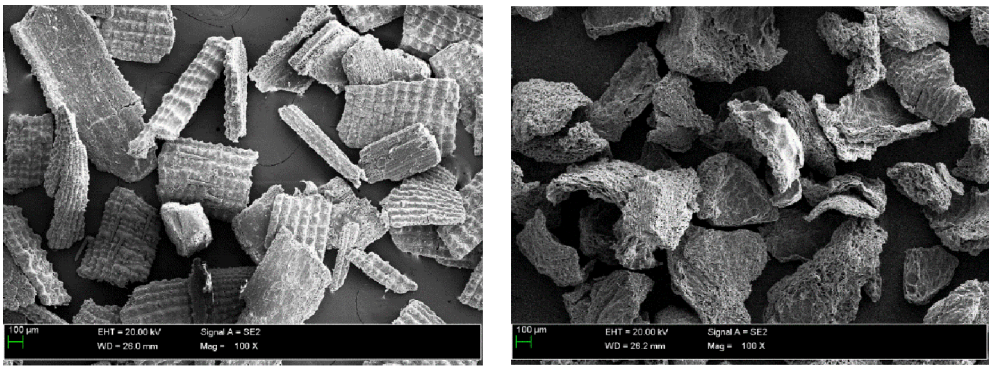

(a) (b)

Fig. 1 SEM images of adsorbent powders **a** RH **b** OPP

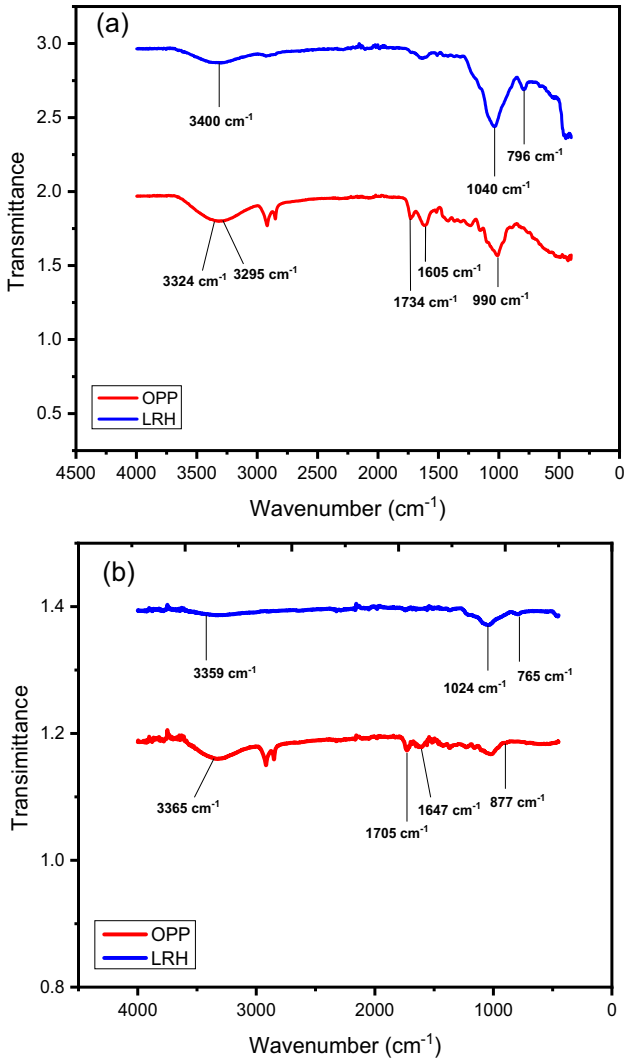

Fig. 2 FTIR spectra of OPP and RH adsorbents **a** before adsorption of arsenic **b** after adsorption of arsenic

Effects of particle size on adsorption efficiency

The average removal efficiencies of the RH and OPP adsorbents for both the 841 µm and 425 µm particle sizes are shown in Fig. 3a and b, respectively. For RH adsorbent, the comparison plots show that the average removal efficiencies of the 425 µm particle size adsorbent (ranging from 78.88 to 94.13%) were greater than that of the 841 µm particle size adsorbent (ranging from 47.57 to 72.74%). A similar trend was observed from the plots in Fig. 3b, which compares the average removal efficiencies of the individual doses of the OPP adsorbent used for both particle sizes. The plots show that the range of values of the average removal efficiencies of the masses of the 425 µm particle size adsorbent (ranging from 82 to 100%) was greater than that of the 841 µm particle size adsorbent (ranging from 71 to 100%). The optimum value of the particle size of the RH was 425 µm.

Effect of contact time on removal efficiency

The effect of contact time of the RH adsorbents with the arsenic solution for its removal efficiency was studied for different masses of the adsorbent; 2 g, 4 g, 6 g, 8 g and 10 g (Fig. 4). Each mass was allowed a maximum of 120 min of contact time with the Arsenic solution. The adsorption behavior for each of the masses is presented in Fig. 4a. For the 2 g mass, the removal efficiency was 71.02% at 20 min of contact. The removal efficiency for the 10 g mass was 89.46% after 20 min of contact and kept increasing until at 100 min of contact, when equilibrium was seen to occur with an efficiency of 95.98%. It was observed that, the optimal removal efficiency occurred with 8 g dosage of adsorbent, which recorded as high as 96.38% removal efficiency. The general observation from the study showed that, the removal efficiency of arsenic by the RH adsorbents increases with increasing contact time with arsenic contaminated solution.

Figure 4b shows the effect of time on the removal efficiency of arsenic by the OPP adsorbents. For all the different masses used, it was observed that the removal efficiency was time-dependent. For the 2 g mass, the removal efficiency was 80% at 20 min of contact with the adsorbate solution. After 80 min, the removal efficiency was 100%, which was the maximum removal efficiency for the mass. After the mass was increased to 4 g, the removal efficiency

Table 1 FTIR spectra assignments for shift observations in adsorbents before and after adsorption

Adsorbent	IR peak before adsorption (cm^{-1})	IR peak after adsorption (cm^{-1})	Shift (cm^{-1})	Assignment
RH	3400	3359	−41	–OH and Si–OH vibrations
	1040	1024	−16	Si–O–Si vibrations and secondary cyclic alcohols C–OH stretching
	796	765	−31	Si–H stretching
OPP	3324	3365	41	Bonded –OH groups
	3295	3266	−29	Bonded –OH groups
	1734	1705	–29	C=O vibrations
	1605.27	1647.64	42.37	C=O vibrations

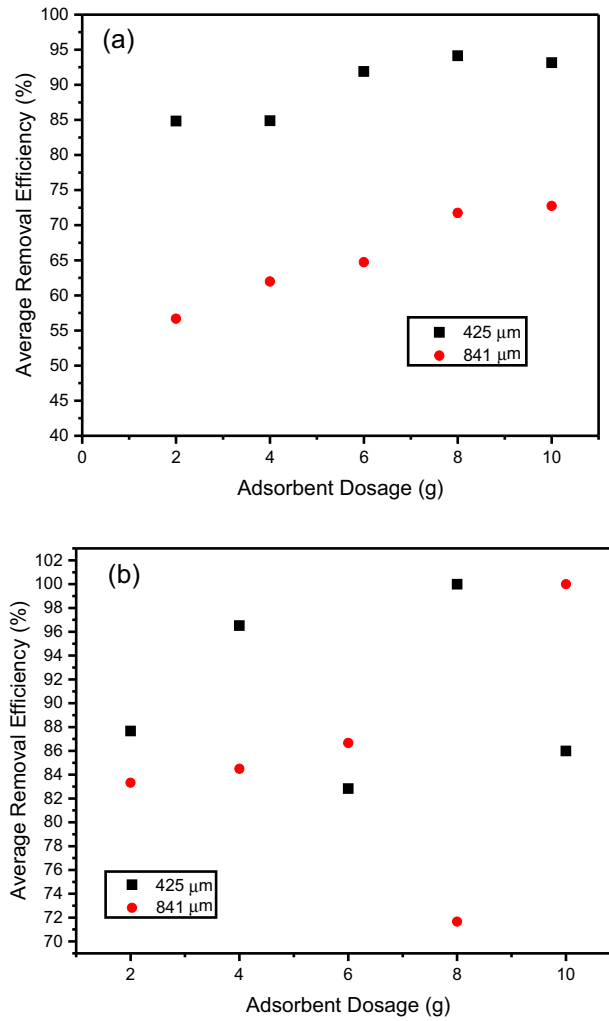

Fig. 3 **a** RH Average removal efficiencies for 425 µm and 841 µm **b** OPP Average removal efficiencies for 425 µm and 841 µm

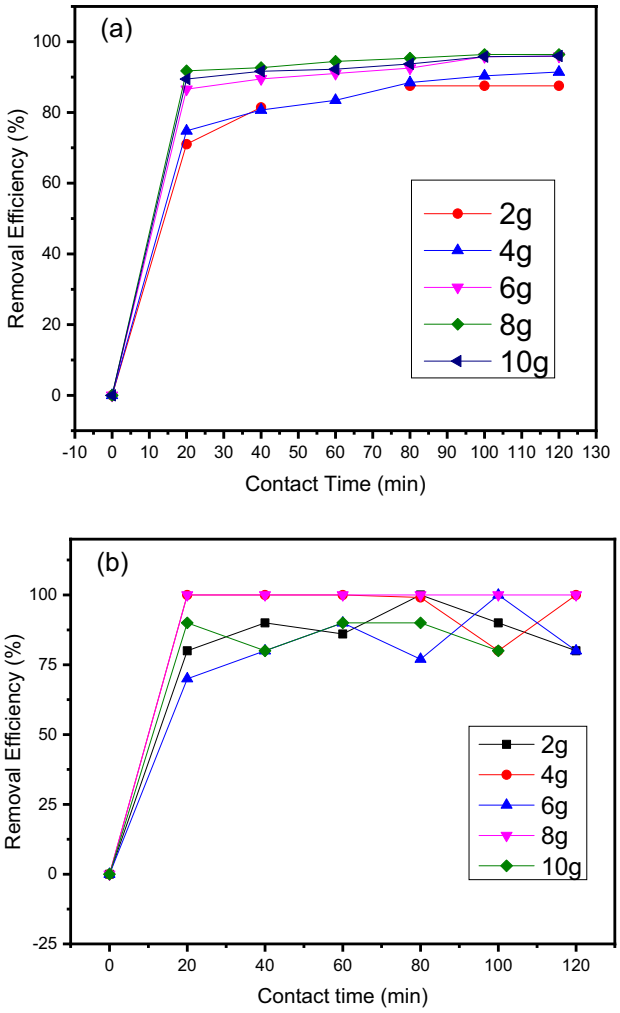

Fig. 4 Effect of contact time on adsorption of Arsenic(V) onto adsorbents **a** RH adsorbents (particle size 425 µm) **b** RH adsorbents (particle size 425 µm)

was 100% at 20 min of contact. The maximum removal efficiency for this mass was 100% and it was seen at 20, 40, 60 and 120 min of contact time when equilibrium was seen to occur. The mass was increased to 6 g and at 20 min of contact time, the removal efficiency was 70%. The maximum removal efficiency for this mass was seen at 100 min of contact time after which equilibrium started to occur with a removal efficiency of 100%. At a mass of 8 g, the percentage removal was 100% and remained at this level throughout 120 min. At a dosage of 10 g, the percentage removal was 90% after 20 min of contact which was the maximum removal efficiency seen for this mass. The general observation of the time dependence of the removal efficiency was that, the removal efficiency was rapid within the first 20 min of contact time followed by a slow and steady increase until equilibrium was achieved. The difference in removal efficiency of arsenic by the various OPP doses was not significant from 2 to 10 g of adsorbent. This is because at the initial stage of adsorption, the surface of the OPP adsorbent is bare resulting in a faster sorption kinetics of the adsorbate onto the surface of the adsorbent, usually through diffusion kinetics. During the later stage of the adsorption process, the kinetics is changed from a diffusion process to more of an attachment-controlled process [32].

Effects of adsorbent dosage on removal efficiency and adsorption capacity

The effect of dosage on adsorption removal efficiency and adsorption capacity of the adsorbents are shown in Fig. 5. For RH adsorbent, the adsorption capacity, q_e (mg/g), of the adsorbent was found to reduce from 9.98 to 0.99 mg/g as the

dosage of the adsorbent was increased for a fixed concentration and volume of the arsenic solution.

Similarly, the effect of the OPP adsorbent dosage was studied for its removal efficiency and adsorption capacity and the results are shown in Fig. 5b. The mass of the adsorbent was increased from 2 to 10 g, keeping the concentration of the solution constant at 100 ug/L and the volume of the solution constant at 100 mL. It was observed that the removal efficiency of arsenic by the OPP adsorbent increased with increase in the mass of the adsorbent. The optimal removal efficiency was 100% at dosage of 4 g. It was also observed that the adsorption capacity reduced slightly (from 4.945 to 4.905) as dosage increases.

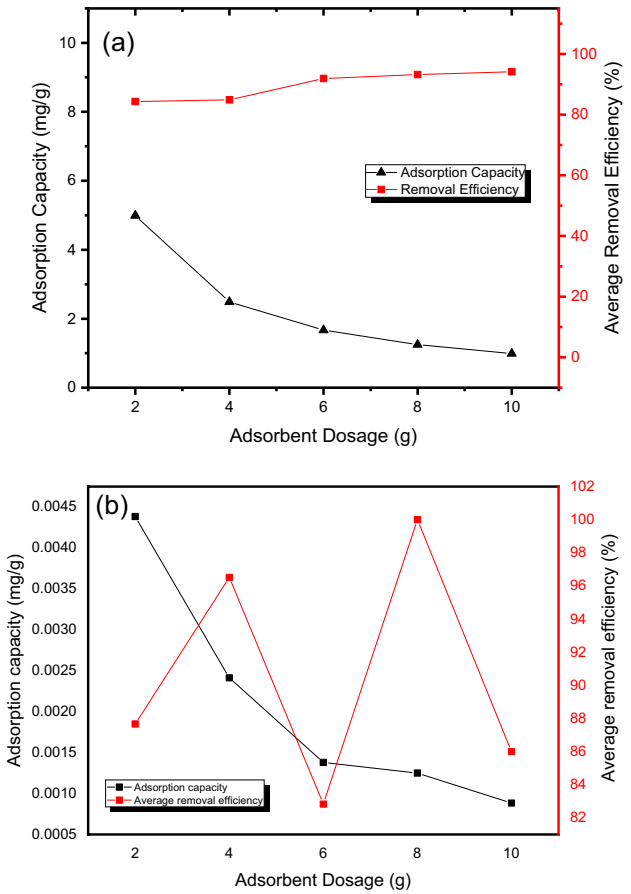

Fig. 5 Effects of adsorbent dosage on removal efficiency and adsorption capacity **a** RH adsorbent **b** OPP adsorbent

Adsorption isotherm and kinetic studies

The various parameters for the pseudo-first order (PFO), pseudo-second order (PSO) and inter-particle diffusion models for RH and OPP adsorbents are given in Tables 2 and 3, respectively. The isotherm adsorption modeling fit parameters are presented in Table 4 for both adsorbents. The adsorption data were found to obey the PSO kinetic model with R square value of 1.00. The R-square value for the Freundlich isotherm model fit was 1.00 compared with the near zero R-square value of the Langmuir isotherm model fit. The adsorption kinetic models for OPP showed that the correlation parameter, R^2 values ranged 0.31–0.58 for the PFO adsorption of arsenic onto the OPP adsorbents. However, the PSO model showed a much better fit to the experimental data with a goodness of fit R^2 value of approximately 0.96. The isothermal adsorption parameter $R^2 = 1.00$ for Langmuir isotherm fit compared with $R^2 = 0.99$ of the Freundlich isotherm model. The computed adsorption capacity, q_m, was 4.84 mg/g for the Langmuir model, which is closer to the experimental value of 4.93 mg/g (Table 4). This is complemented by the value of R_L is 0.0026, which accurately describes a favorable adsorption according to Langmuir isotherm model since it lies between 0 and 1.

Discussion

Rice husks and orange peels were prepared as adsorbents for removal of arsenic from aqueous media. The adsorbents were pulverized into two sizes 841 and 425 µm. The SEM image of the RH shows multiple indented surfaces, whereas that of the OPP had several smaller pores. The

Table 2 Adsorption kinetic model for RH adsorbent

Mass (g)	Experimental	Pseudo-first-order			Pseudo-second-order			Intra-particle diffusion	
		Computed			Computed			Computed	
	q_e (mg/g)	K_1 (mg/g/min)	q_e (mg/g)	R^2	K_2 (mg/g/min)	q_e (mg/g)	R^2	R^2	K_{ipd} (mg/g/min)
2	4.99	0.03955	0.19	0.34	8.25	4.99	1	0.5924	0.40793
4	2.49	0.04219	0.11	0.43	7.24	2.49	1	0.5926	0.20399
6	1.67	0.03364	0.08	0.31	17.77	1.67	1	0.59183	0.13602
8	0.99	0.00036	0.94	0.08	61.57	0.99	1	0.64048	0.09494
10	1.25	0.04567	0.04	0.55	33.82	1.25	1	0.59153	0.10201

Table 3 Adsorption kinetic model for OPP adsorbent

Mass (g)	Experimental.	Pseudo-first-order			Pseudo-second-order			Intra-particle diffusion	
		Computed			Computed			Computed	
	q_e (mg/g)	K_1 (mg/g/min)	q_e (mg/g)	R^2	K_2 (mg/g/min)	q_e (mg/g)	R^2	R^2	K_{ipd} (mg/g/min)
2	4.91	−0.05062	0.48	0.58	0.0140	6.605	0.96	0.59	0.40124
4	4.91	−0.02358	0.63	0.32	0.0137	6.636	0.96	0.59	0.40235
6	4.92	−0.02379	0.62	0.32	0.0137	6.363	0.96	0.59	0.40254
8	4.93	−0.02420	0.56	0.31	0.0137	6.649	0.96	0.59	0.40318
10	4.92	−0.02352	0.61	0.32	0.0139	6.626	0.96	0.60	0.40240

Table 4 Adsorption isotherm models for adsorbents

Adsorbent	Langmuir isotherm				Freundlich isotherm		
	R^2	q_m (mg/g)	b (L/g)	R_L	R^2	K_f (mg/g)	n (L/g)
RH	7.8×10^{-16}	2757	−0.0064	1.00	1.00	1.04	1.00
OPP	1.00	4.84	3785.60	0.0026	0.99	4.63	−68.68

indented surfaces and the several smaller pores indicate potential adsorbent sites.

The removal efficiencies of the adsorbents were found to be particle size dependent. The smaller particle size 425 µm was found to demonstrate greater removal ability than 841 µm particle size for both adsorbent. This was mainly because of the increase in the adsorption sites for the smaller sizes. Again, the adsorbent with the smaller particle sizes has larger surface area enabling it to have a significant influence on the transport of particles during the adsorption process [24, 33, 34].

The adsorption capacity, q_e (mg/g), of the RH adsorbent was found to reduce as the dosage of the adsorbent was increased for a fixed concentration and volume of the arsenic solution. This apparent decrease in the adsorption capacity can be attributed to the heterogeneous nature of RH surface sites which comprise sites having a wide spectrum of binding energies. For lower masses of the RH adsorbent, all the sites have adequate exposure to arsenic for adsorption and the saturation of the surface is faster resulting in higher value of adsorption capacity, q_e (mg/g). When the mass is increased, the number of higher energy sites is reduced leaving a greater portion of lower energy sites occupied, which results in lower values of q_e (mg/g) [35]. The results of effect of dosage on adsorption capacity for OPP revealed a similar pattern as in the RH output. The reduction in the adsorption capacities for OPP was attributed to lower binding energy sites as well [36].

The FTIR spectra for before and after adsorption are presented in Fig. 4a and b for both rick husk and orange peels. The spectra show a shift of -41 cm^{-1}, -16 cm^{-1} and -31 cm^{-1} for the wavenumber peaks of 3400 cm^{-1}, 1040 cm^{-1} and 796 cm^{-1}, respectively for RH before and after adsorption of arsenic; indicating that these groups play a role in the chemisorption process. The spectra bands of OPP adsorbent before and after adsorption of As(V) show that, there was a shift of 41 cm^{-1} and -29 cm^{-1} in the adsorption wavenumber at the peaks are 3324 cm^{-1} and 1734 cm^{-1}, respectively. This is suggestive of the involvement of these groups in the chemisorption process. Although the magnitudes of shifts are different, this finding is supported by previous work in the literature [34] where the authors recorded a shift of (29 cm^{-1}) and (42 cm^{-1}) in the absorption wave number of peaks at 3295 cm^{-1} and 1605 cm^{-1}, respectively. They attributed a small post As(V) adsorption peak of 877 cm^{-1} to the metal to oxygen bond.

The isotherm and kinetic models were explored along the data obtained from the batch adsorption studies for the optimum particles size 425 µm. The adsorption data for RH could be described by Freundlich model and the process therefore as chemisorption involving heterogeneous surface. The OPP adsorption data were best described by Langmuir isotherm modeling as presented by the *R*-square values in Table 4. The Langmuir model showed enhanced binding due to a partial increase in quantity of availability of adsorption monolayer sites for arsenic [37]. The 0.99 *R*-square value for the Freundlich confirmed the great adherence also unto the Freundlich model. Both adsorbents were found to show *R*-square values which demonstrates that the pseudo-second order (PSO kinetic model) can be used to describe their adsorption data.

Implications

The implications of the results are quite significant. Firstly, it demonstrates that the adsorbents were able to remove arsenic pollutant to a reasonable extent from the aqueous media. Organic wastes, RH and OPP were not chemically or thermally activated for this adsorption process, and it therefore clearly shows the possibility of utilizing raw organic or agricultural wastes for various environmental engineering applications.

Secondly, the results showed a higher percentage removal efficiency for arsenic without releasing any other chemical pollutant into the aqueous media. This therefore complements the non-chemical preparation process of the adsorbents. The removal efficiency plots for both adsorbents define the variation in the potential of the adsorbents at the pollutant removal but clearly shows acceptable level of percentage in water treatment applications.

Lastly, considering the availability of the RH and OPP, the envisaged water treatment technology may be sustainable and reasonably affordable. Environmental Engineers therefore have the task of transforming experimental output to technology.

Conclusions

The study investigated the potential of organic wastes RH and OPP as adsorbents of arsenic from aqueous solution. The maximum removal efficiencies recorded for RH, and OPP are 95.98% and 100%, respectively. These arsenic adsorption efficiencies are indicative of a high level of potential for any of these local materials to be used for the removal of arsenic from aqueous solutions. Smaller particle sizes are encouraged for higher removal efficiency. The outcome of this study shows the necessity to explore local materials with high iron oxide content for the adsorption of Arsenate(V) from aqueous solutions. The removal efficiency for OPP was found to increase with increasing dosage of adsorbent till equilibrium was established at 8 g.

With respect to OPP, it was observed that the removal efficiency was time-dependent and only marginal changes occurred after 20 min contact time for all dosages considered. The isotherm and kinetic models for OPP were described by the Langmuir isotherm and the pseudo-second-order (PSO) models, respectively, whereas the isotherm and kinetic models for RH were described by Freundlich model and PSO model, respectively. Indeed, the 0.99 *R*-square value for OPP kinetic modeling also makes it a possible candidate for Freundlich model subscriber. The experimental output of this study indicates that the adsorbents RH and OPP (with smaller particles sizes less than 500 µm) are better for arsenic removal.

Appendix

Presentation of results from atomic adsorption spectroscopy (AAS) characterization

Concentrations of arsenic in solution after treatment with different masses of RH adsorbents with grain size of 425 µg/L, at different contact times.

Contact time (min)	Concentration (µg/L)					
	1 g	2 g	4 g	6 g	8 g	10 g
0	100.00	100.00	100.00	100.00	100.00	100.00
20	32.22	28.98	25.20	13.42	4.27	10.54
40	26.65	18.56	19.30	10.51	5.65	8.33
60	22.88	6.125	16.54	8.98	2.56	7.75
80	16.54	12.46	11.52	7.43	5.29	6.25
100	14.22	12.46	9.64	4.23	7.36	4.22
120	14.21	12.46	8.56	4.11	7.21	4.02

Concentrations of arsenic in solution after treatment with different masses of RH adsorbents with grain size of 841 µg/L, at different contact times.

Contact time (min)	Concentration (µg/L)					
	1 g	2 g	4 g	6 g	8 g	10 g
0	100.00	100.00	100.00	100.00	100.00	100.00
20	15.41	37.71	28.41	30.42	27.72	22.44
40	92.72	51.00	25.12	34.60	29.63	31.13
60	85.00	59.00	19.34	37.90	25.66	27.73
80	11.73	42.22	19.52	37.86	24.21	13.25
100	13.62	33.24	16.67	30.82	19.39	17.20
120	96.21	36.81	12.50	40.17	17.32	15.62

Concentrations of arsenic in solution after treatment with CG granules with different concentrations of Fe_3O_4 nanoparticles, at different contact times.

Contact time (min)	Concentration (µg/L)		
	1% Fe_3O_4	5% Fe_3O_4	10% Fe_3O_4
0	100.00	100.00	100.00
20	22.30	19.80	24.90
40	22.80	20.60	3.37
60	6.55	13.80	7.48
80	15.50	10.80	2.70
100	9.45	8.03	12.50

Contact time (min)	Concentration (µg/L)		
	1% Fe_3O_4	5% Fe_3O_4	10% Fe_3O_4
120	2.35	19.00	5.68

Concentrations of arsenic in solution after treatment with different masses of OPP adsorbents, at different contact times.

Contact time (min)	Concentration (µg/L)				
	1 g	2 g	3 g	4 g	5 g
0	100	100	100	100	100
20	20.2	19	18.1	16	18.7
40	19.4	19	18	15.3	18
60	19.3	18	18	15	17
80	19.1	17.8	17	13.4	16.4
100	19	14.5	14.4	13	16.3
120	16.1	15	14	13.1	14

Supplementary Information The online version contains supplementary material available at https://doi.org/10.1007/s40095-022-00551-z.

Acknowledgements Materials, Consumables, and Equipment usage were fully sponsored by Office of Research, Innovation and Development (ORID; Project number UGRF/10/ILG-083/2016 – 2017), University of Ghana, Ghana. We appreciate the technical support provided by Grace Karikari Arkorful, Laboratory Technologist at Materials Science and Engineering Department of the University of Ghana, Legon, Ghana.

Author contributions ANSA: Methodology, Investigation, draft preparation, and Writing. LNWD: Writing—review and editing, resources, validation. YDB: Methodology, writing—review and editing, supervision. PKA: Formal Analysis, and Writing—review and editing. DN: Methodology, writing—review and editing, supervision. AA: Investigation, draft preparation, and resources. EA: Conceptualization, formal analysis, Validation, review, editing, and supervision.

Funding The funders had no role in the design of the study; in the collection, analyses, or interpretation of data; in the writing of the manuscript, or in the decision to publish the results.

Declarations

Conflict of interest The authors declare no conflict of interest.

References

1. Smith, A.H., Lingas, E.O., Rahman, M.: Contamination of drinking-water by arsenic in Bangladesh: a public health emergency. Bull. World Health Organ. **78**, 1093–1103 (2000)
2. Choong, T.S., et al.: Arsenic toxicity, health hazards and removal techniques from water: an overview. Desalination **217**(1–3), 139–166 (2007)
3. Rahaman, M.S., Mise, N., Ichihara, S.: Arsenic contamination in food chain in Bangladesh: a review on health hazards, socioeconomic impacts and implications. Hyg. Environ. Health Adv. **2**, 100004 (2022)
4. Baboo, H., et al.: A comprehensive and systematic study of fluoride and arsenic contamination and its impacts in India. Sustain. Water Res. Manag. **8**(4), 1–19 (2022)
5. Huntsman-Mapila, P., et al.: Characterization of arsenic occurrence in the water and sediments of the Okavango Delta NW Botswana. Appl. Geochem. **21**(8), 1376–1391 (2006)
6. Huntsman-Mapila, P., et al.: Arsenic distribution and geochemistry in island groundwater of the Okavango Delta in Botswana. In: Anthony, J., Jones, A. (eds.) Sustaining Groundwater Resources, pp. 55–67. Springer, Berlin (2011)
7. Bowell, R., et al.: Environmental impact of former gold mining on the Orangi River, Serengeti NP Tanzania. Biogeochemistry **28**(3), 131–160 (1995)
8. Serfor-Armah, Y., et al.: Levels of arsenic and antimony in water and sediment from Prestea, a gold mining town in Ghana and its environs. Water Air Soil Pollut. **175**(1), 181–192 (2006)
9. Amasa, S.: Arsenic pollution at Obuasi Goldmine, town, and surrounding countryside. Environ. Health Perspect. **12**, 131–135 (1975)
10. Amonoo-Neizer, E.H., Amekor, E.: Determination of total arsenic in environmental samples from Kumasi and Obuasi Ghana. Environ. Health Perspect. **101**(1), 46–49 (1993)
11. Ahmad, K., Carboo, D.: Speciation of As(III) and As(V) in some Ghanaian gold tailings by a simple distillation method. Water Air Soil Pollut. **122**(3), 317–326 (2000)
12. Smedley, P.L.: Arsenic in rural groundwater in Ghana: part special issue: hydrogeochemical studies in sub-Saharan Africa. J. Afr. Earth Sci. **22**(4), 459–470 (1996)
13. Babu, D.S., Nidheesh, P.: Treatment of arsenite contaminated water by electrochemically activated persulfate oxidation process. Sep. Purif. Technol. **282**, 119999 (2022)
14. Mobar, S., Bhatnagar, P.: Arsenic bioremediation potential of arsenite oxidizing bacteria isolated from geogenic and anthropogenically contaminated soil. Pollution **8**(4), 1137–1149 (2022)
15. Turpeinen, R., et al.: Influence of microbes on the mobilization, toxicity and biomethylation of arsenic in soil. Sci. Total Environ. **236**(1–3), 173–180 (1999)
16. Zhao, Y., et al.: Preparation of layered double-hydroxide nanomaterials with a uniform crystallite size using a new method involving separate nucleation and aging steps. Chem. Mater. **14**(10), 4286–4291 (2002)
17. Sushil, S., Batra, V.S.: Catalytic applications of red mud, an aluminium industry waste: a review. Appl. Catal. B Environ. **81**(1–2), 64–77 (2008)
18. Kanel, S.R., et al.: Removal of arsenic(III) from groundwater using low-cost industrial by-products-blast furnace slag. Water Qual. Res. J. **41**(2), 130–139 (2006)
19. Yeo, K.F.H., et al.: Arsenic removal from contaminated water using natural adsorbents: a review. Coatings **11**(11), 1407 (2021)
20. Dehghani, M.H., Maroosi, M., Heidarinejad, Z.: Experimental dataset on adsorption of Arsenic from aqueous solution using Chitosan extracted from shrimp waste; optimization by response surface methodology with central composite design. Data Brief **20**, 1415–1421 (2018)
21. de Gennaro, B., et al.: Zeolite-rich composite materials for environmental remediation: arsenic removal from water. Appl. Sci. **10**(19), 6938 (2020)
22. Ayele, A., et al.: Comparative utilization of dead and live fungal biomass for the removal of heavy metal: a concise review. Sci. World J. **2021**, 1–10 (2021)
23. Bahar, M.M., et al.: As(V) removal from aqueous solution using a low-cost adsorbent coir pith ash: equilibrium and kinetic study. Environ. Technol. Innov. **9**, 198–209 (2018)

24. Ali, S.H., Emran, M.Y., Gomaa, H.: Rice husk-derived nanomaterials for potential applications. In: Makhlouf, A.S.H., Ali, G.A.M. (eds.) Waste Recycling Technologies for Nanomaterials Manufacturing, pp. 541–588. Springer, Berlin (2021)
25. Faust, S.D., Aly, O.M.: Chemistry of Water Treatment. CRC Press, Boca Raton (2018)
26. Imran, M., et al.: Kinetic and equilibrium studies for cadmium biosorption from contaminated water using Cassia fistula biomass. Int. J. Environ. Sci. Technol. **16**(7), 3099–3108 (2019)
27. Mahramanlioglu, M., Kizilcikli, I., Bicer, I.: Adsorption of fluoride from aqueous solution by acid treated spent bleaching earth. J. Fluorine Chem. **115**(1), 41–47 (2002)
28. Roulia, M., Vassiliadis, A.A.: Sorption characterization of a cationic dye retained by clays and perlite. Microporous Mesoporous Mater. **116**(1–3), 732–740 (2008)
29. Ho, Y.-S., McKay, G.: Pseudo-second order model for sorption processes. Process Biochem. **34**(5), 451–465 (1999)
30. Kajjumba, G.W., et al.: Modelling of adsorption kinetic processes—errors, theory and application. In: Advanced Sorption Process Applications, pp. 1–19(2018)
31. Morcali, M.H., Zeytuncu, B., Yucel, O.: Platinum uptake from chloride solutions using biosorbents. Mater. Res. **16**(2), 528–538 (2013)
32. Weber, W., Morris, J.: Intraparticle diffusion during the sorption of surfactants onto activated carbon. J. Sanit. Eng. Div. Am. Soc. Civ. Eng. **89**(1), 53–61 (1963)
33. Amin, M.N., et al.: Removal of arsenic in aqueous solutions by adsorption onto waste rice husk. Ind. Eng. Chem. Res. **45**(24), 8105–8110 (2006)
34. Khaskheli, M.I., et al.: Use of orange peel waste for arsenic remediation of drinking water. Waste Biomass Valoriz. **2**(4), 423–433 (2011)
35. Biswas, B.K., et al.: Effective removal and recovery of antimony using metal-loaded saponified orange waste. J. Hazard. Mater. **172**(2–3), 721–728 (2009)
36. Abid, M., et al.: Arsenic (V) biosorption by charred orange peel in aqueous environments. Int. J. Phytoremed. **18**(5), 442–449 (2016)
37. Ahmad, I., et al.: Biosorption and health risk assessment of arsenic contaminated water through cotton stalk biochar. Surf. Interfaces **29**, 101806 (2022)

International Journal of Energy and Environmental Engineering (2023) 14:661–670
https://doi.org/10.1007/s40095-022-00541-1

ORIGINAL RESEARCH

High efficient solar cells through multi-layer thickness optimization using particle swarm optimization and simulated annealing

Hamed Kargaran[1] · Elahe Bayat[1] · Aliakbar Hassanzadeh[1] · Ghasem Alahyarizadeh[1]

Received: 27 April 2022 / Accepted: 18 September 2022 / Published online: 26 September 2022

Abstract

In a comparative study, a solar cell structure's layer thicknesses were optimized using particle swarm optimization (PSO) and simulated annealing (SA). The ideal short-circuit current density was considered as the cost function for both algorithms to minimize the number of function evaluations (NFEs) needed to obtain the optimal thicknesses of the structure layers (ZnO and MoOx layers), separately and simultaneously, being single- and multi-layer optimization. The results were compared to those of genetic algorithm (GA) and brute-force methods that have been reported in the literature. In the single-layer optimization, the results obtained by PSO indicated that the maximum required NFEs for optimizing ZnO was 33.1 ± 23.16 compared to 81 for the brute-force method and 78.16 ± 1.65 for the GA. The PSO method needed 19.6 ± 11.7 NFEs for optimizing the MoOx layer, while, as was reported in Ref. Vincent (E 13:1726 2020), GA optimized this layer by 13.05 ± 3.24 in the best manner by the Roulette wheel method. Both single-based and population-based approaches were implemented for the SA. The results obtained by SA indicated that the required NFEs were estimated higher than that of the GA due to the small search space. The required NFEs for two-layer optimization using PSO amount to 111.27 ± 60.1, which is considerably lower than the 1758.77 ± 39.75 of GA. The NFEs are significantly lower than the similar value obtained using the brute-force approach and GA, even with the highest SD value. In the case of two-layer optimization, SA estimated 65.63 ± 21.1 and 575.76 ± 301.64 NFEs using single-based and population-based methods, respectively.

Keywords Particle swarm optimization (PSO) · Simulated annealing (SA) · Solar cell · Optimization · Efficient thickness

Introduction

Any nation's progress is fueled mainly by its access to electrical energy. Electricity generation is possible in a variety of ways. One of these alternatives is solar energy, a limitless energy source. The community employs renewable energy to produce clean energy [1]. It is predicted that in 2100, between 30 and 65% of the total energy supply will be allocated to renewable sources. Abundant solar energy, without pollution, is sustainable and endless and can meet all human energy needs. After 2008, the price of PV c-Si modules fell by 45% to $ 2.21 per Watt. The cost of PV power generation for centralized systems is estimated at $ 0.03–$ 0.2 per Watt-hour. Studies indicate that solar energy-based technologies have the potential to become the most important source of energy for human needs now and in the future [1–3]. High-performance solar cells are an attractive proposition [4]. Many researchers are putting in a lot of effort to improve solar photovoltaic cells' efficiency to generate more electrical energy in any specific bandwidth area. The selection of different materials such as CdTe, GaN, GaAs, Ge, InP, a-SiH causes a change in the bandgap, a change in the efficiency of the photovoltaic cell [5].

Improving the efficiency and design of solar cells is the solution to the supply–demand problem. One method used to optimize the efficiency of the solar cell is making multi-layered connections with more materials solar cells, which can effectively use the all-solar spectrum to convert it into electricity by changing the bandwidth limits [6–8]. The Brute-Force method is the most common problem-solving technique to achieve the optimum solar cell structure. It acts as the possible solution to a problem by examining individual answers, determining the result of expressing a problem whether it satisfies or not, and is used when the problem size is limited. This algorithm is known as Generate and Test,

✉ Ghasem Alahyarizadeh
g_alahyarizadeh@yahoo.com

[1] Faculty of Engineering, Shahid Beheshti University, Tehran, Iran

which offers all possible solutions to a problem. It is a simple problem-solving technique that is easy to implement and always suggests a solution if available. The computational cost of the Brute-Force technique grows as the problem size grows since it is directly proportional to the number of candidate solution [9]. However, this algorithm does not work for optimizing solar cell efficiency due to many parameters (e.g., number of layers and their thicknesses, materials, and doping) and high permutations. So, better optimization techniques will be required since real-world problems are highly complicated. One of the tools for simulating and evaluating the performance of PV systems is to build an accurate mathematical model with the help of experimental measurement data of solar cells and photovoltaic (PV) modules.

Ahmed A. Zaki Diab et al. used the Coyote Optimization Algorithm (COA) to optimize solar cells and PV modules. Using this algorithm, they extracted unknown parameters from the single-diode, two-diode, and three-diode equivalent circuit models. The simulation results and the statistical measurement in this work support the COA algorithm's superiority and reliability not only for the extraction parameter of PV modules but also in different operational scenarios [10]. Meta-heuristic algorithms provide satisfactory results in terms of solution quality and convergence speed. Anouar Farah et al. used a comprehensive Rao- learning optimization algorithm (CLRao-1) to achieve an accurate model of photovoltaic cells. Rao-1 was chosen for its simplicity, ease of understanding and implementation, and for evaluating the effectiveness of the algorithms through PV cells and three equivalent circuit modules. The results of experimental and simulated data were highly consistent. In addition, the algorithm achieved the best results in terms of reliability and accuracy [11]. Youssef Kharchouf et al. have proposed the differential evolution (DE) technique to improve the performance of solar photovoltaic systems. It relies on the Lambert W function and an initial meta-heuristic step to select the optimal jump coefficient and cross-parameters for each specific voltage-current characteristic, which can improve the DE convergence characteristics by using the meta-heuristic strategy [12]. Ashraf Mohamed Hemeida et al. used the multi-objective multi-verse optimization (MOMVO) algorithm to optimize hybrid microgrid systems (HMGS), which are the main target of the hybrid system design process as objective functions. The feasibility study of using HMGS for rural power systems leads to increased access to energy [13].

In all optimization problems, the goal is to find the minimum or maximum value. In many cases, population-based algorithms are frequently suggested to solve complex problems. Three popular, widely used and highly similar techniques involving the Genetic Algorithm (GA), Particle Swarm Optimization (PSO), and Simulated Annealing (SA) are chosen from the numerous proposed techniques. Even though GA has been well established since it was first introduced, SA and PSO algorithms have garnered more interest in optimization-related topics. GA is one of the most popular evolutionary algorithms that work with a population of individuals evolving according to a set of rules such as selection, crossover, and mutation (moving through the perspective of fitness) [14].

The PSO algorithm is another example of a swarm intelligence population-based algorithm [15]. PSO is a robust stochastic optimization technique. It is compatible with optimizing the nonlinear function in multidimensional space, used for several real-world problems [16]. SA is an optimization technique successfully used to solve many optimization problems. This optimization technique is based on the behavior of dense materials at low temperatures that simulates the natural annealing process, such as freezing and crystallizing a liquid or coolant and metal annealing [17–21]. Optimization problems are divided into two categories based on the type of decision variables: discrete and continuous optimizations. Models with discrete decision variables are discrete optimization problems, whereas the continuous optimization method uses continuous decision variables. The goal of a discrete optimization problem is to find an object from a countable set, such as an integer, permutation, or graph. Due to the comprehensiveness and multiplicity of continuous optimization algorithms, employing these algorithms in discrete optimization is important and challenging.

This paper provides the best and most appropriate optimization method for multi-layer thickness optimization of a solar cell by comparing an optimization problem solved by Premkumar Vincent et al. with the GA through the PSO and SA algorithms optimization [22]. In that work, the authors used the GA, a discrete optimization method, to perform the calculations in the reference. However, in this work, we investigate the challenge of the efficiency of continuous algorithms in the inherently discrete problem, using methods PSO and SA. The main goal is to focus on the number of required operations to achieve optimum cost function, their effects on the quality of the solution, and the solution time of each algorithm by observing.

Methodology

Solar cell structure

The solar cell structure is similar to the structure optimized in reference [22]. Figure 1 demonstrates the solar cell structure, which consists of 5 layers. Solar cell simulation was performed by the Finite-Difference Time-Domain (FDTD) software. FDTD is the gold standard for modeling nanophotonic devices, processes, and materials. This finely-tuned implementation of the FDTD method delivers reliable,

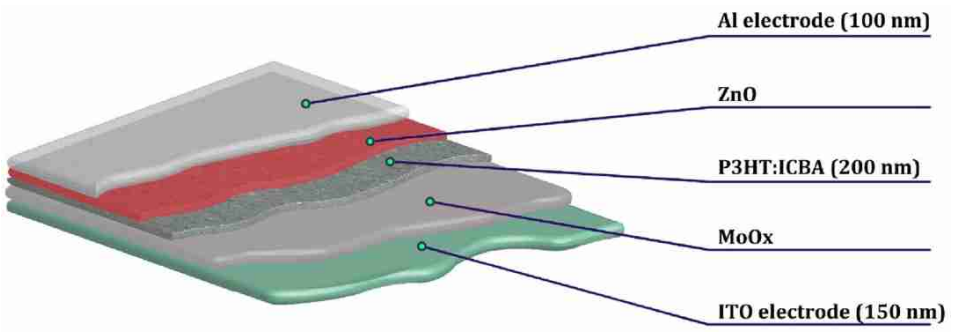

Fig. 1 The solar cell structure [22]

powerful, and scalable solver performance over a broad spectrum of applications. FDTD is a state-of-the-art method for solving Maxwell's equations in complex geometries [23]. The thicknesses of two layers of ZnO and MoOx are considered variable parameters for optimization, and the Jsc parameter is considered a parameter determining the solar cell performance and response. In the paper presented by Premkumar Vincent et al. [22], simulations were performed using this data and the GA algorithm with different methods including Random, Roulette wheel, Tournament and Breeder methods, and their best answer is considered the optimal design. The presented results indicated that the GA algorithm implementation results in a considerably faster and more precise search method than the brute-force method in both single-layer and multi-layer optimizations. The best-case roulette wheel achieved 1758.77 ± 39.75 NFEs which are significantly fewer than 2511 NFEs by brute-force method. This study aims to simulate based on the presented data using the PSO and SA algorithms and compare the results with the obtained results by the GA algorithm. We used the FORTRAN compiler to implement the PSO and SA algorithms for optimization. We utilized FDTD as a cost function in this procedure.

Particle swarm optimization algorithm

In 1995, an article on PSO was presented at the evolutionary calculations Congress for the first time [24]. In a PSO algorithm, atoms, called particles, fly or swim through supermassive space. Each particle searches for the best position over time in a multidimensional space when flying or swimming. Then, it modifies its position according to its own experience, including present velocity and position and the best previous position experienced by itself and its neighbors [25].

The PSO algorithm is set up with a group of random particle combinations with a definite answer and then searches for optima by updating generations. Each particle flies at a velocity of v_i through the search space R_d, which is adjusted according to its best previous answer, $\mathrm{pBest_i}$, and its best previous answer, gBest. In other words, PSO uses $\mathrm{pBest_i}$ and gBest to change the current search point to prevent particles from "flying" in one direction. The velocity is updated as a linear combination of position and velocity vectors. The particle i is represented as

$$\chi_i = \left(\chi_{i1}, ..., \chi_{iD}\right). \tag{1}$$

The previous best position (the position that gives the best fit value) is recorded for the i particle and is represented as $\mathrm{pBest_i} = (\mathrm{p_{i1}}, \ldots, \mathrm{p_{iD}})$. The best particle index among all population particles is indicated by the symbol gBest, which indicates the best overall. The rate of change of position (velocity) for particle i is shown as v_i by the following equation: $v_i = (v_{i1}, \ldots, v_{iD})$. Particles are manipulated according to the following equations:

$$\begin{aligned} v_{id} =& w \times v_{id} + c_1 \times rand1() \times \left(pBest_i - \chi_{id}\right) \\ &+ c_2 \times rand2() \times \left(gBest_i - \chi_{id}\right) \end{aligned} \tag{2}$$

$$\chi_{id} = \chi_{id} + v_{id} \tag{3}$$

where w is the inertia weight decreases along with iterations, $\mathrm{x_{id}}$ is the current position for the particle, v_{id} is the current velocity for particle i, c1 and c2 are the acceleration constants, rand() is a random number, $\mathrm{pBest_i}$ is the best value for particle i, and gBest is the best particle achieved over all iterations.

The algorithm can be summarized as follows:

(1) Randomly initialize the position and the velocity of all particles in the search space.
(2) Evaluate the fit value of each particle.
(3) Determine the best individual value function. $\mathrm{pBest_i}$ compares each particle with its current fit value. If the current fit value is acceptable, the current fit value is assigned to $\mathrm{pBest_i}$.
(4) Determine the best current value function in the whole population. If the best current fit value is better than gBest, the best current fit value is assigned to gBest.
(5) For each particle, the particle velocity is updated (Eq. 2),

(6) Update the particle position (Eq. 3).
(7) Repeat steps 2–6 until a stop criterion is met or a predefined number of iterations is completed [20, 21].

Simulated annealing algorithm

SA was introduced in 1983 by Kirk Patrick, Glatt, and Wake. One of the most significant benefits of SA is its ability to optimize problems independent of specialized knowledge or overall structure in calculations [26]. This algorithm is a solution-based meta-heuristic optimization technique inspired by the metallurgical annealing process [27–29]. By changing the solution gradually (like the cooling process of metal), SA pursues new solutions by adding a small perturbation to the old solution via the search space and reducing the temperature parameter T over time. The algorithm explores a stochastic acceptance criterion if the cost value of the new solution is not adequate before accepting it. Thus, a probability inspired by the Boltzmann probability distribution [26] is used to select the uphill moves that may help the optimization procedure escape from local minima.

$$w \propto \exp\left(-E/(KT)\right) \tag{4}$$

where k is Boltzmann's constant (It is equal to 1 for SA), E energy and T temperature.

This probability is a decreasing function of both the order of magnitude of the cost value reduction and the temperature parameter. As the temperature decreases, the probability of its acceptance decreases, and eventually, SA turns into a classical local search.

The general procedure for the SA algorithm can be summarized as follows:

(1) Guess an initial solution C and select an initial temperature T.
(2) Find another solution, namely C_{next}, by modifying C's last answer..
(3) Calculate the energy difference of $\Delta E = f(C_{next})\text{-}f(C)$.
(4) If $\Delta E < 0$, go to Step 9.
(5) Generate a random number, namely R, between 0 and 1.0.
(6) If $R < \exp(-\Delta E/T)$, go to Step 9.
(7) Repeat Steps 2 ~ 6 for the number of predetermined steps for the given temperature.
(8) If no new configuration C_{next} is accepted, go to Step 10.
(9) Decrease the temperature T, replace C with C_{next}, and go to Step 2.
(10) Cool the environment by setting T to a lower value.
(11) Repeat Steps 1–10 until no further improvement is obtained [26].

Results and discussion

Single-layer optimization

ZnO optical spacer layer

The first optimization step was performed by considering the thickness constant of the MoOx layer at 10 nm and changing the ZnO layer as the optical separator layer from 0 to 80 nm. Then the optimization was carried out using the PSO and SA algorithms by considering that the obtained

Table 1 The results of all three GA, PSO and SA algorithms to optimize the ZnO layer

Comparison results for ZnO single-layer optimization					
Optimized ZnO Thickness = 30 nm					
This work, PSO	Parameter	Selected method			
	Population	5			
	Mean (simulations)	33.1 ± 23.16			
This work, SA	Parameter	Single-based		Population-based	
	Population	1		2	
	Mean (simulations)	29.98 ± 18.2		38.29 ± 26.08	
Ref. GA [22]	Parameter	Selected method			
		Random	Roulette	Tournament	Breeder
	Population	20	80	70	60
	Generation	40	10	30	10
	Mutation prob (%)	80	15	60	75
	Mean (simulations)	78.42 ± 1.82	80.47 ± 0.50	78.16 ± 1.65	79.17 ± 1.37
Ref. Brute-force method [22]	Number of Simulations	81			

optimum thickness by the genetic algorithm for the ZnO layer was 30 nm which presented the maximum value of Jsc current of 116.67 A/m^2 [22]. Table 1 reports the results from the PSO and SA algorithms, as well as the genetic algorithm and Brute-Force method from Reference [22]. According to the results, the PSO algorithm with a population of 5 could reach optimum thickness by 33.1 ± 23.16 NFEs, comparable with 78.16 ± 1.65 for the genetic algorithm (Tournament selection method with 70 population) and 81 NFEs for the Brute-Force. The required number of function evaluations related to SA algorithms with populations 1 and 2 are 29.98 ± 18.2 and 38.29 ± 26.08 NFEs, respectively. As can be seen, both PSO and SA algorithms with smaller population sizes require fewer simulations comparable with the results presented in Ref. [22]. However, as observed for SA optimization, the number of function evaluations in the population-based method is higher than in single-based method optimization. It is due to the essence of the SA method, which presents acceptable results for complicated problems. Figures 2 and 3 show the number of iterations (NI) and the number of function evaluations (NFEs) as a function of the population size for optimizing the ZnO layer with the PSO and SA algorithm, respectively. As seen in these figures, although the number of function evaluations (NFEs) increases with the population size, the number of iterations (NI) decreases, which compensates the increase of NFEs. In all simulations, the NFEs for SA and PSO algorithms are lower than reported in Ref. [22]. Comparing the PSO and SA results shows that the required NFEs obtained through the single-based SA method (29.98 ± 18.2)

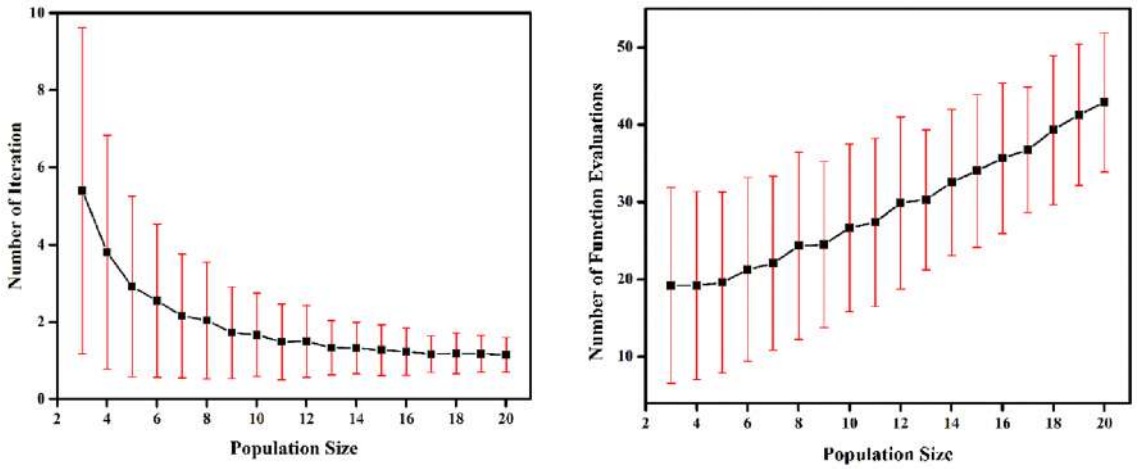

Fig. 2 The number of iterations and number of function evaluations as a function of the population size for optimizing ZnO layer with PSO algorithm

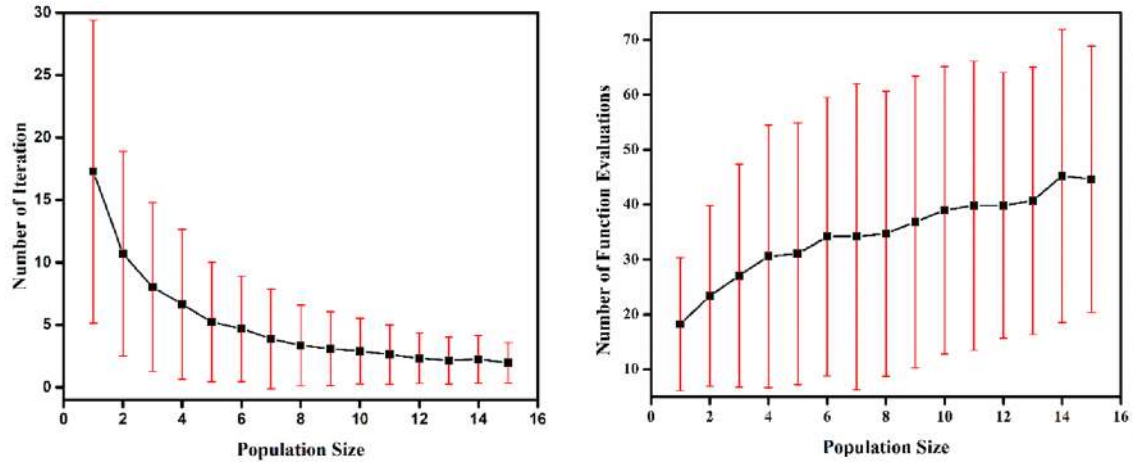

Fig. 3 The number of iterations and number of function evaluations as a function of the population size for optimizing ZnO layer with SA algorithm

are lower than the PSO (33.1 ± 23.16). However, the PSO method performs significantly better than the population-based SA (38.29 ± 26.08).

MoOx optical spacer layer

The MoOx layer was the next layer that required optimization. Similar to the previous step, the thickness of the ZnO layer was held constant at 30 nm, and the MoOx layer's thickness was varied from 0 to 30 nm to get the best Jsc current value of 116.67 A/m^2 [22]. The obtained results of optimizing this layer through the PSO and SA algorithm have presented in Table 2, compared with the presented results by genetic algorithm and Brute-Force method obtained in Ref. [22]. The best results obtained by GA were for the Roulette wheel selection model, which shows the least 13.05 ± 3.24 NFEs by a population size of 20 to reach the best Jsc, while the NFEs required for the PSO algorithm with a population of 5 is 19.6 ± 11.7 and for the SA algorithm is 18.26 ± 12.12 with a population of 1 in single-based. In this case, due to the nature of the problem and small search space, the number of function evaluations for population-based SA optimization is higher than the Brute-Force method (31 simulations), so the only single-based method was considered in this step. Figures 4 and 5 show the number of iterations and the number of function evaluations as a function of the population size for optimizing the MoOx layer with the PSO and SA algorithm. As seen in these figures, same as the ZnO layer, the number of function evaluations increases

Table 2 The results of all three GA, PSO and SA algorithms to optimize the MoOx layer

Comparison results for MoOx single-layer optimization					
Optimized MoOx Thickness = 8 nm					
This work, PSO	Parameter	Selected method			
	Population	5			
	Mean (simulations)	19.6 ± 11.7			
This work, SA	Parameter	Single-based		Population-based	
	Population	1		–	
	Mean (simulations)	18.26 ± 12.12		–	
Ref. GA	Parameter	Selected method			
		Random	Roulette	Tournament	Breeder
	Population	15	5	15	15
	Generation	20	100	30	80
	Mutation prob (%)	80	75	75	80
	Mean (simulations)	30.91 ± 0.31	13.05 ± 3.24	30.97 ± 0.16	30.97 ± 0.18
Ref. Brute-force method	Number of simulations	31			

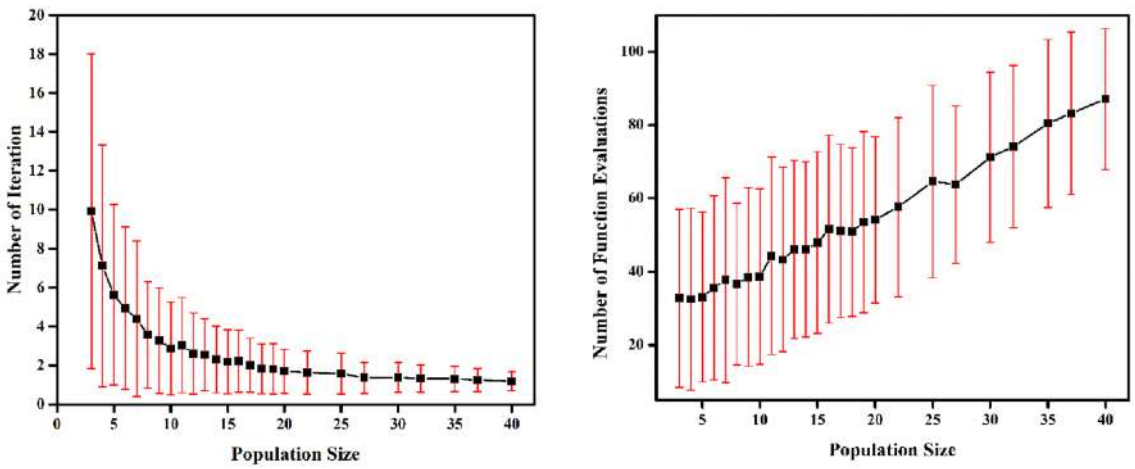

Fig. 4 The number of iterations and number of function evaluations as a function of the population for optimizing MoOx layer with PSO algorithm

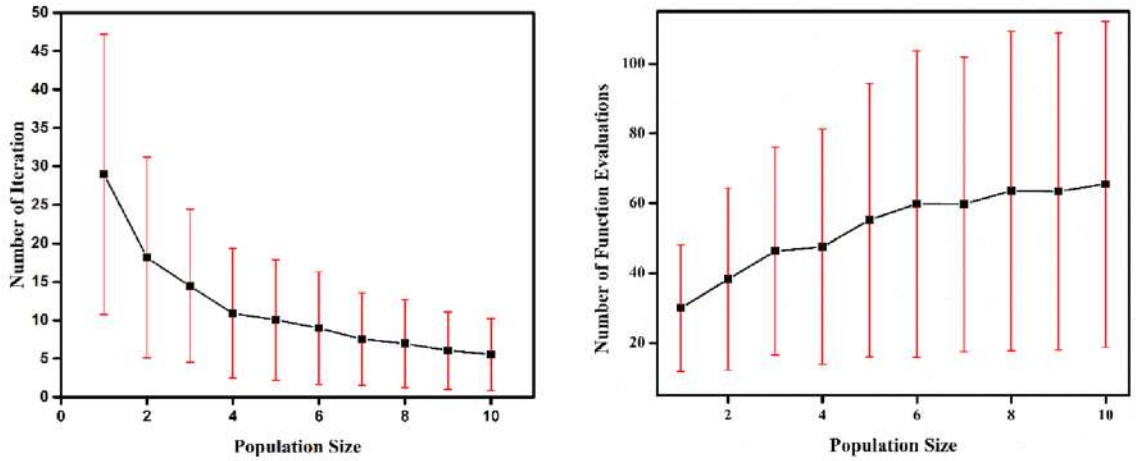

Fig. 5 The number of iterations and number of function evaluations as a function of the population for optimizing MoOx layer with SA algorithm

with the population size, and the number of iterations per simulation decreases. As a comparison of the PSO and SA results, it is observed that the required NFEs obtained through the single-based SA method (18.26 ± 12.12) are lower than the PSO (19.6 ± 11.7). However, the population-based is not applicable for optimizing the layer with small search space.

Multi-layer optimization (ZnO + MoOx)

Multi-layer optimization of the solar cell requires a large number of simulations, resulting in a considerable increase in the computational costs required to perform these simulations. Optimization algorithms are very effective in shrinking the number of simulations and maintaining the same level of accuracy in cases where multiple layers have to be optimized simultaneously. In the last section, the thickness of two layers of ZnO and MoOx were optimized simultaneously. In this regard, ZnO and MoOx layer thicknesses varied from 0 to 80 nm and 0 to 30 nm, respectively. According to the reported results in reference [22], the optimized thicknesses of the ZnO layer (24 nm) and MoOx layer (8 nm) were achieved by 2511 function evaluations with the brute-force method and 1758.77 ± 39.75 function evaluations by the GA algorithm (in the best case of using roulette wheel method). The population size was considered 5 to implement the PSO. As seen in Table 3, the required number of function evaluations for two-layer optimization using PSO amounts to 111.27 ± 60.1, which is considerably lower than GA. Even with the highest SD

Table 3 Comparison of results for multi-layer optimization by GA, PSO and SA

Comparison results for multi-layer optimization					
Optimized ZnO Thickness = 24 nm, Optimized MoOx Thickness = 8 nm					
This work, PSO	Parameter	Selected method			
	Population	5			
	Mean (simulations)	111.27 ± 60.1			
This work, SA	Parameter	Single-based		Population-based	
	Population	1 (success rate: 80.2%)		15	
	Mean (simulations)	65.63 ± 21.11		575.76 ± 301.64	
Ref. GA	Parameter	Selected method			
		Random	Roulette	Tournament	Breeder
	Population	500	1000	500	500
	Generation	90	90	80	90
	Mutation prob (%)	10	90	20	50
	Mean (simulations)	2391.34 ± 38.13	1758.77 ± 39.75	2428.84 ± 34.57	2256.80 ± 70.15
Ref. Brute-force method	Number of Simulations	2511			

value, this value is much lower than the corresponding value from the brute-force method and GA algorithm [22]. Two optimization methods performed by SA, single-based and population-based (The population size was considered 15) show the required number of simulations for two-layer optimization was 65.63 ± 21.11 and 575.76 ± 301.64, respectively. The single-based method presents the lower required number of simulations; however, this method has an 80% success rate, and 20% of simulations could not find the optimum result. The population-based method presents 575.76 ± 301.64 number of simulations with a 100% success rate, which is significantly lower than the GA.

Figures 6 and 7 illustrate the NFE and NI as a function of population size for simultaneous optimization of ZnO and MoOx layers. As a result, the PSO can be considered the best optimization method with a 100% success rate in multi-layer optimization while same as in previous sections, single-based SA exhibits the lowest required NFEs (65.63 ± 21.11), and population-based SA shows the highest required NFEs (575.76 ± 301.64).

Conclusion

The layer thicknesses of a solar cell structure were optimized using two PSO and SA optimization algorithms. The ideal short-circuit current density was considered to be both algorithms' cost function (objective function). ZnO and MoOx layer thicknesses were separately and simultaneously optimized. The optimization processes

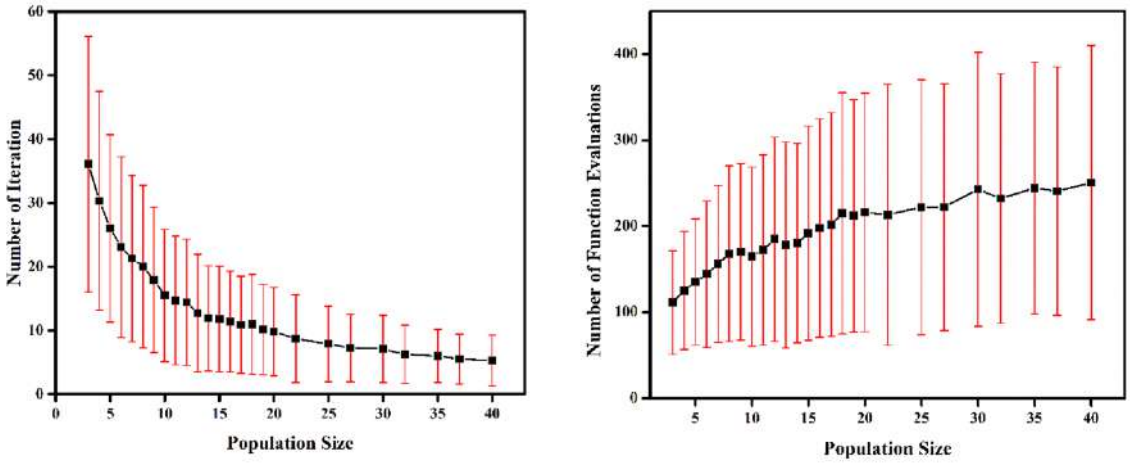

Fig. 6 The number of iterations and number of function evaluations as a function of the population for optimizing Multi-Layer: ZnO and MoOx layers with PSO algorithm

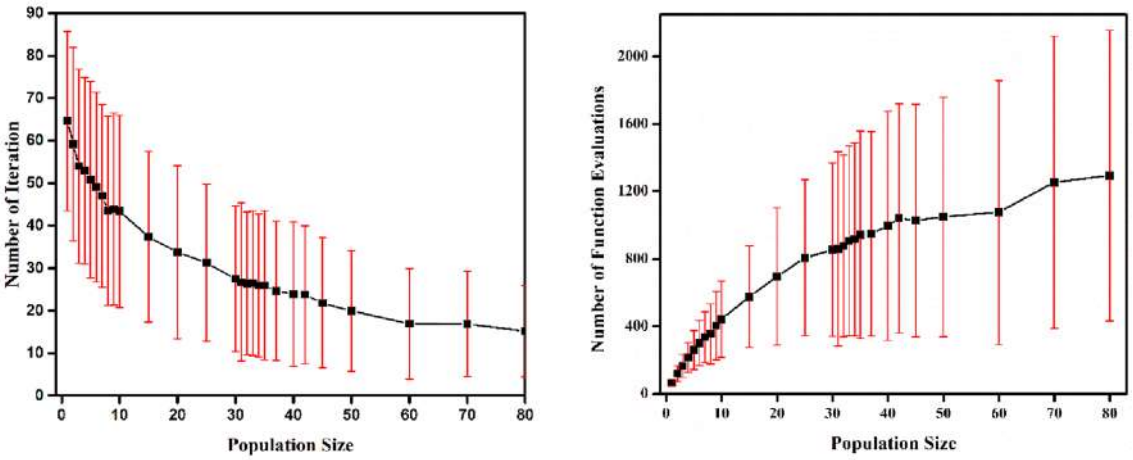

Fig. 7 The number of iterations and number of function evaluations as a function of the population for optimizing Multi-Layer: ZnO and MoOx layers with SA algorithm

were carried out by considering the varying thickness of ZnO between 0 and 80 nm, while constant MoOx thickness at 10 nm and the varying thickness of MoOx between 0 and 30 nm with constant ZnO thickness at 30 nm to reach the best Jsc at 116.62 A/m^2. The obtained results by PSO indicated that the maximum number of required function evaluations for optimizing ZnO was 33.1 ± 23.16 compared to 81 for the brute-force method and 78.16 ± 1.65 for the genetic algorithm. This method required 19.6 ± 11.7 number of function evaluations to optimize the MoOx layer, whereas the best optimization achieved by GA using the Roulette wheel method was 13.05 ± 3.24. The required number of function evaluations for two-layer optimization using PSO amounts to 111.27 ± 60.1, which is considerably lower than the 1758.77 ± 39.75 of GA. Even with the highest SD value, this value is much lower than the corresponding value from the brute-force method and GA algorithm. The SA algorithm was also implemented by two single-based and population-based approaches. For ZnO optimization by SA, the maximum required function evaluations were estimated 29.98 ± 18.2 and 38.29 ± 26.08 by single-based (1 population) and population-based (2 populations), respectively. The obtained results indicated that the number of function evaluations in the population-based method is higher than those in the single-based method. This phenomenon was also observed in MoOx optimization. The number of function evaluations required for the SA algorithm was 18.26 ± 12.12 with a population of 1 in single-based. In this case, due to the small search space, the higher population resulted in more the number of function evaluations than the Brute-Force method. The required number of function evaluations for two-layer optimization was obtained 65.63 ± 21.11 for single-based and 575.76 ± 301.64 for population-based with a population size of 15. The results indicated that the population-based method presented 575.76 ± 301.64, the number of function evaluations with a 100% success rate significantly lower than the GA. They also showed that the single-based method demonstrated a lower required number of simulations with an 80% success rate. The 20% of simulations in the single-based method could not find the optimum result due to the many locally optimal solutions of the objective function. Also, a comparison between the obtained results by PSO and SA shows that the required NFEs obtained through the single-based SA are always lower than the PSO in all cases. However, the PSO method performs significantly better than the population-based SA. For example, for multi-layer optimization, the number of required NFEs in single-based SA is 65.63 ± 21.11, significantly lower than PSO, 111.27 ± 60.1. In this case, the highest required NFEs is for population-based SA, which is 575.76 ± 301.64. The use of optimization algorithms in more advanced and complicated solar cell systems with more layers, like quantum well-based solar cells, and by taking into account additional parameters such as materials and doping concentration of each layer under study, can minimize a computational cost, thereby minimizing the required laboratory capacity in this area as much as possible.

Acknowledgements The support from Shahid Beheshti University is gratefully acknowledged.

Declarations

Conflict of interest There is NO Competing Interest. The authors declare no competing financial and non-financial interests.

References

1. Li, G., Li, M., Taylor, R., Hao, Y., Besagni, G., Markides, C.N.: Solar energy utilisation: current status and roll-out potential. Appl. Therm. Eng. (2022). https://doi.org/10.1016/j.applthermaleng.2022.118285
2. Korfiati, A., Gkonos, C., Veronesi, F., Gaki, A., Grassi, S., Schenkel, R., Volkwein, S., Raubal, M., Hurni, L.: Estimation of the global solar energy potential and photovoltaic cost with the use of open data. Int. J. Sustain. Energy Plan. Manag. **9**, 17–29 (2016). https://doi.org/10.5278/ijsepm.2016.9.3
3. Güney, T.: Solar energy and sustainable development: evidence from 35 countries. Int. J. Sustain. Dev. World Ecol. **29**, 187–194 (2022). https://doi.org/10.1080/13504509.2021.1986749
4. Kannan, N., Vakeesan, D.: Solar energy for future world: - a review. Renew. Sustain. Energy Rev. **62**, 1092–1105 (2016). https://doi.org/10.1016/J.RSER.2016.05.022
5. Milichko, V.A., Shalin, A.S., Mukhin, I.S., Kovrov, A.E., Krasilin, A.A., Vinogradov, A.V., Belov, P.A., Simovski, C.R.: Solar photovoltaics: current state and trends. Phys. Usp. **59**, 727–772 (2016). https://doi.org/10.3367/UFNE.2016.02.037703/XML
6. King, R.R., Karam, N.H., Ermer, J.H., Haddad, M., Colter, P., Isshiki, T., Yoon, H., Cotal, H.L., Joslin, D.E., Krut, D.D., Sudharsanan, R., Edmondson, K., Cavicchi, B.T., Lillington, D.R.: Next-generation, high-efficiency III-V multijunction solar cells. Conf. Rec. IEEE Photovolt. Spec. Conf. (2000). https://doi.org/10.1109/PVSC.2000.916054
7. Pakhanov, N.A., Andreev, V.M., Shvarts, M.Z., Pchelyakov, O.P.: State-of-the-art architectures and technologies of high-efficiency solar cells based on III–V heterostructures for space and terrestrial applications. Optoelectron. Instrum. Data Process. **54**, 187–202 (2018). https://doi.org/10.3103/S8756699018020115
8. Yamaguchi, M.: Japanese R and D activities of high efficiency III-V compound multi-junction and concentrator solar cells. Energy Procedia. **15**, 265–274 (2012). https://doi.org/10.1016/J.EGYPRO.2012.02.031
9. Miller, B., Ranum, D.: Problem-solving with algorithms and data structures release 3.0, Franklin, Beedle & Associates (2013)
10. DIab, A.A.Z., Sultan, H.M., Do, T.D., Kamel, O.M., Mossa, M.A.: Coyote optimization algorithm for parameters estimation of various models of solar cells and PV modules. IEEE Access **8**, 111102–111140 (2020). https://doi.org/10.1109/ACCESS.2020.3000770
11. Farah, A., Belazi, A., Benabdallah, F., Almalaq, A., Chtourou, M., Abido, M.A.: Parameter extraction of photovoltaic models using a comprehensive learning Rao-1 algorithm. Energy Convers.

Manag. **252**, 115057 (2022). https://doi.org/10.1016/J.ENCONMAN.2021.115057
12. Kharchouf, Y., Herbazi, R., Chahboun, A.: Parameter's extraction of solar photovoltaic models using an improved differential evolution algorithm. Energy Convers. Manag. **251**, 114972 (2022). https://doi.org/10.1016/J.ENCONMAN.2021.114972
13. Hemeida, A.M., Omer, A.S., Bahaa-Eldin, A.M., Alkhalaf, S., Ahmed, M., Senjyu, T., El-Saady, G.: Multi-objective multi-verse optimization of renewable energy sources-based micro-grid system: real case. Ain Shams Eng. J. **13**, 101543 (2022). https://doi.org/10.1016/J.ASEJ.2021.06.028
14. Alavi, M., Yoo, Y., Vogel, D.R.: Using information technology to add value to management education. Acad. Manag. J. **40**, 1310–1333 (2017). https://doi.org/10.5465/257035
15. Ardito, C., Costabile, M.F., De Marsico, M., Lanzilotti, R., Levialdi, S., Roselli, T., Rossano, V.: An approach to usability evaluation of e-learning applications. Univers. Access Inf. Soc. **43**, 270–283 (2005). https://doi.org/10.1007/S10209-005-0008-6
16. Boehner, K., DePaula, R., Dourish, P., Sengers, P.: How emotion is made and measured. Int. J. Hum. Comput. Stud. **65**, 275–291 (2007). https://doi.org/10.1016/J.IJHCS.2006.11.016
17. Meer, K.: Simulated annealing versus metropolis for a TSP instance. Inf. Process. Lett. **104**, 216–219 (2007). https://doi.org/10.1016/J.IPL.2007.06.016
18. Niknam, T.: An approach based on particle swarm optimization for optimal operation of distribution network considering distributed generators. IECON Proc. Indus. Elect. Conf. (2006). https://doi.org/10.1109/IECON.2006.347222
19. Niknam, T., Firouzi, B.B., Nayeripour, M.: An efficient hybrid evolutionary algorithm for cluster analysis. World Appl. Sci. J. **4**(2), 300–307 (2008)
20. Rajan, C.C.A., Mohan, M.R.: An evolutionary programming based simulated annealing method for solving the unit commitment problem. Int. J. Electr. Power Energy Syst. **29**, 540–550 (2007). https://doi.org/10.1016/J.IJEPES.2006.12.001
21. Saber, A.Y., Senjyu, T., Yona, A., Urasaki, N., Funabashi, T.: Fuzzy unit commitment solution—A novel twofold simulated annealing approach. Electr. Power Syst. Res. **77**, 1699–1712 (2007). https://doi.org/10.1016/J.EPSR.2006.12.002
22. Vincent, P., Sergio, G.C., Jang, J., Kang, I.M., Park, J., Kim, H., Lee, M., Bae, J.H.: Application of genetic algorithm for more efficient multi-layer thickness optimization in solar cells. Energies **13**, 1726 (2020). https://doi.org/10.3390/EN13071726
23. Anabestani, H.: Investigation on performance enhancement of micro-sized IR photodetectors, UWSpace. http://hdl.handle.net/10012/17406 (2021)
24. Kennedy, J., Eberhart, R.: Particle swarm optimization. Proc. ICNN'95 Int. Conf. Neural Netw. **4**, 1942–1948 (1942). https://doi.org/10.1109/ICNN.1995.488968
25. Kennedy, J.F., Eberhart, R.C., Shi, Y.: Swarm intelligence, vol. 512. Morgan Kaufmann Publishers, San Francisco (2001)
26. Niknam, T., Amiri, B., Olamaei, J., Arefi, A.: An efficient hybrid evolutionary optimization algorithm based on PSO and SA for clustering. J. Zhejiang Univ. A **10**, 512–519 (2009). https://doi.org/10.1631/JZUS.A0820196
27. Kirkpatrick, S., Gelatt, C.D., Vecchi, M.P.: Optimization by simulated annealing. Science **80**(220), 671–680 (1983). https://doi.org/10.1126/SCIENCE.220.4598.671
28. Rutenbar, R.A.: Simulated annealing algorithms: an overview. IEEE Circuits Devices Mag. **5**, 19–26 (1989). https://doi.org/10.1109/101.17235
29. Siddique, N., Adeli, H.: Simulated annealing its variants and engineering applications. Inte. J. Artif. Intell. Tools (2016). https://doi.org/10.1142/S0218213016300015

International Journal of Energy and Environmental Engineering (2023) 14:627–641
https://doi.org/10.1007/s40095-022-00539-9

ORIGINAL RESEARCH

Capping carbon emission from green data centers

Tathagata Bhattacharya[1] · Mostafa Rahgouy[4] · Xiaopu Peng[2] · Taha Takreeti[4] · Ting Cao[3] · Jianzhou Mao[4] · Amit Das[4] · Xiao Qin[4] · Apurba Sinha[5]

Received: 16 February 2022 / Accepted: 9 September 2022 / Published online: 10 October 2022

Abstract
The world has witnessed a global surge in energy consumption and carbon footprint since the industrial revolution. Data centers are claimed to be the second most significant contributor of the havoc greenhouse gasses. This paper deals with modeling carbon footprint of green data centers. Initially, we use a panel dataset of a green data center that mostly relies on green energy resources for power. Our study reveals that in spite of massive renewable energy usage, the carbon footprint trend of this data center is quite significant. Alongside, due to massive nuclear energy usage in this data center, a hefty amount of nuclear waste is generated causing a global threat to sustainability. This is a novel paper that pinpoints that though green data centers claim they are zero-carbon data centers but the reality is different. We prove that green data centers also emit significant amount of greenhouse gasses and cause danger to sustainability. Alongside, we provide a nuclear footprint estimator that effectively calculates the nuclear emission and carbon footprint from the data center each hour. We also provide a remedy to this entire situation and provide a carbon footprint model in this paper that optimizes the total carbon emission from this green data center.

Keywords Energy modeling · Power management · Green energy · Brown energy · Carbon footprint · Nuclear estimator

Introduction

Starting with the aviation industry to car manufacturers, and from electrical industries to agricultural plants [1], the globe is trying to manage carbon emission smartly. Data centers are not exceptions; capping carbon footprint has become a prime focus for developing large-scale data centers. Data centers consume a massive amount of energy to fulfill its daily energy demands. Unsurprisingly, powering and cooling a data center are expensive in terms of energy demand [2]. This enormous power demand results in emitting a significant amount of carbon into the air [3]. This carbon emission causes a threat to global sustainability [4]. Nowadays, data centers are responsible for almost 2 percent of global carbon emission [5], which is causing global warming along with ice melt at the poles [6]. In what follows, we describe our motivation behind the study of global carbon footprint.

Massive brown energy usage

Electric grids burn mostly coal energy to meet the ever-increasing power demand of the data centers throughout the globe. A report of the Lawrence Berkeley National Laboratory claims that the US data centers consume up to 70 billion Kilowatt-hours of energy which costs around dollar 7 billion [7]. Another report states that these data centers consume over 1000 W/m2 of power—more than 10 times that required by a commercial office space [8]. Scientists estimate that a large-scale data center uses the energy of

✉ Tathagata Bhattacharya
tzb0063@auburn.edu

Xiao Qin
xqin@auburn.edu

Apurba Sinha
m.sinha0686@gmail.com

[1] Auburn University, Montgomery, USA

[2] Lander University, Greenwood, USA

[3] Truman State University, Kirksville, USA

[4] Department of Computer Science and Software Engineering, Shelby Center for Engineering Technology, Samuel Ginn College of Engineering, Auburn University, Auburn, AL 36849-5347, USA

[5] Department of Computer Science and Software Engineering, Guru Gobind Singh Educational Society Technical Campus, Bokaro, India

almost 25,000 households [9]. One of the most crucial factors that add to the expense of powering a data center is cooling. For a standard data center, the cost of cooling can be significantly high [10]. Reports assert that an efficient cooling system of a data center consumes 24% of the total energy consumption, whereas a least efficient cooling system can consume up to 61% of total energy. On average, a cooling system consumes 40% of the total data center energy [11]. Today IT sector uses 7% of the global electricity; it is expected to consume 13% of the global electricity no sooner [12]

Power management and energy-saving techniques have been deployed to build energy-efficient data centers [13]. All these cutting-edge technologies come at the cost of huge expenditure, intensive labor, and excellent infrastructure. Most of the existing schemes overlook modeling clean energy resources (e.g., solar and wind). Renewable energy resources [14] can bring a panacea in this situation. Researchers claim that photovoltaic cells can produce up to 1.5 MW power [15]. Brown energy resources give the way to green energy resources, which further boost energy efficiency of future data centers.

Global carbon footprint

Carbon dioxide is one of the principal greenhouse gasses that causes the rise in the earth's average temperature [16]. To mitigate excessive carbon emission, engineers ought to cap the carbon emission of the data centers. Data centers are estimated to produce the fastest-growing carbon footprint [17]. Data centers are responsible for 2% of the global carbon footprint [18], and the growth is expanding. Reports claim that data centers can produce carbon dioxide of 171,630 kg [19]. Now the question arises, how do data centers produce such a hefty amount of co_2. Electric grids burn a hefty amount of brown energy resources to meet the never-ending power needs of the data centers [20]. This tremendous power consumption leads to increased emission of greenhouse gasses, especially Carbon Di Oxide causing an increase in the earth's average temperature by1.5 to 2 degrees [21].

Although a carbon tax has been imposed on the data centers to cap the carbon footprint [3], such a tax does not help the overall situation. The curve in the rapid growth of carbon dioxide ever since the industrial revolution has been steep [21]. Today parallel and cloud computing powered by virtualization has proved to be effective in capping the carbon footprint of data centers [22]. Using green energy to curb the carbon footprint is an optimum solution. It is evident that green slots reduce carbon footprint by 39% [23]. Alongside, smart grids are furnishing a green revolution for the future data centers managing their carbon footprint [24]. Therefore, green computing is expected to bring forth much-needed positive environmental changes.

Global sustainability

Fastest-growing data centers and IT industry causes impose a financial burden accompanied by environmental degradation [25]. Today the total energy cost of operating data centers is approaching $14 billion a year; such a high cost is going to be $50 billion per year in the recent future by 2020 [26]. Total cooling cost is estimated to be around $7 billion according to the reports [27]. An array of models predicts that data centers would swallow 10 percent more energy every year, thereby generating massive e-waste and greenhouse gasses. Energy resources of data centers are significantly dependent on brown energy resources such as coal and natural gas. Therefore, it is evident that by 2030, the natural resources for non-renewable energy will deplete causing an environmental dis-balance [28]. Now coming to heat dissipation, data centers are the cause of massive heat emission [29]. Apart from wasting billions of dollars in meeting the energy demand, data centers are one of the true factors behind climate change [30]. Due to the increase in atmospheric greenhouse gasses, the global temperature has increased 1.5 to 2.5 degrees [31]. This global warming results in ice melting at the poles leading to devastation.

To battle with this evil, google and yahoo have incorporated evaporative cooling techniques [32]. Governments are focusing on green energy deals to save the climate. We are shifting our focus from traditional data centers to zero-carbon data centers. Companies like Google are trying to make 100% carbon–neutral arrangements [33]. It is prudent to adopt clean energy to fulfill the energy demand of data centers. These clean energy resources intend to mitigate financial burden, to cut back carbon footprint, and most importantly, to ensure sustainability of the earth.

Our contributions

It is evident that world needs to focus on reducing the carbon emission to prevent the damage in sustainability. Extensive technologies such as workload consolidation and virtual machines (VM) migration, geographical load balancing are capable of mitigating the carbon emission issue of data centers at high cost. Leading-edge solutions like workload scheduling and power management lack efficiency standards and quality of services [34]. The globe needs easy, simple, reliable, and affordable solutions to handle the surge in carbon footprint and energy consumption. To deal with this challenging situation, we come up with a carbon footprint model to curtail carbon emission from data centers by predicting carbon footprint.

The primary contribution of the paper is detecting the flaws in the current green data center and providing the solution to overcome this situation. To execute our plan, we initially investigate the power consumption and carbon footprint of a green data center. We deliberately show that though green data centers claim they are zero-carbon data centers, eventually that is a myth. We also assert that though this data center mostly relies on green energy resources, the carbon footprint from the brown energy resources is significantly high. During peak hours, these data centers still use a massive amount of brown energy resources to meet their never-ending power demand. Also, this data center uses nuclear energy as a significant energy resource; but the nuclear waste from this data center can cause a severe threat to sustainability. Therefore, it is prudent to optimize the energy resources to cap the carbon footprint from this data center. Our model serves this purpose by effectively reducing the carbon emission from the data center while meeting its power demand. We summarize the overall contributions in this paper as follows.

We investigate and detect the flaws in green data centers.
We extend our carbon footprint calculator (see sec3.3) of the data center powered by heterogeneous energy resources to measure carbon footprint and nuclear footprint of the data center.
We display the yearly and daily energy usage trend and carbon footprint graph for the data center. We also specify the diversity of heterogeneous energy resources used in this data center.
We optimize the energy resources and their usage to limit the CO2 emission from the green data center.
Through series of evaluations, we prove the efficiency and accuracy of our model in terms of capping carbon emission from the data center.

Background of carbon capping

To maintain the ecological balance, engineers and researchers have come up with several power consumption and CO2 production models customized for data centers. This section presents the background of energy-efficient computing that brings solidarity and uniqueness to our research.

Capping carbon footprints from data centers

To control power usage effectiveness or PUE, the IBM management and management technology (MMT) is very effective in scanning the power usage of a data center [35]. Once we aim toward energy efficiency, we set a step ahead in reducing the carbon footprint. Today, green computing has opened a new horizon for the energy-efficient computing community to cap carbon dioxide elimination from data centers. Researchers delve into the development of novel technologies like virtualization, live VM migration, geographical load balancing, scheduling policies, and to name just a few. Virtualization by consuming less energy and creating negligible e-waste contributes toward reducing the carbon footprint from data centers [36]. Renewable energy-aware workload allocation algorithm to cap carbon footprint of the data center is claimed to be efficient [37]. Unlike the above techniques, our solution has its root in power modeling in a way to reduce the carbon emission from data centers by efficiently substituting green energy for brown energy resources while meeting data centers' energy requirements.

Power consumption of data center

Electric grids are a significant power resource of data centers. These electric grids are a huge consumer of brown energy (e.g., coal, hard coal, and petroleum). The data center architecture is very difficult decipher [38]. Power engineers use feature extraction, a very common technique to model the energy optimization of data centers [39]. Measuring the raw power consumption through hardware and software has been intrinsic research toward power optimization [40]. Current data centers depend on PDUs to optimize energy efficiency because these techniques are less portable [41]. Although PDUs are extremely efficient, the expensiveness and scalability issue of PDUs prevent the wide adoption of this approach. Hardware performance counters (HPC) today are ubiquitous in data centers for measuring power consumption as well as predicting energy consumption [42]. Along with these, CPU power dissipation with free cooling, clock gating or using split plane power, scientists are dealing up with the massive energy consumption of the data centers [43]. Energy-efficient cloud management and energy-efficient resource allocation have also grabbed eyes in terms of energy conservation in a data center [44]. Prior efforts have put forward several models derived from data gleaned by HPCs, but in some cases, such data are misleading and the error rate shows flaws in HPCs [45]

Power modeling

Data centers comprise a variety of components, the energy consumption models of which are summarized in this subsection. Servers are very an essential piece in a data center as the servers correspond to significant load requirements. Hence, constructing a power model for servers is crucial in reducing the total energy consumption of data centers. Server power models depend on other collaborating components. Roy et al. devised a simple yet elegant server power model, which is a summation of the load consumption of

CPU and memory [46]. Lewis et al. developed a server power-consumption model as a function of the total energy consumed by processor, memory, DD-RAM, SD-RAM, the semiconductor chips, and hard disks [47]. Apart from that, Orangerie et al. orchestrated server energy as a function of the energy consumption of system boot and system halt [48]; Li et al. constructed a power model as a function of energy consumed by active virtual machines running on servers [49].

Cooling is crucial in data centers to dispose of heat generated by the high power consumption in the server [50]. Cooling consumes approximately 50% energy of a standard data center; hence, it is imperative to model cooling energy consumption as well as maintain the quality of service or QoS [51]. Starting from the cooling fans, over the positioning of cool air into the system causes power inefficiencies [13]. To address this issue, a simple cooling power model came up to express fan power consumption as a function of the temperature of the air outside a data center and hot air exhaled by IT racks in the data center [52]. Other models capture cooling power consumption as a function of the fan speed of CRAH systems and the idle and dynamic power usage of CRAH units of data centers [53].

Machine learning techniques compel the researchers have investigated supervised and unsupervised learning models for power consumption in the data center. For instance, Beral et al. demonstrated a way of modeling expected processor and disk usage based on the M5P algorithm [54]. Khargharia et al. applied a decision tree to map a power-consumption model with current system behavior [55]. Dhiman et al. piloted a GMM-based approach for power prediction following an unsupervised learning method with an error below 10% [56]. Reinforcement learning enables power managers to dynamically create new power control policies during the run-time from information gathered via RL [57]. Moreno et al. developed a MLP-based neural network to predict power from clients' historical data [58]. Recently, *iOverbook*—an autonomous, online, and intelligent overbooking strategy—has drawn attention in the field of power modeling [59]. After analyzing the time and space complexities, Li et al. proposed an embedded software power model by the virtue of the backpropagation artificial neural network (B-ANN) [60]. Recent technology development has given birth to Data Center Energy-Efficient Resource Scheduling (DCEERS), Green Cloud, Elastic Tree, and DENS [61]. Intelligent Transportation Cloud Data Center [62], VM allocation algorithms for IoT platforms [63], auto-scaling energy-efficient VM migration [64] or dynamic workload placement [65] are current trends in capping the surge in energy consumption of the data centers.

All the aforementioned models have significantly contributed to reducing the power consumption of data centers from the perspectives of cooling and server power consumption. But no technology is a complete solution to the overall problem. Each of these models, technological developments have their flaws. Therefore, it is very complex to do a combination and permutation of all these energy-efficient technologies while running a complex data center. Therefore, it remains an open issue to the model power consumption of data centers powered by a diversity of energy resources. To fill this technological gap, we propose a power-consumption model for modern data centers that are powered by a mixture of green and brown energy to reduce the cost and carbon footprint.

System overview

In the beginning, we design a data center framework to understand the underpinning architecture of a data center. Section 3.1 defines the overall structure of a data center.

In what follows, we outline the system architecture in Sect. 3.1. In Sect. 3.2, we discuss the methodology applied to the development of the model.

System architecture

Figure 1 describes the framework of a medium-scale green *data center*, which compromises a large number of components like physical nodes, UPS, Battery, chillers, and other heterogeneous energy resources. We elaborate on each of these components below.

- *Nodes*: Computational resources draw significant energy from data centers to provide high-performance computing and storage capacity.
- *UPS*: UPS offers an uninterrupted power supply.

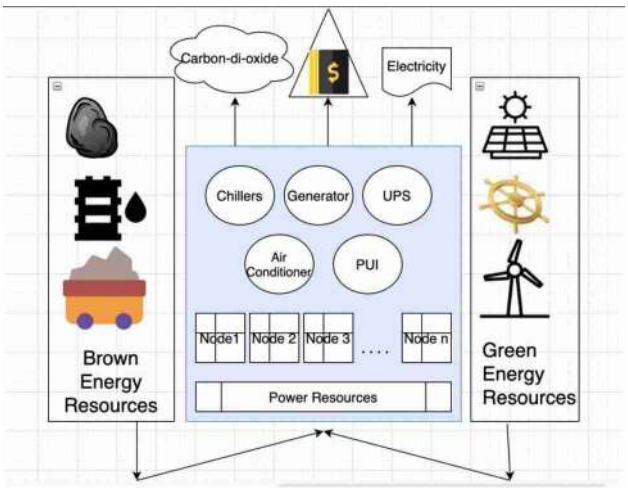

Fig. 1 The framework orchestrates a diversity of green and brown energy sources to maximize the energy efficiency of data centers

- *Air Conditioner*: Air conditioning systems are deployed to cool down the data centers.
- *Chillers*: Chillers are also used to cool down data centers with chilled water.
- *Cooling Tower*: Cooling towers work as a great source of cooling for data centers.
- *Generator*: Generators produce power from green and brown energies.
- *Battery*: Batteries facilitate energy storage for data centers.

More often than not, data centers consume a massive amount of energy from brown energy resources (see, for example, Coal and Petroleum at the left of Fig. 1), thereby releasing an enormous amount of heat and greenhouse gasses in the air to cause a major adverse impact on the environment. Recent evidence confirms that data centers consume energy as large as that of 25,000 households and 100 to 200 times of electricity consumed by standard office space[66]. This high brown energy consumption threatens the sustainability due to a massive carbon emission from this data center. The high energy cost can be curtailed by deploying green energy like solar and wind (see the green energy box at the right of Fig. 1). On the other hand, green energy causes no significant threat to the environment. Plus, green energy can be cost-effective as well while ensuring the energy supply for the data centers.

Instead of using massive coal, petroleum and fossil fuel energy, we advocate for green-energy-enabled data centers powered by solar, nuclear, wind, and hydro-energy to optimize the hefty energy demand and diminish the operational cost of the data centers. Clean energy not only reduces energy costs but also fulfills the UN sustainability goals by lowering greenhouse gas emissions in the air thus ensuring sustainability of the world [67]. Our dataset shows that solar, wind, nuclear and hydro-energies are notable sources of energy to eliminate brown energy usage. The data center in our system architecture makes use of the plenty of solar energy available during day time as a source of power while charging the UPS to use batteries during nighttime. Also, the energy from the turbine and wind can supply power demand to the data centers at night, thereby meeting the energy demand of the data center at night. Nuclear energy is employed as a backup plan. Though nuclear energy produces significantly less carbon dioxide (0.0264555 lb co2 from 12gm/kWh nuclear energy) but comes up with high amount of radioactive rays causing severity to the eco-system and mankind [68]. It is arguably true that the usage of green energy leads to the sustainability of future data centers.

Methodology

While designing a model to cap carbon emission from the data center, our second initiative is defining a creative methodology to experiment. To initialize in a methodical approach, we investigate the popular modeling approaches to obtain a rich dataset of energy usage per hour. We decided that we are not going to make a prediction with our model. Instead, we try to design a model that will prove to reduce the carbon dioxide emission from the data center in future. After harnessing the dataset, we portray the energy usage in graphical forms to come up with a clear picture of a data center's energy consumption and carbon footprint at any particular time of the day. This analysis strategy helps us in building a theoretical underpinning of our model. In what follows, we articulate our research methodology.

- **A pilot study.** Initially, we graphically plot the energy, power consumption and carbon emission trend from the data center. We categorically portray these graphical trends to illustrate the difference of energy and power usage along with carbon emission during each month, weekday and weekend, and each day.
- **Regression.** After a thorough analysis, we decide to implement linear, polynomial and lasso regression to predict a model for reducing the carbon footprint from the data center. We also determine to evaluate the efficiency and efficacy of our model in terms of their comparative study.
- **Other models** Finally, we would propose how can we bring panacea in this scenario and design the energy equation that will lower the carbon footprint for the future data centers.

Nuclear estimator

To deal with the carbon footprint of the data centers, we need to know the carbon emission from the data center per hour. Since, we did not have the data of carbon footprint from this data center, we design our own carbon footprint calculator. This calculator determines the carbon footprint of a data center if we can plug in the energy values in this calculator as an input. Therefore, we initially searched for the amount of carbon emission from the brown and green energy resources per hour. Once we get the values, we tune them in the calculator to find the total carbon footprint generated by burning the brown and green energy resources per hour. We have mentioned the heterogeneous resources and their symbols used to determine the carbon footprint of the data center in Table 1.

Let $t = \{\alpha, \beta\}$ denote a set of energy types, in which α and β represent green energy and brown energy, respectively.

Table 1 Symbol and annotation

Symbol	Annotation
$\alpha 1$	Hydro-pump energy
$\alpha 2$	Solar energy
$\alpha 3$	Nuclear energy
$\alpha 4$	Wind energy
$\beta 5$	Coal energy
$\beta 6$	Biomass energy
$\beta 7$	Fossil gas
$\beta 8$	Oil energy
$\gamma 1$	Carbon footprint of green energy
$\gamma 2$	Carbon footprint of brown energy
δ	Total carbon footprint
δ	Green energy
δ	Brown energy

The calculator presented in Algorithm 1 measures carbon footprint according to a given energy type in set t.

Algorithm 1: Carbon Footprint Calculator

```
Input  : α, β (KWh)
Output δ(lbph)
if α == α3 then
    return radioactive emission= 0.01 * α3
end
if t ==  α then
    return γ1= 0.04078552 * α1 + 0.110231 * α2 +
    0.0264555 * α3 + 0.0242508 * α4
end
else if t ==  β then
    return γ2 = 2.21 * β1 + (2 * 2.41) * β2 + 0.92 * β3 +
    2.11 * β4
end
δ = γ1 + γ2
```

Carbon footprint Calculator 1 detects the carbon footprint from both green and brown energy resources in a data center. Also, to modify the pre-existing carbon footprint calculators, we decide to add nuclear emission calculator. The data for carbon footprint for the brown energy resources are available at [69]. The amount of carbon footprint and nuclear emission(only for nuclear energy) generated from the green energy resources can be obtained from [70–73]. We do our little bit of calculations and play with these value and brought to a specific unit pound-per-hour(lbph). The nuclear emission is calculated in millirem per year. Then, we used simple arithmetic operations to find the amount of lbph of CO2 emissions per KWh burning of the different fuels. Though we include nuclear energy in this algorithm, one may opt for pruning the nuclear energy usage from the model. Nuclear energy resources contribute a very less carbon footprint, but such resources are highly radioactive. It is evident that nuclear energy's radioactivity causes cell damage, impotency, and cancer [74]. Because we are focusing on sustainability, we ensure that nuclear energy only plays a supporting role in our model. Also, it was initially considered that biomass is a zero-carbon energy resource [75]. Recent studies, however, indicate that burning biomass produces a carbon footprint double the amount of that produced by coal energy. For this reason, we treat biomass as brown energy in the model though it is traditionally classified as renewable energy [73].

Results and discussion

Data collection and data handling

Data collection for this research has been crucial in terms of reliability, authenticity and scalability. Although we explore a lot of information on energy efficiency, renewable energy usage, and power modeling of data centers, we could not accumulate a data center's public data on energy resources and energy usage. Fortunately, we have the detailed configuration of a data small-scale data center managed by Auburn University. We make use of the Auburn data center's configuration fed into the energy-consumption model [76] to estimate energy usage and energy resources. We opt for applying this model to project the energy usage of the Auburn data center because the model has been well validated in the literature. Thanks to our carbon footprint calculator, we could calculate the carbon emission from this data center per hour. After obtaining the panel dataset, we perform multiple machine-learning algorithms to exploit the entire scenario. We segmented the dataset into *yearly, weekday- weekend and heterogeneous* energy usage and carbon emission of the data center to proceed with the different aspects of our experiment.

Yearly energy consumption

Figure 2 orchestrates the brown and green energy usage of a data center per hour over one year. Figure 3 plots the carbon footprint of a data center per hour powered by brown and green energy resources. Figure 2 reveals that this data center uses a significant amount of green energy resources in this case(which is quite an exception). Though brown energy resource usage is quite elevated in Fig. 2, still we observe this data center uses more green energy in meeting the energy requirement. On a contrary, Fig. 3 indicates that even the less amount of brown energy usage in this data center produces much more carbon dioxide than that by the leading green energy resources. This reveals that the data center power usage needs an energy-intensive model to cap

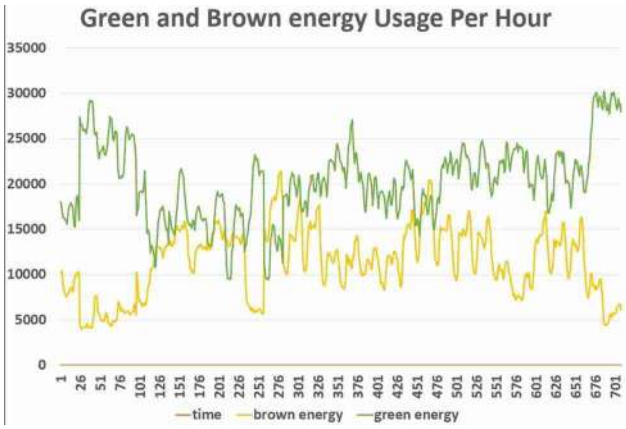

Fig. 2 This line chart defines the brown and green energy consumption of a data center per hour over a period of one year. The x-axis determines time in hour, where the y-axis denotes the energy usage in kwh. The maximum and minimum usage of brown energy resources in this figure is 22000 KWh and 3500 KWh, respectively, whereas the maximum and minimum green energy usage in this figure is 30000 KWh and 9500 KWh, respectively

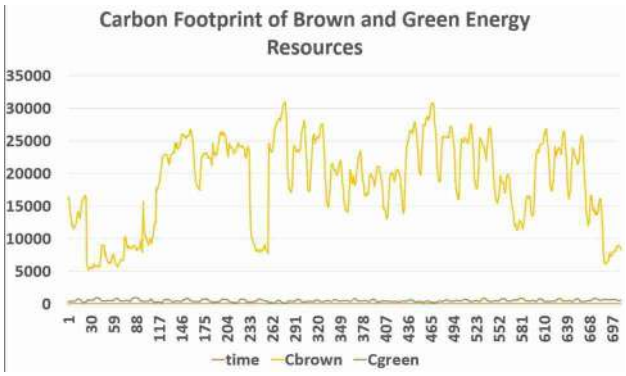

Fig. 3 This line chart defines the carbon footprint from a data center due to brown and green energy usage per hour over a period of one year. The x-axis determines time in hour, where the y-axis denotes the carbon footprint in pound per hour (lbph). The maximum and minimum carbon dioxide emission from brown energy resources in this figure is 32000 lbph and 5000 lbph, respectively, whereas the maximum and minimum carbon footprint from green energy usage in this fig is around 100 lbph and 26 lbph, respectively. Here, Cbrown and Cgreen represent carbon footprint of brown and green energy resources, respectively

its carbon footprint. To reduce the carbon emission from this data center, the energy resources must be carefully investigated and designed.

Figure 4 depicts the energy consumption cost of a data center per hour over a year. Figures 5 and 6 orchestrate the brown energy and green energy consumption of the data center per hour over a year. Figures 4 and 5 have a strong correlation. These two figures are related proportionally to each other. We notice, whenever there is a surge in energy demand and brown energy consumption increases, the cost

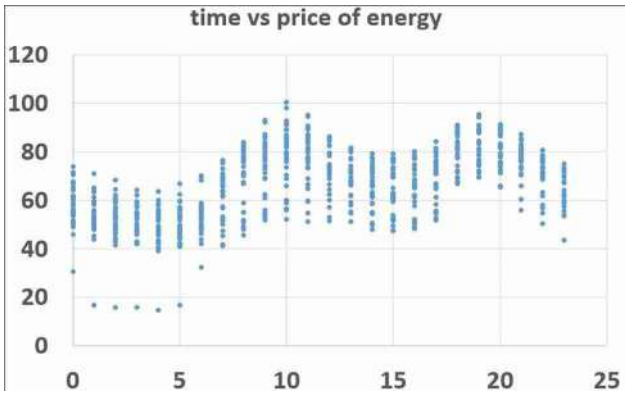

Fig. 4 The scatter plot defines the relationship between time and price of the energy consumption. The x-axis determines time in hour, where the y-axis denotes the cost of the energy usage per hour in dollar. The maximum cost in this figure is around dollar 100 per hour, whereas the minimum cost is around dollar 19 per hour

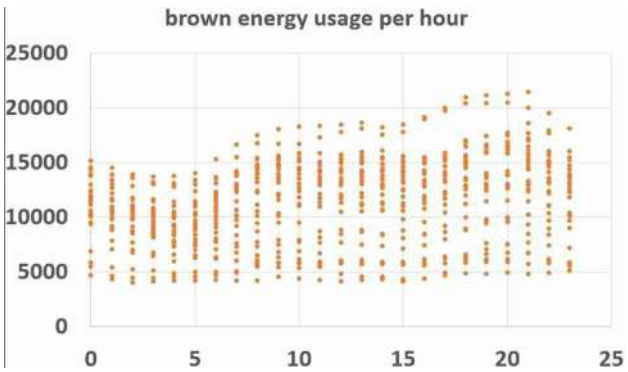

Fig. 5 This scatter plot defines the brown energy usage per hour in a data center over a period of one year. The x-axis determines time in hour, where the y-axis denotes the energy usage in kwh

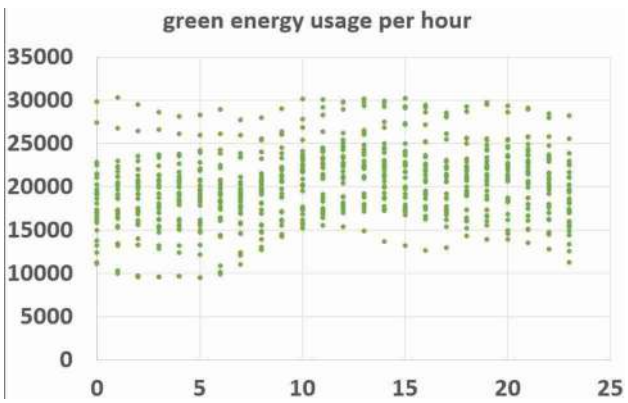

Fig. 6 This image defines the brown energy usage per hour in a data center over a period of one year. The x axis determines time in hour, where the y axis denotes the energy usage in kwh.

of energy consumption per hour also increases. For example, during the peak hours, from 10 AM to 8 PM, the cost and the brown energy usage are at their peak. Since, renewable energy resources (solar, wind, hydro-energy, etc.) are gifts of nature, they do not cost any significant amount(except nuclear energy). Therefore, we can conclude that excessive usage of brown energy solemnly increases the cost as well as the carbon footprint of the data center significantly. To deal with this situation, one needs to build a carbon footprint model comprising significant green energy resources and minimalist brown energy resources. This model can reduce power usage, increase cost efficiency and most importantly cap the

In this section, we portray the energy consumption and carbon footprint of the data center over the weekdays and weekends.

Figures 7, 8, 9 detail the energy consumption of the data center over the weekend. This scatter plot portrays that the data center uses significantly more green energy resources to meet the never energy demand. Since the total energy consumption on weekends is less, the data center uses less brown energy resources to reduce the carbon footprint. Figure 9 orchestrates the carbon footprint of the data center over the weekend. This scatterplot signifies that even less brown energy usage on the weekends could not impact the carbon emission much.

Figure 8 details the energy consumption of the data center on the weekdays. This scatter plot portrays that the data center uses significantly more brown energy resources to meet the ever-surging energy demand. Since the total

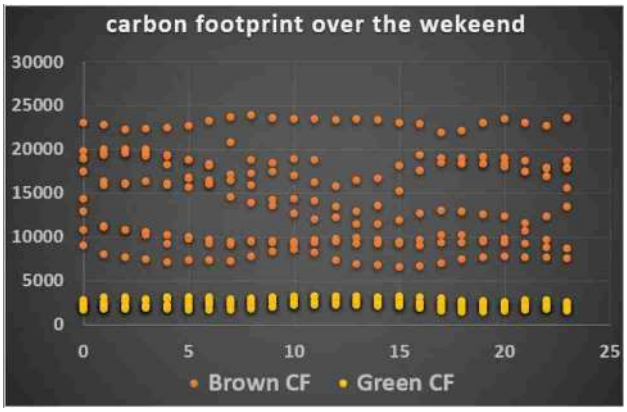

Fig. 7 The scatter plot defines the carbon footprint from brown and green energy usage over the weekend. The x-axis determines time in hour, where the y-axis denotes the carbon footprint in lbph. The maximum and minimum usage of carbon footprint from brown energy resources in this figure is 23000 lbh and 4000 lbph, respectively, whereas the maximum and minimum carbon footprint from green energy usage in this figure is 200 lbph and 11 lbph, respectively. Here, Cbrown and Cgreen represent carbon footprint of brown and green energy resources, respectively

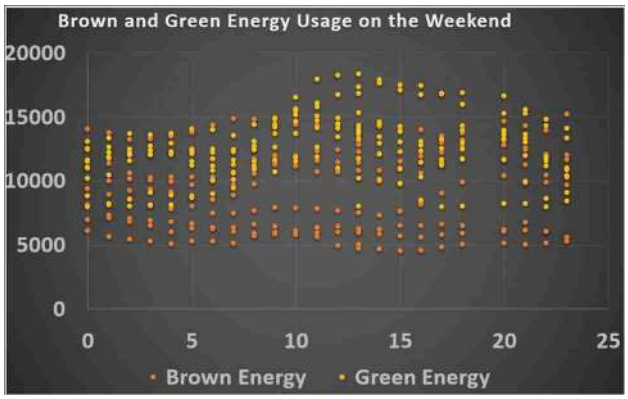

Fig. 8 The scatter plot defines the brown and green energy usage over the weekends. The x-axis determines time in hour, where the y-axis denotes the energy usage in kwh. The maximum and minimum usage of brown energy resources in this figure is 15000 KWh and 4000 KWh, respectively, whereas the maximum and minimum green energy usage in this fig is 18000 KWh and 9000 KWh, respectively

energy consumption on the weekdays is more, the data center uses more brown energy resources and less green energy resources to fulfill the energy requirement of the data center. This massive brown energy usage due to peak data traffic leads to an increase in carbon footprint significantly. Figure 10 portrays the surge in carbon emission due to the huge consumption of brown energy resources.

In terms of energy cost, the data center ends up paying more dollars on weekdays than weekends. Figure 11 portrays that weekend energy consumption cost is far less than that on the weekdays. On the same note, we observe that the amount of brown energy usage is significantly high to meet the power requirement of the data center. This indicates that the massive carbon footprint from the data center is not only

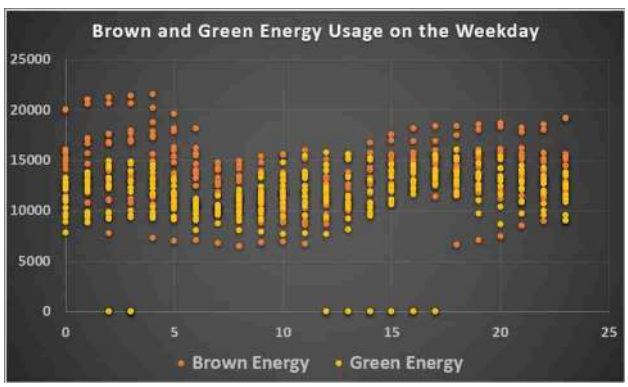

Fig. 9 The scatter plot defines the brown and green energy usage over the weekdays. The x-axis determines time in hour, where the y-axis denotes the energy usage in kwh. The maximum and minimum usage of brown energy resources in this figure is 23000 KWh and 8000 KWh, respectively, whereas the maximum and minimum green energy usage in this fig is 15000 KWh and 400 KWh, respectively

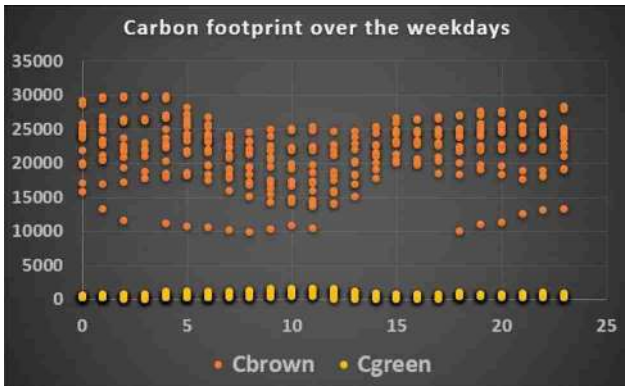

Fig. 10 The scatter plot defines the carbon footprint from brown and green energy usage over the weekend. The x-axis determines time in hour, where the y-axis denotes the carbon footprint in lbph. The maximum and minimum usage of carbon footprint from brown energy resources in this figure is 32000 lbph and 11,000 lbph, respectively, whereas the maximum and minimum carbon footprint from green energy usage in this figure is 167 lbph and 98 lbph, respectively. Here, Cbrown and Cgreen represent carbon footprint of brown and green energy resources, respectively

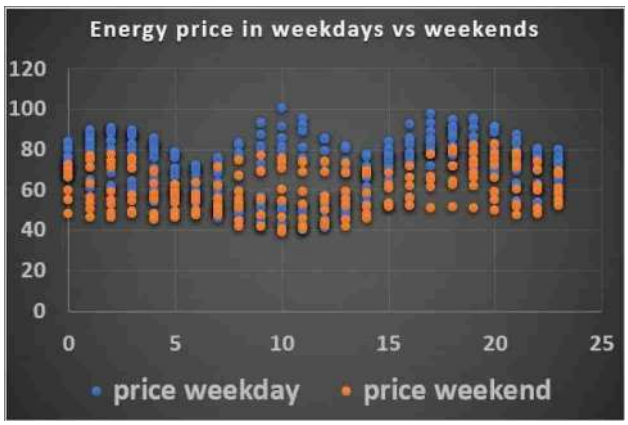

Fig. 11 The scatter plot defines the energy cost over the weekend and weekdays. The maximum energy cost on a weekday is dollar 110 during 10 AM to 3 PM and that during a weekend is dollar 75

significant damage due to brown energy usage, but ends up spending billions of dollars to buy those energy resources. Therefore, it is evident that this data center needs an efficient carbon footprint model that will cut down brown energy resources significantly while using more clean energy.

Heterogeneous energy resources

Figures 12 and 13 show the histogram of brown and green energy consumption of our data center. This histograms plot the frequency of brown and green energy usage. Figures 12 and 13 advocate that the frequency of high green energy consumption is evident in this data center.

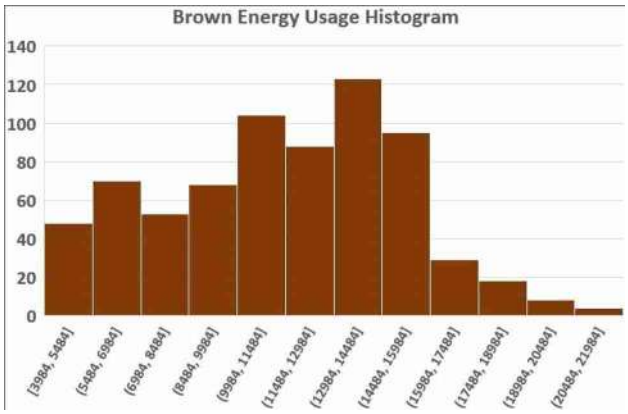

Fig. 12 The histogram details the brown energy consumption of our data center. The x-axis represents the amount of energy usage in KWh, and the y-axis represents the frequency of the energy consumption. The highest frequency (120) of brown energy lies between 12,984 and 14,484 KWh

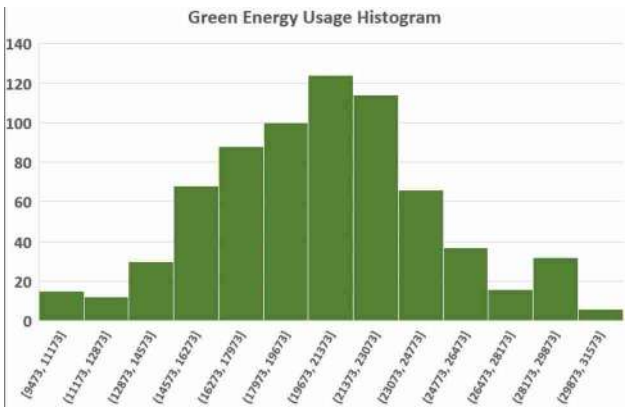

Fig. 13 The histogram details the green energy consumption of our data center. The x-axis represents the amount of energy usage in KWh, and the y-axis represents the frequency of the energy consumption. The highest frequency (120) of green energy lies between 19,673 and 23,373 KWh

Figure 14 depicts the details of various brown energy resources used to meet the power requirement of the data center. This image describes that hard coal and oil are significant sources of powering the data center, whereas biomass and coal also contribute to the carbon footprint of the data center. We describe, how hard coal and oil produce massive carbon footprint with regard to other brown energy resources like coal, biomass, etc. (see Sect. 3.3).

Figure 15 depicts the details of various green energy resources used to meet the power requirement of the data center. This image describes that wind, nuclear, and water reservoirs are the significant green energy resources to power the data center. Whereas solar, hydro-pumps, waste, and rivers also contribute to the energy supply of the data center. We describe, how nuclear energy produces

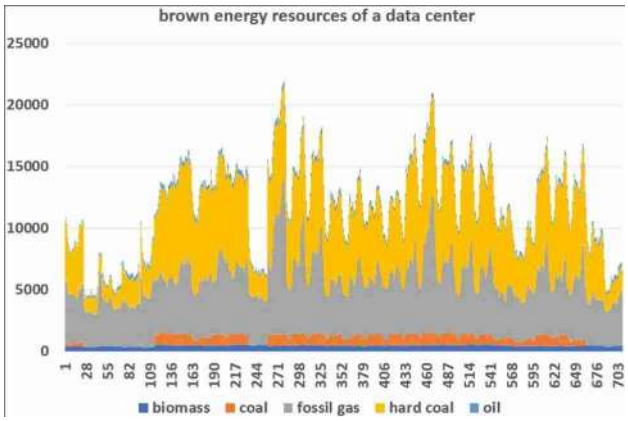

Fig. 14 This 2D chart depicts the various brown energy resource usage in a data center. Among all the other energy resources, hard coal and oil contribute to the maximum energy supply for the data center. Here, y-axis represents energy usage in KWh for various brown energy resources

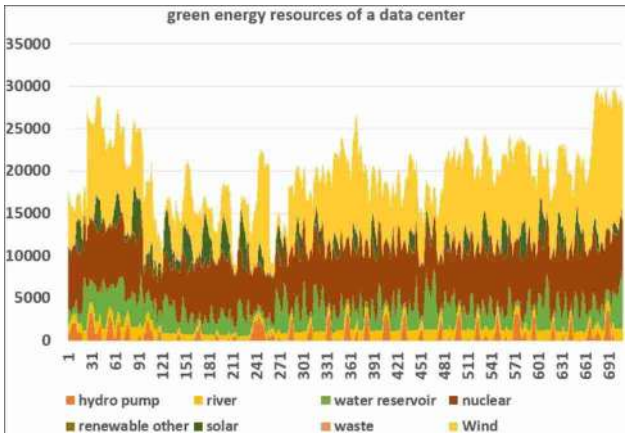

Fig. 15 This 2D chart depicts the various brown energy resource usage in a data center. Among all the other energy resources, hard coal and oil contribute to the maximum energy supply for the data center. Here, y-axis represents energy usage in KWh for various brown energy resources

radioactive emissions causing damage to mankind and animals (see Sect. 3.3). This signifies that the power source of brown energy needs to be designed properly to reduce the carbon emission and nuclear emissions from the data center.

Figure 16 represents the carbon footprint of the data center intrinsically. This line chart depicts that the rise in the total carbon footprint of the data center is solely due to the carbon footprint of brown energy resources over time. If we carefully investigate Fig. 16, we will find that the carbon footprint of the green energy resource is significantly less than that of the brown energy resources. Despite focusing on more green energy usage, this data center fails to cap the carbon dioxide emission from it. Therefore, this gives

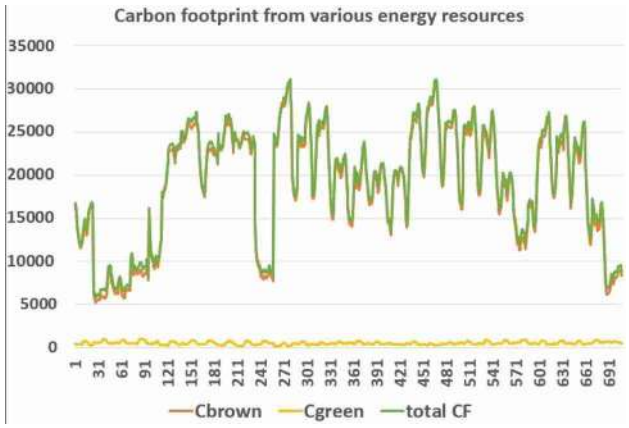

Fig. 16 The line chart plots the carbon footprint trend from brown and green energy along with the total carbon footprint. The Y-axis represents the carbon emission per hour in lbh. This chart signifies that though the overall brown energy usage is lesser than green energy resources, the carbon footprint of brown energy exceeds the carbon footprint of green energy. Thus, total carbon footprint also increases significantly. Here, Cbrown and Cgreen represent the carbon footprint of brown and green energy; whereas total CF represents the total carbon footprint of the data center

us a strong motivation to build an efficient carbon footprint model that will lower the carbon emission intensity from this data center.

Modeling energy usage

In our prior study reported in [5], we developed a power model to predict the power usage of a data center. This paper focused on the prediction accuracy of the algorithm in determining the future power consumption of the data center. But our current paper centers around capping the carbon footprint from a data center.

The aim of this paper is to build a model using maximum green energy resources. Also, our model should cap maximum carbon footprint from this data center. To provide a model for capping carbon footprint, we apply three different regression models, i.e., linear regression, polynomial regression, and lasso regression. These three models predict the carbon footprint of the green data center using the same energy resources but based on different statistical parameters. Turns out, all these three statistical models work fine to predict the carbon footprint of the data center. But here, we do not focus on prediction accuracy and efficacy. Rather our goal here is to determine the model that caps maximum carbon footprint from this data center. We plot the graph of actual and predicted carbon footprint from these models to determine the best model for capping carbon footprint for the green data centers. The best model from this graph (see 17) will provide an important measure for the network and

power engineers in reducing carbon dioxide emissions by just plugging in the energy values.

To do a pilot study, we initialized our experiment by checking the flaws of the data. After a quick reshaping and removing the skewness of the data, we start our experiment. We decide to proceed further in the following way:

- Initially, we decide to plot the dataset and find the relationship among each of the attributes. This gave us an idea of selecting the modeling strategy.
- Next, we split the dataset into random training and testing dataset. We finalize linear, polynomial, and lasso regression strategies to create the carbon footprint model for the data centers.
- Later, we decide to evaluate these models based on R squared value, p value, and other decision parameters.
- To understand the importance of each model, we came up with model plotting and thus decide the best model for capping the carbon footprint.
- Once figuring out the best possible modeling strategy, we design the carbon footprint reduction model of the data center.

The model evaluation is done based on p value, R squared value, mean squared error adjusted R squared values. Also, we plot the relationship between each attributes of the panel dataset to provide readers with a detailed graphical view. Also, once we plot the actual vs predicted carbon footprint for each model. We provide the details on how and why we claim that the particular model is great for capping the carbon emission from the data center.

Initially, we decide to use three candidate modeling techniques: linear regression, polynomial regression and lasso regression to predict the carbon footprint for future. In this case, we try to incorporate as much green energy as possible. The reason behind incorporating more green energy is to reduce the energy price as well as the carbon emission from the data center. But to meet the power hunger during the peak hours the data center requires some brown energy resources. Therefore, we decide to include fossil gas as one of the brown energy resources for the carbon footprint model. Though fossil gas is a traditional energy resource, but it causes less carbon emission and provides high power with lesser amount. Once we build the models with linear, polynomial and lasso regression, we intend to evaluate our model efficiency in predicting the future carbon footprint for future. We decide to define the efficiency parameters of these three models via Table 2.

Table 2 denotes the evaluation parameters of three modeling techniques. In terms of significance (denoted by the p value), all the models reject null hypothesis and prove to be significant. The standard R squared value suggests that these models have goodness of fit.

Table 2 The residual standard evaluation parameters

Parameter	Linear	Polynomial	Lasso
P value	< 2.2e−16	< 2.2e−16	< 2.2e−16
R^2	0.8957	0.8964	0.8257
Adjusted R^2	0.8956	0.8962	0.8981
Residual SE	1927	1920	2032
Mean squared error	4887	5016	3971

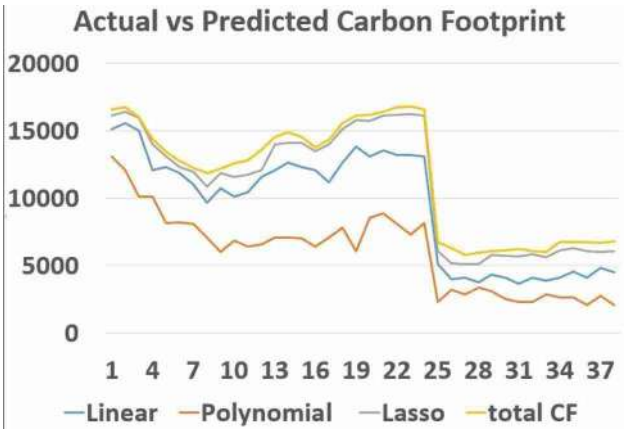

Fig. 17 This plot determines the relation between actual carbon footprint from the data center with predicted carbon footprint of the data center based on linear, polynomial and lasso regression model. The x-axis determines time, while the y-axis denotes the carbon footprint per hour

Error and mean squared error (MSE) suggest that lasso regression predicts the carbon footprint quite accurately, whereas linear regression and polynomial regression models have significant MSE. There lies the conflict. We can say that though lasso regression does a phenomenal job in predicting the carbon footprint accurately, the linear and polynomial model actually caps the carbon footprint of the data center. These two models of carbon footprint produce less carbon footprint and thus point toward sustainability. In other words, polynomial regression turns out to cap maximum carbon footprint from the data center than lasso regression and linear regression model. We have to always remember, here our aim is to build such a model that will reduce the current carbon footprint of this green data center for a better sustainable approach. Though in Fig. 17, the lasso regression has a high prediction accuracy, here we are more eager to see a model that will deplete the current carbon emission of this data center.

Figure 17 suggests that the polynomial regression is doing a phenomenal job in reducing the carbon footprint. The figure advocates that lasso regression is doing a phenomenal job in terms of prediction accuracy. But to cap the carbon footprint, we need to rely on linear and polynomial

regression. Now the question comes why we are saying both the linear and polynomial models are effective in terms of capping the carbon footprint. When we were modeling the carbon footprint of the data center, we introduced some linear parameters in the polynomial equation along with their second degree. This helped us in tuning the polynomial model to cap the carbon emission from the data center.

$$\begin{aligned} CarbonFootprint = &-2.291e+03 \times solar + 4.746e \\ &+03 \times solar^2 + -1.069e+04 \times wind \\ &+2.2369e+01 \times waste + -2.581e \\ &+04 \times waterreservoir + -3.247e \\ &+04 \times river + -2.763e+04 \times river^2 \\ &+-2.753e+00 \times hydropump \\ &+.240e+00 \times fossilgas \end{aligned} \tag{1}$$

In Eq. 1, we have used mostly green energy resources. It is worth noting that, to reduce wastage and balancing sustainability, we incorporate waste energy in our equation. Including waste energy and eliminating nuclear energy in out carbon footprint equation makes the model efficient, sustainable and green. Also, Eq. 1 is incorporated only one brown energy resource which is fossil gas. It is worth depicting that burning small amount of fossil gas produces significantly large amount of energy while contributing to less carbon footprint; hence, adding a single brown energy resource in our research equation has produced a better, stable and efficient model to reduce carbon emission. Our experiment gives rise to two case studies. The case studies are mentioned in Sect. 6.

Case studies

While experimenting with carbon footprint capping from data centers we come across two significant case studies. These case studies are mentioned below:

- Weekend carbon footprint capping(see 6.1)
- Carbon capping during peak hours(see 6.2)

These two case studies are described in the following subsections.

Weekend carbon footprint capping

While experimenting with the data, we decide to evaluate our model on the weekday weekend data. Though for weekdays, the model fits perfectly and there is no exception, model evaluation for weekends depicts a different scenario.

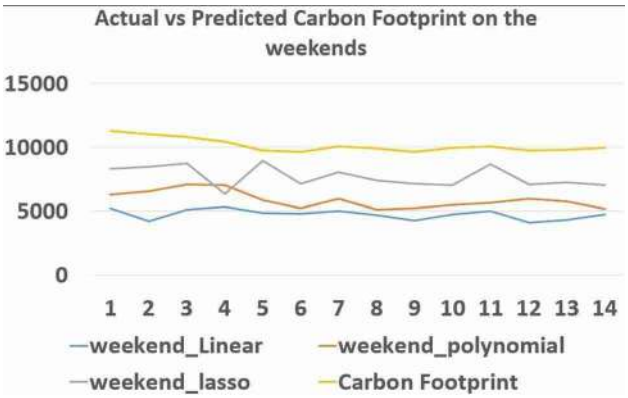

Fig. 18 This plot determines the relation between actual carbon footprint from the data center with predicted carbon footprint of the data center based on linear, polynomial and lasso regression model over the weekends. The x-axis determines time, while the y- axis denotes the carbon footprint per hour

Therefore, we feed the weekend data into three regression models and it turns out that the linear regression model caps maximum carbon footprint.

Figure 18 depicts the actual vs predicted carbon footprint over the weekends. Figure 18 reveals that the linear model works best in capping the carbon footprint of the data center over the weekends. This is probably because the data center power load over the weekends is significantly less. Limited brown energy usage over the weekends probably contributed to determining the best model to reduce carbon emission over the weekends. This result compels us to determine that along with our general carbon footprint model to limit the carbon footprint from the data center, we will look into more specific models in future research.

Carbon capping during peak hours

While analyzing the energy trend and carbon emission from the data center during peak hours, we realize, data centers burn massive brown energy resources during peak hours(see Sect. 4). Therefore, to meet the power demand during peak hours, we propose to store maximum green energy during non-peak hours. To store green energy resources, we may use various technical products like UPS(for solar energy), large above-ground tanks or in underground caverns (for wind energy), or pumped hydroelectric storage(for hydro-energy), etc. Modern technology today allows us to efficiently manage waste. We may think to use the waste energy efficiently to supply power during the peak hours for this data center.

Conclusion

In this study, we aim to construct a carbon footprint model to optimize the energy efficiency of green data centers. Thanks to the various modeling strategies, we propose a model to cap the carbon footprint of a green data center. More specifically, we updated our carbon footprint calculator with an effective algorithm to detect nuclear emissions from nuclear energy resources. Our intensive experiments demonstrate that our model is conducive to capping the carbon footprint of the data centers powered by brown and green energy. Our experimental results confirm that our model consistently declines carbon and nuclear emission from the data center.

As mentioned in the objectives(see Sect. 1), the main aim of this project was to limit massive brown energy usage of the data centers, capping the global carbon footprint, and make the data centers more sustainable. Our paper has produced a significant model that relies massively on clean energy resources that cause minimum carbon emission. Also, we focus on sustainability by not including nuclear energy as a power resource of this data center as it is still difficult to manage nuclear waste. Our nuclear and carbon footprint calculator is strong evidence that we are extremely dedicated to ensuring our mission and our objectives are properly maintained. Summarizing as a whole, we can claim that our paper ensures traditional energy usage reduction along with sustainability and carbon emission reduction.

As a future research direction, we intend to design statistical models at a micro-level. We want to develop an individual carbon footprint model for peak–non-peak hours of the day, weekend–weekdays, etc. In a second future direction, we want to explore the horizon of geographical load balancing strategy in capping power demand and carbon emission. Combining our carbon footprint model and the geographical load balancing will achieve superior efficiency, sustainability, and novelty in our research.

Declarations

Conflict of interest The authors declare that they have no conflict of interest.

References

1. Chowdhury, G.: Carbon footprint of the knowledge sector: what's the future?. J. Document. (2010).
2. Siriwardana, J., Jayasekara, S., Halgamuge, S.K.: Potential of airside economizers for data center cooling: A case study for key australian cities. Appl. Energy **104**, 207–219 (2013)
3. Khosravi, A., Andrew, L.L., Buyya, R.: Dynamic vm placement method for minimizing energy and carbon cost in geographically distributed cloud data centers. IEEE Trans. Sustain. Comput. **2**(2), 183–196 (2017)
4. Darda, S., Papalas, T., Zabaniotou, A.: Biofuels journey in Europe: currently the way to low carbon economy sustainability is still a challenge. J. Clean. Prod. **208**, 575–588 (2019)
5. Bhattacharya, T., Qin, X.: Modeling energy efficiency of future green data centers. In: 2020 11th International Green and Sustainable Computing Workshops (IGSC). IEEE, pp. 1–3 (2020).
6. Ivanova, D., Wood, R.: The unequal distribution of household carbon footprints in Europe and its link to sustainability. Glob. Sustain. **3** (2020).
7. Shehabi, A., Smith, S., Sartor, D., Brown, R., Herrlin, M., Koomey, J., Masanet, E., Horner, N., Azevedo, I., Lintner, W.: United states data center energy usage report (2016).
8. Stein, J.: More efficient technology will ease the way for future data centers. In: Proceedings (2002).
9. Dayarathna, M., Wen, Y., Fan, R.: Data center energy consumption modeling: A survey. IEEE Commun. Surv. Tutorials **18**(1), 732–794 (2015)
10. Parolini, L., Sinopoli, B., Krogh, B. H.: Reducing data center energy consumption via coordinated cooling and load management. In: Proceedings of the 2008 Conference on Power Aware Computing and Systems*, HotPower*, vol. 8, pp. 14–14 (2008).
11. Bertoldi, P.: A market transformation programme for improving energy efficiency in data centres. In: ACEEE Summer Study on Energy Efficiency in Buildings, pp. 9–14 (2014).
12. Sadler, R.: Video demand drives up global co_2 emissions. Clim. News Netw. (2017).
13. Zapater, M., Ayala, J.L., Moya, J.M., Vaidyanathan, K., Gross, K., Coskun, A. K.: Leakage and temperature aware server control for improving energy efficiency in data centers. In: 2013 Design, Automation & Test in Europe Conference & Exhibition (DATE). IEEE, pp. 266–269 (2013).
14. Ciarreta, A., Espinosa, M.P., Pizarro-Irizar, C.: Is green energy expensive? Empirical evidence from the Spanish electricity market. Energy Policy **69**, 205–215 (2014)
15. Morini, A.A., Hotza, D., Ribeiro, M.J.: Embodied energy and carbon footprint comparison in wind and photovoltaic power plants. Int. J. Energy Environ. Eng., pp. 1–11 (2021).
16. Florides, G.A., Christodoulides, P.: Global warming and carbon dioxide through sciences. Environ. Int. **35**(2), 390–401 (2009)
17. Whitehead, B., Andrews, D., Shah, A., Maidment, G.: Assessing the environmental impact of data centres part 1: background, energy use and metrics. Build. Environ. **82**, 151–159 (2014)
18. GeSI, S.: Enabling the low carbon economy in the information age. A Report by The Climate Group on behalf of the Global eSustainability Initiative (GeSI) (2008).
19. IEA, I.: Co2 emissions from fuel combustion highlights (2012)
20. Kong, F., Liu, X.: A survey on green-energy-aware power management for datacenters. ACM Comput. Surv. (CSUR) **47**(2), 1–38 (2014)
21. Bouley, D.: Estimating a data center's electrical carbon footprint. Schneider electric white paper library, pp. 14–22 (2011)
22. Ren, C., Wang, D., Urgaonkar, B., Sivasubramaniam, A.: Carbonaware energy capacity planning for datacenters. In: 2012 IEEE 20th International Symposium on Modeling, Analysis and Simulation of Computer and Telecommunication Systems, pp. 391–400 (2012)
23. Goiri, I., Haque, M.E., Le, K., Beauchea, R., Nguyen, T.D., Guitart, J., Torres, J., Bianchini, R.: Matching renewable energy supply and demand in green datacenters. Ad Hoc Netw. **25**, 520–534 (2015)
24. Asad, Z., Chaudhry, M.A.R.: A two-way street: Green big data processing for a greener smart grid. IEEE Syst. J. **11**(2), 784–795 (2016)

25. Le, K., Bilgir, O., Bianchini, R., Martonosi, M., Nguyen, T.D.: Managing the cost, energy consumption, and carbon footprint of internet services. ACM Sigmetrics Perform. Eval. Rev. **38**(1), 357–358 (2010)
26. Poess, M., Nambiar, R.O.: Energy cost, the key challenge of today's data centers: a power consumption analysis of tpc-c results. Proc. VLDB Endowm. **1**(2), 1229–1240 (2008)
27. Pakbaznia, E., Pedram, M.: Minimizing data center cooling and server power costs. In: Proceedings of the 2009 ACM/IEEE International Symposium on Low Power Electronics and Design, pp. 145–150 (2009).
28. McNerney, M.: The data center dilemma: Is our data destroying the environment? (2019). https://www.datacenterknowledge.com/industry-perspectives/data-center-dilemma-our-data-destroying-environment.
29. Liu, Y., Wei, X., Xiao, J., Liu, Z., Xu, Y., Tian, Y.: Energy consumption and emission mitigation prediction based on data center traffic and pue for global data centers. Glob. Energy Interconnect. **3**(3), 272–282 (2020)
30. Karl, T.R., Knight, R.W., Easterling, D.R., Quayle, R.G.: Indices of climate change for the united states. Bull. Am. Meteor. Soc. **77**(2), 279–292 (1996)
31. Uddin, M., Darabidarabkhani, Y., Shah, A., Memon, J.: Evaluating power efficient algorithms for efficiency and carbon emissions in cloud data centers: a review. Renew. Sustain. Energy Rev. **51**, 1553–1563 (2015)
32. Weerts, B.A., Gallaher, D., Weaver, R.: Green data center cooling: Achieving 90% reduction: Airside economization and unique indirect evaporative cooling. In: 2012 IEEE Green Technologies Conference. IEEE, 2012, pp. 1–6
33. Laine, J., Heinonen, J., Junnila, S.: Pathways to carbon-neutral cities prior to a national policy. Sustainability **12**(6), 2445 (2020)
34. Ni, J., Bai, X.: A review of air conditioning energy performance in data centers. Renew. Sustain. Energy Rev. **67**, 625–640 (2017)
35. Bose, R., Roy, S., Mondal, H., Chowdhury, D. R., Chakraborty, S.: Energy-efficient approach to lower the carbon emissions of data centers. *Computing*, pp. 1–19 (2021).
36. Agarwal, S., Nath, A.: Desktop virtualization and green computing solutions. In: Proceedings of the Second International Conference on Soft Computing for Problem Solving (SocProS 2012), December 28–30, 2012. Springer, pp. 1439–1449 (2014).
37. Renugadevi, T., Geetha, K.: Task aware optimized energy cost and carbon emission-based virtual machine placement in sustainable data centers. J. Intell. Fuzzy Syst. no. Preprint, pp. 1–13 (2021)
38. Greenberg, A., Lahiri, P., Maltz, D. A., Patel, P., Sengupta, S.: Towards a next generation data center architecture: scalability and commoditization. In: Proceedings of the ACM Workshop on Programmable Routers for Extensible Services of Tomorrow, pp. 57–62 (2008).
39. Kodama, Y., Itoh, S., Shimizu, T., Sekiguchi, S., Nakamura, H., Mori, N.: Power reduction scheme of fans in a blade system by considering the imbalance of cpu temperatures. In: 2010 IEEE/ACM Int'l Conference on Green Computing and Communications Int'l Conference on Cyber, Physical and Social Computing. IEEE, pp. 81–87 (2010).
40. Bircher, W.L., John, L.K.: Core-level activity prediction for multicore power management. IEEE J. Emerg. Sel. Top. Circ. Syst. **1**(3), 218–227 (2011)
41. Smith, J.W., Khajeh-Hosseini, A., Ward, J. S., Sommerville, I.: Cloudmonitor: Profiling power usage. In: 2012 IEEE Fifth International Conference on Cloud Computing. IEEE, pp. 947–948 (2012).
42. Chen, H., Shi, W.: Power measuring and profiling: the state of art. Handb. Energy-Aware Green Comput., pp. 649–674 (2012).
43. Jain, A., Mishra, M., Peddoju, S. K., Jain, N.: Energy efficient computing-green cloud computing. In: 2013 International Conference on Energy Efficient Technologies for Sustainability. IEEE, pp. 978–982 (2013).
44. Buyya, R., Beloglazov, A., Abawajy, J.: Energy-efficient management of data center resources for cloud computing: a vision, architectural elements, and open challenges. *arXiv preprint* arXiv:1006.0308 *(2010)*.
45. Wu, X., Chang, H.-C., Moore, S., Taylor, V., Su, C.-Y., Terpstra, D., Lively, C., Cameron, K., Lee, C. W.: Mummi: multiple metrics modeling infrastructure for exploring performance and power modeling. In: Proceedings of the Conference on Extreme Science and Engineering Discovery Environment: Gateway to Discovery, pp. 1–8 (2013).
46. Roy, S., Rudra, A., Verma, A.: An energy complexity model for algorithms. In: Proceedings of the 4th Conference on Innovations in Theoretical Computer Science, pp. 283–304 (2013).
47. Lewis, A.W., Ghosh, S., Tzeng, N.-F.: Run-time energy consumption estimation based on workload in server systems. HotPower **8**, 17–21 (2008)
48. Orgerie, A.-C., Lefevre, L., Guerin-Lassous, I.: Energy-efficient´ bandwidth reservation for bulk data transfers in dedicated wired networks. J. Supercomput. **62**(3), 1139–1166 (2012)
49. Li, Y., Wang, Y., Yin, B., Guan, L.: An online power metering model for cloud environment. In: 2012 IEEE 11th International Symposium on Network Computing and Applications. IEEE, pp. 175–180 (2012)
50. Zhang, Q., Meng, Z., Hong, X., Zhan, Y., Liu, J., Dong, J., Bai, T., Niu, J., Deen, M.J.: A survey on data center cooling systems: Technology, power consumption modeling and control strategy optimization. J. Syst. Archit., p. 102253 (2021).
51. Abbas, A., Huzayyin, A., Mouneer, T., Nada, S.: Effect of data center servers' power density on the decision of using in-row cooling or perimeter cooling. Alex. Eng. J. **60**(4), 3855–3867 (2021)
52. Liu, Z., Chen, Y., Bash, C., Wierman, A., Gmach, D., Wang, Z., Marwah, M., Hyser, C.: Renewable and cooling aware workload management for sustainable data centers. In: Proceedings of the 12th ACM SIGMETRICS/PERFORMANCE joint international conference on Measurement and Modeling of Computer Systems, pp. 175–186 (2012).
53. Meisner, D., Wenisch, T. F.: Does low-power design imply energy efficiency for data centers? In: IEEE/ACM International Symposium on Low Power Electronics and Design. IEEE, pp. 109–114 (2011).
54. Berral, J. L., Gavalda, R., Torres, J.: Adaptive scheduling on power-aware managed data-centers using machine learning. In: 2011 IEEE/ACM 12th International Conference on Grid Computing. IEEE, pp. 66–73 (2011).
55. Khargharia, B., Luo, H., Al-Nashif, Y., Hariri, S.: Appflow: Autonomic performance-per-watt management of large-scale data centers. In: 2010 IEEE/ACM Int'l Conference on Green Computing and Communications & Int'l Conference on Cyber, Physical and Social Computing. IEEE, pp. 103–111 (2010).
56. Dhiman, G., Mihic, K., Rosing, T.: A system for online power prediction in virtualized environments using gaussian mixture models. In: Proceedings of the 47th Design Automation Conference, pp. 807–812 (2010).
57. Shen, H., Tan, Y., Lu, J., Wu, Q., Qiu, Q.: Achieving autonomous power management using reinforcement learning. ACM Trans. Des. Autom. Electron. Syst. (TODAES) **18**(2), 1–32 (2013)
58. Moreno, I.S., Xu, J.: Neural network-based overallocation for improved energy-efficiency in real-time cloud environments. In: 2012 IEEE 15th International Symposium on Object/Component/ServiceOriented Real-Time Distributed Computing. IEEE, pp. 119–126 (2012).
59. Caglar, F., Gokhale, A.: ioverbook: intelligent resourceoverbooking to support soft real-time applications in the cloud. In: 2014

IEEE 7th International Conference on Cloud Computing. IEEE, pp. 538–545 (2014).
60. Li, Q., Guo, B., Shen, Y., Wang, J., Wu, Y., Liu, Y.: An embedded software power model based on algorithm complexity using backpropagation neural networks. In: 2010 IEEE/ACM Int'l Conference on Green Computing and Communications & Int'l Conference on Cyber, Physical and Social Computing. IEEE, pp. 454–459 (2010).
61. Shuja, J., Bilal, K., Madani, S.A., Khan, S.U.: Data center energy efficient resource scheduling. Clust. Comput. **17**(4), 1265–1277 (2014)
62. Zhang, W., Qi, Q., Deng, J.: Building intelligent transportation cloud data center based on soa. In: Research Anthology on Architectures, Frameworks, and Integration Strategies for Distributed and Cloud Computing. IGI Global, pp. 1084–1096 (2021).
63. Zhou, Z., Shojafar, M., Alazab, M., Abawajy, J., Li, F.: Afed-ef: an energy-efficient vm allocation algorithm for iot applications in a cloud data center. IEEE Trans. Green Commun. Netw. **5**(2), 658–669 (2021)
64. Saxena, D., Singh, A.K.: A proactive autoscaling and energyefficient vm allocation framework using online multi-resource neural network for cloud data center. Neurocomputing **426**, 248–264 (2021)
65. Ajibola, O.O., El-Gorashi, T.E., Elmirghani, J.M.: Energy efficient placement of workloads in composable data center networks. J. Lightwave Technol. **39**(10), 3037–3063 (2021)
66. Dayarathna, M., Wen, Y., Fan, R.: Data center energy consumption modeling: a survey. IEEE Commun. Surv. Tutorials **18**(1), 732–794 (2016)
67. Fonseca, L.M., Domingues, J.P., Dima, A.M.: Mapping the sustainable development goals relationships. Sustainability **12**(8), 3359 (2020)
68. Henry, H.F.: Is all nuclear radiation harmful? JAMA **176**(8), 671–675 (1961)
69. How much carbon dioxide is produced when different fuels are burned? [Online]. Available: https://www.eia.gov/tools/faqs/faqphp?id=73&t=11
70. Hydropower built back better and greener. https://iha-project.webflow.io/
71. How much co2 does one solar panel create. https://www.treehugger.com/ how-much-co-does-one-solar-panel-create-4868753
72. Wind energy's carbon footprint. https://www.factcheck.org/2018/03/wind-energys-carbon-footprint/
73. How can nuclear combat climate change? https://www.world-nuclear.org/nuclear-essentials/ how-can-nuclear-combat-climate-change.aspx
74. Questions about radiation. https://www.nrc. gov/about-nrc/radiation/related-info/faq.html
75. Čuček, L., Varbanov, P.S., Klemeš, J.J., Kravanja, Z.: Total footprints-based multi-criteria optimisation of regional biomass energy supply chains. Energy **44**(1), 135–145 (2012)
76. Song, S.L., Barker, K., Kerbyson, D.: Unified performance and power modeling of scientific workloads. In: Proceedings of the 1st International Workshop on Energy Efficient Supercomputing, pp. 1–8 (2013s).

International Journal of Energy and Environmental Engineering (2023) 14:719–741
https://doi.org/10.1007/s40095-022-00545-x

ORIGINAL RESEARCH

Using active/passive methods to control of MHD conjugate heat transfer of power-law fluids: a numerical entropy analysis by LBM

Mohammad Nemati[1] · **Mohammad Sefid**[1]

Received: 27 June 2022 / Accepted: 11 October 2022 / Published online: 8 November 2022

Abstract

Trying to understand to what extent active methods (the angle of placement chamber + the change of temperature of the barrier included inside the chamber) and passive methods (the application of MF + HAP) can be used in controlling and managing EP regarding to HT of non-Newtonian FF has been one of the goals of this numerical study. Since in this study, in addition to convection process, heat conduction in the solid is also considered, in addition to Ha, PL index, Ra, HAPC, TMF, the barrier temperature and the chamber inclination angle, TCR is presumed as the controller variable. The utmost momentous obtained outcomes are as follows: (A) On average, a decrease of up to 38% in the flow power and a decrease of up to 45% in HT amount are the result of an augmentation of in the value of Ha and PL index. (B) The impact of exerting MF becomes more noticeable with diminish in PL index. Augmentation of Ha to the highest value causes decline in the mean Nu by about 52% and 18% for $n = 0.75$ and $n = 1.25$, respectively. (C) To achieve a flow with higher power and higher the mean Nu, MF can be used non-uniformly, especially TMF1. The more noticeable influence of changing TMF is the result of augmentation of the amount of Ha. The influence of the change in TMF to the shear thickening fluid is lowest. (D) As TCR increases, the maximum mean Nu is acquired, in which case the impact of increasing Ha and the HAPC becomes more pronounced. (E) The minimum amount of HT, current power and MF influence is obtained when the chamber is at an angle of + 90°, in which case the mean Nu is up to about 75% less than the zero angle. (F) Although enhancement of HAPC reduces the mean Nu, it nevertheless increases the flow power and influence of MF on EP. In the case of heat production, the increment of in EP is the result of the enhancement of in Ha, unlike in other cases. (G) EP and current vigor increase by placing the barrier at hot temperature while the mean Nu diminishes. The contribution of MF in EP increases with enhancement of block temperature. (H) Be value increases with increment of HAPC, augmentation of Ha and decrement of TCR, and maximum Be value is obtained at an angle of + 90°.

Keywords Conjugate heat transfer · Power-law fluid · Heat absorption/production · Non-uniform magnetic field · Entropy production · Lattice Boltzmann method · Variable barrier thermal boundary condition · Inclination angle of chamber

List of symbols

B	MF vigor
Be	Number of Bejan
c	Discrete lattice velocity
F	Exterior force
f	Function of the density distribution
g	Energy distribution function
f^{eq}	Equilibrium density distribution function
g^{eq}	Equilibrium energy distribution function
g	Gravity vector
h	MF distribution function
h^{eq}	Equilibrium MF distribution function
H	Chamber height and length
Ha	Hartmann number
HAPC	Coefficient of HAP
k	Coefficient of thermal conductivity
n	Power-law index
Nu	Number of Nusselt
p	Pressure
Pr	Number of Prandtl
Q	Volumetric HAP
Ra	Number of Rayleigh
S	Entropy value in total mode

✉ Mohammad Nemati
mohammadnemati.lbm@gmail.com;
mohammadnemati@stu.yazd.ac.ir

Mohammad Sefid
mhsefid@yazd.ac.ir

[1] Faculty of Mechanical Engineering, Yazd University, Yazd, Iran

S_F EP arising from fluid friction
S_M EP arising from MF
S_H EP arising from HT
T Temperature
TCR Ratio of thermal conductivity $\left(\frac{k_s}{k_f}\right)$
TMF Type of magnetic field applied
$\mathbf{u}$ (u, v) Macroscopic velocities
$\mathbf{x}$ (x, y) Lattice coordinates

Greek symbols

α Coefficient of thermal diffusivity
β Coefficient of thermal expansion
τ^* Relaxation time associated with flow field
τ^{**} Relaxation time associated with temperature field
τ^{***} Relaxation time associated with MF
υ Kinematic viscosity
θ Dimensionless temperature
ρ Density
φ Enclosure placement angle
μ Dynamic viscosity
Ψ Dimensionless stream function
ω Weighting coefficient

Subscripts

c Cold
f Fluid
h Hot
s Solid

Introduction

One of the methods for controlling heat transfer (HT) caused by convection processes, including natural convection HT (NCHT), is to use the impact of magnetic field (MF) on fluid flow (FF). The analysis of FF subjected to MF is known as magnetohydrodynamics. This new medium can be used in an alternating MF for estimating and measuring X-ray experiments or for heating cellular tissues that have magnetic properties. The motivation that has led to make a detailed study of the behavior of magnetohydrodynamics in different conditions attractive and mandatory is the wide application of this physical branch, including applications in foundry, health and food industries [1–4]. It is necessary to check FF under non-uniform MF from two aspects: (1) FF is not always under uniform MF. Sometimes, depending on the conditions, the variable MF affects the flow. (2) To achieve a specific goal, there is a need to apply non-uniform MF in different ways. In addition to the fact that the characteristics of the current are controlled by the presence of MF, and the direction of applying this parameter also has special effects in such a way that it is possible to achieve different currents by using this parameter [5–8].

The main characteristic of fluids with non-Newtonian behavior is existence of nonlinear communication between tensors of stress and shear rate. This characteristic leads to different fluid behavior in different conditions. Unlike Newtonian fluid, where viscosity is a constant coefficient relating stress and shear rate, such a fixed parameter cannot be defined in non-Newtonian fluids. One of the most widely used models of this category of fluids is the power-law (PL) model, which has the ability to model extensive range of fluids. Most of the fluids in nature and used in industries reveal their non-Newtonian behavior, among which it can refer to the blood flow in the veins [9–12].

Since sometimes it is necessary to build a device for HT in electronic equipment that has a special shape, so it is very vital to investigate the design of chambers with different shapes in which HT occurs. Simplicity in the simulation of square and rectangular enclosures is the most obvious reason for the lack of research related to non-square enclosures. The placement of the chamber with special shapes in unwanted positions makes it important to check the shaped chambers [13–16].

One of the influencing parameters on FF fields is the presence of heat absorption/production (HAP), which sometimes has an impact in a desired and sometimes undesired way. In order to achieve a specific goal, researchers simultaneously examine HAP and MF on FF, which these activities has increased in recent years, because this phenomenon happens in momentous cases such as the nuclear industry and chambers where combustion occurs [17–20].

The concept of conjugate HT refers to that, in addition to the process of convection the fluid inside the industrial equipment, sometimes it is impossible not to consider HT inside the solid wall [21–23]. In this process, a part of HT occurs inside the solid wall and then the fluid is involved and the overall HT occurs. Investigating this phenomenon is due to its frequent use in different industries. As an example, the heat transferred in the wall of the combustion chamber cannot be ignored [24–26].

Respect to the outstanding capabilities of Lattice Boltzmann method (LBM) in the numerical analysis of complex flows, including multiphase flows, flows under the effect of MF, and combustion simulation, in the last three decades, it has received a lot of attention from engineering experts. The two main stages that are the basis of this method are as follows: the collision stage and the streaming stage. The most famous model for performing the collision phase is the LBGK model. In this model, single relaxation time (SRT) is used [27–30]. It is possible to understand some salient features of LBM in Fig. 1.

The study of entropy production (EP) as a measure of the destruction of workability is a very momentous issue to achieve an optimal design in energy systems. The basis of the science of EP goes back to the studies of Kelvin and

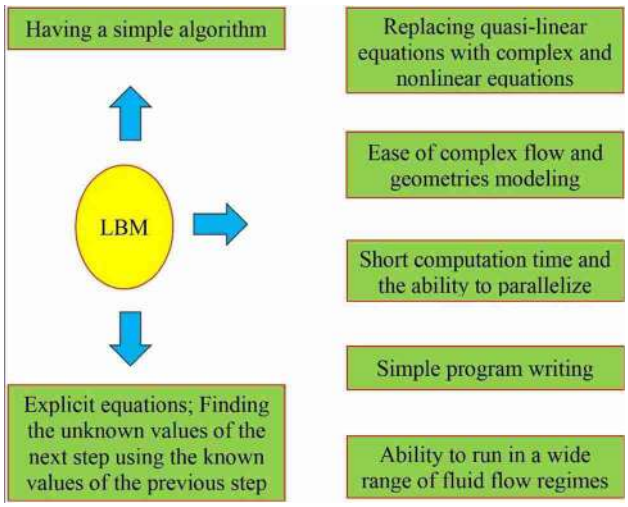

Fig. 1 Some features of LBM

Clausius on the irreversible aspects of the second law of thermodynamics. After the studies of Kelvin and Clausius, theories based on preliminary principles raised by them, it was developed. However, the study of EP caused by temperature difference by classical thermodynamics remained untested, which motivated many researchers to analyze applied engineering problems based on the second law of thermodynamics. Among the different sources of EP, we can mention HT caused by limited temperature difference, fluid viscosity and mass transfer [31–34].

Since LBM has been used in the existing simulation and considering the multiplicity of keywords related to the subject of the available perusal, a review of past studies with emphasis on priority over recent years is presented below. The most considerable achievements are stated so that the innovation and necessity of the available research can be clearly identified.

- Numerical study using SIMPLE algorithm on simulation of nanofluid NCHT inside an inclined square chamber contains thermogenic fins under uniform MF (Khetib et al. [35]): (1) It is possible to use the shape and placement of the fin embedded inside the chamber as a passive method to control the flow and HT characteristics. (2) The reduction of EP and the mean Nu results with the augmentation of MF power. These effects are controlled by changing the tilt angle of the chamber.
- Numerical study using control volume method to simulate nanofluid NCHT inside a rectangular chamber containing two hot triangular obstacles (Alqaed et al. [36]): (1) The decrease in Be and increase in mean Nu and EP are the result of augmentation of the strength of buoyancy forces (augmentation of Ra). (2) If the Ra is low (conduction prevails over convection), the amount of HT and EP does not change noteworthy due to the augmentation of Ha. (3) To manage FF, the inclination angle of the chamber can be used in such a way that the maximum amount of mean Nu is obtained in inclination angle of 30 degrees.
- Numerical study by LBM in the analysis of PL fluids HT under uniform MF (Aghakhani et al. [37]): (1) For flow management and control, it is possible to benefit from the variable aspect ratio of the chamber, so that the convection effects are significantly reduced with an augmentation of in the aspect ratio. (2) To reduce the effect of MF, it is enough to augmentation of the cavity aspect ratio and the fluid PL index.
- NCHT study in a square enclosure with considering the heat conduction effects in the conductor wall (Ferhi et al. [38]): (1) Although sometimes MF may unintentionally affect FF, its effects can be controlled by changing the angle of the chamber (or by changing the angle of application of the MF). (2) The irreversibility amount and the share of HT in EP are strongly dependent on the values of Ra, Ha and ratio of thermal conductivity (TCR), so that the lowest EP is the result for the lowest value of TCR.

So far, many methods have been proposed to control of HT in enclosures and heat exchangers, which are divided into active methods (with energy consumption) and passive methods (without energy consumption). In active methods, an external factor such as a MF or an oscillator causes a change in FF and increases the convection coefficient. But in passive methods, without using an external source and only with measures such as changing the geometry of the chamber such as making the walls wavy or changing the angle of chamber placement along with adding materials such as nanoparticles to the fluid, the rate of HT can be increased [39–45].

Taking into consideration the researches reviewed above, it is clear that the influence of HAP and non-uniform MF on NCHT in a novel inclined irregular hexagonal chamber involving a square block in different temperatures with LBM not reviewed. This numerical study, which has been analyzed considering the first and second laws of thermodynamics, reveals to what extent it is possible to influence the amount of HT and EP by using passive and active methods. The reason for using LBM in this simulation is the ease of applying the boundary conditions between the solid and fluid surfaces, which is the reason why this method is superior to other methods of proportional fluid dynamics in fluid flow modeling. The most great goal in carrying out this simulation is to try controlling and managing FF with various methods in order to achieve the desired flow characteristics in the face of desired or unwanted phenomena. This simulation can be helpful and effective for modeling

in high-efficiency design of equipment such as electronic coolers and thermal insulators.

After reading of this article, it is possible to understand how it is possible to influence the characteristics of the flow (Including the amount of HT, the flow power and the amount of EP) with low-cost or even simple method. Also, this numerical study can give a suitable perspective to those interested in the field of heat transfer, which can be done with tools such as LBM to accurately analyze fluid flow problems in order to obtain the best state to have a favorable flow. This study, which contains an extension of LBM, showed that this method is a powerful tool in CFD that can model complex flows problems more easily.

Methodology

A view of the geometry of the problem under investigation is depicted in Fig. 2a. Regarding to φ symbol, the chamber is placed at different angles while a square-shaped impediment with dimensions $0.3H \times 0.3H$ in the position (0.3H, 0.35H) at the variable temperature embedded inside the chamber. Based on $\varphi = 0$, the main factor of NCHT is the temperature difference of the vertical wall (hot) and the walls on the right side of the chamber (cold), while the horizontal walls is assumed to be adiabatic. 0.1H is considered as the thickness of the conductive wall, which is placed in the neighborhood of the vertical wall, and through this, the heat of the wall is transferred to the fluid. The uniform HAP with a vigor of Q affects on FF. Three different shapes are chosen to exert MF to affect FF. The assumptions made in this simulation are presented in Fig. 3 while the correspond values for existing simulation are presented in Fig. 4.

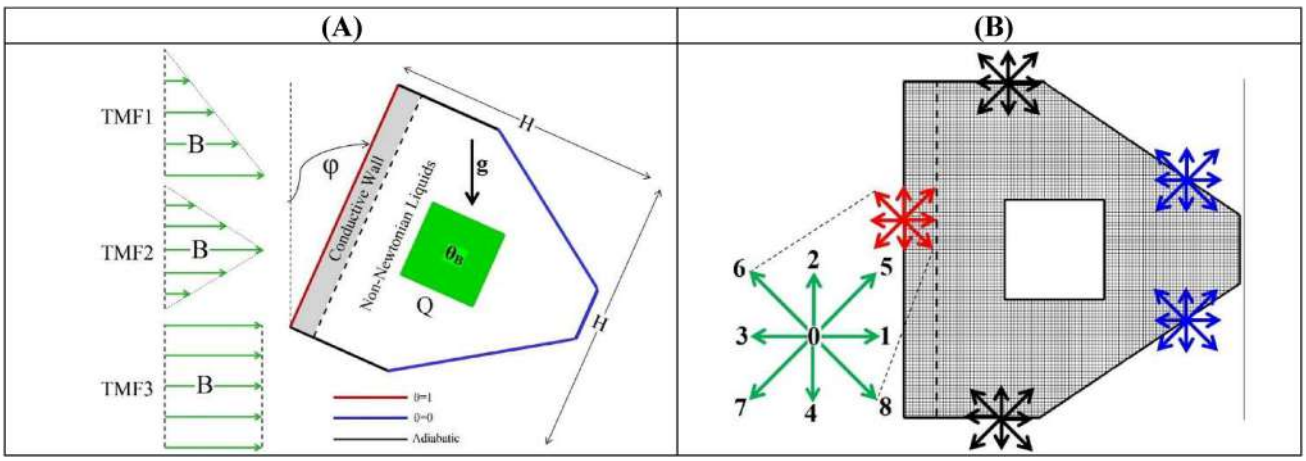

Fig. 2 **a** A view of the studied geometry. **b** A sketch of computational domain along with D_2Q_9 lattice arrangement

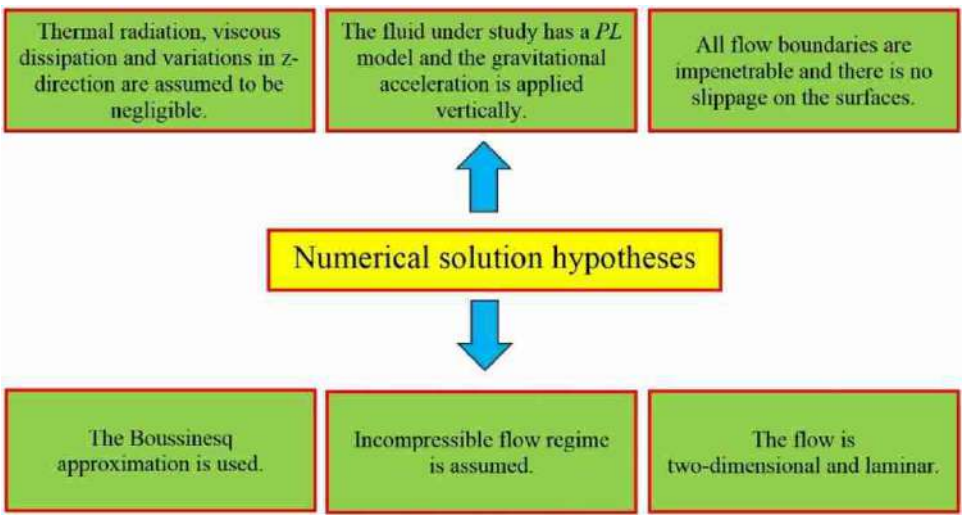

Fig. 3 Assumptions used for numerical solution in present simulation

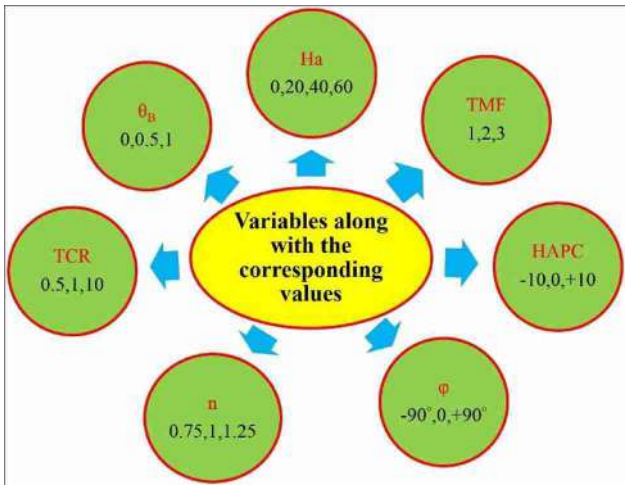

Fig. 4 The values range of the investigated variables

Considering the dimensionless variables in solving the equations and analyzing the outcomes according to Eq. (1) and according to the assumptions included in Fig. 3, the dimensionless basic equations in the analysis of PL fluid on FF and HT are declared according to Eqs. (2) to (10) [46–48]. In PL model for fluid, dynamic viscosity (μ), kinematic viscosity (υ) and shear rate tensor (γ) are determined according to Eqs. (11) to (13) [49–51]. The relationship that reveals the thermal interaction between the conductive wall and the fluid is proposed according to Eq. (14) [52]. The stream function (Ψ) is determined according to Eq. (15).

$$X=\frac{x}{H},\ Y=\frac{y}{H},\ U=\frac{uH}{\alpha\sqrt{\mathrm{Ra}}},\ V=\frac{vH}{\alpha\sqrt{\mathrm{Ra}}},\ \upsilon_0=\frac{\mu_0}{\rho},\ \mathrm{Pr}=\frac{\upsilon_0 H^{2-n}}{\alpha^{2-n}},\ \theta=\frac{T-T_c}{T_h-T_c},\ \mathrm{TCR}=\frac{k_s}{k_f}$$
$$\mathrm{Ha}=BH^n\sqrt{\frac{\sigma\alpha^{1-n}}{\mu_0}},\ \mathrm{Ra}=\frac{\beta\theta g H^{2n+1}}{\upsilon_0\alpha^n},\ P=\frac{pH^2}{\rho\mathrm{Ra}\alpha^2},\ \mathrm{HAPC}=\frac{QH^2}{\rho C_p\alpha},\ \alpha=\frac{\upsilon_0}{\mathrm{Pr}},\ S=s\frac{T_0^2H^2}{k_f(T_h-T_c)^2} \tag{1}$$

$$\frac{\partial U}{\partial X}+\frac{\partial V}{\partial Y}=0 \tag{2}$$

$$U\frac{\partial U}{\partial X}+V\frac{\partial U}{\partial Y}=-\frac{\partial P}{\partial X}+\frac{\mathrm{Pr}}{\mathrm{Ra}^{\frac{(2-n)}{2}}}\left[\frac{\partial}{\partial X}\left(2\chi\frac{\partial U}{\partial X}\right)+\frac{\partial}{\partial Y}\left(\chi\frac{\partial U}{\partial y}\right)+\frac{\partial}{\partial Y}\left(\chi\frac{\partial V}{\partial X}\right)\right] \tag{3}$$

$$U\frac{\partial V}{\partial X}+V\frac{\partial V}{\partial Y}=-\frac{\partial P}{\partial Y}+\mathrm{Pr}\,\theta-\frac{\mathrm{Pr}\,\mathrm{Ha}^2}{\sqrt{\mathrm{Ra}}}V+\frac{\mathrm{Pr}}{\mathrm{Ra}^{\frac{(2-n)}{2}}}\left[\frac{\partial}{\partial X}\left(\chi\frac{\partial V}{\partial X}\right)+\frac{\partial}{\partial Y}\left(2\chi\frac{\partial V}{\partial y}\right)+\frac{\partial}{\partial X}\left(\chi\frac{\partial U}{\partial Y}\right)\right] \tag{4}$$

$$U\frac{\partial\theta}{\partial X}+V\frac{\partial\theta}{\partial Y}=\frac{1}{\sqrt{\mathrm{Ra}}}\left(\frac{\partial^2\theta}{\partial X^2}+\frac{\partial^2\theta}{\partial Y^2}+\mathrm{HAPC}\theta\right) \tag{5}$$

$$\chi=\left\{2\left[\left(\frac{\partial U}{\partial X}\right)^2+\left(\frac{\partial V}{\partial Y}\right)^2\right]+\left(\frac{\partial V}{\partial X}+\frac{\partial U}{\partial Y}\right)^2\right\}^{\frac{(n-1)}{2}} \tag{6}$$

$$S_{\mathrm{TOT}}=S_{\mathrm{H}}+S_{\mathrm{F}}+S_{\mathrm{F}} \tag{7}$$

$$S_{\mathrm{H}}=\left[\left(\frac{\partial\theta}{\partial X}\right)^2+\left(\frac{\partial\theta}{\partial Y}\right)^2\right] \tag{8}$$

$$S_{\mathrm{F}}=10^{-4}\chi\left[\left(\frac{\partial U}{\partial Y}+\frac{\partial V}{\partial X}\right)^2+2\left(\left(\frac{\partial U}{\partial X}\right)^2+\left(\frac{\partial V}{\partial Y}\right)^2\right)\right] \tag{9}$$

$$S_{\mathrm{M}}=10^{-4}\mathrm{Ha}^2V^2 \tag{10}$$

$$\mu=\mu_0\left\{2\left(\frac{\partial U}{\partial X}\right)^2+\left(\frac{\partial V}{\partial X}+\frac{\partial U}{\partial Y}\right)^2+2\left(\frac{\partial V}{\partial Y}\right)^2\right\}^{\frac{(n-1)}{2}} \tag{11}$$

$$\upsilon(x,t)=\frac{\mathrm{Pr}}{\mathrm{Ra}^{\frac{(2-n)}{2}}}|\gamma|^{(n-1)}=\upsilon_0|\gamma|^{(n-1)} \tag{12}$$

$$|\gamma|=\sqrt{2\gamma_{ij}\gamma_{ij}}\ \text{and}\ \gamma_{ij}\equiv 0.5\left(\frac{\partial u_i}{\partial x_j}+\frac{\partial u_j}{\partial x_i}\right) \tag{13}$$

$$\frac{\partial\left(k_s\frac{\partial\theta}{\partial X}\right)}{\partial X}+\frac{\partial\left(k_s\frac{\partial\theta}{\partial Y}\right)}{\partial Y}=0 \tag{14}$$

$$U=\frac{\partial\Psi}{\partial Y}\ \text{and}\ V=-\frac{\partial\Psi}{\partial X}\ \text{OR}\ \frac{\partial^2\Psi}{\partial X^2}+\frac{\partial^2\Psi}{\partial Y^2}=\frac{\partial U}{\partial Y}-\frac{\partial V}{\partial X} \tag{15}$$

Production of heat: HAPC > 0, Absorption of heat: HAPC < 0,

Fluid with shear thinning behaviour: $n<1$, Fluid with shear thickening behaviour: $n>1$

Newtonian fluid: $n=1$, The subscript zero refers to the Newtonian fluid

Unlike the conventional CFD methods, LBM is based on the mesoscopic kinetic equation, which uses the set of behavior of particles in a system to simulate the continuous mechanics of a system. Due to the local nature of calculations, common hardware has the ability to parallelize. The main advantage of this model is its simplicity. This method is rapidly expanding and progressing, and many physical phenomena have not yet been investigated by this method. Considering all the mentioned cases and according to the characteristics shown in Fig. 1, LBM is used for this simulation. To augmentation of the precision of calculations, instead of using two distribution functions (for temperature and flow fields), three distribution functions are used in the existing work. That is, a separate function is considered for MF, and in this way, the impact of MF is not considered only as a term source. The equations related to this numerical solution method are shown in Eqs. (16) to (30) [53].

$$f_i\left(\mathbf{x}+\mathbf{c}_i,t+1\right)=\mathbf{c}_i\mathbf{F}_i+f_i(\mathbf{x},t)+\frac{\left[f_i^{eq}(\mathbf{x},t)-f_i(\mathbf{x},t)\right]}{\tau^*} \tag{16}$$

$$\mathbf{F}_i=-3\rho\omega_i\frac{\mathrm{Ha}^2\upsilon(x,t)}{H^2}v+3\omega_i\rho\mathbf{g}\beta\theta \tag{17}$$

$$g_i\left(\mathbf{x}+\mathbf{c}_i,t+1\right)=\frac{Q}{(\rho C_p)}(T-T_c)+g_i(\mathbf{x},t)+\frac{\left[g_i^{eq}(\mathbf{x},t)-g_i(\mathbf{x},t)\right]}{\tau^{**}} \tag{18}$$

$$h_i\left(\mathbf{x}+\mathbf{c}_i,t+1\right)=h_i(\mathbf{x},t)+\frac{\left[h_i^{eq}(\mathbf{x},t)-h_i(\mathbf{x},t)\right]}{\tau^{***}} \tag{19}$$

$$f_i^{eq}=\frac{3\omega_i}{2}\left(\frac{\mathbf{c}_i^2B^2}{2}-\left(\mathbf{c}_i.B\right)\right)+\rho\omega_i\left(1+3\mathbf{c}_i.\mathbf{u}+\frac{9}{2}\left(\mathbf{c}_i.\mathbf{u}\right)^2-\frac{3}{2}\mathbf{u}.\mathbf{u}\right) \tag{20}$$

$$g_i^{eq}=\omega_iT\left(1+3\mathbf{c}_i.\mathbf{u}\right) \tag{21}$$

$$h_{ix}^{eq}=\lambda_i\left(B_x+3\mathbf{c}_{ix}(vB_x-uB_y)\right) \tag{22}$$

$$h_{iy}^{eq}=\lambda_i\left(B_y+3\mathbf{c}_{iy}(uB_y-vB_x)\right) \tag{23}$$

$$\omega_0^f=4/9,\ \omega_{1-4}^f=1/9,\ \omega_{5-8}^f=1/36 \tag{24}$$

$$\begin{aligned}\mathbf{c}_0&=0\\ \mathbf{c}_{1-4}&=\left[\cos\left(\frac{(i-1)\pi}{2}\right),\sin\left(\frac{(i-1)\pi}{2}\right)\right]\\ \mathbf{c}_{5-8}&=\sqrt{2}\left[\cos\left(\frac{(i-5)\pi}{2}+\frac{\pi}{4}\right),\sin\left(\frac{(i-5)\pi}{2}+\frac{\pi}{4}\right)\right]\end{aligned} \tag{25}$$

$$\lambda_0=1/3 \text{ and } \lambda_{1-4}=1/6 \tag{26}$$

$$\tau^*=3\upsilon+0.5 \tag{27}$$

$$\tau^{***}=3\alpha+0.5 \tag{28}$$

$$\tau^{***}=3\eta+0.5 \tag{29}$$

$$\begin{aligned}&\rho=\sum_{i=0}^{8}f_i,\quad \rho=\sum f_i,\ \mathbf{u}=\frac{1}{\rho}\sum\mathbf{c}_if_i,\\ &T=\sum g_i,\ B_x=\sum h_{ix}\text{ and }B_y=\sum h_{iy}\end{aligned} \tag{30}$$

Achieving the correct outcomes from the simulation requires the accuracy and correctness of applying the boundary conditions. Since all flow boundaries are smooth or diagonal, the bounce back model is used in LBM. Regarding to this model and taking into account Fig. 2b, the distribution functions outside the boundary assumed known (Specified in the streaming step) while the input functions to the solution domain are unknown [27–29]. An example of how to apply these boundary conditions (velocity and temperature) is provided in Eqs. (31) to (34) for $\varphi=0$.

Boundary conditions on hot wall:
$$\begin{cases}f_1(0,j)=f_3(0,j),\ f_5(0,j)=f_7(0,j),\ f_8(0,j)=f_6(0,j)\\ g_1(0,j)=T_h[\omega(1)+\omega(3)]-g_3(0,j),\ g_5(0,j)=T_h[\omega(5)+\omega(7)]-g_7(0,j),\\ g_8(0,j)=T_h[\omega(6)+\omega(8)]-g_6(0,j)\end{cases} \tag{31}$$

Boundary conditions on upper cold wall:
$$\begin{cases}f_8(i,j)=f_6(i,j),\ f_4(i,j)=f_2(i,j),\ f_7(i,j)=f_5(i,j),\ f_3(i,j)=f_1(i,j)\\ g_8(i,j)=-g_6(i,j),\ g_4(i,j)=-g_2(i,j),\ g_7(i,j)=-g_5(i,j),\ g_3(i,j)=-g_1(i,j)\end{cases} \tag{32}$$

Boundary conditions for interaction of fluid and conductive wall:
$$\left\{f_1(0.1H,j)=f_3(0.1H,j),\ f_5(0.1H,j)=f_7(0.1H,j),\ f_8(0.1H,j)=f_6(0.1H,j)\right. \tag{33}$$

$$\text{Boundary conditions on upper adiabatic wall: } \begin{cases} f_4(H,j) = f_2(H,j),\ f_6(H,j) = f_8(H,j),\ f_7(H,j) = f_5(H,j) \\ g_0(H,j) = g_0(H,j),\ g_4(H,j) = g_4(H,j),\ g_7(H,j) = g_7(H,j), \\ g_1(H,j) = g_1(H,j),\ g_2(H,j) = g_2(H,j),\ g_3(H,j) = g_3(H,j), \\ g_6(H,j) = g_6(H,j),\ g_5(H,j) = g_5(H,j),\ g_8(H,j) = g_8(H,j) \end{cases} \tag{34}$$

The algorithm used to perform the numerical solution using LBM is in accordance with Fig. 5.

The amount of irreversibility created due to the rotation of the fluid inside the chamber is measured by a parameter called entropy, which is alluded according to Eq. (35). The share of HT in EP is measured by a parameter called number of Bejan (Be), and this parameter is according to Eq. (36). The predominance of HT share in EP is determined by Be > 0.5. The dimensionless quantity that is used as a scale to measure HT in this study is mean Nu, which expresses the ratio of convection HT to conduction HT and is exhibited according to Eq. (37) [53].

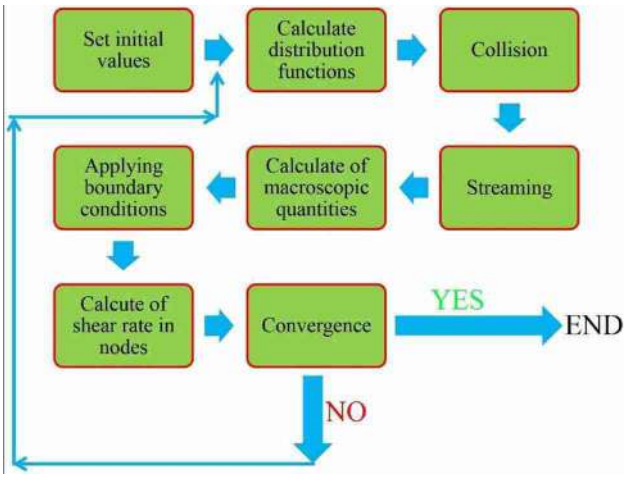

Fig. 5 The process of simulation in LBM

$$S = \frac{\int S_{\mathrm{TOT}} \mathrm{d}\widetilde{V}}{\widetilde{V}},\ \widetilde{V}\text{: Volume} \tag{35}$$

$$\mathrm{Be} = \frac{S_{\mathrm{H}}}{S_{\mathrm{F}} + S_{\mathrm{H}} + S_{\mathrm{M}}} \tag{36}$$

$$\mathrm{Nu} = \frac{1}{H}\int_0^1 -\left(\frac{\partial \theta}{\partial X}\right)_{X=W} \mathrm{d}Y \tag{37}$$

In order to have accurate outcomes and to make sure that the outcomes are not dependent on the size of the selected mesh, the independent check of the selected mesh size is presented in Table 1. Since the solution domain is considered square and H×H according to Fig. 2, regarding to Table 1, by choosing a 100×100 grid size, it can be sure that the outcomes are independent of the selected grid because a noticeable change is not observed for the larger dimensions of the network. The Fortran code written to compare with the conducted studies is shown in Figs. 6, 7 and 8. By observing the small difference between the outcomes, it can be sure of the high efficiency of the code and easily present and analyze the results.

Results and discussion

Displays Fig. 9 parts (a)–(c) isotherms in exchange for variations of Ha, TCR and φ. There are two important points that need to be explained: (1) The linear temperature distribution inside the wall is the result of the high thermal resistance of the wall, which is caused by the low TCR. Observation

Table 1 Mean Nu for different mesh sizes at TCR = 10, HAPC = 0, TMF2, $\varphi = -90°$, $\theta_{\mathrm{B}} = 0.5$

		Mesh size	60×60	80×80	100×100	120×120	140×140
Ha = 0	$n = 0.75$	Nu	2.96	3.09	3.18	3.22	3.24
		Error (%)	–	4.11	2.65	1.25	0.65
		$\lvert\Psi_{\max}\rvert$	0.091	0.101	0.108	0.113	0.117
	$n = 1.25$	Nu	2.44	2.49	2.52	2.538	2.549
		Error (%)	–	1.81	1.15	0.75	0.45
		$\lvert\Psi_{\max}\rvert$	0.046	0.048	0.051	0.0525	0.054
Ha = 60	$n = 0.75$	Nu	1.454	1.495	1.52	1.533	1.541
		Error (%)	–	2.75	1.21	0.91	0.51
		$\lvert\Psi_{\max}\rvert$	0.023	0.0246	0.027	0.0288	0.0295
	$n = 1.25$	Nu	2.29	2.32	2.34	2.35	2.35
		Error (%)	–	1.08	0.79	0.41	0
		$\lvert\Psi_{\max}\rvert$	0.0365	0.0371	0.039	0.039	0.039

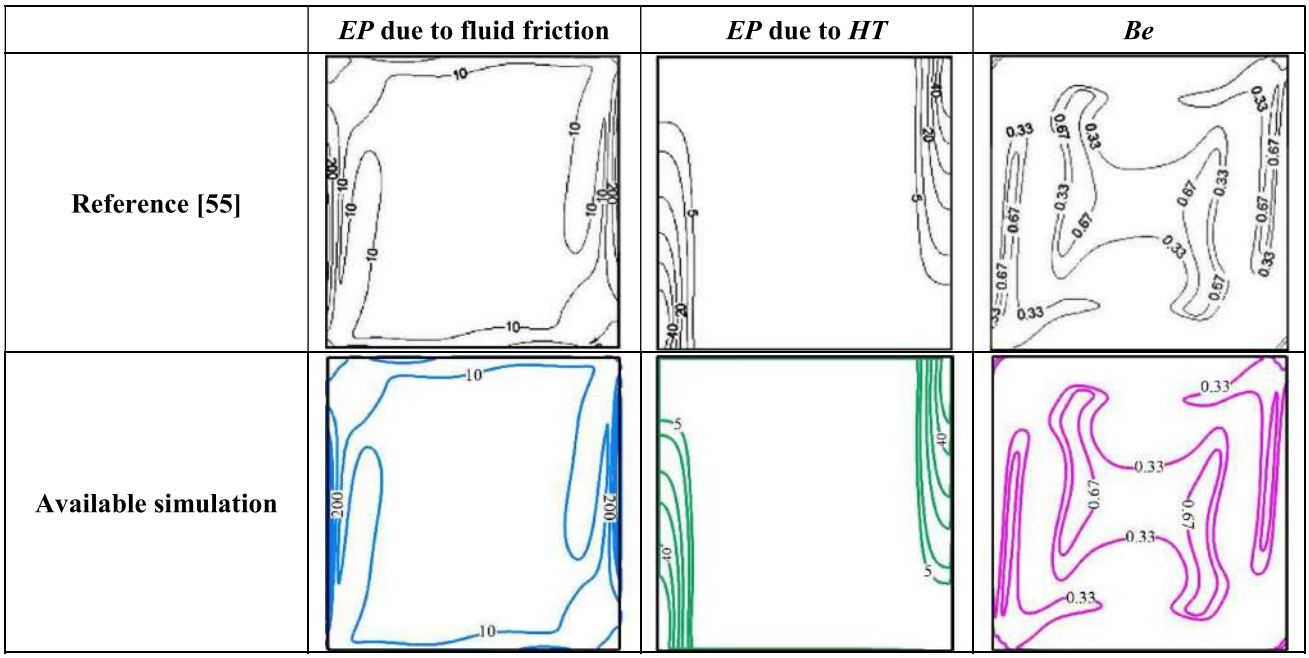

Fig. 6 Comparison of the present code and reference [55] based on EP

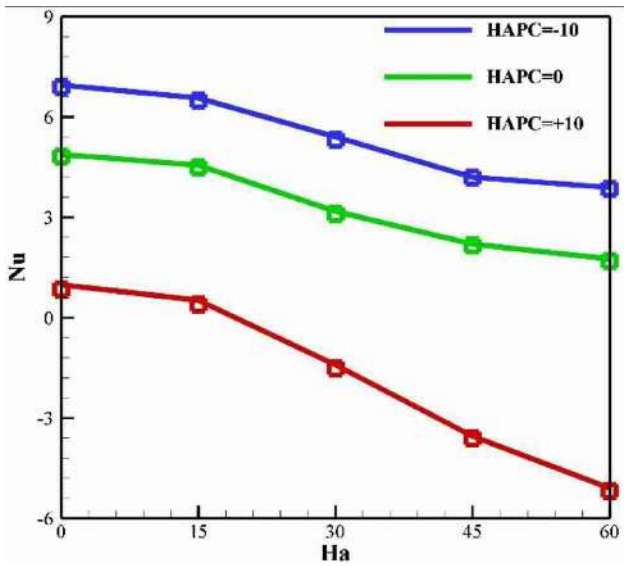

Fig. 7 Comparing the outcomes of the present code (solid lines) with references [54] (square symbol) for Ra = 10.[5]

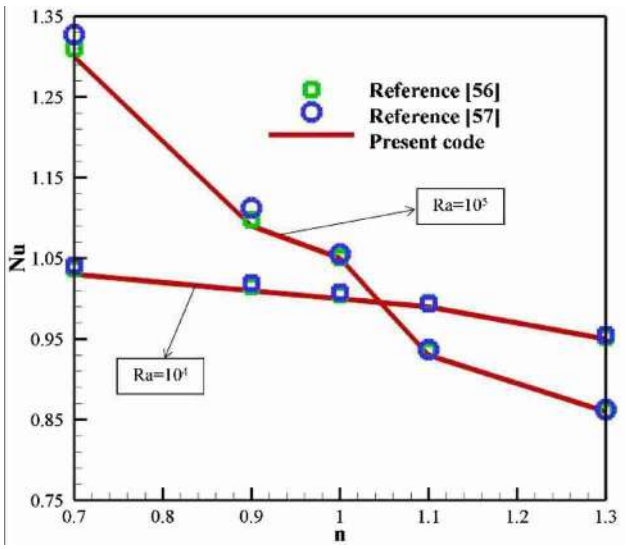

Fig. 8 Comparing the outcomes of the present code with references [56] and [57]

of nonlinear behavior for temperature distribution occurs while TCR value grows. Based on Fourier's conduction law, the nonlinear temperature distribution inside the conductor wall increases dramatically. The expansion of the isotherms becomes possible with the augmentation of the TCR value, especially at the angles of 0 and − 90°. This phenomenon is not seen in $\varphi = +90°$. Because at $\varphi = +90°$, since the heat source is at the top and the cold source is at the bottom, the lowest convection performance occurs. (2) Respect to the dominance of conduction over the convection at $\varphi = +90°$, in all values of TCR, there is no remarkable variation in streamlines with augmentation of MF strength. However, in the other two φ values, the decline in the distortion of the isotherms is the result of the augmentation of in the Ha value. A substantial decline in the compactness of isotherms can be seen with the augmentation of Ha, especially around the cold walls and conductive wall. This phenomenon reveals that the convection effects are reduced. It can

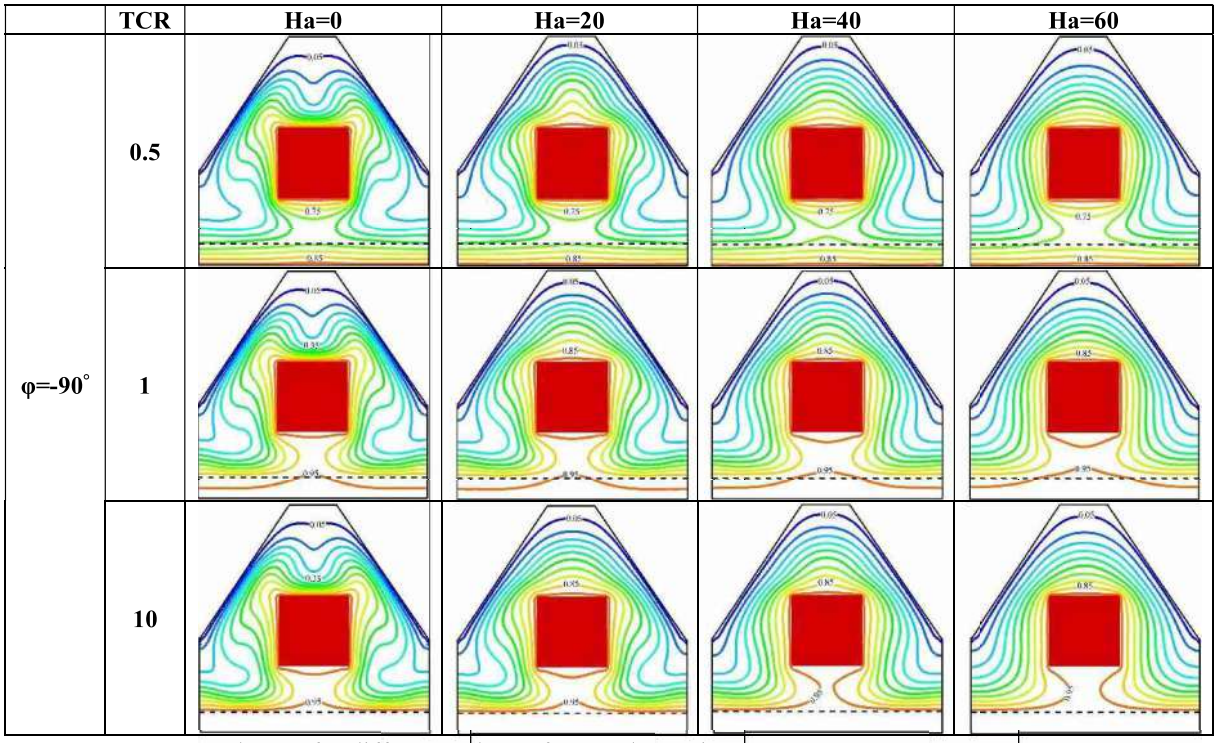

(A). Isotherms for different values of *Ha* and *TCR* in **HAPC = 0, TMF3, θ_B = 1, n = 0.75, λ = -90**

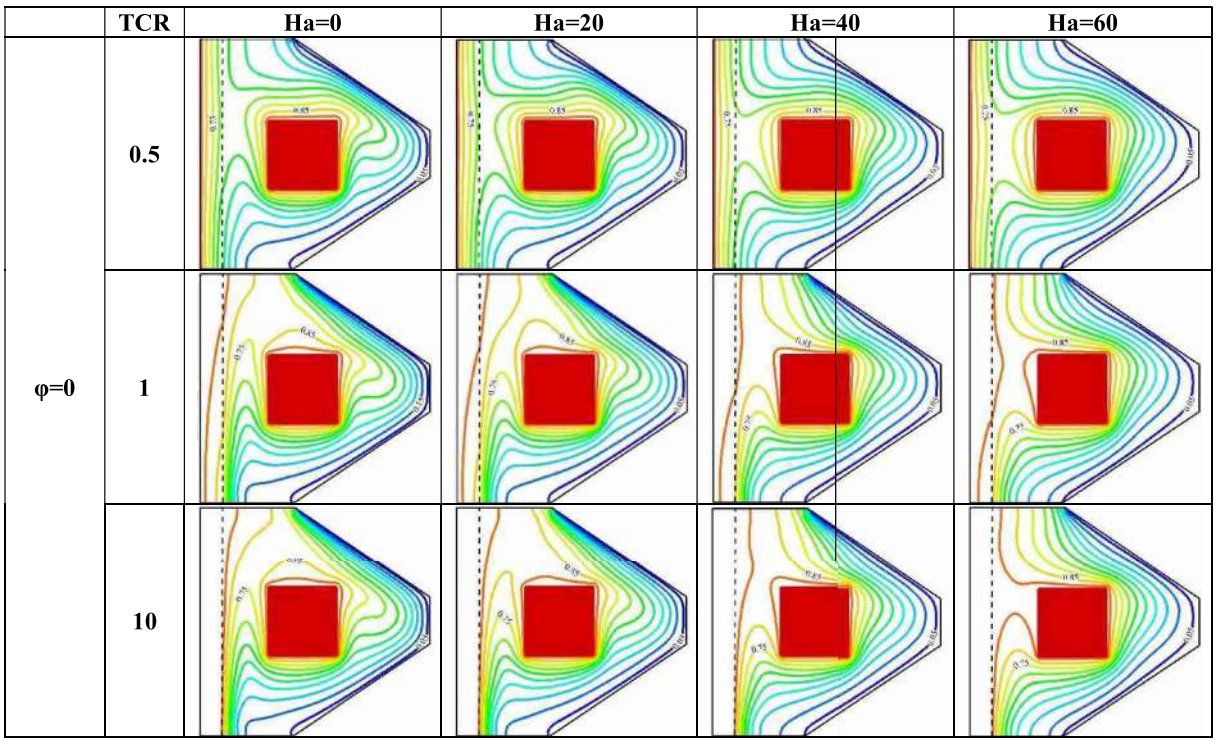

(B). Isotherms for different values of *Ha* and *TCR* in **HAPC = 0, TMF3, θ_B = 1, n = 0.75, λ = 0**

Fig. 9 Isotherms for different values of Ha and TCR in **a** HAPC = 0, TMF3, $\theta_B = 1$, $n = 0.75$, $\lambda = -90°$, **b** HAPC = 0, TMF3, $\theta_B = 1$, $n = 0.75$, $\lambda = 0$, **c** HAPC = 0, TMF3, $\theta_B = 1$, $n = 0.75$, $\lambda = +90°$ and **d** Streamlines and entropy lines for different values of Ha and λ in HAPC = 0, TMF3, $\theta_B = 1$, $n = 0.75$, TCR = 10

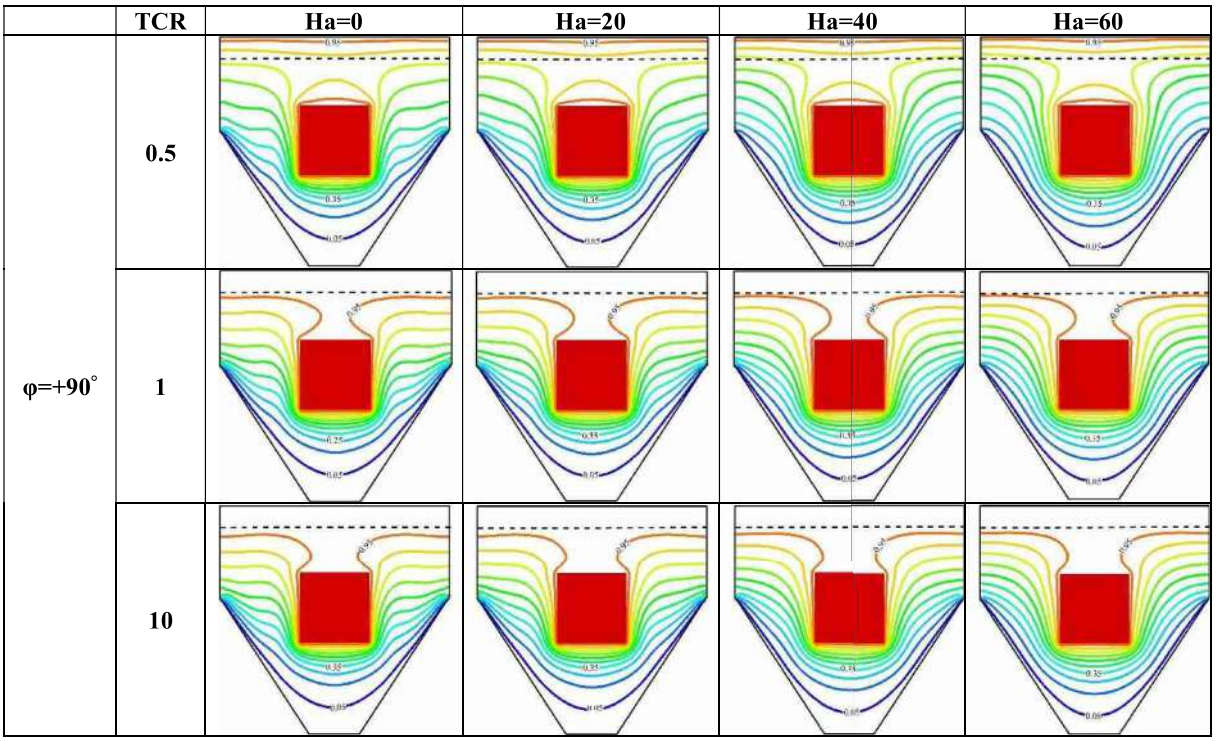

(C). Isotherms for different values of *Ha* and *TCR* in $\mathbf{HAPC = 0, TMF3, \theta_B = 1, n = 0.75, \lambda = +90^{\circ}}$

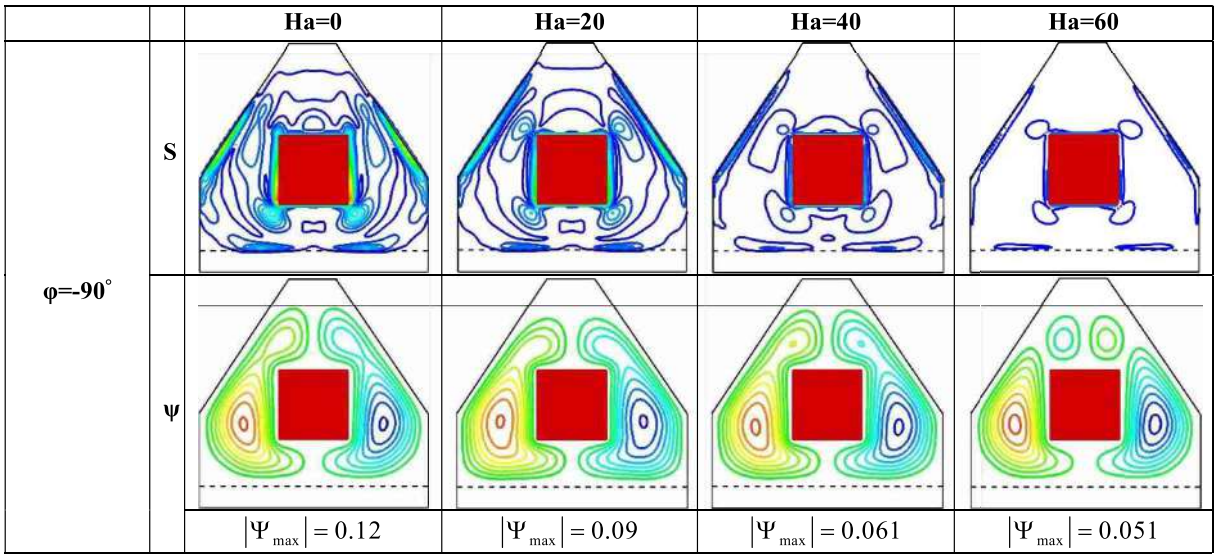

Fig. 9 (continued)

be inferred from Fig. 9 part (d): (1) The pattern of streamlines changes with changing φ. In $\varphi = 0$, the fluid rotates around the hurdle, creating a clockwise vortex, while at the other two angles, two symmetrical vortices form on either side of the hurdle while rotating in opposite directions. The flow vigor formed inside the chamber can be changed by changing φ so that the current vigor at $\varphi = 0$ is about twice as much and 4.3 times higher than angles of $\varphi = -90^{\circ}$ and $\varphi = +90^{\circ}$, respectively. (2) Increment of Ha leads to a noticeable decrease in flow vigor because MF exerts a resisting force on FF, contrary to the gravitational force according to Eq. (3). Enhancement of Ha from zero to 60 reduces the flow vigor by about 72%, 59%, and 51% for $\varphi = 0$, $\varphi = -90^{\circ}$, and $\varphi = +90^{\circ}$, respectively. (3) As Ha values increases, the

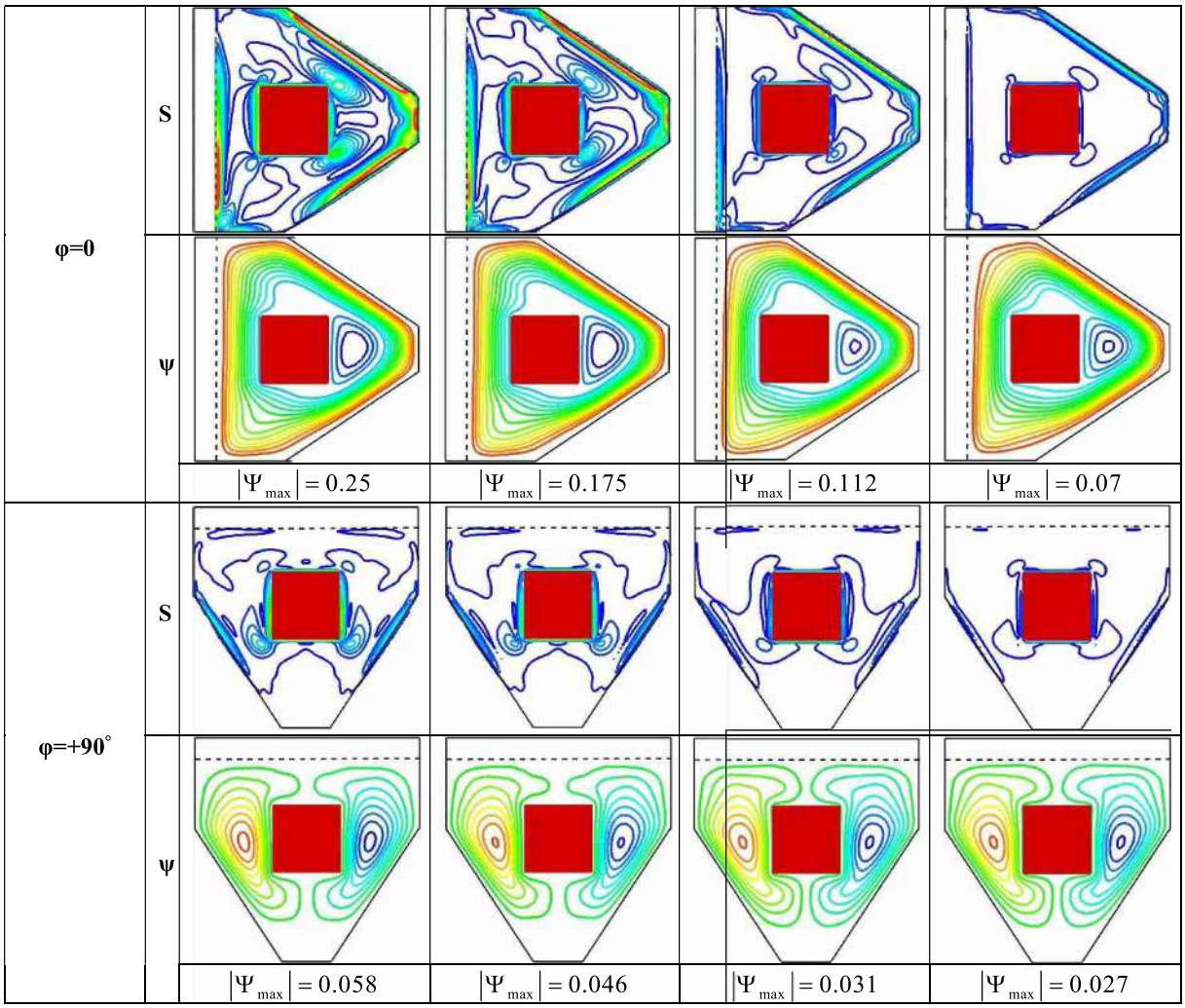

(D). Streamlines and entropy lines for different values of *Ha* and λ in **HAPC = 0, TMF3, θ_B = 1, n = 0.75, TCR = 10**

Fig. 9 (continued)

amount of EP decreases with respect to the entropy lines. Because based on Eqs. (7) to (10) in addition to reducing the speed and temperature gradients, the velocity value also decreases. (4) It may be assumed that the augmentation of in EP results from an increase in the amount of Ha according to Eq. (14), but it should be noted that increment of Ha also decreases velocity value and velocity gradient. The sum of these factors leads to a reduction in the amount of irreversible inside the chamber. The lower impact of MF on the reduction of EP for $\varphi = +90°$ is evident, as well as the least amount of irreversibility belongs to this angle. At all three angles of inclination, there is the highest amount of EP in the vicinity of the impediment is due to HT. Also near the cold walls and the conductor wall there is a high density of lines, where there are the most velocity variations.

Regarding to Fig. 9, it can be observed explicitly that by variation the chamber placement position, the amount of HT and FF power can be controlled.

Based on Fig. 10, which presents the mean Nu, several momentous points can be stated: (1) For $\varphi = +90°$, the lowest mean Nu value results. Because in this situation, hot and cold walls are placed at the top and bottom of the chamber, respectively. Based on the Rayleigh–Benard phenomenon, this situation is the worst case for the convection process to occur. In comparison of $\varphi = 0$ and $\varphi = -90°$, the highest the mean Nu value is related to $\varphi = 0$, because in this situation, the chamber is heated from the side wall. Because in the chambers that are heated from the side surfaces, by creating a small temperature difference, the phenomenon of convection occurs. However, cavities heated from the upper

and lower surfaces must reach a critical value in order for the convection effects to be observed. (2) Increment of TCR leads to enhancement of the value of the mean Nu, which is much less for $\varphi = +90°$ than the other two angles. For example, increasing the TCR from 0.5 to 10 results in an increase of about 3.5, 3.2, and 2 times of mean Nu for 0, −90, and +90 angles, respectively. (3) Enhancement of Ha reduces the mean Nu due to decreasing the flow vigor and temperature gradient near the walls. There is only one exception, and that is at $\varphi = +90°$ for TCR = 0.5, in which MF has no effect on the mean Nu. Because in this situation, thermal conduction is the most dominant type of HT. (4) The higher TCR, the more obvious the impact of the MF. In general, the least influence of MF is when the heat source is at the top of cavity.

According to Table 2, several points can be stated: (1) Increment of Ha leads to decreasing the amount of EP. For specimen, in TCR = 1, augmentation of Ha from zero to 60 reduces the entropy by about 66, 66, and 88 percent for the angle 0f 0, −90°, and +90°, respectively. (2) The maximum amount of entropy produced and the impact of MF are related to the state in which the chamber is heated from the side wall. (3) With augmentation of TCR value, due to

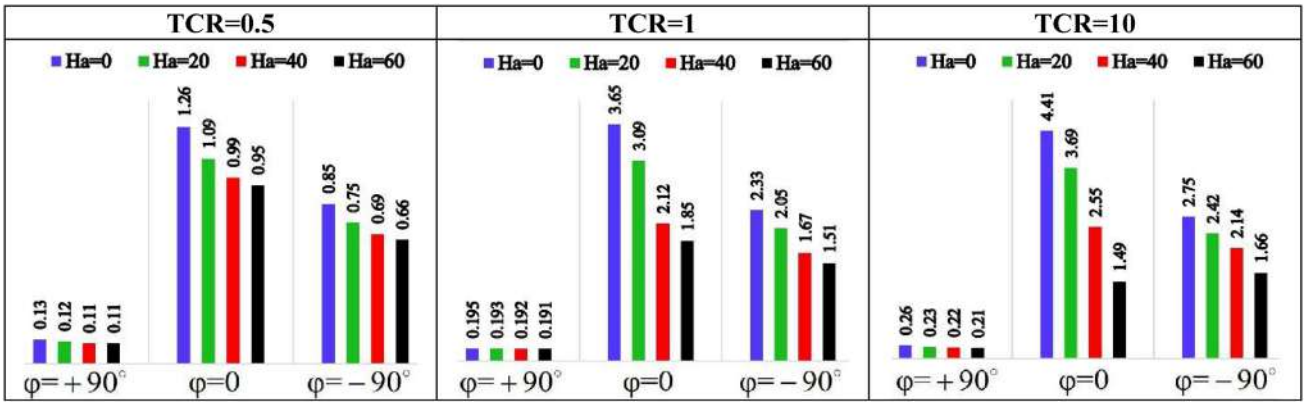

Fig. 10 Mean Nusselt number for different values of Ha, λ and TCR in HAPC = 0, TMF3, $\theta_B = 1$, $n = 0.75$

Table 2 Values of EP for the different Ha, TCR and λ in HAPC = 0, TMF3, $\theta_B = 1$, $n = 0.75$

	TCR = 0.5			TCR = 1			TCR = 10		
	$\varphi = -90°$	$\varphi = 0$	$\varphi = +90°$	$\varphi = -90°$	$\varphi = 0$	$\varphi = +90°$	$\varphi = -90°$	$\varphi = 0$	$\varphi = +90°$
Ha = 0	29.15	32.75	31.85	38.05	41.55	40.57	38.15	44.25	42.05
Ha = 20	28.65	31.74	31.21	37.25	40.54	39.35	37.55	42.11	39.93
Ha = 40	27.95	30.45	29.95	36.15	38.65	37.32	36.24	38.94	38.15
Ha = 60	27.91	29.15	28.98	35.19	36.15	35.31	35.45	36.72	36.71

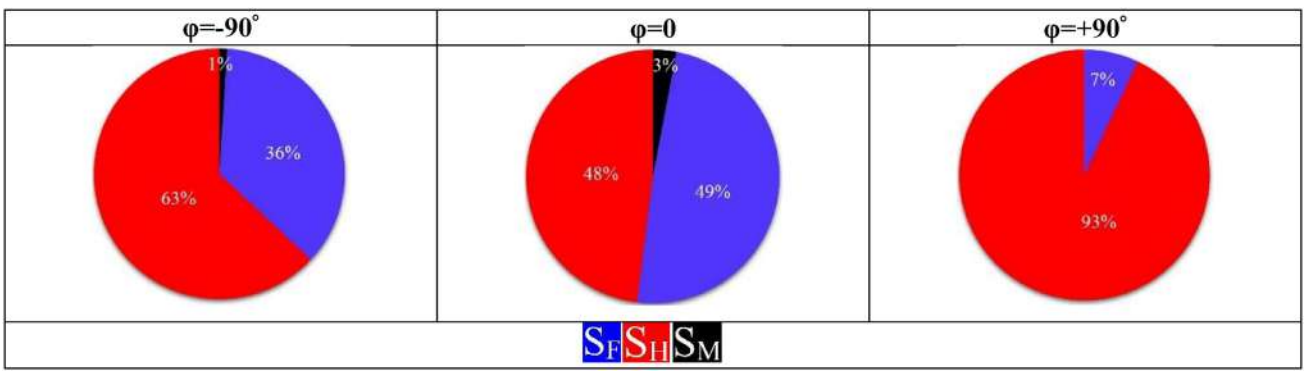

Fig. 11 The contribution of each entropy-generating factor in creating the total entropy for λ changes in HAPC = 0, TMF3, $\theta_B = 1$, $n = 0.75$, Ha = 20, TCR = 10

		HAPC=-10	HAPC=0	HAPC=+10
n=0.75	ψ	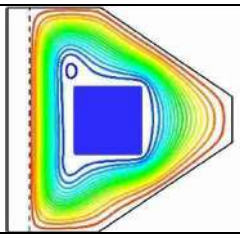	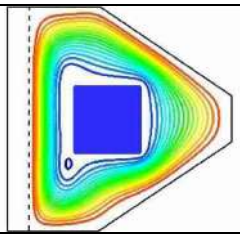	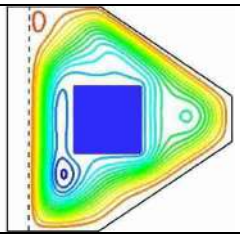
		$\lvert\Psi_{max}\rvert = 0.145$	$\lvert\Psi_{max}\rvert = 0.175$	$\lvert\Psi_{max}\rvert = 0.195$
	θ	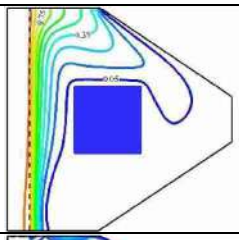	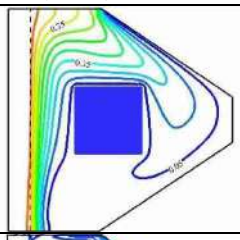	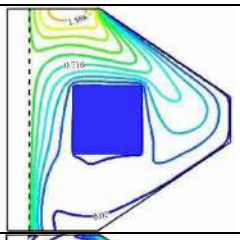
	S	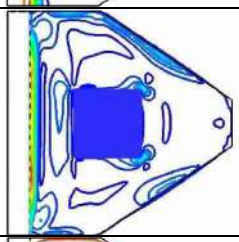	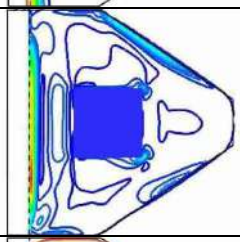	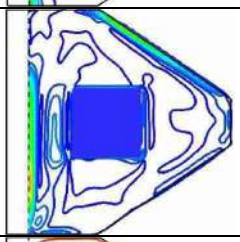
n=1.25	ψ	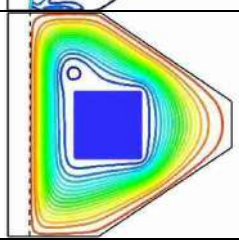	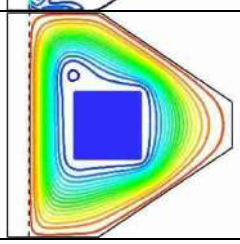	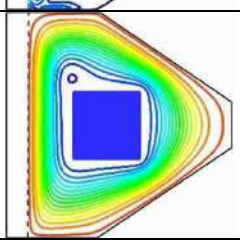
		$\lvert\Psi_{max}\rvert = 0.079$	$\lvert\Psi_{max}\rvert = 0.085$	$\lvert\Psi_{max}\rvert = 0.091$
	θ	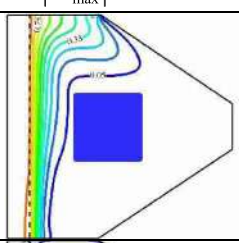	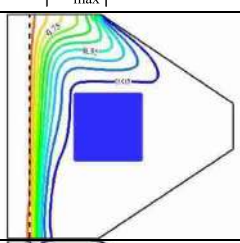	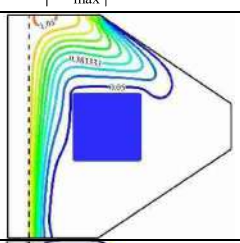
	S	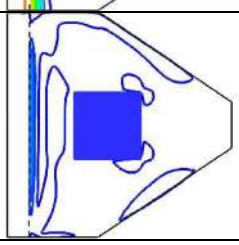	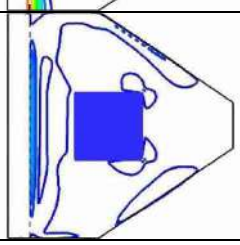	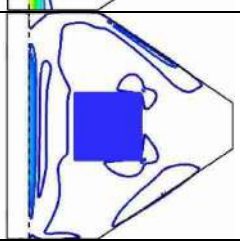

(A). Streamlines, isotherms and entropy lines for different values of *HAPC* and *PL* index in

$\mathbf{TCR = 10, TMF3, \theta_B = 0, \lambda = 0, Ha = 0}$

Fig. 12 Streamlines, isotherms and entropy lines for different values of HAPC and PL index in **a** TCR = 10, TMF3, $\theta_B = 0$, $\lambda = 0$, Ha = 0 and **b** TCR = 10, TMF3, $\theta_B = 0$, $\lambda = 0$, Ha = 60

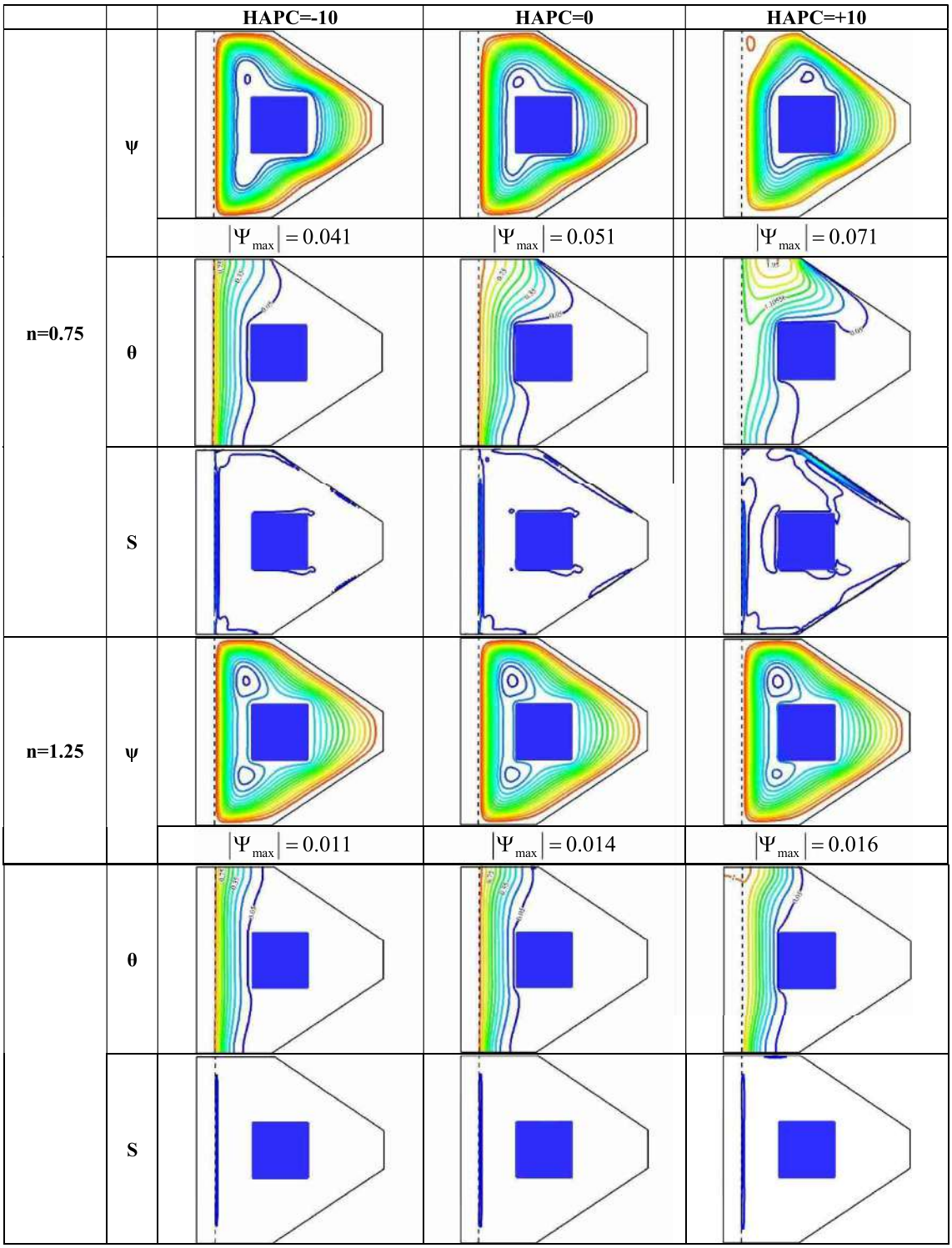

(B). Streamlines, isotherms and entropy lines for different values of *HAPC* and *PL* index in $\mathbf{TCR = 10, TMF3, \theta_B = 0, \lambda = 0, Ha = 60}$

Fig. 12 (continued)

increasing the share of HT and convection effects in EP, the total EP increases to about 32%.

As shown in Fig. 11, the share of HT in EP for $\varphi = +90°$ is greater than the other two angles, while the highest share of fluid friction in EP belongs to $\varphi = 0$. It is momentous to note that the share of the MF in EP varies according to the angle of the chamber, so that the largest share is related to the state where $\varphi = 0$. For $\varphi = +90°$, the percentage of MF in EP is less than 1%.

It is necessary to make a few points about Fig. 12: (1) In all modes, increment of HAPC increases the current vigor, which is more pronounced in $n = 0.75$. In the absence of MF, this impact for $n = 1.25$ and $n = 0.75$ is about 15% and 34%, respectively, while for Ha = 60, it is about 73% and 45%. Because augmentation of the fluid velocity of rotation is the result of augmentation of HAPC, which results in more convection effects. The pattern of streamlines for $n = 1.25$ is almost the same in all cases, but in $n = 0.75$, in the heat generated state, the shape of the streamlines changes and a vortex counterclockwise begins to form at the top left. (2) Because the barrier is located at cold temperature, the compactness of isotherms the near to the conductor wall is high and the scattering and extent of the lines across the chamber is significantly reduced compared to Fig. 9. The interspersing and obliquity of the isotherms increase remarkably throughout the chamber with augmentation of HAPC. As HAPC increases, the gradient of temperature around the conductor wall diminishes, indicating a decrease in HT from the wall to the fluid. In the mode of heat production, the temperature of the fluid reaches more than 1 because in this case, the fluid temperature increases remarkably. In Ha = 60, except for HAPC = + 10 in $n = 0.75$, isotherms are generally a function of X, and the lines are parallel to the vertical wall and have a slight curvature, indicating that conduction is the predominant HT process in these cases. (3) In addition to a very considerable decrease in entropy with increasing Ha, an increase in HAPC dramatically increases the concentration of the entropy lines, especially at $n = 0.75$. Because augmentation of HAPC, in addition to enhancement of the share of HT, also increases the share of other entropy factors. The further scattering of entropy lines across the chamber is particularly interesting in Ha = 60 and $n = 0.75$ heat generation modes, especially in the vicinity of the hindrance. The insignificancy of the impact of MF with the power of Ha = 60 on the reduction of entropy in $n = 1.25$ is quite obvious.

Temperature in dimensionless mode is depicted in Fig. 13 for changes in PL index, HAPC and Ha. Explainable points are as follows: (1) The temperature decreases near the conductive wall to reach the cold barrier temperature around $X = 0.3$. After this area, the temperature of the fluid increases and then, in interaction with the cold wall, the temperature of the fluid decreases. The augmentation of in the fluid temperature inside the chamber is the result of the augmentation of in HAPC value and the highest temperature is seen in HAPC > 0. As the PL index increases, the difference in temperature profiles due to the HAPC changes decreases. This indicates that the least impact of HAPC is obtained when the fluid is considered to be shear thickening. (3) Applying MF with power of Ha = 60 reduces the difference in temperature profiles, especially at $n = 1.25$, which is very clear. The smoothness of fluid movement is the result of enhancement of viscosity because there is a direct relationship between PL index and viscosity. An augmentation of in PL index leads to an augmentation of in viscosity. This factor leads to the reduction of convection effects, and as a result, the reduction of MF effect is evident. In Ha = 60, due to the linearization of temperature profiles, the dominance of conductivity over convection is well defined. A very momentous point in $n = 0.75$ and Ha = 60 is that the temperature reaches more than 1.2, which discloses that the fluid temperature is much higher than the wall and there must be reverse HT.

Given Fig. 14, which exposes the mean Nu in exchange for Ha, HAPC, and PL index changes, it is important to mention a few points: (1) To have less HT, using MF can be effective. In all values of PL index and HAPC, the application of MF leads to decrement of in the mean Nu, which is intensified by decrement of PL index and increasing HAPC. At $n = 0.75$, growth of Ha from zero to 60 reduces the mean Nu number by 21% and 144% for HAPC = + 10 and HAPC = − 10, respectively. This impact for the $n = 1.25$ is about 15% and 65%, respectively. Respect to Fig. 9 in HAPC = + 10, the fluid temperature inside the chamber reaches more than unit, in HAPC = + 10, the lowest mean Nu is seen, to the extent that in $n = 0.75$ and Ha = 60, the mean Nu is negative. This reveals that not only is heat not transferred from the wall to the fluid, but there is also HT from the fluid to the wall (see Fig. 13).

The important points about Table 3 that depict the EP for changes in HAPC, Ha and PL index: (1) For HAPC ≤ 0, augmentation of Ha always leads to decreasing the entropy value, but for HAPC > 0, increasing MF vigor increases the entropy. (2) Increasing PL index decreases entropy value and reduces the impact of MF in this decrease. (3) In HAPC = − 10, the least effect of MF is seen.

The contribution of HT to the formation of total entropy increases dramatically with increasing HAPC. Be in HAPC = + 10 is about 29% higher than HAPC = 0 and 44% higher than HAPC = − 10, respectively. The important point is that the contribution of MF to the production of entropy increases with increasing HAPC. These cases are presented in Fig. 15.

The impact of changing the temperature boundary condition of the barrier embedded inside the chamber is investigated in Fig. 16. The important contents are as follows: (1)

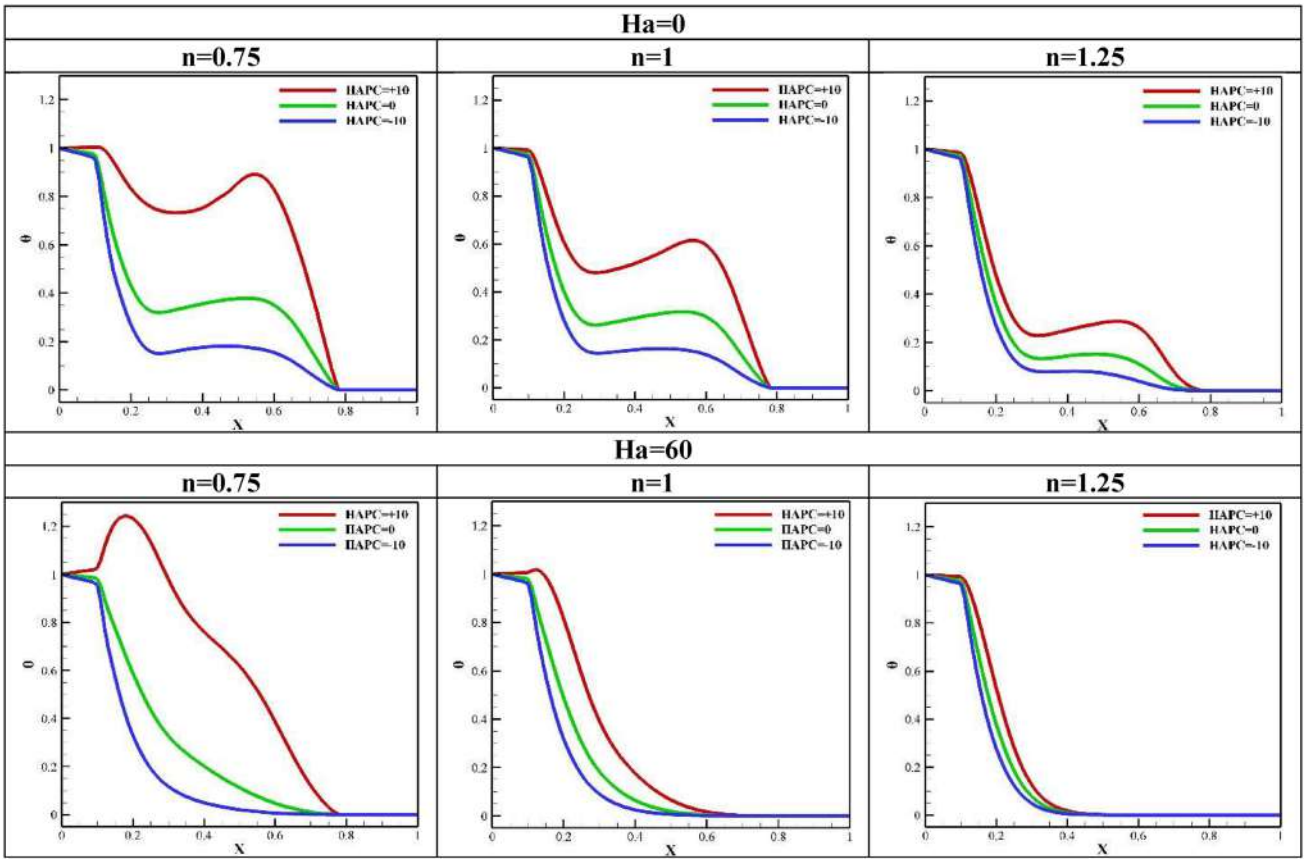

Fig. 13 Dimensionless temperature for different values of HAPC, Ha and PL index in TCR = 10, TMF3, $\theta_B = 0$, $\lambda = 0$

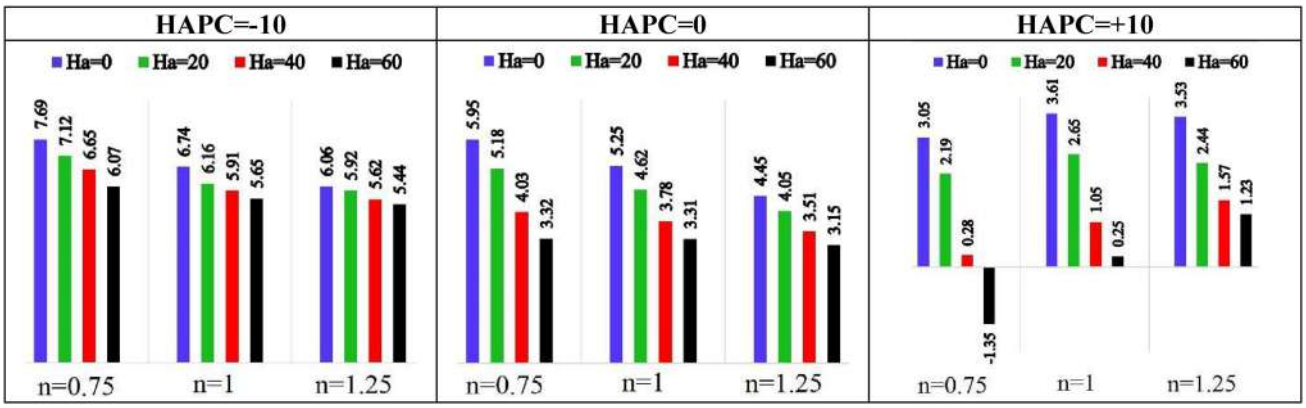

Fig. 14 Mean Nusselt number for different values of Ha, HAPC and PL index in TCR = 10, TMF3, $\theta_B = 0$, $\lambda = 0$

Table 3 The amount of entropy generated for the different values of Ha, HAPC and PL index in TCR = 10, TMF3, $\theta_B = 0$, $\lambda = 0$

	HAPC = − 10			HAPC = 0			HAPC = + 10		
	$n = 0.75$	$n = 1$	$n = 1.25$	$n = 0.75$	$n = 1$	$n = 1.25$	$n = 0.75$	$n = 1$	$n = 1.25$
Ha = 0	38.55	31.15	26.84	44.55	34.81	27.85	94.05	50.05	33.15
Ha = 20	34.75	28.65	25.49	39.55	32.25	26.75	99.25	52.35	33.95
Ha = 40	30.51	26.78	24.96	35.05	29.02	25.62	105.17	54.09	34.31
Ha = 60	28.15	26.19	24.85	30.85	27.85	25.05	113.15	56.65	35.09

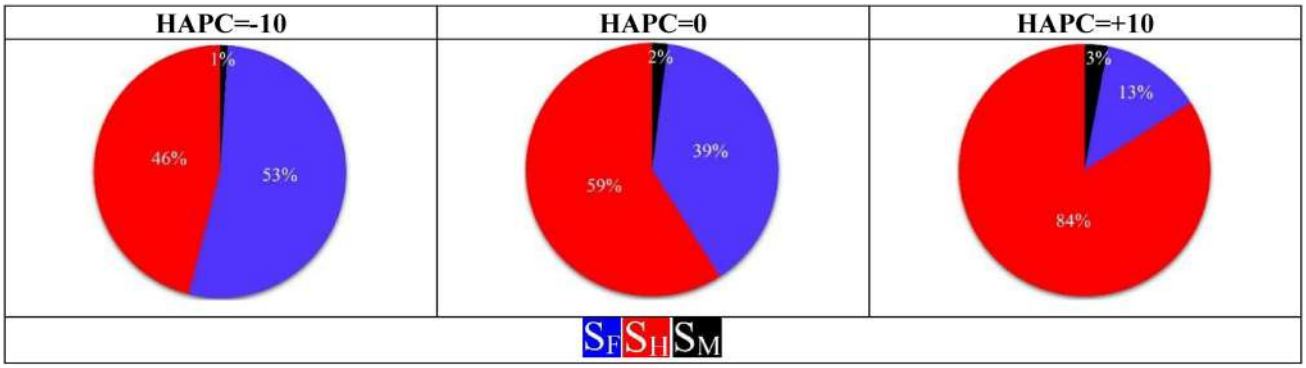

Fig. 15 The contribution of each entropy-generating factor in creating the total entropy for HAPC changes in TCR = 10, TMF3, $\theta_B = 0$, $\lambda = 0$, Ha = 20, $n = 0.75$

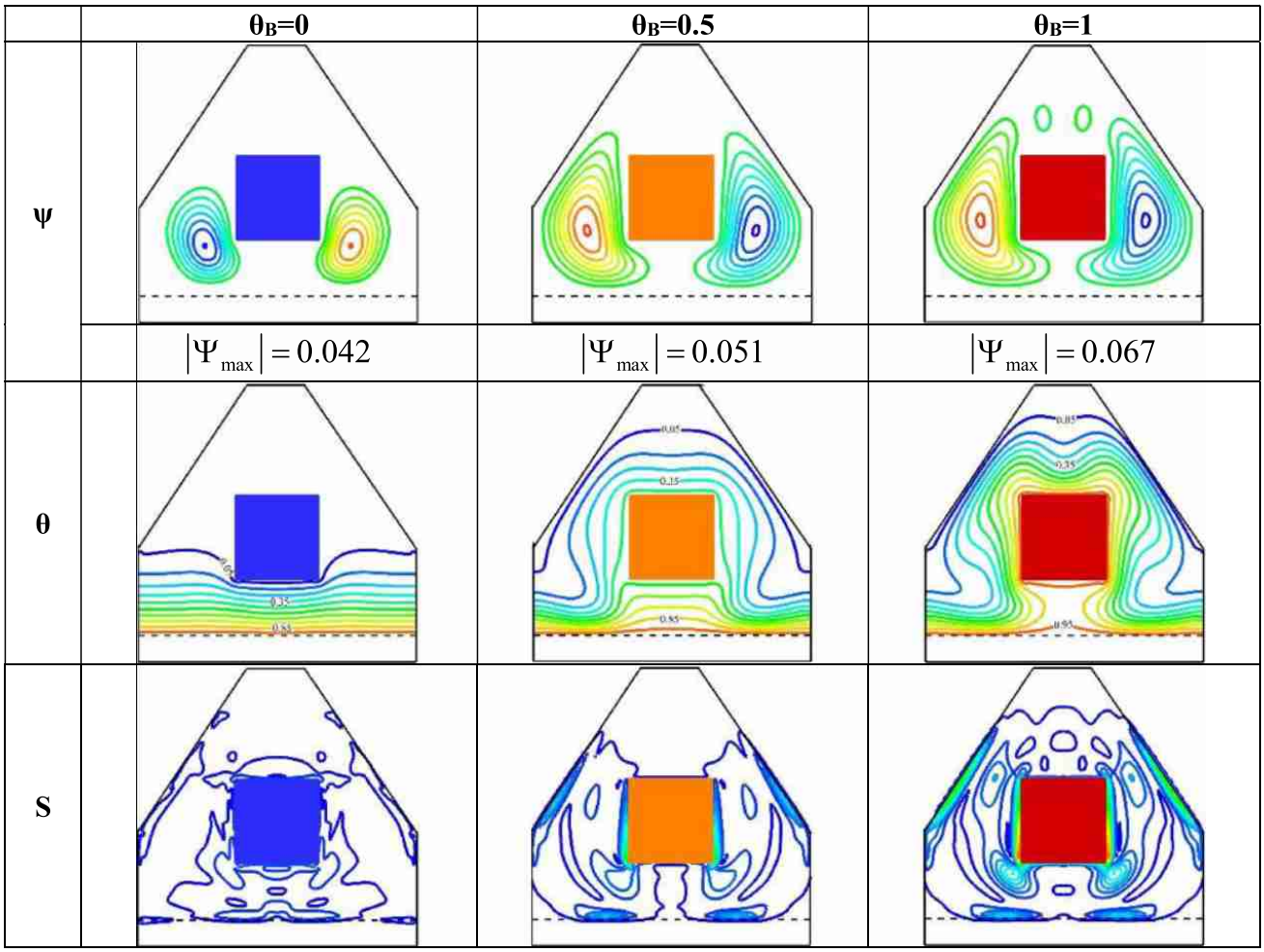

Fig. 16 Streamlines, isotherms and entropy lines for different values of θ_B in TCR = 10, TMF2, $\lambda = -90°$, Ha = 20, HAPC = 0, $n = 1$

According to Eqs. (24) and (25), the obstacle temperature boundary conditions strongly affect the formed flow. As the barrier temperature increases, the vigor and shape of the flow change visibly, so that the current vigor in $\theta_B = 1$ is about 59% and 31% higher than $\theta_B = 0$ and $\theta_B = 0.5$, respectively. As the barrier temperature increases, the symmetrical streamlines formed around the barrier expands upwards. (2) Pure conduction is visible when barrier temperature is equal

to 0.5. This can be understood when the isotherms are parallel to the conductor wall. Increasing the barrier temperature leads to the expansion of isotherms at the surface of the chamber and due to the curvature of the lines, the increase of convection effects is visible. (3) Like the symmetrical shape of vortices, the shape of entropy lines is symmetrical. It is well known that entropy increases with enhancement of the barrier temperature, especially in the near of diagonal walls, because there is an increase in speed and temperature gradients. In $\theta_B = 1$, the highest concentration of lines is seen in the vicinity of the barrier, which indicates a high irreversibility in this area.

The synchronic impact of Ha, fluid type and barrier temperature on the mean Nu in Fig. 17 is exhibited: (1) The mean Nu decreases with enhancement of the barrier temperature. As shown in Fig. 15, the reduction and augmentation of in the concentration of isotherms in the proximity of the conductor wall and the cold walls, respectively, are the result of the augmentation of in the block temperature. (2) The influence of barrier temperature change increases with

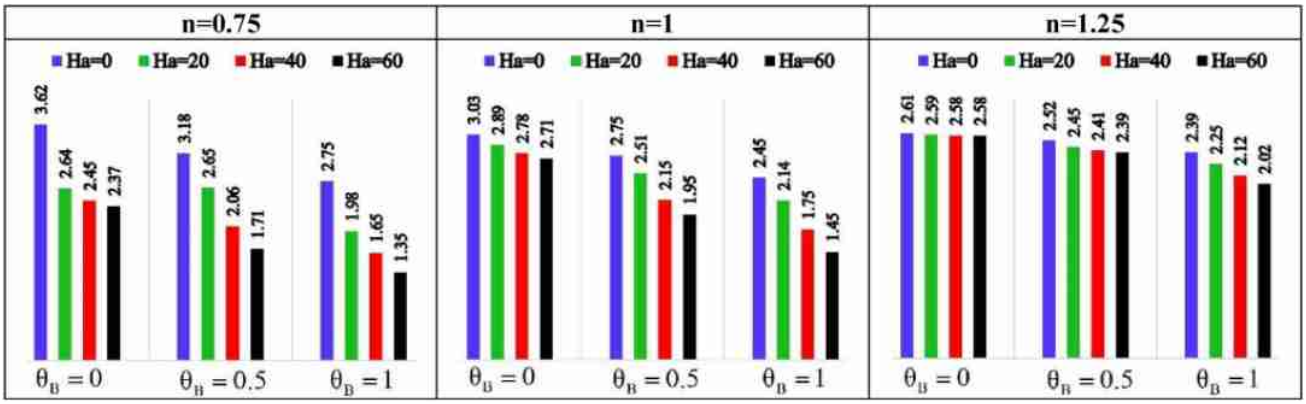

Fig. 17 Mean Nusselt number for different values of Ha, θ_B and PL index in TCR = 10, TMF1, HAPC = 0, $\lambda = -90°$

Table 4 The amount of entropy generated for different values of Ha, θ_B and PL index in TCR = 10, TMF1, HAPC = 0, $\lambda = -90°$

	$n=0.75$			$n=1$			$n=1.25$		
	$\theta_B=0$	$\theta_B=0.5$	$\theta_B=1$	$\theta_B=0$	$\theta_B=0.5$	$\theta_B=1$	$\theta_B=0$	$\theta_B=0.5$	$\theta_B=1$
Ha=0	37.51	40.25	45.03	33.75	36.25	38.45	27.59	28.64	29.74
Ha=20	34.51	36.95	39.99	31.15	33.75	34.99	27.03	27.75	28.49
Ha=40	31.75	33.01	34.15	29.15	30.81	31.35	26.41	27.05	27.41
Ha=60	29.25	29.35	29.78	28.01	28.65	29.22	26.21	26.35	26.71

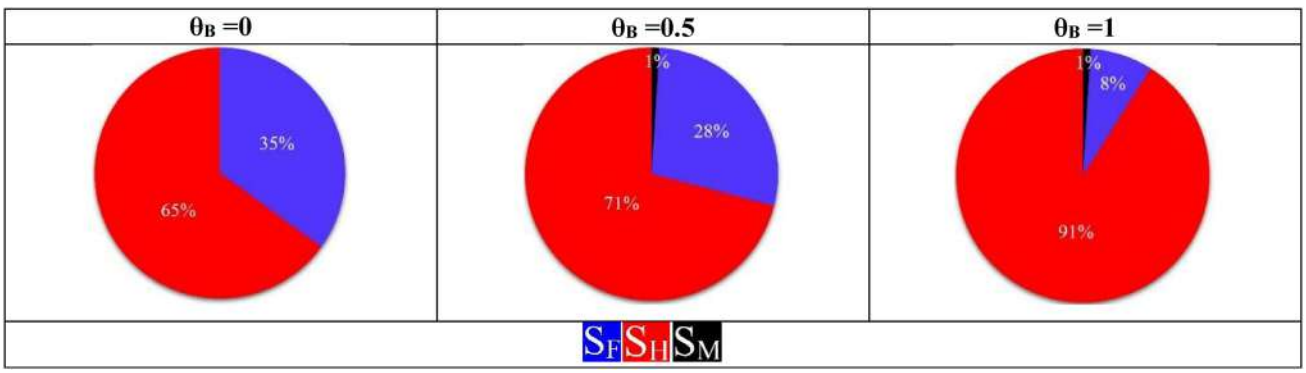

Fig. 18 The contribution of each entropy-generating factor in creating the total entropy for θ_B changes in TCR = 10, TMF2, $n = 1$, $\lambda = -90°$, Ha = 20, HAPC = 0

decreasing PL index. The augmentation of in convection effects caused by the augmentation of in obstacle temperature leads to an augmentation of in the effectiveness of MF. For specimen, in the absence of MF, augmentation of θ_B from 0 to 1 reduces the mean Nu by 25%, 19% and 8.5% for $n=0.75$ and $n=1.25$, respectively. The trivial of the impact of MF applied on $n=1.25$ in $\theta_B=0$ is remarkable regarding to the domination of thermal conductivity.

The increase in EP can be seen clearly in Table 4 by enhancement of the barrier temperature. The trend of changes in EP value similar to the mean Nu is reportaged.

The insignificance of the impact of MF on EP at $\theta_B=0$ is significant according to Fig. 18. Another important point is the augmentation of in the share of HT in EP with the augmentation of the block temperature, which is very substantial.

In order to depict the impact of the kind of MF applied, the vertical velocity for Ha changes for $n=0.75$ and $n=1.25$ is expressed in Fig. 19. It should be explained that: (1) The fluid velocity decreases with increment of Ha, which has a greater impact on $n<1$ than on $n>1$. (2) Via MF applying non-uniformly, less volumetric force (Lorentz resistive force) is applied to the fluid in the opposite direction to gravity (According to the kind of application according to Fig. 2a) This factor causes the fluid velocity to be higher than the uniform mode and the fluid to circulate more easily inside the chamber and the convection effects to be stronger. (3) The higher velocity of the fluid for $n=0.75$ compared to the $n=1.25$ indicates that an augmentation of in PL index leads to an increase in the viscosity of the fluid according to Eq. (6).

The impact of change in TMF applied on the maximum values of flow and the mean Nu is expressed in Table 5. (1) The change in the kind of application of MF changes the amount of HT and the flow vigor so that the application in the form of TMF3 has the lowest mean Nu and the vigor of the flow. (2) The least influence of changing TMF belongs to $n=1.25$, because in this situation there are the least effects of convection. (3) The larger Ha, the more vivid the impact of changing TMF.

Figure 20 exhibits that the share of MF in the total EP varies with the change in the rheological behavior of the fluid, so that with increasing PL index this share decreases remarkably. Also, due to the augmentation of in the viscosity of fluid with augmentation of PL index regarding to Eq. (9),

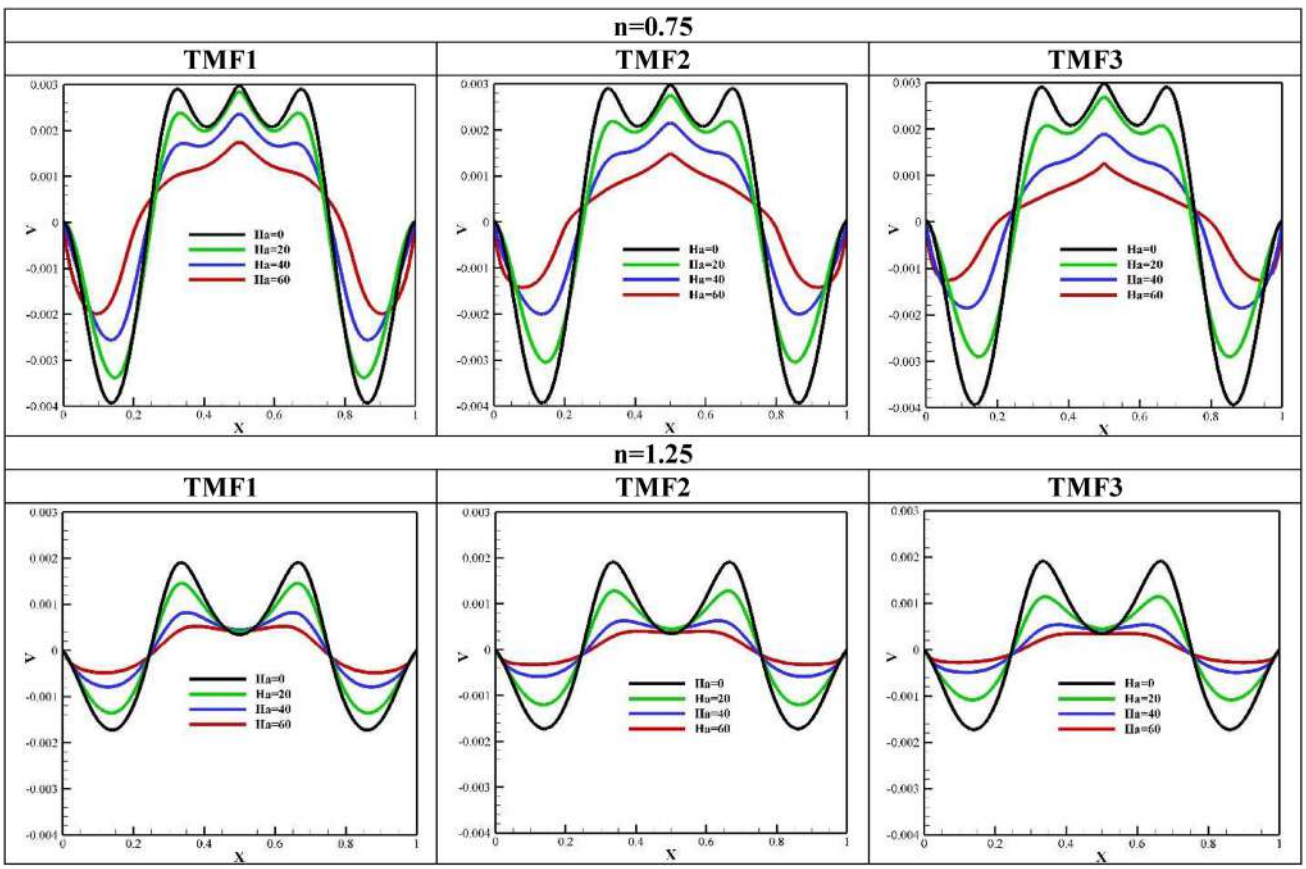

Fig. 19 Vertical velocity for different values of Ha, TMF and PL index in TCR = 10, HAPC = 0, $\lambda = -90°$, $\theta_B = 1$

Table 5 The mean Nu for different values of Ha, TMF and PL index in TCR = 10, HAPC = 0, $\lambda = -90°$, $\theta_B = 0.5$

	TMF1			TMF2			TMF3		
	$n=0.75$	$n=1$	$n=1.25$	$n=0.75$	$n=1$	$n=1.25$	$n=0.75$	$n=1$	$n=1.25$
$\lvert\Psi_{max}\rvert$									
Ha = 0	0.108	0.091	0.051	0.108	0.087	0.051	0.108	0.091	0.051
Ha = 20	0.089	0.081	0.048	0.085	0.074	0.046	0.073	0.071	0.043
Ha = 40	0.062	0.065	0.043	0.045	0.051	0.042	0.031	0.037	0.035
Ha = 60	0.053	0.055	0.041	0.027	0.038	0.039	0.018	0.028	0.033
Nu									
Ha = 0	3.18	2.75	2.52	3.18	2.75	2.52	3.18	2.75	2.52
Ha = 20	2.65	2.51	2.45	2.54	2.48	2.44	2.38	2.45	2.41
Ha = 40	2.06	2.15	2.41	1.91	2.05	2.38	1.78	1.85	2.28
Ha = 60	1.71	1.95	2.39	1.52	1.75	2.34	1.41	1.55	2.21

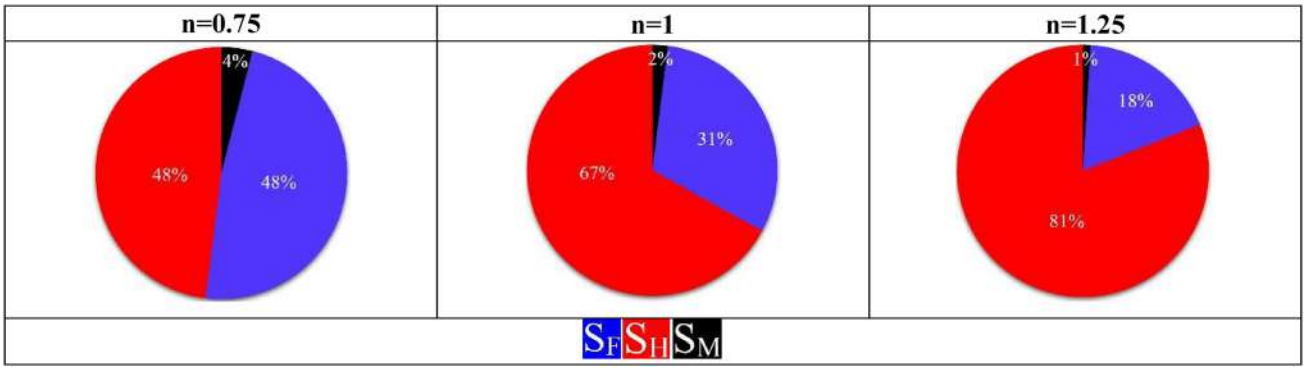

Fig. 20 The contribution of each entropy-generating factor in creating the total entropy for PL index changes in TCR = 1, TMF2, $\theta_B = 0.5$, $\lambda = -90°$, Ha = 20, HAPC = 0

the share of fluid friction in EP decreases and the share of HT in EP increases.

Conclusions

The following points can be summarized about the simulation of NCHT of PL fluids under the impact of uniform HAP. The inclined irregular hexagonal chamber involving a square hurdle in different temperatures under study is exposed to three different shapes of MF. The correctness of the obtained outcomes by LBM corroborated qualitatively and quantitatively with reliable references.

- The reduction of the velocity of fluid movement, the power of fluid rotation and the mean Nu is the result of the augmentation of Ha, so that on average these effects are up to 41% more for $n=0.75$ compared to $n=0.125$.
- TMF can be used to control flow characteristics. By using this momentous variable, it is possible to achieve desired flow and HT easily. A more obvious reduction of HT and fluid rotation power is possible via MF applying in the form of TMF3 (uniform). To make the change of TMF more visible, it is necessary to use a fluid with low viscosity.
- The reduction of convection effects and the predominance of thermal conductivity as the main mechanism of HT results from the augmentation of in PL index. The mean Nu value up to about 45% for $n=0.125$ is less than $n=0.75$. For MF control, changing the value of PL index can be a suitable choice so that the lowest MF influence is obtained in $n=0.125$.
- One of the tools to control HT is to place a barrier in the path of FF. By changing the barrier temperature, it can be managed the flow strength, EP and HT. Although the lowest value of the mean Nu is obtained for the highest value of the obstacle temperature, however, the effectiveness of the MF is more obvious. To lower the EP value, it is enough to keep the obstacle at a low temperature.
- By designing the chamber in such a way that it is positioned at an angle of + 90 degrees, the MF effect can be minimized and less mean Nu and EP can be achieved. Reducing the influence of MF, changing the type of fluid, and changing TMF are all possible by reducing TCR.

- In order to achieve a higher Be value, augmentation of Ha and HAPC, using a fluid with high viscosity, and reducing TCR are suitable solutions. To augmentation of the share of MF in EP, it is enough to design in such a way that $n = 0.75$, $\varphi = 0$, HAPC $= +10$ and Ha $= 0$ are selected.
- Based on the obtained outcomes, for HAPC $= +10$, the total EP increases with enhancement of Ha, and in return, in HAPC ≤ 0, increment of Ha leads to a decrease in the amount of EP.
- To develop the existing work and in order to gain a deeper understanding of fluid behavior in different conditions and to better manage the amount of HT, it is suggested to simulate the present work in the porous medium by considering the effects of thermal radiation.

Acknowledgements This article is the result of the efforts of the authors of the article, Mohammad Nemati and Mohammad Sefid. This article is part of the doctoral thesis of Mr. Mohammad Nemati. The main goal of this article is to try to achieve optimal conditions to achieve a desired flow. In this article, which has been developed with the development of LBM, an attempt has been made to show how active and passive methods can affect the amount of heat transfer and entropy.

Author contributions MN contributed to project administration, writing—review and editing, formal analysis, methodology, conceptualization, and writing—original draft. MS contributed to formal analysis, supervision, and writing—review and editing.

Funding There is no funding source.

Availability of data and material The data and material are available and can be presented in the case of needed.

Declarations

Conflict of interest There is no conflict of interest.

Ethical approval This article does not contain any studies with human participants or animals performed by any of the authors.

Informed consent Informed consent was obtained from all individual participants included in the study.

References

1. Khashi'ie, N.S., Arifin, N.M., Pop, I.: Magnetohydrodynamics (MHD) boundary layer flow of hybrid nanofluid over a moving plate with Joule heating. Alex. Eng. J. **61**(3), 1938–1945 (2022)
2. Amine, B.M., Redouane, F., Mourad, L., Jamshed, W., Eid, M.R., Al-Kouz, W.: Magnetohydrodynamics natural convection of a triangular cavity involving Ag-MgO/water hybrid nanofluid and provided with rotating circular barrier and a quarter circular porous medium at its right-angled corner. Arab. J. Sci. Eng. **46**(12), 12573–12597 (2021)
3. Akgül, A., Siddique, I.: Novel applications of the magnetohydrodynamics couple stress fluid flows between two plates with fractal-fractional derivatives. Numer. Methods Partial Differ. Equ. **37**(3), 2178–2189 (2021)
4. Hellinger, P., Papini, E., Verdini, A., Landi, S., Franci, L., Matteini, L., Montagud-Camps, V.: Spectral transfer and Kármán–Howarth–Monin equations for compressible hall magnetohydrodynamics. Astrophys. J. **917**(2), 101 (2021)
5. Islam, T., Alam, M., Asjad, M.I., Parveen, N., Chu, Y.M.: Heatline visualization of MHD natural convection heat transfer of nanofluid in a prismatic enclosure. Sci. Rep. **11**(1), 1–8 (2021)
6. Roy, N.C.: MHD natural convection of a hybrid nanofluid in an enclosure with multiple heat sources. Alex. Eng. J. **61**(2), 1679–1694 (2022)
7. Borrelli, A., Giantesio, G., Patria, M.C.: Exact solutions in MHD natural convection of a Bingham fluid: fully developed flow in a vertical channel. J. Therm. Anal. Calorim. **147**(10), 5825–5838 (2022)
8. Mourad, A., Abderrahmane, A., Younis, O., Marzouki, R., Alazzam, A.: Numerical simulations of magnetohydrodynamics natural convection and entropy production in a porous annulus bounded by wavy cylinder and Koch snowflake loaded with Cu–water nanofluid. Micromachines **13**(2), 182 (2022)
9. Ali, L., Ali, B., Liu, X., Iqbal, T., Zulqarnain, R.M., Javid, M.: A comparative study of unsteady MHD Falkner–Skan wedge flow for non-Newtonian nanofluids considering thermal radiation and activation energy. Chin. J. Phys. **1**(77), 1625–1638 (2022)
10. Ibrahim, M.G., Asfour, H.A.: The effect of computational processing of temperature-and concentration-dependent parameters on non-Newtonian fluid MHD: applications of numerical methods. Heat Transf. **51**(4), 2977–2994 (2022)
11. Ismael, A., Eldabe, N.T., Abouzeid, M., Elshabouri, S.: Entropy generation and nanoparticles Cu O effects on MHD peristaltic transport of micropolar non-Newtonian fluid with velocity and temperature slip conditions. Egypt. J. Chem. **65**(9), 715–722 (2022)
12. El-Dabe, N., Abou-Zeid, M.Y., Mohamed, M.A., Abd-Elmoneim, M.M.: MHD peristaltic flow of non-Newtonian power-law nanofluid through a non-Darcy porous medium inside a non-uniform inclined channel. Arch. Appl. Mech. **91**(3), 1067–1077 (2021)
13. Alesbe, I., Aljabair, S., Jalil, J.M.: An efficient numerical simulation of 2D natural convection in an inclined cavity with internal heat generation using differential quadrature method. Walailak J. Sci. Technol. (WJST). **18**(13), 20601–20617 (2021)
14. Rana, P., Kumar, A., Gupta, G.: Impact of different arrangements of heated elliptical body, fins and differential heater in MHD convective transport phenomena of inclined cavity utilizing hybrid nanoliquid: artificial neutral network prediction. Int. Commun. Heat Mass Transf. **1**(132), 105900 (2022)
15. Sefid, M., Jahromi, B., Jahangiri, R.: The effect of magnetic field and nanoparticle shape on heat transfer in an inclined cavity with uniform heat generation/absorption. Comput. Methods Eng. **40**(2), 109–126 (2022)
16. Dhia Massoudi, M., Ben Hamida, M.B., Mohammed, H.A., Almeshaal, M.A.: MHD heat transfer in W-shaped inclined cavity containing a porous medium saturated with Ag/Al2O3 hybrid nanofluid in the presence of uniform heat generation/absorption. Energies **13**(13), 3457 (2020)
17. Khan, M.R., Mao, S., Deebani, W., Elsiddieg, A.M.: Numerical analysis of heat transfer and friction drag relating to the effect of Joule heating, viscous dissipation and heat generation/absorption in aligned MHD slip flow of a nanofluid. Int. Commun. Heat Mass Transf. **1**(131), 105843 (2022)
18. Abdulkadhim, A., Hamzah, H.K., Ali, F.H., Yıldız, Ç., Abed, A.M., Abed, E.M., Arıcı, M.: Effect of heat generation and heat absorption on natural convection of Cu-water nanofluid in a wavy enclosure under magnetic field. Int. Commun. Heat Mass Transf. **1**(120), 105024 (2021)

19. Dar, A.A.: Effect of thermal radiation, temperature jump and inclined magnetic field on the peristaltic transport of blood flow in an asymmetric channel with variable viscosity and heat absorption/generation. Iran. J. Sci. Technol. Trans. Mech. Eng. **45**(2), 487–501 (2021)
20. Gambo, J.J., Gambo, D.: On the effect of heat generation/absorption on magnetohydrodynamic free convective flow in a vertical annulus: an Adomian decomposition method. Heat Transf. **50**(3), 2288–2302 (2021)
21. Al-Farhany, K., Al-Chlaihawi, K.K., Al-dawody, M.F., Biswas, N., Chamkha, A.J.: Effects of fins on magnetohydrodynamic conjugate natural convection in a nanofluid-saturated porous inclined enclosure. Int. Commun. Heat Mass Transf. **1**(126), 105413 (2021)
22. Siddiqa, S., Begum, N., Hossain, M.A., Abrar, M.N., Gorla, R.S., Al-Mdallal, Q.: Effect of thermal radiation on conjugate natural convection flow of a micropolar fluid along a vertical surface. Comput. Math. Appl. **1**(83), 74–83 (2021)
23. Premachandran, B., Balaji, C.: Conjugate mixed convection with surface radiation from a horizontal channel with protruding heat sources. Int. J. Heat Mass Transf. **49**(19–20), 3568–3582 (2006)
24. Rao, G.M., Narasimham, G.S.: Laminar conjugate mixed convection in a vertical channel with heat generating components. Int. J. Heat Mass Transf. **50**(17–18), 3561–3574 (2007)
25. Sudhakar, T.V., Balaji, C., Venkateshan, S.P.: Optimal configuration of discrete heat sources in a vertical duct under conjugate mixed convection using artificial neural networks. Int. J. Therm. Sci. **48**(5), 881–890 (2009)
26. Choi, C.Y., Kim, S.: Conjugate mixed convection in a channel: modified five percent deviation rule. Int. J. Heat Mass Transf. **39**(6), 1223–1234 (1996)
27. Lei, T., Wang, Z., Luo, K.H.: Study of pore-scale coke combustion in porous media using lattice Boltzmann method. Combust. Flame **1**(225), 104–119 (2021)
28. Bisht, M., Patil, D.V.: Assessment of multiple relaxation time-lattice Boltzmann method framework for non-Newtonian fluid flow simulations. Eur. J. Mech.-B/Fluids **1**(85), 322–334 (2021)
29. Shan, F., Du, H., Chai, Z., Shi, B.: Lattice Boltzmann modeling of the capillary rise of non-Newtonian power-law fluids. Int. J. Numer. Methods Fluids **94**(3), 251–271 (2022)
30. Gohari, E.M., Sefid, M., Malooze, A.R., Mozafari-Shamsi, M.: Hydrodynamic simulation of liquid–solid fluidized bed with non-Newtonian power-law fluids using SPM-LBM method. J. Mech. Eng. **51**, 245–250 (2022)
31. Shahsavar, A., Entezari, S., Askari, I.B., Jamei, M., Karbasi, M., Shahmohammadi, M.: Investigation on two-phase fluid mixture flow, heat transfer and entropy generation of a non-Newtonian water-CMC/CuO nanofluid inside a twisted tube with variable twist pitch: numerical and evolutionary machine learning simulation. Eng. Anal. Bound. Elem. **1**(140), 322–337 (2022)
32. Al-Chlaihawi, K.K., Alaydamee, H.H., Faisal, A.E., Al-Farhany, K., Alomari, M.A.: Newtonian and non-Newtonian nanofluids with entropy generation in conjugate natural convection of hybrid nanofluid-porous enclosures: a review. Heat Transf. **51**(2), 1725–1745 (2022)
33. Mliki, B., Abbassi, M.A.: Entropy generation of MHD natural convection heat transfer in a heated incinerator using hybrid-nanoliquid. Propuls. Power Res. **10**(2), 143–154 (2021)
34. Gal, S., Kolsi, L., Hassen, W., Ben Ali, N., Ben Khedher, N., Chamkha, A.J.: Three-dimensional study of magnetohydrodynamic natural convection, entropy generation, and electromagnetic variables in a nanofluid filled enclosure equipped with inclined fins. ACS Omega **7**(14), 12365–12373 (2022)
35. Khetib, Y., Alahmadi, A.A., Alzaed, A., Azimy, H., Sharifpur, M., Cheraghian, G.: Effect of straight, inclined and curved fins on natural convection and entropy generation of a nanofluid in a square cavity influenced by a magnetic field. Processes **9**(8), 1339 (2021)
36. Alqaed, S., Mustafa, J., Sharifpur, M.: Numerical investigation and optimization of natural convection and entropy generation of alumina/H2O nanofluid in a rectangular cavity in the presence of a magnetic field with artificial neural networks. Eng. Anal. Bound. Elem. **1**(140), 507–518 (2022)
37. Aghakhani, S., Pordanjani, A.H., Karimipour, A., Abdollahi, A., Afrand, M.: Numerical investigation of heat transfer in a power-law non-Newtonian fluid in a C-shaped cavity with magnetic field effect using finite difference lattice Boltzmann method. Comput. Fluids **15**(176), 51–67 (2018)
38. Ferhi, M., Djebali, R., Al-Kouz, W., Abboudi, S., Chamkha, A.J.: MHD conjugate heat transfer and entropy generation analysis of MWCNT/water nanofluid in a partially heated divided medium. Heat Transf. **50**(1), 126–144 (2021)
39. Thapa, S., Samir, S., Kumar, K., Singh, S.: A review study on the active methods of heat transfer enhancement in heat exchangers using electroactive and magnetic materials. Mater. Today Proc. **1**(45), 4942–4947 (2021)
40. Miri Joibary, S.M., Siavashi, M.: Effect of Reynolds asymmetry and use of porous media in the counterflow double-pipe heat exchanger for passive heat transfer enhancement. J. Therm. Anal. Calorim. **140**(3), 1079–1093 (2020)
41. Zaboli, M., Ajarostaghi, S.S., Noorbakhsh, M., Delavar, M.A.: Effects of geometrical and operational parameters on heat transfer and fluid flow of three various water based nanofluids in a shell and coil tube heat exchanger. SN Appl. Sci. **1**(11), 1–7 (2019)
42. Sheikholeslami, M., Gorji-Bandpy, M., Ganji, D.D.: Review of heat transfer enhancement methods: focus on passive methods using swirl flow devices. Renew. Sustain. Energy Rev. **1**(49), 444–469 (2015)
43. Sidik, N.A., Muhamad, M.N., Japar, W.M., Rasid, Z.A.: An overview of passive techniques for heat transfer augmentation in microchannel heat sink. Int. Commun. Heat Mass Transf. **1**(88), 74–83 (2017)
44. Akbarzadeh, S., Valipour, M.S.: Heat transfer enhancement in parabolic trough collectors: a comprehensive review. Renew. Sustain. Energy Rev. **1**(92), 198–218 (2018)
45. Ullah, H., Hayat, T., Ahmad, S., Alhodaly, M.S.: Entropy generation and heat transfer analysis in power-law fluid flow: finite difference method. Int. Commun. Heat Mass Transf. **1**(122), 105111 (2021)
46. Zhang, R., Aghakhani, S., Pordanjani, A.H., Vahedi, S.M., Shahsavar, A., Afrand, M.: Investigation of the entropy generation during natural convection of Newtonian and non-Newtonian fluids inside the L-shaped cavity subjected to magnetic field: application of lattice Boltzmann method. Eur. Phys. J. Plus **135**(2), 184 (2020)
47. Hussain, S., Zeeshan, M.: Irreversibility analysis for the natural convection of Casson fluid in an inclined porous cavity under the effects of magnetic field and viscous dissipation. Int. J. Therm. Sci. **1**(179), 107699 (2022)
48. Rostami, S., Ellahi, R., Oztop, H.F., Goldanlou, A.S.: A study on the effect of magnetic field and the sinusoidal boundary condition on free convective heat transfer of non-Newtonian power-law fluid in a square enclosure with two constant-temperature obstacles using lattice Boltzmann method. J. Therm. Anal. Calorim. **144**(6), 2557–2573 (2021)
49. Chen, Z., Shu, C.: Simplified lattice Boltzmann method for non-Newtonian power-law fluid flows. Int. J. Numer. Methods Fluids **92**(1), 38–54 (2020)
50. Kefayati, G., Bassom, A.P.: A lattice Boltzmann method for single-and two-phase models of nanofluids: Newtonian and non-Newtonian nanofluids. Phys. Fluids **33**(10), 102008 (2021)
51. Kebriti, S., Moqtaderi, H.: Numerical simulation of convective non-Newtonian power-law solidliquid phase change using the

lattice Boltzmann method. Int. J. Therm. Sci. **1**(159), 106574 (2021)
52. Kiani-Oshtorjani, M., Kiani-Oshtorjani, M., Mikkola, A., Jalali, P.: Conjugate heat transfer in isolated granular clusters with interstitial fluid using lattice Boltzmann method. Int. J. Heat Mass Transf. **15**(187), 122539 (2022)
53. Rahman, A., Nag, P., Molla, M.M., Hassan, S.: Magnetic field effects on natural convection and entropy generation of non-Newtonian fluids using multiple-relaxation-time lattice Boltzmann method. Int. J. Mod. Phys. C **32**(01), 2150015 (2021)
54. Teamah, M.A., El-Maghlany, W.M.: Augmentation of natural convective heat transfer in square cavity by utilizing nanofluids in the presence of magnetic field and uniform heat generation/absorption. Int. J. Therm. Sci. **1**(58), 130–142 (2012)
55. Ilis, G.G., Mobedi, M., Sunden, B.: Effect of aspect ratio on entropy generation in a rectangular cavity with differentially heated vertical walls. Int. Commun. Heat Mass Transf. **35**(6), 696–703 (2008)
56. Khezzar, L., Siginer, D., Vinogradov, I.: Natural convection of power law fluids in inclined cavities. Int. J. Therm. Sci. **1**(53), 8–17 (2012)
57. Kefayati, G.R.: Mesoscopic simulation of magnetic field effect on natural convection of power-law fluids in a partially heated cavity. Chem. Eng. Res. Des. **1**(94), 337–354 (2015)

International Journal of Energy and Environmental Engineering (2023) 14:937–948
https://doi.org/10.1007/s40095-023-00557-1

ORIGINAL RESEARCH

Effect of various nanoparticle biodiesel blends on thermal efficiency and exhaust pollutants

Shahab Imran[1] · M. Gul[1,2] · M. A. Kalam[1,3] · N. W. M. Zulkifli[1] · M. A. Mujtaba[1] · M. N. A. M. Yusoff[1] · M. S. N. Awang[1]

Received: 4 October 2022 / Accepted: 15 January 2023 / Published online: 4 February 2023

Abstract

The transport sector produces one-third of the world's greenhouse gasses. World consumption of nonrenewable energy through vehicles increases the interest in studies of different nanoparticle biodiesel blend behavior in a diesel engine. In this research, a comprehensive approach is taken using a wide variety of appraised nanoparticles to make blends. The CI diesel engine's engine performance and emission characteristics are studied with Malaysian commercial fuel using various nanoparticles (TiO_2, Al_2O_3, CuO, CeO_2, CNT, and GNP) blend to discover the best one. 100 ppm of each nanoparticle is used to make a blend via the ultrasonic technique. Mechanical and emission performance is tested in diesel engines (Yanmar TF 120 M) with 100% engine load at variable engine speed (2100-900 rpm). Graphical presentation and comparison of each fuel blend are discussed in this paper. All the ternary blends have shown improved engine performance. Al_2O_3 has shown a 3.68% reduction in BSFC when compared to neat B10. The average highest BTE recorded is a 14.59% increase when the B10 + TiO_2 blend is used, followed by CNT and CeO_2. Al_2O_3 has shown a 21.84% and 86.20% reduction in CO and HC when compared to B10, while CNT and GNP have shown a 6.03% and 2.06% of reduction in NOx emission when compared with B10.

Keywords Diesel engine · Nanoparticles · Engine performance · And emissions

Abbreviations

ASTM	American Standard for Testing Materials
UN	United Nations
DI	Direct injection
CI	Compression ignition
B10	10% Biodiesel + 90% diesel
ppm	Parts per million
Mr	Molar mass
CNT	Carbon nanotubes
TiO_2	Titanium dioxide
Al_2O_3	Aluminum oxide
CuO	Copper oxide
CeO_2	Caesium oxide
GNP	Graphene nanoparticles
BP	Brake power
BT	Brake torque
BTE	Brake thermal efficiency
BSFC	Brake-specific fuel consumption
CO	Carbon monoxide
CO_2	Carbon dioxide
HC	Hydrocarbons

Introduction

Energy conservation is one of the biggest concerns in the field of engineering. The world population is gradually increasing, requiring more energy every day. Asia is the most populated continent around the globe and consumes 41% of the earth's energy produced [1]. Vehicles play a very big role in consuming the energy of the world via using fossil fuels. An alternative is approached to fulfill the world's demand for energy and reduce environmental pollution by using renewable biofuels. 50% of the greenhouse gasses produced will be from the transport sector by 2030 [2].

✉ Shahab Imran
shahab@um.edu.my; kalam@um.edu.my

[1] Centre of Energy Science, Department of Mechanical Engineering, University of Malaya, 50603 Kuala Lumpur, Malaysia

[2] Department of Mechanical Engineering, Faculty of Engineering and Technology, Bahauddin Zakariya University, Multan 60000, Pakistan

[3] School of Civil and Environmental Engineering, University of Technology Sydney, Ultimo, NSW, Australia

According to UN 17 global sustainable development goals, we will be focusing on two goals. No.11: sustainable cities and communities and No. 13: climate change [3]. The transport sector plays the biggest role in global warming by emitting greenhouse gases [4]. Scientists believe that fossil fuel production is declining in its production, and alternative is required to replace it. Biofuels have less emission of greenhouse gases as compared with diesel fuels. Production of biodiesel was started with the high production of palm oil in Indonesia to reduce dependency on diesel fuel. Palm biodiesel is biodegradable and renewable and is used as an alternative fuel [5].

When compared to diesel fuel, biodiesel has superior properties in oxygen content, flash point, cetane number, etc. Thus, biodiesel shows a reduction in harmful exhaust emissions like CO, HC, and NOx [6]. Because of its lower calorific values, pure biodiesel has a low brake thermal efficiency (BTE), which can be improved by mixing it with diesel [7]. Biodiesel has some drawbacks when compared to pure diesel, like higher emission of NOx, lower calorific value, and poor oxidation stability, which can be improved by adding different nanoparticles. [8, 9] In Asia, biodiesel is produced using palm oil in Indonesia and Malaysia. By 2021, B30 will be commercialized in Indonesia and B20 in Malaysia, while B10 and B20 are currently being used currently in Malaysia and Indonesia [10, 11].

Overall, biodiesel decreases the engine's mechanical performance while having a positive effect on engine exhaust gasses instead of NOx. The mechanical performance of the engine could be improved by using fuel additives (nanoparticles), and it has been proven by various researchers [12–15]. Nanoparticles have shown a reduction in NOx and carbon emission while enhancing engine performance such as brake thermal efficiency (BTE), brake-specific fuel consumption (BSFC), and brake power (BP) [14].

Sathiyamoorthi et al. [16] conducted an experiment where they used CeO_2 in lemongrass oil biodiesel to evaluate the performance, combustion, and emission of a diesel engine. HC and CO emission was both reduced by 18.18 and 33.31%, while BSFC and BTE increased by 10.8 and 2.87%. There was a significant increase in cylinder pressure and heat release as well. These findings match with the [17] that oxygen in CeO_2 particles provided extra oxygen that eases the combustion. Janakiraman et al. [18] report has shown that CeO and TiO_2 have shown an increase in Engine performance. Al_2O_3 has shown a very positive emission of gasses from diesel engines when compared to base fuel. CO and HC emissions decreased as complete combustion was eased due to oxygen being more in ppm that aid combustion [13, 19–21]. Higher concentrations of nanoparticles are more effective with engine efficiency. Kumar et al. [22] used 50 and 100 ppm of TiO_2 and found that 100 ppm in biodiesel gives 114% more increase when compared to 50 ppm. Sandeep et al. [23] found that adding CNT to biodiesel improves BTE by 2.24% and reduces BSFC by 20.68% because nonmetallic nanoparticles possess excellent thermal conductivity and surface deficits. [24] No study has been conducted where various nanoparticles (at least 6) are tested at the same standards and compared [12].

The literature review has always shown significant improvement in the efficiency of the engine and a positive influence on the emission of gasses when a small amount of different nanoparticles is added to fuel [12, 15, 20, 23, 25, 26]. It can be seen from the literature review that no technical review has been done with various nanoparticles in the same standard fuel to compare different ternary blends in engine testing. Malaysian B10 is widely available and is the best base oil that could be used for comparison, so that country could get benefit from this paper as well. Many experiments have been done using not more than three nanoparticles. A comprehensive comparison between nanoparticle biodiesel blends could not be achieved for a particular fuel since different fuels are used in each paper. Some nanoparticles have oxygen atoms, which promote complete combustion inside the engine [27, 28]. 100 ppm of each nanoparticle is added in B10 to make different samples. Then, a comprehensive investigation is carried out using one cylinder diesel engine. BP, BT, BSFC, and engine efficiency are compared accordingly. Emissions such as CO_2, CO, and HC were compared, and the result can be used in future research to choose the mixture of nanoparticles that could give maximum performance and less harmful gaseous emissions. Though no experimental investigations have been carried out using these many nanoparticles as an additive in biodiesel on the same standard biodiesel, engine performance and emission characteristics for various nanoparticles as additives in biodiesel blends were limited.

Materials and method

Commercial diesel B10 (diesel with 10% palm biodiesel blend) fuel was bought from Shell, Malaysia, and used as the base fuel. Sigma-Aldrich, Malaysia, provided nanoparticles (TiO_2, Al_2O_3, CuO, CeO_2, CNT, GNP).

Samples preparation

The molar mass of each nanoparticle was taken into consideration to make the concentration 100 ppm. Different masses of each nanoparticle were taken to make 100 ppm as the molar mass of each nanoparticle is different. Sodium dodecyl sulfate is used as a surfactant to increase the concentration of dispersant, and nanoparticles are well dispersed [29].

A magnetic stirrer was used for basic physical mixing of nanoparticle additives and B10 at 60 °C, 700 rpm speed

for 1 h, followed by ultrasonication with 20 kHz frequency, pulse ratio of 2 s, and maximum rated power of 500 W for 30 min as shown in Fig. 1a, b. Ultrasonicator was used as an extra tool that is used to vibrate the particles in the liquid for better satisfactory mixing [30]. Table 1 describes the concentrations and other specifications of nanoparticles used for making ternary blends (fuel samples) for the diesel engine's performance and emission analysis.

The size of all nanoparticles was < 100 nm, as specifications were mentioned on the container.

Physicochemical properties of fuel samples

The viscosity index (VI), density, and kinematic viscosities at 100 and 40 °C were estimated by using Anton Paar, Graz Austria branded automatic Stabinger viscometer SVM 3000 according to ASTM D7042 standard. While calorific values were measured by using IKA, UK branded C2000 basic calorimeter according to ASTM D4809 standard.

Experimental setup of engine

For this study, the University of Malaya provided a diesel engine test setup [Model: Yanmar (TF 120 M)] to evaluate the engine performance and emission characteristics of various fuel samples. A schematic diagram of the experimental test setup is shown in Fig. 1. The diesel engine specifications are provided in Table 2.

Initially, B10 (commercial diesel) was utilized to investigate the performance and exhaust emission characteristics of a CI engine. The graduated measuring cylinder

Table 1 Concentration and other specifications of nanoparticles used

No	Fuels samples	Additive concentration	Size of nanoparticle (nm)	Color of nanoparticle
1	B10	–	–	
2	B10 + TiO_2	100 ppm	< 25	White/offwhite
3	B10 + Al_2O_3	100 ppm	< 50	White
4	B10 + CuO	100 ppm	< 50	Black
5	B10 + CeO_2	100 ppm	< 80	Offwhite
6	B10 + CNT	100 ppm	< 100	Black
7	B10 + GNP	100 ppm	< 100	Black

B10 is commercialized Malaysian fuel that is used as base oil

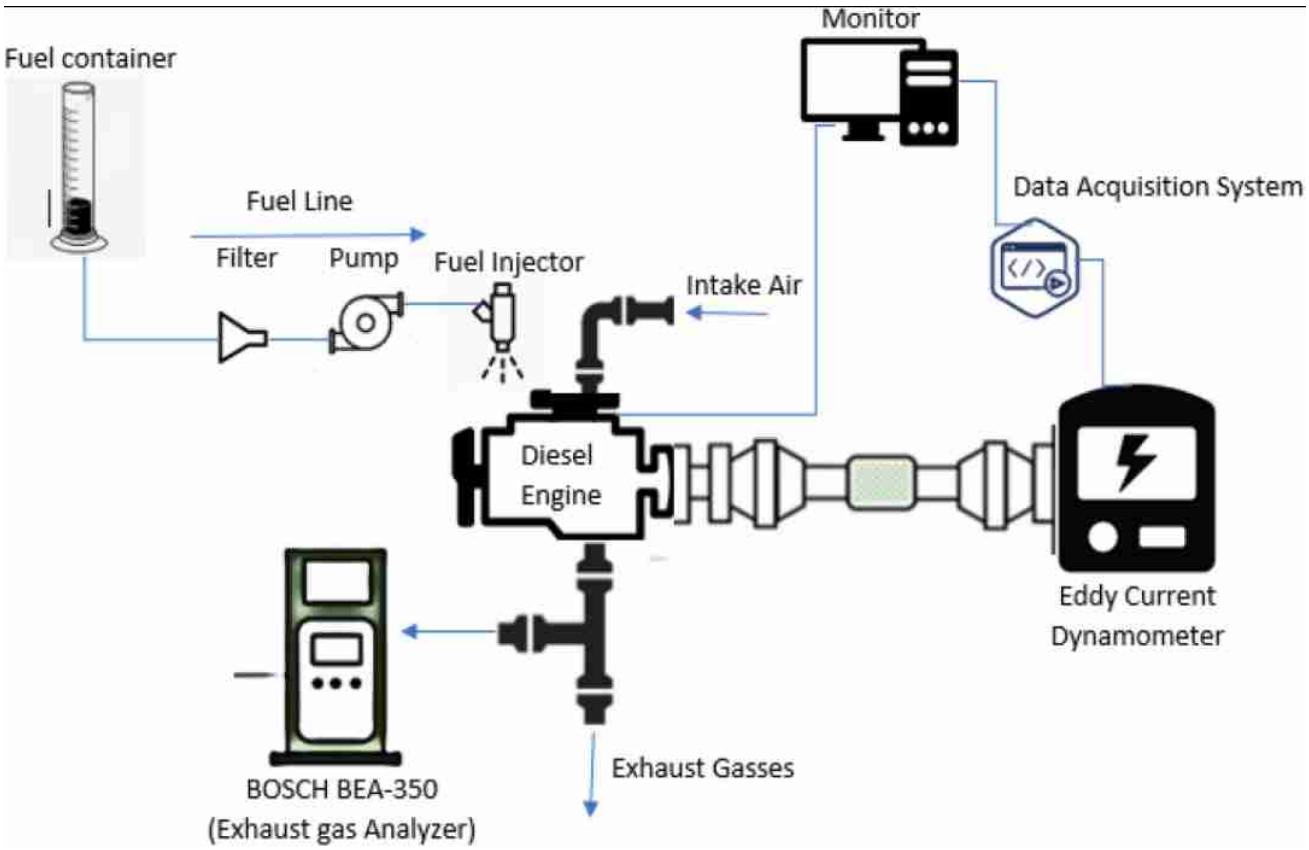

Fig. 1 Schematic diagram of the experimental setup

Table 2 Diesel engine specifications

Engine description	Specification
Number of cylinders	1
Induction	Radiator cooling
Stroke × cylinder bore × (mm)	96×92
Displacement	0.638
Ratio of compression	17.70
Engine speed at Max (rpm)	2400
Power at Max (kW)	7.70
Time of injecting (°)	17°BTDC
The pressure of injection (kg/cm^2)	200
Power take-off position	Flywheel side
Connecting rod length (mm)	149.50

is used as a fuel container to measure the fuel flow rate as the fuel decrease in volume and timing be noted manually. During the single test run, three readings were taken for every 10 ml by clicking the stopwatch for the respective engine speed, and the results were averaged. Brake torque and brake power were taken from (DASTEP8). BSFC is calculated using Eq. (1), while time is time taken for 1 kg of fuel to burn. BTE is calculated using Eq. (2), while Cv is the calorific value and *m* is the mass flow of fuel. Engine exhaust gasses (CO, HC, and NOx) were measured via a BOSCH gas analyzer, and the specification is mentioned in Table 3.

$$\mathrm{BSFC} = \frac{0.01}{\mathrm{Bp} \times \mathrm{Time}} \tag{1}$$

$$\mathrm{BTE} = \frac{\mathrm{Bp}}{m \times \mathrm{Cv}} \tag{2}$$

At first, the setup was running with B10 (commercial diesel) to know the steady operational conditions and engine characteristics, followed by ternary fuel blends (B10, B10 + TiO_2, B10 + Al_2O_3, B10 + CuO, B10 + CeO_2, B10 + CNT, and B10 + GNP). The diesel engine was flushed with B10 after every successful test to remove any traces left in the engine of the previous blend. Experimental results were obtained at full (100%) engine load with varying engine speeds (2100–900) rpm. All the test samples were conducted on the same day to obtain more accurate comparative results.

Result and discussion

Physicochemical properties of fuel samples

The physicochemical properties of all fuel samples are described in Table 4. In most cases, the calorific value is proportional to the engine's thermal efficiency. Calorific value depends on the element type, the bond between atoms, and the Mr of the molecule. B10 + GNP has shown the highest calorific value due to the long chain of carton and hydrogen atoms, making its molecular mass the highest. In most cases, engine combustion does not burn the fuel completely as time and oxygen supply are limited between strokes. A viscosity factor requires the eligibility of the oil while entering the inlet valve. The viscosity factor could be neglected as the inlet value used is efficient in providing a good flow. All the blends have shown almost the same value for density, and each nanoparticle's concentration is low in the blends.

Performance analysis

Performance parameters like Torque, brake power, BTE, and BSFC were evaluated for all ternary blends of fuel samples at 100% load with varying engine speeds and are deliberated below.

Brake Torque (BT) and Brake Power (Bp)

Brake torque and power were produced at 100% engine load while engine speed was running from high to low. Maximum brake power values for all the samples were recorded at 2100 engine speeds 6.86894, 6.92218, 6.81793, 6.85626, 6.89914, 6.91473, and 6.89057 for B10, B10 + TiO_2, B10 + Al_2O_3, B10 + CuO, B10 + CeO_2, B10 + CNT, and B10 + GNP, respectively. As the engine speed decreases, the break power produced for all the samples decreases dramatically. [31] The average Bp for the engine speed from 2100 to 900 rpm is 4.97668, 5.05844, 5.04415, 5.02306, 5.05328, 5.10219, and 5.08782 for B10, B10 + TiO_2, B10 + Al_2O_3, B10 + CuO, B10 + CeO_2, B10 + CNT and B10 + GNP, respectively. There is an increase in Bp for all the nanoparticles used as a blend. CNT and GNP have shown the highest value of BP followed by TiO_2, CeO_2, Al_2O_3, and CuO. CNT and GNP have carbon atoms in them. They provide further combustion in the cylinder. Fuel is denser in the solid

Table 3 Specifications for gas analyzers

Apparatus	Technique	Evaluate	Evaluated Range	Precision
BOSCH BEA 350	Flame ionization detector (FID)	HC	0–9999 ppm	±1 ppm
	Nondispersive infrared	CO	0–10% vol	±0.001% vol

Table 4 Physicochemical properties of all fuel samples

Blend (100 ppm)	Calorific value (MJ/Kg)	Viscosity index	Viscosity (mm^2/s)		Density (g/cm^3) at 15 °C
			At 40 °C	At 100 °C	
B10	44.9453	+219.5	2.7997	1.1802	0.8280
B10 + CuO	44.2737	+98.2	2.9713	1.1895	0.8290
B10 + GNP	45.3969	+339.5	2.7715	1.2008	0.8288
B10 + CNT	44.1505	+71.8	2.9134	1.1289	0.8287
B10 + TiO_2	43.7040	+149.2	2.9237	1.1991	0.8289
B10 + CeO_2	43.2207	+116.7	2.9464	1.1929	0.8286
B10 + Al_2O_3	44.1703	+99.5	3.0396	1.2109	0.8289

state. Thus, more carbon atoms are there to burn in a small volume of fuel [32]. Al_2O_3 had better Bp than CuO [20]

The average brake torque has a direct relation with the average brake power. In this experiment, maximum brake torque occurs between 1500 and 1800 rpm and the average values are 32.173545, 32.783675, 32.743, 32.526075, 32.723495, 32.878585, and 32.973495 for B10, B10 + TiO_2, B10 + Al_2O_3, B10 + CuO, B10 + CeO_2, B10 + CNT, and B10 + GNP, respectively. Compared to B10, all the ternary fuel blends have shown great improvement and the average increase are 1.67, 1.64, 1.16, 1.69, 2.58, and 2.50% for B10 + TiO_2, B10 + Al_2O_3, B10 + CuO, B10 + CeO_2, B10 + CNT, and B10 + GNP, respectively. Because of the occurrence of complete combustion, the value of BT is enhanced for ternary fuel blends compared to B30 fuel. Thus, more work is produced, and the mean pressure in the engine cylinder is higher, resulting in an increase in BT and force by the piston [33] (Figs. 2, 3).

Brake-specific fuel consumption

BSFC was calculated while the engine was running at 100% load with speed increasing from 2100 to 900 rpm, as illustrated in Fig. 4. Generally, BSFC increases as the engine speed decrease with time. Minimum BSFC was recorded at 2100 rpm with the values of 0.5241, 0.51903, 0.50869, 0.49639, 0.4895, 0.52063, and 0.48657 for B10, B10 + TiO_2, B10 + Al_2O_3, B10 + CuO, B10 + CeO_2, B10 + CNT, and B10 + GNP. Average BSFC values for all the tested fuels were 0.58021 (B10), 0.57185(B10 + TiO_2), 0.55882(B10 + Al_2O_3), 0.57795(B10 + CuO), 0.57799 (B10 + CeO_2), 0.56514 B10 + CNT), and 0.56682 (B10 + GNP). All the nanoparticle's ternary fuel samples have shown reduced fuel consumption as the value of BSFC is lower. Compared to B10, all the ternary fuel blends (B10 + TiO_2, B10 + Al_2O_3, B10 + CuO, B10 + CeO_2, B10 + CNT and B10 + GNP) have shown an average of 1.44, 3.68, 0.3895, 0.3826, 2.597, and 2.307% fall in BSFC. Ternary fuel blends caused volumetric efficiency to increase and a lower amount of work is needed for the compression stroke, thus causing improvement in BSFC values [34, 35].

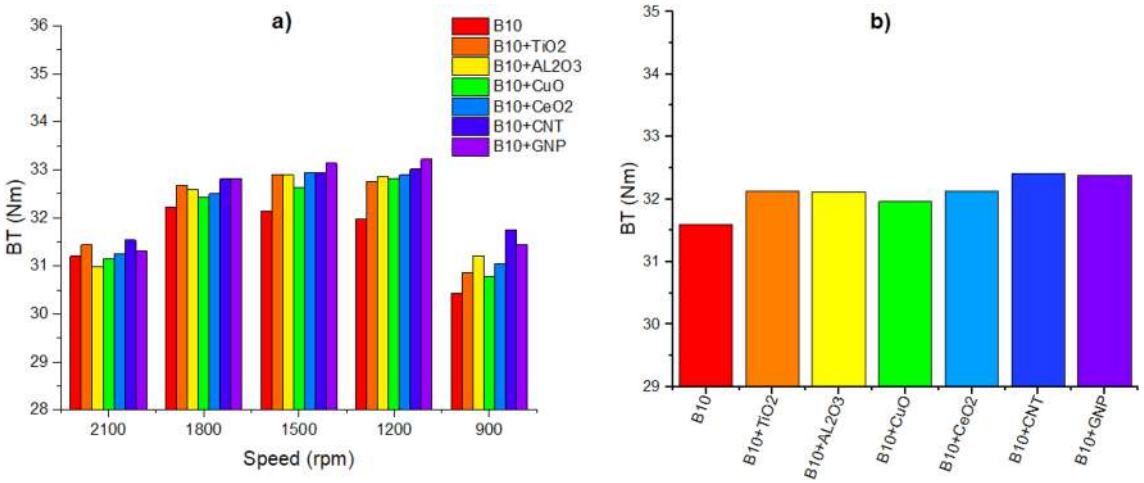

Fig. 2 **a** BT reported from engine testing with variable engine speed. **b** Mean BT of all the fuel samples

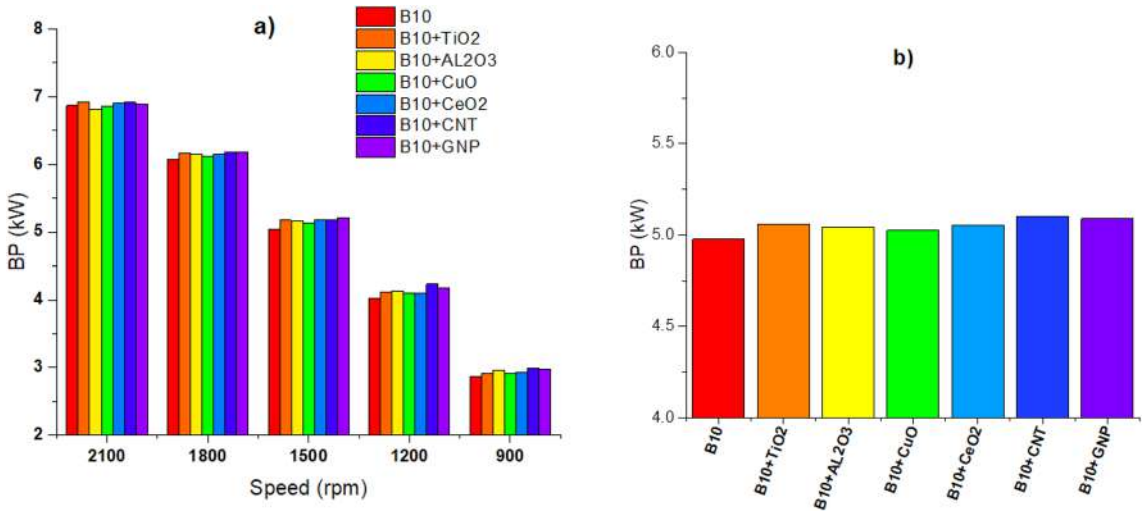

Fig. 3 **a** BP reported from engine testing with variable engine speed. **b** Mean Bp of all the fuel samples

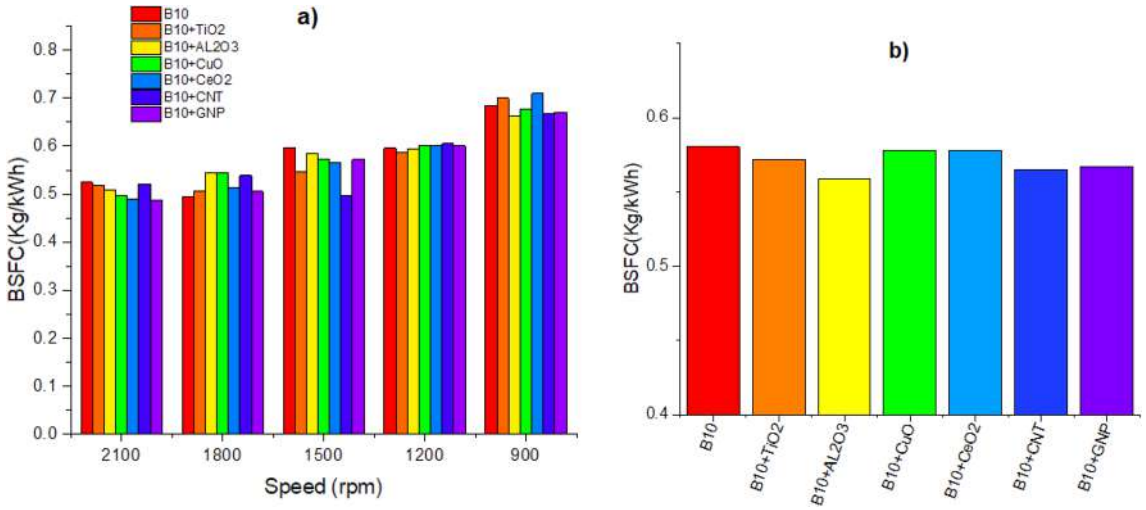

Fig. 4 **a** BSFC evaluated for all the fuel blends at different engine speeds. **b** Mean BSFC of all the fuel samples

Nanoparticles act as an acting catalyst for better and more vigorous combustion causing better heat release and higher cylinder pressure [36]. In addition, nanoparticles in ternary fuel blends act as microfuel droplets, causing an extra explosion in the cylinder. Thus, better and more vigorous fuel combustion results in better BSFC and engine performance [37].

Brake thermal efficiency

BTE was calculated when the engine was running at full load and with the variable engine speed of 2100–900 rpm, as shown in Fig. 5. BTE increases as the engine speed increases due to more work done with a lower fuel intake [38]. The maximum value of BTE in percentage occurs at 2100 rpm when the engine was running in this speed range and the values are 15.28, 15.87, 16.02, 16.38, 17.26, 15.66, and 16.29% for B10, B10 + TiO_2, B10 + Al_2O_3, B10 + CuO, B10 + CeO_2, B10 + CNT, and B10 + GNP, respectively. The average value of brake thermal efficiency of the engine at different engine speeds is 13.98, 14.59, 14.19, 14.21, 14.57, 14.59, and 14.18% for B10, B10 + TiO_2, B10 + Al_2O_3, B10 + CuO, B10 + CeO_2, B10 + CNT, and B10 + GNP, respectively. All the nanoparticle's ternary fuel blend has shown an increase in overall engine efficiency. Some nanoparticles act as an oxidizing agent causing better thermal efficiency, thus increasing engine efficiency due to the extra oxygen provided in it. Mujtaba et al. [14] reported as well that TiO_2 has shown the greatest improvement in engine efficiency compared to the rest of the nano additives. Titanium and cesium

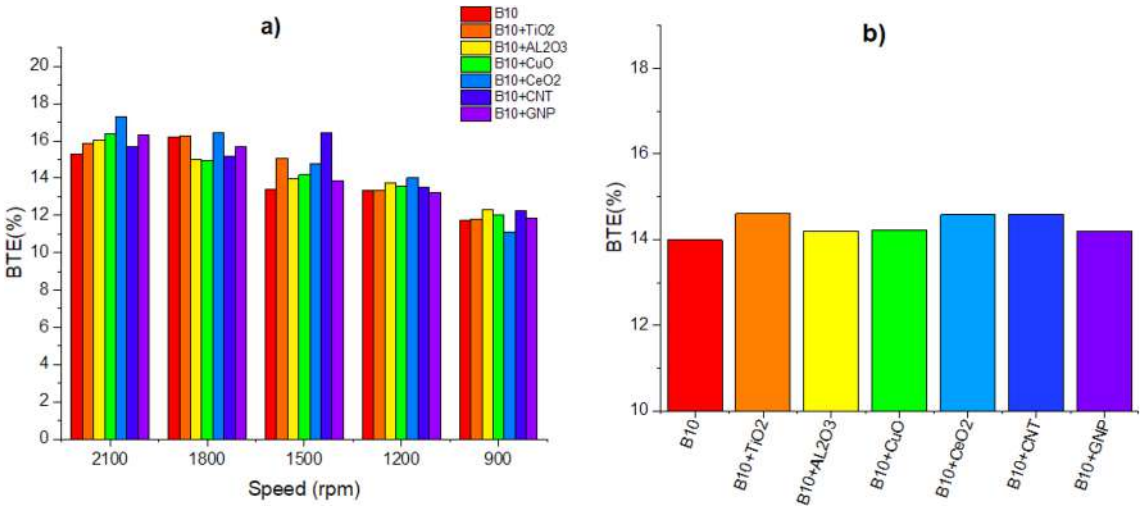

Fig. 5 **a** BTE (%) evaluated for all the fuel blends individually at different engine speeds. **b** Average BTE (%) of all the fuel samples

nanoparticles have a weaker bond, and the outer shell of the electron is bigger, so it can easily lose the oxygen atoms causing better combustion, thus on top of the efficiency count. [39] Engine performance increases because of the combustion of the nanoparticle ternary fuel blends droplet that causes microexplosion inside the cylinder, enhancing the overall combustion. [37]

Emission analysis

Carbon oxides

Carbon monoxide is one of the most harmful gas in the air that causes cancer, tuberculosis, and chest infections [40]. Diesel engines excrete CO gas according to the type of fuel burned in them. The fuel–air mixture ratio in the cylinder before combustion plays a big role in the count of CO emissions [41]. In this experiment, CO emission is counted when the engine was running at full load from 2100 to 900 rpm. The average value for three engine runs is illustrated in the graph. The percentage volume of CO emission increases as the engine speed decreases over time. The highest percentage emission of CO occurs at an engine speed of 900 rpm, and the values are 8.39, 7.504, 6.35667, 7.699, 7.91633, 8.104, and 7.93333 for B10, B10 + TiO_2, B10 + Al_2O_3, B10 + CuO, B10 + CeO_2, B10 + CNT, and B10 + GNP, respectively. The average percentage decrease of CO emissions when compared to B10 are 9.78, 21.84, 17.10, 6.38, 4.26, and 5.61% for B10 + TiO_2, B10 + Al_2O_3, B10 + CuO, B10 + CeO_2, B10 + CNT, and B10 + GNP, respectively. All the oxygenated nanoparticle's ternary fuel bends have shown a great reduction in CO emission due to the extra oxygen atom they carry, causing vigorous and complete combustion of fuel. [25] Al_2O_3 and CuO are the most approachable nanoparticles when the goal is to reduce the CO emission due to their lower reactivity, causing the oxygen atom to be released with a small amount of heat during the reaction [42] (Fig. 6).

CO_2 is the second most abandoned gas emitted from diesel engines after nitrogen [27]. CO_2 is a greenhouse gas affecting the ozone layer, but it has poor health effects compared to CO. CO affects the ozone layer and the health of humans more than CO_2 [43], 44. CO_2 emission was recorded when the engine was running at full load with a variety of speeds from 2100 to 900 rpm. CO_2 emissions reduce gradually as the engine speed decreases from 2100 to 900 with an interval of 300 rpm. Maximum release of CO_2 occurs at an engine speed of 2100 rpm, and the values are 10.56333, 10.99, 10.26, 10.29, 10.5, 10.75667, 10.40667 for B10, B10 + TiO_2, B10 + Al_2O_3, B10 + CuO, B10 + CeO_2, B10 + CNT, and B10 + GNP, respectively. The average value of CO2 released in percent by total volume by each ternary fuel blend is 8.39667, 8.67267, 8.97067, 8.848, 8.392, 8.73867, and 8.364 for B10, B10 + TiO_2, B10 + Al_2O_3, B10 + CuO, B10 + CeO_2, B10 + CNT, and B10 + GNP, respectively. All of the nanoparticles have shown higher release of CO_2 because nanoparticle ternary fuel blends aid complete combustion, thus causing more release of CO_2 compared to B10 (Malaysian commercialized Fuel) [12] (Fig. 7).

Hydrocarbons

HC is released from the diesel engine's exhaust due to the incomplete combustion of the hydrocarbons in the fuel [31]. Lower the emission of HC means better and full combustion is occurring, thus releasing more heat and pressure. HC was recorded when the engine was running at full load

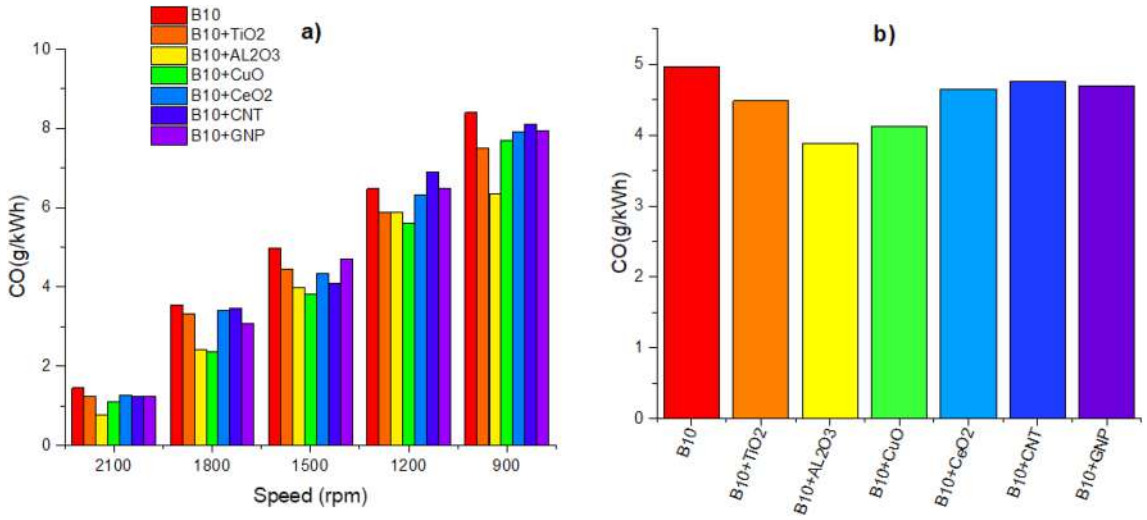

Fig. 6 **a** CO emission recorded from a diesel engine with variable engine speed. **b** Mean emission of CO for all the fuel blends

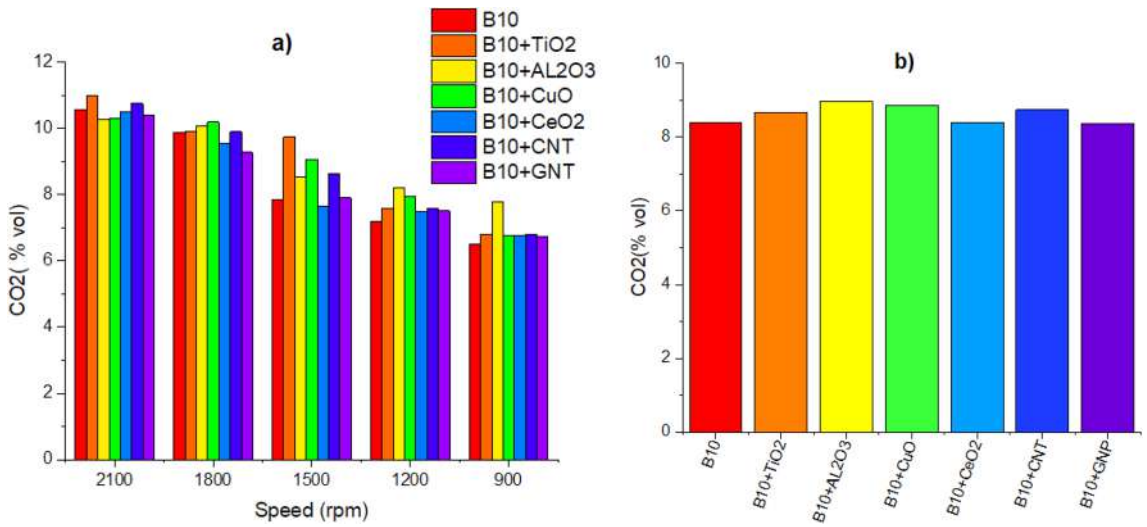

Fig. 7 **a** CO_2 emission recorded from a diesel engine with variable engine speed. **b** Mean emission of CO_2 for all the fuel blends

with a variety of engine speeds (2100–900) rpm. Maximum emission of HC occurs at the engine speed of 900 rpm, and the values are 137.33333, 112, 76.66667, 109.66667, 112.66667, 120.33333, and 122 for B10, B10 + TiO_2, B10 + Al_2O_3, B10 + CuO, B10 + CeO_2, B10 + CNT, and B10 + GNP, respectively. Nanoparticles ternary fuel blends have shown a promising reduction in the emission of HC with average percentages compared to B10 that are 41.12, 86.20, 63.76, 32.38, 29.22, and 27.93% for B10 + TiO_2, B10 + Al_2O_3, B10 + CuO, B10 + CeO_2, B10 + CNT, and B10 + GNP. Ghanbari et al. [45] and Najafi [37] have even reported that HC emission decreases when the nanoparticle's ternary fuel blends are used. The oxidation reaction of unburned HC is initiated due to the high temperature in the cylinder [46, 47] (Fig. 8).

Nitrogen oxides

NOx is one of the most harmful gasses released from engine combustions. NOx is produced mainly by the transport sector and causes health hazards, ozone formation, and acid rain [48]. Most nanoparticle blends increment the NOx in the environment [12, 14, 26, 49, 50]. NOx emission is evaluated at the full engine load with engine speed varying from 2100 to 900 rpm. Figure 9 states the NOx emission of all seven blends, the average value of 0.16564, 0.1867, 0.21964, 0.20824, 0.19944, 0.15566, and 0.16164 g/kWh of NOx released by B10, B10 + TiO_2, B10 + Al_2O_3, B10 + CuO, B10 + CeO_2, B10 + CNT, and B10 + GNP. Throughout the testing, as engine speed decreases, NOx production decreases as well because at lower engine speed

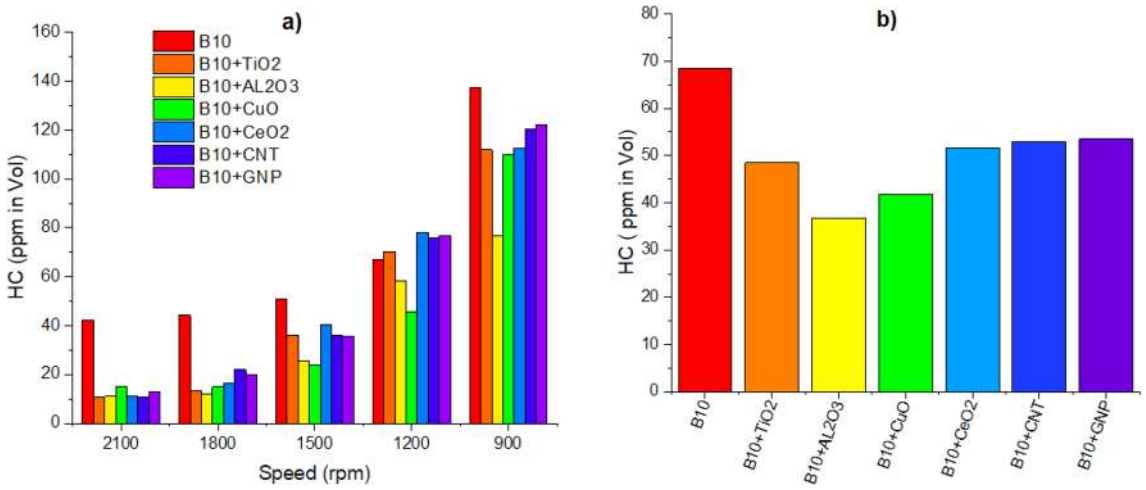

Fig. 8 **a** HC emission recorded from a diesel engine with variable engine speed. **b** Mean emission of HC for all the fuel blends

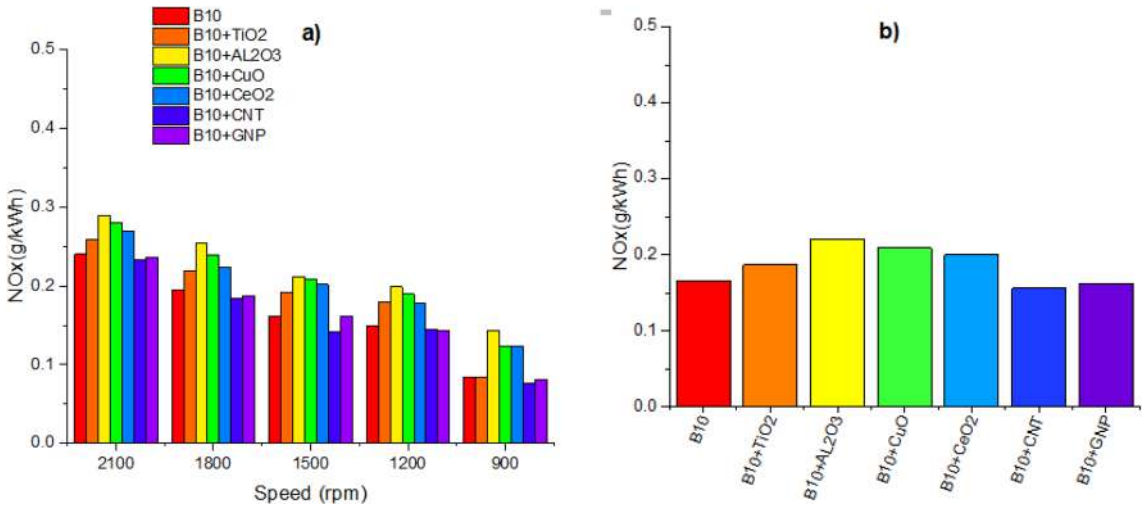

Fig. 9 **a** NOx emission recorded from a diesel engine with variable engine speed. **b** Mean emission of NOx for all the fuel blends

combustion occurs at a lower rate, thus lower heat production. NOx increment depends on the internal cylinder pressure and temperature [51]. Compared to B10, the CNT and GNP blends have decreased the average emission of NOx by 6.03 and 2.06%, while other blends have shown an increase in NOx average emission by 32.7, 26.1, 20.6%, and 13.2% for B10 + Al_2O_3, B10 + CuO, B10 + CeO_2, and B10 + TiO_2, respectively. CNT and GNP have caused a delay in ignition timing and better-premixed combustion, triggering lower emissions of NOx [52]. Gad et al. [50] have also shown lower NOx emissions when CNT is used as a fuel additive. Oxygen-carrying nanoparticles have shown an increment in released NOx; this extra oxygen creates better combustion, thus causing cylindrical temperature and pressure to elevate, which promotes NOx production also explained by Örs et al. [49].

Future recommendation

Metal-based and carbon-based nanoparticles ternary fuel blends have shown different levels of improvements in diesel engine performance and emissions. For example, Al_2O_3 reduces the emission of HC and CO while having poor mechanical performance. On the other hand, CNT and GNP show good mechanical performance while having higher emissions of CO and HC. In future studies, Al_2O_3 + CNT and TiO_2 + CNT could be used for positive gas emissions and better engine performance.

Conclusion

In this research, B10 (Malaysian commercial diesel) was used as base oil. Seven samples were made with different nanoparticles. An additional, ultrasonic technique was utilized for the complete and proper mixing of nanoparticles in B10. The physicochemical properties of samples were measured under the consideration of ASTMD6751 standards. Then, these seven samples were tested in a single-cylinder diesel engine for further comparison. Mechanical and emission performance is concluded below accordingly at variable engine speed (2100–900 rpm) with 100% engine load. There is an increase in BT and BP with all the nanoparticles used when compared to pure B10. CNT and GNP have shown the highest value, followed by TiO_2.All the ternary fuel blends have shown a reduction in BSFC. Al_2O_3 + B10 has a 3.68% reduction compared to B10, followed by CNT and GNP. An increase in BTE could be distinguished with all the ternary fuel blends. The average highest BTE recorded is 14.59% when the B10 + TiO_2 blend is used, followed by CNT and CeO_2. (Al_2O_3, CuO, TiO_2, and CeO_2) from lowest to highest have shown a great reduction in CO emission. Al_2O_3 has an average percentage reduction of 21.84% in CO emission compared to B10. Higher emission of CO_2 means that better combustion is occurring in the engine. B10 emits the lowest CO_2 when compared to other ternary fuel blends. All the ternary fuel blend has shown a reduction in HC emission. Al_2O_3 followed by CuO and TiO_2 has shown the greatest reduction by a percentage of 86.20, 63.76, and 41.12% when compared to B10. All the oxygen-carrying nanoparticles have shown an increment in NO_x emission, while CNT and GNP have reduced it by 6.03 and 2.06%. TiO_2, followed by CNT, has shown the best engine performance. All nanoparticles have reduced CO emissions. CNT and GNP are the only nanoparticles that reduce NO_x. Therefore, for better engine performance, TiO_2 is recommended.

Appendix

Uncertainty of the result when the engine is running at different speeds at full load using B10 (commercial diesel).

Uncertainty for BT(Nm) when using B10										
Engine speed (rpm)	Three test runs			Min–Max value		Accuracy of the system ± 0.2 Nm		Average value	Percentage uncertainty (%)	
	Test 1	Test 2	Test 3	Min	Max	Min − 0.2	Max + 0.2		Min −	Max +
2100	31.18386	31.18386	31.18386	31.18386	31.18386	30.98386	31.38386	31.18386	0.641357	0.641357
1800	32.4041	31.99735	32.26852	31.99735	32.4041	31.79735	32.6041	32.22332	1.252683	1.252683
1500	32.26852	32.13293	32.13293	32.13293	32.26852	31.93293	32.46852	32.17813	0.83163	0.83163
1200	31.99735	31.99735	31.99735	31.99735	31.99735	31.79735	32.19735	31.99735	0.625052	0.625052
900	30.37037	30.50595	30.50595	30.37037	30.50595	30.17037	30.70595	30.46076	0.879787	0.879787
Percentage uncertainty in the value of BT									0.846102%	0.846102%
Other Percentage uncertainties of different values when using B10:										
Percentage uncertainty in the value of BSFC									1.6128%	1.6129%
Percentage uncertainty in the value of BTE									1.8345%	1.8346%
Percentage uncertainty in the value of CO_2 emission									0.71%	0.71%
Percentage uncertainty in the value of CO emission									0.83%	0.83%

Uncertainty for BT(Nm) when using B10										
Engine speed (rpm)	Three test runs			Min–Max value		Accuracy of the system ± 0.2 Nm		Average value	Percentage uncertainty (%)	
	Test 1	Test 2	Test 3	Min	Max	Min − 0.2	Max + 0.2		Min −	Max +
Percentage uncertainty in the value of HC emission									0.83%	0.83%
Percentage uncertainty in the value of NO_x emission									1.14%	1.14%

Supplementary Information The online version contains supplementary material available at https://doi.org/10.1007/s40095-023-00557-1.

Acknowledgements The authors would like to acknowledge the University of Malaya and the Ministry of Higher Education Malaysia through the Fundamental Research Grant Scheme FP142-2019A-(FRGS/1/2019/TK03/UM/01/1). On behalf of all authors, the corresponding author states that this research has no conflict of interest.

References

1. Eia, U.: Annual energy outlook 2015: with projections to 2040. DOE/EIA-0383 (2017)
2. REN21: Renewables 2016: global status report; REN21. In: Secretariat Paris (2016)
3. Nations, U.: The sustainable development goals report 2019 (2019). https://doi.org/10.18356/55eb9109-en
4. Uusitalo, V., Leino, M., Kasurinen, H., Linnanen, L.: Transportation biofuel efficiencies from cultivated feedstock in the boreal climate zone: case Finland. Biomass Bioenerg. **99**, 79–89 (2017). https://doi.org/10.1016/j.biombioe.2017.02.017
5. Kalam, M.A., Masjuki, H.H.: Biodiesel from palmoil—an analysis of its properties and potential. Biomass Bioenerg. **23**(6), 471–479 (2002). https://doi.org/10.1016/S0961-9534(02)00085-5
6. Ong, H.C., Masjuki, H.H., Mahlia, T.M.I., Silitonga, A.S., Chong, W.T., Yusaf, T.: Engine performance and emissions using Jatropha curcas, Ceiba pentandra and Calophyllum inophyllum biodiesel in a CI diesel engine. Energy **69**, 427–445 (2014). https://doi.org/10.1016/j.energy.2014.03.035
7. Silitonga, A.S., Shamsuddin, A.H., Mahlia, T.M.I., Milano, J., Kusumo, F., Siswantoro, J., Dharma, S., Sebayang, A.H., Masjuki, H.H., Ong, H.C.: Biodiesel synthesis from Ceiba pentandra oil by microwave irradiation-assisted transesterification: ELM modeling and optimization. Renew Energy **146**, 1278–1291 (2020). https://doi.org/10.1016/j.renene.2019.07.065
8. Rizwanul Fattah, I.M., Masjuki, H.H., Kalam, M.A., Wakil, M.A., Ashraful, A.M., Shahir, S.A.: Experimental investigation of performance and regulated emissions of a diesel engine with *Calophyllum inophyllum* biodiesel blends accompanied by oxidation inhibitors. Energy Convers. Manage. **83**, 232–240 (2014). https://doi.org/10.1016/j.enconman.2014.03.069
9. Silitonga, A.S., Masjuki, H.H., Mahlia, T.M.I., Ong, H.C., Chong, W.T., Boosroh, M.H.: Overview properties of biodiesel diesel blends from edible and non-edible feedstock. Renew. Sustain. Energy Rev. **22**, 346–360 (2013). https://doi.org/10.1016/j.rser.2013.01.055
10. Yusoff, M.N.A.M., Zulkifli, N.W.M., Sukiman, N.L., Chyuan, O.H., Hassan, M.H., Hasnul, M.H., Zulkifli, M.S.A., Abbas, M.M., Zakaria, M.Z.: Sustainability of Palm biodiesel in transportation: a review on biofuel standard, policy and international collaboration between Malaysia and Colombia. BioEnergy Research **14**(1), 43–60 (2021). https://doi.org/10.1007/s12155-020-10165-0
11. Elisha O, Fauzi A, Anggraini E. Analysis of production and consumption of palm-oil based biofuel using system dynamics model: case of Indonesia. Int. J. Sci. Res. Sci., Eng. Technol. (2019). https://doi.org/10.32628/IJSRSET1962149
12. Yusof, S.N.A., Sidik, N.A.C., Asako, Y., Japar, W.M.A.A., Mohamed, S.B., Muhammad, N.M.A.: A comprehensive review of the influences of nanoparticles as a fuel additive in an internal combustion engine (ICE). Nanotechnol. Rev. **9**(1), 1326–1349 (2020). https://doi.org/10.1515/ntrev-2020-0104
13. Basha, D.J.S.: An experimental analysis of a diesel engine using alumina nanoparticles blended diesel fuel. In: SAE World Congress 2014, SAE Technical Paper 2014-01-1391 (2014). https://doi.org/10.4271/2014-01-1391
14. Mujtaba, M.A., Kalam, M.A., Masjuki, H.H., Gul, M., Soudagar, M.E.M., Ong, H.C., Ahmed, W., Atabani, A.E., Razzaq, L., Yusoff, M.: Comparative study of nanoparticles and alcoholic fuel additives-biodiesel-diesel blend for performance and emission improvements. Fuel **279**, 118434 (2020). https://doi.org/10.1016/j.fuel.2020.118434
15. Khan, H., Soudagar, M.E., Kumar, R., Safaei, M.R., Farooq, M., Khidmatgar, A., Banapurmath, N., Farade, R., Abbas, M., Afzal, A., et al.: Effect of nano-graphene oxide and n-butanol fuel additives blended with diesel-nigella sativa biodiesel fuel emulsion on diesel engine characteristics. Symmetry **12**, 961 (2020). https://doi.org/10.3390/sym12060961
16. Sathiyamoorthi, R., Sankaranarayanan, G., Pitchandi, K.: Combined effect of nanoemulsion and EGR on combustion and emission characteristics of neat lemongrass oil (LGO)-DEE-diesel blend fuelled diesel engine. Appl. Therm. Eng. **112**, 1421–1432 (2017). https://doi.org/10.1016/j.applthermaleng.2016.10.179
17. Sajith, V., Sobhan, C.B., Peterson, G.P.: Experimental Investigations on the Effects of Cerium Oxide Nanoparticle Fuel Additives on Biodiesel. Adv. Mech. Eng. **2**, 581407 (2010). https://doi.org/10.1155/2010/581407
18. Janakiraman, S., Lakshmanan, T., Chandran, V., Subramani, L.: Comparative behavior of various nano additives in a DIESEL engine powered by novel Garcinia gummi-gutta biodiesel. J. Clean. Product. **245**, 118940 (2020). https://doi.org/10.1016/j.jclepro.2019.118940
19. Sathiamurthi, P., Vinith, K.S.K., Sivakumar, A.: Performance and emission test in CI engine using magnetic fuel conditioning with nano additives. In: 2019; of Conference: (Year). https://doi.org/10.35940/ijrte.C6213.098319
20. Gumus, S., Özcan, H., Ozbey, M., Topaloglu, B.: Aluminum oxide and copper oxide nanodiesel fuel properties and usage in a compression ignition engine. Fuel **163**, 80–87 (2016). https://doi.org/10.1016/j.fuel.2015.09.048
21. Chen, A.F., Akmal Adzmi, M., Adam, A., Othman, M.F., Kamaruzzaman, M.K., Mrwan, A.G.: Combustion characteristics, engine performances and emissions of a diesel engine using nanoparticle-diesel fuel blends with aluminium oxide, carbon nanotubes and silicon oxide. Energy Convers. Manage. **171**, 461–477 (2018). https://doi.org/10.1016/j.enconman.2018.06.004
22. Kumar, A.R.M., Kannan, M., Nataraj, G.: A study on performance, emission and combustion characteristics of diesel engine powered by nano-emulsion of waste orange peel oil biodiesel. Renew. Energy **146**, 1781–1795 (2020). https://doi.org/10.1016/j.renene.2019.06.168
23. Sandeep, K., Rajashekhar, C.R., Karthik, S.R.: Experimental studies on effect of nano particle blended biodiesel combustion on performance and emission of CI engine. IOP Confer. Ser.: Mater. Sci. Eng. **376**, 012019 (2018). https://doi.org/10.1088/1757-899x/376/1/012019
24. Power, A.C., Gorey, B., Chandra, S., Chapman, J.: Carbon nanomaterials and their application to electrochemical sensors: a review. Nanotechnol. Rev. **7**(1), 19–41 (2018). https://doi.org/10.1515/ntrev-2017-0160
25. Baskar, P., Senthilkumar, A.: Effects of oxygen enriched combustion on pollution and performance characteristics of a diesel engine. Eng. Sci. Technol., Int. J. **19**(1), 438–443 (2016). https://doi.org/10.1016/j.jestch.2015.08.011
26. Najafi, G.: Diesel engine combustion characteristics using nanoparticles in biodiesel-diesel blends. Fuel **212**, 668–678 (2017). https://doi.org/10.1016/j.fuel.2017.10.001

27. Speight, J.G.: Chapter 10—combustion of hydrocarbons. In: Speight, J.G. (ed.) Handbook of Industrial Hydrocarbon Processes, 2nd edn., pp. 421–463. Gulf Professional Publishing, Boston (2020). https://doi.org/10.1016/B978-0-12-809923-0.00010-2
28. Fattah, I.M.R., Ong, H.C., Mahlia, T.M.I., Mofijur, M., Silitonga, A.S., Rahman, S.M.A., Ahmad, A.: State of the art of catalysts for biodiesel production. Front. Energy Res. **8**, 101 (2020). https://doi.org/10.3389/fenrg.2020.00101
29. Buksagarmath, P., Rajashekar, C.R.: Studies on effect of various surfactants on stable dispersion of graphene nano particles in simarouba biodiesel. IOP Confer. Ser.: Mater. Sci. Eng. **149**, 012083 (2016). https://doi.org/10.1088/1757-899X/149/1/012083
30. Thanu, D.P.R., Zhao, M., Han, Z., Keswani, M.: Chapter 1—fundamentals and applications of sonic technology. In: Kohli, R., Mittal, K.L. (eds.) Developments in Surface Contamination and Cleaning: Applications of Cleaning Techniques, pp. 1–48. Elsevier (2019). https://doi.org/10.1016/B978-0-12-815577-6.00001-3
31. Proctor, C.L.: Internal combustion engines. In: Meyers, R.A. (ed.) Encyclopedia of Physical Science and Technology, 3rd edn., pp. 33–44. Academic Press, New York (2003). https://doi.org/10.1016/B0-12-227410-5/00350-1
32. Chang, S.-L., Zhou, C.Q.: Combustion and thermochemistry. In: Cleveland, C.J. (ed.) Encyclopedia of Energy, pp. 595–603. Elsevier, New York (2004). https://doi.org/10.1016/B0-12-176480-X/00087-5
33. Hosseini, S.H., Taghizadeh-Alisaraei, A., Ghobadian, B., Abbaszadeh-Mayvan, A.: Effect of added alumina as nano-catalyst to diesel-biodiesel blends on performance and emission characteristics of CI engine. Energy **124**, 543–552 (2017). https://doi.org/10.1016/j.energy.2017.02.109
34. Khalife, E., Tabatabaei, M., Demirbas, A., Aghbashlo, M.: Impacts of additives on performance and emission characteristics of diesel engines during steady state operation. Prog. Energy Combust. Sci. **59**, 32–78 (2017). https://doi.org/10.1016/j.pecs.2016.10.001
35. Murcak, A., Haşimoğlu, C., Çevik, İ, Karabektaş, M., Ergen, G.: Effects of ethanol–diesel blends to performance of a DI diesel engine for different injection timings. Fuel **109**, 582–587 (2013). https://doi.org/10.1016/j.fuel.2013.03.014
36. Saxena, V., Kumar, N., Saxena, V.K.: A comprehensive review on combustion and stability aspects of metal nanoparticles and its additive effect on diesel and biodiesel fuelled C.I. engine. Renew. Sustain. Energy Rev. **70**, 563–588 (2017). https://doi.org/10.1016/j.rser.2016.11.067
37. Najafi, G.: Diesel engine combustion characteristics using nanoparticles in biodiesel-diesel blends. Fuel **212**, 668–678 (2018). https://doi.org/10.1016/j.fuel.2017.10.001
38. Le Anh, T., Reksowardojo, I.K., Wattanavichien, K.: 23—utilization of biofuels in diesel engines. In: Luque, R., Lin, C.S.K., Wilson, K., Clark, J. (eds.) Handbook of Biofuels Production, 2nd edn., pp. 699–733. Woodhead Publishing (2016). https://doi.org/10.1016/B978-0-08-100455-5.00023-0
39. Manchon, A., Belabbes, A.: Chapter One—spin-orbitronics at transition metal interfaces. In: Camley, R.E., Stamps, R.L. (eds.) Solid State Physics, vol. 68, pp. 1–89. Academic Press (2017). https://doi.org/10.1016/bs.ssp.2017.07.001
40. Stork, C., Anguish, D.: Carbon monoxide. In: Wexler, P. (ed.) Encyclopedia of Toxicology, 2nd edn., pp. 423–425. Elsevier (2005). https://doi.org/10.1016/B0-12-369400-0/00184-8
41. Habibullah, M., Masjuki, H.H., Kalam, M.A., Rizwanul Fattah, I.M., Ashraful, A.M., Mobarak, H.M.: Biodiesel production and performance evaluation of coconut, palm and their combined blend with diesel in a single-cylinder diesel engine. Energy Convers. Manage. **87**, 250–257 (2014). https://doi.org/10.1016/j.enconman.2014.07.006
42. Sankaralingam, M., Lee, Y.-M., Nam, W., Fukuzumi, S.: Amphoteric reactivity of metal–oxygen complexes in oxidation reactions. Coord. Chem. Rev. **365**, 41–59 (2018). https://doi.org/10.1016/j.ccr.2018.03.003
43. Sher, E.: Chapter 2—environmental aspects of air pollution. In: Sher, E. (ed.) Handbook of Air Pollution From Internal Combustion Engines, pp. 27–41. Academic Press, San Diego (1998). https://doi.org/10.1016/B978-012639855-7/50041-7
44. Jacobs, D.E.: Housing-related health hazards: assessment and remediation. In: Nriagu, J.O. (ed.) Encyclopedia of Environmental Health, pp. 76–94. Elsevier, Burlington (2011). https://doi.org/10.1016/B978-0-444-52272-6.00351-2
45. Ghanbari, M., Najafi, G., Ghobadian, B., Yusaf, T., Carlucci, A.P., Kiani Deh Kiani, M.: Performance and emission characteristics of a CI engine using nano particles additives in biodiesel-diesel blends and modeling with GP approach. Fuel **202**, 699–716 (2017). https://doi.org/10.1016/j.fuel.2017.04.117
46. Fattah, I.M.R., Masjuki, H.H., Kalam, M.A., Wakil, M.A., Ashraful, A.M., Shahir, S.A.: Experimental investigation of performance and regulated emissions of a diesel engine with Calophyllum inophyllum biodiesel blends accompanied by oxidation inhibitors. Energy Convers. Manage. **83**, 232–240 (2014). https://doi.org/10.1016/j.enconman.2014.03.069
47. Fattah, I.M.R., Masjuki, H.H., Kalam, M.A., Mofijur, M., Abedin, M.J.: Effect of antioxidant on the performance and emission characteristics of a diesel engine fueled with palm biodiesel blends. Energy Convers. Manage. **79**, 265–272 (2014). https://doi.org/10.1016/j.enconman.2013.12.024
48. Thurston, G.D.: Outdoor Air Pollution: Sources, Atmospheric Transport, and Human Health Effects. In: Quah, S.R. (ed.) International Encyclopedia of Public Health, 2nd edn., pp. 367–377. Academic Press, Oxford (2017). https://doi.org/10.1016/B978-0-12-803678-5.00320-9
49. Örs, I., Sarıkoç, S., Atabani, A.E., Ünalan, S., Akansu, S.O.: The effects on performance, combustion and emission characteristics of DICI engine fuelled with TiO2 nanoparticles addition in diesel/biodiesel/n-butanol blends. Fuel **234**, 177–188 (2018). https://doi.org/10.1016/j.fuel.2018.07.024
50. Gad, M.S., Jayaraj, S.: A comparative study on the effect of nano-additives on the performance and emissions of a diesel engine run on Jatropha biodiesel. Fuel **267**, 117168 (2020). https://doi.org/10.1016/j.fuel.2020.117168
51. Semakula, M., Inambao, P.F.: The formation, effects and control of oxides of nitrogen in diesel engines. In: 2018; of Conference: (Year). Corpus ID: 236566453
52. Mei, D., Zuo, L., Adu-Mensah, D., Li, X., Yuan, Y.: Combustion characteristics and emissions of a common rail diesel engine using nanoparticle-diesel blends with carbon nanotube and molybdenum trioxide. Appl. Therm. Eng. **162**, 114238 (2019). https://doi.org/10.1016/j.applthermaleng.2019.114238

International Journal of Energy and Environmental Engineering (2023) 14:961–971
https://doi.org/10.1007/s40095-023-00559-z

ORIGINAL RESEARCH

Maximum power point tracking of a standalone photovoltaic system using electromagnetic field optimization algorithm

Abeer Imdoukh[1] · **Mohamed Zribi**[2]

Received: 12 August 2022 / Accepted: 31 January 2023 / Published online: 1 March 2023

Abstract

There are non-stop efforts being put into enhancing the performance of the available maximum power point tracking methods and proposing new tracking methods. In this paper, a novel maximum power point tracking method based on a physics-inspired metaheuristic algorithm called Electromagnetic Field Optimization algorithm is proposed. The methodology of applying the Electromagnetic Field Optimization method on the maximum power point tracking problem is explained. The proposed method is applied to control the duty cycle of a DC–DC converter in a standalone photovoltaic system. The performance of the proposed method is evaluated against the Cuckoo Search Algorithm method, the Particle Swarm Optimization method, the Perturb and Observe method, and the Incremental Conductance method. A simulation test using MATLAB/Simulink software was conducted for varied sun irradiance levels under fixed temperature and load conditions. An experimental test was also conducted under fixed load and fixed weather conditions. The proposed method achieved tracking efficiencies of 100% and 80.14% in the simulation and experimental tests, accordingly. The superiority of the proposed method over the other applied metaheuristic-based methods is highlighted as the proposed method achieved short tracking times, no steady-state oscillations, and no duty cycle oscillations in both tests. The easiness of tuning the proposed method's parameters is also an advantage of it.

Keywords Photovoltaic system · MPPT · SEPIC · EFO · P&O · CSA

List of Symbols

CO_2	Carbon dioxide
R_i	Input resistance of the DC–DC converter (Ω)
R_{opt}	Optimal internal resistance of PV module (Ω)
D	Duty cycle
D_i	Duty cycle at index i
K	Random index from the neutral field
P	Random index from the positive field
N	Random index from the negative field
D_K, D_P, and D_N	Duty cycles at K, P, and N
L_1, L_2	Inductors of the DC–DC converter (H)
S	MOSFET of the DC–DC converter
D	Diode of the DC–DC converter
C_1	Series capacitor of the DC–DC converter (F)
C_2	Output capacitor of the DC–DC converter (F)
C_{in}	Input capacitor of the DC–DC converter (F)

List of Parameters

N_emp	Number of electromagnetic particles
P_field	A portion of the population assigned to the positive field (ranges between 0.05 and 0.1)
N_field	A portion of the population assigned to the negative field (ranges between 0.4 and 0.5)
Ps_rate	Probability of selecting an electromagnetic particle from the positive field (ranges between 0.1 and 0.4)
R_rate	Probability of changing one electromagnet with a randomly generated electromagnet
r	A random number between [0, 1]

✉ Abeer Imdoukh
aimdoukh@auk.edu.kw

[1] College of Engineering and Applied Sciences, American University of Kuwait, Salmiya, Kuwait

[2] Department of Electrical Engineering, College of Engineering and Petroleum, Kuwait University, Al-Shadadiya, Kuwait

K	Lévy multiplying coefficient
P_a	Probability of discovering and replacing the worst nest by a new nest
w	Inertia weight
c_1, c_2	Acceleration coefficients

List of Abbreviations

PV	Photovoltaic
MPPT	Maximum power point tracking
MPP	Maximum power point
EFO	Electromagnetic field optimization
CSA	Cuckoo search algorithm
PSO	Particle swarm optimization
P&O	Perturb and observe
INC	Incremental conductance
SEPIC	Single ended primary inductor converter
T.E.	Tracking efficiency (%)
T.T.	Tracking time (s)
S.S.O.	Steady-state oscillations
Ave.	Average

List of Constants

φ	The golden ratio (1.618)

Introduction

The escalation of environmental problems and the limitation of natural resources impose the need to take serious steps toward the usage of renewable energies. Many countries all over the world have already started to not only depend on limited natural energy sources (coal, gas, and oil) but also on renewable sources to satisfy their energy demands. According to the International Energy Agency (IEA), the highest increase in CO_2 emissions in 2021 was from the electricity and heat production sectors [1]. CO_2 emissions in 2021 rose above the pre-pandemic level of 2019 [1]. The use of fossil fuels increased as well to meet the electricity demand growth [1]. Although there was an increase in coal use in 2021, renewable energy sources and nuclear power provided a higher share of global electricity generation than coal [1]. In 2020, twenty countries added at least 1 GW of new solar photovoltaics (PV) to become a competitive option for electricity generation since it is a clean, safe, and accessible energy source [2]. Nevertheless, maximum power point tracking (MPPT) is still a concern to extract the maximum available power by a PV module.

The main idea of MPPT relies on the fact that a PV module needs to operate at one unique point in the power-voltage curve of the PV module to transfer the maximum possible power from a PV module to a load. This point is called the maximum power point (MPP). However, the MPP changes when the weather conditions (sun irradiance and surrounding temperature) change. In addition, since the load itself may not be fixed, connecting the load directly to the PV module usually results in operating at a point that is not the MPP. This leads to not extracting the maximum available power. Accordingly, a tracking system should be used to track the MPP and force the PV module to operate at it regardless of the weather conditions and the load values.

Maximum power point tracking is achieved by connecting a DC–DC converter between the PV module and the load. The DC–DC converter matches the input resistance of the DC–DC converter (R_i) to the optimal internal resistance of the PV module (R_{opt}). Resistance matching is accomplished by varying the duty cycle (D) of the control pulse of the transistor switch of the DC–DC converter. Finding the optimal duty cycle can be achieved by using several tracking methods. Figure 1 depicts a block diagram of a standalone PV system.

In this paper, a novel tracking method based on a physics-inspired metaheuristic algorithm called Electromagnetic Field Optimization (EFO) algorithm is proposed. The proposed method was not applied before in the literature to address the MPPT problem. Since tracking efficiency, tracking time, and steady-state oscillations are the main aspects concerned with the performance of a tracking method, the proposed method is developed to find an MPP with high tracking efficiency, short tracking time, and no steady-state oscillations. All of that with the simplicity of tuning the method's parameters on a trial-and-error basis. The performance of the proposed method is assessed against the performances of four well-studied MPPT methods in the literature, namely: the Cuckoo Search Algorithm (CSA) method, the Particle Swarm Optimization (PSO) method, the Perturb and Observe (P&O) method, and the Incremental Conductance (INC) method. A brief overview of some tracking methods is presented next.

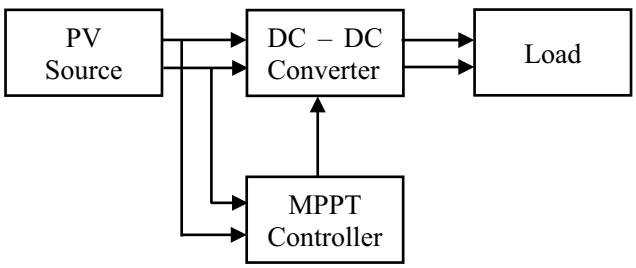

Fig. 1 A block diagram of a standalone PV system connected to a load

Maximum power point tracking methods

MPPT is a well-known and well-studied topic and there are several MPPT tracking methods proposed in the literature. The reader can refer to Refs. [3–13] for a good review of MPPT methods. Nevertheless, some of the tracking methods can be classified as metaheuristic-based control methods, direct control methods, and indirect control methods.

Metaheuristic-based control methods are based on stochastic search algorithms that attempt to find the solutions of optimization problems by randomly exploring the search spaces with the use of intelligent heuristics to guide the search [14]. The search process is directed by certain strategies adopted from nature, biology, or the laws of physics [14]. Several metaheuristic algorithms were applied to solve the MPPT problem. For example, the Cuckoo Search Algorithm (CSA), the Particle Swarm Optimization (PSO) algorithm, the Fruit Fly Optimization Algorithm (FFOA), the Dragonfly Optimization (DFO) algorithm, the Artificial Bee Colony (ABC) algorithm, the Grey Wolf Optimization (GWO), the Genetic Algorithm (GA), and the Bat Algorithm (BA) are some of the algorithms that were applied to solve the MPPT problem [9, 10].

On the other hand, direct MPPT methods are based on simple searching algorithms that find an MPP by using control strategies based on modulation [11, 13]. They are commonly applied MPPT methods due to their simplicity and ease of implementation. The Perturb and Observe (P&O) method, the Incremental Conductance (INC) method, the Parasitic Capacitance (CP) method, the Photovoltaic Array Combination (PAC) method, the Power Feedback (PF) method, and the Actual Measurement (AM) method are some of the direct control methods that were applied to MPPT problem [8, 11]. The methodology of applying the proposed metaheuristic-based EFO method on the MPPT problem is discussed next.

The methodology of applying and evaluating the EFO method

The EFO algorithm is a physics-inspired metaheuristic algorithm that was proposed by Abedinpourshotorban in 2016. The algorithm is inspired by two phenomena: attraction repulsion forces among electromagnets with different polarities, and the golden ratio which is a nature-inspired ratio. The EFO algorithm is a population-based algorithm in which the population consists of electromagnetic particles which are made of electromagnets [15].

Applying the EFO algorithm to the MPPT problem requires having the electromagnetic particles consisting of one electromagnet which represents the duty cycle. Therefore, a total number of N_emp electromagnetic particles representing duty cycles need to be defined first as D_i (where $i = 1, 2, \ldots, N\_\text{emp}$).

The generated duty cycles are then applied to the converter connected to the PV module, and the fitness of each duty cycle is evaluated. The fitness is evaluated by finding the resulting PV power which is calculated by multiplying the sensed PV voltage by the sensed PV current.

The electromagnetic particles are then sorted according to their fitness, and they are divided into three fields based on two parameters. One parameter is the P_field which determines a portion of the population assigned to the positive field (highest fitness) and it ranges between 0.05 and 0.1 [15]. Another parameter is the N_field which determines a portion of the population assigned to the negative field (lowest fitness) and it ranges between 0.4 and 0.5 [15]. The remaining electromagnetic particles are assigned to the neutral field.

Next, three electromagnetic particles are randomly selected from the three fields to generate a new electromagnetic particle by using the algorithm's equation (Eq. 1).

$$D_{\text{new}} = D_K + \left\{\varphi * r * \left(D_P - D_K\right)\right\} - \left\{r * \left(D_N - D_K\right)\right\} \tag{1}$$

where K is a random index from the neutral field, P is a random index from the positive field, and N is a random index from the negative field; D_K, D_P, and D_N are the duty cycles at K, P, and N, respectively. φ is the golden ratio, and r is a random number between [0, 1].

After generating a new electromagnetic particle, the particle is evaluated. If the new electromagnetic particle is fitter than the worst electromagnetic particle in the population, then the worst particle is eliminated, and the new particle is inserted in the sorted population according to its fitness and it obtains a polarity based on its position.

Another way of generating a new electromagnetic particle to diversify the population is by randomly choosing an electromagnetic particle from the positive field if a random number between [0, 1] is less than Ps_rate. Ps_rate is the probability of selecting an electromagnetic particle from the positive field and this probability ranges between 0.1 and 0.4 [15].

To diversify the population more, the algorithm has a parameter, R_rate, which represents the probability of changing one electromagnet of the generated electromagnetic particle with a randomly generated electromagnet [15]. However, the R_rate parameter is not used in the MPPT problem as the electromagnetic particles consist of only one electromagnet (D). The process of generating new electromagnetic particles and evaluating them continues until the

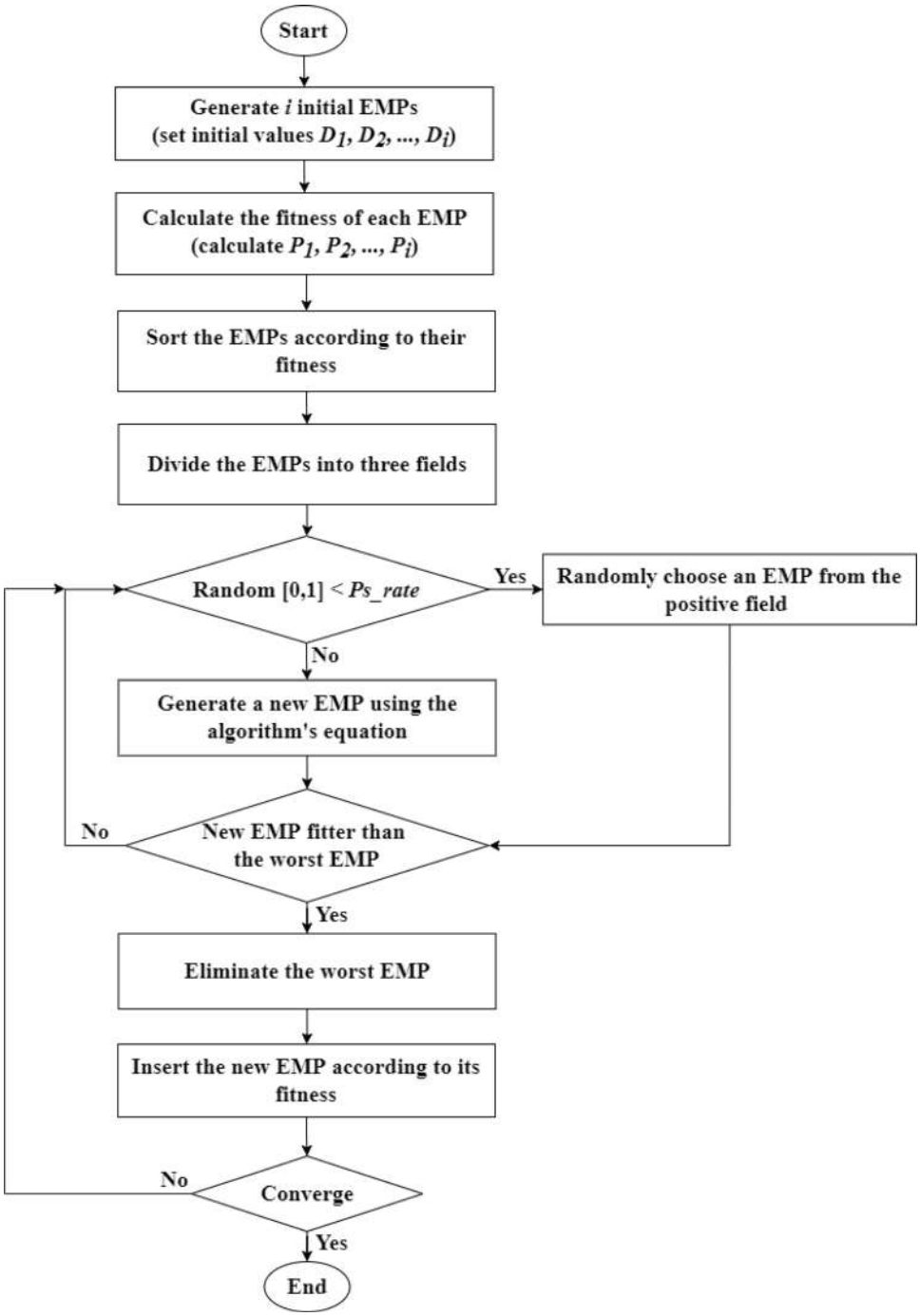

Fig. 2 The flowchart of the EFO MPPT method

MPP is identified. Figure 2 depicts the flowchart of EFO MPPT method.

The performance of the proposed MPPT method is evaluated based on several criteria. The first criterion is the tracking efficiency (T.E.). The tracking efficiency is the ability of the applied method to track the MPP. The tracking efficiency is the ratio between the tracked maximum power and the theoretical maximum power under certain weather conditions.

The second evaluation criterion is the tracking time (T.T.). The tracking time is the time required to reach the MPP under different weather conditions. The less time required to reach to the MPP, the better the MPPT method is.

The third evaluation criterion is the steady-state oscillations (S.S.O.). Oscillations in steady-state result in power losses. Therefore, the less oscillations around the MPP, the better the MPPT method is.

The last evaluation criterion is complexity. The complexity of an MPPT method can be determined by the number

Table 1 Selected parameters for each MPPT method

MPPT method	Selected parameters
EFO	$Ps\_rate = 0.1$ $P\_field = 0.1$ $N\_field = 0.45$
CSA	$K = 1.5$ $P_a = 0.25$
PSO	$w = 0.01$ $c_1 = 0.1$ $c_2 = 2$
P&O	Perturbation step size = 0.005
INC	Perturbation step size = 0.0025

of tuning parameters of the method. In addition, how easily a good combination of the tuning parameters can be found on a trial-and-error basis to find an MPP with highest T.E., shortest T.T., and least S.S.O.

The performance of the proposed EFO MPPT method is assessed against other four well-known MPPT methods (CSA, PSO, P&O, and INC). The selection of the parameters for the five methods is completed on a trial-and-error basis to achieve a good compromise between the tracking efficiency and the tracking time. The number of the population is selected to be 5 for the metaheuristic methods. Table 1 summarizes the selected parameters for each MPPT method.

Simulation results and discussion of the varied sun irradiance test

The aim of the test is to evaluate the performance of the proposed EFO method in tracking MPPs under changing irradiance levels and fixed temperature and load conditions. The performance of the EFO method is compared to the performances of the CSA method, the PSO method, the P&O method, and the INC method under the same testing conditions.

The simulation test is carried out in MATLAB/Simulink software. The five MPPT methods use the PV module voltage and current to generate the optimal voltage. The optimal voltage is compared to a high frequency sawtooth signal (50 kHz) to generate a PWM signal for the MOSFET of a SEPIC DC–DC converter. The simulated standalone PV system is depicted in Fig. 3.

The test starts with a 300 W/m^2 sun irradiance level value. After 0.75 s, a step change is done, and the value of the sun irradiance level becomes 400 W/m^2. This value is kept for another 0.75 s. The last step change in the sun irradiance level is made to obtain a value of 500 W/m^2. The temperature value throughout the test is fixed at 25 °C and the load is fixed at 100 Ω. The studied sun irradiance levels did not exceed 500 W/m^2 and low power ratings approach is adopted since the hardware PV system is implemented in a laboratory setup. Table 2 summarizes the numerical results of the test, and Figs. 4, 5, 6 and 7 depict the graphical results of the test.

The testing results confirm the ability of all the applied MPPT methods in tracking the MPPs under the three irradiance levels. However, the direct MPPT methods (the P&O and the INC methods) achieve the lowest tracking efficiency as compared to the tracking efficiency of the metaheuristic methods (the CSA, the PSO, and the EFO methods). This confirms the disadvantage of the direct MPPT methods discussed in [16–18]; as the PV module would be operating around the MPP but not exactly on it which leads to power losses. The metaheuristic methods achieve 100% tracking efficiencies for all the irradiance levels. This confirms the

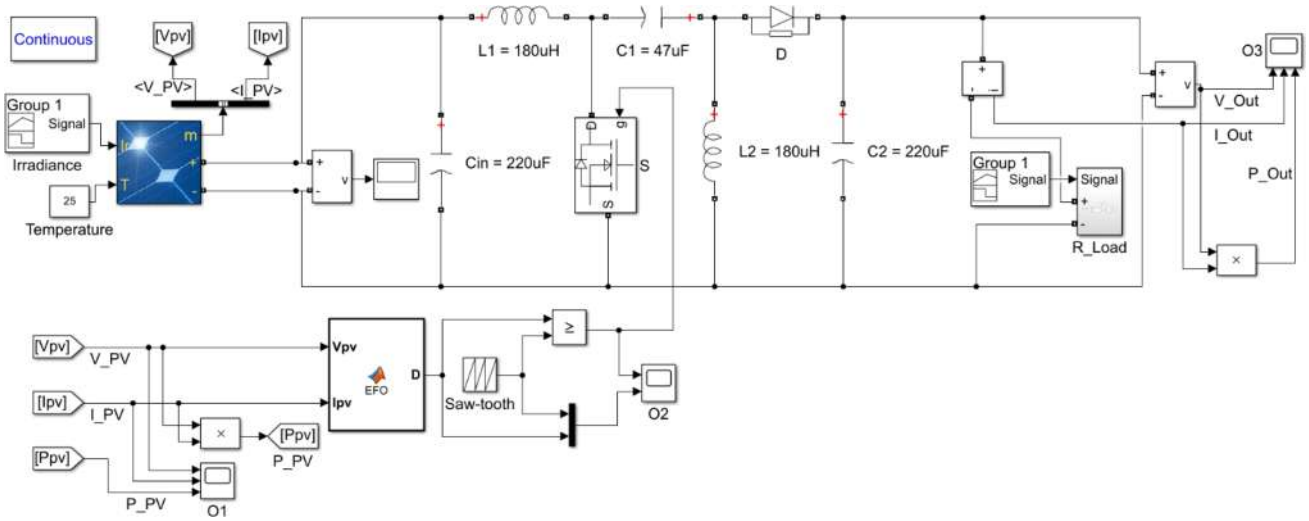

Fig. 3 The simulated standalone PV system in MATLAB/Simulink

Table 2 Simulation results of varied sun irradiance under fixed load and fixed temperature conditions test

MPPT method	EFO	CSA	PSO	P&O	INC
300 W/m^2 sun irradiance level					
PV power (W)	5.75	5.75	5.75	Ave. 5.73	5.75
T.E. (%)	100	100	100	99.67	99.98
T.T. (s)	0.22	0.48	0.49	0.05	0.08
400 W/m^2 sun irradiance level					
PV power (W)	7.75	7.75	7.75	Ave. 7.72	7.75
T.E. (%)	100	100	100	99.64	100
T.T. (s)	0.14	0.20	0.22	0.03	0.04
500 W/m^2 sun irradiance level					
PV power (W)	9.77	9.77	9.77	Ave. 9.74	9.75
T.E. (%)	100	100	100	99.75	99.88
T.T. (s)	0.13	0.23	0.26	0.02	0.05

high tracking efficiency advantage of the metaheuristic methods discussed in [19–21].

The tracking times of the direct MPPT methods are less when compared to the tracking times of the metaheuristic methods. This confirms the fast convergence to the MPP advantage of the direct MPPT methods due to perturbation step size selection as discussed in [16–18]. On the other hand, among the metaheuristic methods, the EFO method achieves the shortest tracking time which demonstrates the superiority of the EFO method over the other metaheuristic methods. It is also worth noting that the tracking times for all the methods decreased after the first step change in the sun irradiance level when compared to the initial tracking times.

The duty cycle of the P&O method suffers from large oscillations compared to the duty cycle of the INC method. This confirms the disadvantage of the P&O method as discussed in [16, 17]. The duty cycles of the metaheuristic methods (the CSA, the PSO, and the EFO methods) are constant at steady-state. This confirms the advantage of not having S.S.O. for the metaheuristic methods discussed in [19–21].

The transient behaviors of the direct MPPT methods (the P&O and the INC methods) are less random during searching for the MPPs compared to the transient behaviors of the metaheuristic methods. The transient behavior of the EFO method demonstrates the least randomness compared to the transient behaviors of the other metaheuristic methods discussed in [19–21]. It is worth mentioning that for all the five MPPT methods, the transient behaviors while searching for the MPPs are less random after the first step change because the first MPP is kept as a reference. The fact that the transient behaviors are less random after the first step change results in shorter tracking times.

The simulation results show that the transfer of power from the PV module to the load is efficient as the efficiency of the designed system ranges between 86% and 88% for the five MPPT methods under varied load values (50–150 Ω) as

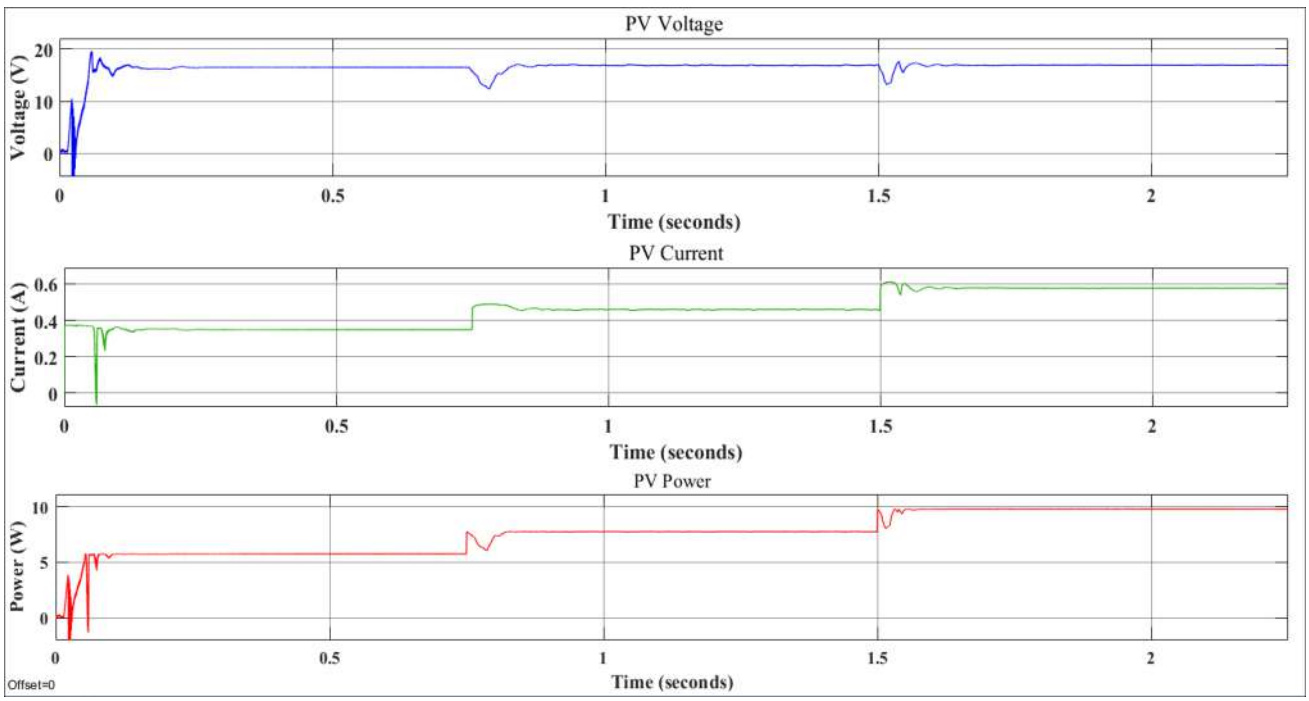

Fig. 4 The voltage, the current, and the power of the PV module versus time when using the EFO method

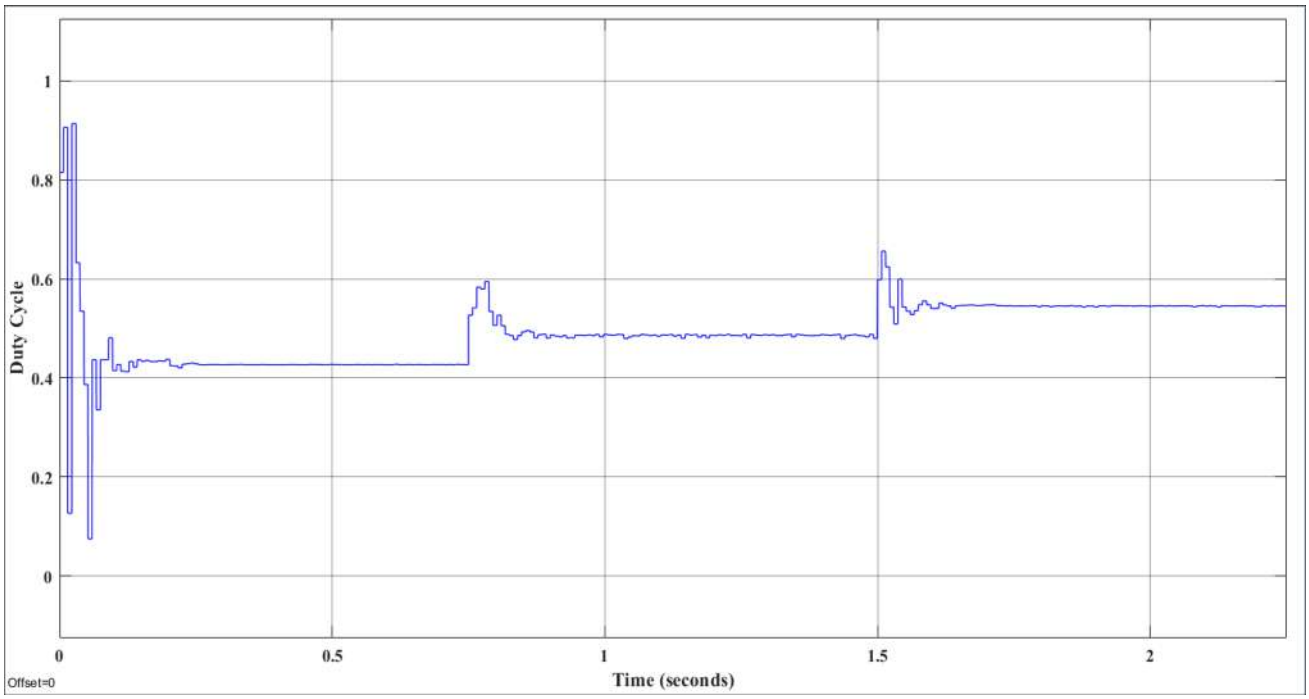

Fig. 5 The duty cycle versus time when using the EFO method

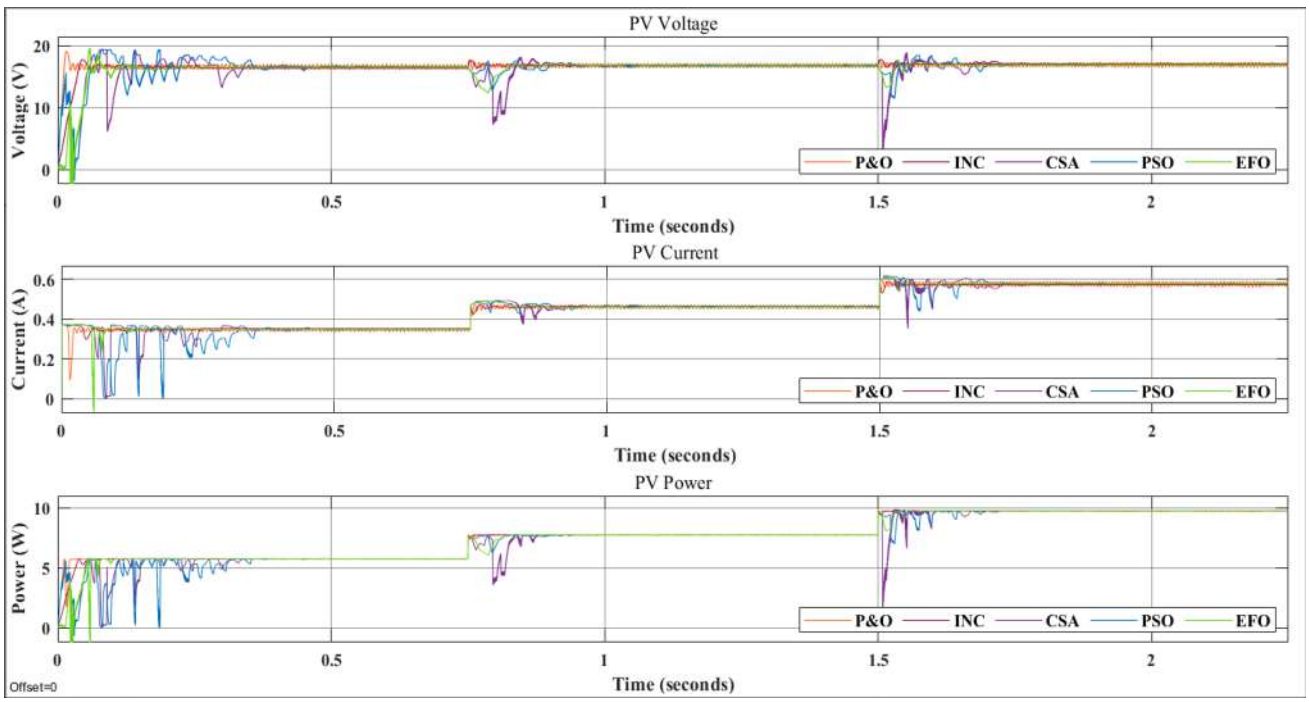

Fig. 6 The voltage, the current, and the power of the PV module versus time when using the five MPPT methods

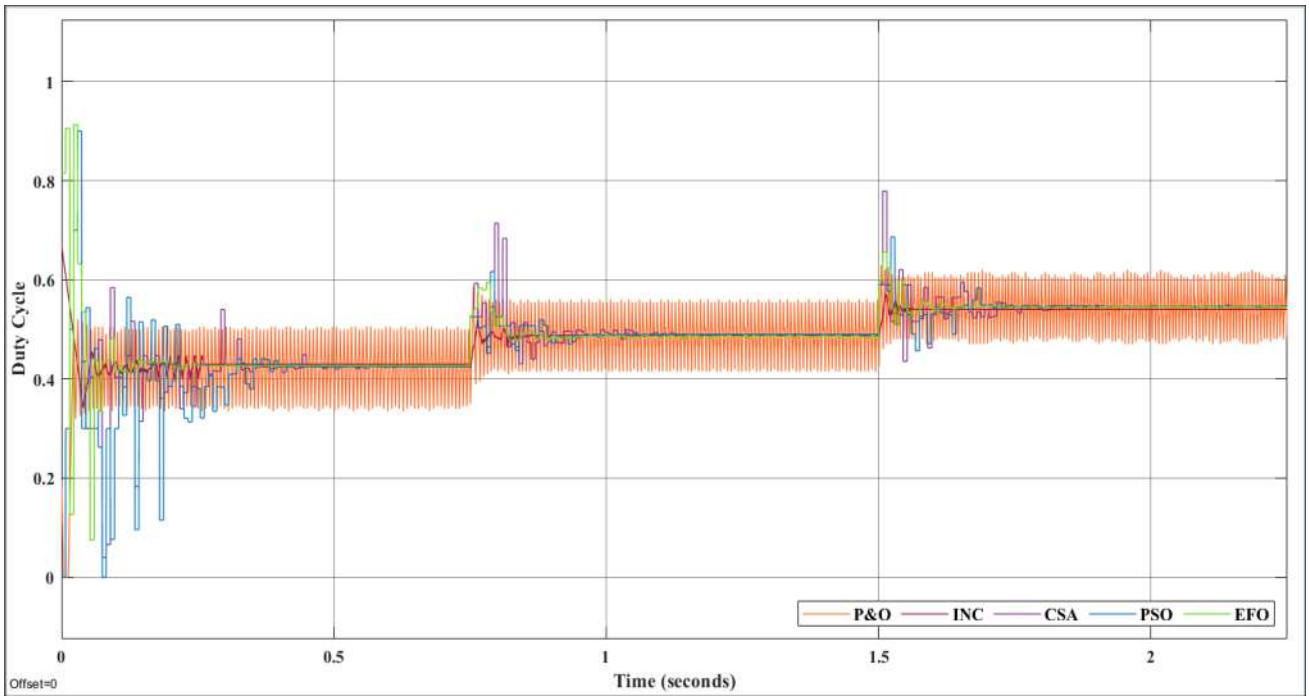

Fig. 7 The duty cycle versus time when using the five MPPT methods

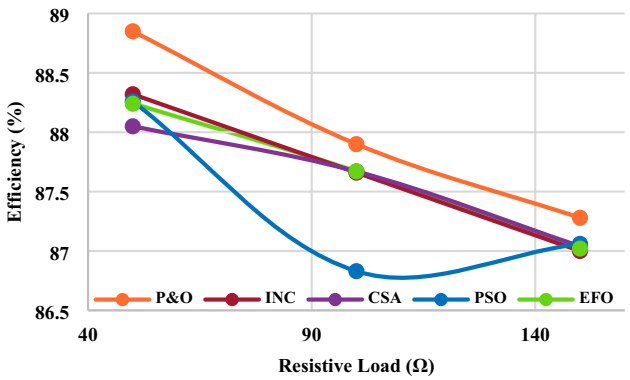

Fig. 8 The efficiency of the system versus the load when using the five MPPT methods

shown in Fig. 8. The electrical efficiency of the chosen PV module ranges between 15.18% and 15.47% for the tested

Table 3 A summary of the simulation results of the five MPPT methods

MPPT method	EFO	CSA	PSO	P&O	INC
T.E	100%	100%	100%	99.59%	99.98%
T.T	Rank 3	Rank 4	Rank 5	Rank 1	Rank 2
S.S.O	No	No	No	Yes	No
Tuning parameters	3	2	3	1	1

Fig. 9 The implemented hardware setup

sun irradiance levels (300–500 W/m^2). Table 3 summarizes the results of the applied methods.

Experimental results and discussion of the fixed load and fixed weather conditions test

A hardware setup for the standalone PV system was implemented to test the performance of the proposed EFO method and compare it to the performance of the P&O method. The implemented hardware setup was inspired from [22]. The setup consists of white LED light bulbs, a

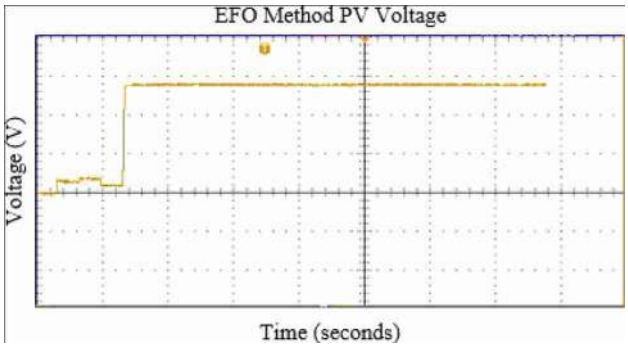

Fig. 10 The experimental voltage of the PV module versus time when using the EFO method

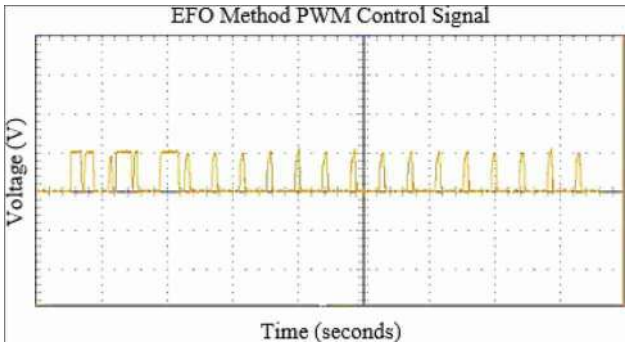

Fig. 11 The experimental PWM control signal versus time when using the EFO method

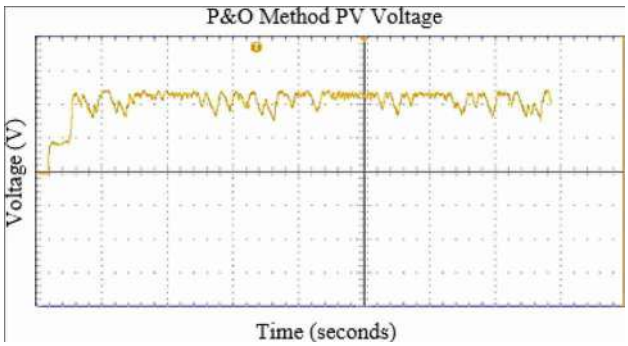

Fig. 12 The experimental voltage of the PV module versus time when using the P&O method

20 W PV module (Newpowa NPA20S-12H), a current and voltage sensor (Zio INA219), a SEPIC converter, Arduino Mega 2560, a resistive load (150 Ω), an oscilloscope, and a digital light and temperature meter. Figure 9 illustrates the implemented hardware setup. The experimental test was conducted under fixed load and fixed weather conditions (sun irradiance level is 33 W/m^2 and surrounding temperature is 25 °C). Figures 10, 11, 12 and 13 depict the

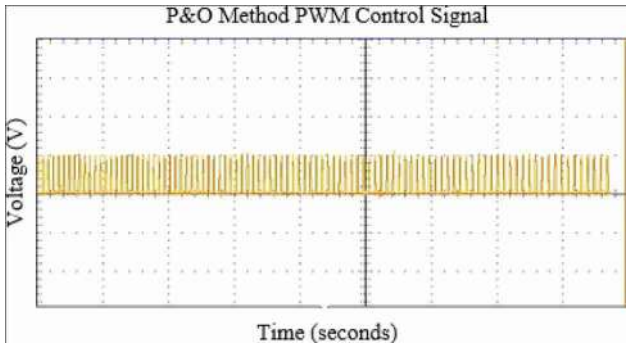

Fig. 13 The experimental PWM control signal versus time when using the P&O method

Table 4 Experimental results of fixed load and fixed weather conditions test

MPPT method	EFO	P&O
PV power (W)	0.45	Ave. 0.56
T.E. (%)	80.14	98.58
T.T. (s)	6.60	3.20
Load power (W)	0.28	Ave. 0.35
Converter efficiency (%)	62.17	62.05

graphical results of the test. The numerical results of the test are summarized in Table 4.

From the conducted test, the P&O method achieved higher tracking efficiency as compared to the tracking efficiency of the EFO method. This contradicts the simulation results as the P&O method exhibits steady-state oscillations which should result in power losses. However, one reason behind the degraded tracking efficiency of the EFO method experimentally could be due to the tuning parameters. The values of the tuning parameters that were used in the experimental test are the same as that of the simulation test. Changing the values of the tuning parameters could improve the performance of the EFO method. Another reason for the degraded tracking efficiency of the EFO method could be the used algorithm to find the correct index to insert a new EMP into the sorted population. The algorithm that was used in the experimental test can be improved or changed to enhance the performance of the EFO method. In addition, a higher precision ratio could be used when comparing the worst EMP with the newly generated EMP to improve the tracking efficiency of the EFO method.

The tracking time of the P&O method is less than the tracking time of the EFO method. This confirms the simulation results and the fast convergence advantage of the P&O method discussed in [16, 17].

Steady-state oscillations around the MPP for the P&O method are clear in the experimental results. However, the

EFO method achieved zero S.S.O. The PWM control signal of the P&O method suffers from large oscillations as compared to the PWM control signal of the EFO method. This confirms the simulation results and the S.S.O. disadvantage of the P&O method as discussed in [16, 17].

Conclusions

This paper proposed the methodology of applying a new maximum power point tracking (MPPT) method, namely the Electromagnetic Field Optimization (EFO) method. The proposed tracking method was not applied before in the literature. The performance of the proposed method was assessed against the performances of four well-studied MPPT methods in the literature, namely: the Cuckoo Search Algorithm (CSA) method, the Particle Swarm Optimization (PSO) method, the Perturb and Observe (P&O) method, and the Incremental Conductance (INC) method. The assessment of the performances of the methods was completed by conducting simulation and experimental tests.

The simulation test was conducted to evaluate the performance of the proposed EFO method in tracking the MPP under changing sun irradiance levels and fixed temperature and load conditions. The EFO method achieved a high tracking efficiency (100%), a short tracking time (0.13 s), no steady-state oscillations, and no duty cycle oscillations in the simulation test. This test highlighted the superiority of the EFO method over the CSA method and the PSO method in terms of the short tracking time as their tracking times were 0.23 s and 0.26 s, accordingly. The simulation results also demonstrated that the transfer of power from the PV module to the load is efficient as the efficiencies of the designed system range between 86% and 88% for the five MPPT methods. The electrical efficiencies of the chosen PV module range between 15.18% and 15.47% for the tested sun irradiance levels (300–500 W/m^2).

On the other hand, the experimental test was under fixed load and fixed weather conditions. The EFO method achieved 80.14% tracking efficiency, 6.6 s tracking time, no steady-state oscillations, and no duty cycle oscillations in the experimental test. The experimental test highlighted a degraded tracking efficiency of the EFO method compared to the P&O method that achieved 98.58% tracking efficiency and 3.2 s tracking time.

As a result, modifications to the EFO method can be made to improve its performance in future experimental tests. Future experimental tests can include slow gradual changes in irradiance and temperature tests, rapid changes in irradiance and temperature tests, and worst-case irradiance tests. In addition, a hybrid method comprising of the EFO method and another MPPT method can be implemented to achieve an improved tracking performance. Addressing the dynamic partial shading problem using the EFO method can also be considered for future research.

Author contributions AI proposed the methodology, investigated the project resources, performed the simulation and the experimental tests, analyzed the results, and drafted, reviewed, and submitted the final manuscript. MZ supervised the work.

Funding The authors have no relevant financial or non-financial interests to disclose.

Declarations

Conflict of interest The authors have no competing interests to declare that are relevant to the content of this article.

References

1. IEA: Global energy review: CO2 emissions in 2021. International Energy Agency (2021). https://iea.blob.core.windows.net/assets/c3086240-732b-4f6a-89d7-db01be018f5e/GlobalEnergyReviewCO2Emissionsin2021.pdf
2. Arthouros, Z: Renewables 2021: global status report. REN21 (2021). https://www.ren21.net/wp-content/uploads/2019/05/GSR2021_Full_Report.pdf
3. Bendib, B., Belmili, H., Krim, F.: A survey of the most used MPPT methods: conventional and advanced algorithms applied for photovoltaic systems. Renew. Sustain. Energy Rev. **45**(1), 637–648 (2015). https://doi.org/10.1016/j.rser.2015.02.009
4. De Brito, M.A.G., Galotto, L., Sampaio, L.P., e Melo, G.D.A., Canesin, C.A.: Evaluation of the main MPPT techniques for photovoltaic applications. IEEE Trans. Ind. Electron. **60**(3), 1156–1167 (2012). https://doi.org/10.1109/TIE.2012.2198036
5. Sarvi, M., Azadian, A.: A comprehensive review and classified comparison of MPPT algorithms in PV systems. Energy Syst. **13**(2), 281–320 (2021). https://doi.org/10.1007/s12667-021-00427-x
6. Bollipo, R.B., Mikkili, S., Bonthagorla, P.K.: Critical review on PV MPPT techniques: classical, intelligent and optimisation. IET Renew. Power Gener. **14**(9), 1433–1452 (2020). https://doi.org/10.1049/iet-rpg.2019.1163
7. Karami, N., Moubayed, N., Outbib, R.: General review and classification of different MPPT techniques. Renew. Sustain. Energy Rev. **68**, 1–18 (2017). https://doi.org/10.1016/j.rser.2016.09.132
8. Mao, M., Cui, L., Zhang, Q., Guo, K., Zhou, L., Huang, H.: Classification and summarization of solar photovoltaic MPPT techniques: a review based on traditional and intelligent control strategies. Energy Rep. **6**, 1312–1327 (2020). https://doi.org/10.1016/j.egyr.2020.05.013
9. Motahhir, S., El Hammoumi, A., El Ghzizal, A.: The most used MPPT algorithms: review and the suitable low-cost embedded board for each algorithm. J. Clean. Prod. **246**, 1–17 (2020). https://doi.org/10.1016/j.jclepro.2019.118983
10. Pal, R.S., Mukherjee, V.: Metaheuristic based comparative MPPT methods for photovoltaic technology under partial shading condition. Energy (2020). https://doi.org/10.1016/j.energy.2020.118592
11. Rezk, H., Eltamaly, A.M.: A comprehensive comparison of different MPPT techniques for photovoltaic systems. Sol. Energy **112**, 1–11 (2015). https://doi.org/10.1016/j.solener.2014.11.010
12. Rezk, H., Fathy, A., Abdelaziz, A.Y.: A comparison of different global MPPT techniques based on meta-heuristic algorithms

for photovoltaic system subjected to partial shading conditions. Renew. Sustain. Energy Rev. **74**, 377–386 (2017). https://doi.org/10.1016/j.rser.2017.02.051
13. Verma, D., Nema, S., Shandilya, A.M., Dash, S.K.: Maximum power point tracking (MPPT) techniques: recapitulation in solar photovoltaic systems. Renew. Sustain. Energy Rev. **54**, 1018–1034 (2016). https://doi.org/10.1016/j.rser.2015.10.068
14. Saka, M.P., Dogan, E.: Recent developments in metaheuristic algorithms: a review. Comput. Technol. Rev. **5**(4), 31–78 (2012). https://doi.org/10.4203/ctr.5.2
15. Abedinpourshotorban, H., Shamsuddin, S.M., Beheshti, Z., Jawawi, D.N.: Electromagnetic field optimization: a physics-inspired metaheuristic optimization algorithm. Swarm Evol. Comput. **26**, 8–22 (2016). https://doi.org/10.1016/j.swevo.2015.07.002
16. Ahmed, J., Salam, Z.: An improved perturb and observe (P&O) maximum power point tracking (MPPT) algorithm for higher efficiency. Appl. Energy **150**, 97–108 (2015). https://doi.org/10.1016/j.apenergy.2015.04.006
17. Alik, R., Jusoh, A.: An enhanced P&O checking algorithm MPPT for high tracking efficiency of partially shaded PV module. Sol. Energy **163**, 570–580 (2018). https://doi.org/10.1016/j.solener.2017.12.050
18. Loukriz, A., Haddadi, M., Messalti, S.: Simulation and experimental design of a new advanced variable step size Incremental Conductance MPPT algorithm for PV systems. ISA Trans. **62**, 30–38 (2016). https://doi.org/10.1016/j.isatra.2015.08.006
19. Nugraha, D.A., Lian, K.L.: A novel MPPT method based on cuckoo search algorithm and golden section search algorithm for partially shaded PV system. Can. J. Electr. Comput. Eng. **42**(3), 173–182 (2019). https://doi.org/10.1109/CJECE.2019.2914723
20. Alshareef, M., Lin, Z., Ma, M., Cao, W.: Accelerated particle swarm optimization for photovoltaic maximum power point tracking under partial shading conditions. Energies **12**(4), 1–18 (2019). https://doi.org/10.3390/en12040623
21. Mirza, A.F., Ling, Q., Javed, M.Y., Mansoor, M.: Novel MPPT techniques for photovoltaic systems under uniform irradiance and partial shading. Sol. Energy **184**, 628–648 (2019). https://doi.org/10.1016/j.solener.2019.04.034
22. Killi, M., Samanta, S.: Modified perturb and observe MPPT algorithm for drift avoidance in photovoltaic systems. IEEE Trans. Ind. Electron. **62**(9), 5549–5559 (2015). https://doi.org/10.1109/TIE.2015.2407854

International Journal of Energy and Environmental Engineering (2023) 14:601–612
https://doi.org/10.1007/s40095-022-00537-x

ORIGINAL RESEARCH

Investigating the effects of nanorefrigerants in a cascaded vapor compression refrigeration cycle

Evidence Akhayere[1] · Victor Adebayo[2] · Michael Adedeji[2] · Muhammad Abid[4] · Doga Kavaz[1,3] · Mustafa Dagbasi[2]

Received: 15 May 2022 / Accepted: 9 September 2022 / Published online: 29 September 2022

Abstract

It is vital, following the Kyoto Protocol, to find environmentally benign and energy-efficient refrigerants, consequently boosting the coefficient of performance (COP). Refrigeration systems are used extensively in the industrial, home, and commercial sectors for cooling, heating, food preservation, and cryogenic purposes. Researchers have successfully employed the application of nanoparticles in cooling systems to achieve improved enhancement, reliability, and efficiency of refrigeration systems because of their higher heat transfer and thermophysical capabilities. The function of numerous variables, however, makes the experimental technique appear to be costly and time-consuming to carry out. This study was, therefore, designed to numerically simulate the performance assessment of a nanoparticle-enhanced Cascaded Vapor Compression Refrigeration Cycle (CVCRC). The focus of this paper is on four distinct SiO_2 nanoparticle nanorefrigerants and their pure fluids: two HFCs as well as two fourth-generation refrigerants (HFOs), namely; R12, R134a, R1234yf, and R-1234ze (E). The results show that adding nanoparticles to the pure refrigerant improves COP, and the highest values were achieved with the R1234ze(E)/SiO2 mixture. Increasing the mass concentration of the nanoparticles leads to an increase in the refrigeration effect, an increase in COP, and a reduction in compressor work. Although R125 had the lowest compressor work of 47.12 kW when SiO2 nanoparticles are introduced, however, is not suitable for refrigeration because of its high GWP values. R1234ze has the second-lowest compressor work of 59.58 kW with the addition of SiO_2, it is consequently more energy efficient and can be used in its place as it has a GWP of 6, among other benefits.

Keywords Nanorefrigerants · COP · Refrigeration · Cascaded vapor compression refrigeration cycle · Compressor work

List of symbols

h	Specific enthalpy (kJ/kg)
ρ	Density
Q	Heat rate (kW)
W	Work rate (kW)
m	Mass flow rate (kg/s)
ω	Mass fraction

Abbreviations

BGS	Barley grass straw
COP	Coefficient of performance
CVCRC	Cascade vapor compression refrigeration system
EDX	Energy dispersive X-ray
FTIR	Fourier-transform infrared spectroscopy
GWP	Global warming potential
HFE	Hydrofluoroethers
HTL	High temperature loop
LTL	Low temperature loop
NS	Nanosilica
SEM	Scanning electron microscopy
XRF	X-ray fluorescence
HC	Hydrocarbon
HFO	Hydrofluoro olefin

Subscripts

c	Condenser
comp	Compressor
ev	Evaporator

✉ Victor Adebayo
vadebayo@ciu.edu.tr

[1] Department of Environmental Science, Cyprus International University, Nicosia, Mersin 10, Turkey

[2] Department of Energy Systems, Cyprus Internatonal University, Nicosia, Mersin 10, Turkey

[3] Department of Bioengineering, Cyprus International University, Nicosia, Mersin 10, Turkey

[4] Department of Energy Systems Engineering, Faculty of Integrated Technologies, Universiti Brunei Darussalam, Jalan Tungku Link BE 1410, Bandar Seri Begawan, Brunei Darussalam

exp	Expansion
NR	Nanorefrigerant
PR	Pure refrigerant

Introduction

The proliferation of refrigeration and air conditioning devices has significantly boosted global energy consumption. Therefore, a small reduction in energy consumption can have a big impact on the global energy situation. This necessitates the use of energy-efficient and high-performance heating, refrigeration, and air-conditioning systems.

Vapor compression cycles are the most common technology for modifying the environment of a closed room through heating or cooling [1]. Due to the high compression requirements, a single cycle system will not be able to efficiently cool processes at extremely low temperatures. To attain the requisite low temperature, cascaded refrigeration systems (CRS) are typically employed. A cascaded cooling system is made up of two cooling cycles linked by a heat exchanger. The heat exchanger acts as a condenser in the low-temperature loop (LTL) and as an evaporator in the high-temperature loop (HTL) [2].

In comparison to a single vapor compression refrigeration system, a cascaded vapor compression refrigeration system may operate at lower evaporation temperatures and compression ratios (in each loop), while yet achieving a better volumetric compressor efficiency [3]. The development of energy-efficient cooling systems is hampered by the poor thermal transport properties of conventional heat transfer fluids. To get around this constraint, a colloid has been developed through the suspension of nanoparticles (NP) into the conventional heat transfer fluids, also referred to as nanofluids [4]. Because of their thermal transfer capabilities, nanofluids have been particularly attractive as advanced working fluids. Nanofluids are made up of extremely small particles (1–100 nm) mixed with ordinary working fluids like water and oil. It is called nanorefrigerant when a refrigerant is used as the base fluid [5].

The nanorefrigerant has a higher thermal conductivity than the base fluid as a result of its superior thermal conductivity. Their higher heat transfer coefficient is also one of their most distinctive features. [6]. As a result, at the liquid, vapor, and the two-phase region of a refrigeration cycle, an increase in heat transfer takes place [7, 8]. According to the literature, the results of such contrary effects are often combined with a COP increase of about 10–20%, depending mainly on the NP and their mass/volume fraction [9].

Conventional refrigerants significantly contribute to global warming and thereby damage the ozone layer. Therefore, the performance of the vapor compression cooling system must be enhanced using a suitable refrigerant. Water was one of the first substances to be utilized as a refrigerant [10]. These water-based refrigeration systems, however, were only used in a few applications due to their numerous drawbacks. The vapor compression refrigeration systems, which used ethyl ether as the refrigerant, were first created by Jakob Perkins [11]. Due to its high boiling point, toxicity, and flammability problems, ethyl ether first seemed to be an excellent refrigerant but did not catch on. Later, the carbon dioxide-powered vapor compression refrigeration system was invented. Due to its nonflammability and lack of hazardous properties, carbon dioxide has numerous uses, particularly in marine refrigeration [10].

The initial vertical ammonia compressor with single acting was developed by David Boyle in 1872. The thermophysical properties of ammonia are excellent, it is widely available, and it is inexpensive[12]. But, ammonia is risky and has a minor flammability issue. A few common building materials, like copper, are also incompatible with it. However, testing on several other fluids, including isobutane, ethyl chloride, methyl and ethyl amines, and methylene chloride, was stopped due to several limitations [10].

The introduction of second-generation refrigerants was necessary because virtually all first-generation refrigerants had safety issues, such as toxicity, flammability, and high operating pressures. Second-generation refrigerants, also referred to as ODS, have been connected to both significant contributions to global warming and ozone layer depletion. This prompted scientists to rethink their search for safer refrigerants. This time, the phrase "safer" refers to hazards to immediate personal safety as well as long-term environmental safety, such as toxicity and flammability [10].

Between 1990 and 2009, the Montreal Protocol drastically decreased CFC emissions. Due to the non-ozone depleting characteristics becoming the major criteria for third-generation refrigerants, two alternatives HFCs and HFEs have emerged. The Montreal Protocol's primary goal was to protect the ozone layer, but it also had the unintended consequence of significantly reducing greenhouse gas emissions. This is true since HFCs emit greenhouse gases at a lower rate than CFCs. Nevertheless, the Kyoto Protocol classifies HFCs as greenhouse gases [13, 14] because of their relatively large GWP, which is many times more than CO_2. Among all greenhouse gases, HFCs are growing at the quickest pace, at a rate of 10–15% annually. Fluorochemicals were still the main topic of attention, though. Many non-fluorochemicals and hydrofluoroether (HFE) chemicals were thoroughly assessed by corporate and public research programs, but only a small number of them showed promise [10].

Several industries have been obliged to adopt a new generation of low-GWP refrigerants, such as HC (hydrocarbon) and HFO (hydrofluoro olefin) refrigerants, to meet regulatory requirements. Due to increasing international concerns

about the GWP of HFC refrigerants. The number of fluorine atoms in HFCs directly affects their atmospheric lifetime and GWP. As a result, HFCs have been scrutinized for their role in greenhouse gas emissions. The growing concern about humanity's effect on global warming has prompted researchers to look for alternative refrigerants with a lower GWP, and natural refrigerants have re-sparked renewed interest [15].

HFOs which are also called fourth-generation refrigerants are unsaturated organic compounds made up of hydrogen, fluorine, and carbon. They have a carbon–carbon double bond, which is a key feature that contributes to their low global warming. These synthetic refrigerants, known as hydrofluoro olefins (HFOs), have a low GWP which is 0.1% of that of HFCs. The HFOs, besides having short atmospheric lifetimes, have many useful properties, including low boiling points, excellent physicochemical properties, and strong vapor pressures at room temperature. As a result, they are thought to be the best HFC alternatives [10].

In this vital phase of the transition from high-GWP to low-GWP systems, this type of study might be tremendously valuable in improving knowledge regarding the application and efficiency of environmentally friendly refrigerants. Although more research is needed to fully understand nanorefrigerants' potential applicability in refrigeration and air conditioning systems, their impact on the thermodynamic efficiency of refrigerants and lubricants suggests they will be employed more frequently in the future [16]. Nanorefrigerant studies are, however, still in the embryonic phase but scientists have recently used nanoparticles in refrigeration systems because thermophysical and heat transfer capabilities could be significantly improved by these nanoparticles. Nanofluid investigations are not limited to thermal conductivity only. Nevertheless, researchers have studied other thermophysical properties as well as viscosity, the tension on the surface, specific heat capacity, etc.

Various studies on the application of nanorefrigerants in various systems are reviewed in this paper and are provided in this section. Subramani and Prakash [17] examined the performance of an Al_2O_3 nanoparticle (size and 50 nm, density 0.26 g/cc) cooling system mixed with lubricating oil (SUNISO 3GS). The results showed that refrigerant cooling in the condenser decreases by 8.3 °C and cooling time by 27%. In addition, power consumption was reduced by 25%, and COP improvement of 33% was achieved. Jwo et al. [18] also investigated the potential of Al_2O_3 nanoparticles as R12/MO additives. The results showed that a greater compression ratio compared to R12 is achieved by using the nanorefrigerant at 0.1 wt.%. Peng et al. [19] investigated the effect of mass fraction on the pressure drop of a boiling R113/CuO nanorefrigerant in a horizontal tube. They concluded that the dispersion of nanoparticles in pure R113 refrigerant increases the drop in pressure. The maximum pressure drop improvement was 20.8%. With a 0.5% mass fraction of CuO nanoparticles distributed in polyester oil, Kedzierski and Gong [20] observed a 275% increase in heat transfer with the base refrigerant R134a. Sun and Yang [8] have investigated nanorefrigerants such as R141b/Cu, R141b/Al_2O_3 and R141b/CuO to find out the effects of material type and quality of vapor on the flow of boiling heat transfer in horizontal tubes with the use of computer-aided tests. The R141b/Cu nanorefrigerant has the highest heat transfer coefficient for the same mass fraction, and R141b/CuO provides the lowest coefficient of heat transfer among the considered nanorefrigerants.

Improvements in heat transfer have been seen in recent studies by the use of Al_2O_3 as nanoparticles in refrigerants, as well as in the reduction of power consumption. Because the heat transfer enhancement reduces the amount of energy required by the compressor to run the working fluid, the system runs more efficiently. Bi et al. [21]examined the R134a/Al2O3 nanorefrigerant in a refrigerator and discovered that a 0.06 wt. percent blend saved 23.24% of energy and increased COP by 18.30 percent. Sabareesh et al. [22] studied how R12/TiO_2/mineral oil could improve a vapor compression cooling system's COP. Based on their findings, compression work decreased by 11% as COP increases in the vapor compression cooling system when the nanorefrigerant is used instead of the R12/MO mixture. The use of nanorefrigerants in domestic refrigerators has been studied by Javadi and Saidur [23] to reduce energy consumption and greenhouse gas emissions. The nanorefrigerants TiO_2-mineral oil-R134a and Al_2O_3-mineral oil-R134a were utilized in mass fractions of 0.06 percent and 0.1 percent, respectively. The nanorefrigerant containing 0.1% TiO_2 nanoparticles showed the highest energy savings. Wang et al. [24] conducted one of the first experimental studies using nanorefrigerant, demonstrating that using TiO_2 nanoparticles in an R134a-based system significantly improves the cooling speed and COP of a domestic refrigerator. Using TiO_2 nanoparticles, Li et al. [25] reported a major increase in the heat transfer coefficient of R11 refrigerant.

In a separate study, Aktas et al. [5] focused on five distinct nanorefrigerants, Al_2O_3 nanoparticles with pure refrigerants; R430a, R436a, R12, R600a, and R134a. The results showed that COP is improved by adding nanoparticles to the pure refrigerants, and the highest increment of 43.93% of COP was obtained by utilizing the R600a/Al_2O_3 mixture. The relationship between thermal power and increased COP performance in some cooling systems was studied by Mahbubul et al. [26]. At the same temperature, the conductivity, dynamic viscosity, and density of the Al_2O_3/R-134a nanorefrigerant rose by 28.58%, 13.68%, and 11%, respectively, when compared to the base refrigerant (R-134a). A nanolubricant of the 40 nm ZnO nanoparticles with PAG oil was prepared by Kumar et al. [27]. The mixture was prepared for 10 h by the magnetic stirrer, then the ultrasonic homogenizer

vibrates the mixture for 15 h to prevent the particles from being clustered. The mixture was then used with R152a refrigerant to develop a nanorefrigerant that decreases the consumption of energy with 0.5% of volume concentration. Kumar et al. [28]evaluated the performance of VCRS with ZrO_2 nanoparticles with R134a and R152a to compare the impact of refrigerant type. ZrO_2 nanoparticles (20 nm) were utilized at 0.01 to 0.06 percent volume concentration. The compressor work for ZrO_2/R152a nanorefrigerant was lower than R152a but higher than R134a. Coumaressin et al. [29] studied the effects of aluminum oxide, copper oxide, titanium oxide, and zinc oxide nanofluids in a vapor compression refrigeration device utilizing R1234yf. Nanofluids are injected directly into the refrigerant in the liquid line after the pump. Using the TK solver, the nanorefrigerant's thermophysical characteristics were assessed. The comparison curves show that Al_2O_3 nanorefrigerant has much better performance than the other nanorefrigerants at 0.55 concentration. The coefficient of performance of Al_2O_3 nanofluid is 28% greater than that of other nanofluids, while power consumption is reduced by 7%.

Although nanorefrigerants have been researched over time, their use in refrigeration is still up for debate. For example, it is observed there is almost no study on the use of nanoparticles with fourth-generation refrigerants. The goal of this research is to examine how nanoparticles affect the thermodynamic efficiency of a cascaded refrigeration system. An investigation into the coefficient of performance (COP) and compressor performance of a cascaded refrigeration system utilizing four different refrigerants, two HFCs as well as two fourth-generation refrigerants (HFOs), namely, the R12, R134a, R1234yf, and R-1234ze (E), in combination with SiO_2 nanoparticles is the goal of this theoretical investigation. The performance of these four nanorefrigerants in a CVCRC is evaluated by introducing SiO_2 nanoparticles at a mass fraction of 0.05%. To investigate the effects of the refrigeration cycle, parameters such as refrigerant type and nanoparticle mass concentration on COP at various evaporation and condensation temperatures. The utilization of SiO_2 nanoparticles synthesized from agricultural waste from the barley plant, which increases sustainability, is another innovative aspect of this research.

Preparation of SiO_2 nanoparticles

Materials and methods

One of the highlights of the research was to synthesize the nanofluid using a sustainable means. Nanosilica was synthesized from the agricultural waste of the barley plant. Barley grass straw (BGS) was collected from levent farm, also hydrochloric acid and sodium hydroxide were prepared for their various molarities, other materials used include furnace, miller equipment, UV reflux bottles, and beakers.

Experimental preparation

The waste straw made from barley was gathered and properly cleansed with distilled water. The barley waste was dried and washed with distilled water, to remove soil particles attached to the straws [30]. After which they were allowed to dry for 24 h at 100 °C in the oven. The dried straw was powdered with the help of a miller and 50 g of the powder was used for preparation. To prepare the nano-enhanced refrigerant fluid, barley grass straw was refluxed in 250 ml of 2 M HCl for 6 h, then heated in a 700 °C furnace for 5 h, the process is the same as described in [31]. The stabilization of the nanoparticle was done by dispersion in deionized water, after which ultra-sonication was carried out to prevent agglomeration and to ensure a pH value of 7.

System description

The CVCRC is divided into two cycles: HTL and LTL. Both cycles have a compressor, condenser, expansion valve, and evaporator, and they are connected by a heat exchanger, which serves as the evaporator in the HTL and the condenser in the LTL at the same time, as shown in Fig. 2. In this study, CO_2 is employed as the working fluid in the LTL loop, whereas one of the four nanorefrigerants is used in the HTL loop. Table 1 summarizes the thermodynamic, environmental, and safety properties of the refrigerants used in this analysis, as obtained from the literature. [33–38]

A schematic of a typical cascaded refrigeration system is given in Fig. 1 and a representative T-S diagram for the CVCRC is presented in Fig. 2. The refrigerant is saturated vapor when it goes into the compressors (points 1 and 5) and saturated liquid when it enters the expansion valves (points 3 and 7). The LTL condenser and the HTL evaporator serve as heat exchangers within the CVCRC. The refrigerant in the HTL cycle evaporates in this heat exchanger, whereas the refrigerant in the LTL cycle condenses into saturated liquid.

The four processes that make up the vapor-compression refrigeration cycle are as follows:

- (1–2), (5–6) isentropically compression of refrigerant in the compressor.
- (2–3), (6–7) constant-pressure condensation,
- (3–4), (7–8) in the expansion valve, adiabatic expansion occurs.
- (4–1), (8–5) constant-pressure evaporation.

Table 1 The thermodynamic, environmental, and safety properties of the refrigerants used

	R125	R134a	R1234yf	R-1234ze (E)	R-744
Chemical formula	C_2HF_5	$C_2H_2F_4$	$C_3H_2F_4$	$C_3H_2F_4$	CO_2
Critical Temperature (°C)	66.02	101.06	94.7	109.36	30.98
Critical Pressure (kPa)	3617.7	4059.28	3382.2	3634.9	7377.3
Critical density (kg/m^3)	573.58	511.899	475.55	489.238	467.6
Boiling point (°C)	−48.09	−26.07	−29.45	−18.97	−78.46
Molecular weight (kg/mol)	120.02	102.032	114.042	114.0416	44.009
GWP*	3170	1300	1	6	1
ODP	0	0	0	0	0
ASHRAE safety group	A1	A1	A2L	A2L	A1
Atmospheric lifetime (years)	29	14	0.030116	NA	200

*Global warming potential with a period of 100 years (CO_2 relative to GWP = 1)

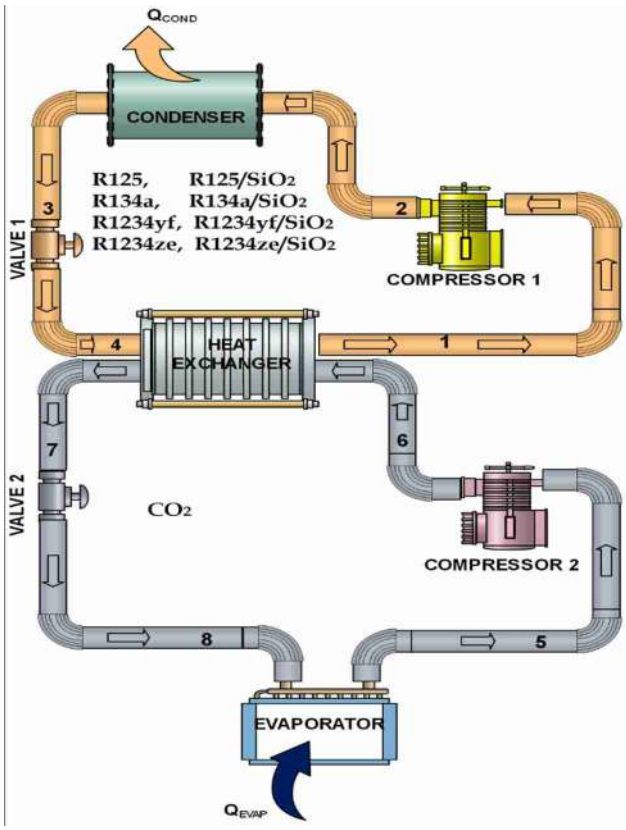

Fig. 1 Schematic of typical cascaded refrigeration system

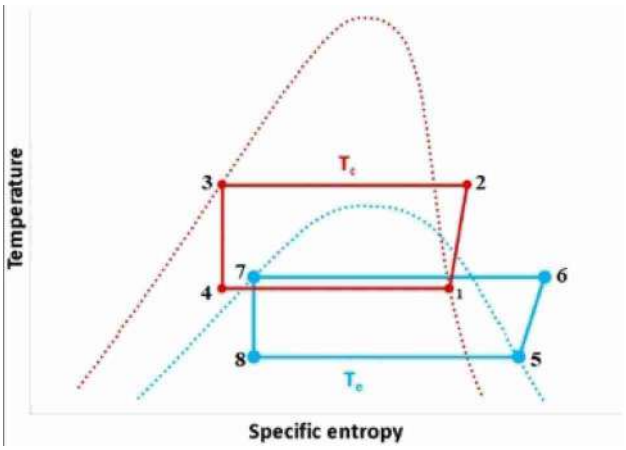

Fig. 2 T-S diagram of a typical cascaded refrigeration system

Theoretical modeling

The mass, energy and entropy balance equations are used to determine the CVCRC's thermodynamic performance, and Table 2 contains the input data used for system analysis. The thermodynamic analysis considers the following assumptions:

- The CVCRC works under steady-state conditions.
- Potential and kinetic energies are insignificant.
- The refrigerant valves are isenthalpic.
- In the CVCRC pipeline, the pressure drops are ignored.
- The nanoparticle distribution in the refrigerant flow is uniform.
- The nanoparticles are not deposited on the solid walls.

For each component of the CVCRC, the mass balance equation is expressed as follows:

$$\sum \dot{m}_{\text{in}} = \sum \dot{m}_{\text{out}} \tag{1}$$

The general energy balance equation for CVCRC is:

$$\sum \dot{m}_{\text{in}} \text{h}_{\text{in}} + \sum \dot{Q}_{\text{in}} + \sum \dot{W}_{\text{in}} = \sum \dot{m}_{\text{out}} h_{\text{out}} + \sum \dot{Q}_{\text{out}} + \sum \dot{W}_{\text{out}} \tag{2}$$

Work, specific enthalpy, and heat transfer rates are represented by W, h, and Q, respectively.

Table 2 Input data

	Low-temperature loop (LTL)	High-temperature loop (HTL)
Refrigerant	CO_2	R125, R134, R1234yf, R-1234ze (E) & R125-SiO_2, R134- SiO_2, R1234yf- SiO_2, R-1234ze (E)- SiO_2
Temperature of the evaporator (°C)	−50	–
Temperature of the condenser (°C)	–	–
Temperature of the evaporator (°C)	–	–
Temperature of the condenser (°C)	45	–
Isentropic efficiency of the compressor (%)	80	80
Heat exchanger effectiveness	90	

Table 3 Energy balance

Components	Energy balance
Evaporator	$\dot{m}_8 h_8 + \dot{Q}_{ev} = \dot{m}_5 h_5$
Compressor I	$\dot{m}_1 h_1 + \dot{W}_{comp1} = \dot{m}_2 h_2$
Compressor II	$\dot{m}_5 h_5 + \dot{W}_{comp2} = \dot{m}_6 h_6$
Condenser	$\dot{m}_3 h_3 + \dot{Q}_c = \dot{m}_2 h_2$
Expansion valve I	$\dot{m}_3 h_3 = \dot{m}_4 h_4$
Expansion valve II	$\dot{m}_7 h_7 = \dot{m}_8 h_8$
Heat exchanger	$\dot{m}_4 h_4 + \dot{m}_6 h_6 = \dot{m}_1 h_1 + \dot{m}_7 h_7$

Table 3 represents the energy balance equations for the CVCRC components.

The CVCRC's overall coefficient of performance for cooling is:

$$\mathrm{COP}_{\mathrm{overall}} = \frac{\dot{Q}_{ev}}{\dot{W}_{comp1} + \dot{W}_{comp2}} \tag{3}$$

The density of a nanorefrigerant (NR) is estimated from the density of nanoparticles (NP) and the density of the base fluid (PR) and the mixture ratio using the equation proposed by Xuan and Roetzel [39], it should be noted, however, that the original equation is modified in this work by substituting mass fraction (ω) for volume fraction.

$$\rho_{NR} = \omega\rho_{NP} + (1-\omega)\rho_{PR} \tag{4}$$

Validation

We considered testing for the accuracy and validity of the results by making a comparison between our results and that of the Hussin et al. [40] experimental study as shown in table. Table 4 shows COP for the pure refrigerant R134a and R134a/SiO_2 nanorefrigerant. It can be observed that the COP results from our theoretical analysis and that of Hussin et al. [40] shows same trend; a raise in the COP with the addition of SiO_2 nanoparticles. In the study performed by Hussin et al. [40], a percentage increase of 23.45% in COP value was recorded with the addition of SiO_2, while a percentage increase of 10.11% was recorded in this study. The large deviation is due to the difference in system parameters used in both studies. Also, for this study, only the COP of HTL loop of the cascade system was considered in this validation.

Table 4 Validation of the study

Density of Nanoparticle: Hussin et al. [40]: 2200 kg/m^3, This study:2400 kg/m^3
Mass concentration: Hussin et al. [40]: 0.5%, This study:0.5%

		COP		COP
Pure R134a	Hussin et al. [40]	3.24	This study	2.461
R134a + SiO_2	Hussin et al. [40]	4.00	This study	2.71

Results and discussion

In this study, the thermodynamic performance of a CVCRC using NR is investigated. The nanosilica was synthesized from the agricultural waste of the barley plant. The density of an NR can be used as a metric to measure the enthalpy of a working fluid because there are no charts or correlations to establish the characteristics of NRs. The EES database may be used to calculate nanorefrigerant enthalpies that correspond to the density, temperature, and pressure of pure refrigerants at any point in time. The density of SiO_2 was experimentally determined to be 2400 kg/m^3. It is worth noting that enthalpy of state point 3 on the T-S diagram is calculated as follows; firstly, for this study the condensation temperature (T_{PR3}) and corresponding pressure (P_{PR3}) are set to 45 °C and 1154 kPa, respectively. The density at point 3 of the various pure refrigerants used in this study (R125, R134a, R1234yf, and R-1234ze (E)) are referred to from EES. Nanorefrigerant density (ρ_{NR}) is calculated using Eq. (4). Based on the density of the NR, the enthalpy at

liquid saturation is determined using pure refrigerant data. The latter enthalpy as determined from EES is used to be the one for point 3. Similarly, entropy for point 3 is determined using the EES database. The enthalpy value of NR, determined in this way, is slightly below that of the pure refrigerant used as the base fluid for the NR.

For state point 1, the temperature (T_{PR1}) and saturation pressure (P_{PR1}) are set to − 14 °C and 183.7 kPa, respectively. Enthalpy and entropy of NR at state point 1 are determined in a similar way to that of state point 3. Enthalpy of NR at point 1 is found to be slightly higher than that of pure refrigerant.

The properties of refrigerants at points 1 and 3 are summarized in Table 5.

Using parameters from points 1 and 3 of the refrigeration cycle, such as pressure and entropy, the enthalpy of points 2 and 4 can be calculated. h_4 at the evaporator's inlet must equal h_3 due to adiabatic expansion in the expansion valve. EES calculates h_1 using s_1 and saturation pressure at point 3. Furthermore, if the compressors' isentropic efficiency is equal to 1 and the refrigeration cycle is ideal, s_1 and s_2 at the compressor's outlet must be equal. The compressor's isentropic efficiency is assumed to be 0.80 in this study.

Results from nanoparticle characterization

To obtain the XRF patterns of SiO_2 nanoparticles, the samples are measured with an X-ray diffractometer (Bruker D8 Advance model). Following that substantial peaks were noticed and recorded over the range of 400–4000 cm^{-1} utilizing (IR Prestigue–21 Shimadzu, Japan) to explore the characteristics of nanoparticles. This analysis is critical for identifying the functional groups in nanoparticles. It was important to perform EDX analysis to determine the constituent elements. In the SEM analysis, the EDX generates X-rays based on the principle of electrons focused primarily on the specimen. As a result, it is possible to provide a complete depiction of the constituent elements [32].

Figure 3 shows the FTIR spectra of produced silica nanoparticles after calcination at 700 °C. The domineer peaks point to the occurrence of silica. Vibrations related to the stretching of silicon bonds (Si–O–Si) for NS synthesized from BGS cause the peak at 1080 cm^{-1}. In addition, the vibrations have a low critical stretching peak. In the FTIR, NS synthesized from BGS has a transmission spectrum of 400–4000 cm^{-1}. A peak at 2250 cm^{-1} was also linked to an aromatic methyl group's C=H bond stretching. The peak at 800 cm^{-1} revealed siloxane linkages (Si–O–Si) framing silica from silicon, demonstrating that the findings of this study are consistent with previous findings. Figure 3 also shows SEM images in which no aggregation and less agglomeration was observed in the structures. At around 2.0 keV, a significant silicon peak was seen, indicating that 88.6% of silicon was synthesized.

Some basic properties of the synthesized barley grass nanosilica (SiO_2) are tabulated in Table 6.

Results of the sensitivity analysis

For all refrigerant couplings at constant evaporator temperature (T_{ev} = − 50 °C), Fig. 4 examines the effect of condenser temperature on overall CVCRC COP. As the condenser temperature rises from 25 to 50 °C, the total COP decreases in all situations. Among the refrigerant couples studied, the R1234ze/SiO_2(NR)-CO_2 refrigerant pair has the highest overall COP value, while the R125-CO_2 refrigerant couple has the lowest overall COP value.

The effect of the condenser temperature on the CVCRC evaporator's heat transfer rate is seen in Fig. 5. The figure depicts a declination trend, in which the heat of evaporation of the refrigerants increases as the temperature increases. The evaporator heat rate is increased by lower condenser temperatures. It was also discovered that adding silicon

Table 5 Properties of nanorefrigerants at points 1 and 3

State point	T_{PR}(°C)	ρ_{PR}(kg/m^3)	h_{PR}(kJ/kg)	ω	ρ_{SiO_2}(kg/m^3)	ρ_{NR}(kg/m^3)	T_{NR}	h_{NR}(kJ/kg)
R125/SiO$_2$								
1	− 15	25.54	325.67	0.0005	2400	26.73	− 13.7	326.34
3	45	1048	262.66	0.0005	2400	1049	44.93	262.55
R134a/SiO$_2$								
1	− 15	8.293	241.48	0.0005	2400	9.489	− 11.51	243.60
3	45	1125	115.80	0.0005	2400	1126	44.85	115.58
R1234yf/SiO$_2$								
1	− 15	10.5	353.39	0.0005	2400	11.69	− 12.04	355.35
3	45	1012	261.14	0.0005	2400	1013	44.82	260.88
R-1234ze (E)/SiO$_2$								
1	− 15	6.831	373.64	0.0005	2400	8.028	− 10.84	376.57
3	45	1092	263.02	0.0005	2400	1093	44.84	262.78

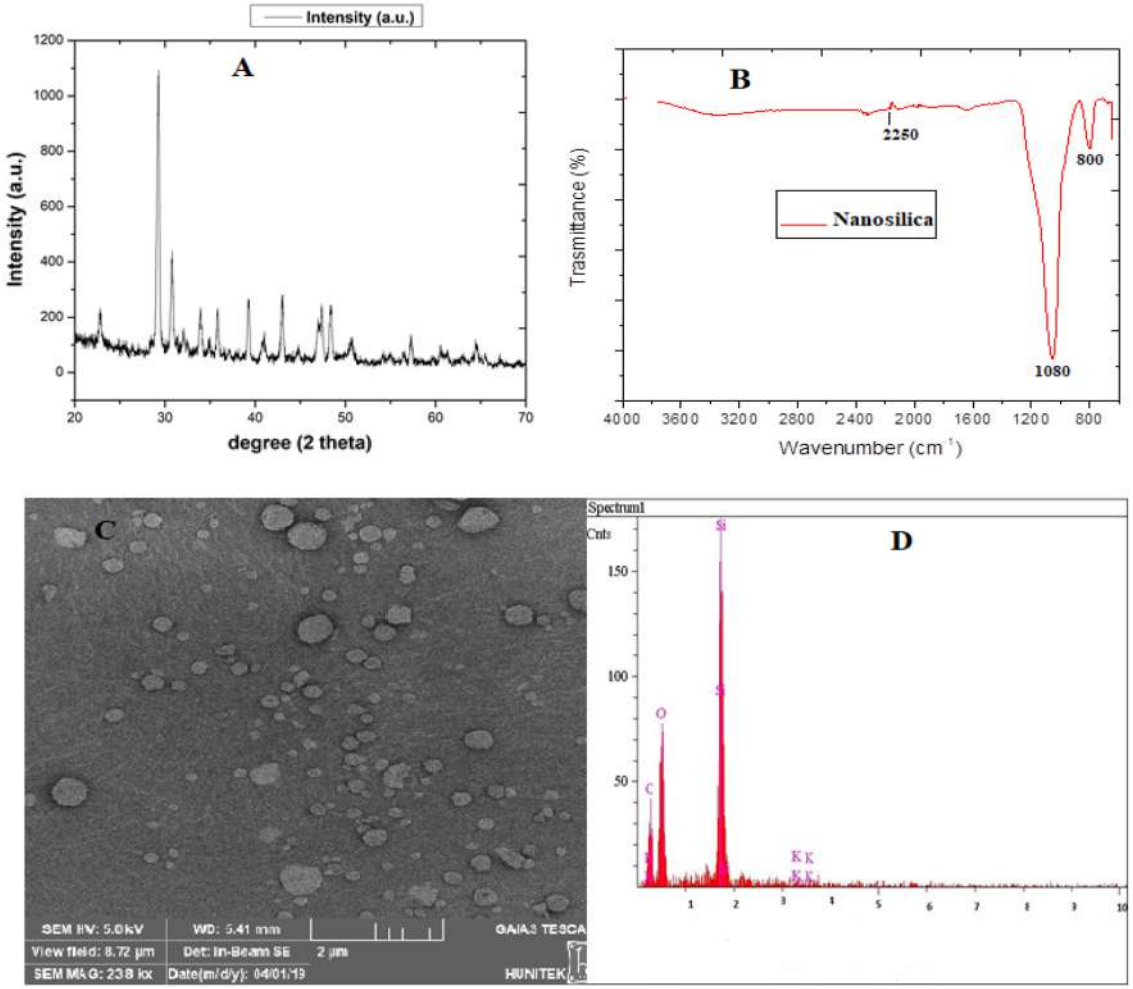

Fig. 3 **A** Xrd Images of Nanosilica, **B** Ftir of Nanosilica, **C** Sem Images of Nanoparticles, **D** Edx images of nanoparticles

Table 6 Synthesized barley grass nanosilica (SiO_2) properties

Property	
Density (kg/m^3)	2400
Thermal conductivity (W/m.K)	1.380
Specific heat capacity (J/kg.K)	968.9
Particle size (nm)	100

oxide (SiO_2) nanoparticles to the base refrigerants enhanced the evaporator's heat transfer rate.

The influence of evaporator temperature on the overall COP of the CVCRC is illustrated in Fig. 6, while the condenser temperature remains constant at 45 °C. The COP of the CVCRC increases as the evaporator temperature rises from − 55 °C to − 40 °C for all refrigerant pairs. The R1234ze/SiO_2-CO_2 refrigerant pair has the highest COP, with a 23.95% increase when the evaporator temperature is adjusted from − 55 °C to − 40 °C while the condenser

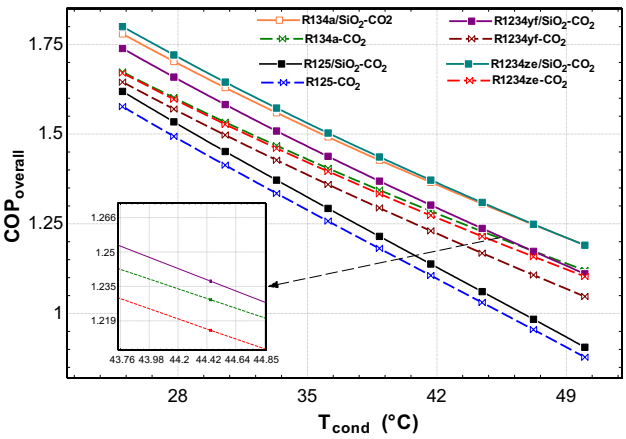

Fig. 4 Effect of condenser temperature on overall COP at $T_{evap} = -50$ °C

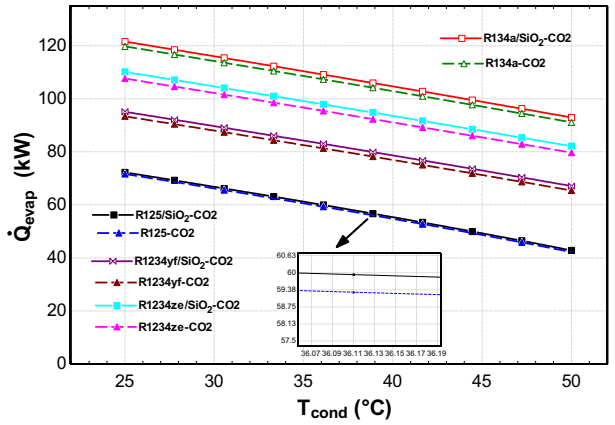

Fig. 5 Effect of Condenser Temperature on Evaporator load at $T_{evap} = -50$ °C

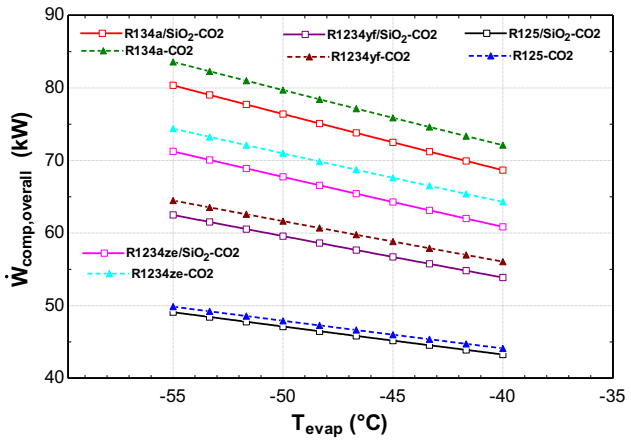

Fig. 7 Effect of Evaporator temperature on Overall compressor work ($T_{cond} = 45$ °C)

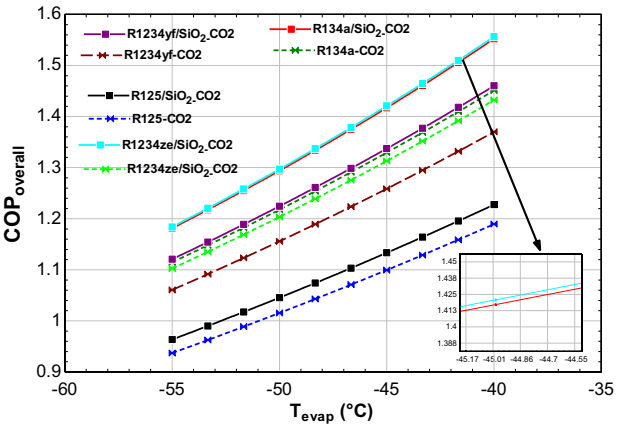

Fig. 6 Effects of Evaporator temperature on Overall COP at $T_{cond} = 45$ °C

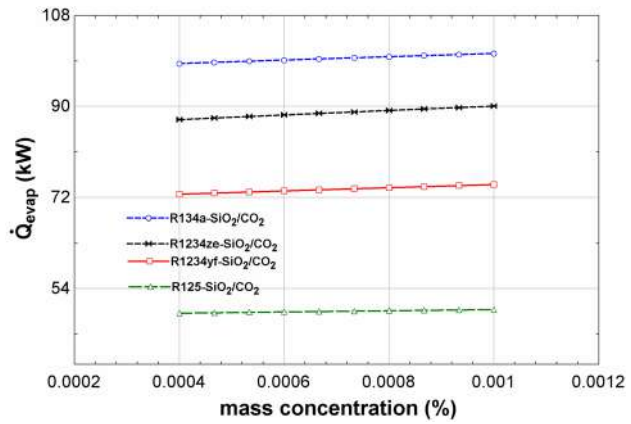

Fig. 8 Effect of mass concentration of nanoparticle on the refrigeration effect

temperature is kept at 45 °C. Krishnan et al. [41] reported a similar trend and observations in a similar investigation.

At a constant condenser temperature of 45 °C, Fig. 7 shows the effect of evaporator temperature on compressor work. As predicted, the compressor consumes less energy at higher evaporator temperatures while the condenser temperature remains constant. It was observed that compressor work decreased by adding silicon oxide (SiO_2) nanoparticles to the base refrigerants. A rise in COP was caused by an increase in Q_e and a decrease in W_{comp}, as per Eq. (4). This means that less energy is consumed for the same refrigeration capacity. Among the refrigerants investigated, R134a-CO_2 had the highest compressor work while R125/SiO_2-CO_2 had the lowest compressor work in all conditions at a constant condenser temperature.

Figure 8 depicts the effect of increasing the mass concentration of the SiO_2 nanoparticles on the refrigeration effect of the CVCRC. Increasing the mass concentration from 0.04% to 0.1% leads to an increase in the refrigeration effect. This is because more nanoparticles per unit mass of refrigerant improve the heat transfer coefficient and thus the cooling effect.

Figure 9 shows the influence of nanoparticle mass concentration on overall compressor work and COP of the CVCRC employing four different nanorefrigerants. For the four nanorefrigerants, the work of the compressor decreases as the mass concentration increases. The mobility of the nanoparticle within the nanorefrigerant contributes to the pressure of the nanorefrigerant, which requires the compressor to do less work to achieve the required condenser pressure. As a result, the quantity of work required by the compressor is greatly reduced. The COP increases as mass concentration rises. Because there are more nanoparticles per unit of refrigerant, the heat transfer coefficient and COP are greatly enhanced [42]. Odunfa and Oseni [42] likewise noted and documented this facts and pattern.

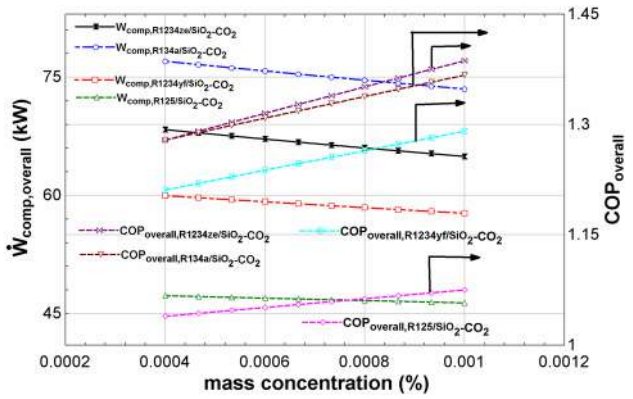

Fig. 9 Effect of mass concentration of the nanoparticles on the overall compressor work and COP

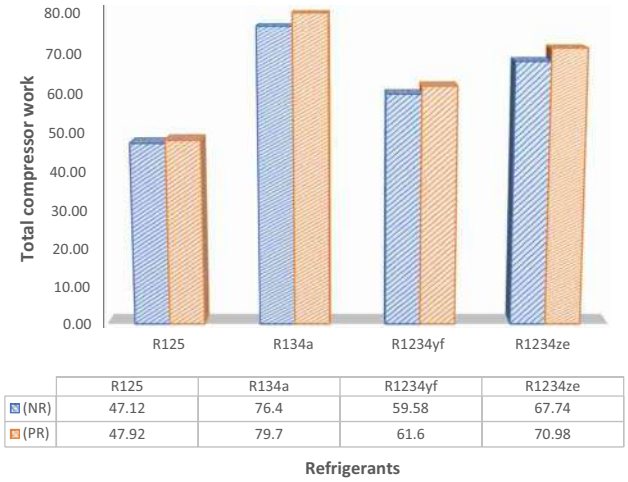

	R125	R134a	R1234yf	R1234ze
(NR)	47.12	76.4	59.58	67.74
(PR)	47.92	79.7	61.6	70.98

Fig. 11 Comparison of total compressor work for different refrigerant pairs

The CVCRC COP was determined to be 1.045, 1.015, 1.294, 1.218, 1.224, 1.156, 1.297, and 1.203 for R125/SiO2-CO2, R125-CO2, R134a/SiO2-CO2, R134a-CO2, R1234yf/SiO2-CO2, R1234yf-CO2, R1234ze/SiO2-CO2, and R1234ze-CO2 refrigerant. The results demonstrate that the best performing HFC refrigerant (with and without nanoparticles) is R134a, while the best performing fourth generation refrigerant (with and without nanoparticles) is R1234ze; exhibiting a very close margin to the best performing HFC refrigerant (Fig. 10).

In Fig. 11, it was observed that compressor work decreases by adding silicon oxide (SiO_2) nanoparticles to the base refrigerants. This occurs because the nanoparticles enhance heat transfer performances and decrease energy consumption in the compressor. From Fig. 8, it is seen that the usage of R125 nanorefrigerant in high temperature loop of the CVCRC system decreases compressor work by 1.66%, 4.1% when R134a nanorefrigerant is used, 3.27% when R1234yf nanorefrigerant is used and 4.56% when R1234ze nanorefrigerant is used.

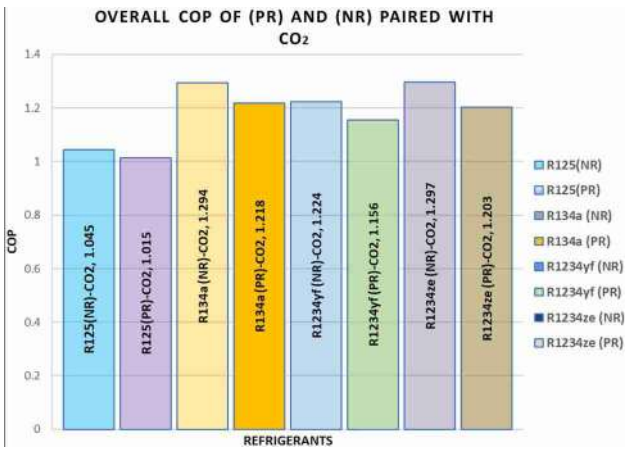

Fig. 10 COP comparison of the CVCRC for all cases of refrigerant couples ($T_{evap} = -50$ °C, $T_{cond} = 40$ °C)

Conclusion

Comparing the effects of adding SiO_2 nanoparticles to different refrigerants was carried out in this study. The nanosilica was synthesized from the agricultural waste of the barley plant. One major aim of the research was to synthesize the nanofluid using a sustainable means. A numerical model is adopted for the thermodynamic analysis of the system and the results were based on the coefficient of performance (COP), compressor work, mass concentration, evaporation heat, and condenser heat. It was difficult to determine the enthalpy of the nanorefrigerant due to the fact there is a scarcity of correlation or experimental data in this field. As a result, calculations for the enthalpy of nanorefrigerants in the refrigerant cycle were made using a density prediction method for nanorefrigerants. Findings from the study indicates that the thermal properties of refrigerant fluids are improved by adding nanoparticles, which increases the refrigeration system's performance.

In the cycles using nanorefrigerants, the COP was shown to be greater. R1234ze/SiO_2-CO_2 refrigerant couple had the highest COP, followed by the R134a/SiO_2-CO_2 under all of the conditions investigated in the study. Increasing the evaporator temperature from − 55 to − 40 °C led to an increase in the COP for all refrigerant pairs.

The results indicate that adding 0.05% mass concentration of SiO_2 nanoparticles to base refrigerants improves the overall performance of the CVCRC over pure-base refrigerants.

Addition of SiO_2 nanoparticles resulted to a reduction in compressor work. Despite the fact that R125 had the

lowest compressor work. In its place, R1234ze, the refrigerant with the second-lowest compressor work can be used, with the addition of SiO_2 compressor work is reduced to 59.58kW from 61.6 kW. It also has a GWP of 6, and may be successfully used in newly designed systems instead of R134a. The use of nanoparticles therefore, improves the refrigeration cycle's performance by improving heat transfer in heat exchangers and lowering the compressor's power consumption.

Moreover, the nanoparticle is likely dispersed in the liquid rather than the gas phase. Therefore, this work brings together a number of approximations and gives a useful tool for scholars to use in their work. Analytical models for predicting physical properties have gotten very little attention. More work will be required to make this study popular. Additionally, more investigation is still needed to determine how other nanoparticle properties affect a vapor compression refrigeration system.

References

1. Mahbubul, I.M., Saidur, R., Amalina, M.A.: Influence of particle concentration and temperature on thermal conductivity and viscosity of Al2O3/R141b nanorefrigerant. Int. Commun. Heat Mass Transf. **43**, 100–104 (2013)
2. Adebayo, V., Abid, M., Adedeji, M., Dagbasi, M., Bamisile, O.: Comparative thermodynamic performance analysis of a cascade refrigeration system with new refrigerants paired with CO2. Appl. Therm. Eng. (2020). https://doi.org/10.1016/j.applthermaleng.2020.116286
3. Kumar, V.: Comparative analysis of cascade refrigeration system based on energy and exergy using different refrigerant Pairs. J. Therm. Eng. **6**(1), 106–116 (2020)
4. Sanukrishna, S.S., Vishnu, A.S.: Nanorefrigerants for energy efficient refrigeration systems. J. Mech. Sci. Technol. **31**(8), 3993–4001 (2017)
5. Aktas, M., Dalkilic, A.S., Celen, A., Cebi, A., Mahian, O., Wongwises, S.: A theoretical comparative study on nanorefrigerant performance in a single-stage vapor-compression refrigeration cycle. Adv. Mech. Eng. **7**(1), 138725 (2015)
6. Celen, A., Çebi, A., Aktas, M., Mahian, O., Dalkilic, A.S., Wongwises, S.: A review of nanorefrigerants: flow characteristics and applications. Int. J. Refrig. **44**, 125–140 (2014)
7. Fang, X., Wang, R., Chen, W., Zhang, H., Ma, C.: A review of flow boiling heat transfer of nanofluids. Appl. Therm. Eng. **91**, 1003–1017 (2015)
8. Sun, B., Yang, D.: Flow boiling heat transfer characteristics of nano-refrigerants in a horizontal tube. Int. J. Refrig. **38**, 206–214 (2014)
9. Alawi, O.A., Sidik, N.A.C., Kherbeet, A.S.: Nanorefrigerant effects in heat transfer performance and energy consumption reduction: a review. Int. Commun. Heat Mass Transf. **69**, 76–83 (2015)
10. Gupta, S., Karanam, N.K., Konijeti, R., Dasore, A.: Thermodynamic analysis and effects of replacing HFC by fourth-generation refrigerants in VCR systems. Int. J. Air-Conditioning Refrig. **26**(02), 1850013 (2018)
11. Perkins, J.: Apparatus for producing ice and cooling fluids. Br. Pat., no. 6662, 1834
12. Nagengast, B.A.: A history of refrigerants. CFCs Time Transit. (1989)
13. de Chazournes, L.B.: Kyoto protocol to the united nations framework convention on climate change. UN's Audiov. Libr. Int. Law (http//untreaty. un. org/cod/avl/ha/kpccc/kpccc. html). (1998)
14. Montzka, S.A., Hall, B.D., Elkins, J.W.: Accelerated increases observed for hydrochlorofluorocarbons since 2004 in the global atmosphere. Geophys. Res. Lett. (2009). https://doi.org/10.1029/2008GL036475
15. Fluorochemicals, D.: DuPont fluorochemicals develops next generation refrigerants–new sustainable alternatives would offer practical solutions. Press Release. Wilmington, DE, USA (09.02. 06). (2006)
16. Kasaeian, A., Hosseini, S.M., Sheikhpour, M., Mahian, O., Yan, W.-M., Wongwises, S.: Applications of eco-friendly refrigerants and nanorefrigerants: a review. Renew. Sustain. Energy Rev. **96**, 91–99 (2018)
17. Subramani, N., Prakash, M.J.: Experimental studies on a vapour compression system using nanorefrigerants. Int. J. Eng. Sci. Technol. **3**(9), 95–102 (2011)
18. Jwo, C.S., Jeng, L.Y., Teng, T.P., Chang, H.: Effects of nanolubricant on performance of hydrocarbon refrigerant system. J. Vac. Sci. Technol. B Microelectron. Nanom. Struct. Process. Meas. Phenom. **27**(3), 1473–1477 (2009)
19. Peng, H., Ding, G., Jiang, W., Hu, H., Gao, Y.: Measurement and correlation of frictional pressure drop of refrigerant-based nanofluid flow boiling inside a horizontal smooth tube. Int. J. Refrig. **32**(7), 1756–1764 (2009)
20. Kedzierski, M.A.: Effect of CuO nanoparticle concentration on R134a/lubricant pool-boiling heat transfer. J. Heat Transf. (2009). https://doi.org/10.1115/1.3072926
21. Bi, S., Shi, L., Zhang, L.: Application of nanoparticles in domestic refrigerators. Appl. Therm. Eng. **28**(14–15), 1834–1843 (2008)
22. Sabareesh, R.K., Gobinath, N., Sajith, V., Das, S., Sobhan, C.B.: Application of TiO2 nanoparticles as a lubricant-additive for vapor compression refrigeration systems–an experimental investigation. Int. J. Refrig. **35**(7), 1989–1996 (2012)
23. Javadi, F.S., Saidur, R.: Energetic, economic and environmental impacts of using nanorefrigerant in domestic refrigerators in Malaysia. Energy Convers. Manag. **73**, 335–339 (2013)
24. Wang, R. X., Hao, B., Xie, G.Z., Li, H.Q.: A refrigerating system using HFC134a and mineral lubricant appended with n-TiO2 (R) as working fluids. In: Proceedings of the 4th International Symposium on HAVC, Tsinghua University Press, Beijing, China, 2003, pp. 888–892
25. Li, P., Wu, X., Li, H., Wang, W.: Investigation of Pool boiling heat transfer of R11 with TiO~ 2 nano-particles. J. Eng. Thermophys. **29**(1), 124 (2008)
26. Mahbubul, I.M., Saadah, A., Saidur, R., Khairul, M.A., Kamyar, A.: Thermal performance analysis of Al2O3/R-134a nanorefrigerant. Int. J. Heat Mass Transf. **85**, 1034–1040 (2015)
27. Kumar, D.S., Elansezhian, R.: ZnO nanorefrigerant in R152a refrigeration system for energy conservation and green environment. Front. Mech. Eng. **9**(1), 75–80 (2014)
28. Kumar, V.P.S., Baskaran, A., Subaramanian, K.M.: A performance study of vapour compression refrigeration system using ZrO2 nano particle with R134a and R152a". Int. J. Sci. Res. Publ. **6**, 410–421 (2016)
29. Coumaressin, N.A.T., Palaniradja, K.: Experimental Analysis of a Refrigeration system using Al2O3/CuO/TiO2/ZnO-R1234yf Nanofluids as refrigerant. Int. J. Res. Eng. Appl. Manag. **4**(08), 69–75 (2018)
30. Bhattacharya, M., Mandal, M.K.: Synthesis of rice straw extracted nano-silica-composite membrane for CO2 separation. J. Clean. Prod. **186**, 241–252 (2018)

31. Essien, E.A., Kavaz, D.: Effective and reusable nano-silica synthesized from barley and wheat grass for the removal of nickel from agricultural wastewater. Environ. Sci. Pollut. Res. **26**(25), 25802–25813 (2019)
32. Akhayere, E., Vaseashta, A., Kavaz, D.: Novel magnetic nano silica synthesis using barley husk waste for removing petroleum from polluted water for environmental sustainability. Sustain. **12**(24), 1–16 (2020). https://doi.org/10.3390/su122410646
33. Handbook, A.: ASHRAE handbook–fundamentals. Atlanta, GA. (2009)
34. McLinden, M.J.O., Thol, M., Lemmon, E.W.: Thermodynamic properties of trans-1, 3, 3, 3-tetrafluoropropene [R1234ze (E)]: measurements of density and vapor pressure and a comprehensive equation of state. (2010)
35. Steven Brown, P.E.J.: Methodology for estimating thermodynamic parameters and performance of alternative refrigerants. ASHRAE Trans. **114**: 230 (2008)
36. Steven Brown, P.E.J.: HFOs: new, low global warming potential refrigerants. ASHRAE J. **51**(8), 22 (2009)
37. Di Nicola, C., Di Nicola, G., Pacetti, M., Polonara, F., Santori, G.: P− V− T Behavior of 2, 3, 3, 3-Tetrafluoroprop-1-ene (HFO-1234yf) in the vapor phase from (243 to 373) K. J. Chem. Eng. Data. **55**(9), 3302–3306 (2010)
38. Del Col, D., Torresin, D., Cavallini, A.: Heat transfer and pressure drop during condensation of the low GWP refrigerant R1234yf. Int. J. Refrig. **33**(7), 1307–1318 (2010)
39. Xuan, Y., Roetzel, W.: Conceptions for heat transfer correlation of nanofluids. Int. J. Heat Mass Transf. **43**(19), 3701–3707 (2000)
40. Hussin, M.H.C., Mahadi, M.A.S., Sanuddin, A., Khalil, A.N.M., Rahim, Y.A.: Experimental performance of R134a/SiO2 in refrigeration system for domestic use. J. Adv. Res. Fluid Mech. Therm. Sci. **95**(1), 145–163 (2022)
41. Krishnan, B.P., Vijayan, R., Gokulnath, K.: Performance analysis of a nano refrigerant mixtures in a domestic refrigeration system. Adv. Nat. Appl. Sci. **11**(6), 508–516 (2017)
42. Odunfa, M.K., Oseni, O.D.: Numerical simulation and performance assessment of a nanoparticle enhanced vapour compression refrigeration system. J. Power Energy Eng. **9**(11), 33–49 (2021)

International Journal of Energy and Environmental Engineering (2023) 14:871–887
https://doi.org/10.1007/s40095-022-00553-x

ORIGINAL RESEARCH

Solar drying in a ventilated attic: case study of cassava slices

Zokagon Aristide Tieu[1,2] · Paul Magloire Ekoun Koffi[2] · Abé Simon Yapi[1] · Prosper Gbaha[2]

Received: 7 April 2022 / Accepted: 19 November 2022 / Published online: 15 December 2022

Abstract

In constantly sunny regions of the world such as most African countries, due to the availability of sunlight, metal roofs that are constantly exposed to the sun offer opportunities for many solar thermal applications. This study focuses on the numerical and experimental investigation of solar drying in a ventilated attic. The constructed prototype attic has three PVC pipes used as chimneys, and the roof is painted black. It was modeled using the equations of heat and mass transfers occurring during drying. The food commodity subjected to drying was cassava. The resulting system of equations was solved using the classical fourth-order Runge–Kutta method. The MATLAB R2014a language is used for the simulations. The drying of 6 kg of cassava in the prototype took 3 days. The obtained experimental results were compared with the theoretical points. The mean relative error ($E\%$) was used as a parameter for model validation. Its values of less than 14% obtained for temperatures and humidities are evidence that the theoretical points accurately represented the behavior of the attic during solar drying. The drying efficiency varied from 25% on the first day to 0.2% on the last day. The calculated payback period is 2 months. This method can be easily implemented and would be helpful to farmers in rural Africa.

Keywords Solar drying · Ventilated attic · Modeling · Heat transfer · Mass transfer · Cassava

List of symbols

a	Constant (4×10^{-5}), accuracy
C	Specific heat (J/kg K), difference between initial and final moisture contents (kg/kg db)
D	Diameter (m)
e	Thickness (m)
F	Geometrical factor
G	Solar radiation (W/m^2)
$G(i,\gamma)$	Global solar radiation on tilted surface ($i=10°$: tilt angle, ($\gamma=0$: azimuth angle) (W/m^2)
G_r	Grashof number
g	Acceleration of gravity (N/kg)
Hr	Relative humidity (%)
h	Coefficient of heat exchange (W/m^2 k), hour angle (°)
i	Angle (°), ith observations
K	Runge–Kutta parameter
K_T	Daily clearness index
L	Length (m), latitude (°)
LL	Local longitude (°)
LST	Local standard time (time shown by our clocks)
L_{vap}, L_v	Latent heat of evaporation (J/kg)
MRE	Mean relative error (%)
M_{ev}	Mass of water evaporated (kg)
m	Mass (kg)
$\dot{m}$	Air mass flow rate (kg/s)
N	Number of observations
N_u	Nusselt number
n	nTh iteration of Runge–Kutta, number of the days in the year
P	Pressure (Pa), perimeter (m)
$Ps(T)$	Pressure of the vapor in the saturation state (mmHg)
P_r	Prandtl number
R_B	Beam radiation tilt factor
R_a	Rayleigh number
S	Surface (m^2)
SL	Standard longitude (°)
T	Temperature (°C, K)
t	Time step (s)
(t)	Instantaneous
U	Overall heat loss (W/m^2 K)
V	Air speed (m/s), volume (m^3)

✉ Zokagon Aristide Tieu
tieu_aristide@yahoo.fr

[1] Laboratoire de Technologie, Université Félix Houphouet-Boigny, 22 BP 582 Abidjan 22, Abidjan, Côte d'Ivoire

[2] Laboratoire d'Energie Nouvelle et Renouvelable, Institut National Polytechnique Félix Houphouet-Boigny, BP 581 Yamoussoukro, Côte d'Ivoire

X Cassava moisture content (kg/kg db)
Y Air absolute humidity (kg/kg)

Greek letters

α Absorptivity, air thermal diffusivity (m^2/s)
β Reverse of the average temperature (k^{-1})
ρ_G Ground albedo
η Efficiency (%)
σ Stefan–Boltzmann constant (5.67×10^{-8} W/(m^2 K^4))
λ Conductivity (W/m K)
δ Declination (°)
μ Dynamic viscosity (Pa s)
ν Air kinetic viscosity (m^2/s)

Subscripts

0 Anhydrous cassava, extraterrestrial
a Air, ambient
B Beam
D Diffuse
b Of the plywood
*b*1 Upper face of the vertical plywood on the shelves
*b*2 Lower face of the vertical plywood on the shelves
*b*1*pr* From upper face of the vertical plywood on the shelves towards cassava slices
*b*2*pr* From lower face of the vertical plywood on the shelves towards cassava slices
c Of the roof
cab By convection under the ceiling and outside air
*cb*1 From the roof towards upper face of the vertical plywood on the shelves
cbe By conduction in the plywood of the ceiling
*cb*1*f* By convection between upper face of the vertical plywood on the shelves and drying air
*cb*2*f* By convection between lower face of the vertical plywood on the shelves and drying air
cce By convection between the roof and outside air
ccf By convection between the roof and drying air
cpr Between the roof and the floor
cprf By convection between cassava slices and drying air
cplf By convection between drying air and the floor
cv From the roof towards heaven vault
exp Experimental
f Of drying air
h Hydraulic
i *i*Th observation
o Outside
pl Of the Floor
*plb*2 From the floor towards lower face of the vertical plywood on the shelves
plpr From the floor towards cassava slices.
po Of polystyrene
pr Of cassava slices
theor Theoretical
v Of heaven vault, of vaporization, vapor

Introduction

The sun is a real blessing for the world and in particular for many African countries [1]. Mastering all its applications such as drying, steam and electricity production, water distillation and desalination, heating, cooling and refrigeration would contribute to the development of the continent. It is free, inexhaustible and always available. If sufficiently exploited, many of the world's energy supply problems would be solved. The biggest advantage of solar energy over other forms of energy is that it is clean and can be supplied without polluting the environment [2]. On the other hand, for most of the world's developing countries, the best way to reduce hunger is to fight food loss. Cassava accounts for 32% of the world's production of roots and tubers, which are crucial foods in poor countries. It is a food widely consumed in sub-Saharan Africa and in Asian and Latin American countries. In its raw state, it is a perishable and heavy product, as it has a high water content, which makes storage and long-distance trade complicated and expensive. Drying the roots is the simplest method of preservation. The main market for dry cassava is food, feed, as well as industrial food and non-food uses. Nigeria was by far the world's largest producer of cassava with more than 51 million tons per year, followed by Thailand with about 30 million tons per year. But today, Cambodia is the leader. Côte d'Ivoire is the 10th world producer [3]. In rural areas of Africa, most people are not aware of the existence of appropriate methods for processing their products. Therefore, they face great losses of their crops. Traditional sun drying is the most common use of solar radiation on the continent. Due to the dust generated on the crops, the non-uniform drying, the attack of rodents, domestic animals and thieves, this method must be abandoned. Time must also be spent monitoring the crops during rainfall [4]. The poor-quality products that often result from this drying method are difficult to preserve and sell on the market. This keeps farmers poor. Conventional dryers that use fossil fuels or electric power to heat the air are not appropriate because of their cost, and burning fossil fuels has bad environmental impacts. The less expensive method that facilitates the drying process increases the quality of the dried products and their market value is the use of solar dryers [5, 6]. As many developing countries are concerned with this problem, more and more researches are being done on solar dryers. Norton [7] presented a review on solar dryers; he demonstrated that

Table 1 Heat transfer equations in the different parts of the prototype

Heat transfers in the roof

$$m_c C_c \frac{dT_c}{dt} = \alpha S_c G(i,\gamma) - \sigma F_{cpr} S_c \left(T_c{}^4 - T_{pr}{}^4\right) - \sigma F_{cv} S_c \left(T_c{}^4 - T_v{}^4\right) - \sigma F_{cb1} S_c (T_c{}^4 - T_{b1}{}^4) - h_{ccf} S_c \left(T_c - T_f\right) - h_{cce} S_c \left(T_c - T_a\right) \quad (1)$$

Heat transfers in drying air

$$m_f C_f \frac{dT_f}{dt} = \dot{m}_a c_a \left(T_a - T_f\right) + m_0 C_{\text{vap}} (T_f - T_{pr}) \frac{dX}{dt} + h_{ccf} S_c \left(T_c - T_f\right) + h_{cprf} S_{pr} \left(T_{pr} - T_f\right) + h_{cplf} S_{pl} \left(T_{pl} - T_f\right) + h_{cb1f} S_b \left(T_{b1} - T_f\right) - m_0 \frac{dX}{dt} L_{\text{vap}} \quad (2)$$

Heat transfers in cassava slices

$$m_{pr} C_{pr} \frac{dT_{pr}}{dt} = \sigma F_{cpr} S_{pr} \left(T_c^4 - T_{pr}^4\right) + \sigma F_{b1pr} S_{pr} \left(T_{b1}^4 - T_{pr}^4\right) + \sigma F_{b2pr} S_{pr} \left(T_{b2}^4 - T_{pr}^4\right) + \sigma F_{plpr} S_{pr} \left(T_{pl}^4 - T_{pr}^4\right) + h_{cprf} S_{pr} \left(T_f - T_{pr}\right) + \frac{\lambda_{pr}}{e_{pr}} S_{pr} \left(T_f - T_{pr}\right) + m_0 \frac{dX}{dt} L_{\text{vap}} \quad (3)$$

Heat transfer in the vertical parts of the drying shelves

$$\frac{m_b C_b}{2} \frac{dT_{b1}}{dt} = \sigma F_{b1pr} S_b \left(T_{pr}^4 - T_{b1}^4\right) + \sigma F_{cb1} S_c \left(T_c^4 - T_{b1}^4\right) + h_{cb1f} S_b \left(T_f - T_{b1}\right) + \frac{\lambda_b}{e_b} S_b \left(T_{b2} - T_{b1}\right) \quad (4)$$

$$\frac{m_b C_b}{2} \frac{dT_{b2}}{dt} = \sigma F_{b2pr} S_b \left(T_{pr}^4 - T_{b2}^4\right) + \sigma F_{plb2} S_{pl} \left(T_{pl}^4 - T_{b2}^4\right) + \frac{\lambda_b}{e_b} S_b \left(T_{b1} - T_{b2}\right) + h_{cb2f} S_b \left(T_f - T_{b2}\right) \quad (5)$$

Heat transfers in the ceiling

$$m_{pl} c_{pl} \frac{dT_{pl}}{dt} = \sigma F_{plpr} S_{pl} \left(T_{pr}^4 - T_{pl}^4\right) + h_{cplf} S_{pl} \left(T_f - T_{pl}\right) + U_{pl} S_{pl} \left(T_a - T_{pl}\right) - \sigma F_{plb2} S_{pl} \left(T_{pl}^4 - T_{b2}^4\right) \quad (6)$$

effective solar drying must take into account climatic conditions, preparation and crop characteristics in the design of the solar dryer. Azwin et al. [8] review the work on the use of solar thermal energy in the drying process; they outlined the advantages of using solar dryers and presented some improvements to make them more efficient. Mallikarjuna et al. [9] presented a paper in which the experimental results obtained from solar drying of green chili and okra in an indirect solar dryer were presented. They also calculated the yields of the solar collector and the drying efficiency. Cetina-Quinones et al. [10] studied the performance of two thermal storage materials (limestone and beach sand) in an indirect solar dryer; they noticed that limestone performs better than beach sand. Purusothamana and Valarmathi [11] performed a numerical study of a greenhouse solar dryer; they noticed that with forced convection, the temperature in the dryer is higher than with natural convection. Tomar et al. [12] studied different solar dryers for tropical foods. Benaouda et al. [13] performed an experimental study on a forced convection solar dryer. They then developed a mathematical model for their device. It should be noted that a new trend in the study of solar dryers is the use of numerical methods. The goal is to predict the behavior of a particular crop during solar drying or the thermal behavior of solar dryers as a function of climatic conditions. Several numerical models have therefore been developed by many researchers. Merlin Simo et al. [14] and other researchers [15, 16] have presented many works on numerical methods for solar drying of wood and for solar drying of foodstuffs [17–19]. Mondaca et al. [20] developed a numerical model for the drying of papaya slices; the comparison of experimental results with theoretical results was used for the validation of the model. Tieu et al. [4] used the fourth-order Runge–Kutta method to model the moisture growth in the drying air for solar drying of cassava. Many other research papers such as [21–24] discuss the use of established semi-empirical models to predict the drying kinetics of different crops. The sun is always present in Côte d'Ivoire as well as in many other African countries, and the metal roofs always exposed to the sun are a real source of energy. They can be used for drying food crops. To date, no scientific study dealing with the use of ventilated attics for solar drying has been reported elsewhere, except by this author [4, 24]. In this study, a numerical approach is used to predict the thermal behavior of a ventilated attic during solar drying of cassava slices. The thermal performance of the prototype is also evaluated. The setup is the one used in [4]. The heat transfer and mass transfer equations are used for modeling. The experimental results obtained during the solar drying of cassava in the device are compared to the predicted points for the model validation. In order to show its advantages over the traditional method, the prototype is then compared to the traditional solar drying through an economic study and an efficiency comparison.

Material and methods

Design of the prototype ventilated attic

The prototype used is presented in Fig. 1. It is covered with a blackened corrugated aluminum-zinc sheet. Three PVC pipes, 1.5 m high and 50 mm in diameter each, are used as chimneys and separated of 34.5 cm to each other. The sides and the ceiling are made with 10-mm-thick plywood.

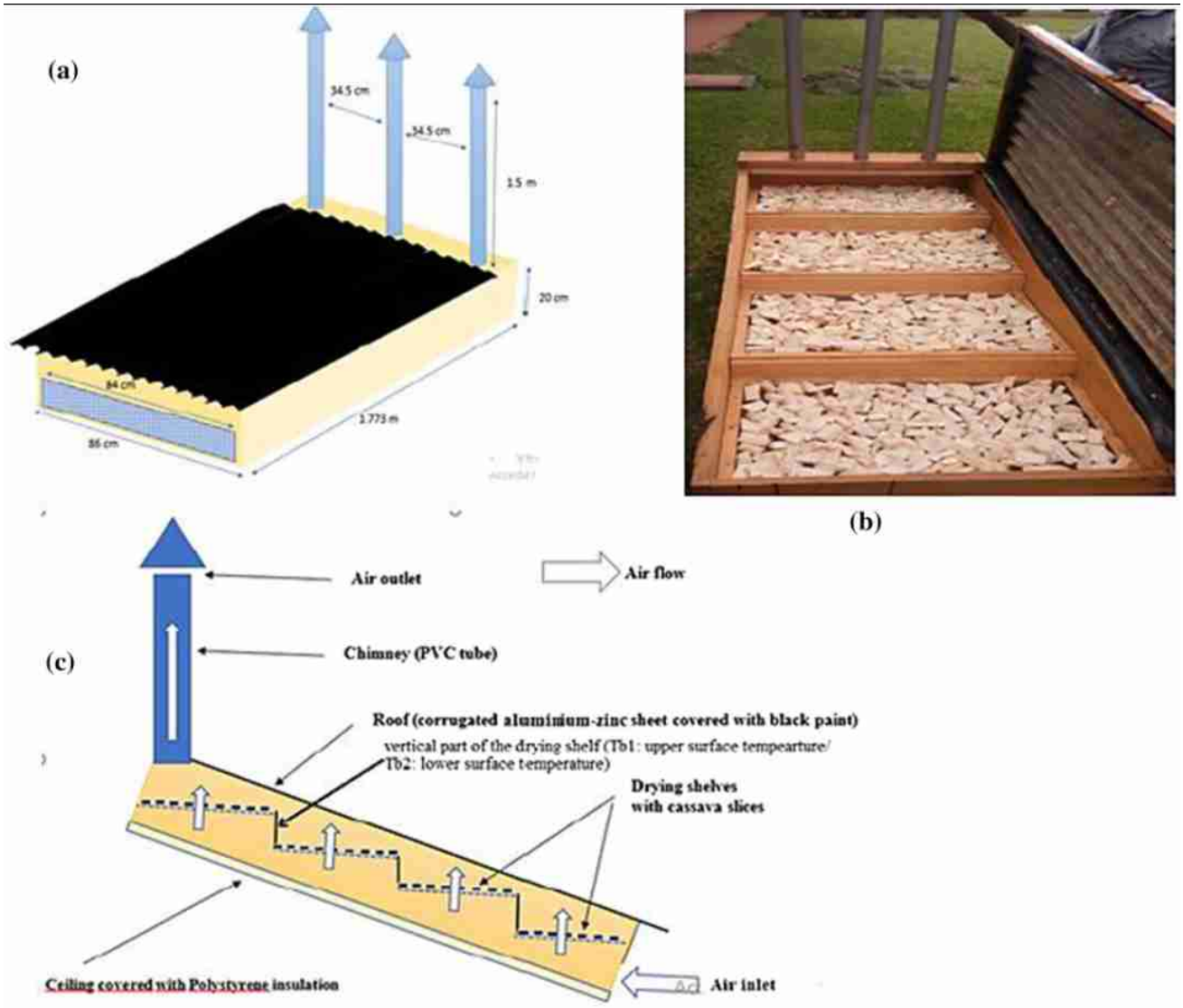

Fig. 1 **a** Overview, **b** inside of the prototype with cassava slices and **c** profile view of the prototype ventilated attic [4]

There are four drying shelves in the attic, made with nylon net fixed on a wooden frame of 44.3 cm × 84 cm dimensions. They are arranged like stairs along the roof and separated by vertical plywood to prevent moist air of the lower shelf from passing through the one above. Each one is charged with 1.5 kg of cassava slices. The ceiling is covered with an 8-cm-thick layer of polystyrene to impede heat from crossing it. The space under and on the trays allows free air circulation by natural convection. The prototype is 1.773 m long, 0.86 m large. The air inlet has a surface of 84 cm × 4 cm. and the whole thing is mounted on a 2.5-m height support and tilted southward at $i = 10°$. We stop drying when we no longer see any change in the weight of cassava.

Mathematical modeling of the prototype

Simplification assumptions

- All components of the prototype are homogeneous.
- The characteristic of air is constant in the attic.
- Temperature and moisture content of the cassava are uniform in the attic.
- Conductive heat transfer between the cassava slices and the drying shelves is neglected.
- Only the temperatures of the roof, drying air, cassava and the floor are concerned as well as the relative humidity of the drying air and the moisture content of the cassava.

Heat transfer equations

Heat transfer in the attic components occurs by convection, radiation and conduction. For the heat transfer equations, we use the method of Simo-Tagne et al. [18]. They are given in Table 1.

Mass transfers in the attic

See Table 2.

Runge–Kutta method for heat transfer equations

The Runge–Kutta algorithm for heat transfer is given as follows after giving initial conditions (the system of equations and functions used are defined in "Appendix" section):

$$\begin{cases} K_{11}=h*f(T_{cn},T_{prn},T_{fn},T_{b1n},T_{b2n},T_{pln},t_n) \\ K_{21}=h*g(T_{cn},T_{prn},T_{fn},T_{b1n},T_{b2n},T_{pln},t_n) \\ K_{31}=h*l(T_{cn},T_{prn},T_{fn},T_{b1n},T_{b2n},T_{pln},t_n) \\ K_{41}=h*m(T_{cn},T_{prn},T_{fn},T_{b1n},T_{b2n},T_{pln},t_n) \\ K_{51}=h*n(T_{cn},T_{prn},T_{fn},T_{b1n},T_{b2n},T_{pln},t_n) \\ K_{61}=h*p(T_{cn},T_{prn},T_{fn},T_{b1n},T_{b2n},T_{pln},t_n) \end{cases} \tag{17}$$

$$\begin{cases} K_{12}=h*f(T_{cn}+\frac{K_{11}}{2},T_{prn}+\frac{K_{21}}{2},T_{fn}+\frac{K_{31}}{2},T_{b1n}+\frac{K_{41}}{2},T_{b2n}+\frac{K_{51}}{2},T_{pln}+\frac{K_{61}}{2},t_n+\frac{h}{2}) \\ K_{22}=h*g(T_{cn}+\frac{K_{11}}{2},T_{prn}+\frac{K_{21}}{2},T_{fn}+\frac{K_{31}}{2},T_{b1n}+\frac{K_{41}}{2},T_{b2n}+\frac{K_{51}}{2},T_{pln}+\frac{K_{61}}{2},t_n+\frac{h}{2}) \\ K_{32}=h*l(T_{cn}+\frac{K_{11}}{2},T_{prn}+\frac{K_{21}}{2},T_{fn}+\frac{K_{31}}{2},T_{b1n}+\frac{K_{41}}{2},T_{b2n}+\frac{K_{51}}{2},T_{pln}+\frac{K_{61}}{2},t_n+\frac{h}{2}) \\ K_{42}=h*m(T_{cn}+\frac{K_{11}}{2},T_{prn}+\frac{K_{21}}{2},T_{fn}+\frac{K_{31}}{2},T_{b1n}+\frac{K_{41}}{2},T_{b2n}+\frac{K_{51}}{2},T_{pln}+\frac{K_{61}}{2},t_n+\frac{h}{2}) \\ K_{52}=h*n(T_{cn}+\frac{K_{11}}{2},T_{prn}+\frac{K_{21}}{2},T_{fn}+\frac{K_{31}}{2},T_{b1n}+\frac{K_{41}}{2},T_{b2n}+\frac{K_{51}}{2},T_{pln}+\frac{K_{61}}{2},t_n+\frac{h}{2}) \\ K_{62}=h*p(T_{cn}+\frac{K_{11}}{2},T_{prn}+\frac{K_{21}}{2},T_{fn}+\frac{K_{31}}{2},T_{b1n}+\frac{K_{41}}{2},T_{b2n}+\frac{K_{51}}{2},T_{pln}+\frac{K_{61}}{2},t_n+\frac{h}{2}) \end{cases} \tag{18}$$

$$\begin{cases} K_{13}=h*f(T_{cn}+\frac{K_{12}}{2},T_{prn}+\frac{K_{22}}{2},T_{fn}+\frac{K_{32}}{2},T_{b1n}+\frac{K_{42}}{2},T_{b2n}+\frac{K_{52}}{2},T_{pln}+\frac{K_{62}}{2},t_n+\frac{h}{2}) \\ K_{23}=h*g(T_{cn}+\frac{K_{12}}{2},T_{prn}+\frac{K_{22}}{2},T_{fn}+\frac{K_{32}}{2},T_{b1n}+\frac{K_{42}}{2},T_{b2n}+\frac{K_{52}}{2},T_{pln}+\frac{K_{62}}{2},t_n+\frac{h}{2}) \\ K_{33}=h*l(T_{cn}+\frac{K_{12}}{2},T_{prn}+\frac{K_{22}}{2},T_{fn}+\frac{K_{32}}{2},T_{b1n}+\frac{K_{42}}{2},T_{b2n}+\frac{K_{52}}{2},T_{pln}+\frac{K_{62}}{2},t_n+\frac{h}{2}) \\ K_{43}=h*m(T_{cn}+\frac{K_{12}}{2},T_{prn}+\frac{K_{22}}{2},T_{fn}+\frac{K_{32}}{2},T_{b1n}+\frac{K_{42}}{2},T_{b2n}+\frac{K_{52}}{2},T_{pln}+\frac{K_{62}}{2},t_n+\frac{h}{2}) \\ K_{53}=h*n(T_{cn}+\frac{K_{12}}{2},T_{prn}+\frac{K_{22}}{2},T_{fn}+\frac{K_{32}}{2},T_{b1n}+\frac{K_{42}}{2},T_{b2n}+\frac{K_{52}}{2},T_{pln}+\frac{K_{62}}{2},t_n+\frac{h}{2}) \\ K_{63}=h*p(T_{cn}+\frac{K_{12}}{2},T_{prn}+\frac{K_{22}}{2},T_{fn}+\frac{K_{32}}{2},T_{b1n}+\frac{K_{42}}{2},T_{b2n}+\frac{K_{52}}{2},T_{pln}+\frac{K_{62}}{2},t_n+\frac{h}{2}) \end{cases} \tag{19}$$

$$\begin{cases} K_{14}=h*f(T_{cn}+K_{13},T_{prn}+K_{23},T_{fn}+K_{33},T_{b1n}+K_{43},T_{b2n}+K_{53},T_{pln}+K_{63},t_n+h) \\ K_{24}=h*g(T_{cn}+K_{13},T_{prn}+K_{23},T_{fn}+K_{33},T_{b1n}+K_{43},T_{b2n}+K_{53},T_{pln}+K_{63},t_n+h) \\ K_{34}=h*l(T_{cn}+K_{13},T_{prn}+K_{23},T_{fn}+K_{33},T_{b1n}+K_{43},T_{b2n}+K_{53},T_{pln}+K_{63},t_n+h) \\ K_{44}=h*m(T_{cn}+K_{13},T_{prn}+K_{23},T_{fn}+K_{33},T_{b1n}+K_{43},T_{b2n}+K_{53},T_{pln}+K_{63},t_n+h) \\ K_{54}=h*n(T_{cn}+K_{13},T_{prn}+K_{23},T_{fn}+K_{33},T_{b1n}+K_{43},T_{b2n}+K_{53},T_{pln}+K_{63},t_n+h) \\ K_{64}=h*p(T_{cn}+K_{13},T_{prn}+K_{23},T_{fn}+K_{33},T_{b1n}+K_{43},T_{b2n}+K_{53},T_{pln}+K_{63},t_n+h) \end{cases} \tag{20}$$

$$\begin{cases} T_{c(n+1)}=T_{cn}+\frac{1}{6}(K_{11}+2K_{12}+2K_{13}+K_{14}) \\ T_{pr(n+1)}=T_{prn}+\frac{1}{6}(K_{21}+2K_{22}+2K_{23}+K_{24}) \\ T_{f(n+1)}=T_{fn}+\frac{1}{6}(K_{31}+2K_{32}+2K_{33}+K_{34}) \\ T_{b1(n+1)}=T_{b1n}+\frac{1}{6}(K_{41}+2K_{42}+2K_{43}+K_{44}) \\ T_{b2(n+1)}=T_{b2n}+\frac{1}{6}(K_{51}+2K_{52}+2K_{53}+K_{54}) \\ T_{pl(n+1)}=T_{cn}+\frac{1}{6}(K_{61}+2K_{62}+2K_{63}+K_{64}) \end{cases} \tag{21}$$

$$t_{n+1} = n * h; \quad n = n + 1 \tag{22}$$

A MATLAB language in the version R2014a was used for generation of the results. And values calculated were saved in an excel sheet.

Heat transfer coefficients

See Table 3.

Other variables and constants involved in the equations

Geometrical factors

For ease of calculation, it is assumed that each horizontal portion of the drying shelves, the vertical plywood on the left and the roof portion above form a three-sided enclosure, and the following expression is used ($b=6.5$ cm, $c=45$ cm, $p=44.3$ cm) [31] (Fig. 2).

$$F_{cp} = \frac{c + p - b}{2.c} \tag{35}$$

The same assumption is made for the drying racks and the ceiling. We therefore have the following values.

$$F_{cpr} = F_{plpr} = 0.914;\ F_{cb1} = F_{plb2} = 0.08;\ F_{b1pr} = F_{b2pr} = 0.48 \tag{36}$$

For radiation from the roof to the sky, $F_{cv}=1$.
Heaven vault temperature [32]:

$$T_v = 0.0552Ta^{1.5} \tag{37}$$

The specific heat and thermal conductivity of cassava and the latent heat of evaporation [33]:

$$c_{pr} = 837 + 33.5\frac{X}{1+X} \tag{38}$$

$$\lambda_{pr} = 0.49 - 0.44\exp(-0.206X) \tag{39}$$

$$L_{\text{vap}} = 4186.8 * (597 - 0.56T_{pr}) \tag{40}$$

The specific heat, density, conductivity, dynamic viscosity and thermal diffusivity of air are given as follows [18]:

$$C_a = 1835 - 0.734T_a \tag{41}$$

$$\rho_a = \frac{353}{(T_a + 273.15)} \tag{42}$$

$$\lambda_a = 7.57 * 10^{-5}T_a + 0.0242 \tag{43}$$

$$\mu_a = 1.718 * 10^{-5} + 4.620 * 10^{-8}T_a \tag{44}$$

$$\nu_a = 10^{-5}0.0146T_a + 1.8343 \tag{45}$$

For the plywood used in the prototype, the specific heat and conductivity are given by:

$$C_b = 103.1 + 3.867 * T_b \tag{46}$$

$$\lambda_b = \frac{0.2003 * \rho_b}{-0.0038 * T_b^2 - 0.0505 * T_b + 1002.6} + 0.02378 \tag{47}$$

To determine the density of each element, a piece of 25 cm^2 is weighed with an electronic balance of precision 0.01 g and the mass obtained is divided by its volume (Table 4).

Validation of the model and experimental setup uncertainties

The statistical parameter used to evaluate the quality of this modeling is the MRE (mean relative error). It has been used by many other researchers [18, 28, 36]. The measured values are compared to the calculated values to validate the model using Eq. (48).

$$MRE = \frac{100}{N}\sum_{i=1}^{N}\frac{\left|T_{i,exp} - T_{i,theor}\right|}{T_{i,exp}} \tag{48}$$

Here are the measuring instruments we used: A Kipp & Zonen CMP 10 pyranometer was used for solar radiation. To weigh the samples, we used a Mettler PL 1200 electronic balance. A hot wire anemometer was used to measure the internal air velocity. Two FY-11 thermo-hygrometers were used to measure air temperature and humidity inside and outside the device (in the shade). Twelve Voltcraft PL-120-T2 thermometers connected to k-type probes were used for the other temperatures. Since these are not suitable for wet surfaces, we wrapped the probe tips with thin plastic before placing them in contact with the cassava slices to measure their temperature. For the wind direction, we used a wind vane.

There are no statistical treatment data available; therefore, only type B uncertainty is considered. We assume that all measurands are uniformly distributed. The standard uncertainties (u) are expressed as (a: accuracy of the measuring instrument) [37]:

$$u = a/\sqrt{3} \tag{49}$$

Economic analysis of the prototype

As expressed by Simo Tagne et al. [38], the payback period (PBP) of a solar drying device is calculated taking into account the initial investment (ii), the money (price of electric energy) that can be saved per year using the prototype (SM) and the maintenance cost for two years (20% of initial investment). It is expressed as:

$$PBP = \frac{1.2 * ii}{SM} \tag{50}$$

ii is the money spent for building the device (47,300 F cfa/76.72$ US) (see "Appendix" section for details), SM is calculated by multiplying the energy received from the sun in a year (E^y) by the price of a kwh of energy in Côte d'Ivoire (89.75 F cfa/0.14$ US). Considering 20 working days for each month of the year, we can write:

$$E^y = \sum_{m=1}^{12}\left(\sum_{d=1}^{20}E^d\right) \tag{51}$$

Based on the values of solar irradiation estimated by Tofighi [39], the average global solar irradiation in Côte d'Ivoire is 5.01 kwh/m^2/day.

Results and discussion

Weather conditions and instrument measurement standard uncertainties

The experiments took place at the INPHB (Institut National Polytechnique Houphouet Boigny) in Yamoussoukro (Latitude: $L = 6.8206$ N, longitude: $l = 5.2767$ W). The diurnal variations of relative humidity and air temperature, the temperatures of the components of the prototype as well as those of the mass and temperature of the cassava with solar radiation were recorded. The drying of 6 kg of cassava slices in the prototype lasted for 3 days, from November 8 to 10, 2019. The overall solar radiation, ambient relative humidity, and ambient temperature for these days are plotted

Table 2 Mass transfer equations in the prototype

The mass transfer equation [4, 18, 25]

$$m_f \frac{dY_i}{dt} = \dot{m}(Y_o - Y_i) - m_0 \frac{dX}{dt} \quad (7)$$

Cassava drying curve [26, 27]

$$\log\left(\frac{X-X_f}{C}\right) = -at \quad (8)$$

$$x(t) = C \cdot e^{-at} + x_f \quad (9)$$

$$m_0 \frac{dx}{dt} = -a \cdot m_0 \cdot Ce^{-at} \quad (10)$$

Equation (8) is defined as a function and written as follows:

$$\frac{dY_i}{dt} = Y_i(t)' = \frac{\dot{m}}{m_f}(Y_o(t) - Y_i(t)) + \frac{m_0}{m_f} a \cdot Ce^{-at} \quad (11)$$

$$f(Y_{i,n}, t_n) = \frac{\dot{m}}{m_f}(Y_o(t_n) - Y_{i,n}) + \frac{m_0}{m_f} a \cdot Ce^{-at_n} \quad (12)$$

$$Hr_1 = 83\%; m_1 = 6 \text{ kg and } x_1 = 1.63 \text{ kg/kg d.b. and } T_1 = 30.1\ ^\circ\text{C}; m_0 = \frac{m_1}{1+x_1} \quad (13)$$

The Runge–Kutta Algorithm for mass transfer is given as follows [27–29]

$$K_1 = h * f(Y_{i,n}, t_n); K_2 = h * f\left(Y_{i,n} + \frac{K_1}{2}, t_n + \frac{h}{2}\right); K_3 = h * f\left(Y_{i,n} + \frac{K_2}{2}, t_n + \frac{h}{2}\right) \quad (14)$$

$$K_4 = h * f(Y_{i,n} + K_3, t_n + h); Y_{i,n+1} = Y_{i,n} + \frac{1}{6}(K_1 + 2K_2 + 2K_3 + K_4) \quad (15)$$

$$t_{n+1} = n * h; \quad n = n + 1; \quad (16)$$

in Fig. 3. All morning on the first day, the sky remained overcast until noon when the sky cleared. The maximum solar radiation value was 1025 W/m^2 at 12:45. The relative humidity was between 68 and 83%. The maximum ambient temperature was 34 °C. We started to measure from 9:30 am because of the cloudy sky. On the second day, the sky was a bit clear around 7:55 am, so we started the measurements from 8:00 am but the sky remained overcast all day with a few moments of clearing around 10:00 and 16:00. The maximum solar radiation for this day was 844 W/m^2 at 10:30 am. The temperature remained low with a maximum value of 32.3 °C, as for the relative humidity, its minimum value for this day was 74%. The last day was sunny with some cloudy periods between 11:45 and 14:00. The maximum ambient temperature was 33.7 °C, and the minimum relative humidity was 63%. Solar radiation reached a maximum value of 1046 W/m^2 at 13:30. We started the measurements from 7:00 am. The standard uncertainty of measurement instruments used is given in Table 5.

Comparison of the points predicted by the model and the experimental values

The experimentally obtained values and the predicted points are plotted and compared. The calculated mean relative errors ($E\%$) are used for model validation, as mentioned above.

Drying kinetics

Figure 4 shows the numerical and experimental evolution of cassava moisture content. The experimental drying kinetic curve has three parts corresponding to the 3 days of drying. For the 1st and 2nd days, due to the presence of free water in the cassava slices, we observed a rapid decrease in water content. For the last day, despite high solar radiation, we observe a small decrease in water content. Indeed, the resistance to drying increases with time because of the internal bonds between remaining water and the material. The water content of the cassava decreased from 1.63 kg/kg on the 1st day at 9:30 a.m. to 0.122 kg/kg at 2:00 p.m. on day 3. This final moisture content is acceptable. The value obtained by Koua et al. [28] was 0.13 kg/kg. The rapid decrease in sunlight in the afternoon of the first day of drying has an immediate impact on the drying kinetics. And since the subsequent rapid decrease in drying rate is not accounted by our model, the discrepancy between the experimental and predicted points at the end of the first day and the beginning of the second day is observed. However, both curves have almost the same trend. The value of E% that we obtain here is 13.62%. It is satisfactory. Indeed, Hii et al. [36] obtained a value of 12.1% which is close to ours, for the modeling of the water content of cocoa beans, and Simo Tagne et al. [18] obtained 15.29% for the modeling of the drying curve of red chilli.

Temperature and humidity in the attic

In Fig. 5, the experimental and calculated evolutions of the relative humidity and temperature of the drying air are compared. The maximum drying air temperatures measured were 37.9 °C, 35 °C, and 38.2 °C for the 1st, 2nd, and 3rd days, respectively. For these 3 days, the relative humidity of the drying air measured ranged from 83 to 55%, 88% to 61%, and 90% to 50%, respectively. These higher internal temperature and lower relative air humidity than outside allow

Table 3 Heat transfer coefficients

Thermal transfer by conduction occurring in the vertical parts of the drying shelves and the wooden part of the floor

$$h_{cbe} = \frac{\lambda_b}{e_b} \tag{23}$$

Thermal convection between the roof and outside air [18]

$$h_{cce} = 5,67 + 3,86V_a \tag{24}$$

The thermal convection coefficient is expressed as follows:

$h_c = \frac{N_u \lambda_a}{D_h}$ (λ_a : is air conductivity); N_u (Nusselt number) and D_h (hydraulic diameter) (25)

For the roof (h_{ccf}) [17]

$$N_{uc} = \frac{0.677P_r^{1/2}G_{rc}^{1/4}}{[0.95+P_r]^{1/4}} \tag{26}$$

$$G_{rc} = \frac{(g.\cos\alpha)\beta(T_c-T_f)(L_c)^3}{v^2}; D_{hc} = \frac{4*S_c}{P_c}; \beta = \frac{2}{T_c+T_f}; \alpha = (90^\circ - i) \tag{27}$$

For the ceiling floor (h_{cplf}) [30]

$$N_{upl} = 1 + 1.44 * \left[\frac{\left|1-\frac{1708}{R_{apl}*cosi}\right|+1-\frac{1708}{R_{apl}*cosi}}{2}\right] * \left[1 - \frac{1708*(\sin(1.8))^{1.6}}{R_{apl}*cosi}\right] + \frac{\left|\left(\frac{R_{apl}*cosi}{5830}\right)^{1/3}-1\right|+\left(\frac{R_{apl}*cosi}{5830}\right)^{1/3}-1}{2} \tag{28}$$

$$R_{apl} = \frac{g.\beta(T_{pl}-T_f)(D_{hpl})^3}{av}; D_{hpl} = \frac{L_{pl}}{\cos i}; \beta = \frac{2}{T_{pl}+T_f} \tag{29}$$

For the vertical surfaces of the drying shelves [31]

$$N_{ub} = \left[0,825 + \frac{0,387R_{ab}^{\frac{1}{6}}}{\left[1+\left(\frac{0.492}{P_r}\right)^{\frac{9}{16}}\right]^{\frac{8}{27}}}\right]^2 \tag{30}$$

$$R_{ab} = \frac{g\beta(T_b-T_f)D_{hb}^3}{\alpha v}; \beta = \frac{2}{T_b+T_f}; D_{hb} = L_b \tag{31}$$

For cassava slices [17]

$$N_{upr} = 0.54\left(G_{rpr}.P_r\right)^{1/4} \tag{32}$$

$$G_{rpr} = \frac{g\beta(T_{pr}-T_f)D_{hpr}^3}{v^2};\ \beta = \frac{2}{T_{pr}+T_f};\ D_{hpr} = \sqrt[3]{\left(V_{pr}\frac{6}{\pi}\right)}; V_{pr} = 7\ \text{cm}^3 \tag{33}$$

Global thermal loss coefficient of the floor of the prototype

$$U_{pl} = \frac{1}{\left(h_{cplf}+\frac{e_{po}}{\lambda_{po}}+\frac{e_b}{\lambda_b}+h_{cab}\right)} \tag{34}$$

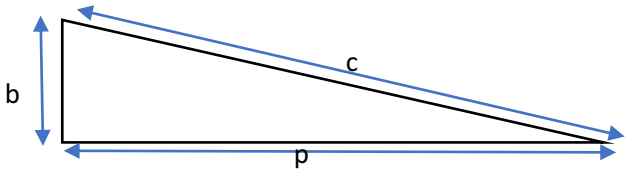

Fig. 2 Approximation for geometrical factor calculation

drying to take place in the attic since air drying potential is increased. It can also be seen that the numerical predictions evolve synchronously with the experimental points. We obtained the values $E\% = 8.85\%$ for the relative humidity and $E\% = 4.35\%$ for the drying air temperature. The deviations observed on the first day may be due to the high amount of moisture released by the cassava into the drying air, which causes a decrease in temperature and an increase in relative humidity. In Fig. 6, the experimental and numerical variations of the roof temperature are compared. This figure shows a good correspondence between measured predicted points. The value of $E\%$ calculated was 4.05%.

In Fig. 7, we can see the variations of the calculated and measured temperatures of the floor and cassava slices. The

Table 4 Parameter of plywood, polystyrene and aluminum-zinc sheet of the prototype

Components	Aluminum-zinc sheet	Plywood	Polystyrene
Surface (m^2)	1.548	0.164	1.512
Mass (kg)	2.1	0.843	2.9
Density (kg/m^3)	2707	514	16
Specific heat (J/kg °C)	875		1450 [34]
Absorptivity	0.91		
Conductivity (W/m K)		0.15 [35]	0.03 [34]

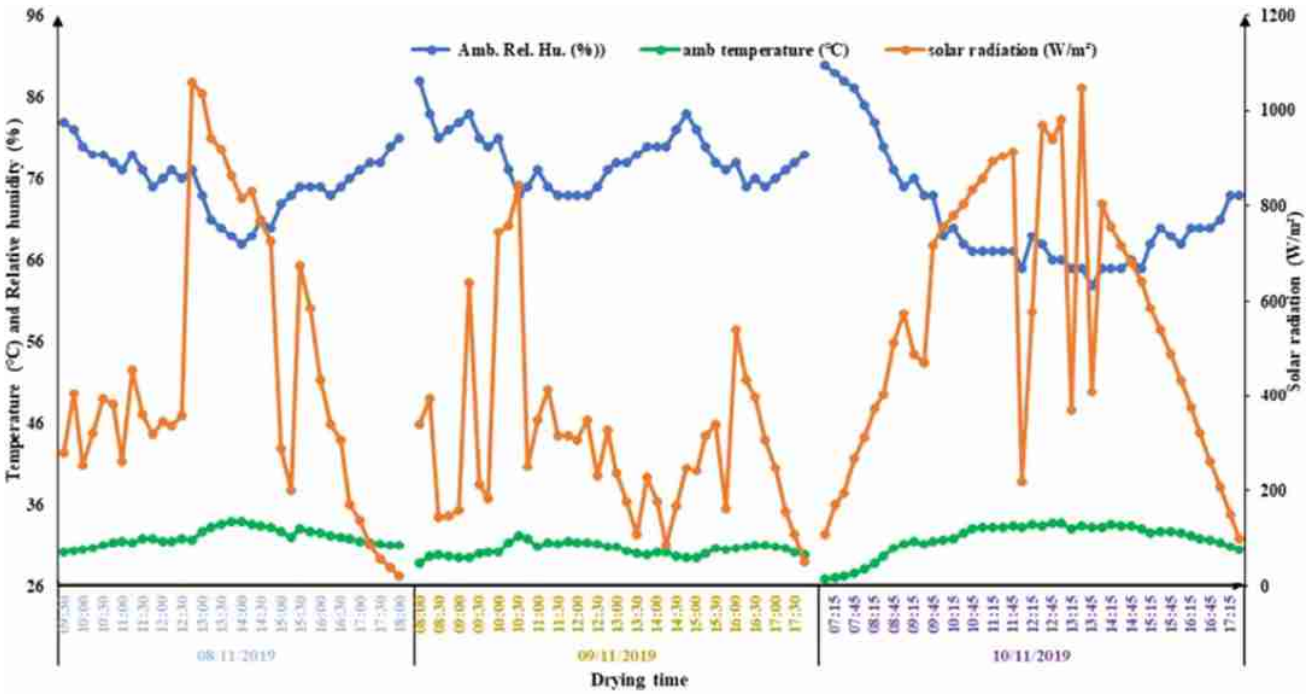

Fig. 3 Ambient air temperature, relative humidity, and global solar radiation

Table 5 Least count, range and standard uncertainties of measuring instruments

Instruments used	Least count	Range	Standard uncertainty (u)
Pyranometer Kipp & Zonen CMP 10	1 W/m^2	0–4000 W/m^2	0.6 W/m^2
Balance Mettler PL 1200	0.01 g	0–200 g	0.006 g
FY-11 thermo-hygrometers	1 °C 1%	− 50 °C to 70 °C 10–99%	0.6 °C 0.6%
Voltcraft PL-120-T2 thermometers connected to k-type probes	1 °C	− 200 °C to 1372 °C	0.6 °C
A hot-wire anemometer	0.1 m/s	0–20 m/s	0.06 m/s

average relative errors calculated are $E\% = 4.7\%$ for the cassava slices and $E\% = 2.84\%$ for the floor. There are certainly some deviations between the predicted and experimental points. They show that not all the mechanisms developed in the heat and mass transfer occurring in the prototype are considered by our model. However, the calculated and experimental curves have almost the same trend. And these values of $E\%$ obtained (lower than 10% as recommended by Rosa et al. [40]) are satisfactory; they show a good correspondence between predictions and experiment. Other researchers have obtained higher values [18, 41]. All the values of the MRE obtained are gathered in Table 6.

Figure 8 shows the temperatures of all components of the prototype. The black roof is the hot source due to the energy received from the sun during the day. Its temperature is higher than all other components of the prototype. The maximum values are 69.2 °C (at 13:15), 57 °C (at 10:30), and 69 °C (at 11:45) for the 1st, 2nd, and 3rd day, respectively. The drying air temperature is the highest internal temperature. Its average values were 34.8 °C, 32.17 °C, and 34.55 °C successively on these 3 days. The cassava temperature was higher than the ambient temperature, but the floor temperature remained lower. This is because heat transfer by radiation between the cassava and the roof and by convection between the roof and the indoor air is significant. As for the floor, it does not receive any radiation from the roof. Figure 9 shows the evolution of the water content of the product as well as the variations of humidity inside and outside. The wind direction has an influence on the prototype. When the wind blows from east to west or in the opposite

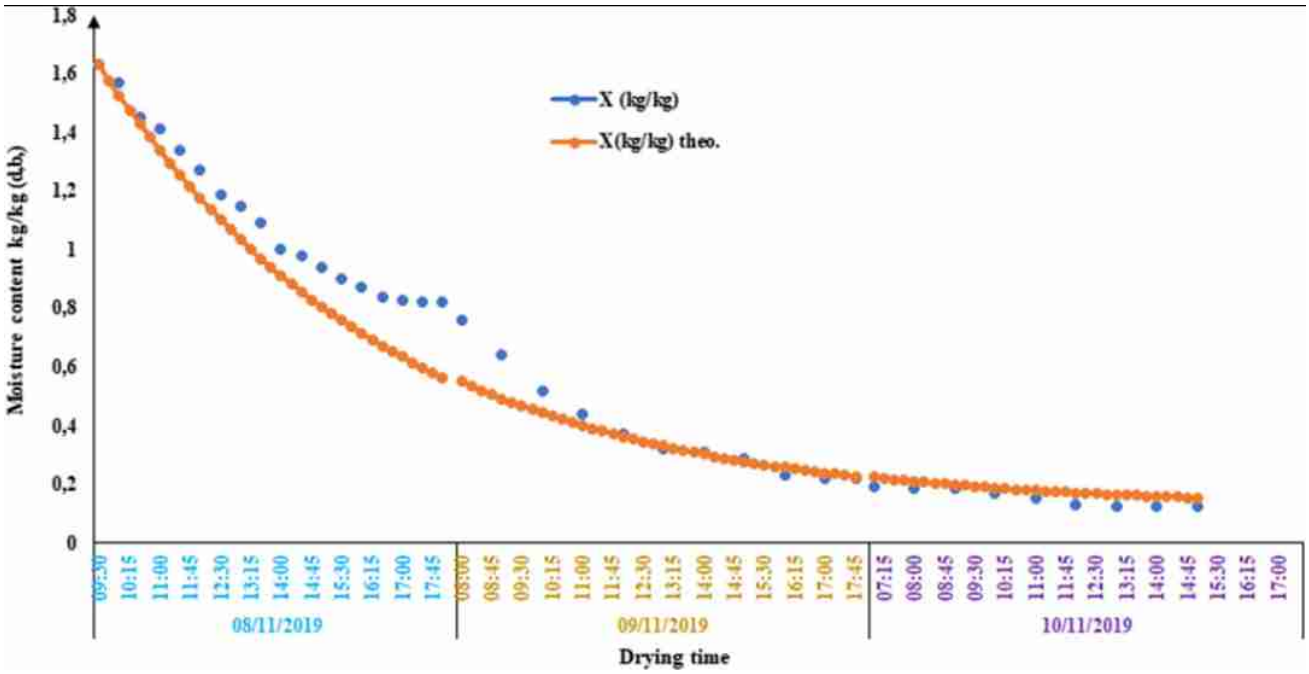

Fig. 4 Experimental and numerical moisture content versus drying time ($E\% = 13.62\%$)

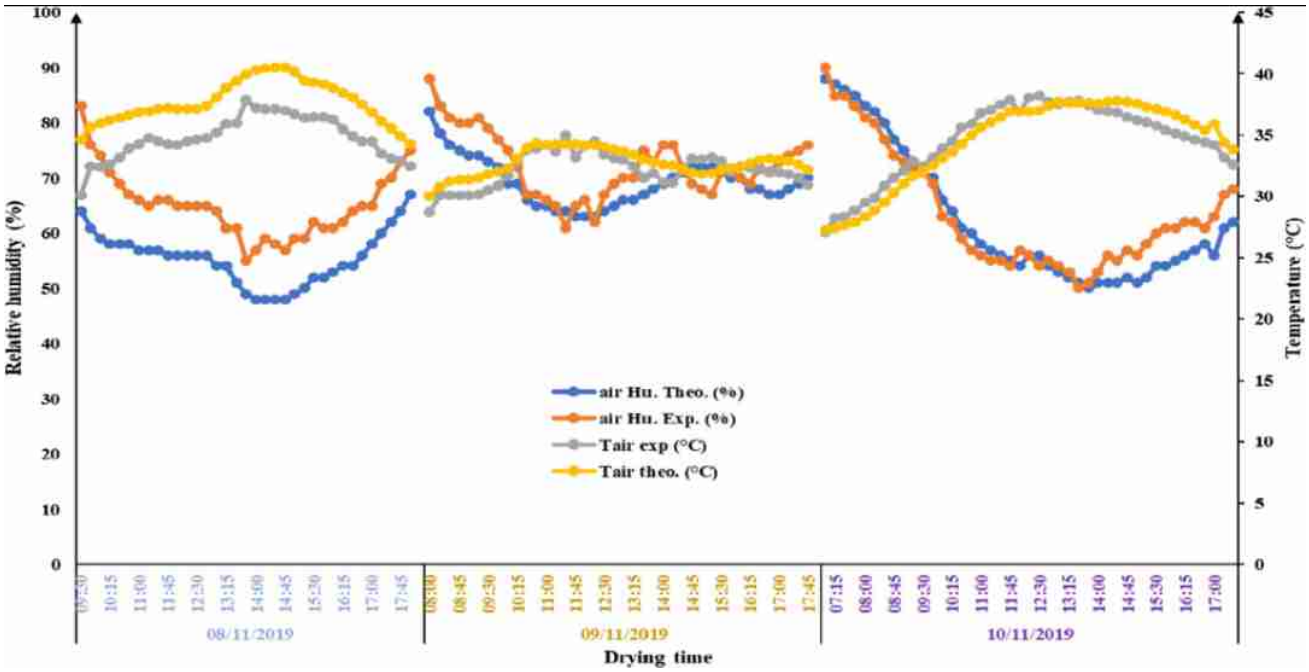

Fig. 5 Theoretical and experimental drying air temperature ($E\% = 4.35\%$) and relative humidity ($E\% = 8.85\%$)

direction, the temperature and humidity of the air in the attic are more influenced by the sunshine. The internal temperature is higher and the internal relative humidity is lower than outside as we can observe in this study. But when the wind blows from south to north, the influences of the humidity of the outside air and the water content of the product on the drying air can be observed [4].

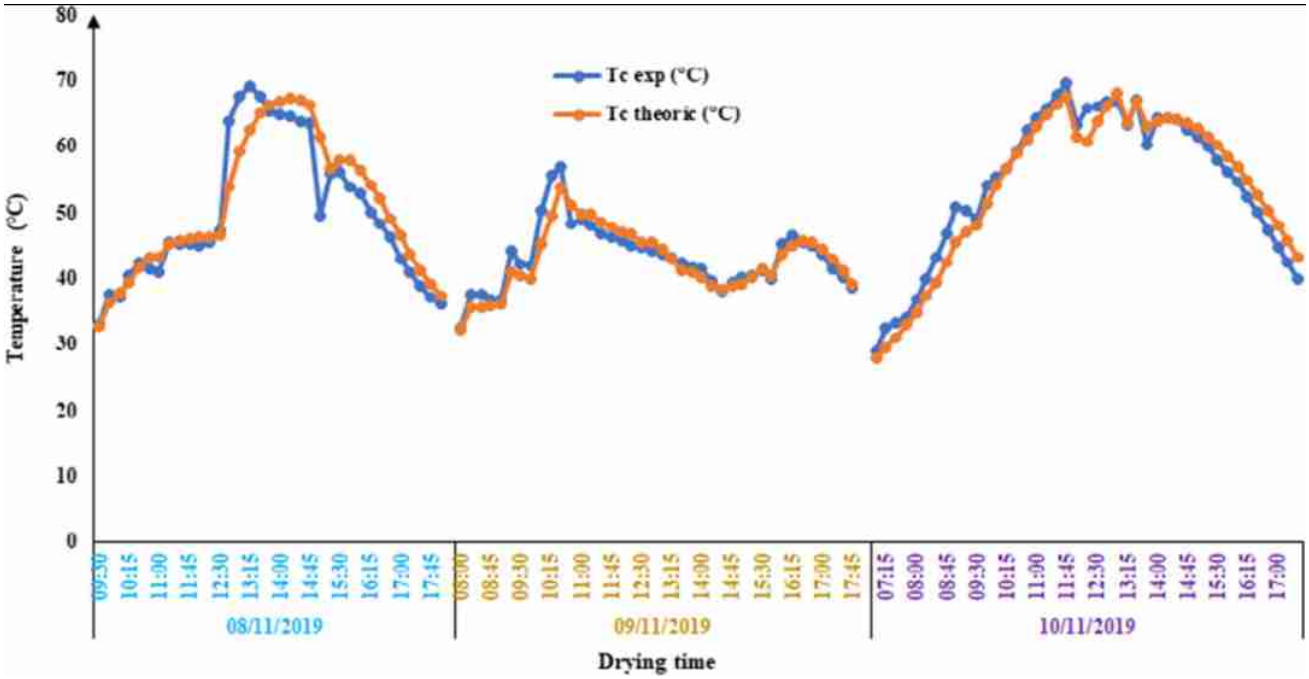

Fig. 6 Roof experimental and numerical temperature evolutions ($E\% = 4.05\%$)

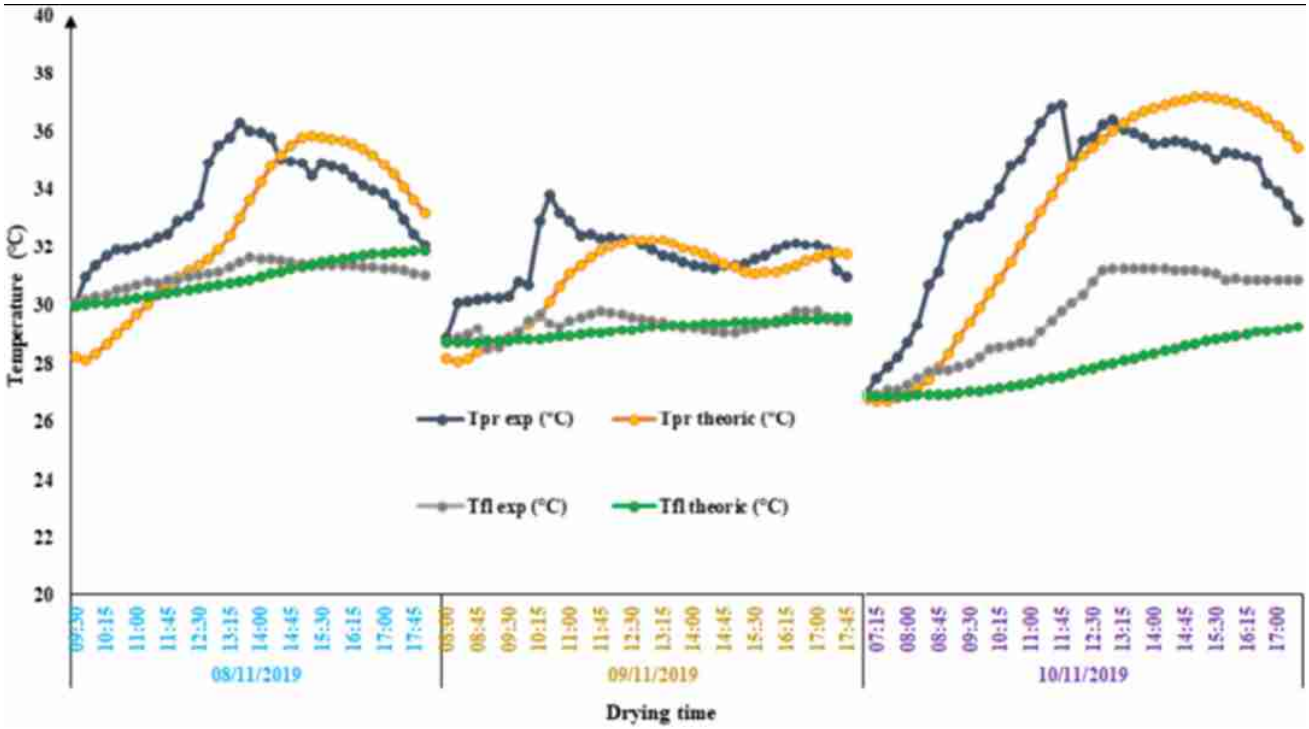

Fig. 7 Experimental and calculated temperatures of cassava slices (T_{pr}) ($E\% = 4.7\%$) and the floor (T_{fl}) ($E\% = 2.84\%$)

Drying efficiency

The efficiency of a solar drying system can be expressed in terms of the ratio of heat used for evaporation of moisture from the material to the total incident solar radiation [22, 42]. Sometimes the drying potential of the ambient air is taken into account [43], but in our case, a rapid decrease in drying rate is observed in the absence

Table 6 Parameter modeled and corresponding MRE values

Parameter modeled	*E*%
Drying curve	13.62
Drying air relative humidity	8.85
Drying air temperature	4.35
Black roof temperature	4.05
Cassava slices temperature	4.7
Temperature of the floor	2.84

of sunlight. Therefore, we consider this potential negligible. The drying efficiency is given by Eq. (61) and plotted in Fig. 10. In this equation, L_v is latent heat of water evaporation, and it is calculated using the mean value of temperature in the prototype.

$$\eta = \frac{M_{ev} \cdot L_v}{S_c \cdot \int G(i,\gamma)\mathrm{d}t} * 100 \tag{52}$$

The drying efficiency varied from 0.2 to 25%. The average value was 6.48%. Considering the amount of solar radiation received and the amount of water removed from the cassava each day, the average values of efficiency were 9.13%, 6.12% and 0.2% for the 1st, 2nd, and 3rd days, respectively. The drying efficiency decreases because the amount of water evaporated decreases with the drying time. This is due to the increasing resistance of cassava to drying. The same decrease in drying efficiency was observed by Mallikarjuna Goud et al. [9] and by [22, 42]. This average drying efficiency is higher than 4.3% obtained for open-sun drying by [44] and lower than traditional drying efficiency, 13.5% obtained by [45]. The choice of crop drying in the attic should not be based on efficiency but on safety, product quality, the durability and cost of the drying device and availability of construction materials [45]. The initial investment is 47,300 Fcfa (76.62 $ US) (see Table 7); there is almost no maintenance cost. Drying 6 kg of cassava slices takes 3 days with about 10 h of drying per day. Considering 20 working days, we can dry at least twice 6 kg of cassava, which corresponds to 60 h of drying per month, so $E^y = 3607.2$ Kwh/year. SM = 323,746.2 Fcfa/year (504.67 $ US/year). The payback time is therefore a maximum of 2 months for drying cassava slices. Traditional sun drying may seem advantageous compared to this method, because there is almost no cost for a device to be spent by farmers nor any particular skill. But this old method has many limitations. It is labor-intensive, and the dried products are often of poor quality due to infestations and drying is only possible when the sun is shining [46, 47].

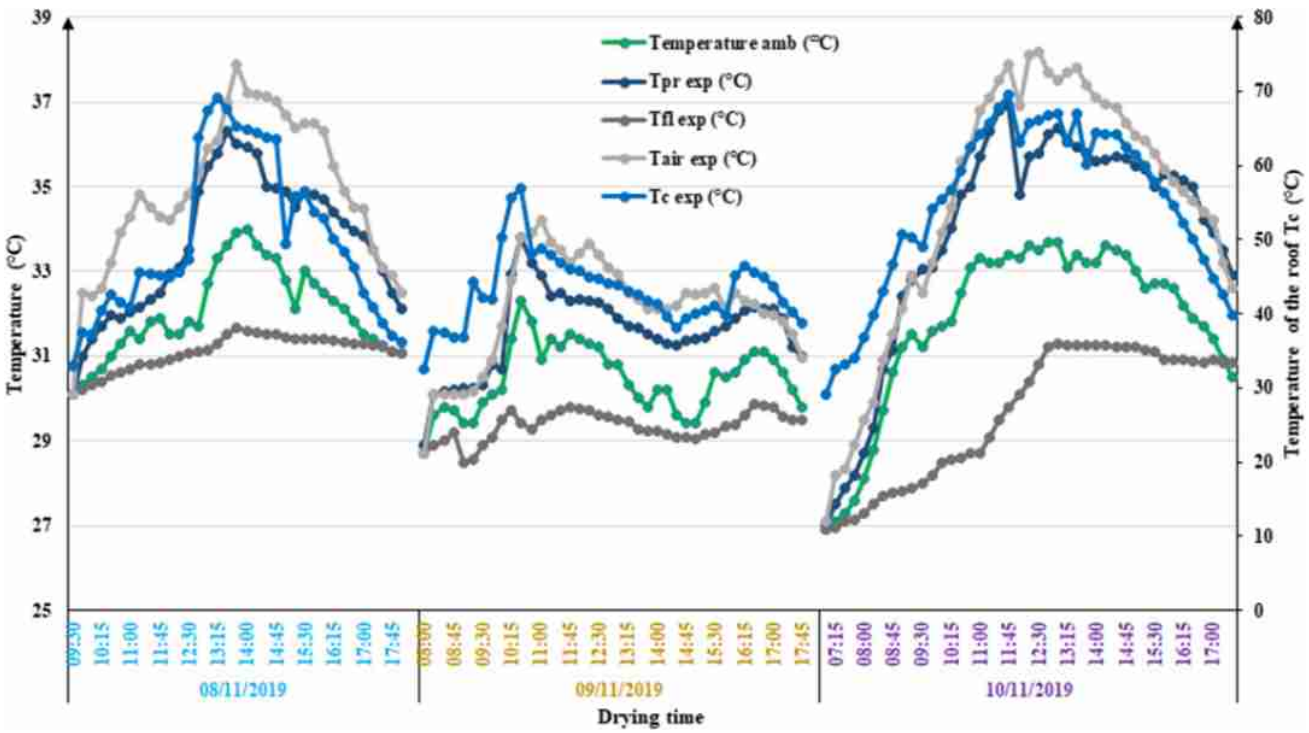

Fig. 8 Temperatures of all the components of the prototype with solar radiation and ambient air temperature

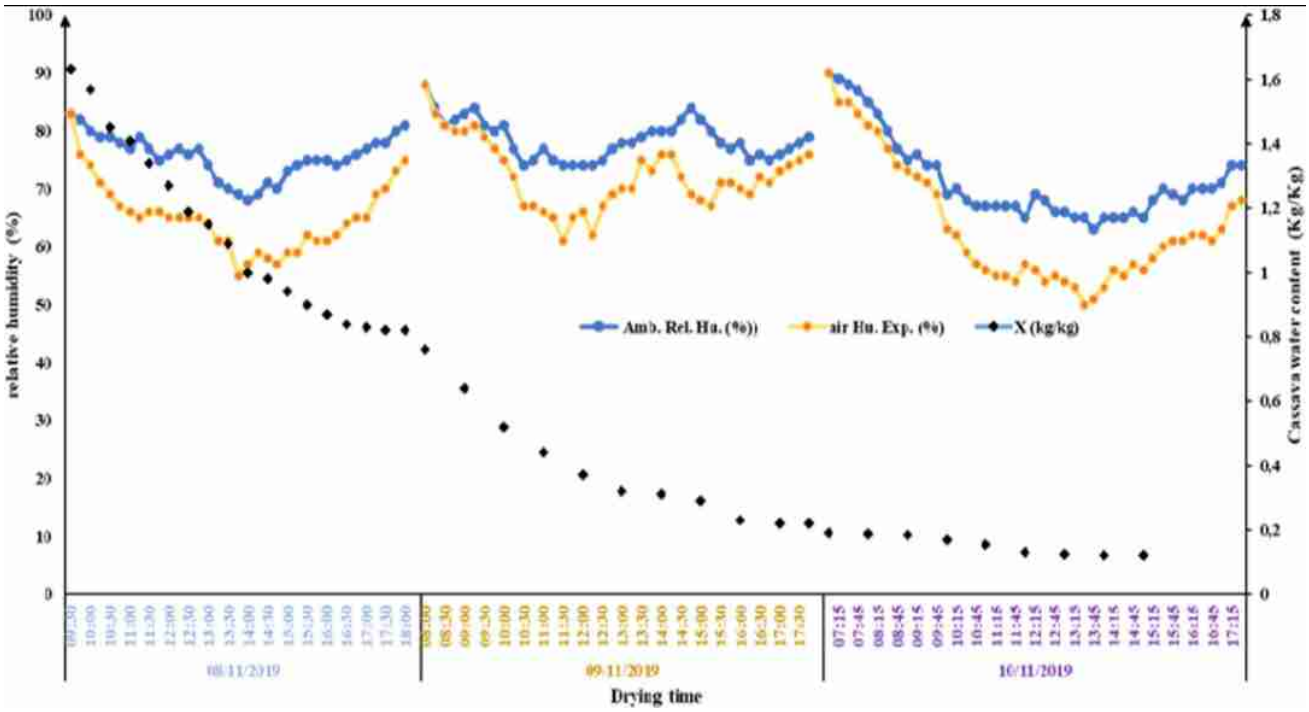

Fig. 9 Evolutions of drying air and outside air relative humidity and cassava moisture content

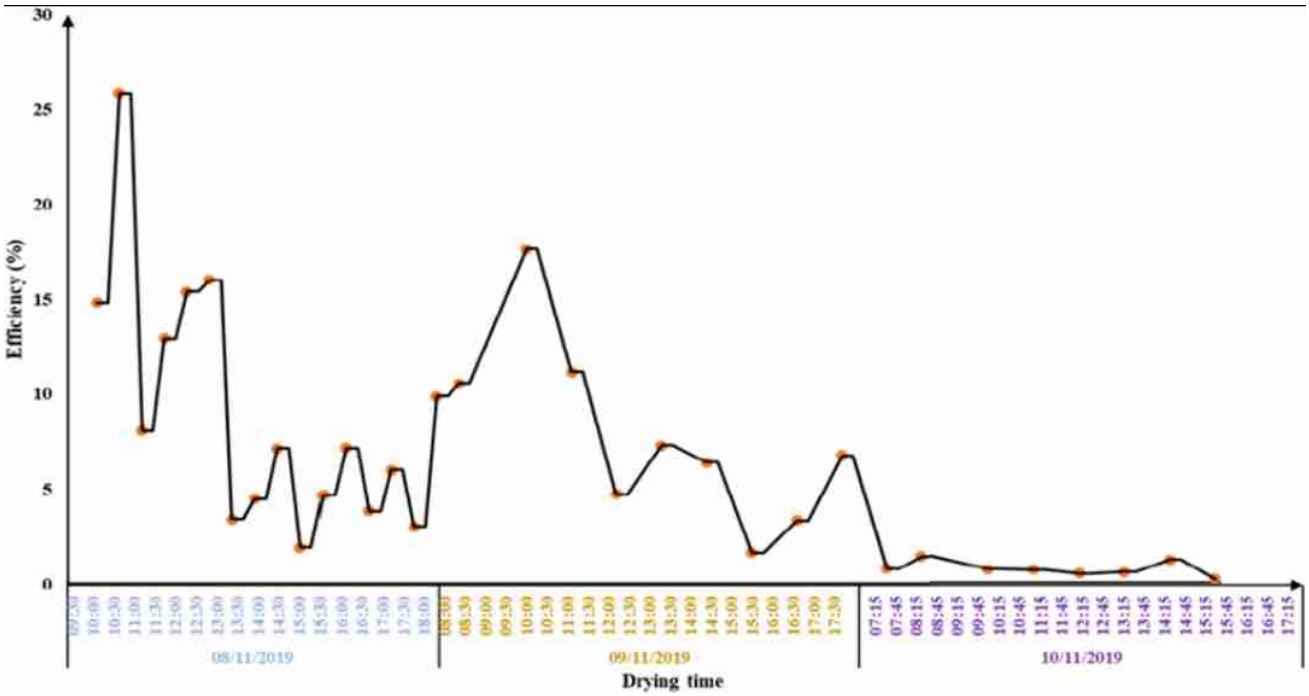

Fig. 10 Drying efficiency in the prototype

Table 7 The cost of manufacturing this prototype

Material	Cost (F cfa)/U.S. $
A sheet of plywood (2 × 1.5 m^2, 10 mm thick)	7000/11.14
A nylon net (1.5 m^2)	1000/1.59
A layer of polystyrene (3 m^2, 4 cm thick)	9000/14.32
Spikes	1500/1.39
A blackened aluminum-zinc corrugated sheet (2 × 1 m^2)	3500/5.57
PVC pipe (4.5 m long and 50 mm in diameter)	4500/7.16
Wood (for the frame of the prototype and the shelves)	4500/7.16
Iron net for the air inlet (0.25 m^2)	1000/1.59
Two hinges	800/1.27
Manufacturing cost	15,000/23.87
Total	47,300/76.72

The currency used in Côte d'Ivoire is the F cfa

Conclusion

Modeling of a ventilated attic used for solar drying has been undertaken and successfully completed. The theoretical study is conducted using a system of equations for the heat and mass transfers that occur during cassava drying. This system is solved by the fourth-order Runge–Kutta method. Experimental results were obtained from solar drying of 6 kg of cassava in the constructed prototype. The temperatures of the prototype components, drying air humidity, and mass changes of cassava slices were recorded along with the weather conditions. The estimated values were compared to the measured data. The calculated mean relative errors ($E\%$) show a good agreement between experiment and calculation. Indeed, its values lower than 14% are in agreement with the results obtained in several research works. The drying efficiency decreases with the drying time. Its average value was 6.48%. This ventilated attic can be easily implemented in all sunny rural areas to avoid post-harvest losses of food. The estimated payback period is only 2 months. In the future, we would like to study the feasibility of drying other food products in such a device, in real size and under different climatic conditions. A cheap and locally available type of insulation will also be studied for the ceiling.

Appendix

The system of equations for heat transfer in the attic was written as follows:

$$\begin{aligned}\frac{dT_c}{dt} &= T_c{}' \\ &= \frac{S_c}{m_c C_c}(\alpha_c G(i,\gamma) - \sigma F_{cpr}\left(T_c{}^4 - T_{pr}{}^4\right) \\ &- \sigma F_{cv}\left(T_c{}^4 - T_v{}^4\right) - \sigma F_{cb1}\left(T_c{}^4 - T_{b1}{}^4\right) \\ &- h_{ccf}\left(T_c - T_f\right) - h_{cce}\left(T_c - T_a\right))\end{aligned} \tag{53}$$

$$\begin{aligned}\frac{dT_{pr}}{dt} &= T_{pr}{}' \\ &= \frac{1}{m_0 c_{pr}}(\sigma F_{cp} S_c\left(T_c{}^4 - T_{pr}{}^4\right) + \sigma F_{plpr} S_{pl}\left(T_{pl}{}^4 - T_{pr}{}^4\right) \\ &+ \sigma F_{b1pr} S_{b1}\left(T_{b1}{}^4 - T_{pr}{}^4\right) + \sigma F_{b1pr} S_{b2}\left(T_{b2}{}^4 - T_{pr}{}^4\right) \\ &+ h_{cprf} S_{pr}\left(T_f - T_{pr}\right) + \frac{\lambda_{pr}}{e_{pr}} S_{pr}(T_f - T_{pr}) + \dot{m}_{pr} L_{\text{vap}})\end{aligned} \tag{54}$$

$$\begin{aligned}\frac{dT_f}{dt} &= T_f{}' \\ &= \frac{1}{m_a C_a}(\dot{m}_a c_a\left(T_a - T_f\right) + h_{ccf} S_c\left(T_c - T_f\right) \\ &+ h_{cprf} S_{pr}\left(T_{pr} - T_f\right) + h_{cplf} S_{pl}\left(T_{pl} - T_f\right) \\ &+ h_{cb1f} S_{b1}\left(T_{b1} - T_f\right) + h_{cb2f} S_{b2}\left(T_{b2} - T_f\right) - \dot{m}_{pr} L_{\text{vap}})\end{aligned} \tag{55}$$

$$\begin{aligned}\frac{dT_{b1}}{dt} &= T_{b1}{}' \\ &= \frac{2}{m_{b1} C_b}(\sigma F_{b1pr} S_{b1}\left(T_{pr}{}^4 - T_{b1}{}^4\right) + \sigma F_{cb1} S_c\left(T_c{}^4 - T_{b1}{}^4\right) \\ &+ h_{cb1f} S_{b1}\left(T_f - T_{b1}\right) + \frac{\lambda_b}{e_b} S_{b1}\left(T_{b2} - T_{b1}\right))\end{aligned} \tag{56}$$

$$\begin{aligned}\frac{dT_{b2}}{dt} &= T_{b2}{}' \\ &= \frac{2}{m_{b1} C_b}(\sigma F_{b1pr} S_{b1}\left(T_{pr}{}^4 - T_{b2}{}^4\right) + \sigma F_{plb2} S_{pl}\left(T_{pl}{}^4 - T_{b2}{}^4\right) \\ &+ h_{cb2f} S_{b1}\left(T_f - T_{b2}\right) + \frac{\lambda_b}{e_b} S_{b1}\left(T_{b1} - T_{b2}\right))\end{aligned} \tag{57}$$

$$\begin{aligned}\frac{dT_{pl}}{dt} &= T_{pl}{}' \\ &= \frac{S_{pl}}{m_{pl} c_{pl}}(\sigma F_{plp}\left(T_{pr}{}^4 - T_{pl}{}^4\right) + h_{cfpl}\left(T_f - T_{pl}\right) \\ &+ U_{pl}\left(T_a - T_{pl}\right) - \sigma F_{plb2}\left(T_{pl}{}^4 - T_{b2}{}^4\right))\end{aligned} \tag{58}$$

Each equation of heat transfer is defined as a function; then, we pose [32]:

$$\begin{cases} T_c' = f(T_c, T_{pr}, T_f, T_{b1}, T_{b2}, T_{pl}, t) \\ T_{pr}' = g(T_c, T_{pr}, T_f, T_{b1}, T_{b2}, T_{pl}, t) \\ T_f' = l(T_c, T_{pr}, T_f, T_{b1}, T_{b2}, T_{pl}, t) \\ T_{b1}' = m(T_c, T_{pr}, T_f, T_{b1}, T_{b2}, T_{pl}, t) \\ T_{b2}' = n(T_c, T_{pr}, T_f, T_{b1}, T_{b2}, T_{pl}, t) \\ T_{pl}' = p(T_c, T_{pr}, T_f, T_{b1}, T_{b2}, T_{pl}, t) \end{cases} \tag{59}$$

Initial conditions for the Runge–Kutta algorithm, for the first day:

$$m_0 = 2.28 \text{ kg}; h = 15 \text{ min} = 900 \text{ s}; \quad i = 1; t(i) = 0; Y_{11} = 22.55 \text{ g/kg}; \dot{m} = 0.013 \frac{\text{kg}}{\text{s}} \tag{60}$$

Ambient air absolute humidity [48]:

$$Y_o = \frac{0.622}{\frac{P}{Hr \cdot Ps(T)} - 1} \ (Hr\,(\%) \text{ measured value}, \ P = 101325 \text{ Pa}) \tag{61}$$

$$Ps(T) = e^{\left[46{,}784 - \frac{6435}{T+273{,}15} - 3{,}868.\ln(T+273{,}15)\right]} \ (\text{mmHg}) \tag{62}$$

Relative humidity in the attic is calculated using Eq. (57). Temperature in the attic and water vapor pressure at the saturation state is given by [18, 49]:

$$Ps(T)_i = e^{\left[\frac{-5.8*10^3}{T} + 1.391 - 4.864*10^{-2}T + 4.17*10^{-5}T^2 - 1.445*10^{-8} + 6.545 lnT\right]} \tag{63}$$

$$T_i = \frac{(1+Y_o)(0.24+0.46Y_i)T_f + (1+Y_i)(0.24+0.46Y_o)T_a}{(1+Y_o)(0.24+0.46Y_i) + (1+Y_i)(0.24+0.46Y_o)} \tag{64}$$

The solar radiation on the tilted roof is calculated using the following equations [2]:

$$G(i,\gamma) = R_B \cdot G_B + G_D\left(\frac{1+\text{Cos}i}{2}\right) + \rho_G G\left(\frac{1-\text{Cos}i}{2}\right); G_B = G - G_D; \tag{65}$$

$$\frac{G_D}{G} = 1.390 - 4650K_T + 5.531K_T^2 - 3.108K_T^3; K_T = \frac{G}{G_0}; \tag{66}$$

$$R_B = \frac{\text{Sin}(L-i)\text{Sin}\delta + \text{Cos}(L-i)\text{Cos}\delta\text{Cosh}}{\text{Sin}(L)\text{Sin}\delta + \text{Cos}(L)\text{Cos}\delta\text{Cosh}}; \quad \delta = 23.45 * \text{Sin}\left(\frac{360}{365}(284+n)\right) \tag{67}$$

$$G_0 = 1366.1 * (1 + 0.033 cos\left(\frac{360n}{365}\right)) \ (Sin(L)Sin\delta + Cos(L)Cos\delta Cosh) \tag{68}$$

$$h = 15.\Big\{LST + \Big(9.87 * sin\Big[\frac{360}{182}.(n-81)\Big] - 7.5 * cos\Big[\frac{360}{364}.(n-81)\Big] - 1.5 * sin\Big[\frac{360}{364}.(n-81)\Big]\Big) - 4(SL-LL) - 12\} \tag{69}$$

(The cost of the 2.5 m high stand on which the prototype is mounted is not included.)

The actual cost of installing this attic depends on the size of the house on which it will be installed. Sloped roofs are common on houses; blackened aluminum-zinc corrugated sheet can be obtained to order. But what is not found everywhere on rural homes is the ceiling covered with insulation as well as the chimneys and drying shelves, which are the real new expense. Once properly installed on a house, the only thing that could generate replacement costs is the nylon netting on the drying racks (so they must be removable).

Data availability The datasets generated during the current study are available from the corresponding author on reasonable request.

Declarations

Conflict of interest On behalf of all authors, the corresponding author states that there is no conflict of interest.

References

1. Agbo, E.P., Edet, C.O., Magu, T.O., Njok, A.O., Ekpo, C.M., Louis, H.: Solar energy: a panacea for the electricity generation crisis in Nigeria. Heliyon (2021). https://doi.org/10.1016/j.heliyon.2021.e07016
2. Soteris, A.: Kalogirou: Solar Energy Engineering Processes and Systemes. Elsevier, San Diego (2014)
3. Vernier, P., N'Zué, B., Zakhia-Rozis, N.: Le manioc, entre culture alimentaire et filière agro-industrielle. Presses agronomiques de Gembloux et Éditions Quæ, Gembloux (2018)
4. Tieu, A., Yapi, A.S., Gbaha, P.: Modeling of humidity evolution during solar drying of cassava in a ventilated attic. Int. J. Innov. Appl. Stud. **34**, 521–531 (2021)
5. Ndukwu, M.C., Diemuodeke, E.O., Abam, F.I., Abada, U.C., Eke-emezie, N., Simo-Tagne, M.: Development and modelling of heat and mass transfer analysis of a low-cost solar dryer integrated with biomass heater: application for West African Region. Sci. Afr. (2020). https://doi.org/10.1016/j.sciaf.2020.e00615
6. Ndukwu, M.C., Simo-Tagne, M., Bennamoun, L.: Solar drying research of medicinal and aromatic plants: an African experience with assessment of the economic and environmental impact. Afr. J. Sci. Technol. Innov. Dev. (2020). https://doi.org/10.1080/20421338.2020.1776061
7. Norton, B.: Characteristics of different systems for the solar Drying of Crops. In: Solar Drying Technology, vol. 10, pp. 978–981. Springer (2017)

8. Kamarulzaman, A., Hasanuzzaman, M., Rahim, N.A.: Global advancement of solar drying technologies and its future prospects: a review. Sol. Energy **221**, 559–582 (2021)
9. Goud, M., Reddy, M.V.V., Chandramohan, V.P., Lingayat, A., Raju, V.R.K., Suresh, S.: Experimental investigation of drying kinetics of green chilli and okra using indirect solar dryer with evaluation of dryer performance. Int. J. Ambient Energy (2021). https://doi.org/10.1080/01430750.2021.1946145
10. Cetina-Quinones, A.J., Lopez Lopez, J., Ricalde-Cab, L., El-Mekaoui, A., San-Pedro, L.: Experimental evaluation of an indirect type solar dryer for agricultural use in rural communities: relative humidity comparative study under winter season in tropical climate with sensible heat storage material. Sol. Energy (2021). https://doi.org/10.1016/j.solener.2021.05.040
11. Purusothamana, M., Valarmathi, T.N.: Computational fluid dynamics analysis of greenhouse solar dryer. Int. J. Ambient Energy (2018). https://doi.org/10.1080/01430750.2018.1437567
12. Tomar, V., Tiwari, G.N., Norton, B.: Solar dryers for tropical food preservation: thermophysics of crops, systems and components. Sol. Energy (2017). https://doi.org/10.1016/j.solener.2017.05.066
13. Nour-Eddine, B., Belkacem, Z., Abdellah, K.: Experimental study and simulation of a solar dryer for spearmint leaves (*Mentha spicata*). Int. J. Ambient Energy **36**, 50–61 (2015)
14. Simo-Tagne, M., Bennamoun, L., Leonard, A., Rogaume, Y.: Modeling, numerical simulation and validation of a convective dryer in steady conditions: a case study of tropical woods. Int. J. Model. Simul. (2019). https://doi.org/10.1080/02286203.2019.1575111
15. Simo-Tagne, M., Bennamoun, L.: Numerical study of timber solar drying with application to different geographical and climatic conditions in Central Africa. Sol. Energy (2018). https://doi.org/10.1016/j.solener.2018.05.070
16. Simo-Tagne, M., Bonoma, B., Bennamoun, L., Monkam, L., Léonard, A., Zoulalian, A., Rogaume, Y.: Modeling of coupled heat and mass transfer during drying of ebony wood using indirect natural convection solar dryer. Drying Technol. (2019). https://doi.org/10.1080/07373937.2018.1544144
17. Simo-Tagne, M., Tagne, A.T., Ndukwu, M.C., Bennamoun, L., Akong, M.B.O., El Marouani, M., Rogaume, Y.: Numerical study of the drying of cassava roots chips using an indirect solar dryer in natural convection. AgriEngineering (2021). https://doi.org/10.3390/agriengineering3010009
18. Simo-Tagne, M., Ndukwu, M.C., Zoulalian, A., Bennamoun, L., Kifani-Sahban, F., Rogaume, Y.: Numerical analysis and validation of a natural convection mix-mode solar dryer for drying red chili under variable conditions. Renew. Energy (2019). https://doi.org/10.1016/j.renene.2019.11.055
19. Simo-Tagne, M., Macmanus, C.N.: Study on the effect of conical and parabolic solar concentrator designs on hybrid solar dryers for apricots under variable conditions: a numerical simulation approach. Int. J. Green Energy (2021). https://doi.org/10.1080/15435075.2021.1914632
20. Lemus-Mondaca, R.A., Zambra, C.E., Vega-Gálvez, A., Moraga, N.O.: Coupled 3D heat and mass transfer model for numerical analysis of drying process in papaya slices. J. Food Eng. **116**, 109–117 (2013)
21. Stéphane, K.A., Yao, N., Konan, K., Bruneau, D., Traore, A., Diby, K.A., Saraka, J.K.: A numerical model of cocoa beans drying kinetics in an indirect solar and air crossing dryer. Int. J. Innov. Appl. Stud. **23**, 717–731 (2018)
22. Hidalgo, L.F., Candido, M.N., Nishioka, K., Freire, J.T., Vieira, G.N.A.: Natural and forced air convection operation in a direct solar dryer assisted by photovoltaic module for drying of green onion. Sol. Energy. **220**, 24–34 (2021)
23. Pechaporn, P., Morakot, K., Raksuda, S., Prysathryd, S., Chinnathan, A.: Effect of temperature and shape on drying performance of cassava. Agric. Nat. Resour. (2017). https://doi.org/10.1016/j.anres.2017.12.004
24. Tieu, Z.A., Gbaha, P., Diby, K.A.: Étude expérimentale d'un grenier séchoir solaire à convection naturelle: application au séchage du cacao et du manioc. Afr. Sci. **15**, 80–95 (2019)
25. Bentayeb, F., Bekkioui, N., Zeghmati, B.: Modelling and simulation of a wood solar dryer in a Moroccan climate. Renew. Energy **33**, 501–506 (2008)
26. Apollinaire, K.-N.S.: Contribution à l'étude du séchage solaire de la banane plantain, de la mangue et du manioc: essais de désorption, sorption et modélisation. Thèse de doctorat troisième cycle. Laboratoire d'énergie solaire. Université de Cocody - Abidjan, Côte d'Ivoire. https://bibliotheque.uvci.edu.ci (2020). Accessed 7 Apr 2020
27. Koua, B.K., Fassinou, W.F., Gbaha, P., Siaka, T.: Etude expérimentale de la cinétique de séchage du manioc dans un séchoir solaire directe muni d'un circulateur thermique. Rev. Ivoire Sci. Technol. **9**, 11–26 (2007)
28. Koua, K.B., Gbaha, P., Koffi, E.P.M., Fassinou, W.F., Touré, S.: Modelling of thermal behaviour of a direct solar drier possessing a chimney: application to the drying of cassava. Indian J. Sci. Technol. **4**, 1609–1618 (2011)
29. Koua, B.K., Koffi, E.P.M., Gbaha, P., Touré, S.: Thermodynamic analysis of sorption isotherms of cassava (*Manihot esculenta*). J. Food Sci. Technol. **51**, 125–140 (2012)
30. Huetz, J., Petit, J.P.: Notions de transfert thermique par convection, Techniques de l'Ingenieur, traité de Génie énergetique A 1 540. 1990. http://japanstuff.free.fr/Sauvegarde/Scolaire/Projet%20d'%C3%A9tude/docs/a1540%20transferts%20thermiques.pdf (2021). Accessed 3 Jan 2021
31. Incropera, F.P., Dewit, D.P., Bergam, T.L., Lavine, A.S.: Fundamentals of Heat and Mass Transfer. Wiley, River-street (2007)
32. Kabidi, K.: Expérimentation et modélisation du comportement énergétique et thermique d'un séchoir solaire sous le climat de la région de Rabat. THÈSE DE DOCTORAT, UNIVERSITÉ MOHAMMED V – AGDAL, FACULTÉ DES SCIENCES, Rabat, 2014. https://thesesenafrique.imist.ma (2020). Accessed 7 Apr 2020
33. Koua, B.K., Koffi, E.P.M., Gbaha, P.: Evolution of shrinkage, real density, porosity, heat and mass transfer coefficients during indirect solar drying of cocoa beans. J. Saudi Soc. Agric. Sci. **18**, 72–82 (2019)
34. Info-Energie en auvergne, CAUBE Haute-Loire: GUIDE DES MATERIAUX ISOLANTS. http://www.cg43.fr/sites/cg43/IMG/pdf/guide_des_materiaux__isolants (2022). Accessed 13 May 2022
35. LECAHIER 106: LE CONTREPLAQUÉ Dans la construction NF EXTÉRIEUR CTB-X. http://www.lecontreplaque.com/wp-content/uploads/2015/10/CAHIER-106-2015.pdf (2022). Accessed 13 May 2022
36. Hii, C.L., Law, C.L., Law, M.C.: Simulation of heat and mass transfer of cocoa beans under stepwise drying conditions in a heat pump dryer. Appl. Therm. Eng. **54**, 264–271 (2013)
37. Dumka, P., Mishra, D.R.: Energy, exergy and techno-economic analysis of novel solar stills for sea coastal area. Int. J. Ambient Energy (2021). https://doi.org/10.1080/01430750.2021.1945489
38. Simo-Tagne, M., Etala, H.D.T., Tagne, A.T., Ndukwu, M.C., El Marouani, M.: Energy, environmental and economic analyses of an indirect cocoa bean solar dryer: a comparison between natural and forced convections. Renew. Energy (2022). https://doi.org/10.1016/j.renene.2022.02.015
39. Tofighi, A.: Solar energy balance in Yamoussoukro. Renew. Energy **8**, 919–922 (1993)
40. Pinto, L., Rosa, G.S., Moraes, M.A.: Moisture sorption properties of chitosan. LWT Food Sci. **43**, 415–420 (2010)

41. Fu, B.A., Chen, M.Q., Huang, Y.W.: Heat transfer caracteristics on lignite thin layer during hot air forced convective drying. Fuel **154**, 132–139 (2015)
42. Poonia, S., Singh, A.K., Jain, D.: Mathematical modelling and techno-economic evaluation of hybrid photovoltaic-thermal forced convection solar drying of Indian Jujube (*Zizyphus mauritiana*). J. Agric. Eng. **55**, 74–88 (2018)
43. Altobelli, F., Condorı, M., Duran, G., Martinez, C.: Solar dryer efficiency considering the total drying potential. Application of this potential as a resource indicator in north-western Argentina. Sol. Energy **105**, 742–759 (2014)
44. Hii, C.L., Law, C.L.: Solar drying of major commodity products. In: Solar Drying: Fundamentals, Applications and Innovations. C.L. Hii, S.V. Jangam, S.P. Ong and A.S. Mujumdar, Singapore (2012)
45. Minka, C.J.: Solar drying in Africa. In: Proceeding of Workshop Held in Dakar, Sénégale: Potential Improvements to Traditional Solar Crop Dryers in Cameroon: Research and Development. International Development Research Centre, Ottawa (1986)
46. Compendium, GIZ HERA Cooking Energy Energypedia. https://energypedia.info/wiki/Solar_Drying#Open-Drying (2022). Accessed 16 July 2022
47. VijayaVenkataRaman, S., Iniyanb, S., Goic, R.: A review of solar drying technologies. Renew. Sustain. Energy Rev. (2012). https://doi.org/10.1016/j.rser.2012.01.007
48. Jeannot, Y.: L'air Humide. CNRS, Paris (2005)
49. Daguenet, M.: Les séchoirs solaires: théorie et pratique. UNESCO, Paris (1985)

International Journal of Energy and Environmental Engineering (2023) 14:905–920
https://doi.org/10.1007/s40095-022-00555-9

ORIGINAL RESEARCH

Mitigation of greenhouse gas emissions from power generation through cofiring coal and raw glycerol: a theoretical feasibility study

Alex O. Dutra[1] · **Marcio L. de Souza-Santos**[1]

Received: 10 June 2022 / Accepted: 4 December 2022 / Published online: 17 January 2023

Abstract

A theoretical technical feasibility investigation aiming to decrease the rate of greenhouse emissions per unit of generated power from fossil fuel plants is presented. To that end, the FGSIG/GT (fuel glycerol integrated gasifier/gas turbine) concept is applied. High-ash coal and raw glycerol—that last deriving from renewable fuel (biodiesel) production—are mixed to form a slurry, which is pumped into the gasifier. The gas stream emerging from that reactor is cleaned by cyclones and filters to decrease the concentration of suspended solids in the stream as well as its granulometry. Before combustion, the fuel gas temperature is decreased to values below the dew points of alkaline compounds in it, thus significantly reducing their concentrations in the gas stream, therefore allowing its injection into commercial gas turbines. Energy recovering is accomplished by two Rankine cycles. The exergetic efficiency is chosen as an objective function to optimize the gasification process. The results reveal a diverging aspect of the RG/solid-fuel ratio influence on the gasification efficiency when comparing with the obtained in previous works where biomasses were fed to the FGSIG/GT process. Due to that highly pressurized process, the whole power generation is optimized resulting in first law efficiencies around 45%, which is noticeable having in mind the relatively low heating values of the presently considered fuels. Additionally, it is important to stress that the objective of this investigation is not just to decrease the overall CO_2 emitted per unit of power output from a station consuming fossil fuel and shift, at least part of that, to one derived from a renewable source.

Keywords High-ash coal · Raw glycerol · Fluidized bed · Gasification · Thermoelectric generation

Abbreviations

CE	Chemical contribution to the exergetic efficiency
CGE	Cold gas efficiency
DSC	Dry solid content of a slurry
EE	Exergetic efficiency
FGSIG/GT	Fuel glycerol slurry integrated gasifier/gas turbine power generation process
HAC	High-ash coal
RG	Raw glycerol
TE	Thermal contribution to the exergetic efficiency
Z	Vertical coordinate inside the gasifier, where Z = 0 is the base of gas distributor surface

✉ Marcio L. de Souza-Santos
dss@unicamp.br

Alex O. Dutra
alexdutra86@gmail.com

[1] University of Campinas, Campinas, SP, Brazil

Introduction

Despite the trend toward renewable power generation, coal is still among the most employed sources of electric power around the planet. Thus, emissions of greenhouse gases from units consuming that fuel will continue to be a preoccupation into the foreseeable future. Additionally, in several countries, a substantial portion of the available coal contains elevated ash fractions [1–3]. Nonetheless, mitigations of those effects are possible. Among the alternatives, there is the mixing of that fossil fuel with biomass or biomass-derived fuels such as raw glycerol (RG), which is a residue from biodiesel production. That production has increased substantially. Just in Brazil, the biodiesel production has surpassed 6.5 million m^3/year [3, 4] and RG represents 11% of that.

Refining of raw glycerol (RG) is not economically feasible [5, 6]. Despite some applications in fuel enhancement, a sizable portion is still discarded as residue. The combination of those factors suggests that, at least in some regions and particular situations, mixing RG and coal might mitigate the

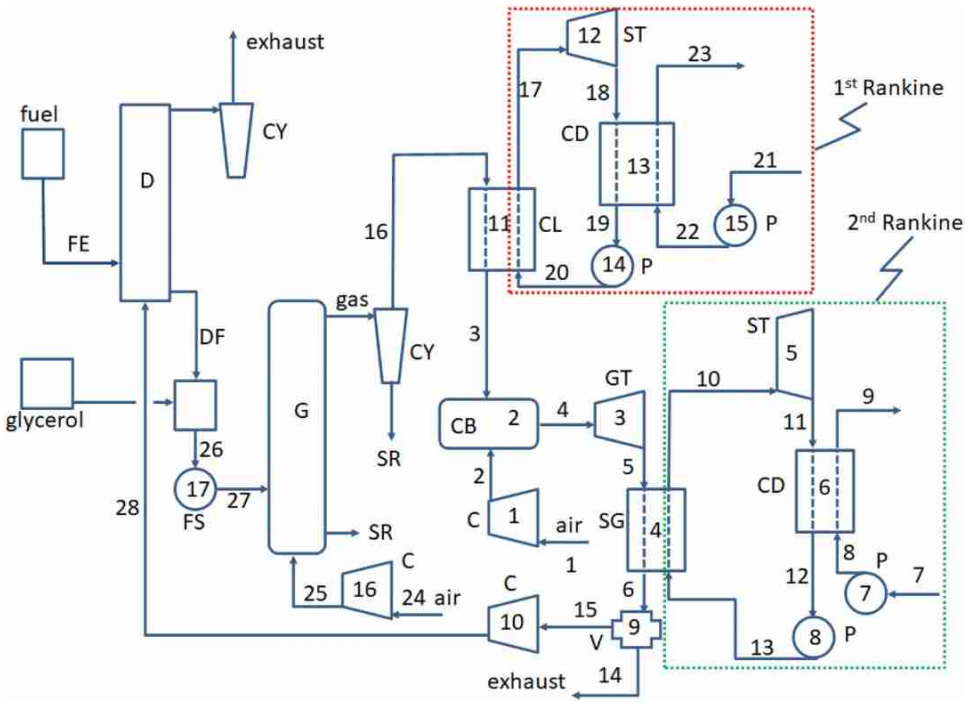

Fig. 1 Scheme of the fuel glycerol slurry integrated gasifier/gas turbine (FGSIG/GT) process; Configuration A. Streams and equipment are numbered to allow power generation simulations and energy-recuperating cycles are encircled. C = compressor, CB = combustor, CD = condenser, CL = cleaning system, CY = cyclone, D = dryer, DF = dried fuel, FE = screw feeding, FS = Fuel glycerol slurry pumping, G = gasifier, GT = gas turbine, SG = steam generator, SR = solid residue, ST = steam turbine, P = water pump, V = valve or splitter

overall carbon dioxide emission per unit of generated electricity. Assuming a worst-case scenario, the present study investigates the application for cases where high-ash coal (HAC) is applied as fuel, but the results might be applied to coal in general.

State of art

Recent studies [7–9] showed that increases of 20 to 30% on the efficiency of power generation are possible if RG is mixed with conventional fuels and that mixture is used to drive units operating under the concept of fuel glycerol slurry integrated gasifier/gas turbine (FGSIG/GT).

There are works on mixing raw glycerol and coal as well as RG combustion [10–12] but no studies on those mixtures consumed by power generation processes have been found in the published literature. In this sense, this is an introductory work on mitigating the emissions of greenhouse gases per mass unit of consumed coal to generate power through the mixing of that fuel with a residual derived from biomass production.

Proposed approach

The schemes of main possibilities of such units are shown in Figs. 1 and 2 [7].

At Configuration A (Fig. 1), the wet solid fuel is fed into dryer (D). Upon leaving that stage, it is mixed with RG and the slurry pumped into the gasifier (G). The produced gas steam is cleaned to decrease its alkaline concentration and the maximum size of carried particles to allow injection into commercially available combustors (CB). The first Rankine branch, composed by equipment 11 to 15, is used to recover part of the energy related to the alkaline condensation. The second Rankine cycle (equipment 4 to 8) provides the energy recovering from the gas turbine (GT) exhaust (stream 5). Part of that energy is also used during the fuel drying stage.

The fuel drying stage is not required at Configuration B, and the wet fuel is mixed with water and/or RG directly before being pumped into the gasifier (G).

A previous study [7] showed that, for the case of biomass as fuel, both configurations led to similar efficiencies. Since Configuration B (Fig. 2) dispenses the solid fuel drying step—which probably would result in capital, maintenance, and operational cost savings—it has been chosen for the present investigation.

It is also worthwhile stressing that both proposals involve pressurized gasification of solid fuel. The feeding of fuel particles into a pressurized vessel raises several critical obstacles. For instance, if Archimedes screws are employed, compact blocks of fuel would enter the reactor (either combustor or gasifier). Those would not be easily disintegrated, leading to inefficient combustion or gasification. The application of cascade feeding consisting of a series of lock-hoppers has been proposed and applied [13, 14]. However, such a method requires discontinuous operations and demands injections of inert gas (usually nitrogen) to prevent spontaneous fuel combustion inside the hoppers. Those factors add to the power plant capital, operational, and maintenance costs.

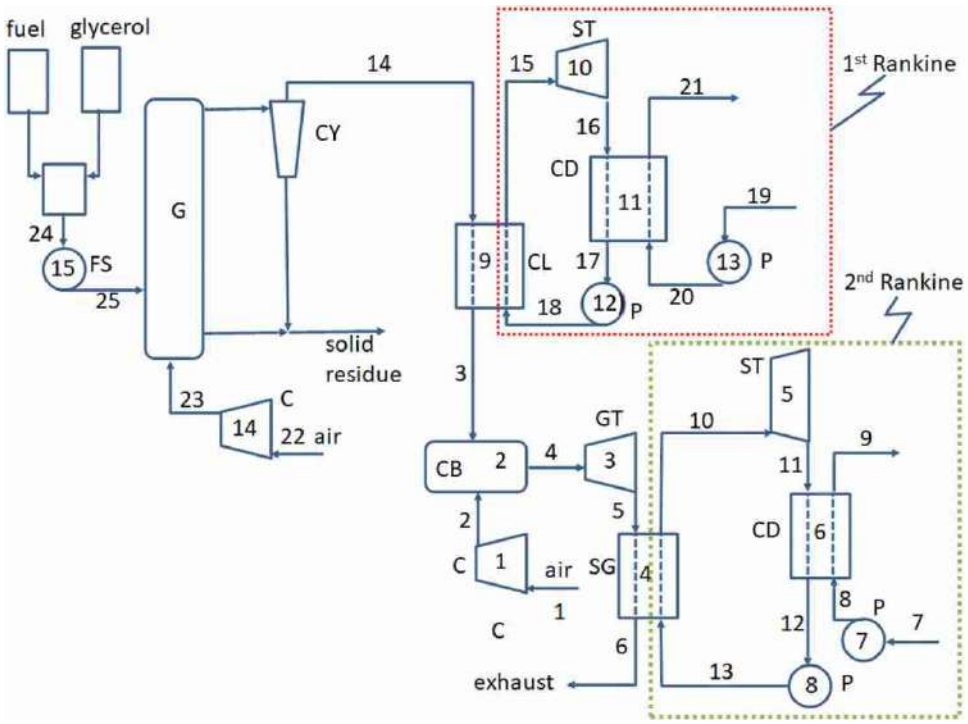

Fig. 2 Scheme of the fuel glycerol slurry integrated gasifier/gas turbine (FGSIG/GT) process; Configuration B. Streams and equipment are numbered to allow power generation simulations. C = compressor, CB = combustor, CD = condenser, CL = cleaning system, CY = cyclone, FS = fuel glycerol slurry pumping, G = gasifier, GT = gas turbine, SG = steam generator, ST = steam turbine, P = water pump, V = valve or splitter

Water slurry feeding has been proposed [2, 15–17]. However, just the evaporation of added water uses almost all potential fuel combustion enthalpy. That renders any gasification technique unfeasible. This obstacle can be surpassed through the application of liquid hydrocarbons [16], which is proposed here, and therefore differs from a previous study [2] when HAC water slurry was applied.

Additionally, to ensure the continuous operation of the generation plant, it has been assumed that the solid fuel could be pumped using water as slurry liquid even when RG may not be available.

Objective

This theoretical investigation intends to find the optimum ratio between the inflows of HAC and RG that could result in the highest efficiency obtainable from the FGSIG/GT (fuel glycerol slurry integrated gasifier/gas turbine) generation process.

Specific objectives

The specific objectives are:

a. Optimize the pressurized fluidized bubbling bed gasifier receiving a slurry of HAC glycerol. The gasification exergetic efficiency was used as objective function.
b. Optimize the whole FGSIG-GT process aiming to maximize its first law efficiency.

Methodology

This theoretical study employs two simulation software.

The Comprehensive Simulator of Fluidized and Moving Beds (CeSFaMB©)[1] was applied for optimizing the gasification step. Such a program has been validated [18–25] and used in many investigations [2, 7–9, 18–33]. Its mathematical code is composed of 95 coupled differential equations describing the mass and energy continuities at the bed and freeboard. It considers more than 30 solid and gaseous chemical species as well as their reactions (homogeneous and heterogeneous). The results allow studying the temperature and composition profiles of gaseous and solid phases. Simulation results also provide many engineering parameters employed in equipment design. Details of the mathematical model behind CeSFaMB© as well as examples of its application can be found elsewhere [18].

The IPES© software is employed to optimize the whole power generation process. Its mathematical core is composed by equations describing the first and second laws of thermodynamics around each equipment. Physicochemical properties of gas and liquid mixtures in each follow are computed using Redlich–Kwong–Soave relations to correct deviations from ideal behavior. Levenberg–Marquardt algorithm and finite difference to the Jacobian are applied to allow the solution equation system. After processing, the temperature,

[1] www.csfmb.com.

Table 1 Proximate analysis of a typical HAC

Component	Mass percentage (wet basis)
Moisture	1.57
Volatile	18.49
Fix carbon	31.24
Ash	48.70

Table 2 Ultimate analysis of a HAC

Species	Mass percentage (dry basis)
Carbon	42.12
Hydrogen	2.71
Nitrogen	0.74
Oxygen	2.67
Sulfur	2.28
Ash	49.47

composition, pressure, and many other properties of each stream of the simulated process are provided. The simulator has been applied in several studies [2, 7–9, 26–34].

The main steps of this work are listed below:

1) First round of gasifier optimization. During this step, the injection rate of air into the gasifier and the rate of RG added to the basic HAC–water slurry were varied. The ratios between RG and HAC feeding rates are described by the dry solid content (DSC), which is the mass percentage of solid in the slurry..
2) All other variables, including the gasifier main geometric characteristics as well as the HC feeding rate, its particle size distribution and other properties, were kept constant. The operational conditions leading to feasible bubbling fluidized bed operations were found by preliminary simulations. The gasification exergy efficiency (EE) was employed as optimization function.
3) For each DSC leading to the highest EE, the gasifier diameter was added as variable.
4) Once the gasifier with the highest EE operational condition was found, the characteristics of the exiting gas stream are used to simulate the whole power generation process described in Fig. 2. The first law of thermodynamics efficiency was used as the objective function to optimize the process.

Premises

During this theoretical investigation, the following has been assumed:

1) The gasification reactor works under the bubbling fluidized bed technique. Other types of reactors–such as circulating beds and entrained flow–might be employed. However, bubbling beds are less stringent regarding the range of size and density of feeding particles. Any rock much denser or larger than the average in the bed would drop on the distributor and might be withdrawn without interrupting the reactor's continuous operation [15, 35].
2) The composition of a typical HAC was assumed and is described in Tables 1 and 2 [2].
3) The dry-basis HAC high heating value was taken as 18.11 MJ/kg [2].
4) The sphericity of feeding HAC particles was taken as 0.7, which is within the typical characteristics of grinded coal.
5) A particle size distribution of feeding HAC has been chosen, and led to an average particle size of 1.1 mm. This is the usual operational range of bubbling fluidized beds [18, 35]
6) The real and apparent particle densities of the feeding HAC have been set as 1830 and 1680 kg/m^3 [2].
7) Proper commercially available pumps should be able to handle up to 40% DSC slurries [36–38]. However, manufacturers [39, 40] indicate that 60% DSC slurries might be pumped as well. In view of that, the range of DSC investigated here was set between 40 and 60%.
8) For this initial study, the feeding rate of HAC was set as 10 kg/s (wet basis). Scaling up or down should not sensibly affect the results achieved at this investigation.
9) The mass flow of RG was varied between 4 and 8 kg/s. Preliminary simulations showed that range could provide relatively high gasification efficiency. Additionally, contingencies involved in providing RG to the power plant location should be kept in mind. Therefore, a minimum flowrate of liquid water to be mixed with the HAC is kept. That should allow obtaining a pumpable slurry, even when RG might not be available. Such mixture would provide a slurry close to 60% DSC. Given the flow of solid fuel, that flow of water would be 6.67 kg/s.
10) Since the gasification takes place in a fluidized bed, the exposed-core model has been applied to model the heterogeneous reactions between the solid fuel and gases [18].
11) The coated-inert particle model (CIP)–which assumes that the feeding liquid fuel coats solid particles in the bed–was used for reactions between gases and RG [41].
12) The gasifier operational pressure was set at 4 MPa. That should decrease the equipment volume and might improve the overall power generation efficiency when compared to lower operational pressures. Additionally, air compression from ambiance conditions to that pressure can be accomplished by commercial compressors without the need of intercooling [42].
13) Besides investigating the proposal for HAC and keeping the worst-case scenario perspective as well as to follow

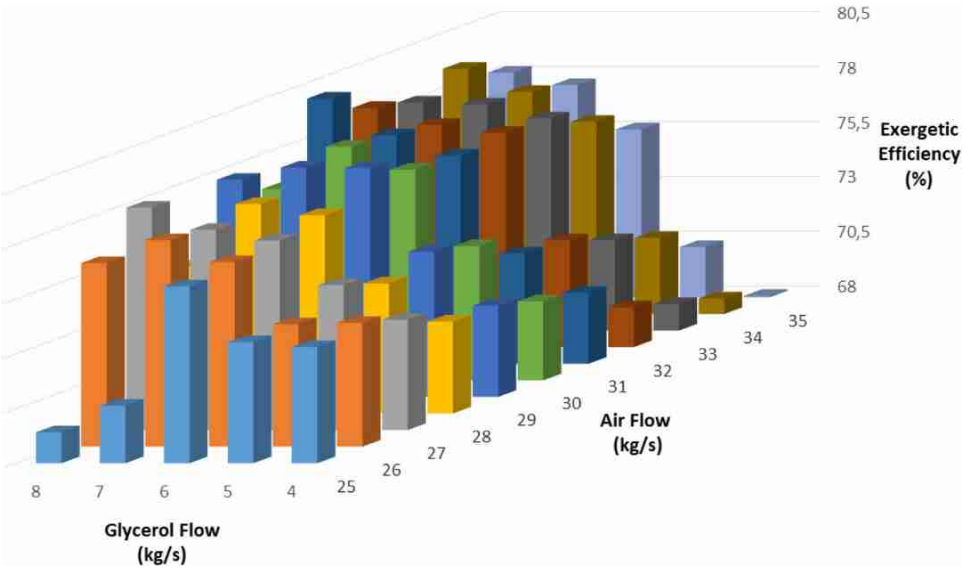

Fig. 3 Gasification exergetic efficiency against the airflow and RG injection rates

the value applied in previous works [7–9], the RG heating value was set at 16.80 MJ/kg [43].

14) The maximum temperature of gas injection into the gas turbine has been limited to 1700 K [44].
15) During the first round of gasifier optimization, its bed internal diameter was kept at 10 m, bed height at 4 m, and freeboard height at 6 m. Such values were reached after preliminary simulations, which provided high gasification efficiency and stable fluidization. It is worth remembering that the following conditions should be ensured to allow viable bubbling fluidization operations [18, 35]:

- The gas superficial velocity in the bed should not surpass the transport velocity value.
- Particle temperatures cannot surpass the ash softening point.
- Steady state must be maintained.
- No particle segregation may occur.

Future works might explore changes on those assumptions.

Discussions related to economic aspects are not within the scope of the present work.

Results and discussions

First round of gasifier optimization

As mentioned above, aiming to maximize the gasification EE, at this first round of optimization the air and RG injection rates of into the gasifier were varied.

It is also important to notice that the produced gas exergy reflects two main factors. One is related to its enthalpy, which tends to increase with the temperature of the produced gas. That aspect of the exergy is called here as thermal exergy (TE). The other is related to the concentrations of fuel species—such as hydrogen, carbon monoxide, and methane—in the produced gas stream. This has been named chemical exergy (CE). The gasifier exergetic efficiency (EE) is given by the ratio between produced gas exergy (TE plus CE) against the total exergy entering the equipment, or exergies brought by the injected air as well as by the feeding solid fuels.

Using CeSFaMB©, various combinations between gasifier dimensions and injected airflow rates were simulated, thus allowing to study all internal details–such as temperature, composition, pressure, and fluidization parameters—of each phase (emulsion, bubbles, and particles) along the whole reactor's interior. Simulations also provided important engineering parameters.

Figure 3 summarizes the gasification EE for each case gasifier bed diameter and airflow rates.

As seen, in general, the EE increases with the concentration of RG in the feeding slurry while decreases for higher air injection rates. The behavior in relation to the RG concentration in the feeding mixture can be understood for the following main reasons:

a) Since the RG coats the HAC particles, it is oxidized before the reactions between gases and HAC begin before heterogenous reactions (few of them endothermic) between gases and the HAC start. Thus, there is a range of operations where higher RG/HAC ratios lead to higher temperatures and increases of the leaving gas TE.
b) Air is injected into the gasifier through the distributor at its basis. During the gasification process, fuel gas species— such as H_2, CO, and CH_4 produced by gasification reactions—are oxidized in the region from the dis-

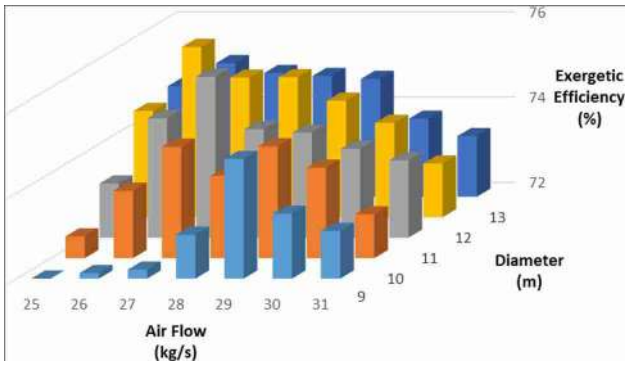

Fig. 4 Gasification exergetic efficiency against the airflow and gasifier internal diameter for the case of RG inject rate at 5 kg/s

tributor until the point where all oxygen expires. That is the bed oxidizing region. Relatively high air ratios tend to decrease the concentration of fuel gases, therefore declining the leaving stream CE.

c) Additionally, it is important to consider the effect of fluidized bed dynamics. Part of the injected air through the distributor is diverted to emulsion and the remaining to the bubble phase. For a given bed diameter, the ratio between the fraction of air flow diverted to the emulsion compared to the diverted to the bubble phase increases when the conditions nearer those found at minimum fluidization one [8, 35]. In bubbling fluidization, the emulsion phase holds almost all particles, which rapidly reacts with the incoming oxygen, while the oxygen in the bubbles must diffuse to the emulsion phase before reacting with the fuels in the bed. Operations where the injected oxygen is completely exhausted closer to the distributor allow for larger layers of the reactor to be at reducing condition than operations farther the minimum fluidization condition. Thus, conditions nearer minimum fluidization favor higher concentration of fuel gases in the exiting stream. That explains why certain operations with lower air ratio led to higher CE of the exiting gas stream.

d) As many other effects are involved in such a complex process [18, 35], straightforward or monotonic variation of EE against just two variables is seldom found.

Second round of gasifier optimization

During this optimization stage, the gasifier internal diameter was introduced as variable. Therefore, for each RG injection rate, the EE was computed against the airflow rate and the bed diameter. As an example, Fig. 4 shows the results when 5 kg/s of RG injection was set.

Since higher airflow injections into the gasifier move the operation toward complete or stoichiometric air–fuel ratio, the temperature in the bed increases. Despite higher temperatures, the oxidation of fuel gases (such as H_2, CO, and CH_4) decreases their concentration in the stream exiting the gasifier. An optimum point could be found within the studied range.

According to the simulations, for a given gasifier bed diameter, a maximum EE value could be found for an intermediate air injection rate. This is explained by the above comments on the interplay between TE and CE.

It is also valuable noticing that combustion reactions are usually faster than gasification ones. Gas fuel seldom survives in the region where oxygen is available. Moreover, particles are in direct contact with solid and liquid fuels in the emulsion phase while no such fuels are present inside the bubbles. Therefore, the available oxygen is consumed faster in the emulsion phase than in the bubble one. Oxygen remains in the bubbles longer or at higher positions in the bed [18]. Greater differences of oxygen concentration between bubbles and emulsion provoke faster rates of mass transfer between those phases. If the bed conditions are closer to the minimum fluidization ones, smaller bubbles are formed, which leads to greater interface area between bubbles and emulsion per unit of bed volume. That explains why the oxygen is exhausted closer to the distributor surface when the bed fluidization dynamics approach those found at minimum fluidization regimes. Above that position, flue gases can accumulate. Thus, at a given airflow rate, higher concentrations of combustible gas species can be achieved for wider beds, thus increasing the CE of gasifier leaving stream. Lager equipment would lead to higher capital costs. Optimizations considering economic aspects are left to future investigations.

The best results obtained after completing those two stages of gasifier optimization are summarized in Table 5, shown in Appendix 1.

Table 6 lists the most important inputs and outputs of those optimum operations, and is also presented in Appendix 1.

It is worth mentioning that due to the high compression, the temperature of injected air is relatively high. In the present cases, its energy was enough to evaporate all water in the feeding slurry.

The compositions of produced gas streams are shown in Table 7 (see Appendix 1).

As seen, the best results regarding EE were reached for the operation with the maximum rate of glycerol added to the slurry with HAC, or DSC near 40%.

Details of the temperature, composition, and reaction rates throughout the gasifier can be seen at Appendix 2. Those also help to understand the operational details of that reactor.

Table 6 also reveals that, within the studied range, the gasification exergy and the cold gas efficiencies increase with the glycerol–coal ratio. The main reasons for that have been described above. Therefore, increases on that ratio leads to higher temperatures in the fluidized bed, as shown in Fig. 5.

Figure 6 shows the influence of slurry's RG concentration on the gasification EE. Here the interplay between TE and CR

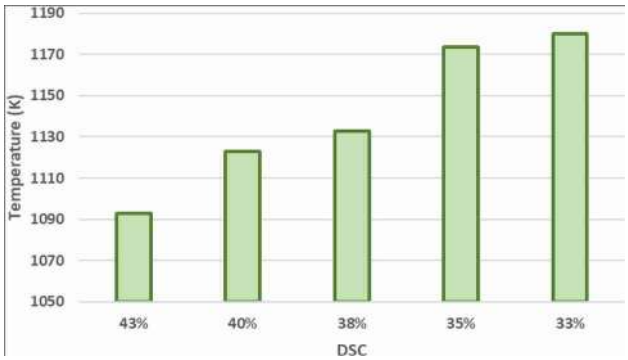

Fig. 5 Temperature in the fluidized bed in each case

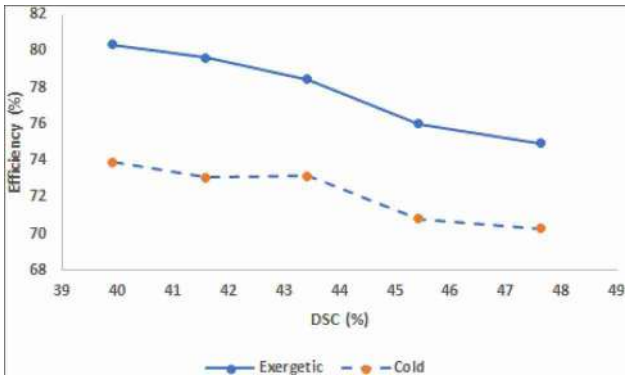

Fig. 6 Exergetic and cold efficiency in each case

becomes even clearer. Higher RG/solid-fuel ratio (or lower DSC) tends to increase the fluidized bed temperature, thus augmenting the TE while not significantly decreasing the CE.

Power generation process optimization

Once the optimum gasifier geometry and operational conditions were found, the produced gas characteristics were used as input data related to stream 14 (Fig. 2) and the entire power generation process could be optimized. For that, the IPES© software was applied and the overall power generation efficiency was chosen as the optimization function.

The main limitations for that search have already been listed among the premises.

The optimization procedure was repeated for each rate of glycerol consumption, which can be translated into the slurry DSC.

As an example, the main conditions or characteristics of the various involved streams in the process are listed in Table 3.

The best results for the process, at each rate of glycerol added to the HAC, are summarized in Table 4.

As verified, within the studied range, both first and second law efficiencies increase with the rate of consumed glycerol. Those behaviors are also shown in Figs. 7 and 8.

Table 3 Main characteristics of the power generation process (Configuration B, Fig. 2) consuming slurry with 39.9% DSC

Stream	Fluid	Temperature (K)	Pressure (kPa)	Flow (kg/s)
1	Air	298.0	101.3	166.4
2	Air	938.0	4085.0	166.4
3	Fuel gas	800.0	4085.0	51.6
4	Gas	1699.9	4080.0	218.0
5	Gas	921.2	120.0	218.0
6	Gas	400.0	115.0	218.0
7	Cooling water	298.0	115.0	700.0
8	Cooling water	298.0	130.0	700.0
9	Cooling water	328.6	125.0	700.0
10	Steam	880.0	9995.0	39.0
11	Steam	381.1	125.0	39.0
12	Water	362.8	120.0	39.0
13	Water	363.0	10,000.0	39.0
14	Fuel gas	1176.8	4090.0	51.6
15	Vapor	880.0	9995.0	9.0
16	Steam	381.1	125.0	9.0
17	Steam	345.6	120.0	9.0
18	Water	345.9	10,000.0	9.0
19	Cooling water	298.0	115.0	165.0
20	Cooling water	298.0	130.0	165.0
21	Cooling water	328.9	125.0	165.0
22	Air	298.0	101.3	32.0
23	Air	938.9	4100.0	32.0
24	Slurry	298.0	101.3	16.7
25	Slurry	298.1	4010.0	16.7

The above pictures illustrate how the power generation plant first and second law efficiencies increase with the concentration of glycerol in the consumed HAC slurry. That happens when the thickness of liquid layer coating of feeding fuel particles increases. Such behavior was not observed during previous studies where the RG was added to other fuels [8, 9]. This is primarily due to the significantly lower porosity of HAC (around 8%) when compared with biomasses (near 50%) [8, 9]. The reasons for that can be better understood by the following reasoning:

- Gases in the emulsion must react with the RG coating before reaching the solid particles.
- The total carbon conversion is a composition between the conversions of carbon in the liquid and in the solid fuel.
- For very porous particles, the participation of carbon conversion from the solid fuel is comparable to the participation of carbon conversion from the liquid fuel. Thicker RG layers around the solid particle increase the resistance for gases to reach the porous particles. Thus, after a given threshold of RG ratios in the feeding slurry, the total carbon conversion might decrease.
- If the solid particle porosity decreases, the participation of carbon conversion from the solid on the total carbon conversion decreases. Thus, the abovementioned threshold is found for higher RG ratios in the feeding slurry.

Table 4 Main power generation parameters for each case

Parameter	DSC (%)				
	47.63	45.43	43.43	41.59	39.90
Consumed mechanical power (MW)[1]	100.76	108.66	120.84	127.65	136.66
Generated by turbines (MW)	201.39	216.68	239.01	256.07	272.63
Net generated power (MW)	100.63	108.02	118.17	128.42	135.97
Rate of energy inputted by the fuels (MW)[2]	235.24	250.61	265.97	281.34	296.70
First law efficiency (%)	42.78	43.10	44.43	45.65	45.83
Rate of exergy inputted by fuels (MW)	282.00	298.60	315.40	332.30	349.20
Second law efficiency (%)	35.68	36.18	37.47	38.65	38.94

[1]Consumed by compressors and pumps

[2]Mass flows times their combustion enthalpies at 298 K and 101.325 kPa.

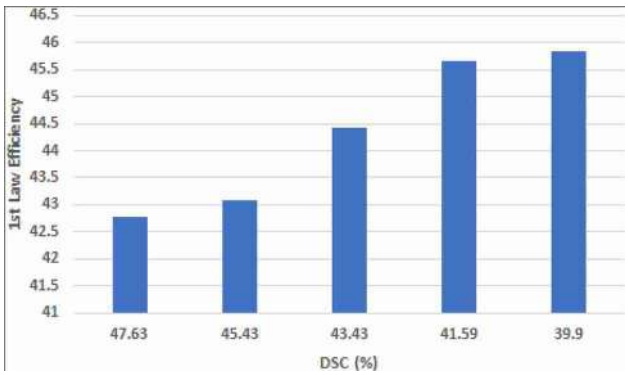

Fig. 7 First law efficiency for the process

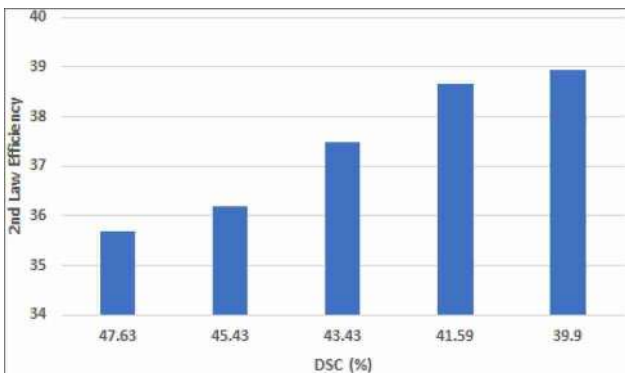

Fig. 8 Second law efficiency for the process

The present power generation alternative may also work even when no RG is available, and only water is used to prepare the slurry. The optimizations of power generation processes applying those two possibilities would be left for future studies.

Finally, it is worth commenting that due to the possibility of feeding solid particles to a pressurized gasifier and injection of exhausted gas from combustion at relatively high temperature into the gas turbine, the power generation first law efficiency reached 45%, which is notable having in mind the relatively low heating values of the presently considered fuels. More conventional power generations [33, 45–49] present efficiencies in the range from 31 to 46%. Furthermore, it is important to emphasize that the present alternative shows the possibility of shifting part of the CO_2 emission due to the use of fossil fuel to release derived from a renewable source.

Conclusions

Since glycerol is a residue derived from a renewable fuel source (biomass) during the production of biodiesel, the present theoretical feasibility work explored the possibility of an efficient process, which allows mitigating the emissions of greenhouse gases (mainly CO_2) from power generation consuming nonrenewable fuel such as coal. That can be achieved by mixing the raw glycerol (RG) with coal to form a slurry, which can be pumped the FGSIG/GT process. It is worth mentioning that slurry feeding greatly simplifies introducing particle solids into highly pressurized vessels, thus accomplishing higher overall power generation efficiencies than operations at lower pressures. The gasifier has been optimized aiming maximizing its exergetic efficiency by varying the RG/coal ratio in the feeding slurry as well as the gasifier basic dimensions. After that, the whole proposed power generation process was optimized having its first law efficiency as objective function.

Despite the low combustion enthalpies of the feeding high-ash coal and RG, the achieved 45% overall power generation first law efficiency is a good indication that similar strategy may be applied to situations where higher coal quality and RG is available.

Furthermore, it is important to emphasize that the present alternative shows the possibility of shifting part of the CO_2 emission due to the use of fossil fuel to emission from a renewable source. It is also worth stressing that no similar work, i.e., application of mixtures of low-rank coal and glycerol for power generation, has been found in the literature.

Future investigations should address other points, such as:

- The economic aspects of the present proposal.

- Improvements in the energy recuperation cycles.
- Influence of coal quality, as well as its particle sizes.
- The possibility of applying other gasification techniques, such as circulating fluidized bed and entrainment flow reactors.

Appendix 1

Important tables mentioned in the text are presented below (Tables 5, 6, 7).

Table 5 Main results for each rate of RG injection into the gasifier

Parameter	DSC (%)				
	47.63	45.43	43.43	41.59	39.90
Flow of RG (kg/s)	**4**	**5**	**6**	**7**	**8**
Air flow rate (kg/s)	25	26	28	31	32
Bed diameter (m)	14	12	11	11	11
EE (%)	74,93	75,99	78,43	79,63	80,34
Bed average temperature (K)	1093,04	1123,05	1132,61	1173,42	1180,13
Cold gas efficiency (%)	70,29	70,85	73,14	73,06	73,9

Table 6 Most important parameters related to gasification operations for various DSC

Main input parameter	DSC (%)				
	47.63	45.43	43.43	41.59	39.90
Flow of glycerol (kg/s)	4	5	6	7	8
Flow of wet coal (kg/s)	10	10	10	10	10
Flow of added water (kg/s)	6.67	6.67	6.67	6.67	6.67
Flow of injected air (kg/s)	25	26	28	31	32
Temperature of injected air (K)	938.9	938.9	938.9	938.9	938.9
Temperature of pumped slurry (K)	298	298	298	298	298
Bed internal diameter (m)	14	12	11	11	11
Bed height (m)	4	4	4	4	4
Freeboard internal diameter (m)	14	12	11	11	11
Freeboard height (m)	6	6	6	6	6
Slurry injection position (m)[a]	0.5	0.5	0.5	0.5	0.5
Average pressure inside the gasifier (MPa)	4.1	4.1	4.1	4.1	4.1
Main output parameter					
Oxygen ratio	0.3225	0.3143	0.3184	0.3328	0.3254
Exergetic efficiency (%)	74.93	75.99	78.43	79.63	80.34
Carbon conversion (%)	96.18	95.38	96.97	97.97	97.75
Cold gas combustion enthalpy (MJ/kg)	4.95	5.08	5.19	5.06	5.18
Hot gas combustion enthalpy (MJ/kg)	5.53	5.68	5.83	5.77	5.88
Bed average temperature (K)	1093.0	1123.1	1132.6	1173.4	1180.1
Cold gas efficiency (%)	70.29	70.85	73.14	73.06	73.9
Hot gas efficiency (%)	89.26	90.39	93.11	94.56	95.18
Flow of solids discharged from the bed (kg/s)	0.30	0.34	0.39	0.33	0.31
Flow of elutriated solids (kg/s)	5.34	5.61	5.83	6.22	6.37
TDH – Transport disengaging height (m)	4.213	4.303	4.36	4.40	4.42
Rate of energy provided by fuels (MW)	235.24	250.61	265.97	281.34	296.70
Total rate of energy entering the equipment (MW)	252.40	268.45	285.19	302.61	318.67
Rate of energy leaving with the hot gas (MW)	225.30	242.64	265.53	286.14	302.99
Rate of energy leaving with cold gas (MW)	177.41	190.20	208.60	221.09	235.48
Average temperature of leaving gas stream (K)	1088.2	1119.0	1134.1	1177.3	1176.8
Pressure loss at the distributor (kPa)	0.21	0.23	0.27	0.33	0.35
Pressure loss in the bed (kPa)	24.51	22.78	22.77	21.5	21.54
Minimum fluidization velocity (m/s)	1.9×10^{-3}	2.2×10^{-3}	3.0×10^{-3}	2.7×10^{-3}	3.9×10^{-3}
Superficial gas velocity at bed middle (m/s)	0.019	0.028	0.035	0.040	0.039
Rate of exergy brought by fuels (MW)	282.00	298.60	315.40	332.30	349.20
Rate of exergy brought by injected air (MW)	16.81	17.48	18.83	20.84	21.52
Total entering rate of exergy (MW)	298.8	316.1	334.2	353.1	370.7
Total leaving rate of exergy with the gas (MW)	223.9	240.2	262.1	281.2	297.9
Total leaving rate of exergy (MW)	226.1	243.8	267.3	287.3	304.7
Ratio between the exergy of leaving gas and the total entering the equipment (%)	74.93	75.99	78.43	79.62	80.35

[a]Above the gas distributor surface

Table 7 Produced gas composition (molar percentage) for each case

Species	DSC (%)				
	47.63	45.43	43.43	41.59	39.90
H_2	19.97	20.15	20.25	19.61	19.98
H_2O	15.37	15.56	14.84	15.11	14.93
H_2S	0.21	0.22	0.20	0.20	0.19
NH_3	0.05	0.05	0.03	0.03	0.03
NO	0.00	0.00	0.00	0.00	0.00
NO_2	0.00	0.00	0.00	0.00	0.00
N_2	38.54	38.04	38.37	39.10	38.66
N_2O	0.00	0.00	0.00	0.00	0.00
O_2	0.00	0.00	0.00	0.00	0.00
SO_2	0.18	0.15	0.14	0.12	0.11
CO	13.94	14.66	15.38	15.79	16.11
CO_2	10.46	9.99	9.54	9.04	8.94
HCN	0.00	0.00	0.00	0.00	0.00
CH_4	1.24	1.15	1.23	0.98	1.01
C_2H_4	0.02	0.02	0.01	0.01	0.01
C_2H_6	0.01	0.01	0.01	0.01	0.01
C_3H_6	0.00	0.00	0.00	0.00	0.00
C_3H_8	0.00	0.00	0.00	0.00	0.00
C_6H_6	0.01	0.01	0.01	0.00	0.00
Tar	0.00	0.00	0.00	0.00	0.00

Appendix 2

To provide a more complete view, the following figures illustrate a few aspects of the gasifier operation under those conditions. Those have been obtained by the application of CeSFaMB© software.

Figures 9 and 10 picture the temperature profiles in the bed and freeboard, respectively.

As expected at bubbling fluidized bed operations, the temperatures are uniform and relatively low, which allows for easier control as well many advantages when compared with other techniques [18, 35].

Figure 11 shows that complete cracking and coking of tar generated during the fuel pyrolysis near its feeding position (Z = 0.5 m) could be achieved. Thus, the produced gas would be free of Tar. Such prevents operational problems and maintenance costs to clean the produced gas.

Figure 12 allows observing the fast development and destruction of Tar near the fuel feeding position, which is far below the bed top. Therefore, well-designed equipment would allow sufficient bed height to complete those reactions before gas with Tar passes to the freeboard region; otherwise, the risk of jeopardizing the gas cleaning system increases. Additionally, the fuel feeding position is above the oxidation region, thus allowing the volatiles—rich in hydrogen, methane, and carbon monoxide—to survive and improve the quality of the produced gas.

Figure 13 shows other important heterogeneous reactions occurring in the emulsion. It becomes clear how fast fuel oxidation is when compared with gas–solid reactions. That also explains the surge of temperatures near the distributor (Z = 0), as shown in Fig. 9, as well as the fast decline of oxygen near that position (Fig. 14).

The concentration profiles of other important gas species throughout the gasifier interior are presented in Fig. 15.

Drying and evaporation of water entering with the slurry is paramount for hydrogen production (see reaction R.3 in Appendix 3). The rates of those reactions are also pictured in Fig. 9, while Fig. 16 illustrates the main homogeneous ones.

That figure demonstrates the key role played by the shift reaction (R.41 in Appendix 3) throughout the bed, which continues in the freeboard.

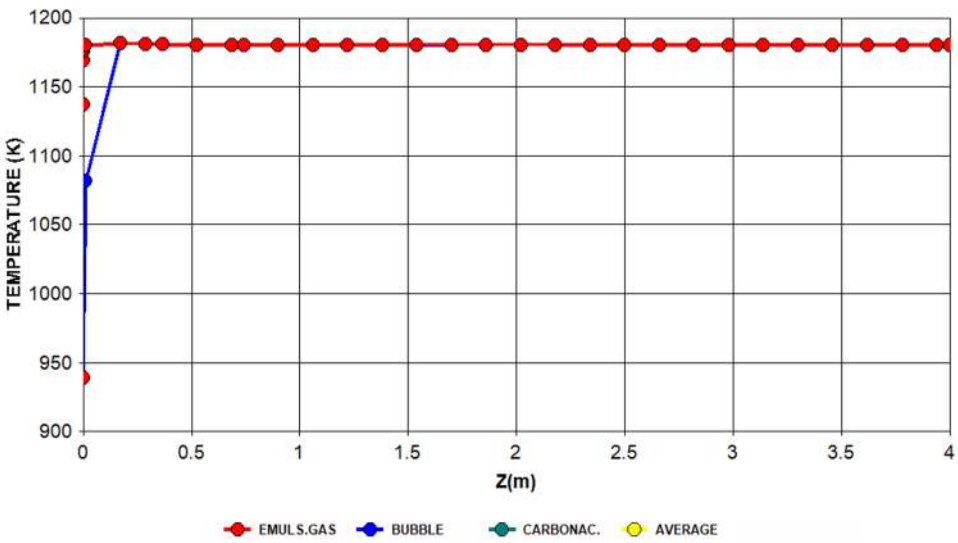

Fig. 9 Temperature profiles inside the gasifier bed

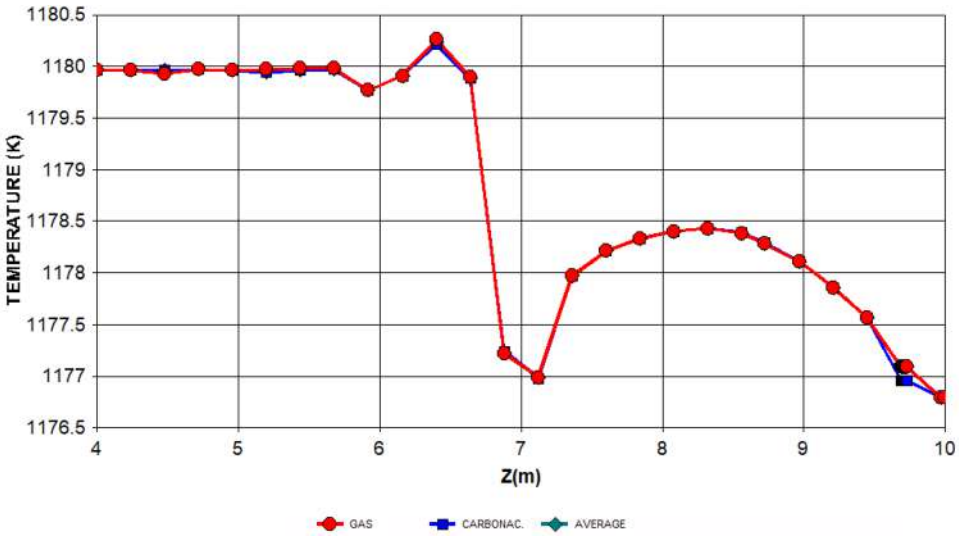

Fig. 10 Temperature profiles inside the gasifier freeboard

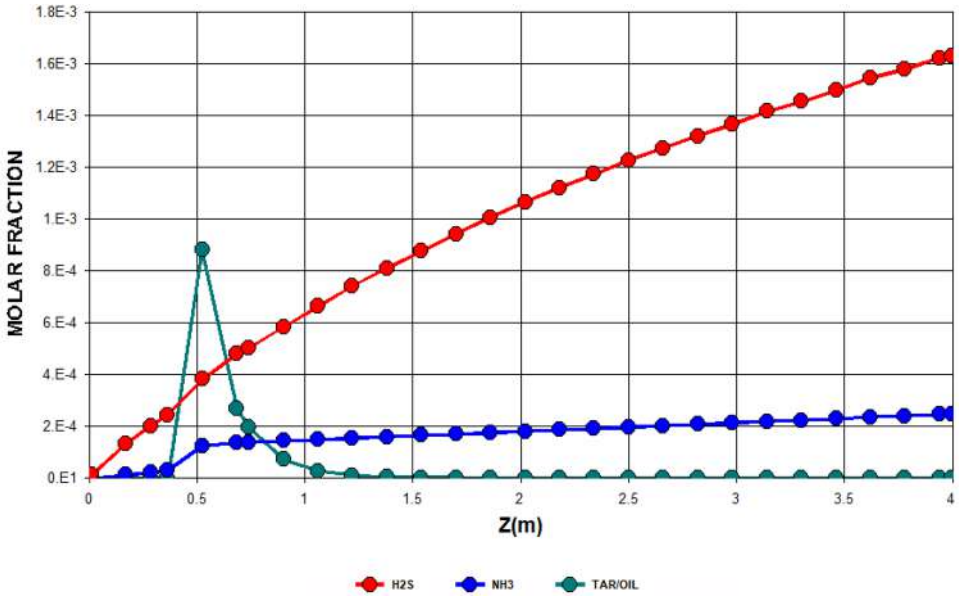

Fig. 11 Molar fractions of Tar, H_2S, and NH_3 throughout the gasifier

Appendix 3

A list of main reactions and processes considered by the simulator (CeSFaMB©) is presented below:

$$\mathrm{CH}_{a_{32}}\mathrm{O}_{a_{33}}\mathrm{N}_{a_{34}}\mathrm{S}_{a_{35}} + \left(\frac{a_{32}}{4} - \frac{a_{33}}{2} + \frac{a_{34}}{2} + a_{35}\right)\mathrm{O}_2 \rightarrow \mathrm{CO}_2 + \frac{a_{32}}{2}\mathrm{H}_2\mathrm{O} + a_{34}\mathrm{NO} + a_{35}\mathrm{SO}_2 \quad \text{(R.1)}$$

$$\mathrm{CH}_{a_{32}}\mathrm{O}_{a_{33}}\mathrm{N}_{a_{34}}\mathrm{S}_{a_{35}} + (1 - a_{33})\mathrm{H}_2\mathrm{O} \leftrightarrow \left(1 + \frac{a_{32}}{2} - a_{33} - a_{35}\right)\mathrm{H}_2 + \mathrm{CO} + \frac{a_{34}}{2}\mathrm{N}_2 + a_{35}\mathrm{H}_2\mathrm{S} \quad \text{(R.3)}$$

$$\mathrm{CH}_{a_{531}}\mathrm{O}_{a_{551}}\mathrm{N}_{a_{546}}\mathrm{S}_{a_{563}} + \mathrm{CO}_2 \leftrightarrow 2\mathrm{CO} + a_{551}\mathrm{H}_2\mathrm{O} + \left(\frac{a_{531}}{2} - a_{551} - \frac{3a_{546}}{2} - a_{563}\right)\mathrm{H}_2 + a_{34}\mathrm{NH}_3 + a_{35}\mathrm{H}_2\mathrm{S} \quad \text{(R.4)}$$

$$\mathrm{CH}_{a_{531}}\mathrm{O}_{a_{551}}\mathrm{N}_{a_{546}}\mathrm{S}_{a_{563}} + \left(2 - \frac{a_{531}}{2} + a_{551} + \frac{3}{2}a_{546} + a_{563}\right)\mathrm{H}_2 \leftrightarrow \mathrm{CH}_4 + a_{551}\mathrm{H}_2\mathrm{O} + a_{34}\mathrm{NH}_3 + a_{35}\mathrm{H}_2\mathrm{S} \quad \text{(R.5)}$$

$$\mathrm{CH}_{a_{32}}\mathrm{O}_{a_{33}}\mathrm{N}_{a_{34}}\mathrm{S}_{a_{35}} + (2 - a_{33})\mathrm{NO} \leftrightarrow \left(\frac{a_{32}}{2} - a_{35}\right)\mathrm{H}_2 + \mathrm{CO}_2 + \left(1 + \frac{a_{34}}{2} - \frac{a_{33}}{2}\right)\mathrm{N}_2 + a_{35}\mathrm{H}_2\mathrm{S} \quad \text{(R.6)}$$

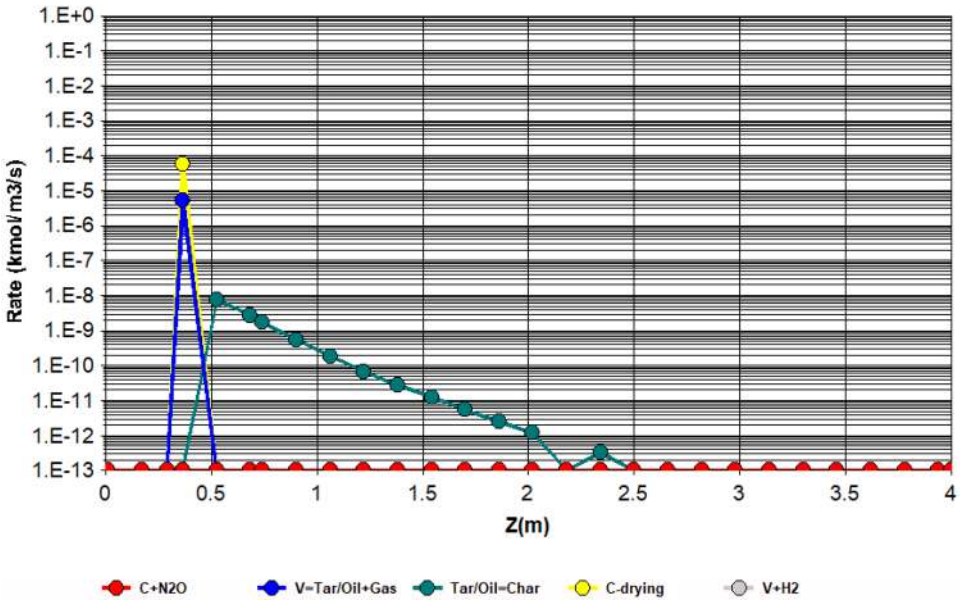

Fig. 12 Rates of Tar decomposition in the emulsion phase

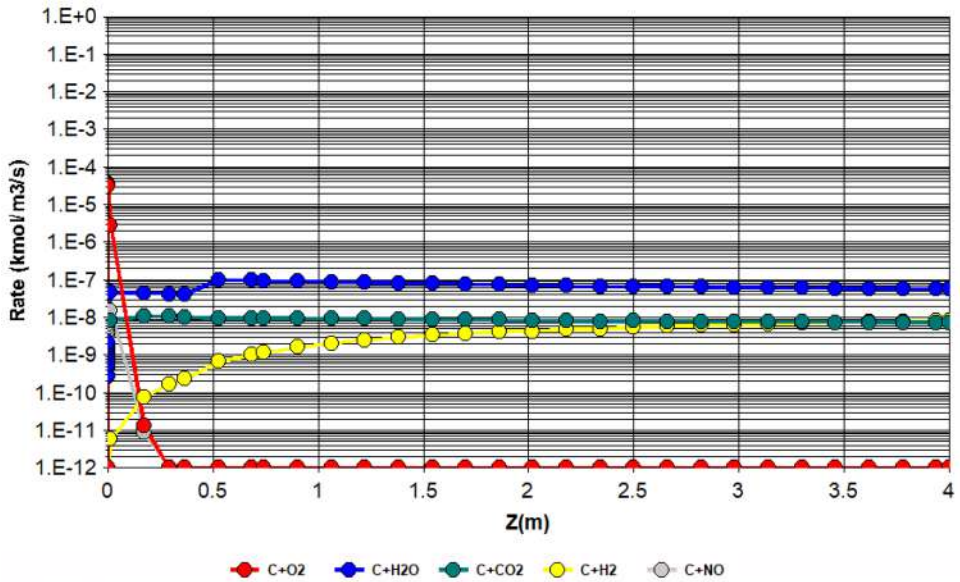

Fig. 13 Main gas–solid reaction rates

$$\text{Fuel}_{\text{daf}} \rightarrow \text{Volatile} + \text{Char}_1 \quad \text{(R.7)}$$

$$\text{Volatile} \rightarrow \text{Gases} + \text{Tar} \quad \text{(R.8)}$$

$$\text{Wet Carbonaceous Solid} \rightleftarrows \text{Dry Carbonaceous Solid} + H_2O \quad \text{(R.10)}$$

$$CH_{a_{32}}O_{a_{33}}N_{a_{34}}S_{a_{35}} + (2 - a_{33})NO \leftrightarrow \left(\frac{a_{32}}{2} - a_{35}\right)H_2 + CO_2 + \left(1 + \frac{a_{34}}{2} - \frac{a_{33}}{2}\right)N_2 + a_{35}H_2S \quad \text{(R.12)}$$

$$CH_{a_{531}}O_{a_{551}}N_{a_{546}}S_{a_{563}} + (1 - a_{551})N_2O \leftrightarrow \left(\frac{a_{531}}{2} - a_{563}\right) H_2 + CO + \left(1 + \frac{a_{34}}{2} - \frac{a_{33}}{2}\right)N_2 + a_{35}H_2S \quad \text{(R.13)}$$

$$\text{Tar} \rightarrow \text{Char}_2 \quad \text{(R.14)}$$

$$CO + H_2O \rightleftarrows CO_2 + H_2 \quad \text{(R.41)}$$

$$2CO + O_2 \rightleftarrows 2CO_2 \quad \text{(R.42)}$$

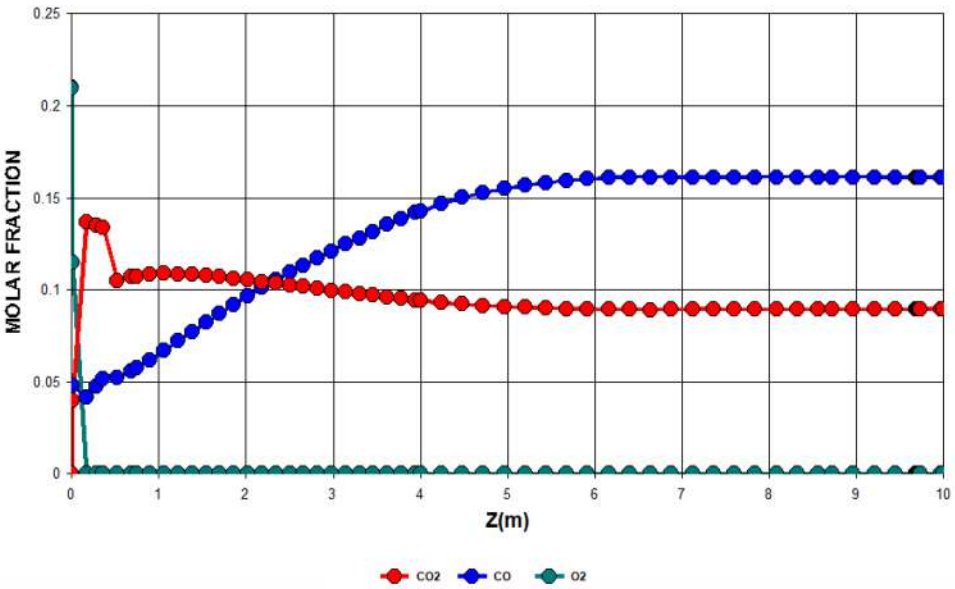

Fig. 14 Concentration of CO_2, CO, and O_2 throughout the equipment

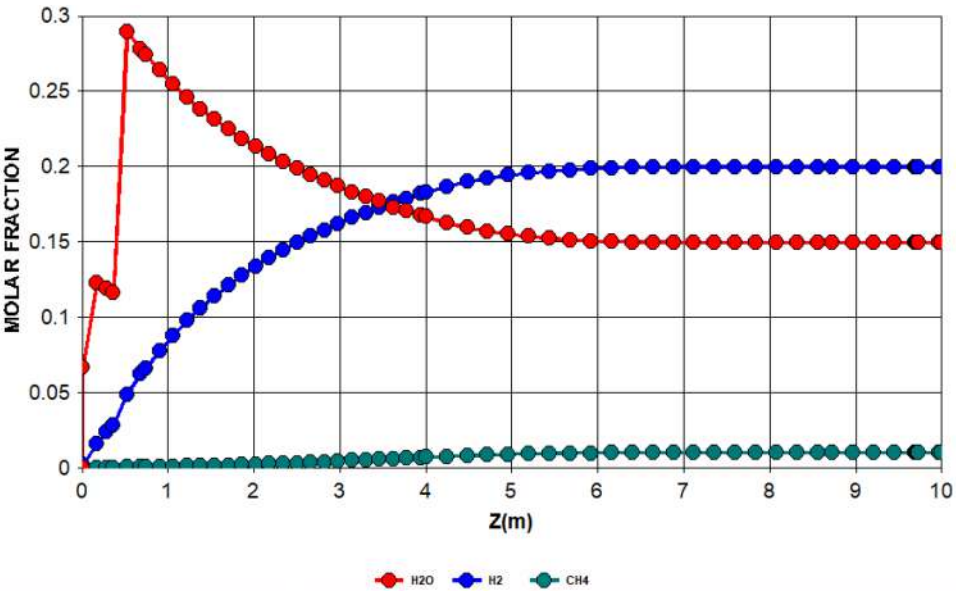

Fig. 15 Concentration of H_2O, H_2, and CH_4 throughout the equipment

$$2H_2 + O_2 \rightleftarrows 2H_2O \quad \text{(R.43)}$$

$$CH_4 + 2O_2 \rightleftarrows CO_2 + 2\,H_2O \quad \text{(R.44)}$$

$$2C_2H_6 + 7O_2 \rightleftarrows 4CO_2 + 6H_2O \quad \text{(R.45)}$$

$$4NH_3 + 5O_2 \rightleftarrows 4NO + 6H_2O \quad \text{(R.46)}$$

$$2H_2S + 3O_2 \rightleftarrows 2SO_2 + 2H_2O \quad \text{(R.47)}$$

$$N_2 + O_2 \rightleftarrows 2NO \quad \text{(R.48)}$$

$$\text{Tar} + O_2 \rightleftarrows \text{Combustion Gases} \quad \text{(R.49)}$$

$$\text{Tar} \rightarrow \text{Gases} \quad \text{(R.50)}$$

$$\text{Tar} + H_2 \rightarrow CH_4 + \text{Other Light Gases} \quad \text{(R.51)}$$

$$C_2H_4 + 3O_2 \rightleftarrows 2CO_2 + 2H_2O \quad \text{(R.52)}$$

$$2C_3H_6 + 9O_2 \rightleftarrows 6CO_2 + 6H_2O \quad \text{(R.53)}$$

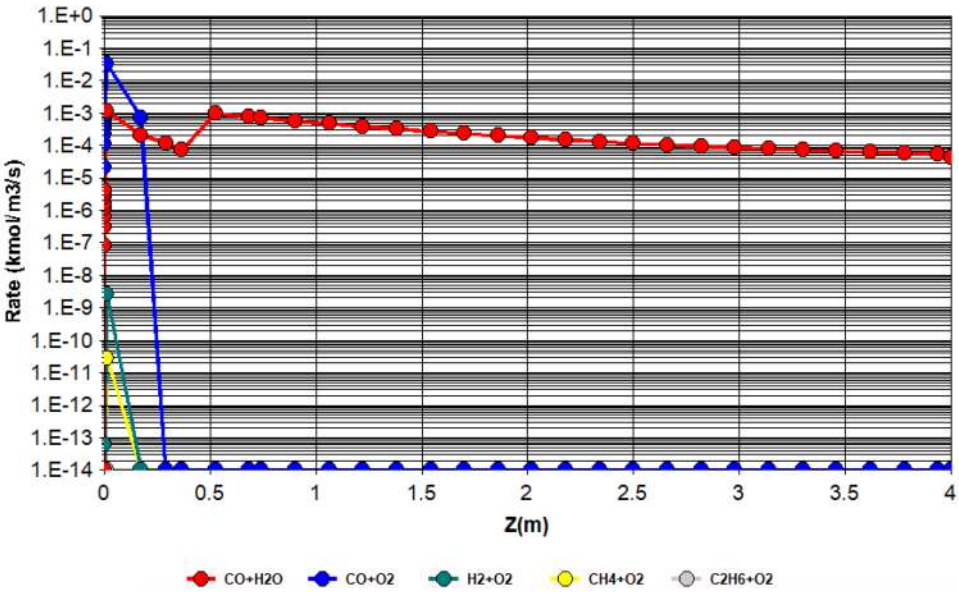

Fig. 16 Main gas–gas reaction rates

$$C_3H_8 + 5O_2 \rightleftarrows 3CO_2 + 4H_2O \quad \text{(R.54)}$$

$$2C_6H_6 + 15O_2 \rightleftarrows 12CO_2 + 6H_2O \quad \text{(R.55)}$$

$$4HCN + 3O_2 \rightleftarrows 4CO + 2N_2O + 2H_2 \quad \text{(R.56)}$$

$$CH_4 + H_2O \rightleftarrows CO + 3H_2 \quad \text{(R.71)}$$

$$C_2H_4 + 2H_2O \rightleftarrows 2CO + 4H_2 \quad \text{(R.72)}$$

$$C_2H_6 + 2H_2O \rightleftarrows 2CO + 5H_2 \quad \text{(R.73)}$$

$$C_3H_6 + 3H_2O \rightleftarrows 3CO + 6H_2 C_3H_6 + 3H_2O \rightleftarrows 3CO + 6H_2 \quad \text{(R.74)}$$

$$C_3H_8 + 3H_2O \rightleftarrows 3CO + 7H_2 \quad \text{(R.75)}$$

$$C_6H_6 + 6H_2O \rightleftarrows 6CO + 9H_2 \quad \text{(R-76)}$$

$$CH_4 + CO_2 \rightleftarrows 2CO + 2H_2 \quad \text{(R-77)}$$

$$2NO_2 + 2NH_3 \rightleftarrows 4NO + 3H_2 \quad \text{(R.81)}$$

$$2NO + 2NH_3 \rightleftarrows 2N_2O + 3H_2 \quad \text{(R.82)}$$

$$3N_2O + 2NH_3 \rightleftarrows 4N_2 + 3H_2O \quad \text{(R.83)}$$

$$NO_2 + 2H_2 \rightleftarrows NO + H_2O \quad \text{(R.84)}$$

$$2NO + 2H_2 \rightleftarrows N_2O + H_2O \quad \text{(R.85)}$$

$$N_2O + H_2 \rightleftarrows N_2 + H_2O \quad \text{(R.86)}$$

$$NO_2 + CO \rightleftarrows NO + CO_2 \quad \text{(R.87)}$$

$$2NO + CO \rightleftarrows N_2O + CO_2 \quad \text{(R.88)}$$

$$N_2O + CO \rightleftarrows N_2 + CO_2 \quad \text{(R.89)}$$

$$NH_3 + CO \rightleftarrows HCN + H_2O \quad \text{(R.90)}$$

$$2N_2 + O_2 \rightleftarrows 2N_2O \quad \text{(R.91)}$$

$$2N_2O + O_2 \rightleftarrows 4NO \quad \text{(R.92)}$$

$$2NO + O_2 \rightleftarrows 2NO_2 \quad \text{(R.93)}$$

References

1. Kurose, R., Ikeda, M., Makino, H.: Combustion characteristics of high ash coal in a pulverized coal combustion. Fuel **80**, 1147–1455 (2001). https://doi.org/10.1016/S0016-2361(01)00020-5
2. de Souza-Santos, M.L.: Lima EHS (2015) introductory study on fuel-slurry integrated gasifier/gas turbine (FSIG/GT) alternative for power generation applied to high-ash or low-grade coal. Fuel **143**, 275–284 (2022). https://doi.org/10.1016/j.fuel.2014.11.060. AccessedonJanuary18
3. Brazilian Ministry of Mines and Energy 2019 report. https://www.gov.br/mme/pt-br/acesso-a-informacao/arquivos/auditorias/2019/

arquivos-1/relatoriogestaomme-2019.pdf. Accessed on October 14, 2021.
4. Oil, Natural Gas and Biofuels Statistical Yearbook 2021, https://www.gov.br/anp/pt-br/centrais-de-conteudo/publicacoes/anuario-estatistico/oil-natural-gas-and-biofuels-statistical-yearbook-2021. Accessed on January 18, 2022.
5. Pachauri, N., He, B.: Value-added utilization of crude glycerol from biodiesel production: a survey of current research activities. In: ASABE meeting presentation, 066223, Portland, Oregon 9–12 July 2006 (2000)
6. Leoneti, A.B., Aragão-Leoneti, V., DeOliveira, S.V.W.B.: Glycerol as a by-product of biodiesel production in Brazil: alternatives for the use of unrefined glycerol. Renewab Energy **45**, 138–145 (2012). https://doi.org/10.1016/j.renene.2012.02.032
7. de Souza-Santos, M.L.: Proposals for power generation based on processes consuming biomass-glycerol slurries. Energy **120**(1), 959–974 (2017). https://doi.org/10.1016/j.energy.2016.12.005
8. de Souza-Santos, M.L., Camara, M.A.: Theoretical study on the effect of glycerol fraction in slurries with biomass consumed by a power generation process. Energy Fuels (2017). https://doi.org/10.1021/acs.energyfuels.7b02996
9. Cadavez, C., de Souza-Santos, M.L.: Efficiency of a power generation alternative regarding the composition of feeding biomass-glycerol slurry. Theoret Assess Energy **214**, 2022 (2021). https://doi.org/10.1016/j.energy.2020.118967
10. Raza, M., Inayat, A., Abu-Jdayil, B.: Crude glycerol as a potential feedstock for future energy via thermochemical conversion processes: a review. Sustainability **13**, 12813 (2021). https://doi.org/10.3390/su132212813
11. Rodrigues, A., Bordado, J.C., Galhano dos Santos, R.: Upgrading the glycerol from biodiesel production as a source of energy carriers and chemicals—a technological review for three chemical pathways. Energies **10**(11), 1817 (2017)
12. Bohon, M.D., Metzger, B.A., Linak, W.P., King, C.J., Roberts, W.L: Glycerol combustion and emissions. In: Proceedings of the Combustion Institute (2010).
13. Mills, D.: Pneumatic Conveying Design Guide, 3rd edn. Butterworth-Heinemann, Oxford (2016). https://doi.org/10.1016/C2014-0-02678-0
14. Vimalchand, P., Peng, W.W., Liu, G.P., Peng, W.W., Liu, G.: High pressure feeder and method of operating to feed granular or fine materials US20110146153A1 (2011). 17 Jul 2011. https://www.google.com/patents/US20110146153. Accessed 31 May 31 2021
15. Anthony, E.J.: Fluidized bed combustion of alternative solid fuels; status, successes and problems of the technology. PECS **21**(3), 239–268 (1995). https://doi.org/10.1016/0360-1285(95)00005-3
16. Breault, R.W.: Gasification processes old and new: a basic review of the major technologies. Energies **3**, 216–240 (2010). https://doi.org/10.3390/en3020216
17. Laugwitz, A., Grabner, M., Meyer, B.: Availability analysis of integrated gasification combined cycle (IGCC) power plants. In: Power Plant Life Management and Performance Improvement, Woodhead Publishing Limited (2011). https://doi.org/10.1533/9780857093806.1.110.
18. de Souza-Santos, M.L.: Solid Fuels Combustion and Gasification: Modeling, Simulation, and Equipment Operation, 2nd edn. New York, CRC Press (2010)
19. de Souza-Santos, M.L.: Modelling and simulation of fluidized-bed boilers and gasifiers for carbonaceous solids. Ph.D. Dissertation, University of Sheffield, United Kingdom (1987)
20. de Souza-Santos, M.L.: Comprehensive modelling and simulation of fluidized-bed boilers and gasifiers. Fuel **68**(1507–1521), 2022 (1989)
21. de Souza-Santos, M.L.: Comprehensive simulator (CSFMB) applied to circulating fluidized bed boilers and gasifiers. Open Chem. Eng. J. **2**, 106–118 (2008)
22. de Souza-Santos, M.L.: CSFB applied to fluidized-bed gasification of special fuels. Fuel **88**(826–833), 2022 (2009). https://doi.org/10.1016/j.fuel.2008.10.035.AccessedonJanuary18
23. Krzywanski, J., Zylka, A., Czakiert, T., Kulicki, K., Jankowska, S., Nowak, W.: A 1.5D model of a complex geometry laboratory scale fluidized bed CLC equipment. Powder Technol. (2016). https://doi.org/10.1016/j.powtec.2016.09.041
24. Zylka, A., Krzywanski, J., Czakiert, T., Idziak, K., Sosnowski, M., De Souza-Santos, M.L., Sztekler, K., Nowak, W.: Modeling of the chemical looping combustion of hard coal and biomass using ilmenite as the oxygen carrier. Energies (2020). https://doi.org/10.3390/en13205394.AccessedOctober19
25. de Souza-Santos, M.L.: Application of comprehensive simulation of fluidized-bed reactors to the pressurized gasification of biomass. J. Braz. Soc. Mech. Sci. **16**, 376–383 (1994)
26. de Souza-Santos, M.L., Chavez, J.V.: Preliminary studies on advanced power generation based on combined cycle using a single high-pressure fluidized bed boiler and consuming sugar-cane bagasse. Fuel **95**, 221–225 (2012)
27. de Souza-Santos, M.L., Chavez, J.V.: Development of studies on advanced power generation based on combined cycle using a single high-pressure fluidized bed boiler and consuming sugar cane bagasse. Energy Fuels **26**, 1952–1963 (2012). https://doi.org/10.1021/ef2019935
28. deSouza-Santos, M.L., Chavez, J.V.: Second round on advanced power generation based on combined cycle using a single high-pressure fluidized bed boiler and consuming biomass. Open Chem. Eng. J. **6**, 41–47 (2012). https://doi.org/10.2174/1874123101206010041
29. de Souza-Santos, M.L., Ceribeli, K.: Technical evaluation of a power generation process consuming municipal solid waste. Fuel **108**, 578–585 (2012). https://doi.org/10.1016/j.fuel.2012.12.037
30. de Souza-Santos, M.L., Beninca, W.A.: New strategy of fuel-slurry integrated gasifier/gas turbine (FSIG/GT) alternative for power generation applied to biomass. Energy & Fuel **28**(4), 2697–2707 (2014). https://doi.org/10.1021/ef500317a
31. de Souza-Santos, M.L., Bernal, A.F.B., Rodriguez-Torres, A.F.: New developments on fuel-slurry integrated gasifier/gas turbine (FSIG/GT) alternative for power generation applied to biomass; configuration requiring no steam for gasification. Energy & Fuels **29**(6), 3879–3889 (2015). https://doi.org/10.1021/acs.energyfuels.5b00775
32. de Souza-Santos, M.L.: Very high-pressure fuel-slurry integrated gasifier/gas turbine (FSIG/GT) power generation applied to biomass. Energy Fuels **29**, 8066–8073 (2015). https://doi.org/10.1021/acs.energyfuels.5b02093
33. Mantovani, H.B., de Souza-Santos, M.L.: Theoretical analysis of power generation applying supercritical steam and high-pressure combustion chamber consuming biomass slurry. Int. J. Energy Environ. Eng. (2021). https://doi.org/10.1007/s40095-021-00432-x
34. de Souza-Santos, M.L.: A study on thermo-chemically recuperated power generation systems using natural gas. Fuel **76**, 593–601 (1997). https://doi.org/10.1016/S0016-2361(97)00059-8
35. Basu, P.: Combustion and Gasification in Fluidized Beds. CRC Press, Boca Raton, FL (2006)
36. Bair, W.G., Tarman, P.B.: Slurry Pumping Techniques for Feeding high-Pressure Coal Gasification Reactors. Institute of Gas Technology, Chicago, IL (1977)
37. He, W., Park, C.S., Joseph, N.M.: A rheological study on the pumpability of co-mingled biomass and coal slurries. In: Proceedings of the Pittsburgh Coal Conference, Pittsburgh, PA, PCC - Proceedings. Jan., 2008. (2008)
38. He, W., Park, C.S., Norkeck, J.M.: Rheological study of comingled biomass and coal slurries with hydrothermal pretreatment.

Energy Fuels **23**(10), 4763–4767 (2009). https://doi.org/10.1021/ef9000852
39. GIW Industries, Inc: Centrifugal Slurry Pump Concentration Limit Testing Phase 1. The Florida Institute of Phosphate Research, Bartow, FL (2005)
40. Shijazhuang Minerals Equipment Co., Personal correspondence . Retrieved from sales33@cnmineralsequipment.com. Acessed 04 Aug 2020.
41. de Souza-Santos, M.L.: Theoretical models for rates of heterogeneous reactions during combustion and gasification of liquid fuels in fluidized beds. Brazilian Journal of Chemical Engineering **35**(2), 679–690 (2018). https://doi.org/10.1590/0104-6632.20180352s20160495
42. Boyce, P.M.: Axial Flow Compressors. http://www.netl.doe.gov/File%20Library/Research/Coal/energy%20systems/turbines/handbook/2-0.pdf. Accessed on August 2015.
43. Bala-Litwiniak, A., Radomiak, H.: Possibility of the utilization of waste glycerol as an addition to wood pellets. Waste Biomass Valoriz **10**, 2193–2199 (2019). https://doi.org/10.1007/s12649-018-0260-7
44. Mitsubishi Heavy Industries. Gas Turbines. Mitsubishi Heavy Industries, Ltd. Global Website|MHI Selects "Best Innovation 2011" Awards (2011). Accessed June 2022
45. Larson, E.D., Williams, R.H., Leal, M.R.L.V.: A review of biomass integrated gasifier/gas turbine combined cycle technology and its application in sugarcane industries, with an analysis for Cuba. Energy Sustain. Dev. **5**(1), 54–76 (2001). https://doi.org/10.1016/S0973-0826(09)60021-1
46. Manente, G., Lazzaretto, A.: Innovative biomass to power conversion systems based on cascaded supercritical CO 2 Brayton cycles. Biomass Bioenerg. **69**, 155–168 (2014). https://doi.org/10.1016/j.biombioe.2014.07.016
47. Consonni, S., Larson, E.D.: Biomass-gasifier/aeroderivative gas turbine combined cycles: part A – technologies and performance modeling. J. Eng. Gas Turbine Power **118**(3), 507–515 (1996). https://doi.org/10.1115/1.2816677
48. Consonni, S., Larson, E.D.: Biomass-gasifier/aeroderivative gas turbine combined cycles: Part B – performance calculations and economic assessment. J. Eng. Gas Turbine Power **118**(3), 516–525 (1996). https://doi.org/10.1115/1.2816678
49. Department of Energy, Office of Fossil and Carbon Management, https://www.energy.gov/fecm/science-innovation/office-clean-coal-and-carbon-management/advanced-energy-systems/transformative. Accessed on August 30, 2022

International Journal of Energy and Environmental Engineering (2023) 14:743–755
https://doi.org/10.1007/s40095-022-00546-w

ORIGINAL RESEARCH

Assessment of a diaphragm thermoacoustic Stirling engine using the energy standpoint and genetic algorithm

Shahryar Zare[1] · Maedeh makki[2] · Masoud Rasooli[3] · Hassan Shafiee Alavi[4] · A. R. Tavakolpour-Saleh[1]

Received: 26 May 2022 / Accepted: 17 October 2022 / Published online: 31 October 2022

Abstract

This paper presents a novel method to estimate the design parameters of a diaphragm thermoacoustic Stirling engine and investigate the stable limit cycle (sufficient condition) of the engine dynamic using the genetic algorithm and system energy changes. In this regard, first, the parametric equations are extracted by employing both the governing equations of the engine and energy standpoint. Next, V_{c0} (initial volume of compression space), R_q (pneumatic resistance), V_{h0} (initial volume of expansion space), and hot gas temperature (T_h) are taken as the design parameters in this study. Genetic algorithm and parametric equations were then utilized to estimate the chosen design parameters. Next, the sufficient condition of the engine is evaluated based on the estimated design parameters. The simulated outcomes are shown that the sufficient condition is satisfied by the estimated design parameters. Afterward, the simulated results are validated using experimental data gathered from the constructed SUTech-SR-3 engine. Comparing the extracted data eventuates a proper method of estimating design parameters and satisfying the sufficient condition related to the SUTech-SR-3 engine. It is worth noting that in this research, the dynamic of the thermoacoustic Stirling engine has investigated using a mechanical point of view. Also, in this paper, only the dynamic behavior of the engine has been investigated, and the production power and work have not been studied.

Keywords Diaphragm thermoacoustic Stirling engine · Thermoacoustic engine · Stirling engine · Genetic algorithm

Abbreviations

A'	Cross-sectional area of the looped tube (m^2)
A	Cross-sectional area of pistons (m^2)
K_y	Stiffness of power piston (N/m)
K_x	Stiffness of displacer piston (N/m)
m	Total gas mass (kg)
m_h	Gas mass of expansion space (kg)
m_c	Gas mass of compression space (kg)
M_y	Power piston mass (kg)
M_x	Displacer piston mass (kg)
P_{atm}	Ambient pressure (Pa)
P_1	The pressure of compression space (pa)
P_0	Initial pressure (*pa*)
P_2	The pressure of expansion space (*pa*)
R_q	Flow resistance (Ns/m^5)
R	Ideal gas constant ($Jkg^{-1}K^{-1}$)
V_h	Expansion space (m^3)
V_c	Compression space (m^3)
T_h	Hot gas temperature (K)
T_c	Cold gas temperature (K)
x	The motion of displacer piston (m)
y	The motion of power piston (m)
V_{h0}	Initial expansion space (m^3)
V_{c0}	Initial compression space (m^3)

Greek symbols

ρ	Density (Kg/m^3)
φ	Phase difference between piston movements (degree)

✉ Shahryar Zare
s.zare@sutech.ac.ir

[1] Department of Mechanical and Aerospace Engineering, Shiraz University of Technology, Shiraz, Iran

[2] Department of Mechanical, Sharif University of Technology, Tehran, Iran

[3] Kish Branch, Islamic Azad University, Kish, Iran

[4] Department of Computer Engineering, Shiraz Branch, Islamic Azad University, Shiraz, Iran

Introduction

The increasing daily demand of the world's population for energy leads the majority of researches toward the extraction of novel green energies [1, 2]. Solar energy as one of the main sources of today's green energies extensively used

worldwide has a big disadvantage that is the requirement of high-performance converters. Thermoacoustic converters are presented as a novel technology converting solar to electrical energy. Ceperley et al.[3] first announced the idea of making these types of engines in 1979, and later Backhause and Swift [4, 5] constructed the preliminary design of such engines. These thermoacoustic engines are working based on the Stirling cycle [6] and that is the reason they are sometimes regarded as the Stirling thermoacoustic engines [7]. These Stirling thermoacoustic engines can also be called a novel version of free-piston Stirling engines [8, 9]. The lack of dynamic parts such as crankshafts and pistons in the overall structure of such engines makes them more fascinating in terms of design and manufacture for scientists due to the extreme final cost of such products. On the other hand, this phenomenon results in arduous design process to achieve a stable oscillating for the engine while having a nonlinear dynamic behavior.

Various types of thermoacoustic Stirling engines were designed and developed, which consist of two main parts containing looped tubes and a core section. Other parts of the engine including the inertance, compliance, resonator, and diaphragm are regarded as the facilitators [10]. The diaphragm is also utilized as the phase shifter between pressure changes and the fluid flow rate in the core section of the motor [11, 12]. As stated earlier, removing the dynamic mechanical parts in such engines positively affects the performance; however, creating a stable limit cycle in their nonlinear dynamic is a major challenge that needs to be taken care of while considering the sufficient condition for the engine design. In better words, the necessary (unstable dynamic behavior at the startup) and sufficient (stable dynamic behavior at the engine after the startup) conditions are required for a stable run of thermoacoustic Stirling engines. It is worth noting that the necessary condition is automatically met by satisfying the sufficient condition in the dynamics of the engine [13, 14]. Although there have been numerous researches on examining how the necessary condition of such engines works, most of them were based on investigating the dominant poles of the linear closed-loop dynamic system of the engines [15, 16]. Moreover, investigating the sufficient condition of thermoacoustic engines is another area that became the focus of many other pieces of research. To date, the sufficient condition has been investigated via the numerical methods and direct solution of the governing equation for the systems. Abduljalil et al. [17] used the experimental data gathered from the fluctuation of the internal pressure in the chamber to investigate sufficient conditions of the thermoacoustic Stirling engines. Besides, the sufficient condition of thermoacoustic Stirling engines using the CFD method was investigated by Yu et al. [18]; they employed numerical methods to solve the momentum and continuity equations simultaneously. Lalit et al. [19] investigated the optimization of different parts of such engines and analyzed the sufficient condition by representing a nonlinear computational method. Aside from the previous worthwhile researches to examine the behavior of the nonlinear thermoacoustic engines in stable oscillation conditions, one can mention the design criteria undertaken in an old version of such engines (free-piston Stirling engines). Tavakolpour-Saleh and Zare proposed a method by the utilization of energy changes in the system where the sufficient condition of an oscillator such as a free-piston Stirling engine would automatically be evaluated when applied. In this method, first, an energy function is selected based on the dynamic of the engine. Then, the existence of the stable limit cycle is investigated by the time derivative of the energy function; if the mean value of the time derivative in a working cycle is zero, then the sufficient condition is satisfied [20]. This method can be used to study the sufficient condition the diaphragm Stirling engine for the first time in this article.

Presenting a design method being able to estimate the principal design parameters before fabricating the engine can thus facilitate the construction process of thermoacoustic engines. In this regard. Zare and Tavakolpour-Saleh [21] employed linear mechanical-acoustic equations, presented by De Waele [22], to design an engine with the desired frequency. But there is a need to provide a design method for diaphragm thermoacoustic Stirling engines considering nonlinear dynamics. Thus, the paper goal is to know what the design parameters should be in order to satisfy the sufficient condition in engine dynamics. To this end, the principle of system energy changes and the genetic algorithm technique can be used, which will be explained in detail in the next sections. Also, this method can be presented as a multi-physical software to design these engines.

With the concepts stated above, there is no comprehensive study that simultaneously estimates the preliminary design parameters using the genetic algorithm and investigates the sufficient conditions related to the dynamics of engines. In this regard, first, a parametric equation to evaluate the sufficient condition is extracted based on the energy viewpoint. Afterward, the estimated parametric equations are used on finding the unknown parameters in the design process. This method is also analyzed by means of the characteristics of the SUTech-SR-3 engine. Ultimately, the simulated results are verified with the available experimental data.

Diaphragm thermoacoustic Stirling engine

The thermoacoustic Stirling engines generally consist of two sets of components. The first ones are related to the main engine parts including the engine loop and core [23, 24]. The other components are known as facilitators which include

inertance, resonator, compliance, and diaphragm [25, 26]. Diaphragm thermoacoustic Stirling engines are indeed thermoacoustic Stirling engines where the diaphragm is utilized as a facilitator as well as a phase shifter [27, 28]. As it is illustrated in Fig. 1a–c, one can clearly see the diaphragm thermoacoustic Stirling engine SUTech-SR-3, which is consisted of two diaphragms. These two diaphragms perform different tasks of phase shifter (Diaphragm No.1) and power receiver (Diaphragm No.2). The core section has three parts including a hot heat exchanger, cold heat exchanger, and a regenerator part, which are shown in Fig. 1b. Also, the two-dimensional scheme of the engine is shown in Fig. 1c.

As stated earlier, the diaphragm thermoacoustic Stirling engine is a novel type of free-piston Stirling oscillator [8]. Based on this idea, a mechanical model can be presented for the diaphragm thermoacoustic Stirling engines, which is demonstrated schematically in Fig. 2 [8].

Based on Fig. 2, the mechanical model of the diaphragm thermoacoustic Stirling engine, therefore, consists of two power pistons (diaphragm 2 with an attached mass) and a displacer (diaphragm 1 with internal gas mass). This simplified equivalence is necessary to be able to apply theories related to free-piston Stirling engines on the diaphragm thermoacoustic Stirling engines.

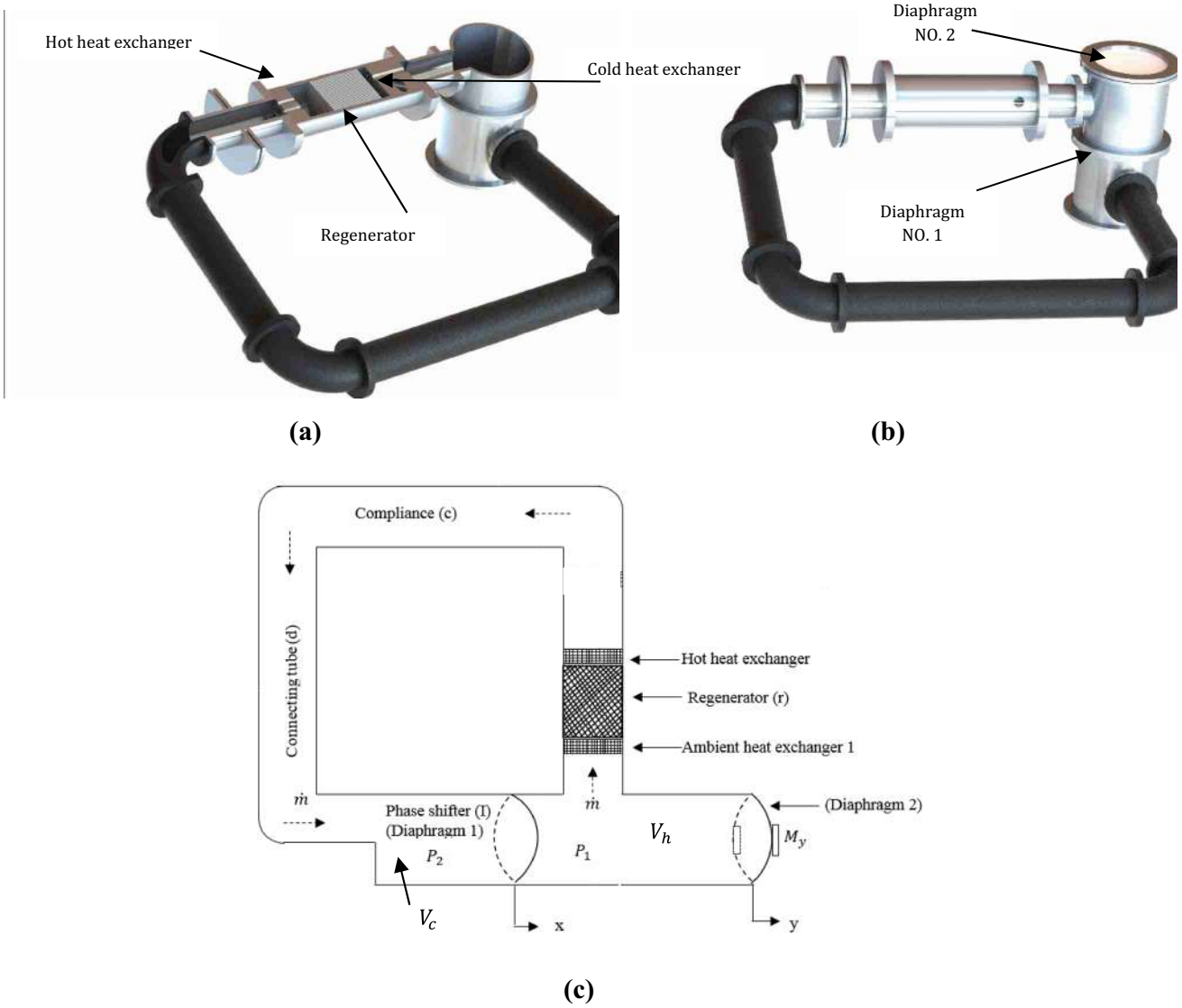

Fig. 1 Diaphragm thermoacoustic Stirling engine photograph: **a** a cross-sectioned view of the engine core, **b** scheme view, **c** scheme view in 2-D

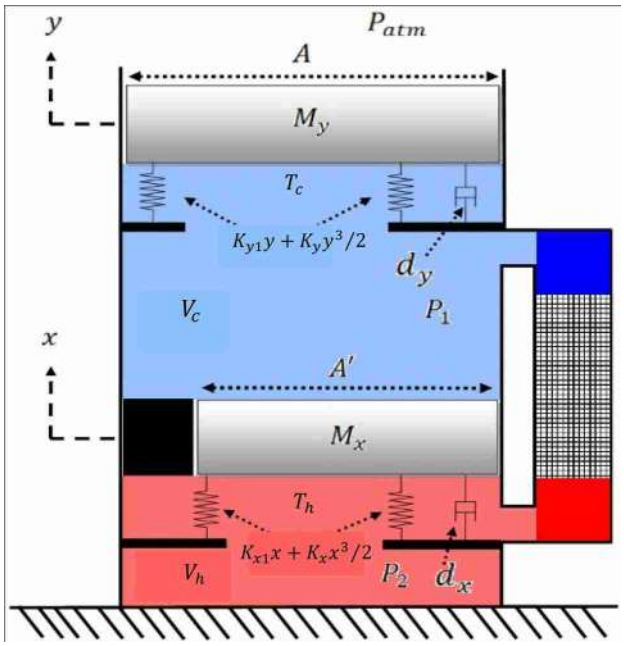

Fig. 2 The mechanical model of a diaphragm thermoacoustic Stirling engine

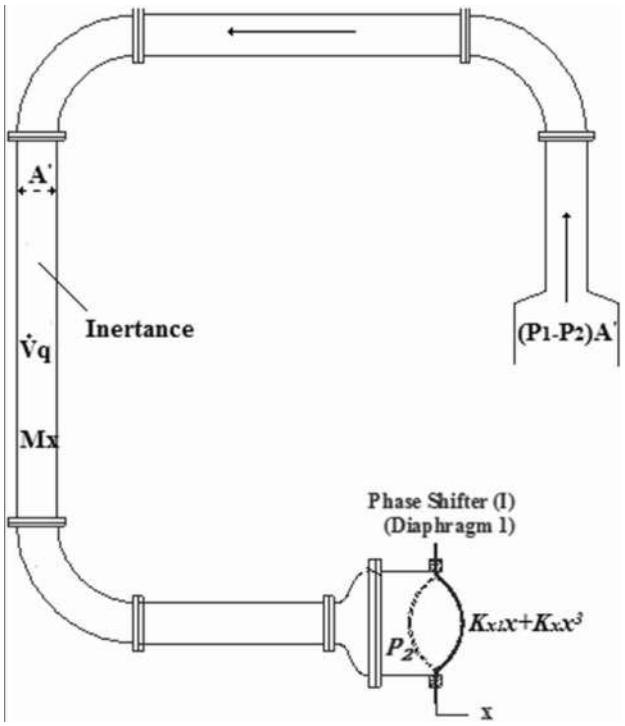

Fig. 3 Looped-tube section and forces exerted on it

Mathematical background

To study the stable limit cycle in the dynamics of the engine, it is essential to extract the governing equations first. According to Figs. 2 and 3 as well as ref. [8], the mechanical equations can be extracted (see Eqs. (1) and (2)). By comparing between Figs. 2 and 3, it can be found that M_x (displacer piston mass in the mechanical model) is equal to the gas mass inside the tube. As seen in Figs. 1–3, the core section of the diaphragm thermoacoustic engine contains hot and cold heat exchangers as well as a regenerator, which results in a pressure difference between compression and expansion spaces. Hence, the pressure difference relation due to area changes and friction can be defined as can be seen in Eq. (4)[29, 30]. It is important to note that in this study the dynamic of the diaphragm thermoacoustic Stirling engine is investigated via the free-piston Stirling (with help of the mechanical model) point of view and energy balances (for the thermal and the mechanical) part. Also, the engine specifications (SUTech-SR-3) including the value and dimensions of the equipment are explained in Sect. 5 and Table 1. According to Fig. 2, the total mass inside the engine chamber can be obtained by summing the gas mass in the compression (m_c) and expansion (m_h) spaces, which is shown in Eq. (5).

$$M_y\ddot{y} + d_y\dot{y} + K_{y1}y + K_y y^3 = \left(P_1 - P_{\text{atm}}\right)A \tag{1}$$

Table 1 Values of design parameters of SUTech-SR-3

Parameter	Value	Parameter	Value
A'	0.00314 (m^2)	M_y	0.097 (kg)
P_0	100 (kpa)	ρ	4.81 (kg/m^3)
T_c	300 K	R	287(N m kg^{-1} K)
φ	121 (degree)	–	–

$$M_x\ddot{x} + d_x\dot{x} + K_{x1}x + K_x x^3 = \left(P_1 - P_2\right)A' \tag{2}$$

where

$$\begin{aligned} P_1 &= \left(m - \frac{\Delta P V_h}{RT_{\text{h}}}\right)\left(\frac{V_h}{RT_{\text{h}}} + \frac{V_{\text{c}}}{RT_{\text{c}}}\right)^{-1} \\ &= \frac{mRT_{\text{h}}T_{\text{c}} - \left(b_1\dot{x} + b_2\dot{x}x + b_3\dot{y} + b_4\dot{y}x\right)}{a_1 y + a_2 x + a_3} \end{aligned} \tag{3}$$

$$P_2 - P_1 = R_q\dot{V}_q = R_q\left(\dot{V}_h - \dot{V}_{\text{c}}\right) = R_q(A\dot{x} - A(\dot{y} - \dot{x})) \tag{4}$$

$$m = m_h + m_c = \frac{\left(P_1 + \Delta P\right)V_h}{RT_{\text{h}}} + \frac{P_1 V_{\text{c}}}{RT_{\text{c}}} \tag{5}$$

In the mechanical model, it is assumed that all thermal power provided by the hot heat exchanger is being used up by heat losses in the tubes, the deformation of the membranes, and the acoustic energy to the environment transferred by membrane 2.

By substituting Eqs. (3) to (5) into Eqs. (1) and (2), the final governing equations are obtained as:

$$M_y\ddot{y} + d_y\dot{y} + K_{y1}y + K_y y^3 = \left(\frac{mRT_hT_c - \left(b_1\dot{x} + b_2\dot{x}x + b_3\dot{y} + b_4\dot{y}x\right)}{a_1y + a_2x + a_3} - P_{atm}\right)A \tag{6}$$

$$M_x\ddot{x} + d_x\dot{x} + K_{x1}x + K_x x^3 = -R_qAA'(2\dot{x} - \dot{y}) \tag{7}$$

where

$$a_1 = T_hA \tag{8}$$

$$a_2 = T_cA - T_hA \tag{9}$$

$$a_3 = T_cV_{h0} + T_hV_{c0} \tag{10}$$

$$b_1 = 2R_qAT_cV_{h0} \tag{11}$$

$$b_2 = 2R_qA^2T_c \tag{12}$$

$$b_3 = -R_qAT_cV_{h0} \tag{13}$$

$$b_4 = -R_qA^2T_c \tag{14}$$

Notably, the dynamic Eqs. (6) and (7) are extracted from the suggested model for a diaphragm thermoacoustic Stirling engine [8]. Thus, the power piston and displacer stated in the previous sections are shown in Fig. 2.

To further study the dynamics of the engine, Eqs. (6) and (7) are required to be in a matrix form:

$$\begin{bmatrix} M_y & 0 \\ 0 & M_x \end{bmatrix}\begin{bmatrix} \ddot{y} \\ \ddot{x} \end{bmatrix} + \begin{bmatrix} K_{y1} & 0 \\ 0 & K_{x1} \end{bmatrix}\begin{bmatrix} y \\ x \end{bmatrix} + \begin{bmatrix} d_y & 0 \\ -R_qAA' & d_x + 2R_qAA' \end{bmatrix}\begin{bmatrix} \dot{y} \\ \dot{x} \end{bmatrix} + \begin{bmatrix} K_yy^3 \\ K_xx^3 \end{bmatrix} + \begin{bmatrix} -\left(\frac{mRT_hT_c - \left(b_1\dot{x} + b_2\dot{x}x + b_3\dot{y} + b_4\dot{y}x\right)}{a_1y + a_2x + a_3} - \frac{mRT_hT_c}{T_cV_{h0} + T_hV_{c0}}\right)AA_r \\ 0 \end{bmatrix} = 0 \tag{15}$$

It is clear from Eq. (15) that the governing equations for diaphragm thermoacoustic engines are consisted of four separate forces including the resulting forces due to the accelerator mass, friction force, the force due to the movement of the diaphragm, and the force arises from pressure changes. The power generated (P_W) can also be easily obtained by multiplying the value of each mentioned force (F) by the velocity of the movement ($\dot{v}$) related to the dynamic parts:

$$P_W = F\dot{v} \tag{16}$$

The power of each component is therefore obtained by multiplying the forces in Eq. (10) by the velocity changes ($[\dot{y}, \dot{x}]$) as:

$$\begin{bmatrix} \dot{y} \\ \dot{x} \end{bmatrix}^T\begin{bmatrix} M_y & 0 \\ 0 & M_x \end{bmatrix}\begin{bmatrix} \ddot{y} \\ \ddot{x} \end{bmatrix} + \begin{bmatrix} K_{y1} & 0 \\ 0 & K_{x1} \end{bmatrix}\begin{bmatrix} y \\ x \end{bmatrix} + \begin{bmatrix} \dot{y} \\ \dot{x} \end{bmatrix}^T\begin{bmatrix} K_yy^3 \\ K_xx^3 \end{bmatrix} + \begin{bmatrix} \dot{y} \\ \dot{x} \end{bmatrix}^T\begin{bmatrix} d_y & 0 \\ -R_qAA' & d_x + 2R_qAA' \end{bmatrix}\begin{bmatrix} \dot{y} \\ \dot{x} \end{bmatrix} + \begin{bmatrix} \dot{y} \\ \dot{x} \end{bmatrix}^T\begin{bmatrix} -\left(\frac{mRT_hT_c - \left(b_1\dot{x} + b_2\dot{x}x + b_3\dot{y} + b_4\dot{y}x\right)}{a_1y + a_2x + a_3} - \frac{mRT_hT_c}{T_cV_{h0} + T_hV_{c0}}\right)AA_r \\ 0 \end{bmatrix} = 0 \tag{17}$$

The total energy of the system (E_t) can also be acquired as:

$$E_t = \frac{1}{2}\begin{bmatrix} \dot{y} \\ \dot{x} \end{bmatrix}^T\begin{bmatrix} M_y & 0 \\ 0 & M_x \end{bmatrix}\begin{bmatrix} \dot{y} \\ \dot{x} \end{bmatrix} + \frac{1}{2}\begin{bmatrix} y \\ x \end{bmatrix}^T\begin{bmatrix} K_{y1} & 0 \\ 0 & K_{x1} \end{bmatrix}\begin{bmatrix} y \\ x \end{bmatrix} + \frac{1}{4}\begin{bmatrix} y \\ x \end{bmatrix}^T\begin{bmatrix} K_yy^3 \\ K_xx^3 \end{bmatrix} \tag{18}$$

where the first and the second segments are related to kinematic energy (E_k) and the potential energy (E_p), respectively.

$$E_t = E_k + E_p \tag{19}$$

The time derivative of Eq. (13) can be written as:

$$\frac{dE_t}{dt} = \frac{d}{dt}\left(E_k + E_p\right) = \begin{bmatrix} \dot{y} \\ \dot{x} \end{bmatrix}^T\begin{bmatrix} M_y & 0 \\ 0 & M_x \end{bmatrix}\begin{bmatrix} \ddot{y} \\ \ddot{x} \end{bmatrix} + \begin{bmatrix} \dot{y} \\ \dot{x} \end{bmatrix}^T\begin{bmatrix} K_{y1} & 0 \\ 0 & K_{x1} \end{bmatrix}\begin{bmatrix} y \\ x \end{bmatrix} + \begin{bmatrix} \dot{y} \\ \dot{x} \end{bmatrix}^T\begin{bmatrix} K_yy^3 \\ K_xx^3 \end{bmatrix} \tag{20}$$

The three matrices of Eq. (17) represent the total energy of the system. On the other hand, the energy of the system can also be written as:

$$\frac{dE_t}{dt} = \frac{d}{dt}\left(E_k + E_p\right) = \dot{E}_{in} - \dot{E}_{out} \tag{21}$$

By combining Eqs. (17) and (21), the $\dot{E}_{in}$ and $\dot{E}_{out}$ are obtained as follows:

$$\dot{E}_{in} = \begin{bmatrix} \dot{y} \\ \dot{x} \end{bmatrix}^T\begin{bmatrix} \left(\frac{mRT_hT_c - \left(b_1\dot{x} + b_2\dot{x}x + b_3\dot{y} + b_4\dot{y}x\right)}{a_1y + a_2x + a_3} - \frac{mRT_hT_c}{T_cV_{h0} + T_hV_{c0}}\right)AA_r \\ 0 \end{bmatrix} \tag{22}$$

$$\dot{E}_{\text{out}} = \begin{bmatrix} \dot{y} \\ \dot{x} \end{bmatrix}^T \begin{bmatrix} d_y & 0 \\ -R_q AA' & d_x + 2R_q AA' \end{bmatrix} \begin{bmatrix} \dot{y} \\ \dot{x} \end{bmatrix} \tag{23}$$

The change of total energy related to a stable system is equal to zero when a stable limit cycle occurs due to the movement of diaphragms (or pistons). Therefore, Eq. (21) can be written as:

$$\dot{E}_{\text{in}} - \dot{E}_{\text{out}} = 0 \tag{24}$$

The time-averaging related to a fluctuating system in a working cycle, therefore, has to be zero according to refs. [7, 9]:

$$\left\langle \dot{E}_{\text{in}} \right\rangle_{2\pi} - \left\langle \dot{E}_{\text{out}} \right\rangle_{2\pi} = 0 \tag{25}$$

Substituting Eqs. (17) and (18) into Eq. (20), one can conclude to Eq. (26):

$$\dot{y}\left(\frac{mRT_h T_c - \left(b_1\dot{x} + b_2\dot{x}x + b_3\dot{y} + b_4\dot{y}x\right)}{a_1 y + a_2 x + a_3} - \frac{mRT_{\text{h}}T_{\text{c}}}{T_{\text{c}}V_{h0} + T_{\text{h}}V_{\text{c0}}} \right) AA_{r2\pi} - d_y\dot{y}^2 - R_q AA'A\dot{y}\dot{x} + \left(d_x + 2R_q AA'\right)\dot{x}^2 \tag{26}$$

As stated, this paper attempts to analyze the dynamics of Stirling engine with the help of mechanical model. On the other hand, the mechanical model also shows that the diaphragm thermoacoustic Stirling engine is actually the advanced type of the free-piston Stirling engine. Thus, the movement of pistons is in a periodic and oscillatory manner; their stable moving patterns can be estimated with cosine definitions as:

$$y = A_1 cos(t) \tag{27}$$

$$x = B_1 cos(t + \varphi) \tag{28}$$

By substituting Eqs. (27) and (28) as well as their derivatives into Eq. (20):

$$-\frac{1}{2}d_y A_1^2 + \frac{1}{2}R_q AA'A_1B_1\cos(\varphi) - \frac{1}{2}B_1^2\left(d_x + 2R_q AA'\right) - \frac{1}{2\pi}\int_0^{2\pi} AA_rA_1\sin(t)\left(\frac{mRT_{\text{h}}T_{\text{c}} + b_1B_1 sin(t+\varphi) + b_2B_1^2 sin(t+\varphi)cos(t+\varphi) + b_3A_1 sin(t) + b_4B_1A_1\sin(t)cos(t+\varphi)}{a_1A_1 cos(t) + a_2B_1 cos(t+\varphi) + a_3} \right) dt = 0 \tag{29}$$

Equation (29) is an indicative design expression that can be used to investigate the sufficient condition of a diaphragm thermoacoustic Stirling engine; in other words, a stable limit cycle is obtained while the equation is satisfied. It is worth noting that K_{y1}, M_x, M_y and K_{y1} are not directly engaged in Eq. (29), but have the effect in the phase difference in the same formula.

As stated earlier, by using the energy phenomenon and the change of energy in the system, one can also estimate the engine design parameters. The diaphragm thermoacoustic Stirling engine has two stable limit cycles that are correlated to each other, and its individual cycles are related to the power piston and displacer. In fact, the dynamic of the engine includes two coupled second-order equations. As a result, two limit cycles will be formed in the engine dynamics at the stable oscillations condition, which are related to the movement of the power and displacer pistons in the presented mechanical model (or the movement of the diaphragms in the engine structure). With these explanations, a pseudo-energy equation is defined for each piston:

$$E_{\text{p}} = \frac{1}{2}M_y\dot{y}^2 + \frac{1}{2}K_{y1}y^2 + \frac{1}{4}K_y y^4 \tag{30}$$

$$E_{\text{d}} = \frac{1}{2}M_x\dot{x}^2 + \frac{1}{2}K_{x1}x^2 + \frac{1}{4}K_x x^4 \tag{31}$$

As seen, the potential and kinetic energies related to each of the pistons (Fig. 2) are considered as terms of the pseudo-energy equations.

Derivation of Eqs. (30) and (31) leads to:

$$\dot{E}_{\text{p}} = M_y\dot{y}\ddot{y} + K_{y1}y\dot{y} + K_y y^3\dot{y} \tag{32}$$

$$\dot{E}_{\text{d}} = M_x\dot{x}\ddot{x} + K_{x1}x\dot{x} + K_x x^3\dot{x} \tag{33}$$

Using the engine governing equations of (6) and (7), Eqs. (32) and (33) can be rewritten as:

$$\dot{E}_{\text{p}} = \left(\frac{mRT_{\text{h}}T_{\text{c}} - \left(b_1\dot{x} + b_2\dot{x}x + b_3\dot{y} + b_4\dot{y}x\right)}{a_1 y + a_2 x + a_3} - P_{\text{atm}} \right) A\dot{y} - d_y\dot{y}^2 \tag{34}$$

$$\dot{E}_{\text{d}} = d_x\dot{x}^2 - R_q AA'(2\dot{x} - \dot{y})\dot{x} \tag{35}$$

As stated earlier, although the chosen pseudo-energy equations for individual pistons were independent, the time derivation of such equations was eventually coupled. Also, the stable piston movements were estimated in a cosine form (Eqs. (27) and (28)). Considering this cosine movement as well as the zero magnitudes of average time derivation of the

pseudo-energy equation while forming a stable limit cycle, the equations of (34) and (35) are defined as follows:

$$\left(\frac{mRT_{\mathrm{h}}T_{\mathrm{c}}-\left(b_1\dot{x}+b_2\dot{x}x+b_3\dot{y}+b_4\dot{y}x\right)}{a_1y+a_2x+a_3}-P_{\mathrm{atm}}\right)A\dot{y}-d_y\dot{y}_{2\pi}^2=0 \tag{36}$$

$$\langle d_x\dot{x}^2-R_qAA'(2\dot{x}-\dot{y})\dot{x}\rangle_{2\pi}=0 \tag{37}$$

Eventually, the two equations of (36) and (37) can be summarized as:

$$\begin{aligned}-\frac{1}{2}d_yA_1^2-\frac{1}{2\pi}\int_0^{2\pi}\frac{\beta_1\sin(t)}{a_1A_1cos(t)+a_2B_1cos(t+\varphi)+a_3}\mathrm{d}t\\-\frac{1}{2\pi}\int_0^{2\pi}\frac{\beta_2\sin(t)sin(t+\varphi)}{a_1A_1cos(t)+a_2B_1cos(t+\varphi)+a_3}\mathrm{d}t\\-\frac{1}{2\pi}\int_0^{2\pi}\frac{\beta_3\sin(t)sin(t+\varphi)cos(t+\varphi)}{a_1A_1cos(t)+a_2B_1cos(t+\varphi)+a_3}\mathrm{d}t-\\\frac{1}{2\pi}\int_0^{2\pi}\frac{\beta_4\sin(t)^2}{a_1A_1cos(t)+a_2B_1cos(t+\varphi)+a_3}\mathrm{d}t\\-\frac{1}{2\pi}\int_0^{2\pi}\frac{\beta_5\sin(t)^2cos(t+\varphi)}{a_1A_1cos(t)+a_2B_1cos(t+\varphi)+a_3}\mathrm{d}t=0\end{aligned} \tag{38}$$

$$\frac{1}{2}\left(d_x-2R_qAA'\right)B_1^2+\frac{1}{2}R_qAA_1B_1A'\cos(\varphi)=0 \tag{39}$$

where

$$\beta_1=mRT_{\mathrm{h}}T_{\mathrm{c}}AA_1 \tag{40}$$

$$\beta_2=b_1B_1AA_1 \tag{41}$$

$$\beta_3=b_2B_1^2AA_1 \tag{42}$$

$$\beta_4=b_3AA_1^2 \tag{43}$$

$$\beta_5=b_4B_1AA_1 \tag{44}$$

By solving Eqs of (38) and (39) simultaneously, the unknown design parameters of an engine can be identified by assuming constant values of other engine parameters. On the other hand, with the help of soft computation methods like the genetic algorithm and the former two equations, these unknown parameters of the engine (assuming more than two) can also be identified which is discussed in the next section.

Results and discussion

As mentioned earlier, a method based on energy phenomenon and the employment of the genetic algorithm for designing engines is presented. The first step toward this goal is to select the parameters that are needed to be estimated using this method. After approximating these parameters, it is required to investigate the sufficient condition (creating a stable limit cycle in engine dynamics) to determine whether it is satisfied or not. The four parameters of the V_{c0}, R_q, V_{h0} and T_{h} were chosen as the design parameters in this section. The reason for this selection is that they can be preferably altered during the design and manufacturing phase.

The detailed characteristics of the diaphragm thermoacoustic Stirling engine in the current study (SUTech-SR-3) are clarified in Table 1.

The genetic algorithm operators ought to be determined first as stated in Table 2.

The second step in this process is the selection of the cost function. The genetic algorithm true targets are reached if only the two extracted values related to the parameters of Eqs. (38) and (39) converge to zero. With these said the cost function is defined as:

$$C.F=|\mathrm{Eq.}(38)|+|\mathrm{Eq.}(39)| \tag{45}$$

Using the genetic algorithm toolbox in MATLAB software, one can estimate the unknown design parameters. Figure 4 clearly illustrates the trend of cost function after 193 generations. The ultimate value, in this case, has converged to the value of 0.0000000035 indicating the correctness of such method. It is worth noting that the stop value was set to 0.00000001 for the current study.

The selected parameters at the initial step are evaluated and reported in Table 3.

After obtaining the values generated using the genetic algorithm, such values have to be investigated to determine whether they satisfy the sufficient condition of the engine or not. To this end, the parameters are inserted in Eq. (28):

$$|\mathrm{Eq.}(29)|=0.000023 \tag{46}$$

The very slight value of Eq. (46) being close to zero indicates the satisfaction of sufficient condition of the engine. This can also be verified by numerically investigating Eqs. (6) and (7) that are the main sets of equations in an engine. Figure 5 depicts the velocity change of the mass connected to the diaphragm 2 (power piston). On the other hand, the power piston displacement shows a very stable form, which is clearly illustrated in Fig. 6. Employing the data mentioned in Figs. 5 and 6, the phase plane related to the power piston can be depicted as shown in Fig. 7. The limit cycle is evident in Fig. 7 that indicates the sufficient condition of the engine based on estimated parameters

Table 2 Genetic algorithm characteristics

Parameter	Type/value
Population size	400
Range of parameter	[0,1]
Selection strategy	Stochastic
Mutation	Uniform
Crossover	Scattered

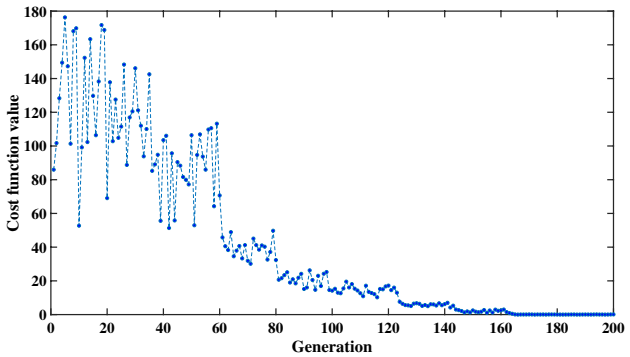

Fig. 4 Convergence of genetic algorithm

Table 3 The estimated parameters using the genetic algorithm

Design parameter	Value
T_h (K)	476
R_q (Ns/m^5)	12,960
V_{h0} (m^3)	0.000191
V_{c0}(m^3)	0.000342

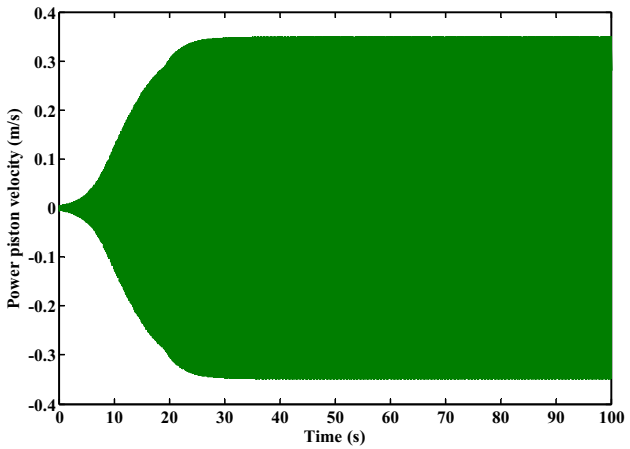

Fig. 5 Power piston velocity change related to the mass attached to diaphragm 2

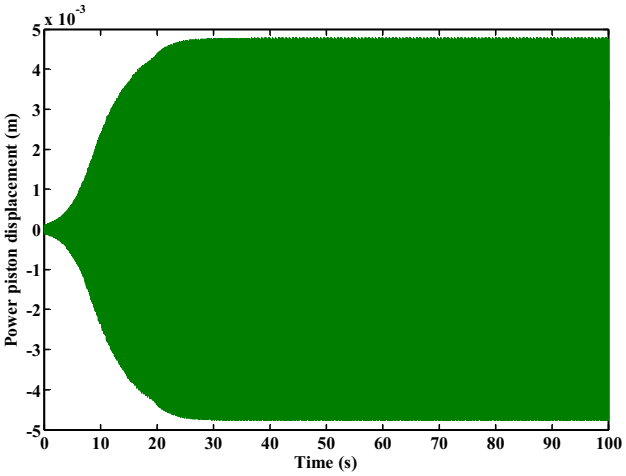

Fig. 6 Power piston displacement related to the mass attached to diaphragm 2

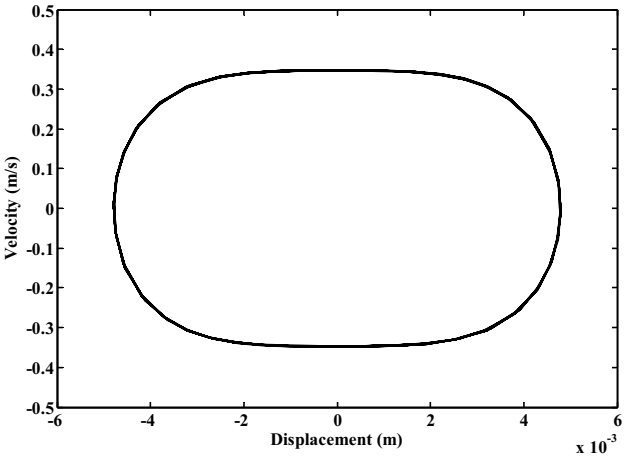

Fig. 7 Phase plane of the power piston (M_y) related to the mass attached to diaphragm 2

using the genetic algorithm. The numerical data presented here are to be validated using resulted experimental values of SUTech-SR-3 in the subsequent section.

It is also possible to study the stable limit cycle based on the pressure fluctuations (i.e., P_1 and P_2). According to Eqs. (1)–(5) and the obtained design parameters, the pressure changes in the compression and expansion space are simulated as can be seen in Figs. 8 and 9.

Finally, the process employed here to design and investigate the sufficient condition of the diaphragm thermoacoustic Stirling engine is illustrated in the flowchart as shown in Fig. 10.

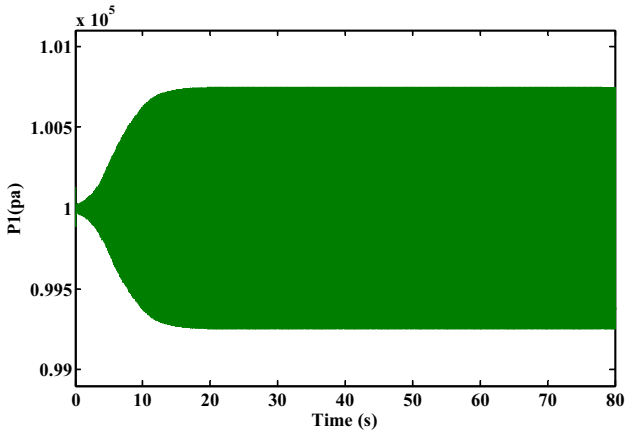

Fig. 8 Pressure variations in compression space

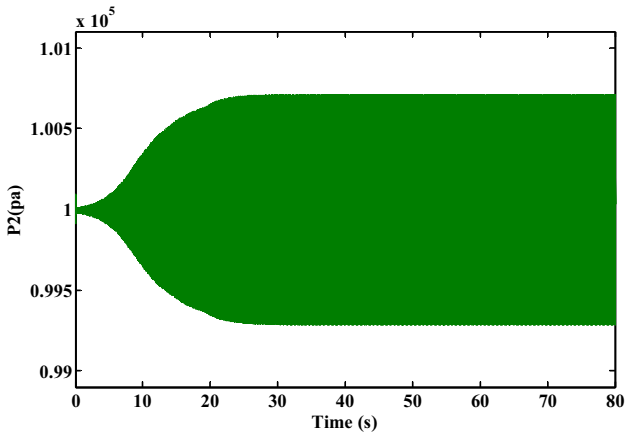

Fig. 9 Pressure variations in expansion space

Experimental results

Initializing and constructing the engine were accomplished according to the estimated results in the previous section. As mentioned, the diaphragm thermoacoustic Stirling engine is named SUTech-SR-3. The core section of this engine consists of three parts including a hot heat exchanger, ambient heat exchanger and regenerator. The hot and cold heat exchangers are made up aluminum block (30 mm in diameter and 20 mm in length). Monitoring the hot temperature was done using a power supply assigned in a proper position through the element wires (with 1.8 mm in diameter). Also, the length and diameter of the regenerator are 37 mm and 30 mm, respectively. In the SUTech-SR-3 structure, the length of the looped tube is about 1.6 m (PVC pipe with a diameter of 20 mm). The voltage difference due to the back-and-forth movement of the mass attached to diaphragm No.2 is extracted and reported in Fig. 11. This was simply done by connecting an accelerator sensor (Freescale MMA7361) to the mass and a NI-USB6009 14-bit resolution data acquisition system. (The data collection process is shown in Fig. 12.) It is important to note that the electromagnetic is not used to gain power from reciprocating motion of the mass connected to diaphragm No. 2 in the present work. The values of acceleration are also obtained and illustrated in Fig. 13. Drawing the phase plane is required to investigate the sufficient condition of the SUTech-SR-3 engine. To this end, the velocity change and the movement of the power piston have to be carefully monitored during the stable limit cycle of the dynamic engine. Integrating the experimental driven data, the velocity variation related to the power piston is obtained and depicted in Fig. 14. The movement values of the power piston can also be generated using the same procedure and integrating the data for a second time (Fig. 15). Using the experimental results for the velocity and movement of the power piston, the practical phase plane of the engine can be simply drawn. According to Fig. 16, the stable limit cycle of the engine is formed in the phase plane. Eventually, the resemblance of the limit cycle in one piston results in the existence of the same limit cycle in the other piston since both the equations of the system are coupled (Eqs. (1) and (2)). It is important to note that the experimental frequency of the engine (resonance frequency) is measured as 13.8 Hz.

Also, Table 4 demonstrates the comparison between simulated and experimental design parameters. As seen, outcomes show that the presented method can predict the design parameters, well.

Conclusion

In this study, the diaphragm thermoacoustic Stirling engine-related design parameters, the according to sufficient condition, were investigated using the genetic algorithm for the first time. To this end, an estimated parametric equation for the engine was considered by employing energy phenomena relations. To do so, two pseudo-energy equations and their related derivatives were defined for individual pistons, estimating the design engine parameters. Using the resulted equations and genetic algorithm, the four main design parameters of the engine including V_{c0}, R_q, V_{h0} and T_h were

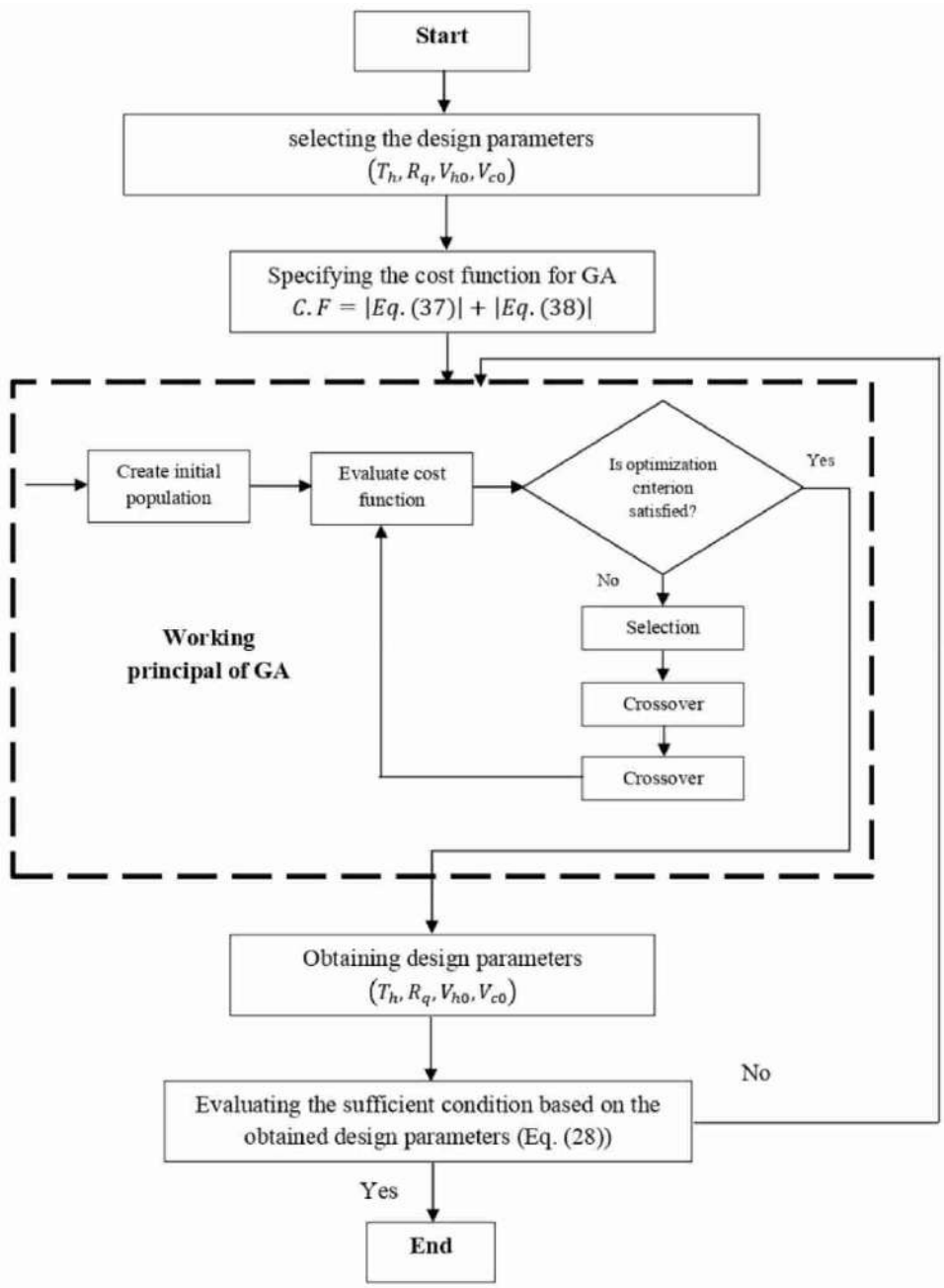

Fig. 10 Flowchart presenting the design process of diaphragm thermoacoustic Stirling engine

estimated. The sufficient condition of the engine was analyzed using the estimated parameters and parametric sets of equations. The presented model predicted a stable movement of the constructed *SUTech-SR-3* engine based on the four extracted values. This claim was later validated using the experimental results of the mentioned engine, and a very good agreement was reached comparing such data. This accomplishment revealed that the presented methods can be applied to other oscillators in terms of both manufacturing and investigating the sufficient condition of engines in their dynamic phase. This is mainly because the above-mentioned method was successfully applied on the two oscillators of free-piston Stirling engines and diaphragm thermoacoustic Stirling engines. It is important to note that the value of T_{h} is

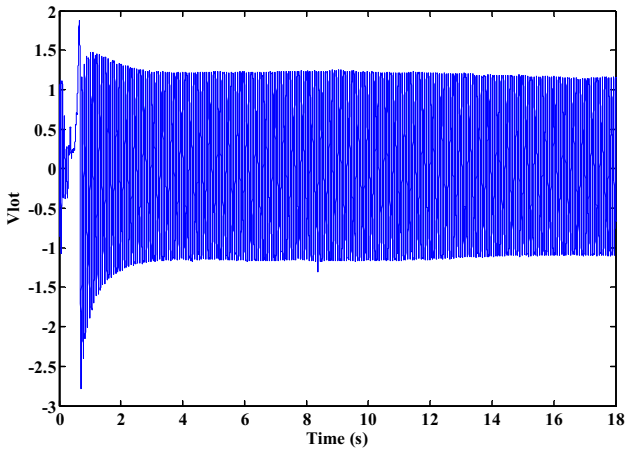

Fig. 11 The voltage changes due to the movement of mass attached to diaphragm No.2 (power piston)

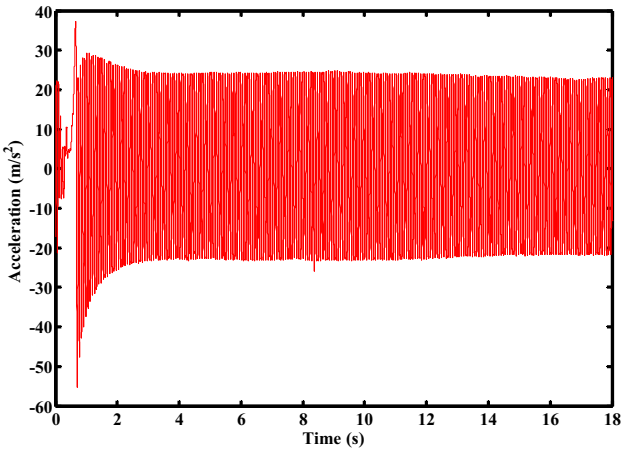

Fig. 13 Experimental data of the power piston acceleration

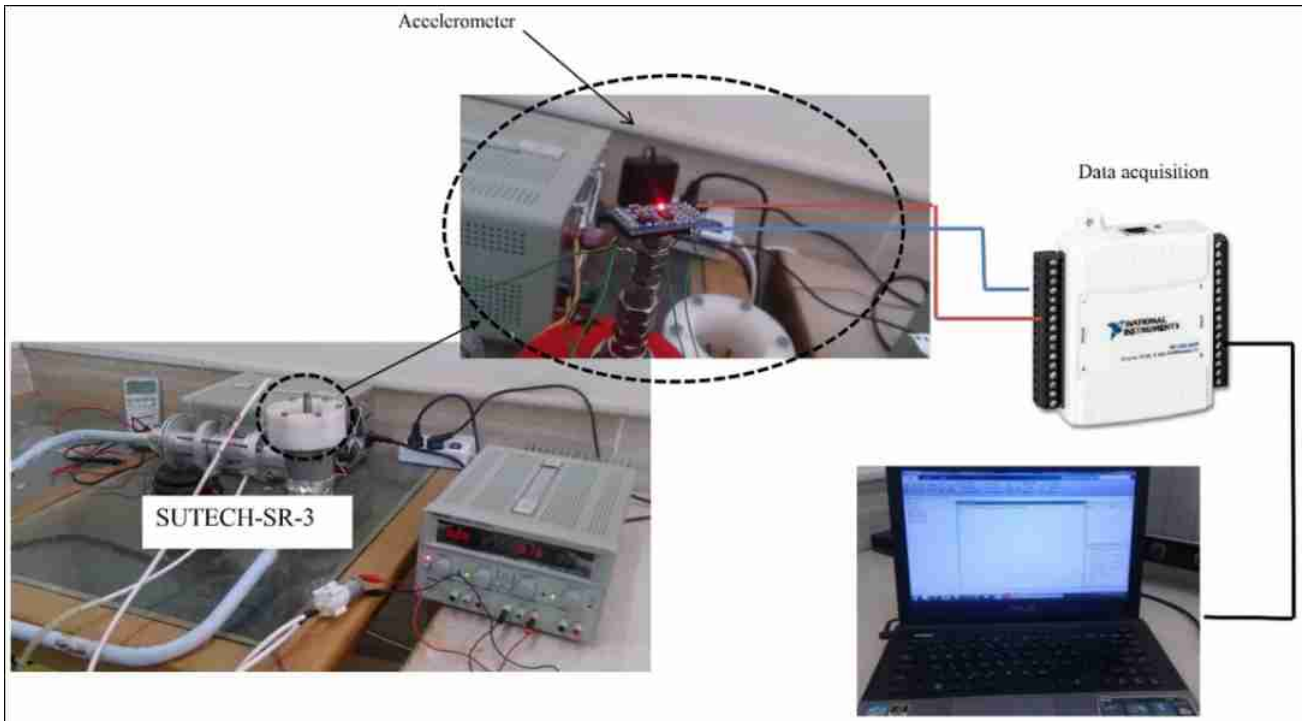

Fig. 12 Experimental rig

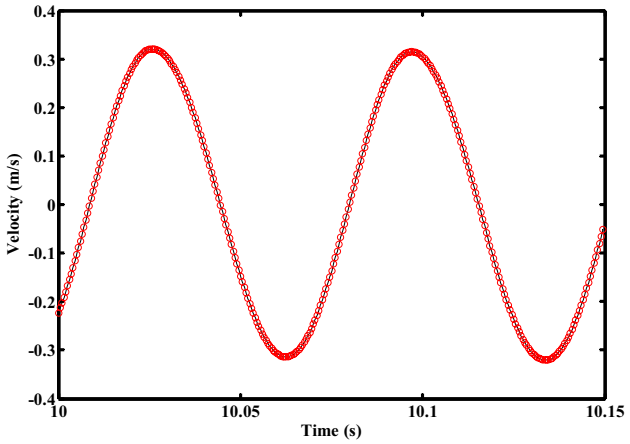

Fig. 14 Experimental data of the power piston velocity

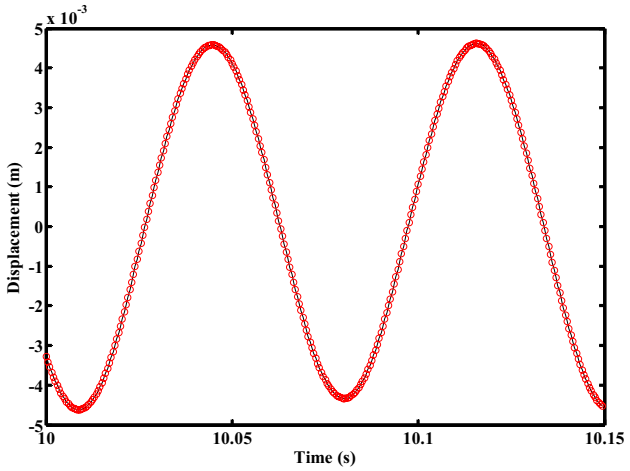

Fig. 15 Experimental data of the power piston movement

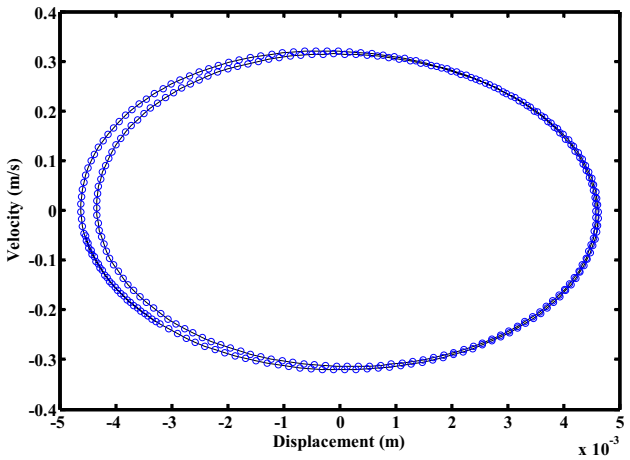

Fig. 16 Experimental phase plane of power piston (mass connected to diaphragm No. 2)

Table 4 Comparison between simulated and practical values of design parameters

Design parameter	Simulated value	Practical value	Error analysis
T_h	493 (k)	488 (k)	1%
R_q	12960	13450	3.6%
$V_{h0}(m^3)$	0.000191 (m^3)	0.000198 (m^3)	3.5%
$V_{c0}(m^3)$	0.000342 (m^3)	0.000364 (m^3)	6%

only related to the hot source temperature section, and this value can be varied during the engine loop.

Declarations

Conflict of interest The authors declare that they have no conflict of interest.

References

1. Zhang, B., et al.: Dynamic energy conversion and management strategy for an integrated electricity and natural gas system with renewable energy: deep reinforcement learning approach. Energy Convers. Manag. **220**, 113063 (2020)
2. Xu, J., et al.: Numerical study on a heat-driven piston-coupled multi-stage thermoacoustic-Stirling cooler. Appl. Energy **305**, 117904 (2022)
3. Ceperley, P.H.: A pistonless Stirling engine—the traveling wave heat engine. J. Acoust. Soc. Am. **66**(5), 1508–1513 (1979)
4. Backhaus, S., Swift, G.: A thermoacoustic Stirling heat engine. Nature **399**(6734), 335–338 (1999)
5. Backhaus, S., Swift, G.W.: A thermoacoustic-Stirling heat engine: detailed study. J. Acoust. Soc. Am. **107**(6), 3148–3166 (2000)
6. Dhuchakallaya, I., Jearsiripongkul, T., Saechan, P.: Acoustic field improvement through adjustable resonator to enhance the performance of thermoacoustic-Stirling engine. Energy Rep. **8**, 979–985 (2022)
7. Swift, G.W.: Thermoacoustics: A unifying perspective for some engines and refrigerators. Acoust. Soc. Am. (2003)
8. Zare, S., Tavakolpour-Saleh, A.: Modeling, construction, and testing of a diaphragm thermoacoustic Stirling engine. Energy Convers. Manag. **243**, 114394 (2021)
9. Tavakolpour-Saleh, A., Zare, S.: Justifying performance of thermo-acoustic Stirling engines based on a novel lumped mechanical model. Energy **227**, 120466 (2021)
10. Chen, G., et al.: Multi-physics coupling in thermoacoustic devices: A review. Renew. Sustain. Energy Rev. **146**, 111170 (2021)
11. Steiner, T., de Chardon B.: Evolution of a diaphragm beta Stirling engine to a displacer-less thermoacoustic design. In: 17th international stirling engine conference. 2016
12. Steiner, T.W., Archibald, G.D.: A high pressure and high frequency diaphragm engine: comparison of measured results with thermoacoustic predictions. Appl. Energy **114**, 709–716 (2014)
13. Nouh, M., Aldraihem, O., Baz, A.: Onset of oscillations in traveling wave thermo-acoustic-piezo-electric harvesters using circuit analogy and SPICE modeling. J. Dyn. Syst. Meas. Contr. **136**(6), 061005 (2014)

14. Penelet, G., Watanabe, T., Biwa, T.: Study of a thermoacoustic-Stirling engine connected to a piston-crank-flywheel assembly. J. Acoust. Soc. Am. **149**(3), 1674–1684 (2021)
15. Roshwalb, A., et al.: Performance of a traveling wave thermoacoustic-piezoelectric energy harvester: an electrical circuit analogy approach. J. Intell. Mater. Syst. Struct. **25**(11), 1372–1383 (2014)
16. Aldraihem, O., Baz, A. Onset of self-excited oscillations of traveling wave thermo-acoustic-piezoelectric energy harvester using root-locus analysis. J. Vibr. Acoust. **134**(1), (2012).
17. Abduljalil, A.S., Yu, Z., Jaworski, A.J.: Non-linear phenomena occurring during the start-up process of a travelling-wave looped-tube thermoacoustic engine. Proc. Inst. Mech. Eng. Part A J. Power Energy **226**(7), 822–836 (2012)
18. Yu, G., et al.: Study of nonlinear processes of a large experimental thermoacoustic-Stirling heat engine by using computational fluid dynamics. J. Appl. Phys. **102**(7), 074901 (2007)
19. Lalit, M., Karlsson, M., Åbom, M.: An engineering nonlinear model for thermoacoustic engines. ICSV22, pp. 12–16 Florence, Italy (2015).
20. Tavakolpour-Saleh, A., Zare, S.: An averaging-based Lyapunov technique to design thermal oscillators: a case study on free piston Stirling engine. Energy **189**, 116127 (2019)
21. Zare, S., Tavakolpour-Saleh, A.: Design of a traveling wave thermo-acoustic engine based on genetic algorithm. Int. J. Energy Res. **43**(14), 8790–8801 (2019)
22. De Waele, A.: Basic treatment of onset conditions and transient effects in thermoacoustic Stirling engines. J. Sound Vibr. **325**(4–5), 974–988 (2009)
23. Hu, J., et al.: Analysis of a displacer-coupled multi-stage thermoacoustic-Stirling engine. Energy **145**, 507–514 (2018)
24. Iniesta, C., et al.: Energy and efficiency evaluation of feedback branch design in thermoacoustic stirling-like engines. Energies **12**(20), 3867 (2019)
25. Dhuchakallaya, I., Saechan, P.: Performance Improvement of a Thermoacoustic Stirling Engine With In-Line Phase-Adjuster. J. Energy Resour. Technol., **144**(5) (2022).
26. Kisha, W., et al.: Asymmetrically heated multi-stage travelling-wave thermoacoustic electricity generator. Energy **235**, 121312 (2021)
27. Tan, J., Wei, J., Jin, T.: Onset and damping characteristics of a closed two-phase thermoacoustic engine. Appl. Therm. Eng. **160**, 114086 (2019)
28. Senga, M., Hasegawa, S.: Energy conversion of thermoacoustic engines with evaporation and condensation. Int. J. Heat Mass Transf. **165**, 120385 (2021)
29. Zare, S., Aghajanzadeh, O.: An investigation on the effects of gas pressure drop in heat exchangers on dynamics of a free piston Stirling engine. Int. J. Eng. **30**(2), 294–302 (2017)
30. Zare, S., Tavakolpour-Saleh, A.: Free piston Stirling engines: a review. Int. J. Energy Res. **44**(7), 5039–5070 (2020)

International Journal of Energy and Environmental Engineering (2023) 14:921–936
https://doi.org/10.1007/s40095-022-00556-8

ORIGINAL RESEARCH

Technical and economic feasibility assessment of low and high salinity water flooding: a simulation-based approach

Furqan Alvi[1] · **Haris Ahmed Qureshi**[1]

Received: 14 August 2022 / Accepted: 18 December 2022 / Published online: 5 January 2023

Abstract

Waterflooding is renowned improved oil recovery method worldwide to recover medium to light crude oil. LSWF is an emergent IOR method which reduces the quantity of residual oil saturation by implementing waterfloods of low salt concentration. LSWF can increment the oil recovery up to 10–20% compared to simple waterflooding. A synthetic 3D simulation model is generated in this study using commercial black oil simulator (Eclipse 100). Two base cases of low and high salinity water flooding are simulated, and impact of low salinity water flooding on FOE, FOPR, FOPT, FPR, FSPR, FSPT is analyzed. Sensitivity analyses of injection water salinity, relative permeability curves, grid refinement, Low salinity slug size and end point saturation effects are also conducted (LASLTFNC). LSWF enhances the oil recovery efficiency by 17% compared to HSWF. Sensitivity of wettability (relative permeability curves) exhibits maximum recovery of 75.96% in presence of strongly water wet system. Similarly, sensitivity of grid refinement exhibits variation in ultimate recovery of 5.24% between LSWF base case and refined grid case. Sensitivity of injection water salinity from 1000 to 35,000 PPM (sea water) results in ultimate recovery between 60.88 and 75.96%, respectively. The continuous injection of LS water is not economical for whole production life therefore the injection of slug can help in the withdrawal of almost similar volume of oil with better cost. Economic analysis of five different LSWF cases and one HSWF case is carried out to evaluate the most economically viable injection scenario. From case-1 to case-6, injection of low salinity water for 450 days followed by high saline water turns out to be the most optimum case with NPV of 20.422 million dollars.

Keywords Low salinity water flooding · EOR · Wettability alteration · Slug injection · Grid refinement recovery efficiency · Economic analysis

Introduction

In this modern era, the thirst for energy resources is increasing day by day and the demand for global energy resources will raise to 40% by 2035 [1]. Oil and gas will be one of the key energy sources to fulfill this energy demand in future [2]. The pace of discovering new hydrocarbon reserves is quite low to cope up the ever-increasing thirst of fossil fuel. So, the EOR/IOR of the existing oil reservoirs is fundamental for industry to sustain the demand and supply. Studies have suggested that more than 70% of the global oil reserves do not have enough energy to produce through primary recovery technique [3].

Oil recovery in any EOR method depends on sweep and displacement efficiency of the applied technique either it increases the sweeping efficiency by pushing the remaining oil in unswept region or increase in displacement efficiency by residual oil saturation reduction. Residual oil saturation depends on the capillary number which can be decreased by reducing IFT or by alteration of rock's wettability to water wet [4].

Waterflooding is renowned improved oil recovery method worldwide to recover medium to light crude oil. Waterflooding was initially employed for maintenance of reservoir pressure after primary depletion, but it is proved as very efficient oil recovery mechanism in terms of sweep efficiency and displacement of oil towards the production well at an economic rate. Waterflooding can increase the oil recovery from 10 (primary recovery phase) even up to 40% of the OOIP [5, 6].

✉ Haris Ahmed Qureshi
haris.ahmed@mpcl.com.pk

[1] Mari Petroleum Company Limited, Islamabad, Pakistan

Conventionally, the contribution of injected water properties to displacement efficiency and oil recovery was not studied in detail, but in last several years, extensive research is done which shows that optimized composition and salinity of injected water can affect the rock/fluid interaction in favorable way to improve oil recovery. LSWF is an emergent IOR method which reduces the quantity of residual oil saturation by implementing waterfloods of low salt concentration. The injected brine disturbs the initial rock/oil system equilibrium and alters the initial wettability of rock by adsorption/Desorption of ions and make it more water wet to recover more trapped oil. LSWF is cheap and environment friendly technique, and it does not need any expensive chemical to be added. Water treatment to formulate low salinity water comprises of two stages: Nano-filtration and reverse osmosis [7]. In the first step, hardness of brine is reduced by removal of contaminates like sulfates and other divalent cation (Ca^{+2} or Mg^{+2}). LSWF can be applied in any phase of the oil recovery process. LSWF can increment the oil recovery up to 10% compared to simple waterflooding (high salinity water) for equal injection volume depending on formation minerology and brine composition [3].

LSWF shows promising results in both sandstone & carbonate reservoirs but LSWF application in carbonate reservoir has found erratic response in comparison to sandstone reservoirs. This may be the result of heterogeneity in carbonates, deficiency of certain clay and minerals favorable for LSWI and good bonding energy between polar components in crude oil and carbonate surfaces.

Tang and Morrow was the first one to observe the effect of LSWF on recovery efficiency by natural imbibition of low salt brine [8]. Filoco and Sharma proposed that oil recovery efficiency will be enhanced only if the salinity of connate water is reduced along with injected brine solution and confirms the effect of wettability alteration (Mixed wet to water wet) in enhanced recovery [9]. Hussain et.al suggested that pressure drop and permeability reduction due to fines migration is one of the reasons for increased oil recovery efficiency. (Mohammad Al Thani 2014) evaluated five different LSWF cases with different brine salinity and concluded that LSWF can enhance the recovery more than 5% on field scale. [10] employed LSWF, conventional waterflooding and polymer flooding and combination of it and found that improved IOR process selection depends on the different reservoir forces dominating over the field development process, reservoir heterogeneity, rock wettability and permeability. [11] develop several injection scenarios and observed that LSWF is sensitive to end point saturation, injection water salinity, low salinity slug and witnessed 22% incremental oil recovery by LSWI compared to HSWI. [12] in his paper evaluated the effect of coupling LSWF and steam flooding and detect promising results. The steam reduces the oil viscosity while LS water shifts the wettability to water wet system. He concluded that this technique could produce up to 15% of OOIP after secondary and tertiary methods. [3] in his review concluded that LSWF have a potential to improve recovery factor but the underpin factors are numerous depending on specific reservoir conditions, development scenarios and rock fluid interaction. [13] in his study compared the recovery outputs of different salinity water injection cases and concluded that recovery efficiency increases with decreasing water salinity. [14] develop a mathematical model coupling multicomponent ion exchange, water and oil phases and solubility of carbonates which then evaluates the effect of these variables on recovery efficiency. He concluded that recovery efficiency is dependent on brine composition and dissolution of calcite ion from surface of rock [14]. [15] couples LSWF and polymer flooding to improve heavy oil recovery and concluded that individual methods provide 5% of additional oil recovery while combination of both could increase recovery from 7.5 to 10% of OOIP.

The objectives of this study are to measure the impact of various salinity water injection on recovery efficiency and evaluate the sensitivity of different relative permeability curves (Wettability) on ultimate oil recovery efficiency. Observe the effect of grid refinement, Different Slug Sizes, End Point Saturation on both low and high salinity base cases and evaluate optimum water salinity injection case and to conduct the economic analysis of different water salinity injection scenarios and analyze the most cost-effective injection scenario.

Materials and methods

To simulate the low salinity waterflooding model, it is compulsory to start brine tracking feature in black oil simulator (Eclipse 100). Low salinity feature is introduced by keyword "LOWSALT" in RUNSPEC section of eclipse data file [16]. Two different profiles of relative permeability curve should be introduced for high and low salinity brine, in this way it permits the user to adjust the water–oil relative permeability, saturation and capillary pressure end points as a function of salt concentration in brine [17]. Keyword "LSALTFNC" in PROPS specifies the relative permeability curve to be assign, this function employs weighting factor which ranges from 0 to 1 to characterize as either low or high salinity brine is injected, with "0" representing high salinity and "1" representing low salinity properties to be used, any value in between allows the simulator to incorporate between the capillary pressure and relative permeability profiles to get correct profile for the specified salinity [11]. "SATNUM" and "LWSLTNUM" keywords in REGIONS are the low salinity oil–water saturation function region number which specifies the saturation table utilize to estimate relative permeability and capillary pressure in individual grid block.

"PVTWSALT" keyword defines the water PVT in case of low salinity brine injection with regards to salt concentration. The density and salt content of injected brine is introduced by keyword "BDENSITY" and "WSALT." The keyword "SALTVD" in SOLUTION supplies salt concentration table at different depths for each region of equilibration [18].

Favorable conditions for LSWF

Many conditions are proposed in different studies to see the impact of low salt brine flooding. Some of them are:

1. Significant clay amount must be present in porous formation [19].
2. Trapped oil containing polar components (Acidic or basic organic molecules). LSWF effects are not visible in refined oil as polar components are not present in it.
3. The concentration of injected brine is also a critical factor, and it is sensitive to ionic concentration. Ideally it must be in range of 1000–2000 ppm, but difference can be detected up till 5000 ppm.
4. Formation water must present and should contain divalent cations (Ca^{+2} or Mg^{+2}).
5. In some cases, fines production usually observed with water production but in LSWF it is not apparent as it can cause possible formation damage.
6. Reservoir temperature is an important factor in LSWF, but it appears to have no influence on the results of LSWI.

This project is conducted on commercial black oil simulator (Eclipse 100). A variety of synthetic models will be generated to analyze and test. The inputs to various parameters in the study are extracted from previous research work to conduct the study in a logical way. A basic 3D synthetic static simulation model will be created.

The assumptions for the reservoir under consideration are:

1. The pressure of reservoir is more than bubble point pressure i.e., undersaturated reservoir and therefore no gas cap will be present.
2. The reservoir is homogeneous and isotropic throughout. Rock and fluid properties will be similar and constant in every layer of the reservoir.

Enhanced recovery mechanism of low salinity water flooding

Increased interest in low salinity Waterflooding application results in several field and laboratory scale assessments of this method. Still, the exact mechanism of incremental oil recovery by LSWI is ambiguous. Complex interaction of rock, crude oil and injection water makes it quite difficult to understand the exact phenomena rather it is assumed to be an outcome of different processes underwent in a reservoir. Different mechanisms that held responsible to incremental oil recovery in several research articles are as follows:

Fines migration

[20] in their study proposed a relationship between fines migration, amount of clay present and additional oil recovery by low salinity water during study on Berea sandstone cores consists of low and high clay content. Core having high clay content exhibits high oil recovery compared to low clay content core by low salinity water injection. They suggest that introduction of low salinity brine results in expansion of double layer between clay particles due to their destabilization. Release of fine or clay fragments exposes the underlying layer, which enhances water wetness of the system and thereby improves oil recovery. Another belief is that release of clay particles potentially block pore throats or high permeability streaks and divert flowing water into unswept region which improves microscopic displacement.

Multi-component ion exchange (MIE)

[21], suggested multicomponent ion exchange as an incremental oil recovery mechanism between injected LSW and connate water. Polar oil component with assistance of positively charged ion connects with negatively charged clay surface. Four mechanisms of organic matter desorption onto clay surface are effected by cation exchange capacity in low salinity water environment, namely; cation bridging, cation exchange, water bridging and ligand bonding/bridging. Lager confirmed this phenomenon of cation exchange by flooding core with brine (Nacl) till traces of divalent cations (Ca^{+2} and Mg^{+2}) left.

PH effect

[10], observed increase in pH of effluent in presence of low salinity water. He concluded that enhanced oil recovery has the same mechanism of alkaline flooding by reducing the interfacial tension between water and oil phase by surfactant generation and alteration of wettability to more water wet state. They accounted cation exchange and carbonate dissolution as cause for increase in pH. Austad et.al (2010) explained relationship between water salinity and pH. In the presence of acidic gases such as CO_2, the pH of connate water is very low due to which divalent cations (Ca^{+2} and Mg^{+2}) absorbs cation exchange matter which are clay mineral. Injection of low ion concentrated water disrupts the equilibrium and causes desorption of divalent cations.

Electrical double layer effect

Electric double layer effect is another mechanism documented in the literature by which LSWF improves oil recovery. According researches, connate water contains significant amount of Ca^{+2} or Mg^{+2} ions which screens off formation of negative charge at connate water pH at water/oil and solid/water interface which accounts for repulsive forces suppression. Injection of low salinity water with lower amount of divalent cations reduces the screen off potential. This results in double layer expansion (water layer) across clay particle and oil. Oil desorbs from clay particle surface when repulsive force overcomes the binding force, this increases ultimate oil recovery efficiency.

Synthetic model construction

A synthetic 3D simulation model is generated in this study using commercial black oil simulator (Eclipse 100). The model contains of $50 \times 50 \times 3$ grid blocks having dimension $400 \times 400 \times 12$ ft in *X*, *Y* and *Z* axes, respectively. Each grid block size in *X* and *Y* axes is 8 ft, while it measures 4 ft in *Z*-direction. The proposed model is heterogenous for different rock layers. Water and oil are two active phases offered in this simulation model with connate water salinity of 35 kg/m3 which is equally saline to sea water. Two active wells exist in the reservoir model: Injector and producer, both wells are located diagonal to each other. Injector is located on grid block 1, 1 and producer on 50, 50 in I, J location. Injector and producer wells are completed from top to bottom and controlled by reservoir fluid volume (RESV) with flow rate of 500 bbl/day.

Two base cases were developed based on the above-mentioned model: one is low salinity case with continuous water injection of salinity 0.35 lb/stb (1000 PPM) and the other one is high salinity case with continuous water injection of salinity 12.27 lb/stb (35,000 PPM). The simulation model is run for the period of 5 years from 2019 to 2024 in both cases with injection rate of 500 bbl/day. 3D visualization of synthetic model configured with injector and producer is shown in (Figs. 1, 2, 3).

Model properties

The data utilized in the construction of synthetic waterflooding models during this study are extracted from the literature review. As reservoir is heterogenous the porosity of the reservoir models varies from 0.17 to 0.25 and permeability value ranges between 200 and 900 mD. The density of oil, water and gas at surface condition is 49.94, 62.5 and 0.05 $lb/ft^{3,}$ respectively. The reference pressure is 4000 psia for oil and water, water formation volume factor is 1.038 rb/stb, water and rock compressibility are 4.6E-5. The initial viscosity of oil and water at surface conditions is 0.628 and 0.318 cp, respectively. In generation of synthetic model Capillary pressure data are neglected due to unavailability. The simulated model takes on single salt in the injected brine for simplicity. From the literature review it is evident that low salinity effects are visible only under 1.75 lb/stb (5000 PPM) of salt concentration so all the simulated cases for low salinity sensitivity analyses is conducted under this range.

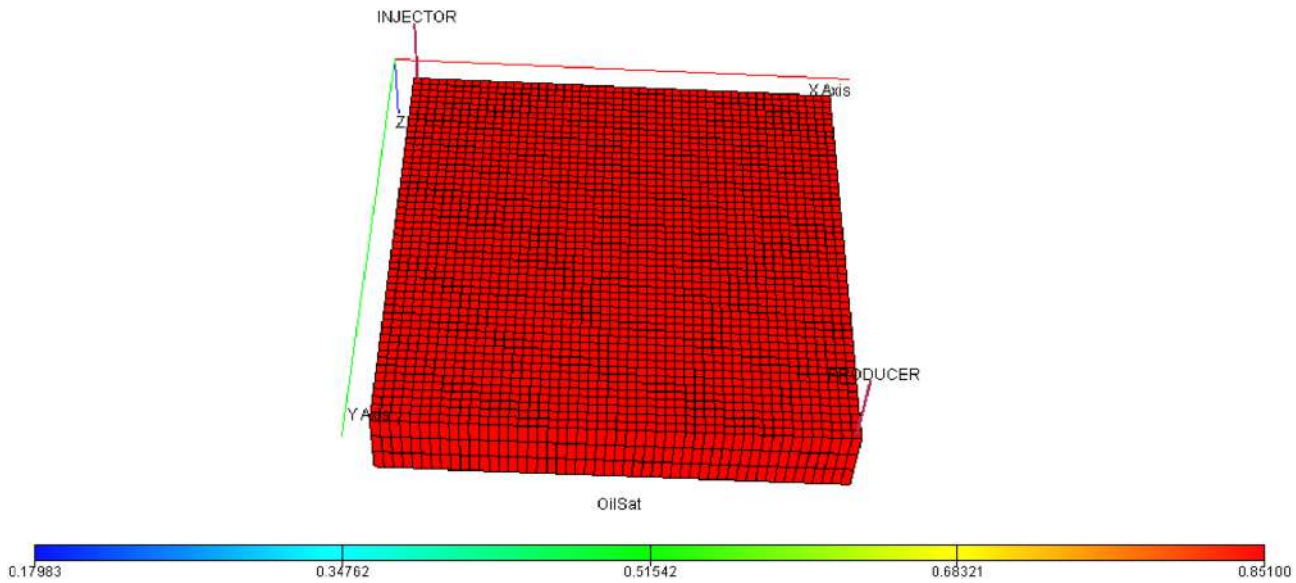

Fig. 1 3D visualization of synthetic model showing oil saturation distribution and well placement

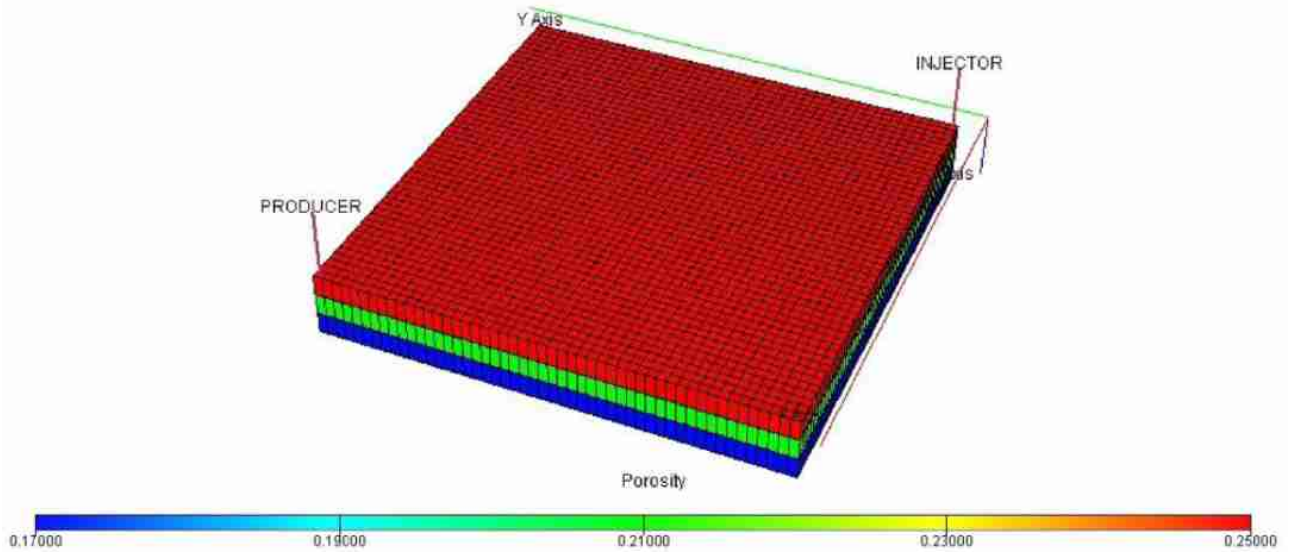

Fig. 2 Variation in porosity pattern

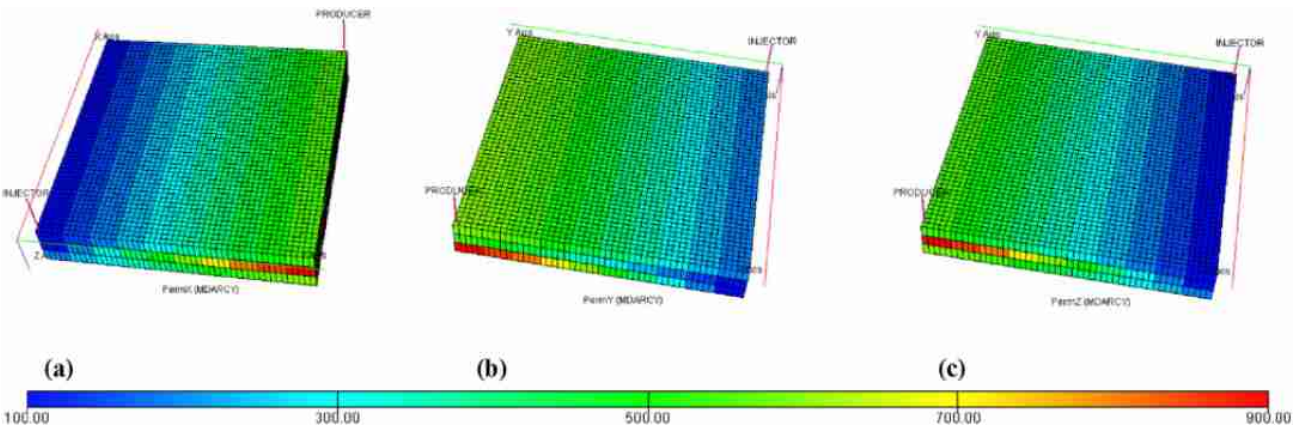

Fig. 3 Variation in permeability pattern in *X*, *Y* and *Z*-dimension

Results and discussion

The base case designed for low salinity waterflooding involves continuous injection of low saline water (1000 ppm) for the production period of 5 years. Similarly, base case of high salinity waterflooding uses continuous injection of high saline water (sea water) or 35,000 ppm from start till end of production life. After conducting the numerical simulation utilizing the data and the assumptions proposed in the preceding section, the following results have been plotted, and their explanation has been provided with each outcome.

1. Field Oil Equivalent (Oil Recovery Efficiency)
2. Field Oil Production Rate
3. Field Oil Production Total
4. Average Field Pressure
5. Field Salt Production Rate
6. Field Salt Production Total

Effect of salinity on oil recovery efficiency

(Fig. 4) corresponds to result of salinity on oil recovery efficiency, from the plot it is visible that recovery with continuous injection of high salinity water results in 60% recovery of the pore volume while recovery factor gets to 77% from constant injection of low salinity water. This reflects that recovery efficiency enhanced with decrease in water salinity. The oil recovery from high salinity case

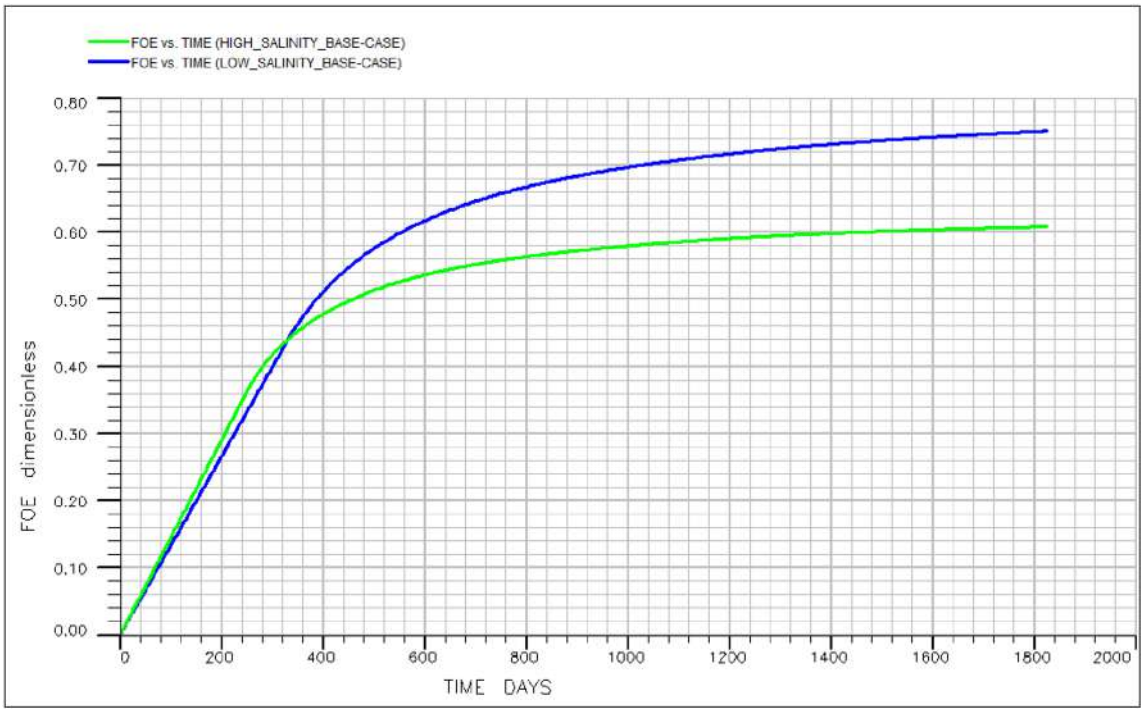

Fig. 4 Assessment of oil recovery efficiency in base cases

is still high which is because of existing homogeneity in some areas of the reservoir model.

Effect of salinity on field oil production rate and cumulative oil production

(Fig. 5) illustrates the flow rate of oil and cumulative oil production during production life of the field. The plot shows that oil flows initially at 500 stb/day. The initial flow rate in high salinity and low salinity injection case lasts till 242 days and 330 days, respectively. The flow rate starts to drop quickly onwards because water breakthrough at the perforations and WOR gets increase at every interval of time. The rate slows down and flows at very low rate of 20 stb/day from 1200 days until end of production in high salinity case while in low salinity case it stabilized around 1500 days and flows at 25 stb/day until production stops. The delay in water breakthrough in low salinity case sustains the initial flow rate to a longer period than high salinity injection case. The cumulative oil production for low salinity case is 243723 STB, while is 209052 STB in high salinity case. The cumulative oil volume is similar till 274 days in both high and low salinity cases. It shows that low salinity effect requires 274 days to become visible. The shorter the time required to visible low salinity effect the better it is for project economics.

Effect of salinity on field average pressure

The following (Fig. 6) represents average pressure for both cases, the initial pressure is 3998 psia, as oil is withdrawn from the reservoir, pressure starts to decline slightly in both cases until the waterflooding effects visible in the reservoir. The pressure drop in low salinity Waterflooding is more compared to high salinity waterflooding, but the difference is quite small. The pressure at the conclusion of first year of production is 3991 in high salinity and 3987 in low salinity case. This difference in pressure shrinks with every year of production and remains 1.5 psia at the end of production. The observed results depict the difference in salinity cause some change in pressure but that are not much significant.

Effect of salinity on rate of salt production and cumulative salt production

The following (Fig. 7) exhibits salt production rate and cumulative salt production, it shows salt production starts

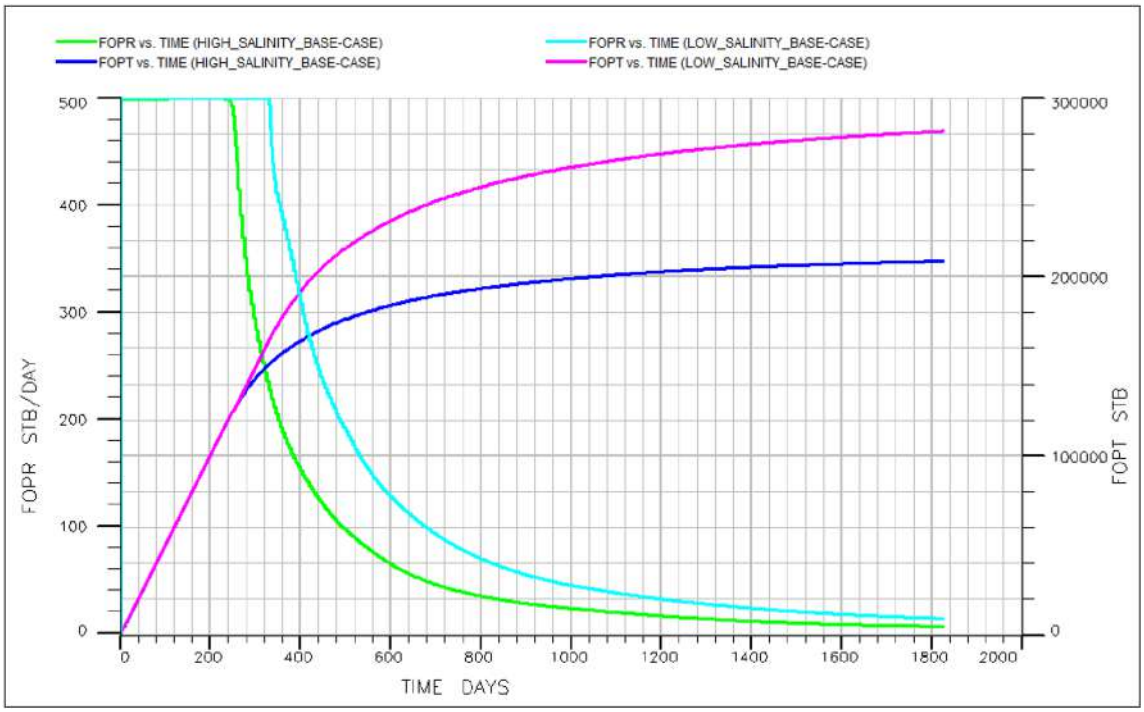

Fig. 5 Assessment of rate of oil production and cumulative oil production in base cases

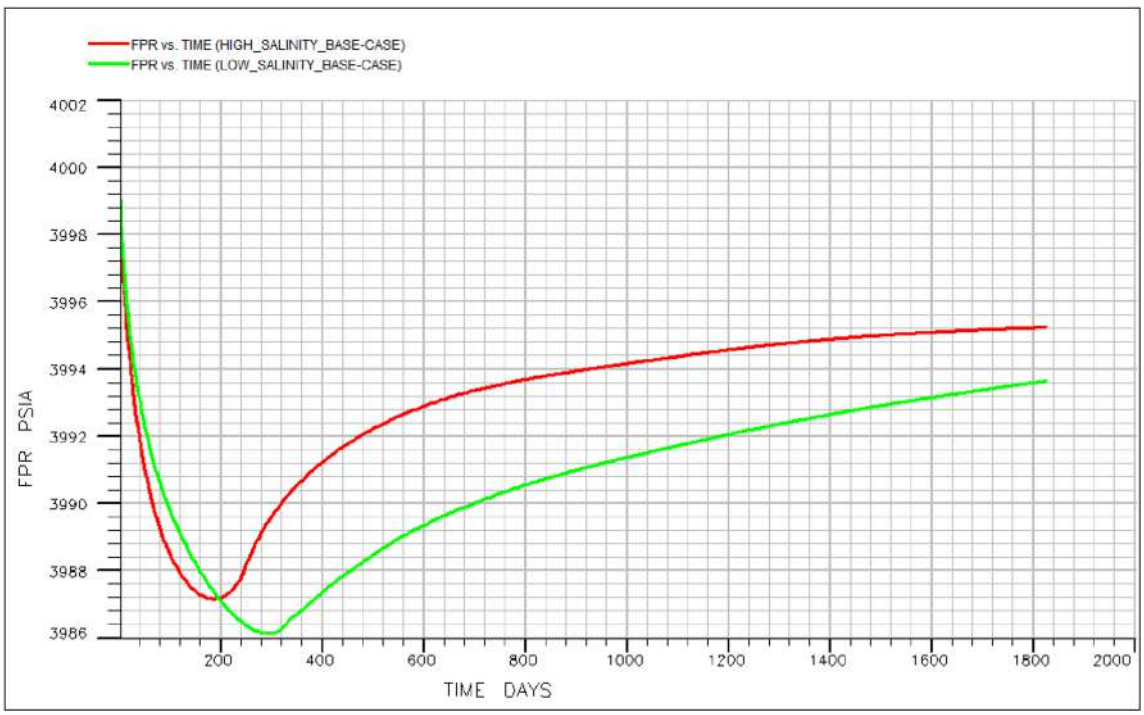

Fig. 6 Assessment of average field pressure

around 240 days in high salinity case and rapidly increases within no time and achieves the rate of 3700 lb/day while in low salinity it starts after 330 days and increases to 38 lb/day at the conclusion of first year. The rate at the conclusion of production is 5839 lb/day for high salinity and 164 lb/day for low salinity case. The total salt production is 88 M Lb

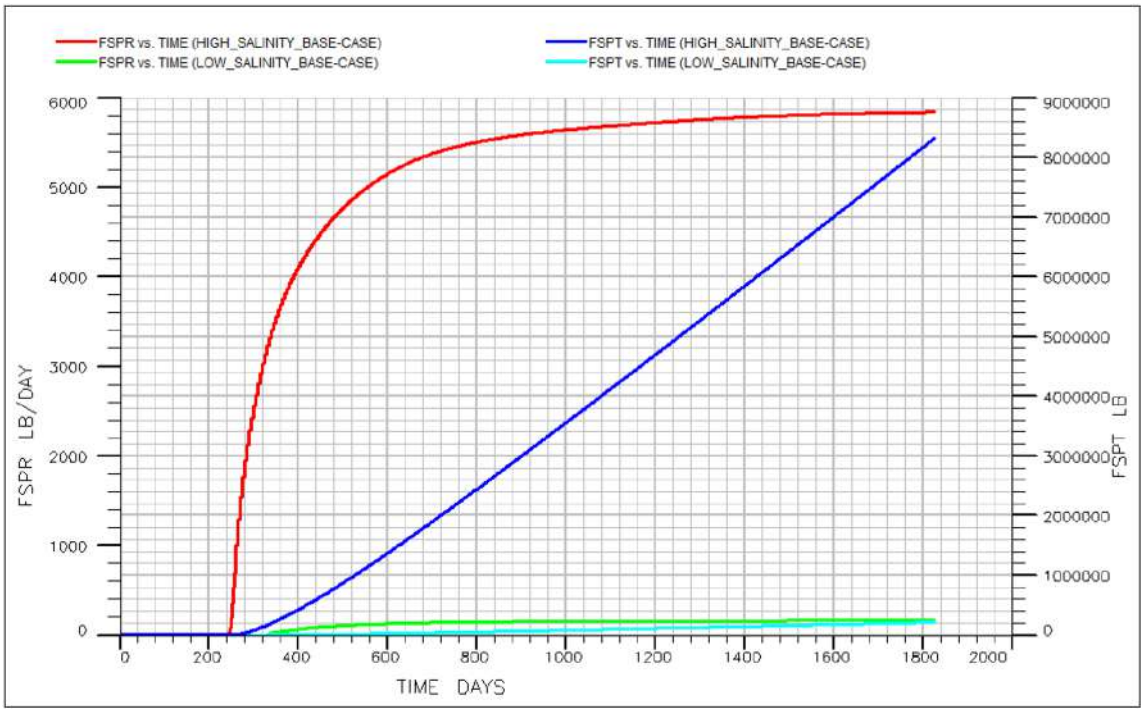

Fig. 7 Assessment of salinity effect on rate and cumulative salt production

in high salinity case which is much higher than 0.25 M Lb in low salinity case.

Sensitivity analysis

The base case is analyzed to evaluate the sensitivity of injection water salinity, reservoir water salinity, relative permeability curves interpolation, grid refinement and slug size effect.

Injection water salinity effect

To analyze the impact of water salinity on oil recovery factor, six different cases were analyzed including the base case with injection water salinity of 35,000 ppm of TDS (12.25 lb/stb) in moderately salinity reservoir of 50,000 ppm or 17.52 lb/stb. Rest of the injection water salinity values are 1000, 2000, 3000, 4000 and 5000 ppm, respectively. The results of different salinity water injection into high salinity reservoir are shown in (Fig. 8) and (Table. 1).

It shown in Fig. 8 and Table 1 that decrease in injection water salinity enhances the ultimate recovery efficiency. High salinity water of 35,000 ppm offers 60.88% of oil recovery, which in comparison to injection of 1000-ppm salinity water offers 24.77% less oil than it. It should be noticed here from Table 1 that injection salinity of 5000 ppm offers no improvement to oil recovery compared to high salinity injection case, which endorses the fact that positive effects of low salinity water are visible for injection water salinity less than 5000 ppm.

Relative permeability effect

LSWF strongly rely on the saturation function and relative permeability interpolation and therefore very much dependent on wettability. Corey's correlation is employed to generate different wettability profiles to analyze the sensitivity of rocks wettability on recovery factor. Relative permeability effects on high salinity connate water reservoir are observed because most reservoirs contain high mineralogical concentration. effect of relative permeability on both low and high salinity injection case is analyzed. The result from high salinity water injection into high salinity connate water reservoir is shown in (Fig. 9) and corresponding recovery efficiencies with Corey's parameters is shown in (Table 2).

The result shows highest recovery of 75.19% in case 4 which is highly water wet system and lowest recovery factor of 48.15% for case 3 which is strongly oil wet system. Partial water wet system offers 72.28% recovery which is higher than recovery efficiency of 59.73% of partially oil wet system.

Table 3 and Fig. 10 show the results of low salinity water flooding in different wettability reservoirs. Maximum recovery of 75.96% is obtained in base case which possess

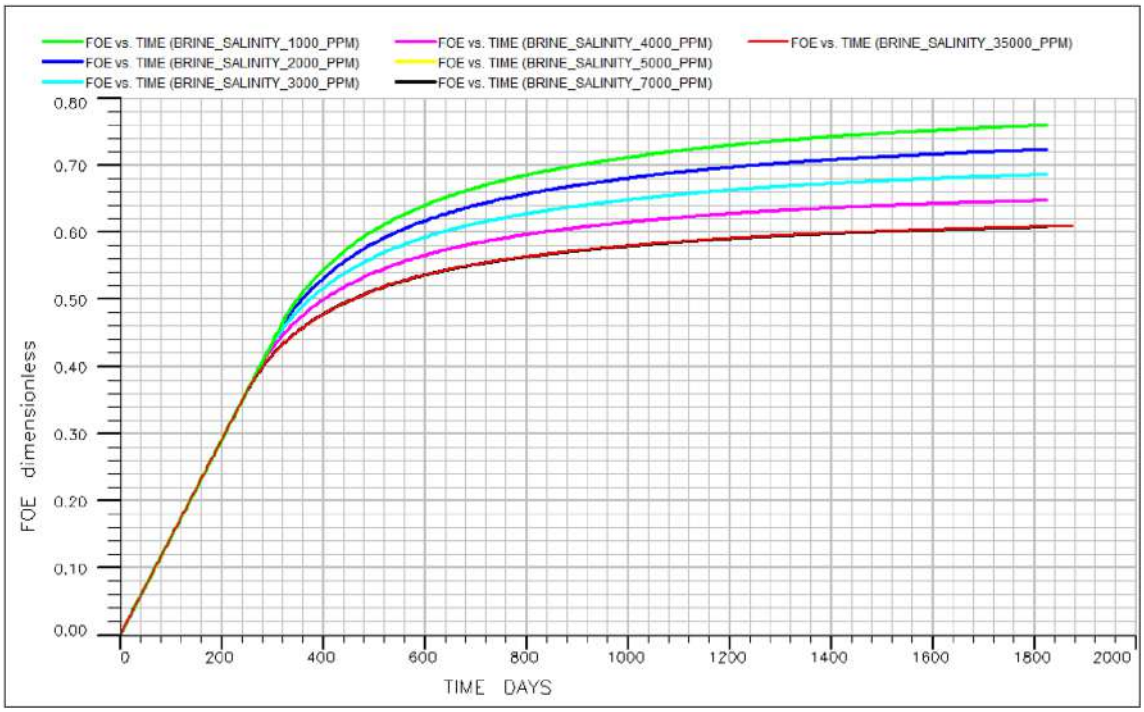

Fig. 8 Assessment of injection water salinity on recovery efficiency in highly saline reservoir

Table 1 Different salinity cases with reservoir and injection water salinity effect on recovery efficiency in highly saline reservoir

Case	Reservoir water salinity (PPM)	Injection water salinity (PPM)	Recovery efficiency (%)	Improvement from base case (%)
Base Case	71,000–75,000 (3000–6000 ft)	35,000	60.88	0.0
Case 1	71,000–75,000 (3000–6000 ft)	5000	60.80	−0.001
Case 2	71,000–75,000 (3000–6000 ft)	4000	64.78	6.40
Case 3	71,000–75,000 (3000–6000 ft)	3000	68.62	12.71
Case 4	71,000–75,000 (3000–6000 ft)	2000	72.34	18.82
Case 5	71,000–75,000 (3000–6000 ft)	1000	75.96	24.77

strongly water wet system and lowest recovery of 54.79% achieved in highly oil wet system.

It is visible from (Fig. 10) and (Table 3), the low salinity water injection gives improved results from high salinity water injection in initially partially or highly oil wet reservoirs but the injection of low salinity water injection in partially or highly water wet reservoir gives slight improvement which is not economical compared to the cost of low salinity water. So, the selection of low salinity water injection depends extremely on the initial reservoir wettability.

Grid refinement effect

Grid refinement is very much concerned with the adequate inference of the real reservoir behavior with mathematical model. The error arises due to coarsening of grid blocks creates local truncation errors which causes numerical dispersion error. So, the selection of optimum grid block length is essential to achieve certain physical system estimates. Grid refinement is conducted on low salinity and high salinity base cases and results are shown in (Fig. 11) and (Table 4).

The difference in recovery factor from high salinity base case and refined case is 2.77% and Low salinity base case and refined case is 5.24%. The difference is bit higher in low salinity cases than high salinity cases because of changes in wettability by low saltwater injection.

Low salinity slug size effect

Low salinity water flooding depends on the volume of water injected because the cost of low salinity water is

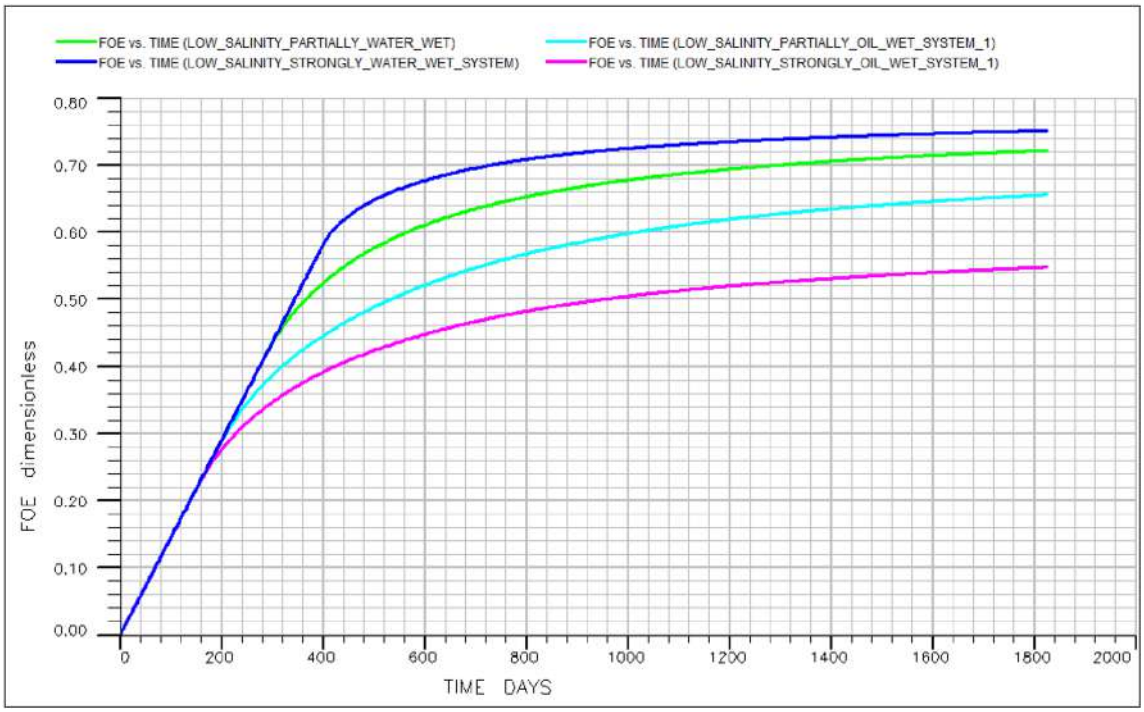

Fig. 9 Effect of relative permeability on recovery efficiency by high salinity water injection

Table 2 Different relative permeability rocks effect on recovery efficiency by high salinity water injection

Case	Corey's equation parameters				Recovery efficiency (%)
	S_{orw}	S_{wc} or S_{wi}	K_{rw} (S_{orw})	K_{ro} (S_{wc})	
Base case (HSWF)	0.2	0.15	0.42	0.75	60.80
Case 1	0.20	0.10	0.70	1.0	59.73
Case 2	0.10	0.22	0.60	0.70	72.28
Case 3	0.33	0.10	0.70	0.90	48.15
Case 4	0.10	0.25	0.30	0.70	75.19

Case 1 partially oil wet system, Case 2 partially water wet system, Case 3 Strongly oil wet system, Case 4 strongly water wet system

Table 3 Different relative permeability rocks effect on recovery factor by low salinity water injection

Case	Corey's equation parameters				Recovery efficiency (%)
	S_{orw}	S_{wc} or S_{wi}	K_{rw} (S_{orw})	K_{ro} (S_{wc})	
Base case (LSWF)	0.20	0.15	0.8	0.9	75.96
Case 1	0.20	0.10	0.70	1.0	65.58
Case 2	0.10	0.22	0.60	0.70	72.15
Case 3	0.33	0.10	0.70	0.90	54.79
Case 4	0.10	0.25	0.30	0.70	75.12

Case 1 partially oil wet system, Case 2 partially water wet system, Case 3 Strongly oil wet system, Case 4 strongly water wet system

expensive. The continuous injection of low salinity water for the complete production period can be costly to execute economically. In this study, low salinity base case is flooded with 1000 ppm or 0.35 lb/stb salinity brine for the period of 150, 300, 450, 600 and 750 days followed by brine injection of 35,000 ppm or 12.27 lb/stb for the remaining production life. The results shown in (Fig. 12) demonstrates the dependency of oil recovery on slug size.

(Table 5) shows when the injected volume increase from 72,226 to 144,435 STB the incremental recovery obtained is around 2.39%. on the other hand, from case 2 to case 5 the incremental recovery is 2.5%. The combined increased in recovery from case 1 to case 5 is 4.89% which is not much important compared to the volume of low salinity water injected.

End point saturation effect

Low salt weighting factor vs salt concentration (LSALTFNC) specifies the quantity of low and high salinity saturation profiles and relative permeability tables that will be used for different brine salinities. In this study three "LSALTFNC" were used as shown in (Table 6). In both base case and case 1 less data from low salt profile is used. On the other hand, in case 2 low salt profile is used until water salinity is less than 4000 ppm and utilize high salt profile for water salinity greater than 4000 ppm.

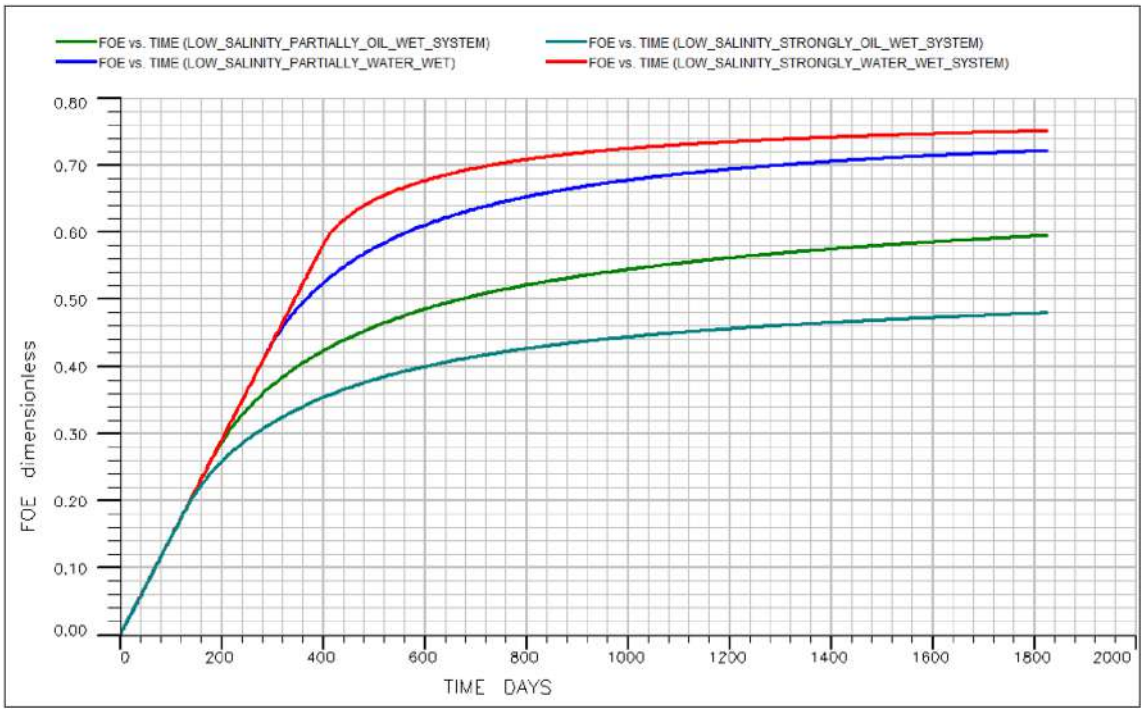

Fig. 10 Assessment of relative permeability on recovery efficiency by low salinity water injection

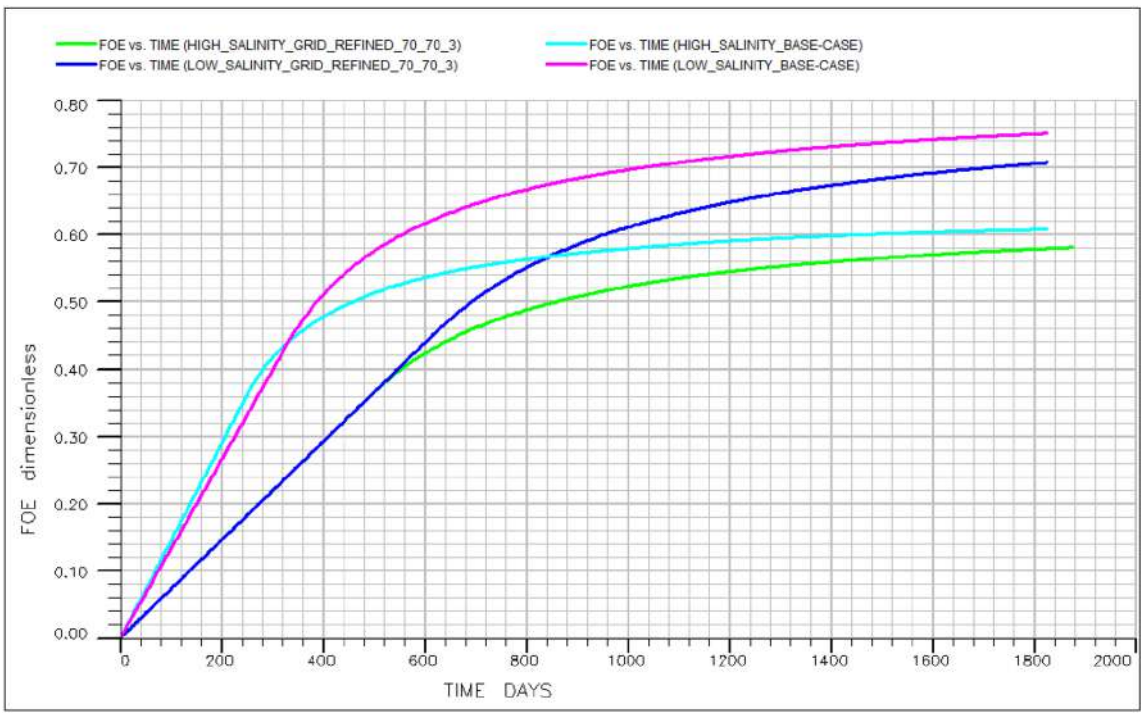

Fig. 11 Effect of grid refinement on recovery efficiency of low and high salinity base cases

Table 4 Grid refinement effect on recovery efficiency

Cases	Description	Recovery efficiency (%)
Case 1	High salinity base case with 50×50×3 grids in *X*, *Y* and *Z* dimension	60.88
Case 2	High salinity refined case with 70×70×3 grids in *X*, *Y* and *Z* dimension	58.11
Case 3	Low salinity base case with 50×50×3 grids in *X*, *Y* and *Z* dimension	75.96
Case 4	Low salinity refined case with 70×70×3 grids in *X*, *Y* and *Z* dimension	70.72

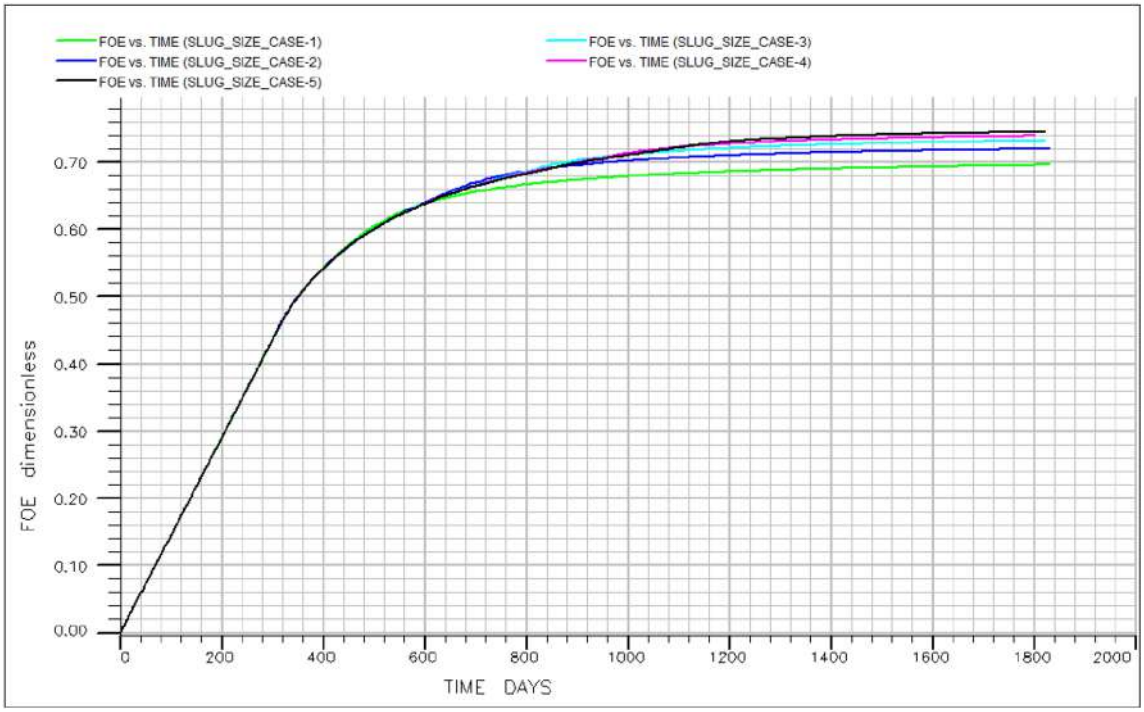

Fig. 12 Assessment of different slug sizes on oil recovery efficiency

Table 5 Oil recovery and volume injected for different slug sizes

Cases	Low salinity water flooding				Recovery efficiency (%)
	Time steps	Time (days)	Injection rate (STB/day)	Injected volume (STB)	
Case 1	5	30	500	72,226	69.57
Case 2	10	30	500	144,435	71.96
Case 3	15	30	500	216,648	73.13
Case 4	20	30	500	288,866	73.88
Case 5	25	30	500	346,643	74.46

(Fig. 13) shows maximum recovery factor for case 2 and minimum for case 1. The maximum recovery could be the reason of low salinity water flooding performance.

Economic analysis

The success of any EOR/IOR project depends on the economic feasibility of the development strategy. The implementation of any enhanced oil project does not need only technical ability, but it must also overcome the economic constraint in the successful execution of the project. Most fundamental principle of finance is time value of money. A dollar earn today is more valuable than the dollar obtained in future because the dollar earn today can be capitalized to earn more than a dollar received in future.

In actual we cannot inject low salinity water continuously throughout the production period of project because it will not be cost effective and can potentially reduce the project's overall profit if incremental oil recovery is not enough to justify the expense [11].

Table 6 Different tables for low salt weighting factor versus salt concentration

Base case			Case 1			Case 2		
Salt concentration (PPM)	F1	F2	Salt concentration (PPM)	F1	F2	Salt concentration (PPM)	F1	F2
0	1.0	1.0	0	1.0	1.0	0	1.0	1.0
1000	0.8	1.0	1000	0.6	1.0	1000	1.0	1.0
4000	0.2	1.0	4000	0.2	1.0	4000	1.0	1.0
5000	0.0	0.0	5000	0.0	0.0	5000	0.0	0.0
35,000	0.0	0.0	35,000	0.0	0.0	35,000	0.0	0.0
50,000	0.0	0.0	50,000	0.0	0.0	50,000	0.0	0.0

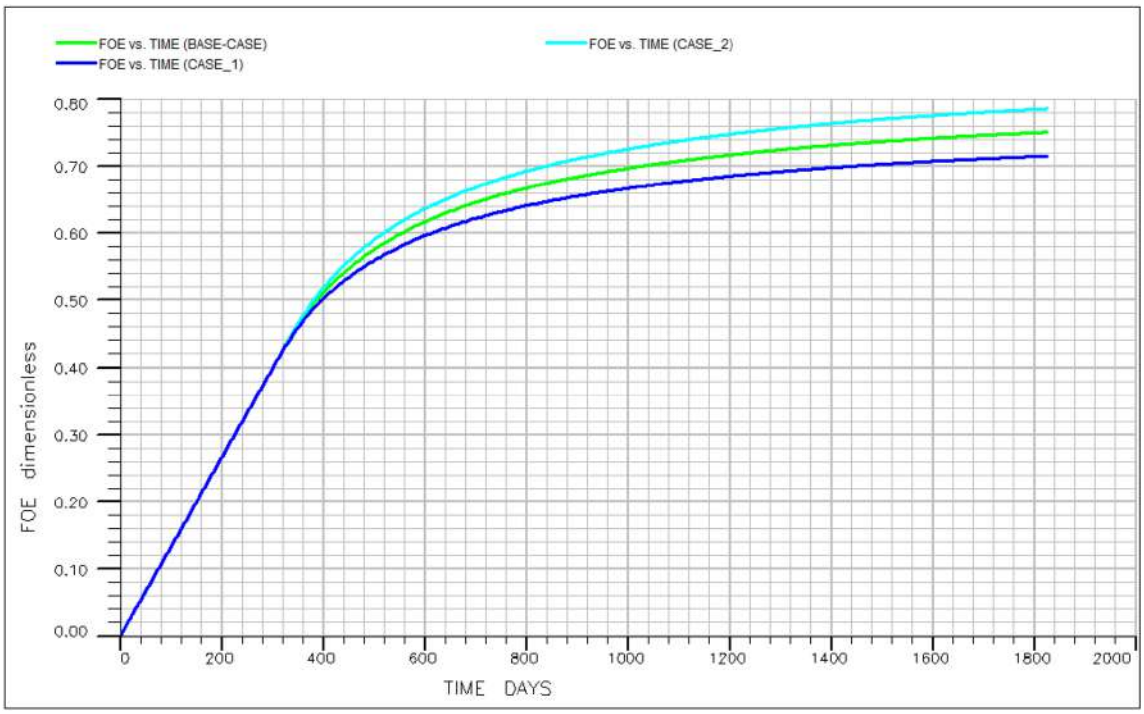

Fig. 13 Oil recovery factor for low salt weighting factor versus salt concentration

The economic feasibility of injecting low salinity water in reservoir development is influenced by following factors [18].

1. Volume of incremental oil recovery
2. Desalination cost of water

The economic parameters are not persistent and can change slightly and sometimes significantly depending on the operating condition and location. Therefore, petroleum economist must carefully consider all the available information and resources to done economic evaluation of any reservoir development project.

The successful application of low salinity water flooding project is characterized by volume of incremental oil over conventional high salinity sea water flooding. To determine the ideal case for LSWF in our project, Net present value criteria is used. NPV is the algebraic sum of all the cash flows occur during the project life cycle after discounting. The selection of a project depends on the positive value of NPV calculated on discount rate. NPV is calculated by using this formula

$$\mathrm{NPV} = \sum_{n=0}^{t} \frac{\mathrm{CF}n}{(1+i)^n} \tag{1}$$

where 't' = project's lifetime, 'n' = time period of investment, 'i' = discount rate and 'CF_n' = cash flow in time(n).

To appraise the cash flows, occur during the production life of the project in each scenario is calculated by using the following expression.

$$CF = \text{Oil Revenue} - \text{Low Salinity Water Injection Cost} \quad (2)$$

Assumptions for economic study

1. Synthetic model is supposed to be producing at residual oil saturation.
2. The properties of the model have no compatibility issues with models PVT and rock properties.
3. Five different LSWF cases were analyzed to evaluate the most economically viable injection scenario.

(1) **Scenario 1:** Low Salinity Water Injection of 1000 PPM for 150 days followed by high salinity water injection of 35,000 PPM for the rest of production life.

(2) **Scenario 2:** Low Salinity Water Injection of 1000 PPM for 300 days followed by high salinity water injection of 35,000 PPM for the rest of production life.

(3) **Scenario 3:** Low Salinity Water Injection of 1000 PPM for 450 days followed by high salinity water injection of 35,000 PPM for the rest of production life.

(4) **Scenario 4:** Low Salinity Water Injection of 1000 PPM for 600 days followed by high salinity water injection of 35,000 PPM for the rest of production life.

(5) **Scenario 5:** Continuous Injection of low Salinity water of 1000 PPM throughout the production life of the reservoir.

4. The price of oil per barrel is assumed to be 100 dollars and discount rate is fixed to 15%.
5. Cost of sea water desalination to obtain fresh water is averaged to be 10 dollars/barrel.
6. High salinity water cost is assumed to be zero, as it is easily available in sea.
7. To simplify the complexity of waterflooding project, only the cost of water desalination is supposed to be the main expense of the project. No operating and any other facility expense are included.
8. Variation of Interest rate, discount factor, oil prices and rising inflation are not considered in this study.

Economic analysis of results

(Fig. 14) depicts the cumulative volumes of oil production and freshwater injection in different injection cases. It is visible from the (Fig. 14) that volume of oil production increases with increased volume freshwater injection. Case 5 gives the maximum oil production of 0.28 MMSTB, while case 1 gives minimum oil production of 0.23 MMSTB, respectively.

Similarly, (Fig. 15) describes the precise net present values of all injection scenarios including all simulation cases and continuous high and low salinity base cases. the

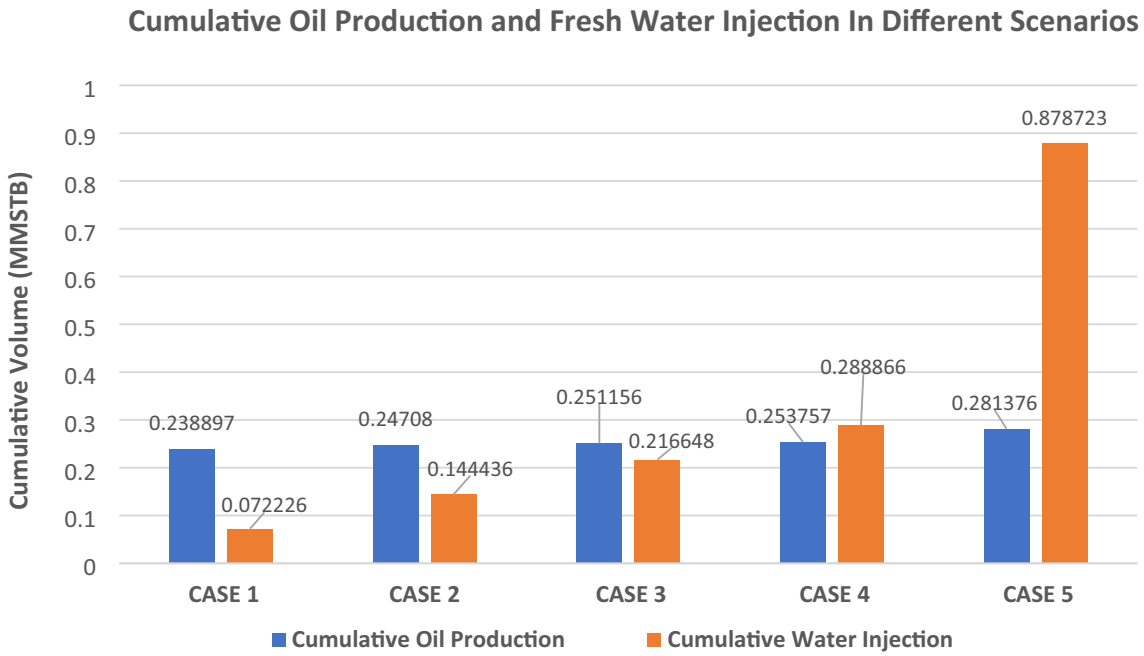

Fig. 14 Cumulative oil production and fresh water injection volumes in different flowing scenarios

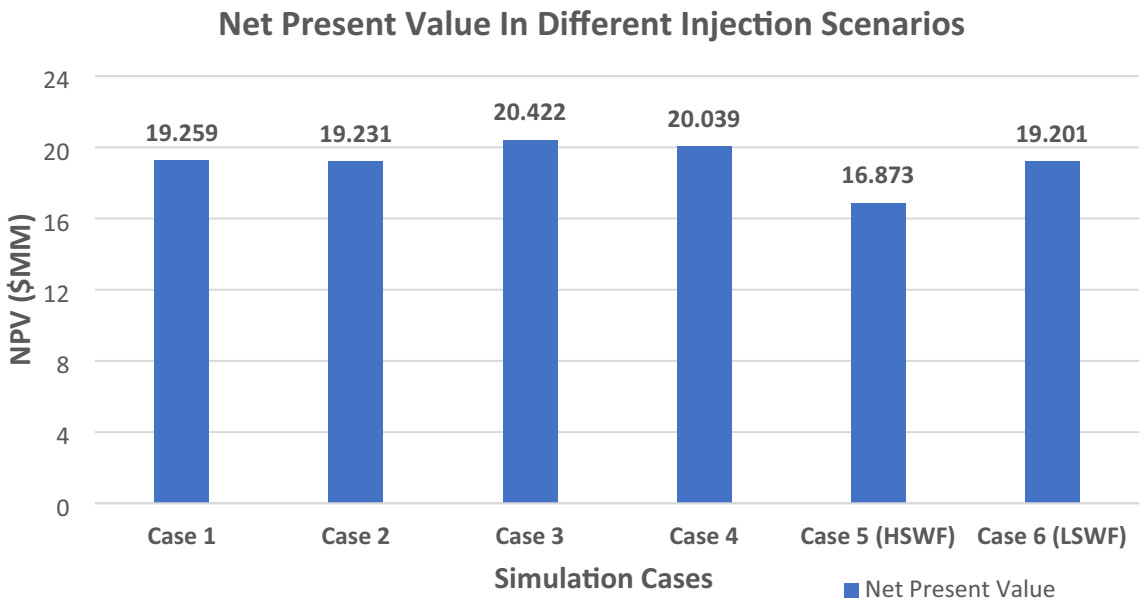

Fig. 15 Comparison among NPV's of different flowing scenarios

NPV increases with volume of low salinity water injection and offers minimum NPV for continuous low salinity water injection and offers maximum value for case 3 which injects LS water for 450 days and HS water for the rest of production life. There is minor difference in NPV between Case 1 and Case 2.

Recommendations for future work

Low salinity water flooding exhibits great potential to enhance oil recovery efficiency from this study and gives positive effect on results. However, the following are few recommendations proposed to address in future work.

1. This study is based on simulation of synthetic model with not much heterogeneities involved therefore, a smooth increase in oil recovery has been observed due to homogeneous nature of reservoir. Real field cases possess more complexity in terms of faults acting as permeability barriers, depositional environment etc. It is recommended for future research to build a model incorporating full field data to evaluate the potential of low salinity water flooding.
2. Evaluation of rock and fluid properties could be conducted in future research, as it is evident from literature review that polarity of oil and clay content can influence the ultimate oil recovery efficiency by low salinity waterflooding.

Conclusion

In view of the simulation outputs of injecting low salinity and high salinity injection cases, following conclusions can be drawn:

1. LSWF is found to be more efficient technique compared to HSWF to enhance the oil recovery by secondary recovery method. Injection of high salinity water results in ultimate recovery efficiency of 60% of pore volume while continuous injection of low salinity water results in incremental oil recovery of 17% provided the equal volume of injection water. Recovery factor for all the simulated cases increases with decrement in injection water salinity and offers similar recovery efficiency for injection water having salinity more than 5000 ppm. In other words, low salinity effects can be visible between 0 and 5000 ppm.
2. The initial flow rate of 500 STB/D in high salinity and low salinity injection case lasts till 242 days and 330 days, respectively, and drops as water breakthrough at perforations. The late onset of water breakthrough in low salinity injection case results in sustained higher oil flow for longer period than high salinity waterflooding case. Similarly, the difference in impact of LSWF and HSWF on average reservoir pressure is very minute.
3. The maximum oil recovery is obtained if reservoir is strongly water wet and minimum recovery if its strongly oil wet. In this case the maximum recovery of 75.96 and 75.19% is obtained by LSWF and HSWF, respectively, with strongly water wet system. The LSWF relative per-

meability curves and feasibility of this method can be evaluated if residual oil saturation is known.

4. Grid refinement is proved to be vital to minimize the numerical dispersion and accurately estimates certain physical system. The difference in recovery factor from high salinity base case and refined case is 2.77% and Low salinity base case and refined case is 5.24%.
5. Slug size of LS water affects the ultimate oil recovery and increases as slug size increases. When the slug size (injected water) is 72,226 bbl, ultimate recovery is 69.57% which increases by 4.89% to 74.46% in case-5 when injected water volume increased to 346,643 bbl.
6. End point saturation describes the application of low or high salinity profile. Case 2 provides the maximum recovery efficiency of 79.2% due to better performance of LS water followed by base case and case-1.
7. Economic analysis of all the cases reveals maximum NPV of case 3 that is 20.422 million dollar and case 5 gives minimum NPV of 16.873 million dollars.

Funding There is no funding attached to this research.

Data availability The data are presented in the manuscript.

Declarations

Conflict of interest Author declares that there is no conflict of interest.

References:

1. Matsuo, Y., Yanagisawa, A., Yamashita, Y.: A global energy outlook to 2035 with strategic considerations for Asia and Middle East energy supply and demand interdependencies. Energ. Strat. Rev. **2**(1), 79–91 (2013)
2. Chandrashegaran P.: Low salinity water injection for EOR. In: SPE Nigeria Annual International Conference and Exhibition (2015)
3. Derkani, M.H., Fletcher, A.J., Abdallah, W., Sauerer, B., Anderson, J., Zhang, Z.J.: Low salinity waterflooding in carbonate reservoirs: review of interfacial mechanisms. Coll. Interfaces **2**(2), 20 (2018)
4. Aladasani A, Bai B, Wu Y.S, Okasha Q.: 3D Simulation of low salinity, polymer, conventional, water-flooding & combination ior methods–heterogeneous and varying wetting conditions. In: SPE/IATMI Asia Pacific Oil and Gas Conference and Exhibition (2015)
5. Muther, T., Qureshi, H.A., Syed, F.I., Aziz, H., Siyal, A., Dahaghi, A.K., Negahban, S.: Unconventional hydrocarbon resources: geological statistics, petrophysical characterization, and field development strategies. J. Petrol. Explor. Prod. Technol. (2021). https://doi.org/10.1007/s13202-021-01404-x
6. Muther, T., Syed, F.I., Dahaghi, A.K., Negahban, S.: Socio-inspired multi-cohort intelligence and teaching-learning-based optimization for hydraulic fracturing parameters design in tight formations. J. Energy Resour. Technol. (2021). https://doi.org/10.1115/1.4052182
7. VODE, P.O.P.O.O.: Performance of nano-filtration and reverse osmosis processes for wastewater treatment. Mater. Tehnol. 51(3) 541–548 (2017)
8. Tang, G.-Q., Morrow, N.R.: Influence of brine composition and fines migration on crude oil/brine/rock interactions and oil recovery. J. Petrol. Sci. Eng. **24**(2–4), 99–111 (1999)
9. Sharma, M.M., Filoco, P.R.: Effect of brine salinity and crude-oil properties on oil recovery and residual saturations. SPE J. **5**(03), 293–300 (2000)
10. Snosy M.F, Abu El Ela M, El-Banbi A, Sayyouh H.: Comprehensive investigation of low salinity waterflooding in carbonate reservoirs. Journal of Petroleum Exploration and Production Technology.1–24 (2021)
11. Mahmood, B.S., Ali, J., Nazhat, S.B., Devlin, D.: A sensitivity study on low salinity waterflooding. Mod. Environ. Sci. Eng **4**, 231–236 (2017)
12. Al-Saedi, H.N., Flori, R.E., Al-Jaberi, S.K.: Eliminate the role of clay in sandstone: EOR low salinity water flooding. J. Petrol. Explor. Prod. Technol. **9**(2), 1475–1483 (2019)
13. LOW J.L.: LOW SALINITY WATER FLOODING SIMULATION STUDY (2013)
14. Omekeh A.V, Friis H.A, Evje S. and Fjelde I.: A model for low salinity flooding experiments: dissolution and ion exchange. Journal of Porous Media 18 (3) (2015)
15. Gbadamosi, A., Patil, S., Shehri, D.A., Kamal, M.S., Shakil Hussain, S.M., Al-Shalabi, E.W., Hassan, A.M.: Recent advances on the application of low salinity waterflooding and chemical enhanced oil recovery. Energy Rep. **8**, 9969–9996 (2022)
16. Hasanov, B.: Application of low salinity water injection to NORNE field E-segment. Norwegian University of Science and Technology, Norwegian. Department of Petroleum Engineering and Applied Geophysics (2010)
17. Khan, M.J., Muther, T., Aziz, H., Mubeen-ur-Rehman, M.: Investigating the impact of injection-water salinity and well strategies on water mobility and oil production in an oil-wet reservoir. Model Earth Syst. Environ. **7**(1), 247–260 (2021). https://doi.org/10.1007/s40808-020-00934-3
18. Althani M.: An evaluation of low salinity waterflooding in carbonates using simulation and economics: colorado school of mines (2014)
19. Afolabi, F., Mahmood, S.M., Yekeen, N., Akbari, S., Sharifigaliuk, H.: Polymeric surfactants for enhanced oil recovery: a review of recent progress. J. Petrol. Sci. Eng. **208**, 109358 (2022)
20. Aziz, H., Muther, T., Khan, M.J., Syed, F.I.: A review on nanofluid water alternating gas (N-WAG): application, preparation, mechanism, and challenges. Arab. J. Geosci. **14**(14), 1416 (2021). https://doi.org/10.1007/s12517-021-07787-9
21. Syed F.I, Dahaghi A.K, Muther T.: Laboratory to field scale assessment for EOR applicability in tight oil reservoirs. Petroleum Science (2022)

International Journal of Energy and Environmental Engineering (2023) 14:687–697
https://doi.org/10.1007/s40095-022-00543-z

ORIGINAL RESEARCH

Conversion of solar irradiance determined by satellite images to electrical energy using photovoltaic technology (a case study of northeastern state (NES) of Nigeria)

Mohammed K. Salihu[1] · **Ali Danladi**[2] · **D. W. Medugu**[2]

Received: 30 June 2022 / Accepted: 18 September 2022 / Published online: 1 October 2022

Abstract

This study determined solar irradiance by satellite images and converted it into electrical power using different type's photovoltaic technology. The process was done using the Aeronautical reconnaissance coverage geographical information system (ArcGIS). The mean annual global solar irradiance were calculated for the entire NES, while ArcGIS weighting overlay was used to determine the suitability area for the conversion. According to the study, Yobe received the higher global solar irradiance with an annual mean value of 2264.69 kWh/m^2/year, followed by Borno 2244.94 Kwh/m^2/year, Bauchi 2208.52 Kwh/m^2/year, Gombe 2167.03 Kwh/m^2/year Adamawa 2154.93 Kwh/m^2/year, while Taraba has the least amount of global solar irradiance of 2017.96 kWh/m^2/year. The suitable areas for Adamawa, Bauchi, Borno, Gombe, Taraba, and Yobe are as follows: 12,042.2, 17,069.1, 39,426.3, and 6755.99 Km^2, 4924.82, and 23,215.5 Km^2, respectively. And the electrical energy determined for different types of photovoltaic technology, i.e., Single-crystalline-silicon, Multi-crystalline-silicon, Amorphous-Silicon and Cadmium-Telluride for Adamawa, 194.3 MW, 179.8, 77.73 MW and 140.7 MW, Bauchi 306.4, 283.4, 122.6 and 222.1 MW Borno1101, 1019, 440.5 and 798.5 MW Gombe, 132.2, 122.3, 52.90 and 95.87 MW, Taraba 19.06, 17.63, 7.623 and 13.83 MW, Yobe 623.0, 576.3, 294.2 and 451.7 MW, respectively. It has been concluded that northeast states are blessed with abundant solar irradiance, which is suitable for installing a photovoltaic station, and single crystalline silicon is the best photovoltaic technology.

Keywords Satellite image · Electrical energy · Solar irradiance · And photovoltaic

Abbreviations

NES	Northeast states
L	Spectral radiance measured over spectral bandwidth of a channel in Wm−2sr^{-1} μm^{-1}
DN	Digital number value recorded,
L_{max}	Radiance measured at detector saturation in Wm−2sr^{-1} μm^{-1},
L_{min}	Lowest radiance measured by detector in Wm−2sr^{-1} μm^{-1},
Ø	Azimuth angle
θ	Polar angle
Ω	Solid angle
sc-Si	Single-crystalline Silicon
mc-Si	Multi-crystalline Silicon
a-Si	Amorphous Silicon
CdTe	Cadmium-Telluride
PV	Photovoltaic
$\overline{G}$ =	The monthly mean global solar radiation on a horizontal surface (kWh/m^2/day),
G_o	The monthly mean extra-terrestrial solar radiation on a horizontal surface (kWh/m^2/day)
$\overline{S}$ =	The monthly mean daily bright sunshine hours (Hours),

✉ Mohammed K. Salihu
mohamedks122@gmail.com

Ali Danladi
alishalangwa@gmail.com

D. W. Medugu
dalemedugu@yahoo.com

[1] Department of Physics, University of Maiduguri,, Maiduguri, Nigeria

[2] Department of Pure and Applied Physic, Adamawa State University, Mubi, Nigeria

S_o	The maximum possible monthly mean daily sunshine hours (Hours), a and b are regression constants depending on on-site location
I_{sc}	Is the solar constant (= 1367 Wm−2),
Ø	The latitude of the site,
δ	The solar declination
ω_s	The mean sunrise hour angle for the given month, and
n	The number of days of the year starting from the first of January.
δ	The solar declination
KWh/m^2/year	Kilo-Watt-hour per meter square per year
E_P	Electric power generation potential per year (kWh/year)
A_R	Annual solar radiation received per unit horizontal area (kWh/m^2/year)
T_A	Calculated total area of suitable land (m2)
A_F	The area factor,
η	PV system efficiency

Introduction

Global solar irradiance measurements are used to study the transformation of energy within the Earth–atmosphere system and its variation in time and space and to analyze the properties and distribution of the atmosphere concerning its constituents [1]. A satellite image is a representation of electromagnetic radiation from the Earth, which rely on either the electromagnetic radiation, reflected, scattered, or absorbed on the surface of the Earth [2]. Satellite images are captured in either panchromatic or multispectral format. A panchromatic idea is one spectral band with a black-and-white resolution that refers to the pixel size of the satellite image [3]. Solar irradiance calculated by satellite images is measured in Watt/meter^2/ster^{-1}/μm^{-1}. Average the energy transfer values in Watt per square meter on the ground, at one steradian (three-dimensional angle from a point on Earth's surface to the sensor), per micro-wavelength [4]. Satellite images cover a large area with high time resolutions, leading to the identification and forecasting of the weather. The information leads to the estimation of solar radiation at the ground level. Comparing solar irradiance determined by satellite data to meteorological ground measurements, satellite images estimated hourly irradiance shown to be the best option for places far away more significant than 25 km from meteorological data station. Thus, estimating data from satellite images can be a good option for forecasting solar radiation on the ground. Related studies were conducted in different parts of the world, using different approaches to determine solar radiation potential and photovoltaic (PV) installations. Below are some of the researches made in various parts of the world.

Aras et al. [5] developed empirical models to predict global solar irradiance. Mekonnen [6] applied physical and empirical models with inputs of various meteorological data to estimate the monthly mean solar irradiance. Poudyal et al. [7] estimated total solar irradiance using cloud transmittance factor. Besharat et al. [8] determined global irradiance as one of the most critical parameters needed in solar applications. Mabuchi et al. [9] determined the global solar irradiance using empirical models. Yisehak [10] analyzed empirical models in calculating solar irradiance. Auwal and Darma [10] & Innocent et al. [11] used the Angstrom-Prescott model to determine global solar irradiance. Rajiv and Singhal [12] predicted global solar radiation using an artificial neural network. Salihu et al. [13] mapped the spectral radiance over Mubi town using satellite images Landsat 7 ETM. Alhassan and Elseddig [14] used sunshine duration-based models to estimate solar radiation. Alkasim et al. [15] used an empirical model to estimate global solar irradiance. Xiao et al. [16] studied the properties of the Photovoltaic (PV) system to optimize the operation of the maximum power point tracker (MPPT). Mills et al. [17] proposed the electricity rate design of PV systems. Hocaoglu et al. [18] studied the temperature effect on the PV module. Zhou et al. [19] studied the strength of PV modules. Parida et al. [20] carried out a significant review of major solar photovoltaic technologies. Khan and Ahmad [21] determined the available solar energy when supplying a small load. Gaurav et al. [22] discussed how solar energy could be converted into electrical energy using PV cells. Vladimır et al. [23] investigated the PV system and its long-term behavior. Asmae and Khalid [24] suggested a way to find the optimum daily operation of a PV system. Maria and Carlos [25] calculated the amount of electric energy in a photovoltaic (PV) system. Nouar et al. [26] estimated the relevance of solar photovoltaic modules for various weather conditions.

Almost all the research reviews cited above used meteorological station data to determine or estimate the amount of global solar irradiance or utilized the amount of solar radiance obtained from meteorological stations to convert to electrical energy using PV technology. Nevertheless, this research determined global solar irradiance by satellite image data and converted to electric power using different PV technologies. Recently, Northeastern Nigerian is facing challenges of energy generation and sustainable utilization. The available energy resources currently relied on in Nigeria are exhaustible and will be depleted because of the increasing demand. Nigerian electric energy sector depends solemnly on hydroelectric and thermal electric generation companies. Electrical energy consumption in Nigeria Territories is the lowest per capita in the northeastern part, and the consumption tariff is higher than

anywhere else in the country. This research will figure out ways of a lasting solution for electrical energy for the entire northeastern state of Nigeria.

This study aims to convert the solar irradiance determined by satellite images to electrical energy using photovoltaic technology and in other to achieve we have to determine the amount of global solar irradiance, estimate the suitability area, and convert the amount Global solar irradiance to electrical power.

Methodology

Research area

This research will focus on the NES of Nigeria, comprising Borno, Adamawa, Bauchi, Yobe, Taraba and the Gombe States. The region lies between Latitude (07°98′69″—12°18′71″) and Longitude (09°84′52″ – 13°17′40″). NES of Nigeria lies within a high sunshine region, and the solar radiation is fairly well distributed. The annual solar radiation varies from 12.6 MJ/m^2/day in coastal latitudes to 25.2 MJ/m^2/day in the far north [10]. Photovoltaic systems provide the energy necessary through the sun's renewable and environmentally friendly source. The zones have been categorized geographically into semi-desert Sahelian savanna in the north and central part and Mandara plateau in the southern region. As agriculturally based zones, the rural areas of the zone economy relied heavily on livestock and crop farming before the Boko haram insurgency. The states' capitals are major trade and service centers that need electrical energy to boost the zone's economy (Fig. 1).

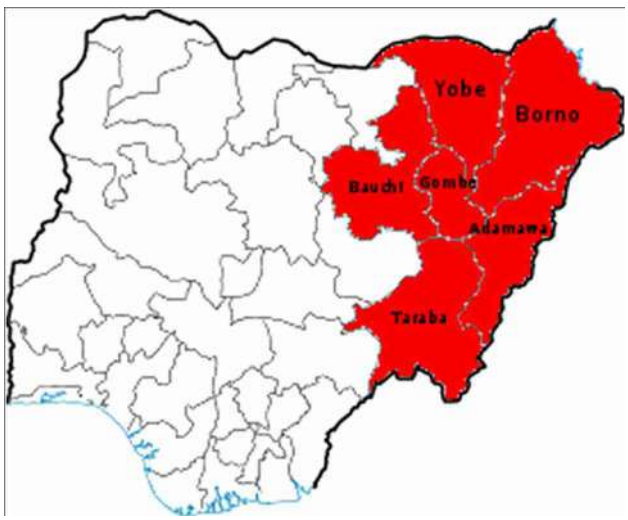

Fig. 1 Map of Nigeria showing the North Eastern States

Data sources

(a) Meteorological data will be collected from each state's meteorological station for 2009–2018.

(b) Satellite imagery data will be downloaded from Solargis global solar model. It has been delivered for the Global Solar Atlas (https://globalsolaratlas.info/) covering the period 2009–2018.

Data processing

Satellite image data processing

Data processing involves converting pixel digital number (DN) to radiance using bias and gain values specified to the individual pixel.

$$L = Gain \times DN + Bias \tag{2.1}$$

where:

L = spectral radiance measured over spectral bandwidth of a channel in $Wm^{-2}sr^{-1}\ \mu m^{-1}$,

DN = digital number value recorded,

Gain = $(L_{max} - L_{min})/255$ = slope of response function,

Bias = L_{min} = intercept of response function,

L_{max} = radiance measured at detector saturation in $Wm^{-2}sr^{-1}\ \mu m^{-1}$,

L_{min} = lowest radiance measured by detector in $Wm^{-2}sr^{-1}\ \mu m^{-1}$,

the equation can also express it as

$$L\lambda = (L_{max} - L_{min})/255\, x\, DN + L_{min} \tag{2.2}$$

L_{max} and L_{min} for the two used bands were obtained from the metadata of the downloaded images, as shown in Table 1.

Global solar irradiance determined by satellite images is measured in Watt/meter^2/ster^1/μm^1. That is, the amount of energy transfer (Watt), per square meter, for one steradian (three-dimensional angles from a point on Earth's surface to the sensor), per micro-meter (wavelength), being needed to convert it into KWh/m^2/year, so we have to do some mathematical expression as shown below:

Imaginary sphere surrounding the point source of radiation.

Table 1 L_{max} and L_{min} values of Landsat data obtained from the image metadata

Band	Satellite/Sensor	L_{max} ($Wm^{-2}sr^{-1}\ \mu m^{-1}$)	L_{min} ($Wm^{-2}sr^{-1}\ \mu m^{-1}$)
6.1	Landsat7/ETM + Low	17.04	00.00
6.2	Landsat7/ETM + High	12.65	03.20

$$\frac{Area\ of\ unit\ sphere\ (\omega)}{Area\ of\ sphere\ A} \tag{2.3}$$

$$steradian(\Omega) = \frac{\omega}{A} = \frac{4\pi.1^2}{4\pi.r^2} \tag{2.4}$$

$$\omega = \frac{A}{r^2}\text{steradian} \tag{2.5}$$

The differential solid angle in spherical coordinate considers a different variation of the direction

$$d\omega = \frac{dA}{r^2} \tag{2.6}$$

a pair of angle $\Omega\ (\varnothing, \theta)$.

$\varnothing$ is an azimuth angle: $0 \leq \varnothing \leq 2\pi$.

θ is polar angle: $0 \leq \theta \leq \pi$

$$dA = (r\sin\theta d\varnothing).(rd\theta) = r^2\sin\theta d\theta d\varnothing \tag{2.7}$$

Differential solid angle

$$d\omega = \frac{dA}{r^2} = \frac{r^2\sin\theta d\varnothing d\theta}{r^2} = \sin\theta d\theta d\varnothing \tag{2.8}$$

Consider a finite solid angle in spherical coordinate

$$\Omega = \iint d\omega = \int_{\theta=0}^{\pi}\int_{\varnothing=0}^{2\pi} \sin\theta d\theta d\varnothing = 4\pi \tag{2.9}$$

Now solid angle steradian $(\Omega) = 4\pi$ steradian.

Meteorological data processing

The suitable correlation for estimating solar radiation was formulated by Angstroms and modified by Prescott. [27] The equation is given as follows:

$$\frac{\overline{G}}{G_o} = a + b\frac{\overline{S}}{S_o} \tag{2.11}$$

$$G_o = \frac{24}{\pi}I_{sc}\left(1 + 0.033\cos\frac{360n}{365}\right)\left((\omega_s\sin\lambda\sin\delta + \cos\lambda\cos\delta\sin\omega s\right) \tag{2.12}$$

$$\delta = 23.45\sin\left(360\frac{284n}{365}\right) \tag{2.13}$$

$$S_0 = \frac{2}{15}\omega_s \tag{2.14}$$

Thus, the *sunrise time* will be

$$\omega_s = 12 - \left[\frac{\cos^{-1}(-\tan\delta\tan\varphi)}{15}\right] \tag{2.15}$$

And the *sunset time* will be

$$\omega_s = 12 + \left[\frac{\cos^{-1}(-\tan\delta\tan\varphi)}{15}\right] \tag{2.16}$$

where

$\overline{G}$ = The monthly mean global solar radiation on a horizontal surface (kWh/m^2/day),

G_o= the monthly mean extra-terrestrial solar radiation on a horizontal surface (kWh/m^2/day).

$\overline{S}$ = The monthly mean daily bright sunshine hours (Hours),

S_o=, the maximum possible monthly mean daily sunshine hours (Hours),

a and b are regression constants depending on on-site location.

I_{sc}= is the solar constant (= 1367 Wm^{-2}),

$\varnothing$= the latitude of the site,

δ = the solar declination,

ω_s= the mean sunrise hour angle for the given month, and.

n = the number of days of the year starting from the first of January.

δ = the solar declination.

Determine the suitable area

ArcGIS Weighted Overlay tool was used to determine the most suitable area to complete the suitability modeling. Cartographic maps will be generated using ArcGIS 10.4.1. Those mapping will reveal the availability of land in the study areas (Table 2).

Conversion of solar radiation acquired to electrical energy

The electric power generation potential per year is based on the average annual solar radiation per unit surface area per day, the total appropriate location, and the efficiency of the PV panel. Equation (2.17) was used to estimate the yearly solar electric power generation potential [28].

$$E_P = A_R.T_A.A_F.\eta \tag{2.17}$$

where,

Table 2 Typical efficiency of solar panels, (source; [29])

Solar cell technology	Efficiency (%)
Single-crystalline Silicon (sc-Si)	20.0
Multi-crystalline Silicon (mc-Si)	18.5
Amorphous Silicon (a-Si)	8.00
Cadmium-Telluride (cdTe)	14.5

E_P = Electric power generation potential per year (kWh/year).

A_R = Annual solar radiation received per unit horizontal area (kWh/m^2/year).

T_A = Calculated total area of suitable land (m^2).

A_F = the area factor indicates what fraction of the calculated areas can be covered by solar panels.

The efficiency (η) of different PV technologies used for this study is shown in Table 2.

Results and discussions

Results obtained from satellite image data

The annual mean global solar irradiance of NES of Nigeria from 2009 to 2018 was calculated using the ArcGIS solar radiation analysis tools, as shown in Fig. 2 and Table 3:

Regarding methodology, we used the global solar irradiation calculation tool in ArcGIS software to calculate the mean annual global solar irradiance maps based on the satellite image. Also, we used meteorological station data to calculate the mean yearly global solar irradiance of the entire NES, while we used Arcgis weighting overlay to determine the suitability area for the conversion.

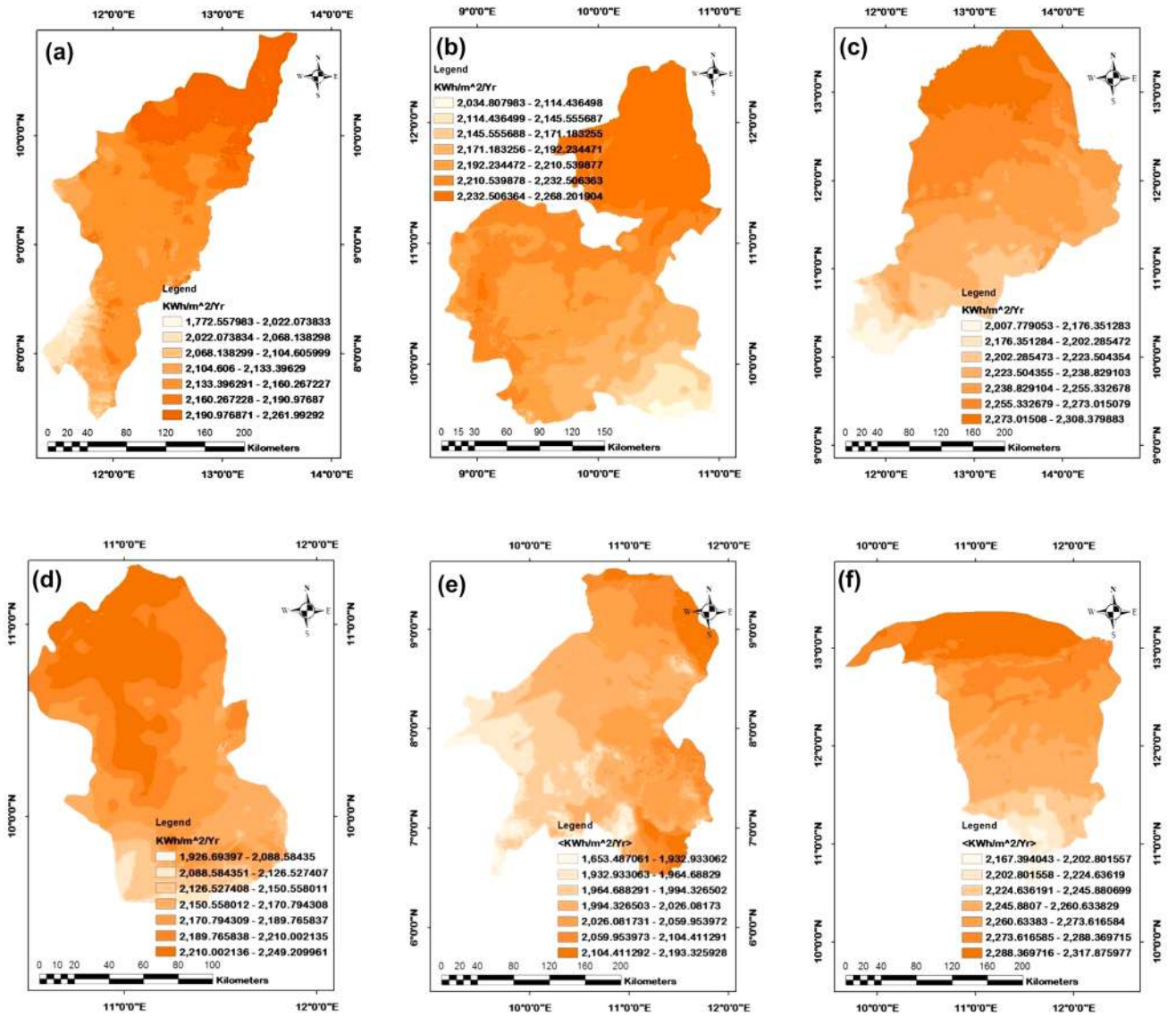

Fig. 2 **a** Global solar irradiance (KWh/m^2/Yr) of Adamawa state **b** Global solar irradiance (KWh/m^2/Yr) of Bauchi State **c** Global solar irradiance (KWh/m^2/Yr) of Borno state **d** Global solar irradiance (KWh/m^2/Yr) of Gombe State **e** Global solar irradiance (KWh/m^2/Yr) of Taraba state **f** Global solar irradiance (KWh/m^2/Yr) of Yobe State

According to this research, the annual mean global solar irradiance obtained from satellite image data for the NES is shown in Fig. 2. In which Yobe received the higher global solar irradiance with an annual mean value of 2264.69 kWh/m^2/year, followed by Borno 2244.94 Kwh/m^2/year, Bauchi 2208.52 Kwh/m^2/year, Gombe 2167.03 Kwh/m^2/year Adamawa 2154.93 Kwh/m^2/year, while Taraba has the least amount of global solar irradiance of 2017.96 kWh/m^2/year which are in ranges with the previous carried by so far by other researchers [11, 13, 15] (Figs. 3 and 4).

The result obtained from meteorological stations data

The annual mean global solar irradiance of NES of Nigeria from 2009 to 2018 was calculated using a suitable correlation for estimating solar radiation, formulated by Angstroms and modified by Prescott. The result is shown in Table 4 and Fig. 9.

Also, for meteorological station data, the annual mean global solar irradiance was calculated using the following parameters, i.e., declination angle, latitude e and sunset hour angle, and regression constants a and b, respectively. The global solar irradiance was calculated using Eq. 2.11, as shown in Table 4 and Fig. 9 [13, 15, 27].

Correlation between satellite image data and meteorological data

The correlated results between the two data are shown in Table 5, Figs. 5 and 6:

A correlation between meteorological and satellite global Solar irradiance values of NES was calculated, and the coefficient of determination R^2 value of 0.985 shows a good

Table 3 Mean annual Global solar irradiance (KWh/m^2/Yr) of NES determined by satellite Images

	Adamawa	Bauchi	Borno	Gombe	Taraba	Yobe
Min	1772.56	2034.81	2007.78	1926.63	1653.49	2167.39
Max	2261.99	2268.21	2308.38	2249.21	2193.33	2317.88
Mean	2154.93	2208.52	2244.94	2187.03	2017.96	2264.69

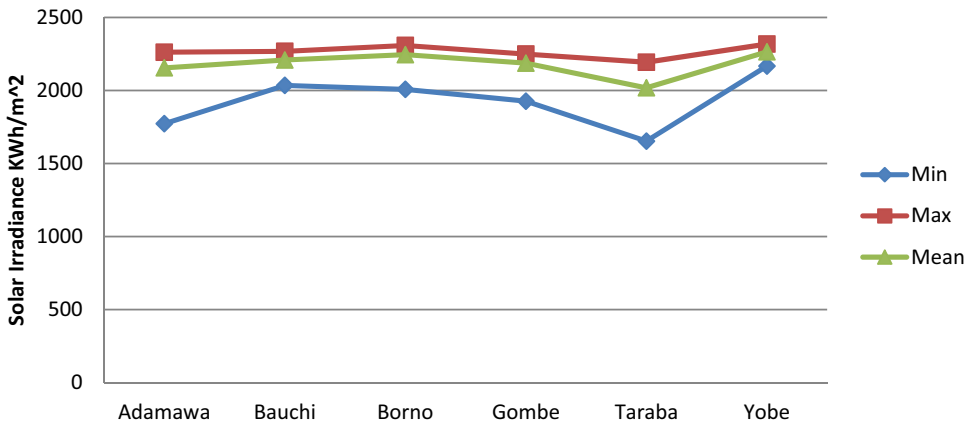

Fig. 3 Graph of mean annual global solar irradiance of NES determined by satellite Image

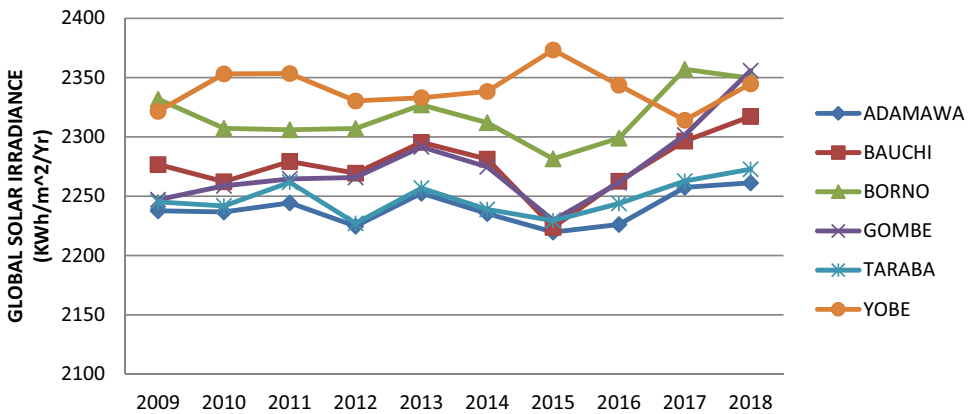

Fig. 4 Graph of mean global yearly solar irradiance (KWh/m^2/Yr) determined by meteorological station data

Table 4 Mean annual solar irradiance (KWh/m^2/Yr) determined by meteorological data

	2009	2010	2011	2012	2013	2014	2015	2016	2017	2018
Adamawa	2237.7	2236.7	2244.4	2224.8	2252.5	2235.4	2219.8	2226.2	2257.5	2261.3
Bauchi	2276.7	2262.3	2279.4	2269.5	2295.4	2281.3	2223.7	2262.7	2296.5	2317.3
Borno	2331.8	2307.3	2306.1	2307.2	2327.0	2312.0	2281.6	2299.0	2357.1	2349.5
Gombe	2247.1	2258.8	2264.7	2265.8	2291.6	2274.7	2229.8	2261.5	2301.6	2355.9
Taraba	2245.2	2241.8	2261.8	2227.2	2256.9	2238.9	2229.4	2243.9	2262.8	2272.8
Yobe	2321.6	2353.2	2353.5	2330.4	2333.1	2338.4	2373.4	2343.6	2314.2	2344.7

Table 5 Mean annual global solar irradiance (KWh/m^2/Yr) determined by both meteorological and satellite data

	Meteorological solar irradiance	Satellite solar irradiance
Adamawa	2239.62	2154.93
Bauchi	2276.48	2208.52
Borno	2317.85	2244.94
Gombe	2275.14	2187.03
Taraba	2148.07	2017.96
Yobe	2340.59	2264.69

correlation between meteorological and satellite determined values [11, 27].

The result obtained in the determined suitability area

These showed the suitability area determined for the calculation of potential electrical energy in Fig. 2.

We used the ArcGIS Weighted Overlay tool to determine the most suitable area to complete the suitability modeling. Slope, aspect, global solar irradiance, distance from roads, and grid network were used as input raster.

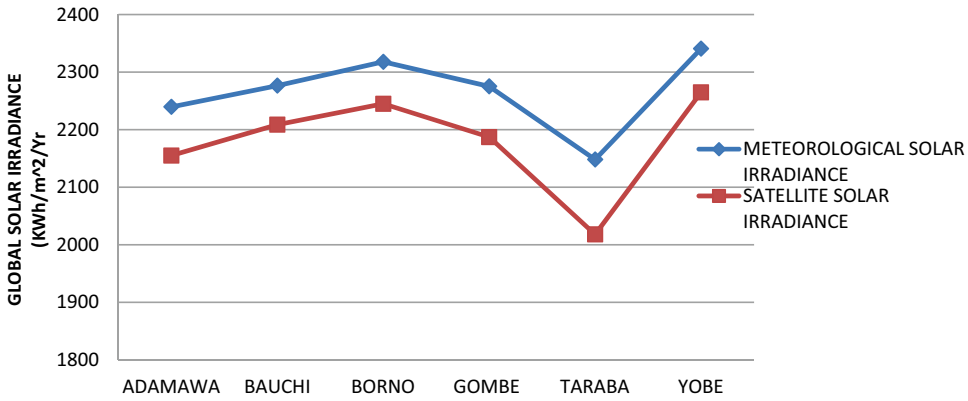

Fig. 5 A graph of mean annual global solar irradiance (KWh/m^2/Yr) determined by both meteorological and satellite data

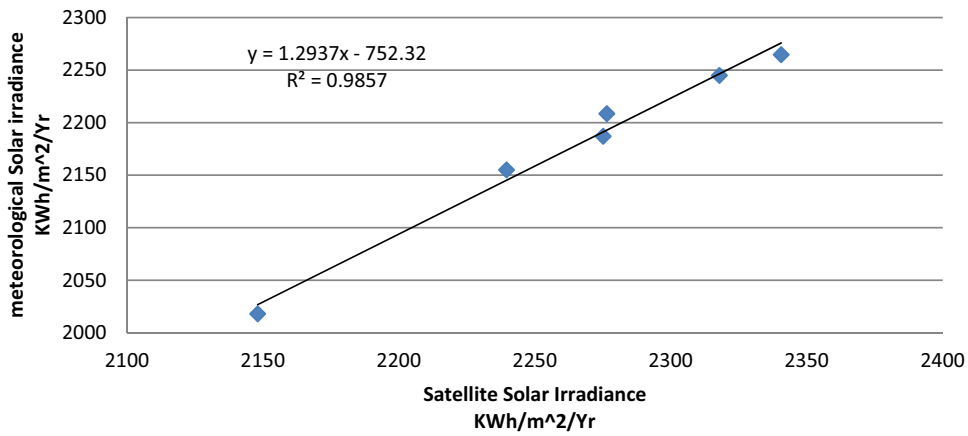

Fig. 6 A correlation graph between meteorological and satellite determined global solar irradiance

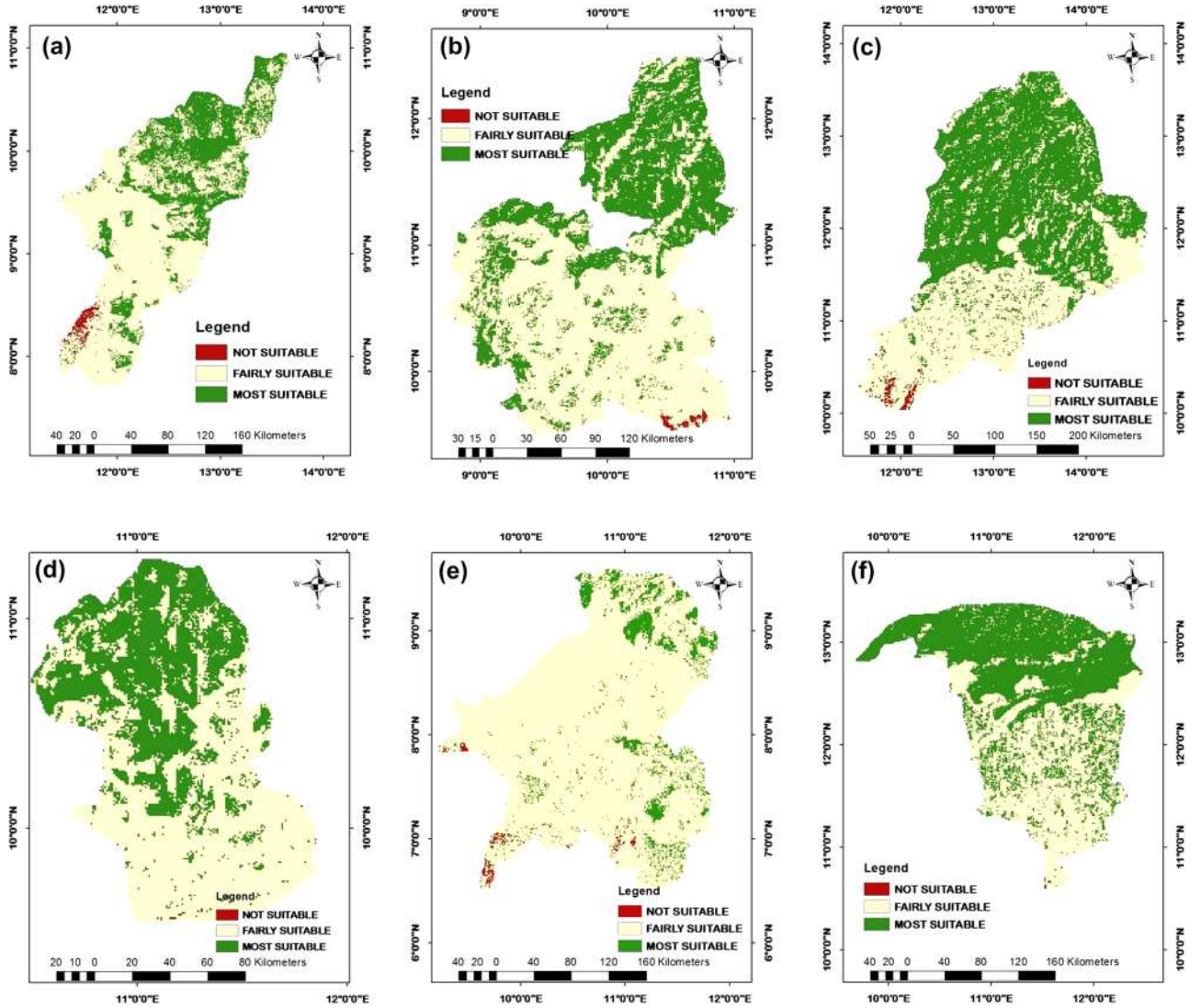

Fig. 7 **a** shows a map of a determined suitable site in Adamawa state **b** shows a map of a relevant committed area in Bauchi state **c** shows a map of a determined right place in Borno state **d** shows a map of the suitable bound site for the Gombe state **e** shows a map of a committed suitable site in Taraba state **f** shows a map of a right-bound site in Yobe state

Table 6 The summary of the determined suitability area of NES

	Adamawa	Bauchi	Borno	Gombe	Taraba	Yobe
Not suitable	509.69	215.45	537.08	15.16	617.84	23.69
Fairly suitable	24,174	30,662.2	32,395.2	10,483.1	53,260.5	21,475.3
Most suitable	12,042.2	17,069.1	39,426.3	6755.99	4924.82	23,215.5

Slopes were expressed in percentages. Percentage of Slope is calculated using the ArcGIS; the most suitable solar station area is located on flat ground. The flatter the site, the more critical the region will be. The Slope must be less than 3% for a suitable solar station area.

We used ArcGIS spatial analyst's aspect tool to calculate the aspect in nine different directions that the slopes were facing North N, Northeast NE, Northwest NW, East E, Southeast SE, South S, Southwest SW, West W, and flat

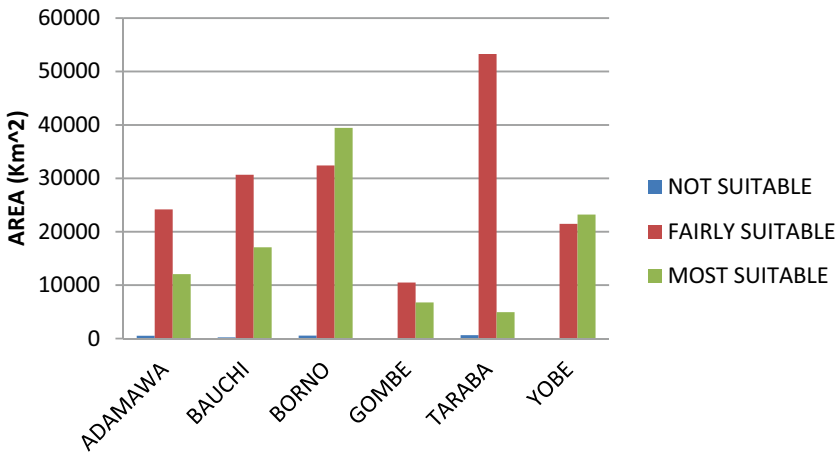

Fig. 8 A Graph of determining relevant areas

Table 7 Summary of electric power generated (MW) of NES with different solar cell technology

Cells	Adamawa	Bauchi	Borno	Gombe	Taraba	Yobe
Sc-Si	194.3	306.4	1101	132.2	19.06	623.0
Mc-Si	179.8	283.4	1019	122.3	17.63	576.3
a-Si	77.73	122.6	440.5	52.9	7.623	294.2
CdTe	140.9	222.1	798.5	95.87	13.82	451.7

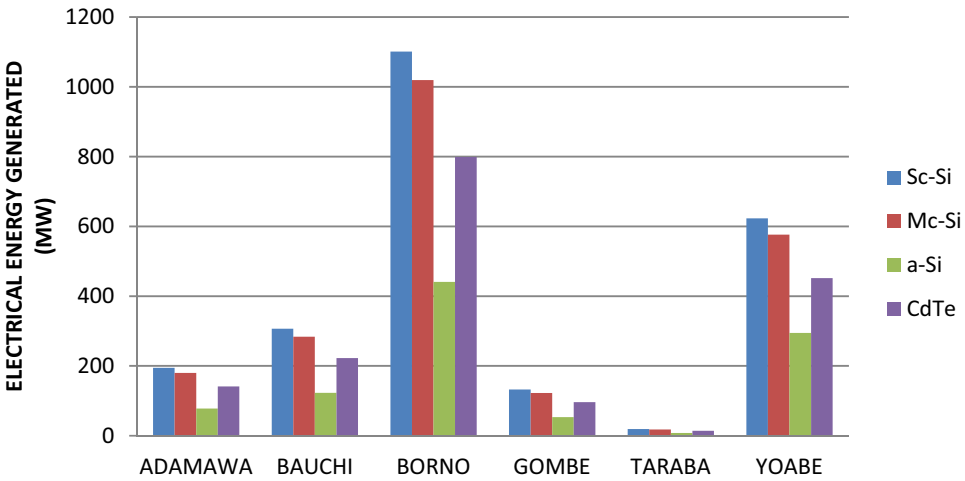

Fig. 9 A graph of relentless electric energy (MW) of different solar cell technology

areas, the flat area and south facing slopes, i.e., SE and SW mark the best and most suitable.

Due to our Nigerian factors, the road and grid network always goes hand to hand and was created a distance raster from the street's shape file. It was done using the Euclidean Distance function tools in ArcGIS and selected less than 1 km as the most suitable.

In high temperatures, modules with insufficient voltage may be unable to charge a lead acid battery fully. While the output current from a PV Module is directly related to the amount of sunlight striking the surface, the output voltage is reasonably consistent under most sunlight conditions. The voltage is, however, affected by temperature. The suitable temperature conditions for crystalline PV installation are Standard Test Conditions (STC) irradiance of 1000 W/m^2 cell temperature of 25 °C.

The input criteria were reclassified into a standard preference scale indicated as unsuitable, reasonably suitable, and most appropriate. The more favorable the criteria range, the higher the value. The standards were weighted according to their importance. Global solar irradiance is the essential criterion weighted at 45%. Topographical Slope was 25%, topographical aspect 15%, nearest to the road and grid network 10%, and temperature 5%, respectively. The constraints layers slope, aspect, distance from roads and grid network, temperature, and annual

mean global solar irradiance were multiplied together and produced the final constraints layer for the entire NES as shown in Fig. 7, Table 6 and Fig. 8, respectively, while the suitable area obtained for Adamawa, Bauchi, Borno, Gombe, Taraba, and Yobe are; 12,042.2, 17,069.1, 39,426.3, and 6755.99, 4924.82, and 23,215.5 Km.^{2}, respectively [28]

The result obtained in conversion of global solar irradiance into electrical energy

The potential electrical energy (MW) determined is shown in Table 7 and Fig. 9.

The potential electric energy was calculated using PV efficiency, as shown in Table 2 for four different PV technologies. Annual potential electric energy generation from a suitable area was computed using Eq. (2.7), as shown in Table 7 and Fig. 9. Furthermore, the electrical energy is determined for different types of photovoltaic technology, which shows that Single-crystalline-silicon (Sc-Si) is the best PV technology, followed by Multi-crystalline-silicon (Mc-Si), Amorphous-Silicon (a-Si) and Cadmium-Telluride (CdTe) due to their efficiencies as shown in Fig. 9, Tables 7 and 2, respectively.

Conclusions

The northeast zone of Nigeria is blessed with abundant global solar irradiance. It is revealed that the Sahel/desert area such *as* Yobe received the higher global solar irradiance, followed by Borno, Bauchi, Gombe, and Adamawa, while Taraba has the least amount of global solar irradiance as shown in Fig. 2. It has been observed that most suitability areas are connected to higher global solar irradiance values. The suitable areas for Adamawa, Bauchi, Borno, Gombe, Taraba, and Yobe are shown in Fig. 2. An increase in global solar irradiance is found to have relied on topographical factors which are critical in the conversion of solar irradiance to electrical energy, and different types of photovoltaic technology determine the electrical energy, i.e., Sc-Si, Mc-Si, a-Si and CdTe as shown in and Figs. 6 and 9. Moreover, it has been observed that Sc-Si is the best PV technology, followed by Mc-Si, a-Si, and CdTe least based on their efficiencies [30].

The study is limited to conversion of solar irradiance determined by satellite images to electrical energy using photovoltaic technology in the northeastern state of Nigeria. It is recommended for other research on quantitatively electrical energy consumption of each state in the northeastern zone of Nigeria and to be compared with the one given by the national grid and that determined by solar irradiance for the lasting solution to power shortage in the zone.

References

1. Petty, G.W.: The first course in atmospheric radiation. Sun dog, Madison, Wisconsin (2006)
2. Lillesand, T.M., Chipman, J.W., Kiefer, R.W.: Remote sensing and image interpretation. Wiley, Hoboken (2008)
3. Clifford, N., French, S., Valentine, G.: Critical methods in geography. SAGE, Thousand oaks (2010)
4. Oesch, E.D.: validating satellite observed thermal emission with in-situ measurements over an urban surface. Remote Sens. Environ. **104**, 201–210 (2006)
5. Aras, H., Balli, O., Hepbasli, A.: Global solar potential part 1: model development. Energy Sour. Part B **1**(3), 303–315 (2006)
6. Mekonnen, S.A.: Solar energy assessment in Ethiopia: modelling and measurement. Addis Ababa University (2007)
7. Poudyal K. N. Bhattarai B. K. Sapkota B. & Kjeldstad B. (2012) Estimating global solar radiation using sunshine duration in Himalaya region research. J. Chem. Sci. **2**(11):20–25, ISSN 2231–606 Noyes. J. Chem. Sci.www.isca.in
8. Besharat, F., Dehghan, A.A., Faghih, A.R.: Empirical models for estimating global solar radiation: a review and case study. Renew. Sustain. Energy Rev. **21**, 798–821 (2013)
9. Nnabuchi, M.N, Ekpe, J.E. & Ibeh, G.F.: Estimation of global solar radiation in Onitsha and Calabar using empirical models. Commun. Appl. Sci. **1**(1):25–37 (2013) ISSN 2201–7372
10. Yisehak, A.: Comparison of different empirical models in the estimation of mean global solar radiation using Sunshine durations measured at dire Dawa, Ethiopia a project submitted to the Department of physics, college of Natural and Computational Sciences, School of Graduate Studies Haramaya University (2014)
11. Auwal, M. & Darma, T.H. Estimation of global solar radiation for Kano state Nigeria based on meteorological data IOSR J. Appl. Phys. (IOSR-JAP) e-ISSN: 2278–4861.**6**(6):19–23 www.iosrjournals.org
12. Innocentk, A.J, Jacob, O.E, Chibuzo, G.C., James I. Odeh, D.O.: Estimating global solar radiation in Gusau, Nigeria. Int. J. Res. Eng. Technol. (IMPACT: IJRET) 3(2):27–32 (2015) ISSN(E):2321–8843;ISSN(P): 2347–4599
13. Salah, A., Saleh, H.: Impact of urban expansion on surface temperature in Baghdad, Iraq using remote sensing and GIS technique Department of Physics, College of Science Al-Nahrain University. J. Al-Nahrain Univ. **13**(1), 48–59 (2010)
14. Salihu, M. K. Bello Y. I. & Japari A.: Mapping the spatial distribution of spectral radiance over Mubi town using satellite images landsat 7 Etm+ Research journal's J. Geogr. **3**(3):1–7 (2016) ISSN 2349–5367
15. Alhassan A.T., Ali E.J.: Sunshine duration-based models for predicting global solar radiation. UKSim-AMSS 19th International Conference on Modelling & Simulation (2017)
16. Alkasim, A., Dikko, A.B. & Eyube, E.S.: An empirical model for the estimation of global and diffuse solar radiation over yola, northeastern Nigeria based on air Temperature IJRDO-J. Appl. Sci. **3**(9):14–24 (2017) ISSN: 2455–6653
17. Xiao, W., Ozog, N., Dunford, W.G.: Topology study of photovoltaic interface for maximum power point tracking. IEEE Trans. Ind. Electron **54**(3), 1696–1704 (2007)

18. Mills, A., Wiser, R., Barbose, G., Golove, W.: The impact of retail rate structures on the economics of commercial photovoltaic systems in California. Energy Policy **36**(9), 3266–3277 (2009)
19. Hocaoglu, F.O., Gerek, O.N., Kurban, M.: The effect of model generated solar radiation data usage in hybrid (Wind–PV) sizing studies. Energy Convers. Manag. **50**, 2956–2963 (2009)
20. Zhou, W., Lou, C., Lu, L., Yang, H.: Current status of research on optimum sizing of stand-alone hybrid solar-wind power generation systems. Appl. Energy **87**(2), 380–389 (2010)
21. Parida, B., Iniyan, S., Goic, R.: A review of solar photovoltaic technologies. Renew. Sustain. Energy Rev. **15**, 1625–1636 (2011)
22. Khan, M.M., Ahmad, M.J.: Estimating global solar radiation using clear sky radiation in Yemen. J. Eng. Sci. Technol. Rev. **5**(2), 12–19 (2012)
23. Gaurav, T., Mohd, I. Raj K.S.: Generation and transmission of electrical power through solar power satellite (SPS) Int. J. Modern Eng. Res. (IJMER) **3**(1): 595–598 (2013) ISSN: 2249–6645 www.ijmer.com
24. Saly, V., Vary, M., Packa, J., Firicky, E., Perny, M., Kubica, J.: Performance and testing of a small roof photovoltaic system. J. Electric. Eng. **65**(7s), 15–19 (2014)
25. Berrada, A., Loudiyi, K.: Optimal modeling of energy storage system. Int. J. Model. Optim. **5**(1), 71–77 (2015)
26. Sampedro, M.S.R.G., Gonzalez, C.S.: Spanish photovoltaic learning curve. Int. J. Low-Carbon Technol. **11**, 177–183 (2016)
27. Aoun, N., Bouchouicha, K., Chenni, R.: Performance evaluation: A mono-crystalline photovoltaic module under different weather and sky conditions. Int. J. Renew. Energy Res. **7**(1), 292–297 (2017)
28. Medugu, D.W., Yakubu, D.: Using angstrom model to estimate mean monthly global solar radiation in Yola (Nigeria). Adv. Appl. Sci. Res. **2**(2), 414–421 (2011)
29. Gastli, A., Charabi, Y.: Solar electricity prospects in Oman using GIS-based solar radiation maps. Renew. Sustain. Energy Rev. **14**(2), 790–797 (2011)
30. National Renewable Energy Laboratory of the USA. https://www.nrel.gov. Accessed 20 June 2021
31. Rahimikhoob, A.: Estimating global solar radiation using artificial neural network and air temperature data in a semi-arid environment. Renew. Energy **35**(9), 2131–2135 (2010). https://doi.org/10.1016/j.renene.2010.01.029

International Journal of Energy and Environmental Engineering (2023) 14:777–789
https://doi.org/10.1007/s40095-022-00548-8

ORIGINAL RESEARCH

Optimization of hybrid grid-tie wind solar power system for large-scale energy supply in Cameroon

Kitmo[1] · Guy Bertrand Tchaya[1] · Noël Djongyang[1] · on behalf of all the authors

Received: 17 June 2022 / Accepted: 21 October 2022 / Published online: 15 November 2022

Abstract

In several countries around the world, the transition from fossil fuels to renewable energies is considered an inevitable trend for the reduction of greenhouse gas emissions and the protection of the environment. It also helps to minimize dependence on fossil fuels which are exhausted over time. In Cameroon, the use of renewable energies appears as an alternative for commercial companies which depend enormously on the public sector which is the only supplier of electricity thanks to hydroelectric dams. Installing solar power systems and wind power systems can help businesses and industrial facilities directly use electricity generated from clean energy sources. Moreover, the need to reduce electricity costs and to move toward solutions that improve the environment from being polluted is felt. In this article, the results of an optimization study for a cement plant in Garoua Province, Cameroon, show that the hybrid wind and solar grid-tied energy systems in Scenario 1 are considered more efficient; on the environmental, economic and technical level than the solar energy systems connected to the electrical grid in scenario 2. The robustness and feasibility of this system thanks to the Homer Pro software and the optimization by particle swarm shows a reduction in the cost of the installation as well as a contribution to the protection of the environment. The optimal configuration of the hybrid power system connected to the grid includes wind energy with a capacity of 300 kW and solar energy with a capacity of 1500 kW, this system has a net present cost (NPC) of 5,596,978 USD, the cost of energy (COE) of 0.0847 USD/kWh, the investment cost of 1,140,000 USD and the operating cost of 384,877 USD.

Keywords Renewable energy · Cameroon · Homer · Optimization · COE

List of symbols

HOMER	Hybrid optimization of multiple energy resources
NPC	Net present cost
COE	Cost of energy
PVs	Photovoltaic source
NPVG	Number of photovoltaic panels
WTs	Wind turbine source
PPV	Photovoltaic real power
PWT	Wind turbine
CESS	Energy system of storage cost
Copt	Cost of operation
Ccap	Capital cost
ESS	Energy system of storage cost
PSO	Particles swarm optimization
PV	Photovoltaic
STC	Standard temperature condition

✉ Guy Bertrand Tchaya
tchayaguiy@gmail.com

Kitmo
Kitmobahn@gmail.com

[1] Department of Renewable Energy, National Advanced School of Engineering of Maroua, Maroua, Cameroon

Introduction

The policy of developing renewable energy sources is considered an unavoidable trend in the world today [1, 2] because of its significant contribution to limiting greenhouse gas emissions, protecting environment and reducing dependence on fossil fuels which are exhausted over time[3]. In recent years, renewable electricity has experienced considerable global growth, especially solar and wind energy. Solar energy reached a total installed capacity of 760 GWp. On the other hand, the global wind power market grew to 93 GW in 2020 and brought the total installed capacity of global wind power to 743 GW. The investment cost of solar and wind energy projects has continued to decline [4, 5] due to technological innovation, changes in market efficiency by intelligent systems or e-commerce, new policies and

benchmark business models. Nowadays, clean and green energy is increasingly used as part of the urgent need for energy transition [3].

Many companies and industrial parks around the world have improved the use of renewable energy [6] and the roadmap to 100% clean energy with detailed actions that respect commercial conventions. The RE100 initiative [7] has spread throughout Europe, the Americas, Africa, and Asia–Pacific since its launch in 2014. The research results of Emanuele Taibi et al. [8] have identified the application potential of renewable energy for industrial applications and proposed the development of a detailed technology roadmap to further explore this potential. The International Energy Agency (IEA) [9] has estimated that the lower investment costs of wind and solar energy will open the possibility of applying and reducing greenhouse gas emissions in the industrial sector.

Recently, the United Nations Industrial Development Organization (UNIDO) [9] explored the possibility of developing clean energy through Industrial Revolution 4.0. According to research by Meng, Y et al. [10], renewable electricity was considered as one of the solutions to improve energy efficiency and sustainability in smart manufacturing factories. Charles Rajesh Kumar. J conducted an extensive literature survey on the energy consumption of the Indian manufacturing sector and the importance of sustainable energy for the industrial sector [11]. The results of this study also showed that renewable energies were the only option for the sustainable development of the industrial production sector. In Cameroon, grid-connected solar projects (GCSP) have been developed in recent years and are considered a useful solution to help ensure energy security and combat climate change [12].

The government of Cameroon has published mechanisms and policies [13] to develop the solar energy source while the wind energy source (WES) still lags behind [14]. However, policies supporting solar power, including rooftop solar and wind power, have been questioned and they are awaiting new policy mechanisms by the government during the next years. Because, the standards of connection to the electrical networks require a revolution as there is evolution in the design of the components of the power electronics (DCPE) [15].

The increasing production of electricity in rural areas of industrial sites is necessary to meet the electricity demand of companies [16], because the development of manufacturing plants is very strong and fast, there are, for example, industrial parks and processing areas. This scenario not only exerts pressure on the electricity companies which are few in Cameroon, but can also directly affect the activities of investors. If there is a power outage [17] in the factory due to lack of electricity, business and production activities will come to a near standstill, and the damage will not only affect the economy but also on the reputation of the company [18, 19] or of the electricity supplier. Therefore, businesses in Cameroon can actively create isolated on-site power sources using solar power, wind power systems to reduce the cost of purchasing electricity from the utility grid, and can even get more profit by selling the excess solar energy to the distribution grid [20], so it will reduce the burden of electricity shortage, help to ensure the energy security of the factory and the Garoua region especially where it exists significant deposits in solar and wind. It is also a profit for the activities of companies which can operate autonomously [21].

Many studies select renewable electricity technologies for the industrial sector around the world. M. Hasan et al. [19] worked on the optimization of renewable energy systems for the industrial sector using HOMER software. Mixed integer linear programming has been used by Scheubel et al. [22] to optimize the power and heat supply system to minimize annual costs and implement energy system optimization for several companies in the German industrial sector. Schulz, J et al. [23] investigated on-site renewable energy generation plants and optimization, methods for simulating hybrid power systems in manufacturing plants to reduce their reliance on the national power grid. The results also showed that some simulation software such as TRNSYS, orbs, Balmorel, DER-CAM, HOMER Pro, MARKAL & TIMES, Energy Plan, Top Energy, can allow optimization of complex systems, but Homer Pro is widely used in analysis of renewable energy systems.

In this article, the results of the research on the optimal configuration and environmental, economic and technical efficiency of the plant of the cement manufacturing plant, CIMENCAM in the province of Garoua, Cameroon, are calculated using the Homer Pro software and the analysis of the robustness and feasibility of this method are made using advanced algorithms, such as particle swarm optimization (PSO) [24].

The locality of Garoua in northern Cameroon was chosen for several reasons: There are significant deposits of photovoltaic solar energy and wind energy in this area. The region of Garoua has factories with large capacities in demand for electrical energy [24], there are for example the CIMENCAM factories, the Brasseries du Cameroun. Then, the northern region of Cameroon is only supplied by a single source of electricity, which is the Lagdo dam, located in the Garoua region. Finally, there is too much load shedding in this area of the North interconnected network (NIN), which needs to be reinforced. Using a solar power system combined with wind power can reduce factory electricity costs and help create products that meet green standards and increase competitiveness in the Cameroonian market. The results of the study will help determine the importance of renewable energy technologies for industrial facilities in general and unfired brick factories in particular in

Cameroon. In addition, the Cameroonian government aims to develop a decentralized production policy [25] with a view to autonomy in green and intelligent zones (ZVI).

Literature review

Renewable energies have attracted several countries in recent years because of their non-polluting nature [26]. A considerable research is done for their development and implementation. Some studies [27] are done on the components needed for the exploitation of renewable resources and others are done on the materials used for the production of renewable energy. However, it is important to know the design techniques of these renewable sources in order to reduce the costs of production, transmission and distribution [28]. In the world in general and in Africa in particular, a lot of research is done to evaluate the potential of these inexhaustible natural resources [29]. In this work, a study is made on the feasibility and the rentability of the methods of fusion of these various sources. A specification is made to estimate the performance of a photovoltaic installation integrated to the building in a scenario 2 and an installation made of a hybrid photovoltaic and wind source connected to the electrical grid [30]. Cameroon is one of the countries that have realized the need to migrate to renewable energy. Thus, [31] has worked on the wind resource in the three regions of Northern Cameroon, while [32] has studied the feasibility of a purely renewable energy transition in the region of Bafoussam as well [33], which proves that the Great North of Cameroon is full of important wind and photovoltaic energy deposits compared to the region of Southern Cameroon. [34] presents the optimization of a grid-connected photovoltaic system and a hybrid wind-photovoltaic system for grid integration. The work of [35] and [36] show that the region of Garoua has an important photovoltaic energy deposit with an average sunshine that varies between 900 and 950 W/m^2. In the same way, [37] shows that the Garoua region has a significant potential for wind energy with a wind speed that varies around 6 m/s during the months of August and October. The Cameroonian government decided to improve the Northern Interconnected Network (NINL) line, which is experiencing numerous load shedding problems due to the failure of the Lagdo dam. The Lagdo dam is located in the Garoua region, which also has major manufacturing and processing factories for raw materials. The availability of photovoltaic and wind resources is an advantage for factories and companies to operate autonomously, as they would use decentralized production. In this work, it is shown that the hybridization of photovoltaic/wind sources with an energy storage system and a photovoltaic/thermal power plant combined with an energy storage system would be a guarantee for the continuity of the service with a capacity of 150 MW [38], but unfortunately the cost of the installation is not taken into consideration in the evaluation of the performance. In this work, it is shown that the hybridization of a photovoltaic plant and a wind power plant connected to the grid has a better performance with an economic cost.

Methodology

In this study, the grid-tied hybrid wind and solar power system in a cement manufacturing plant was economically and technically analyzed using Hybrid Optimization of Multiple Energy Resources (HOMER) software [39]. This microgrid system simulation program is created and developed by the US National Renewable Energy Laboratory to optimize microgrid systems and facilitate comparison of power sources in hybrid mode. The HOMER program simulates a variety of system configurations, eliminates unfeasible configurations, organizes viable configurations according to total net present cost (NPC) in the optimization process, and the feasible configuration with the lowest NPC is the configuration of the most optimal hybrid power system according to the available resources [40].

This study will simulate two scenarios using the renewable energy systems of the cement manufacturing plant to assess the environmental, economic and technical effectiveness of different scenarios, so that the most feasible scenario can be evaluated and considered. The two grid-connected renewable energy scenarios are used as follows:

Scenario 1: Using the grid-tied hybrid wind and solar power system.

Scenario 2: Using only the grid-tied rooftop solar power system similar to other industrial plants applying rooftop solar power in Cameroon.

The optimization of renewable power systems at the non-fired brick factory according to two scenarios is illustrated as can be seen in Fig. 1.

Site selection

The location of the cement manufacturing plant in the case study is selected in Garoua province as can be seen in Fig. 2. The solar power potential and wind power potential are determined with the help of the National Aeronautics and Space Administration (NASA) which provides the databases in the HOMER Pro program. From these data, the average global solar radiation in the Garoua area is about 4.55 kWh/m^2/day, as shown in Fig. 3. The highest global solar radiation value is about 5 0.4 kWh/m^2/day, while December has the lowest overall solar radiation value of around 3.4 kWh/m^2/day. The average value of the clarity index is around 0.45.

On the other hand, the wind energy in this location is quite good because it is near the sea with an average

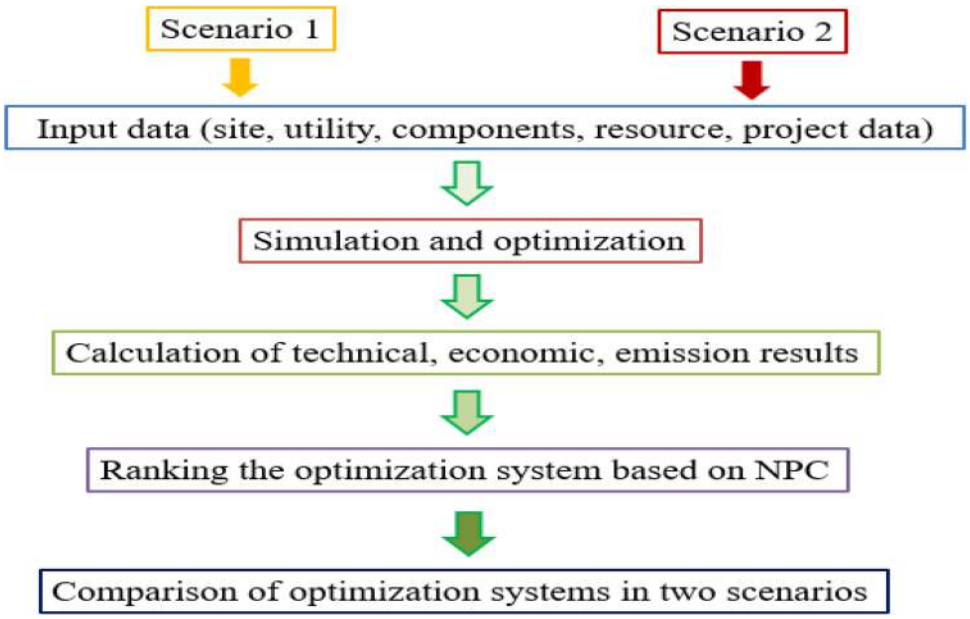

Fig. 1 Optimized calculation framework for renewable power systems

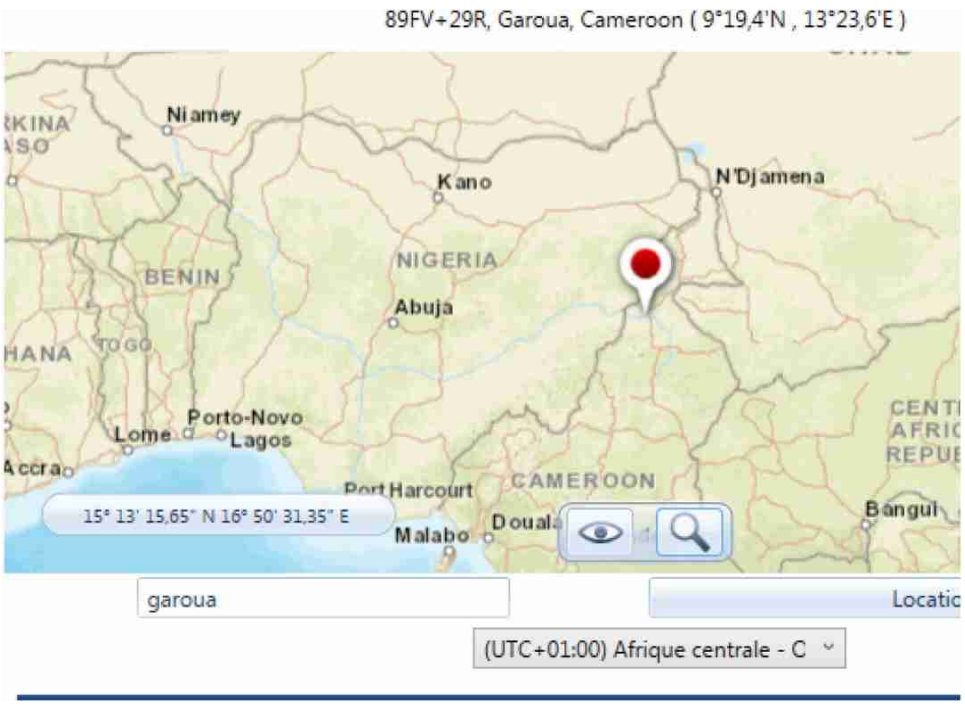

Fig. 2 Location of the research area in Garoua province

annual wind speed of about 5.04 m/s as shown in Fig. 4, November has the highest wind speed of 6 m/s and May has the lowest wind speed of 4 m/s.

Configuration and energy supplied

The photovoltaic system's hourly output power is defined as in Eq. (1).

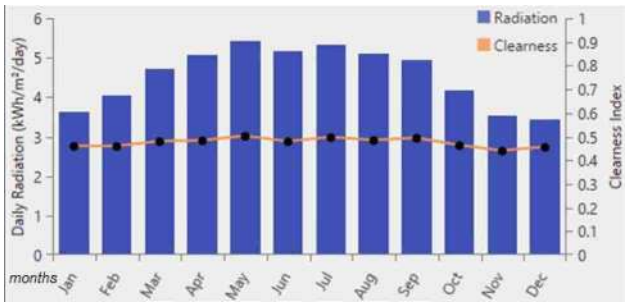

Fig. 3 Global solar radiation in the project area

Fig. 4 Wind speed at an altitude of 10 m in the project area

$$P_{\mathrm{PV}} = D_{\mathrm{PV}}\zeta_{\mathrm{PV}}\left(\frac{I_T}{I_S}\right)[1+\phi_P(T_C - T_S)] \tag{1}$$

where D_{PV} is the rated capacity of PV array, ζ_{PV} the derating factor (80%),

I_T the incident solar irradiation in kW/m^2, I_S the standard solar irradiation in kW/m2, ϕ_P the coefficient of the solar power, T_C the temperature of the PV cell in °C, and T_S is the standard PV cell temperature.

The temperature of the PV cell can be also calculated as in Eq. (2).

$$T_c = T_a + I_T\frac{T_{c,\mathrm{NOCT}} - T_{a,\mathrm{NOCT}}}{I_{T,\mathrm{NOCT}}}\left(1 - \frac{\partial_{\mathrm{PV}}}{0.9}\right) \tag{2}$$

where T_a the temperature (°C), ∂_{PV} is the efficiency of the PV cell, and NOCT is the nominal operating cell temperature.

The power law to determine the wind speed necessary for a specific location for a given hub height is defined in Eq. (3), where τ is the power law exponent.

$$U = U_{\mathrm{refer}}\left(\frac{\chi}{\chi_{\mathrm{refer}}}\right)^{\tau} - \tau \tag{3}$$

$$\gamma = \frac{\gamma - \mu_\lambda}{1 + \mu_\lambda} \tag{4}$$

where U is wind speed (m/s) at the hub height, U_{refer} is wind speed (m/s) at the reference height, χ is hub height, $\chi_{\mathrm{refer}} = 24$ is reference height.

The $P_{\mathrm{WT}}(U)$, wind turbine power output.is defined in Eq. (5)

$$P_{\mathrm{WT}}(U) = \begin{cases} 0, \mathrm{for} U < U0 \\ aU^3, \mathrm{for} U_0 < U < U_{\mathrm{rs}} \\ P_{\mathrm{rs}}, \mathrm{for}\ U_{\mathrm{rs}} < U < U_1 \\ 0, \mathrm{for}\ U > U_1 \end{cases} \tag{5}$$

where U_1 is cutout speed (m/s).

Parameters a and b are constant, P_{rs} is rated power, U_{rs} is rated speed (m/s), $U0$ is cut speed (m/s).

$$b = \frac{U_0^3}{U_{\mathrm{rs}}^3 - U_0^3} \tag{6}$$

$$a = \frac{P_{\mathrm{rs}}}{U_{\mathrm{rs}}^3 - U_0^3} \tag{7}$$

When using HOMER, TNPC is calculated using Eq. (8), where C_Ψ is the overall yearly cost (USD/year) and CRF is the capital recovery factor, $C_{\Psi,\mathrm{Cap}}$ is the capital cost, $C_{\Psi,\mathrm{Rep}}$, the replacement costs, considering the system. The cost of energy can be calculated as in Eq. (8). E_T is the total energy production.

$$\mathrm{COE} = \frac{C_\Psi}{E_T} \tag{8}$$

$$C_\Psi = C_{\Psi,\mathrm{Cap}} + C_{\Psi,\mathrm{Rep}} + C_{\Psi,O\&M} \tag{9}$$

$$\mathrm{TNPC} = \frac{C_{O\Psi}}{\mathrm{CRF}} \tag{10}$$

$$\mathrm{CRF} = \frac{\gamma(1+\gamma)^n}{\gamma(1+\gamma)^n - 1} \tag{11}$$

$$\mathrm{LCE} = \sum_{\tau=1}^{\kappa} BrEi - \kappa \tag{12}$$

The total produced energy can be manage as follows:

$$N_{\mathrm{PV}}P_{\mathrm{Photovol}}(t) + N_{\mathrm{WT}}P_{\mathrm{WTurbine}}(t) - P_{\mathrm{splus}} = P_{\mathrm{Load}}(t) \tag{13}$$

$$N_{\mathrm{PV}} \succ 0, N_{\mathrm{WT}} \succ 0. \tag{14}$$

The optimized system can be, On the other hand, evaluated using PSO algorithms. This is formulated considering:X_m the position, V_i, velocity, pbest, the best position and C_1 and C_2 weighing coefficients values are:

$$\omega_{\max} = 0.8, \omega_{\min} = 0.3 \tag{15}$$

$$X_m = \left(x_{m,1}, x_{m,2}, x_{m,3}, L, x_{m,n}\right) \tag{16}$$

And $c_1 = c_2 = 0.2$

$$S_{j\psi}^{i+1} = S_{j\psi}^{i} + v_{j\psi}^{i+1},\ k = 1, 2, \cdots, n; \psi = 1, 2, \cdots, m \tag{17}$$

$$\begin{aligned} S_{\mathrm{kd}}^{i+1} &= \omega v_{\mathrm{kd}}^{i} + c_1 * \mathrm{rand}\left(\mathrm{pbest}_{\mathrm{kd}} - s_{\mathrm{kd}}^{i}\right) \\ &\quad + c_2 * \mathrm{rand}\left(\mathrm{gbest}_{\mathrm{kd}} - s_{\mathrm{kd}}^{i}\right) - S_{\mathrm{kd}} - \mathrm{kd} \end{aligned} \tag{18}$$

pbest is the best position and gbest is the best values generated and evaluated. S_{kd} Is score at position kd.

$$\omega_f = \omega_{\max} - \frac{\omega_{\max} - \omega_{\min}}{f_{\max}} f \tag{19}$$

$$\mathrm{Pbest}_a = \left(\mathrm{pbest}_{a,1}, \mathrm{pbest}_{a,2}, L, \mathrm{pbest}_{a,b}\right) \tag{20}$$

$$\mathrm{Gbest}_a = \left(\mathrm{gbest}_{a,1}, \mathrm{gbest}_{a,2}, \ldots . \mathrm{gbest}_{a,b}\right) \tag{21}$$

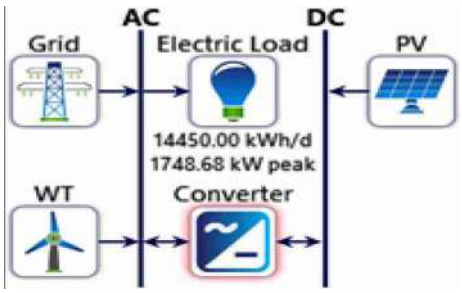

Fig. 5 Proposed hybrid power system

The configuration of the hybrid grid-tied renewable energy system in the locality of Garoua is depicted in Fig. 5. The hybrid power system consists of the main components such as the power grid, solar panels, wind turbines and inverters grid-tied solar. In normal operation, the electrical load will primarily use electricity supplied from renewable energy sources such as wind power and solar power. The cement manufacturing plant can directly use electricity from clean energy sources, including solar and wind power, to reduce electricity costs and help protect the environment, because the system Hybrid power uses less electricity from fossil fuel sources. The cement manufacturing plant uses many energy-intensive devices and operates continuously all day, as shown in Fig. 6, so the daily average electricity consumption is quite high with a value of approximately 14,450 kWh per day. The highest load capacity is in the periods from 4:00 to 10:00 a.m. and from 1:00 to 3:00 p.m.

The specifications of the main components of the hybrid power system are shown in Table 1, in which the capacity of the solar and wind power systems will include many different values to find the optimal configuration. Solar and wind power capacity values are selected within the appropriate range of investment capacity and priority to serve the primary feedstock of the cement manufacturing plant. The solar panels are installed on the roofs of the factory with a suitable angle of inclination.

The purchase price of electricity from the medium voltage power grid is calculated on average, according to the regulations of the Cameroon Electricity Company (ENEO), and this purchase price is calculated to increase on average of 6% per year according to ENEO's annual plan. On the other hand, the price of rooftop solar is temporarily calculated at 0.06 USD/kWh, this is a price that is expected to decrease from the old price of rooftop solar in 2020 of 0.0838 USD/kWh according to the roadmap to build the Cameroonian government's annual renewable energy FIT price. The price of solar energy is stable throughout the 20-year project life cycle under the power company's power purchase agreement.

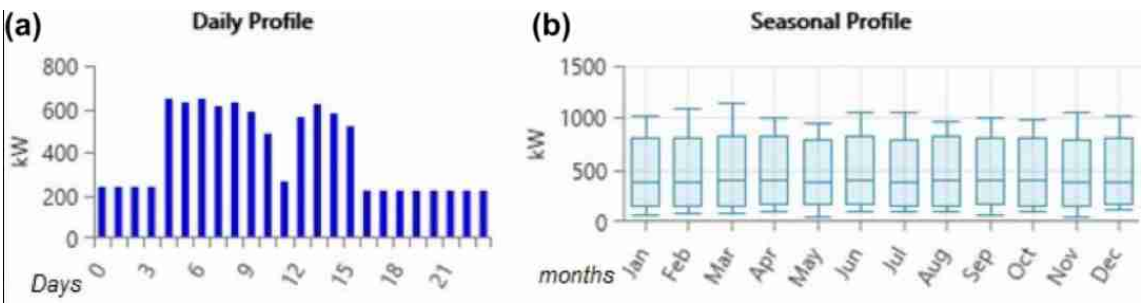

Fig. 6 Daily 6(**a**) and monthly 6(**b**) power load profile of cement manufacturing plant

The cost of the renewable energy system in Table 2 is based on the actual cost of solar energy and wind energy in the market in Cameroon.

This study will simulate two scenarios using renewable energy in the cement manufacturing plant as follows:

Scenario 1: Grid-tied hybrid wind and solar power system.

Scenario 2: Grid-tied rooftop solar power system.

Finally, a comparison of optimization grid-tied renewable power systems between two scenarios is executed to find the best optimal scenario.

Results and discussion

Scenario 1 (grid-tied hybrid wind and solar power system)

The simulation results in Table 3 showed that a hybrid power system containing three wind turbines with a rated capacity of 300 kW, and the solar array with a total capacity of 1500 kW is the most optimal configuration due to the minimum NPC cost of $5,596,978, while the COE cost of $0.0847/kWh, the investment cost of $1,140,000, and the operating cost of $384,877.

Figure 7 shows the electricity production of wind turbines, solar panels and the electricity grid during the year. The solar power system generates most of the electricity from April to September while the most electricity comes from the wind turbines from October to January of the following year. It can be seen that the rate of electricity generation from the grid is 52.1%, while the rate of electricity generated from renewable energy sources reaches more than 47%, of which solar energy accounts for 35, 4% and wind energy represents 12.5%. Generating a large amount of renewable electricity has helped save the cost of purchasing the manufacturing plant's power grid. The grid-tied hybrid power system generates electricity of 5,274,250 kWh/year to meet the plant's power demand, while the amount of excess solar energy sold to the local power grid is 434 246 kWh/year. This result corresponds to the Cameroonian policy of using solar energy on the roofs to meet mainly the needs of electrical load on site. The grid-connected hybrid power

Table 1 Input parameters for simulation

Component	Power (kW)	Life time (year)	Notes
Solar power	1000, 1100, 1200, 1300, 1400, 1500	25	Solar and wind power capacity values are selected in the suitable range of the investment capability and priority to serve the main power load of the non-fired brick factory
Wind power	100, 200, 300	10	
Utility Grid	Ensuring sufficient and continuous supply for electrical loads in the factory		Electricity purchase price: $0.077/kWh (Grid electricity price is calculated to increase by an average of 6% per year) Price of solar power: $0.06/kWh (The price of solar power is stable throughout the project life cycle of 20 years under the power purchase contract of the power company)

Table 2 Cost of renewable power system

Component	Investment expenses	Replacement costs	O&M expenses
Solar power	$550 $/kW	$550 $/kW	$11/kW/year
100 kW Solar grid-tied inverter	$5000	$5000	$100/year
100 kW wind system	$80,000	$70,000	$1600/year

Table 3 Cost of renewable power system

System	PV (kW)	WT	NPC($)	COE($)	Operating cost($/year)	Initial capital($)	Renewable fraction (%)
Quantity	1500	3	5.60 M	0.0847	384,877	1.14 M	47.5

Fig. 7 Electric production from the grid-tied hybrid power system

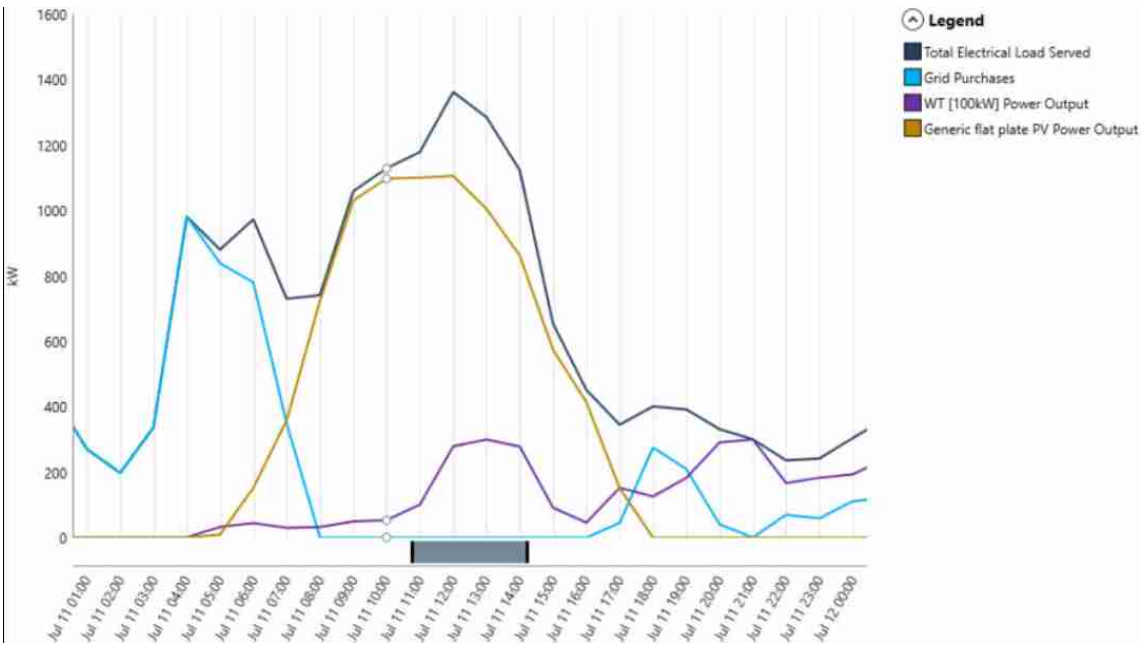

Fig. 8 Typical day power generation results in scenario 1

system ensures that the plant can work stably, continuously, without power failure during the year.

Figure 8 shows the results of electricity production from energy sources on a typical day of July 11. Daytime electric loads mainly use electricity from solar energy, and they are also added from wind energy, the amount of electricity from the power grid is quite small, and they are supplied only in the event of adverse weather conditions. During the day to ensure the highest rate of renewable energy production. Meanwhile, the nighttime electrical load uses a lot of grid power, a small part is supplied by wind power when wind conditions are favorable. Therefore, Scenario 1 shows a fairly flexible combination of wind power and solar power in the process of supplying renewable electricity to meet the electricity consumption demand for working in the factory and minimizing the proportion of grid energy from fossil energy sources.

Figure 9 illustrates the statistical results of the frequency of buying and selling solar power to the power grid during the year of the hybrid power system. It can be seen that the power grid provides electricity to serve the plant load

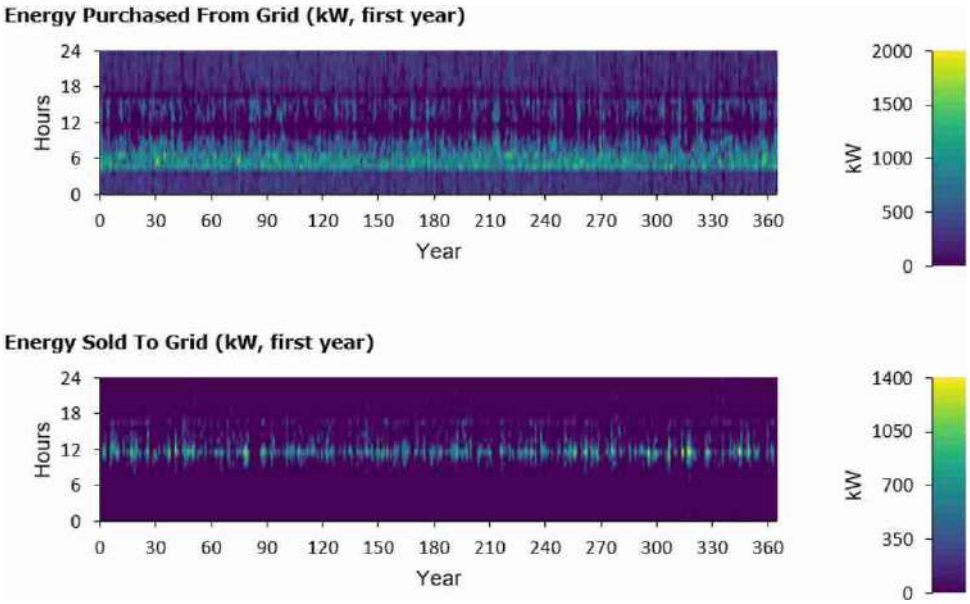

Fig. 9 Electricity purchase and sale of solar power

mainly from 4:00 to 8:00 a.m. due to the highest capacity of the plant load and there is not much of sun and wind to operate wind and solar equipment during this period. On the other hand, the frequency of solar power sales to the power grid during the year is concentrated around noon, when the solar power generation capacity is highest and the plant load capacity is lowest during the day. At many times of the year, another portion of excess solar power can be sold to the power grid using power generation from wind turbines to power the load under the right wind conditions during the day, which will increase the profitability for the investor.

The results of the environmental analysis showed that the use of a hybrid wind and solar system reduced the use of grid energy and that the cement manufacturing plant only emits CO2 emissions de 2,400,000 kg/year into the environment, thus helping to reduce environmental pollution.

Scenario 2 (grid-tied rooftop solar power system)

In Scenario 2, the calculation result in Table 4 shows that the grid-connected solar power system with a capacity of 1,500 kW is the most optimal configuration due to the minimum NPC cost of $6,122,231, while the COE cost is about $0.0951/kWh, the investment cost $900,000, as well as the operating cost worth $450,959.

The amount of electricity generated from PV generators and the power grid during the year is shown in Fig. 10. In this case, the electricity generation rate from the power grid is 63.7%, while that the rate of electricity generated from solar energy sources reaches 36.3%. The solar power system provides an amount of electricity of 2,034,531 kWh to meet the electricity demand of the factory, while the amount of excess solar energy sold to the local grid is 287,194 kWh per year. The power grid in this scenario will supply 3,567,604 kWh/year to ensure the stable operation of the plant, without power outages during the year.

Figure 11 depicts the results of electricity production from energy sources on a typical day of August 16. Daytime power charging gives priority to the use of electricity from solar energy, the missing part is further supported by the power grid at times of unfavorable weather during the day to ensure stable operation of the power load. Meanwhile, nighttime power load operation utilizes the entire power grid.

The result of the environmental analysis also showed that the factory emits CO2 emissions of about 2,868,354 kg/year into the environment due to the use of a rooftop solar energy system.

Table 4 Cost of renewable power system

System	PV (kW)	WT	NPC($)	COE($)	Operating cost($/year)	Initial capital($)	Renewable fraction (%)
Quantity	1500	3	6,12 M	0.0951	450,959	900.000	35.9

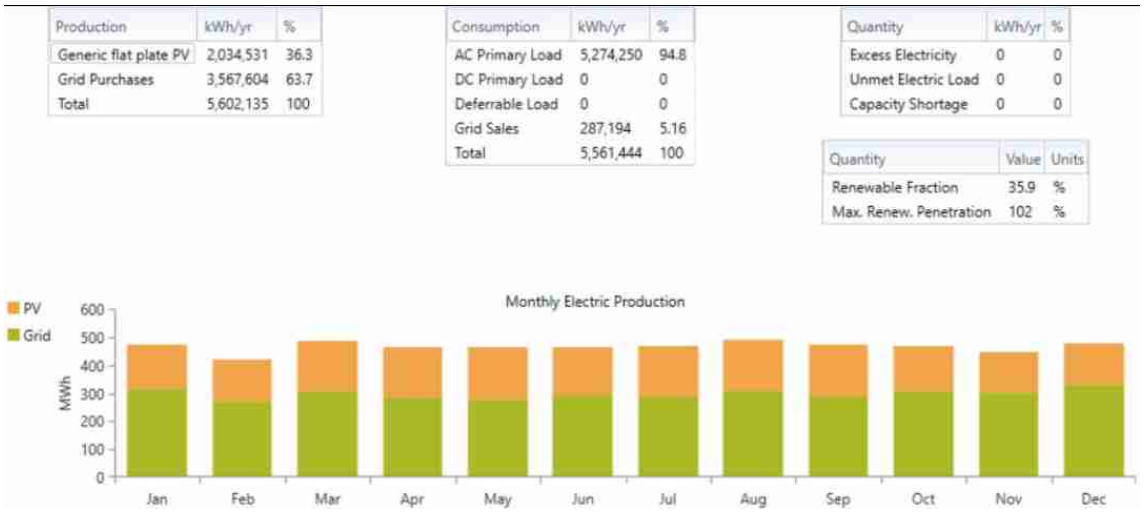

Fig. 10 Electric production from the grid-tied rooftop solar power system

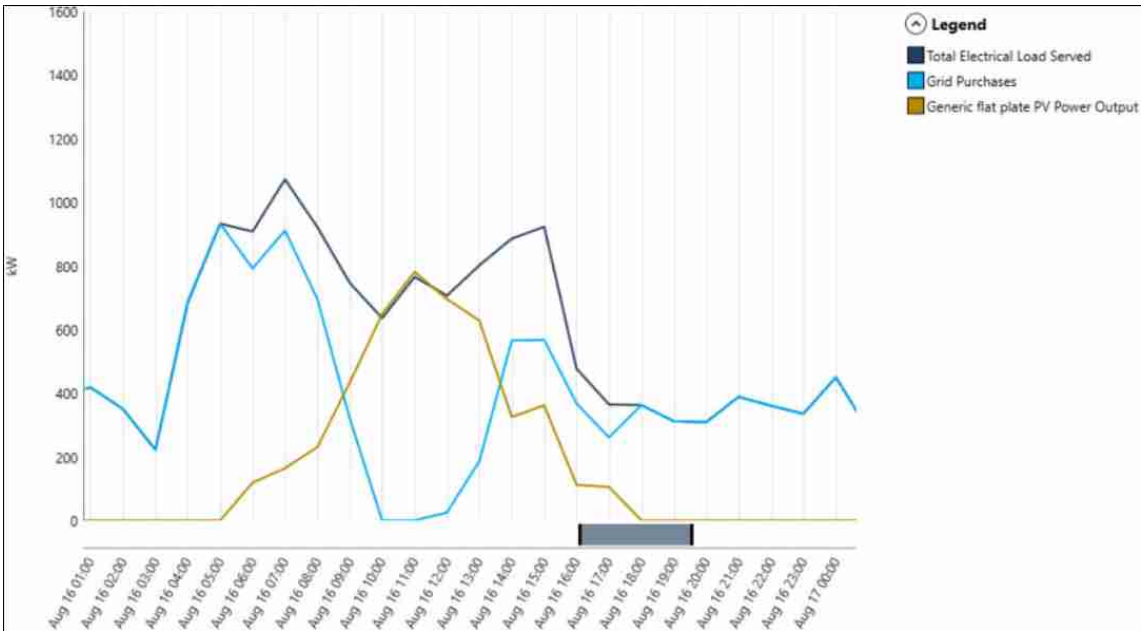

Fig. 11 Typical day power generation results in scenario 2

Optimal configuration system

The results of the comparison of economic factors in the two scenarios are shown in Fig. 12. The grid-tied hybrid power system in Scenario 1 has a higher initial investment cost, with higher operating and maintenance costs, lower maintenance and more benefits from the surplus solar energy sold to the grid. Energy is and is purchased from the grid, so Scenario 1 will result in a more optimal configuration due to lower NPC and COE costs.

Figure 13 shows the relationship between the amount of electricity purchased from the distribution grid and the total net present cost. Purchasing so much electricity from the power grid will increase the total net present cost and reduce the optimal capacity of the renewable energy system.

The result of reducing greenhouse gas emissions in Fig. 14 shows that the use of renewable energy systems can

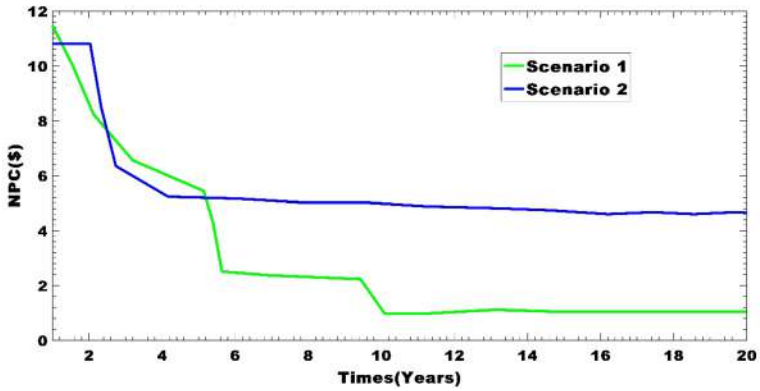

Fig. 12 The comparison results of the economic factors of the two scenarios

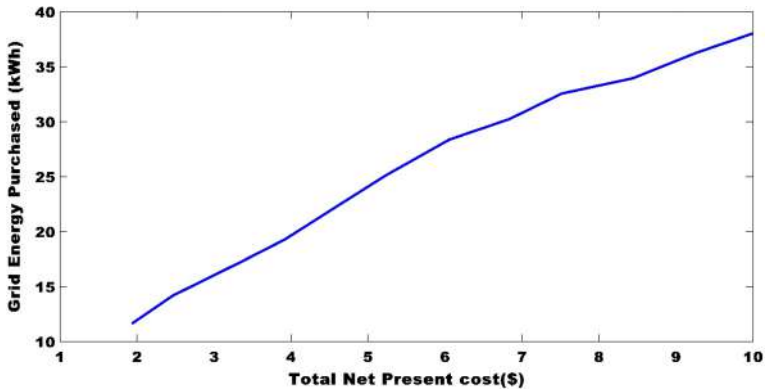

Fig. 13 The relationship between the amount of electricity purchased from the grid and the total net present cost

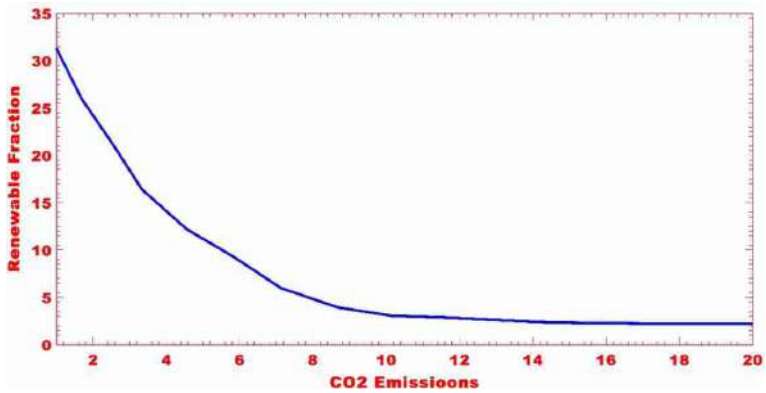

Fig. 14 Results of reduction in greenhouse gas emissions

reduce greenhouse gas emissions, but the emissions depend on the proportion of renewable electricity for factory load. The renewable electricity rate in Scenario 1 is about 11.6% higher than Scenario 2, so it can help the cement manufacturing plant emit less CO2 emissions of about 468,354 kg per year in the environment due to the reduction of electricity generated from the medium voltage supply of the utility grid.

Conclusion

In this paper, the results of the optimization study of the grid-connected renewable energy system in the cement manufacturing plant located in Garoua province, Cameroon, were calculated. The grid-tied hybrid wind and solar power systems of Scenario 1 are considered to bring more environmental, economic and technical efficiency than the grid-tied solar power systems of Scenario 2. The optimal power system configuration hybrid includes wind power

with a capacity of 300 kW and solar power with a capacity of 1500 kW, the system has an NPC cost of 5,596,978 USD, a COE cost of approximately 0.0847 USD /kWh, an investment cost of 1,140,000 USD and an operating cost of 384,877USD. Installing renewable energy capacity will force the plant investor to purchase as much power from the utility grid and will increase the total net present cost, which should reduce the system's optimal capacity of renewable energy. On the other hand, the use of a renewable energy system will also help the plant to reduce greenhouse gas emissions, but the emissions depend on the proportion of renewable electricity for the load of the plant. The rate of renewable electricity from a hybrid wind and solar grid-tied system in Scenario 1 is approximately 11.6% higher than that from a solar grid system in Scenario 2, so it can help the factory emit less CO2 emissions of about 468,354 kg per year to the environment due to less electricity generated by the utility grid. Thus, the use of hybrid wind and solar systems can reduce the electricity costs of the cement manufacturing plant and help create products that meet green standards, thereby increasing competitiveness in the Cameroonian market. The research findings can help determine the importance of applying renewable electricity technologies to industrial facilities in general and cement manufacturing plants in particular in Cameroon. Moreover, this initiative, which is innovative for Cameroon in particular, presents a solution for making industries autonomous from utility power and at the same time reinforces the Northern Interconnected Network (NIN).

This work, which aimed to assess the feasibility of strengthening the North interconnected network (RIN), in order to solve the problem of load shedding in the area due to the growing demand for electricity, presents an aspect that is not addressed. It would be advantageous to calculate the harmonic distortion rate to assess the quality of the energy produced by this multi-source plant.

Declarations

Conflict of interest No competing financial interests have been declared by the authors for this paper.

References

1. Serda, M., Becker, F.G., Cleary, M., et al.: For sustainable development: future trends in renewable energy and enabling technologies. Uniw śląski **7**, 343–354 (2020)
2. Li, L., Lin, J., Wu, N., et al.: Review and outlook on the international renewable energy development. Energy Built Environ. **3**, 139–157 (2022). https://doi.org/10.1016/J.ENBENV.2020.12.002
3. Prăvălie, R., Bandoc, G.: Nuclear energy: between global electricity demand, worldwide decarbonisation imperativeness, and planetary environmental implications. J. Environ. Manag. **209**, 81–92 (2018). https://doi.org/10.1016/J.JENVMAN.2017.12.043
4. Xiao, M., Junne, T., Haas, J., Klein, M.: Plummeting costs of renewables—are energy scenarios lagging? Energy Strateg. Rev. **35**, 100636 (2021). https://doi.org/10.1016/J.ESR.2021.100636
5. Ouyang, X., Lin, B.: Levelized cost of electricity (LCOE) of renewable energies and required subsidies in China. Energy Policy **70**, 64–73 (2014). https://doi.org/10.1016/J.ENPOL.2014.03.030
6. Butturi, M.A., Lolli, F., Sellitto, M.A., et al.: Renewable energy in eco-industrial parks and urban-industrial symbiosis: a literature review and a conceptual synthesis. Appl. Energy **255**, 113825 (2019). https://doi.org/10.1016/J.APENERGY.2019.113825
7. Hsu, A., Höhne, N., Kuramochi, T., et al.: Beyond states: harnessing sub-national actors for the deep decarbonisation of cities, regions, and businesses. Energy Res. Soc. Sci. **70**, 101738 (2020). https://doi.org/10.1016/J.ERSS.2020.101738
8. Taibi, E., Gielen, D., Bazilian, M.: The potential for renewable energy in industrial applications. Renew. Sustain. Energy. Rev. **16**, 735–744 (2012). https://doi.org/10.1016/J.RSER.2011.08.039
9. - International Energy Agency I Renewable Energy for Industry From green energy to green materials and fuels Cédric Philibert
10. Meng, Y., Yang, Y., Chung, H., et al.: Enhancing sustainability and energy efficiency in smart factories: a review. Sustainability **10**, 4779 (2018). https://doi.org/10.3390/SU10124779
11. Rajesh Kumar, C.J., Majid, M.A.: Renewable energy for sustainable development in India: current status, future prospects, challenges, employment, and investment opportunities.Energy Sustain Soc. (2019) https://doi.org/10.1186/s13705-019-0232-1
12. Kitmo, T.G.B., Djongyang, N.: Optimization of the photovoltaic systems on the North Cameroon interconnected electrical grid. Int. J. Energy Environ. Eng. **2021**, 1–13 (2021). https://doi.org/10.1007/S40095-021-00427-8
13. Setting the pace for a sustainable energy transition in Central Africa: the case of Cameroon | IEEE Journals & Magazine | IEEE Xplore. https://ieeexplore.ieee.org/abstract/document/9579016. Accessed 28 Sep 2022
14. Kitmo, D.R., Kidmo, D.K., et al.: Optimization of the power flow of photovoltaic generators in electrical networks by MPPT algorithm and parallel active filters. Energy Rep. **7**, 491–505 (2021). https://doi.org/10.1016/J.EGYR.2021.07.103
15. Djidimbélé, R., Ngoussandou, B.-P., Kidmo, D.K., et al.: Optimal sizing of hybrid systems for power loss reduction and voltage improvement using PSO algorithm: case study of Guissia rural grid. Energy Rep. **8**, 86–95 (2022). https://doi.org/10.1016/J.EGYR.2022.06.093
16. Heffron, R., Körner, M.F., Wagner, J., et al.: Industrial demand-side flexibility: a key element of a just energy transition and industrial development. Appl. Energy **269**, 115026 (2020). https://doi.org/10.1016/J.APENERGY.2020.115026
17. Letcher, T.M.: Storing electrical energy. Manag. Glob. Warm Interface Technol. Hum. Issues **16** 365–377 (2019) https://doi.org/10.1016/B978-0-12-814104-5.00011-9
18. Fakih, A., Ghazalian, P., Ghazzawi, N.: The effects of power outages on the performance of manufacturing firms in the MENA region. Rev. Middle East Econ. Financ. **16**, 20200011 (2020). https://doi.org/10.1515/RMEEF-2020-0011
19. Cissokho, L.: The productivity cost of power outages for manufacturing small and medium enterprises in Senegal. J. Ind. Bus. Econ. **46**, 499–521 (2019). https://doi.org/10.1007/S40812-019-00128-8/TABLES/14
20. Temene Hermann, D., Donatien, N., Konchou Franck Armel, T., René, T.: Techno-economic and environmental feasibility study

with demand-side management of photovoltaic/wind/hydroelectricity/battery/diesel: a case study in Sub-Saharan Africa. Energy Convers. Manag. **258**, 115494 (2022). https://doi.org/10.1016/J.ENCONMAN.2022.115494
21. Nfah, E.M., Ngundam, J.M.: Feasibility of pico-hydro and photovoltaic hybrid power systems for remote villages in Cameroon. Renew. Energy **34**, 1445–1450 (2009). https://doi.org/10.1016/J.RENENE.2008.10.019
22. Scheubel, C., Zipperle, T., Tzscheutschler, P.: Modeling of industrial-scale hybrid renewable energy systems (HRES)—the profitability of decentralized supply for industry. Renew. Energy **108**, 52–63 (2017). https://doi.org/10.1016/J.RENENE.2017.02.038
23. Schulz, J., Leinmüller, D., Misik, A., Zaeh, M.F.: Renewable onsite power generation for manufacturing companies—technologies, modeling, and dimensioning. Sustainability **13**, 3898 (2021). https://doi.org/10.3390/SU13073898
24. Sawle, Y., Gupta, S.C., Bohre, A.K.: Optimal sizing of standalone PV/Wind/Biomass hybrid energy system using GA and PSO optimization technique. Energy Procedia **117**, 690–698 (2017). https://doi.org/10.1016/J.EGYPRO.2017.05.183
25. Kenfack, J., Lewetchou, K.J., Bossou, O.V., Tchaptchet, E.: How can we promote renewable energy and energy efficiency in Central Africa? A Cameroon case study. Renew. Sustain. Energy Rev. **75**, 1217–1224 (2017). https://doi.org/10.1016/J.RSER.2016.11.108
26. Pearl-Martinez, R., Stephens, J.C.: Toward a gender diverse workforce in the renewable energy transition. Sustain. Sci. Pract. Policy **12**, 8–15 (2017). https://doi.org/10.1080/15487733.2016.1190814 9
27. Murshed, M., Ahmed, R., Kumpamool, C., et al.: The effects of regional trade integration and renewable energy transition on environmental quality: evidence from South Asian neighbors. Bus. Strateg. Environ. **30**, 4154–4170 (2021). https://doi.org/10.1002/BSE.2862
28. Al-Shahri, O.A., Ismail, F.B., Hannan, M.A., et al.: Solar photovoltaic energy optimization methods, challenges and issues: a comprehensive review. J. Clean. Prod. **284**, 125465 (2021). https://doi.org/10.1016/J.JCLEPRO.2020.125465
29. Gorjian, S., Sharon, H., Ebadi, H., et al.: Recent technical advancements, economics and environmental impacts of floating photovoltaic solar energy conversion systems. J. Clean. Prod. **278**, 124285 (2021). https://doi.org/10.1016/J.JCLEPRO.2020.124285
30. Alphonse, S., Jacques, B., et al.: Optimization PV/Batteries system: application in Wouro Kessoum Village Ngaoundere Cameroon. J Power Energy Eng **9**, 50–59 (2021). https://doi.org/10.4236/JPEE.2021.911003
31. Kidmo, D.K., Bogno, B., Ngohe Ekam, P.-S., et al.: Hydropower generation potential and prospective scenarios for sustainable electricity supply for the period 2022–2042: a case study of the NIN zone of Cameroon. Energy Rep. **8**, 123–136 (2022). https://doi.org/10.1016/J.EGYR.2022.06.090
32. Tonsie Djiela, R.H., Tiam Kapen, P., Tchuen, G.: Wind energy of Cameroon by determining Weibull parameters: potential of a environmentally friendly energy. Int. J. Environ. Sci. Technol. **188**(18), 2251–2270 (2020). https://doi.org/10.1007/S13762-020-02962-Z
33. Gormo, V.G., Kidmo, D.K., Ngoussandou, B.P., et al.: Wind power as an alternative to sustain the energy needs in Garoua and Guider, North Region of Cameroon. Energy Rep. **7**, 814–829 (2021). https://doi.org/10.1016/J.EGYR.2021.07.059
34. Koholé, Y.W, Fohagui,F.C.V, Tchuen, G.: A holistic overview of Cameroon renewable energy sources: potentials, achievements, challenges and perspectives. (2022) https://doi.org/10.1080/01430750.2022.2068065
35. Yaouba, B.M., Welba, C., et al.: An experimental and case study on the evaluation of the partial shading impact on PV module performance operating under the Sudano-Sahelian climate of Cameroon. Front. Energy Res. **10**, 967 (2022). https://doi.org/10.3389/FENRG.2022.924285
36. Kitmo, Tchaya, G.B., Djongyang, N., et al.: Optimization of the smart grids connected using an improved P&O MPPT algorithm and parallel active filters. J. Sol. Energy. Res. **6**, 814–828 (2021). https://doi.org/10.22059/JSER.2021.320173.1196
37. Ibrahim, I.D., Hamam, Y., Alayli, Y., et al.: A review on Africa energy supply through renewable energy production: Nigeria, Cameroon, Ghana and South Africa as a case study. Energy Strateg. Rev. **38**, 100740 (2021). https://doi.org/10.1016/J.ESR.2021.100740
38. Aqachmar, Z., Campana, P.E., Bouhal, T., et al.: Electrification of Africa through CPV installations in small-scale industrial applications: energetic, economic, and environmental analysis. Renew. Energy **197**, 723–746 (2022). https://doi.org/10.1016/J.RENENE.2022.07.106
39. Bahramara, S., Moghaddam, M.P., Haghifam, M.R.: Optimal planning of hybrid renewable energy systems using HOMER: a review. Renew. Sustain. Energy Rev. **62**, 609–620 (2016). https://doi.org/10.1016/J.RSER.2016.05.039
40. Dogahe, S.A., Javaran, E.J., Abdolzadeh, M.: Energy and economic analysis of photovoltaic, concentrating photovoltaic, and combined concentrating photovoltaic/thermal-organic rankine cycle power plants in Iran. Environ. Prog. Sustain. Energy **41**, e13763 (2022). https://doi.org/10.1002/EP.13763

International Journal of Energy and Environmental Engineering (2023) 14:563–572
https://doi.org/10.1007/s40095-022-00535-z

ORIGINAL RESEARCH

Effect of different concentrations of phosphorus and nitrogen on the growth of the microalgae *Chlorella vulgaris*

Lilian Tavares[1] · Matheus Haddad Nudi[2] · Pedro Augusto Arroyo[3] · Rodrigo Felipe Bedim Godoy[4,5] · Elias Trevisan[2]

Received: 6 June 2022 / Accepted: 9 September 2022 / Published online: 26 September 2022

Abstract

The growth curve is an important characteristic to estimate microalgae biomass production for biofuel generation, since they can measure the variation between concentrations of limiting factors of culture medium. Therefore, this work aimed to evaluate the development of *Chlorella vulgaris* with triplicate cultivation of three different concentrations of nitrogen and phosphorus (Treatment 1: 0.50 g L^{-1} $Ca(NO_3)_2{\cdot}4H_2O$ and 0.13 g L^{-1} KH_2PO_4, Treatment 2: 0.50 g L^{-1} $Ca(NO_3)_2{\cdot}4H_2O$ and 0.39 g L^{-1} KH_2PO_4, Treatment 3: 1.50 g L^{-1} $Ca(NO_3)_2{\cdot}4H_2O$ and 0.13 g L^{-1} KH_2PO_4,). Growth curve using Gompertz model presented high R^2 ($0.96 \leq R^2 \leq 0.99$) in the three studied treatments. In the thirteenth day, turbidity in the treatment with higher nitrogen concentration (203.67 NTU) was 2.15 times higher than the first treatment (94.56 NTU) and 1.78 times higher than the treatment with higher level of phosphorus (113.9 NTU). We therefore observed a major biomass production, chlorophylls and carotenoids in the treatment with higher concentration of nitrogen, while in high levels of phosphorus the growth is not statistically significant from the first treatment with lower nitrogen and phosphorus concentration (p value > 0.05). In the end of cultivation, there was an increase of 203.12% in chlorophyll-a in the third treatment compared to the first treatment and of 246.42% in comparison with the second treatment. For carotenoids, the highest increase was seen compared to the first treatment (192%) than for the second treatment (137.5%). Therefore the treatment with lower phosphorous concentration in the cultivation medium presented slightly higher chlorophyll concentration and smaller carotenoids with the treatment with higher phosphorus concentration. The ash content demonstrated that this microalgae have a great potential for energy use.

Keyword Biofuel · Carotenoids · Chlorophyll · Nutrients

Introduction

Biofuel are energetic chemicals produced by biological processes or derived from the biomass of autotrophic living beings such as plants, microalgae and cyanobacteria [1, 2]. It has received worldwide attention as a potential alternative to substitute fossil fuels [2, 3] due to the climate change concern as a consequence of burning those fossil fuels generating CO_2 emissions [1, 4, 5]. Finding the low cost production of biofuels will start to address energy security and climate change concern [6].

There are several feedstocks for biofuel production, among them are vegetable and used oils, animal fats and microalgae [7, 8], mainly those microalgae with higher lipid

✉ Lilian Tavares
lilian.tavares5454@gmail.com

Matheus Haddad Nudi
matheus.h.nudi@gmail.com

Pedro Augusto Arroyo
paarroyo@uem.br

Rodrigo Felipe Bedim Godoy
rodrigofelipe7@hotmail.com

Elias Trevisan
eliastrevisan@yahoo.com.br

[1] Environmental Engineer, Umuarama, PR, Brazil

[2] Department of Environment, State University of Maringá (UEM), Umuarama, PR, Brazil

[3] Department of Chemical Engineering, State University of Maringá, Maringá, PR, Brazil

[4] Centre de Recherche sur les Interactions Bassins Versants-Écosystèmes Aquatiques (RIVE), Université du Québec à Trois-Rivières, Trois-Rivières, QC, Canada

[5] Interuniversity Research Group in Limnology (GRIL), Université de Montréal, Montreal, QC, Canada

content for jet fuel, biodiesel and biogasoline production [9]. Microalgae are photosynthetic beings that combine water, carbon dioxide and light to generate biomass being considered as a potential raw material for the next generation biofuel [10–13]. Advantages to use microalgae includes fast growth rates, high lipid proclivity as well as the ability to synthesize value-added bioproducts [14]. The lipids and carbohydrates present in the microalgal cells might be used, respectively, to biodiesel and bioethanol production [15]. A recent study has indicated that microalgae biomass can generate 121, 104 L of biodiesel per hectare [16].

Studies related to the use of microalgae to produce biofuel have increased over the years [3, 4, 9, 11, 17]. There are diverse benefits for microalgae biofuel generation due to its rich energy content, inexpensive culture procedures, inflated growth rate, high capacity of CO_2 fixation and release of O_2 to the atmosphere [3], although there are also challenges to make the microalgae biofuel economically viable and durable [9]. For biodiesel production, the main method is transesterification, in which the oil or fat extracted from the biomass, is converted into fatty acid methyl or ethyl esters [18].

The growth of microalgal biomass is expressed by a curve that can vary according to the nutrients and culture conditions, such as temperature, light and pH [19]. The growth curve has been used in many studies to monitor the variation of biomass over time [20–22] and to identify the stationary phase [23]. The parameters associated with biomass production include dry biomass concentration [22, 24] and turbidity [25, 26].

According to Andrade and Filho [19], growth curve is divided into five phases, which are the lag phase, in which occurs the adaptation of the microalgae in the medium; the log phase that is characterized as having a higher growth rate; growth reduction phase also called transition; stationary phase, with no more growth and the decline phase, which due to substrate limitation or accumulation of toxic metabolites, there is cell death.

Nutrients are indispensable for microalgae growth and depending on the amount needed, they can be divided between micro and macronutrients [27]. According to Lourenço [28], micronutrients are, for example, boron, copper, zinc, and molybdenum, and act in the enzymatic activity and also in the cell structure. Macronutrients regulate the metabolic activities and participate in the energy exchange, and can be carbon, nitrogen, hydrogen, phosphorus, calcium, magnesium, and potassium.

The main nutrients for the culture medium, also called limiting nutrients of the microalgae, are nitrogen and phosphorus. Nitrogen is the most abundant as a mineral element, and when in low concentrations, there is a decrease in algal biomass, and when in abundance, the cell division rate increases remarkably. Andrade and Filho [19], says that phosphorus is linked to the metabolic processes of the microalgae, and therefore is the most important limiting factor when related to primary productivity. Knowing that, microalgae can be applied for nutrients remediation of industrial and domestic sewage [29, 30].

Previous studies have indicated that nitrogen and phosphorus are key elements for development of *Chlorella vulgaris* even using wastewater as culture medium with low and high concentration of nitrogen [31, 32]. Comparing three different forms of nitrogen (Urea, NH_4Cl and $NaNO_3$), Arabian [33] found that $NaNO_3$ was the most suitable nitrogen-form for the increase of *Chlorella vulgaris* biomass. In another study using *Chlorella vulgaris*, this microalgae compared to other species presented the highest phosphate removal capacity [34].

The microalgae *Chlorella vulgaris* has been used in many studies for biomass production with several different objectives [5, 35, 36], due to high applicability for the pharmaceutical products industry and health food as feed supplement [37]. This microalgae has great resistance, high adaptability to diverse environmental conditions and high lipids and biomass production [38, 39], and based on the aforementioned information, this study aimed to evaluate the growth of the microalgae, in cultivations with different concentrations of nitrogen and phosphorus. Through this general objective, we divided in some specific objectives such as to analyze the growth curve for each treatment, to evaluate the response in biomass and pigments production of *Chlorella vulgaris* in three treatments, to identify which condition it would be more suitable (increasing Nitrogen or increasing phosphorus) for biofuel production and to analyze the ash content for each treatment. The general hypothesis of this work is that increasing the concentration of nutrients in the cultivation medium in comparison with the first treatment (with reduced nutrients concentration), there will have an increase in biomass and pigments production. The significance of this paper is demonstrated, besides in the methodology applied that can be reproduced by other researches, in the comparison between three situations in *Chlorella vulgaris* biomass production for possible application in biofuels production.

Materials and methods

Cultivation of microalgae

The microalgae *Chlorella vulgaris* was cultivated in the Laboratory of Pollution, in the Department of Environment—DAM of the State University of Maringá (UEM)—Umuarama campus. The microalgae strain was provided by Professor Dr. Pedro Augusto Arroyo, coordinator of the Laboratory of Heterogeneous Catalysis and Biodiesel (LCH-Bio) of the UEM—Maringá campus.

Table 1 Composition of *Detmer''s Medium*

Reagent	Quantity (g L^{-1})
$Ca(NO_3)_2{\cdot}4H_2O$	1.0
KCl	0.25
$MgSO_4{\cdot}7H_2O$	0.55
KH_2PO_4	0.26
$FeSO_4{\cdot}7H_2O$	0.02
Solution A_5*	1.0 mL L^{-1}

Source: Watanabe [40]

Table 2 Composition of solution A_5*

Reagent	Quantity (g L^{-1})
H_3BO_3	1.0
$MnCl_2{\cdot}4H_2O$	0.25
$ZnCl_2$	0.55
$CuSO_4{\cdot}5H_2O$	0.08
$3(NH_4)_2O{\cdot}7MoO_2{\cdot}4H_2O$	0.018

Source: Watanabe [40]

The used culture mediums were made from a variation in the concentrations of Detmer's Medium (Table 1 and 2; [40]), which is the culture proposed in the literature for the type of microalgae used. In Table 1 the macronutrients are highlighted, while in Table 2 are the micronutrients necessary for the development of microalgae. Among the macronutrients, as a source of nitrogen, the Calcium Nitrate Tetrahydrate ($Ca(NO_3)_2{\cdot}4H_2O$) and the Potassium dihydrogen phosphate (KH_2PO_4) as phosphorus supply source. In addition to these, there are potassium chloride (KCl), magnesium sulfate heptahydrate ($MgSO_4{\cdot}7H_2O$) and Iron(II) sulfate heptahydrate ($FeSO_4{\cdot}7H_2O$). For the formulation of the A5 solution, the reagents Boric acid (H_3BO_3), Manganese (II) Chloride ($MnCl_2{\cdot}4H_2O$), Zinc chloride ($ZnCl_2$), Copper(II) sulfate ($CuSO_4{\cdot}5H_2O$), Ammonium heptamolybdate tetrahydrate ($3(NH_4)_2O{\cdot}7MoO_2{\cdot}4H_2O$).

These modifications were only done in the reagents nitrate ($Ca(NO_3)_2{\cdot}4H_2O$) and phosphate (KH_2PO_4) shown in Table 3.

Culture conditions

The experiment consisted of microalgae cultivation in three different treatments, done in triplicate for 14 days, starting on 18 October 2019 and ending on 31 October 2019, characterized as day 0 to 13. To this end, cultivation was performed at room temperature with continuous photoperiod (24 h) provided by four 40 W tubular fluorescent lamps, with light intensity of approximately 1800 lux and aeration from aerators (Big Air model A320 with capacity of 3.5 L min^{-1}).

In order to obtain parameters for growth monitoring, daily monitoring of turbidity, chlorophyll and carotenoids was performed. Turbidity analyses were performed using a Del Lab model DLT-WV turbidimeter. Pigments were evaluated according to the methodology proposed by He et al. [41, 42].

Biomass recovery and drying

After the 14 days, to obtain the biomass in the three treatments, the microalgae from the erlenmeyers undergo coagulation and flocculation for their decantation and recovery in the Jar-Test model PoliControl model FlocControl III, using 20 mg L^{-1} of the flocculant Tanfloc, at 450 Rpm for 20 s of fast mixing, and 30 rpm for 20 min of slow mixing. Then the biomass was filtered on filter paper and later taken for drying on watch glass in the oven for a period of 24 h and 60 °C.

Characterization of the biomass

Determination of chlorophyll and carotenoids

To obtain the concentration of chlorophyll and carotenoids, initially, 4 mL of culture were centrifuged in a METROTERM MTD III PLUS model centrifuge at 3000 rpm for 40 min.

After removing the supernatant, 4 mL of 95% ethanol was added to the sedimented biomass to suspend the contents. Subsequently, it was kept at 4 °C, for 12 h, and in a light-free environment. After cooling, the suspended cells were centrifuged at 3000 rpm for 15 min.

Then, absorbance analyses were performed in a FEMTO 700 spectrophotometer at A470, A649, and A665 wavelengths. From the results obtained, the concentrations of chlorophyll a, b and total, as well as carotenoids, were determined according to Eqs. 1, 2, 3 and 4 [41, 42], respectively.

$$Chl_a\left(\text{mg L}^{-1}\right) = 13.95\,A_{665} - 6.88\,A_{649} \quad (1)$$

$$Chl_b\left(\text{mg L}^{-1}\right) = 24.96\,A_{649} - 7.32\,A_{665} \quad (2)$$

$$Chl_{tot}\left(\text{mg L}^{-1}\right) = Chl_a + Chl_b \quad (3)$$

Table 3 Concentrations of nitrate and phosphate for each treatment

Treatment	$Ca(NO_3)_2{\cdot}4H_2O$ (g L^{-1})	KH_2PO_4 (g L^{-1})
First (1)	0.50	0.13
Second (2)	0.50	0.39
Third (3)	1.50	0.13

Adapted from Watanabe [40]

$$Car_{tot}\left(\text{mg L}^{-1}\right) = \frac{1000\,A_{470} - 2.05\,Chl_a - 114.8\,Chl_b}{245} \quad (4)$$

Ash content

To determine the ash content, we used the proposal of Wychen and Laurens [43] of the National Renewable Energy Laboratory, in duplicates, where 100 mg of dry biomass were incinerated in the muffle EDG brand EDG-CON model 1P 7000 at 575 °C for 3 h, then, already at room temperature, weighed again. For the calculation, Eq. (5) was used.

$$\%\text{ash} = 100 \times \frac{\text{Mcrucible} + \text{ash} - \text{Mcrucible}}{\text{Dry weight sample}} \quad (5)$$

Data analysis

To determine the growth curve, the nonlinear regression model proposed by Gompertz was used, where the estimation of the parameters is done by minimizing the sum of squares of the errors, thus demonstrating the points of the growth curve in order to obtain a better understanding [44]. To verify possible differences between treatments, chlorophyll, carotenoids and ash content were employed Student's T-test. Assumptions such as homoscedasticity and normality were tested adopting $p < 0.05$ as significance.

Results and discussion

Through the relationship between turbidity and time in days, we can obtain the growth curve for the three treatments studied using the Gompertz model, and their fitting equations (Fig. 1). Turbidity is a parameter that can be applied for the evaluation of the growth curve of microalgae cultivation [25, 45]. As turbidity measures the capacity of a light scattering into the water, it is influenced by the presence of suspended particles. This parameter therefore might be used to monitor microalgae biomass growth [46]. The increase of biomass implies in higher turbidity values. Use of turbidity

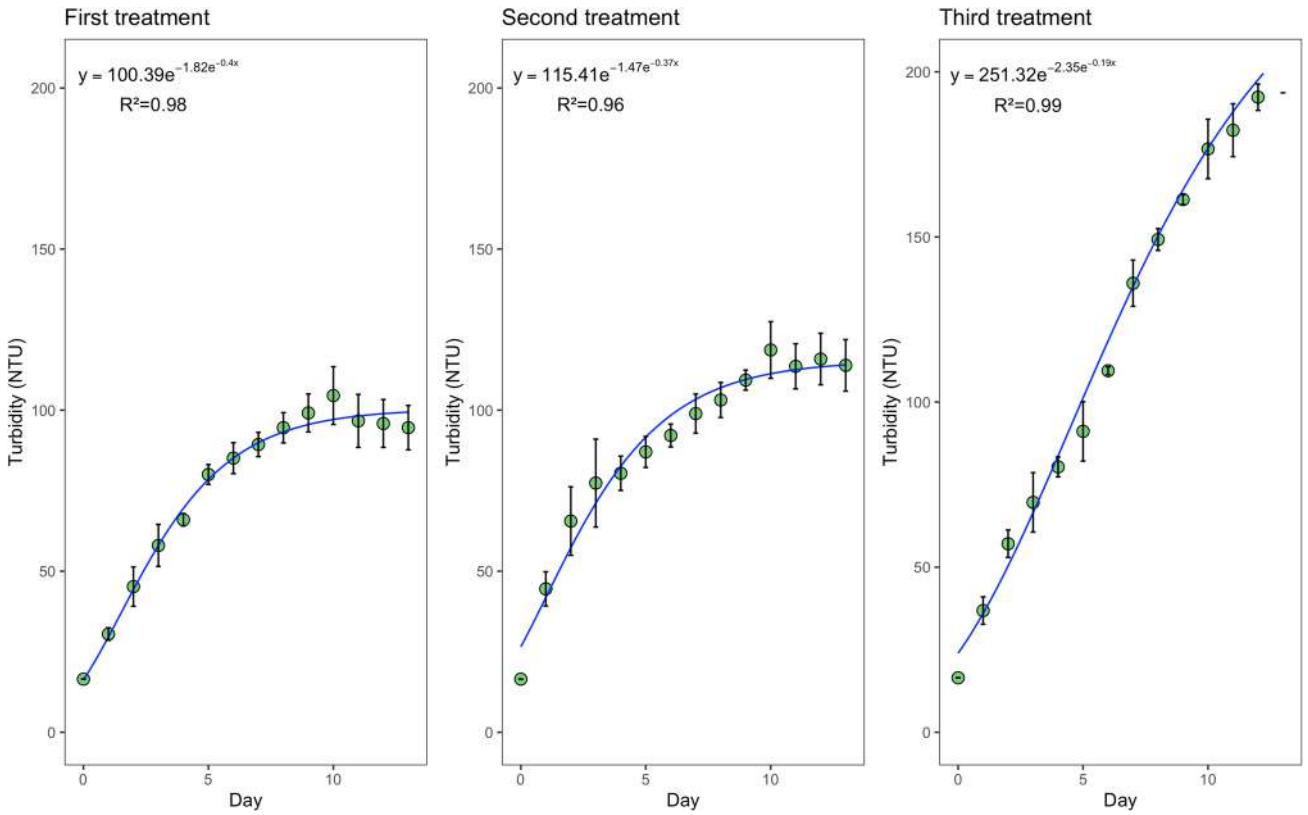

Fig. 1 Growth curve using Gompertz model for the three treatment performed in this study. First treatment: with half concentration of nitrate and phosphate of the original cultivation medium. Second treatment: with three times higher of phosphate and half of nitrate. Third treatment: with three times higher of nitrate and half of phosphate. For the growth curve is used average turbidity with error bars indicating the standard deviation

as a parameter to monitor *Chlorella vulgaris* growth has already been reported [47].

We can see that for the three treatments the nonlinear model presented a high R^2 ($0.96 \leq R^2 \leq 0.99$) with the best result for the third treatment ($R^2 = 0.99$). It means that the model explains at least 96% of turbidity variation over the period of cultivation. These results are similar with the result obtained by Praveen et al. [48] for biomass concentration of *Chlorella* sp., when the authors using Gompertz model found a R^2 of 0.99 for an autotrophic cultivation mode over 14 days of cultivation. Besides that, Gompertz model was also a good mathematical tool to estimate cells density of *Botryococcus braunii* with a R^2 of 0.98 in 13 days of cultivation [49]. In addition, modifications in the Gompertz model can also present a high R^2 for evaluation of biomass productivity of Chlorolla vulgaris in bubble column photobioreactors using wastewater as nutrients source [50]. In another study, Ajala and Alexander [51] verified that the Gompertz model presented stronger correlations with the biomass concentration in 14 days of cultivation for *Scenedesmus obliquus* ($R^2 = 1$;$R^2 = 0.99$), and *Oocystis minuta* ($R^2 = 0.99$;$R^2 = 0.99$) than *Chlorella vulgaris* ($R^2 = 0.90$;$R^2 = 0.95$) in N/P ration of 7:1 and 4:1, respectively. Sousa et al. [52] found that the Gompertz model perfectly fitted the *Chlorella vulgaris* growth in different operating conditions. As demonstrated by our results and previous studies, Gompertz model has been recognised as a strong mathematical tool to model the biomass growth of *Chlorella vulgaris* and other species. In our result, the best fit was observed for the third treatment with an increase of nitrogen concentration.

In relation to the growth curve, was possible to ascertain that in all treatments there was no adaptation period of microalgae to the medium in which it was exposed. This may have occurred due to the influence of the initial inoculum, due to the same conditions of light and temperature to which these microalgae had been subjected, not verifying, therefore this phase when verified may be for a very short period of time, as in the case of being removed still in exponential phase [53].

The cell growth phases for treatments 1 and 2 were similar, since for both the stationary phase started on day 6. Treatment 2 with a higher concentration of phosphorus in the cultivation medium, presented higher values of turbidity after the tenth day. Pereira and Branco [54], analyzed the effect of phosphorus on the growth of the specie *Schizomeris leibleinii Kützing*, and concluded that it has tolerance to variations of this nutrient, even though it is a limiting factor for growth. Kozlowska-Szerenos et al. [55] found that deficit in phosphorus content reduced the *Chlorella vulgaris* growth by 30–40% in comparison with the control. Despite that, phosphorus is present less than 1% in algal biomass, being required at least 0.03–0.06% of the cultivation medium composition to sustain algae growth [56]. In our results, the treatment 1 with lower phosphorus concentration presented a reduction of 16.97% of turbidity value found in treatment 2 in the thirteenth day ($\text{turbidity}_{\text{treatment 1}} = 94.56$ NTU; $\text{turbidity}_{\text{treatment 2}} = 113.9$ NTU).

Parallel to this, treatment 3 kept growing, reaching higher turbidity values (turbidity = 203.67 NTU). Treatment 3 presented an increase of 115.38% in relation to treatment 1 and of 78.81% in relation to treatment 2. This is due to the fact that it has a nitrogen concentration three times higher, and for being a nutrient that requires a large amount for chemical reactions and also for the composition of DNA [10]. Treatments 1 and 2, which had equal values of nitrogen, reached the stationary phase in the same time and occurred when all the nutrient was absorbed, while for treatment 3 it was possible to observe that there was still the nutrient in the medium. Beuckels et al. [57] affirm that microalgae can accumulate more phosphorous in higher concentrations of nitrogen, while in lower concentrations of nitrogen the accumulation of phosphorus by microalgae is reduced. This fact could be one of the possible explanations for the higher biomass production in the treatment with higher nitrogen concentration even in lower phosphorus concentration compared to treatment 2. According to Yaakob et al. [56], nitrogen concentration significantly influence biomass and biochemical compositions of microalgae growth. However, it is also important to point out that nitrogen limitation as well as excessive nitrogen source might affect negatively reducing the growth rate and productivity of microalgae [58]. Slinksienė et al. [59] found the highest biomass production of *Chlorella* sp. using a nitrogen source from landfill leachate of 0.08 g L^{-1} of concentration, it was not in the highest nitrogen concentration tested by the authors. Complementarily, Zhuang et al. [60] also found the highest productivity in an intermediate range of nutrients compared to extreme high concentrations.

Table 4 shows the comparison made from the student's T-test, to find out if there is a significant difference (p value < 0.05) between the treatments, using the turbidity of treatment 1 as a parameter for treatment 2, which has a higher phosphorus concentration, and treatment 3, which has a high nitrogen concentration. A significant difference was observed between treatments 1 and 3, and no difference between treatments 1 and 2.

Our results shows higher productivity in higher levels of nitrogen than phosphorus. Fu et al. [61] found that the excess of phosphorus under nitrogen limitation also increase microalgae biomass. The effect of higher concentrations of nutrients (one or both increasing) on microalgae biomass is corroborated by Mostert and Grobbelaar [62] and Fu et al. [61]. Figler et al. [63] tested different nitrogen and phosphorus concentrations with different N:P ratios to see the response in a green algae growth. Different from our results,

Table 4 Comparison of turbidity between the first treatment and the second and third treatments

Days	Treatment 2	Treatment 3
0–1	No*	No
1–2	No	No
2–3	No	Yes
3–4	No	Yes
4–5	No	Yes
5–6	No	No
6–7	No	Yes
7–8	No	Yes
8–9	No	Yes
9–10	No	Yes
10–11	No	Yes
11–12	No	Yes
12–13	Yes	Yes

Significance: p value < 0.05

*No: the difference is not significant

Yes: the difference is significant

the authors did not found that in higher N:P ratios with higher nutrients concentration would be better for growth of the green algae *Coelastrum morus*. Different species of microalgae can react differently under nutrients increasing.

Chlorophylls and carotenoids were affected according to the crop variation (Fig. 2). Regarding chlorophylls, when under treatment 1 and 2, they remained between 0.5 and 1.5 mg L^{-1}, and for treatment 3, the concentrations were between 0.5 and 3.5 mg L^{-1}. Carotenoids followed similar trends to that found for chlorophyll, but in smaller proportions, where treatments 1 and 2 are between 0.05 and 0.25 mg L^{-1}, and treatment 3 close to the values 0.05 and 0.45 mg L^{-1}. Our results of chlorophylls for treatment 1 (lower P concentration) and treatment 2 (three times P concentration) followed the results found by Kozlowska-Szerenos et al. [55], in which they found that deficiency in phosphorus did not affect the total chlorophyll content in the *Chlorella vulgaris* cultivation in comparison with the control. This result was also observed by Kozłowska-Szerenos et al. [64], where the authors did not find any significant difference between the total chlorophyll content seen in the cultivation with phosphorous deficiency in relation to the control.

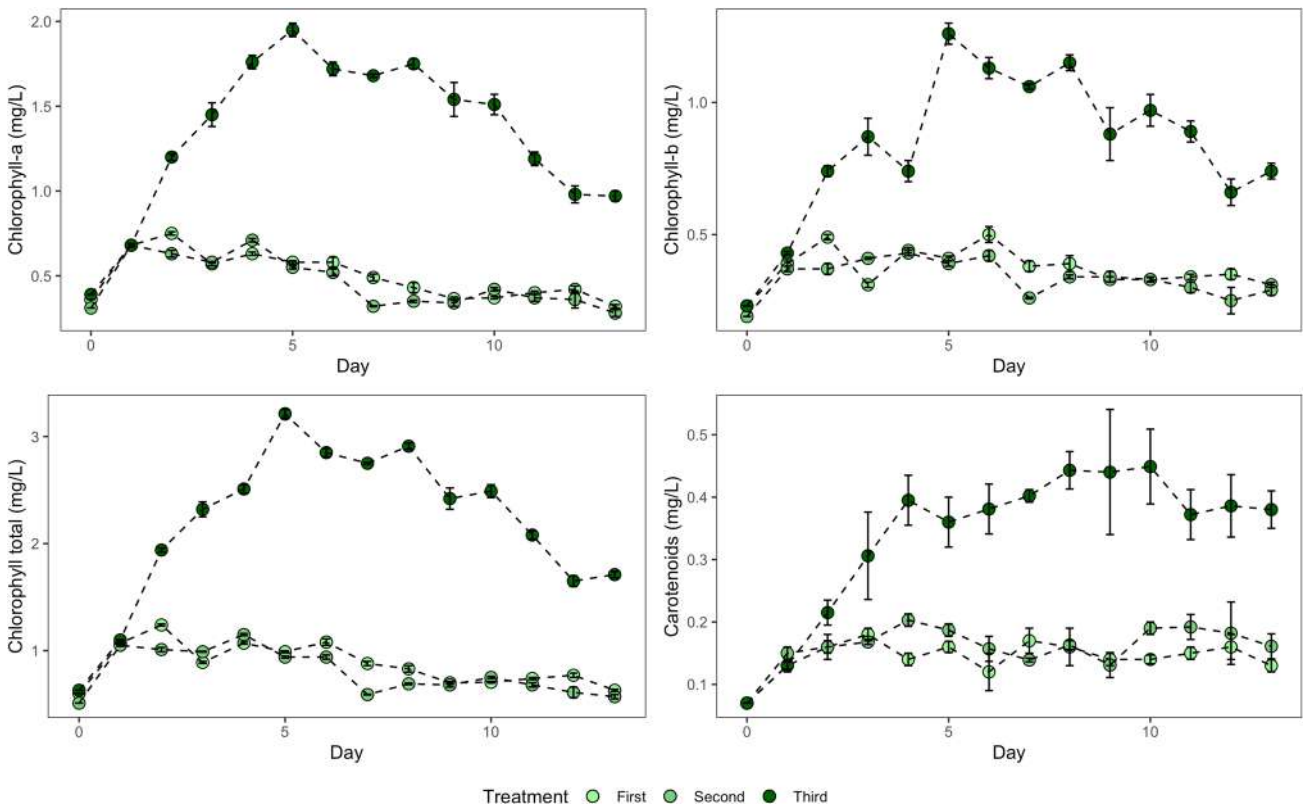

Fig. 2 Concentration of Chlorophyll-a, Chlorophyll-b, Chlorophyll-Total and carotenoids over the period of cultivation. The error bars means the standard deviation

Concentration of carotenoids varied over the days of cultivation with the maximum concentration seen in the tenth day for the third treatment (carotenoids = 0.45 mg L^{-1}). This result is similar for the result found by Jalal et al. [65], where the authors found the maximum carotenoid concentration in the tenth day for the cultivation of *Isochrysis* sp. and after there was a decreased.

This difference between treatments for chlorophyll and carotenoids is marked, as in the growth curve, by the effect of the limiting factor nitrogen. All three treatments showed concentration peaks followed by a decrease, if the nitrogen supply is high in the culture medium, there is an increase of chlorophylls and carotenoids in the cell [28] and as it decreases, and goes through a stress situation, its amount decreases, because the degradation process begins [66].

The variations found, analyzing each treatment separately, may occur mainly due to chlorophylls and carotenoids belong to the photosynthetic system of microalgae, called pigments [67]. He et al. [41] analyzed that a long exposure time of chlorophylls to high light intensity causes them to degrade, while the carotenoid content increases because it is the protective pigment of the photosynthetic system. This would explain the contrast of decreasing chlorophyll and increasing carotenoid on the fifth day of the experiment onwards.

It was found that as with turbidity, statistically there is considerable difference in chlorophyll and carotenoid concentrations between treatments 1 and 3, but that the difference is not significant between treatments 1 and 2 (Table 5 and 6). However, in the period 0–4 days treatments 1 and 3 showed no significant difference for carotenoids, and for chlorophyll this difference was not observed until day 5 of the experiment. Compared to growth there is a proximity to the situation where the beginning of the differentiation of increased turbidity occurred. This demonstrates that a distinction occurred between the nutritional treatments, as well as the relationship between growth and chlorophyll.

Table 5 Comparison between the total Chlorophyll concentration of treatment 1 and treatments 2 e 3

Days	Treatment 2	Treatment 3
0–1	No	No
1–2	No	No
2–3	No	No
3–4	No	Yes
4–5	No	No
5–6	No	Yes
6–7	No	Yes
7–8	No	Yes
8–9	No	Yes
9–10	No	Yes
10–11	No	Yes
11–12	No	No
12–13	No	Yes

Significance: p value < 0.05

Table 6 Comparison between the carotenoid concentration of treatment 1 and treatments 2 e 3

Days	Treatment 2	Treatment 3
0–1	No	No
1–2	No	No
2–3	No	No
3–4	No	No
4–5	No	Yes
5–6	No	Yes
6–7	No	Yes
7–8	No	Yes
8–9	No	Yes
9–10	No	Yes
10–11	No	No
11–12	No	Yes
12–13	No	Yes

Significance: p value < 0.05

Our results shows that in the end of the cultivation period there was an increase of 203.12% in Chlorophyll-a concentration in the third treatment compared to the first treatment and an increase of 246.42% in relation to the second treatment. In relation to the Chlorophyll-b, there was an increase of 138.70% in the third treatment compared to the first treatment and an increase of 155.17% in relation to the second treatment. In relation to carotenoids, there was an increase of 192% in the third treatment in relation to the first treatment and an increase of 137.5% in relation to the second treatment.

The ash content of the three treatments was considered optimal (Table 7), because the values were less than 5%, and satisfactory if compared to the results found by Rodrigues and Seckler [68] which was 5% and by Braga et al. [69] of 4.66%, which also explains that a low ash content is desirable because it is a measure of inorganic parts of biomass such as iron, sodium, potassium, magnesium and phosphorus, thus being directly linked to the energy value, because it reaches significantly its content.

The final temperature that the biomass was submitted is essential for the determination of the ash content, because the content will be higher at lower temperature due to incomplete

Table 7 Ash content for each treatment

Treatment	Ash content (%)
1	4.82
2	4.89
3	3.53

combustion, and lower at high temperature where there is increased vaporization of chlorine and various minerals such as potassium [70].

Through the T-test, it was found that the variations in the values of the percentages were not significant.

This experimental study therefore provides important evaluation about the *Chlorella vulgaris* growth under different nutrients enriched treatments. Our results indicated that even in three times higher phosphate concentration, there is no significant difference for the treatment with the lowest phosphate concentration with lower nitrogen concentration. Our results suggest, for example, in cultivation with objective to have a higher productivity, it is necessary to supply a higher nitrate concentration, to have higher biomass and pigments production. Besides that, even in the treatment with higher nitrate concentration, lower ash content was observed, which it means a higher energetic potential use using the biomass produced by this treatment.

Conclusion

The results of the Gompertz model fitting the growth curves over time presented high R^2 for *Chlorella vulgaris*. It was also seen by previous studies as mentioned previously, and our results also indicated that this model is very strong to model the biomass growth of *Chlorella vulgaris*. We also found that, for the conditions presented, nitrogen is more related to increase biomass than phosphorus. Although some previous studies mentioned previously, have also indicated that increase in phosphorus concentration can increase microalgae biomass. Consequently with increased biomass, higher concentrations in the cultivation time for the nitrogen enriched treatment were observed.

Through our experiments, we can conclude that the third treatment with higher concentration of nitrate presented a higher value of turbidity, which indicates higher biomass in the thirteenth day, higher concentration of Chlorophyll-a, Chlorophyll-b and Carotenoids. The most expressive increase was compared to the second treatment (with three times the phosphate concentration than the first treatment) with 246.42% of increase in Chlorophyll-a concentration. It indicate therefore that increase in phosphate does not necessarily mean increase in the pigments concentration, although increase in phosphate increased the value of turbidity compared to the first treatment. Finally, the ash content has shown a great potential of use of the microalgae for its energy value, and despite having changes in the percentages, this value is not considerable.

For future studies, we suggest to add analysis of carbohydrates, lipids and protein content after the cultivation period to have a better understanding in which situation would be more suitable for biofuel production.

Acknowledgements We authors would like to thank the help and suggestions provided by the professors Dr. Emerson Luiz Botelho Lourenço and Dr. Ricardo Puziol de Oliveira for the elaboration of this work.

Funding The authors did not receive support from any organization for the submitted work.

Declarations

Competing interests The authors have no competing interests to declare that are relevant to the content of this article.

References

1. Machado, I.M., Atsumi, S.: Cyanobacterial biofuel production. J. Biotechnol. **162**(1), 50–56 (2012)
2. Rodionova, M.V., Poudyal, R.S., Tiwari, I., Voloshin, R.A., Zharmukhamedov, S.K., Nam, H.G., et al.: Biofuel production: challenges and opportunities. Int. J. Hydrogen Energy **42**(12), 8450–8461 (2017)
3. Hossain, N., Mahlia, T.M.I., Saidur, R.: Latest development in microalgae-biofuel production with nano-additives. Biotechnol. Biofuels **12**(1), 1–16 (2019)
4. Chen, H., Wang, X., Wang, Q.: Microalgal biofuels in China: the past, progress and prospects. GCB Bioenergy **12**(12), 1044–1065 (2020)
5. Sheng, Y., Mathimani, T., Brindhadevi, K., Basha, S., Elfasakhany, A., Xia, C., Pugazhendhi, A.: Combined effect of CO_2 concentration and low-cost urea repletion/starvation in *Chlorella vulgaris* for ameliorating growth metrics, total and non-polar lipid accumulation and fatty acid composition. Sci. Total Environ. **808**, 151969 (2022)
6. Peralta-Yahya, P.P., Keasling, J.D.: Advanced biofuel production in microbes. Biotechnol. J. **5**(2), 147–162 (2010)
7. Miao, X., Wu, Q.: Biodiesel production from heterotrophic microalgal oil. Bioresour. Technol. **97**, 841–846 (2006)
8. Sousa-Aguiar, E.F., Appel, L.G., Bicudo, A.A., Fonseca, I., Fraga, A.C., Zonetti, P.C.: Some important catalytic challenges in the bioethanol integrated biorefinery. Catal. Today **234**, 13–23 (2014)
9. Moshood, T.D., Nawanir, G., Mahmud, F.: Microalgae biofuels production: a systematic review on socioeconomic prospects of microalgae biofuels and policy implications. Environ. Chall. **5**, 100207 (2021)
10. Wojciechowski, J., Straube, A., Cavalcante, K.P., Miranda, F.E.: Isolamento e Cultivo de Microalga (Microalgae Isolation and Cultivation). Univerdade Federal do Paraná, Curitiba (2013)
11. Nagappan, S., Devendran, S., Tsai, P.C., Dahms, H.U., Ponnusamy, V.K.: Potential of two-stage cultivation in microalgae biofuel production. Fuel **252**, 339–349 (2019)
12. Salama, E.S., Govindwar, S.P., Khandare, R.V., Roh, H.S., Jeon, B.H., Li, X.: Can omics approaches improve microalgal biofuels under abiotic stress? Trends Plant Sci. **24**(7), 611–624 (2019)
13. Han, W., Jin, W., Li, Z., Wei, Y., He, Z., Chen, C., et al.: Cultivation of microalgae for lipid production using municipal wastewater. Process Saf. Environ. Prot. **155**, 155–165 (2021)
14. Pugazhendhi, A., Nagappan, S., Bhosale, R.R., Tsai, P.C., Natarajan, S., Devendran, S., et al.: Various potential techniques to

reduce the water footprint of microalgal biomass production for biofuel—a review. Sci. Total Environ. **749**, 142218 (2020)
15. Correa, D.F., Beyer, H.L., Possingham, H.P., Thomas-Hall, S.R., Schenk, P.M.: Global mapping of cost-effective microalgal biofuel production areas with minimal environmental impact. GCB Bioenergy **11**(8), 914–929 (2019)
16. Suparmaniam, U., Lam, M.K., Uemura, Y., Lim, J.W., Lee, K.T., Shuit, S.H.: Insights into the microalgae cultivation technology and harvesting process for biofuel production: a review. Renew. Sustain. Energy Rev. **115**, 109361 (2019)
17. Jaiswal, K.K., Banerjee, I., Singh, D., Sajwan, P., Chhetri, V.: Ecological stress stimulus to improve microalgae biofuel generation: a review. Octa J. Biosci. **8**, 48–54 (2020)
18. Parente, E.S.: Biodiesel: uma aventura tecnológica num país engraçado (Biodiesel: a technological adventure in a funny country). Editora Tecbio, Fortaleza (2003)
19. Andrade, D.S., Filho, A.C.: Microalgas de águas continentais (*Microalgae of continental waters*). Londrina: IAPAR. v.3 (2014)
20. Sforza, E., Pastore, M., Spagni, A., Bertucco, A.: Microalgae-bacteria gas exchange in wastewater: how mixotrophy may reduce the oxygen supply for bacteria. Environ. Sci. Pollut. Res. **25**(28), 28004–28014 (2018)
21. Romero-Martínez, L., Moreno-Andrés, J., Acevedo-Merino, A., Nebot, E.: Photocatalytic inactivation of microalgae: efficacy and cell damage evaluation by growth curves modeling. J. Appl. Phycol. **31**(3), 1835–1843 (2019)
22. González, J.F., Cuello, T.B., Calderón, A.J., Calderón, M., González, J., Carmona, D.: Cultivation of autochthonous microalgae for biomass feedstock: Growth curves and biomass characterization for their use in biorefinery products. Energies **14**(15), 4567 (2021)
23. Islam, Z., Khatoon, H., Minhaz, T.M., Rahman, M.R., Hasan, S., Mahmud, Y., et al.: Data on growth, productivity, pigments and proximate composition of indigenous marine microalgae isolated from Cox's Bazar Coast. Data Brief **35**, 106860 (2021)
24. Chuka-ogwude, D., Ogbonna, J.C., Moheimani, N.R.: Depth optimization of inclined thin layer photobioreactor for efficient microalgae cultivation in high turbidity digestate. Algal Res. **60**, 102509 (2021)
25. Hermadi, I., Setiadianto, I.R., Al Zahran, D.F.I., Simbolon, M.N., Saefurahman, G., Wibawa, D.S., Arkeman, Y.: Development of smart algae pond system for microalgae biomass production. In: IOP Conference Series: Earth and Environmental Science, vol. 749(1), p. 012068). IOP Publishing (2021)
26. Thoré, E.S., Schoeters, F., Spit, J., Van Miert, S.: Real-time monitoring of microalgal biomass in pilot-scale photobioreactors using nephelometry. Processes **9**(9), 1530 (2021)
27. Franco, A.L.C., Lôbo, I.P., Almeida J.A.N., Cruz, R.S., Menezes, R.S., Teixeira, C.M.L.L.: Biodiesel de microalgas: avanços e desafios (Microalgae Biofuel: advances and challenges). Química Nova (2013)
28. Lourenço, S.O.: Cultivo de Microalgas Marinhas (Cultivation of marine microalgae). 1. ed. São Carlos: RIMA (2006)
29. Leite, L.S., Hoffmann, M.T., Daniel, L.A.: Microalgae cultivation for municipal and piggery wastewater treatment in Brazil. J. Water Process Eng. **31**, 100821 (2019)
30. Khanzada, Z.T.: Phosphorus removal from landfill leachate by microalgae. Biotechnol. Rep. **25**, e00419 (2020)
31. Wu, Y.H., Hu, H.Y., Yu, Y., Zhang, T.Y., Zhu, S.F., Zhuang, L.L., Zhang, X., Lu, Y.: Microalgal species for sustainable biomass/lipid production using wastewater as resource: a review. Renew. Sustain. Energy Rev. **33**, 675–688 (2014)
32. Fadeyi, O., Dzantor, K., Adeleke, E.: Assessment of biomass productivities of *Chlorella vulgaris* and Scenedesmus obliquus in defined media and municipal wastewater at varying concentration of nitrogen. J. Water Resour. Prot. **8**(2), 217–225 (2016)
33. Arabian, D.: Investigation of Effective Parameters on the Productivity of Biomass and Bio-cement as a Soil Improver from Chlorella vulgaris. Geomicrobiol. J. (2022). https://doi.org/10.1080/01490451.2022.2078445
34. Osorio, J.H.M., Del Mondo, A., Pinto, G., Pollio, A., Frunzo, L., Lens, P.N.L., Esposito, G.: Nutrient removal efficiency of green algal strains at high phosphate concentrations. Water Sci. Technol. **80**(10), 1832–1843 (2019)
35. Martins, C.F., Trevisi, P., Coelho, D.F., Correa, F., Ribeiro, D.M., Alfaia, C.M., et al.: Influence of *Chlorella vulgaris* on growth, digestibility and gut morphology and microbiota of weaned piglet. Sci. Rep. **12**(1), 1–12 (2022)
36. Ren, H., Zhu, G., Ni, J., Shen, M., Show, P.L., Sun, F.F.: Enhanced photoautotrophic growth of Chlorella vulgaris in starch wastewater through photo-regulation strategy. Chemosphere **307**, 135533 (2022)
37. El-Naggar, N.E.A., Hussein, M.H., Shaaban-Dessuuki, S.A., et al.: Production, extraction and characterization of *Chlorella vulgaris* soluble polysaccharides and their applications in AgNPs biosynthesis and biostimulation of plant growth. Sci. Rep. **10**, 3011 (2020). https://doi.org/10.1038/s41598-020-59945-w
38. Lee, R.: Phycology, 4th edn. United States of America by Cambridge University Press, New York (2008)
39. Dalal, S.R., Hussein, M.H., El-Naggar, N.E.A., Mostafa, S.I., Shaaban-Dessuuki, S.A.: Characterization of alginate extracted from Sargassum latifolium and its use in *Chlorella vulgaris* growth promotion and riboflavin drug delivery. Sci. Rep. **11**(1), 1–17 (2021)
40. Watanabe, A.: List of algal strains in collection at the institute of applied microbiology, University of Tokyo. J. Gen. Appl. Microbiol. **6**, 283–292 (1960)
41. He, Q., Yang, H., Hu, C., Wu, L.: Effect of light intensity on physiological changes, carbon allocation and neutral lipid accumulation in oleaginous microalgae. Biores. Technol. **191**, 219–228 (2015)
42. He, Q., Yang, H., Wu, L., Hu, C.: Effect of light intensity o physiological changes, carbon allocation and neutral lipid accumulation in oleginous microalgae. Biores. Technol. **191**, 219–228 (2015)
43. Wychen, S.V., Laurens, L.M.L.: Summative Mass Analysis of Algal Biomass—Integration of Analytical Procedures. National Renewable Energy Laboratory, Golden (2013)
44. Souza, G.S.: Introdução aos modelos de regressão linear e não-linear (Introduction to linear and non-linear regression models). Brasília: Embrapa- SPI/Embrapa-SEA, 489 (1998)
45. Flores, G., Rodriguez-Mata, A.E., Amabilis-Sosa, L.E., Gonzalez-Huitron, V.A., Hernández-González, O., Lopéz-Peréz, P.A.: A turbidity sensor development based on NL-PI observers: experimental application to the control of a Sinaloa's River Spirulina maxima cultivation. Open Chem. **18**(1), 1349–1361 (2020)
46. Ferrando, N.S., Benitez, H.H., Gabellone, N.A., Claps, M.C., Altamirano, P.R.: A quick and effective estimation of algal density by turbidimetry developed with *Chlorella vulgaris* cultures. Limnetica **34**(2), 397–406 (2015)
47. Aguirre, R.N.J., Palacio, B.J.A., Correa, O.I.C., Hernández, A.E.: Ensayos de bioestimulación algal con diferentes relaciones nitrógeno: fósforo, bajo condiciones de laboratorio. Revista Ingenierías Universidad de Medellín **6**(11), 11–21 (2007)
48. Praveen, K., Abinandan, S., Kavitha, M.S., Natarajan, R.: Biochemical responses from biomass of isolated *Chlorella* sp., under different cultivation modes: non-linear modelling of growth kinetics. Braz. J. Chem. Eng. **35**, 489–496 (2018)
49. Hanief, S., Prasakti L., Budiman, A., Cayono, R.B., Pradana, Y.S.: Growth kinetic of Botryococcus braunii microalgae using

logistic and gompertz models. In: AIP Conference Proceedings, vol. 2296(1), p. 020065. AIP Publishing LLC (2020)
50. Blanco, G.C., Stablen, M.J., Tommaso, G.: Cultivation of *Chlorella vulgaris* in anaerobically digested gelatin industry wastewater. Water Supply **21**(5), 1953–1965 (2021)
51. Ajala, S.O., Alexander, M.L.: Assessment of *Chlorella vulgaris*, *Scenedesmus obliquus*, and *Oocystis minuta* for removal of sulfate, nitrate, and phosphate in wastewater. Int. J. Energy Environ. Eng. **11**(3), 311–326 (2020)
52. Sousa, C.A., Sousa, H., Vale, F., Simoes, M.: Microalgae-based bioremediation of wastewaters-Influencing parameters and mathematical growth modelling. Chem. Eng. J. **425**, 131412 (2021)
53. Mata, T.M., Martins, A.A., Caetano, N.S.: Microalgae for biodiesel production and other applications: a review. Renew. Sustain. Energy Rev. **14**, 217–232 (2010)
54. Pereira, J.L., Branco, L.H.Z.: Influência do nitrato e fosfato no crescimento de *Schizomeris leibleinii* Kützing (Chaetophorales, Chlorophyta). Acta Bot. Bras. **21**, 155–162 (2007)
55. Kolozlowska-Serenos, B., Zielinski, P., Maleszewski, S.: Involvement of glycolate metabolism in acclimation of Chlorella vulgaris cultures to low phosphate supply. Plant Physiol. Biochem. **38**(9), 727–734 (2000)
56. Yaakob, M.A., Mohamed, R.M.S.R., Al-Gheethi, A., Aswathnarayana, G.R., Ambati, R.R.: Influence of nitrogen and phosphorus on microalgal growth, biomass, lipid, and fatty acid production: an overview. Cells **10**(2), 393 (2021)
57. Beuckels, A., Smolders, E., Muylaert, K.: Nitrogen availability influences phosphorus removal in microalgae-based wastewater treatment. Water Res. **77**, 98–106 (2015)
58. Chen, X., Li, Z., He, N., Zheng, Y., Li, H., Wang, H., et al.: Nitrogen and phosphorus removal from anaerobically digested wastewater by microalgae cultured in a novel membrane photobioreactor. Biotechnol. Biofuels **11**(1), 1–11 (2018)
59. Slinksienė, R., Sendzikiene, E., Mikolaitiene, A., Makareviciene, V., Paleckiene, R., Ragauskaite, D.: Use of microalgae biomass for production of granular nitrogen biofertilizers. Green Chem. Lett. Rev. **15**(2), 415–425 (2022)
60. Zhuang, L.L., Azimi, Y., Yu, D., Wu, Y.H., Hu, H.Y.: Effects of nitrogen and phosphorus concentrations on the growth of microalgae Scenedesmus. LX1 in suspended-solid phase photobioreactors (ssPBR). Biomass Bioenergy **109**, 47–53 (2018)
61. Fu, L., Li, Q., Yan, G., Zhou, D., Crittenden, J.C.: Hormesis effects of phosphorus on the viability of *Chlorella regularis* cells under nitrogen limitation. Biotechnol. Biofuels **12**(1), 1–9 (2019)
62. Mostert, E.S., Grobbelaar, J.U.: The influence of nitrogen and phosphorus on algal growth and quality in outdoor mass algal cultures. Biomass **13**(4), 219–233 (1987)
63. Figler, A., Márton, K., Bácsi, I.: Effects of nutrient content and nitrogen to phosphorous ratio on the growth, nutrient removal and desalination properties of the green alga *Coelastrum morus* on a laboratory scale. Energies **14**(8), 2112 (2021)
64. Kozłowska-Szerenos, B., Bialuk, I., Maleszewski, S.: Enhancement of photosynthetic O_2 evolution in Chlorella vulgaris under high light and increased CO_2 concentration as a sign of acclimation to phosphate deficiency. Plant Physiol. Biochem. **42**(5), 403–409 (2004)
65. Jalal, K.C.A., Shamsuddin, A.A., Nurzatul, N.Z., Rahman, M.F., Rozihan, M.: Growth and total carotenoid, chlorophyll a and chlorophyll b of tropical microalgae (*Isochrysis* sp.) in laboratory cultured conditions. J. Biol. Sci. **13**(1), 10 (2013)
66. Markou, G., Nerantzis, E.: Microalgae for high-value compounds and biofuels production: a review with focus on cultivation under stress conditions. Biotechnol. Adv. **31**, 1532–1542 (2013)
67. Spolaore, P., Joannis-Cassan, C., Duran, E., Isambert, A.: Commercial applications of microalgae. J. Biosci. Bioeng. **101**, 87–96 (2006)
68. Rrodrigues, T.T.M., Seckler, M.M.: Investigação dos produtos de pirólise da microalga *Chlorella vulgaris* usando PY-GC/MS (Investigation of the pyrolysis products of the microalgae Chlorella vulgaris using PY-GC/MS). Anais do XV Safety, Health and Environment World Congress. Porto, Portugal, 2015, pp. 298–301 (2015)
69. Braga, R.M., Almeida, H.N., Calixto, G.Q., Freitas, J.C.O., Melo, D.M.A., Resende, F.M.: Caracterização energética e pirólise rápida Py-CG/MS das microalgas chlorella vulgaris e spirulina platensis (Energetic characterization and rapid Py-CG/MS pyrolysis of the microalgae C*hlorella vulgaris* and S*pirulina platensis*) . In: 8° Congresso Brasileiro de Pesquisa e Desenvolvimento em Petróleo e Gás, 2002, Curitiba, PR. Anais do 8° PDPETRO. Curitiba: [s.n.] (2002)
70. Liu, J., Pan, Y., Cao, X., Xue, S., Yao, C., Wang, H.: Determination of ash content and concomitant acquisition of cell compositions in microalgae via thermogravimetric (TG) analysis. Algal Res. **12**, 149–155 (2015)

contain 26 articles

Springer

زمستان ۱۴۰۲

December 24